AD A 113 969

AGARD-CP-305

# AGARD

## ADVISORY GROUP FOR AEROSPACE RESEARCH & DEVELOPMENT

7 RUE ANCELLE 92200 NEUILLY SUR SEINE FRANCE

AGARD CONFERENCE PROCEEDINGS No. 305

# Medium, Long and Very Long Wave Propagation
# (At frequencies less than 3000 kHz)

DTIC
S ELECTE D
APR 2 9 1982
H

## NORTH ATLANTIC TREATY ORGANIZATION

DISTRIBUTION AND AVAILABILITY
ON BACK COVER

82 04 30 001

# REPRODUCTION QUALITY NOTICE

This document is the best quality available. The copy furnished to DTIC contained pages that may have the following quality problems:

- Pages smaller or larger than normal.

- Pages with background color or light colored printing.

- Pages with small type or poor printing; and or

- Pages with continuous tone material or color photographs.

Due to various output media available these conditions may or may not cause poor legibility in the microfiche or hardcopy output you receive.

☐ If this block is checked, the copy furnished to DTIC contained pages with color printing, that when reproduced in Black and White, may change detail of the original copy.

NORTH ATLANTIC TREATY ORGANIZATION

ADVISORY GROUP FOR AEROSPACE RESEARCH AND DEVELOPMENT

(ORGANISATION DU TRAITE DE L'ATLANTIQUE NORD)

AGARD Conference Proceedings No.305

# MEDIUM, LONG AND VERY LONG WAVE PROPAGATION

## (AT FREQUENCIES LESS THAN 3000 KHZ)

Edited by

Dr J.S.Belrose
Communications Research Centre
Dept. of Communications
P.O.Box 11490, Station H
Ottawa K2H 8S2
Canada
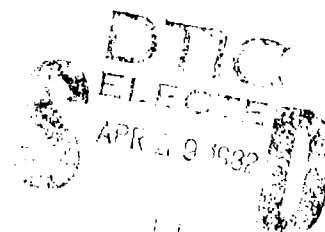
# THE MISSION OF AGARD

The mission of AGARD is to bring together the leading personalities of the NATO nations in the fields of science and technology relating to aerospace for the following purposes:

Exchanging of scientific and technical information;

Continuously stimulating advances in the aerospace sciences relevant to strengthening the common defence posture;

Improving the co-operation among member nations in aerospace research and development;

Providing scientific and technical advice and assistance to the North Atlantic Military Committee in the field of aerospace research and development;

- Rendering scientific and technical assistance, as requested, to other NATO bodies and to member nations in connection with research and development problems in the aerospace field;

Providing assistance to member nations for the purpose of increasing their scientific and technical potential;

Recommending effective ways for the member nations to use their research and development capabilities for the common benefit of the NATO community.

The highest authority within AGARD is the National Delegates Board consisting of officially appointed senior representatives from each member nation. The mission of AGARD is carried out through the Panels which are composed of experts appointed by the National Delegates, the Consultant and Exchange Programme and the Aerospace Applications Studies Programme. The results of AGARD work are reported to the member nations and the NATO Authorities through the AGARD series of publications of which this is one.

Participation in AGARD activities is by invitation only and is normally limited to citizens of the NATO nations.

†ρ

ii

# THEME

The ELF band (30 3000 Hz) has very serious deficiencies when compared with conventional radio communications bands. Its restricted bandwidth implies low data rates, and because the very large wavelength whatever transmitting antenna could be built would be inefficient, as measured by radiated power. For special applications however, where part of the propagation path involves lossy media such as rock, earth, soil and water, ELF offers the possibility of communications whereas the conventional bands offer none. Even at VLF (3 30 kHz) where the wavelength is up to two orders of magnitude smaller, efficient transmitting antennas must be enormous costly structures, and transmitter powers great if global communications are desired and to points under the sea or beneath the ground. The LF band (30 300 kHz) provides for communications to intermediate distances, shorter than the global distances afforded by VLF, but longer than ground wave distances characteristic of the MF broadcasting band (535 1605 kHz) . . . although MF sky wave signals propagate to much greater distances with relatively low loss at night. Propagation conditions change with increasing frequency, toward the top of MF band (3000 kHz) where the band merges with and the propagation becomes characteristic of the HF band.

Use of the various frequency bands (at least above 10 kHz) is extensive and covers a wide range of communications and navigation applications: such as the Omega navigation system (10 14 kHz); VLF global communications (14 30 kHz), principally military communications: DECCA, Loran-C and other position fixing and navigation systems (70 130 and 1605 2000 kHz); non directional beacons (200 325 kHz); broadcasting (150 285 and 535 1605 kHz); radio communications in various frequency bands ranging from the ELF through MF, and as well broadcast of time and frequency standards, etc.

While use of these bands is not increasing, their use is not decreasing either. Much new propagation information has been obtained, principally at ELF and VLF frequencies since the last AGARD Symposium on this topic; and while new communication technologies that permit automation, transmission of data and SSB voice over narrow bandwidths and spread spectrum modulation techniques have been developed, these have not seen application below 3000 kHz. It was intended that this symposium would, by means of review papers, summarize the current state of our knowledge in this frequency band in areas of propagation, antennas and radio communications technology; present recently acquired data and knowledge; and speculate on trends and future use of these bands.

## ELECTROMAGNETIC WAVE PROPAGATION PANEL

Chairman:    Dr J.Aarons                    Deputy Chairman:   Dr J.Belrose
             AF Geophysics Laboratory                          Communications Research Centre
             Hanscom Field                                     Department of Communications
             Bedford, Mass. 01731                              P.O. Box 11490, Station H
             USA                                               Ottawa K2H 8S2
                                                               Canada

### PROGRAMME COMM' ITEE

Chairman:                Dr J.Belrose, Ca

Programme Committee:     Dr Lange-Hesse, Ge
                         Dr T.Larsen, No
                         Dr B.Burgess, UK
                         Mr M.Fonteyne, Fr

Local Coordinator:       Col. d'Aviation Ir. C.Sprenkels
                         Commandant 22eme Wing, Logistique
                         Quartier Roi Albert 1er
                         Rue de la Fusée, 70
                         B-1130 Brussels

### PANEL EXECUTIVE

L/Col. J.B.Catiller
AGARD/NATO
7, rue Ancelle
92200 Neuilly-sur-Seine
France

# CONTENTS

† Abstract Only

# THE PROPAGATION MEDIUM: AN OVERVIEW

John S. Belrose
Communications Research Centre
Department of Communications
Ottawa, Ontario

## ABSTRACT

This paper is an overview on electron and ion number densities and collision frequency height profiles in the lower E - and D-regions of the ionosphere (heights below 100km). Ion chemistry is not addressed in detail, but reference is made to current work in this area.

1.      INTRODUCTION

In the propagation of ELF and VLF radio waves to great distances, the waves are confined within the space between the earth and the ionosphere. This space acts as a waveguide, and the concept is applicable for characterizing the field-strength as a function of frequency and distance. At LF and MF frequencies ionospheric attenuation increases rapidly with frequency, and the maximum in the absorption of ionospheric radio waves lies in the frequency range 100kHz to 1000kHz. (dependent on frequency and distance). In describing propagation at these higher frequencies it is found useful to interpret the experimental data, and to calculate field strength by the wave-hop method of propagation. That is the total field comprises a ground wave and a skywave reflected once or more than once from the ionosphere.

Whatever the method of interpreting propagation data or calculating field-strength, the electrical conductivity of the upper and lower boundaries of the media are important. The upper boundary is characterized by the electron and ion density distributions and the collision frequency height profile. The lower boundary by a homogeneous smooth earth having an effective but variable conductivity and dielectric constant, although some calculations have been described in which the actual topographical earth surface profile is taken account of. This overview is concerned with the characteristics of the upper ionospheric boundary, with the E - and D-regions, particularly for heights below 100km.

Rocket-borne ion mass spectrometer observations carried out since 1963, together with improved measurements of electron concentrations have lead to our present knowledge of the lower ionosphere. The unique character of the D-region arises from the presence of chemically active minor neutral constituents, and the relatively high ambient pressures which permit three-body reactions to occur. Ideas concerning the production and loss of the ionization have remained unchanged now for several years, c.f. Thomas [1974], Reid [1977] and Mitra [1981], only our knowledge of the importance of various processes has improved.

Of particular importance for the ionospheric reflection of VLF, LF and MF radio waves is the electron density-height gradient, and this is not measured very accurately by ground-based experiments. Nor is the electron concentration for densities less than about $100cm^{-3}$, which is of particularly important for the lower frequencies. At VLF frequencies and below, the ion densities becomes important, the degree of which increases with decrease in frequency. Ion concentrations are particularly important at night, and at times of solar geophysical disturbances when electron production rates at low heights are large. Because effective electron loss rates are high ion densities are correspondingly high.

2.      COLLISION-FREQUENCIES

Collisions between electrons and neutral molecules are of great importance to some aspects of radio wave propagation, particularly for the role they play in the attenuation of radio waves. The collision frequency-height profile may be estimated from laboratory studies of the mobility of electrons in atmospheric gases, in combination with rocket-borne measurements of atmospheric temperature and density (or pressure), or it may be determined quite independently from an analysis of radio wave propagation. There is much evidence both in radio and meteorological pressure data to establish that the collision frequency-height profile changes with season, latitude, and at least on some occasions with solar activity. The variability from day-to-day and with season is undetectably small during summer months and at low latitudes. At high latitudes in winter the day-to-day variability can exceed the seasonal change.

Several formula have been used to relate $\nu_m$, the mono-energetic collision frequency used with generalized magneto-ionic theories, to atmospheric gas pressures. The one used by the author and his colleagues [Belrose et. al., 1967] is $\nu_m = 1.04 \times 10^8 p (mm~Hg)~sec^{-1}$. Collision frequency height profiles calculated from this formula for 30, 45 and 60°N were compared by these authors with collision frequencies deduced from some selected rocket-borne and ground based radio wave propagation experiments. These data are reproduced here in Figures 1 to 3. It should be noted that a given value of collision occurs at a lower height in winter than in summer, and this fact is revealed in the phase-height of reflection of VLF steep incidence radio waves (see Figure 4). A particular electron production rate will be found at the height of a particular pressure isopleth.

On this assumption, then, the seasonal variation of atmospheric pressure is complex, since (see Figure 5), there is an anomaly in the reflexion height versus seasonal variation in April.

There is a little doubt that collision frequency in the L-region varies with solar activity [Schlapp, 1959], and at high latitudes with energetic particle precipitation [Schlegel et. al., 1980], but similar variations have not so far been reliably observed in the D-region, except on a few occasions. In Figure 6 we show an example when the height of the 10mb pressure level over middle Europe at midnight appears to correlated with a strong 27-day periodicity in solar activity during the months of January and February 1961. High solar activity is associated with an increase in the height of the 10mb pressure level, and presumably also with pressures above this level. A peculiar feature of these data is the sudden cessation

in the correlation in March, 1962, even thought the strong 27-day periodicity in solar flux
continued for several cycles.  It is likely that such a phenomenon when it does occur is feature
of the winter atmosphere.

3.          ELECTRON DENSITIES:  BACKGROUND INFORMATION

          In Figure 7 we show an electron density-height profile measured by a rocket-borne experiment on
16 April, 1964 over Wallops Island [Mechtly et. al., 1967] at a time when the solar zenith angle was $60^{\circ}$.
This particular profile clearly shows different layers (or ledges) of ionization that are thought to be
characteristic of the lower ionosphere.

These are:

1.  A region above 85km, the base of the E-layer which is the simplest part of the D-region;

2.  A region where the electron density increases rapidly, the so-called "ledge" region around 82-85km;

3.  A region between the ledge and 70km, the D-layer;

4.  A region between 50-70km, the so-called C-layer, where negative ions becomes appreciable; and

5.  The region below 50km where there are no electrons under normal quiet solar conditions, but this is
    the region where ion densities are large and of increasing complexity.

          While the main purpose of this paper is to review what is known about electron densities and
their variation with latitude, time of day, season and solar cycle, and at times of geophysical disturbance;
we will begin by a brief discussion of the sources of ionization and of the height distributions of neutral
consituents and positive and negative ion composition.

3.1     SOURCES OF IONIZATION

          The important sources of ionization of the quiet D-region are: 1) photo ionization of nitric
oxide (NO) by Lyman $\propto$ radiation; 2) solar x-rays; 3) solar uv ionization of excited molecular oxygen $O_2$ ('$\Delta$g);
and 4) galactic cosmic rays (GCR) which are the principle source of ionization at heights below
70km under normal quiet conditions.  Representative ionization rates in the quiet daytime middle latitude
D-region for solar minimum conditions and a solar zenith angle of $60^{\circ}$, and at night are shown in Figures 8
and 9 [after Thomas, 1974].  While electron production rates are small during nighttime, nevertheless they
are sufficient to maintain ionization densities during nighttime, and during the polar night at high latitudes
[Belrose et. al., 1966], sufficient reflect VLF and LF radio waves.  Clear evidence for a nocturnal variation
in nighttime ionization rates can be seen in Figure 4.  Note that the phase height of reflection for VLF
radio waves continuously increases after sunset, until about one-hour after local midnight, when the phase
height  continuously decreases until dawn.  The most likely source for such nighttime rates that could
result in such a variation is the photoionization of NO by Lyman$\propto$ radiation in the night glow.

          A times electron production by solar x-rays (at the time of a solar flare), and by particle
precipitation  can overwhelmingly dominate these regular processes.  Solar particle events (SPE) can
produce small to very intense ionization in the D-region, particularly at high magnetic latitudes.  The
principle sources of ionization during these events are solar protons  between 1 and 100MeV and solar
electrons having energies >10keV.  The initial disturbance on the sun produces prompt effects due to
ionization by solar x-rays (SXR) in the 0.5 to 10.$\overset{o}{A}$ range (the shorter the wavelength the deeper the
penetration into the atmosphere).  Subsequent geomagnetic storm associated effects, and storm after effects
are due to precipitation into the D-region of high energy particles (HEP), electrons, of magnetospheric
origin (from the radiation belts)

          An extreme ionization rate profile for the 4 August, 1972 SPE over Chatanika, Alaska is shown
in Figure 10 [after Reagan and Watt, 1976].  This was the largest solar proton event ever observed.
Comparison of Figures 8 and 10, and in Figures 10 itself, reveals that the electron production rates at
60km are almost five order of magnitude greater than normal (normal being ionization rates due to galactic
cosmic rays).

3.2     ELECTRON LOSS RATES

          Once electrons production rates are known or assumed, the ambient electron density can be calculated
from:

$$\frac{dNe}{dt} = q(h) - \Psi(h)Ne^2(h)$$

or if $Ne(h)$ and $q(h)$ are known the effective recombination rate $\Psi(h)$ may be determined.  This is the most
simple form of the continuity equation.  Nevertheless the height variation of $\Psi(h)$ provides some insight
into the chemistry of the region.

          Montbriand and Belrose [1979] made a study of the diurnal and seasonal variations of the steady
state loss coefficient ($dNe/dt \approx 0$)   for quiet periods over Ottawa employing partial reflection electron
density data and calculated electron production rates.  The results obtained for diurnal variation were
based on electron density-height profiles deduced earlier by Coyne and Belrose [1972].

          In order to identify season variations of $\Psi$, quiet intervals were selected on the basis of electron
content below 76km (ratio meter records, c.f. Belrose [1972]).  The selection was made for the periods of
highest ratios (least electron densities below 76km) in each month.  Furthermore the periods selected
(morning or afternoon) had to exhibit regular solar control, also judged from the ratio meter records.

The measurements were made at $\chi = 68.6^0$, which is the smallest value that could be studied seasonally. The dashed curves in Figure 11 are the results obtained from this study. Note that for h > 75km, and particularly at a height $\approx$ 85km $\psi$ varies seasonally by more than order of magnitude. Smallest values are found in winter when mesospheric temperatures are low. Near 75km there is neither a diurnal (results for this are not shown) or a seasonal variation. Below this height $\Psi$ decreases, a result which is also apparent in the data obtained during large solar x-rays flares [Montbriand and Belrose, 1972].

This height variation for h<75km, is in sharp contrast with results obtained during a major solar proton event, when $\Psi$ increases rapidly with decrease in height.

A strong day-night variation in $\Psi$ is expected, because at night electron loss to form negative ions is expected to dominate recombination loss. The curve labelled 6 in Figure 12 is taken to be representative of the $\Psi$(h) variation at night (actually these data were measured at totally during a solar eclipse). The $\Psi$(h) results obtained during strong solar proton disturbances are smaller at all heights. Sellers and Stroscio [1975] compare these and other data obtained during SPE events with theoretical predictions. Prasad and Mohanty [1980] have employed a simplified positive ion model to study electron production and loss rates at 80km and have compared their results with electron densities measured at this height under quiet solar geophysical conditions.

## 3 3    HEIGHT DISTRIBUTION OF NITRIC OXIDE

Measurements of NO concentrations in the D - and E-regions have been obtained from rocket observations of the flurescence of the NO $\gamma$-bands in day glow [c.f. Beran and Bangert, 1979], and from positive ion densities measured by mass spectrometers [Swider, 1978; Arnold and Kranskowsky, 1979]. Diurnal and seasonal measurements of NO in the low E-region have also been derived from satellite data [Stewart and Cravens, 1978; Cravens and Stewart, 1978]. A summary of various number density models for NO, reproduced from Bergan and Bangert [1979] is shown in Figure 13. The two profiles labelled by dates were measured by there authors during the Western European Winter Anomaly Campaign 1975/76.

## 3.4    HEIGHT DISTRIBUTION OF $O_3$ and $O_2$ ('$\Delta g$)

Similarly, the $O_2$('$\Delta g$)    concentration profiles can be determined by optical measurements [Beran and Bangert, 1979] or derived from positive ion measurements [Arnold and Krankowsky, 1979]. The optical measurements are of the infared atmospheric band of oxygen at 1.27$\mu$m from which the $O_3$ density profile can be derived. The $O_2$('$\Delta g$) profile is obtained from the $O_3$ density profile by multiplying by the Einstein transition coefficient. The profiles in Figure 14 are reproduced from the paper by Bergan and Bangert [1979].

## 3.5    POSITIVE AND NEGATIVE ION DENSITIES

Since the major source of ionization in the quiet D-region is thought to be photoionization of NO by solar L$\alpha$ radiation this should give rise to NO + (ion mass 30), as the dominant positive ion in the D-region. However, rocket-borne ion mass spectrometers, beginning with those of Narcissi and Bailey [1965] have shown that below about 82km altitude the dominant positive ion species are water clusters of the type $H^+(H_2O)n$ [c.f. Thomas, 1974; Reid, 1977; Arnold and Krankowsky, 1977]. Since the lifetime of NO ions at 80km is of the order of $10^3$ sec, a reaction path must exist that is fast enough to convert NO ions into water cluster ions in a time which is much less than this [Reid, 1977]. The rapid increase in the number density of water cluster ions for heights below about 82km, c.f. Figure 15 [from Narcissi et. al., 1972] is undoubtly associated with the sudden change in effective electron loss rates at these heights. Arnold et. al. [1980] have discussed evidence for a strong temperature control of the ionospheric D-region deduced from ion composition measurements ... a factor that is thought to be in part a cause of the variability of electron densities at heights near 80km under geomagnetical quiet conditions. in winter.

Negative ion chemistry strongly controls the diurnal changes in electron density particularly at heights below 70km. Because of the much greater mobility of electrons, they are the important factor in determining atmospheric conductivity, strongly affecting the propagation of ELF and VLF radio waves. Free electrons are removed by attachment to neutral molecules to form negative ions. Electrons in turn may be detached from negative ions through photodetachment, or associated detachment reactions, a factor that is particularly important at dawn [c.f. Peterson, 1976]. At lower altitudes where electron densities become negligeable and negative ions become the primary negative charge conductors, hydration may effect conductivity by stabilizing negative ions against electron detachment. Negative ion mass spectrometer measurements have been carried out by the two groups that have also been instrumental in measuring positive ion densities, but unfortunately the two sets of measurements have produced conflicting results [Narcissi et. al., 1971 and 1972; and Arnold et . al., 1971]. These differences have recently been discussed by Keesee et. al. [1979]. D-region negative ion chemistry, omitting negative ion clusters has been analyzed by Wisemberg and Kockcarts [1980].

The height variation of the ratio of negative ion to electron number density ($\lambda$) has been discussed by many researchers during the last decade, and earlier. While it is generally agreed by most that $\lambda \sim 0$ at 85km (or above), the extremes in the values that have been estimated at 65km reach/or exceed three orders of magnitude [c.f. Montbriand and Belrose, 1979]. While a day/night difference seems to have been established (c.f. a selection of a few results in Figure 16, and those obtained from other sources given by Mitra [1981], there is no clear difference between results obtained under quiet and disturbed solar geophysical conditions. This is in contrast with the differences found for electron loss rates, and measured and inferred differences in ion chemistry.

## 4. D-REGION MODELLING

D-region modelling is an art that has been practised by only a few, due largely to the complexity of the region, which has been revealed during the past two decades by the many rocket measurements of electron densities, positive and negative ion densities and neutral densities. A rather detailed model, including very many reactions must be employed to correctly model the ion chemistry and to determine a model that is self consistent with all available data, including laboratory measurements of rate coefficients for each specific reaction.

The atmospheric model of Keneshea et. al. [1979] is the most detailed and most complete atmospheric model of the ionosphere and lower thermosphere. Heaps and Heimerl [1980] have carried out a sophisticated computer simulation of ion species and densities in the D-region. Their analysis has shown a qualitative agreement between predictions and detailed positive ion composition measured in situ, indicating that the positive ion chemistry is correctly modelled. Comparison of simulated and experimental electron density profiles show that the experimental values lie consistently below those predicted. The mass spectrometer measurements of negative ions show little agreement with current predictions.

Others, e.g., Chakrabarty and Chakrabarty [1981] have tried to model electron and positive ion densities using a simplified approach, which can be more readily modified in attempting to bring theory and experiment into agreement [c.f. Mitra, 1981].

## 5. D-REGION ELECTRON DENSITIES

### 5.1 TECHNIQUES FOR MEASURING ELECTRON DENSITIES

Measurements of electron concentration in the D-region, and the relative merits of various ground-based and rocket-borne experiments have been reviewed by Thrane [1974]. Of the various rocket borne experiments the Faraday rotation experiment, first used by Jespersen et. al. [1966] has found considerable favour [c.f. Mechtly and Smith, 1968; Bennet et. al., 1972, and Beynon and Williams, 1976]. Differential absorption experiments have been employed by Kane [1961] using a CW transmitter; and by Belrose et. al. [1972] using pulsed transmissions from the ground, alternatly switching between right-and-left-hand circular polarization. In association with the basic experiment (Faraday rotation or differential absorption) plasma probe experiments have usually been used to provide height resolution. A few experiments have been flown employing ground-to-rocket LF propagation [Hall et. al., 1965 and 1973, Seliga, 1968] and VLF propagation [Nagano et. al., 1978]. The ground based methods are: 1) the partial reflection experiment, first developed by Gardner and Pawsey and used most extensivily by Belrose and his colleagues [Belrose, 1970; Belrose et. al., 1972a; Coyne, 1973]; 2) The pulsed wave interaction experiment, developed by Fejer [1955, 1970] and used by Smith and his colleagues [1967a, b, c; Coyne, 1973; by Thrane, 1967 and by Cole et. al., 1969]; and 3) electron density profiles inferred somewhat indirectly from VLF/LF propagation [c.f. overview by Belrose and Segal, 1974]. The partial reflection experiment has been the one most extensively employed for synoptic studies of the D-region [Belrose, 1972].

### 5.2 D-REGION STRUCTURE

In section 3 we discussed the fact that the D-region electron density profile contains two ledges (or layers) below the daytime E-layer. Only a few profiles, however, clearly show the presence of a C-layer, below the D-layer, except at dawn, although the presence of underlying ionization having number densities below those which can be reliably measured (N<100 electrons can often be inferred from ground based experiments. On occasion a ledge below 70km is clearly discernable [Coyne and Belrose et. al., 1972], even at midday.

### 5.3 VARIATION WITH LATITUDE

The most extensive and continuous studies from which one can infer certain features of the global morphology of ionization in the D-region and lower E-region, are those of ionospheric absorption. George [1971] studied absorption data measured during IGY and IQSY (active and quilt sun years) at some 28 stations. Swentek [1976] made absorption measurements on board a ship sailing from the summer to the winter hemisphere. And Swentek et. al., [1978] have noted an asymmetry in winter anomalous absorption observed at Lindau (51.6°N) and Ushuaia (54.8°S).

In regards to global modelling of electron density profiles, the most extensive statistical studies are those of Rawer et. al., [1978] and McNamara [1979]. We will not attempt to reproduce or duplicate these works, instead we will illustrate only a few representative profiles measured at equatorial (Thumba), middle (Wallops Island and Ottawa) and at high latitudes (Resolute Bay). A great number of profiles have been measured at middle latitudes in Europe, by rocket borne experiments. Some of these data will be discussed in Section 5.7.

We show in Figure 17 electron density profiles measured over Thumba, India during morning hours by rocket-borne experiments on different days in 1968/70 [Kane, 1969]. In Figures 18 and 19 we show electron density profiles measured at Ottawa in March 1971 and May 1970, for selected undisturbed days under regular solar control [Coyne and Belrose 1972]. In figure 20 we show profiles measured at a high latitude location Resolute Bay. Resolute Bay is a unique location. It is near the centre of the polar cap, well above the auroral oval. In winter the sun never rises ($\chi>98°$) and in the summer the sun never sets ($\chi<83°$).

A number of features illustrated in these data deserve attention:
1) There is no marked difference between profiles measured at equatorial and at middle latitudes. The electron densities at $\chi = 60°$ are $\sim$ 100cm$^{-3}$ at 60km, and 1000cm$^{-3}$ at $\sim$ 80km;

2) With regard to the profiles for Ottawa, a diurnal asymmetry is clearly evident, which does not seem to have any preferred level. The electron densities in May were considerably higher than March. In particular the ledge that formed toward mid day near 70km in the May profiles was absent during the

March period. The ledge near 82km in the 75° morning profile occured over the whole of the morning period in which densities could be measured at this height;

3) Notice the absence of electron at heights <75km at noon in March over Resolute Bay($\chi$ = 80°), whereas in summer measurable electron densities are found at lower heights. This is a spring phenomenon since profiles for September, not shown, are similar to the summer profiles. The absence of electrons at low heights at noon in March must be a feature of the chemistry of the D-region, which has been in darkness for several months during the winter polar night. This absence of electrons is made clear in the profiles shown in Figure 21; compare the profiles for Resolute Bay and Churchill, measured during the same period in March, at the same solar zenith angle ($\chi$ = 80°).

## 5.4    VARIATION OVER DAWN

One of the most regular features noticeable in diurnal course of LF/VLF field strength and phase variation is the abrupt change that occurs at dawn. Only a few observations of electron density profiles over dawn have been obtained. In Figure 22 we show the now "classic" electron density profiles over dawn measured by wave interaction [Smith et. al., 1967]. In Figure 23 we compare ground based and rocket data for $\chi \sim 90°$, measured at middle and low latitudes.

Synoptic measurements of the D-region electron densities using the differential absorption partial reflection experiment have been made at Ottawa from one hour before sun rise to one hour after sunset for each month in all seasons over several years. Generally for $\chi > 85°$ the signal-to-noise ratio is inadequate, but this is not always the case. In Figure 24 we show two ratio meter records in which Ax/Ao (76km) was measured over dawn. This amplitude ratio, measured at a particular height, is inversely proportional to the integrated electron density below the reference height. Note that for the record of 28 December, 1973, which is a typical example of the variation over dawn, this ratio first decreased, then increased, and for $\chi < 85°$ Ax/Ao decreased continuously, reaching lowest values at noon. Clearly the electron density below 76km during the dawn transition increased, decreased, and increased again, i.e., the electron densities were a maximum at mid day. The latter phases of this change at dawn (for $\chi < 85$) is clearly evident in Figure 25, which shows electron densities at fixed heights versus solar zenith angle for March, 1971, c.f. the variation at 69km.

If the layer which formed at dawn is produced by the rapid photo detachment of electrons from a bank of negative ions that was in equilibrium with nighttime production mechanisms, then its subsequent decay before photoionizing radiation from the sun reaches it indicates that the effective recombination rate of electrons with positive ions is higher than that of positive and negative ions at this heights.

An interesting feature of the observations is the apparent lack of such a variation over dawn on some days in winter, c.f., the Ax/Ao record for the 30 January, 1972 (also shown in Figure 24).

## 5.5    WINTER VARIABILITY

The occurence of periods of enhanced ionization, known as the winter anomaly, is a well known feature of the middle latitude D-region and this phenomenon has received considerable attention. The variability of the winter D-region is not confined to periods of enhanced ionization as the ratio meter records show. The mid day amplitude ratio Ax/Ao at 76km throughout the winters of 1969-70, 1970-71 and 1971-72 are shown in Figure 26 to 28. The appropriate summer ratios are plotted in Figures 26 and 27 by the solid and dashed lines (morning and afternoon ratios). The high degree of variability in the electron densities below76km over Ottawa during the winter is readily apparent. Furthermore it is clear that periods of low (high ratios), as well as high (low ratios) ionization can exist. In Figure 29 we show average electron density profiles for 1969/70, averaged according to the Ax/Ao ratio measured at 76km.

The winter variability is due to two causes, which may on some occasions occur together:

1) Geomagnetic Post storm effects (GPE) which are not confined to winter, but the phenomenon is more easily observed in winter when electron densities at low heights are small. The magnitude of the effect however appears to be enhanced in winter;

2) Winter day of anomalous absorption of the "meteorological type".

## 5.6    GEOMAGNETIC POST STORM EFFECTS

There is no doubt that D-region ionization changes follow geomagnetic storms. [Belrose and Thomas, 1968]. There is also evidence that storm "after effects" have a seasonal variation and that the winter season is more strongly affected. Lauter and Knuth [1967] have suggested that precipiation and ionization due to energetic electrons leaking out of the Earth's outer radiation belt, injected there during a geomagnetic storm is the cause of the post storm effect. Belrose and Thomas [1968] have however stressed that a part of the cause of the enhanced electron density may be the result of meteorological influence of dynamical processes leading to chemical changes in the D-region.

The precipitation explanation has been backed by the results of Larsen et. al., [1976], who made co-ordinated studies of electron precipitation measured by means of a satellite, and D-region electron densities, measured by partial reflection measurements at Ottawa. Lauter et. al., [1979 a,b] and Oksman et.al. [1981] came to the same conclusion.

A very clear example of a post storm effect is evident in data already illustrated. In Figure 27 note the decrease in Ax/Ao ratio, lasting several days, which followed the geomagnetic storm of 14 December, 1970. The diurnal variation of electron densities for the 16 December, 1970 is shown in Figure 30, which illustrates features which were earlier indirectly inferred from VLF/LF propagation. Note the rapid increase in electron density at dawn ($\psi$ values 90 to 100°). The chain dotted curves in this figure represent the variation observed on a normal undisturbed day. The N(h) profiles during the dawn and dusk periods, to illustrate diurnal asymmetry is shown in Figure 31. The N(h) profiles in Figure 32 illustrate

the development and the decay of the phenomena. A profile for 14 December is not shown, since a "representative" profile cannot be given for the storm day due to the irregular variations in electron density.

## 5.7    WINTER DAY OF ANOMALOUS ABSORPTION OF THE "METEOROLOGICAL TYPE"

The results of the Western European 1975/76 D-region Winter Anamaly Campaign, reference Offerman [1979] provide the clearest evidence for the importance of dynamical and related photochemical effects. Electron precipitation was excluded as a significant cause of ionization in the D-region for a major anomaly observed on 21 January, 1976. Beran and Bangert [1979] clearly show that the observed ionization increase was associated with increases in NO, $O_2(^1\Delta g)$ and decreases in water cluster ions due to increased temperatures. Ihrane el. al., [1979] have calculated the effective electron loss rate $\psi = q/Ne^2$ cm$^3$ sec$^{-1}$, and their results for this parameter are shown in Figure 33 (the curve labelled 21 January, 1976 El Arenosillo). On this figure we show also the quiet day results deduced by Montbriand and Belrose [1979] for Ottawa; and the extremes observed by Larsen et. [1976], the two curves labelled 23 January and 24 February 1972. It should be noted that electron production on these two days was dominated by electron drizzle precipitation, associated with post storm effects.

It is clear that the winter anomaly is very complex. The enhanced electron densities are due on different occasions to high energy particle (HEP) precipitation, to increases in constituents such as NO, $O_2(^1\Delta g)$, and decreases in electron loss rates due in part to decreases in water cluster ions. Decreased electron loss rates in the height range 80-90km can occur at times when electron "drizzle" dominates production (the 23 January, 1972 curve) and when such a phenomena is absent (21 January, 1976). According to the results shown in Figure 33 it would appear that decreased electron loss rates for heights >75km can be associated with increased electron loss rates below this height. The winter anomaly phenomena is still under study and discussion [Sato, 1980, 1981; Manson, 1981].

## 5.8    GEOPHYSICAL DISTURBANCE EFFECTS

Different types of disturbances in the upper atmosphere can change its properties as a propagation medium for electromagnetic waves. Thrane [1979] has recently reviewed the most important of these disturbances, and has discussed the possibility of predicting their effect on the atmosphere, once they have occured.

## 5.8.1    SOLAR X-RAY FLARE (SXR) EFFECTS

One type of ionospheric disturbance which has long been known to be caused by enhanced solar x-rays (SXR) accompanying certain solar flaresis called sudden ionospheric disturbance. Two of the SXR flare effects are the immediate increase in ionization densities throughout the D-region and the lowyering of the base of that region. The increased ionization density results in increased absorption of HF radio waves, which cause short wave fade outs (SWF). The lowering of the base of the ionosphere and the increase in the electron density gradient causes sudden phase anomalies (SPA) on LF and VLF circuits, and usually an amplitude increase in LF field strength. Other effects are the sudden absorption of cosmic noise (SCNA).

Figures 34 and 35 show as an example the effects of a very large SXR flare that occurred on 8 July 1968. In Figure 34 we show the SCNA observed on a polar directed 30MHz riometer at Ottawa, and in Figure 35 the electron density height profiles as deduced from partial reflection observations at various times during the event (these times are indicated on Figure 34).

## 5.8.2    SOLAR PROTON EVENTS

Following within a few minutes to a few hours after certain solar flares, so called proton flares [c.f. Cook and Davies, 1979; Heckman, 1979; Smart and Shea, 1979], a very strong disturbance can occur. These disturbances are confined to the polar caps, i.e., magnetic shell latitudes $\Lambda > 60^o$. Hence the named polar cap absorption (PCA), so named because of the intense absorption that occurs on HF circuits. The cause of these disturbances is known to be due to solar protons, in the range 80-100 MeV, although in some cases heavier nuculei and especially alpha particles and solar electrons (>10keV) are present.

In Figure 36 we show day time electron density profiles measured by various techniques [Kane, 1959, 1961; Ulwick, 1971; Reagan and Watt, 1976] for solar proton events (SPE) of different magnitude (as judged by the amount of absorption observed on a 30MHz zenith riometer). D-region electron densities extending to $5 \times 10^4$ electrons cm$^{-3}$ at 70km were measured; useful data being obtained down to altitudes as low as 45km. Positive ion densities are clearly large at low heights, extending downward to the height limits of the experiments.

Nighttime electron densities, (see Figure 37) are orders of magnitude smaller, especially at low heights [c.f. Belrose, 1972; Swider and Narcisi, 1975; Regean and Watt, 1976]. While the change from day-to-night during the course of an event is partly due to the changing spectra of precipitating protons, the dominant change is due to a change in electron loss rates. At night electrons are lost to form negative ions. For example during the course of the 2 November, 1969 event, see Figures 36 and 37, the height where $N = 10^3$ electrons cm$^{-3}$ changed from 48km at noon on 2 November, 1969 to 72km at midnight on the 3 November (local time at Churchill).

For both solar flare events and solar proton events, the increase in electron densities at D-region heights (50-80km) is associated with a drastic reduction in electron loss coefficient $\psi(=q/Ne^2)$, see Figures 11 and 12, which, at least for SPE's is associated with a drastic reduction in water cluster ions and emergence of NO$^+$ and $O_2^+$ ions as the principle positive ions in the middle D-region.

## 5.8 3 HEP EFFECTS

High energy particle (electron) events, unlike SXR flare and SPE events occur very irregularly in both space in time. Nocturnal anomalies in LF field strength associated with changes in the earth's magnetic field occur frequently, even at middle latitudes [Lauter and Sprenger, 1952; Belrose 1968]. At high latitudes, if the HEP event occurs during daytime on the path, there is a rather detailed correlation between LF propagation and auroral absorption. Minimum phase heights and maximum field strengths correlate with maximum in auroral absorption measured at path midpoint [Belrose, 1968]. If the event occurs at night, auroral absorption and changes in the earths magnitude are well correlated in time, if not in detail, but there is no detailed correlation with LF propagation. Phase and amplitude of LF signals fluctuate more rapidly, and usually, the mean amplitude is depressed as well as the phase height. These differences are due in part to the localized nature of the events (daytime events seem to be more widespread), and in part to the heights where enhanced election densities are found. In Figure 37 we show day and nighttime electron density profiles measured during various HEP events, which are classified according to the absorption observed on a 30MHz zenith riometer. All events except the 7.2ʼ nighttime event were measured by in rockets by Jespersen and Landmark [1968]. The strong nighttime event was deduced by Hargreaves [1980] from the incoherent scatter radar at Chatanika, Alaska, during an auroral absorption spike event. This was the only event of the several that be observed that was sufficiently wide spread to fill of the beam of 30MHz wide beam riometer that he used to select and classify the events.

Clearly, during "usual" HEP events, nighttime electron densities at 100km can exceed day E-layer densities, and while the ionization increase occurs at all heights throughout D-region the electron density gradient is steep, and only small electron densities aᵢ found at h < 70km; except for very intense spike events. During daytime large electron densities (greater by an order of magnitude from normal) are observed to heights as low as 60km. This difference is largely due to the formation of negative ions at night, but also, except for the nighttime spike events, the energy spectra for HEP events are in general softer for nighttime than for daytime events.

## 6.    CONCLUSIONS

Geophysical disturbances affect the upper atmosphere in a very complex way. Even the regular D-region is perplexing; when compared with the E-layer where the ions are primarily molecular, consisting of $NO^+$ and $O_2^+$. Recombinations of these ions are straight forward and involve dissociative recombination processes for which rates are fairly well known. The geomagnetic post storm effect (GPE) is one of the many phenomena that affects LF and MF field strenghts, and VLF phase. Its persistance for several days after the storm is clear evidence for a fairly uniform precipitation and ionization due to energetic electrons leaking out of the Earth's radiation belts. It is also interesting to note that during the most intense of solar geophysical disturbance, the SPE, D-region chemistry is simplist. Dynamical circulation and temperature effects, particularly during winter months have a strong influence on electron production, due to changes in trace constituents such as NO, and on electron loss rates. There is a strong temperature dependance on D-region ion composition which is the reason for the correlation that is sometime observed between D-region ionization densities and statospheric warnings [Belrose, 1967]. The C-layer is also not so simple or first thought. While the normal ionization rates are well known to be galactic cosmic rays, the loss rates can apparently be variable indicating that the chemistry for this region is complicated.

Special campaigns, such as the very extensive winter anomaly campaign of 1975/76, and the several high latitude campaigns carried out in earlier years, have greatly increased our knowledge of the D-region, and while the gross features are well understood, there are inconsistences in the data which prevent a detailed quantative interpretation. Negative ion densities have not been reliably measured.

### REFERENCES

Arnold, F., J. Kissel, D. Krankowsky, H. Wieder, and J. Zahringer, J. atmosph. terr. Phys, 33, 1169-1175, 1971.
Arnold, F. and D. Krankowsky, Dynamical and Chemical Coupling of the Neutral and Ionized Atmosphere (ed. by B. Granda and J.A.O. Holtet, Reidel Doordrecht - Boston, p. 93, 1977.
Arnold, F. and D. Krankowsky, J. atmosph. terr. Phys., 41, 1127-1140, 1979.
Arnold, F., D. Krankowsky, E. Zettwitz and W. Joos, J. atmosph. terr. Phys., 42, 249-256, 1980.
Belrose, J.S., Nature, 214, 660, 1967.
Belrose, J.S., AGARD lecture Series No. 29, Radio Wave Propagation, CFSTI Accession No. N68-37825, 1968.
Belrose, J.S., Proc. of Cospar Symposium on Solar Particle Event of November, 1969, AFCRL 72-0474, Special Reports No. 144, pp. 243-258, 1969.
Belrose, J.S., J. atmosph, terr. Phys., 32, 567, 1970.
Belrose, J.S., COSPAR Symposium Record on D-and E-region Ion Chemistry, Aeron. Rep. No. 48, Univ. of Ill, Urbana, 1972.
Belrose, J.S., L.R. Bode and L.W. Hewitt, Electron Density Profiles in Ionosphere and Exosphere (ed. Frihagen), North Holland Pub. Co., Amsterdam, 1966.
Belrose, J.S., and I.A. Bourne, Ground Based Radio Wave Propagation Studies of the Lower Ionosphere, vol. 1, 79-94, Def. Res. Board, Canada, 1967.
Belrose, J.S., and L. Thomas, J. atmosph. terr. Phys., 30, 1127, 1968.
Belrose, J.S., M.J. Burke, T.N.R. Coyne and J.E. Reed, J. Geophys. Res. 77 4829, 1972a.
Belrose, J.S., D.B. Ross and A.G. McNamara, J. atmos. terr. Phys., 34, 627-640, 1972b.
Belrose, J.S. and B. Segal, COSPAR Sympsium on Methods of Measurements and Results of Lower Ionosphere Structure, 77-109, Akademic - Verlag-Berlin, 1974.
Bennett, F.D.C., J.E. Hall, and P.H.G. Dickinson, J. atmos. terr. Phys., 34, 1321, 1972.
Beran, D. and J. Bangert, J. atmosph. terr. Phys., 41, 1091-1095, 1979.
Beynon, W.J.G. and E.R. Williams, J. atmos. terr. Phys., 38, 1319-1325, 1976.
Chakrabarty, D.K. and P. Chakrabarty, J. atmosph. terr. Phys., 43, 23-29, 1981.
Cole, A.R., A.J. Ferraro and H.S. Lee, Nature, 222, 761, 1969.
Cook, F.E. and P. Davies, STPP, 1, 229-238, 1979.
Coyne, T.N.R., J. Geophys. Res., 78, 206-217, 1973.
Coyne, T.N.R., J. Geophys. Res., 78, 8276-8288, 1973.
Coyne, T.N.R., and J.S. Belrose, Radio Sci., 7, 163-174, 1972.

Cravens, T.E. and A.I. Stewart, J. Geophys. Res. ., 2246-2252, 1978.
Fejer, J.A., J. atmosph. terr. Phys., 7, 322, 1955.
Fejer, J.A., J. atmosph. terr. Phys., 32, 597, 1970.
George, P.L., J. atmosph. terr. Phys., 33, 1893-1906, 1971.
Hall, T.E., Planet, Space Sci., 21, 119, 1973.
Hall, T.E. and J. Fooks, Planet, Space Sci., 13, 1013, 1965.
Hargreaves, J.K., J. atmosph. terr. Phys., 42, 783-789, 1980.
Heaps, M.G. and J.M. Heimerl, J. atmosph. terr. Phys., 42, 733-742, 1980.
Heckman, G., STPP, 1, 322-349, 1979.
Jespersen, M., H. Haug, and B. Landmark, Electron Density Profiles in Ionosphere and Exposphere (ed.
    J. Frihagen), pp. 27-30, North-Holland, Amsterdam, 1966.
Jespersen, M. and B. Landmark, Ionospheric Radio Communication (ed. K. Folkestad), Plenum Press, N.Y.,
    pp. 73-80, 1968.
Kane, J.A., J. Geophy. Res., 64, 133-139, 1959.
Kane, J.A., J. atmos. terr. Phys., 23, 338-347, 1961.
Kane, J.A., NASA-GSFC, Report X-615-69-499, 1969.
Keesee, R.G., N. Lee, and A.W. Castleman, J. Geophys. Res., 84, 3719-3722, 1979.
Keneshea, T.J., S.P. Zimmerman and C.R. Philbrick, Planet. Space Sci., 27, 365-401, 1979.
Larsen, T.R., J.B. Reagan, W.L. Imhof, L.E. Montbriand and J.S. Belrose, J. Geophys. Res., 81, 2200, 1976.
Lauter, E.A., and K. Sprenger, Zeit f. Met., 6, 161-173, 1952.
Lauter, E.A. and K. Knuth, J. atmosph. terr. Phys., 29, 411, 1967.
Lauter, E.A., A. Grafe, B. Nikutowski, J. Taubenheim, R. Treumann, C.U. Wagner, Space Res. 19, 351, 1979.
Lauter, E.A., A. Grafe, B. Nikutowski, J. Taubenheim and C.U. Wagner, Gerl. Beitr. Geophy., Leipzig., 88,
    73, 1979b.
Manson, A.H., J. Geophys. Res., 86, 1633-1635, 1981.
McNamara, L.F., Radio Sci., 14, 1165-1173, 1979.
Mechtly, E.A. and L.E. Smith, J. atmos. terr. Phys., 30, 1555, 1968.
Mechtly, E.A., S.A. Bowhill, L.G. Smith and H.W. Knoebel, J. Geophys. Res., 72, 5239-5245, 1967.
Mitra, A.P., J. atmosph. terr. Phys. 43, 737-752, 1981.
Montbriand, L.E. and J.S. Belrose, Radio Sci., 7, 133-142, 1972.
Montbriand, L.E. and J.S. Belrose, J. Geophys. Res., 84, 1921-1929, 1979.
Nagaro, I., M. Mambo, and I. Kimura, Planet, Space Sci., 26, 219-227, 1978.
Narcisi, R.S., and A.D. Bailey, J. Geophys. Res., 70, 3687-3700, 1965.
Narcisi, R.S., A.D. Bailey, L. Della Lucca, C. Sherman and D.M. Thomas, J. atmosph. terr. Phys., 33, 1147-1159,
    1971.
Narcisi, R.S., A.D. Bailey, L.E. Wlodyka and C.R. Philbrick, J. atmos. terr. Physics., 34, 647-658, 1972.
Offerman, D., J. atmosph. terr. Phys., 41, 1047, 1979.
Oksman, J., C.U. Wagner, K. Kaila and E.A. Lauter, Planet space Sci., 29, 405-413, 1981.
Peterson, J.E., J. Geophys. Res., 81, 1433-1435, 1976.
Prasad, B.S.N. and S. Mohanty, Radio Sci., 15, 1017-1023, 1980.
Rawer, K., D. Bilitza, and S. Ramakrishnan, URSI International Reference Ionosphere, Brussels, 1978.
Reid, G.C., Planet, Space Sci., 25, 275,1977.
Reagan, J.B. and T.M. Watt, J. Geophys. Res., 81, 4579-4596, 1976.
Sato, T., J. geophys. Res., 85, 197-105, 1980.
Sato, T., J. Geophys. Res., 86, 1636-1638, 1981.
Schlapp. D.M., J. atmosph. terr. Phys., 16, 340-343, 1959.
Schlegel, K., H. Kohl and K. Rinnert, J. Geophys. Res., 85, 710-714, 1980.
Schwentek, H., J. atmosph. terr. Phys., 38, 89-92, 1976.
Schwentek, H., W. Elling and M. Peres, J. atmosph. terr. Phys., 42, 545-552, 1980.
Seliga, T.A., J. Geophys. Res., 73, 6783, 1968.
Sellers, B. and M.A. Stroscio, J. Geophys. Res., 80, 2241-2246, 1975.
Smart, D.F. and M.A. Shea, STPP, 1, 406-427, 1979.
Smith, R.A., Ground-Based Radio Wave Propagation Studies of the Lower Ionosphere, Vol. 1, pp. 235-278,
    Def. Res. Board, Canada, 1967a.
Smith, R.A., I.A. Bourne, R.G. Loch, and T.N.R. Coyne, Ibid., 300-318, 1967b.
Smith, R.A., T.N.R. Coyne, R.G. Loch and I.A. Bourne, Ibid., 335-357, 1967c.
Stewart, A.I. and T.E. Cravens, J. Geophys. Res., 83, 2453-2456, 1978.
Swider, W., J. Geophys. Res., 83, 4407-4410, 1978.
Swider W. and R.S. Narcisi, J. Geophys. Res., 80, 655-664, 1975.
Thomas, L. Radio Science, 9, 122-136, 1974.
Thrane, E.V., Ground-Based Radio Wave Propagation Studies of the Lower Ionosphere, Vol. 1, pp. 321-326,
    Def. Res. Board, Canada, 1967.
Thrane, E.V., COSPAR Symposium on Methods of Measurements and Results of Lower Ionosphere Structure, Akademic
    Verlag, Berlin, 1974.
Thrane, E.V., AGARD Lecture Series No. 99, Aerospace Propagation Media Modelling and Prediction Schemes for
    Modern Communications, Navigation, and Surveillance Systems, Tech. Edit, and Reproduction Ltd., London,
    1979.
Thrane, E.V., B. Grandal, O. Hagen, F. Ugletveit, W. Bangert, D. Beran, M. Friedrich, A. Loidl and
    H. Schewentek, J. atmosph. terr. Phys., 41, 1097-1103, 1979.
Ulwick, J.C., Space Res, 11, 1181-1187, 1971.
Wisemberg, J. and G. Kockarts, J. Geophys. Res., 85, 4642-4652, 1980.
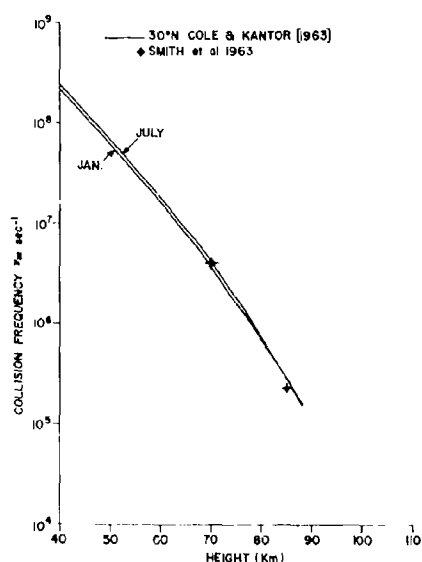
Figure 1
Collision frequency-height profile
for 30°N latitude.
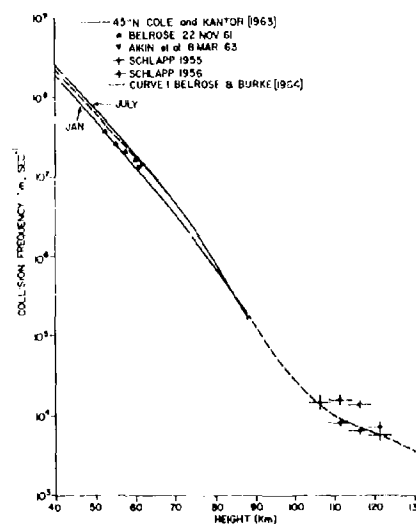


Figure 2
Collision frequency-height profile for
45°N latitude.
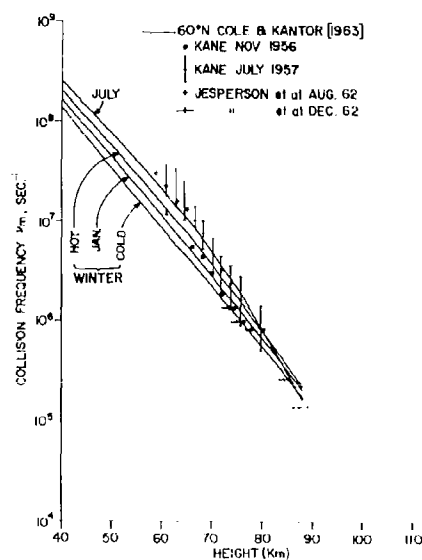


Figure 3
Collision frequency-height profile
for 60°N latitude.
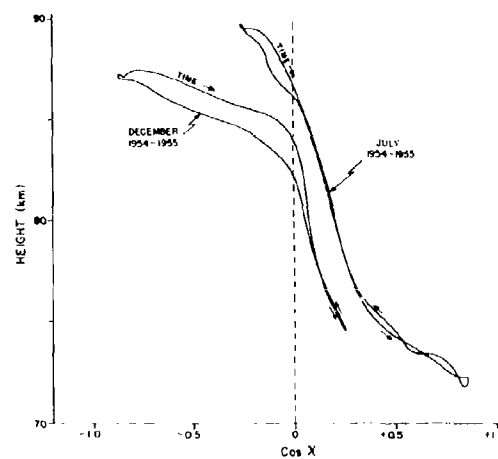


Figure 4
Diurnal variation of VLF (16kHz) phase height of
reflection for the Rugby-Cambridge transmission
in December and July during 1954-55 (Sunspot
minimum years).

Figure 5
Seasonal variation of VLF (16kHz) phase height of reflection for the Rugby-Cambridge transmission at constant solar zenith angle, and at midnight and noon during 1954-55 (sunspot minimum years).



Figure 6
Day-to-day variation of the height of the 10mb pressure level over middle Europe at midnight, and of solar activity (10.7cm solar flux) for equinoxal and winter months, 1961-62.
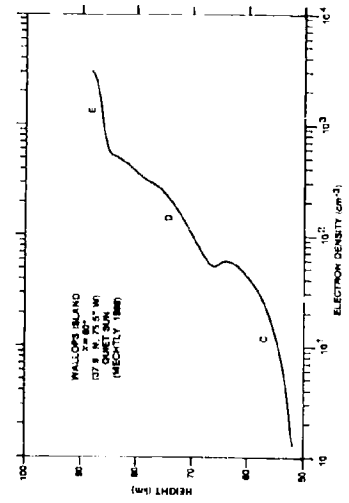


Figure 7
Electron density-height profile over Wallops Island, Va., 16 April, 1964, $\chi = 60°$, quiet sun [after Mechtly, 1968].



Figure 8
Ion pair production rates versus height for mid-latitudes, day ($\chi = 60°$), quiet sun [after Thomas, 1974].

Figure 10
Ion pair production rates versus height over Chatanika, Alaska, during a major solar proton event on 4 August, 1972 [after Reagan and Watt, 1976].
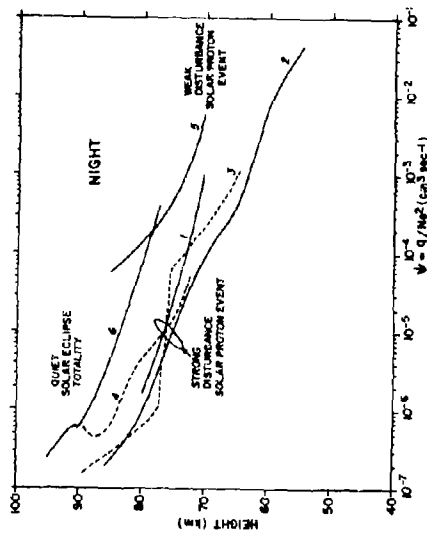


Figure 12
Effective electron loss rates versus height on quiet and disturbed nights.



Figure 9
Ion pair production rates versus height for mid-latitudes, midnight, quiet sun [after Thomas, 1974]



Figure 11
Effective electron loss rates versus height over Ottawa on quiet days ($\lambda = 68.6°$), for summer and winter, and during a large solar proton and large solar x-rays flare events.
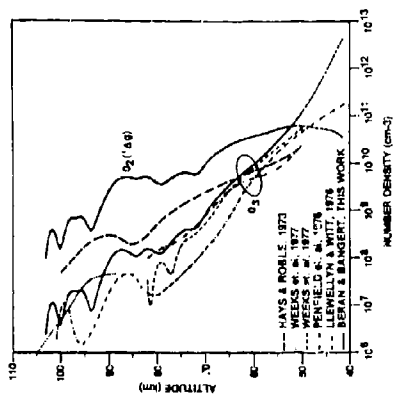
Figure 14
Height distributions of $O_3$ and $O_2$ ($^1\Delta g$) number densities, measured at various places and times [after Bergan and Bangert, 1979].



Figure 16
Height distributions of negative ion to electron ratio $\lambda$ from various sources for both quiet and disturbed and day and night conditions.



Figure 13
Height distributions of NO number densities, measured at various places and times [after Bergan and Bangert, 1979].



Figure 15
Rocket-borne mass spectrometer observations of the positive ion composition for a solar zenith angle of 20° at Cassino Brazil on 12 November, 1966 [after Narcissi et. al., 1972].

Figure 18
Electron density height profiles over Ottawa,
Ontario in March, 1971, averaged data for selected
undisturbed days.



Figure 20
Averaged electron density height profiles over Resolute Bay, N.W.T., in March
and July, 1965 (quiet sun). Note the profile measured by a rocket experiment
[Kane, private communications, 1969].



Figure 17
Electron density height profiles measured over Thumba, India during morning hours at
various solar zenith angles in March, 1978/70 [after Kane, 1969].
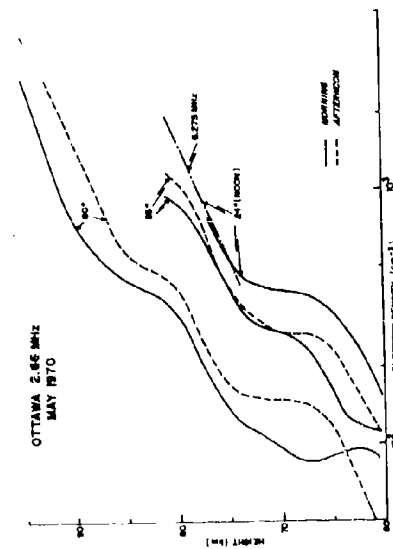


Figure 19
Electron density height profiles over Ottawa, Ontario in May, 1970, averaged
data for selected undisturbed days.
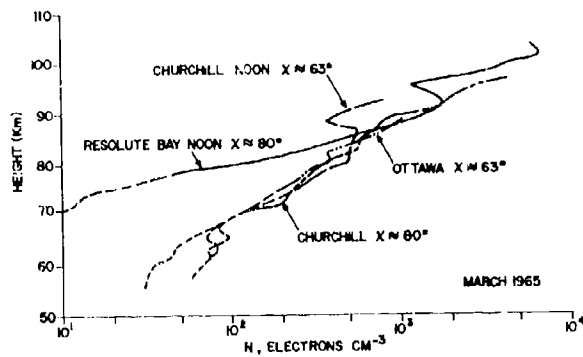
**Figure 21**
Averaged electron density height profiles over Ottawa, Churchill and Resolute Bay, in March 1965 (quiet sun)



**Figure 22**
Electron density heigh profile over Armidale N.S.W., for night, dawn and daytime periods in 1963-65 [after Smith et. al., 1967c].
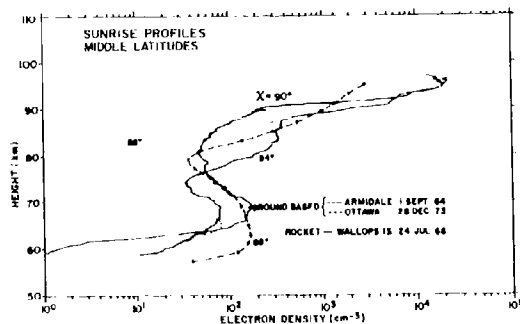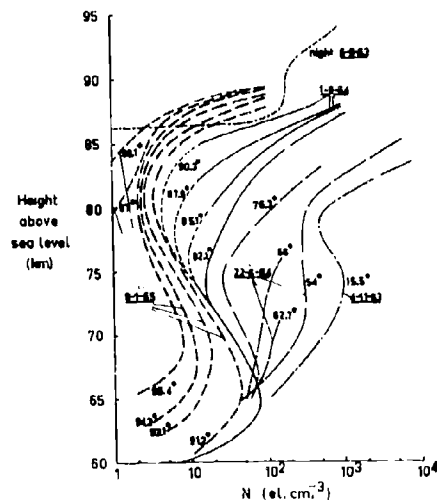


**Figure 23**
Electron density height profiles at sunrise ($\chi \sim 90^\circ$) measured by different techniques, places and times.
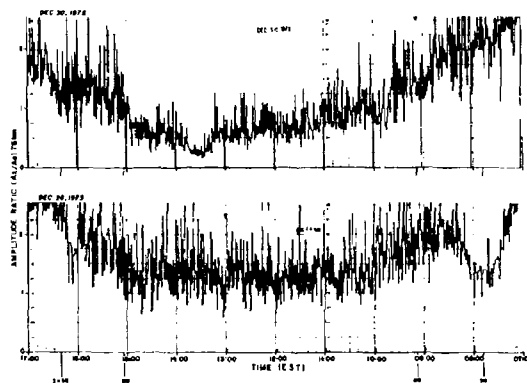
Figure 24
Ratio meter records (Ax/Ao at 76km) for a 2.66MHz
partial reflection experiment at Ottawa, Ontario
on two selected days in December. Note the
variation over dawn (solar zenith angles of
90 and 80° are marked). The lower record
(28 December, 1973) is considered to be
typical, the upper record (30 December, 1972)
is unusual in that the dawn development of
C-layer was not observed.

Figure 25
Diurnal variation of electron densities at fixed
heights over Ottawa, for selected quiet periods
in March 1971.
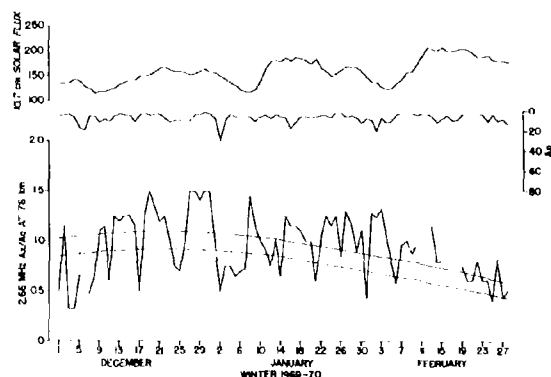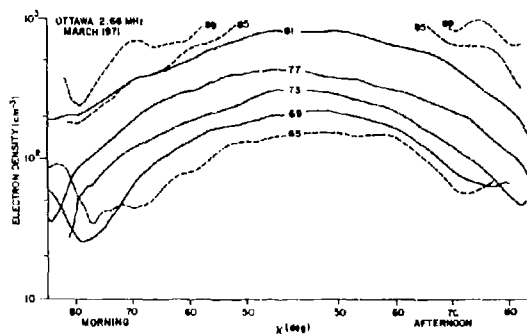




Figure 26
Day-to-day variation of Ax/Ao at 76km for a
2.66 MHz partial reflection experiment at
Ottawa, averaged midday values for the winter
of 1969-70. The magnetic index Ap and 10.7cm
solar flux values are also plotted on the
figure.
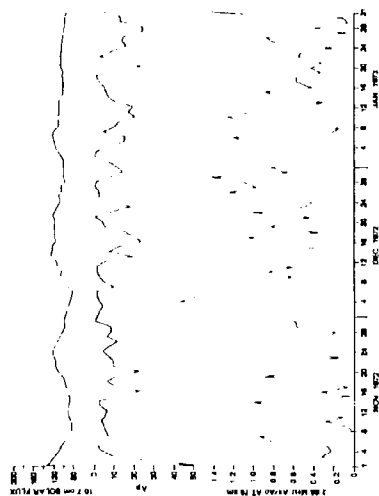
Figure 27
Day-to-day variation of Ax/Ao at 76km for a 2.66MHz partial reflection experiment at Ottawa, averaged midday values for the winter of 1970-71. The magnetic index Ap and 10.7cm solar flux values are also plotted on the figure.



Figure 29
Average midday electron density height profiles over Ottawa, Ontario for 1969-70. Note that the data are selected according the amount of ionization below 76km as judged by the Ax/Ao ratio.
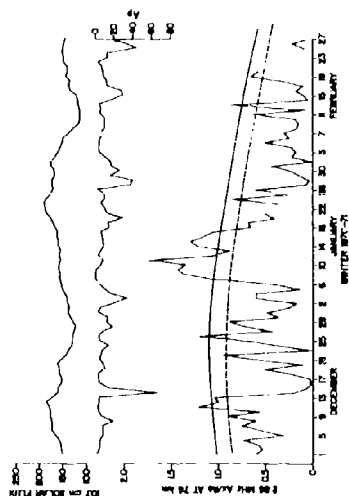


Figure 28
Day-to-day variation of Ax/Ao at 76km for a 2.66 MHz partial reflection experiment at Ottawa, averaged midday values for the winter of 1972-73. The magnetic index Ap and 10.7cm solar flux values are also plotted on the figure.
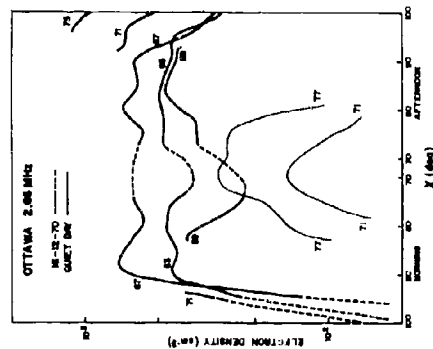


Figure 30
Diurnal variation of electron density at fixed heights over Ottawa on a geomagnetic post storm (GPS) day, 16 December 1970, compared with the variation observed on a typical lightly ionized quiet winter day.

Figure 31
Electron density height profiles over Ottawa at dawn, dusk and midday on a geomagnetic post storm (GPS) day, 16 December 1970.

Figure 32
Electron density height profiles over Ottawa at noon, showing development and decay of the GPS event illustrated in Figures 30 and 31. Note that a profile for the storm day, 14 December, 1970, is not included, since electron densities were very irregular and it was not possible to select a "representative" profile.

Figure 33
Effective electron loss rates on anomalous winter days over Ottawa and El Arencsilio, Spain.
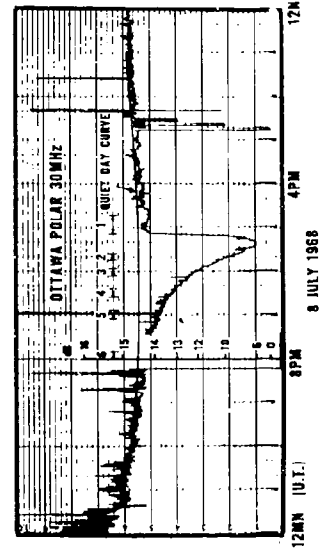
Figure 34
30 MHz polar riometer absorption during a major solar x-ray flare on 8 July, 1968. Note the time intervals marked 1 to 6, which correspond to periods selected to deduce electron densities (height profiles (see Figure 35).

Figure 35
Electron density height profiles at various times during a major solar x-ray flare on 8 July, 1968



Figure 36
Daytime electron density height profiles during solar proton events of various magnitude, as judged by the magnitude of absorption observed on a 30MHz zenith riometer. Note that positive ion densities are also shown for the 2 November, 1979 event.
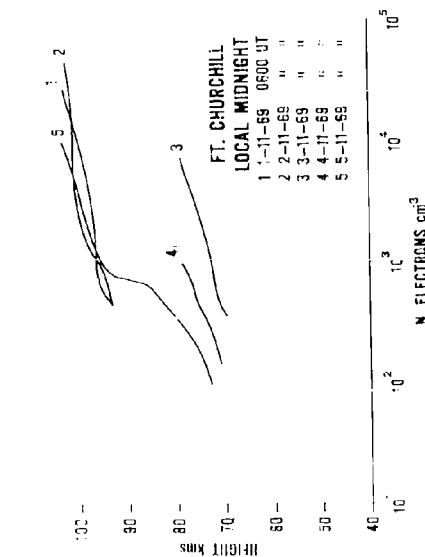


Figure 37
Nighttime electron density profiles during the course of a solar proton event on 2 November, 1969. Note that the profile labelled 3 should be compared with the daytime profile labelled 14dB in Figure 36.



Figure 38
Electron density height profiles during high energy particle (HEP) events (auroral absorption), measured during day and night. The data are sorted according to the magnitude of absorption on a 30 MHz zenith riometer.
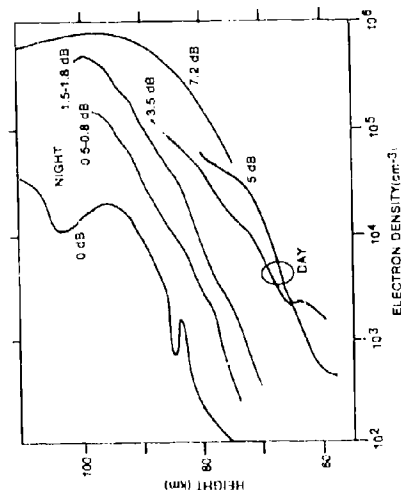
# STUDIES OF THE D-REGION BY THE PARTIAL REFLECTION OF MF RADIO WAVES

by

W.A.Flood, H.N.Turner, T.F.Shirley and S.D.Collins
US Army Research Office
Dept. of the Army, P.O. Box 12211
Research Triangle Park
N.C.27709, USA

## Abstract

During the period May 1976-October 1978, a series of coordinated measurements of the D region above Raleigh, N. C. were carried out at a frequency of 2.66 MHz. Four experiments were performed. The first experiment was concerned with the validity of the Randomly Phased Angular Spectrum (RPAS) approximation which is central to the measurement of ionospheric winds. Our results show that for D region echoes the RPAS approximation is valid. The second experiment utilized measurements of the complex spatial correlation coefficient of D region echoes to estimate the half power, half cone angle of arrival of D region echoes. The mean half cone angle was found to increase between 68-80 kilometers and then to remain constant at a value of $13^\circ$. Above 80 kilometers the variance of the angle of arrival increased with altitude. The implications of these cone angle measurements on the accuracy of D region electron density profiles measured by the "partial reflection" technique are discussed.

A series of carefully screened noon-time values of D region electron density profiles derived from the "partial reflection" technique have been analyzed to determine seasonal variations of electron density over the altitude range 68-88 kilometers. Examples of days of anomalous winter absorption are clearly evident.

Amplitude distribution of D region echoes were analyzed by means of a Chi-squared test and found to support the hypothesis that the echoes were drawn from a Rayleigh population. We take this result and the fact that D region echoes are continuous with altitude as evidence that the source of D region echoes is volume backscattering from fluctuations of refractive index.

## Introduction

The goals of the program were to determine the characteristics of D region (60-90 kilometers) backscattering and the effects of these characteristics upon the accuracy of experimentally-derived D region electron density profiles and D region "winds." Particular goals were:

(1) The investigation of the validity of the randomly phased angular spectrum approximation (hereafter abbreviated RPASA).

(2) Measurements of the cone angles of arrival of D region echoes and the effects of the cone angles on the accuracy of D region electron density profiles measured by the partial reflection technique.

(3) Measurements of noon time values of D region electron density profiles to establish the seasonal variation of D region electron densities.

(4) The examination of the amplitude distribution of D region echoes.

## The Validity of the RPASA

The electric field intensity of waves backscattered from the ionosphere can be described by an angular spectrum of plane waves. The Fourier transform of this angular spectrum is the spatial correlation function of the field intensity measured in the observation plane. The spatial cross correlation function is defined by an ensemble average:

$$R(x,\Delta x, y, \Delta y, z, \tau) = \left\langle E(x,y,z,t) \, E^*(x+\Delta x, y+\Delta y, z, t+\tau) \right\rangle$$

In the theory applied to ionospheric drift measurements, it is assumed that the spatial cross correlation function is independent of x and y which, if true, implies that non-zero electric fields exist over an infinite plane. One can therefore hypothesize that the process is ergodic and that a spatial average is equivalent to an ensemble average. Consequently:

$$R(\Delta x, \Delta y, \tau) = \lim_{\substack{L_x \to \infty \\ L_y \to \infty}} \frac{1}{4 L_x L_y} \int_{-L_x}^{L_x} \int_{-L_y}^{L_y} E(x,y,z,t) \, E^*(x+\Delta x, y+\Delta y, z, t+\tau) \, dy \, dx \qquad ...(1b)$$

Equation (1b) is clearly independent of x and y. In all of the preceding, it has been assumed that the process is stationary in a temporal sense so that the results are independent of the absolute time.

In the usual realization of the ionospheric drift experiment, measurements from at least three spaced receivers are used to deduce the spatial cross correlation function from a temporal average:

$$R(x, \Delta x, y, \Delta y, \tau) = \lim_{T \to \infty} \frac{1}{2T} \int_{-T}^{T} E(x,y,z,t) \, E^*(x+\Delta x, y+\Delta y, z, t+\tau) \, dt \qquad ...(2)$$

It should be clear that equation (2) has an explicit dependence on the absolute position, (x, y, z), as well as $\Delta x$ and $\Delta y$. Nonetheless, experimenters equate equations (1) and (2). One can show that the only way this can be true is if the angular spectrum is randomly phased--that is, if

$$\overline{F(s_1, s_2, t) \, F^*(s_1', s_2', t)} = \overline{|F(s_1, s_2, t)|^2} \, \delta(s_1 - s_1') \, \delta(s_2 - s_2') \qquad ...(3)$$

where the overbar indicates a temporal average and $F(s_1, s_2, t)$ is a component of the angular spectrum of plane waves having complex amplitude $F(s_1, s_2, t) \, ds_1 \, ds_2$ traveling in a direction specified by direction cosines $s_1, s_2, s_3$ where:

$$s_1^2 + s_2^2 + s_3^2 = 1 \qquad ...(4)$$

One can also show that no physically realizable angular spectrum can be exactly randomly phased, but that a spectrum may be approximately randomly phased so that equating (2) and (1) may be justified for relatively small values of $\Delta x$ and $\Delta y$.

Now that we have attempted to formalize the problems in mathematical terms, it is instructive to cast the problem in physical terms. What we really require is that the spatial cross correlation function is approximately independent of the absolute position of the measurement system--that is, that the RPASA is approximately satisfied. The spatial correlation function should not be a strong function of the absolute position of the receivers. One way to check this approximation is to measure the spatial cross-correlation function at, say, one-half wavelength separation at a number of absolute positions, and see just how "equal" they are.

There has been only one experimental investigation of the validity of the RPASA. von Biel (1969) developed a technique to measure the spatial correlation of the complex fields reflected from the ionosphere. Using near normal incidence echoes, von Biel concluded that D region echoes at his location (New Zealand) did not have a randomly phased angular spectrum.

Von Biel's technique was implemented at Raleigh, N. C. with a 125 kilowatt (peak pulse power), 2.66 Mhz transmitter, a circularly polarized transmitting array and a receiving array of 5 co-linear, horizontal dipoles whose feed points were spaced one-half wavelength apart. The polarization of the transmitting array could be switched in the interpulse period from left to right hand circular and the array was equipped with a T-R switch for use in a D region "partial-reflection" experiment. In the experiments to be described herein, the von Biel phasing networks were switched on a pulse-to-pulse basis between pairs of dipoles separated by one-half wavelenth (RPASA experiment) or between pairs of dipoles separated by increasingly larger multiples of one-half wavelength (CONE ANGLE experiment). Echo amplitudes were sampled for each transmitted pulse at 2 kilometer intervals between 60 and 98 kilometers altitude. These samples were digitized with an eight bit A/D converter and stored on magnetic tape for later data processing.

## 1.0 Randomly Phased Angular Spectrum Experiment

A necessary condition for the validity of the RPASA is that measured values of the complex correlation coefficient be a function only of the separation between the two sample points and not of the absolute positions of the sampling points. The receiving array of five dipoles spaced one-half wavelength apart enabled four determinations of the complex correlation coefficient for half wavelength separations over a range of absolute positions which extended to two wavelengths.

Variations in the four correlation measurements could be caused by sampling errors, noise and interference, or a true position dependence. An error analysis, Turner (1977), showed that unless the signal to interference ratio was very high, the phase of the measured correlation function was subject to serious error. Furthermore, at large separation distances, where the magnitude of the correlation function is small, relatively low levels of interference can cause large errors in the measurement of the magnitude of the correlation function. For signal to interference ratios of greater than 10 db and for separations such that the magnitude of the true correlation was not small, the effect of interference on the measured magnitude of the correlation function was found to be tolerable.

Records taken on days of exceptionally low interference levels showed that reducing the averaging time from 20 minutes to 5 minutes produced changes of less than 3% in magnitude of the correlation coefficient. Data processing was restricted to records of 20 minutes' duration at altitudes where the signal to interference ratio was at least 10 db. Some measurements of the phase as well as the magnitude of correlation coefficient for half wavelength separations were obtained on days of exceptionally low interference levels and one example will be shown and discussed.

## 1.1 E Region Tests of System Operation

Echoes from a quiet E region, characterized by very slowly fading, large amplitude echoes from a very restricted range of altitudes, were used to test system operation. Figure 1 is a plot of the magnitude and phase of the complex correlation function of an echo from a quiet E region. The correlation coefficient was evaluated for spacings of $\frac{\lambda}{2}$, $\lambda$, $\frac{3\lambda}{2}$ and $2\lambda$ and the individual data points have been connected by straight lines.

The magnitude of the correlation function is essentially unity at all the observed spacings, consistent with a nearly specular reflection from the E region. The phase plot, on the other hand, is quite irregular. Since the average specular E region returns are expected to be vertically incident, eight phase plots of quiet E region echoes were averaged to produce a plot of phase offset with respect to the reference antenna. (The average phase offsets were similar to a contour plot of the field site). When the average phase offsets were subtracted from the phases plotted in Figure 1, the resulting phase plot was linear with separation distance and consistent with an apparent zenith angle of 0.45 degrees. (The corrected phase plot is also shown in Figure 1).

E region tests (made with very high signal to interference ratio echoes) are evidence that the experimental system can measure the complex correlation function of the incident fields.

## 1.2 D Region Results

Data acquired during the period May 1976 through October 1976 consisted of 20 minute data runs taken around local noon with a pulse repetition frequency of 16 Hz. A summary of the correlation measurements as a function of altitude is presented in Table 1. The quantity PSD (percent standard deviation) defined by:

$$PSD = \frac{\sigma}{M} \times 100\%$$

$$...(5)$$

where M and $\sigma$ are the means and the rms fluctuation about that mean for each data run. $\sigma$ and the PSD are used only as a measure of the variability of the four measured values of the correlation function for that run.

In Table 1, N is the number of individual 20 minute observations at each altitude for which the signal to interference ratio was greater than 10 db and $\overline{M}$ and $\overline{PSD}$ are the averages of the N means and N PSDs at each altitude. The largest PSD value at each altitude is also shown. It should be noted that for altitudes of 68-78 kilometers, the largest PSD is the result of the same 20 minute observation. The low values of the average PSD ($\overline{PSD}$) indicate that the remaining PSDs were much lower for altitudes with N greater than unity.

The mean values of correlation magnitudes obtained over the five month period are listed for reference only. Measurements were taken around noon local time, but the seasonal variation in solar zenith angle could have affected the outcome of the measurements. The acquisition of data was governed by interference levels, and data could not be regularly obtained on a day-to-day basis. Thus, seasonal patterns in the correlation measurements, if present, would not be evident. The "standard deviations" listed in Table 1 serve only to illustrate the spread of the values from which the averages were obtained.

The PSD for the one 20 minute observation at 78 km was the only observation which could not be explained on the basis of the prevailing signal to interference ratio. Therefore, it seems reasonable to conclude that, within experimental error, the magnitude of the spatial correlation coefficient for normal incidence D region echoes at Raleigh is essentially independent of the absolute position of the receiving antennas.

To the extent that the magnitude of the correlation function is independent of position, the RPASA is valid. However, the phase of the correlation function has not been shown to be independent of position since, except on relatively rare occasions, the signal to interference ratio of D region echoes was not large enough to permit reliable phase measurements to be made. An example of one such rare occasion on which phase measurements were possible is shown in Figure 2.

In Figure 2, the magnitude of the correlation coefficient for each pair of observing stations at each altitude are closely grouped, as might be expected for complex correlation functions which are independent of position. The phase plots have the same form, but there are obvious offsets between them. The significance of the phase "offsets" has already been discussed. The similarity of the phase plots is indicative of the fact that interference levels were well below D region echo levels on this occasion. We conclude that D region echoes satisfy the RPASA in a local sense--that is, over distances of at least the RPASA is satisfied and equating equations (1) and (2) seems valid in the Raleigh area.

## 2. Cone Angle of Arrival of D Region Echoes

The array of five dipole antennas and the validity of the RPASA make possible the estimation of the half power width of the angular power spectrum. The angular spectrum is denoted by:

$$\overline{|F(s_1, s_2, t)|^2} \, ds_1 \, ds_2$$

= power density associated with plane waves with direction cosines between $S_1$, $S_2$, and $S_1 + ds_1$ and $S_2 + ds_2$

The angular power spectrum and the spatial correlation function are Fourier transform pairs. Assume that the two dimensional correlation function is isotropic and is of the form:

$$\rho(\Delta x, \Delta y) = \frac{R(\Delta x, \Delta y, 0)}{(0,0,0)} = \exp\{-B^2 r^2\} \qquad \ldots (6)$$

The one dimensional (isotropic) angular power spectrum is:

$$\overline{|F(s,t)|^2} = \left(\frac{\pi}{B^2}\right)^{1/2} \exp\left\{-\left(\frac{\pi s}{B}\right)^2\right\} \qquad \ldots (7)$$

where $\overline{|F(s,t)|^2}$ is the angular power spectrum of the backscattered echoes as a function of s, the sine of the zenith angle. We define the half power width of the angular spectrum by:

$$\frac{|F(s,t)|^2}{\overline{|F(0,t)|^2}} = 0.5 \qquad \ldots (8)$$

where $S_{1/2} = \sin\theta_{1/2} = .27 B$. $\qquad \ldots (9)$

Least squared fits of the experimentally determined spatial correlation functions for separations of $\frac{\lambda}{2}, \lambda, \frac{3\lambda}{2}$ were made to estimate the parameter B in equation (6) and these estimates used to determine the half power angle of D region echoes from equation (9).

Turner's (1977) analysis of the effects of interference on the determination of the magnitude of the spatial correlation evaluated at large separations, where the magnitude value may be low, showed that the correlation value is likely to be in error due to interference. Almost all values of the magnitude of D region spatial correlation coefficient at the two wavelength separation were too low to use in the least squared fitting procedure.

Figure 3 is a plot of the measured magnitude and phase of the spatial correlation function at altitudes of 68, 72, and 76 kilometers on one occasion. It is not an atypical set of curves but phase measurements could be made only on rare occasions. Note that the 76 km data imply the widest angular spectrum. The rms error in fitting the data points for the 72 km at $\lambda$, $\lambda$, $3\lambda$ and $2\lambda$ was .023. The possible rms error caused by interference was estimated to be .058. Since the error in the curve fit is less than might be expected due to interference, (6) is said to be a "good" fit to the 72 kilometer correlation data and the cone estimate is likewise classified "good." Because similar error values were found for many other spatial correlation curves, it was concluded that (6) is adequate for cone angle estimation.

Equation (7) predicts signals from angles which are larger than is physically possible. We expect the Gaussian approximation to the true angular spectrum will fail at large zenith angles. The experimental data, to be presented next, indicate half power spectral widths, $\theta_{1/2}$ of less than 25 degrees so that truncation of the angular spectrum at $\varphi = 90$ degrees should cause no serious errors.

## 2.1 Cone Angle Experimental Results.

The cone angle of arrival data obtained from D region measurements made around local noon during the period May 1976 through October 1976 are plotted in Figure 4. For each altitude, Table II lists the following:

$N$ = number of cone angle estimates at each altitude

$\overline{\theta_{1/2}}$ = mean of the N estimates of each altitude

$\sigma_{1/2}$ = standard deviation of the N estimates

$\theta_{1/2\,max}$ = largest of the N estimates of the half power width at that altitude.

The most striking feature of Figure 4 and Table II is the rapid rise in cone angle between 68 and 78 kilometers. Most of the data below 78 kilometers were obtained with X wave polarization because of the generally stronger X wave returns at lower altitudes. The increase in cone angles between 68 and 78 kilometers is caused at first by the increase in effective scattering volume and then by the rapid rise in X wave absorption which causes the X wave amplitude to decrease with increasing altitude. Consequently, stronger X wave echoes at lower altitudes ( and larger zenith angles) tend to dominate the measurement so that over the range 72-78 kilometers, the cone angle of arrival increases.

Above 82 kilometers, where both the X and O wave amplitudes increase with altitude, the mean cone angle is approximately constant at 12-13 degrees but the standard deviation, $\sigma_{1/2}$, increases with altitude. Note that the higher altitude data have very high signal to interference ratios so that interference is not the cause of the increased cone angle variability at the higher altitudes.

## 2.2 Effects of Cone Angle Results on the Partial Reflection Experiment

D region echoes are frequently assumed to come from a horizontal slab centered at a height $R_0$ of thickness $L = \frac{c\tau}{2}$ where c is the vacuum velocity of light and $\tau$ is the pulse duration. Because of the curvature of the wave front, not all of the scattering volume is contained within the slab. The percentage of the scattering volume contained in the horizontal slab is most important in assessing altitude "smearing."

Cross sections of two scattering volumes are shown in Figure 5. The volumes are portions of spherical shells of thickness L. The semiangular extent of the shells is $\theta_{1/2}$ and the figure illustrates the cases $\theta_{1/2} < \theta_B$ and $\theta_{1/2} > \theta_B$ where $\theta_B$ is the angle at which the outer edge of the spherical shell is at the height of the bottom of the horizontal slab.

It can be shown that for 2-4 km spatially extended pulses in the D region, as the cone angle approaches $\theta_B$, approximately 50% of the scattering volume lies at altitudes below the horizontal slab and significant altitude smearing is present. The cone angle data of the previous section suggest that, for X waves, increased altitude smearing is present at ranges where $A_x$ decreases with altitude. Consequently, regions where $\frac{\partial \overline{A_x}}{\partial h}$ is negative can present problems for the partial reflection experiment.

## 2.3 Wide Cone Angles and Electron Density Minima.

One of the goals of this research was to identify possible causes of erroneous electron density profiles. Two electron density profiles obtained by the "partial reflection technique" (Belrose & Burke, 1964) are illustrated in Figure 6 and Figure 7. The local minima in electron density at 78 km and 80 km are the portions of the profiles in question. Minima which occur below 72 km are not questioned because of possible inaccuracies in the ratio measurements caused by interference.

Consider the curve of Figure 6. X-wave cone angle measurements are shown on the plot. Note the 22.3 degree cone angle at 78 km where the electron density minimum occurs. A much deeper minimum is shown in Figure 7 at 80 km. An X-wave cone angle measurement at 80 km was not available for the data in Figure 7, but the cone angle had already reached 20.7 degrees at 78 kilometers. The implication of these figures is that local minima in electron density profiles can result from oblique X-wave echoes and altitude smearing. These oblique X-wave echoes are frequently associated with regions where the X-wave amplitudes decrease with increasing altitude while O-wave amplitudes tend to increase with altitude.

While we can frequently associate minima in electron density profiles with minima in X-wave amplitude, this is not always the case as will be seen in a later section. The fact remains, however, that differential scattering volumes for the X and O waves are a real source of error in the partial reflection experiment and these differences are emphasized in regions where the extraordinary wave amplitude decreases with increasing altitudes.

## 3. Seasonal Variation of Noon Time D-Region Profiles

Extensive partial reflection measurements (Belrose and Burke 1964) were made during the period November 1976 - June 1978. The 125 $k_w$ pulse transmitter generated 25 microsecond pulses with repetition rates of either 8 or 16 pulses per second. The 2x2 array of crossed dipoles capable of switching between the X and O modes was used for both transmission and reception.

The receiver had a 100 kiloherz bandwidth and a special wide dynamic range envelope detector; the linearity of the overall receiver was tested under operating conditions and found to be within 0.5 db over a 50 db dynamic range. Furthermore, the receiver employed a programmable gain IF amplifier--the gain could be changed in less than 13 microseconds, the time between samples at every two kilometers, and was used to prevent saturation from the stronger echoes at the higher altitudes.

A digital logic unit controlled the transmitter, receiver gain, and data acquisition. This unit sampled the returns from each transmitted pulse, converted the amplitudes to an eight bit word and stored the samples on magnetic tape for later processing. Each pulse return was sampled every 2 kilometers between 60 and 98 kilometers.

All data were collected with an operator present although the digital logic unit made it possible to collect data, automatically, at preset times. We elected "operator on site" data collection to avoid taping large quantities of invalid, useless "data." In order to aid the "on-site operator" and to guide him in his decision to record echo amplitudes on tape, circuitry was added which caused a small light to flash on each pulse for which interference levels were too high for "valid data." There were many occasions of potential noon-time data runs when the "invalid data" light flashed so frequently that the digital tape recorder was not activated.

The data were handled in ten minute lengths and were subjected to extensive screening procedures. Records were rejected if the signal-to-interference ratio was less than 10 db at too many altitudes or if saturation effects (A/D counts greater than 250) were excessive. The time lagged auto correlation function was also used to screen the data at low altitudes. If the normalized auto correlation function at .25 second lag was less than 0.75, data at that altitude was rejected. Finally, each "run" had to have acceptable O and X wave data over at least a 10-12 kilometer altitude interval before the data were inverted for electron density profiles.

Operator screening on site and the data processing screening outlined above resulted in 75 days of acceptable partial reflection data. While the majority of these days had at least three contiguous, or nearly so, data runs, some days had only one valid 10 minute run.

### 3.1 Calculation of Electron Density Profiles

The theory of the partial reflection technique (Belrose and Burke, 1964; Flood, 1968) leads to the following expression:

$$\frac{\overline{A_x(h)}}{\overline{A_o(h)}} = P(h) \, exp\left\{ -\frac{4\pi}{\lambda} \int_o^h \left[ m_x^i(\jmath) - m_o^i(\jmath) \right] d\jmath \right\} \qquad \ldots(10)$$

where P(h) is the square root of the ratio of the backscattering cross section.
per unit volume of the X wave to that of the O wave
$\lambda$ is the free space wave length
$m_{x,o}^i$ is the imaginary part of the refractive index of the extraordinary or ordinary wave.
$\overline{A_{x,o}(h)}$ is the mean amplitude of the X (O) return at a range h.

If the operating frequency is much greater than plasma frequency, as is the case for 2.66 Mhz and normal D region densities, the modal refractive indices are nearly linear functions of electron density and the Q-L approximation to the Sen Wyller equations (Flood, 1980) can be useful for $m_x^i$ and $m_o^i$. Expressions for P(h) and $m_{x,o}^i$ are given in Appendix A.

Taking the natural logarithm of both sides of equation (10) results in an equation which can be readily inverted by means of a least squared fit to a polynomial approximation to the electron density profile. All of the screened 10 minute data runs were inverted via this technique to produce electron density profiles. The order of the polynomial approximation to the electron density profiles was never greater than one half the number of data attitudes. On the many days when several successive acceptable data runs were available, the electron density profiles for each 10 minute period were averaged to produce one average noon-time profile for that day. A large number of test cases were evaluated to see if there were differences between an average of three successive electron density profiles and the electron density profile determined from an average of three successive $\overline{A_x}/\overline{A_o}$ profiles. While there were differences, they were decidedly minor.

There are some significant observations which can be made at this point. When individual, successive, electron density profiles, based on 10 minute averages, showed pronounced minima in electron density, the electron density profile computed from a 30 minute average of $\overline{A_x}/\overline{A_o}$ also showed a pronounced electron density minimum. When electron density profiles based on 10 minute averages showed slight minima, the average of the three profiles might show no minima at all or might even show a slight minimum at some other altitude. The electron density profile derived from a single 30 minute average of $\overline{A_x}/\overline{A_o}$ could equally well show a slight minimum at a completely different altitude. While slight minima in 10 minute profiles produced average profiles with either no or slight minimum in the average 30 minute profile, deep minima in individual profiles were reproduced in the 30 minute profile. We take this to

mean that deep minima, frequently associated with regions where $\overline{\partial A_i}/_{\partial h}$ is negative, may be caused by altitude smearing, but the slight minima are often artifacts of the data processing procedures.

The 75 days of acceptable noon time profiles were fortunately almost equally divided among the four seasons of the year. The seasonal means and their standard derivations are tabulated in Table IV and plotted in figures 8 and 9. Figure 10 shows the profiles associated with summer, winter and spring/fall averages.

The measurements shown in Figures 8 and 9 indicate that at a mid-latitude station while there is a difference in summer and winter electron densities above 78 kilometers, it is difficult to find a difference below 78 kilometers. This is not surprising in view of the solar control at altitudes above 78-80 kilometers. Further support for this conclusion is provided by Figure 9 which indicates that the spring and fall electron densities are essentially indistinguishable and that above 78 kilometers, mean equinoctial electron densities lie between the means of the summer and winter profiles. The seasonal variation of electron densities above 78 kilometers is clearly evident.

While processing the winter day data, five days were found which had obviously high electron densities--possibly indicative of anomalous winter absorption. The electron density profiles for these days are shown in Figure 11 where the mean values of electron density are clearly greater than the average winter profile + one standard deviation. If these are indeed "days of anomalous winter absorption," they differ somewhat from some previously reported examples of anomalous winter absorption--the electron densities are only 2-4 times the average electron densities at these altitudes.

## 4. Amplitude Distributions of D Region Echoes

Flood (1968) proposed that D region echoes were caused by scattering from volume distributed refractive index fluctuations. If this mechanism is operative, the amplitudes of the echoes should be Rayleigh distributed. The Rayleigh probability density function is:

$$p(A) = \frac{A}{\sigma^2} \, exp\left\{ - \frac{A^2}{2\sigma^2} \right\} \qquad \qquad ...(4.1)$$

where p(A) dA is the probability that the
signal amplitude is between A and A + dA.

The data analyzed consisted of 10 minute runs during which the transmitted and received polarizations were changed on successive pulses from right to left circular ("ordinary," and "extraordinary," respectively). For each transmitted pulse, the return signals were sampled at 2 kilometer intervals over the range 60 to 98 kilometers. Amplitude distribution histograms were computed for both ordinary wave and extraordinary wave polarizations although X wave measurements dominate the lower altitude measurements. At a typical prf of 8 pulses per second, a total of 2,400 "0" and "X" wave returns were available for each 10 minute period. The data were screened for noisy and saturated returns at each altitude. These restrictions effectively set the lowest altitude for which valid data was available at 70 kilometers.

The data samples at each altitude were normalized to the sample mean value and "eight-bin" histograms were computed. The Chi-squared hypothesis test using six degrees of freedom (the amplitudes had been normalized to the mean value of the data run) was applied to the histograms. Acceptance or rejection of the Rayleigh hypothesis was set at the 10% level; i.e., the probability that the differences between the observed (data) distribution of amplitudes and that expected from a true Rayleigh distribution could be caused by sampling error is less than 10%.

A summary of the Chi-squared test results is shown in Table IV. The notation in the table is:

ALT   =   altitude in kilometers
N     =   number of screened 10 minute observations at that altitude
CL%   =   mean confidence limit of the N observations
N 10% =   number of 10 minute observations that were rejected at the 10% level as not being drawn
          from a Rayleigh population.

### Summary of Table 5 Chi-Squared Results

| ALT | 70 | 72 | 74 | 76 | 78 | 80 | 82 | 84 | 86 |
|------|----|----|----|----|----|----|----|----|----|
| N | 20 | 23 | 25 | 23 | 26 | 25 | 23 | 24 | 23 |
| CL% | 42 | 39 | 44 | 39 | 41 | 44 | 51 | 41 | 42 |
| N 10% | 2 | 4 | 2 | 5 | 2 | 2 | 1 | 1 | 2 |

It should be noted that although the Rayleigh hypothesis was accepted or rejected on the 10% level, the average confidence level at each altitude was at least 39%. Consequently, there is a 39% probability that the differences between the observed distributions and Rayleigh distributions were caused by sampling error. We take this as strong support for the hypothesis that the source of D region's back-scatter is scattering from volume distributed fluctuations of refractive index.

## Summary and Conclusions

In the order in which we posited the goals of this program, we have found that:

1.   The RPASA is valid provided the separation between observation points is not much greater than 2 . While the RPASA may hold for larger separations, we have not validated it for such separations. Most of the ionospheric drift experiments do not use larger separation of the receiving antennas.

2.   The cone angle of arrival of D region echoes increases to a mean value of $13^0$ over the altitude range 70-80 kilometers. While the mean value of $13^0$ is maintained over the 80-90 kilometers region, the rms fluctuation about the mean value definitely increases with altitude. In regions where the cone angle is negative, x wave cone angles tend to be large, which implies that significant altitude smearing can take place.

3.   The seasonal variation of noon time D region densities above 78 kilometers is clearly visible.

4.   The amplitude distributions of echoes backscattered from the D region satisfy a Chi-squared test for a Rayleigh distribution with an average 40% confidence level. The strong finding for the Rayleigh hypothesis, coupled with the apparently continuous distribution of echo intensity with altitude, seems to strongly support the contention that the source of D region backscatter at MF frequencies is from volume distributed fluctuations of refractive index--mainly of electron density.

## Acknowledgements

## References

Belrose, J. S. and M. J. Burke. 1964. "A Study of the Lower Ionosphere Using Partial Reflections." J. Geophys. Res. 69, p. 2799.

Flood, W. A. 1968. "Revised Theory for Partial Reflection D Region Measurements." J. Geophy. Res. 73, p. 5585.

Flood, W. A. 1969. Reply. J. Geophys. Res. 74, p. 5183.

Flood, W. A. 1980. "A D Region Mid and High Latitude Approximation to the Sen-Wyller Refractive Index Equations." Radio Sci. 15, 797.

Turner, H. N. 1977. Unpublished thesis presented to the faculty of North Carolina State University. "Some Inherent Limitations to the Accuracy of D Region Electron Density Profiles Obtained by the Differential Absorption Partial Reflection Technique."

von Biel, H. A. 1970. Unpublished thesis presented to the faculty of the University of Canterbury, Christ Church, New Zealand.

Table I. Summary of Position Dependence Data as a Function of Altitude
Antenna Separation is One-Half Wavelength

| h | N | M̄ | P̄S̄D̄% | Maximum PSD% |
|---|---|---|---|---|
| 68 | 5 | 0.79 | 3.4 | 6.0 |
| 70 | 5 | 0.79 | 5.0 | 14.9 |
| 72 | 5 | 0.70 | 5.0 | 13.3 |
| 74 | 4 | 0.69 | 5.7 | 11.4 |
| 76 | 1 | 0.62 | 8.3 | 8.3 |
| 78 | 1 | 0.53 | 28.9 | 28.9 |
| 80 | 1 | 0.83 | 1.9 | 1.9 |
| 82 | 3 | 0.80 | 4.1 | 6.3 |
| 84 | 6 | 0.82 | 2.5 | 4.7 |
| 86 | 7 | 0.86 | 2.2 | 3.3 |
| 88 | 10 | 0.83 | 3.1 | 7.0 |
| 90 | 16 | 0.83 | 2.8 | 6.5 |
| 92 | 18 | 0.81 | 3.9 | 10.6 |
| 94 | 18 | 0.78 | 4.7 | 6.2 |
| 96 | 15 | 0.78 | 3.5 | 6.4 |
| 98 | 14 | 0.76 | 4.7 | 8.3 |

Table II. Cone Angle Summary

| h | N | | | |
|---|---|---|---|---|
| 68 | 6 | 6.75 | 1.736 | 5.8 |
| 70 | 11 | 8.54 | 2.32 | 12.8 |
| 72 | 11 | 10.9 | 2.39 | 15.4 |
| 74 | 10 | 13.7 | 3.28 | 18.8 |
| 76 | 9 | 15.6 | 4.02 | 20.6 |
| 78 | 6 | 17.6 | 4.68 | 22.3 |
| 80 | 6 | 12.7 | 2.72 | 17.1 |
| 82 | 10 | 12.0 | 1.53 | 14.1 |
| 84 | 18 | 12.0 | 2.17 | 15.4 |
| 86 | 30 | 11.8 | 2.24 | 17.9 |
| 88 | 38 | 11.8 | 3.05 | 16.7 |
| 90 | 45 | 12.1 | 3.08 | 20.7 |
| 92 | 49 | 13.3 | 3.04 | 20.3 |
| 94 | 47 | 13.7 | 3.30 | 21.2 |
| 96 | 48 | 13.8 | 4.30 | 21.8 |

Table III. Seasonal Averages of the Electron Density (per $cm^3$) for Raleigh, NC

| Altitude | Winter M | | Spring M | | Summer M | | Fall M | |
|---|---|---|---|---|---|---|---|---|
| 68 | -- | -- | 260 | 44 | -- | -- | -- | -- |
| 70 | -- | -- | 319 | 50 | 216 | 57 | 283 | 34 |
| 72 | 244 | 57 | 337 | 65 | 274 | 63 | 328 | 61 |
| 74 | 328 | 115 | 354 | 82 | 313 | 56 | 330 | 50 |
| 76 | 388 | 140 | 413 | 87 | 356 | 99 | 384 | 47 |
| 78 | 425 | 153 | 495 | 102 | 461 | 179 | 475 | 103 |
| 80 | 647 | 151 | 636 | 161 | 688 | 274 | 620 | 183 |
| 82 | 519 | 188 | 880 | 227 | 896 | 233 | 851 | 243 |
| 84 | 786 | 270 | 1180 | 260 | 1353 | 302 | 1223 | 290 |
| 86 | 1388 | 498 | 1669 | 514 | 1998 | 536 | 1601 | 383 |
| 88 | 2561 | 1063 | 2280 | 950 | 2135 | 339 | -- | -- |

2-9

94  h (km)

90

86

MAG OF R(λ/2,o)

1.0
0.9
0.8
0.7

h (km)

ARG. OF R(λ/2,o) IN DEGREES

20°
10°
-10°
-20°
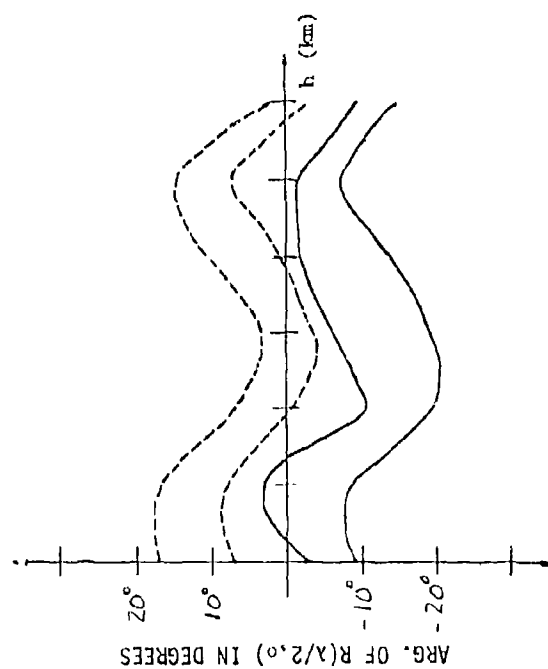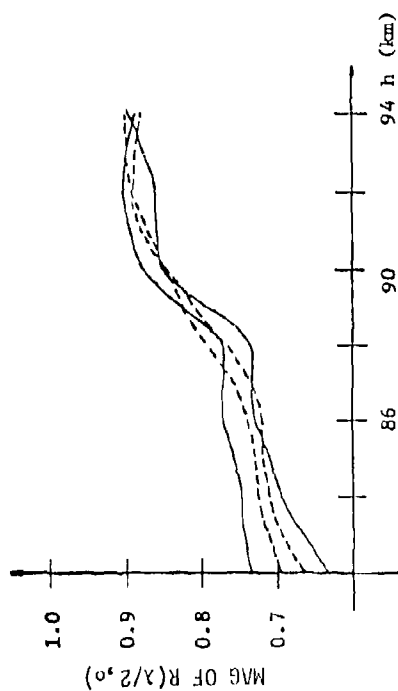
Fig.2  Correlation magnitudes and phases vs. altitude at four positions of λ/2 separation

DISTANCE IN WAVELENGTHS

0.5  1.0  1.5  2.0

MAG. OF R(Δx,o)

1.00
0.75
0.50
0.25

Corrected phase curve
($\theta_x = 0.45°$)

Observed phase curve.

ARGUMENT OF R(Δx,o)

30°
20°
10°
-10°
-20°
-30°
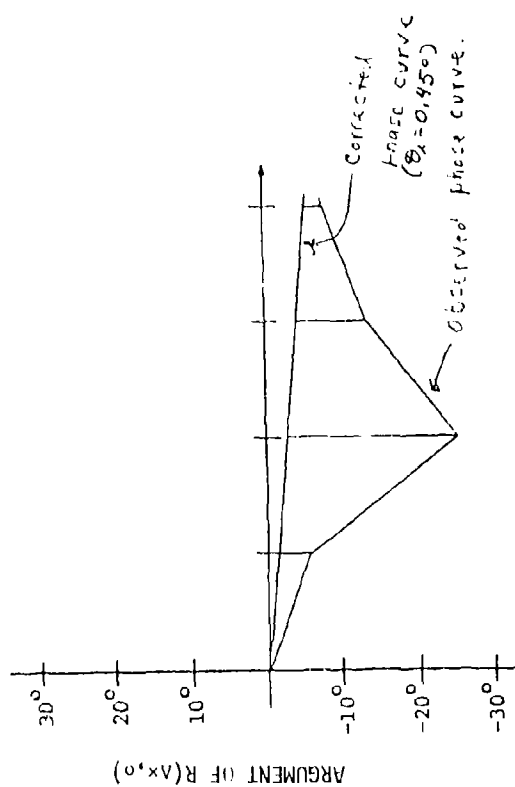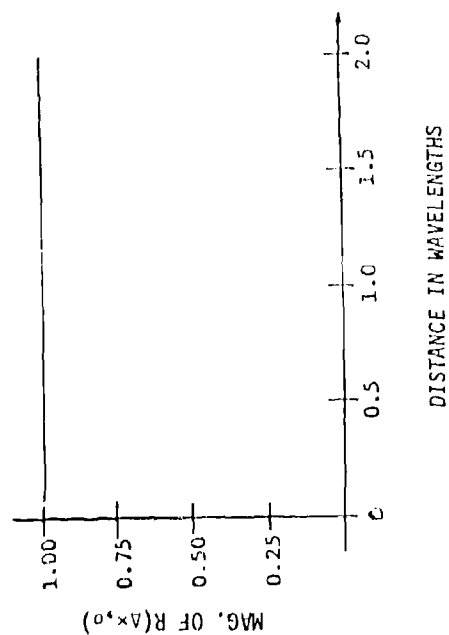
Fig.1  E-region spatial correlation function
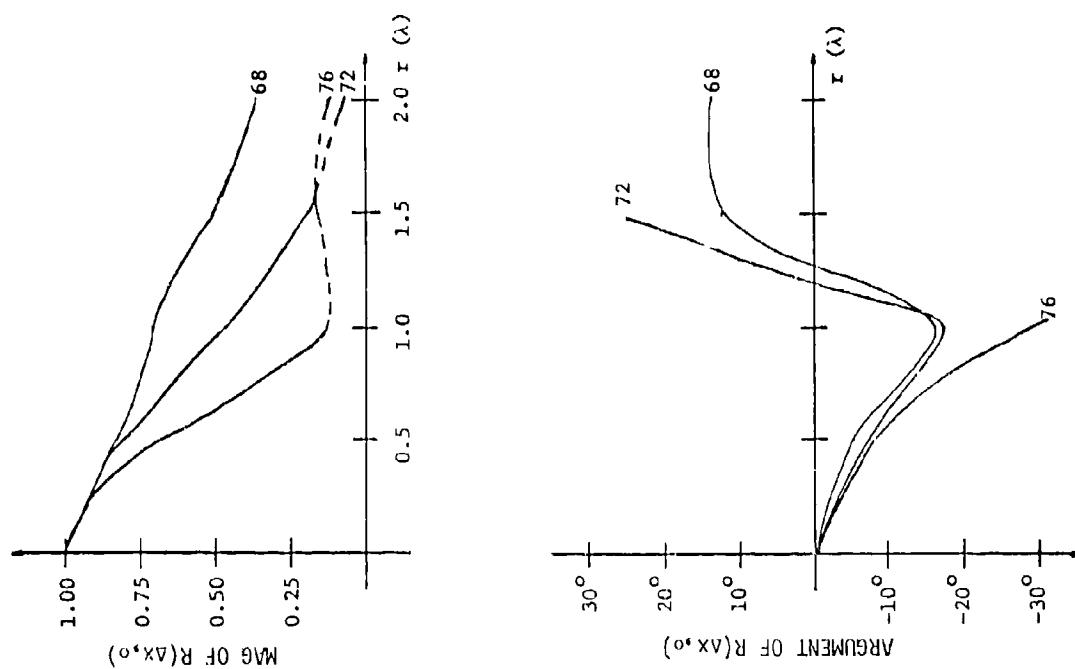
Fig.3   D-region spatial correlation function
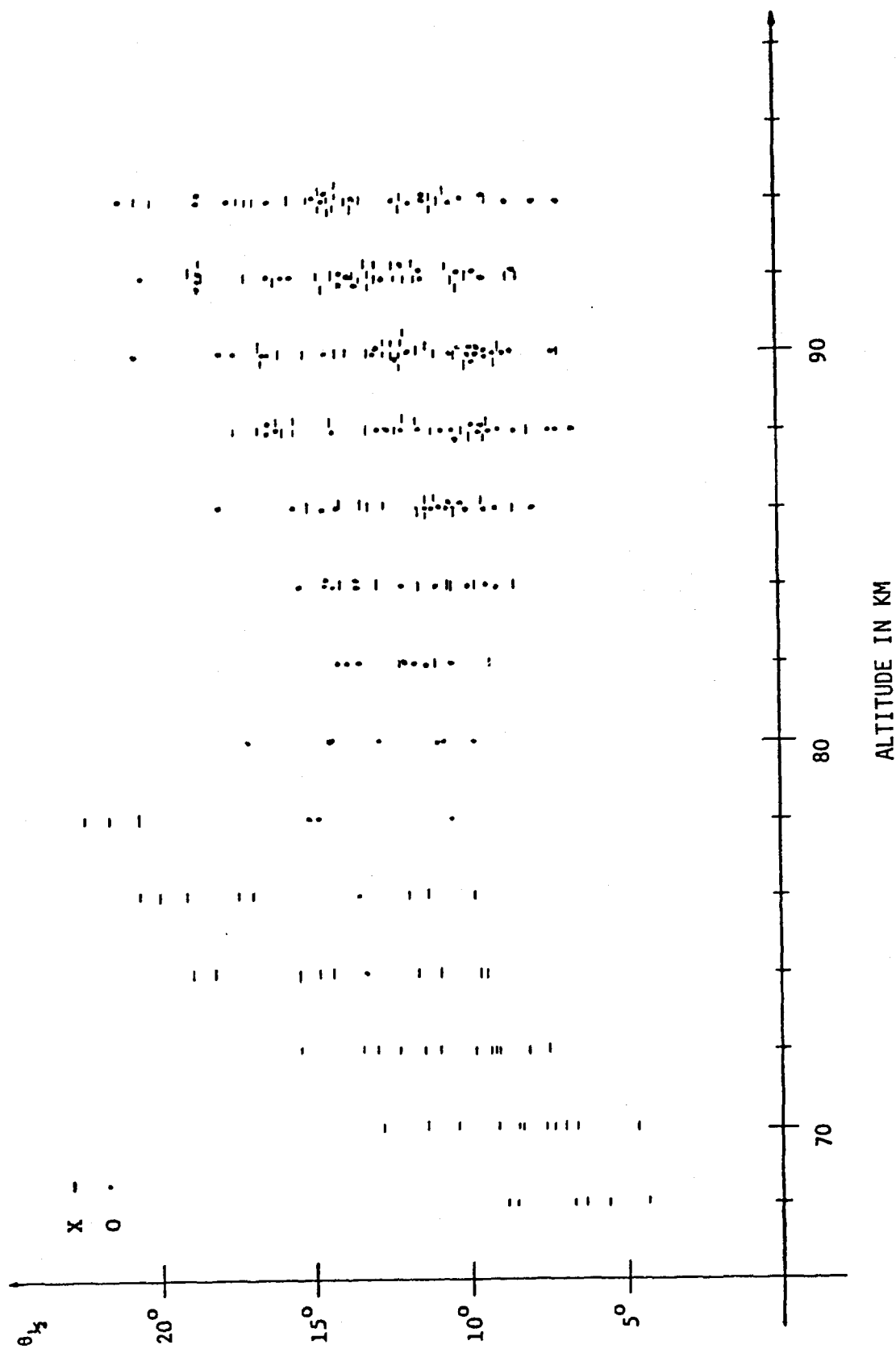
Fig.4    Semi-cone angle of arrival as a function of altitude

ELECTRON DENSITY PER C.C.

ALTITUDE IN KILOMETERS

22.3°
20.6°
18.7°
13.4°
15.4°

100   200  300  500   1000   2000  5000

80

70
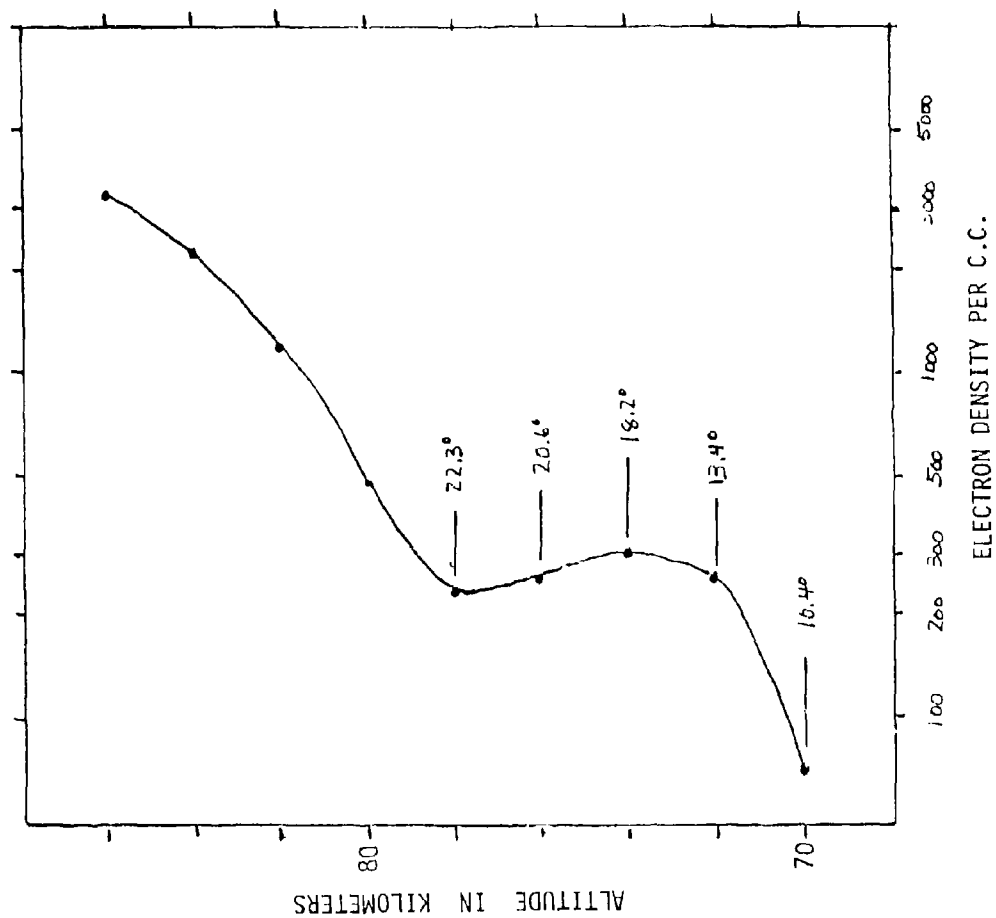
Fig.6   Electron density profile with measured values of $\theta_\frac{1}{2}$ for X wave

$R_0$

$\theta_B$

$\theta_\frac{1}{2}$

5a   $\theta_\frac{1}{2} < \theta_B$

$R_0$

$\theta_B$

$\theta_\frac{1}{2}$

5b   $\theta_\frac{1}{2} > \theta_B$
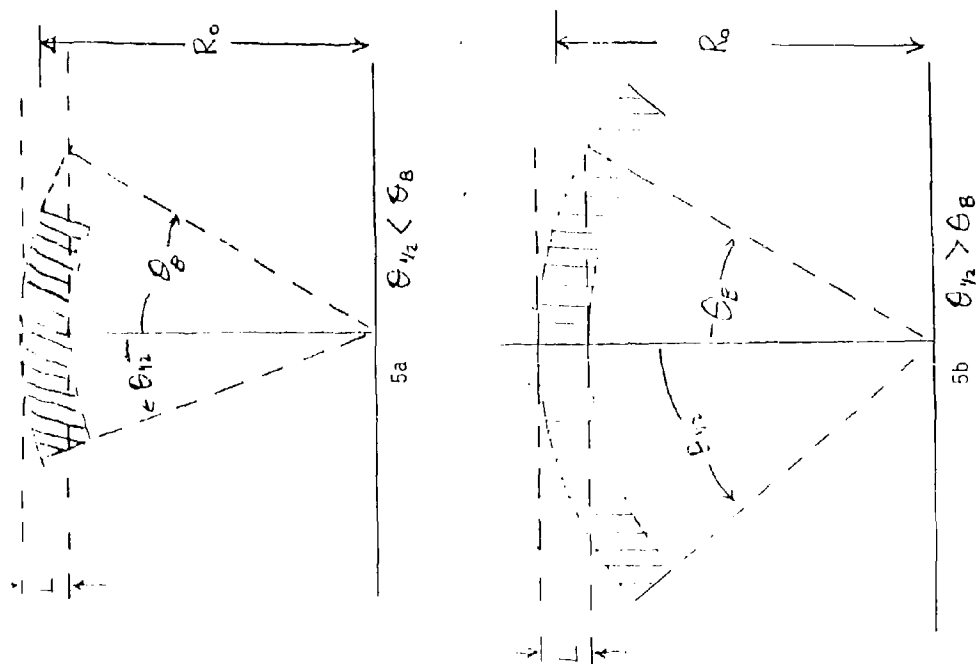
Fig.5   Scattering geometries
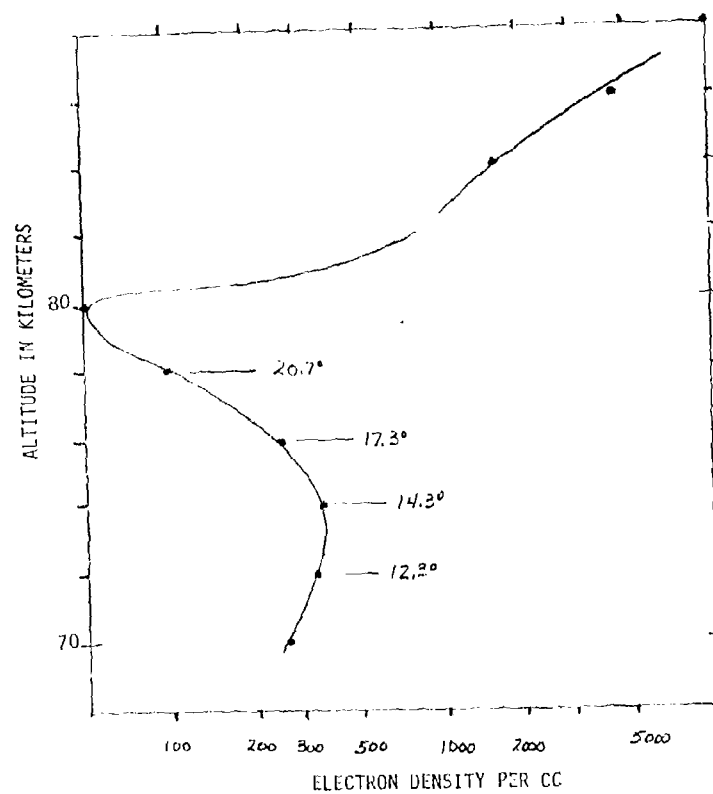
Fig.7   Extreme case of electron density profile minimum with measured values of $\theta_{\frac{1}{2}}$ for X wave
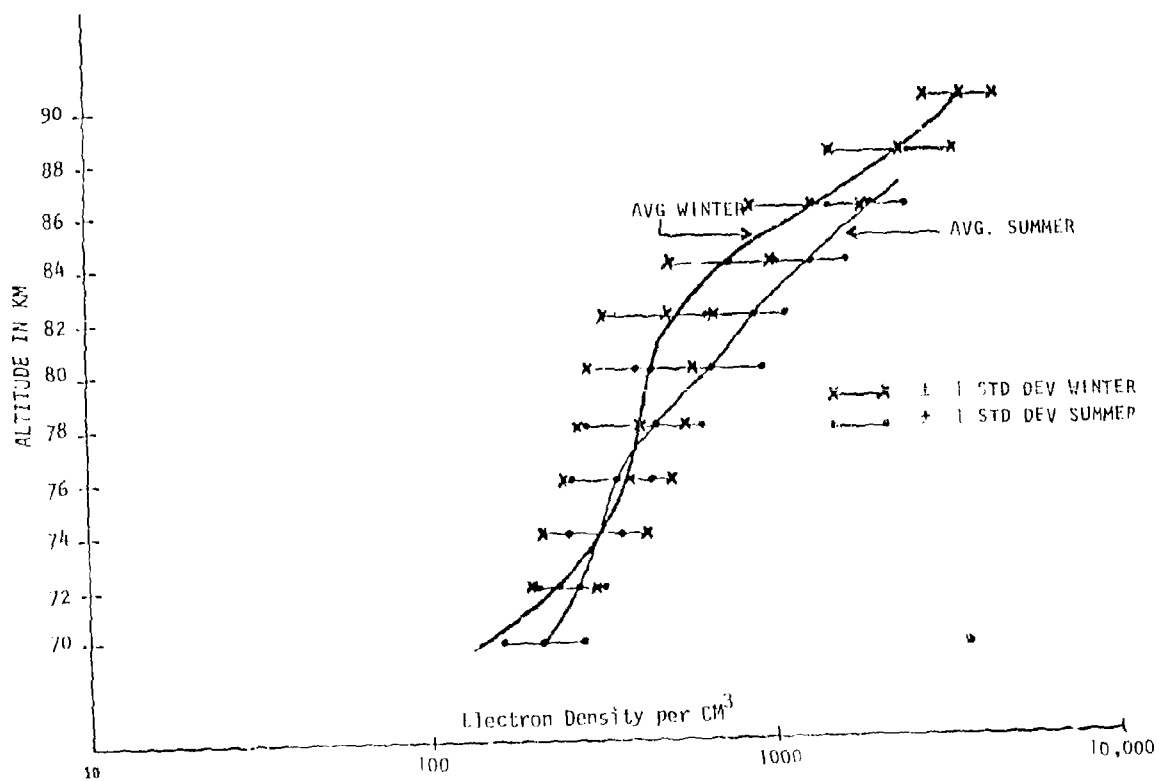


Fig.8   Comparison of average profiles for winter and summer days

ALTITUDE IN KM

x = AVG SPRING NOON
o = AVG FALL NOON

Electron Density per CM$^3$

Fig.9    Equinoctial electron densities



ALTITUDE IN KM

Average Winter Day
├────┤ = x̄ ± 1 σ

⊙  12/31/77
X  1/1/78
△  2/12/78
▢  1/8/77
★  1/9/77
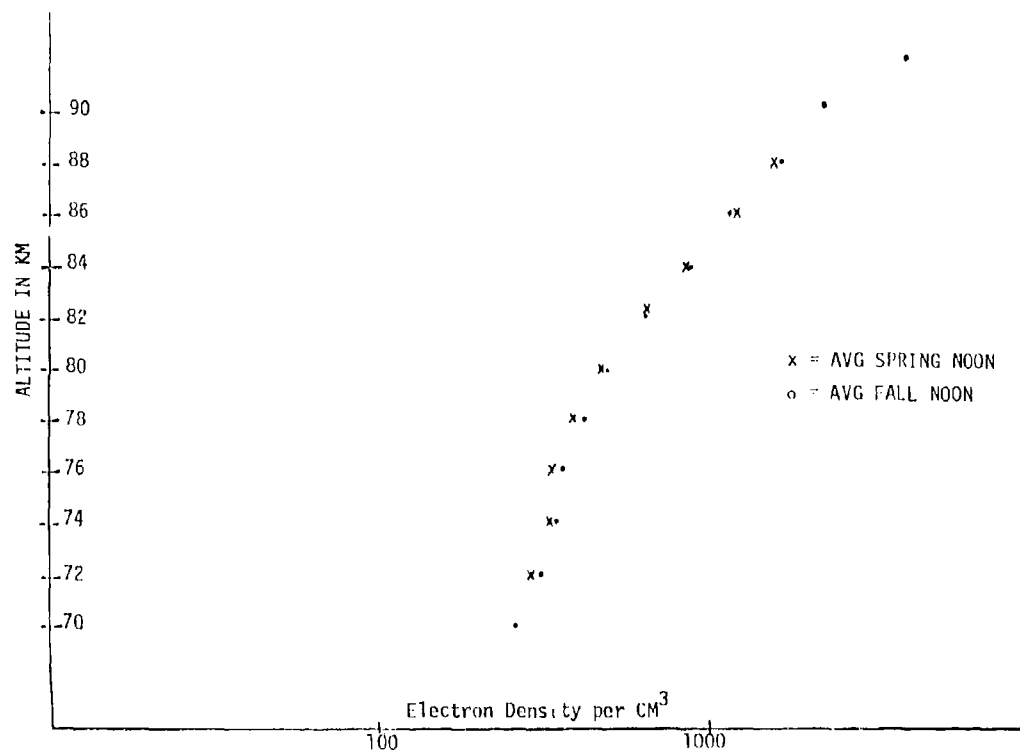
Electron Density per c.c.
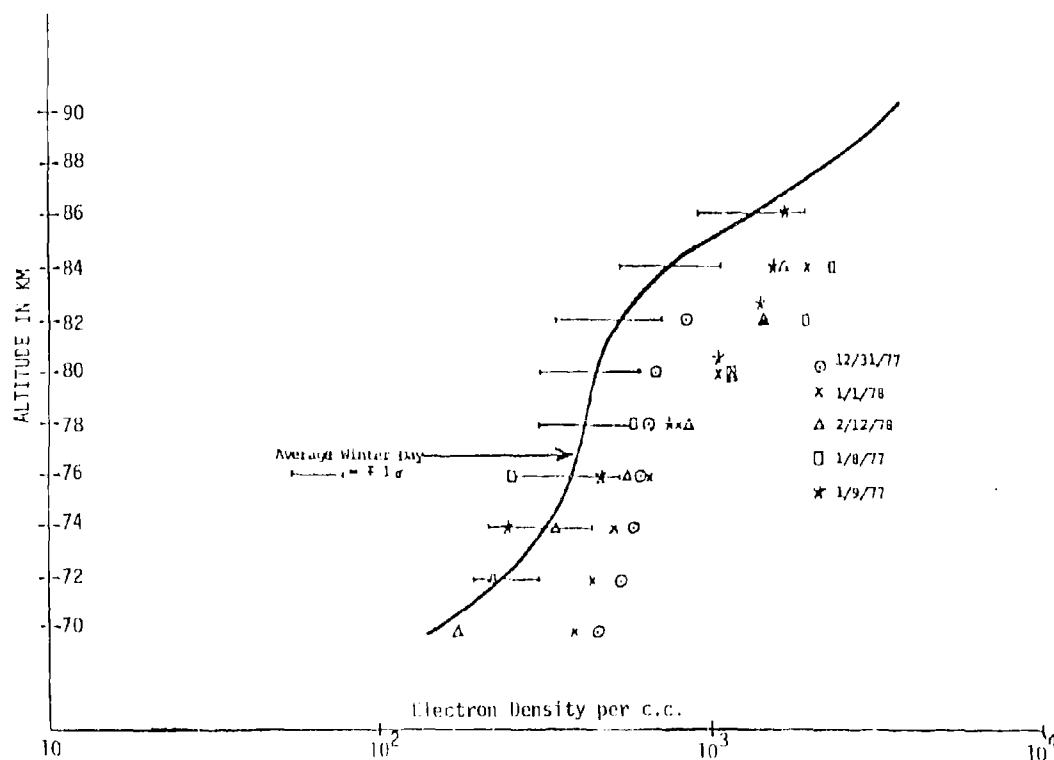
Fig.10    Anomalous winter days

## Appendix A

Following Flood (1980), for angular frequency $\omega$ much greater than the plasma frequency $\omega_p$

$$n_0 = 1 - \frac{\omega_p^2}{2\omega\nu}\left[T_2 + j\frac{5}{2}T_4\right] \tag{A1a}$$

$$n_x = 1 - \frac{\omega_p^2}{2\omega\nu}\left[T_1 + j\frac{5}{2}T_3\right] \tag{A1b}$$

where

$$T_1 = A y_x C_{3/2}(y_x) + B y_0 C_{3/2}(y_0) + D y C_{3/2}(y) \tag{A2a}$$

$$T_2 = A y_0 C_{3/2}(y_0) + B y_x C_{3/2}(y_x) + D y C_{3/2}(y) \tag{A2b}$$

$$T_3 = A C_{5/2}(y_x) + B C_{5/2}(y_0) + D C_{5/2}(y) \tag{A2c}$$

$$T_4 = A C_{5/2}(y_0) + B C_{5/2}(y_x) + D C_{5/2}(y) \tag{A2d}$$

$$A = \cos^2(\phi/2) - \frac{1}{4}\sin^2\phi$$

$$B = \sin^2(\phi/2) - \frac{1}{4}\cos^2\phi$$

$$D = \frac{1}{2}\sin^2(\phi)$$

$\phi$ = angle between the direction of propagation and the magnetic field lines

$$y_x = \frac{\omega - \omega_H}{\nu} \qquad y_0 = \frac{\omega + \omega_H}{\nu} \qquad y =$$

$\omega$ = operating frequency in radians/sec

$\omega_H$ = electron gyro-frequency in radians/sec

$\omega_p^2$ = square of the angular plasma frequency = $\dfrac{Ne^2}{m\varepsilon_0}$

$\nu$ = electron collision frequency $(\text{Sec})^{-1}$

$m$ = electron mass = $9.1 \times 10^{-31}$ kg

$e$ = charge on electron = $1.602 \times 10^{-19}$ coulombs

$\varepsilon_0$ = free space permittivity = $8.854 \times 10^{-12}$ farads/meter

$N$ = electron density (per cubic meter)

$C_p(y)$ = Dingle-Arndt Semi-Conductor Integral

$$C_p(y) = \frac{1}{p!}\int_0^\infty \frac{x^p e^{-x}}{x^2 + y^2}\,dx$$

$\Gamma$ = geomagnetic flux density in Teslas

Finally it can be shown that

$$P(h) = \left\{\frac{T_1^2 + \frac{25}{4}T_3^2}{T_2^2 + \frac{25}{4}T_4^2}\right\}^{1/2} \quad \text{if one can neglect differential absorption within the scattering volume} \tag{A3}$$

# VLF/LF PULSE REFLECTION MEASUREMENTS OF THE POLAR D-REGION
# DURING QUIET AND DISTURBED IONOSPHERIC CONDITIONS

John P. Turtle   John E. Rasmussen   Wayne I. Klemetti   Paul A. Kossey

Propagation Branch, Rome Air Development Center, Hanscom AFB, Ma.   01731

## SUMMARY

This paper describes propagation studies conducted by the U.S. Air Force using a unique short pulse VLF/LF ionosounder to determine the characteristics of the polar D-region during quiet and disturbed conditons.  Data obtained at Thule AB, Greenland, near the center of the polar cap, are presented giving detailed information on the D-regions's height and reflectivity as a function of time.  Under quiet conditions there are marked variations in the D-region due to the effects of diurnal and seasonal changes in solar illumination.  Energetic particle events produce dramatic changes in both the height and reflectivity of the D-region which can exhibit a complex behavior throughout the duration of the event.  The severity of the D-region effects is highly dependent on seasonal illumination conditions.  Data on ionospheric reflectivity are presented to illustrate normal seasonal and diurnal variations.  In addition, data from disturbed periods are presented to show the interaction between propagation parameters and energetic particle ionization, solar ionizing and photodetaching radiations.

## 1.  INTRODUCTION

The propagation of long radio waves is controlled by the lowest regions of the ionosphere. During the daytime this includes the C-layer and the lower D-region and, at night, the lowest part of the E-region.  Observation of changes in the amplitude and phase of VLF/LF signals propagating in the earth-ionosphere waveguide provides a relatively simple ground-based technique for monitoring the state of the lower ionosphere.  The technique has proven to be especially sensitive for detecting ionospheric disturbances, such as those produced by solar x-ray flares, polar cap absorption events (PCA's), and high altitude nuclear detonations.  The observation of continuous-wave (cw) transmissions over very long propagation paths has often been used for such monitoring purposes since such paths provide coverage over very large geographical areas.  A disadvantage of such long path observations is that the effects of relatively localized disturbances (such as energetic particle events in the polar cap) are integrated, or smoothed-out, making it difficult, or impossible, to obtain information on the severity, extent,and structure of the disturbed region of the ionosphere.

Short-path VLF/LF propagation techniques, however, provide data on more localized regions of the ionosphere.  One such technique, developed by the Rome Air Development Center (USAF), is illustrated in Figure 1.  Short VLF/LF pulses (about one rf-cycle at 20 kHz) are radiated from a 130 m vertical antenna, and are received at sites which can be located at various distances from the transmitter.  At the receiver both ground wave and ionospherically reflected sky wave pulses are recorded.  Since the transmitted pulses are so short, less than 100 µs, the sky wave pulses can be observed free from interference with the ground wave pulses, even at distances of several hundred kilometers from the transmitter.  Both the normal (||) and converted (⊥) polarization components of the sky waves can be sensed using orthogonal loop antennas.  Figure 2 gives an example of received waveforms, showing the separation of the ground wave and sky wave pulses.  The received waveforms can be Fourier analyzed to obtain information on the effective reflection heights and the reflection coefficients of the lower ionosphere, over a frequency range from 5 to 35 kHz (Lewis et al., 1973).  As described by Rasmussen et al. (1980), the system, which is essentially a VLF/LF pulse ionosounder, provides a means for studying the reflection properties and structure of the lower ionosphere in the 50 to 90 km altitude range.

This paper describes VLF/LF pulse reflection data obtained in northern Greenland.  The data shown were chosen to illustrate the complex effects of the unique solar illumination conditions in the Arctic on the quiet and disturbed polar ionosphere.  Ionospheric pulse reflection data are described for three solar illumination conditions: (1) day/night, corresponding to periods of the year when the sun rises and sets, such as during March and September ($76° < \chi < 102°$), (2) continuous darkness, such as in December ($\chi > 100°$), and (3) continuous sunlight, such as during the period from May to August ($\chi < 80°$).  The data were obtained over a 106 km path (approximately 90° magnetic azimuth) from Thule Air Base, Greenland (76°33'N, 68°40'W) to Qanaq  Greenland (76°24'N, 69°20'W).

## 2.  VLF/LF PULSE REFLECTION DATA - QUIET POLAR IONOSPHERIC CONDITIONS

Figure 3 shows three-dimensional presentations of pulse ionosounder data obtained under the three solar illumination conditions.  Each of the presentations consists of individual received waveforms stacked one-behind-the-other, with time linearly progressing from bottom-to-top, for a period of one week.  The data are typical for the quiet polar ionosphere as observed on the Thule to Qanaq path.  In Figure 3, each individual waveform is a 30 min average of approximately 650,000 pulses.  The horizontal scale is linear in time (µs), measured from the start of the ground wave.  The ground wave remains fixed in time, while the sky waves move back and forth as the effective ionospheric reflection height changes.  The waveforms represent the instantaneous wave amplitudes as a function of time, as sensed by loop antennas.  The sky wave data corresponds to the normal unconverted component of the ionospherically reflected waves (i.e., the || polarization component). Included with each plot is a representative graph of the diurnal variation in the solar zenith angle. Below each of the three-dimensional plots, are representative 24 hours plots of effective heights of

reflection, and plane wave reflection coefficients for both the normal ( $_{n}R_{\parallel}$ ) and converted ( $_{n}R_{\perp}$ ) sky wave components. The heights of reflection are determined simply from consideration of the relative times of arrival of the ground wave and sky wave pulses, and the geometry of the experiment. The reflection coefficients are derived at 8, 16, and 22 kHz after Fourier analysis of the data (see Lewis et al., 1973).

### 2.1. September ($76° < \chi < 102°$): Day-Night

Figure 3a gives data for a week in September 1976 during which the ionosphere was undisturbed. The data show diurnal patterns resulting from the changing solar illumination. During the night the effective height of reflection for the sky waves was about 90 km, the daytime height was about 78km. Even for the relatively steep incidence angle (about 33°) associated with the Thule data, the nighttime normal polarization reflection coefficients varied typically from about 0.8 at 8 kHz to about 0.5 at 22 kHz. The effective heights of reflection for the converted polarization component of the sky wave were comparable to the normal components throughout the day. The converted reflection coefficients were generally lower but remained relatively constant with the increasing frequency.

### 2.2. December ($\chi > 100°$): Night

Figure 3b shows data acquired over the period of a week in December 1977. During that period, in arctic winter, the sun was far enough below the horizon so that the D-region was not directly illuminated. Thus, as shown in the Figure, the three dimensional display and the reflection heights (about 85 km) and coefficients were essentially constant throughout the week. At Thule, the totally dark period (solar zenith angle $\chi > 100°$) lasts for about one month. It is interesting that VLF/LF pulse ionosounder data acquired over five years showed that the magnitudes of the December reflection coefficients were comparable to those at night in September. However, the December reflection heights were 3 to 4 km lower than those for local midnight in September, or even in June when the D-region is continuously sunlit. The reason for this is not apparent.

### 2.3. June ($\chi < 80°$): Day

At the latitude of Thule, the sun is above the horizon throughout the entire day from early May through the end of August. Even so, as shown by the June 1976 data of Figure 3c, there are still diurnal variations in the effective heights of reflection of the D-region. These heights vary from about 88 km to 75 km depending on the solar zenith angle. Thus, even though the solar zenith angle is below 80° throughout the entire day in June, the D-region ionization produced by Lyman-alpha radiation varies appreciably with the solar zenith angle. As mentioned above, the effective height of reflection at local midnight in June was about 88 km, or approximately 3 km higher than the December-night condition. The heights at local noon in June were about 75 km, the lowest seen throughout the year. The magnitudes of the reflection coefficients were considerably lower in June than at any other time of the year. This suggests that during the summer, the constant solar illumination produces ionization well below 80 km which acts as an absorber of energy from the incident and reflected pulses. Reflections from this ionization are so weak that they cannot be observed with this instrumentation at the relatively steep incidence angle associated with the Thule-Qanaq path.

VLF/LF pulse ionosounder data, such as that illustrated in Figure 3, show that the lower polar ionosphere, even under quiet conditions, exhibits highly variable properties depending on the solar illumination conditions. Other data show that the polar ionosphere is much more dynamic than the mid-latitude ionosphere. In the data derived from the VLF/LF pulse ionosounder, this is clearly seen in the variances associated with the reflection coefficients and reflection heights. The variations are much larger for polar data, than for mid-latitude data, even if only quiet conditions are considered. The ionosounder data also show that the polar ionosphere often experiences changes due to geomagnetic storm activity and precipitation of energetic particles from the sun. These later events, so called Polar Cap Absorption events (PCA's), often cause the polar ionosphere to be severely disturbed for many days, and even weeks. The effects of these disturbances on VLF/LF reflectivity and propagation depend greatly on the solar illumination conditions (or season) as described below.

## 3. VLF/LF PULSE REFLECTIONS, PCA - DISTURBED (PCA) IONOSPHERIC CONDITIONS

The ionosounding path is close to the center of the north polar cap, so that it is ideally suited for observing changes in the reflecting properties of the lower ionosphere due to energetic particle events (Turtle et al.,1980,1981). The effects of PCA's on polar reflection parameters depends on the magnitude of the incoming particle flux and the solar illumination conditions, as illustrated in Figure 4.

Figure 4 shows pulse reflection data acquired during PCA's, under the same three seasonal illumination conditions described in conjunction with Figure 3. Figure 4a shows data acquired in September 1978 when there were light and dark periods during each day; Figure 4b shows data obtained in December 1978 during a period when there was complete darkness; and Figure 4c shows data taken in June 1979 when the sun was always above the horizon. The onsets of the PCA's are clearly seen in all three sets of data, but the data also show that the reflection properties of the disturbed polar ionosphere, from onset through recovery, vary greatly depending on the time of year the events occur.

### 3.1. September ($76° < \chi < 102°$): Day-Night

Figure 5 presents normal polarization reflection data derived from the waveforms of Figure 4a along with corresponding information on the conversion coefficient ( $_{n}R_{\perp}$ ) obtained from waveforms recorded on the orthogonal antenna. This Figure shows the effects of a PCA that occurred in September 1978, when the sun was rising and setting. As seen in the plot of the differential 13 - 25 MeV solar proton data recorded by the IMP 7/8 satellite * (Figure 5d), the onset of the PC

*Particle data obtained from the National Space Science Data Center, Greenbelt, Maryland.

occurred near 1100 UT on September 23 (DAY 266). This PCA was one of the strongest observed (10dB riometer absorption) since the low frequency ionosounder was installed at Thule in 1975.

Before the event, the effective heights of the September ionosphere were varying from 92 km at night to 80 km during daylight hours, as shown in Figure 5a. Shortly after the onset of the PCA, the effective height of reflection dropped to about 51 km. The effects of the PCA were seen in the data until DAY 274, eight days after the onset of the event. The diurnal variation in the reflection heights was smallest on the first day of the event and increased as the incoming particle flux decreased.

The effects of the PCA on the 8 kHz, 16 kHz, and 22 kHz reflection coefficients are shown in Figures 5b and 5c. The magnitudes of both the normal and converted coefficients at these frequencies were generally reduced throughout the duration of the event. The effects on the converted reflection coefficients were especially severe during the daylight hours, as shown in Figure 5c. This indicates that the effects of the geomagnetic field on the reflection processes in the ionosphere below about 70 km were small compared to the electron-neutral collision effects. Even so, the steep incidence data show that the magnetic field effects were not negligible, even during the periods when the effective ionospheric heights were the lowest. However, it is expected that if the observations were made at greater distances from the transmitter (i.e., if the incidence angles on the ionosphere were more grazing), the data would indicate that the disturbed ionosphere could be described phenomenologically as having an almost purely real and isotropic electrical conductivity. It appears that such a simple model would not be appropriate for the relatively steep incidence data shown in Figure 5.

The September 1978 period was one of relatively high solar activity; there were some periods, for example, when the ionosphere was disturbed by PCAs for days at a time, with events following one another and even overlapping. In Figure 5, for example, close inspection of the data shows that a relatively weak event began during DAY 275, less than a day after the ionosphere had fully recovered from the large PCA that began on DAY 266. This small event caused by lower energy protons was not recorded as a PCA by the riometer-absorption indicators. The pulse reflection data show clearly that an energetic particle event did occur, and its effects on VLF/LF ionospheric reflectivity lasted for a number of days. The data demonstrate that VLF/LF propagation parameters are extremely sensitive to the state of the lower ionosphere.

3.2.   December ( $\chi$ > 100°):   Night

Figure 4b shows pulse reflection data typical of that observed during PCA events which occur during periods of continuous darkness at Thule. The onset of the PCA (0.5 dB riometer absorption), seen at approximately 2200 UT on December 11, 1978 (DAY 345), caused the effective reflection height of the ionosphere to drop almost 11 km. This was accompanied by a decrease in the strengths of the reflected sky wave pulses. The recovery of the ionosphere to quiet conditions occurred gradually, over a period of about four days. Some specific details on the effects of the PCA are shown in Figure 6.

Figure 6 shows effective heights of reflection and reflection coefficients derived from the normal and converted polarization data associated with the event shown in Figure 4b. Specific information related to the 8 kHz, 16 kHz and 22 kHz components of the sky waves are described. The onset of the PCA, at approximately 2200 UT, is seen in the plot of 13 - 25 MeV solar proton data (Figure 5d). The solar proton flux data did not return to background (quiet) levels until about four days later.

Figure 6a shows the reflection heights for the normal sky wave at 16.5 kHz over a two week period starting two days before the onset of the PCA. As shown, the undisturbed effective height of reflection before the event was 84 km; during the event, the effective height dropped to as low as 73 km. Similar effects were observed on the 16.5 kHz component of the converted sky wave. It is interesting to note that, although the onset of the PCA was very rapid (as seen in the particle flux data), the onset of the event as seen by the ionosounder was slower, with the peak change in the effective height occurring over a day later. The 11 km drop in the effective height of the ionosphere was about 10 km less than typically observed during other PCA's having similar peak flux levels, which occurred during sunlit conditions at Thule.

Figures 6b and 6c show the normal and converted reflection coefficients, respectively, for 8 kHz, 16 kHz, and 22 kHz, over the same two week period. As shown in Figure 6b, the magnitude of the 8 kHz reflection coefficient was relatively unaffected by the event; however, the 16 kHz and 22 kHz reflection coefficients were reduced about 6 dB during the event. The peak reduction in the coefficients was seen within a few hours of the onset of the event. It is interesting to note that the peak change observed in the effective heights of reflection, however, did not occur until more than a day after the onset of the event. The reflection coefficients and the effective heights of reflection returned to their background, or undisturbed, values closely following the return-to-normal of the particle flux levels, as shown in the Figures.

The data presented in Figure 6 also show the effects of a magnetic storm that followed the PCA. The effects are first seen, in the magnitudes of the reflection coefficients, at about 2400 UT, on DAY 351. As seen in the reflection data, the event lasted three days. Throughout the period slight increases were observed in the effective reflection heights of the normal sky waves. The most pronounced effects, however, were observed in the magnitude of the 22 kHz reflection coefficient which was reduced even more than during the PCA. The manner in which the reflection coefficient data varied with frequency, with a relative null at around 22 kHz, suggests the possibility of two pulse reflections, coming from different ionospheric heights, which interfered to produce the observed pattern (Kossey and Lewis, 1981). From the location of the relative null at 22 kHz, and the incidence angle (38°) associated with the experiment, it is estimated that the interfering reflections came from layers about 14 km apart. One layer at about 84 km would

correspond to the usual effective height observed at Thule in December, the second layer associated with the magnetic disturbance would have been in the E-region at about 98 km.

### 3.3. June ($\chi < 80°$) Day

Figure 7 shows reflection parameters derived from the data in Figure 4c, and illustrates the effects of a PCA (6 dB riometer absorption) that occurred in June 1979 when the sun was continuously above the horizon. Before the onset of the PCA, which began at 0600 UT on June 6 (DAY 157), the effective height of the ionosphere varied from 70 km to 89 km as the solar zenith angle increased. The PCA lowered the effective height to less than 60 km, after which no diurnal variations were seen in the height data until the disturbance effects were over, almost a week later (see Figure 7a). The PCA also suppressed the diurnal effects in the normal and converted reflection coefficients, as shown in Figures 7b and 7c. The reflection coefficient data show significant differences between the two polarization components of the sky waves. During the first two days of the event the magnitudes of the reflection coefficients ($_{\|}R_{\|}$) were larger generally than they were under undisturbed conditions. This suggests that the increased ionization resulting from the event produced a much more sharply bounded reflection layer. As the layer weakened throughout the duration of the event, the reflection coefficients decreased, and by DAY 160 they were actually less than the undisturbed values. Instead of showing an increase the magnitudes of the reflection coefficients of the converted sky wave components ($_{\|}R_{\perp}$) were slightly reduced during the event. This decrease was in accordance with expectations, since the reflections occurred at much lower altitudes, where electron-neutral collisions were relatively large.

On DAY 162, while the ionosphere was recovering, the reflectivity became extremely weak. This effect which was typical of summer events can be seen in Figure 7 where the 22 kHz coefficients were most significantly reduced. Analysis of the data associated with these periods show that such patterns could be caused by the interference of two pulses which were reflected from different layers in the ionosphere, typically about 12 - 14 km apart. This phenomena occurred when the solar zenith angle was relatively large, suggesting that as the solar zenith angle decreased, additional electron production caused the reflections to occur primarily from the lower layer. Whether such ionospheric structure could be observed at more distant receiving locations, or whether the structure would appear at different times during the PCA at such locations is not clear at this time.

### 3.4. February ($89° < \chi < 117°$)

Another example of the complexity of the interaction between solar particles and solar radiation in the ionosphere is illustrated in Figure 8. The Figure shows the effects of a disturbance which occurred in February 1978 during the transition period from night conditions in December to day-night conditions in March. The Figure includes a plot of solar zenith angle showing that at local noon the sun just barely reached the horizon at Thule. The disturbed waveforms, presented in Figure 8b shows the effects of a PCA (6 dB riometer absorption) which began at about 1000 UT on February 13 (DAY 044). This event caused a 28 km drop in noontime reflection height, followed by a gradual return to normal over the next 7 days. Even at night during the first day of the event the reflection height remained below 60 km due to the continued high particle flux rate. For the next several days, however, there was a strong diurnal variation which was not present before or after the event. This variation was probably caused by a combination of particle produced ionization with varying photodetachment and attachment processes. As the sun approached the horizon photodetachment produced increased electron densities, lowering the reflection heights. After local noon, as the solar zenith angle increased, the effective reflection heights increased due to attachment. This type of ionospheric behavior during disturbances is only seen in the pulse ionosounding data for the particular solar illumination conditions which occur at Thule in late January and early February and again in November and early December.

### 4. DISCUSSION

VLF/LF pulse reflection data show that there are marked variations in the lower polar ionosphere due to the effects of diurnal and seasonal changes in solar illumination. These variations differ significantly from those observed at mid- and low-geomagnetic latitudes, even under quiet ionospheric conditions. The data also show that energetic particle events (PCA's) produce dramatic changes in both the effective height and reflectivity of the D-region. The manner in which the disturbances effect the VLF/LF reflectivity of the D-region is highly dependent on the illumination conditions. The steep incidence data described in this report show that the disturbance effects can last for as long as a week or more, and that throughout such periods the effects can vary considerably from day-to-day. The data also reveal that there can be complex structure (layering) within the disturbed ionosphere itself. The data indicate the difficulty in specifying models of the lower polar ionosphere, particularly for disturbed conditions. Such models would not only be highly dependent on the particle flux associated with the disturbance, but also on the time of year (season) in which it occurred. Moreover, the models would necessarily have to be adjusted throughout the duration of the disturbance to account for the changing illumination conditions and the changing energetic particle fluxes.

An attempt was made to determine if the lowest heights of reflection observed during PCA's could be used to obtain estimates of the peak particle fluxes (13 - 25 MeV) associated with the events. Figure 9 shows the results of that study. In the Figure the points on the diagram correspond to the lowest effective 16 kHz heights observed with the VLF/LF ionosounder during an individual PCA, along with the peak particle flux measured for the event. Best exponential fits to the data are shown, also, by the dotted lines. The 'Day' line is for PCA's that occurred when there were some sunlit hours during the disturbances. The 'Night' line (which was obtained from only two data samples) corresponds to events that occurred during periods when the sun was always

below the horizon. Although there is some spread in the data, Figure 9 shows that estimates of the peak particle fluxes can be obtained from the pulse ionosounder reflection height data. It is interesting to note that energetic particle events are usually categorized in terms of the riometer absorption that accompany them. For example, a PCA would be termed 'strong' if the riometer absorption associated with it was 10 dB, but it would be considered 'weak' if the absorption was only 1 dB. A peak 13 - 25 MeV particle flux of about 0.2 - 0.3 particles/cm$^2$ sec sr MeV is not uncommon for 'weak' events. Figure 9 shows that during such events the VLF/LF reflection heights may be as low as about 62 - 64 km, during daylight hours at Thule. These heights would be 12 km lower that those observed during undisturbed ionospheric conditions. Events having one-tenth the particle flux still produce noticeable effects in the ionosounder data. The data illustrate that the observation of VLF/LF signals is an extremely sensitive ground-based technique for monitoring ionospheric disturbances.

Steep incidence VLF/LF pulse reflection data provide relatively direct information on the characteristics and variability of the polar D-region. Long path observations of VLF/LF signals that cross the polar region also provide useful information on the state of the high latitude ionosphere. However, since the polar region may constitute only a relatively small part of such paths, it may be difficult to distinguish clearly the effects of the polar ionosphere on the propagating signals, from those produced on other parts of the paths. The consideration of both long path and short path VLF/LF data, jointly, may provide an effective means for determining useful phenomenological models of the polar ionosphere for use with long wave propagation predictions.

5. REFERENCES

Kossey, P.A., and E.A. Lewis (1981) The Reflection Properties of Conducting Slabs, Rome Air Development Center Technical Report 80-371.

Lewis, E.A., J.E. Rasmussen, and P.A. Kossey (1973) Measurements of Ionospheric Reflectivity from 6 to 35 kHz, J. Geophys. Res., 78, p. 3903-3912.

Rasmussen, J.E., P.A. Kossey, and E.A. Lewis (1980) Evidence of an Ionospheric Reflecting Layer Below the Classical D-Region, J.Geophys. Res., 85, p. 3037-3044.

Turtle, J.P., J.E. Rasmussen, and W.I. Klemetti (1980) Effects of Energetic Particle Events on VLF/-LF Propagation Parameters, 1974-1977, Rome Air Development Center Technical Report 80-307.

Turtle, J.P., J.E. Rasmussen, and W.I. Klemetti (1981) Effects of Energetic Particle Events on VLF/-LF Propagation Parameters, 1978, Rome Air Development Center Technical Report 81-82.
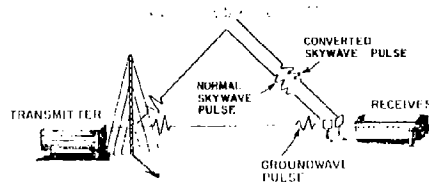
FIGURE 1. Illustration of VLF/LF pulse ionosounding technique.
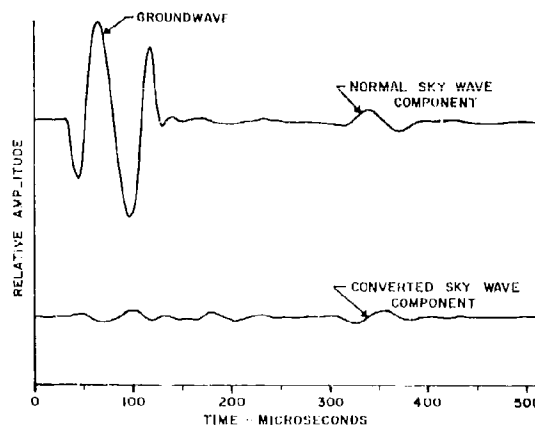
FIGURE 2. Example of received pulse ionosounding waveforms.
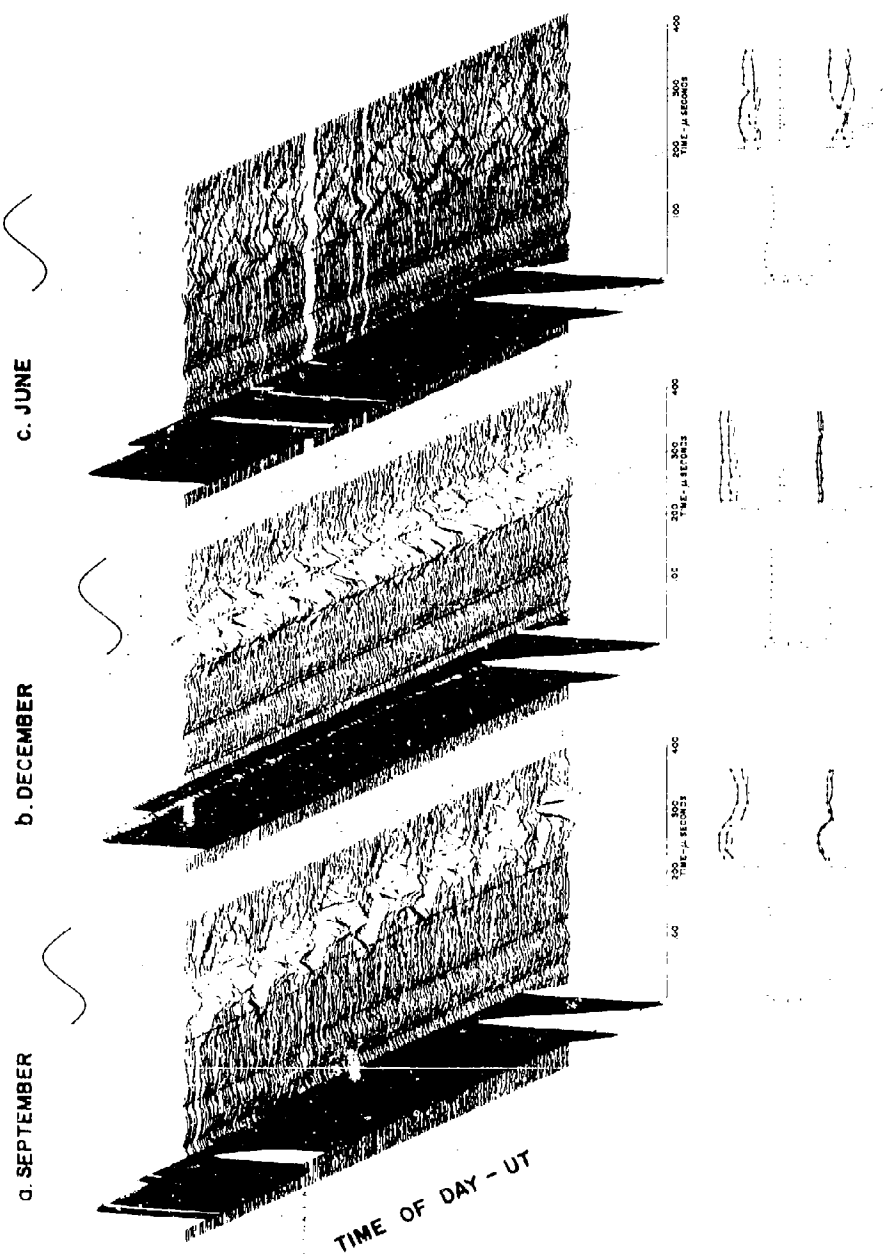
FIGURE 3. Ionosounder waveforms and reflection parameters for undisturbed conditions in September (a), December (b), and June (c). Plots of diurnal solar zenith angle are shown for each season.

TIME OF DAY - UT

a. SEPTEMBER

b. DECEMBER

c. JUNE

a. SEPTEMBER

b. DECEMBER

c. JUNE

TIME OF DAY - UT
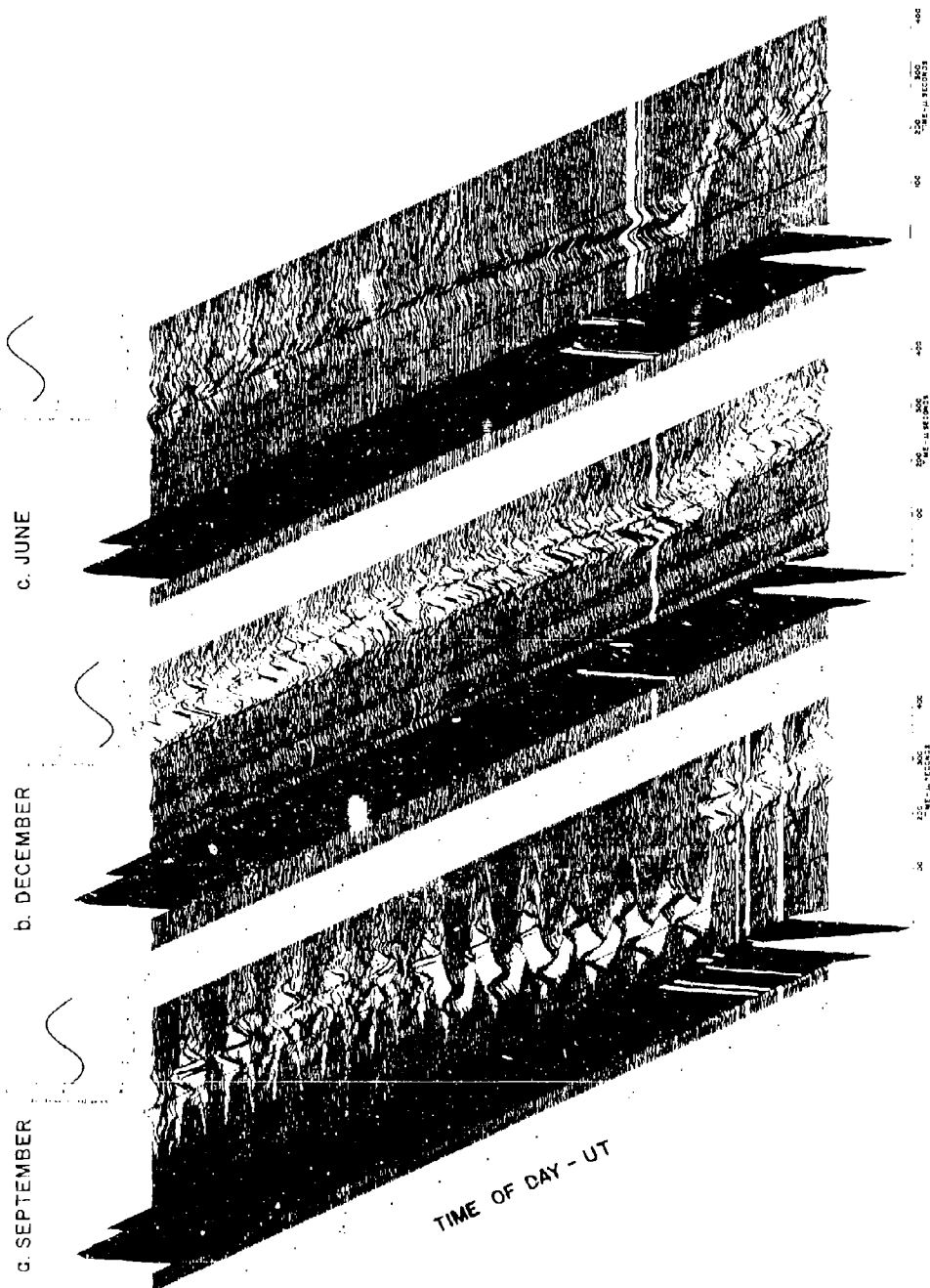
FIGURE 4. Ionosounder waveforms for disturbed conditions in September (a), December (b), and June (c). Plots of diurnal solar zenith angle are shown for each season.
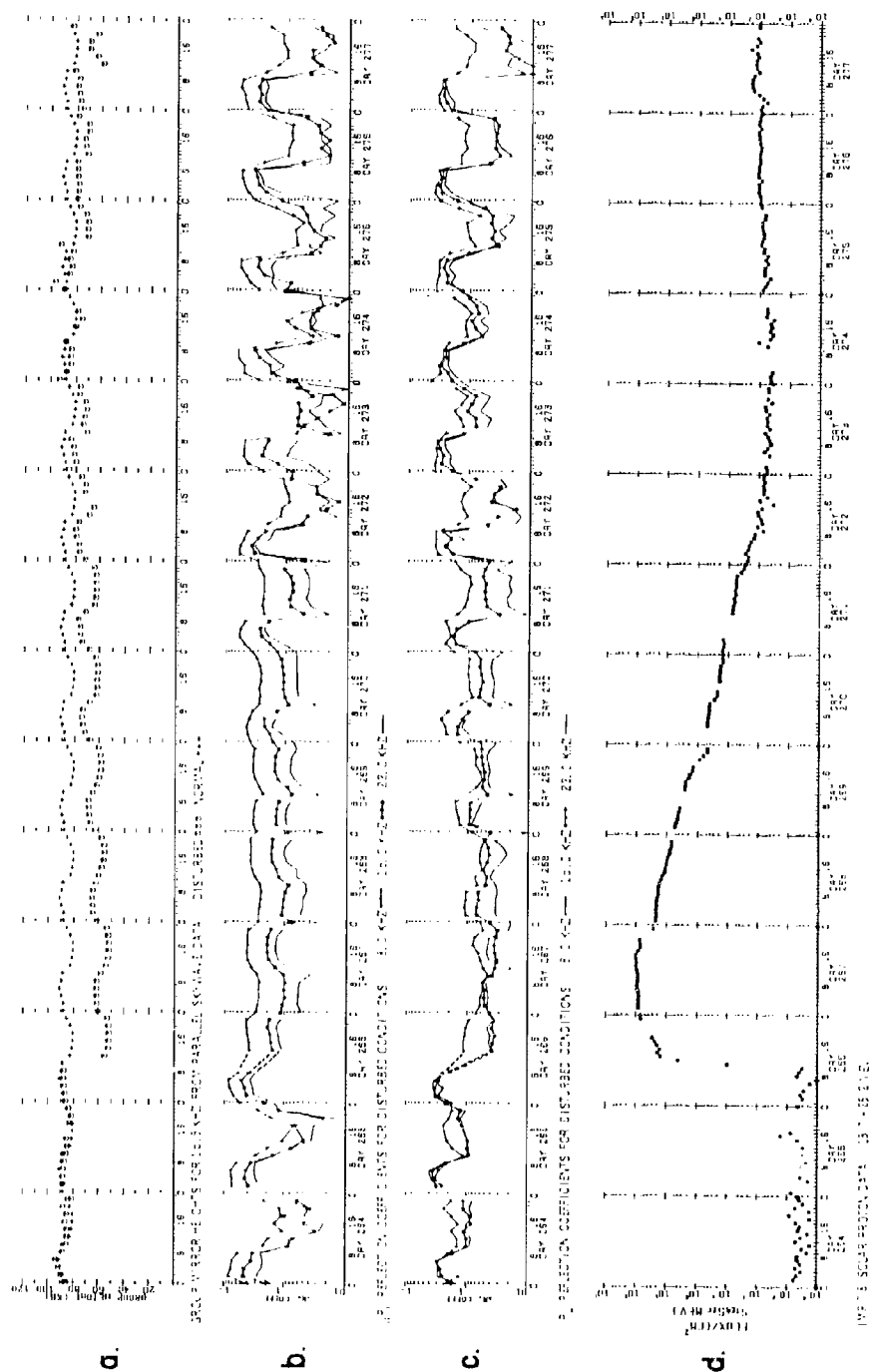
FIGURE 5. Reflection heights and coefficients with satellite proton data for September 23, 1978 (DAY 266) solar particle event.
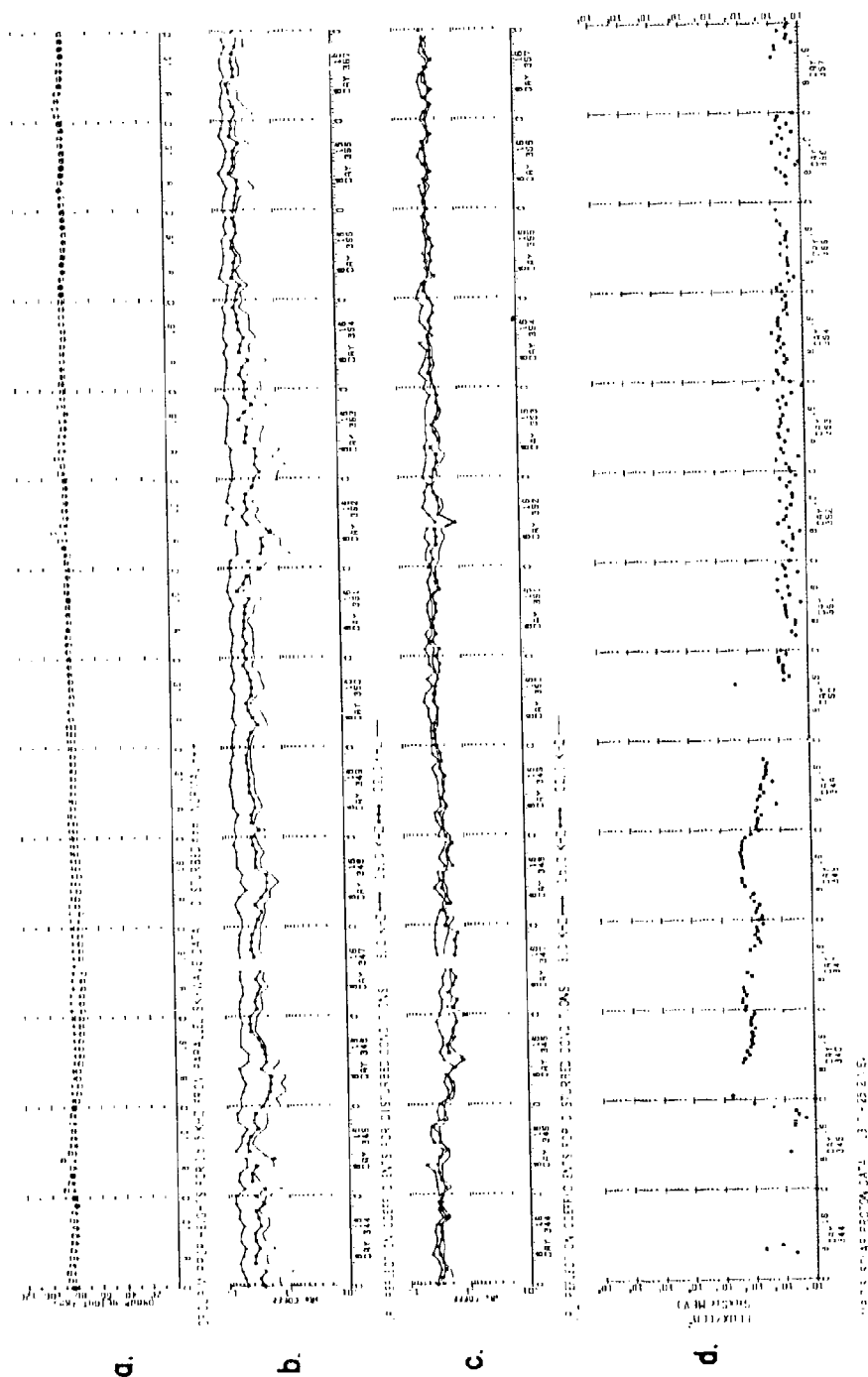
FIGURE 6. Reflection heights and coefficients with satellite proton data for December 11, 1978 (DAY 345) solar particle event.

3-10
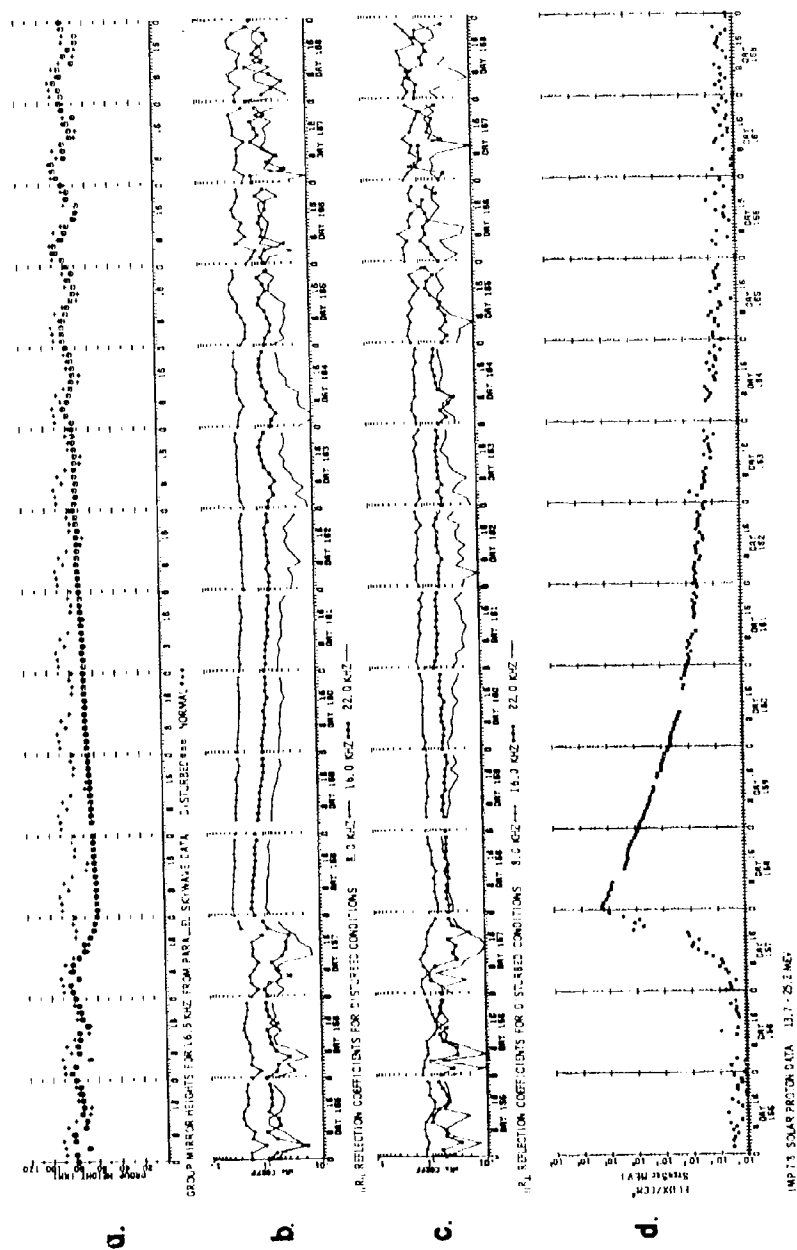


FIGURE 7. Reflection heights and coefficients with satellite proton data for June 6, 1979 (DAY 157) solar particle event.
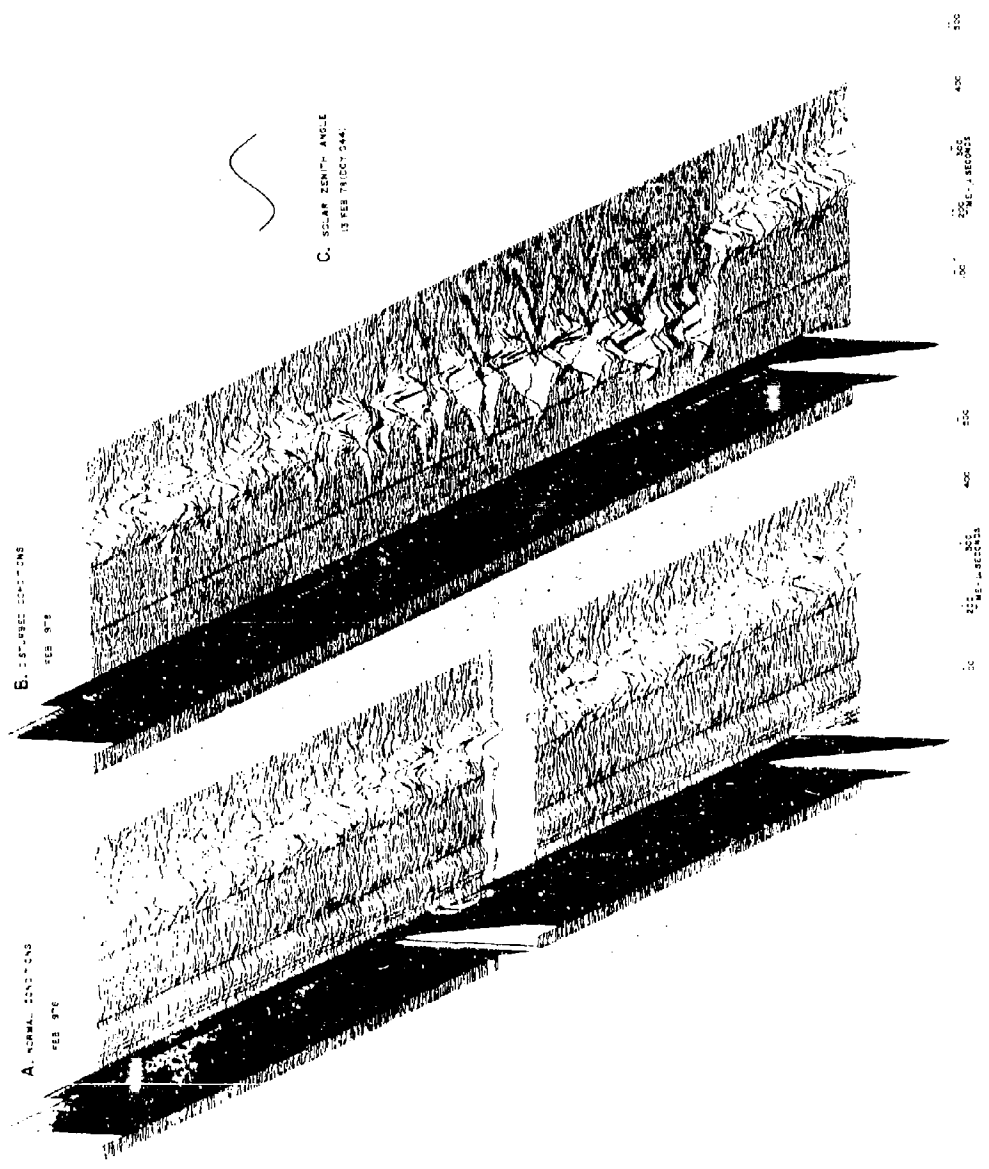
FIGURE 3.  Transponder waveforms for undisturbed conditions in February 1976 and disturbed conditions
in February 1976. Diurnal solar zenith angle curve is shown for February.
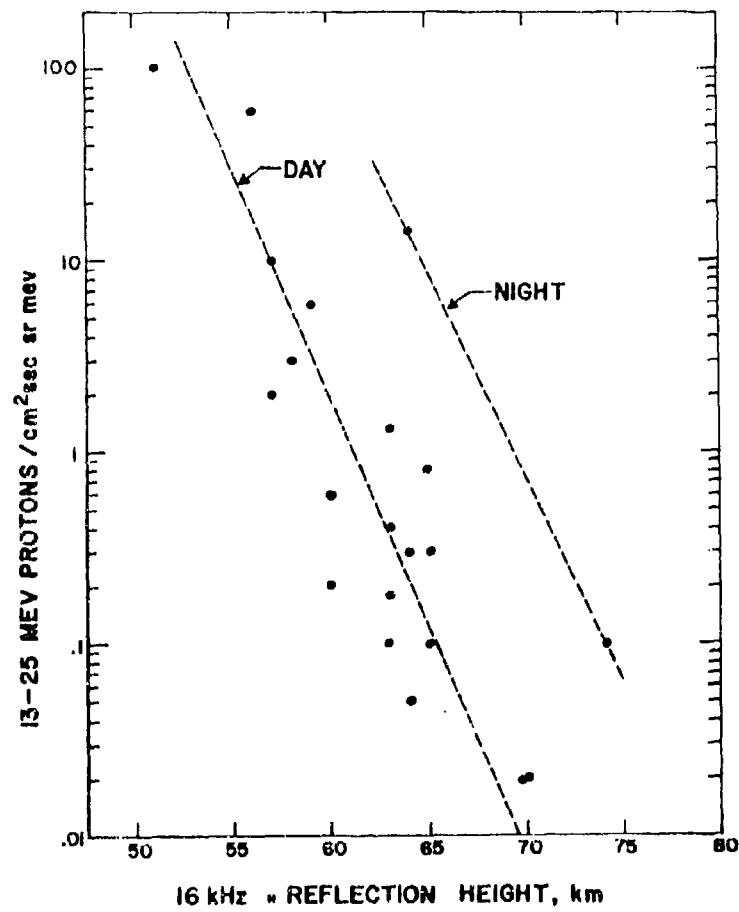
FIGURE 9. Relationship between minimum disturbed 16 kHz reflection heights and 13 - 25 MeV proton flux.

# THE INFLUENCE OF PRECIPITATING ENERGETIC
## PARTICLES ON THE PROPAGATION MEDIUM

W. L. Imhof, R. C. Gunton, J. B. Reagan
R. E. Meyerott, and E. E. Gaines

Lockheed Palo Alto Research Laboratory
Palo Alto, California 94304

and

T. R. Larsen

Norwegian Defence Research Establishment
Kjeller, Norway

## ABSTRACT

From a long term base of satellite measurements with Lockheed payloads, studies have been made of the influence of energetic particle precipitation on the ionosphere at altitudes of importance to long wave propagation. Large enhancements in the electron concentrations in the stratosphere and mesosphere may occur during major solar particle events and also at times of relativistic electron precipitation. Previous studies have shown that direct particle precipitation into the atmosphere can cause VLF and ELF transmission anomalies, but the effects depend in a complex manner on the altitude profiles of ionization,and on the location along the propagation path. Precipitating electrons may often produce large rates of ionization down to altitudes as low as 50 km through direct penetration and weaker but significant ionization down to ~ 20 km through action of the bremsstrahlung produced at higher altitudes. Major solar particle events may cause intense ionization down to altitudes of ~ 20 km. Measurements of the precipitating particles with electron/proton spectrometers and also with bremsstrahlung x ray sensors from several satellites during the 1971-1980 time frame provide the basis for studying the morphology of the propagation medium as related to long-wave signal transmission. From the measured fluxes, energy spectra, and pitch-angle distributions of the particles, ion-pair production profiles are calculated and electron density profiles subsequently obtained with application of effective electron loss rates. The temporal, latitude, longitude, and altitude variations associated with electron precipitation and with major solar particle events will be summarized along with calculations of their effects on ELF propagation. Particular use is made of the nearly simultaneous worldwide measurements of electron precipitation performed via the newly developed satellite bremsstrahlung x-ray technique.

## 1. INTRODUCTION

In 1976 it was established for the first time that anomalous ELF signal propagation strengths can result from the precipitation of energetic particles into the atmosphere (Imhof et al., 1976). Subsequent studies have provided further verification of the importance of this phenomenon to ELF transmission. At VLF frequencies it has been found that electron precipitation can cause long-lived phase disturbances (Larsen et al., 1977; Kikuchi and Evans, 1981). Since particle precipitation clearly plays a significant role in signal transmission it is important for workers in the field to be aware of the morphology of energetic particle precipitation into the atmosphere. The purpose of this paper is to briefly summarize the temporal, latitude, longitude, and altitude variations associated with such precipitation.

In addition to cosmic rays, which are continually impinging on the atmosphere, the primary types of energetic particle precipitation can be classified into the following two groups: (1) electrons of magnetospheric origin and (2) energetic particles associated with solar activity. Each of these categories of precipitation displays a very wide range of intensities, energy spectra, and spatial extents so it is not possible to summarize their characteristics in a simple manner. The matter is further complicated by the lack of comprehensive measurements on a worldwide scale. For example, electron precipitation patterns are so complex and time variable that measurements with a single spectrometer on a satellite do not provide adequate spatial mappings for many purposes and the new remote sensing technique of bremsstrahlung x-ray imaging is needed for quantitative measurement of worldwide patterns of electron precipitation (Imhof et al., 1974).

This review is not intended to be fully comprehensive, but is primarily to provide the reader with an indication of the effectiveness of particle precipitation over different regions of the earth. For magnetospheric electron precipitation the temporal variations in the total inputs over a large area are discussed and the latitude structures given along with spectral variations. Examples of the energy deposition profiles in the atmosphere are also presented with special attention devoted to the stronger events. For solar particle events the spatial extents are discussed with emphasis on the variations in the latitude cutoffs. The distributions of fluxes are indicated along with examples of major events, such as those in August 1972.

## 2. MAGNETOSPHERIC ELECTRON PRECIPITATION

At high latitudes energetic electrons are almost continually precipitating into the atmosphere producing a significant ionization at mesospheric altitudes. Although electron precipitation is an almost continual process, at any given time the precipitating fluxes and energy spectra may be quite structured and varied with latitude (Imhof et al., 1976). Our present knowledge of electron precipitation processes on a worldwide scale is quite limited. Direct measurements from a satellite of precipitating electrons do not provide adequate spatial and temporal coverage. Only with remote sensing techniques can simultaneous mappings of electron precipitation be obtained and in this regard optical

observations provide only limited spectral information and are primarily representative of the lower energy electrons. Bremsstrahlung x-ray measurements from a satellite can provide both intensity and spectral information over a broad range of energies, but to date such observations have been quite limited in number and extent. Here we present a brief summary of the present knowledge of electron precipitation processes at high latitudes.

For measurements of electron precipitation averaged over a large area of the earth the satellite bremsstrahlung x-ray technique is ideally suited. To investigate the dependence of electron precipitation upon geomagnetic activity, the bremsstrahlung x-ray intensities have been taken from 730 passes of a low altitude polar orbiting satellite across the trapping boundary (Imhof et al., 1980). These measurements, taken in a standard geometry, encompass a large area of the atmosphere including the high latitude regions of electron precipitation. The net counting rates from bremsstrahlung x-rays in the energy interval 50-500 keV (after subtraction of local backgrounds associated with the spectrometer and satellite) are plotted in Figure 1 as a function of the geomagnetic index AE. The magnetic local time intervals for electron precipitation encompassed by these presentations are quite broad; the x-ray spectrometer typically viewed a region of the atmosphere spanning an MLT interval of 5-6 hours or some 75° to 90° in longitude. For each of several selected intervals in AE, bars are drawn to indicate median flux levels. The net intensities above the atmospheric and cosmic gamma ray background were generally higher at larger values of the AE index but wide variations in this pattern were observed. For AE > 800 the average flux was a factor of ~ 100 higher than when the index was below 40.

The duration of individual electron precipitation events is an important parameter for describing the morphology of electron precipitation. The time persistence of the total electron precipitation occurring over a wide local time and latitude interval can be studied by considering the x-ray fluxes measured on successive passes of the satellite over the polar cap regions. In Figure 2 the x-ray intensities measured on a second pass are plotted as a function of the flux levels observed on an earlier pass. The noon-noon and midnight-midnight pairs of passes are plotted separately in the right hand section. Some degree of correlation clearly exists between successive passes at nearly the same local time, but there is by no means a one-to-one correspondence. In contrast, there appears to be no significant correlation for successive passes differing by ~ 12 hours in local time. In summary: the time correlation coefficients between pairs of x-ray measurements were significant for delay times of ~ 40 minutes if both members of the pair were either near midnight or noon, but for noon-midnight or midnight-noon pairs the correlations were not significant even at delay times as short as ~ 20 minutes. Clearly, there is a general lack of simultaneous electron precipitation in the noon and midnight sectors.

Energetic electron precipitation at high latitudes is typically characterized by dynamic variations with latitude, longitude and time. The data presented in Figure 3 illustrate the sharp structure that is often encountered and show that major variations in the profiles of flux versus L shell occur even when the longitude and time differences are small. This fine scale structure may or may not be important for ELF/VLF propagation, but in any case one should be aware of the regularity of its appearance.

Although the fine scale temporal and spatial structure in electron precipitation may be of less importance for some wave transmission considerations, the broad scale features are significant. Based on recent data acquired from a low altitude polar orbiting satellite the average noon and midnight latitude profiles have been derived and are presented in Figure 4. These plots are based on nine passes of the satellite for both geomagnetically quiet and disturbed conditions.

From the standpoint of atmospheric effects the energy spectra represent a very important parameter associated with magnetospheric electron precipitation since the energy determines the altitude to which an electron may penetrate into the atmosphere. During electron precipitation events, a wide variety of spectral shapes are known to occur. In some events the spectra extend to relativistic energies and accordingly they are known as Relativistic Electron Precipitation (REP) events.

Examples of the energy spectra of precipitating electrons during some very intense events are shown in Figure 5. Based on these energy spectra, deposition profiles in the atmosphere have been calculated with the computer program, AURORA, (Walt et al., 1968; Walt and Chappel, 1968) taking into account the energy deposited by the bremsstrahlung x-rays produced in the atmosphere by the precipitating electrons. The corresponding ion-pair production profiles are shown in Figure 6. These precipitating electron measurements were taken during a coordinated exercise between ELF transmissi    from the Wisconsin Test Facility (WTF) to receivers at various locations and simultaneous measureme    rom the P72-1 polar orbiting satellite containing a payload of energetic particle spectrometers. This coordinated data set encompassed periods of major geomagnetic disturbance and moderately intense electron precipitation. In all of the examples there is strong ionization at altitudes above ~ 60 km but only during the most intense and hard events does the ionization extend down to 50 km and lower. For the event at 0602 UT on 26 March 1976 the ELF transmission strengths to several receiving stations have been calculated using the waveguide model computer program developed at the Naval Ocean Systems Center (NOSC) (Pappert and Moler, 1974), and the results of these calculations are summarized in Table 1. One can see that signal enhancements are predicted for the receivers at each of the stations. The trend for obtaining enhanced signal strengths during intense auroral zone precipitation of the type often observed is consistent with the measured increase in signal levels. The signal strengths clearly depend upon the details of the ionization profiles along the path and emphasize the need for obtaining complete mappings of electron precipitation.

Table 1.  Comparison of Predicted and Measured ELF Field Strengths for the REP
Event of 26 March 1976.

|  | ELF Field Strengths at 75 Hz during event | | Change in Field Strength during event | |
|---|---|---|---|---|
|  | Predicted (dB wrt 1 A/M) | Measured (dB wrt 1 A/m) | Predicted (dB) | Measured (dB) |
| Connecticut, USA | −143.3 | no meas. | +1.9 | no meas. |
| Maryland, USA | −147.3 | −147.2 | +0.6 | 0.0 |
| Thule, Greenland | −151.3 | −155.0 | +1.0 | +0.5 |
| Tromso, Norway | −153.6 | −155.2 | +1.1 | +2.0 |
| Pisa, Italy | −152.3 | −154.7 | +1.7 | +3.2 |

## 3. PRECIPITATION DURING SOLAR PARTICLE EVENTS

At times of certain solar flares energetic particles are emitted from the sun and these may have good access to the earth's atmosphere over the northern and southern polar caps. When the proton energies extend above a hundred Mev they can produce intense ionization in the atmosphere down to altitudes as low as ~ 20 km. During some solar particle events energetic electrons are also produced but their intensities are usually lower than those of the protons and they generally do not penetrate to such low altitudes. The solar particle access over the polar caps usually extends down to magnetic latitudes somewhere in the range ~ 55° to ~ 65°, generally being lower during times of high geomagnetic activity. Over the polar caps the incident fluxes are much more uniform in space than is generally the case with magnetospheric electron precipitation events. Structure in the spatial distribution may occur, however, and sometimes pronounced north-south asymmetries appear.

The lower latitude cutoffs of proton precipitation during solar particle events have been studied systematically and compared with geomagnetic activity levels (Imhof et al., 1971). In Figure 7 the proton cutoff latitude is plotted as a function of the Kp index. The Kp index certainly does not uniquely determine the cutoff latitude but clearly at times of high geomagnetic activity the cutoff latitudes are lower and a larger polar cap area can be irradiated with solar particles. For certain transmitter-receiver paths such as that from the Wisconsin Test Facility to Tromso the cutoff latitude can have a big effect on the signal transmission strengths. Of particular importance to the signal strengths may be the matter as to whether a transmitter or receiver is located within or outside of the area of irradiation by the solar particles.

The fluxes of energetic particles associated with solar particle events cover a very wide dynamic range. This variability is illustrated in Figure 8 where the total flux for each of the events in the last two solar cycles is plotted at its time of occurrence. Overall there is a trend for greater fluxes to occur near the time of solar maximum in the 11 year cycle, but the data indicate very large deviations from any systematic pattern. The variations are so great that most of the total proton fluence encountered during a solar cycle may appear in only one or two events.

The ion pair production rates produced by solar protons during the major particle events in solar cycles 19 and 20 are shown in Figure 9. The 4 August 1972 event dominates in ion production rate over all of the other events in cycles 19 and 20 at altitudes above 26 km. For comparison, the cosmic ray ionization for solar maximum and minimum is also shown. Clearly, the ionization produced by these major events exceeds that normally produced by cosmic rays by several orders of magnitude.

## 4. SUMMARY

Magnetospheric electron precipitation events are much more common than solar particle events, but they are more localized and do not produce intense ionization below altitudes of ~ 50 km. By producing bremsstrahlung x-rays electron precipitation events can cause ionization down to ~ 20 km but the levels are generally rather low. Measurements of ELF and VLF signals have been made at times of major electron precipitation events, so their importance in affecting the transmissions has been established. However, since the electron precipitation patterns are generally complex and proper mapping measurements with bremsstrahlung x-rays have yet to be made at such times our present knowledge in this area is far from complete.

Solar particle events are much less common than electron precipitation events but when they do occur they can be very effective over an extremely large area and down to altitudes as low as ~20 km. The relatively uniform incidence over a large area provides many advantages for studying in detail the effects on ELF/VLF wave propagation. However, it should be emphasized that at present there are no known cases where ELF signal strength measurements were made at the time of a major solar particle event.

## REFERENCES

Imhof, W. L., J. B. Reagan, and E. E. Gaines, "Solar Particle Cutoffs as Observed at Low Altitudes," J. Geophys. Res., 76, 4276, 1971.

Imhof, W. L., G. H. Nakano, R. G. Johnson, and J. B. Reagan, Satellite observations of bremsstrahlung from widespread energetic electron precipitation events, J. Geophys. Rees., 79, 565, 1974.

Imhof, W. L., T. R. Larsen, J. B. Reagan, and E. E. Gaines, "Ananlysis of Satellite Data on Precipitating Particles in Coordination with ELF Propagation Anomalies," Annual Report on Contract N00014-75-C-0954, covering the period ending 14 March 1976, Lockheed Report No. LMSC/D502063, April 1976.

Imhof, W. L., T. R. Larsen, J. B. Reagan, and E. E. Gaines, "Analysis of Satellite Data on Precipitating Particles in Coordination with Propagation Anomalies", Lockheed Report No. LMSC/D560323, June 1977.

Imhof, W. L., K. W. Nightingale, J. B. Reagan, and G. H. Nakano, "The Morphology of Widespread Electron Precipitation at High Latitudes," J. Atmos. Terr. Phys., 42, 443, 1980.

Kikuchi, J. and D. S. Evans, "VLF Phase Anomalies due to Energetic Electron Precipitation Associated with Substorms" EOS, Trans. Am. Geophys. Union, 62, 366, 1981.

King, J. H., "Solar Proton Influences for 1977-1983 Space Missions", J. Spacecrafts and Rockets, 11, 401, 1974.

Larsen, T. R., W. L. Imhof, and J. B. Reagan, "L-Dependent Energetic Electron Precipitation and Mid-Latitude D-Region Ion Pair Production Profiles," J. Geophys. Res., 81, 3444, 1976.

Larsen, T. R., T. A. Potemra, W. L. Imhof, and J. B. Reagan, "Energetic Electron Precipitation and VLF Phase Disturbances at Middle Latitudes Following the Magnetic Storm of December 16, 1971," J. Geophys. Res., 82, 1519, 1977.

Pappert, R. A., and W. F. Moler, "Propagation Theory and Calculations at Lower (ELF) Extremely Low Frequencies," IEEE Trans. Comm., Vol. COM-22 No. 4, 438-451, April 1974.

Reagan, J. B., R. W. Nightingale, R. E. Meyerott, R. C. Gunton, R. G. Johnson, J. E. Evans, and W. L. Imhof, "Effects of the August 1972 Solar Particle Events on Stratospheric Ozone," Lockheed Report No. LMSC/D650455, October, 1978.

Reagan, J. B., R. E. Meyerott, R. W. Nightingale, R. C. Gunton, R. G. Johnson, J.E. Evans, W. L. Imhof, D. F. Heath, and A. J. Krueger, "Effects of the August 1972 Solar Particle Events on Stratospheric Ozone," J. Geophys. Res., 86, 1473, 1981.

Walt, M., and C. R. Chappell, "Penetration of Particles into the Atmosphere, in Atmospheric Emissions," B. M. McCormac and A. Omholt, eds., Van Nostrand Reinhold Co., New York, New York, 245, 1968.

Walt, M., W. M. McDonald, and W. E. Francis," Penetration of Auroral Electrons into the Atmosphere", in Physics of the Magnetosphere, R. Carovillano and J. F. McClay, eds., Reinhold Publishing Co., New York, New York, 534, 1968.
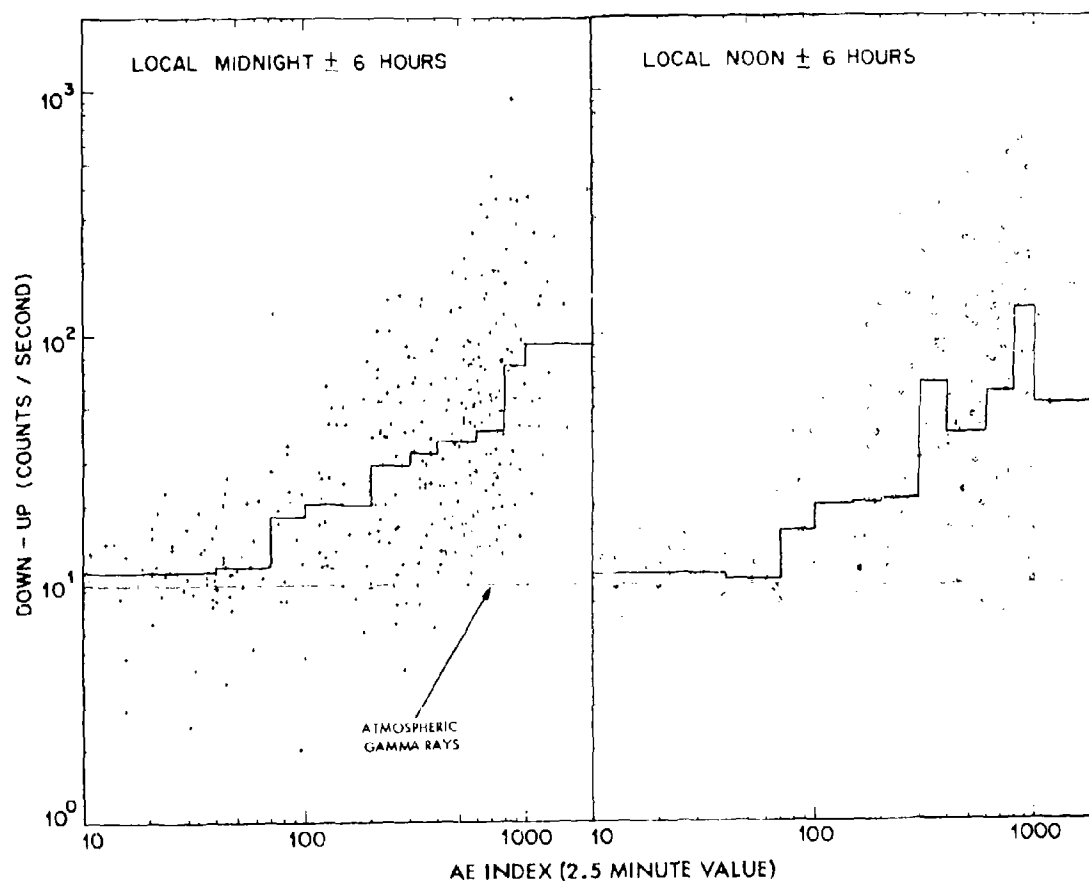
Figure 1. The net (down-up counting rates of Bremsstrahlung X-rays (50-500 keV) plotted as a function of the instantaneous (2.5 min) AE vvalue for observations around local midnight (left-hand section) and around local noon (right-hand section). (From Imhof et al., 1980).
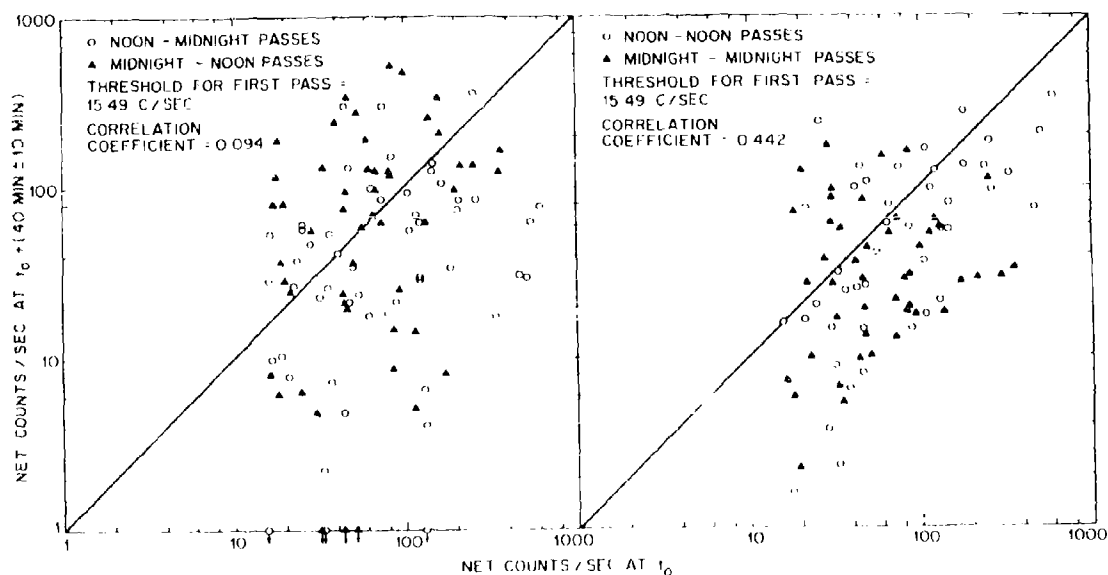


Figure 2. The Bremsstrahlung X-ray intensities measured on a given satellite pass plotted as a function of the intensities observed on a pass ~ 40 min earlier. In the left-hand section the MLT times are the same within ± 2h. For comparison lines are drawn for equal counting rates at both times. (From Imhof et al., 1980).
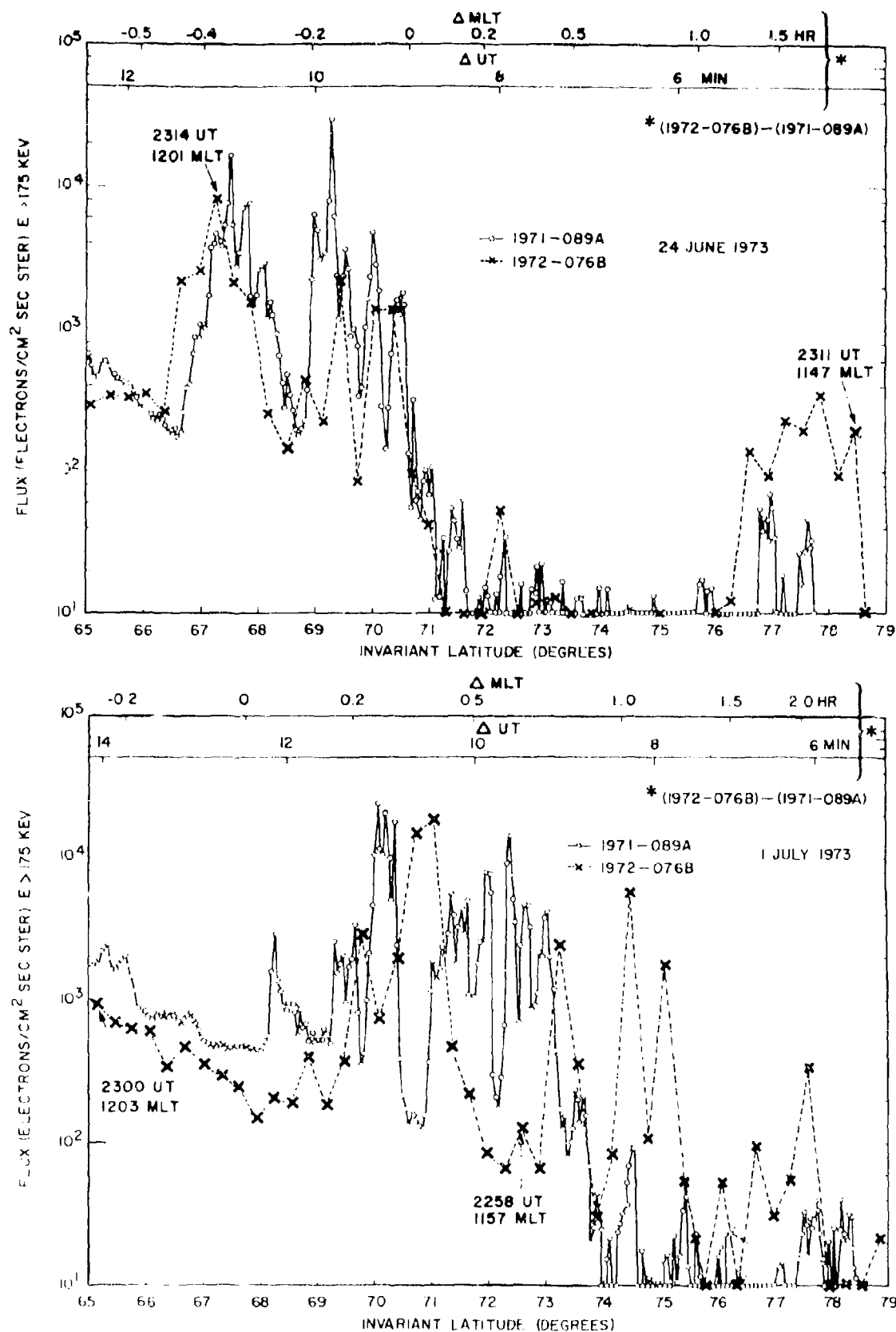
Figure 3. Examples of precipitating electron flux (E > 175 keV) versus latitude profiles measured on co-ordinated passes of the satellites 1971-089A and 1972-076B. (From Imhof et al., 1980).
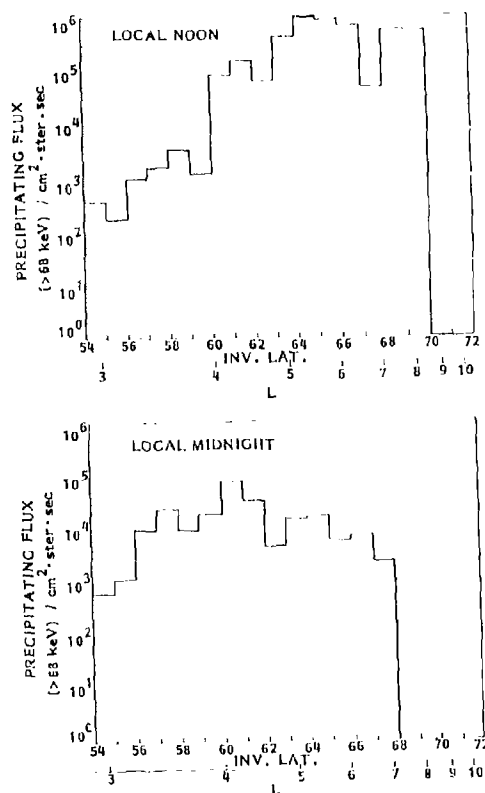
Figure 4. Average noon and midnight latitude profiles of the fluxes of precipitating electrons > 68 keV.
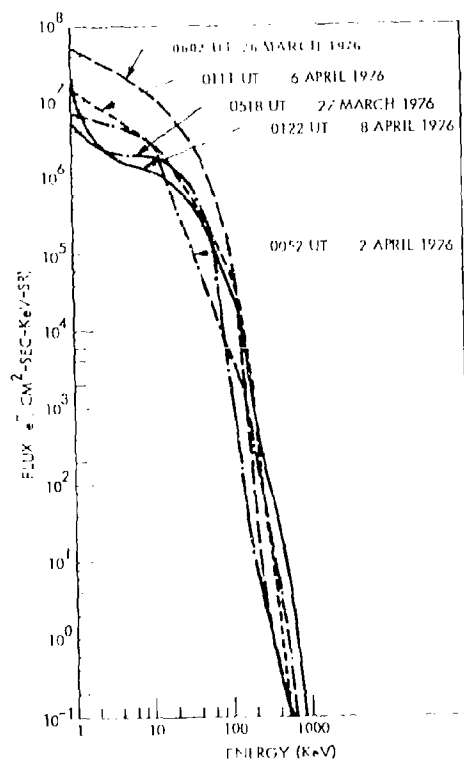


Figure 5. Examples of the energy spectra of precipitating electrons measured during the March-April 1976 coordinations. (From Imhof et al., 1977).
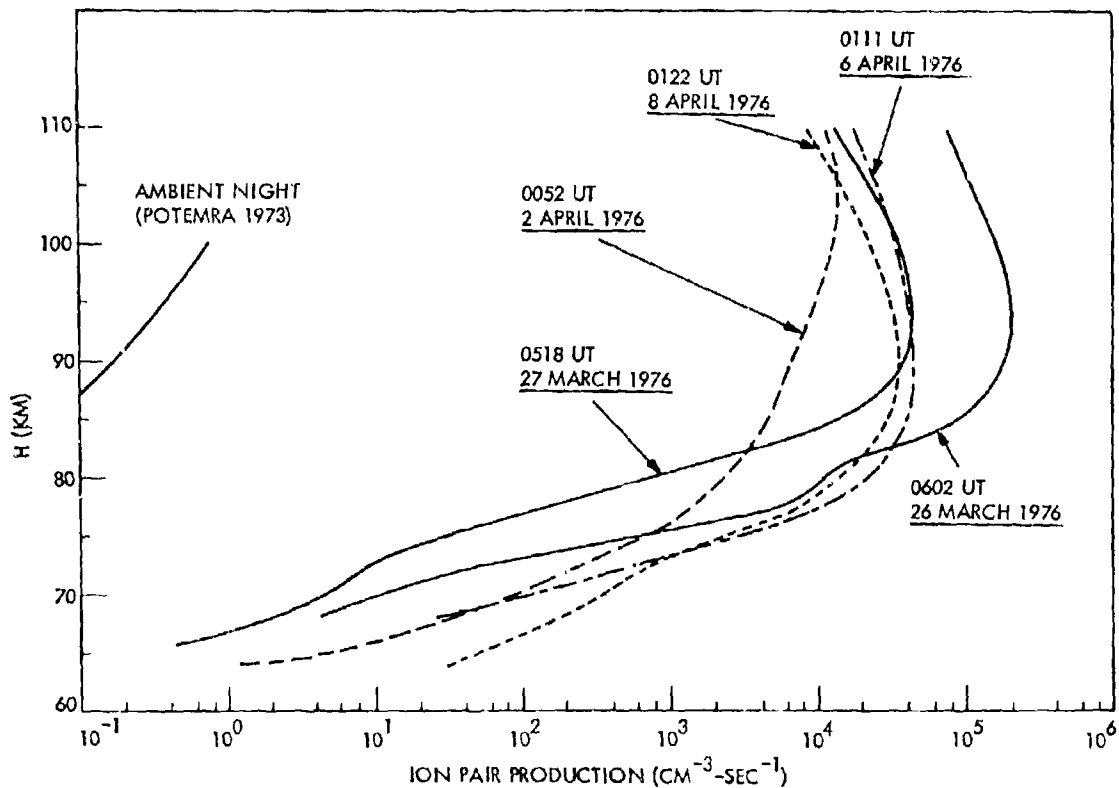
Figure 6.  Ion-pair production rates obtained from the measurements of precipitating electron during selected satellite passes in March-April 1976.  (From Imhof et al., 1977).
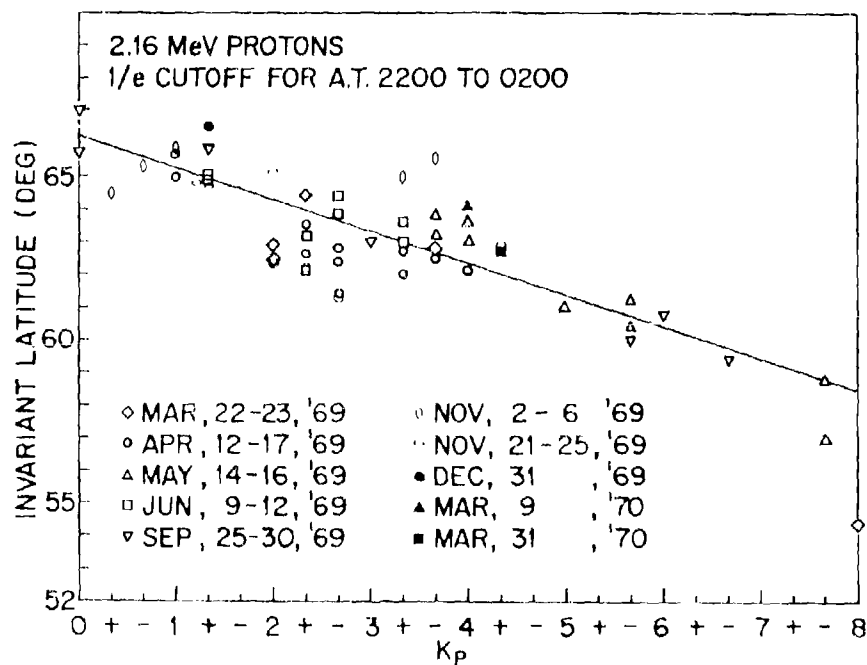


Figure 7.  The 1/e cutoff latitudes for 2.16 MeV protons plotted as a function of Kp.  (From Imhof et al., 1971).
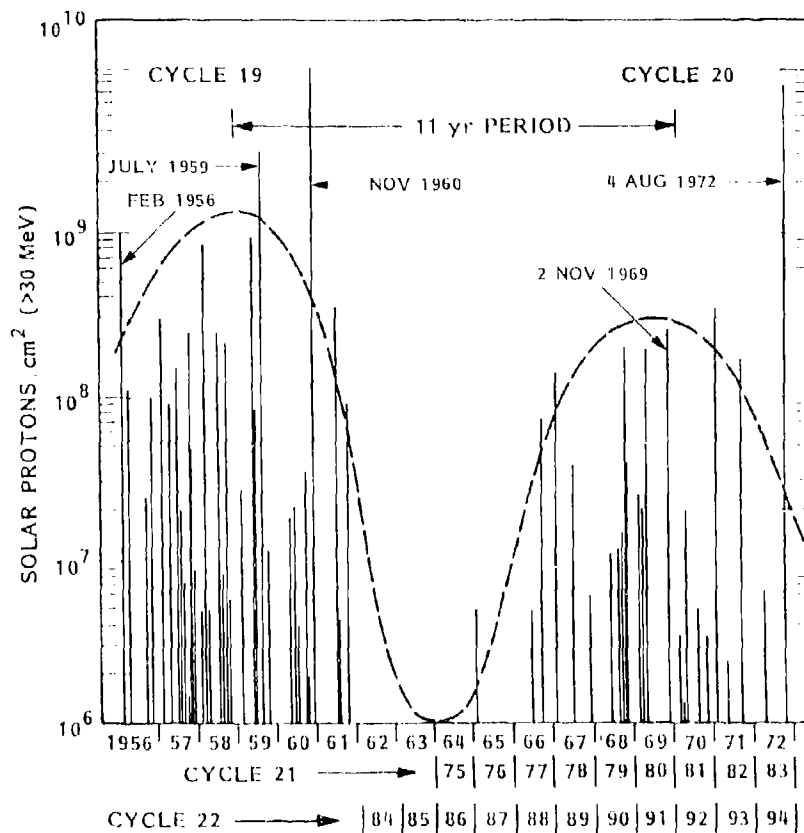
Figure 8
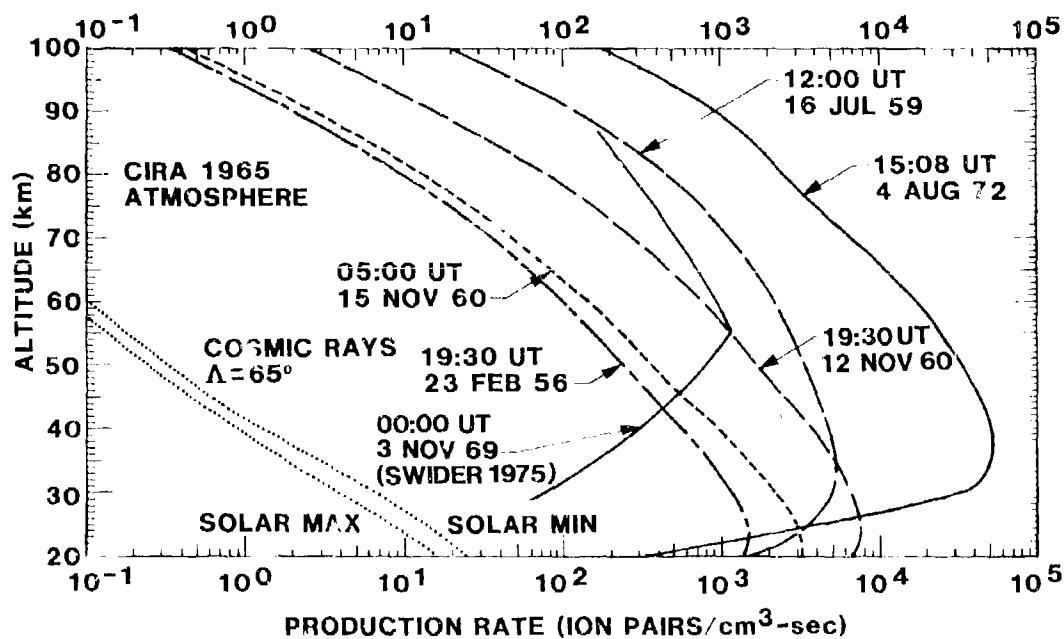


Figure 9

# VLF/LF PULSE REFLECTIONS FROM LAYERS BELOW THE IONOSPHERIC D-REGION

J. E. Rasmussen                P. A. Kossey                J. P. Turtle

Propagation Branch, Rome Air Development Center
Hanscom AFB, Ma. 01731

## SUMMARY

Long wave ionospheric reflectivity data are described from experiments using a VLF/LF pulse
ionosounding system. The sounding technique utilized pulses so short, that even at distances of a few
hundred kilometers from the transmitter, ground wave and ionospherically reflected sky wave pulses
were received separated in time. Pulse reflection data are shown that strongly suggest the simul-
taneous presence of at least two discrete reflections from different heights in the daytime ionosphere.
The upper reflections are identified with the classical D-region, caused primarily by Lyman-α radiation,
while the low-altitude reflections, which occur from shortly before sunrise to shortly after sunset,
are believed to be due to ionization caused by cosmic rays and photodetachment. The variability of the
low altitude daytime ionosphere is described from VLF/LF pulse reflection data obtained during
different seasons, at mid- and low-geomagnetic latitudes, and over different phases of the solar cycle.
Estimates of the effects of the low altitude ionization on the propagation of long radio waves are also
given.

## 1. INTRODUCTION

Observations of the propagation characteristics of long radio waves provide sensitive techniques
for studying the nature of the lowest regions of the ionosphere. One such technique, employing the
transmission and reception of VLF/LF pulses, has been used by the Propagation Branch, Rome Air
Development Center (U.S. Air Force), to obtain a variety of ionospheric reflectivity data at low-, mid-,
and high-geomagnetic latitudes. The system operates basically as an oblique-incidence ionosounder,
as illustrated in Figure 1. Short VLF/LF pulses are transmitted from a vertical antenna and are
observed at receivers located at various distances from the transmitter. Both ground wave and iono-
spherically reflected sky wave pulses are received, and since the transmitted pulses are less than
about 70 μs in length, the sky waves can be observed free from interference with the ground wave, even
at distances several hundred kilometers from the transmitter. Both the normal ($\parallel$) and converted ($\perp$)
polarization components of the sky waves can be sensed by using orthogonal loop antennas. Figure 2
gives an example of received waveforms, showing the separation of the ground wave and sky wave pulses.
The waveforms can be Fourier analyzed to obtain information on the reflection heights and reflection
coefficients of the lower ionosphere over the frequency range from 10 to 50 kHz (see Lewis et al.,1973).
As described by Rasmussen et al.(1980), the VLF/LF ionosounding technique provides a means for studying
the structure within the lower ionosphere itself. This paper describes data showing the nature and
variability of VLF/LF pulse reflections from ionospheric layers below the classical (Chapman-like)
D-region of the daytime ionosphere.

## 2. OBSERVATIONS OF VLF/LF PULSE REFLECTIONS FROM BELOW THE D-REGION

Figure 3 shows VLF/LF pulse ionosounding data recorded on December 26, 1972, under near solar
minimum conditions. The data were received over a 263 km long, magnetically west-to-east, propagation
path from Camden, New York ($43^0$ 18' N, $75^0$ 49' W) to Bethel, Vermont ($43^0$ 48' N, $72^0$ 37' W). Figure 3
shows both the normal and converted polarization components of the ionospherically reflected sky wave
pulses. Each of the three-dimensional displays consist of 288 individual waveforms stacked one behind
the other in linear time progression from bottom-to-top for a 24-hour period. Each individual wave
form was a five minute average of approximately 120,000 pulses and represents the received field strength
as a function of time. The horizontal scales are linear in time, measured from the start of the
ground wave pulses. Included in Figure 3a are the ground wave (0-55 μs), followed by the normal
component of the sky wave, as sensed by a loop antenna oriented in the plane of propagation. The
ground wave had four half-cycles and a spectral maximum at about 36 kHz. Figure 3b shows the con-
verted sky wave pulses as received by an orthogonal loop antenna aligned to a near null on the ground
wave, which therefore appears only vestigially in the Figure.

The nighttime portions of Figure 3, from 0400 to 1200 UT and from 2200 to 0400 UT, show sky
wave reflections beginning at about 160 μs after the start of the ground wave. By attributing this
time delay to a difference in travel distance, an effective reflection height can be calculated using
simple geometry. At night the time delays correspond to an effective reflection height of about
82 km, which would be in the lower part of the ionospheric E-region. The nighttime portion of
Figure 3b shows a converted polarization component of about the same amplitude as the normal component,
indicating a strong interaction of the wave with the geomagnetic field.

The daytime portion of Figure 3a shows weaker pulse reflections of a relatively complicated
nature. To better describe them, Figure 4 shows a number of waveforms selected from Figure 3a in the
period from 1130 to 2330 UT. Inspection of Figure 4 reveals that each daytime reflection consisted
of two basic pulses which were slightly overlapping. The earlier pulse was nearly stationary through-
out the daytime, but the later one had a varying delay, which caused the overlap to be greatest near
local noon and least near sunrise and sunset. At 2130 UT, when the solar zenith angle ($\chi$) at the
mid-point of the path was about $91^0$, there even appeared to be a slight gap, at 150 μs on the time
scale, between the two ionospherically reflected pulses. At 1230 UT, again when the solar zenith
angle was about $91^0$, the later pulse was especially weak, leaving only the earlier one; but, at
1330 UT, when the solar zenith angle was $82^0$, the two pulses were merging. As described by Rasmussen
et al. (1980), the effective heights of the later, higher altitude, pulse reflections seen through-
out the daytime were in general agreement with a ln sec $\chi$ rule, following classical Chapman-like
theory. It is believed that the ionization responsible for the earlier reflections was caused by cosmic
rays and photodetachment, a mechanism proposed previously by other writers in connection with the

C-layer of the ionosphere.

Comparison of the daytime portions of Figure 3a and 3b reveals an important difference between the normal and converted sky wave reflections. The normal low altitude sky waves arrived at about 97 μs, corresponding to an effective reflection height of 63 km, while, in contrast, there was no appreciable component of the converted polarization reflected from such a low altitude. There were later, higher altitude, converted polarization reflections seen during the daytime, but they appeared to arise from wave interactions with ionization above about 68 km, in a manner similar to the higher altitude reflections seen in the normal polarization. The fact that there was essentially no polarization conversion associated with the low altitude (63 km) daytime reflections, suggests that the reflection process was not influenced appreciably by the geomagnetic field, so that the 63 km region of the ionosphere could be regarded as having an almost purely real and isotropic electrical conductivity. In an earlier paper (Rasmussen et al., 1980), the authors described a phenomenological model of the ionosphere in the 63-69 km altitude range which was inferred from the low altitude pulse reflections. The model was a 6 km thick slab having a uniform conductivity of $1.8 \times 10^{-7}$ mhos/m. From this model it was estimated that the peak electron density in the layer which produced the low altitude reflections was about 160 el/cm$^3$, at 63 km altitude.

The model described above was not necessarily unique; i.e., some other assumed layer characteristics might also have been consistent with the observed reflectivity data. Indeed, a large number of C-layer profiles have been proposed by numerous investigators, such as those described by Bain (1974), Krasnushkin and Federov (1966), and Risbeth and Garriot (1969). These experimentally determined layers exhibit widely varying characteristics. This is not surprising in light of the nature of the VLF/LF pulse ionosounding data described in this paper. The data, which were obtained at a number of geomagnetic latitudes, over different seasons, and at different periods of the solar cycle, illustrate the variability of the lower daytime ionosphere.

In the discussions that follow, the prefix CR- is used to distinguish the low altitude (C-Layer) daytime reflections from those associated with the higher altitude, classical D-region of the lower ionosphere.

## 3. MID-LATITUDE WINTER PULSE REFLECTION DATA -- NEAR SOLAR-MINIMUM CONDITIONS

The data shown in Figure 3 were obtained over a mid-geomagnetic (58°N) path under near-solar minimum conditions. For the day shown in Figure 3, the CR-reflections were strong, and relatively distinct from the higher altitude D-region reflections. During this winter measurement period the CR-reflections were seen to exhibit relatively little variability, as illustrated in Figure 5. The data shown there cover a seven day period from December 22 through December 28, 1972. On all the days shown, the CR-reflections can be seen starting at about 1200 UT ($X = 96^0$), and disappearing at about 2200 UT ($X = 96^0$). Although there was some day-to-day variation in the observed waveforms, the shape of the reflected waveforms remained quite constant throughout any given day. Close inspection of the data reveals that there were very weak partial reflections from as low as about 55 km, but that the primary CR-reflections were from altitudes in the 61-63 km range. Furthermore, the variability in the shapes of the reflected pulses indicate that, although they could be simulated as having been reflected from conducting slabs, the thicknesses, conductivities, and ionospheric heights of the slabs would have to be adjusted from day-to-day to account for the differences seen in the data. The data shown in Figure 5 was typical of that obtained during the winter of 1972-73 at Bethel. Although their characteristics varied from day-to-day, CR-reflections were always clearly observed throughout the daylight hours.

## 4. MID-LATITUDE PULSE REFLECTION DATA - NEAR SOLAR-MAXIMUM CONDITIONS

After the 1972-73 winter measurements were completed, the pulse ionosounder was moved to Thule Air Base, Greenland, for use in other programs, and it was not until the winter of 1979-80 that equipment was available for further mid-latitude ionospheric studies. These were conducted over a 245 km path (117° magnetic azimuth) from Forestport, New York (43° 27' N, 75° 05'W) to Troy, New Hampshire (42° 50' N, 72° 12' W), and the data were acquired under near solar-maximum conditions for a period of almost two years.

Figure 6 shows typical winter, spring, and summer reflectivity data, observed at Troy (57° N magnetic latitude). Analysis of the winter data, shown in Figure 6a, reveals that the CR-reflections seen in the daytime, came from about 61-63 km altitudes, similar to those observed at Bethel under solar-minimum conditions in the winter of 1972-73. Typically, however, the average amplitude of the Troy reflections was about one-fourth of that observed at Bethel. In terms of a slab conductivity model, the Troy winter data would indicate that the conductivity was about an order of magnitude lower than that estimated from the earlier Bethel data. The winter Troy data taken near solar maximum, also showed considerably more day-to-day variability in the CR-reflections, when compared to the Bethel data. For example, in Figure 6a, the CR-reflections are relatively strong on December 17 and 20, but are extremely weak on December 18 and December 22. Such large differences were not seen in the solar-minimum data from Bethel, as shown in Figure 5.

During the transition to spring at Troy, as illustrated in Figure 6b, the CR-reflections tended to weaken, but still appeared to be from the 61-63 km region of the lower ionosphere. By summer, as illustrated in Figure 6c, there were days when no CR-reflections could be seen in the data. On other summer days, close inspection of the data reveals that there were extremely weak, just barely discernible, CR-reflections from about 61-63 km altitudes. During the summer the higher altitude, D-region, reflections appeared to come from an effective height of about 69 km at local noon.

It is important to note that the extreme weakness (or absence) of CR-reflections observed during the summer does not indicate necessarily that the C-layer electron concentrations were significantly less than those in the winter. Rather, the data may indicate that the concentrations were at lower altitudes in the summer, resulting in such low effective conductivities that the CR-reflections were

too weak to be observed with the instrumentation used. For example, it is estimated that a concentration of about 100 el/cm$^3$ at 65 km altitude would produce an effective layer conductivity of about 10$^{-7}$ mhos/m, but the same concentration at 55 km altitude would result in a conductivity of less than about 10$^{-8}$ mhos/m. In the latter case, the CR-reflections from the layer would be too weak to be observed with the ionosounder instrumentation. Thus, it is important that more detailed, full-wave, analysis be made of the VLF/LF pulse ionosounding data in order to derive appropriate electron density/conductivity profiles of the lower ionosphere. In doing this, the information from both the CR-reflections and the higher altitude, D-region, reflections should be used.

## 5. LOW LATITUDE PULSE REFLECTION DATA - NEAR SOLAR-MAXIMUM CONDITIONS

Figure 7 shows pulse ionosounding data obtained in May 1980, at a low geomagnetic latitude (25$^0$S) in Brazil. The data were obtained over a 246 km path (125$^0$ magnetic azimuth) from Uniao da Vitoria, Parana (26$^0$ 15' S, 50$^0$ 58' W) to Camboriu, Santa Catarina (27$^0$ 00' S, 48$^0$ 37' W) during a month long ionospheric research program conducted jointly by the Air Forces of the United States and Brazil. The data is for an eight day period, and is typical of that obtained throughout the month. Careful inspection of the daytime portions of the data shows that CR-reflections were observed, and that there was even more day-to-day variability than seen at mid-latitudes. As shown in Figure 7, the reflections varied from being relatively strong on May 17 to being weak on May 20. The heights of the CR-reflections varied from about 65-69 km contrasted with the relatively constant 61-63 km heights observed at mid-latitudes.

The data for May 17, in Figure 7, show leading edges of CR-reflections that were nearly stationary, and distinct throughout the daytime. However, on the other days shown in the Figure, the CR-reflections could only be seen, distinct from D-region reflections, for short periods around sunrise and sunset. In fourteen days of operation at Camboriu, CR-reflections were observed on all but two days. On those two days it is estimated that the conductivity of the ionosphere below the classical D-region was less than about 10$^{-8}$ mhos/m, based on the expected capabilities of the ionosounder instrumentation.

At times, three receivers were operated simultaneously at different locations during the measurement program in Brazil. Figure 8a shows waveforms received on 17 May 1980, at Timbo, S.C. (26$^0$ 50' S, 49$^0$ 16' W), Camboriu, S.C., and Canasvieras, S.C. (27$^0$ 26' S, 48$^0$ 28' W), along a magnetic azimuth of approximately 120$^0$. The three locations were 180 km, 246 km, and 280 km, respectively, from the transmitter. The data were obtained shortly after sunrise (1015 UT, $\chi$ 86$^0$) when the CR-reflections were distinctly separate from the higher altitude D-region reflections. In effect the data provide information on the reflectivity of the ionosphere for three different incidence angles. Based on the times-of-arrival of the CR-reflections and the individual path lengths, it is estimated that the incidence angles ranged from about 53$^0$ (Timbo data) to about 64$^0$ (Canasvieras data). At the shorter ranges (and hence, the steeper incidence angles) there was better resolution of the CR- and D-region reflections, but correspondingly, the reflections were appreciably weaker. For all three locations the CR-reflections had an effective height of reflection of about 67 kilometers.

Figure 8b shows effective plane wave reflection coefficients derived from the CR-reflection waveforms of Figure 8a. The coefficients were obtained by comparing the CR-sky wave Fourier-amplitudes at a given frequency to those of the ground wave, as described by Lewis et al. (1973). The data shown in Figure 8b provide estimates of the reflection properties of the CR-ionization as a function of frequency and incidence angle. These properties can be used to infer a conducting-slab model of the CR-ionization. As described by Kossey and Lewis (1981), an estimate of the slab thickness can be obtained from the frequencies at which the relative nulls occur in the reflection coefficient curves of Figure 8b. The magnitudes of the reflection coefficients are then used in determining an effective slab conductivity. From the data shown in Figure 8b, it was estimated that a 10-km thick slab, having a uniform conductivity of 10$^{-7}$ mhos/m describes (phenomenologically) the ionization that produced the CR-reflections shown in Figure 8a. This model represents a higher altitude, broader, more weakly ionized layer than the 6-km thick slab model described earlier, in conjunction with the mid-latitude Bethel data of Figure 4.

## 6. DISCUSSION

A wide variety of VLF/LF pulse ionosounding data have been obtained showing CR-reflections from ionization below the D-region of the daytime ionosphere. If the ionization responsible for those reflections was produced by cosmic rays and photodetachment (i.e., C-layer ionization), as speculated, it exhibits substantial day-to-day, seasonal, latitudinal, and solar cycle variability.

### 6.1 Day-to-Day Variations

The variability from day-to-day in the strengths and effective heights of the CR-reflections suggest corresponding variations in the electron concentrations and associated conductivities below the D-region. It is estimated that the CR-reflections were from layers having an effective conductivity that varied from about 10$^{-7}$ mhos/m to below 10$^{-8}$ mhos/m, usually within one week's time. This occurred in all the data with the exception of the solar minimum, winter measurements at Bethel, Vt, where the conductivity remained relatively constant. Within a given day, however, the layer characteristics appeared to remain quite constant throughout the daylight hours.

### 6.2. Seasonal Variations

Data obtained at mid-latitude showed the strongest CR-reflections during winter. The reflections tended to weaken through spring, and were barely detectable during the summer months. The strengths of the daytime reflections from the classical D-region, however, did not differ greatly from winter to

summer. These observations suggest that there was a pronounced seasonal effect in the electron concentrations and/or electron distributions with altitude, associated with the C-layer ionization.

### 6.3. Latitudinal Variations

CR-reflection data were obtained simultaneously at mid-geomagnetic latitude (Troy, N.H., 58° N. Magnetic lat.) and at low-geomagnetic latitude (Camboriu, S.C., Brazil, 25° S. Magnetic Lat.) in May 1980. Although the propagation paths were almost the same length, the CR-reflections at Troy had appreciably lower effective heights (61-63 km vs 65-69 km) and were considerably weaker than those observed at Camboriu. Since May corresponds to late spring in Troy, but late fall in Camboriu, it is interesting to speculate to what degree the differences seen in the amplitudes and heights can be attributed to seasonal factors. When the May data from Camboriu was compared with November data from Troy (late fall at both locations) the amplitude relationship was reversed; i.e., the CR-reflections at Troy were stronger.

The lack of suitable polar data and the limited amount of low-latitude data has made it difficult to assess the latitude dependence of the CR-layer; however, in general, the data indicated that the low-latitude layers were weaker, broader, and at higher altitude than at mid-latitude.

### 6.4. Solar Cycle Variations

The mid-latitude CR-reflections observed during near solar-minimum conditions were consistently stronger than those observed near solar-maximum suggesting that the electron concentrations in the C-layer were appreciably larger near solar-minimum. This is in accordance with a modulation mechanism described by Krasnushkin (1966), in which there is an inverse correlation between solar activity and electron concentrations in the C-layer.

### 6.5. C-Layer Effects on Long Wave Propagation

The VLF/LF pulse ionosounding data indicate that the characteristics of the C-layer are highly variable, depending on time-of-day, season, location, and the solar cycle. It is not surprising, therefore, that a large number of C-layer profiles have been proposed by various researchers, from data using different probing techniques. The strongest mid latitude layer deduced from the CR-reflection data was described in terms of a 6 km thick slab, having a conductivity of about $1.8 \times 10^{-7}$ mhos/m. This corresponds to a layer having a maximum electron density of about 100-150 el/cm$^3$, depending on the altitude at which it is located. Bain (1974) has developed a model of the mid-latitude daytime ionosphere, from propagation data, which has an electron density maximum in the C-layer of about 100 el/cm$^3$, at a height of 55 km. Consideration of the effects of such a layer on ELF/VLF/LF propagation by Field and Lewinstein (1978) has produced some interesting results. They show calculated ELF/VLF/LF earth-ionosphere waveguide parameters using daytime models of the ionosphere with, and without, a C-layer (Bain's) to examine the effect of the layer on long range propagation. The model ionospheres used in the calculations are shown in Figure 9a, and the effects of the assumed C-layer on VLF/LF propagation are illustrated for 20 kHz in Figure 9b and for 35 kHz in Figure 9c. The effects of the C-layer on ELF propagation (not shown) were very small; even out to propagation distances as great as 10 Mm, the spread in calculated field strengths between the models was only about 2 dB, at 45 Hz, for example. The effects of the C-layer on VLF/LF were shown to be significantly larger. At 20 kHz the spread between the calculated fields approached a factor of four, or 12 dB, at great distances as shown in Figure 9b. At 35 kHz, the spread was considerably larger, and as shown in Figure 9c, approached a factor of almost forty, or over 30 dB, at the longer ranges. For these calculations it was assumed that the C-layer was present over the entire path length, and hence, the results most likely represent an extreme case. However, the calculations indicate that the C-layer acts as an absorber of energy in long wave propagation. Other calculations by Field indicate that if the C-layer was located at a higher altitude, its effect on long wave propagation would have been significantly less than those shown in Figures 9b and 9c. The same general conclusion would hold if the layer electron concentrations were reduced. The calculations also suggest that more information on the characteristics of the C-layer could be obtained from observation of long-path LF signals, rather than long-path VLF signals.

The variability of the lowest regions of the daytime ionosphere, including its apparent dependence on location, season, and phase of the solar cycle, make it particularly difficult to model. As described in this report, short path VLF/LF ionosounding data can provide information on the reflection properties of that region. It appears, however, that an appropriate combination of such ionosounding data and long path LF propagation data would be even more valuable for deducing the properties of the lower ionosphere and assessing its effects on long wave propagation.

### REFERENCES

Bain, W. C., "The Use of VLF Propagation in Ionspheric Modelling," ELF-VLF Radio Wave Propagation, Proc. of NATO Adv. Study Inst., D. Reidel Publishing Co., 1974.

Field, E. C. and M. Lewinstein, "Analysis of Electron Density-Profiles in the Lower Ionosphere," Rome Air Development Center Technical Report 78-67, 1978.

Kossey, P. A. and E. A. Lewis, "The Reflection Properties of Conducting Slabs," Rome Air Development Center Technical Report 80-371, 1981.

Krasnushkin, P. E. and N. Federov, "Determination of the Electron Density Profile of the Lower Ionosphere from Surface Wave Fields with Allowance for a Possible Ionization Valley," Geomagnetism and Aeronomy, Vol VI, No. 6, p. 839, 1966.

Krasnushkin, P. E., "Influence of the Solar Wind on the C-Layer of the Earth's Ionosphere," Geomagnetism and Aeronomy, : ,. 6, p. 452-453, 1966.

Lewis, L. A., J. E. Rasmussen, and P. A. Kossey, " Measurements of Ionosphere Reflectivity from 6 to 35 kHz," J. Geophys. Res., Vol 78, p. 3903-3912, 1973.

Rasmussen, J. E. , P. A. Kossey, and E. A. Lewis, "Evidence of an Ionspheric Reflecting Layer Below the Classical D-Region," J. Geophys. Res., Vol 85, p. 3037-3044, 1980.

Risbeth, H., and O. K. Garriot, "Introduction to Ionospheric Physics", Academic Press, New York, 1969.
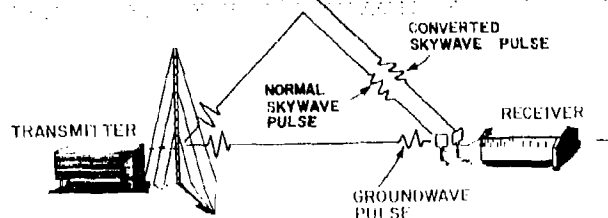


Figure 1. Illustration of VLF/LF pulse ionosounding technique.
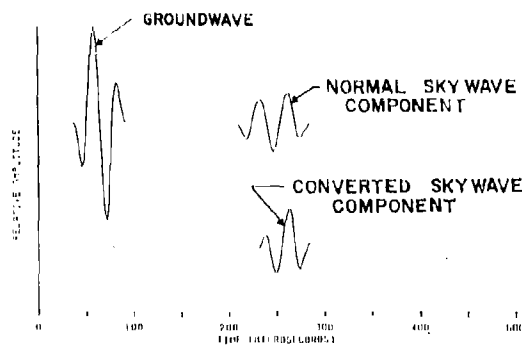


Figure 2. Example of observed pulse ionosounding waveforms.

a.

b.

0400
0200
0000
2200
LOCAL SUNSET
2000
TIME OF DAY-UT
1800
LOCAL NOON
1600
1400
LOCAL SUNRISE
1200
1100
0800
0600
0400

0400
0200
0000
2200
2000
1800
1600
1400
1200
1000
0800
0600
0400

0       100      200      300        0       100      200      300
TIME  MICROSECONDS                  TIME  MICROSECONDS
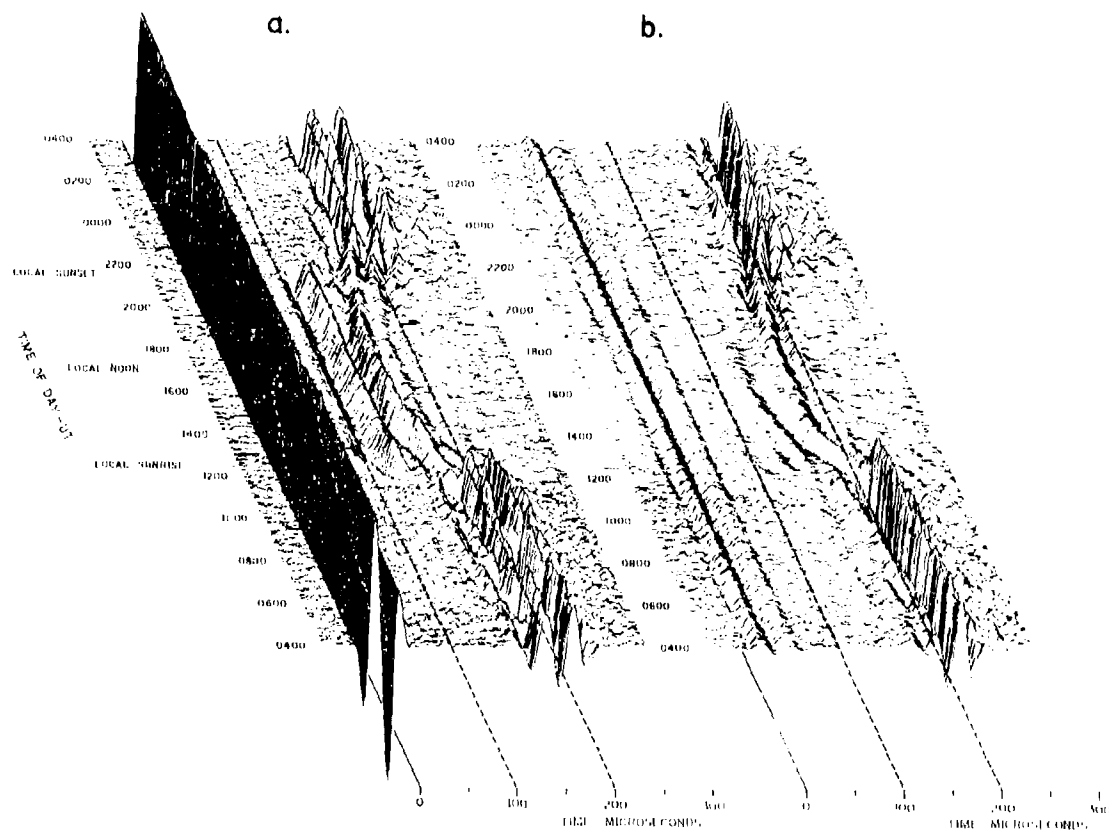
Figure 3.   VLF/LF pulse ionosounding data
obtained over a mid-latitude propagation path.
The transmitter was located at Camden, N.Y. and
the receiver was 263 km to the east at Bethel,
Vermont.   (a) Normal polarization; ground wave
pulses are shown on the left side of the
display, followed by ionospherically reflected
sky wave pulses.  (b) Converted polarization
data.

Figure 4.   Examples of waveforms received at
mid-latitude on December 28, 1972 as a function
of time-of-day and solar zenith angle.

RELATIVE AMPLITUDE

1150 UT   X=101°

1230 UT   X=91°

1330 UT   X=82°

1450 UT   X=75°

1530 UT   X=70°

1630 UT   X=67°

1730 UT   X=67°

1830 UT   X=70°

1930 UT   X=75°

2030 UT   X=82°

2130 UT   X=91°

2230 UT   X=101°

2330 UT   X=111°

0       100      200      300
TIME  MICROSECONDS
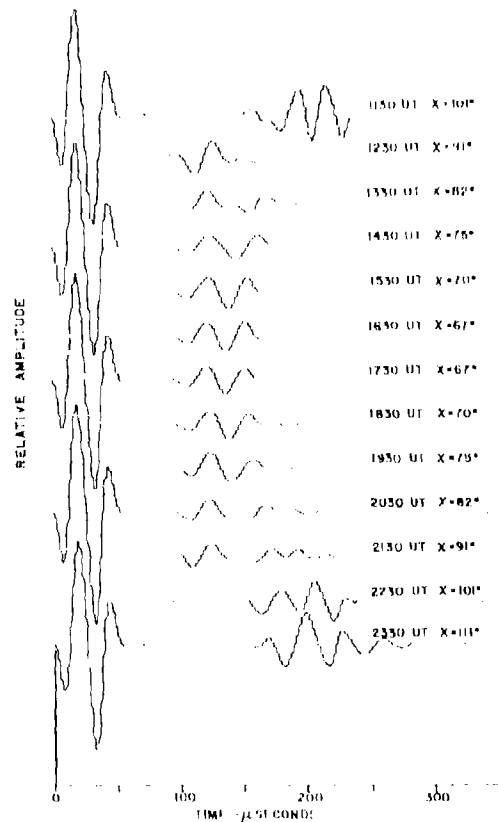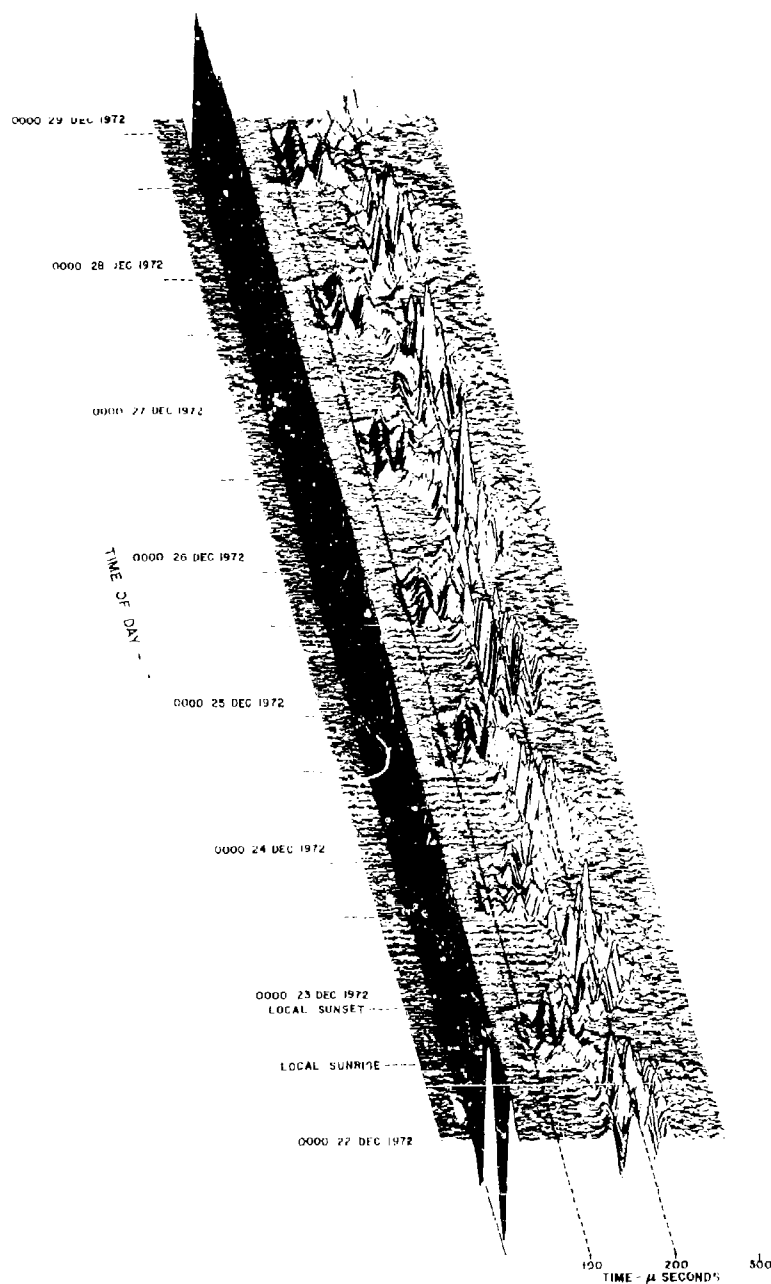
Figure 5. Mid-latitude, winter, pulse ionosounding data obtained near solar-minimum. Normal polarization data covering a seven day period from December 22 through December 28, 1972.
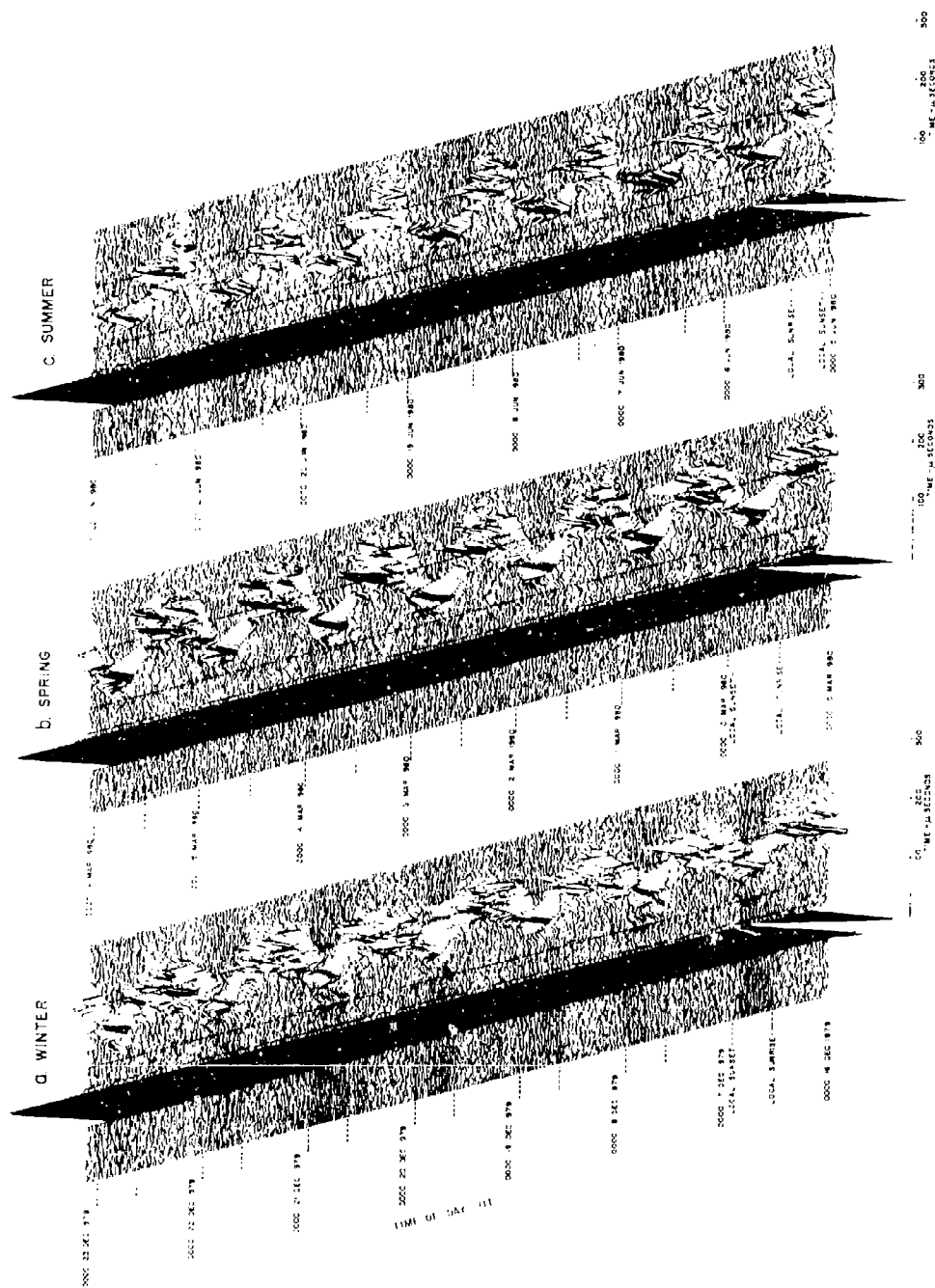
Figure 6. Mid-latitude pulse ionosounding data obtained near solar-maximum conditions over a 615 km path from Forestport, N.Y. to Troy, N.H. Normal polarization data for seven day periods representing (a) winter, (b) spring, and (c) summer.
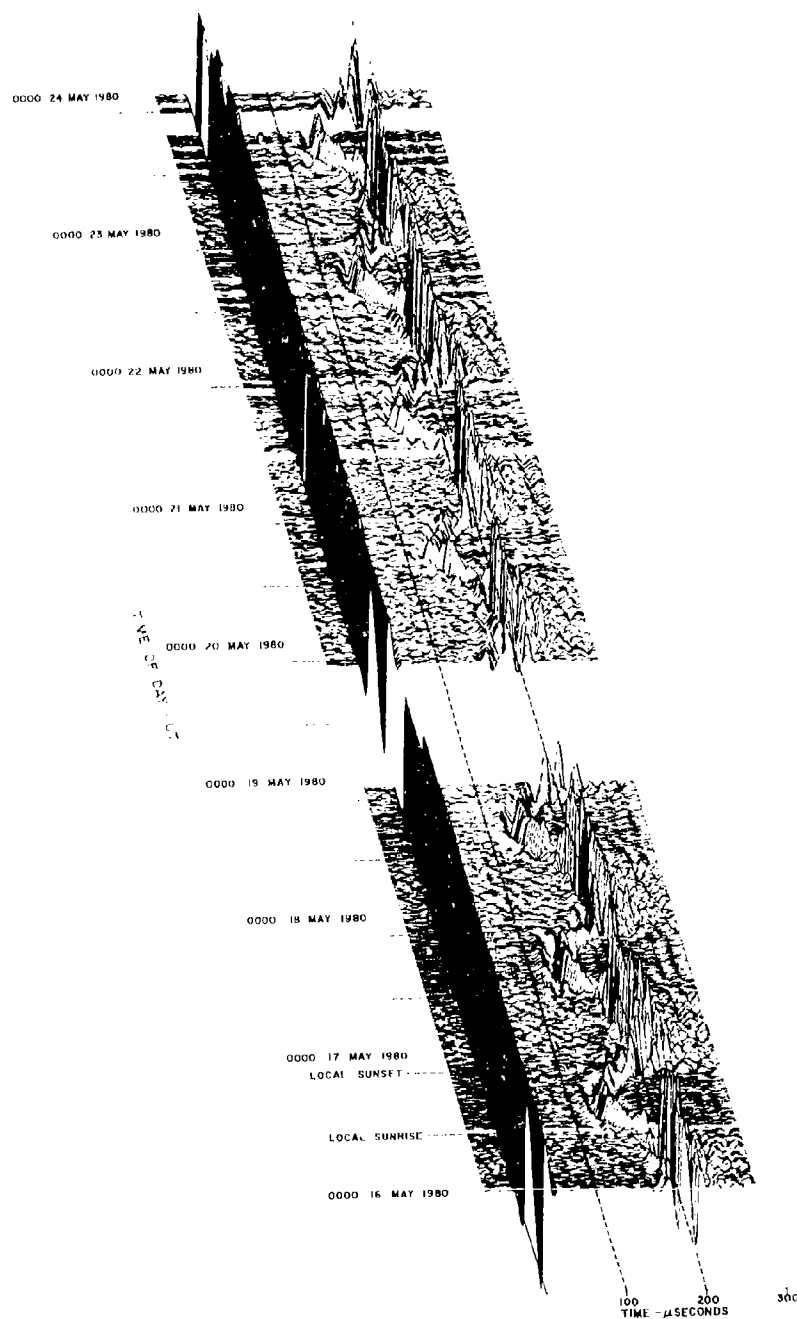
Figure 7. Low-latitude pulse icnosounding data obtained in Brazil over a 246 km path from Uniao da Vitoria, Parana to Camboriu, Santa Catarina. Normal polarization data for an eight day period from May 16 through May 23, 1980.
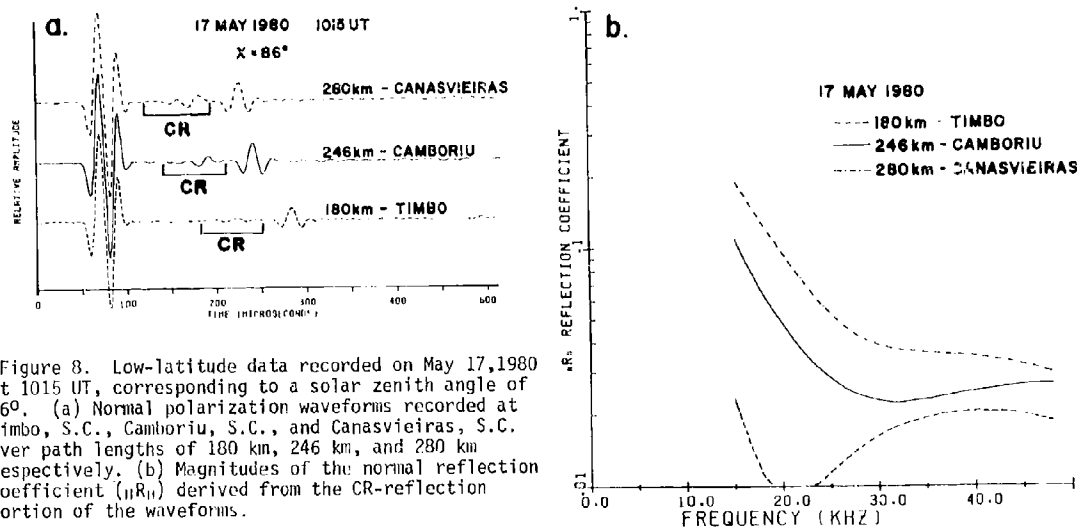
Figure 8. Low-latitude data recorded on May 17,1980 at 1015 UT, corresponding to a solar zenith angle of 86°. (a) Normal polarization waveforms recorded at Timbo, S.C., Camboriu, S.C., and Canasvieiras, S.C. over path lengths of 180 km, 246 km, and 280 km respectively. (b) Magnitudes of the normal reflection coefficient ($_{\parallel}R_{\parallel}$) derived from the CR-reflection portion of the waveforms.
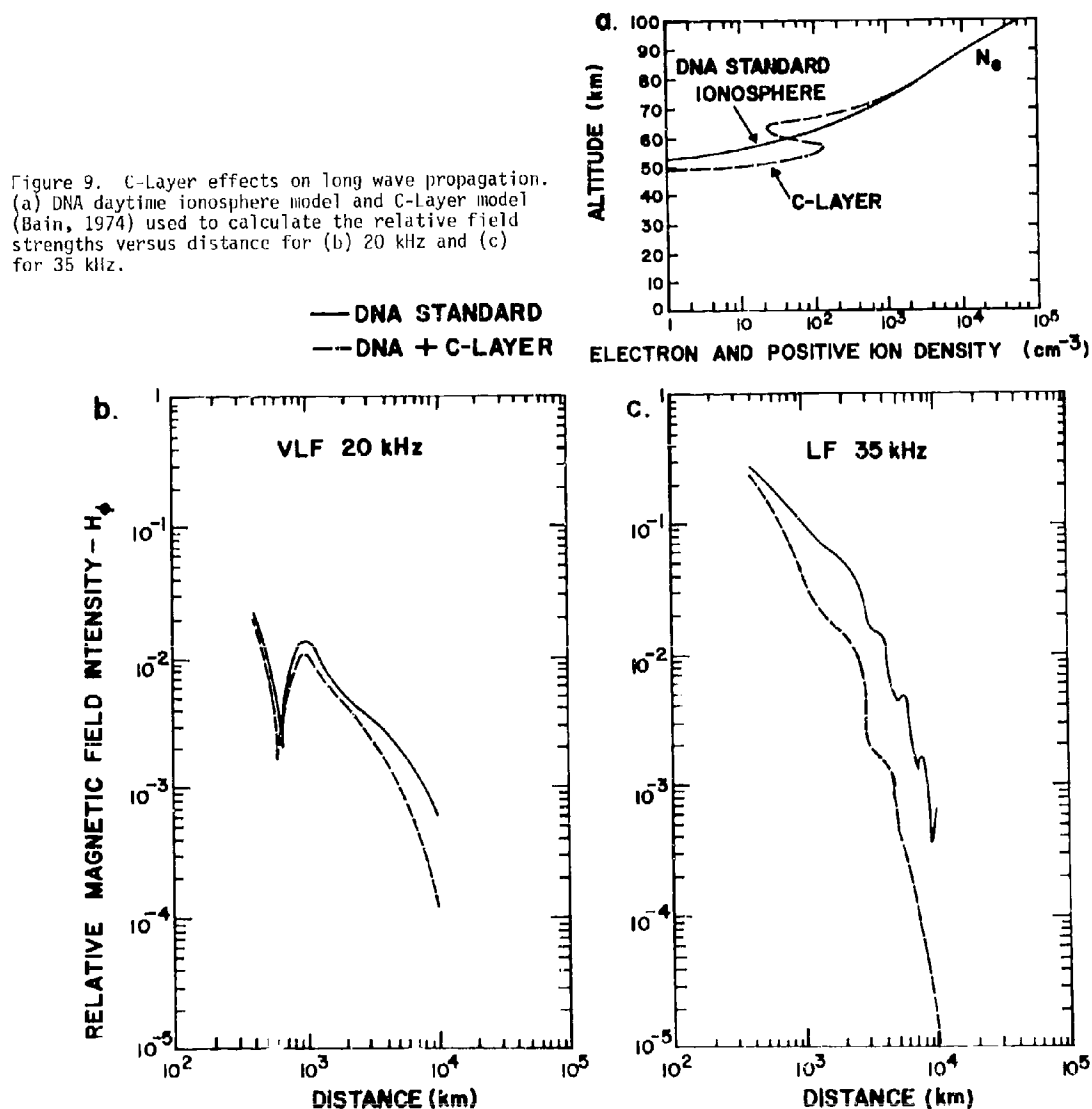
Figure 9. C-Layer effects on long wave propagation. (a) DNA daytime ionosphere model and C-Layer model (Bain, 1974) used to calculate the relative field strengths versus distance for (b) 20 kHz and (c) for 35 kHz.

# VLF-ATMOSPHERICS AS A TOOL FOR PROBING VLF-PROPAGATION CONDITIONS

J. Schäfer and H. Volland
Radioastronomical Institute, University of Bonn
Auf dem Hügel 71, D 5300 Bonn 1, West Germany

## SUMMARY

This paper presents a new technique for receiving and analysing atmospherics signals and for deriving the VLF-propagation conditions. The equipment consists mainly of a receiver/analyser with an on-line desktop computer. The computer controls the observations and analyses the received parameters in real time, so that the results, e. g. the reference height of the lower ionosphere or the strengths and locations of the thunderstorm activity centers, can be printed out immediately or displayed on a world map with a small desktop plotter. The data are also stored on magnetic tape cassettes.

At present, two stations of this kind are operating continuously at Pretoria (South Africa) and Tel Aviv (Israel). A somewhat earlier version is used at Berlin. Further stations are being projected to complete a global network (among these a station in the Antarctic). At the moment, Europe and Africa and parts of South and North America and Asia are covered. These measurements are used to investigate the short and long-term as well as the local and global behaviour of the lightning activity and the VLF-propagation conditions and to elucidate their correlation to atmospheric electric and possibly also external (e. g. solar) parameters. Some results of the measurements, including statistical analyses of the received parameters and typical real time plot charts are shown to demonstrate the methods and capabilities of the present system.

## 1. INTRODUCTION

Lightning strokes are known to produce a wide band of electromagnetic radiation, the VLF-impulsive part of which is called atmospherics. Because of the large antenna lengths and current densities of these natural transmitters and because of the good transmission characteristics of the terrestrial waveguide between earth and ionosphere for VLF-waves, the radiated VLF-impulses can be traced at distances of global scale. The permanent presence of atmospherics (ca. 100 strokes per second over the entire globe) allows one to continuously survey the atmospherics activity and the propagation conditions for VLF-waves, and especially the state of the lower ionosphere, with relatively few recording stations around the world.

The theoretical background of these analyses is a propagation model for VLF-waves depending mainly on (a) the mean reference height of the lower ionosphere along the propagation path, and (b) the mean anisotropy factor, which describes the influence of the geomagnetic field and the plasma collision frequency. Basic calculations on the characteristics of such models have been carried out e. g. by Wait and Spies (1964). Using wave guide mode theory, Volland (1968) has shown the pronounced dispersive behaviour of the spectral parameters of VLF-atmospherics in the frequency band between ca. 3 and 10 kHz, which makes this band suitable for experimental investigations. Based on these theoretical results, a VLF-atmospherics analyser has been developed at the Heinrich-Hertz-Institut, Berlin, (Heydt and Volland, 1968), and subsequently improved in several versions. Besides the direction of incidence (azimuth) of each atmospheric, this receiver determines the spectral amplitudes at two suitable frequencies in the VLF-band as well as the difference in the arrival times between two spectral groups. Extensive model calculations of these spectral parameters for various ionospheric conditions are due to Harth (1972). The main drawback of this first generation of VLF-analysers was the method of data processing. For each atmospheric, one of the spectral parameters could be displayed against the azimuth on an oscillograph screen as a point. Taking a photographic picture of all atmospherics within a time period of e. g. 5 minutes, one could estimate the mean azimuth and the corresponding mean value of the spectral parameter from the clusters on the picture by visual inspection. This complicated and time consuming process and the inefficiency in the recording of the spectral parameters (only one at a time together with the azimuth) inspired the development of a new generation of VLF-atmospherics receivers. This new atmospherics station includes a desktop computer for controlling and analysing the measurements so that it can be operated completely automatically. The calculator collects the spectral parameters and the azimuths of all incoming atmospherics over a time period of 20 minutes. The operation program then performs a statistical analysis of all atmospherics data from each single center of activity. Furthermore, it contains an optimized VLF-propagation model, which is used to directly determine the distance to the thunderstorm centers and the applicable propagation conditions for VLF-waves. A desktop plotter is then enacted to denote the locations and strengths of the activity centers on a map. The received and analysed atmospherics data are printed out in real time and also stored on the internal tape cartridge of the computer for possible a posteriori analysis.

Two of these new stations have been operating continuously for more than one year at Pretoria and Tel Aviv (Schäfer et al., 1980), an older one is installed in Berlin, and another new station will be established in the Antarctic next year. The small size of the equipment its easy handling and its insensibility to external influences allow it to be installed almost everywhere, with its antenna placed on a roof, in an open field or aboard a ship.

## 2. PROPAGATION OF VLF-ATMOSPHERICS IN THE TERRESTRIAL WAVE GUIDE

VLF-atmospherics originate mainly from cloud-to-ground lightning strokes which can be well approximated by vertical electrical dipoles on the ground. The transmitted impulses travel through the atmospheric wave guide between earth and ionosphere, see Fig. 1 (Ingmann et al., 1981), and are transformed on this way according to the propagation conditions, which depend predominantly on the location and the state of the lower ionosphere. The vertical electric field component of an atmospheric at distance $\rho$ from the source over a perfectly conducting earth

$$E(\rho, t)$$

with its complex Fourier transform

$$\hat{E}(\rho, \omega) = |\hat{E}|\, e^{i\phi} = \int_{-\infty}^{+\infty} E(\rho, t)\, e^{i\omega t}\, dt \tag{1}$$

is transformed by the complex transmission function

$$\hat{W}(\rho, \omega, p_1, p_2, \ldots) = |\hat{W}|\, e^{i\Phi} \tag{2}$$

to yield the spectral amplitude

$$\hat{E}(\rho, \omega) \cdot \hat{W}(\rho, \omega, p_1, p_2, \ldots) = |\hat{E}| \cdot |\hat{W}| \cdot e^{i(\phi + \Phi)} = \hat{A} \cdot e^{i\theta} \;. \tag{3}$$

Here, $p_i$ are all the terrestrial parameters which influence the transmission function. Since the earth can be regarded to a very good approximation as perfectly conducting in the far field (more than some 100 km), the parameters $p_i$ describe the state of the lower ionosphere. Simple exponential models for the electron density and the collision number profiles in the lower ionosphere are sufficient for VLF-reflection calculations, because the main reflection takes place at electron densities of only a few hundred electrons/$cm^3$. The electron density profile

$$N(z) = N(z_0)\, \exp(b(z - z_0)) \tag{4}$$

and the electron - neutral particle collision frequency profile

$$\nu(z) = \nu(z_0)\, \exp(-a(z - z_0)) \tag{5}$$

can be combined in the model calculations to form the ratio of the squared plasma frequency $\omega_p^2$ to the collision frequency $\nu$

$$\omega_p^2(z) / \nu(z) = \omega_r(z) = \omega_r(z_0)\, \exp(\beta(z - z_0)) \;, \tag{6}$$

with

$$\omega_r(z_0) = \omega_p^2(z_0) / \nu(z_0) = 3.18 \cdot 10^9\, N(z_0) / \nu(z_0) \qquad (N(z)\ \text{in}\ cm^{-3}) \tag{7}$$

and $\beta = a + b$. $z_0$ is the ionospheric reference height. $\omega_r$ is called the "conductivity parameter"; it is the only relevant parameter for a pure isotropic plasma (no magnetic field). If the terrestrial magnetic field is included, the gyrofrequency $\omega_T$ of the electrons has to be regarded as the second important parameter, which can also be normalized to the collision frequency at $z_0$ to yield the so called "anisotropy factor"

$$\Omega = \omega_T / \nu(z_0) \;. \tag{8}$$

Although $\omega_T$ is actually a 3-component vector for arbitrary directions of propagation, it is the trans-

verse component of the earth's magnetic field that is the most decisive (Wait, 1962), so that the anisotropy factor is related only to that component.

## 3. THE DEPENDENCE OF VLF-ATMOSPHERICS PARAMETERS ON THE PROPAGATION CONDITIONS

The highly dispersive character of the transmission function (2) in the VLF-band offers the opportunity for model calculations of the amplitude and phase relationship between at least two suitable spectral groups in this band. The atmospherics receiver/analyser uses three narrow band receivers at 5, 7 and 9 kHz. The first atmospherics parameter is the Spectral Amplitude "SA" at 5 kHz

$$SA \equiv \hat{A}(\rho, \omega_1, p_1, p_2 \ldots) \qquad . \tag{9}$$

Secondly, the ratio of the amplitudes at 9 and 5 kHz is formed

$$SAR \equiv \hat{A}(\rho, \omega_1, p_1, p_2 \ldots) / \hat{A}(\rho, \omega_2, p_1, p_2 \ldots) \qquad . \tag{10}$$

This parameter is called the Spectral Amplitude Ratio (SAR). The third measured parameter is the time difference in the arrival times of the spectral groups at 6 and 8 kHz, called the Group Delay Time Difference (GDD). It is deduced from the second derivative of the phase $\theta$ in (3) with respect to frequency (Volland, 1968)

$$GDD \equiv \Delta t_g \cong - \frac{\partial^2 \theta(\rho, \omega, p_1, p_2 \ldots)}{\partial \omega^2} \cdot \Delta\omega \qquad . \tag{11}$$

In terms of finite differences this may be written

$$GDD = \Delta t_{gr} \approx \frac{\theta_2 - \theta_m}{\omega_2 - \omega_m} - \frac{\theta_m - \theta_1}{\omega_m - \omega_1} \tag{12}$$

$$= \frac{\theta_2 - 2\theta_m + \theta_1}{\Delta\omega} \qquad , \tag{13}$$

with $\theta_i = \theta(\rho, \omega_i, p_1, p_2 \ldots)$ and $\omega_2 - \omega_1 = \omega_m - \omega_1 = \Delta\omega$. Measuring the phases $\theta_i$ at 5, 7 and 9 kHz, the first derivatives in (12) refer to 6 and 8 kHz, resp., so that their difference gives the time delay between these spectral groups.

Models of these three spectral parameters showing their dependence on the conductivity parameter (6) and the anisotropy factor (8) have been calculated by Harth (1972) at the above mentioned frequencies. He used values of

$$N(z_o) = 300 \, cm^{-3} , \qquad \nu(z_o) = 5 \cdot 10^6 \, s^{-1}$$

and

$$\tag{14}$$

$z_o = 70 \, km , \quad \beta = 0.3 \qquad$ for daytime and

$z_o = 85 \, km , \quad \beta = 0.5 \qquad$ for nighttime propagation conditions.

The anisotropy factor $\Omega$ varies at middle latitudes between ca. -1 for west-east, and ca. +1 for east-west propagation. In Fig. 2, the daytime and nighttime models for GDD and SAR (denoted by their reference heights of 70 and 85 km, resp.) are plotted as function of $\Omega$ in the range between the dotted lines. These parts of the curves are based on a linear dependence of the parameters on distance (Mm 1000 km). Unfortunately, this is only accurate at large distances from the source (beyond ca. 2000 km) where the first mode approximation is sufficient. The higher modes have to be included for consideration at closer distances. This leads to a more complicated non-linear behaviour of the spectral parameters (Harth, 1981 a, b).

In order to account for these deviations from linearity, which are nearly antiparallel for GDD and SAR, the normal range of $\Omega$ (-1 to +1) has been artificially extended, and exponential tails have been added

to the models. Interpolating between the daytime and nighttime models by means of the height dependence given by Volland (1968) and including the exponential extensions one obtains the following functions for GDD and SAR, depending on the anisotropy factor $\Omega$ and the reference height z (in km), see Fig.2,

$$GDD(z,\Omega) = \frac{a}{z^2} + \frac{b}{z} \qquad (usec / Mm) \quad , \tag{15}$$

with

$$a = GDD(85,\Omega) \cdot 1.27\cdot10^3 + 1.61\cdot10^5 \quad ,$$

$$b = GDD(85,\Omega) \cdot 70 + 1.89\cdot10^5 \quad ,$$

$$GDD(85,\Omega) = 29.3 - 3.3 \, \Omega^2 - 7.6 + \exp(-5\Omega - 7) - \exp(5\,\Omega - 7)$$

and

$$SAR(z,\Omega) = \frac{e}{z^3} + \frac{f}{z} \qquad (dB / Mm) \quad , \tag{16}$$

with

$$e = SAR(85,\Omega) \cdot 4.87\cdot10^4 + 2.77\cdot10^6 \quad ,$$

$$f = SAR(85,\Omega) \cdot 78.3 + 3.84\cdot10^2 \quad ,$$

$$SAR(85,\Omega) = 4.8 + 2\,\Omega - \exp(-9\,\Omega - 20) \quad .$$

Because of the greater sensitivity of SA to disturbances and its more complicated statistical distribution, only GDD and SAR are used for the modelling at this stage.

Besides these propagation effects of GDD and SAR of an atmospheric impulse, the source terms (originating in the lightning stroke itself) of these parameters have to be considered. During the course of the measurements, the values of

$$
\begin{aligned}
&7dB \quad \text{for SAR} \qquad \text{and} \\
&-5usec \quad \text{for GDD}
\end{aligned}
\tag{17}
$$

have turned out to fit well. These quantities are in satisfactory agreement with those deduced theoretically by Volland (1981) using a wave guide lightning model.

## 4. METHOD OF MEASUREMENTS AND DATA EVALUATION

The computer collects the data of all atmospherics within a measuring period of 20 minutes. Subsequently, a histogram of the number of atmospherics per azimuth-interval (1.5°) is calculated. A typical example of such a histogram, recorded at the atmospherics station at Tel Aviv, is shown in Fig. 3 (lower panel). Five centers of activity can be clearly discerned. All activity centers are fitted by normal distributions using a fitting routine included in the operations program of the computer. The fact that activity centers can normally be fitted quite well by normal distributions indicates that they can be regarded as point sources. Theoretically, the horizontal magnetic vector of an atmospheric should be exactly orthogonal to the direction of incidence, so that a very narrow peak should be measured (conventional direction finding with double crossed loops is used he ). However, a certain disturbance of the signals is always present which can lead to deflections of up  10° and more for a single atmospheric impulse. Due to the random character of these disturbances, a statistical analysis of an activity center yields the exact position and the strength (atmospherics / min) of that center, even if the rate per minute is very low (down to ca. 2 / min).

Having determined all significant activity centers in the azimuth histogram, the spectral parameters of each of these centers are evaluated using the same fitting procedure with normal distributions. The histograms of GDD, SAR and SA of the three largest activity centers are shown in the upper panel of Fig. 3. The statistical parameters of the spectral and angular measurements are listed in the real time printer output (see inset to azimuth histogram - lower panel). For each parameter ($\phi$ azimuth, $\Lambda$ GDD, r SAR and a SA) are printed the peak value, the width ($1\sigma$) and the total number of impulses (per minute) of the corresponding normal distribution. One notices that the assumption of a normal distribu-

tion again fits quite well for the GDD (in usec) and SAR (in dB) parameters, especially when the pulse rate is high enough (large centers of activity often show pulse rates ten times larger than these, up to 200 per minute and more). This is again due to the unavoidable disturbances of the signals along their propagation paths, and to the internal spread of the values in the sources, but this obviously does not affect the location of the peak values. A more difficult situation arises for the SA parameter. Although its histogram normally follows a logarithmic normal distribution (Volland, 1968), the statistical parameters can sometimes be evaluated only with quite large uncertainties. This happens particularly for very distant sources, when only the large amplitude wing of the distribution can be recorded because the left part is below the receiver threshold. This threshold is defined in the receiver as $0\,dB$. It corresponds to a spectral field strength of ca. $0.8\,uV \cdot m^{-1} \cdot Hz^{-1}$. Measuring SA in DB above this threshold again implies a normal distribution of this parameter.

## 5. DETERMINATION OF THE VLF-PROPAGATION CONDITIONS AND THE DISTANCES OF THE ACTIVITY CENTERS

In order to determine the model values of the spectral parameters at the receiving station, one has to know three independent variables (see Fig. 2):

(a) the reference height $z_o$ of the lower ionosphere,

(b) the anisotropy factor, $\Omega$

(c) the distance of the activity center.

Therefore, by measuring the three independent spectral parameters GDD, SAR and SA, one should theoretically be able to determine the variables. Due to the more complicated distribution of SA, only GDD and SAR are used at this stage of development of the system. An extension of the model including the SA parameter is in progress. For the present, however, one of the independent variables has to be inserted externally into the model. The variable chosen is the reference height of the lower ionosphere. It is determined by the operations program simply as a function of the zenith angle of the sun for any given point on the globe. The universal time (GMT), available in the computer, and a fundamental spherical analysis is used for this task. Now the computer uses an iterative algorithm to determine that unique value of $\Omega$, for which the distances, deduced from the measured GDD and SAR values with the aid of the models in Fig. 2, become equal. Additionally, the mean ionospheric reference height along the propagation path (depending on the mean zenith angle of the sun) is taken into account. By this method, the appropriate $\Omega$ - value is determined internally together with the distance. The parameters $\Omega$, $z_o$ and the distance are printed out immediately. Fig. 3 and Fig. 4, which was taken one hour later, clearly demonstrate the efficiency of the calculation method. As an example, one notices that the two largest activity centers near $38^{o}$ and $304^{o}$ azimuth remain nearly constant in direction and distance (this will be shown in more detail later). Though the GDD and SAR values for these centers change during this time (in a antiparallel manner), the distances are accurate within 0.25% and 2%, resp.. The appropriate $\Omega$ -value for these directions has shifted according to the propagation model (Fig. 2). Generally, the distances are correct to within about 5%. An exception to this rule are those cases, where the propagation direction traverses the terminator at very small angles and where the terminator is very close to the receiver. An optimization of the model for these conditions is being developed.

## 6. MEASUREMENT EXAMPLES

The measured and evaluated atmospherics data are not only printed out, but also stored on the magnetic tape cassette of the computer with a capacity of approximately one month of data recording. The system includes a small desktop plotter (DIN A4) for real time use of the data, which marks the strengths and the locations of the recorded thunderstorm centers directly on a map. Figs. 5 and 6 show two examples of such recordings. Activity centers are marked by a small triangle with a pointer, whose length is proportional to the strength of the center (atmospherics / min) and whose direction gives the time (GMT) like a clock. In Fig. 5, the plot sheet has been in the plotter for 5 hours (8:00-13:00 GMT on 23. June 1981), i.e. during 15 measuring periods. The activity centers at 8:30 and 9:30 GMT, shown in detail in Figs. 3 and 4, can be clearly identified. As already mentioned, the locations of the largest centers in Figs. 3 and 4, near $38^{o}$ and $304^{o}$, remain nearly constant. The first one is a stationary activity center east of the Caspian Sea, which begins to develop at 8:00 GMT and strengthens considerably up to 12:00 GMT. This development is also evident from Figs. 3 and 4. The second example is also a stationary center in the western Mediterranean, which gradually decays during this measuring period. Furthermore, a large activity region develops at around noon in eastern Europe, which exhibits a shift in the location of the peak intensity. This overall picture agrees well with the meteorological condition and frontal system of that day, as verified on the synoptical charts. These weather maps, however, are available only

every 6 hours and give no information on the strength and development of the activity centers.

Fig. 6 shows a similar picture of the recorded thunderstorm activity during 16.5 hours (therefore some overlapping pointers occur), mainly at nighttime propagation conditions. During those times when the strong West African sources are weak (in this case around 2:00 GMT), strong activity centers can be detected in South America. This gives some indication of the range of the system: activity centers in the western direction can be recorded during nighttime at distances of up to 12 000 km, whereas sources in the east are visible only at distances of up to about 7 000 km (during nighttime). Atmospherics sources can generally be detected during the day at distances of only up to 60% of the nighttime values.

The strong sources over the African continent are always detectable at Tel Aviv during nighttime and partly also at daytime. Sources in South America and in the western Atlantic (see Fig. 6) are also often recorded. Together with the station at Pretoria, which records the same sources over the African continent and in South America, and with the station at Berlin, these continuous sets of data are used for optimizing the propagation models of the atmospherics parameters and for investigations of the general characteristics of the propagation conditions and the (half) global lightning activity.

## 7. CONCLUSIONS

A new method of evaluating atmospherics data, including the strength and locations of lightning activity centers and the appropriate VLF-propagation conditions, is presented. The new VLF-atmospherics receiving station is controlled completely automatically by a desktop computer (HP 9825), which also makes a statistical analysis of the received atmospherics data and applies a sophisticated VLF-propagation model for evaluating the parameters of the propagation model as well as the distances and strengths of the activity centers in real time. In order to have an immediate overview, the detected atmospherics sources are plotted directly on a map by means of a small desktop plotter, and the data are additionally stored on magnetic tape cassettes.

The accuracy of direction finding is in general accurate to $0.5^{\circ}$, depending on the stationarity and form of the activity center. The determination of the spectral parameters, as well as the subsequent determination of the distance of an activity center by employing a suitable VLF-propagation model, is possible to an accuracy of around 5%. Further improvement is expected with an increasing number of stations, which, by means of cross-bearings, will assist in the development of optimal models. The maximum range within which thunderstorm can be located extends from ca. 4000 km for eastern centers at daytime to ca. 12 000 km for sources in the western direction during nighttime. The minumum range is around 200 km, at which an unambiguous determination of the distance becomes difficult due to the overwhelming influence of the higher modes.

## 8. REFERENCES

Harth, W. , 1972, "VLF Atmospherics Parameters Described by the Wait and Walters Model", Z. Geophys. , 38, 153.

Harth, W. , 1981a, "Theory of Low Frequency Wave Propagation", Handbook of Atmospherics, H. Volland (ed.), CRC Press, Boca Raton, FL.

Harth, W. , 1981b, "The Higher Order Mode in the Lower VLF-Range Measured at Medium Distances", Current Proceedings.

Heydt, G. , and Volland, H. , 1964, "A New Method for Locating Thunderstorms and Counting their Lightning Discharges from a Single Observing Station", J. Atmos. Terr. Phys. , 26, 780.

Ingmann, P. , Volland, H. , Heydt, G. , 1981, "Observations of the Thunderstorm Activity during July / August 1975 in the European-North American Area by Groundbased Single-Station Technique", Meteorol. Rdsch. , (in print).

Schäfer, J. , Volland, H. , Ingmann, P. , Eriksson, A. J. , Heydt, G. , 1980, "A Network of Automatic Atmospherics Analysators", Proceedings of the symposium on Lightning Technology, NASA Conference Publication 2128, FAA-RD-80-30.

Volland, H. , 1968, "Die Ausbreitung langer Wellen", Vieweg Verlag, Braunschweig

Volland, H. , 1981, "Low Frequency Radio Noise", Handbook of Atmospherics, H. Volland (ed.), CRC Press, Boca Raton, FL.

Wait, J. R. , 1962, "Electromagnetic Waves in Stratified Media", Pergamon Press, Oxford, New York.

Wait, J. R. , and Spies, K. P. , 1964, "Characteristics of the Earth-Ionosphere Waveguide for VLF Radio Waves", Technical Note, NBS, No. 300.
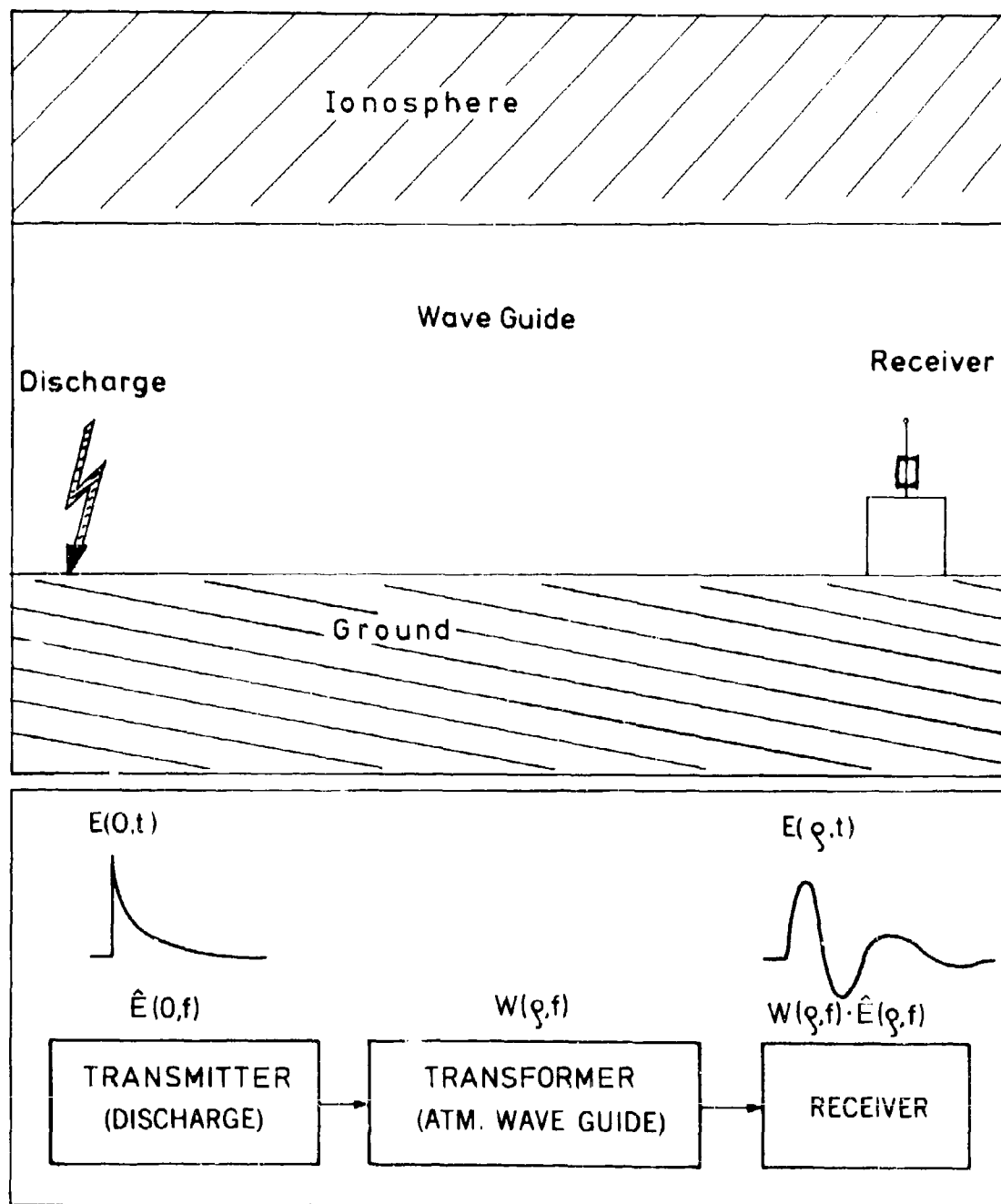
Fig. 1   Schematic diagram of the propagation of VLF-atmospherics through the terrestrial waveguide between earth and ionosphere.
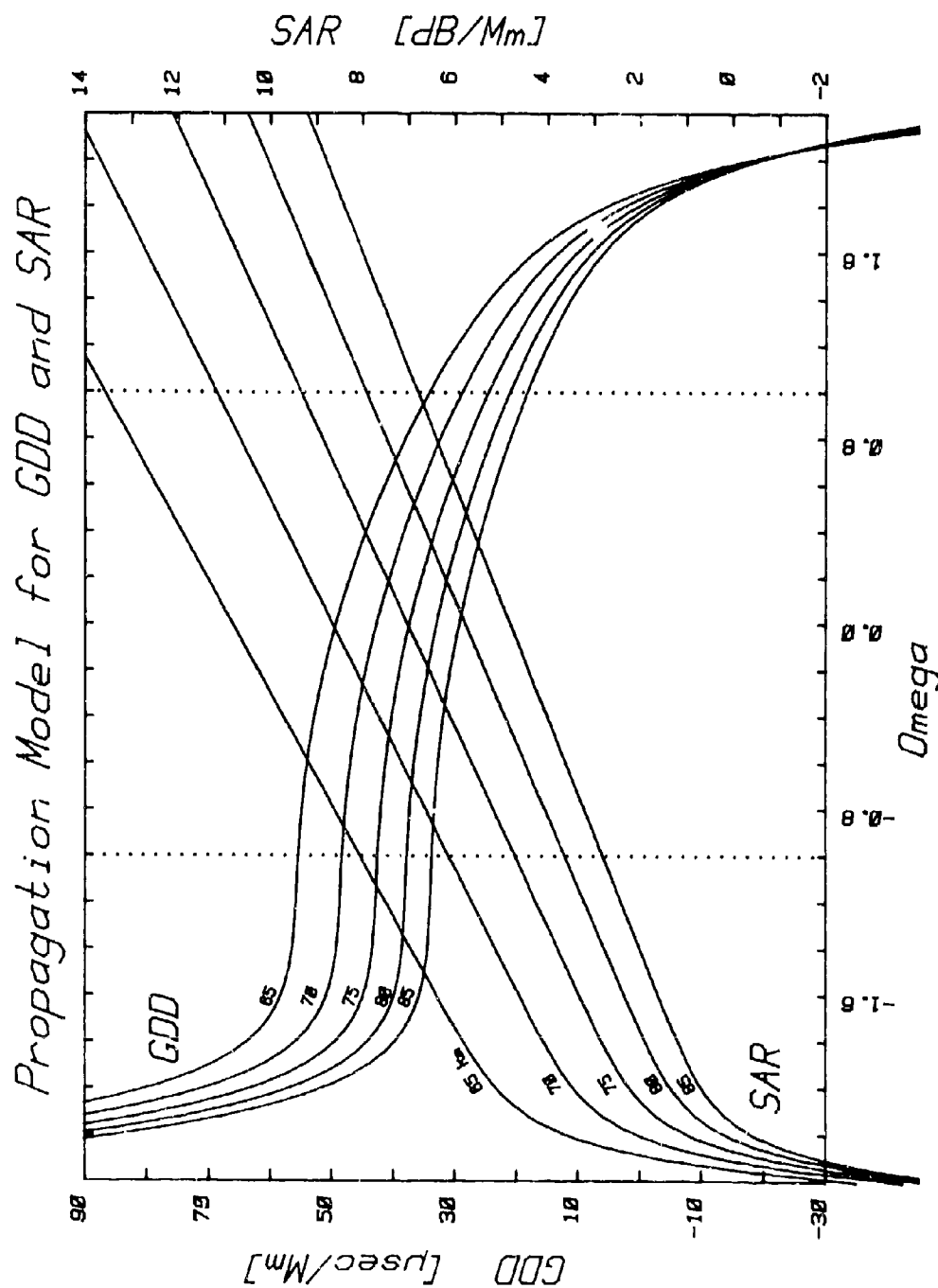
Fig. 2  Propagation models for the atmospherics parameters GDD (Group Delay time Difference, 6 - 8 kHz) and SAR (Spectral Amplitude Ratio, 9 / 5 kHz) as function of the anisotropy factor Omega ($\Omega$, see text) for various ionospheric reference heights $z_0$ (km).
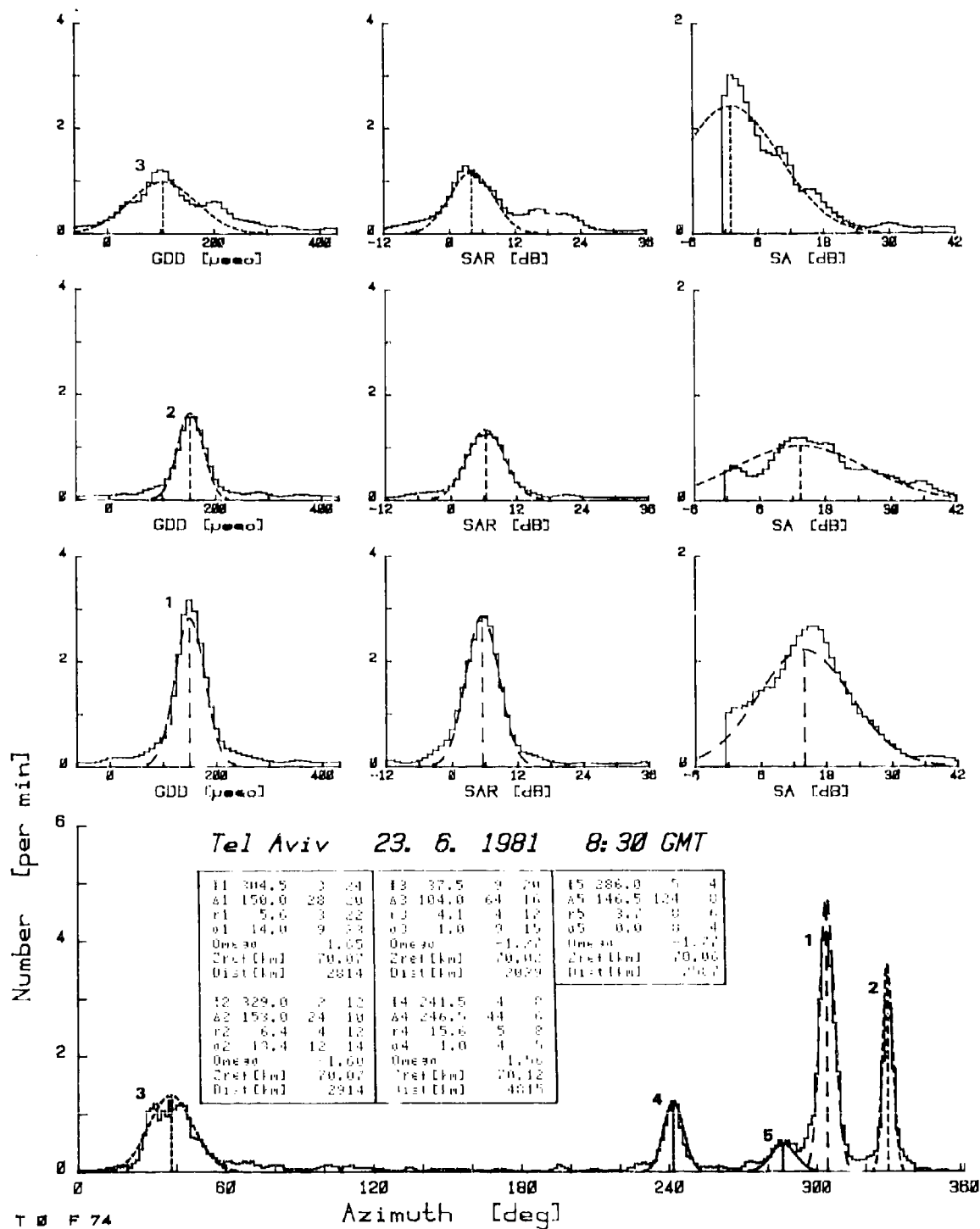
Fig. 3  Histograms of the azimuth and the spectral parameters (GDD, SAR and SA) (of the three largest activity centers) recorded at Tel Aviv in the measuring period 8:20 - 8:40 GMT on 23. June 1981. The inset in the lower panel is the real time printer output of the computer (HP 9825).
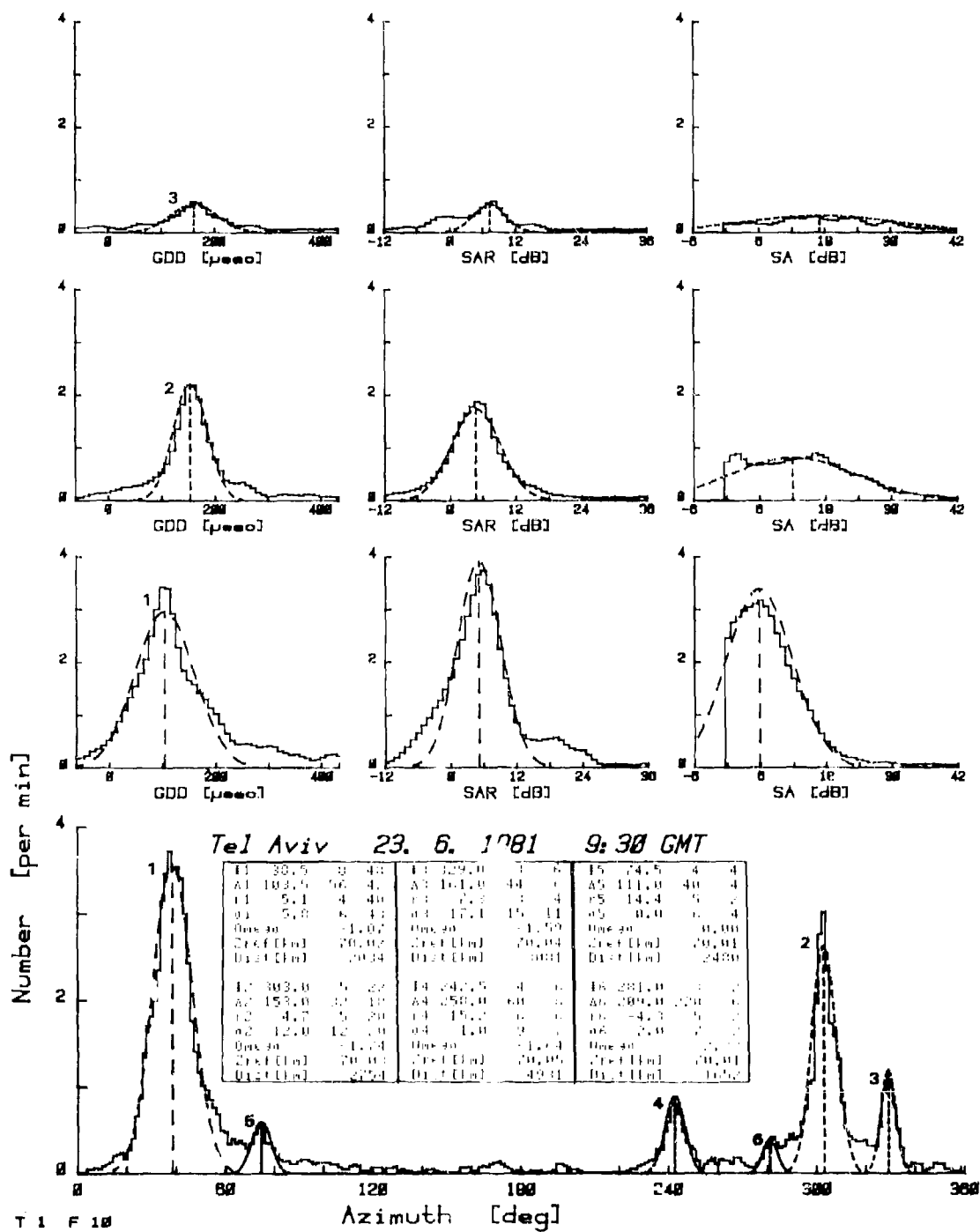
Fig. 4   As Fig. 3 ; for the measuring period 9:20 - 9:40 GMT on 23. June 1981.

Longitude
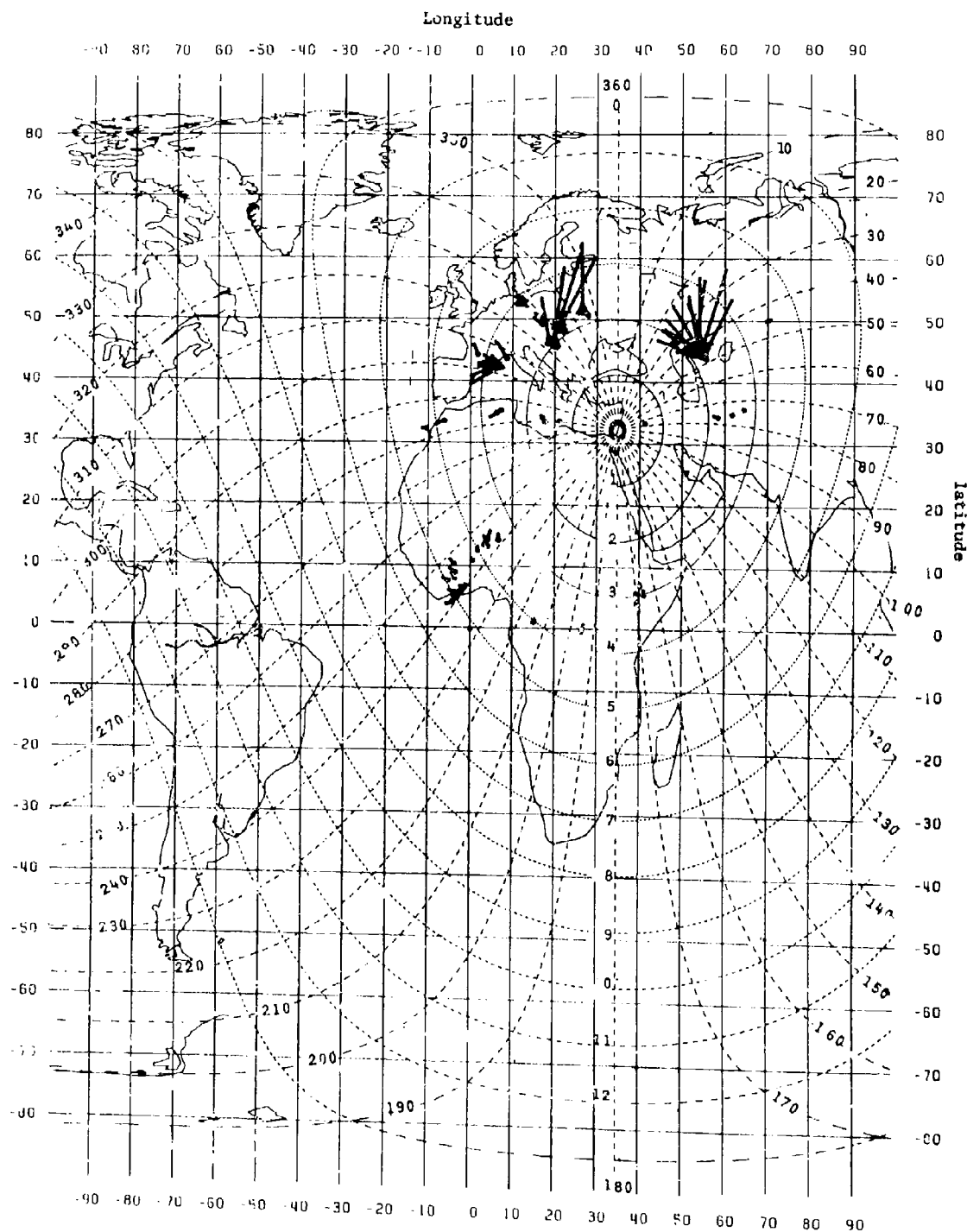


Fig. 5 Thunderstorm activity centers recorded by the Tel Aviv station from 9:00 to 13:00 GMT on 23, June 1981. The length of the pointers is proportional to atmospherics/min, the orientation gives the time (0:00 and 12:00 GMT is North).

**Longitude**
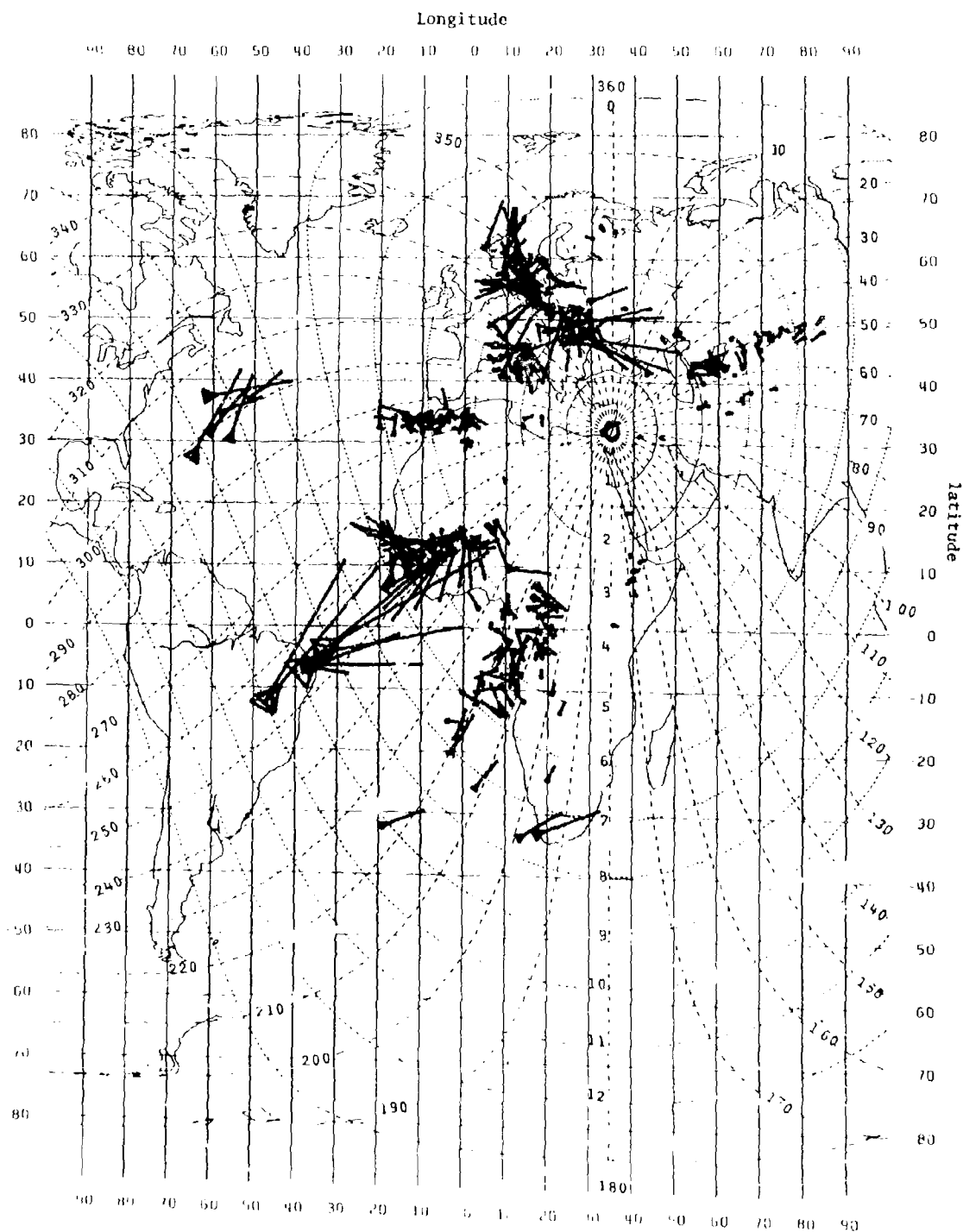


Fig. 6   Thunderstorm activity centers recorded by the Tel Aviv station from 14:00 GMT on 23. June to 6:30 GMT on 24. June 1981. See Fig. 5.

# THE HIGHER ORDER MODE INFLUENCE IN THE LOWER VLF-RANGE
## MEASURED AT MEDIUM DISTANCES

by

W.Harth
Max Planck Institut für Radioastronomie
Bonn, Auf dem Hügel 69
FRG

## ABSTRACT

For a longlasting thunderstorm region over the Bay of Biscay and in Western France the spectral atmospherics parameters GDD (Group Delay Time Difference) and SAR (Spectral Amplitude Ratio) in the lower VLF range have been measured with the atmospherics analyzer in Bonn.

The fluctuation of these parameters with time can be interpreted when we consider the influence and the contribution of higher order modes within these propagation distances (lower than 2000 km). The derived motions of the integral mean activity is in agreement with the wind direction in the 500 mb map.

The field representation is taken from Wait's work including his surface impedance concept.

# INTERACTIONS ONDES-PARTICULES ET ONDE-ONDE
# ENGENDREES PENDANT LES TRANSMISSIONS T.B.F.
# DE KAFJORD, NORVEGE

M. GARNIER et N. CAVACIUTI
Laboratoire de Physique et Dynamique de l'Atmosphère
Université Pierre et Marie Curie, Paris

et

H.C. KOONS et M.H. DAZEY
Space Sciences Laboratory
The Aerospace Corporation
Los Angeles, California

## RESUME

L'intéraction dans la magnétosphère entre des signaux artificiels et les électrons peut entraîner soit une amplification des ondes soit la génération d'ondes de fréquence différente. De plus un signal artificiel peut imposer sa fréquence à un signal naturel de fréquence voisine ou engendrer des bandes de silence dans la magnétosphère.

En 1978 l'Université Pierre et Marie Curie et l'Aerospace Corporation ont installé en Norvège un émetteur d'ondes T.B.F. L'antenne utilisée est une ligne électrique de 15 km environ accordée à la fréquence d'émission. L'Université de Paris utilise un émetteur de 1 KW qui alimente l'antenne avec un courant maximum de 8 ampères. L'Aerospace Corporation utilise l'émetteur TVLF, le courant d'antenne est alors compris entre 20 et 45 ampères.

Les transmissions ont été effectuées lorsque les satellites GEOS 2 et SCATHA étaient près du méridien magnétique de l'émetteur.

Les signaux émis étaient soit à fréquence fixe pulsée, soit une onde entretenue balayée en fréquence. Des signaux associés aux émissions ont été détectés par les récepteurs des satellites à plusieurs reprises.

Le premier type d'émission a permis l'enregistrement de signaux du type PLHR (Power Line Harmonic Radiation). Des émissions déclenchées (ASE), des éléments de choeur et une bande de silence ont aussi été engendrés.

Les deux types d'émission ont engendré ou renforcé le souffle magnétosphérique à une fréquence constante pendant les émissions à fréquence fixe et à une fréquence variable pendant une émission en balayage de fréquence. A deux reprises les émissions à fréquence variable ont imposé leur fréquence aux signaux naturels.

## ABSTRACT

Interactions in the magnetosphere between man-made VLF waves and electrons can produce either an enhacement of the wave or the generation of waves at a different frequency. Furthermore natural emissions can be frequency shifted or modified by a nearby transmitter signal.

Injection of VLF waves into the magnetosphere was initiated in 1978 in Norway by both University of Paris and The Aerospace Corporation. The antenna is a 15 km power line tuned at the transmitted frequency. The University of Paris used a 1 KW transmitter to drive the antenna with a maximum current of 8 amperes. The Aerospace Corporation used the TVLF transmitter with an antenna current between 20 and 45 amperes.

Transmissions were conducted when the SCATHA and GEOS II satellites were near the magnetic meridian of the transmitter.

Transmitted signals were either keyed fixed frequency or continuous waves swept in frequency. Signals correlated with the transmissions were detected by the satellite receivers on several dates.

With the first type of transmission, signals similar to power line Harmonic Radiation (PLHR) were recorded. Artificially stimulated emissions (ASE), chorus elements and magnetospheric induced quiet band are also likely to have been triggered. Both types of transmissions triggered or enhanced hiss at a constant frequency during fixed frequency transmissions or at a variable frequency during a swept frequency transmission.

During swept frequency transmissions in two cases natural emissions were frequency shifted by the man-made signal.

## I. DESCRIPTION DE L'EXPERIENCE ET TRAITEMENT DES DONNEES.

Dès 1975 il a été proposé de tenter d'émettre des signaux artificiels de très basse fréquence vers le satellite GEOS. Une antenne devait être construite en Suède mais du fait du prix élevé de l'opération il a été décidé d'utiliser une ligne électrique comme antenne. Une première ligne a été essayée en Norvège près d'Andenes, il a ainsi été possible, en Mars 1978, d'effectuer des émissions à destination de GEOS I. L'utilisation de cette ligne a alors entraîné d'importantes perturbations sur le réseau de distribution électrique norvégien et l'expérience a du être arrêtée prématurément.

Une autre ligne électrique fut trouvée près de Sortland et l'émetteur TVLF de l'Aerospace Corporation (KOONS H.C. and DAZEY M.H., 1975) a été utilisé en Octobre 1978 pour des émissions vers GEOS II. Plusieurs exemples de signaux reçus seront présentés par la suite. Les émissions pulsées à 1525 Hz ont entraîné de très importantes interférences avec le réseau téléphonique et les émissions ont aussi dû être arrêtées.

Une troisième et dernière ligne électrique fut proposée en 1979 par la Norvège près de Kafjord (?9,4° N ; 20,9° E). Elle est installée sur la montagne et peut être utilisée toute la journée sans aucune interférence avec le réseau téléphonique. Sa longueur totale de 15 km environ est utilisée avec l'émetteur de l'Université de Paris, seulement 10,6 km sont utilisés lors du fonctionnement de l'émetteur TVLF afin d'éviter certaines interférences avec le réseau téléphonique. Des émissions ont eu lieu en Mai et Août 1979 ainsi qu'en Mars, Mai, Août et Octobre 1980.

Ce papier présente quelques résultats obtenus au cours des campagnes d'émission. Au cours de certaines le satellite GEOS II était activé mais l'ensemble des données n'est pas encore disponible. Le satellite américain SCATHA lancé en Janvier 1979 se trouvait, à l'exception de Mars 1979, près du méridien magnétique de Kafjord. Pendant environ deux heures par jour le satellite était activé et recevait en large bande les signaux de très basse fréquence.

Le satellite GEOS II est géostationnaire à une longitude de 36,2 degrés Est. L'orbite de SCATHA a une inclinaison de 7,9 degrés, une période de 23h35 mn, un apogée de 7,78 rayons terrestres et un périgée de 5,32 rayons terrestres. Le spin du satellite est de 1 tour par minute.

Le récepteur VLF de SCATHA utilise 2 antennes pour détecter les composantes magnétique et électrique des émissions. La sensibilité du récepteur est à 1,3 KHz de $5 \times 10^{-7}$ V/m $(Hz)^{1/2}$ pour la composante électrique et de $3 \times 10^{-6}$ $\gamma$ $(Hz)^{1/2}$ pour la composante magnétique.

Les données reçues sont transmises en large bande de 0 à 5 KHz. A un instant donné, les données d'une seule antenne sont transmises. Normalement les antennes sont commutées automatiquement toutes les 16 secondes.

En Mai 1979, l'antenne était accordée à différentes fréquences entre 1200 et 2500 Hz par une self variable. L'émetteur avait une puissance de 1 KW. Deux types d'émission ont été effectués :

- des émissions pulsées - 4 secondes toutes les 12 secondes - à 1280 Hz.

- des balayages de fréquence linéaires de 1350 Hz à 2550 Hz au rythme de 300 Hz toutes les 176 secondes. Cette pente a été choisie en fonction du rythme de balayage du récepteur du satellite GEOS II. Pendant ces émissions l'antenne était accordée tous les 300 Hz à 1500 Hz, 1800 Hz, 2100 Hz et 2400 Hz, il était ainsi possible d'obtenir un courant maximum de 8 ampères. Le temps de commutation était très court devant la durée du balayage.

En Juillet 1980 l'antenne était accordée à 1280 Hz ou à 1420 Hz par une self avec une bande passante de 16 hertz. Pendant 10 minutes toutes les 15 minutes le récepteur du satellite SCATHA était connecté à l'antenne électrique. Différents types de pulsage ou de balayage de fréquence ont été éxécutés.

En Octobre 1980, outre des balayages de fréquence identiques à ceux de Mai 1979, un autre type d'émission a été effectué. Le signal émis était à une fréquence $F_1$ pendant 20 ou 40 secondes puis à une fréquence $F_2$ pendant les 20 ou 40 secondes suivantes.

Les spectrogrammes présentés ont été obtenus à l'Université de Paris à partir des bandes analogiques du satellite SCATHA ou des bardes numériques du satellite GEOS II. L'analyse spectrale a été effectuée en temps réel avec un transformateur de Fourier rapide (FFT) connecté à un miniordinateur. Il est possible d'obtenir soit une analyse FFT en large bande soit une loupe FFT en temps réel de n'importe quelle partie du spectre. La modulation de brillance du terminal graphique du miniordinateur par les spectres successifs permet d'obtenir la présentation classique des spectrogrammes. Le logiciel écrit dans ce but possède une propriété fondamentale : quelle que soit l'amplitude du signal d'entrée, le résultat de la FFT est multiplié par la puissance de 2 qui le ramène au maximum de la dynamique de la modulation de brillance. Il est ainsi possible de détecter des signaux très faibles. Les spectrogrammes présentés par la suite doivent être lus de la façon suivante : une augmentation du niveau du signal n'entraîne pas un noircissement plus important du spectrogramme mais une diminution du noircissement du au bruit.

## II. RESULTATS EXPERIMENTAUX.

### A) SOUFFLE MAGNETOSPHERIQUE - 26 Mai 1979.

Quelques exemples des spectrogrammes obtenus le 26 Mai 1979 sont présentés sur les figures 1 à 4. Les figures 1 et 2a correspondent aux signaux reçus entre 13:36 TU et 13:50 TU. De 13:36 à 13:40 aucune émission n'a été effectuée et l'on remarque la commutation toutes les 16 secondes entre l'antenne magnétique (bruit maximum) et l'antenne électrique. Pendant cette période le satellite reçoit seulement un faible souffle magnétosphérique compris entre 1200 et 1800 Hz et noyé dans le bruit. Une émission à 1280 Hz débute à 13:40 TU, à partir de ce moment le niveau du souffle augmente pendant environ 2 minutes et sa largeur de bande décroit (figure 2a). L'amplification du souffle due à l'intéraction avec notre émission atteint 15 décibels, cette amplification n'existe plus quand vers 14:00 TU débute un balayage de fréquence et la

fréquence du faible souffle est centrée vers 1400 Hz. Pendant 3 minutes de 14:02 TU à 14:05 TU il y a encore amplification du souffle (figure 2b) lorsque la fréquence d'émission est proche de celle du souffle mais cependant avec un retard de l'ordre de 90 secondes.

L'amplification se produit à nouveau à 14:12 TU pendant une émission à fréquence fixe et dure jusqu'à 14:30 TU fin de cette émission (figure 3a). L'amplification est alors de 15 décibels.

De 14:30 TU à 14:42 TU un balayage de fréquence entraîne une nouvelle amplification du souffle à partir de 14:34 TU avec un retard de 3 minutes par rapport au moment où la fréquence d'émission est égale à celle du souffle. Pendant cette émission la fréquence du souffle décroît de 1400Hz à 14:34 TU à 1100 Hz à 14:42 TU alors que la fréquence d'émission augmente.

La fréquence du souffle redevient constante (figure 4b) à partir de 14:42 TU début d'une nouvelle émission à fréquence fixe.

Ces résultats prouvent l'existence d'une étroite corrélation entre les émissions et le niveau de souffle. Une amplification pouvant atteindre 15 décibels prend naissance pendant les émissions à fréquence fixe ou lorsque la fréquence est voisine de celle du souffle. Dans un cas le processus d'amplification se produit pendant tout le balayage et la fréquence du souffle varie avec la fréquence d'émission. Les processus d'amplification s'établissent en 2 minutes environ dans les différents cas.

### B) EMISSIONS EN BANDE ETROITE - 27 Mai 1979.

Les spectrogrammes obtenus le 27 Mai 1979 (figure 5) sont le résultat d'une loupe FFT centrée sur la fréquence d'émission. La fréquence centrale est 1280 Hz pour les émissions à fréquence fixe et varie pendant les balayages de fréquence. Dans ce dernier cas un signal à fréquence fixe a une pente négative sur les spectrogrammes (figure 6a) alors que le signal reçu se manifeste par une ligne pratiquement horizontale (figures 6b et 6c).

Les lignes horizontales à 1140 Hz, 1260 Hz et 1380 Hz de la figure 5a corespondent à des harmoniques du 60 Hz enregistrés sur les bandes avec les signaux, les harmoniques du 50 hertz du réseau électrique européen ne sont pas directement détectables.

Avant 21:42 TU, début d'une émission à 1280 Hz seuls les harmoniques du 60 Hz et du bruit sont détectables. Après 21:42 TU, un faible signal à 1280 Hz est amplifié avec un léger (± 20 Hz) décalage de fréquence. Ce signal similaire aux PLHR décrits par HELLIWELL R.A. et al.1975, a été généré par l'émission. Entre 21:53 TU et 21:55 TU la fréquence du signal augmente - est maintenue constante au voisinage de 1300 Hz - puis décroît après avoir atteint 1350 Hz, ces deux fréquences sont des harmoniques de 50 Hz. Ce phénomène est identique aux interactions onde onde entre les harmoniques des lignes électriques et les émissions de Siple décrites par HELLIWELL R.A. et al. (1975), sa durée - de l'ordre de 2 Minutes - est cependant beaucoup plus importante que celle des phénomènes présentés par HELLIWELL.

Un signal à 1280 Hz est reçu après 21:57 TU et entre 21:59 TU et 22:01 TU, quatre émissions déclenchées (ASE) avec une période voisine de 24 secondes sont reçus quand le niveau de bruit est faible, c'est à-dire sur l'antenne électrique. Ces signaux ont été engendrés par nos émissions. La période de 24 secondes est double de la période de pulsage et peut être expliquée par le fait que - à cause du niveau de bruit sur l'antenne magnétique - un signal sur deux ne peut être détecté.

Deux émissions en balayage de fréquence ont pu être détectées le 27 Mai 1979 - figure 6b entre 21:38 TU et 21:40 TU et figure 6c entre 21:18 TU et 21:19 TU - et ont donné naissance à des signaux pratiquement constants en fréquence sur les spectrogrammes en balayage de fréquence. Ces signaux sont à nouveau liés à des interactions onde-onde puisque l'observation des spectrogrammes en large bande montre l'existence de signaux naturels dont la fréquence est perturbée lorsque celle du balayage lui devient voisine.

Pendant la deuxième période le satellite GEOS II était activé, le dépouillement préliminaire de la bande numérique montre que le balayage de fréquence a aussi été détecté par ce satellite. A cette période la position des deux satellites était très différente :

- GEOS   longitude 36.2 E     L ≈ 6.6
- SCATHA  longitude 43.2       L ≈ 8.4

une analyse comparée des résultats obtenus devrait permettre de comprendre le mécanisme de propagation des ondes entre la zone d'intéraction et les satellites.

### C) SOUFFLE ET CHOEUR - 20 Juillet 1980.

Le 20 Juillet entre 13:25 TU et 14:00 TU se sont succédés différents types de pulsage de la fréquence 1280 Hertz. Jusqu'à 13:26 TU l'émission consiste en une minute composée d'une séquence de pulses de durée croissante jusqu'à 12 secondes. De 13:26 TU à 13:35 TU l'émission consiste en une modulation en signaux carrés de période 10 secondes, de 13:35 TU à 13:45 TU la période est de 60 secondes, de 13:45 TU à 13:50 TU la période est de 2 secondes, à partir de 13:50 TU le premier type d'émission reprend.

A 13:30 TU la ligne de force du champ géomagnétique passant par le satellite rencontre l'altitude 100 km à 0,3° Ouest et 0,3° Sud de Kafjord.

Une bande de souffle de largeur 150 Hz et centrée vers 1250 Hz est détectée à partir de 13:28 TU, son amplitude croît pendant la modulation à 10 secondes et plus fortement pendant celle à 60 secondes, le souffle le plus fort étant reçu entre 13:35 TU et 13:40 TU.

A partir de 13:40 TU et jusqu'à la fin de la modulation à 60 secondes des éléments occasionnels de choeur sont reçus ; le choeur devient permanent pendant la séquence d'émission de pulses de longueur variable.

Il y a une nette corrélation entre ces signaux et notre émission, l'occurrence des éléments de choeur ne semble cependant pas liée à la fréquence de pulsage.

Comme pour les exemples précédents, le signal direct de l'émetteur n'a pas été détecté bien que la présence de sifflements prouve l'existence d'un trajet de propagation entre le guide d'onde terre-ionosphere et le satellite.

D) BANDE DE SILENCE - 20 Octobre 1980.

Le 2 Octobre 1980 le satellite SCATHA a été déclenché à 12:37 TU lorsqu'une émission à 1480 Hz et 1520 Hz avait lieu à Kafjord. Simultanément l'émetteur de Siple émettait une succession de rampes de fréquence montante puis descendante entre 1 et 2 KHz. Les spectrogrammes de la figure 8 montrent la présence designaux-essentiellement constitués d'éléments de choeur - compris entre 1 et 2 KHz. Une bande de silence comprise entre 1500 et 1600 Hz est d'autre part nettement visible. L'ensemble des phénomènes disparaît et le cadencement des antennes redevient visible à partir de 12:54 TU, soit environ 4 minutes après l'arrêt simultané des émissions à Kafjord et à Siple.

Le phénomène observé qui semble nettement corrélé avec les émissions effectuées est analogue à celui décrit par RAGHURAM R. et al,(1977) pour les bandes de silence dans le souffle magnétosphérique et pour lequel une interprétation a été proposée par CORNILLEAU N. et GENDRIN R. (1979). Il faut cependant noter que dans le cas présent la bande de silence est située au-dessus de la fréquence d'émission alors que RAGHURAM R. et al l'observent en-dessous de la fréquence de l'émetteur. La constante de temps de disparition de l'ordre de 4 minutes est supérieure à celles observées par RAGHURAM.

III. INTERPRETATION ET CONCLUSION.

Tous les exemples présentés sont liés à des intéractions entre ondes ou entre ondes et électrons dans la magnétosphère. Le signal direct et sa modulation n'ont cependant pas été clairement mis en évidence du fait de la très faible puissance d'émission. Nous apportons ainsi la preuve que s'il existe, le niveau minimum de signal nécessaire pour exciter les intéractions est très faible.

L'absence de modulation sur les signaux reçus peut s'expliquer par une augmentation de la constante de temps des intéractions ondes particules dans la magnétosphère extérieure par rapport à la plasmasphère. Les constantes de temps décrites ici -quelques minutes - sont de 5 à 10 fois supérieures à celles observées aux latitudes plus faibles L = 4 par HELLIWELL R.A. et al. Ceci implique que les électrons doivent se réfléchir plusieurs fois d'une hémisphère à l'autre avant le développement complet des phénomènes.

Si cette hypothèse est justifiée, l'utilisation d'un code de modulation très lent devrait permettre de mettre en évidence la modulation. Un tel code a été utilisé le 1er Octobre 1978 et sera utilisé à l'avenir.

Le 1er Octobre 1978 entre 17:12 TU et 17:20 TU l'émetteur était pulsé 10 secondes toutes les minutes, la fréquence était de 1525 Hz et le courant d'antenne de 40 ampères. Afin de mettre en évidence la modulation dans les signaux reçus les données ont été divisées en périodes d'une minute en synchronisme avec l'émetteur, chaque minute a été ensuite décomposée en six périodes de 10 secondes de telle sorte que l'émetteur était actif pendant une seule de ces six périodes.

Les spectres ainsi obtenus ont été accumulés, si la modulation est détectée, on doit trouver un signal voisin de la fréquence d'émission pendant seulement une période. C'est le cas figure 9 pendant la première période au voisinage de 1530 Hz.

La même technique a été utilisée de 17:20 TU à 17:24 TU et de 17:36 TU à 17:43 TU lorsque la modulation était de 10 secondes toutes les 30 secondes. Un signal à 1525 Hz est visible figure 10 pendant la première période et un signal voisin de 1530 Hz est visible figure 11. Nous avons ainsi clairement mis en évidence la réception du signal en provenance de l'émetteur.

En conclusion, les signaux de très basse fréquence émis à partir du sol peuvent se propager hors de la plasmasphère et entraîner des intéractions ondes-particules. Le niveau nécessaire à ces intéractions est très faible et les constantes de temps augmentent avec L.

Bien que le satellite soit très proche du méridien magnétique de l'émetteur, des signaux liés aux émissions ne sont observés qu'une faible fraction ($<$ 10 %) du temps d'émission.

REFERENCES.

CORNILLEAU N., GENDRIN, R., 1979, "VLF transmitter induced quiet bands : a quantitative interpretation" J. Geophys.Res., 84, 882.

HELLIWELL R.A., 1967, "A theory of discrete VLF emissions from the magnetosphere", J. Geophys. Res., 72, 4773.

HELLIWELL R.A., KATSUFRAKIS J.P., BELL T.F. and RAGHURAM R., 1975, "VLF line radiation with power system radiation" J. Geophys. Res., 80, 4249

KOONS H.C. and DAZEY M.H., 1975, "Transportable VLF transmitter in VLF, VLF radiowave propagation édited by J. HOLTET, D. REIDEL Publishing Co Dordrecht Holland.

RAGHURAM R., BELL T.F., HELLIWELL R.A. and KATSUFRAKIS J.P., 1977, "A quiet band produced by VLF transmitter signal in the magnetosphere" Geophys. Res. Lett. 4, 199.

(a)

(b)

26 MAI 1979 , TU          Figure 1

1280 Hz

(a)

(b)

14-00-00   RAMPE      26  MAI 1979 , TU      Figure 2      14-05-00

FREQUENCE, KHz

(a)

14-25-00      1280   Hz      14-29-30

(b)

14-34-30      RAMPE      14-39-00

26 MAI 1979 , TU      Figure 3

(a)

14-39-00      RAMPE      14-43-00

FREQUENCE , KHz

(b)

14-43-00      1280  Hz      14-48-00

26  MAI  1979 , TU      Figure 4
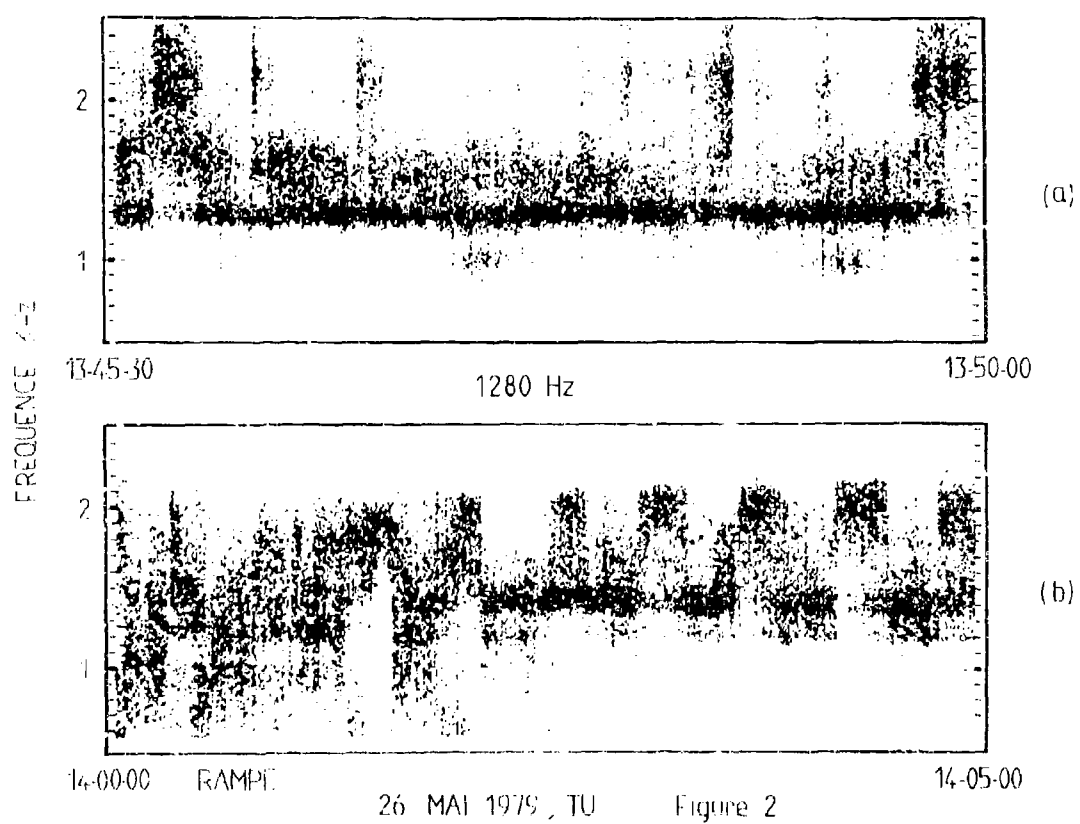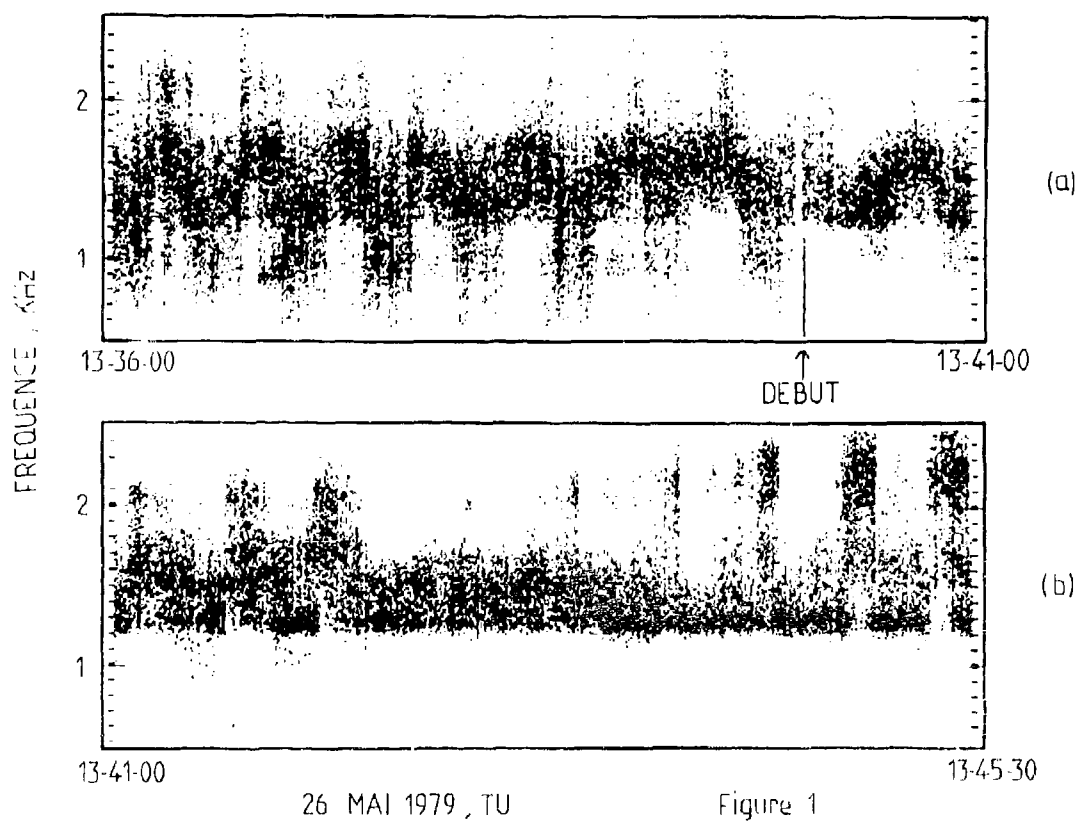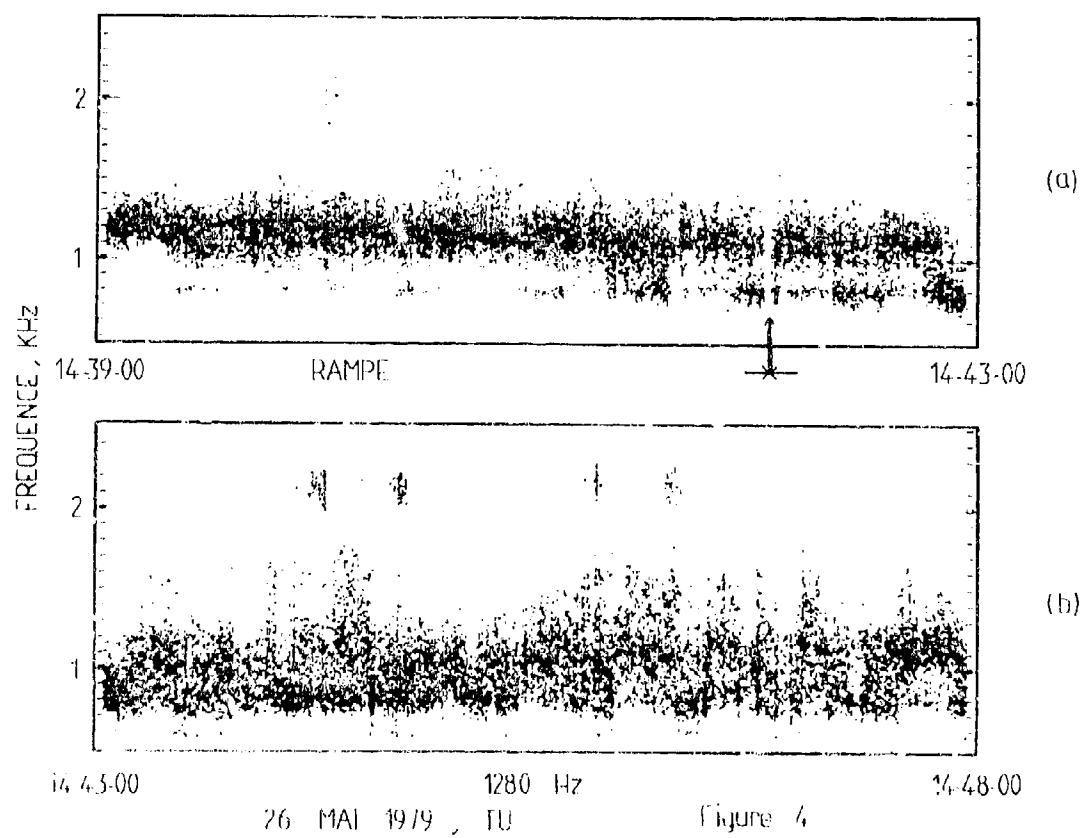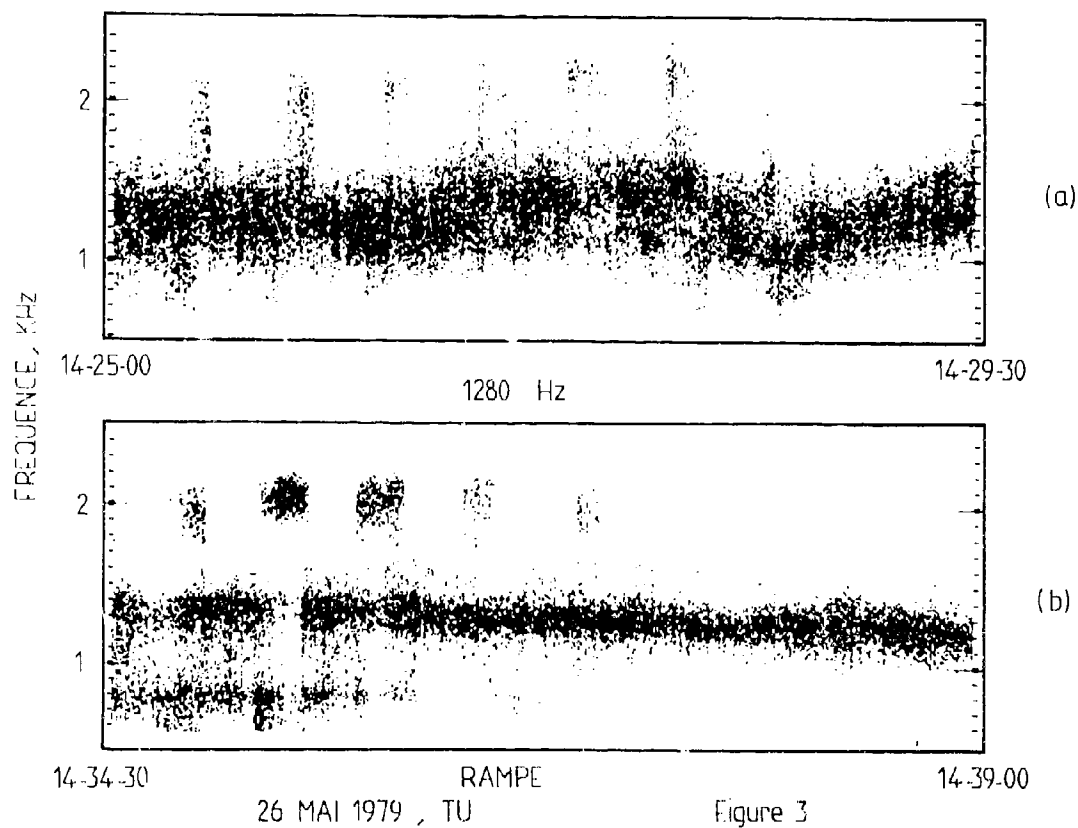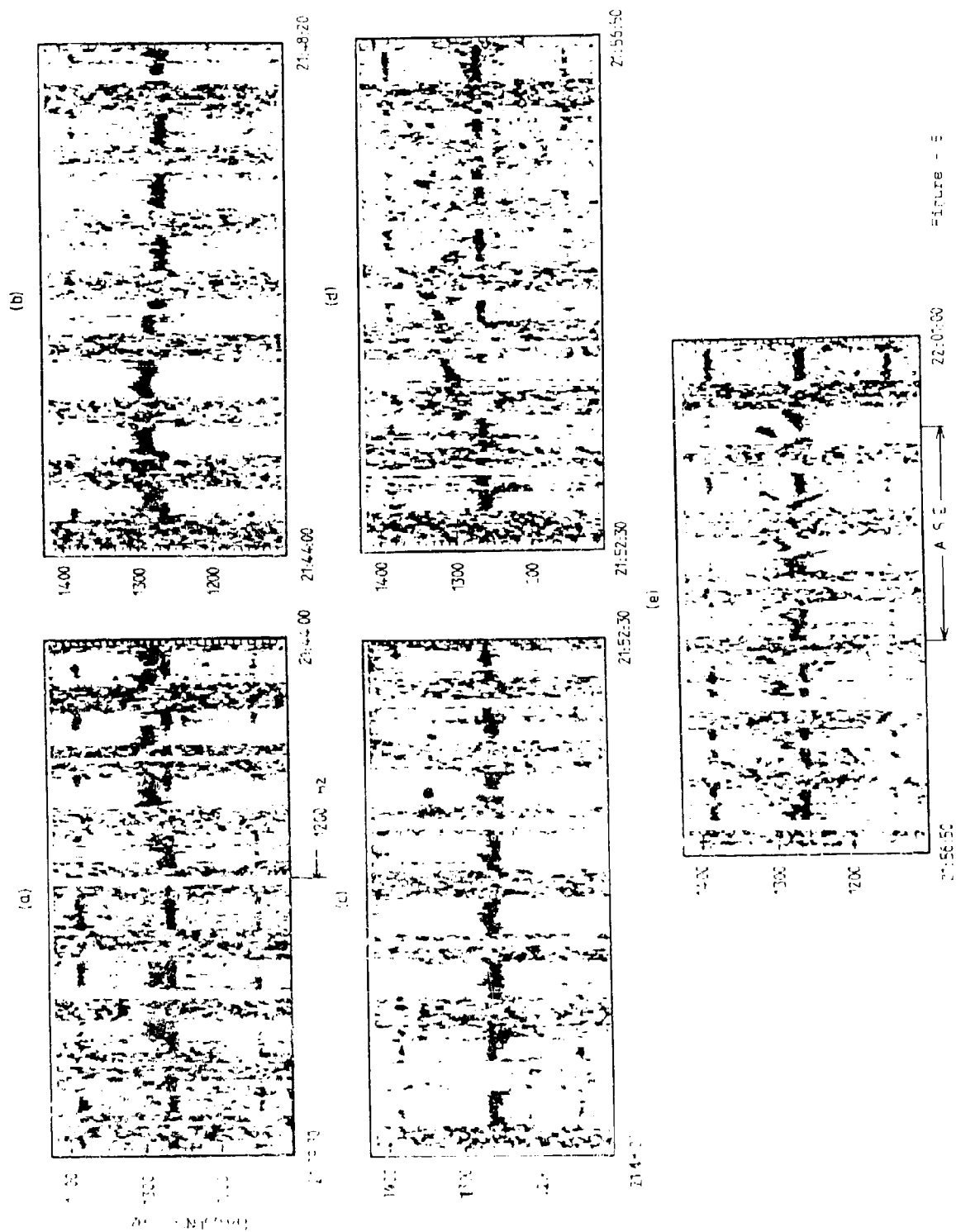
Figure - 8

(a)
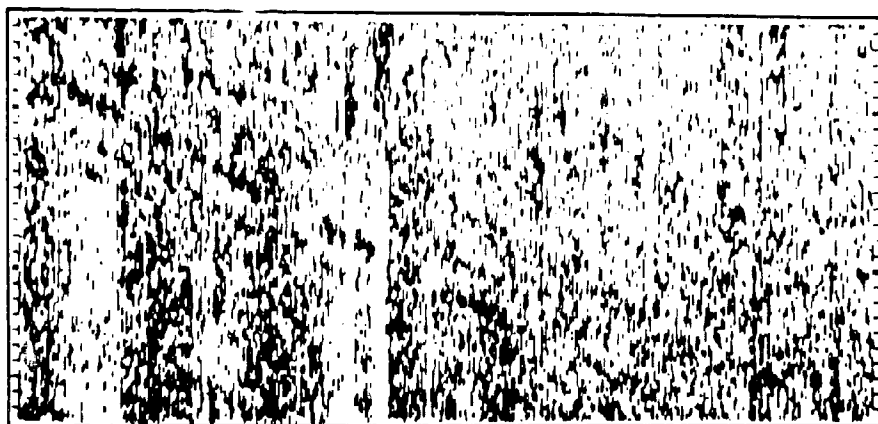
21:34:30                                              21:38:00

(b)

FENETRE GLISSANTE   12,5 Hz  PAR DIVISION
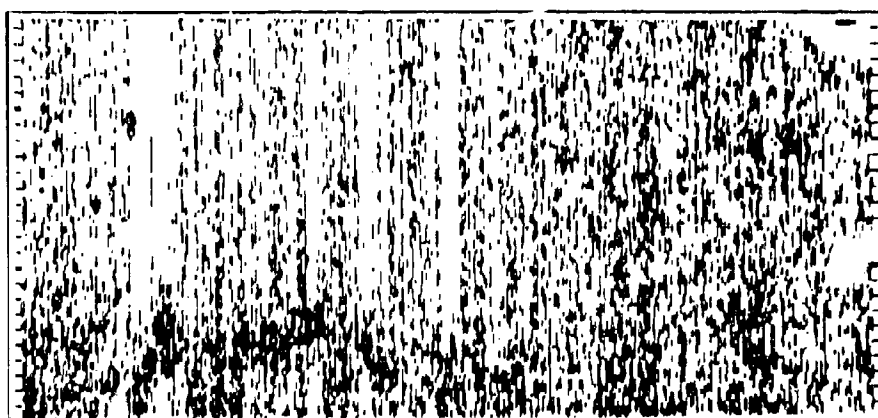
21:38:00      |   SIGNAL      DETECTE   |              21:41:23

(c)
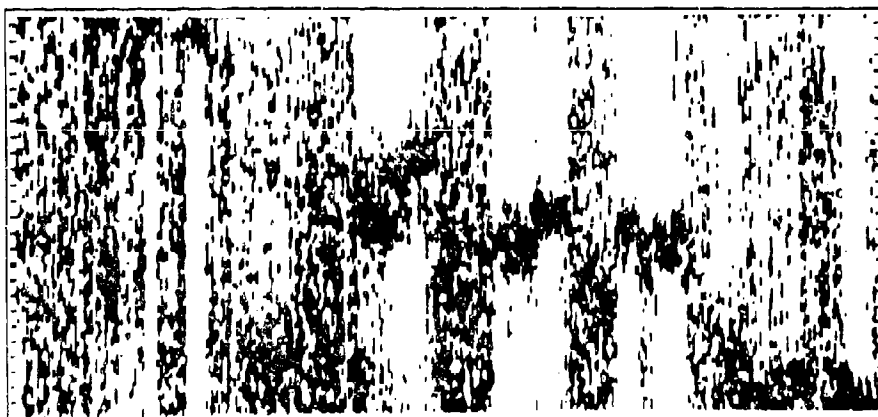
22 16 30              |   SIGNAL   DETECTE   |         22 19 56

22   MAI   1979   TU                    Figure   6
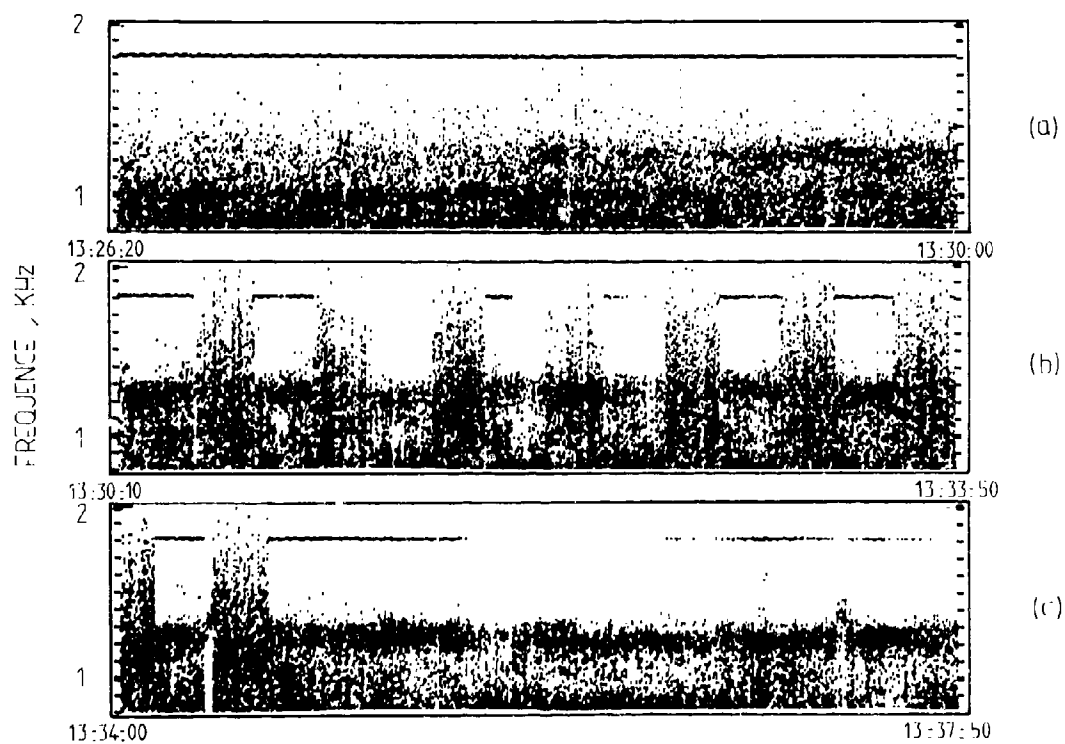
20 JUILLET 1980                    Figure 7



20 JUILLET 1980                    Figure 7

FREQUENCE , KHz

(g)

13:50:10　　　　　　　　　　　　　　　　　13:53:50

(h)

13:54:10　　　　　　　　　　　　　　　　　13:57:50

(i)

13:58:10　　　　　　　　　　　　　　　　　14:01:50
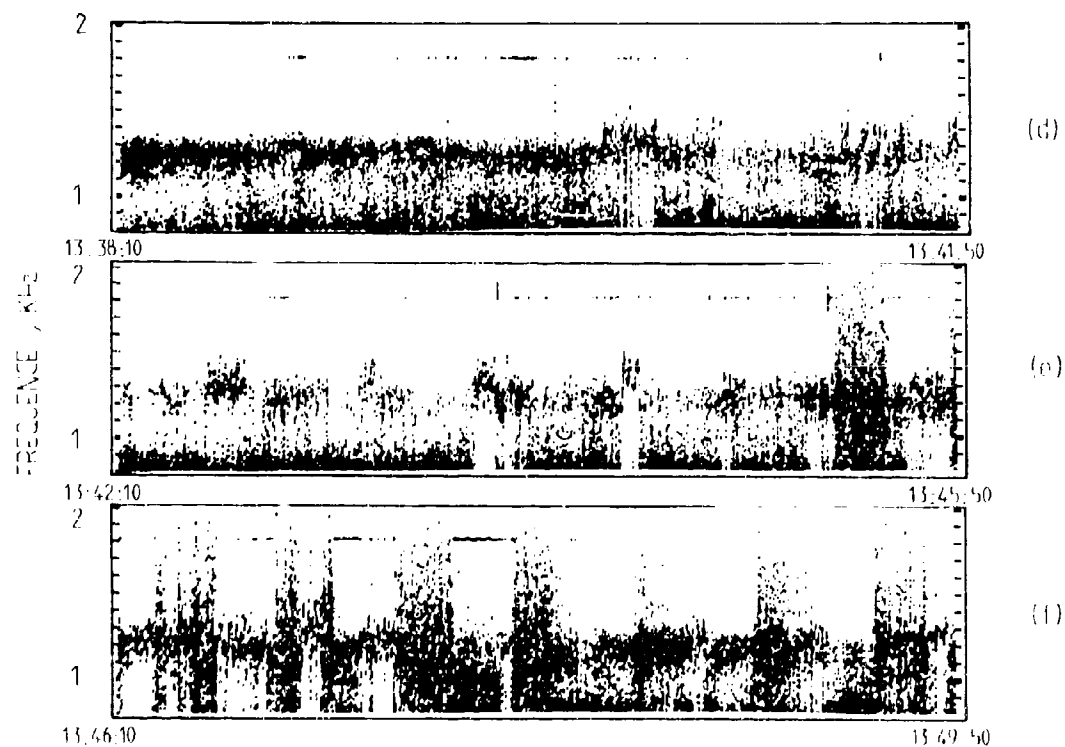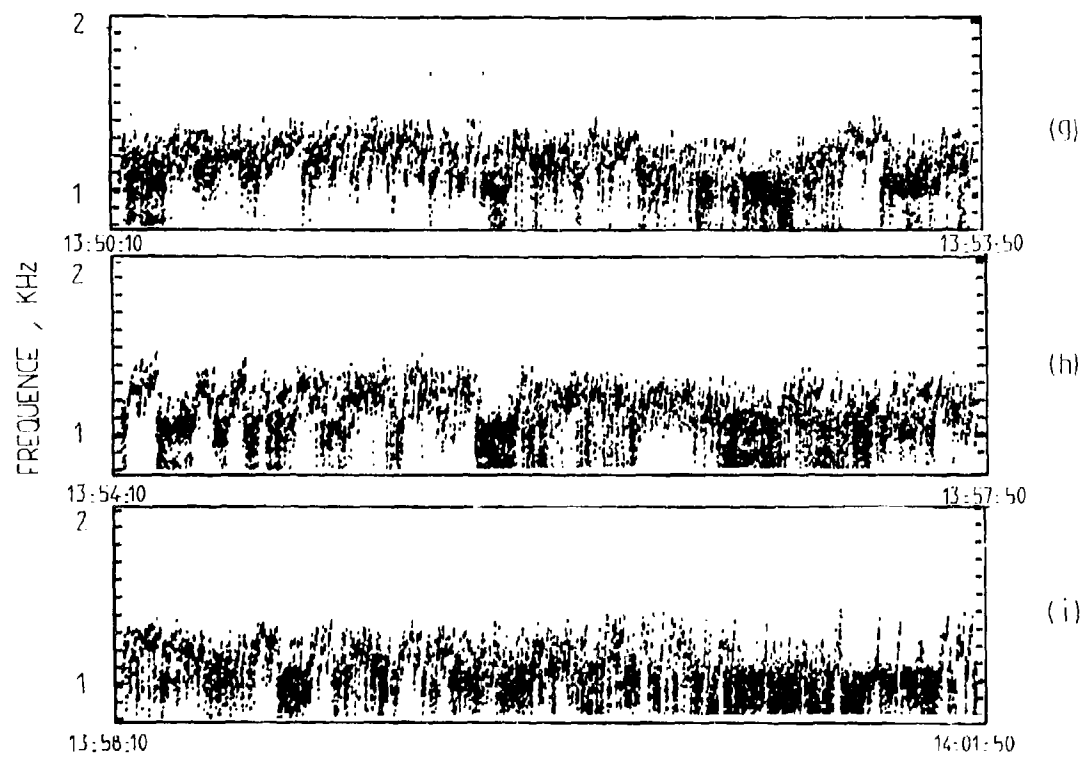
20　JUILLET　1980 , TU　　　　　　Figure　7
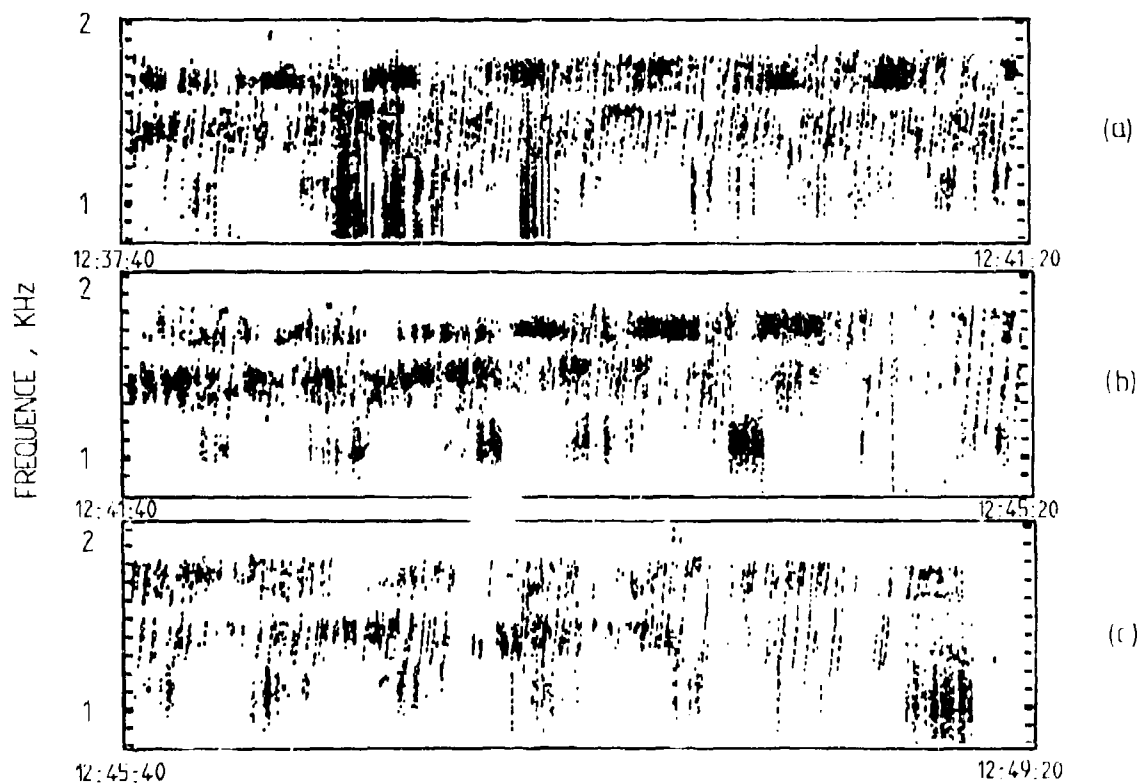
2 OCTOBRE 1980 Figure 8
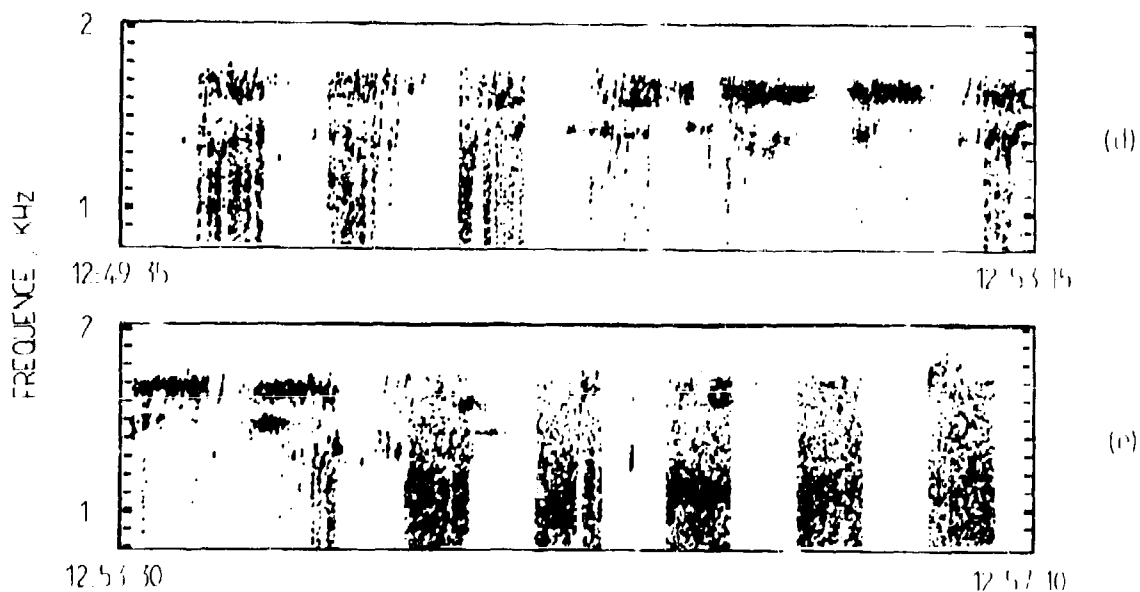
2 OCTOBRE 1980 Figure 8

generated resultant fields are nearly equal in magnitude at a receiver location, rather deep oscillations in the received field strength ma, occur during the period of an orbit. These oscillations often occur during nighttime propagation conditions but can occur during daytime also. Figure 2 shows the signal reception pattern versus distance and time for an airborne transmitting facility flying in good orbit (verticality ≈70%) during daytime. Figure 3 shows the same pattern for a poor orbit (verticality ≈10%) during nighttime. The observed fluctuations range from mild to extreme.
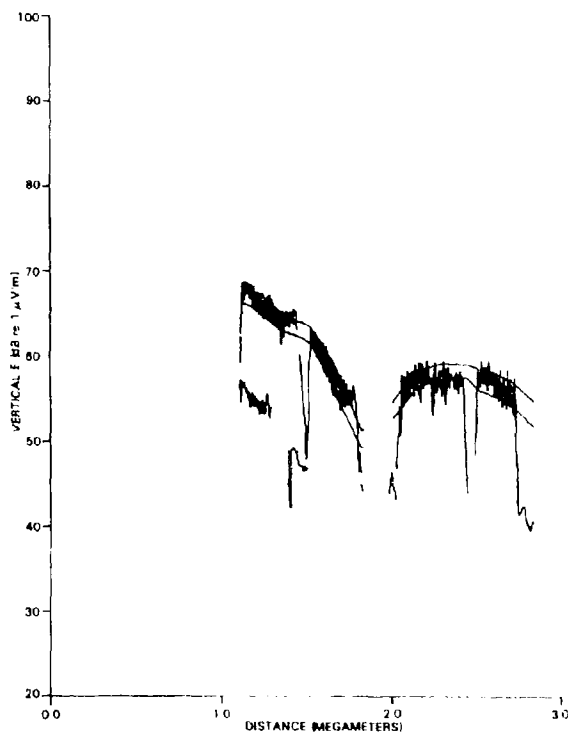


Fig. 2 — Field strength versus distance measured during daylight hours on an aircraft flying radially toward an airborne broadcasting facility in good orbit near Jacksonville, Florida on March 27, 1971, with the frequency being 19.4 kHz
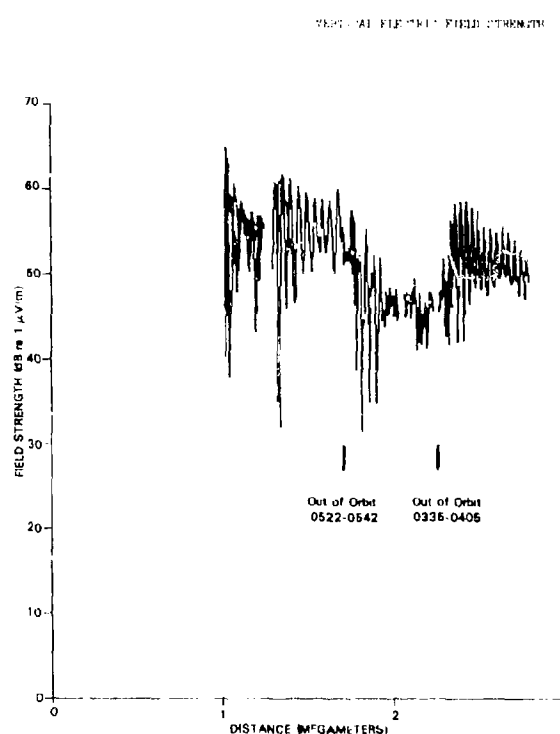
Fig 3 — Field strength versus distance measured during nighttime hours on aircraft flying radially toward airborne broadcasting facility in poor orbit near Jacksonville, Florida on April 5, 1971, with the frequency being 25.6 kHz

An important task of airborne VLF facilities is to broadcast wideband spread-sprectrum VLF communication signals. These signals may be distorted by the propagation through the waveguide and by the variation in aircraft direction in orbit. To determine the deleterious results caused by these circumstances, it is necessary to examine the correlation of the received signal with an exact replica of the transmitted waveform to estimate the effective signal reduction.

A study of correlation receiver distortion due to propagation effects was performed by Rothmuller [5] for the case of broadcast from a fixed transmitter to a fixed receiver. Rothmuller showed that when two multipath signals interfere at a point, two correlation peaks occur separated in receiver synchronization time $\tau_R$ by approximately the duration of a spread-spectrum signaling element (chip). The maximum value of the correlation could be on the earlier or later correlation peak. In the present report we go a step further by including the effects of aircraft orbit on correlation receiver signal output. We study the condition of a time-varying wideband multipath situation common in airborne facility usage by considering the case in which the signaling elements (chips) are minimum-shift-keying (MSK)

waveforms and the communication decision is based on the coherent integration of a series of such waveforms.

In some circumstances the performance of the correlators depends greatly on which instant within a chip the correlator is synchronized to. It appears probable that a bit decision based on several correlations within a chip period would be superior to a decision based on a single correlation within a chip.

## THEORY

### Elementary Signal Theory

Figure 4 shows schematically the outlines of the communication system under discussion. Figure 5 shows a conceptual version of a receiver and demodulation portion of Fig. 4. The operation of the integrator portion of the equipment in Fig. 5 is to sample the received waveforms $h(t)$ and to multiply them by the desired waveform $h_1(t)$ and $h_2(t)$ and to integrate over a time equal to a bit-keying-element period $T_B$, centered about the time $t_l$ the midpoint of the $l$th expected bit interval. The transmitted waveform is constructed as a linear superposition of $h_1(t)$ and $h_2(t)$ according to

$$h(t) = X_l h_1(t) + Y_l h_2(t).  \tag{1}$$

The outputs of the integrators will yield the values of $X_l$ and $Y_l$ which contain the transmitted information,

$$X_l = (T_B)^{-1} \int_{t_l - T_B/2}^{t_l + T_B/2} h_1(t) h(t) \, dt  \tag{2}$$

and

$$Y_l = (T_B)^{-1} \int_{t_l - T_B/2}^{t_l + T_B/2} h_2(t) h(t) \, dt,  \tag{3}$$

as long as $h_1(t)$ and $h_2(t)$ are orthonormal to each other:

$$(T_B)^{-1} \int_{t_l - T_B/2}^{t_l + T_B/2} h_i(t) h_j(t) \, dt = \delta_{ij.}  \tag{4}$$

Here $\delta_{ij}$ is the Kronecker delta function, equal to zero for $i \neq j$ and equal to 1 for $i = j$.

### Correlation of Orthogonal Waveforms

A set of orthogonal wideband waveforms $h_1(t)$ and $h_2(t)$ can be generated by using a baseband waveform $h_B(t)$ to modulate both a sinusoidal and cosinusoidal wave:

$$h_1(t) = h_B(t) \cos \omega_0 t,  \tag{5}$$

$$h_2(t) = h_B(t) \sin \omega_0 t,  \tag{6}$$

$$h(t) = h_B(t)(X_l \cos \omega_0 t + Y_l \sin \omega_0 t).  \tag{7}$$
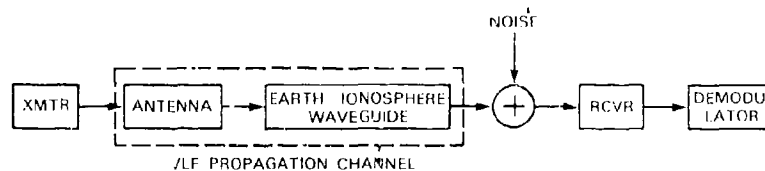


Fig. 4 — Model of the communication system
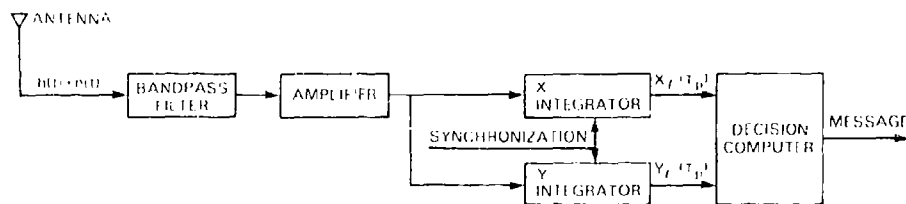
Fig 2 — Model of the receiver-demodulator

The values of $X_l$ and $Y_l$ give the strength of the cosinusoidal and sinusoidal components. A correlation receiver can then be made to extract the value of $X_l$ and $Y_l$:

$$X_l = 2(T_B)^{-1} \int_{t_l - T_B/2}^{t_l + T_B/2} h_B(t)(X_l \cos \omega_0 t + Y_l \sin \omega_0 t) h_B(t) \cos \omega_0 t \, dt \tag{8}$$

and

$$Y_l = 2(T_B)^{-1} \int_{t_l - T_B/2}^{t_l + T_B/2} h_B(t) (X_l \cos \omega_0 t + Y_l \sin \omega_0 t) h_B(t) \sin \omega_0 t \, dt. \tag{9}$$

A propagation delay time of $\tau_p$ modifies the correlator outputs to give new ones which we call $X_l(\tau_p)$ and $Y_l(\tau_p)$:

$$X_l(\tau_p) = 2(T_B)^{-1} \int_{t_l - T_B/2}^{t_l + T_B/2} h_B(t + \tau_p) [X_l \cos \omega_0(t + \tau_p) + Y_l \sin \omega_0(t + \tau_p)]$$
$$\times h_B(t) \cos \omega_0 t \, dt \tag{10}$$

and

$$Y_l(\tau_p) = 2(T_B)^{-1} \int_{t_l - T_B/2}^{t_l + T_B/2} h_B(t + \tau_p) ([X_l \cos \omega_0(t + \tau_p) + Y_l \sin \omega_0(t + \tau_p)]$$
$$\times h_B(t) \sin \omega_0 t \, dt. \tag{11}$$

We find that the vector $\vec{R}_l(\tau_p) = (X_l(\tau_p), Y_l(\tau_p))$ is approximately the phase-rotated version of $\vec{R}_l = (X_l, Y_l)$. We have

$$X_l(\tau_p) = T_B^{-1}(X_l \cos \omega_0 \tau_p + Y_l \sin \omega_0 \tau_p) \int_{t_l - T_B/2}^{t_l + T_B/2} h_B(t) h_B(t + \tau_p) \, dt \tag{12}$$

and

$$Y_l(\tau_p) = T_B^{-1}(- X_l \sin \omega_0 \tau_p + Y_l \cos \omega_0 \tau_p) \int_{t_l - T_B/2}^{t_l + T_B/2} h_B(t) h_B(t + \tau_p) \, dt . \tag{13}$$

Thus we can write this equation in vector form if $\vec{R}_l = (X_l, Y_l)$:

$$\vec{R}_l(\tau_p) = T_B^{-1} \left[ \int_{t_l - T_B/2}^{t_l + T_B/2} h_B(t) h_B(t + \tau_p) dt \right] \begin{bmatrix} \cos \omega_0 \tau_p & \sin \omega_0 \tau_p \\ -\sin \omega_0 \tau_p & \cos \omega_0 \tau_p \end{bmatrix} \vec{R}_l. \tag{14}$$

The magnitude of the vector $\vec{R}_l(\tau_p) = [X_l(\tau_p)^2 + Y_l(\tau_p)^2]^{1/2}$ is given by

$$|\vec{R}_l(\tau_p)| = T_B^{-1}|\vec{R}_l| \int_{t_l - T_B/2}^{t_l + T_B/2} h_B(t) h_B(t + \tau_p) dt. \tag{15}$$

The phase of the vector $\vec{R}_l(\tau_p)$ is given by

$$\phi_l(\tau_p) = arg(X_l(\tau_p) + iY_l(\tau_p)) = arg(X_l + iY_l) + \omega_0 \tau_p \tag{16}$$

Thus, the magnitude of the $\vec{R}_l(\tau_p)$ vector varies slowly with $\tau_p$, and the phase $\phi_l(\tau_p)$ changes rapidly.

*Correlation of Other Orthogonal Waveforms*

A more complicated set of orthogonal waveforms can be generated using two orthogonal baseband waveforms $h_{B1}(t)$ and $h_{B2}(t)$ such that for $i, j = 1, 2$

$$(T_B)^{-1} \int_{t_i - T_B/2}^{t_i + T_B/2} h_{Bi}(t) h_{Bj}(t) \, dt = \delta_{ij} \tag{17}$$

where $\delta_{ij}$ is the Kronecker delta function. The transmitted waveform $h(t)$ is given by

$$h(t) = X_l h_{B1}(t) \cos \omega_0 t + Y_l h_{B2}(t) \sin \omega_0 t. \tag{18}$$

To extract the value of $X_l$ and $Y_l$ from this waveform, we need a correlator receiver to do the following integrations:

$$X_l = 2(T_B)^{-1} \int_{t_i - T_B/2}^{t_i + T_B/2} [X_l h_{B1}(t) \cos \omega_0 t + Y_l h_{B2}(t) \sin \omega_0 t][h_{B1}(t) + h_{B2}(t)] \cos \omega_0 t \, dt \tag{19}$$

and

$$Y_l = 2(T_B)^{-1} \int_{t_i - T_B/2}^{t_i + T_B/2} [X_l h_{B1}(t) \cos \omega_0 t + Y_l h_{B2}(t) \sin \omega_0 t][h_{B1}(t) + h_{B2}(t)] \sin \omega_0 t \, dt. \tag{20}$$

When the time of arrival is changed to $t = t + \tau_p$, we have

$$X_l(\tau_p) = 2(T_B)^{-1} \int_{t_i - T_B/2}^{t_i + T_B/2} [X_l h_{B1}(t + \tau_p) \cos \omega_0(t + \tau_p) + Y_l h_{B2}(t + \tau_p) \sin \omega_0(t + \tau_p)]$$
$$\times [h_{B1}(t) + h_{B2}(t)] \cos \omega_0 t \, dt \tag{21}$$

and

$$Y_l(\tau_p) = 2(T_B)^{-1} \int_{t_i - T_B/2}^{t_i + T_B/2} [X_l h_{B1}(t + \tau_p) \cos \omega_0(t + \tau_p) + Y_l h_{B2}(t + \tau_p) \sin \omega_0(t + \tau_p)]$$
$$\times [h_{B1}(t) + h_{B2}(t)] \sin \omega_0 t \, dt. \tag{22}$$

This gives

$$X_l(\tau_p) = X_l \cos \omega_0 \tau_p T_B^{-1} \int h_{B1}(t + \tau_p)[h_{B1}(t) + h_{B2}(t)] \, dt$$
$$+ Y_l \sin \omega_0 \tau_p T_B^{-1} \int h_{B2}(t + \tau_p)[h_{B1}(t) + h_{B2}(t)] \, dt \tag{23}$$

and

$$Y_l(\tau_p) = -X_l \sin \omega_0 \tau_p T_B^{-1} \int_{t_i - T_B/2}^{t_i + T_B/2} h_{B1}(t + \tau_p)[h_{B1}(t) + h_{B2}(t)] \, dt$$
$$+ Y_l \cos \omega_0 \tau_p T_B^{-1} \int_{t_i - T_B/2}^{t_i + T_B/2} h_{B2}(t + \tau_p) [h_{B1}(t) + h_{B2}(t)] \, dt. \tag{24}$$

If the two baseband modulation functions are sufficiently orthogonal that

$$T_B^{-1} \int_{t_i - T_B/2}^{t_i + T_B/2} h_{B1}(t + \tau_p) h_{B2}(t) \, dt \approx 0 \tag{25}$$

and sufficiently similar that

$$T_B^{-1} \int_{t_i - T_B/2}^{t_i + T_B/2} h_{B1}(t + \tau_p) h_{B1}(t) \, dt = T_B^{-1} \int_{t_i - T_B/2}^{t_i + T_B/2} h_{B2}(t + \tau_p) h_{B2}(t) \, dt, \tag{26}$$

we again obtain

$$X_l(\tau_p) = (X_l \cos \omega_0 \tau_p + Y_l \sin \omega_0 \tau_p) T_B^{-1} \int_{t_i - T_B/2}^{t_i + T_B/2} h_{B1}(t + \tau_p) h_{B1}(t) \, dt \tag{27}$$

and

$$Y_i(\tau_p) = (- X_i \sin\omega_0\tau_p + Y_i \cos \omega_0\tau_p) T_B^{-1} \int_{t_i - T_B/2}^{t_i + T_B/2} h_{B1}(t+\tau_p) h_{B1}(t) \, dt. \tag{28}$$

When the more complicated correlators of Eqs. (19) and (20) are used, and the orthogonal waveforms satisfy the conditions of Eqs. (25) and (26), the type of waveform of Eq. (18) gives a behavior similar to that of Eq. (7).

## Modulation Methods

The values of $\vec{R}_i$ can be modified at the transmitter to initiate the communication of information. In amplitude modulation the magnitude of $\vec{R}_i$ is varied. In phase-shift keying the phase angle $\phi_i$ is modulated. Thus, in general, information may be transmitted by changing the transmitted vector $\vec{R}_i$ in some prescribed way. The stability of the received vector $\vec{R}_i(\tau_p)$ in amplitude and phase is important in the performance of communication systems. In the realistic communication channel the values of $\vec{R}_i(\tau_p)$ will also depend on the noise present. In this study we neglect noise and simply study the effects of propagation on $\vec{R}_i(\tau_p)$.

## MSK Signals

In the field of VLF communications, minimum shift keying (MSK) is a commonly used type of spread-spectrum modulation. MSK is mathematically described in terms of a transmitted waveform $s(t)$, a baseband modulation $u(t)$, and a chip waveform $p(t)$, as follows:

$$s(t) = \text{Re}\left[u(t) e^{i\omega_0 t}\right], \tag{29}$$

$$u(t) = \sum_{n=0}^{\frac{N}{2} - 1} \left[ X_i I_n \, p \, (t - nT) - i \, Y_i \, Q_n \, p \, (t - T/2 - nT)\right], \tag{30}$$

$$\begin{aligned} p(t) &= \sqrt{\frac{2}{T}}\left[\cos\left(\frac{\pi t}{T}\right)\right], \quad -T/2 \leqslant t \leqslant T/2, \\ &= 0, \; |t| > T/2. \end{aligned} \tag{31}$$

This is a specific version of the signal described in general by Eq. (18), in which the orthogonal baseband waveforms $h_{B1}(t)$ and $h_{B2}(t)$ are given by

$$h_{B1}(t) = \sqrt{T} \sum_{n=0}^{\frac{N}{2} - 1} I_n p(t - nT) \tag{32}$$

and

$$h_{B2}(t) = \sqrt{T} \sum_{n=0}^{\frac{N}{2} - 1} Q_n p(t - T/2 - nT). \tag{33}$$

In these above equations $I_n$ and $Q_n$ are pseudorandomly chosen integers of value $+1$ or $-1$. It is assumed that both the transmitter and receiver possess synchronized pseudorandom-number-sequence generators that provide the $I_n$ and $Q_n$ sequences. The frequency $\omega_0$ is the carrier frequency of the broadcast. The time interval $T$ is the duration of a chip. Since two chips are transmitted during each chip duration, the chip length $\tau_c$ is $T/2$. The MSK modulation method gives rise to a constant-amplitude waveform with continuous phase as long as $X_i$ and $Y_i$ are equal to $\pm 1$. The bandwidth of the transmitted signal is inversely related to the chip period. The value of the waveform $s(t)$ depends on one value of $I_n$ and one value of $Q_n$ simultaneously except at the instant when a transition is being

made from one value of $I_n$ or $Q_n$ to the next. At the transition time the amplitude of the waveform undergoing transition is zero, because the $p(t)$ function goes smoothly to zero at the beginning and end of its range. At that instant the value of $s(t)$ depends only on the other integer $Q_n$ or $I_n$. Let us consider the autocorrelation function $B(\tau)$ for the MSK waveform $s(t)$.

$$B(\tau) = \lim_{T' \to \infty} \frac{1}{T'} \int_0^{T'} s(t)s(t + \tau) \, dt. \tag{34}$$

Use of $s(t)$ from Eq. (29) will make $B(\tau)$ nonzero as long as $|\tau| < T$. When $|\tau| > T$, the contributions to $B(\tau)$ will all be from terms having the products $Q_n I_m$, $Q_n Q_m$, and $I_n I_m$ with $n \neq m$. These terms are as often $+1$ as they are $-1$ for an orthogonal or uncorrelated set of $\{Q_n\}$ and $\{I_n\}$; so a summation based on these values should remain small. Thus a large value for the autocorrelation function occurs only for $|\tau| < T$, when $I_n^2$ and $Q_n^2$ terms contribute. Since $I_n^2 = Q_n^2 = 1$, these terms are easy to evaluate. The correlation vector $\vec{R}_i(\tau_p)$ is closely related to the autocorrelation function $B(\tau)$ At very low frequencies the electromagnetic waves may be considered to propagate by distinct waveguide modes or hops. The time delays between dominant modes and hops are small—less than a millisecond [6]—producing the coherent overlap of one chip with its time-delayed image. At some receiver locations the interference of the two waves with each other results in "selective" fading. Such fading is called "selective" because it occurs only for frequencies for which the interference condition is satisfied. At other nearby receiver locations or frequencies the time delays will be such as to produce two pulses which reenforce each other. The propagation channel can be simulated by a multipath model in which $h_T(t)$ is the transmitted wave and the received wave is

$$h_R(t) = \sum_{i=1}^{N} A_i \, h_T \, (t - \tau_i), \tag{35}$$

where $\tau_i$ is the propagation time for the $i$th mode or hop and $A_i$ is the amplitude for the $i$th mode or hop. In the case of earth-ionosphere waveguide propagation sometimes the waves have distinctly different group and phase velocities. Then, we must consider both the phase and group delay times $\tau_p^{(i)}$ and $\tau_g^{(i)}$. The phase delay of the baseband modulation is governed by $\tau_p^{(i)}$, and the group delay is governed by $\tau_g^{(i)}$.

## THE MSK CORRELATION RECEIVER

One can readily evaluate the performance of a correlation receiver for MSK modulation and coherent detection for signal reception on a *single-path* propagation channel. The correlation vector $\vec{R}_i(\tau_p)$ obtained when one uses MSK modulation is explicitly calculated by substituting the expression for $h_{B1}(t)$ from Eq. (32) into Eqs. (27) and (28). The integral $I_B(\tau_p)$, defined as

$$I_B(\tau_p) = T_B^{-1} \int_{t_i - T_B/2}^{t_i + T_B/2} h_{B1}(t + \tau_p)h_{B1}(t) \, dt$$

$$T_B^{-1} \sum_{\substack{n=0 \\ n'=0}}^{\frac{N}{2} - 1} I_n I_{n'} \int_{t_i - T_B/2}^{t_i + T_B/2} p(t - nT)p(t + \tau_p - n'T) \, dt, \tag{36}$$

is readily evaluated. The limits of integration in this equation extend far beyond the region of variable $t$, for which the integrand is nonzero. We can change the integration variable to

$$t' = t - nT. \tag{37}$$

The limits of integration are thereby changed to $t_i + T_B/2 - nT$ and $t_i - T_B/2 - nT$:

$$I_B(\tau_p) = T_B^{-1} \sum_{\substack{n=0 \\ n'=0}}^{\frac{N}{2} - 1} I_n I_{n'} \int_{t_i - T_B/2 - nT}^{t_i + T_B/2 - nT} p(t')p(t' + nT + \tau_p - n'T) \, dt. \tag{38}$$

Since $p(t') = 0$, for $|t'| > T/2$, we need integrate only between $-T/2 \leqslant t \leqslant T/2$. We obtain

$$I_B(\tau_p) = T_B^{-1} \sum_{\substack{n=0 \\ n'=0}}^{\frac{N}{2}-1} I_n I_{n'} \int_{-T/2}^{+T/2} p(t')p[t' + \tau_p + (n - n')T] \, dt. \tag{39}$$

From this formulation we see that the integral depends only on the difference between $n$ and $n'$ and not on the individual values of $n$ and $n'$ separately. Let us define

$$C_k(\tau_p) = \int_{-T/2}^{T/2} p(t')p(t' + \tau_p + kT) \, dt. \tag{40}$$

Since $k = n - n'$, Eq. (39) becomes

$$I_B(\tau_p) = T_B^{-1} \sum_{\substack{n=0 \\ n'=0}} I_n I_{n'} C_{n-n'}(\tau_p)$$

$$= T_B^{-1} \sum_{n=0}^{\frac{N}{2}-1} \sum_{k=n}^{n+1-\frac{N}{2}} I_n I_{n-k} C_k(\tau_p)$$

$$= T_B^{-1} \sum_{n=0}^{\frac{N}{2}-1} \sum_{k=-\left(\frac{N}{2}-1\right)}^{\frac{N}{2}-1} I_n I_{n-k} C_k(\tau_p) U_{n-k}, \tag{41}$$

where

$$U_{n-k} = 1, \qquad \text{if } 0 \leqslant n - k \leqslant \frac{N}{2} - 1,$$

$$= 0, \qquad \text{if } n - k < 0 \text{ or } n - k > \frac{N}{2} - 1.$$

We then interchange the order of summation in Eq. (41) to get

$$I_B(\tau_p) = T_B^{-1} \sum_{k=-\left(\frac{N}{2}-1\right)}^{\frac{N}{2}-1} C_k(\tau_p) \sum_{n=0}^{\frac{N}{2}-1} I_n I_{n-k} U_{n-k}. \tag{42}$$

Because of the orthogonality of the set $\{I_n\}$ with any sequentially shifted copy of itself, we can write

$$\sum_{n=0}^{\frac{N}{2}-1} I_n I_{n-k} U_{n-k} = \frac{N}{2} \delta_{k,0}. \tag{43}$$

This assumes that the binary sequence $\{I_n\}$ has been generated by a method which has "good" auto-correlation properties for the pseudo-noise-coding application [7]. We obtain

$$I_B(\tau_p) = \frac{NT_B^{-1}}{2} C_0(\tau_p). \tag{44}$$

To calculate $C_0(\tau_p)$, we substitute into Eq. (40)

$$C_0(\tau_p) = \int_{-T/2}^{T/2} p(t')p(t' + \tau_p) \, dt. \tag{45}$$

The value of $C_0(\tau_p)$ is symmetric with respect to $\tau_p$ and can be obtained by using elementary integration methods:

$$C_0(\tau_p) = \frac{4}{T} \int_{-\frac{T}{2}}^{T/2-\tau_p} p(t')p(t'+\tau_p)\,dt, \qquad \text{if } \tau_p \geqslant 0,$$

$$= \frac{4}{T} \int_{-\frac{T}{2}}^{T/2-\tau_p} \cos\left[\frac{\pi t'}{T}\right] \cos\left[\pi\left\{\frac{t'+\tau_p}{T}\right\}\right]\,dt'$$

$$= \frac{4}{T} \left[\left\{1 - \frac{|\tau_p|}{T}\right\} \cos\frac{\pi\tau_p}{T} + \frac{1}{\pi}\sin\frac{|\tau_p|}{T}\right] \tag{46}$$

Equations (27) and (28) become

$$X_l(\tau_p) = (X_l \cos\omega_0\tau_p + Y_l \sin\omega_0\tau_p)NT_B^{-1}C_0(\tau_p) \tag{47a}$$

and

$$Y_l(\tau_p) = (-X_l \sin\omega_0\tau_p + Y_l \cos\omega_0\tau_p)NT_B^{-1}C_0(\tau_p). \tag{47b}$$

In matrix form we have

$$\vec{R}_l(\tau_p) = NT_B^{-1}T^{-1} \begin{vmatrix} \cos\omega_0\tau_p & \sin\omega_0\tau_p \\ -\sin\omega_0\tau_p & \cos\omega_0\tau_p \end{vmatrix} \vec{R}_l\, C_0(\tau_p). \tag{47c}$$

A receiver can be adaptively synchronized to the incoming signal by introducing a variable delay $\tau_R$ into the stream of baseband keying elements to generate a family of ideal baseband keying elements $h_{B1}$ and $h_{B2}$. Mathematically this simply means the introduction of the variable $t + \tau_R$ into the expression for $h_{B1}$ in Eqs. (27) and (28) in place of $t$. The selection of the synchronization time $\tau_R$ can greatly affect receiver performance when the actual propagation delay time $\tau_p$ is unknown (or equivalently the clocks that generate the chip streams are not in perfect initial synchronism). Therefore we rewrite Eq. (47c) to exhibit the dependence of system performance on $\tau_R$. We obtain the following expression for $\vec{R}_l(\tau_p, \tau_r)$:

$$\vec{R}_l(\tau_p, \tau_R) = NT_B^{-1} \begin{vmatrix} \cos\omega_0\tau_p & \sin\omega_0\tau_p \\ -\sin\omega_0\tau_p & \cos\omega_0\tau_p \end{vmatrix} \vec{R}_l\, C_0(\tau_p - \tau_R). \tag{48}$$

The magnitude of the components of $\vec{R}_l(\tau_p, \tau_R)$ are proportional to the in-phase and quadrature components of the received radio-frequency carrier wave because of the multipliers $\cos\omega_0\tau_p$ and $\sin\omega_0\tau_p$ in the matrix. However, the magnitude of $\vec{R}_l(\tau_p, \tau_R)$ depends on the propagation delay time $\tau_p$ and on the receiver time $\tau_R$ by the factor $\tau_p = \tau_R$. If the receiver is badly out of synchronization, this factor can be zero or very small. If the receiver is employing phase-shift keying, any change in the propagation time $\tau_p$, even after the receiver is perfectly synchronized on the chip ( $0 \approx |\tau_p - \tau_R| \ll T$), will induce a corresponding phase change in the phase of the vector $\vec{R}_l = (\tau_p, \tau_R)$; that is, the doppler phase variation of the radio-frequency carrier induces an equal doppler shift on the phase angle $\phi_R$. These types of doppler-signal phase variations are often seen when an mobile transmitter or receiver is used. In such a circumstance we cannot assume $\tau_p(t)$ will be constant at each instant within a bit period to permit the factorization shown in Eqs. (21) and (22). However, the other manipulations that we performed on the expression for $\vec{R}$ are all valid up to this point. To obtain the resultant correlation vector $\vec{R}_l(\tau_p, \tau_R)$ if the delay time is slowly changing within a bit period, we must average the instantaneous values of $\vec{R}_l[\tau_p(t), \tau_p]$ over an entire bit period:

$$\vec{R}_l(\tau_p, \tau_R) = NT_B^{-1}T^{-1} \int_{t_i - T_{B/2}}^{t_i + T_{B/2}} \begin{vmatrix} \cos\omega_0\tau_p(t) & \sin\omega_0\tau_p(t) \\ -\sin\omega_0\tau_p(t) & \cos\omega_0\tau_p(t) \end{vmatrix} \vec{R}_l\, C_0[\tau_p(t) - \tau_R]. \tag{49}$$

From this expression one can approximately evaluate the affect on the $\vec{R}_l = [\tau_p(t), \tau_R]$ vector for various conditions of $\tau_p(t)$ and synchronization conditions for a single path propagation.

We have reviewed the elementary cases of a stationary and moving transmitter having a single path of propagation, because this is the simplest case. Linear superposition holds for the waves and correlation procedures; so a resultant from a case having several propagation paths can be obtained by addition of terms from single-path cases.

## TWO PROPAGATION MODES AND A STATIONARY TRANSMITTER

When a stationary transmitter produces a signal at a receiver that comes by two propagation paths, there are two propagation delay times $\tau_{p1}$ and $\tau_{p2}$ and two (real-valued) amplitudes of the two modes $A_1$ and $A_2$. Alternatively, we may say that each mode is described by a complex amplitude, with the magnitude of each complex amplitude being the real amplitude and the phase being related to the propagation time. The voltage impressed on the receiving antenna by the received signal represents a waveform that is the sum of two time-delayed replicas of the initial waveform. Let the subscript $i$ denote the mode index. Then we will get the following expression for the total correlation vector $\vec{R}^T(\tau_R)$:

$$
\vec{R}_l^T(\tau_R) = \sum_{i=1}^{2} \vec{R}_l(\tau_{p,i}, \tau_R)
$$

$$
= NT_b^{-1}T^{-1} \sum_{i=1}^{2} A_i \begin{bmatrix} \cos \omega_0 \tau_{p,i} & \sin \omega_0 \tau_{p,i} \\ -\sin \omega_0 \tau_{p,i} & \cos \omega_0 \tau_{p,i} \end{bmatrix} \begin{bmatrix} X_l \\ Y_l \end{bmatrix} C_0(\tau_{p,i} - \tau_R).
\tag{50}
$$

The behavior of $\vec{R}_l^T(\tau_R)$ as a function of the receiver chip synchronization time $\tau_R$ can be quite different from the behavior when there is only a single path. A splitting of the correlation peak can occur. Indeed, instead of the correlation being best when $\tau_{p,i} = \tau_R$, it could be bad at this time. Numerical examples given later exhibit this circumstance.

## FIELD-STRENGTH EXPRESSIONS

For the case of an antenna trailing behind an airborne transmitting facility, the correlation vectors generated by both the horizontal and vertical components of the antenna are included in $\vec{R}_l^T(\tau_R)$. For an inclined short dipole antenna, the endfire-generated components are modified by $\cos \zeta \sin \gamma$, and the broadside generation depends on $\sin \zeta \sin \gamma$, where $\zeta$ is the angle between the horizontal portion of the inclined dipole and the great circle path to the receiver and $\gamma$ is the inclination angle of the antenna measured from the vertical. The expression for the resultant vertical electric field $E_r(D)$ at distance $D$ from the transmitter can be written as follows [4, p. 332]:

$$
E_r(D) = \cos \gamma \, E_r^{ve} + \sin \gamma \, E_r^{he}.
\tag{51}
$$

In this expression

$$
E_r^{ve} = \frac{-\eta I ds}{h\sqrt{a\lambda}\sin\theta} \sum_q S_q^{1.5} \Lambda_q^e \, G_q^e(z_s) G_q^e(z) \exp(ik_0 D \, S_q - i\pi/4)
\tag{52}
$$

and

$$
E_r^{he} = \frac{-\eta I ds}{h\sqrt{a\lambda}\sin\theta} \sum_q \left[ \Lambda_q^e \, G_q^e(z_s)\Delta_q^e(z_s) \cos \zeta \right.
$$

$$
\left. + \frac{\eta \Lambda_q^h \, G_q^h(z_s)}{Z_{eh}} \sin \zeta \right] S_q^{1/2} \, G_q^e(z) \exp(ik_0 D S_q - i\pi/4).
\tag{53}
$$

The quantities in these expressions are explained in Ref. 4 and are summarized below:

$\Lambda_q^c$      is the excitation factor of the $q$th mode for a vertically polarized electric dipole,

$\Lambda_q^h$      is the excitation factor of the $q$th mode for a horizontally polarized electric dipole,

$G_q^c(z)$      is the height-gain function of the quasi-TM vertical electric-field component,

$G_q^h(z)$      is the height-gain function of the quasi-TE vertical magnetic-field component

$S_q$      is the sine of the complex eigenangle of the $q$th waveguide mode,

$z$      is the height of the receiver,

$z_s$      is the height of the transmitter,

$a$      is the radius of the earth,

$D = a\theta$      is the great-circle distance between the transmitter and the receiver,

$\Delta_q^c(z)$      is the normalized impedance of the quasi-TM-mode fields,

$\Delta_q^h(z)$      is the normalized impedance of the quasi-TE-mode fields,

$Z_{eh}$      is the coupling impedance in the mode $= E_\phi(0)/H_\phi(0)$ at the earth's surface,

$\eta$      is the impedance of free space;

$k_0$      is the free-space propagation constant ($= \omega/c$) for an electromagnetic wave of frequency $\omega_0$,

$h$      is the reference height of the ionosphere.

$\lambda$      is the space wavelength, and

$Ids$      is the current moment.

The dispersion that occurs on each individual waveguide mode is usually minimal when well-behaved types of D- and E-region boundary conditions are present [6]. Each individual waveguide mode can be considered as a dispersionless path over a sufficiently narrow fractional bandwidth. The effect of propagation is to produce several time-delayed images of the transmitted waveform at the receiver. The amplitudes of these waveform images vary independently with time, as the inclined antenna is transported about by the aircraft. This variation with position of the aircraft can be modeled readily by letting the amplitudes $\{A_i\}$ and delay times $\{\tau_{p,i}\}$ vary in an appropriate way.

## CORRELATION EFFECTS OF ANTENNA ROTATION

It is easy to show the effects of rotation by an inclined elevated antenna given the previous development of the mathematics. The horizontal component of the inclined antenna generates both TE and TM modes according to Eq. (53), because the horizontally generated fields have phases and amplitudes different from those generated by the vertical antenna components. The waveguide modal interference pattern for an elevated horizontal antenna differs from that of a vertical antenna. This effect is illustrated in Fig. 6 (taken from Ref. 3), which shows the fields generated by variously inclined antennas at 20 kHz. The amplitudes of the horizontally generated fields vary as the cosine of the angle between the horizontal antenna component and the direction of propagation.

In simulating the effect of this variation on the receiver output vector, we use Eq. (50) for the received correlation vectors, and we use four amplitudes $\{A_i\}$, four phase time delays $\{\tau_i^p\}$, and four group time delays $\{\tau_i^g\}$. Two of the amplitudes represent two vertically generated mode fields and vary as $\sin \gamma$. The other two represent horizontally generated TM mode fields and vary as the product $\cos \zeta \cos \gamma$. The resultant expression for the correlator output is the same as Eq. (50) except that in this case the correlation output is the summation of the outputs for the four individual modes.
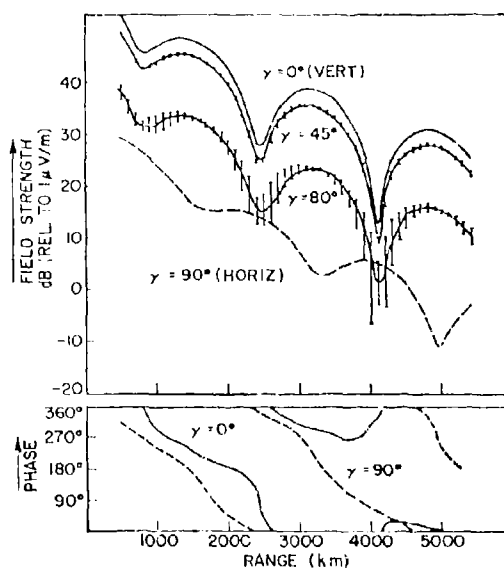
Fig 6 — Predicted variation of field strength and phase with distance for 20 kHz and vertical, inclined, and horizontal antenna inclinations

Denoting the $X_l^{(i)}(\tau_R)$ from the vertically electrically generated modes as $X_l^{(i)ve}(\tau_R)$ and the $X_l^{(i)}(\tau_R)$ from the horizontally electrically generated modes as $X_l^{(i)he}(\tau_R)$, we can write

$$X_l^T(\tau_R) = \cos\gamma \sum_{i=1}^{N'} X_l^{(i)ve}(\tau_R) + \cos\zeta \sin\gamma \sum_{i=1}^{N'} X_l^{(i)he}(\tau_R). \tag{54}$$

Parallel definitions can be made for $Y_l^T(\tau_R)$, $Y_l^{(i)ve}(\tau_R)$ and $Y_l^{(i)he}(\tau_R)$, and we obtain

$$Y_l^T(\tau_R) = \cos\gamma \sum_{i=1}^{N'} Y_l^{(i)ve}(\tau_R) + \cos\zeta \sin\gamma \sum_{i=1}^{N'} Y_l^{(i)he}(\tau_R). \tag{55}$$

The vector $\vec{R}_l^T(\tau_R)$ is a sum of two vectors $\vec{R}_l^{he}(\tau_R)$ and $\vec{R}_l^{ve}(\tau_R)$:

$$\vec{R}_l^T(\tau_R) = \cos\gamma\, \vec{R}_l^{ve}(\tau_R) + \cos\zeta \sin\gamma\, \vec{R}_l^{he}(\tau_R). \tag{56}$$

The vectors $\vec{R}_l^{ve}(\tau_R)$ and $\vec{R}_l^{he}(\tau_R)$ can be parallel, perpendicular, or opposed to each other, depending on circumstances and the value of $\tau_R$. The resultant $\vec{R}_l^T(\tau_R)$ vector can change quite dramatically during a complete orbit. For example, if $\vec{R}_l^{ve}(\tau_R)$ and $\vec{R}_l^{he}(\tau_R)$ are of the same magnitude and phase, there would be one large oscillation of $|\vec{R}_l^T(\tau_R)|$ per orbit (provided $\gamma = 45°$). If $\vec{R}_l^{ve}(\tau_R)$ and $\vec{R}_l^{he}(\tau_R)$ are perpendicular to each other, there would be two oscillations of $|\vec{R}^T(\tau_R)|$ with one cycle $\zeta$. There is a mathematical isomorphism between the phasor $E_r(D)$ and the vector $\vec{R}_l^T(\tau_R)$, since the composition of various phasors which form the complex phasor sum $E_r(D)$ is isomorphic to the composition of various correlation vectors which form the two-dimensional correlation vector sum $\vec{R}_l^T(\tau_R)$. When both TE and TM waveguide mode propagation from an airborne transmitting facility are taken into account, we obtain

$$\vec{R}_l^T(\tau_R) = \vec{R}_l^{ve}(\tau_R)\cos\gamma + \sin\gamma\,[\cos\zeta\, \vec{R}_l^{he}(TM,\tau_R) + \sin\zeta\, \vec{R}_l^{he}(TE,\tau_R)]. \tag{57}$$

The total vector $\vec{R}_I^{\,\prime}(\tau_R)$ is the sum of independently propagated vertical endfire- and broadside-generated components. These components are themselves sums of components which are propagated by different waveguide modes.

## DIAGRAMMATIC REPRESENTATIONS

It is instructive to view diagrams that illustrate the behavior of the various $\vec{R}_I$ vectors as $\tau_R$ and $\zeta$ vary. The following example illustrates what can happen in a particularly severe case of modal interference. Figure 7 depicts the variation of a single-mode correlation output $\vec{R}_I^{(1)ve}(\tau_R)$ from a stationary vertical electric transmitter. Figure 8 shows an output function $R_I^{(2)ve}(\tau_R)$ for a signal coming slightly later on a second-order mode and 180° out of phase with the first. Figure 9 gives the resultant $\vec{R}_I^{\,ve}(\tau_R)$, which is the sum of the correlation outputs of the first and second modes. Figure 10 shows the phase of the vector $\vec{R}_I^{\,ve}(\tau_R)$ as a function of $\tau_R$.
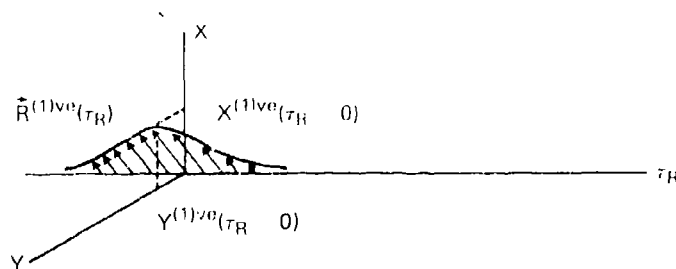
Fig. 7 — Graph of $\vec{R}_I^{(1)ve}(\tau_R)$ versus $\tau_R$ for a stationary vertical electric-dipole transmitter
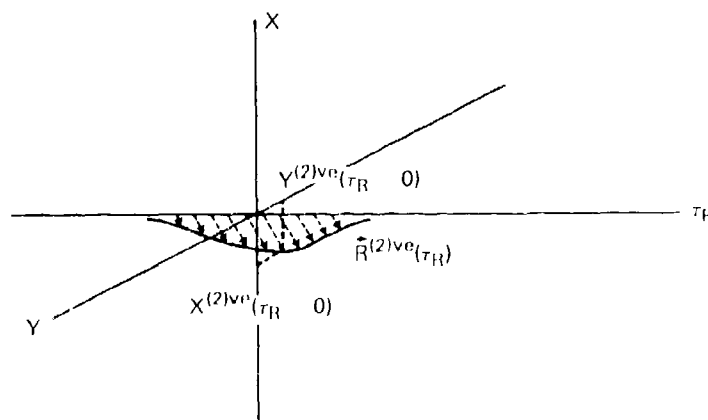
Fig. 8 — Graph of $R_I^{(2)ve}(\tau_r)$ versus $\tau_R$ for a stationary vertical electric dipole transmitter. The phase of this wave is 180° opposite to that illustrated in Fig. 7. The maximum value of $|R_I^{(2)ve}(\tau_R)|$ occurs at slightly greater $\tau_R$ values than does the maximum value of $|R_I^{(1)ve}(\tau_R)|$ shown in Fig. 7.
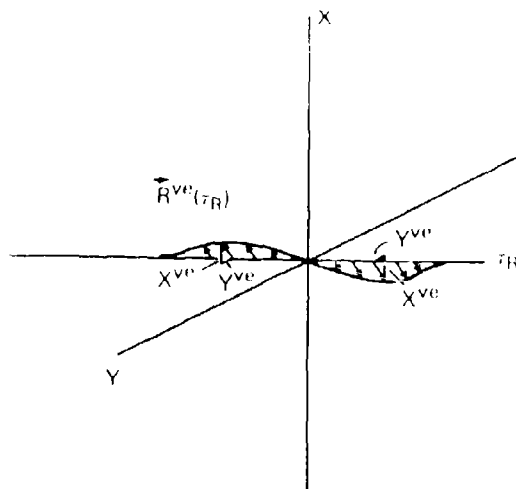
Fig 9 — Graph of $\vec{R}_l^{ve}(\tau_R) = \vec{R}_l^{(1)w}(\tau_R) + \vec{R}_l^{(2)w}(\tau_R)$, showing an abrupt change of phase at $\tau_R = 0$ and a large shift in the value of $\tau_R$ for which $|\vec{R}_l^{ve}(\tau_R)|$ is greatest
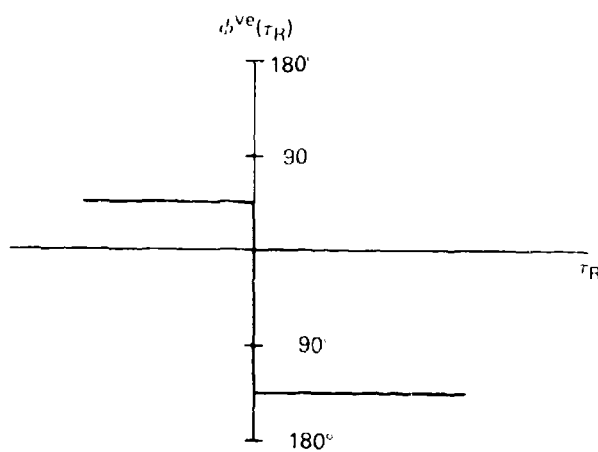


Fig 10 — Graph of $\phi_l^{ve}(\tau_R)$, the angle of the $\vec{R}_l^{ve}(\tau_R)$ vector with the x axis in Fig 9, showing an abrupt shift of phase at $\tau_R = 0$

Figure 11 shows the resultant $\vec{R}_I^T(\tau_R) = \cos\gamma\ \vec{R}_I^{ve}(\tau_R) + \sin\gamma\cos\zeta\vec{R}_I^{he}(\tau_R)$, where $\zeta$ is the angle between the direction of propagation and the endfire direction of the antenna. The angle $\gamma$ is the inclination angle of the antenna; we take $\gamma = 45°$ and $\zeta = 0$ for this example. Figure 12 shows the same resultant except for the condition $\zeta = 180°$. The conditions for $\zeta = 90°$ and $\zeta = 270°$ are both shown by the pattern of Fig. 9, since $\vec{R}_I^T(\tau_R)$ is composed solely of the vertically generated modes in these cases. These figures give a picture of $\vec{R}_I^T(\tau_R)$ at the four cardinal points of an orbit.
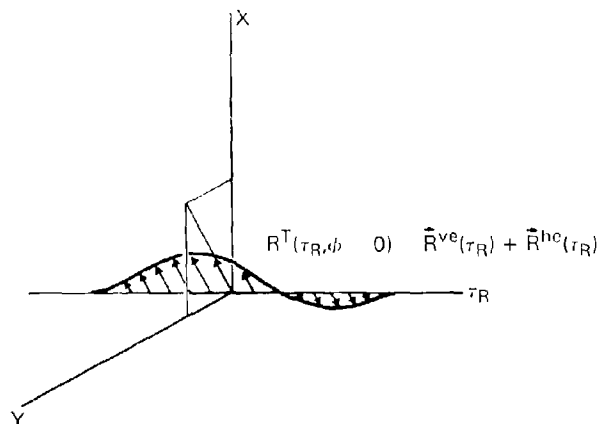


Fig. 11 — Graph of $\vec{R}_I^T(\tau_R)$ for an endfire case ($\cos\zeta = +1$), illustrating the change in the value of $\tau_R$ for which $|\vec{R}_I^T(\tau_R)| = 0$ and the variation in the size of the peak values of $|\vec{R}_I^T(\tau_R)|$ on opposite sides of $\tau_R = 0$. Here a relatively small value of $|\vec{R}_I^{ve}(\tau_R)|$ is assumed.
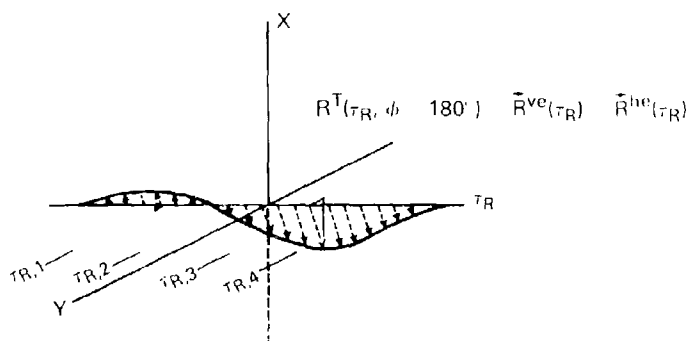


Fig. 12 — Graph of $\vec{R}_I^T(\tau_R)$ for the opposite endfire case ($\cos\zeta = -1$) to the case in Fig. 11. Here the largest value of $|\vec{R}_I^T(\tau_R)|$ occurs for $\tau_R > 0$ whereas, in Fig. 11 it was for $\tau_R < 0$. Synchronization times ($\tau_R$) to be considered in subsequent figures are shown.

In Fig. 12 four sample synchronization times, designated $\tau_{R1}$, $\tau_{R2}$, $\tau_{R3}$, and $\tau_{R4}$, represent possible correlation times that might occur within a receiver. We look at the variation of the correlation vector magnitude $|\vec{R}_i^T(\tau_{R_i})|$ and phase $\phi_i^T(\tau_{R_i})$ during a complete orbit for these times. Figures 13 and 14 show the phase and magnitude of $\vec{R}_i^T(\tau_{R1})$. The phase is constant in this case, because $\vec{R}_i^{ve}(\tau_{R1})$ is greater than and parallel to $\vec{R}_i^{hr}(\tau_{R1})$. The magnitude varies in a mild way. In Figs. 15 and 16 showing the phase and amplitude for the time $\tau_{R2}$, the phase makes two quick successive 180° changes in the neighborhood of $\zeta = 180°$, and the amplitude goes through two successive nulls. Figures 17 and 18 give $\vec{R}_i^T(0)$. This vector varies cosinusoidally, because there is no contribution from the vertical electric antenna component. Figures 19 and 20 show the behavior of $\vec{R}_i^T(\tau_{R3})$, which is similar to the behavior of $\vec{R}_i^T(\tau_{R2})$ except that the nulls occur near $\zeta = 0°$ rather than $\zeta = 180°$. Figures 21 and 22 show the behavior of $\vec{R}_i^T(\tau_{R4})$, which is similar to $\vec{R}_i^T(\tau_{R1})$ except for a shift in orbit angle $\zeta$ of 180°.
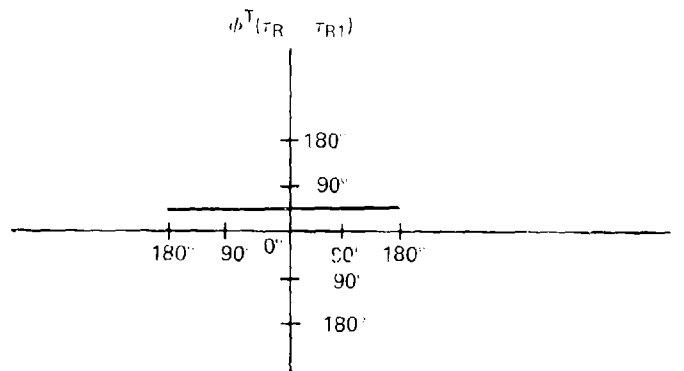


Fig. 13 — Graph of $\phi_i^T(\tau_{R1})$ as the angle of turn $\zeta$ of an inclined antenna changes from $-180°$ to $+180°$ for the synchronization time $\tau_{R1}$. This phase is constant because the contribution of the vertical antenna component always exceeds that of the horizontal component for this synchronization time.
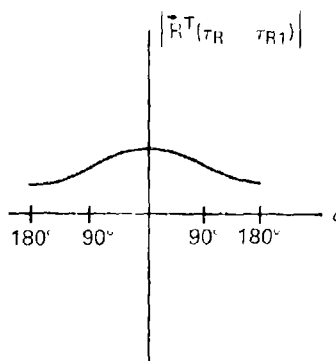


Fig. 14 — Graph of $|\vec{R}_i^T(\tau_{R1})|$ as $\zeta$ varies from $-180°$ to $+180°$. The relatively gentle variation of $|\vec{R}_i^T(\tau_{R1})|$ occurs because $|\vec{R}_i^{ve}(\tau_{R1})| > |\vec{R}_i^{hr}(\tau_{R1})|$
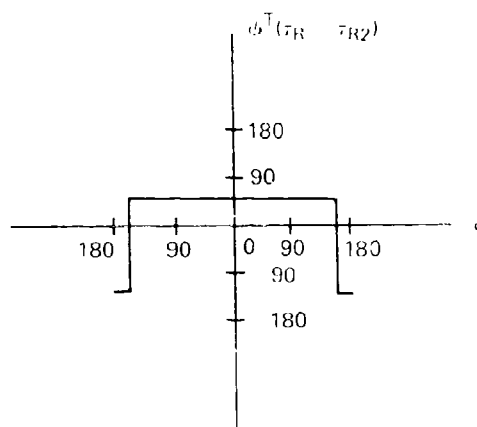
Fig. 15 — Graph of $\phi_i^T(\tau_{R2})$ versus orbit angle $\zeta$. For this lock-on time there are two rapid and large phase changes near $\zeta = 180°$
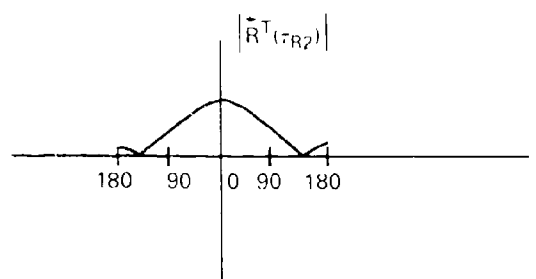


Fig. 16 — Graph of $|\vec{R}_i^T(\tau_{R2})|$ versus orbit angle $\zeta$, showing how this function goes to zero when $\phi_i^T(\tau_{R2})$ is making the abrupt phase transition
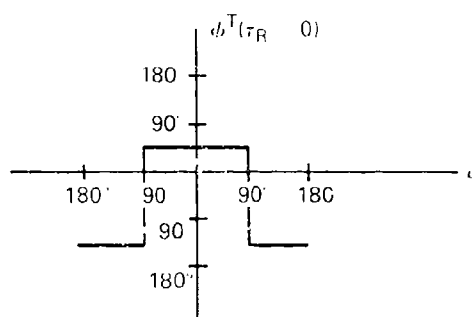


Fig. 17 — Graph of $\phi_i^T(\tau_R = 0)$ versus angle $\zeta$. There is essentially no contribution from the vertical component for this value of $\tau_R$, so the phase is controlled by the horizontal component of the transmitting antenna.
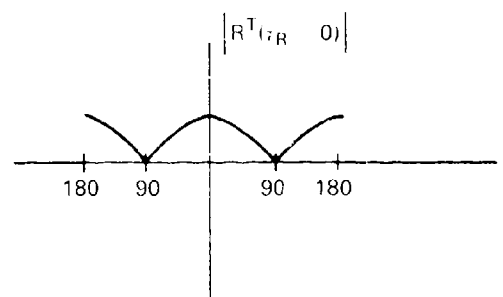


Fig. 18 — Graph of $|\vec{R}_i^T(\tau_R = 0)|$ versus orbit angle $\zeta$. The cosinusoidal variation is caused by the $\cos \zeta$ modulation of the horizontal component. The vertical component contributes essentially zero
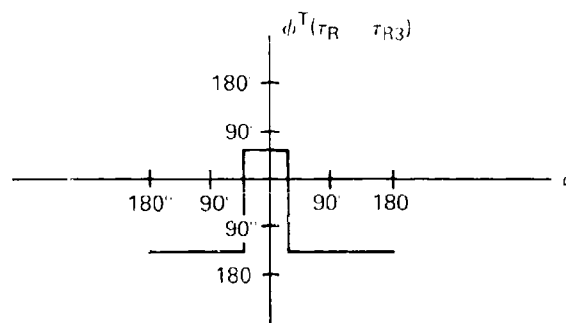


Fig. 19 — Graph of $\phi_i^T(\tau_{R3})$ versus orbit angle $\zeta$. For this synchronization time the abrupt changes in phase occur around the $\zeta = 0$ point rather than around the $\zeta = 180°$ for the $\tau_{R2}$ case illustrated in Fig. 15.
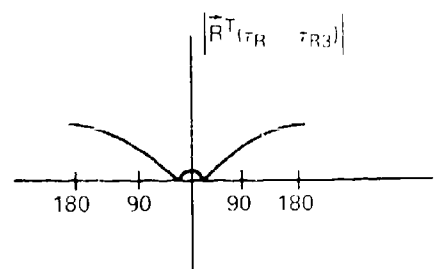


Fig. 20 — Graph of $|\vec{R}_i^T(\tau_{R3})|$ versus orbit angle, $\zeta$. The smallest values of $|\vec{R}_i^T(\tau_{R3})|$ occur for orbit angles near zero degrees rather than near 180° as was the case for $|\vec{R}_i^T(\tau_{R2})|$ as shown in Fig. 10
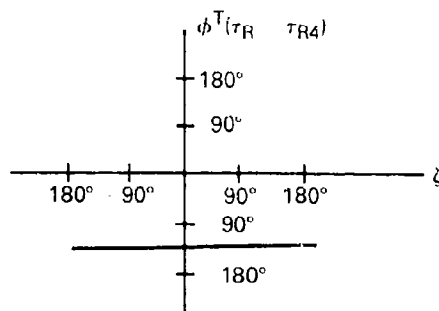
Fig. 21 — Graph of $\phi_l^T(\tau_{R4})$ versus orbit angle $\zeta$. For this receiver time the vertically generated correlation vector dominates; that is $|\vec{R}_l^{ve}(\tau_{R4})| > |\vec{R}_l^{he}(\tau_{R4})|$. No change of phase can occur, since $\vec{R}_l^{ve}(\tau_{R4})$ and $\vec{R}_l^{he}(\tau_{R4})$ are parallel.
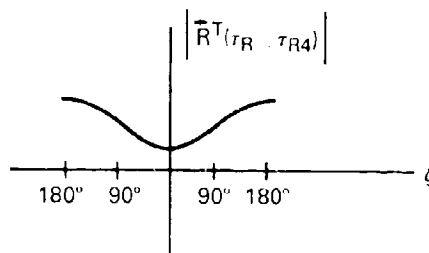


Fig. 22 — Graph of $|\vec{R}_l^T(\tau_{R4})|$ versus orbit angle $\zeta$. For this receiver time the maximum correlation vector occurs for $\zeta = 180°$, whereas for $\tau_{R1}$ the maximum correlation-vector magnitude occurred at $\zeta = 0°$.

Finally, Fig. 23 shows an estimate of $\tau_{Ropt}$, the optimum value of receiver correlation time for different values of orbit angle $\zeta$. This graph shows that $\tau_{R1}$ and $\tau_{R4}$ are preferable when $|\vec{R}_l(\tau_{R1})|$ and $|\vec{R}_l(\tau_{R4})|$ are largest. The phase is constant, and the amplitude varies gently. Relatively mild amplitude behavior occurs for this correlation time because $|\vec{R}_l^{ve}(\tau_{R1})| > |\vec{R}_l^{he}(\tau_{R1})|$. The phase is constant because $\vec{R}_l^{ve}(\tau_{R1})$ is parallel to $\vec{R}_l^{he}(\tau_{R1})$. Although $\vec{R}_l^{he}(\tau_{R1})$ can change the magnitude of $\vec{R}_l^T(\tau_{R1})$, it does not change the phase.
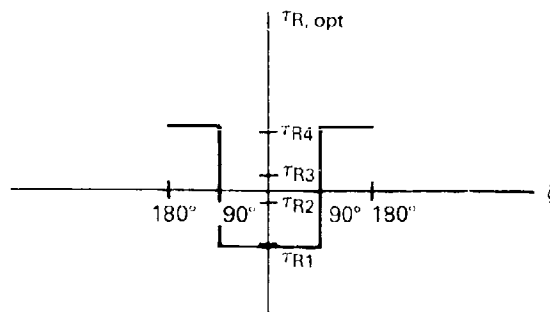


Fig. 23 — Graph showing the values of $\tau_R$ that should be chosen for various orbit angles $\zeta$ for the case illustrated in Figs. 7 through 22.

In the preceding example, there was minimum correlation near the middle of the correlation envelope, and the correlation maximum was greatly displaced from the maximum point of the correlation of either individual multipath signal. Thus, the rather small difference in arrival times $\tau_{p1} - \tau_{p2}$ changes the optimum chip synchronization time $\tau_R$ by a major amount. This effect is fairly easy to explain. The condition described by our equations is a severe case of multipath interference. Two signals come to the receiver antenna offset in time by $\tau_{p1} - \tau_{p2}$. The first and second signals travel independently of each other, so when the first signal pulse arrives, the signal begins to build up. Then the second signal arrives out of phase and cancels out the first signal for a long interval of time while both are strong. Then the first signal goes to zero because its waveform has passed by, while the second signal remains to give an excitation of the antenna again. Thus the strongest portions of each signaling element in this case of interference occur at the beginning and the end of each signaling element. In the middle of the element, the two signals arriving from different paths interfere, and there is a reduction of the field present.

When a receiver tries to synchronize with the signal at its strongest point, it must search for synchronization either at the beginning of the chip or at the end but not in the middle. Thus, if a system were presynchronized with an optimum $\tau_R$ for either of the individual mode delays or for an average of the two mode delays, it would actually be poorly synchronized for optimum operation! For better operation three correlators might be used—one adjusted at the central expected time of arrival of the wave, and one at each end of the chip. If the two waveforms reinforce each other to give the maximum in the middle, the central correlation peak will be large and the two side peaks will be small. If however, an interference condition is present, the middle correlator will be weak and the two side correlators will be strong.

## NUMERICAL CALCULATIONS

### Procedures

We will calculate some values of $\vec{R}_l^T$ for cases that are inspired by realistic mode-theory calculations of the phase and amplitude of VLF waves. For the calculated fields shown in Fig. 6, the waveguide mode constants are given in Table 1.

Table 1 — Constants Used in the Calculations

| | |
|---|---|
| $\Lambda_1 = 0.4$ | $G_1(z) = 1$ |
| $\Lambda_2 = 1.2$ | $G_2(z) = 1$ |
| $S_1 = 1.002 + 0.000689i$ | $\Delta_1(z_s) = -0.02i$ |
| $S_2 = 0.003 + 0.00138i$ | $\Delta_2(z_s) = 0.05i$ |
| $z = 0$ km | $r_0 = 4$ km |
| $G_1(z_s) = 0.965 + 0.259i$ | $z_s = 10$ km |
| $G_2(z_s) = 0.95$ | Radiated power $= 1$ kw |

These constants were used in the following equations to generate the field -strength values in Fig. 6:

$$E_r^{ve}(r, \theta) = i(\mu_0/\epsilon_0)^{1/2} I\ ds^{ve} \sum_n S_n^{1.5} F_n \tag{57}$$

and

$$E_r^{he}(r, \theta) = i(\mu_0/\epsilon)^{1/2} I\ ds^{he} \cos \phi \sum_n \Delta_n(z_s) S_n^{0.5} F_n, \tag{58}$$

where

$$F_n = \frac{1}{(D\lambda h)^{1/2}} \left[ \frac{D/a}{\sin(D/a)} \right]^{1/2} G_n(z) G_n(z_s) \Lambda_n \exp\ (i\pi/4 + ik_0 DS_n). \tag{59}$$

These equations are simplified versions of Eqs. (51) through (53), since they contain only TM-mode constants of an isotropic ionosphere. We calculate $\bar{R}_l^{(l)ve}$ for each mode according to

$$X_l^{(l)ve}(\tau_R, \zeta) = N|A_l^{ve}|\cos[\omega_0\tau_l^{p,ve}(\zeta)] \ C \ (\tau_l^{g,ve}(\zeta) - \tau_R) \tag{60}$$

and

$$Y_l^{(l)ve}(\tau_R, \zeta) = N|A_l^{ve}|\sin[\omega_0\tau_l^{p,ve}(\zeta)] \ C \ (\tau_l^{g,ve}(\zeta) - \tau_R), \tag{61}$$

where

| | |
|---|---|
| $N$ | is a normalizing constant, |
| $A_l^{ve}$ | is amplitude of the $l$th TM mode generated by the vertical component of the transmitting antenna, |
| $\omega_0$ | is the angular frequency of the wave, |
| $\tau_l^{p,ve}(\zeta)$ | is the delay time of the phase of the wave when the aircraft is at angle $\zeta$ of its orbit for the $l$th waveguide mode, and |
| $\tau_l^{g,ve}(\zeta)$ | is the group delay time of the wave when the aircraft is at angle $\zeta$ of its orbit for the $l$th waveguide mode. |

The amplitude is given by

$$A_l^{ve} = S_l^{1.5}G_l(z) \ G_l(z_s)\Lambda_l \exp(i\pi/r + i \ k_0 \cdot DS_l). \tag{62}$$

The phase delay time $\tau_l^{p,ve}(\zeta)$ is obtained by evaluating the phase of $A_l$:

$$\omega_0 \tau_l^{p,ve}(\zeta) = \arg(A_l^{ve}). \tag{63}$$

The group delay time $\tau_l^{g,ve}(\zeta)$ is obtained by evaluating the derivative of the phase of $A_l$:

$$\tau_l^{g,ve}(\zeta) = \frac{\partial}{\partial\omega}[\arg(A_l^{ve})]. \tag{64}$$

The path length $D$ from the transmitting antenna to the receiver location is a function of the orbit angle $\zeta$ and the orbit radius $r$ according to the approximation

$$D = D_0 + r \sin \zeta, \tag{65}$$

where $D_0$ is the distance from the receiver to the center of the orbit. To calculate $\bar{R}_l^{ve}(\zeta, \tau_R)$, we performed summations as indicated in Eqs. (54) through (56).

We calculate the horizontally electrically generated fields in an analogous manner:

$$X_l^{(l)he}(\tau_R, \zeta) = N|A_l^{he}|\cos[\omega_0\tau_l^{p,he}(\zeta)] \ C_0 \ (\tau_l^{g,he}(\zeta) - \tau_R) \tag{66}$$

and

$$Y_l^{(l)he}(\tau_R, \zeta) = N|A_l^{he}|\sin[\omega_0\tau_l^{p,he}(\zeta)] \ C_0 \ (\tau_l^{g,he}(\zeta) - \tau_R). \tag{67}$$

The amplitude of the $i$th mode is given as follows:

$$A_l^{he} = G_l(z)G_l(z_s)\Lambda_l \exp(i\pi/4 + ik_0 \ D \ S_l) \ S_l^{.5} \ \Delta_l(z_s) = A_l^{ve} S_l \ \Delta_l(z_0). \tag{68}$$

The phase and group delay times are given in the same manner as for the vertically generated modes:

$$\omega_0 \tau_l^{p,he}(\zeta) = \arg(A_l^{he}) \tag{69}$$

and

$$\tau_l^{g,he}(\zeta) = \frac{\partial}{\partial\omega}[\arg(A_l^{he})].$$  (64)

Tables 2 and 3 give the numerical values used in making the correlation calculations.

Table 2 — Set of Quantities Used in Calculation
of Correlation Vectors

| Mode | Quantity | Value |
|------|----------|-------|
| 1 | $\|A_1^{ve}\|$ | $1.26500262 \times 10^{-1}$ |
| | $\tau_1^{p,ve}$ | $1.33658211 \times 10^{-2}$ |
| | $\tau_1^{g,ve}$ | $1.34400 \times 10^{-2}$ |
| | $\|A_1^{he}\|$ | $2.52495471 \times 10^{-3}$ |
| | $\tau_1^{p,he}$ | $1.33533157 \times 10^{-2}$ |
| | $\tau_1^{g,he}$ | $1.34400 \times 10^{-2}$ |
| 2 | $\|A_2^{ve}\|$ | $1.11773228 \times 10^{-1}$ |
| | $\tau_2^{p,ve}$ | $1.32437617 \times 10^{-2}$ |
| | $\tau_2^{g,ve}$ | $1.356666 \times 10^{-2}$ |
| | $\|A_2^{he}\|$ | $5.62805237 \times 10^{-3}$ |
| | $\tau_2^{p,he}$ | $1.32562578 \times 10^{-2}$ |
| | $\tau_2^{g,he}$ | $1.356666 \times 10^{-2}$ |

Table 3 — Second Set of Quantities Used in
Calculation of Correlation Vectors

| Mode | Quantity | Value |
|------|----------|-------|
| 1 | $\|A_1^{ve}\|$ | $1.26500262 \times 10^{-1}$ |
| | $\tau_1^{p,ve}$ | $1.33658211 \times 10^{-2}$ |
| | $\tau_1^{g,ve}$ | $1.34400 \times 10^{-2}$ |
| | $\|A_1^{he}\|$ | $2.52495471 \times 10^{-3}$ |
| | $\tau_1^{p,he}$ | $1.3315820 \times 10^{-2}$ |
| | $\tau_1^{g,he}$ | $1.34400 \times 10^{-2}$ |
| 2 | $\|A_2^{ve}\|$ | $1.26500262 \times 10^{-1}$ |
| | $\tau_2^{p,ve}$ | $1.33908211 \times 10^{-2}$ |
| | $\tau_2^{g,ve}$ | $1.356666 \times 10^{-2}$ |
| | $\|A_2^{he}\|$ | $5.62805237 \times 10^{-3}$ |
| | $\tau_2^{p,he}$ | $1.3365820 \times 10^{-2}$ |
| | $\tau_2^{g,he}$ | $1.356666 \times 10^{-2}$ |

## Results

Figures 24 through 29 show $\vec{R}_l^I(\tau_R)$ and $\phi_l^I(\tau_R)$ contours for $\gamma$ values of $90°$, $85°$, $80°$, $60°$, $45°$, and $0°$ with the propagation parameters of Table 2. Figure 30 shows $\vec{R}^{(1)ve}(\tau_R)$, the correlation vector of the first-order mode. Figures 31 through 36 show the correlation vector for propagation parameters of Table 3 for $\gamma$ values of $90°$, $85°$, $80°$, $60°$, $45°$, and $0°$. The "average" chip duration for each of these calculations was $\tau_c = 1$ ms. The total length of each chip is $T = 2\tau_c = 2$ ms. The radius of the orbit is 3 km; the distance from the center of the orbit to the receiver is 4000 km.

Fig. 24a — Amplitude behavior of $\vec{R}_I^T(\tau_R)$ for $\gamma = 90°$, calculated with the parameters of Table 2
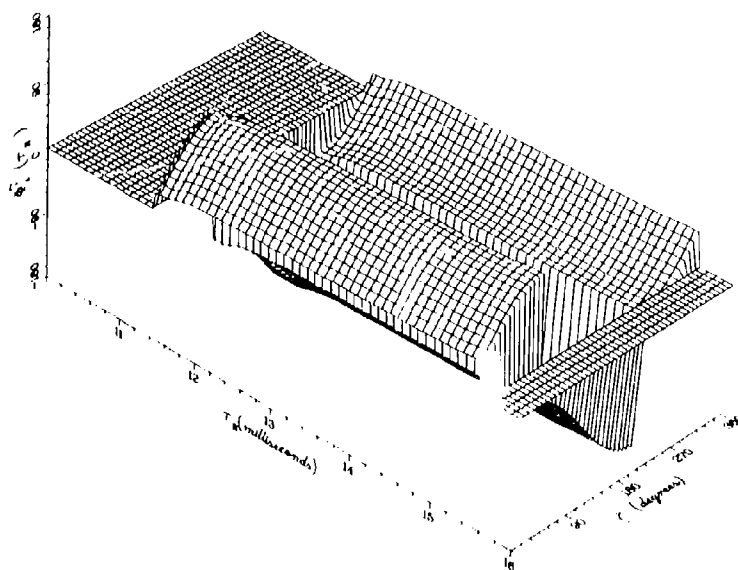


Fig. 24b — Phase behavior of $\vec{R}_I^T(\tau_R)$ for $\gamma = 90°$, calculated with the parameters of Table 2

$$\left| R_\ell^{'T} (\tau_R) \right|$$



Fig. 24c — Amplitude contours corresponding to Fig. 24a

$$\phi_\ell^{T} (\tau_R)$$
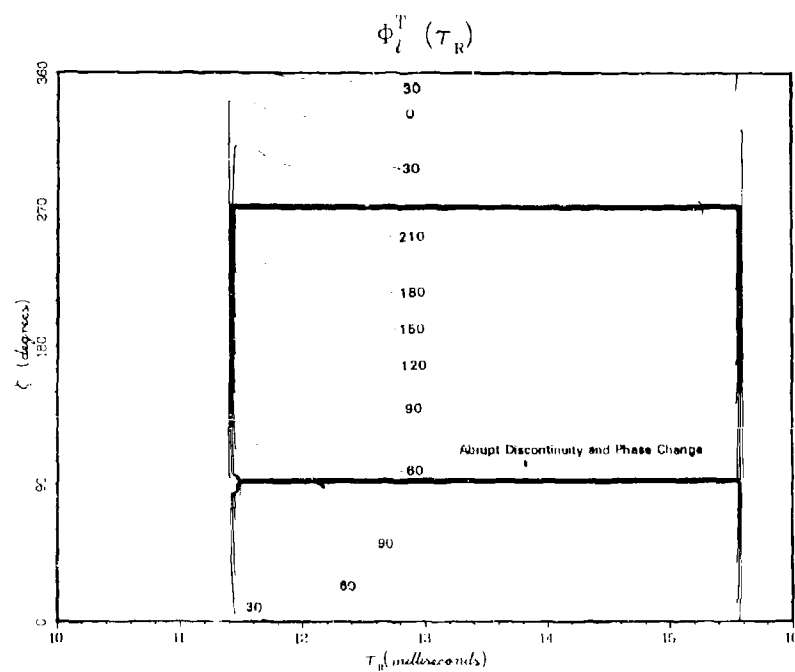


Fig. 24d — Phase behavior corresponding to Fig. 24b

Fig. 25a Amplitude behavior of $\vec{R}_l^T(\tau_R)$ for $\gamma = 85°$,
calculated with the parameters of Table 2
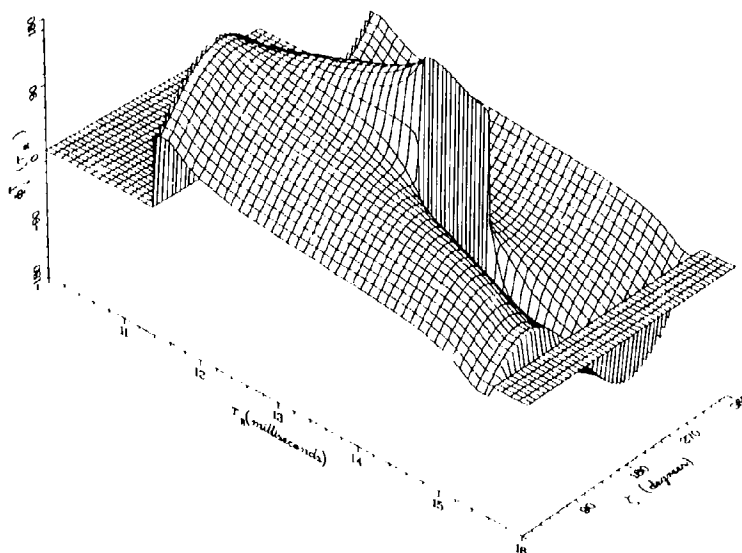


Fig. 25b — Phase behavior of $\vec{R}_l^T(\tau_R)$ for $\gamma = 85°$,
calculated with the parameters of Table 2

$$|R_\ell^T(\tau_R)|$$



Fig. 25c — Amplitude contours corresponding to Fig. 25a

$$\phi_\ell^T(\tau_R)$$
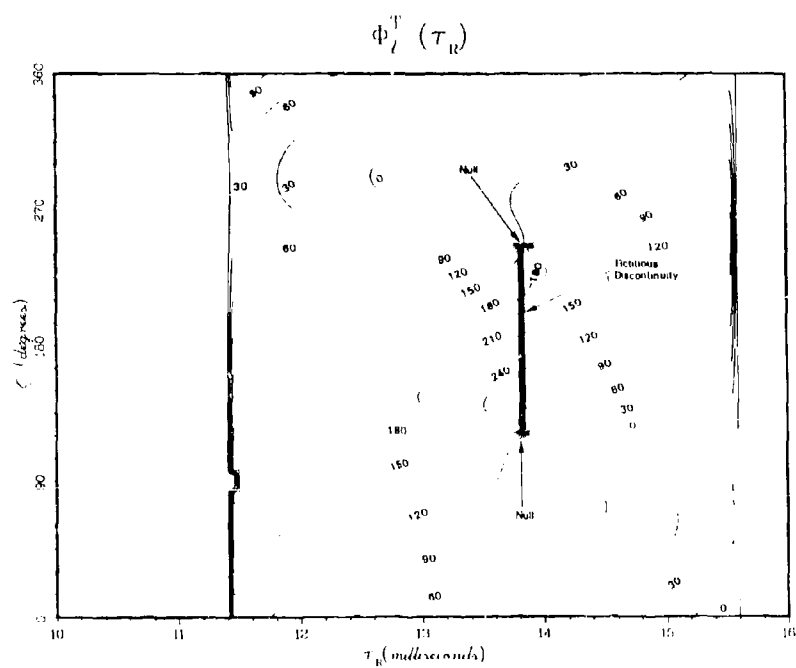


Fig. 25d — Phase behavior corresponding to Fig. 25b

Fig. 26a — Amplitude behavior of $\vec{R}_l^T(\tau_R)$ for $\gamma = 80°$, calculated with the parameters of Table 2
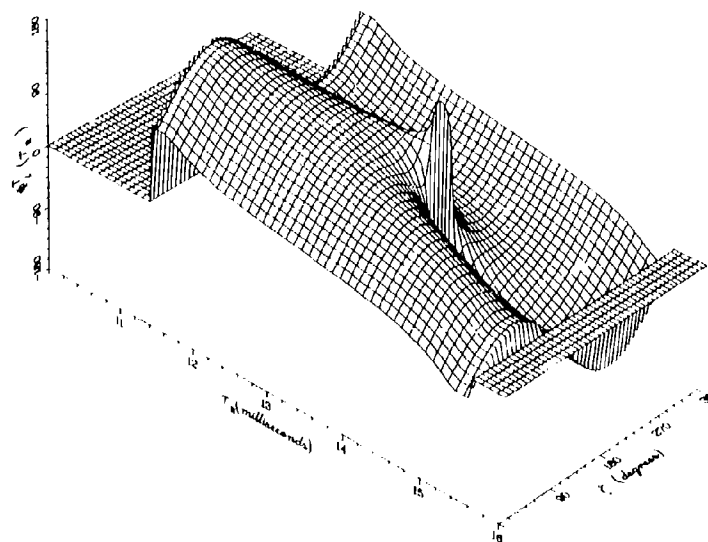


Fig. 26b — Phase behavior of $\vec{R}_l^T(\tau_R)$ for $\gamma = 80°$, calculated with the parameters of Table 2

$$\left| R_\ell^T \left( \tau_R \right) \right|$$
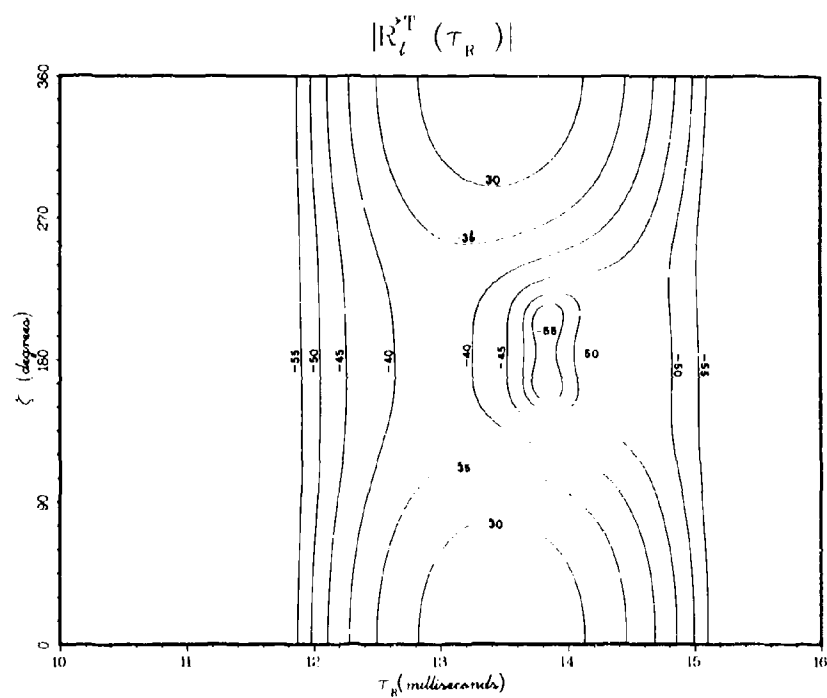
Fig. 26c — Amplitude contours corresponding to Fig. 26a

$$\phi_\ell^T \left( \tau_R \right)$$
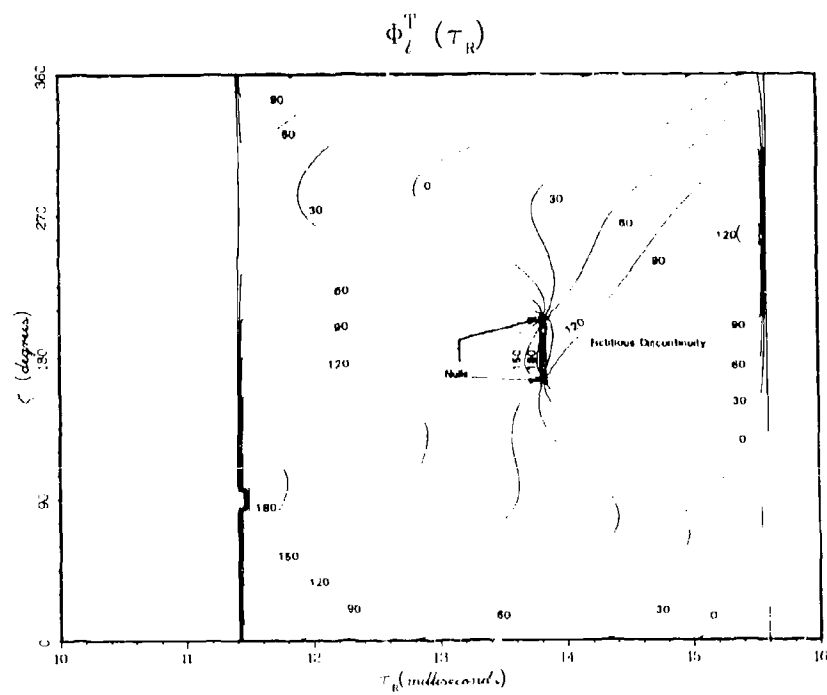
Fig. 26d — Phase behavior corresponding to Fig. 26b
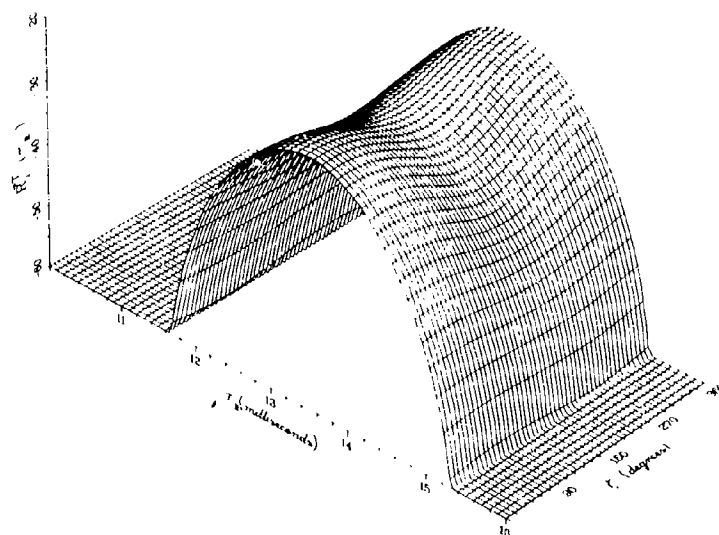
Fig. 27a — Amplitude behavior of $\vec{R}_l^T(\tau_R)$ for $\gamma = 60°$, calculated with the parameters of Table 2
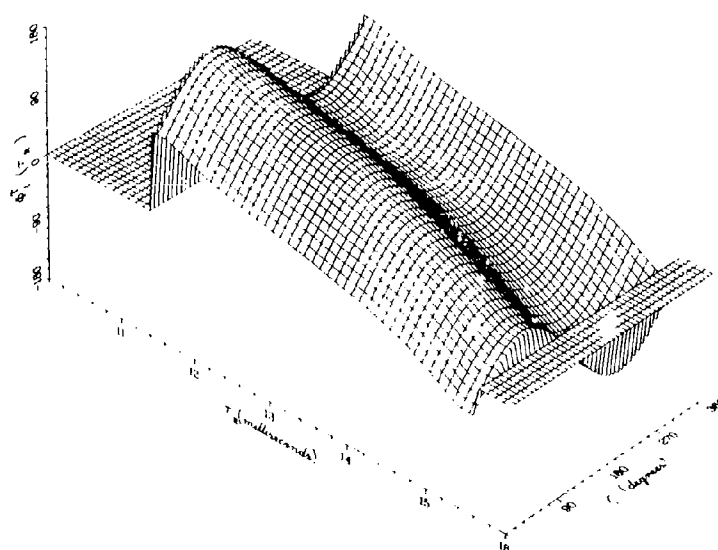


Fig. 27b — Phase behavior of $\vec{R}_l^T(\tau_R)$ for $\gamma = 60°$, calculated with the parameters of Table 2

$$|R_\ell^{\prime T} (\tau_R)|$$
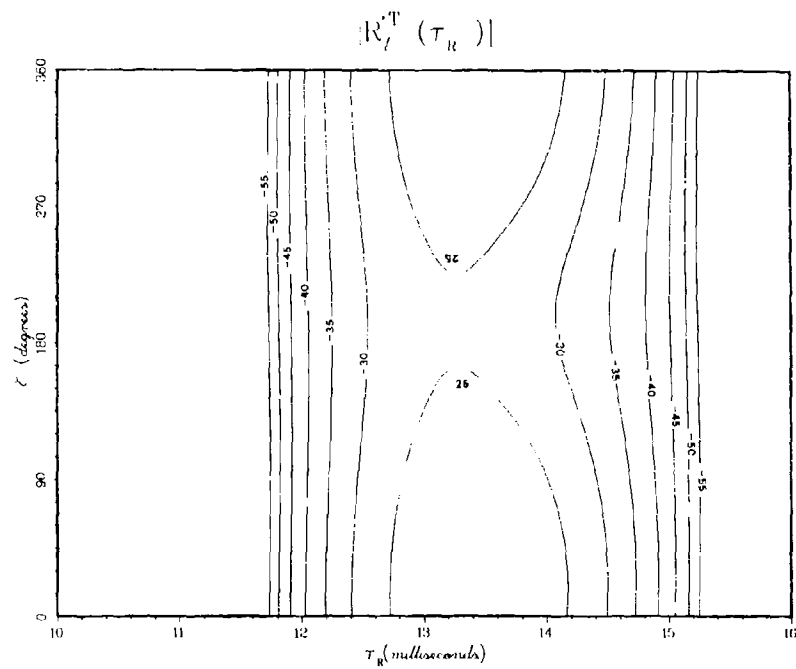


Fig. 27c — Amplitude contours corresponding to Fig. 27a

$$\Phi_\ell^T (\tau_R)$$
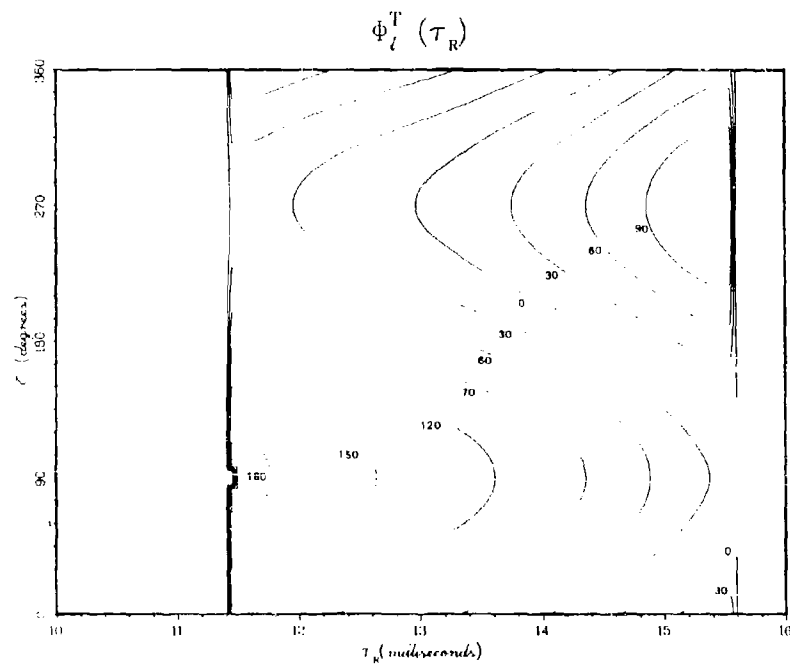


Fig. 27d — Phase behavior corresponding to Fig. 27b
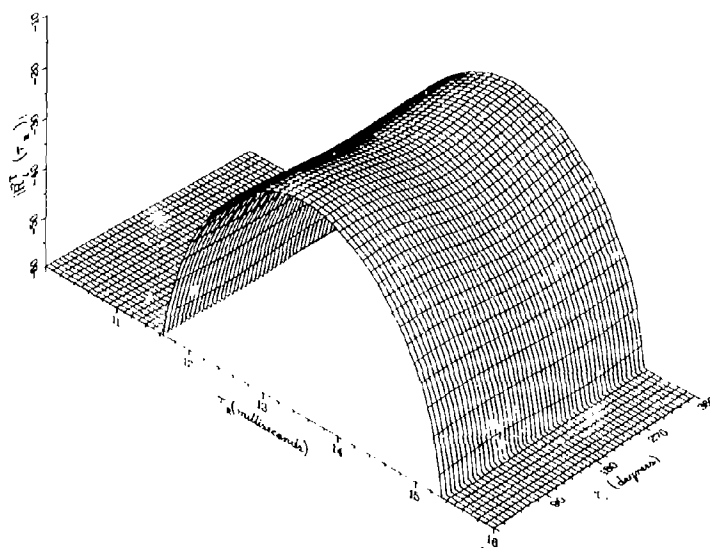
Fig. 28a — Amplitude behavior of $\vec{R}_l^T(\tau_R)$ for $\gamma = 45°$, calculated with the parameters of Table 2
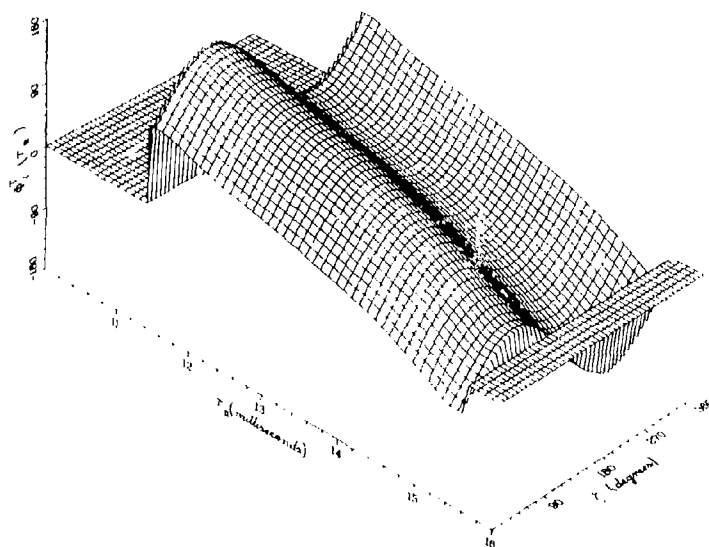


Fig. 28b — Phase behavior of $\vec{R}_l^T(\tau_R)$ for $\gamma = 45°$, calculated with the parameters of Table 2

$$\|R_l^{\cdot T}(\tau_R)\|$$
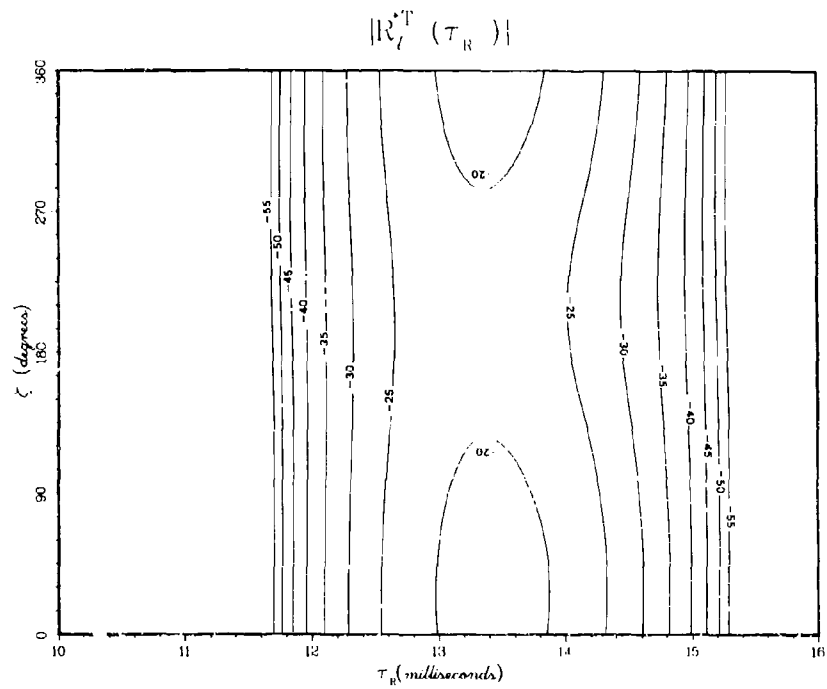


Fig. 28c — Amplitude contours corresponding to Fig. 28a

$$\phi_l^T(\tau_R)$$
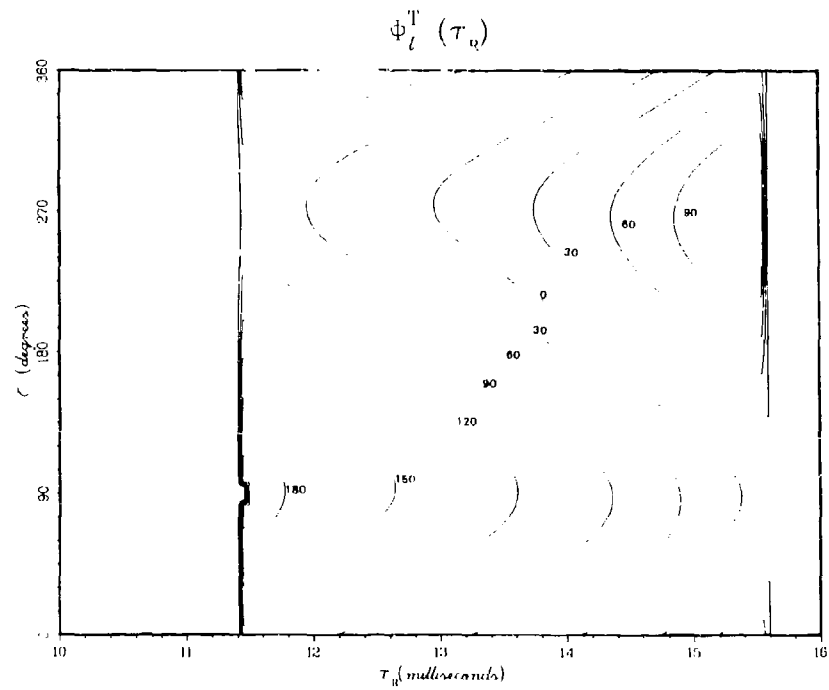


Fig. 28d — Phase behavior corresponding to Fig. 28a
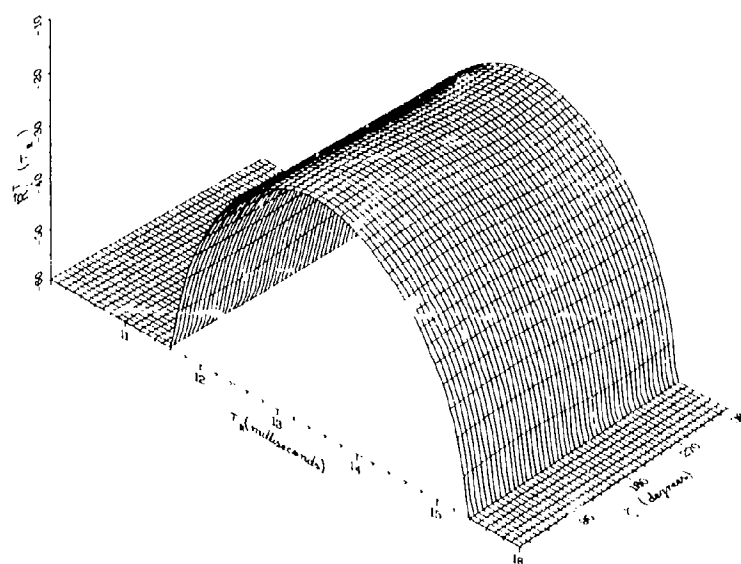
Fig. 29a — Amplitude behavior of $\vec{R}_I^T(\tau_R)$ for $\gamma = 0°$, calculated with the parameters of Table 2
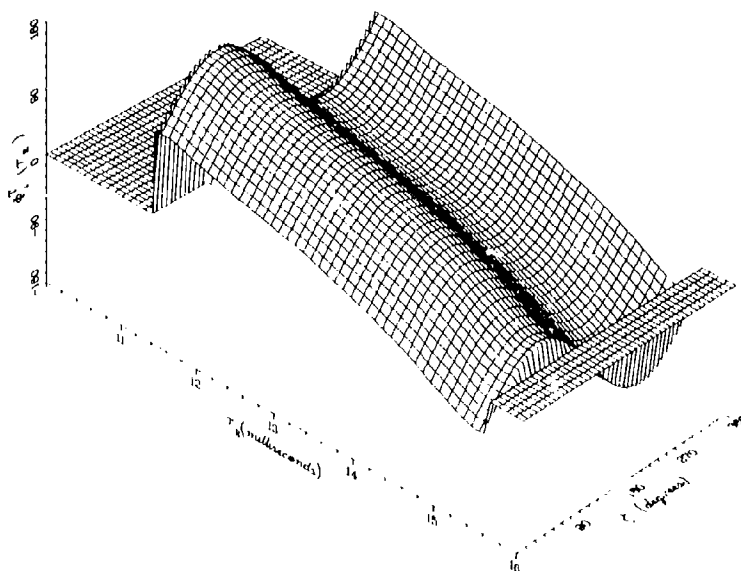
Fig. 29b — Phase behavior of $\vec{R}_I^T(\tau_R)$ for $\gamma = 0°$, calculated with the parameters of Table 2

$$|R_\ell^T (\tau_R)|$$
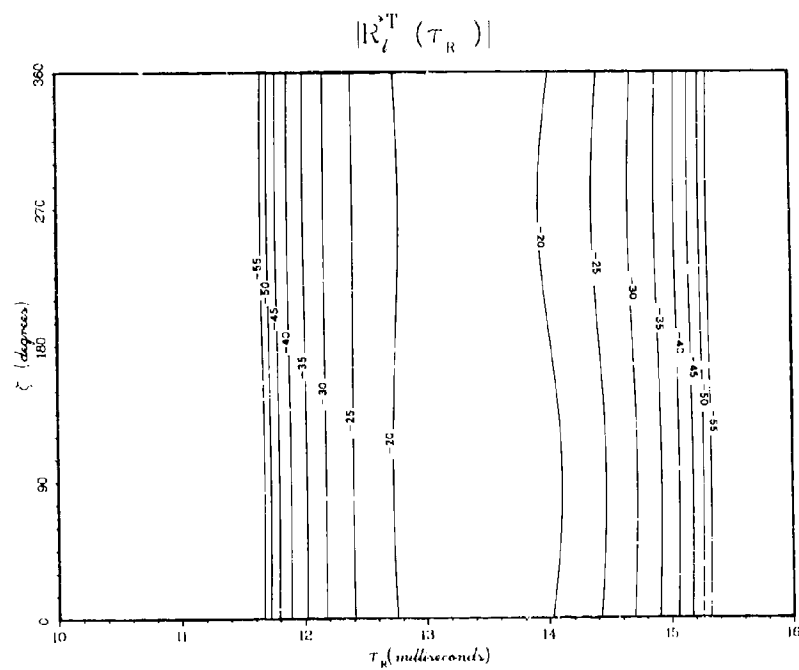
Fig. 29c — Amplitude contours corresponding to Fig. 29a

$$\Phi_\ell^T (\tau_R)$$
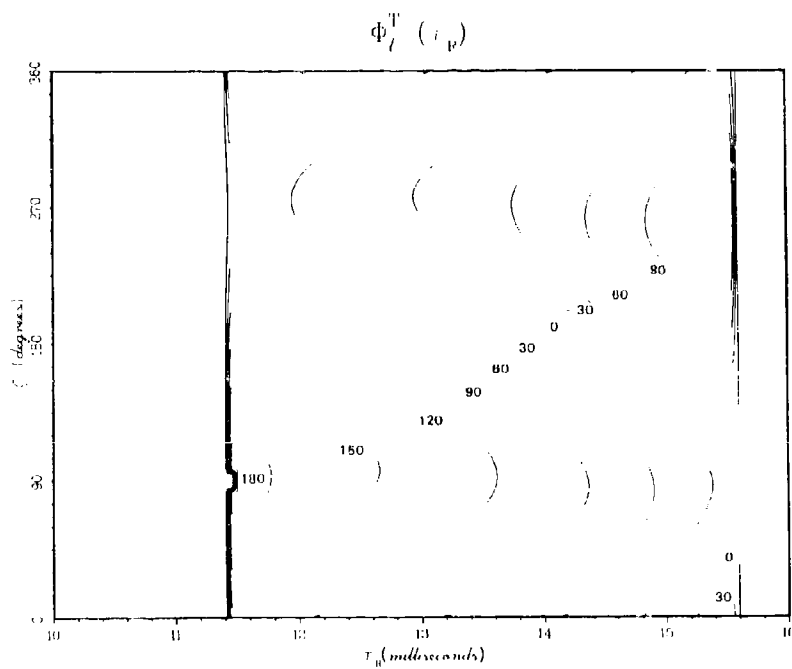
Fig. 29d — Phase behavior corresponding to Fig. 29b
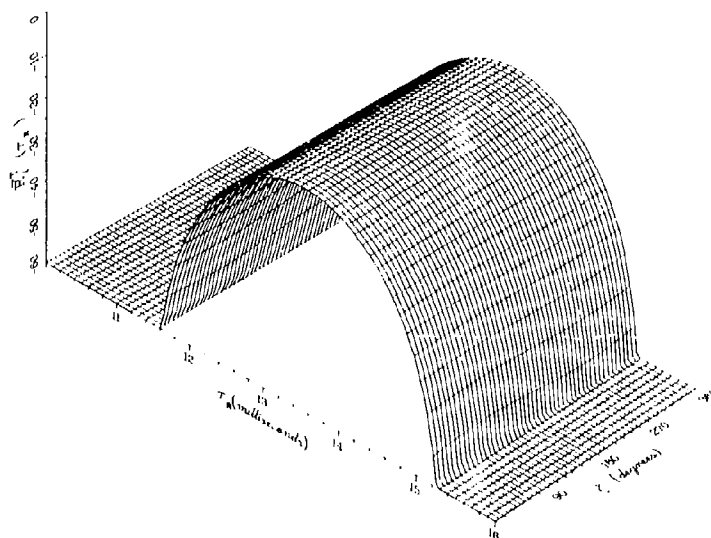
Fig. 30a — Amplitude behavior of $R_I^{(1)}(\tau_R)$ for $\gamma = 0°$, calculated with the parameters of Table 2
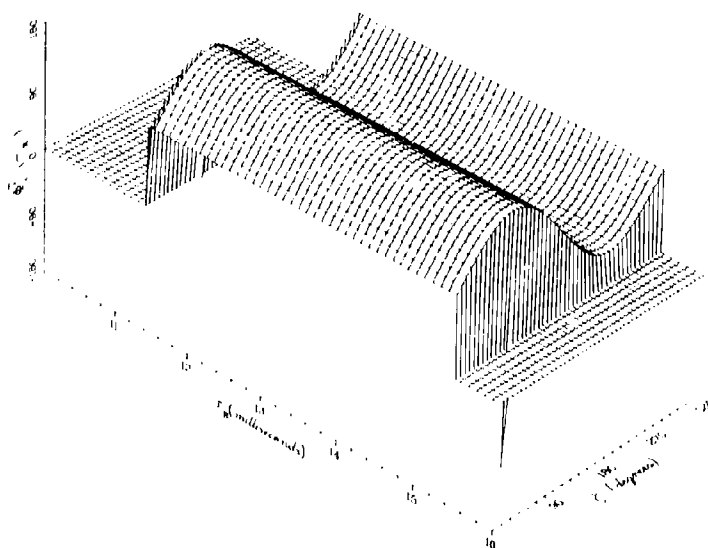


Fig. 30b — Phase behavior of $R_I^{(1)}(\tau_R)$ for $\gamma = 0°$, calculated with the parameters of Table 2

$$\|R_l^{'T}(\tau_R)\|$$
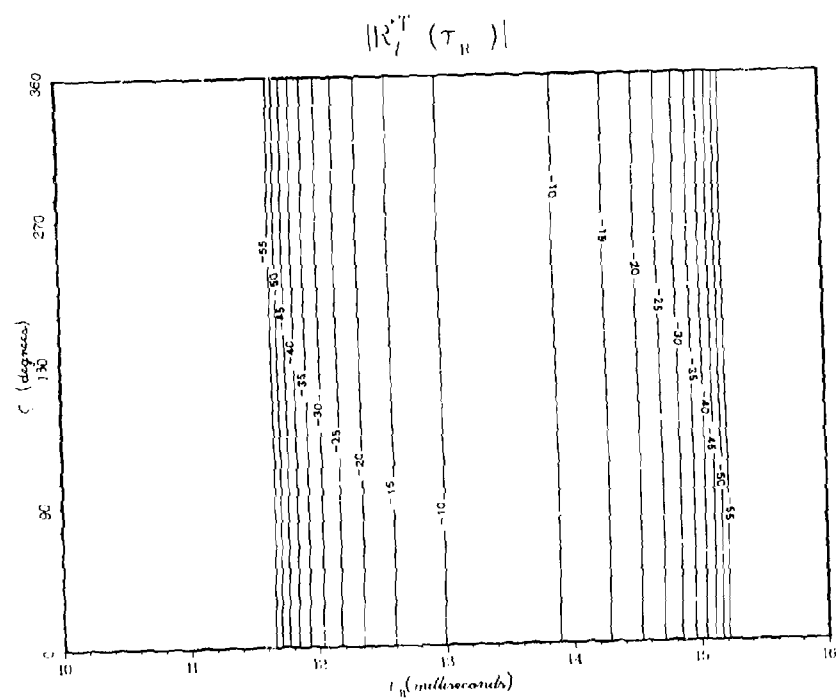


Fig. 30c — Amplitude contours corresponding to Fig. 30a

$$\phi_l^{'T}(\tau_R)$$
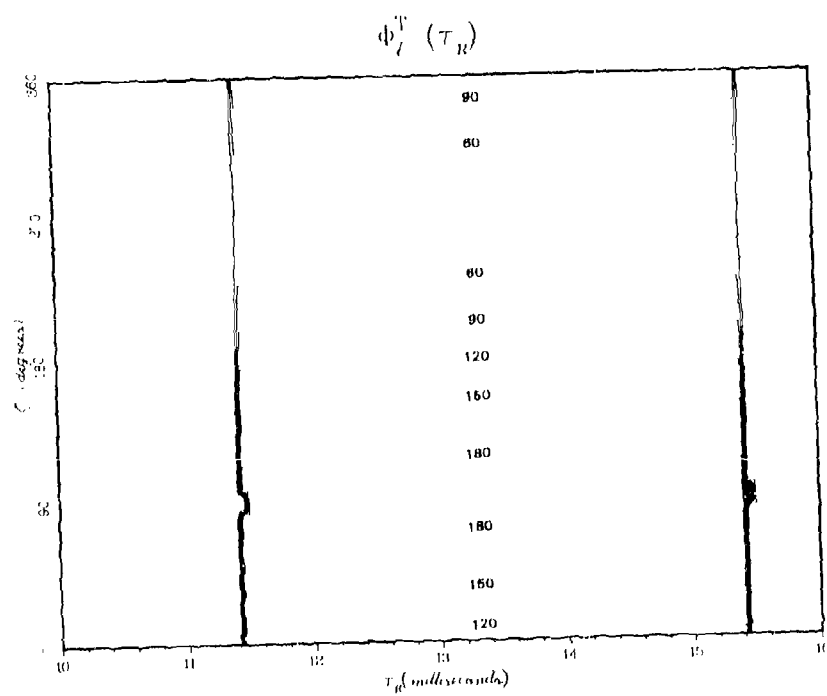


Fig. 30d — Phase behavior corresponding to Fig. 30b
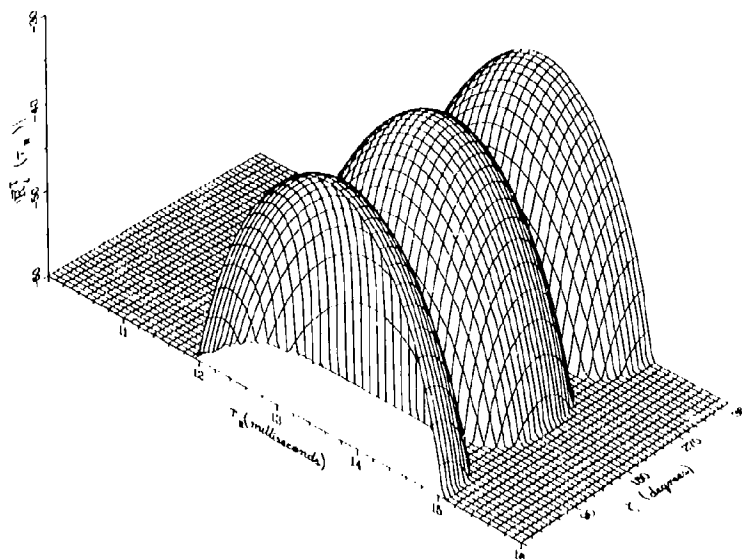
Fig. 31a — Amplitude behavior of $\vec{R}_l^T(\tau_R)$ for $\gamma = 90°$, calculated with the parameters of Table 3
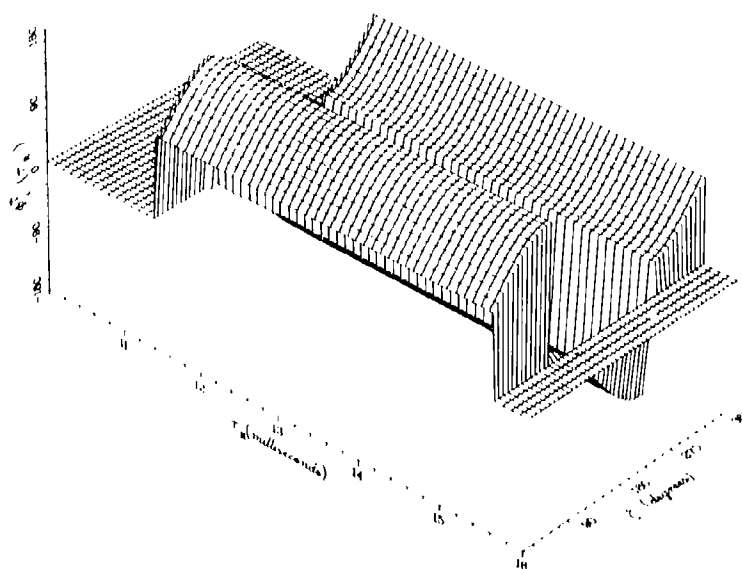


Fig. 31b — Phase behavior of $\vec{R}_l^T(\tau_R)$ for $\gamma = 90°$, calculated with the parameters of Table 3

$$|R_\ell^{'T}(\tau_R)|$$
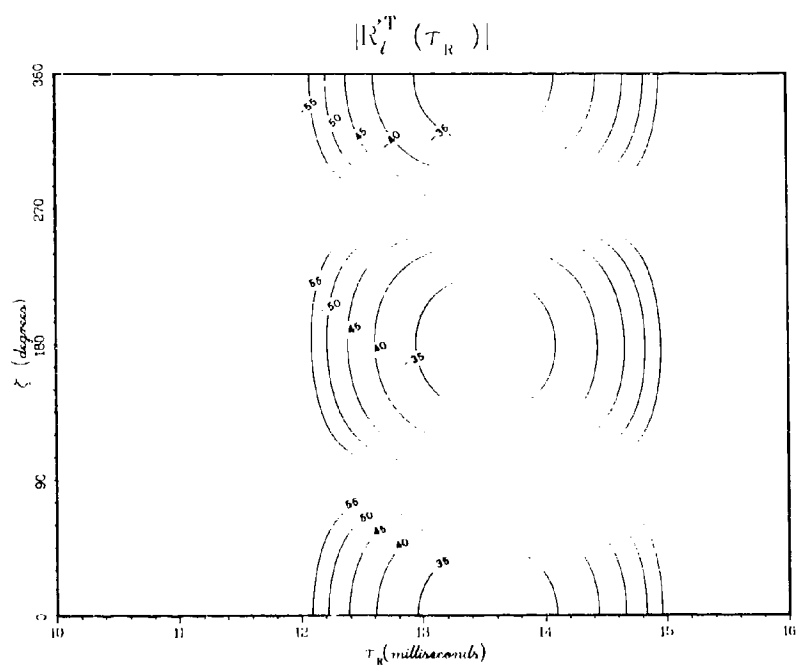


Fig. 31c — Amplitude contours corresponding to Fig. 31a

$$\Phi_\ell^T(\tau_R)$$
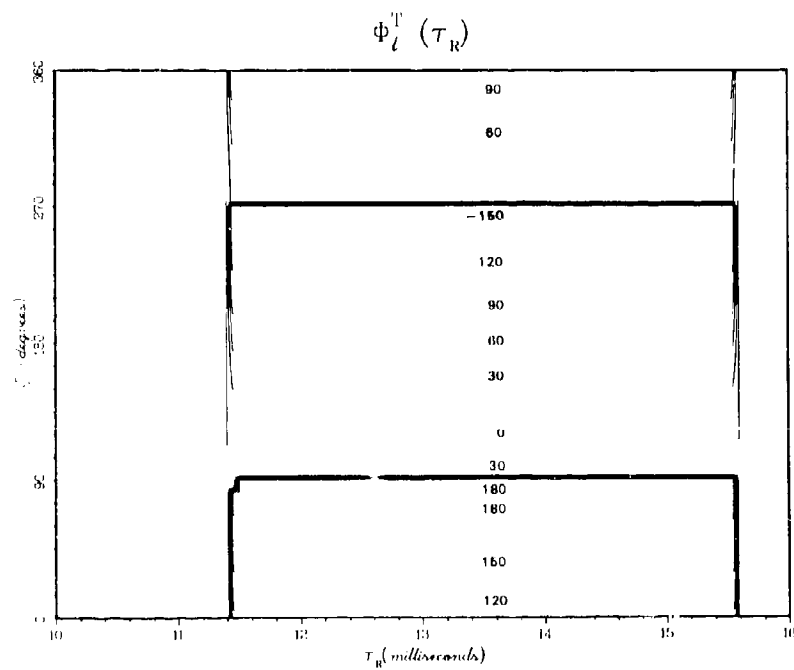


Fig. 31d — Phase behavior corresponding to Fig. 31b
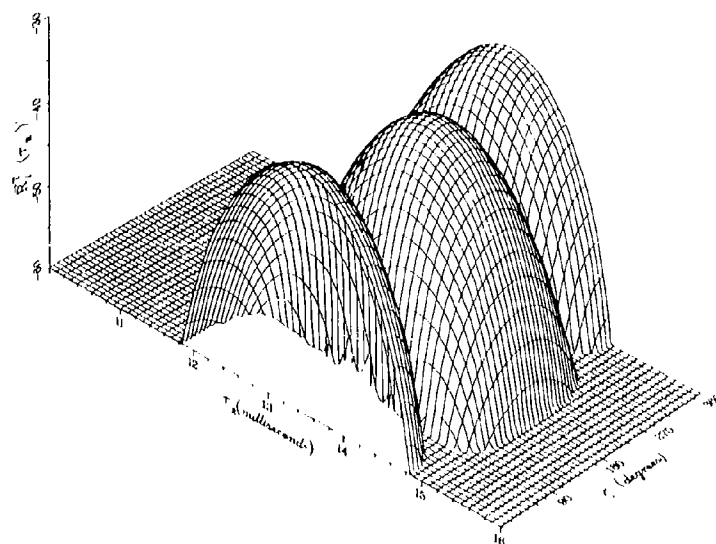
Fig. 32a — Amplitude behavior of $\vec{R}_I^T(\tau_R)$ for $\gamma = 85°$, calculated with the parameters of Table 3
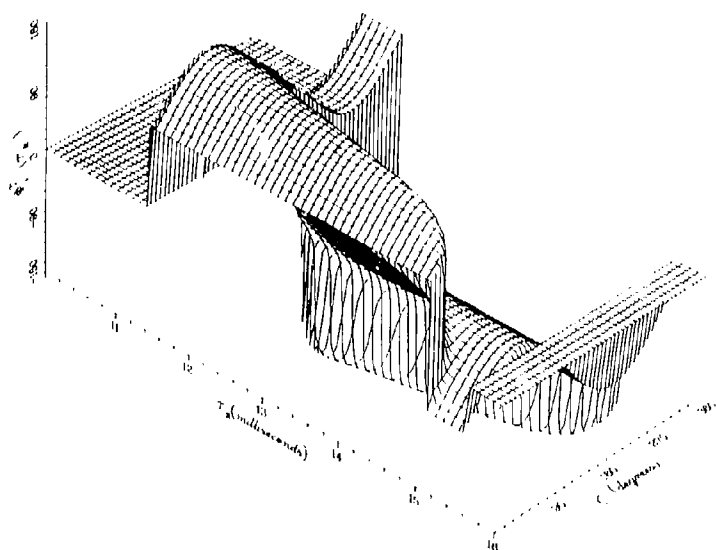


Fig. 32b — Phase behavior of $\vec{R}_I^T(\tau_R)$ for $\gamma = 85°$, calculated with the parameters of Table 3

$$|R_\ell^{'T}(\tau_R)|$$
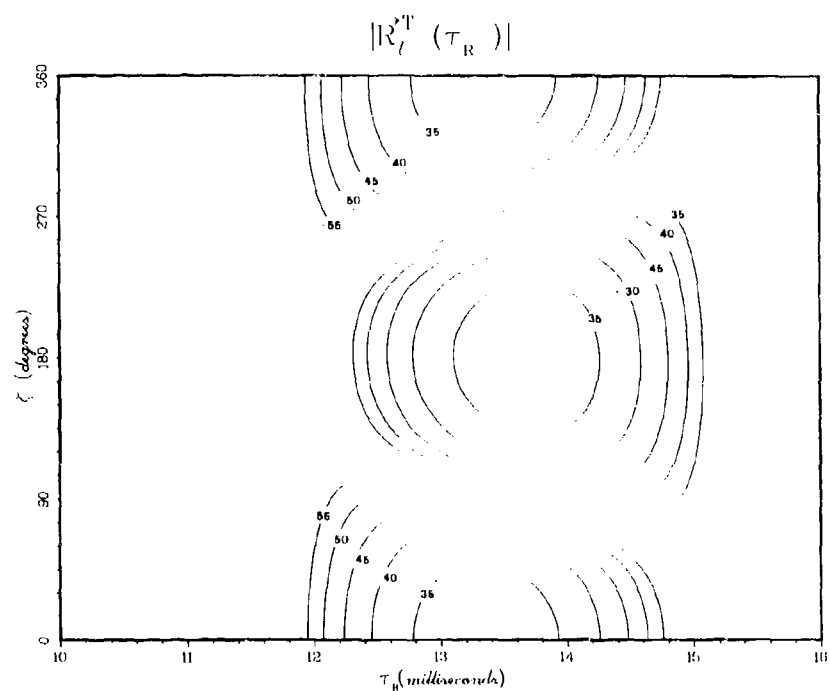


Fig. 32c — Amplitude contours corresponding to Fig. 32a

$$\phi_\ell^T(\tau_R)$$
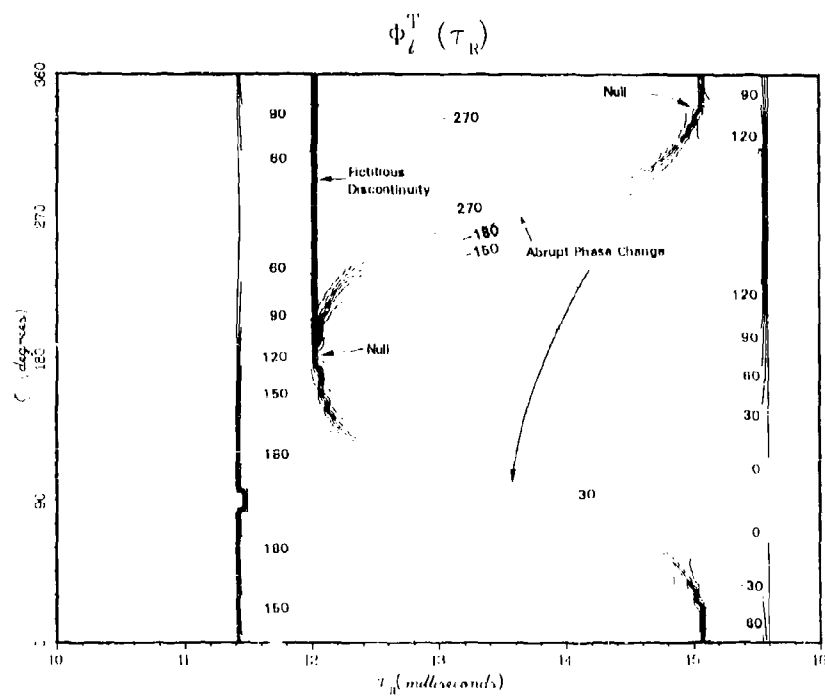


Fig. 32d — Phase behavior corresponding to Fig. 32b
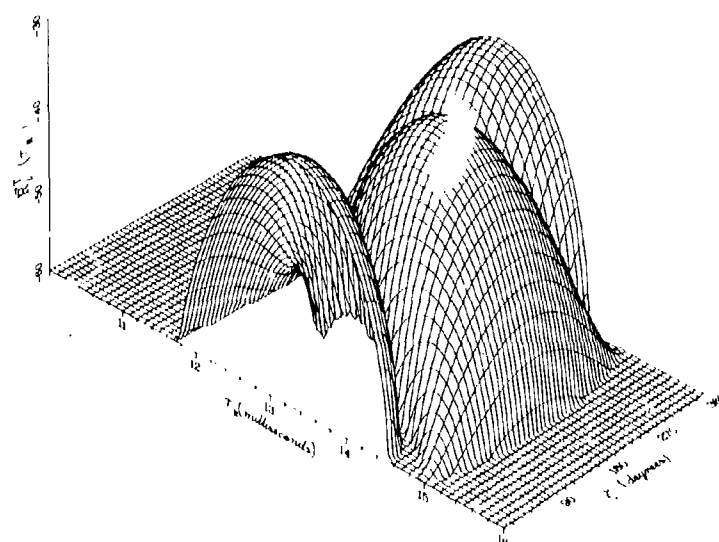
Fig. 33a — Amplitude behavior of $\vec{R}_l^T(\tau_R)$ for $\gamma = 80°$, calculated with the parameters of Table 3
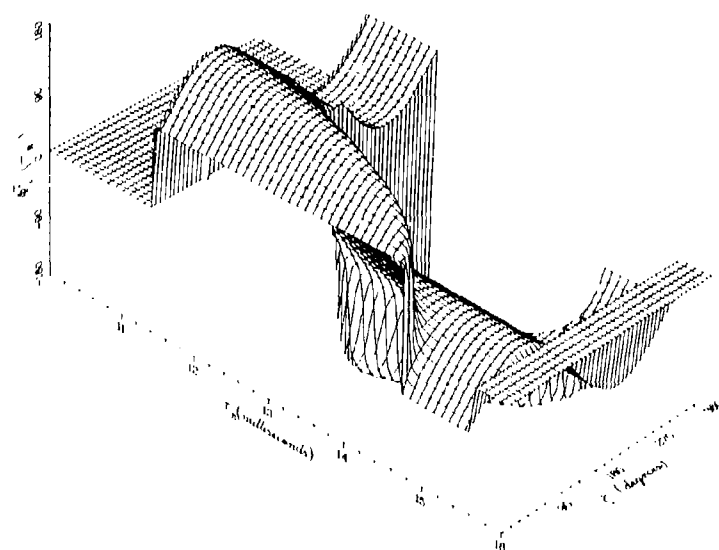


Fig. 33b — Phase behavior of $\vec{R}_l^T(\tau_R)$ for $\gamma = 80°$, calculated with the parameters of Table 3
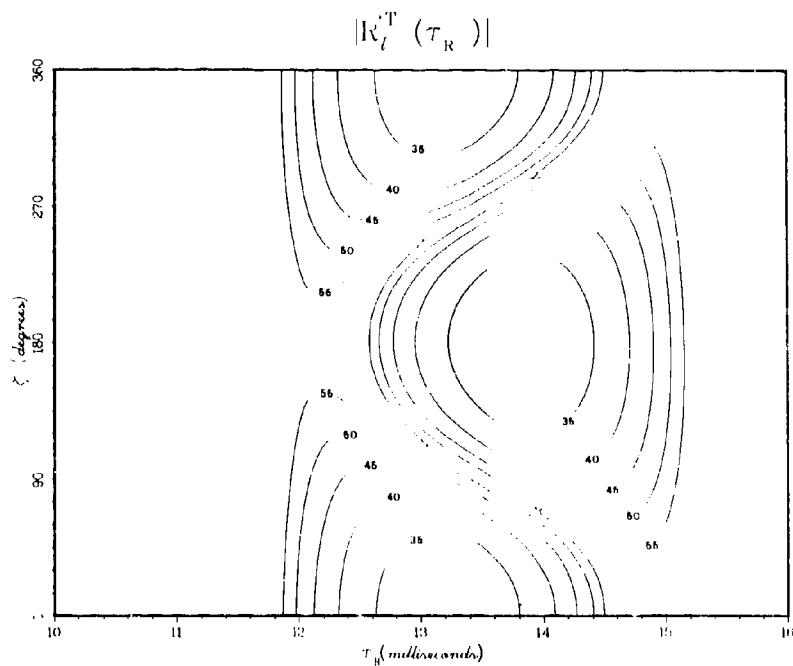
$$|R_i^T (\tau_R)|$$



Fig. 33c — Amplitude contours corresponding to Fig. 33a

$$\phi_i^T (\tau_R)$$
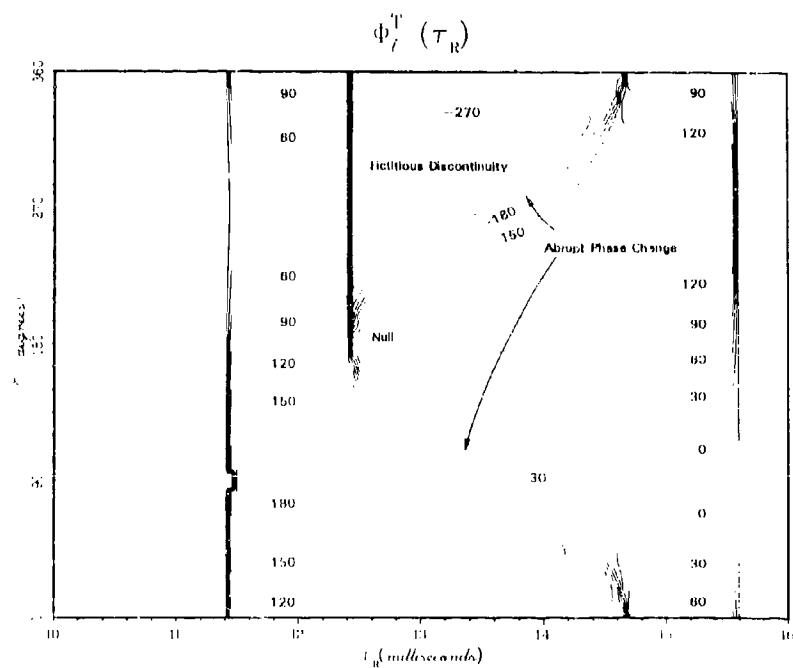


Fig. 33d — Phase behavior corresponding to Fig. 33b
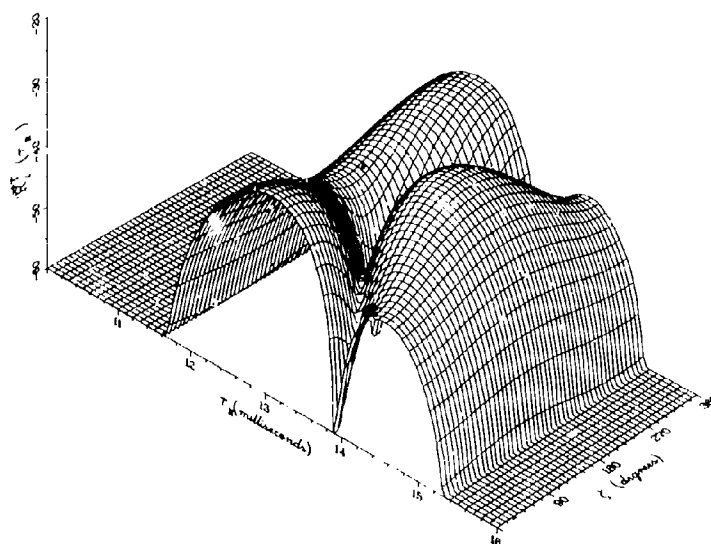
Fig. 34a — Amplitude behavior of $\overline{R}_l^T(\tau_R)$ for $\gamma = 60°$, calculated with the parameters of T...
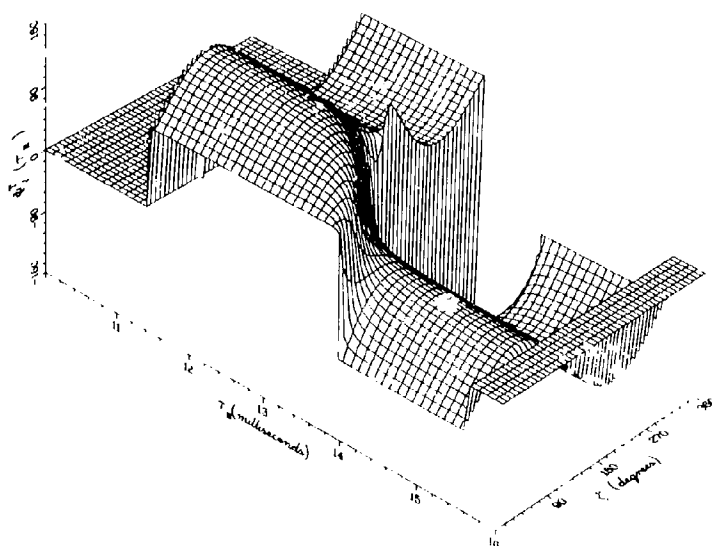


Fig. 34b — Phase behavior of $R_l^T(\tau_R)$ for $\gamma = 60°$, calculated with the parameters of Table 3

$$\left|\vec{R}_l^{'T}\left(\tau_R\right)\right|$$
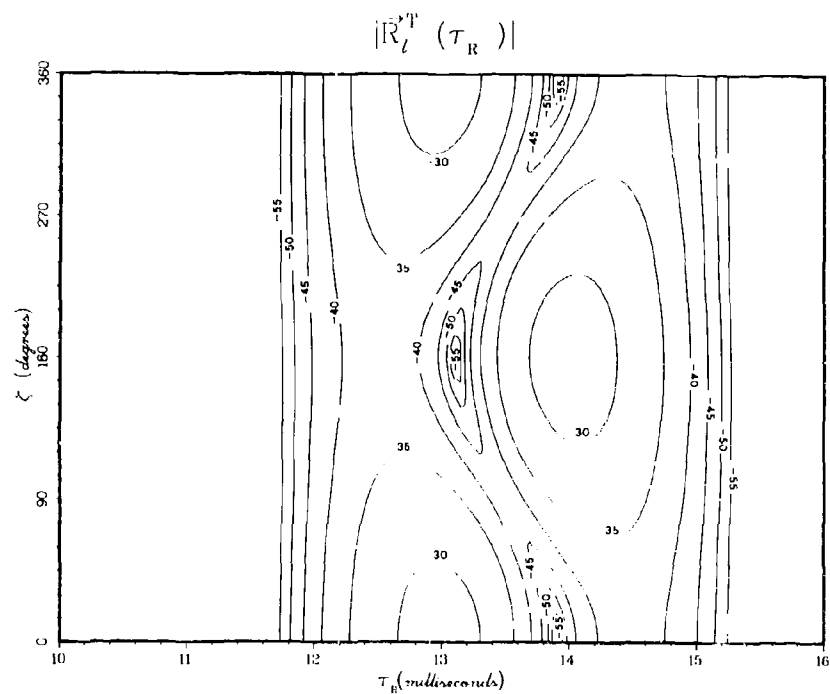


Fig. 34c — Amplitude contours corresponding to Fig. 34a

$$\phi_l^T\left(\tau_R\right)$$
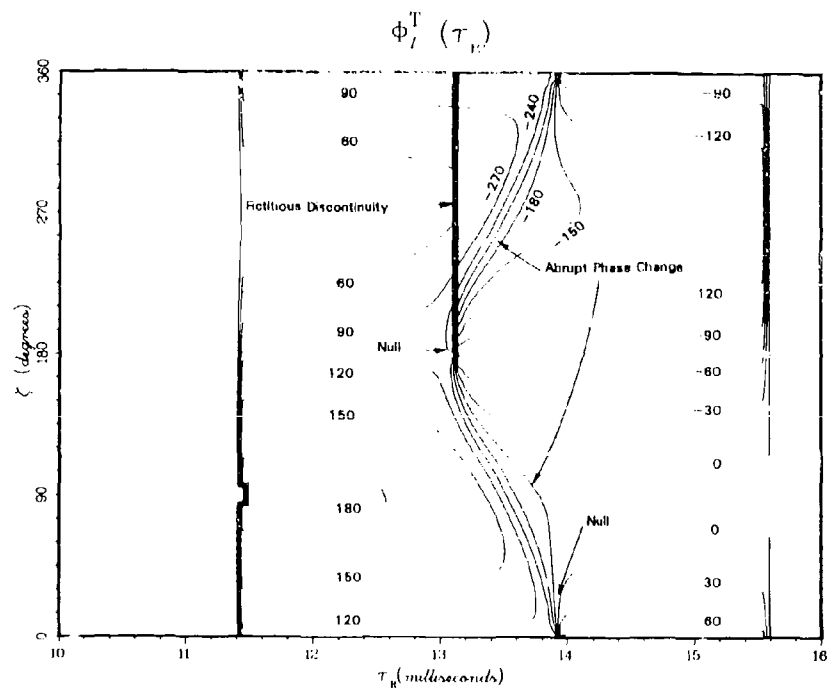


Fig. 34d — Phase behavior corresponding to Fig. 34b
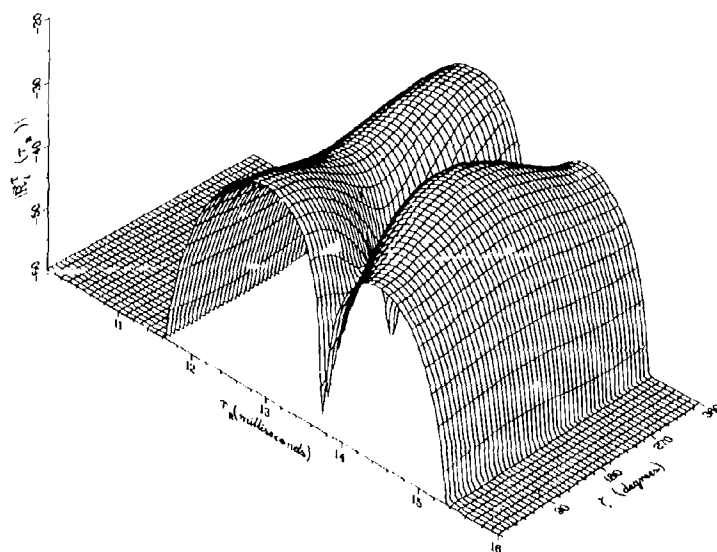
Fig. 35a — Amplitude behavior of $\vec{R}_l^T(\tau_R)$ for $\gamma = 45°$, calculated with the parameters of Table 3
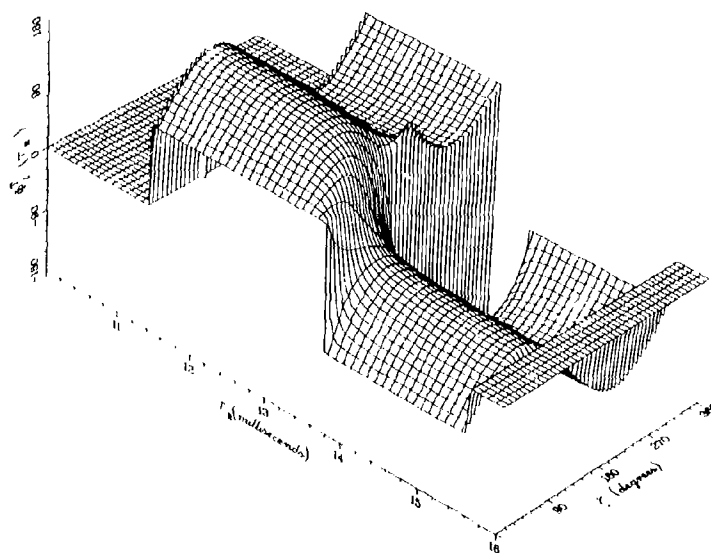


Fig. 35b — Phase behavior of $\vec{R}_l^T(\tau_R)$ for $\gamma = 45°$, calculated with the parameters of Table 3

$$|R_\ell'^{T}(\tau_R)|$$
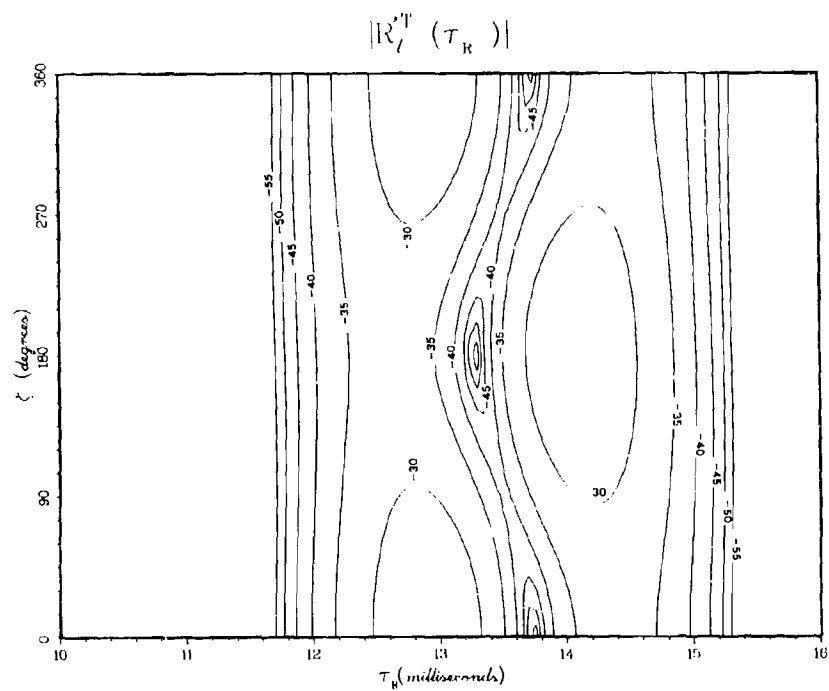


Fig. 35c — Amplitude contours corresponding to Fig. 35a

$$\phi_\ell^{T}(\tau_R)$$
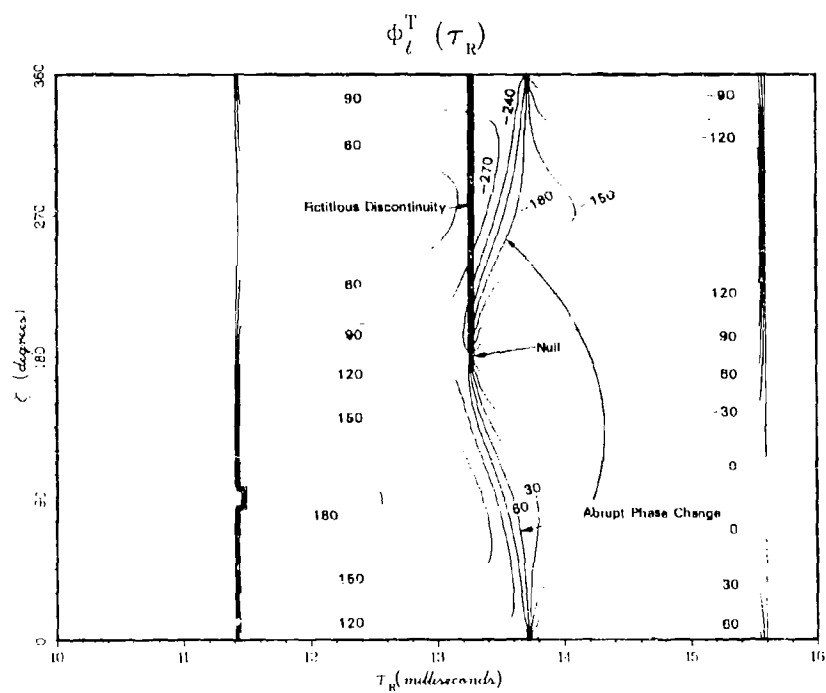


Fig. 35d — Phase behavior corresponding to Fig. 35b
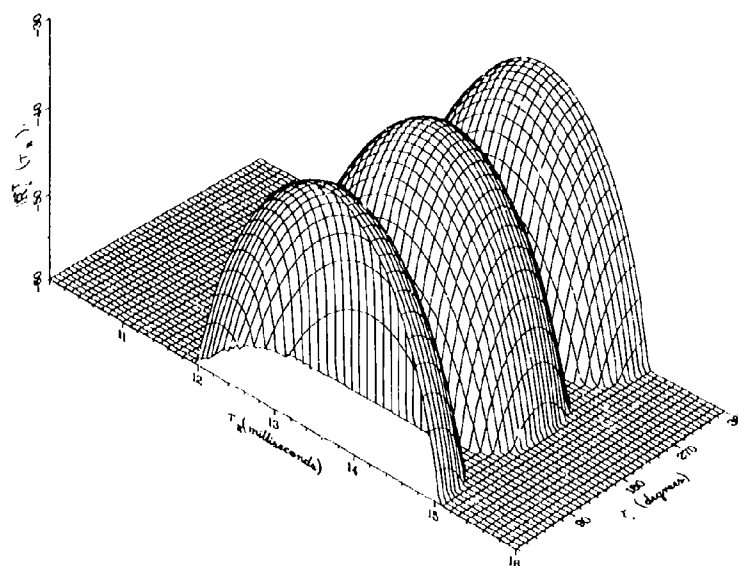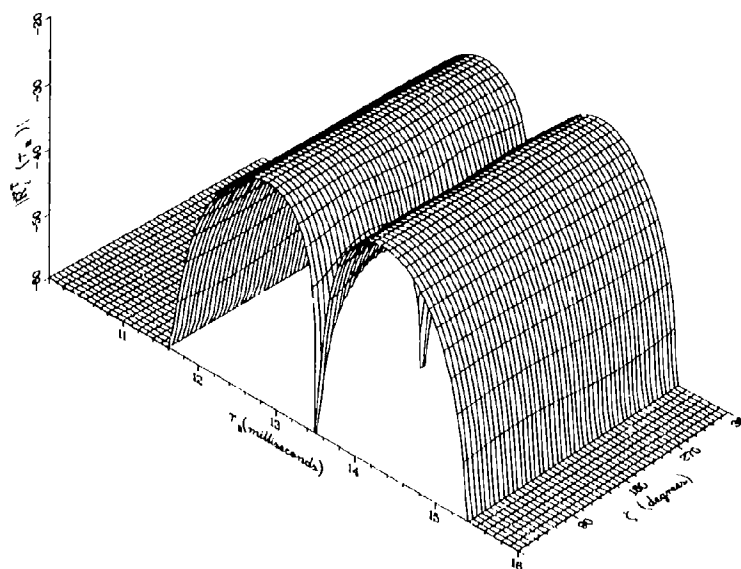
Fig. 36a — Amplitude behavior of $\vec{R}_l^T(\tau_R)$ for $\gamma = 0°$, calculated with the parameters of Table 2
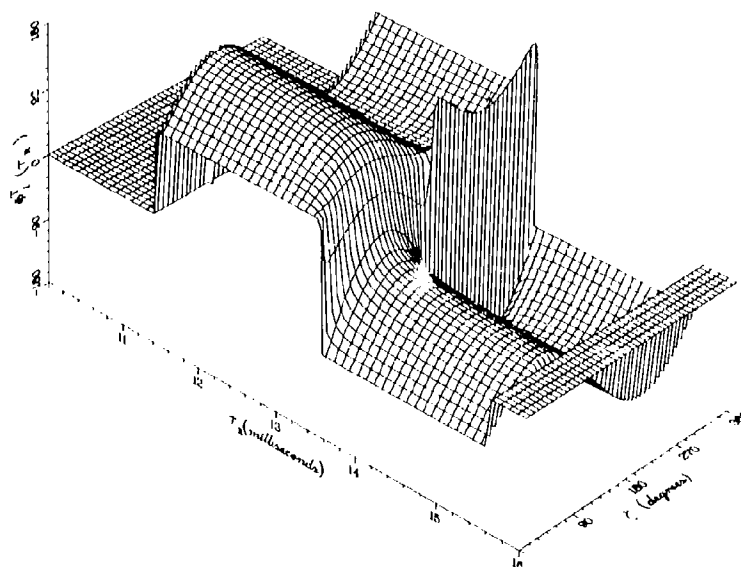


Fig. 36b — Phase behavior of $\vec{R}_l^T(\tau_R)$ for $\gamma = 0°$, calculated with the parameters of Table 3

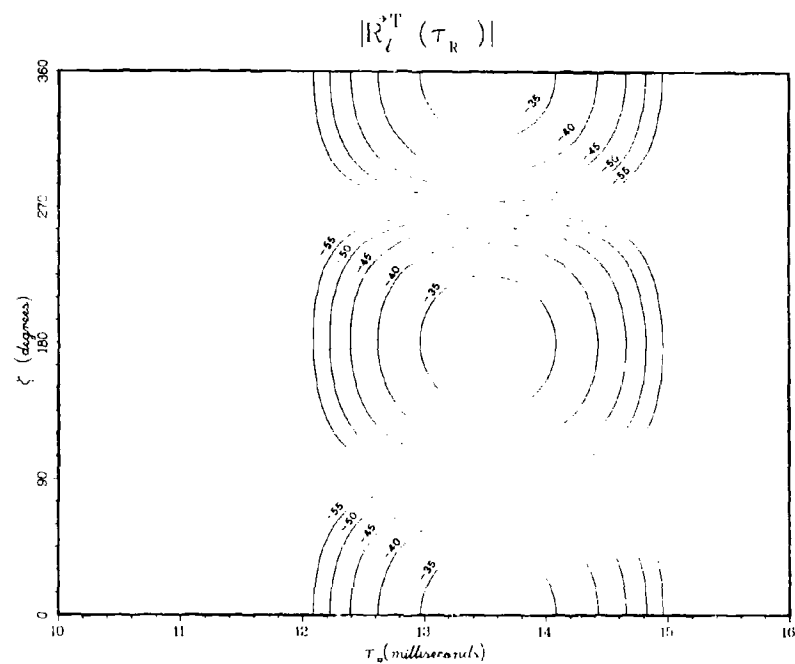$$|R_\ell^{'T}(\tau_R)|$$



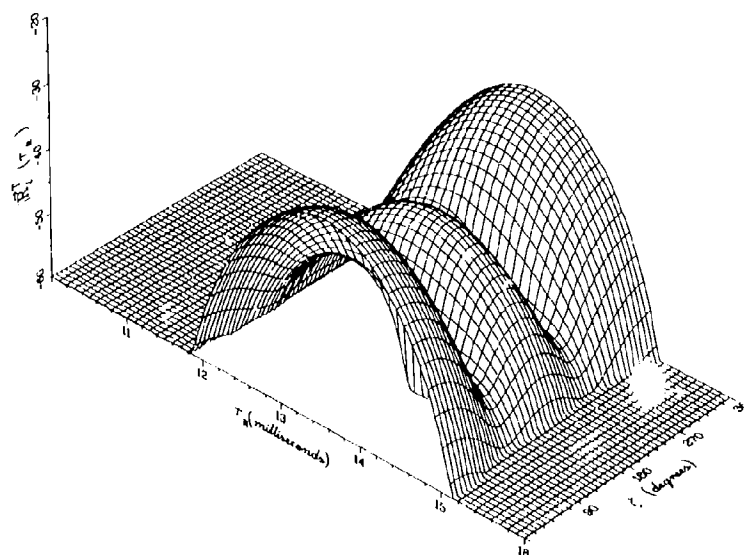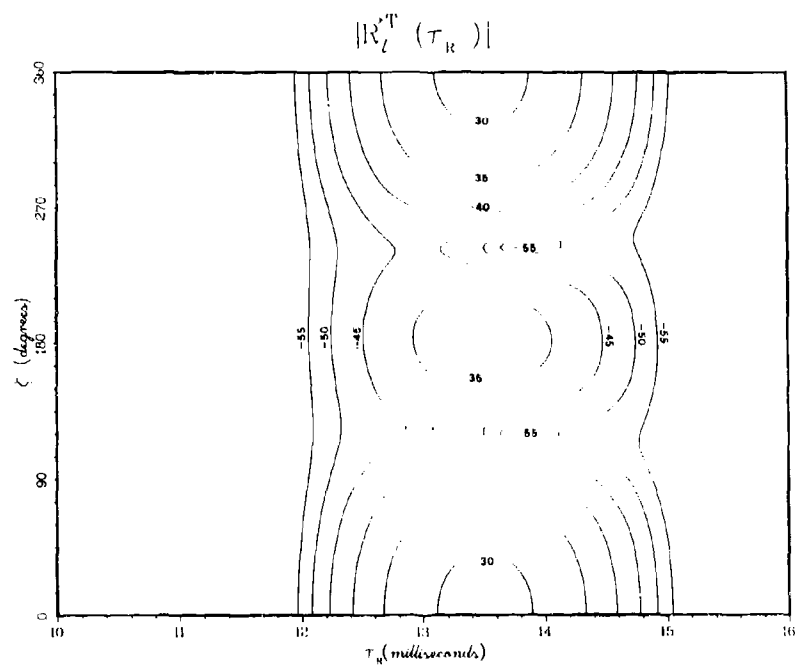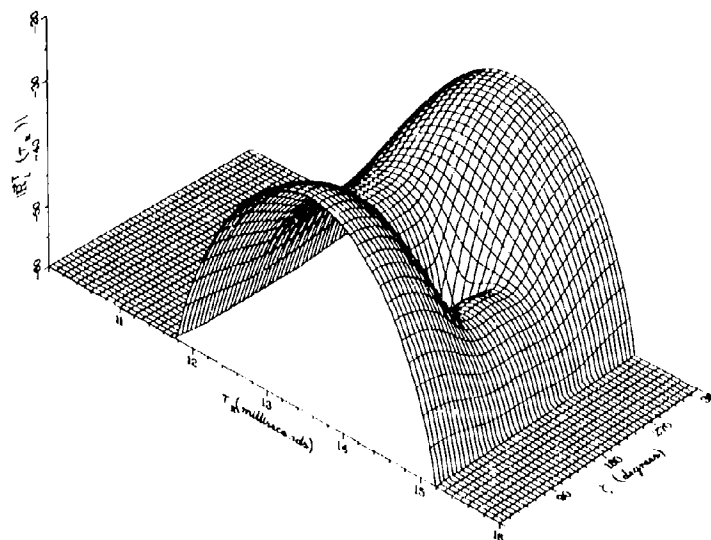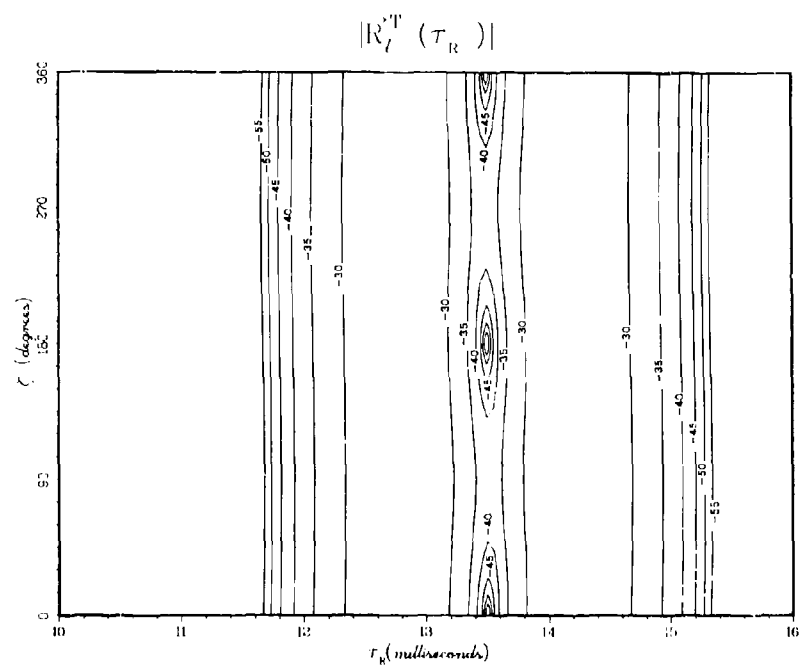Fig. 36c — Amplitude contours corresponding to Fig. 36a

$$\phi_\ell^T(\tau_R)$$
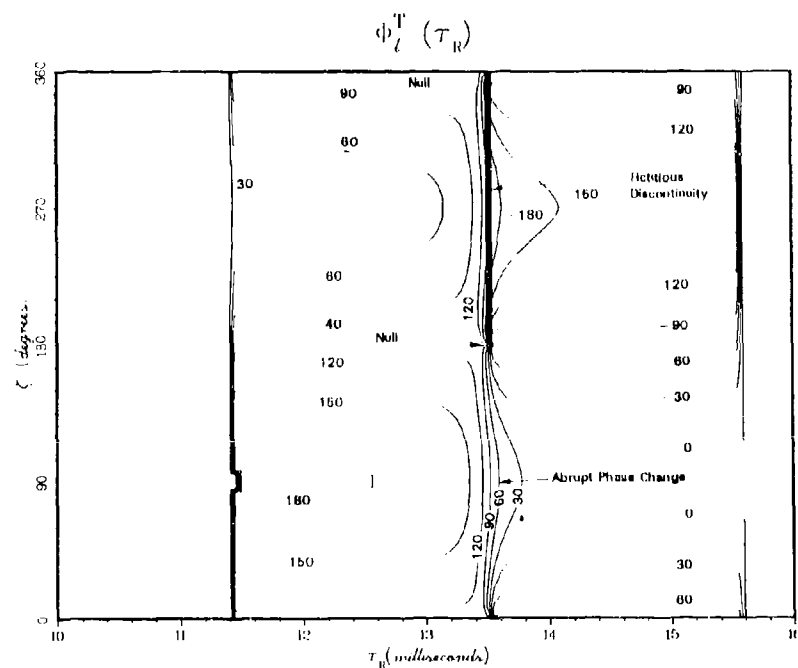


Fig. 36d — Phase behavior corresponding to Fig. 36b

## Discussion

Figure 24 shows the correlator performance for the case of a completely horizontal antenna. For this case $|\vec{R}_l(\tau_R)|$ goes to zero at $\zeta = 90°$ and $270°$, and there are sudden $180°$ phase flips at these angles. The best correlation time appears to be at $\tau_R = 13.5$ ms, which is the middle of the correlation peak.

Figure 25 shows the correlator performance for the case of an antenna with inclination $\gamma = 85°$ from the vertical. For this case it is difficult to say if there is a single best receiver synchronization time $\tau_R$. During most of the orbit it appears that the time $\tau_R = 13.5$ ms would be the best. However, this value of $\tau_R$ appears to give a value of $|\vec{R}_l^T(\tau_R)|$ that is severely reduced at $\zeta = 90°$ and $\zeta = 270°$. For this case a system of selection of three values of $\tau_R$ separated by 1-ms intervals (12.5, 13.5, and 14.5 ms) would give a more stable average performance in the evaluation of $R_l^T(\tau_R)$. The discontinuity in Fig. 25d at $\tau_R = 13.8$ ms, signified by the heavy vertical line, is due to a $360°$ ambiguity which has no real significance except at the nulls ($\zeta = 120°$ and $\zeta = 240°$), where $|\vec{R}_l^T(\tau_P)| \to 0$. Comparison of Figs. 25c and 25d illustrate this feature clearly.

Figure 26 shows the correlation performance for an antenna with $\gamma = 80°$. In the vicinity of $\tau_R = 14.0$ ms and $\zeta = 180°$ there is an abrupt drop of signal and jump in phase. Otherwise the $|\vec{R}_l(\tau_R)|$ function seems fairly well behaved.

Figure 27 shows the behavior of $R_l^T(\tau_R)$ for an antenna with $\gamma = 60°$. The amplitude and phase variation of the correlation are much milder than for the cases with smaller values of $\gamma$, since the vertical electric-field components exceed the horizontal components by at least one order of magnitude at this droop angle. This trend is continued as $\gamma$ is decreased to 45° and then to 0° in Figs. 28 and 29.

Figure 30 gives the value of $R_l^{(1)\text{ive}}(\tau_R)$. It illustrates the case of pure first-order-mode propagation from a vertical electric-dipole source.

The values of the propagation quantities in Table 3 are similar to those of Table 2 except for an adjustment to produce maximum mode cancellation and interference effects. We have made the first-order and second-order vertically generated modes have opposite phase and equal magnitude. We have modified the phase of the horizontally generated modes so they are in the same phase plane with the vertically generated modes to produce maximum field-strength variation. Hence both severe effects appear in Figs. 31 through 36.

Figure 31 gives the behavior of $R_l^T(\tau_R)$ for the propagation parameters of Table 3. The results are almost identical to those of Fig. 24, since $\gamma = 90°$ and the only changes made in the parameters of the horizontally generated modes are to the phase delay times $\tau_l^{\rho,he}$ and $\tau_l^{\rho,he}$.

Figure 32 shows the behavior of $R_l^T(\tau_R)$ for the case of $\gamma = 85°$. The influence of the splitting of the vertically generated function is more evident on the phase plot than on the amplitude plot.

Figure 33 shows the behavior of $R_l^T(\tau_R)$ for the case of $\gamma = 80°$. Here, the influence of the correlation-peak splitting of the vertically generated function is quite evident as the notch in the correlation peak makes its way from side to side through the values of $\tau_R$ and $\zeta$. This is illustrated further in Figs. 34 and 35, which give the graphs for $\gamma = 60°$ and 45°.

Finally, Fig. 36 shows the split correlation peak for a purely vertical antenna being carried around an orbit. Here we find a nearly constant variation of $|R_l^T(\tau_r)|$ versus $\zeta$, and the phase of the correlation function $\phi_l^T(\tau_R)$ varies only moderately with $\zeta$. As a function of $\tau_R$, these variables show the expected splitting.

The phase $\phi_l^T(\tau_R)$ changes gradually with $\tau_R$ in Figs. 27 through 29, whereas in Figs 34 through 36 it changes abruptly at certain $\tau_R$ values but then achieves a constant value again on either side of the change point. This is readily explained using the diagrammatic techniques previously discussed, since in the first case the correlation function for the individual modes $\vec{R}_l^{(1)}(\tau_R)$ are not coplanar, and in the second case they are coplanar, so that only abrupt phase changes are permitted.

## CONCLUSIONS

This report shows possible types of variation of the correlation vector $\vec{R}_l^T(\tau_R)$ when an airborne VLF transmitting system is employed. Use of a single correlator-synchronization time can result in loss of communications because of possible signal degradation and phase change caused by orbital and modal interference effects. Multiple and/or adaptive correlation and decision techniques seem indicated for this channel.

## REFERENCES

1. F.J. Rhoads and W.E. Garner, "An Investigation of the Modal Interference of VLF Radio Waves," Radio Science 2, 539-546 (1967).

2. J.R. Wait and K.P. Spies, "Characteristics of the Earth-Ionosphere Waveguide for VLF Radio Waves," NBS Tech. Note 300, 1964.

3. F.J. Kelly, "VLF Field Strength Variation from an Orbiting Inclined Antenna," Radio Sci. 5, 785-791 (1970).

4. J. Galejs, *Terrestrial Propagation of Long Electromagnetic Waves*, Pergamon Press, New York, 1972, p. 331.

5. I.J. Rothmuller, "Effect of the VLF Propagation Channel on Spread-Spectrum Communication Systems", NELC TR 1834, 4 Aug. 1972.

6. F.J. Kelly, "Multimode and Dispersive Distortion in the Very-Low-Frequency Channel," Radio Sci. 5, 569-573 (1970).

7. W.J. Judge, "Multiplexing using Quasiorthogonal Binary Functions", AIEE Trans. Commun. Electron. 81, 81-83 (1962).

# RELATIVE CHARACTERISTICS OF TE/TM WAVES EXCITED BY AIRBORNE VLF/LF TRANSMITTERS

Paul A. Kossey and Edward A. Lewis
Rome Air Development Center
Hanscom AFB, MA  01731

Edward C. Field
Pacific Sierra Res. Corp.
Santa Monica, CA  90404

## SUMMARY

U. S. Air Force studies of the characteristics of long radio waves, excited by airborne VLF/LF transmitting antennas, are described. These antennas provide a source of both conventionally used Transverse Magnetic (TM) waves and heretofore unused Transverse Electric (TE) waves. A variety of experimental and theoretical studies are described. Included are discussions of TE/TM signal and atmospheric noise data obtained using balloon, rocket and aircraft platforms, and theoretical studies on the propagation of TE/TM waves under both normal and disturbed ionospheric conditions. The exploitation of the TE polarization for improving the range and reliability of VLF/LF air-to-air communications is also considered.

## 1. INTRODUCTION

Conventional Very Low/Low Frequency (VLF/LF) radio transmitting stations have vertical antennas which excite waves of the Transverse Magnetic (TM) polarization in the earth-ionosphere waveguide (see Figure 1). With the advent of systems such as the U.S. Air Force's ARC-96, it is now possible to transmit VLF/LF signals from high speed aircraft. These aircraft are equipped with long trailing-wire antennas which may have lengths in excess of 6-7 kilometers. In high speed operations air-drag forces the antenna into a nearly horizontal position such that the desired vertical component may be only about one-tenth of the total length. In terms of radiated power, such an antenna is in the order of only one-percent as effective as it would be if it was vertical. Because the radiated power from such nearly horizontal antennas is mainly in the Transverse Electric (TE) polarization (see Figure 1), the question naturally arises as to whether or not the TE polarization could be exploited for communication purposes. The answer depends on such factors as the distribution of wave intensity with altitude, azimuth, and range, as well as considerations of the background noise and other interference, and the practicality of installing aircraft receive antennas, etc. This paper describes a variety of experimental and theoretical studies conducted or sponsored by the Propagation Branch, Rome Air Development Center, U.S. Air Force, which addresses a number of these question areas.

## 2. QUALITATIVE CONCEPTS

To the extent that the earth and the ionosphere may be considered to be a flat waveguide for long radio waves, the distribution of field intensity with altitude may be thought of as resulting from the interference of elementary up-going and down-going plane waves reflecting from the boundaries at certain oblique (modal) incidence angles. At these angles the phase changes due to reflection are such that the up-going and down-going plane waves are consistent with each other. For example, for most common types of earth, 45 kHz TM waves incident at angles less than about 87° (below the Brewster angle) may be regarded as reflecting with no large change of phase. On the other hand, the same waves incident on a flat ionosphere at angles greater than about 65° are beyond the quasi-Brewster angle, and reflect with a nearly 180° phase change. Thus, for incidence angles appropriate for long range propagation, the modal structures for TM waves between a flat earth and a flat ionosphere would tend to be the forms shown in Figure 1b. For the efficient coupling to such modes, an electric dipole transmitting antenna should be vertical, and preferably close to the ground.

For TE waves, however, most common surfaces are sufficiently well conducting at low frequencies to give a phase change of nearly 180° on reflection, at all incidence angles. Thus, there is a field cancellation effect at the ground, and the modal structures for TE waves should resemble those illustrated in Figure 1b, which show little or no TE field at low altitudes. Accordingly, the observation of TE waves would require receiver probes at altitudes amounting to an appreciable fraction of the distance between the ground and the ionosphere. Similarly, for the efficient excitation of the TE polarization, the transmitting antenna should be at a high altitude and preferably in a horizontal position. In flight, the ARC-96 transmitting antenna is typically about ninety percent horizontal, and its TE fields should be radiated predominantly in the broadside directions. The TM fields from the vertical component of the antenna, however, should be nearly independent of azimuth.

Strictly speaking, the propagating TE and TM polarizations are not independent because of cross-coupling in the ionosphere due to the geomagnetic field. Thus, there is partial conversion of TM waves into TE waves, and vice-versa. The effect may be especially significant at night. Under normal daytime conditions, or during disturbed ionospheric conditions, VLF/LF waves tend to be reflected at low ionospheric heights where electron-neutral collisions greatly reduce the influence of the earth's magnetic field, and it is generally appropriate to then consider the two polarizations as existing simultaneously, and independently.

## 3. RADC STUDIES OF TE/TM SIGNAL DISTRIBUTIONS WITH ALTITUDE

The altitude distributions of signals from ground-based TM long wave transmitters have been observed in a number of rocket flights conducted by RADC in the 1970's, but the spatial distribution of TE power has been virtually unexplored. In order to observe the TE fields from an ARC-96 transmitter at operational altitudes, RADC designed the balloon probe experiment illustrated in Figure 2. A loop antenna, to sense the vertical magnetic field of the TE waves, was suspended below a standard meteorological balloon. The probe, which included a small VLF receiver and a telemetry transmitter, was flown to an altitude of about 23 km, during a time when signals were available from a number of ground-based and airborne VLF/LF transmitters. During the flight of the probe the loop antenna swung with a random pendulum action, which prevented a strictly quantitative measurement of the observed fields, but

from the manner in which the signals varied as the loop swung, it was possible to infer whether they were predominantly TM or TE. The way in which this was done is illustrated in Figure 2a. For the case of a predominantly TM field, with a horizontal magnetic field, there would be some field linkage, and thus some signal pick-up, when the loop was in position A. As the loop moved towards 0 the signal would decrease to zero, but would increase again as position B was approached. The TM signal amplitude, as a function of time, would therefore give a deeply serrated record, as illustrated in Figure 2b. In the other extreme case shown in Figure 2a, that of a purely TE signal, the magnetic field of the wave is vertical, and essentially there is always some signal induced on the swinging loop. The amplitude-time record would be only slightly undulating, as illustrated.

Data obtained during such a balloon probe experiment are shown in Figure 2c. The data from NAA, a ground based TM transmitter, show the deep serrations expected from the swinging loop. A signal which came from an ARC-96 trailing-wire aircraft flying at high speed (NEACP) shows no evidence of such deep serrations, but is nearly constant. It is surmised from the observations that were made when the balloon was at an altitude of 14 km, that the signal was predominantly TE. The TACAMO signal was from an aircraft that was flown in circles of relatively small radius so that its transmitting antenna hung more vertically than the NEACP antenna. The TACAMO record shown in Figure 2c suggests that its signal contained a more equal mix of TE and TM components, i.e., the signal minima are not as deep as those of NAA, nor are they as nearly constant as the NEACP signal. The NEACP data, although qualitative in nature, represented the first tangible evidence to the Air Force that a predominantly TE- polarized signal could be observed from a trailing-wire aircraft, and provided the impetus for RADC to initiate and conduct further studies relating to the possible future exploitation of those signals to improve the range and reliability of air-to-air communication links.

The next RADC TE/TM experiments involved a new type balloon probe which contained loop antennas for sensing both TE and TM signals, independently (see Figure 3a). This probe swung pendulum-fashion during the balloon ascent, but was released at a pre-set barometric altitude, and allowed to fall. The aero-dynamic design of the probe provided vertical axis stabilization during the descent (typically within about one degree), and as the probe fell, it rotated in azimuth with the plane of the TE loop antenna remaining essentially horizontal. The plane of the TM receiving loop antenna was practically vertical during descent, but rotated azimuthally. An experiment using this 'DART' probe was performed at Churchill, Canada, to observe the 44 kHz signals from an ARC-96 aircraft flying over Lake Superior. The plane flew at an altitude of about 9.4 km in a race-track orbit approximately 100 km by 30 km. During each revolution of about twenty minutes time, all azimuthal aspects of the half-wave (3.4 km) trailing-wire antenna were presented to the receiving package at Churchill, during its ascent. The propagation path was magnetically north, and its average length was about 1300 km. The experiment was conducted under daytime conditions to minimize the effects of ionospheric conversion from one polarization to the other.

During ascent of the probe, the variation of TE amplitude due to the changing aspect of the ARC-96 transmitting antenna showed up very strongly in the data. Data points obtained by plotting relative signal strength against antenna aspect angle, estimated by interpolation in time between signal maxima when the package was at 20.8 km altitude, are shown in Figure 3b. There is excellent agreement with the theoretical pattern of a half-wave dipole in free space.

In Figure 3c, the circle-points show the TE maxima observed as the package ascended. The general trend of these points shows the expected very marked increase of signal with altitude, but the rate of increase appears to be slowing down around 20 km altitude. The TM data shown in Figure 3c were obtained during the axis-stabilized descent portion of the flight, when the loop response to the dominant TE field was minimized. The TM field was about 0.7 μa/m at the ground, and except for minor variations, decreased with increasing altitude. This characteristic agreed with expectations. The TE/TM data in Figure 3c show that, at an altitude of 9.4 km, the TE signal was approximately 12 dB larger than the TM signal, and at 22 km, the TE/TM ratio had increased to about 19 dB. It was estimated during the experiment that the ARC-96 radiated about 11 kw, with all but about two percent of it being in the TE polarization, due to the almost horizontal aspect of its trailing-wire transmitting antenna.

For completeness, field strength-altitude profiles for three ground-based TM transmitters were also recorded. They showed the expected tendency for the TM fields to decrease with increasing altitude. If these TM stations excited any TE wave components during this daytime flight, the amplitudes were too weak to measure with the instrumentation used. This would mean that they must have been at least 20 dB lower than the TM signals.

During this experiment it was also possible to obtain estimates of TE/TM background noise, by replaying the telemetry tapes through a receiver tuned slightly off the 44 kHz ARC-96 frequency. Although telemetry noise placed a limit on the level of atmospheric noise that could be observed from this experiment, it was concluded that the TE-atmospheric noise background was at least 6 dB below the TM noise, even at an altitude of 22 km. In later experiments, using more sensitive equipment, the TE-atmospheric noise was estimated to be at least 12 dB less than the TM noise. More recently a day-time flight of a TE- and TM-instrumented ARCAS rocket provided polarization ratios for 293 individual sferics. At 30 kHz the TM/TE noise ratio was larger than about 15 dB near the earth's surface, but decreased with increasing altitude to about 0 dB at 60 km. Other studies, by the U.S. Navy and Air Force organizations, have estimated that the TE noise is often 20 dB lower than the TM noise. Factors which determine the TM/TE noise ratio at a given altitude include (a) the difference in altitude-amplitude profiles which are, in turn, determined primarily by the boundary conditions at the earth and the ionosphere, (b) the relative strength of the two types of pattern, which may vary with propagation distance, and which depends on the relative effectiveness of the average lightning stroke in exciting the patterns.

## 4. TE/TM SIGNAL DISTRIBUTION WITH RANGE

The results of RADC's early swinging-loop and DART probe experiments indicated a possibility of improving air-to-air long wave communications by exploiting the TE polarization, provided the azimuthal pattern of the trailing-wire antennas could be accepted, and provided that both the transmitting and receiving aircraft were at sufficiently high altitudes. There were no data, from these experiments, on how the TE/TM signals varied with range from the airborne transmitters. To obtain such data, RADC equipped a U-2 aircraft to receive TE/TM signals. This was accomplished in a series of flights in the vicinity of Hawaii. An example of the data received during one such flight is shown in Figure 4. With the transmitting aircraft at 9.75 km, and the U-2 receiving aircraft at 19 km, the received TE signals were substantially greater than the TM signals, over the measurement range of 400-1000 km. The measurements for this flight were limited to about 1000 km due to aircraft electrical noise problems. This noise, from the U-2's generating system, exceeded the background atmospheric noise. In fact, during all the U-2's flights, the internal electrical noise from the harmonics of the aircraft's 400 Hz generator limited the maximum range at which the TE/TM measurements could be made. To alleviate the problem during the U-2 tests, a prototype interference cancellation system was developed and used to extend the measurements range out to about 2000 km. To date, however, the internal aircraft noise on operational aircraft is the primary problem to be overcome if significant increases in communication ranges are to be achieved. Figure 4 illustrates another feature of TE/TM propagation which has been observed on numerous flights. The distances at which the relative nulls of the two signals occur are different, so that there is a 'null-filling' capability which could help to insure more reliable communications if both polarizations were being received.

## 5. COMPUTATIONAL STUDIES

Theoretical studies of excitation factors, height-gains, and attenuation rates further reveal the relative characteristics of TE/TM signals from airborne transmitters. The brief discussions describing these factors, which follow, are incomplete and are meant only to show some of the broad features which tend to characterize the two polarizations.

The fields of the trailing-wire electric dipole in the earth-ionosphere waveguide can be expressed as summations of the elementary waveguide modes, as described earlier in conjunction with Figure 1. For daytime or disturbed ionospheric conditions, when geomagnetic mode-coupling can be neglected, a vertical electric dipole excites only TM modes. Each TM mode, and hence the total field, contains only three components; viz, a vertical electrical field, a transverse magnetic field, a longitudinal electric field, as shown in Figure 1. A horizontal electric dipole excites both TM and TE modes, and, for arbitrary field orientations, excites all six field components shown in Figure 1b. However, for propagation perpendicular to the dipole axis (the situation analyzed here), only the vertical magnetic field, the transverse electric field, and the longitudinal magnetic field are excited. Although these are the same three field components that are present in a pure TE mode (see Figure 1b), the broadside fields are, in fact, composed of complicated combinations of both TM and TM modes. This absence of pure modal excitation has led to the designation 'quasi-modes' for the horizontal electric dipole fields. The contribution of each mode to the total field is proportional to the product of four factors; viz, the excitation factor, the transmitter height-gain factor, the receiver height-gain factor, and the propagation factor. Most of the results described below are for a nominal daytime ionosphere, approximated by an exponential conductivity height-gradient.

### 5.1. Excitation Factors

Figure 5 shows the frequency dependence of the excitation-factor magnitudes of the first three TM modes ($\alpha = 1,2,3$) and the first two TE modes ($\beta = 1, 2$) for ambient daytime conditions and a ground conductivity of $10^{-3}$ mhos/m. The magnitude of the modes give the relative contributions of each mode to the total fields at short distances from ground-based electric dipoles. Effects of elevation and long-path propagation are accounted for in the height-gain and propagation factors, to be given later. The first three TM modes are excited equally at the lower VLF frequencies, but, above about 30 kHz, the higher-order TM modes are much more effectively excited than the first one. The TE modes are excited much more poorly than the TM modes, by four or five orders of magnitude, as shown in Figure 5. The efficiency of TE-mode excitation relative to TM-mode excitation improves as the ground conductivity is reduced. For example, at 20 kHz the TE-mode excitation factors are nearly two orders of magnitude greater for a $10^{-5}$ mhos/m conductivity than for $10^{-3}$ mhos/m. On the other hand, the excitation factor for the lowest TM-mode is less by almost an order of magnitude if the conductivity is changed in the same fashion.

The excitation factors also depend on the state of the ionosphere. The excitation factors as defined here and shown in Figure 5 are inversely proportional to a quantity that becomes the 'height of the ionosphere' in the limit of a sharply bounded ionosphere. For the diffuse ionospheres used here, the excitation factors at the lower VLF frequencies are roughly proportional to the inverse of the average height at which important reflections occur. Thus, one would expect these factors to become somewhat larger under disturbed conditions, when the ionosphere is significantly depressed.

### 5.2. Height-Gain Factors

The height-gain factor of the waveguide mode accounts for the effects of non-zero transmitter and receiver heights. More precisely, the transmitter height-gain factor is the ratio of the mode excitation for the actual transmitter height, h, to the mode excitation for a ground-based transmitter. Similarly, the receiver height-gain factor is the ratio of the mode strength at the receiver height, z, to the TE or TM fields, normalized to a value of unity at the ground. For elevated terminals, the contribution of a given mode to the total field is proportional to the product of the excitation factor, the transmitter height-gain factor, and the receiver height-gain factor. The transmitter and receiver height-gain factors for a given mode are identical, and, therefore, are equal when transmitter and receiver are at the same altitude. In this case, the relative importance of a mode is proportional to the product of the excitation

factor and the square of the height-gain factor computed for the appropriate altitude. Figure 6 shows the computed height-gain factors for the first three TM-modes, for ambient daytime conditions, a conductivity of $10^{-3}$ mhos/m, and a frequency of 40 kHz. These height-gain factors exhibit the classic height-dependences for antennas over a highly conductive ground; the TM mode height-gain factors are of order unity over most of the waveguide, except for some rather sharp nulls; and, above a few kilometers, the TE-mode height-gain factors increase sharply to values well in excess of one-hundred. For elevated antennas, the large TE-mode height-gain factor mitigates the effects of the small excitation factor, and these modes can be excited about as effectively as TM modes.

### 5.3. Attenuation Rates

Modal attenuation rates account for the reduction (over and above cylindrical spreading) in strength suffered by a mode in propagating between the transmitter and receiver. Figure 7 shows calculated attenuation rates versus frequency for the first three TM modes and the first two TE modes for ambient daytime conditions and a ground conductivity of $10^{-3}$ mhos/m. The higher-order modes are more heavily attenuated than lower-order ones, which allows one to neglect the higher terms in the mode sums at large distances. At 40 kHz, however, the attenuation rates for the TE modes differ by only about 2 dB/Mm. Given that the higher-order modes are more effectively excited than the lower ones, it is doubtful that TE mode sums can be truncated throughout the upper LF band under ambient conditions. For moderately disturbed conditions, the higher modes are much more heavily attenuated than the first modes, and the mode sum can be used well into the LF regime. Figure 7 shows that the lowest TE mode is slightly less attenuated than the lowest TM mode. This behavior is in contrast to results found for a perfectly conducting ground. Those results indicated that the first TM-mode attenuation rate was between 2–3 dB/Mm, which was 1–2 dB/Mm less than the lowest TE-mode attenuation rate. The decrease in ground conductivity from perfectly conducting to $10^{-3}$ mhos/m causes the first TM-mode attenuation rate to essentially double, while the TE-mode attenuation rate is relatively unchanged. Other calculations, for an assumed ground conductivity of $10^{-5}$ mhos/m, further show the relative insensitivity of the TE-mode attenuation rate to ground conductivity. For example, at 20 kHz, the first TM-mode attenuation rate is about 8.6 dB/Mm, while the first TE-mode attenuation rate is still only about 3.4 dB/Mm. This large increase in the TM-attenuation rate occurs because the TM ground reflection has a Quasi-Brewster angle effect at the ground, whereas the TE coefficient does not. In summary, TM-mode attenuation rates are more sensitive to changes in ground conductivity than are TE-mode attenuation rates.

In contrast, however, other studies have shown that TE modes are relatively more sensitive to ionospheric conditions. Figure 8 summarizes calculations which provide estimates of how much more the first TE mode is attenuated than the first TM mode over the 10–50 kHz range, for a ground conductivity of $10^{-3}$ mhos/Mm, and for a variety of ionospheric conditions. For undisturbed conditions or frequencies above about 35 kHz there is only a small excess TE-mode attenuation; and, for a weak nuclear or strong polar cap absorption event (PCA) the excess TE-attenuation, although larger, is still relatively moderate. For moderate or severe ionospheric disturbances, however, the excess TE-attenuation becomes very large. An investigation of the TE/TM ionospheric reflection coefficients for oblique incidence angles for the disturbed ionospheric cases reveals that the TE and TM reflection coefficients are generally quite similar, so that the resulting excess TE-mode attenuation may at first seem puzzling. However, in order to satisfy the boundary conditions, it is found that the TE modes must be more steeply incident on the ionosphere than the TM modes. One consequence of this steeper incidence is that the TE reflection coefficient is generally somewhat smaller than the TM coefficient; but, more importantly, the steeper incidence angle causes the skip distance of the TE-mode plane wave to be significantly less than that of the corresponding TM-mode wave. Thus, the TE-mode will generally suffer more ionospheric reflections per a given distance than the TM-mode. These additional reflections cause most of the excess TE-mode attenuation.

### 5.4. Field Strength Versus Distance

Figure 9a shows calculations of TE and TM fields illustrating the effects of elevation for a typical Air Force ARC-96 operational configuration. Normal daytime ambient ionospheric conditions were assumed, and a ground conductivity of $10^{-3}$ mhos/m was used. Both transmitter and receiver were assumed to be at the same altitude, and the trailing-wire transmitting antenna was assumed to be inclined at an angle of ten degrees with respect to the horizontal. In the Figure only a single TM-signal strength curve is shown, since the TM-signal strengths were found to be essentially insensitive to altitudes less than about 16 km. On the other hand, the TE-signal strengths (dotted in Figure 9a) are seen to depend strongly on the aircraft's altitudes. For the 40 kHz example shown, the TE fields substantially exceed the TM fields for altitudes above about 7.6 km. Figure 9b shows calculations similar to those of Figure 9a, but for the case of a moderate spread debris nuclear environment. Comparison of the TE to TM fields in this case is less favorable than for the ambient conditions shown in Figure 9a because of the much larger attenuation rates associated with the TE modes, as described above. Nevertheless, at ranges up to about 1500 km the TE fields are comparable or larger than the TM fields, for aircraft altitudes above 7.6 km. Furthermore, since there may be lower background TE noise, the signal/noise may favor the TE polarization even out to greater distances. It may be that under certain scenarios the most strongly attenuated signal may still be more useful for communication purposes. Of course, in a strong nuclear scenario such questions could be academic, since the signals in both polarizations may suffer prohibitive attenuations.

### 5.5. Field Strength Versus Altitude

When the fields are dominated by a single waveguide mode, the shapes of the field height-profiles are independent of distance from the transmitter, and are essentially the height-gain factors (suitably attenuated) of the dominant mode. For multi-mode propagation, the situation is much more complicated because the field height profiles depend on the height-gain factors of two or more modes. The shape of these profiles depends on transmission range, because the relative contribution of each mode varies with distance. To illustrate this effect, Figure 10 shows height profiles of TE fields, at four distances from a transmitter 4.6 km above ground. The curves apply to 20 kHz, and a ground conductivity of $10^{-3}$ mhos/m. Inspection of Figure 10 shows that the mode structure evolves from the second TE mode

at short distances to the first TE mode at large distances. At intermediate distances (for example, see the 1500 km curve) there is a mixture of the first two modes. A similar evolution with distance from higher to lower modes occurs for the TM fields (not shown in Figure 10). The fact that the first TE mode becomes dominant at 20 kHz, contrasts with the case for 40 kHz, where calculations show that the second TE mode dominates the first out to 10 Mm.

In a recent experiment, RADC launched an ARCAS rocket to over 70 km altitude to record the TE/TM signals from a trailing-wire aircraft flying at an altitude of about 8 km. The rocket was fired at a distance of 1600 km from the transmitter at midday. Figure 11 shows the TE/TM field strengths recorded during that experiment. The TM signal profile was very nearly that expected of the lowest order TM mode. The TE signal profile showed considerably more structure, and, in fact, can be duplicated very closely by assuming that it was made up of the two lowest TE modes, with the second order mode having an amplitude of about 0.8 that of the first order mode. Although the experiment was conducted for an all-sea-water path, the TE amplitude height profile very closely resembles the 1500 km TE profile shown in Figure 10. In other experiments the observed TE structures tended to show various mixing of essentially the two lowest TE modes, whereas the TM structures more closely resembled that expected from a lowest order TM mode.

6. RADC'S PRESENT AND PLANNED TE/TM STUDIES

Present RADC efforts are on studying the effects of PCA events on the ionospheric reflectivity of TE/TM waves, by using VLF/LF pulse ionosounding systems located in northern Greenland. The TE pulses are being radiated from a 3 km-long horizontal antenna, which was configured from an unused powerline on Thule Air Base, Greenland. The TM pulses are being radiated from a 130 meter vertical antenna, also at Thule. The TE/TM ionosounding signals are being received 105 km from Thule, in Qanaq, Greenland, which is located in an almost exactly broadside direction from the TE powerline antenna. The TE/TM ionosounding transmissions consist of a series of extremely short (approximately 100 sec) pulses, precisely controlled in time. At the receiving site, orthogonal loop antennas are used to separate the two polarization components of the ionospherically reflected sky-wave signals. The two systems use different pulse repetition rates, so that the TE/TM reflectivity data can be independently processed and analyzed. A sample of the data being obtained with the TM ionosounding system is shown in Figure 12a. The three-dimensional display shown there consists of data that have been averaged into thirty minute time blocks, and placed one-behind-the-other covering a two week period. Each individual record consists of the received groundwave pulse followed by the ionospherically reflected TM skywave signal. The horizontal scale is linear in time, measured from the start of the groundwave, and the waveforms represent the instantaneous wave amplitude as a function of time. Estimates of effective heights of reflection can be obtained from consideration of the relative times of arrival of the ground-wave and skywave pulses, and the geometry of the experiment. Figure 12a shows data obtained under normal ionospheric conditions in May 1977, when the sun was always above the horizon. The data exhibit a diurnal pattern; at mid-day the effective height of reflection was about 75 km, and at local midnight the effective height was about 85 km. Figure 12b shows data taken in May 1976 during a period in which there was a polar cap absorption event. The effects of the event show up dramatically in the three-dimensional display of the Figure. Within a few minutes of the onset of the event, the effective height of the ionosphere dropped more than 20 km, to below 60 km altitude, and for the next few days the data did not exhibit diurnal features. It took almost a week for the ionosphere to recover to normal conditions, and there was a period during that recovery, starting about three days into the event, in which the skywave pulses were extremely weak. It is important to note that other polar disturbance data, obtained under different solar illumination conditions, displayed strikingly different features, including marked diurnal variations.

Figure 13 is an example of the effects of a PCA on pulses from the RADC TM transmitter and the TE (powerline) transmitter, recorded independently during a period in April 1980 in which a very weak polar cap absorption event occurred. The TM data is similar to that of Figure 12, i.e., it shows received TM groundwave and skywave pulses. The TE data consist essentially only of skywave pulses, since the powerline antenna was almost broadside to the receiving location. The data shown in the Figure is for a PCA that began around local noon on 4 April. At that time the reflection height of the ionosphere dropped from about 85 km to 55 km. Throughout the event the reflection heights for the two polarizations were effectively the same, but the relative amplitude effects on the two polarizations were quite different. In general, the TE amplitudes were much more drastically affected by the event, the amplitudes often being barely discernible. The corresponding TM amplitudes were less than those observed before and after the event, but they were not reduced nearly as much as the TE amplitudes. Other TE/TM ionospheric disturbance data that have been recorded at Thule consistently have shown this trend also. Whether this is due to the particular, near vertical incidence, sounding geometry of the RADC experiments in Greenland, or whether the same relative effects would be seen at more grazing incidence angles, is not know at this time. RADC is planning to conduct other, longer path, TE/TM experiments during PCA's to address such questions.

RADC will be continuing its series of rocket probe experiments to record TE/TM signals from a variety of ground-based and airborne transmitters. These experiments will be similar to the height-gain studies discussed earlier, but the rocket probes (TE/TM receivers) will be launched at Thule Air Base to observe signals that have propagated from mid-latitudes to high-latitudes. Some of these propagation paths will be over poorly conducting earth ($10^{-4}$–$10^{-5}$ mhos/m) so that the relative effects of ground conductivity on the TE/TM waves can be assessed. The rocket probe experiments will be conducted to obtain data under both day and night ambient conditions, and under disturbed (PCA) ionospheric conditions. The data from these studies will be used to determine the feasibility/desirability of extending long wave air-to-air communication links to include mid-to-high latitude paths, as well as present mid-latitude paths. Another important aspect of these studies is to measure the TE fields at high altitude, produced by polarization conversion of the signals from ground-based TM transmitters located at various distances from Thule. This data will be used to assess the degree to which ground-based TM transmitters could produce usable, or interfering, TE signals at aircraft altitudes.

## 7. DISCUSSION

The studies conducted by RADC have shown that Air Force ARC-96 trailing-wire long wave antennas excite TE fields that are often stronger than the conventional TM fields at aircraft altitudes. In addition, the studies have shown that the atmospheric noise background in the TE polarization is significantly less than in the TM polarization, and that under normal ionospheric conditions, TE waves may propagate significantly better than TM waves for paths traversing large areas having very poor surface conductivity. Such paths are often encountered on Air Force mid-to-high latitude communication links. Present air-to-air communication links use the TM polarization only; it is anticipated that if these links exploited the TE polarization as well, greater communication range and reliability could be achieved for the same transmitter power. In order to fully realize these potential improvements some equipment changes, and/or operational procedures may be required. For example, the azimuthal TE pattern of a trailing-wire transmitter is a figure-of-eight, with most of the power going in the two broadside directions. This may require some attention to orientation of flight paths, especially at the longer communication ranges. Also, receiving antennas may require some geometric and/or electric compensation to decouple them from TM atmospheric noise or other interfering signals. Presently, it appears that the limiting factor in fully exploiting the TE/TM polarizations for air-to-air communications, is the on-board, internally generated, noise from the aircrafts' generators. Until this severe problem is overcome, it will not be possible to fully exploit the TE polarization's very low ambient noise characteristic.

The relative extent to which TE/TM communications are degraded under disturbed ionospheric conditions requires further study. The efforts to date indicate that TE waves may suffer more attenuation than TM waves under stressed ionospheric conditions, but since the signal-to-noise ratio, in the presence of possible interfering signals, determines useful communication ranges, all these factors must be taken into account in assessing the relative merits of the two polarizations in operational scenarios. Further studies are required in this regard.

The intent of this paper has been to describe specific RADC involvement in determining the relative characteristics of TE/TM waves excited by airborne transmitters. As such, there has been no attempt to include discussions of very excellent, related, efforts undertaken over the past few years by a number of organizations and individuals outside of RADC. The authors apologize for these necessary omissions.



a. WAVE POLARIZATIONS

b. FAMILIES OF PROPAGATION MODES
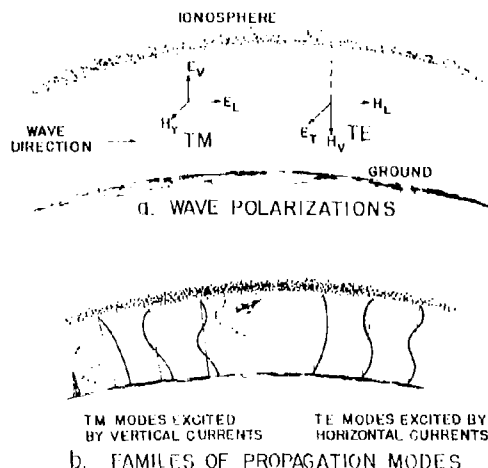
FIGURE 1. Characteristics of TM and TE modes.

a.   b.
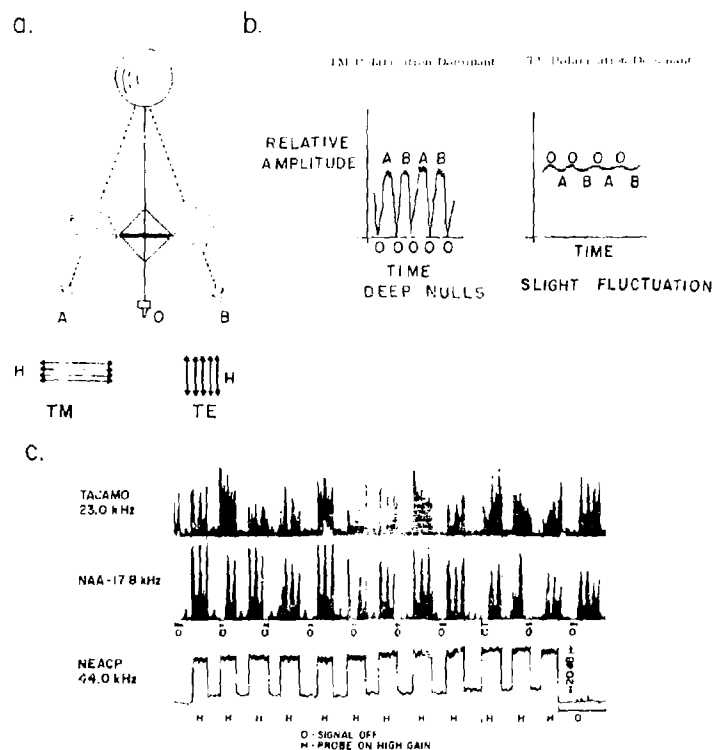


FIGURE 2.   Swinging-loop balloon probe experiment.  (a) the swinging
loop, (b) expected signal variations, (c) experimental data.

b.

a.

c.
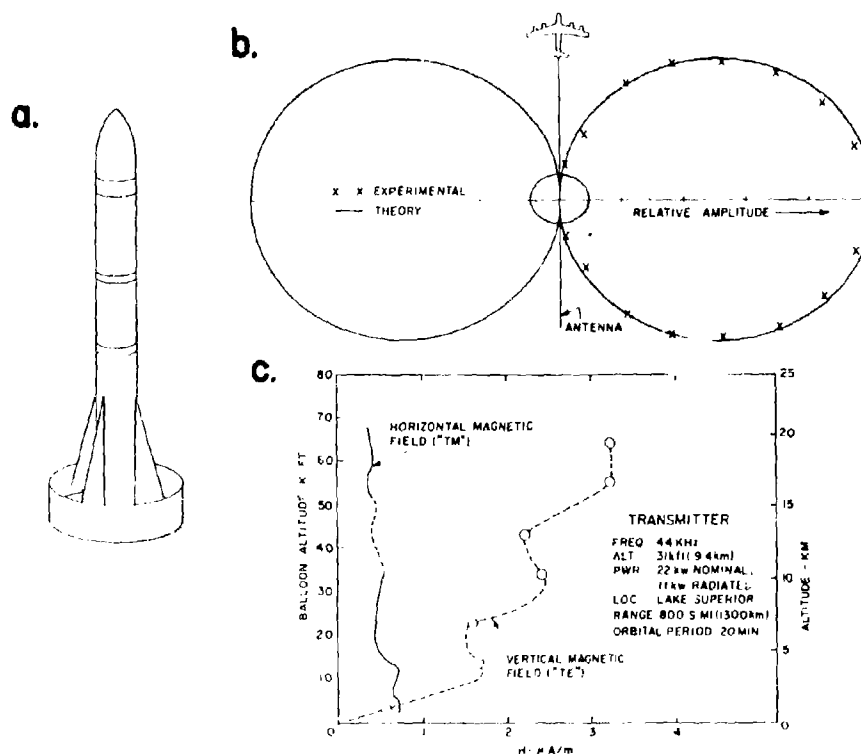


FIGURE 3.   Dart-probe experiment.  (a) the probe, (b) observed TE transmitting antenna
pattern, (c) TE/TM altitude profiles.
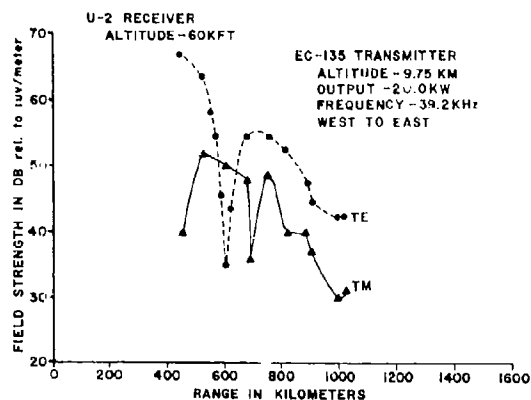
FIGURE 4.  TE/TM signal strengths as a function of distance, U-2 experiment.
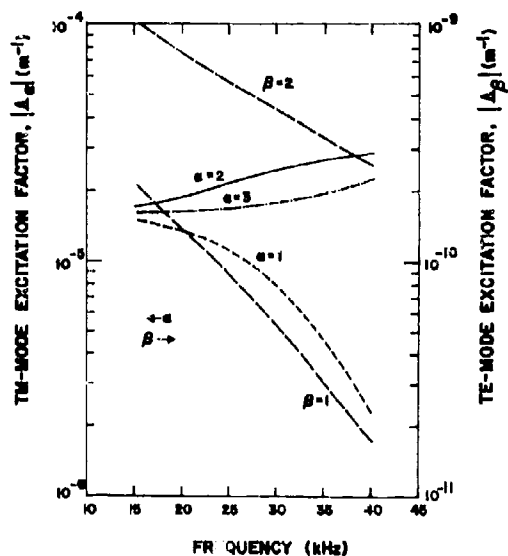


FIGURE 5.  Excitation factor vs. frequency for lowest three TM modes ($\alpha = 1,2,3$) and lowest two TE modes ($\beta = 1,2$): ambient day, $\sigma_g = 10^{-3}$ mhos/m.
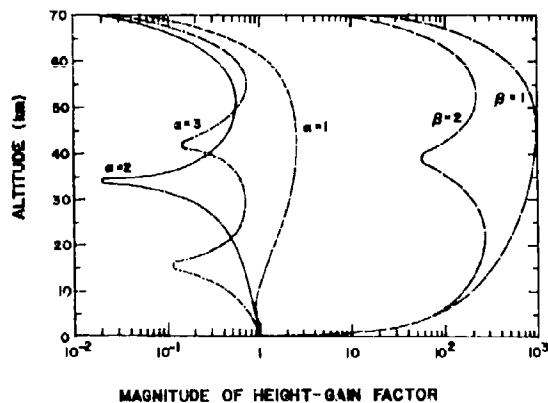


FIGURE 6.  Height-gain factor for lowest three TM modes ($\alpha=1,2,3$) and lowest two TE modes ($\beta=1,2$):  40 kHz, ambient day, $\sigma_g = 10^{-3}$ mhos/m.
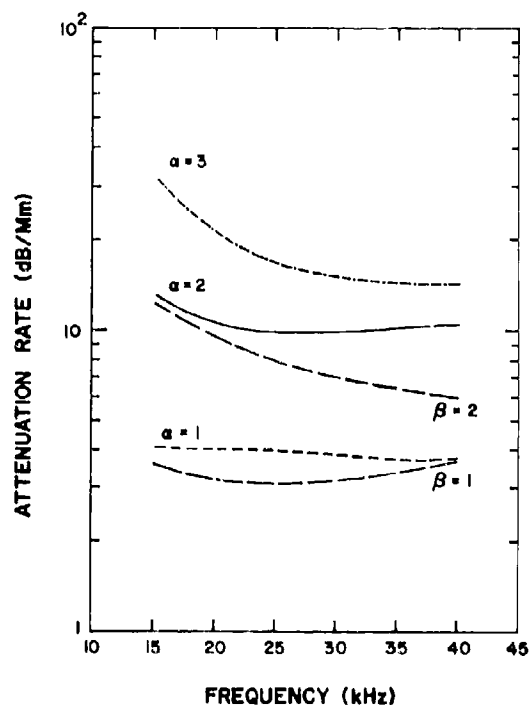


FIGURE 7.  Attenuation rate vs. frequency for lowest three TM modes ($\alpha=1,2,3$) and lowest two TE modes ($\beta=1,2$): ambient day, $\sigma_g = 10^{-3}$ mhos/m.
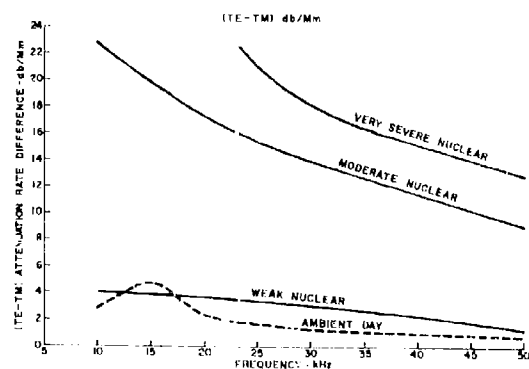


FIGURE 8.  Computed TE/TM relative attenuation rates.
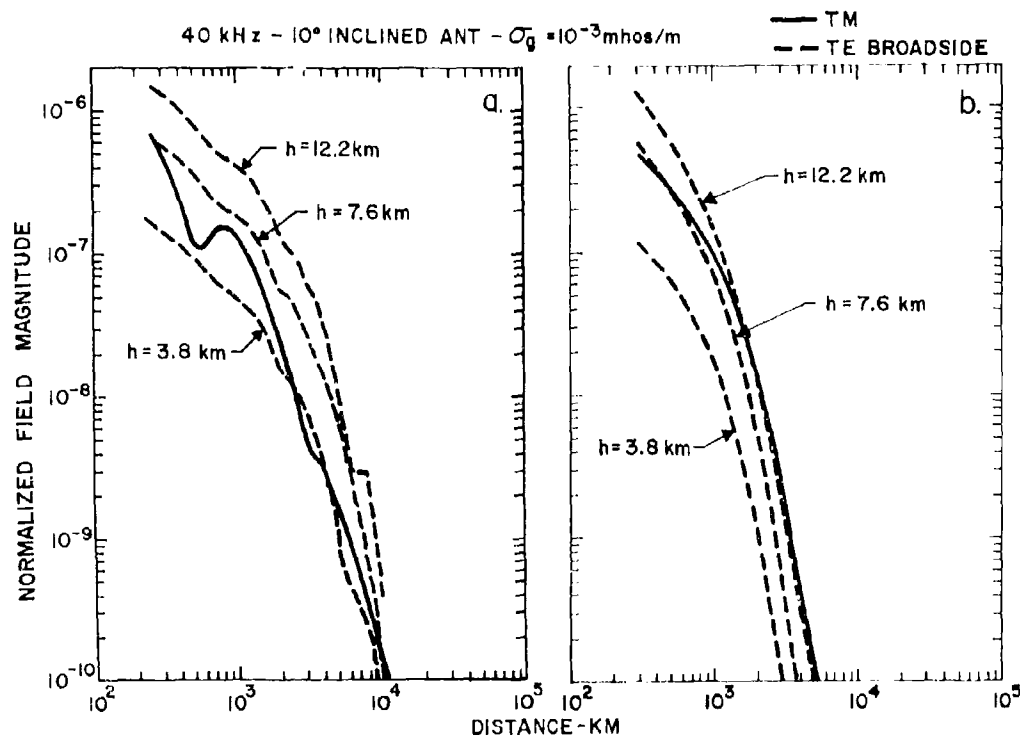
FIGURE 9. Computed TE/TM signal strengths as a function of distance and aircraft altitudes. (a) ambient ionospheric conditions, (b) moderate spread debris nuclear environment.
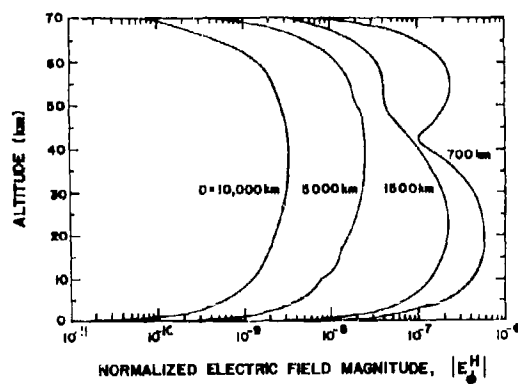


FIGURE 10. Profiles of electric field strength at several distances from an NED transmitter 4.6 km above the ground: 20 kHz, ambient day, $\sigma_g = 10^{-3}$ mhos/m.
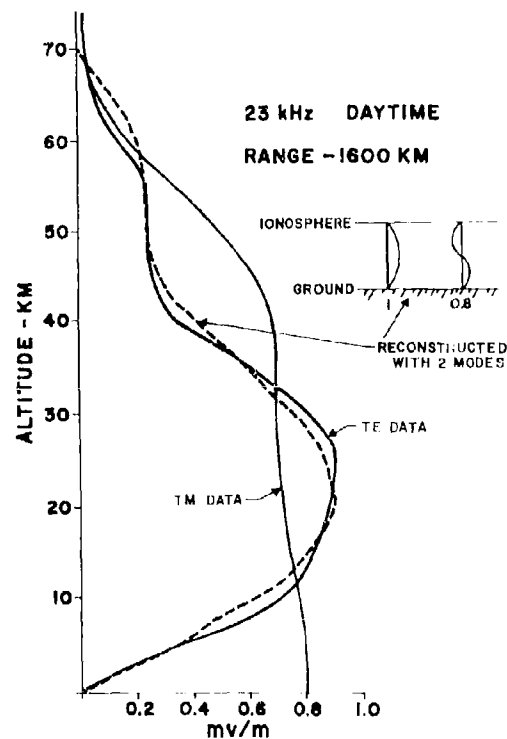
FIGURE 11. Rocket-probe TE/TM height gain profiles.

RECEIVED PARALLEL WAVEFORM DATA

A  DISTURBED CONDITIONS
MAY 1976

B  NORMAL CONDITIONS
MAY 1977

C  SOLAR ZENITH ANGLE
( MAY 76  (DOY 122)

TIME  μ SECONDS

TIME  μ SECONDS
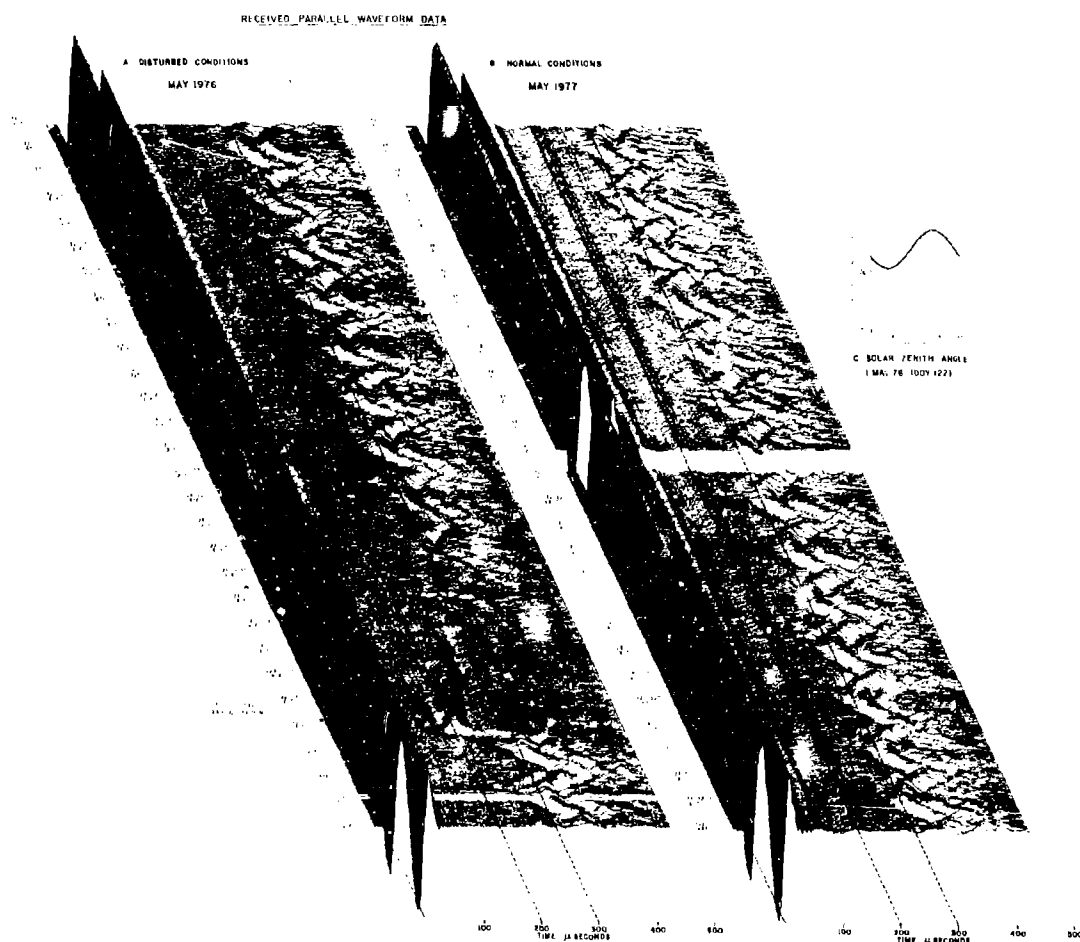
FIGURE 12.  TM pulse ionosounding data obtained over a 105 km path in northern Greenland.
(a) May, ambient conditions, (b) PCA disturbed.

PCA EFFECTS ON TM REFLECTIVITY

PCA EFFECTS ON TE REFLECTIVITY

REFLECTION HEIGHT (KM)

REFLECTION HEIGHT (KM)
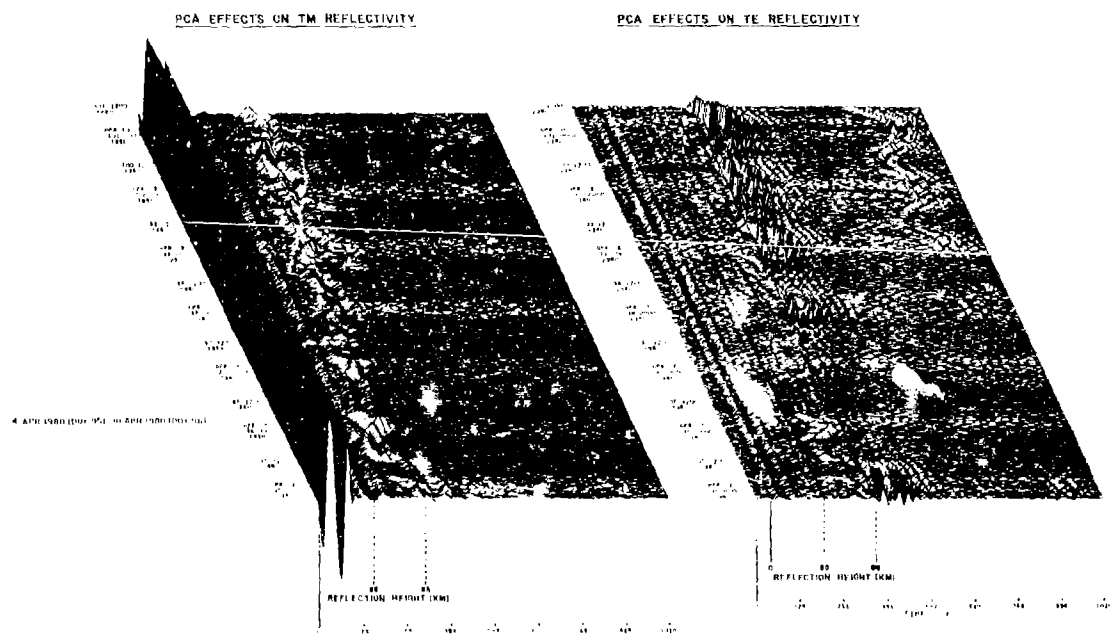
FIGURE 13.  PCA effects on TE/TM reflectivity observed on a 105 km path in northern Greenland.

# PHASE AND AMPLITUDE PERTURBATIONS ON VLF SIGNALS RECEIVED IN THE SEA

C J RIGDEN
COMMUNICATION DIVISION
Admiralty Surface Weapons Establishment
Portsdown
Portsmouth, Hants
England

## SUMMARY

This paper presents the results of an experimental investigation into the stability of VLF signals from the GBR (16 kHz) transmitter when received in the sea. The results of the investigation show the effect of a rough sea surface on these signals. The measured phase and amplitude perturbations on the signals are very small when received above the sea surface or in the sea under calm conditions, but as the sea surface roughness increases so the perturbations on the signals received in the sea increase significantly. The results obtained can be explained by a simple model which takes into account the variations in sea path length for the VLF signals, caused by sea surface waves passing over the receiving aerial.

## 1. INTRODUCTION

It is well known that radio waves in the VLF and lower LF bands (3-150 kHz) propagate to a certain extent into the sea. However, as the VLF/LF signals pass through the air/sea interface and propagate into the sea, they are subject to phase and amplitude perturbations. These perturbations may well be significant, and have to be considered in future developments exploiting VLF/LF for under sea communications or navigation.

Theoretical models have been proposed to describe the magnitude of the signal perturbations in different sea states. There has, however, been little direct experimental measurement of these perturbations, although extensive experience with present VLF/LF systems has not indicated that any anomalous effects exist.

As part of the D/ASWE communications research programme, measurements have been made of the magnitude of phase and amplitude perturbation on the 16 kHz transmission from the GBR transmitter at Rugby, England, when received on a submerged aerial on a submarine. These measurements are compared with similar measurements made above the sea surface. The trials were carried out in early 1978, and the results are presented in this paper.

## 2. PROPAGATION OF VLF SIGNALS IN THE SEA

Above the sea surface, VLF radio waves propagate horizontally with a nearly vertical E field, and a horizontal H field which is perpendicular to the direction of propagation. At a frequency of 16 kHz, the wavelength in free space is 18.75 km.

The relative permeability of the sea is the same as for air, and so the H field of the propagating wave is continuous through the air-sea interface. However, the conductivity of the sea is not zero, and the relative permittivity is much greater than unity. By using Maxwells equations, as in Figure 1, it can be shown that a VLF signal at 16 kHz in sea water, with a conductivity of 4 siemens and relative permittivity of 81, has a wavelength of 12.5 metres, and as the wave propagates through the water it is attenuated by 4.3 dB per metre of pathlength. Hence a model for propagation of VLF signals into the sea is derived in Figure 2, which shows that the resultant radio wave in the sea propagates downwards almost perpendicular to the sea surface, with a horizontal E field in space quadrature with the horizontal H field.

In practice, this means that the VLF signal levels at the terminals of a small receiving loop aerial just above and just below the sea surface will be the same. As the aerial is moved vertically down into the sea, the signal amplitude will be decreased by 4.3 dB, and the phase retarded by 0.5 radians, for every metre of sea path, when compared with the signal at the sea surface.

Conversely, if the aerial is at a fixed vertical position in the sea, and the air-sea interface is perturbed by sea surface waves, the vertical sea path between the sea surface and the aerial will vary as sea waves pass over the aerial. It is to be expected that this path length variation will cause phase and amplitude variation in the received signal. Since it is possible for sea surface waves to have peak to trough heights of several metres, the perturbations on the VLF signals may be significant.

In the design of VLF communication and navigation systems with underwater reception, it is important to know not only the maximum variations in signal strength and phase, but also the rates of change of these parameters. These rates will depend on the period and height of the sea surface waves above the aerial, and are difficult to predict in detail. Hence a field trial was organised for early 1978 to make direct measurements on the 16 kHz component of the Rugby transmissions received in the sea. From these measurements statistics on the phase and amplitude perturbations were obtained, as described below.

## 3. METHOD OF MAKING MEASUREMENTS

To make the required measurements a special receiver was designed and built in ASWE to monitor the VLF transmission from Rugby. Basically the receiver system, with subsequent calibration and analysis, is capable of making simultaneous measurements of the amplitude and phase of a received signal at 16 kHz. In the submarine installation the VLF signals were received on a crossed loop aerial system and fed through a linear amplifier to the ASWE receiver.

For the amplitude measurements, the incoming VLF signals were filtered in the receiver to enhance the Rugby 16 kHz signal relative to other VLF signals, and the radio signal was recorded directly onto one channel of a 4-channel tape recorder. On return to the laboratory, the recordings were fed into a detector which gave an output voltage level directly proportional to the recorded 16 kHz signal strength, and the whole system was calibrated using a front end attenuator.

The phase measurements were made by comparing the incoming 16 kHz signal with a very stable locally generated 16 kHz reference. An output voltage level from this comparison was a direct measure of the relative phase of the incoming signals and the 16 kHz reference. This output voltage was passed through a low pass filter with 100 Hz cut-off. Simultaneous quadrature (sine and cosine) phase comparisons were made, and recorded on two FM channels of the tape recorder so that unambiguous values of phase change could be calculated in the subsequent analysis. During the trials Rugby was keyed in the normal F1 mode ie 2 tone FSK with tones at 16 kHz and 15.95 kHz. The output voltage from the phase comparator was thus constant, or only slowly varying, when the 16 kHz component of the Rugby signal was present, and was a 50 Hz sine wave when the 15.95 kHz component was received. The 50 Hz component was removed during the subsequent computer analysis.

In the receiver design, care was taken to ensure that the measured phase variations were not caused by amplitude variations in the incoming signal, and calibration checks showed that signal phase could be measured independent of signal amplitude over an input signal range of 35 dBs. This dynamic range was found to be sufficient for all variations experienced in a given location and mean aerial depth. However, prior to making measurements at a given location and aerial depth, a front end signal attenuator was adjusted to ensure that the signal levels were within the desired working range of the ASWE receiver.

The tape recordings of signal amplitude and phase were made, as described above, for periods of 15 minutes in various sea states. On return to ASWE the recordings were fed through a specially designed interface to a computer for analysis.

## 4.    RESULTS AND ANALYSIS

### 4.1    Phase Measurements

Examples of the output from the phase comparator portion of the ASWE receiver are shown in Figures 3 to 7. The examples shown are from measurements made under the following conditions:

(a)   Above the sea surface in the submarine  - Figure 3

(b)   In the sea – Sea State 1              - Figure 4

(c)   In the sea – Sea State 3              - Figure 5

(d)   In the sea – Sea State 4/5            - Figure 6

(e)   In the sea – Sea State 5/6            - Figure 7

Each figure shows the output from the sine and cosine channels with the 50 Hz component removed by computer analysis.

When receiving the signal above the sea surface on the submarine, (Figure 3), there are small short term fluctuations at the signal phase.

There is also, however, a slow variation of approximately $10^{-3}$ Hz superimposed on the output. This is attributed to the difference in absolute frequency of the standard at the Rugby transmitter and the local reference (approximately 1 part in $10^7$). The frequency of the slow variation is two orders of magnitude less than the perturbation effects being studied, and was removed by computer calculation prior to the analysis of the results.

Inspection of the results shown in Figures 1 to 7 shows that passage of VLF signals through the air–sea interface for reception in the sea does introduce phase perturbation on the signals. As the sea becomes rougher so these effects become more pronounced.

### 4.2    Analysis of Phase Measurements

Both the maximum phase change and the rate of phase change of the signal perturbations are important parameters. To display both parameters simultaneously in graphical form, analysis was carried out to provide statistics on the magnitude of phase changes in given time intervals. The phase changes over a given time period were measured and for a given sea state, plots were made of the cumulative probability distribution of these phase changes for each of the sample intervals. It was found that these distributions can be described, to a good approximation, by Gaussian probability distribution functions. As an example of this, Figure 8 shows the cumulative probability distributions of phase changes over sample intervals from 1 to 8 seconds in Sea State 5/6. Superimposed on each diagram is the Gaussian distribution curve taking a standard deviation value in each case which gives the best fit. In many cases the two curves are indistinguishable.

Using the Gaussian statistics model, the measurements in all sea states and above the sea are summarised in Figure 9, which shows the standard deviations for phase changes plotted against sample intervals for sample intervals from 1 to 60 seconds.

From this figure, it is seen that when the 16 kHz transmission from Rugby is received above     the phase perturbations are very small. The standard deviation is less than $4^0$ for any sample interval.

Once reception takes place under the sea surface more pronounced perturbations are observed on the signals. The perturbations increase significantly with increasing sea state. For example, for Sea States 5/6 the standard deviation for perturbations over, say a 35 second sample interval approaches 40°.

An interesting feature of the results in Figure 9, is that for a given sea state the observed standard deviation of phase changes have minimum values at certain sample intervals. For example in the Sea State 5/6 these minima occur at multiples of 10 seconds, whilst for Sea State 4/5 they occur at multiples of 8 seconds, and for Sea States 2 and 3 at multiples of 4-5 seconds.

These minima are attributed to the natural period of the sea waves for the given sea states. The minimum in phase change can be expected when samples are taken at multiples of a wave period of the sea surface waves. It is interesting that these effects are so pronounced and are correlated over several wave periods.

### 4.3    Amplitude Measurements

As described above, recordings of amplitude fluctuations were made simultaneously with the phase measurements. Figure 10 shows, as an example, the amplitude variations in the received signal level, observed over a 10 minute period for reception in the sea in the Sea State 5/6 conditions.

Similar amplitude recordings were made for all different sea state conditions. For signals received above the sea surface the amplitude variations were within $\pm 1$ dB, and, in a manner similar to the phase perturbation effects, when signals were received in the sea, the amplitude fluctuations increased in magnitude with increasing sea surface roughness.

### 4.4    Analysis of Amplitude Measurements

To analyse the amplitude perturbations, rather than repeat all the analysis as carried out for the phase perturbations, it was decided to see whether there was any correlation between the amplitude and phase perturbations.

This was done by producing scatter diagrams of the values of amplitude changes against the simultaneous values of phase changes over given sample intervals. The resultant scatter diagrams for Sea State 5/6 conditions are shown in Figure 11.

The solid line drawn in each figure represents the slope of 4.3 dBs per 0.5 radians (ie the expected amplitude and phase changes at 16 kHz for 1 metre of sea path). The correlation coefficients range from 0.77 for 1 second sample intervals to 0.97 for the 4 second case.

In view of the high degree of correlation between the amplitude and phase perturbations it is inferred that the amplitude perturbations can be described by similar statistics to those which describe the phase perturbations.

Also this high degree of correlation, with approximate slope of 4.3 dBs per 0.5 radians, is taken as substantiation of the simple concept that the phase and amplitude perturbations superimposed in VLF signals received in the sea, are caused by the variations in signal path length in the sea, as sea surface waves pass over the receiving aerial.

### 5.    CONCLUSIONS

A series of sea trials has been carried out to investigate whether perturbations are superimposed on VLF signals as they pass through the air-sea interface to be received on submerged aerials.

It was found that significant phase and amplitude perturbations are indeed impressed on the 16 kHz transmission from the Rugby transmitter when received in the sea. The magnitude of the perturbations increases with increasing sea surface roughness.

The perturbations are attributed to the varying distance traversed by the radio signals in the sea, as the sea surface waves pass over the aerial.

There is a high degree of correlation between the amplitude and phase perturbations. The expected relationship of 4.3 dB amplitude change for 0.5 radians phase change for 16 kHz radio waves is well substantiated.

The phase and amplitude perturbations on VLF signals due to the sea surface roughness can be described, to a good approximation, by Gaussian probability distribution functions.

There is some correlation between the magnitude of the signal perturbations over given time intervals and the sea wave period. The standard deviations of the perturbations are markedly less for intervals between samples which are multiples of the sea wave period.

MAXWELLS EQUATIONS PREDICT EM WAVE PROPAGATION
OF THE FORM

$$Hz = H_o \epsilon^{(jwt - \Psi x)} \qquad \text{IN THE x DIRECTION}$$

WHERE $\Psi = \mu\mu_o jw(\epsilon\epsilon_o jw + \sigma)$

---

IN THE SEA, AT LOW FREQUENCIES $\sigma >> /w\epsilon/$

AND SO $\Psi \rightarrow \alpha + j\alpha$ $\qquad$ WHERE $\alpha = \sqrt{\dfrac{w\mu\mu_o\sigma}{2}}$

HENCE WAVE EQUATION SOLUTION FOR IN THE SEA
PROPAGATION IS

$$Hz = H_o \epsilon^{jwt} \underbrace{\epsilon^{-\alpha x}}_{\text{ATTENUATION}} \underbrace{\epsilon^{-j\alpha x}}_{\text{PHASE}}$$

---

AT 16 kHz

$\alpha = 0.5$ $\qquad$ (ASSUMING $\sigma = 4$ SIEMENS)

.. ATTENUATION $= 0.5$ NEPERS/M $= 4.3$ dB/M

AND PHASE VARIATION $\qquad = 0.5$ RADIANS/M

(WAVE LENGTH $\qquad = 12.5$ M)

FIGURE 1 — EM WAVE PROPAGATION IN THE SEA
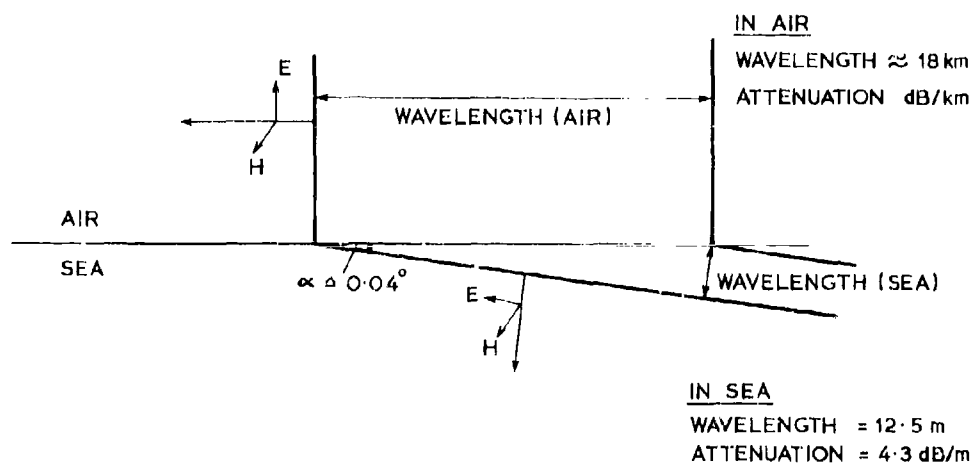


FIGURE 2 — PROPAGATION OF 16 kHz VLF SIGNALS INTO THE SEA
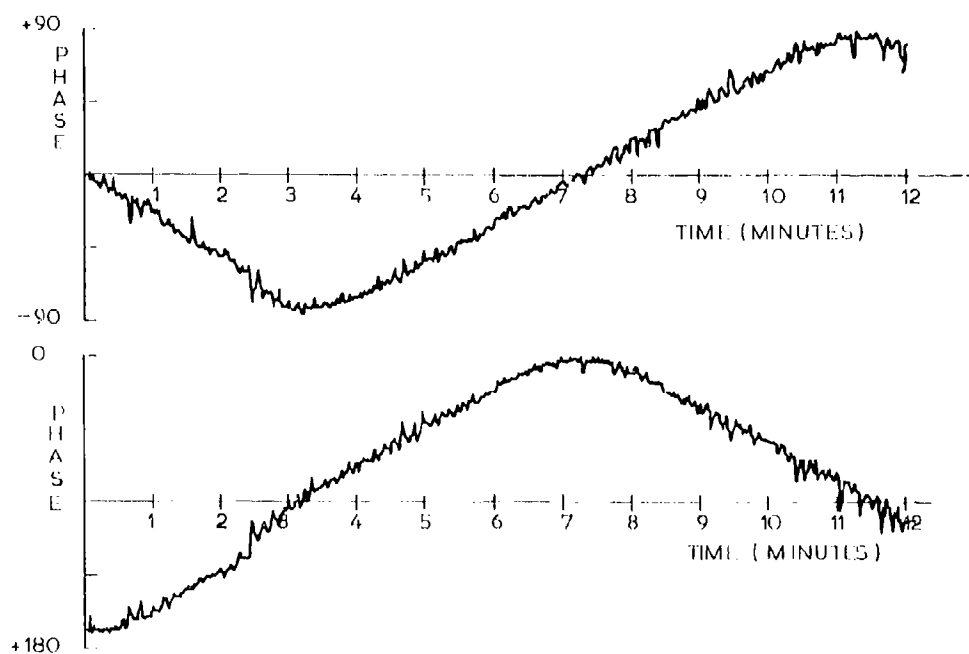
FIGURE 3 — PHASE VARIATIONS ON 16 kHz SIGNAL ABOVE SEA SURFACE
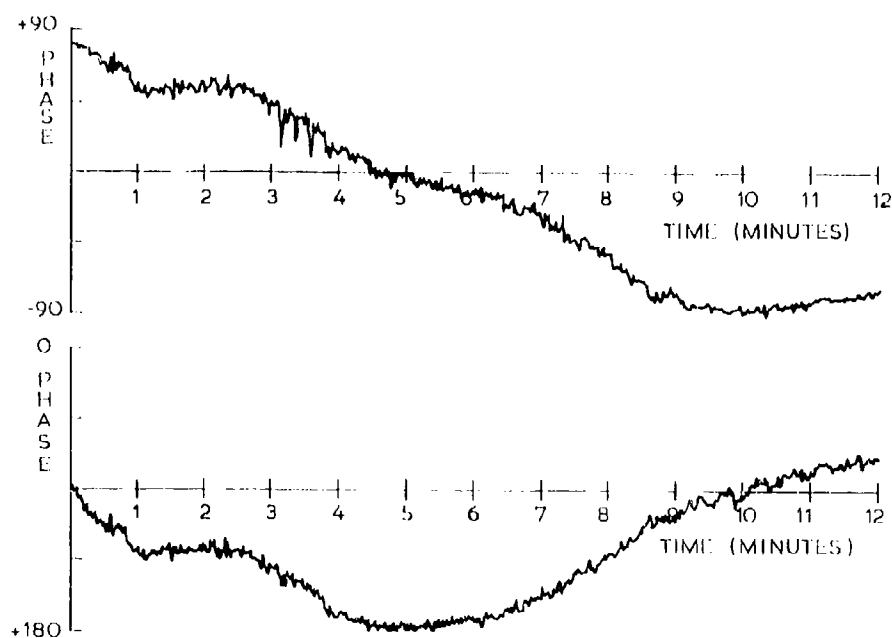


FIGURE 4 — PHASE VARIATIONS ON 16 kHz SIGNAL IN SEA — SEA STATE 1
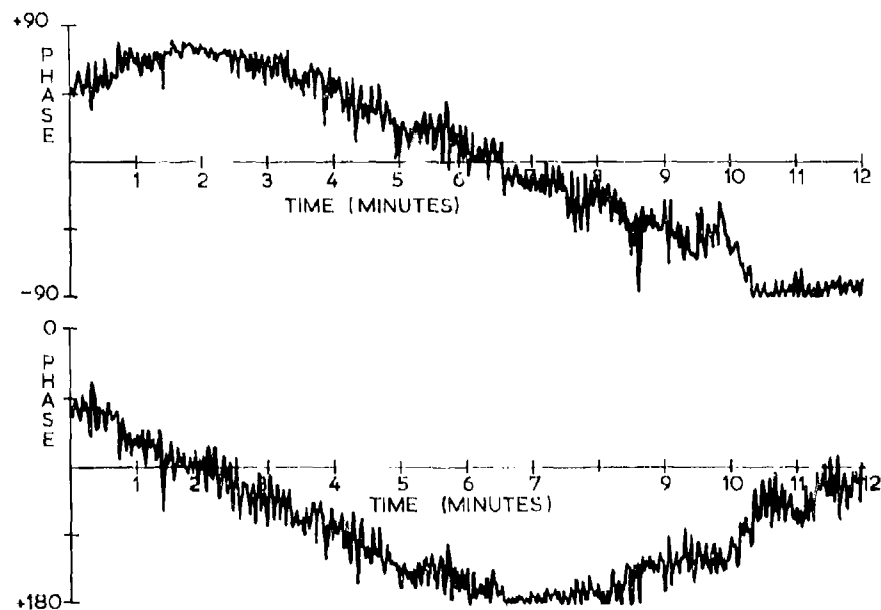
FIGURE 5 — PHASE VARIATIONS ON 16 kHz SIGNAL IN SEA — SEA STATE 3
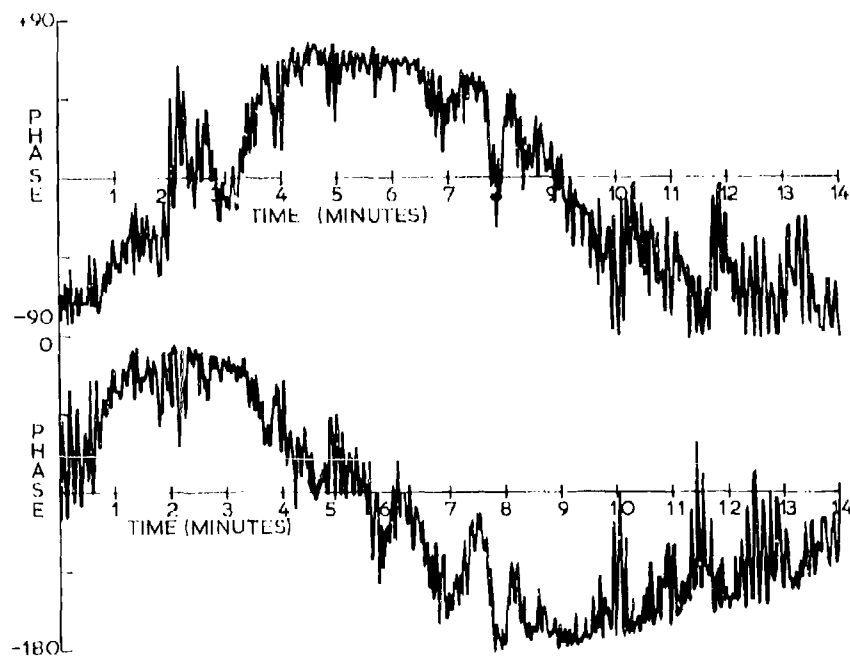


FIGURE 6 — PHASE VARIATIONS ON 16 kHz SIGNAL IN SEA — SEA STATE 4/5
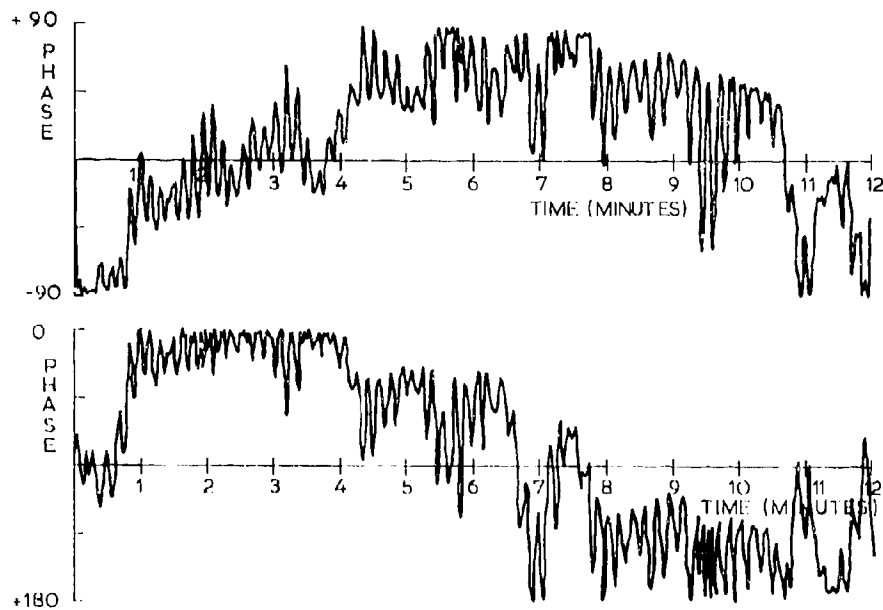
FIGURE 7 — PHASE VARIATIONS ON 16 kHz SIGNAL IN SEA — SEA STATE 5/6

SEA STATE = 5 /6
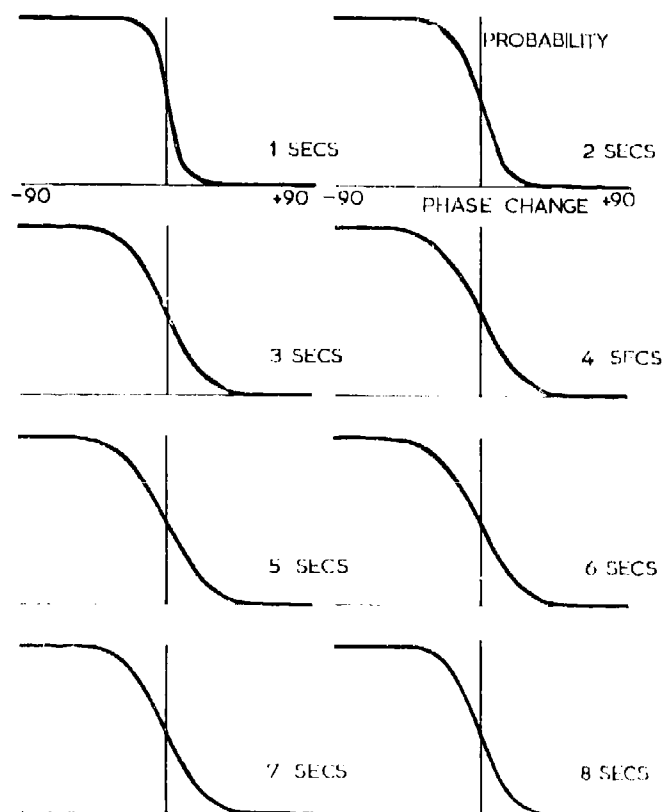


FIGURE 8 — CPDF OF PHASE CHANGES OVER GIVEN SAMPLE INTERVALS
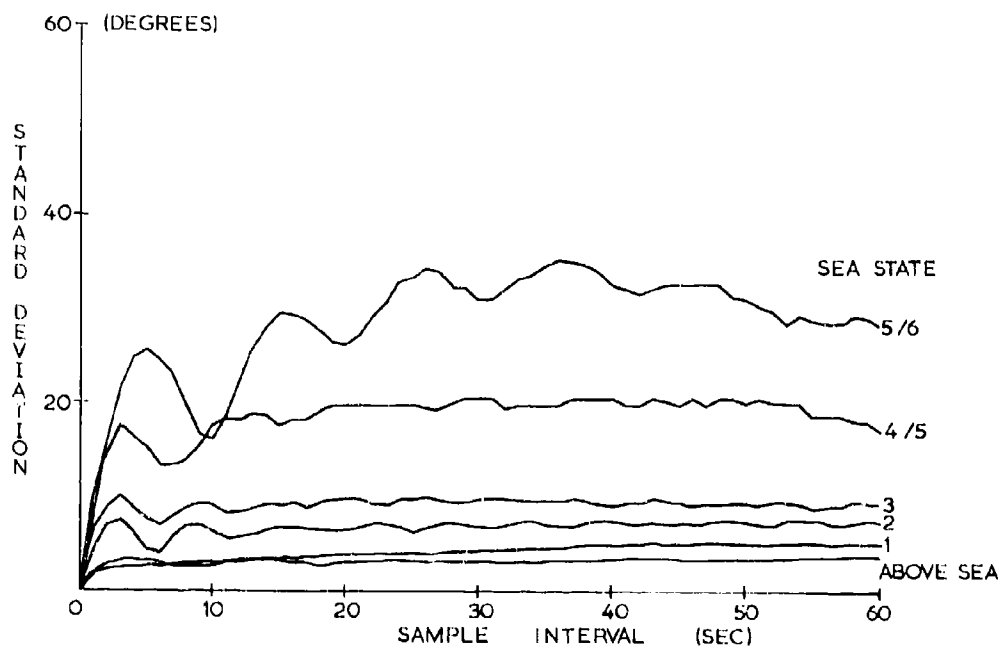
FIGURE 9 — STANDARD DEVIATION OF PHASE PERTURBATIONS FOR GIVEN SAMPLE INTERVALS
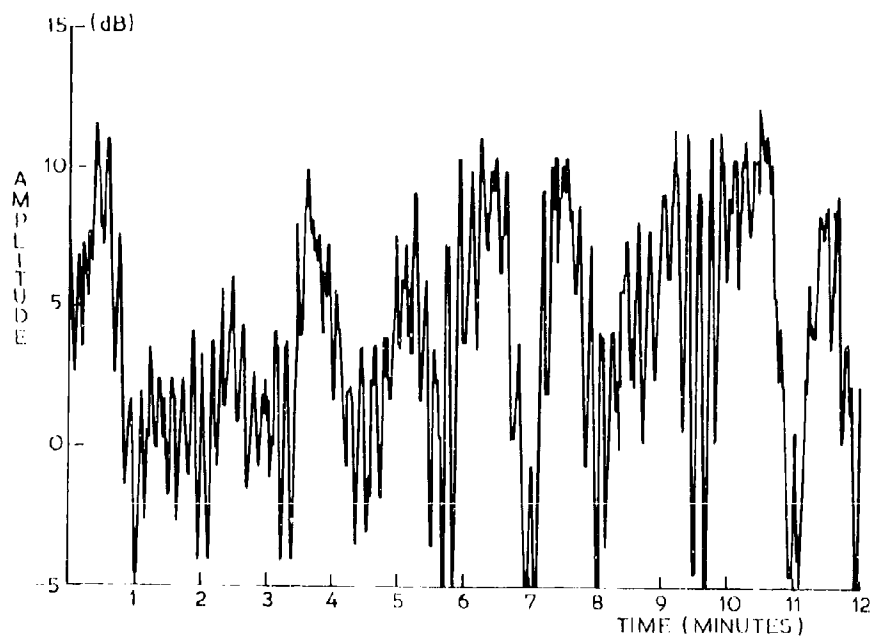


FIGURE 10 — AMPLITUDE VARIATIONS ON 16 kHz SIGNAL IN SEA — SEA STATE 5/6
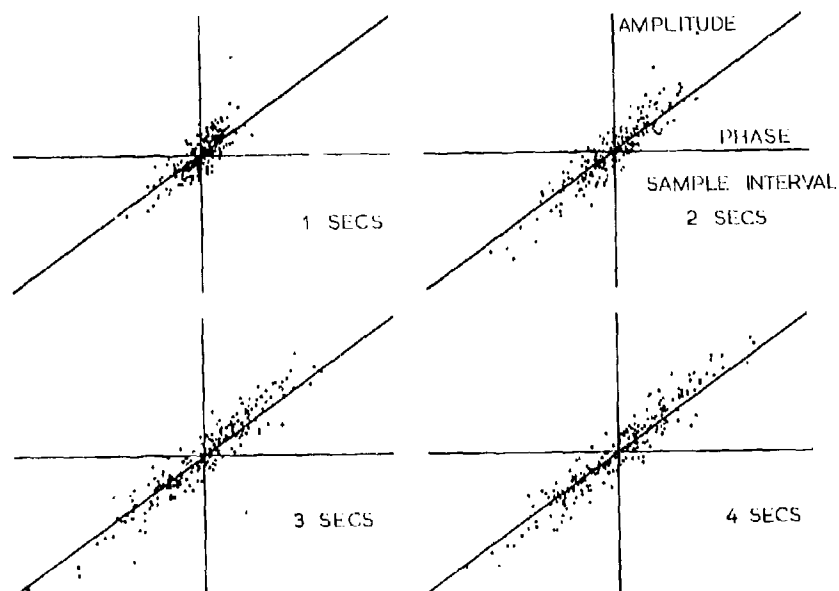
FIGURE 11 — CORRELATION BETWEEN PHASE AND AMPLITUDE VARIATIONS ON 16 kHz
SIGNALS IN SEA — SEA STATE 5/6

# ATMOSPHERIC VLF RADIO NOISE AT ELEVATED RECEIVERS:
## HORIZONTAL AND VERTICAL POLARIZATION

by

F.J.Kelly
E.O.Hulburt Center for Space Research
Ionospheric Effects Branch
Space Science Division
Naval Research Laboratory
Washington, D.C. 20375, US

and

J.P.Hauser and F.J.Rhoads
Information Technology Division
Naval Research Laboratory
Washington, D.C. 20375, US

## INTRODUCTION

The communication effectiveness of any radio circuit or link strongly depends on the signal-to-noise ratio in the receiver. At very low frequencies the propagated radio noise generated by lightning discharges, referred to as atmospheric radio noise, is frequently the dominant system noise.

Many workers have studied atmospheric radio noise [1-7]. In particular, Ref. 3 decribes a computer model which predicts the atmospheric radio noise generated by thunderstorms in all regions of the world and then calculates the propagation of the noise to a receiver at any point on the earth's surface. By performing this computation over a grid of receiver locations, a map of the intensity of atmospheric radio noise can be generated [8] similar to those given in Ref. 1. However, as with most work in this field, only the vertical electric component of the noise is calculated.

In recent years interest has grown in the use of horizontal electric polarized waves for high-altitude air-to-air communication. This polarization should be advantageous, because it is operationally easier for a high-speed high-altitude jet aircraft to trail a horizontal long wire antenna, which preferentially excites transverse electric radio waves and because the vertically polarized lightning strokes are thought to be less effective in generating horizontally polarized noises. Therefore, a requirement exists to be able to accurately predict these noise levels.

The theoretical and experimental effects associated with horizontally polarized VLF-wave transmission and reception have been treated by several authors [9-13]. Also, the use of airborne, horizontally polarized transmitting and receiving antennas for communications at VLF has been discussed several times [14-17]. The WAVEGUID computer program [11] contains the algorithms necessary to compute all the electric and magnetic components of a propagating electromagnetic wave in a given waveguide mode at any height above the ground, if the vertical electric component of the wave at the ground is known. The COMPWR and NOISLAN programs produced by the Westinghouse Georesearch Laboratory (WGL) [3] calculate the amplitudes of the vertical electric VLF noise in the three dominant quasi-transverse-magnetic (quasi-TM) waveguide modes from each equivalent atmospheric noise source. By combining these programs, NRL has now developed a working computer-program model for predicting the horizontally and vertically polarized atmospheric noise at any location, season, time of day, and altitude. This noise program should assist in the prediction of system performance.

## THE PROGRAMS THAT FORM THE NOISE-PREDICTING MODEL

References 3 and 11 give complete descriptions of the COMPWR, NOISLAN, and WAVEGUID programs. The following subsections briefly describe the features of each program essential to the new program.

## Description of COMPWR and NOISLAN

The atmospheric-noise model is built on thunderstorm-day data, from which vertical electrical noise intensity is derived. The thunderstorm-day is a weather statistic which gives over a 30-day interval the number of days during which at least one thunderstorm occurred in the vicinity of the observation site. The data base used by the program represents observations collected over several decades and at thousands of locations. In addition the model uses data on the diurnal variation and variability of thunderstorm occurrences. Algorithms convert thunderstorm days into the number and type of lightning discharges per unit area on the earth's surface. Also, the current moments, waveforms, and power spectral densities of the pulses are calculated. The resultant source powers are combined into equivalent noise "transmitters" representing 5° by 5° areas of the earth's surface. These 5° by 5° areas are further combined into 15° by 15° areas. The program decides, based on the proximity and power of the equivalent noise transmitters, whether to use 5° by 5° or 15° by 15° areas in the final computations.

After COMPWR establishes the location, power, and standard deviation of the power for each equivalent noise transmitter, the NOISLAN program then computes the resulant vertical electric field at the specified receiver location using the propagation equation

$$E_{n,z}^{(i)}(0) = K \sqrt{\frac{P_r^{(i)} \mid \Lambda_{n,t}^{(i)} \mid \mid \Lambda_{n,r} \mid}{f h_i^{(i)} h_r a \, \sin(d^{(i)}/a)}} \; 10^{-\alpha_n^{(i)} d^{(i)}/2 \times 10^{\circ}}. \tag{1}$$

where

$E_{n,z}^{(i)}(0)$     is the vertical electric component of the atmospheric noise contribution of the $i$th noise source in the $n$th waveguide mode at the surface of the waveguide, in volts per meter,

$K$     is a normalizing constant equal to $1.58 \times 10^6$,

$P_r^{(i)}$     is the vertical effective radiated power (VERP) of the $i$th equivalent noise transmitter in watts,

$\Lambda_{n,t}^{(i)}$     is the excitation factor of the $n$th waveguide mode at the $i$th transmitter locations,

$\Lambda_n$     is the excitation factor of the $n$th waveguide mode at the receiver location,

$f$     is the frequency in hertz,

$h_t^{(i)}$ and $h_r$ are the effective ionospheric heights in meters at the $i$th transmitter and at the receiver respectively,

$a$     is the earth's radius in meters,

$d^{(i)}$     is the path length from the $i$th transmitter to the receiver in meters,

and

$\alpha_n^{(i)}$     is the effective attenuation rate in decibels per megameter (1000 km) for the $n$th mode from the $i$th transmitter.

The effective attenuation rate $\alpha_n^{(i)}$ is computed from the combination of several attenuation terms as follows:

$$\alpha_n^{(i)} = M^{(i)} \left[ \alpha_{o,n} + \left(d^{(i)}\right)^{-1} \sum_{l=1}^{L} \Delta \alpha_{I,l,n}^{(i)} \, \Delta d_l \right] + \left(d^{(i)}\right)^{-1} \sum_{k=1}^{K} \Delta \alpha_{G,k,n}^{(i)} \, \Delta d_k. \tag{2}$$

In Eq. (2), $M^{(i)}$ is a directional factor and is given by

$$M^{(i)} = 1 - k \sin \phi_o^{(i)}. \tag{3}$$

where $\phi_o^{(i)}$ is the direction of propagation of the wave from the $i$th transmitter with respect to geographic north and $k$ is given by

$$k = (10^4/f)^i \, K_{10\text{kHz}} \, e^{-B|\theta-90|}. \tag{4}$$

in which

$\theta$          is the colatitude of the receiver in degrees,

$f$          is the frequency in hertz,

$K_{10kHz}$     is a constant that for west-to-east propagation equals 0.68 during the day and 0.70 at night and for east-to-west propagation equals 1.10 during the day and 2.00 at night,

and

$\beta$          is a constant that equals 0.04 during the day and 0.03 at night.

Also in Eq. (2), $\alpha_{a,n}$ is the attenuation rate (day or night) of the $n$th-order mode over seawater for the isotropic case, $\Delta\alpha_{I,I,n}^{(i)}$ is the differential ionospheric attenuation rate in effect for the incremental distance $\Delta d_l$ along the path, $\Delta\alpha_{G,k,n}^{(i)}$ is the differential ground attenuation rate due to ground conductivities other than seawater, and $\Delta d_k$ is the distance segment of the propagation path within a given conductivity area. The differential ionospheric attenuation term is obtained from

$$\Delta\alpha_{I,I,n}^{(i)} = f [2A \cos^2\theta_l + B(\sin |\chi_l|) \sin^2\theta_l]. \tag{5}$$

where

$\theta_l$       is the colatitude of the $k$h segment of the propagation path in degrees,

$\chi_l$       is the solar zenith angle of the $k$h segment of the propagation path,

$A$       equals $2.2 \times 10^{-5}$ dB/Mm-Hz,

and

$B$       equals $2.8 \times 10^{-5}$ dB/Mm-Hz.

The values in Eq. (2) for $\Delta\alpha_{G,k,n}^{(i)}$ are the differences between the attenuation rate of seawater for the isotropic case $\alpha_{a,n}$ and the attenuation rates for the lower ground conductivities as stated in the equation

$$\Delta\alpha_{G,k,n}^{(i)} = \alpha_{G,k,n}^{(i)} - \alpha_{a,n}.$$

where values of $\alpha_{G,k,n}^{(i)}$ and $\alpha_{a,n}$ are those given by Wait and Spies [18] for $h = 70$ km and $\beta = 0.3$ km$^{-1}$ for day and $h = 90$ km and $\beta = 0.5$ km$^{-1}$ for night with $\Omega = 0$ (with their parameter $\beta$ *not* being the same as the parameter $\beta$ in Eq. (4)). However, Ref. 18 is incomplete, because no theoretical data were obtained for some of the lower values of ground conductivity for the second-order and third-order modes. When the theoretical data were not available, the authors of the NOISLAN program appear to have extrapolated data according to an unspecified procedure. The values of $\Delta d_k$ are computed from a digitized version [3, pp. 4-19] of a map of VLF ground conductivity developed for NRL by Morgan [19].

The field-strength contributions from each transmitter and each mode are then summed in an RMS manner, thus giving the vertical electric field strength $E_z(0)$ of the noise at the ground for a specific hour of the day, month, location, and frequency:

$$E_z(0) = \left[ \sum_{n=1}^{3} \sum_{i=1}^{N} (F_{n,z}^{(i)})^2 \right]^{1/2}. \tag{6}$$

NOISLAN also computes the standard deviation of the noise $\sigma_n$ and the voltage deviation $V_d$. However, a discussion of these two parameters is not pertinent to this report.

Additi    Options for COMPWR and NOISLAN

Two options have been added to the WGL model. The first involves a change in the part of the WGL model contained in program COMPWR. The original version of COMPWR has been designated

as option 1 of the COMPWR program, and the modification to be described has been designated as option II. COMPWR computes the average vertical effective radiated power (VERP) and the standard deviation of the VERP for each equivalent noise transmitter for each month of the year. COMPWR then multiplies the average VERP by a diurnal modifier to give the VERP for each hour of the day. Option II involves changes to the diurnal modifiers as well as inclusion of an additional set of modifiers to adjust the average VERP. These changes were developed empirically [20,21].

Another option has been added in the form of a modification to the NOISLAN program. The original version of NOISLAN has been designated as option I, and the new modification has been designated as option II. The modification involves the terms $\Lambda_{n}$, and $\Lambda_{n}^{(1)}$ from Eq. (1) and $\alpha_{a,n}$ and $\Delta\alpha_{G,k,n}^{(1)}$ from Eq. (2). In option 1 of the NOISLAN program the values for these terms are those given by Watt [22], who in turn derived the values from the work of Wait and Spies [18]. However, the computer program used to generate the data of Ref. 18 (in many cases) could find no solution for the second-order and third-order modes, especially for the lower values of ground conductivity. Further, the accuracy of Wait's second-order-mode and third-order-mode roots has been questioned by Pappert et al. [23]. Because of these problems, it was decided to recompute the appropriate mode parameters using the WAVEGUID program. These parameters were then used to compute the aforementioned terms from Eqs. (1) and (2). The values of the propagation parameters computed from the WAVEGUID program agreed with the values used in the NOISLAN program for the first-order mode, but disagreed (as noted by Pappert [23]) for the second-order and third-order modes. Since the second-order and third-order modes often carry more horizontally polarized energy than does the first-order mode, accurate computation of the higher order modes is important in the prediction of high-altitude atmospheric radio noise. The WAVEGUID mode-parameter solutions are believed to be more accurate than those of Refs. 18 and 22. Option II, therefore, has been included in NOISLAN to use the newly calculated parameters. Also there has been interest in extending the VLF atmospheric noise model upward in frequency to cover the lower end of the LF spectrum (30 to 60 kHz). This extension would not be possible using the results of Refs. 18 and 22 but would be possible by use of the WAVEGUID program.

### Description of WAVEGUID

The WAVEGUID computer program was originally developed at the Naval Electronics Laboratory Center to predict the vertical electric field received at a point on the earth's surface produced by a vertical electric transmitting antenna at another point on the earth's surface. It was later extended to give the crosspolarized (horizontal) components of the field at any height in the earth-ionosphere waveguide and even in the ionosphere itself [11, 24, 25]. The basic formulation of the equations for the fields are given in Ref. 13. The net resultant vertical electric field at the earth's surface is represented as a summation of waveguide-mode fields:

$$E_z(0) = \frac{i\sqrt{\mu_0/\epsilon_0}}{\sqrt{d\lambda h}} \, Ids \, \sqrt{\frac{d/a}{\sin(d/a)}} \, \sum_n [\sin^{3/2}\theta_n \, \Lambda_n \, \exp(i\pi/4 + ik_0 d\sin\theta_n)], \qquad (7)$$

where

| | |
|---|---|
| $\theta_n$ | is the eigenangle of the $n$th waveguide mode, |
| $Ids$ | is the dipole moment (ampere-meter) of the vertical antenna located on the earth's surface, |
| $\Lambda_n$ | is the excitation factor of the $n$th waveguide mode, |
| $a$ | is the radius of the earth, |
| $d$ | is the great-circle distance between the transmitter and the receiver, |
| $h$ | is the reference height of the ionosphere (used in the definition of $\Lambda_n$), |
| $k_0$ | $= \omega/c$ is the free-space propagation constant of the wave, |
| $\lambda$ | is the wavelength of the wave, |

and

$\mu_0$ and $\epsilon_0$    are the magnetic permeability and dielectric constant of free space.

Each waveguide mode is characterized by its own value of attenuation rate $\alpha_n$ and phase velocity $v_p^n$, which are related to the eigenangle of the $n$th waveguide mode $\theta_n$ according to

$$\alpha_n = 0.02895 \, \omega \, \text{Im}(\sin \theta_n) \tag{8}$$

and

$$v_p^n = \frac{c}{\text{Re}(\sin \theta_n)}, \tag{9}$$

where $\alpha_n$ is measured in decibels per 1000 km (dB/Mm) and $c$ is the speed of light.

The values of the waveguide-mode eigenangles depend on the reflection coefficients of the ground and the ionosphere. Because of its anisotropy, the ionosphere has four reflection coefficients ${}_{\parallel}R_{\parallel}(\theta_n)$, ${}_{\perp}R_{\parallel}(\theta_n)$, ${}_{\parallel}R_{\perp}(\theta_n)$, and ${}_{\perp}R_{\parallel}(\theta_n)$ for a given angle of incidence $\theta_r$. The ground is assumed to be isotropic and to have reflection coefficients ${}_{\parallel}\bar{R}_{\parallel}(\theta_n)$ and ${}_{\perp}\bar{R}_{\perp}(\theta_n)$, which are calculable from the eigenangle, ground conductivity, and dielectric constant. The WAVEGUID program uses a procedure for calculating the ground and ionospheric reflection coefficients referenced to any height $z$ in the waveguide. References 26, 27, and 28 discuss the reflection coefficients further. The eigenangle $\theta_n$ for a given waveguide mode is obtained by satisfying the mode equation

$$0 = \left\| \begin{bmatrix} {}_{\parallel}R_{\parallel}(\theta_n) & {}_{\perp}R_{\parallel}(\theta_n) \\ {}_{\parallel}R_{\perp}(\theta_n) & {}_{\perp}R_{\perp}(\theta_n) \end{bmatrix} \begin{bmatrix} {}_{\parallel}\bar{R}_{\parallel}(\theta_n) & 0 \\ 0 & {}_{\perp}\bar{R}_{\perp}(\theta_n) \end{bmatrix} - \begin{bmatrix} 1 & 0 \\ 0 & 1 \end{bmatrix} \right\|. \tag{10}$$

This matrix equation is simply rewritten

$$F(\theta_n) = ({}_{\parallel}R_{\parallel} \, {}_{\parallel}\bar{R}_{\parallel} - 1)({}_{\perp}R_{\perp} \, {}_{\perp}\bar{R}_{\perp} - 1) - {}_{\perp}R_{\parallel} \, {}_{\parallel}\bar{R}_{\parallel} \, {}_{\parallel}R_{\perp} \, {}_{\perp}\bar{R}_{\perp} = 0. \tag{11}$$

where the dependence of the reflection coefficient on $\theta_n$ has been suppressed to simplify the notation. The new variable $F(\theta_n)$ is defined also. Each value of $\theta_n$ which satisfies Eq. (11) is the eigenangle of the $n$th waveguide mode. The excitation factor $\Lambda_n$ for the $n$th waveguide mode is obtained from

$$\Lambda_n = -i \, \frac{kh}{2} \, \sin \theta_n \, \frac{(1 + {}_{\parallel}\bar{R}_{\parallel})^2 (1 - {}_{\perp}\bar{R}_{\perp} \, {}_{\perp}R_{\perp})}{{}_{\parallel}\bar{R}_{\parallel} \, \dfrac{\partial F(\theta)}{\partial \theta}\bigg|_{\theta = \theta_r}}. \tag{12}$$

where the variable $F(\theta)$ is as defined in Eq. (11). In addition to the vertical electric field $E_z$ for a given waveguide mode having eigenangle $\theta_n$, in general there exist five other nonzero field components $E_x$, $E_y$, $H_x$, $H_y$, and $H_z$ within the waveguide for each mode.

These extra fields arise because the ionosphere is anisotropic on account of the earth's magnetic field. Propagation through and reflection from such an anisotropic medium rotates the plane of polarization of the incident wave to generate crosspolarized reflected fields. Alternatively one could consider the linearly polarized wave transmitted from the vertical electric dipole antenna to be a linear superposition of right-handed and left-handed circularly polarized waves, each reflected with a different amplitude at the ionosphere. The ionospheric reflection causes a mixture of wave polarizations at a reception point on or above the earth's surface. The fields at height $z$ are related to the vertical electric fields at the earth's surface $E_z(0)$ in a given waveguide mode by the following functions of reflection coefficients and Hankel functions:

$$E_z(z)/E_z(0) = f_{\parallel}(z), \tag{13}$$

$$E_x(z)/E_z(0) = g(z)/S. \tag{14}$$

$$E_y(z)/E_z(0) = -\frac{{}_{\parallel}R_{\perp}(1 + {}_{\perp}\bar{R}_{\perp}) \, f_{\perp}(z)}{S(1 + {}_{\parallel}\bar{R}_{\parallel})(1 - {}_{\perp}\bar{R}_{\perp} \, {}_{\perp}R_{\perp})}. \tag{15}$$

$$H_z(z)/E_z(0) = - \frac{_{\parallel}R_{\perp}(1 + {}_{\perp}\bar{R}_{\perp}) f_{\perp}(z)}{\eta(1 + {}_{\parallel}\bar{R}_{\parallel})(1 - {}_{\perp}\bar{R}_{\perp \perp}R_{\perp})}, \tag{16}$$

$$H_y(z)/E_z(0) = \frac{f_{\parallel}(z)}{\eta \, S}, \tag{17}$$

and

$$H_x(z)/E_z(0) = \frac{_{\parallel}R_{\perp}(1 + {}_{\perp}\bar{R}_{\perp})}{i\,\eta\,k\,S(1 + {}_{\parallel}\bar{R}_{\parallel})(1 - {}_{\perp}\bar{R}_{\perp \perp}R_{\perp})} \, \frac{df_{\perp}(z)}{dz}. \tag{18}$$

where

$$f_{\parallel}(z) = \exp\left[\frac{z-D}{a}\right] \frac{F_1 \, h_1(q) + F_2 \, h_2(q)}{F_1 \, h_1(q_d) + F_2 \, h_2(q_d)}, \tag{19}$$

$$f_{\perp}(z) = \frac{F_3 \, h_1(q) + F_4 \, h_2(q)}{F_3 \, h_1(q_d) + F_4 \, h_2(q_d)}, \tag{20}$$

and

in which

$$g(z) = \frac{1}{ik} \, \frac{d}{dz} \, [f_{\parallel}(z)]. \tag{21}$$

$$F_1 = - \left[ H_2(q_0) - i \, \frac{n_0^2}{N_F^2} \left[\frac{ak}{2}\right]^{1/3} (N_F^2 - S^2)^{1/2} \, h_2(q_0) \right], \tag{22}$$

$$F_2 = H_1(q_0) - i \, \frac{n_0^2}{N_F^2} \left[\frac{ak}{2}\right]^{1/3} (N_F^2 - S^2)^{1/2} \, h_1(q_0), \tag{23}$$

$$F_3 = - \left[ h'_2(q_0) - i \, \left[\frac{ak}{2}\right]^{1/3} (N_F^2 - S^2)^{1/2} \, h_2(q_0) \right], \tag{24}$$

$$F_4 = h'_1(q_0) - i \, \left[\frac{ak}{2}\right]^{1/3} (N_F^2 - S^2)^{1/2} \, h_1(q_0), \tag{25}$$

$$q = \left[\frac{2}{ak}\right]^{-2/3} \left[ C^2 - \frac{2}{a}(h - z) \right]. \tag{26}$$

and

$$q_d = \left[\frac{2}{ak}\right]^{-2/3} \left[ C^2 - \frac{2}{a}(h - D) \right]. \tag{27}$$

with

$$q_0 = \left[\frac{2}{ak}\right]^{-2/3} \left[ C^2 - \frac{2h}{a} \right]. \tag{28}$$

$$H_j(q) = h'_j(q) + \frac{1}{2} \left[\frac{2}{ak}\right]^{2/3} h_j(q), \quad j = 1, 2, \tag{29}$$

$$n^2 = 1 - \frac{2}{a}(h-z), \tag{30}$$

$$n_0^2 = 1 - \frac{2}{a} h, \tag{31}$$

and

$$N_F^2 = \epsilon/\epsilon_0 - j \, \frac{\sigma}{\omega \epsilon}. \tag{32}$$

In these expressions

| | |
|---|---|
| $a$ | is the radius of the earth, |
| $z$ | is the height of the receiver above ground, |
| $N_g$ | is the index of refraction of the ground surface, |
| $D$ | is the reference altitude in the waveguide for evaluating the mode parameters and the reflection coefficients, |
| $k$ | is the propagation constant of the waves in free space $(= \omega/c)$, |
| $S$ and $C$ | are the sine and cosine of the eigenangle $\theta_n$, |
| $h_1(q)$ and $h_2(q)$ | are the modified Hankel functions of order 1/3, |

and

| | |
|---|---|
| $\eta$ | is the impedance of free space. |

Using these relations, one can obtain a desired field of a given mode at any altitude $z$, if one knows the vertical field in that mode at the earth's surface. The NOISLAN prediction program calculates the vertical noise fields in the three strongest quasi-TM waveguide modes in making its noise prediction. So, the values of $E_z(0)$ for the three most important modes are available, and one can obtain the crosspolarized fields at any height $z$ by applying Eqs. (13) through (18) to the NOISLAN $E_z(0)$ values.

## HORNS Program and Approximations

The HORNS portion of the atmospheric-noise model predicts high-altitude atmospheric noise at any polarization by using the functions of the WAVEGUID program, as summarized in Eqs. (13) through (18), and the values of $E_z(0)$ computed by the NOISLAN program. Equations (13) through (18) may be rewritten in a notation more appropriate to the summation of fields from many sources:

$$E_{n,z}^{(i)}(z) = f_{\parallel,n}^{(i)}(z)\, E_{n,z}^{(i)}(0). \tag{13'}$$

$$E_{n,x}^{(i)}(z) = g_n^{(i)}(z) E_{n,z}^{(i)}(0)/S_n^{(i)} \tag{14'}$$

$$E_{n,y}^{(i)}(z) = \frac{-\,_\parallel R_{\perp,n}^{(i)}(1 + \,_\perp \overline{R}_{\perp,n}^{(i)}) f_{\perp,n}^{(i)}(z) E_{n,z}^{(i)}(0)}{S_n^{(i)}\,(1 + \,_\parallel \overline{R}_{\parallel,n}^{(i)})\,(1 - \,_\perp \overline{R}_{\perp,n}^{(i)} R_{\perp,n}^{(i)})}. \tag{15'}$$

$$H_{n,z}^{(i)}(z) = \frac{-\,_\perp R_{\perp,n}^{(i)}(1 + \,_\perp \overline{R}_{\perp,n}^{(i)}) f_{\perp,n}^{(i)}(z) E_{n,z}^{(i)}(0)}{\eta(1 + \,_\parallel \overline{R}_{\parallel,n}^{(i)})(1 - \,_\perp \overline{R}_{\perp,n}^{(i)} R_{\perp,n}^{(i)})}. \tag{16'}$$

$$H_{n,y}^{(i)}(z) = -\frac{f_{\parallel,n}^{(i)}(z)\, E_{n,z}^{(i)}(0)}{\eta\, S_n^{(i)}}. \tag{17'}$$

and

$$H_{n,x}^{(i)}(z) = \frac{_\parallel R_{\perp,n}^{(i)}(1 + \,_\perp \overline{R}_{\perp,n}^{(i)})}{i\eta k S_n^{(i)}(1 + \,_\parallel \overline{R}_{\parallel,n}^{(i)})(1 - \,_\perp \overline{R}_{\perp,n}^{(i)}\,_\perp R_{\perp,n}^{(i)})} \frac{df_{\perp,n}^{(i)}(z)}{dz}\, E_{n,z}^{(i)}(0). \tag{18'}$$

In these expressions the field symbols such as $E_{n,z}^{(i)}(z)$ refer to the field strength produced by the $i$th noise source in the $n$th waveguide mode. The symbols for the height gain functions such as $f_{\parallel,n}^{(i)}(z)$, refer to these functions in the $n$th waveguide mode and from the $i$th transmitter. Likewise the ground and ionospheric reflection coefficients refer to particular modes and to waves from a particular noise source.

After the individual contributions to the components of the noise field have been calculated, the vertically polarized electric and magnetic noise fields may be obtained by analogy to Eq. (6):

$$E_z(z) = \left[ \sum_{i=1}^{N} \sum_{n=1}^{3} |E_{n,z}^{(i)}(z)|^2 \right]^{\frac{1}{2}}$$  (33)

and

$$H_z(z) = \left[ \sum_{i=1}^{N} \sum_{n=1}^{3} |H_{n,z}^{(i)}(z)|^2 \right]^{\frac{1}{2}}.$$  (34)

A random-phase approximation has been made in deriving Eqs. (33) and (34). In other words, no correlations are assumed among the elements $E_{n,z}^{(i)}$ in the sum of Eq. (33) or among the elements $H_{n,z}^{(i)}$ of Eq. (34). For different values of $i$ (different sources) the random-phase approximation is undoubtedly correct, since there is no correlation in the arrival time of energy from different sources. However, for different values of $n$ (different modes from the same source) the random-phase approximation is less accurate, since some correlation exists among the arrival times of different modes from the same source. However, since the noise "transmitter" locations are only the noise power centroids for noise sources in their respective areas and not the noise sources themselves, the actual propagation paths from each lightning discharge to the receiver are not known. Thus one cannot accurately calculate the phase angles of the various modes, leaving the random-phase approximation as the best alternative.

To obtain equations for the horizontally polarized noise fields, one must first select a horizontal axis direction $x'$ along which the noise is to be specified. The previously used coordinates $x$, $y$, and $z$ are defined in relation to the direction of propagation of a wave: $z$ is the vertical direction, $x$ is horizontal in the direction of propagation of the wave, and $y$ is horizontal perpendicular to the direction of wave propagation. Since the equivalent sources are at different bearings from the receiving location, one cannot simply add the $H_{n,y}^{(i)}(z)$ field to that from another source such as $H_{n,y}^{(i+1)}(z)$, because they will not be parallel. Instead one must find the contribution of the various fields to a resultant component fixed in space using the normal processes of vector resolution and vector addition. One then obtains the total horizontal fields in the fixed $x'$ directions as follows:

$$E_{x'}(z) = \left[ \sum_{i=1}^{N} \sum_{n=1}^{3} | E_{n,x}^{(i)}(z) \cos\theta_{x,x'}^{(i)} + E_{n,y}^{(i)}(z) \sin\theta_{x,x'}^{(i)} |^2 \right]$$  (35)

and

$$H_{y'}(z) = \left[ \sum_{i=1}^{N} \sum_{n=1}^{3} | H_{n,x}^{(i)}(z) \cos\theta_{x,x'}^{(i)} + H_{n,y}^{(i)}(z) \sin\theta_{x,x'}^{(i)} |^2 \right]^{\frac{1}{2}}.$$  (36)

The resultant noise predictions $E_{x'}(z)$ and $H_{y'}(z)$ are real numbers, and the waveguide-mode field amplitudes $E_{n,x}^{(i)}$, $E_{n,y}^{(i)}$, $H_{n,x}^{(i)}$, and $H_{n,y}^{(i)}$ are complex phasors. Hence one must use the absolute magnitudes of these contributions in Eqs. (35) and (36).

To determine $H_{n,z}^{(i)}(z)$ from $E_{n,z}^{(i)}(0)$ according to Eq. (16'), one needs knowledge of $\theta_n^{(i)}$, the eigenangle of the $n$th waveguide mode that carries the wave from the $i$th noise transmitter, and of the ionospheric and ground reflection coefficients for this propagating mode. How can one obtain $\theta_n^{(i)}$? One could determine $\theta_n^{(i)}$ from the WAVEGUID program using an appropriate anisotropic ionosphere model by iteratively solving Eq. (11), as is normally done with this program. However, this procedure is time consuming when applied to noise predictions, because it ordinarily requires several iterations to settle on a satisfactory value of $\theta_n$. This undertaking could become expensive and tedious, since there may be as many as 70 significant thunderstorm atmospheric noise sources, each having a different bear-

ing from the receiver location. Since the angle of arrival of energy from each source would be different, a new calculation of $\theta_n$ would be required for each case. An alternative method has been used in the present version of the program.

The approximation for $\theta_n$ in the present program is to substitute the eigenangle $\theta_n$ which has already been calculated for the quasi-TM mode with an isotropic ionosphere. This procedure makes the assumption that the field expressions in Eqs. (13') thorugh (18') are not sensitive to the value $\theta_n$. This assumption was tested and partially verified for a sample of noise predictions. Certainly this method of selecting $\theta_n$ is arbitrary, and it might be improved in subsequent versions of the program. Once $\theta_n$ is selected, it is used for the evaluation of all the factors that enter into the computation of the elevated fields. The geomagnetic field strength and direction at the receiver location is calculated using a dipole model of the earth's field. The $i$th azimuth angle required to evaluate the ionospheric reflection coefficients is evaluated using this geomagnetic model and a knowledge of the direction to the $i$th equivalent noise source.

The atmospheric-noise model calculates the high-altitude electromagnetic fields propagated in three quasi-TM modes in the earth-ionosphere waveguide. The fields generated by the vertical component of the lightning stroke but propagated in the quasi-transverse-electric (quasi-TE) modes are ignored. This deficiency of the prediction model may be remedied in future versions. It seems reasonable that the contributions by the quasi-TE mode to the horizontal electric and vertical magnetic field should be comparable to the contributions by the quasi-TM mode, hence the observed noise might exceed the predicted values by 3 dB.

The atmospheric-noise model also ignores the contributions of the horizontal component of the lightning discharge, because it has been assumed that the horizontal discharges are much weaker than the vertical discharges. Recent detailed analyses of lightning discharge paths [29] suggest that a substantial elevated horizontal component of the discharge channel existed in several thoroughly analyzed cloud-to-ground discharges. This strong horizontal component would be inconsistent with our present noise model and suggests an important topic for further investigation. A detailed statistical study of lightning-channel structures and of received noise polarizations would be useful in assessing this question.

## COMPARISON OF PREDICTIONS WITH OBSERVATIONS

The predictions of the vertical noise fields on the ground obtained from COMPWR and NOISLAN can be readily compared with data. From 1958 through 1967, at first the National Bureau of Standards (NBS) and after a reorganization the Environmental Science Services Administration (ESSA) supervised a worldwide network of atmospheric-radio-noise recording stations [30]. Measured long-term noise data at 13 kHz from 12 of these stations have been compared with COMPWR/NOISLAN predictions. Figures 1 and 2 show a comparison between the NBS experimental data and the predictions using option II of COMPWR and options I and II of NOISLAN.

Whereas many data exist for vertically polarized atmospheric electric noise, few data are available for vertically polarized magnetic noise. The Mitre Corporation has made a few nearly simultaneous measurements of the vertically and horizontally polarized magnetic noise fields at high altitudes using loop antennas. The Mitre Corporation personnel used a horizontal loop antenna extended behind a jet aircraft in measuring the vertical magnetic field strength. The receiver used for the measurements was an RCA VLF amplitude-probability-distribution receiver loaned by NRL for the experiments. A pair of orthogonal-crossed-loop antennas were used in measuring the horizontal magnetic field. The experimenters state (G. Hirst, private communication) that their crossed-loop system did not have an omni-directional reception pattern, because of induced coupling from the aircraft structure. The crossed-loop antennas were coupled to produce a response to elliptically polarized horizontal magnetic noise fields. Neither the directions of the major and minor axes of the ellipse nor the direction of rotation of the
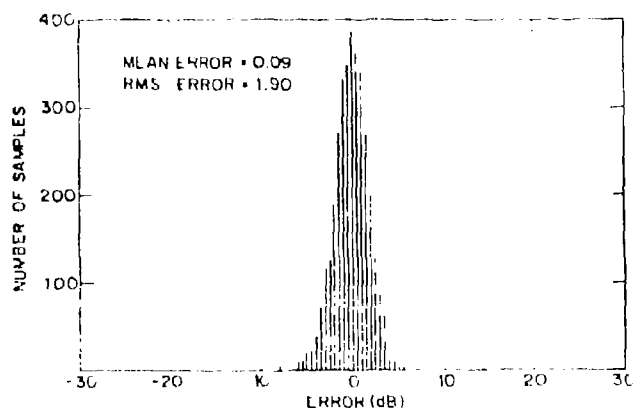
Fig. 1 — Histograms of errors (observed values minus predicted values) in predicting vertically polarized electric noise at 13 kHz using NOISLAN option I and COMPWR option II

Fig. 2 — Histogram of errors (observed values minus predicted values) in predicting vertically polarized electric noise at 13 kHz using NOISLAN option II and COMPWR option II.
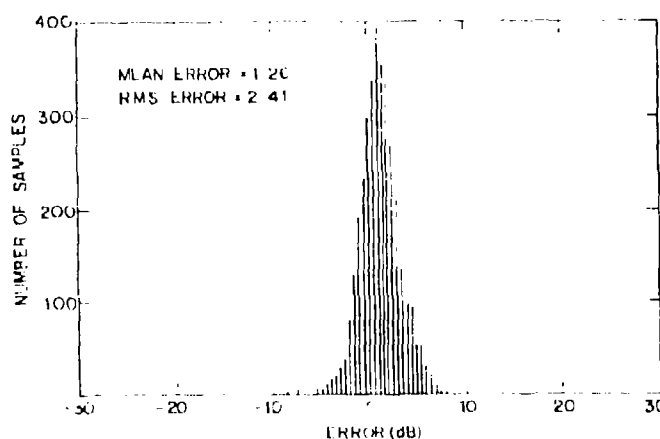


elliptically polarized waves are available. These parameters are important in comparing the data with detailed theoretical predictions from the atmospheric-noise program. They were not important to the Mitre measurement program. In spite of these difficulties, the Mitre data are valuable at present, because they are practically all the data there are. The voltage outputs of the crossed-loop antennas were added together with a 90° phase shift, as is normally done in a crossed-loop system. The resultant field strengths were then normalized to the value of the vertical electric field that an equivalent TM propagation wave would possess to give the observed magnetic-field value. These are the values of $E_z$ presented in Figs. 3 through 8 and in Table 1. The values of $\mathcal{H}_z$, where $\mathcal{H}_z = \eta H_z$, with $\eta$ being the impedance of free space, were those measured on the horizontal loop antenna.

From Figs. 3 through 8 and from Table 1, one can note that the equivalent vertical electric noise field $E_z$ is predicted to be relatively constant from day to night and that it exceeds the equivalent vertical magnetic noise field $\mathcal{H}_z$ by about 30 dB during the day and by about 15 dB during the night. The smaller predicted value of $\mathcal{H}_z$ during the day is directly related to the smaller value of the ionospheric reflection coefficient $_\|R_1$ that describes the change of wave polarization from vertical electric to vertical magnetic (Eq. (16')).

An interesting case of disagreement with the model is observed in Fig. 4, where the noise data, taken immediately after sunrise at the receiver, have a separation of $\mathcal{H}_z$ from $E_z$ more characteristic of nighttime than daytime conditions. Such a case could occur if about 50% of the noise sources were in
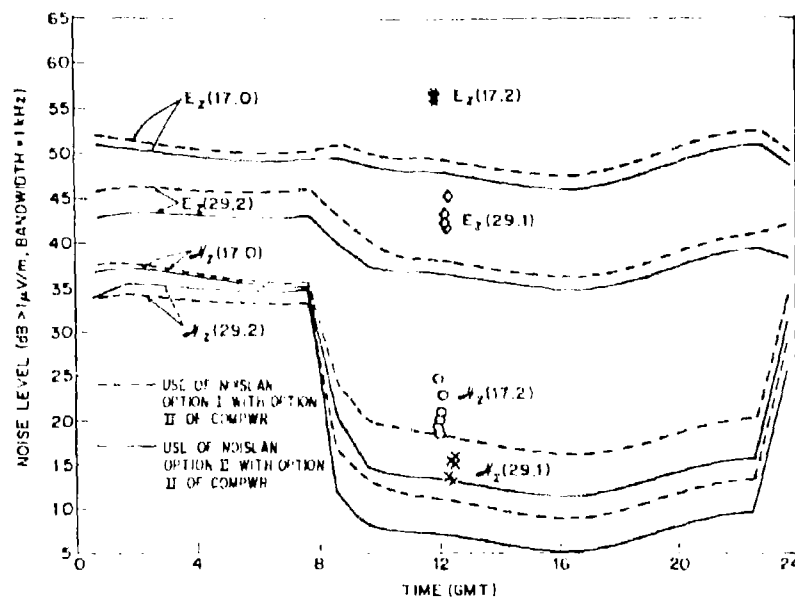
Fig. 3 — Predicted values (lines) and observed values (symbols) of the $E_z$ and $H_z$ components of RMS atmospheric noise at a 10 km altitude at 47°N, 55°W on July 15, 1976. The numbers in parentheses give the frequency in kilohertz
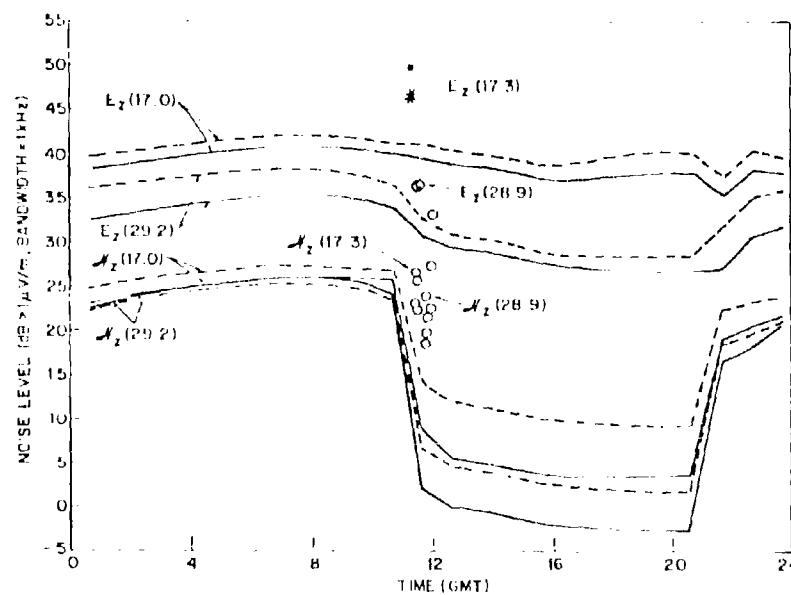


Fig. 4 — Predicted and observed values of RMS atmospheric noise at a 10 km altitude at 44°N, 65°W on February 20, 1976
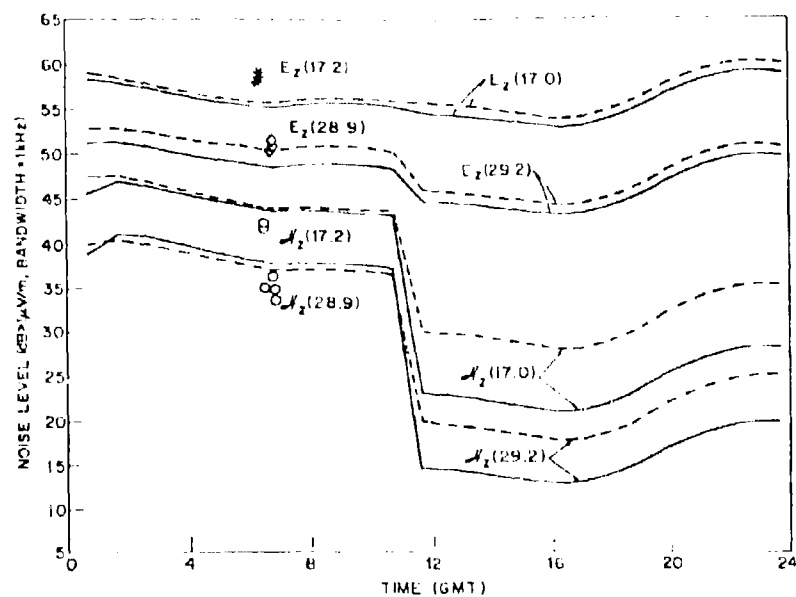
Fig. 5 — Predicted and observed value of RMS atmospheric noise at a 10-km altitude
at 38°N, 82°W on August 17, 1976
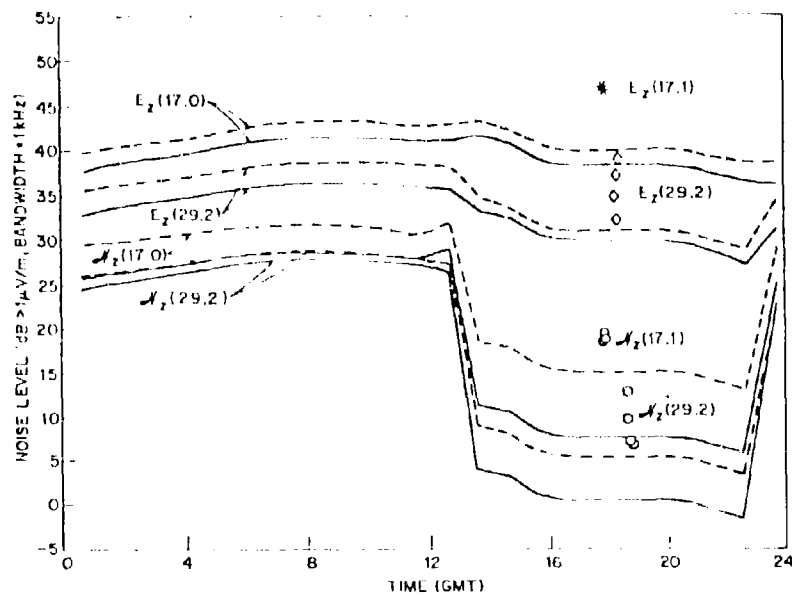


Fig. 6 — Predicted and observed values of RMS atmospheric noise at a 10-km altitude
at 39°N, 90°W on January 23, 1976
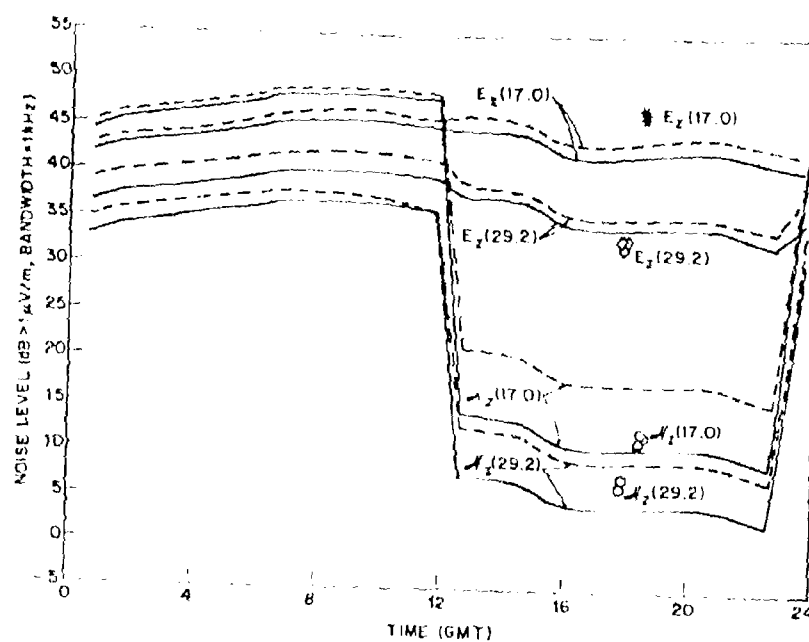
Fig 7 — Predicted and observed values of RMS atmospheric noise at a 10-km altitude at 28°N, 80°W on February 3, 1976
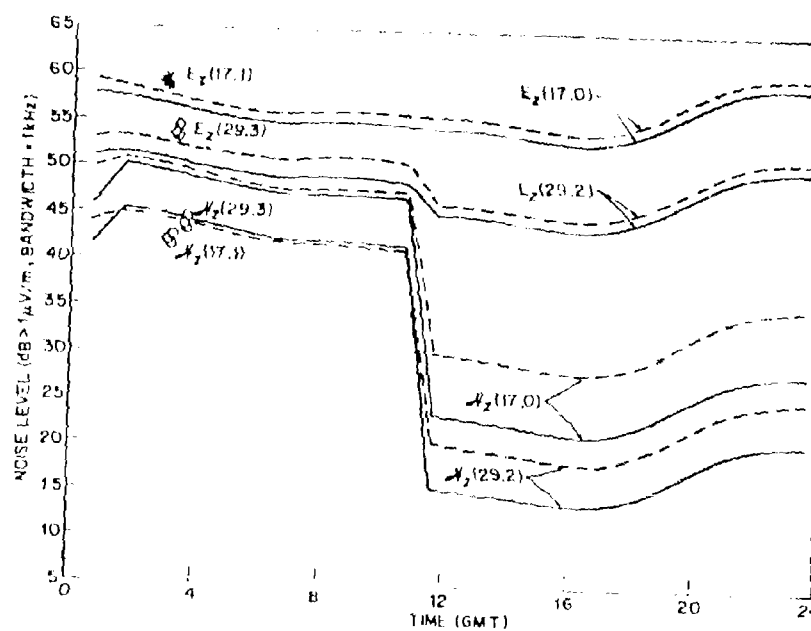


Fig 8 — Predicted and observed values of RMS atmospheric noise at a 10 km altitude at 38°N, 84°W on August 17, 1976

Table 1 — Summary of Predicted and Observed Separations of
RMS Noise as Shown in Figs. 3 thorough 8

| Location | $E_z - H$, RMS-Noise Separation (dB) | | | | | | | | | | | |
| --- | --- | --- | --- | --- | --- | --- | --- | --- | --- | --- | --- | --- |
| | Daytime | | | | | | Nighttime | | | | | |
| | ≈ 17 kHz | | | ≈ 29 kHz | | | ≈ 17 kHz | | | ≈ 29 kHz | | |
| | Opt. I | Opt.II | Obs. | Opt. I | Opt.II | Obs. | Opt. I | Opt.II | Obs. | Opt. I | Opt.II | Obs. |
| 47°N, 55°W | 31.0 | 34.5 | 35.6 | 27.0 | 29.5 | 28.4 | 14.0 | 13.5 | — | 12.5 | 6.5 | — |
| 44°N, 65°W | 29.0 | 34.5 | — | 26.5 | 29.5 | — | 15.0 | 15.0 | 23.2* | 13.5 | 9.5 | 13.0* |
| 38°N, 82°W | 26.0 | 32.0 | — | 26.5 | 30.5 | — | 12.0 | 12.0 | 18.1 | 13.5 | 11.0 | 16.1 |
| 39°N, 90°W | 25.0 | 31.0 | 28.2 | 26.0 | 29.5 | 26.6 | 12.0 | 13.0 | — | 10.0 | 9.0 | — |
| 28°N, 80°W | 26.5 | 32.0 | 35.4 | 26.5 | 30.0 | 26.2 | -2.5 | -3.0 | — | 4.0 | 3.0 | — |
| 38°N, 84°W | 26.0 | 32.0 | — | 26.0 | 30.0 | — | 8.0 | 8.0 | 16.9 | 8.5 | 7.0 | 10.2 |

*Measurements taken during the transition from night to day

the nighttime portion of the globe and if the effect of passage of the nighttime quasi-TM waves through the terminator region did not suppress the $\mathscr{H}_z$ fields but simply propagated them forward in quasi-TI modes. A future improved version of the noise prediction model may be constructed to take this quasi-TE conversion into account.

In general the measured data are several dB higher than the predictions. However, almost all the $E_z$ measurements are within 1 standard deviation of the predicted levels based on the values of $D_u$ given in CCIR Report 322 [1]. Table 1 presents a summary of predicted and observed $E_z - \mathscr{H}_z$ noise separations. The use of option II of the NOISLAN program with option II of COMPWR yields better predictions of $E_z - \mathscr{H}_z$ noise separation for daytime at ≈17 kHz than does the use of option I of NOISLAN with option II of COMPWR. Other than for daytime at ≈17 kHz the predictions are not better from use of option II of NOISLAN rather than of option I. For both options the predictions for daytime fit the data quite well but the predictions for nighttime do not fit so well. The results are encouraging, but more noise data are needed to fully determine the accuracy of the model.

## ADDITIONAL DEVELOPMENT OF THE MODEL

Several possibilities exist for further development of the atmospheric-noise model. Incorporation of TL-mode propagation with conversion at the terminator may be a helpful addition. Also, the extension of the model's frequency range up to 60 kHz would be useful, since the range from 30 to 60 kHz not currently covered is of operational concern. Such an extension would first require a modification of the COMPWR and NOISLAN programs to predict TM noise up to 60 kHz. The propagation parameters could be found using the WAVEGUID program with an appropriate ionospheric model, just the way option II of NOISLAN was prepared. The validity of the extended NOISLAN model could be checked against 51-kHz vertical noise data collected by NBS [30]. In preparation for this comparison effort, the available 51-kHz NBS noise data have been digitized. Results of the analysis may be published in the future.

# REFERENCES

1. "World Distribution and Characteristics of Atmospheric Radio Noise," Proc. of the CCIR Xth Plenary Assembly, Geneva, 1963, Report 322, International Telecommunications Union, Geneva, 1964.

2. A.D. Spaulding, C.J. Roubique, and W.Q. Crichlow, "Conversion of the Amplitude-Probability Distribution Function for Atmospheric Radio Noise from One Bandwidth to Another," J. Res NBS, (Radio Prop.) 66D (No. 6), 713-720 (1962).

3. E.L. Maxwell, D.L. Stone, R.D. Croghan, L. Ball, and A.D. Watt, "Development of a VLF Atmospheric Noise Prediction Model," Westinghouse Georesearch Laboratory Report 70-1H1-VLF NO-R1, 1970.

4. J.C. Williams, "Thunderstorms and VLF Radio Noise," Ph.D. thesis, Harvard University, Division of Engineering and Applied Physics, 1959.

5. E.L. Maxwell and D.L. Stone, "Natural Noise Fields from 1 cps to 100 kc," Trans. IEEE PGAP AP-11 (No. 3), 339-343 (1963)

6. V.D. Rubtsov, "Distribution of the Envelope of a Mixture of Atmospheric Noise and a Narrowband Signal," Radio Eng. and Electronic Phys. 21 (No. 3), 133-135 (1976).

7. V.A. Yepanechnikov, "The Distribution of Intervals to the Nearest Pulse in Poisson-Poisson Trains," Radio Eng. and Electronic Phys. 21 (No. 7), 129-131 (1976)

8. J.P. Hauser and F.J. Rhoads, "Coverage Predictions for the Navy's Fixed VLF Transmitters," NRL Memorandum Report 2884, 1974.

9. F.J. Kelly, "VLF Field Strength Variations from an Airborne Trailing-Wire Antenna," Radio Sci. 5 (No. 5), 785-791 (1970).

10. J. Galejs, Terrestrial Propagation of Long Electromagentic Waves, Pergamon, New York, 1972.

11. R.A. Pappert, W.F. Moler, and L.R. Schockey, "A Fortran Program for Waveguide Propagation which Allows for Both Vertical and Horizontal Dipole Excitation," NELC Interim Report 702, 1970, p. 72.

12. J. Galejs, "ELF and VLF Fields of a Horizontal Electric Dipole," IEEE Trans. Antennas Propagation AP-16 (No. 6), 689-700 (1968).

13. R.A. Pappert, "Effects of Elevation and Ground Conductivity on Horizontal Dipole Excitation of the Earth-Ionosphere Waveguide," Radio Sci. 5 (No. 3), 579-590 (1970).

14. F.J. Kelly, F.J. Rhoads, I.P. O'Neal, and M.Y. McGowan, "Very-Low-Frequency (VLF) Propagation Predictions for Disturbed Conditions," NRL Report 8017, 1976.

15. R.J. Gallenberger and J.E. Bickel, "Horizontal and Vertical Atmospheric Noise Measurements at VLF up to 20,000 ft Altitude," NELC Technical Report 1793, 1971.

16. C.W. Meyer, "MEECN Technical Test Plan for Transverse Electric (TE) Field Measurements," Defense Communications Agency, 960-TP-70-41, 1975.

17.  J.E. Bickel, "Measurements of Vertical and Horizontal VLF Fields Excited by an Elevated, Arbitrarily Oriented Antenna," NELC Technical Report 1833, 1972.

18.  J.R. Wait and K.P. Spies, "Characteristics of the Earth-Ionosphere Waveguide for VLF Radio Waves," NBS Technical Note 300, 1964.

19.  R.R. Morgan, "World-Wide VLF Effective-Conductivity Map," Westinghouse Electric Corporation Report 8013F-1, 1968.

20.  J.P. Hauser and F.J. Rhoads, "Analysis of a VLF Atmospheric Noise Prediction Model," paper given at USNC/URSI 1973 Meeting Aug. 21-24, Commission VIII, Session 1.

21.  J.P. Hauser, "Further Analysis of a VLF Atmospheric Noise Model," paper given at USNC/URSI 1974 Meeting, Oct. 14-17, Commission VIII, Session 2.

22.  A.D. Wait, *VLF Radio Engineering*, International Series of Monographs on Electromagnetic Waves, Vol. 14, Pergamon, 1967.

23.  R.A. Pappert, E.E. Gossard, and I.J. Rothmuller, "A Numerical Investigation of Classical Approximations used in VLF Propagation," Radio Sci. 2 (No. 4), 387-400 (1967).

24.  C.H. Sheddy, R. Pappert, Y. Gough, and W. Moler, "A Fortran Program for Mode Constants in an Earth-Ionosphere Waveguide," NELC Interim Report 683, 1968.

25.  R.A. Pappert and L.R. Schockey, "A Program for Computing Earth Ionosphere ELF/VLF Excitation Factors for Satellite-borne Antennas," NELC Interim Report 741, 1974.

26.  R.N. DeWitt, F.J. Kelly, and G.A. Chayt, "Lower Ionosphere Effects on the Propagation of Waves from an ELF/VLF Source in the Magnetosphere," Radio Science 11, (No. 3   189-197 (1976)

27.  K.G. Boaden, *Radio Waves in the Ionosphere*, Cambridge Univ. Press, 1961.

28.  J.R. Wait, "Electromagnetic Waves in Stratified Media," International Series of Monographs on Electromagnetic Waves, Vol. 3, Pergamon, 1962.

29.  P.R. Krehbiel, M. Brook, and R.A. McCrory, "An Analysis of the Charge Structure of Lightning Discharges to Ground," J. Geophys. Res. 84 (No. C5), 2432-2456 (1979).

30.  W.Q. Crichlow, C.A. Samson, R.I. Disney, and M.A. Jenkins, "Quarterly Radio Noise Data," NBS Technical Note 18 series, 1960

DISCUSSION EPP FALL 81 MEETING
MEDIUM, LONG, AND VERY LONG WAVE PROPAGATION
(AT FREQUENCIES LESS THAN 3000 KHZ)

SESSION 3

PAPER: 17. VLF PROPAGATION IN DISTURBED ENVIRONMENTS
AUTHOR: E. C. Field
COMMENTER: J. S. Belrose
QUESTION: In Figure 9 you show that during an intense disturbance the mode structure in the field-strength versus distance curve essentially disappears. Under normal conditions the first major minimum in the field strength, on a wave hop theory, is the place where the ground and sky wave are approximately equal and in antiphase. This must mean then that under intense disturbance conditions there is no skywave at least for distances < 600 Km where the signal must be essentially ground wave only? At greater distances is this also the situation?
RESPONSE: Although both the wave hop and waveguide mode methods give satisfactory results, the wavehop method is not amenable to simple physical interpretation at VLF under conditions where the earth-ionosphere waveguide is severely constricted. For example it is very difficult to explain the well known phenomenon of waveguide cutoff in terms of a ground-wave and a superposition of skywaves. In figure 9, the single propagating waveguide mode is made up of a large number of terms in the skywave series. Moreover for the conditions shown, the track width of the ground wave extends into the depressed lower ionosphere.

PAPER: 17. VLF PROPAGATION IN DISTURBED ENVIRONMENTS
AUTHOR: E. C. Field
COMMENTER: F. P. Schmerling
QUESTION: In answer to Dr. Belrose's question, I would expect the sky wave reflection coefficient to increase with obliquity. On very simple grounds a disturbance could decrease the sky wave amplitude at nearly vertical incidence sufficiently to wipe out the first interference minimum, but still provide some contribution at oblique incidence (longer range).

RESPONSE: My response to Dr. Belrose's question applies to this comment as well.

PAPER. 17. VLF PROPAGATION IN DISTURBED ENVIRONMENTS
AUTHOR: E. C. Field
COMMENTER: J. B. Reagan
QUESTION: Since there have been many cases of solar proton events occurring while transpolar VLF propagations were underway, have you used any of these events to test the validity of your modeling work?

RESPONSE: Yes, although I have not discussed the transpolar propagation data in my oral presentation. However, a brief discussion of the agreement between experiment and theory is given in the written version of the paper, as is a list of references.

PAPER: 18. MULTIPATH VLF PROPAGATION EFFECTS IN CORRELATION RECEIVERS
AUTHOR: F. J. Kelly
COMMENTER: T. J. Beahn
QUESTION: Have you considered using some of the techniques employed in adaptive equalizers? For example, you can represent the various modes as attenuated and shifted (in time) versions of the original signal. One can then use the psuedorandom sequence as a probe of the channel characteristics and determine just what attenuation and shifts you are dealing with. Perhaps one could obtain better performance with such a model of its channel.

RESPONSE: Personally, I do not know enough about advanced receiver design of the type you describe to say much about it. Undoubtedly, some type of adaptive system might be designed for these circuits under favorable circumstances.

PAPER: 18. MULTIPATH VLF PROPAGATION EFFECTS IN CORRELATION RECEIVERS
AUTHOR: F. J. Kelly
COMMENTER: J. S. Belrose
QUESTION: The correlation techniques that you are proposing must be like spread spectrum techniques used at HF to eliminate multi-path efforts due to "multi-hop" signals. Applying this to VLF, if we spread the energy over a sufficient frequency band that the multi-path signals were not correlated, spread spectrum techniques should work for the VLF situation. Is this in fact what you are saying?
RESPONSE: The MSK spread-spectrum signals discussed in my paper are not of wide enough bandwidth to separate the multipath completely. So my paper deals with the consequences of this circumstance.

PAPER : 21. ATMOSPHERIC VLF RADIO NOISE AT ELEVATED RECEIVERS : HORIZONTAL AND VERTICAL POLARIZATION
AUTHOR : F. J. Kelly
QUESTIONER : C. R. Swanson
QUESTION : Most receivers with which I am familiar use non-linear signal processing to exploit the impulsive nature of VLF noise. Performance may be equivalent to 15 Db gain compared with Gaussian noise. You have addressed only the RMS value. Would you care to comment on the applicability of your work?

RESPONSE : The original WGR Model contains a method for predicting the $V_d$ of the noise. We have

not modified the original algorithms for these quantities.
(Note: $V_d$ is the difference between the RMS and average values of the noise)

# LF PROPAGATION:  AN OVERVIEW

John S. Belrose
Communications Research Centre
Department of Communications
Ottawa, Canada

## ABSTRACT

Propagation at frequencies in the LF band (30-300kHz) alter with change in frequency as would be expected for a transition band between VLF and MF.  But there is a drastic difference between propagation characteristics in these adjacent bands.  Ionospheric attenuation therefore increases rapidly with frequency, particularly during summer daytime.  This overview is inadequate in that many features of LF propagation are scarcely touched on, or not mentioned at all, however reference is made to published work where the detail can be found.  The overview addresses principally those areas where our knowledge is inadequate, particularly where our knowledge of propagation on a global scale is far from complete.

## 1.    INTRODUCTION

As noted in the theme of this symposium, the LF band (30-300kHz) is useful for communications to intermediate distances, shorter than the global reach of ELF/VLF but longer than the ground-wave spans characteristic of the MF band during daytime when the absorption of the ionospheric reflected wave is great. By this we mean communications to distances ranging from hundreds to several thousand kilometers.

The amplitude of the skywave, for waves steeply reflected from the ionosphere, increases rapidly with increase in frequency, especially during summer daytime, and the maximum in the absorption of the sky wave occurs in this frequency band (in the frequency range 100-300kHz), see Figure 1.  At oblique incidence this frequency band for which absorption is a maximum is shifted to higher operating frequencies, because to a fair approximation, an oblique incidence wave suffers an attenuation on reflection from the ionosphere similar to a vertical incidence frequency of effective frequency fcosi, where i = angle of incidence on the ionosphere.  On this interpretation of LF field strength, the frequency range of the MF broadcast band, for a transmission distance of 1500km, spans the frequency band of maximum absorption, since for a 1600kHz wave, fcosi = 278kHz, whereas at 500kHz, fcosi = 86kHz.

In preparing this overview we have concluded that there have been no significant new advances in our knowledge about the propagation of LF radio waves since the extensive discourse by Belrose [1968]; see also Belrose and Segal [1974] and Burgess and Jones [1975], and for a list of some more recently published works CCIR Document [1978-1982].  In the present paper we will address only the more important aspects of LF propagation, with particular emphasis on those that need to be further studied.

## 2.    GEOGRAPHICAL ARRANGEMENT OF EXPERIMENTS

Except for a few specific experiments, e.g., the measurement of LF field strengths in an aircraft by Burgess, and by Kelly [1981] which will be described in the next paper; by the Naval Ocean Systems Centre, we will see some of there results in Morfitt's [1981] overview;  and studies of Loran-C propagation, see Doherty's [1981] overview; LF propagation has been studied extensively only in Canada and in Europe, essentially by three groups of researchers.  These were the early work by Ratcliffe and his colleagues at Cambridge, UK, by Lauter and his colleagues in Europe and by Belrose and his colleagues in Canada.  The author had the opportunity to study LF propagation in both geographical regions, since his early work was carried out at Cambridge during 1953-1957, just long enough to observe the change from solar minimum to solar maximum. Latter work (1957-1974) was carried out in Canada.

It is useful at the outset to consider the geographical arrangement of the experiments, i.e., the geographic/magnetic latitudes of the propagation paths, since one of the principal differences in propagation in there two regions, the diurnal variation in phase (to be described), is undoubtly associated with a difference in magnetic    latitude.   In Canada, all propagation paths studied lay above 45$^0$ geographic, 55$^0$ magnetic (magnetic invariant) latitude; in Europe all paths studied were more narrowly restricted, 50 - 60$^0$ geographic and 45 - 57$^0$ magnetic latitude.  See polar maps shown in Belrose [1968].

## 3.    THE RADIATION FIELD AND ITS MEASUREMENT

Except for a few experiments, e.g., Loran C measurements, the field strengths measured were of continuous wave signals hence the total field record is then the resultant of the field due to the wave diffracted by the ground and the field due to the skywave.  In the simple experiment only the amplitude of the total field is measured, see Figures 2-4, and the phase and amplitude of the skywave are inferred from this simple record at times when it is in or out-of-phase w.r.t. the groundwave.  On this interpretation sometimes described as a "quasi-phase method", a diurnal variation of the phase and amplitude of the skywave can in some instances be inferred.

If the transmitted frequency is stabilized, and a similar primary frequency standard is employed at the receiving site, the total-field record in both phase amplitude can be recorded, see Figures 5-8.

It is sometimes found useful to register the recorded phase and amplitude of the total-field on a polar plot, see Figure 9.  Such a record is called a NORLII, a normal loop induction locus; normal meaning that the total field record has been recorded employing a loop antenna in the place of propagation.

Another experiment, referred to as an oscillating-loop-experiment, has been employed to infer the polarization of the skywave [Belrose, 1968]. In this experiment the loop is oscillated continuously through some small angle about the bearing of the propagation path, and the apparent radio bearing, as well as other parameters of the signal are inferred from the signal at the two extremities of the loop swing and the minimum signal.

The total-field record has also been measured in an aircraft, and again maximum and minima on the record are inferred to be times when the sky and ground-waves are in-or out-of-phase, see Figures 10 and 11. In some experiments the phase of the total-field has been recorded, but this parameter has not found useful, because the position of the aircraft was not known with sufficient accuracy to remove the dominate phase change due change in position of the aircraft.

In interpreting total field records measured in Europe and Canada, attention should be drawn to another difference, besides that of magnetic latitude. In Europe the ground conductivity typically has a conductivity of $5 \times 10^{-3}$ S/m, and some of propagation paths studied lay partly or almost entirely over sea water. A few paths however were over mountainous regions. In Canada a conductivity of $<2 \times 10^{-3}$ S/m is more typical, and paths which traverse the Laurentian shield and arctic land have conducties of $0.3 \times 10^{-3}$ S/m. The skywave to-ground-wave ratio is therefore much greater for LF propagation paths in Canada compared with similar propagation paths in Europe.

## 4. DIURNAL VARIATIONS OF PHASE

In Figure 2 we have shown total-field records recorded at Cambridge, UK, for several LF propagation paths, for different frequencies and distances. On the assumption that the skywave in reflected without a change in phase, and taking account of the phase lag of the ground wave due to the finite conductivity of the earth, the curve in Figure 12, shows the morning variation of the phase height of reflection that is consistent with these data. The skywave is assumed to be in-phase and out-of-phase with the ground wave, at times of maxima and minima on the field strength records. The curves in Figure 13 show phase heights inferred by Starich and Taumer [1966] for the Bresov-Kolberg path (fcosi = 27kHz) for the first half of 1962 (records like those shown in Figure 3). The heights shown here are somewhat greater than those in Figure 12, which may be due to the fact that there authors ignored the phase delay of the ground wave. The total field record for LCH (Tryvasshoegda) near Oslo received at Kuhlungsborn (54.6/660/12.7kHz), see Figure 4, is consistent with the observation that the phase height varied regularly over the day, and is a minimum shortly after local noon.

This diurnal variation in phase is in contrast with data shown in Figures 5 and 7, for propagation between Halifax and Ottawa, 973km distant. For these records, the phase of the total-field was measured directly. The phase lag decreased rapidly at dawn, does not change during the daytime, and increased at dusk. While sky and ground-waves have not been separately inferred for these records, it should be noted, that since the pattern is essentially similar at all frequencies, this would suggest that the skywave was greater than the ground wave even in summer. The amplitude of the total field record does exhibit sharp minima at some frequencies during the dawn and dusk transitions. Because of the low ground conductivity, the sky-wave to ground-wave ratio would be expected to be much greater than for the European paths described above. It must be inferred therefore that the skywave phase does vary in a trapizoidal way, similarly at all frequencies observed.

Such a diurnal variation would be consistent with reflection from a layer produced by a source of ionization that was constant day or night, such as galactic cosmic rays or energetic particles. The rapid decrease at dawn is then due to photodetachment of electrons from a bank of negative ions that was in equilibrium with the nocturnal electron production rates, and the attachment rates of electrons to form negative ions. In Europe the ionization density in this lowest the C-layer must be much lower, and reflection occurs from the D-layer, although there is an amplitude and polarization change during the dawn transition.

It was noted in our overview paper on the propagation medium that ionization on a few days in winter can be rather low. In Figure 14 we show the amplitude ratio Ax/Ao at 76km for a 2.66MHz partial reflection experiment at Ottawa. This ratio is inversely proportional to the average electron density below the reference height, and for Ax/Ao > 1.5 there are almost no electrons below 76km. Notice that Ax/Ao > 1.5 December 4, 1972 and so the electron density in the C-layer was undetectably low. In Figure 15 we show records for this period, actually for 1 and 2 December, 1972 for 32.8kHz propagated over the Ottawa-Halifax path. Compare the observed variation of phase with the record for 19 November, 1972 which is the typical pattern that is regularly observed. The signal amplitude change during the daytime is also different from normal. While the signal minima during the dawn transition and the maximum near sunrise are typical, the deep minima after sunrise and before sunset are not characteristic of propagation over this path. Such a variation is more like that observed routinely on European path, see below. The discontinuity in the phase/record during the dusk transition is likely due to the small signal amplitude at this time. It should be noted also that the apparent phase lag decrease during the morning exceeds the 25-30μ-sec, which is typical for this path.

The records in Figure 16 show observations at a higher frequency, 130.8kHz observed for a path Ottawa to Great Whale River, 1111km distant. This is to be compared with the record for 32.8Hz propagated over the same path. This is a tracing of the actual record, which is 10μ-sec full scale (1 cycle at the reference frequency of 100kHz). Notice that at both frequencies the phase change occurs during a period of about 1½ hours, and the total change is essential identical at both frequencies (about 25 -μsec).

5.      DIURNAL VARIATION OF AMPLITUDE

        The data in Figure 17 are typical of the daily and seasonal change in skywave, inferred from
records of the total field (Figure 3) observed in Europe.  The amplitude of the skyway decreases at dawn
($\chi = 98^0$), then increases again near sunrise, and decreases reaching a minimum shortly after sunrise.
Only the second decrease is evident in these records.  The skywave amplitude then increases, reaching a
maximum at midday.  The midday maximum is especially pronounced in winter.

        The variation during the day is in contrast with the variation observed at Canadian latitudes,
see Figures 6 and 8.  While a signal  minimum during the sunrise change is clearly evident, and the amplitude
increases after this minimum, and there is little or no variation during the day (there is no midday maximum).
The daily pattern is somewhat irregular on some frequencies because these are records for individual days,
the data in Figure 17 are averaged over the month.  The daily pattern of amplitude change for 32.8kHz
propagated over the Ottawa-Halifax path (32.8/973(6.8)kHz), see Figure 15, on an unusual day, 1 December, 1972,
when the ionization density below 76km was low, is like that observed regularly in Europe.

6.      AMPLITUDE VARIATION WITH SOLAR CYCLE

        In Figure 1, we have shown data for amplitude versus frequency, and distance since effective
frequency fcosi is plotted, during sunspot minimum years.  These data, except data point labelled 8, have
been inferred from total field records for European propagation paths.  Data points 8 are for Loran
transmissions (early measurements at 180kHz), recorded at relatively high latitude in Canada during summer
months.Similar curves have been drawn for data recorded during sunspot maximum years.  The curves in
Figure 18 reveal the differences between sunspot minimum and maximum years.  During sunspot maximum years
waves of frequency below about 100kHz are more strongly reflected than during sunspot minimum years,
whereas waves at frequencies above about 100kHz skywaves are more strongly absorbed.

        Observations covering the same frequency/distance range at higher magnetic latitudes (in Canada)
are not available.  For the transmission paths studied there are clearly inconsistencies between the
seasonal and solar cycle variations observed, compared with those at lower magnetic latitudes in Europe.
As an example the observed field strengths over the path Comfort Cove, Newfoundland to Ottawa path
(70.4/1700 (11.3) kHz) are shown in Figure 19.  The seasonal variation for this transmission is opposite
to that expected, in that field strengths are higher in summer than in winter, particularly in winter at
midnight during solar maximum years (1959-61).  Furthermore the field strengths are greater during sunspot
minimum years (1964-65), particularly at night.

        At very high latitudes the change in field-strength over the epoch of the solar cycle is similar
to the observed in Europe, see Figure 20 for the transmission Thule to Churchill (77.15/2200(10.7)kHz), at
least during winter months, but the magnitude of the change is larger.  The diurnal variation is particularly
large in winter and equinoxal periods during sunspot maximum years, is almost non-existent in summer during
this epoch of the solar cycle; and, while not evident in the data given here, the sun effectively looses
control of the field strength over dawn at soltice in sunspot minimum years [see Belrose and Ross, 1967].

7.      SOLAR/GEOPHYSICAL DISTURBANCE VARIATIONS AND POST MAGNETIC STORM EFFECTS

        LF propagation has been employed as a synoptic tool to study the effects of solar geophysical
disturbances [Belrose, 1968].  Particularly, the winter variability has been studied [Lauter et. al., 1976],
and post magnetic storm effects.  The variations during solar-x-ray-flare events have been studied, the
effects of solar proton events (SPE) and high energy particle events (HEP), which, at the lower frequencies
are observed at magnetic latitudes of 50$^0$ and below. [Lauter and Taubenheim, 1970].

        In this overview we will not discuss in detail the observed variations, except for an extreme
example of a SPE of 10 November, 1960.  On this occasion the diurnal variation of LF phase and amplitude,
for high latitude paths, disappeared entirely.  The causitive flare, see Figure 21, occured shortly after
sunrise on the 12 November, 1960.  The time of the flare is indicated by the  rrow marked FL on the
Ottawa-Churchill phase record (curve(e)).  The solar flare effect (SFE) can be observed by the sudden
increase in signal amplitude for the Comfort Cove-Ottawa transmission (Curve (d)).  The SPE began
coincident with a magnetic storm sudden commencement (SC) and a sudden enhancement of cosmic rays (SECR)
observed at ground level.  The dawn and dusk periods at path mid-point are marked by the short broken
vertical lines,  indicating the times of $\chi = 102^0$ and 90$^0$ 50' (ground sunrise).  Note the decrease in
phase lag associated with the SPE for the Ottawa-Churchill path (curve (e)), and also that the normal
increase in phase lag at dusk was absent on 12 November.  In fact the nighttime phase height of reflection
during 12-13 November was the same as the day time height (50km) on the 12 November.  No decrease in phase
lag was observed at dawn on the 13 November.  SECR's on the 13 and 15 November prevented the observation
of the return to normal after the major event of 12 November.  The signal amplitudes for the various LF
propagation paths (curves (a), (b) and (d)... the pen stopped  inking for the record (c)) also reveal
no diurnal variation during 13 November.  Particularly marked is the Thule-Churchill path (curve (a)), since
before the SPE the signal amplitudes were off-scale during nighttime and low during the day, see the record
for 10 November.  The weaker then normal nighttime field strengths during the night of 10-11 November, 1960
is believed to be the result of a weak SPE, perhaps following the flare of 10 November.

        While the diurnal variation in phase height of reflection is always depressed during a SPE and
the magnitude of the diurnal change is reduced, the 12 November, 1960 SPE is the only occasion (in some
15 years of continuous observations) that no diurnal variation was observed during an SPE.  The nighttime
signal amplitudes are always less than normal during a SPE.  The day time amplitude can be less or greater
than normal, or the same as normal during an SPE, depending on the magnitude of the event and the latitude
of the path.

8.    CONCLUSIONS

There is currently a lack of (new) propagation data from which revised ionospheric reflection coefficients as a function of frequency, distance, time of year, solar and geomagnetic activity and other parameters can be derived, and there are inconsistencies in some of the available data, which make it impossible to describe in detail LF propagation on a global scale. More measurements are needed to establish differences between middle, low and high latitudes. An alternative approach is to calculate LF field strengths from models of D-region electron and ion densities, and some progress has been made in this area. Reference is made to Belrose and Segal [1974] and papers presented in Session VI of this Symposium, in which numerical modelling of the propagation medium is addressed. While there is a need for new experimental work, no propagation measurements are planned, and therefore new knowledge rests heavily on the shoulders of those concerned with numerical modelling of the medium. The electron and ion density height profiles must however be accurately known, because of the sensitivity of propagation to changes in height, shape and particularly gradient of the profiles. Ground conductivities at low frequencies are also inadequately known, and these have a great influence, particularly for areas where conductivities are low, on the propagation of the ground wave, and on the parameters affecting reception and transmission of the sky-waves at the terminals of the transmission path.

REFERENCES

Belrose, J.S., Low and Very Low Frequency Radio Wave Propagation, AGARD Lecture Series 29, pp 1V-1-1V-115, CFSTI Accession No. N68-37825, 1968.

Belrose, J.S. and D.B. Ross, Some Remarks on Ionization Changes in the Lower Ionosphere Inferred from the Propagation of Long Radio Waves, Ground-Based Radio Wave Propagation Studies of the Lower Ionosphere, Vol. 2, pp. 480-489, Defence Research Board, Canada, 1967.

Belrose, J.S. and B. Segal, On Interpretation of CW Propagation Data for Long Radio Waves, Methods of Measurements and Results of Lower Ionosphere Structure pp. 77-109,COSPAR Symposium, Akademic-Verlag, Berlin, 1974.

Burgess, B. and T.B. Jones, The Propagation of LF and VLF Radio Waves with Reference to Some System Applications, Radio Elect. Engr., 45, 47, 1975.

CCIR Documents [1978-1982], Skywave Propagation and Circuit Performance at Frequencies Between About 30kHz and 500 kHz, Report 265-4 (Mod F), DOC 6/1042, 1981.

Doherty, R.H. and J.R. Johler, Loran C: An Overview of Operational and Propagation Characteristics, Paper No. 39, this Conference Proceedings, 1981.

Kelly, F., F.J. Rhoads, J.A. Murray and D.J. Baker, Low Frequency Radio Wave Propagation in the Atlantic and Mediterranean Area,Paper No. 24, this Conference Proceedings, 1981.

Lauter, E.A. and J. Taubenheim, Anomalies of Lower Ionosphere Ionization in Medium Latitudes, Ann. Geophys, 26, 631-641, 1970.

Lauter, E.A., J. Taubenheim, G. Entzian, J. Bremer, G.V. Cossart and G. Klein, Middle Atmosphere Processes and Lower Ionosphere in Winter, Heinrich-Hertz-Institute, Berlin, Report HHI-STP No. 7, 1976.

Morfit, D.G., Numerical Modelling of the Propagation Medium at ELF/VLF/LF, Paper No. 32, this Conference Proceedings, 1981.

Starick, E. and F. Taumer, A Method of Field-strength Computation of the Daily Propagation of Long-Waves, O.I.R.T. Radio and Television, 3, 28-36, 1966.

Figure 2
Total field record for 11 March, 1955 received on a vertical antenna at Cambridge. Transmissions labelled Purple, Black, Red and Green are Decca Navigator transmitters in Denmark; and Berlin, Motala and Kalunborg are broadcast transmitters. The horizontal dashed line is the estimated ground wave amplitude. Times of ground sunrise at path midpoint (SR) is marked.
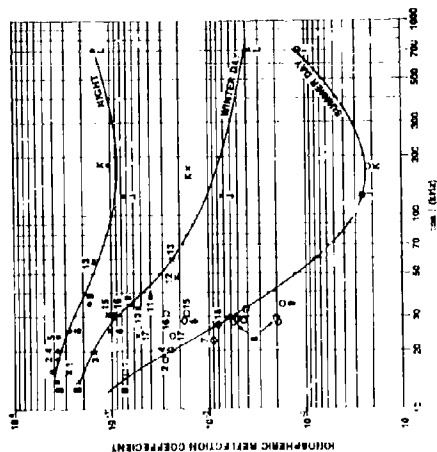
Figure 1
Ionospheric reflection coefficient versus fcosi, where f is the wave frequency and i the angle of incidence on the ionosphere, for winter days, summer days and night (sunspot minimum data).
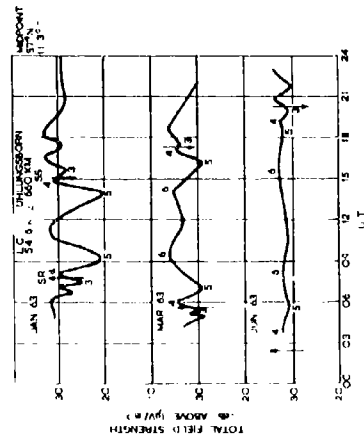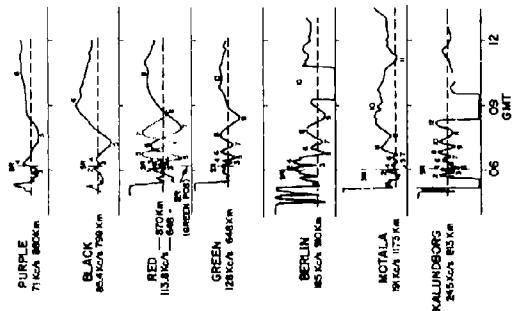
Figure 4
Total field records, monthly average for January, March and June, 1963 received on a loop antenna for the LCH (Tryvasshoegda - Kuhllungborn transmission (54.6/u60(12.7)kHz).

Figure 3
Averaged phase course of the total field strength for various months in 1963/64 for the Rilcuis-Kolberg path (164/1.09(32.7)kHz) [after Starick and Taumer, 1966].
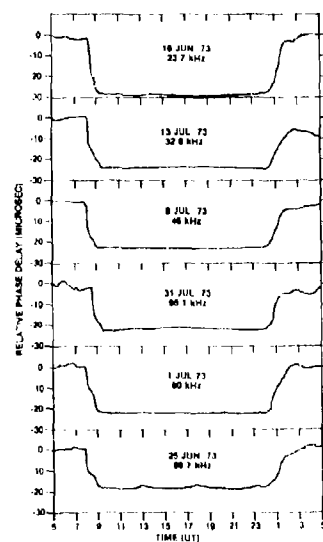
Figure 5
Phase of total field records at various frequencies
for the Ottawa-Halifax path (973km) in summer, 1973.
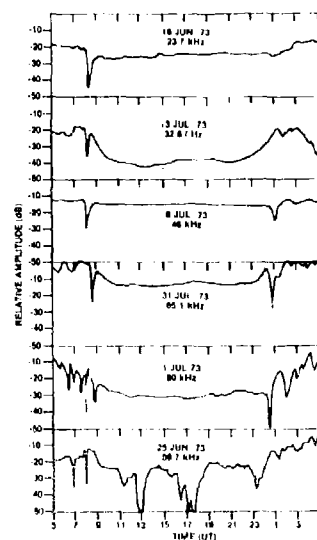


Figure 6
Amplitude of total field records at various
frequencies for the Ottawa-Halifax path
(973km) in summer, 1973.
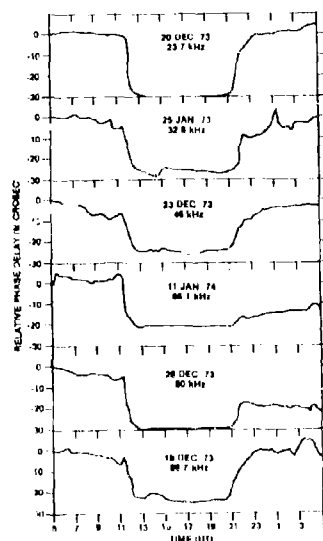


Figure 7
Phase of total field records at various frequencies
for the Ottawa-Halifax path (973km) in winter, 1973.
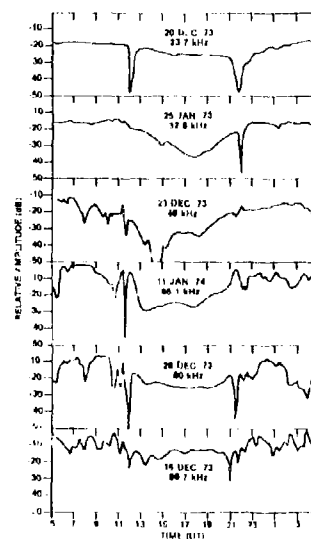


Figure 8
Amplitude of total field records at various
frequencies for the Ottawa-Halifax path
(973km) in winter, 1973.
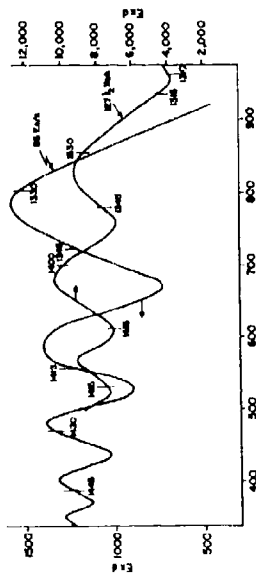
Figure 10
Rolling worth interference patterns
(super position between ground and
skywaves) observed at 85 and 127½kHz
during a daytime flight from Copenhagen
to Farnborough on 13 March, 1951.
GMT times are marked on the curves.
(after K. Weekes, private
communications, 1955).



Figure 12
Diurnal variation of reflection
heights for LF waves obliquely
reflected from the ionosphere,
deduced from the total field
records given in Figure 2
(no phase change on reflection).



Figure 5
Normalized loop induction locus (polar plot of phase and
amplitude) at 45kHz for the Ottawa-Halifax path (973km),
on 8 July, 1972.
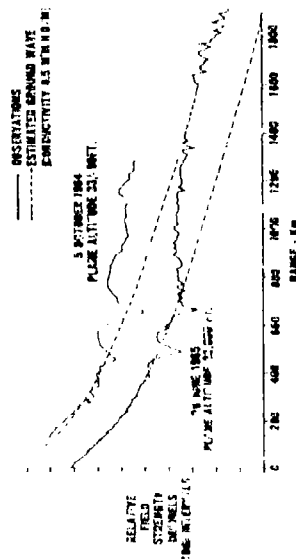


Figure 11
Total field record versus distance on a daytime flight from Ottawa
to Moosonee and Churchill. The two curves are arbitrarily separated
by 2dB relative field strength for clarity.
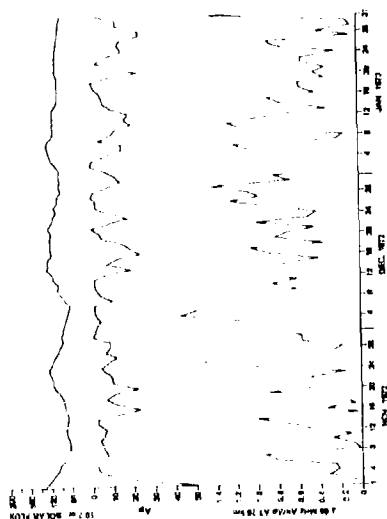
Figure 14
Day-to-day variation of the amplitude ratio Ax/Ao at 76km for a 2.66MHz partial reflection experiment at Ottawa, during the winter of 1972/73. The magnetic index Ap and 10.7cm solar flux index are also plotted on the record.



Figure 16
Morning variation of phase of the total field for 32.8 and 130.8kHz transmissions between Ottawa and Great Whale River, 1111km distant in September, 1972.
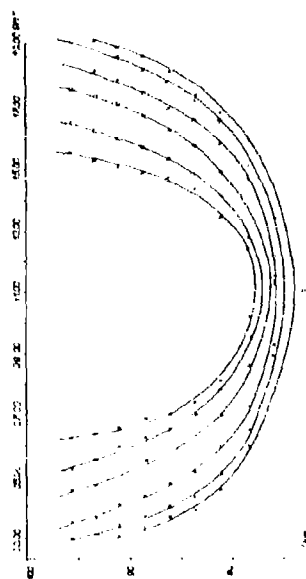


Figure 13
Diurnal variation of reflection heights for the Brasov/Kolberg path (156.1/182.27)kHz for the first half of 1972 (after Stanick and Teuner, 1956).
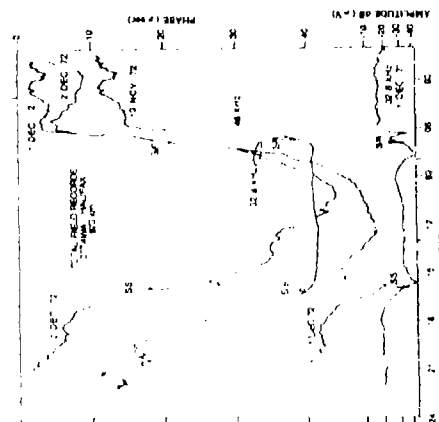


Figure 15
Diurnal variation of phase and amplitude at 32.8kHz for the Ottawa/Halifax path on 1-2 December, 1972 when the ionization densities below 76km were much less than normal.
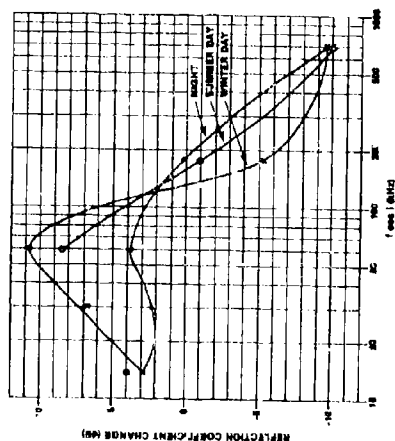
Figure 18
Change in amplitude (dB scale) of
reflection coefficients over the
epoch of the solar cycle (solar
maximum/solar minimum values)
for winter days, summer days and
night.



Figure 19
Field strength (uv/m) of total field records
for the Comfort Cove–Ottawa path (70.384/
163?(11.3)kHz), showing seasonal and solar
cycle changes. Note: 1959-61 were solar
maximum years, 1964-65 solar minimum years.
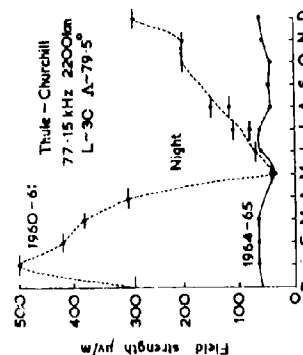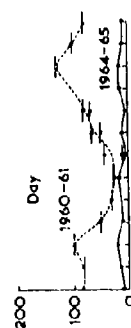


Figure 20
Field strength (uv/m) of total
field records for the Thule–
Churchill path (77.15/2200(12)kHz)
showing seasonal and solar cycle
changes. Note 1960/61 were solar
maximum years, 1964/65 solar
minimum years.

Figure 17
Early course of reflection coefficients during the first half
of 1963-64, as deduced from total field records as shown in
Figure 5 (after Stanwick and Taubner, 1966).
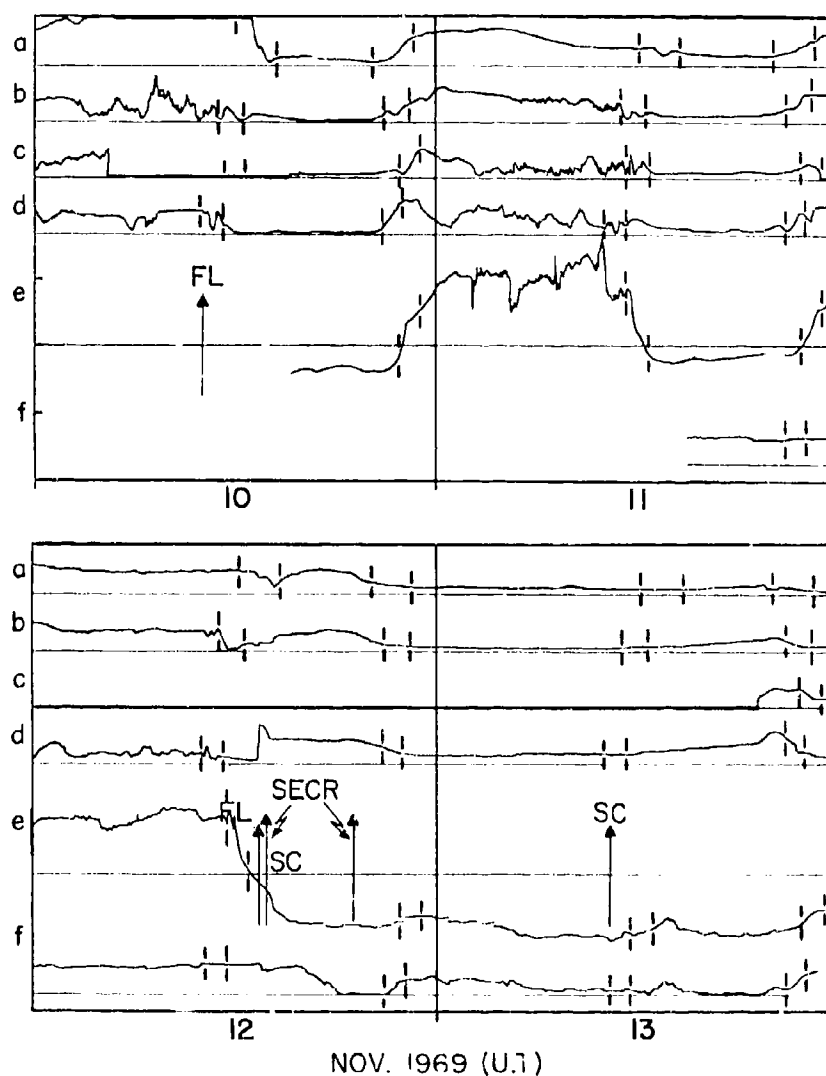
Figure 21

The effect of a solar proton event (SPE) on LF transmission for the 12 November 1969 event. The various curves labelled (a) to(d)are records of total field strength for the transmissions Thule-Churchill, Goose Bay-Churchill, Ottawa-Churchill, and Comfort Cove-Ottawa; curve(e)is the record for the phase of the Ottawa-Churchill transmission; and curve(f)is a riometer record made at Mont-Joli on a polar directed antenna (Mont-Joli is near the midpoint of the Comfort Cove-Ottawa path). All frequencies were 70-80kHz, distances 1900-2200km.

# LOW FREQUENCY RADIO WAVE PROPAGATION IN THE ATLANTIC

## AND MEDITERRANEAN AREAS

Francis J. Kelly
E.O. Hulburt Center for Space Research
Space Science Division

F. J. Rhoads and D. J. Baker
Information Technology Division

J. A. Murray
Space Systems Division

Naval Research Laboratory
Washington, D. C. 20375

## ABSTRACT

During 1976 and 1977 the Naval Research Laboratory conducted eighteen long range aircraft flights in the Atlantic and Mediterranean Sea area to measure and record the field strength of low frequency radio waves from transmitting stations in Iceland, Scotland, Morocco, and Greece, under daytime and nighttime conditions. The experimental data have been compared with the wave hop propagation model of Berry and areas of agreement and disagreement are noted. In particular, the nighttime waves at about 1 Mm, seem to oscillate with distance even more dramatically than the current model predicts. The daytime fields over all-water paths are often in good agreement with theory; but ground conductivity changes and rough terrain effects not contained in available computer models, appear to influence the received fields. We will discuss the unsatisfactory state of mathematical propagation models for this frequency regime and suggest some areas for improvement.

1.      INTRODUCTION

Since the time of Marconi's first trans-Atlantic communications experiment, the electromagnetic waves in the LF frequency band have been used for long range communications and navigation. Researchers into the propagation of these waves have been reported by many famous scientists; the names of Sommerfeld, Debye, Watson, Norton, Wait, Galejs, Fock, van der Pol and Bremmer, Budden, Hollingworth, Pitteway, Belrose, Burgess and many other noted and able researchers come immediately to mind. Even after many excellent studies, uncertainty about the propagation of these waves remains. There are still some poorly understood and modelled aspects of propagation in the LF band. Undoubtedly the basic framework for understanding the propagation exists in Maxwell's electromagnetic theory and our knowledge of the ionosphere, but the implementation of these ideas into a comprehensive predictive model has not been complete and satisfactory.

During the 1960's and early 1970's Berry and his coworkers developed an excellent computer model for the propagation of low frequency waves based on their researches into a wave-hop model of propagation. This model is very attractive because it is comprehensive, inexpensive, and based on ionospheric electron density profiles. The comparison of this predictive program with experimental results has been minimal because soon after the development of the program, sponsor interest in the research was reduced. The developers of the program were not able to check its predictions against experimental data. Fortunately the U.S. Navy has continued to recognize the value of a

well-calibrated propagation prediction tools in this frequency band, and we have been able to pursue the logical next steps in the development of a comprehensive LF Prediction Program.

2.     DAYTIME EXPERIMENT

    LOW FREQUENCY RADIO PROPAGATION EXPERIMENTS

During September, 1976, a series of low frequency radio propagation experiments were performed in the Atlantic and Mediterranean Sea areas utilizing and NRL RP-3A aircraft to measure field strength continuously with distance from the Navy LF transmitters in Iceland, Scotland, Morocco, and Greece.  During these experiments monitors were established near the four transmitting antenna sites to provide a measure of the power radiated from the transmitting antennas.  High quality tape recordings of the transmitted signals were made to provide a reference for comparison with the signal received and recorded on the aircraft.  In addition, two Singer NM12-AT Field Intensity meters were used to make strip chart recordings of the field intensity on the aircraft.  Field strength data were collected along the nine flight paths shown in Figure 1.  Figure 2 gives the flight schedule.

Figure 3 is a photograph of the aircraft used in this experiment.  In addition to the long wire antenna shown in the figure, three orthogonal loop antennas were mounted inside the tail radome.  A block diagram of the recording and measurement system installed in the aircraft is shown in Figure 4.  The recorded data can be used to provide field strength information on more transmitters than could be monitored simultaneously using the field intensity meters, and since accurate timing is maintained and recorded on the aircraft and ground station recordings, the phase delay and the transfer function of the propagation channel can be determined from further laboratory analysis of the recordings.

This report will present a portion of the field strength data obtained during these flights along with some theoretical predictions of the vertical electric fields based on a wave-hop and on a waveguide-mode computer program [Refs 1 and 2].  The theoretical predictions from the wave-hop program are based on a time varying ionosphere adopted by Berry and Jones [Ref 3].  In the present report all wave-hop model predictions are for a receiver on the earth's surface, since the wave-hop program of Reference 1 uses only this receiver altitude.  The wave-hop program could be modified along the lines of Reference 4 to obtain field strength predictions for elevated receiver locations; but, this has not been done at the present time.

Figure 5 shows the field strength versus distance data measured on the September flight from Rota to Athens from the 57.0 kHz transmitter at Bouknadel, Morocco.  The aircraft was flying at an altitude of 11,000 feet during the time of the measurement.  The solid line shows the theoretical field strength versus distance as predicted by the wave-hop program for a ground based receiver.

Figure 6 shows field strength versus distance data measured on the 58.3 kHz transmission from Greece measured on the flight from Rota to Athens and on the return flight (11,000 Ft. $\pm$ 1,000 ft. on both flights.)  The overall repeatability of the data over these two flights is very good.  The reason for the difference in measured fields at the range of 2,400 km is unknown.  The data taken on the flight from Athens to Rota at a distance greater than 380 km were measured using the fore and aft loop on the aircraft.  The other data were taken using the long wire antenna.

To illustrate the effect of ionosphere electron density changes and of receiving aircraft height above the ground, figures 7 and 8 show theoretical predictions of field strength versus distance at two altitudes on 58.3 kHz using a $\beta$ = .5 km$^{-1}$, h = 70 km and a $\beta$ = .3 km$^{-1}$, h = 72.0 km ionosphere

1525 Hz



1$^{ere}$    periode

2$^e$    periode

3$^e$    periode

4$^e$    periode

5$^e$    periode
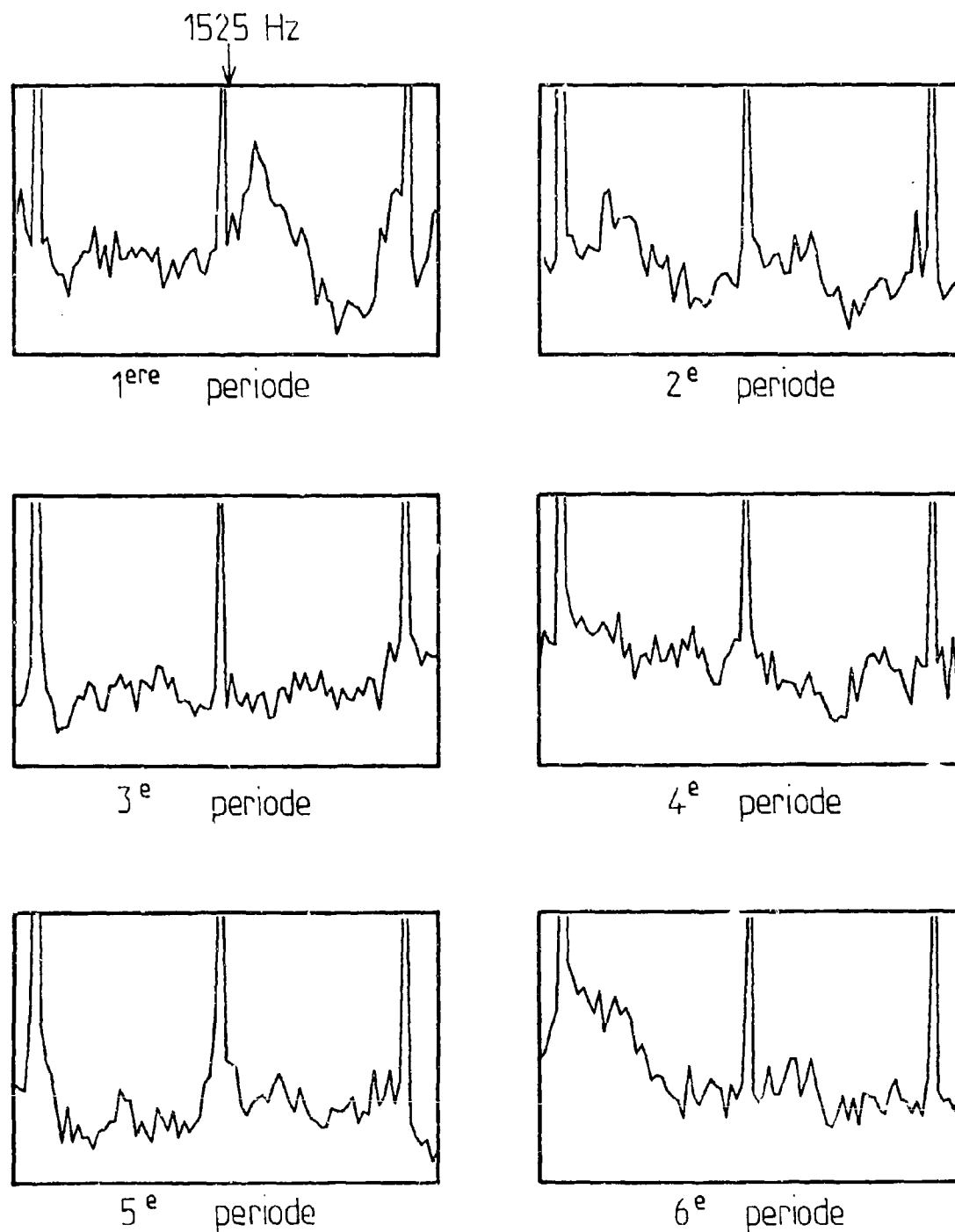
6$^e$    periode

1$^{er}$ OCTOBRE   1978

17h12 à 17h20 , TU

GEOS II

Figure   9
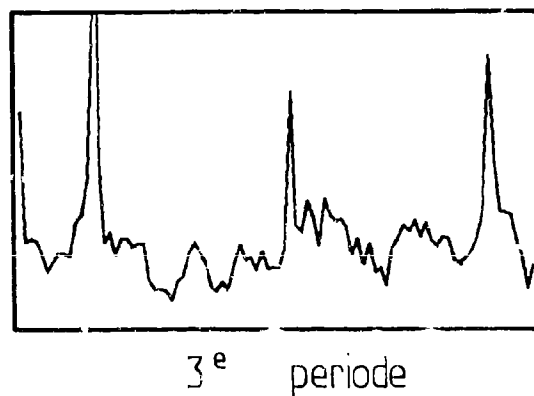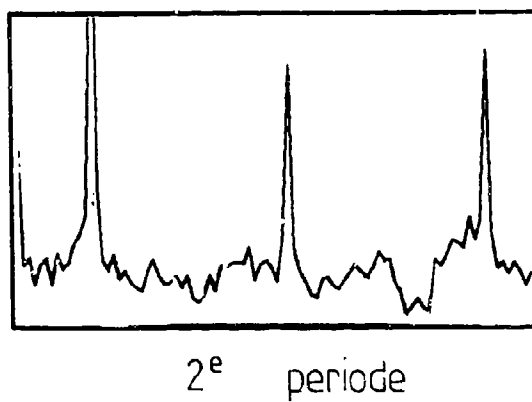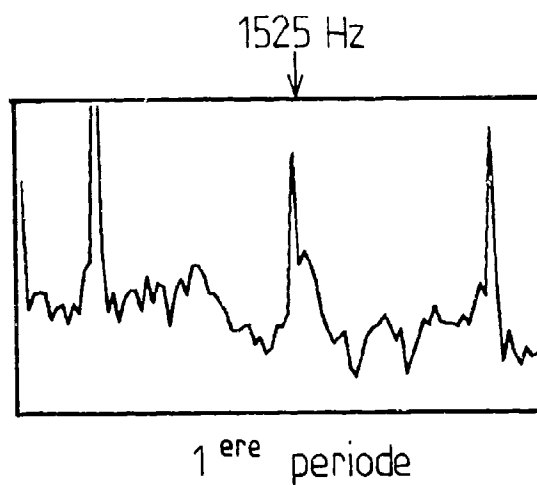
1525 Hz
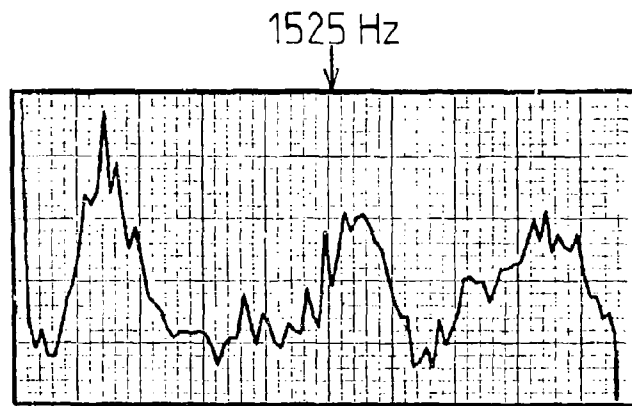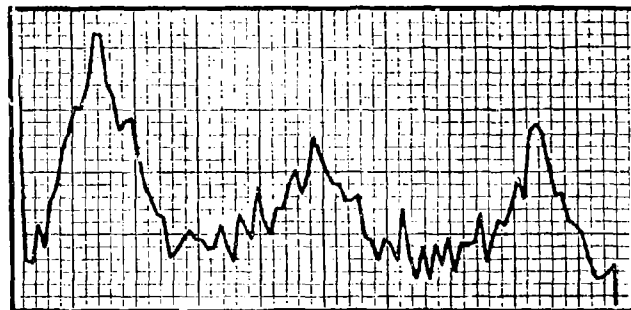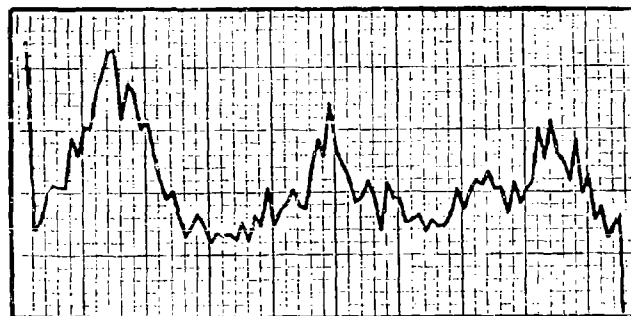
1 <sup>ere</sup> periode

2 <sup>e</sup> periode

3 <sup>e</sup> periode

1 <sup>er</sup> OCTOBRE 1978

17h20 à 17h24, TU

GEOS Ⅱ

Figure 10

1525 Hz

1 ere periode

2 e periode

3 e periode

1 er OCTOBRE 1978

17h20 à 17h24, TU

GEOS Ⅱ

Figure 10

1525 Hz

1<sup>ere</sup> periode

2<sup>e</sup> periode

3<sup>e</sup> periode

1<sup>er</sup> OCTOBRE 1978

17h36  à  17h43 , TU

GEOS II

Figure   11

# GENERATION OF ELF AND VLF WAVES BY MODULATED HF HEATING OF THE POLAR ELECTROJET

P. Stubbe, H. Kopka and M.T. Rietveld

Max-Planck-Institut für Aeronomie
3411 Katlenburg-Lindau 3, Germany


R.L. Dowden

Department of Physics
University of Otago, Dunedin, New Zealand

## SUMMARY

Modulated heating of the lower ionosphere, with modulation frequencies in the ELF and VLF range, gives rise to a corresponding modulation of the electron temperature and, thus, of the electrical conductivity. If a polar electrojet current exists, the current density is modulated, and an ELF or VLF signal is generated. Experiments have been performed to test this mechanism, using the new ionospheric Heating facility at Ramfjordmoen near Tromsø, Norway. It has been found that this mechanism is sensitive in the full ELF range and for VLF frequencies exceeding 7 kHz (which is the upper limit of our VLF receiver).

## 1. INTRODUCTION

Modulation of currents flowing in the lower ionosphere is a powerful means of generating ELF and VLF waves. A HF wave with a frequency in the low MHz range experiences strong absorption in the D and E region of the ionosphere, thereby raising the electron temperature. For the conditions of our experiment, an enhancement of the electron temperature by more than a factor of ten seems to be within reach (STUBBE and KOPKA, 1979). After switching off the HF wave, the electron gas cools down within a time of the order of 1 ms at 90 km (more above, less below 90 km). By using an amplitude modulated HF wave, with the modulation frequency f in the ELF or VLF range, electron temperature oscillations with frequency f are imposed, giving rise to corresponding oscillations of the elements of the conductivity tensor. Thus, if a dc current exists in the lower ionosphere, an ac current will be superimposed upon it, and the ionospheric portion illuminated by the HF wave will be turned into a huge antenna, radiating at the modulation frequency f.

These experiments were performed by using the Heating facility at Ramfjordmoen near Tromsø (geographic co-ordinates 69.6°N, 19.2° E, dip angle 78°, L value 6.2) which has been built by the Max-Planck-Institut für Aeronomie in cooperation with the University of Tromsø. The Heating facility was designed to generate an effective radiated power (ERP) of up to 360 MW in the frequency range 2.5 to 8 MHz. For a more detailed description of the Heating facility see STUBBE and KOPKA (1979).


## 2. EXPERIMENTAL SET-UP

ELF and VLF signals from the modulated ionosphere were received at Lavangsdalen, a low noise site 17 km from the Heating station, with two vertical loop antennas of 50 m² area oriented in the N-S and E-W directions. The antenna and pre-amplifier response, for a constant magnetic field input, peaks at 1000 Hz, is 3 dB down at 450 Hz and 3000 Hz, and 10 dB down at 250 Hz and 6000 kHz. A low pass filter in the pre-amplifier (after the first stage) cuts off at 7 kHz. This represents an extension of the bandwidth of the previously reported system (STUBBE, KOPKA and DOWDEN, 1981).

In addition to this system there have recently been installed two buried "micropulsation" loops (in N-S and E-W directions) whose response, together with preamplifiers, peaks at 10 Hz and is 3 dB down at 4 Hz and 20 Hz. It is capable of receiving signals in the micropulsation range (Pc 1 and 2) and ELF signals up to approximately 30 Hz. The signal produced by these loops is used to frequency modulate a carrier wave of 8.5 kHz by ± 360 Hz. These two frequency modulated signals at ~ 8.5 kHz are then combined with their corresponding E-W or N-S broadband VLF signals (200-7000 Hz) and are telemetered to the Heating station via UHF links.

At the Heating station the combined broad band and FM signals are recorded on magnetic tape and then further processed as follows. The FM carrier, after filtering to remove the broad band VLF, is fed into a phase-locked loop demodulator. This demodulated signal can then be fed into a spectrum analyser.

The two broad band VLF signals are fed into two synchronous detectors which use the heating transmitter modulation as reference. This gives the in-phase and quadrature-phase (i.e. cartesian components) of the received signal in a 32 Hz bandwidth. These four values (two for N-S and two for E-W) are digitized and used by a microcomputer to calculate, in real time, the equivalent amplitude and phase of the two circularly polarized modes (R and L) of which the received signal is assumed to be composed.

These synchronous detectors are also able to provide directly the amplitude and phase of the N-S or E-W signal. By narrowing the bandwidth of one of these synchronous detectors from 32 Hz to ~ 1 Hz it was also possible to synchronously detect signals from the output of the FM demodulator, i.e. from the "micropulsation" loop, as is shown below.

All sweep and fixed frequencies are generated digitally and derived from a frequency standard. It is possible to use amplitude modulation frequencies less than 15 Hz and greater than 200 Hz. Frequencies between these two values could not be used because of transmitter power supply filter resonances. We are mostly using sweep frequency modulation, mainly to find the frequency response of the ionospheric ELF-VLF generation mechanism. The sweep rate is typically ~ 100 Hz/s. In the experiments reported here, we have used three types of modulation: From full to zero power (100/0), half to zero power (50/0), and full to half power (100/50).

## 3. RESULTS AND DISCUSSION

Samples of typical and unusual sweep frequency results are shown in Figs. 1 to 4. The ERP values indicated in the graphs correspond to the full power available at the time of the particular experiment. The average power (averaged over one modulation cycle) follows from the specified type of modulation, i.e. 50% of full power for (100/0), 25% for (50/0), and 75% for (100/50). Before commenting on these results, it may be helpful to briefly discuss the agents and mechanisms determining the observed ELF-VLF signal strength, B, and its dependence on frequency, f.

(1) Electron temperature modification: The electron temperature enhancement caused by the powerful HF wave peaks in the vicinity of the altitude where $f_o \mp f_L \cos\Theta = \nu_e$ ($f_o$ = HF frequency, $f_L$ = electron gyrofrequency, $\nu_e$ = electron collision frequency, $\Theta$ = angle between external magnetic field and $\underline{k}$ vector of the HF wave; + for ordinary (o), - for extraordinary (x) HF mode). The electron collision frequency, $\nu_e$, is proportional to the neutral density and to the electron temperature, $T_e$. The peak altitude thus increases with decreasing $f_o$, with increasing $T_e$ (i.e. with increasing ERP), and with a change of the HF mode from x to o. The $T_e$ maximum increases with decreasing $f_o$ and is larger for x-mode than for o-mode heating. The width of the $T_e$ maximum is larger for higher $f_o$ and o-mode heating. $T_e$ as a function of ERP shows a weak increase with ERP for small ERP's (rotational excitation regime), followed by a very strong increase (runaway regime), and again a weak increase thereafter (vibrational excitation regime) (see STUBBE and KOPKA, 1979).

(2) Source current: The source current at any given altitude is proportional to the driving dc electric field strength, $E_o$, and to the electron density, $N_e$. It is approximately proportional to the amplitude of the electron temperature modulation, $\Delta T_e$, caused by the amplitude modulated HF wave. $\Delta T_e$ depends strongly on $\omega\tau$ ($\omega = 2\pi f$, $\tau$ = electron cooling time). In the lower D-region we have $\omega\tau \ll 1$ which means that $T_e$ is fully modulated, i.e. $\Delta T_e \approx 1/2 (T_{e2}-T_{e1})$ ($T_{e2}$, $T_{e1}$ = electron temperature belonging to the maximum and minimum HF power within one modulation cycle, respectively). In the upper D-region, on the other hand, we have $\omega\tau \gg 1$, leading to $\Delta T_e \approx 1(T_{e2}-T_{e1})/2\omega\tau$. For the modulation frequency range under consideration, $\Delta T_e$ is independent of f up to about 70 km altitude. The $\Delta T_e$ maximum and the height of the maximum increase with decreasing f. Due to the nonlinear relation between $T_e$ and ERP, $\Delta T_e$ should depend not only on the difference between maximum and minimum ERP within one modulation cycle, but also on the average ERP. In particular, $\Delta T_e$ should decrease with increasing average ERP once the runaway regime is passed.

(3) Self-absorption of HF wave: Since the absorption coefficient of a HF wave depends on $T_e$, i.e. on ERP, the relation between energy flux, S, and ERP is not linear. Above the altitude where $f_o \mp f_L \cos\Theta = \nu_e$, S increases more slowly than ERP. This adds another nonlinear contribution to the dependence of $T_e$, $\Delta T_e$, or source current on ERP.

(4) Phase spreading: If the vertical dimension of the source region, d, exceeds half the wavelength of the generated ELF-VLF wave, destructive or constructive interference of waves originating at different altitudes takes place. Minima occur at frequencies obeying $d=n\lambda(f)$ ($\lambda$ = wavelength, n=1,2,...), while the intermediate maxima decrease with increasing n. Phase spreading thus leads to an overall decrease of B with increasing f. L-mode waves are not affected by phase spreading because their refractive index is small, but R-mode (whistler mode) waves can be affected if they are generated at altitudes where $N_e$ is large enough for the refractive index to considerably exceed 1. The required electron density is of the order $10^4$ cm$^{-3}$ for f = 1 kHz, less for higher, more for lower frequencies.

(5) Attenuation of ELF-VLF waves: At altitudes where the electron gyrofrequency is of the order of the collision frequency or exceeds the collision frequency, the L mode wave is heavily attenuated for sufficiently large electron densities. For f = 1 kHz, attenuation becomes prohibitive if $N_e$ exceeds about $10^5$ cm$^{-3}$. The attenuation increases with increasing f. The generation of L-mode waves is thus restricted to the lower portion of the D region, while R-mode waves can be generated at any altitude.

(6) Mode coupling: Since the vertical scale lengths for electron density and collision frequency changes are much smaller than the free space wavelength, mode coupling should be significant, even though the critical coupling condition cannot be satisfied for the frequency range and the geometry of our experiments. Inspection of Equ. (19.2) of BUDDEN (1961) shows that mode coupling should be strongest in the vicinity of the X=Z level ($X = \omega_e^2/\omega^2$, $Z = \nu_e/\omega$) since Max(X,Z) >> 1 and since the scale lengths for X and Z are of the same order of magnitude.

(7) Wave guide resonance: Constructive interference of the primary ELF-VLF wave and the secondary earth-ionosphere reflected waves should give rise to approximately equally spaced maxima in the B(f) curve. Since the horizontal dimension of the radiating ionospheric portion (~ 25 km) is typically much less than the free space wavelength, B should drop as 1/r (r = distance from the source region), provided $2\pi r \gg \lambda$. Otherwise, B drops more sharply than 1/r. Thus, the enhancement of the maxima relative to the average level is at the most

$$\sum_{n=o}^{\infty} \frac{1}{(2n+1)} R_E^n R_L^n$$

($R_E$, $R_L$ = earth and ionosphere reflection coefficient, respectively). It is assumed in this simple expression that the source altitude, $z_o$, and the reflection altitude are equal. The maxima occur at the fre-

quencies $f = nc/2z_o$ (n = 1,2,...). With $z_o$ = 75 km, which is probably a reasonable guess, the first maximum occurs at 2 kHz.

Although all of the mechanisms and agents discussed here are simple to understand, their joint action may lead to very complicated B(f) curves, and it will be difficult to interpret any given B(f) curve in a unique fashion. A detailed knowledge of the $N_e(z)$ profile would be required for this task, but unfortunately electron density profiles were not available to us for the period of the experiments reported here.

Let us now turn back to the experimental results. In looking through Figs. 1 - 4, we notice that almost all of the curves possess very pronounced peaks, roughly at multiples of 2 kHz. Phase spreading of the R-mode wave, in conjunction with mode coupling, and wave guide resonance are possible candidates to explain this feature. Phase spreading, however, should be much more variable, and it would be difficult to explain why the first maximum almost always lies close to 2 kHz. We therefore tend to believe that the main peaks in the B(f) curves are due to wave guide resonance. Intermediate maxima, which can be seen in some of the curves, could however be due to phase spreading. Since the results shown here were collected within 4 days, it is well possible that the ionospheric conditions were rather similar within these days, and it is likely, therefore, that at other periods phase spreading could turn out to be more important. Previous results (STUBBE, KOPKA and DOWDEN, 1981), obtained with one loop (and thus not decomposed into R- and L-mode), give support to this expectation.

Another consistent feature is the striking similarity between the R and L curves. This speaks for the importance of mode coupling. Without mode coupling, we would expect widely different R and L results because of the large differences in the refractive indices. Fig. 4 shows the two most dissimilar cases found in our Oct. 81 data, but even there a correspondence of the main features exists.

Fig. 1, showing B(f) for (100/0), (50/0) and (100/50) modulation, depicts a typical case: The (50/0) sweep is more than half as strong as the (100/0) sweep and is also stronger than the (100/50) sweep. This can be understood in terms of the self-absoption mechanism and of the nonlinear relation between $T_e$ and ERP as outlined in section (1).

In Fig. 2, a comparison is presented of B(f) for x-mode and o-mode heating. We notice that x-mode heating causes much stronger ELF-VLF signals than o-mode heating. The general features of the two sets of curves, however, are quite similar. Only the maxima around 5 kHz, appearing in the o-mode curves, are absent in the x-mode curves. Since x-mode heating is more efficient than o-mode heating around the altitude where the $T_e$ peak occurs, but less efficient at higher altitudes, we may conclude that Fig. 2 corresponds to a situation in which the source current peak lies close to the $T_e$ peak. It is conceivable that in an ionosphere with less ionization in the lower D region and more ionization in the upper D region o-mode heating gives rise to stronger ELF-VLF signals than x-mode heating, but this remains to be seen in future experiments.

Fig. 3 shows two atypical cases. While usually the first two peaks in the B(f) curves are of comparable strength, we have here a clearly dominating second peak in the upper panel and a dominating first peak in the lower panel. Such transitory behaviour lasts for about 30 to 60 min, whereupon the B(f) curves return to their normal shapes in which they may persist for many hours.

Recently we have been able for the first time to detect ELF signals at frequencies around 10 Hz, using the micropulsation loops described above. Fig. 5 shows a spectrum of such in the upper panel and B versus time, obtained with a synchronous detector with 1 Hz bandwidth, in the lower panel. From what we have learned thus far, these signals, when they occur, can be as strong or even stronger than the ELF-VLF signals in the hundreds of Hz to several kHz range. However, while the latter can be excited at any time when the magnetometers indicate the presence of an ionospheric current, the first require rather special ionospheric conditions to be excited. We have not yet been able to fully determine these conditions, but it appears that strong magnetic disturbances are not favourable, probably because they are accompanied by strong ionization in the lower D region. This would prevent efficient heating of the upper D region and E region from where these signals are expected to originate.

REFERENCES

BUDDEN, K.G., 1961, "Radio waves in the ionosphere", University Press, Cambridge.

STUBBE, P., and KOPKA, H., 1979, "Ionospheric modification experiments in northern scandinavia - A description of the Heating project", Report MPAE-W-02-79-04, Max-Planck-Institut für Aeronomie.

STUBBE, P., KOPKA, H., and DOWDEN, R.L., 1981, " Generation of ELF and VLF waves by polar electrojet modulation: Experimental results", J. Geophys. Res. 86, 9073-9078.

OCT. 7, 1981, 01.01 - 01.04 UT

$f_o = 2.759\,MHz$, o-mode, ERP = 260 MW
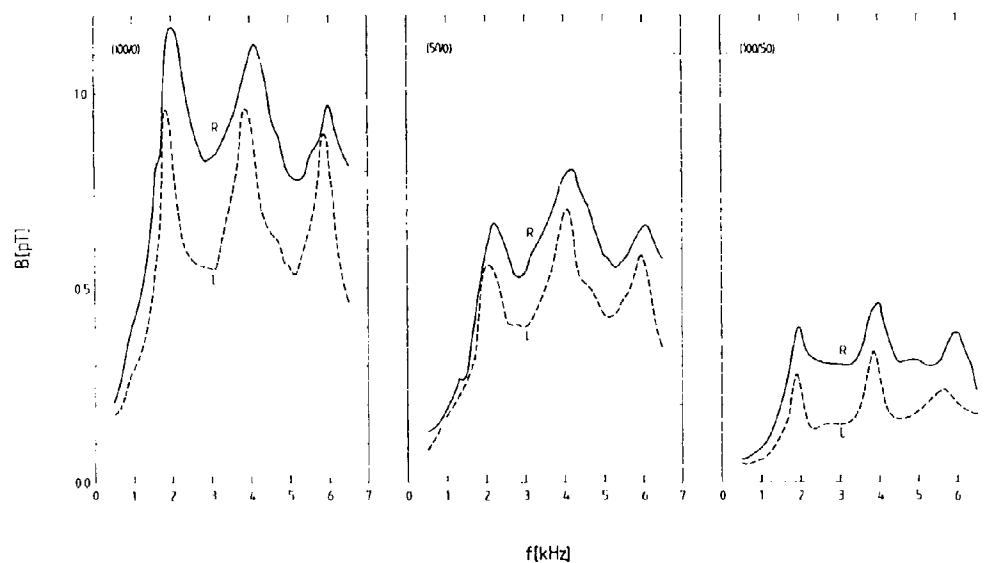


Fig. 1

R- and L-mode amplitude vs. modulation frequency for (100/0), (50/0), and (100/50) sweeps.

OCT. 9, 1981

$f_o = 2.759\,MHz$, ERP=260 MW, (100/0)

18.27 UT, x-mode          18.24 UT, o-mode
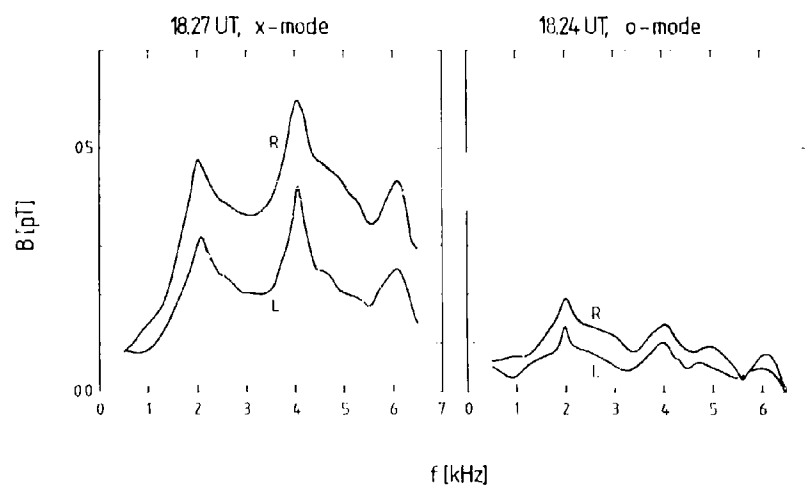


Fig. 2

R- and L-mode amplitude vs. modulation frequency for x- and o-mode heating.

OCT. 10, 1981
19.54 UT
$f_o = 2.759$ MHz
x-mode
ERP = 225 MW
(100/0)

OCT. 10, 1981
19.28 UT
$f_o = 2.759$ MHz
x-mode
ERP = 225 MW
(100/0)
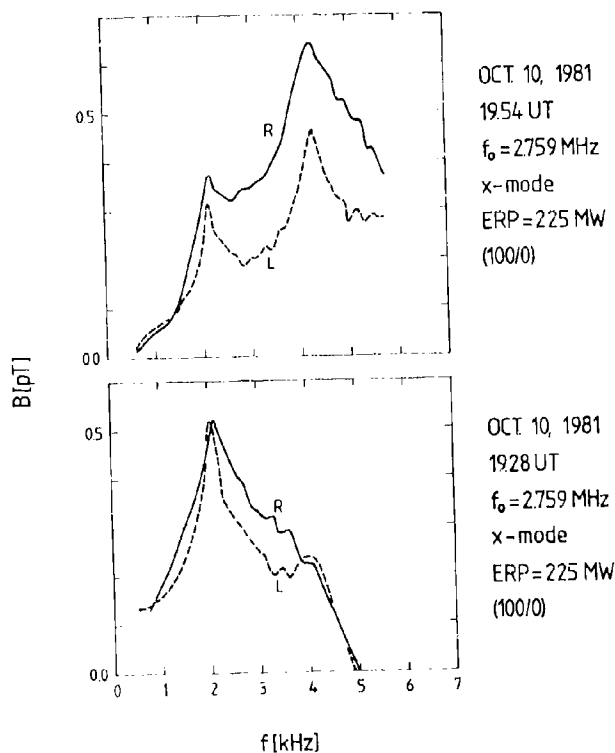
Fig. 3

R- and L-mode amplitude vs. modu-
lation frequency; two atypical cases.

OCT 10, 1981
19.08 UT
$f_o = 2.759$ MHz
x-mode
ERP = 225 MW
(100/0)

OCT. 7, 1981
01.53 UT
$f_o = 2.759$ MHz
o-mode
ERP = 260 MW
(100/0)
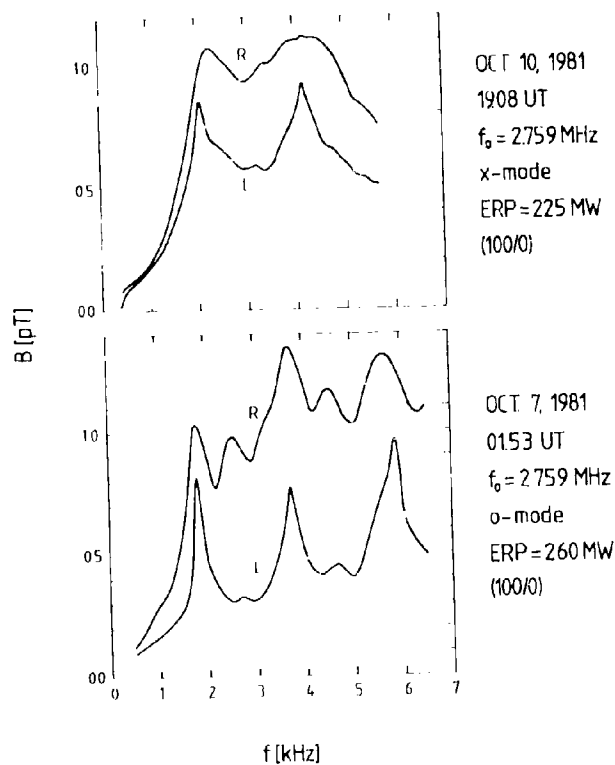
Fig. 4

R- and L-mode amplitude vs. modu-
lation frequency; two cases of
dissimilar behaviour of R- and
L-mode.

SEPT. 9, 1981

$f_0 = 2.759$ MHz    x-mode

ERP=260 MW    f=12 Hz
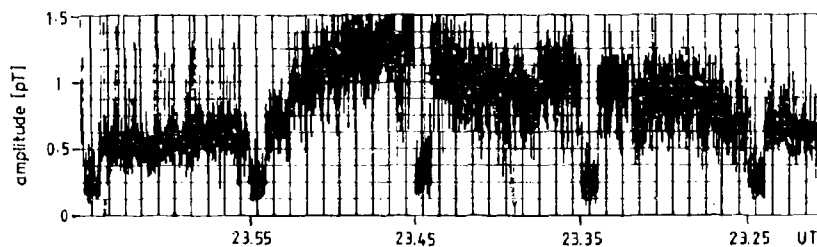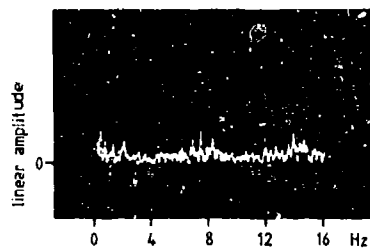


Fig. 5

Upper panel: ELF spectrum, showing a sharp line at the the
modulation frequency 12 Hz. Lower panel: Amplitude of 12 Hz
signal vs. time. The heater was on 9 minutes and off 1 minute.

DISCUSSION EPP FALL 81 MEETING
MEDIUM, LONG, AND VERY LONG WAVE PROPAGATION
(AT FREQUENCIES LESS THAN 3000 KHZ)


SESSION 1

PAPER: 1 - The Propagation Medium - An Overview
AUTHOR:J. S. Belrose
COMMENTER:E. R. Schmerling
QUESTION: We all understand what a disturbed day is. What is your criteria for a quiet day? Many years ago Dr. Becker showed an example of the quietest nights he could find using the Kp index as a criteria. On two occasions during the course of the night, the bottom of the ionosphere was lifted up and lowered by 50 kilometers in a period of 3 hours.
RESPONSE:It is easy to pick a quiet day in summer, its a day under regular solar control and there have been no geophysical disturbances, mainly measured by the parameter of magnetic storminess for several days prior. In winter it is not very easy because as I said there is a variability that goes on which is not correlated with magnetic activity. We have winter days of anomalous absorption during periods when there has been no magnetic storms for ten to twenty days before-hand. Our quiet day was a day: (1) with low electron densities at low heights; (2) no magnetic storms for at least 15-20 days before; (3) no outbursts from the sun on the day chosen; and (4) the electron production and loss processes were under regular solar control, that is the ionization density varied regularly with the solar zenith angle. The first criteria was the one that selected the kind of days we called "quiet."
The parameter observed was the ratio between the two magneto-ionic components in a partial reflection experiment $A_x/A_o$ at 76 kilometers.
In other words the days chosen had small electron densities below 76 kilometers.


PAPER: 2. STUDIES OF THE D-REGION BY THE PARTIAL REFLECTION OF MF-RADIO WAVES
AUTHOR: W. Flood
COMMENTER: J. S. Belrose
COMMENT: I would agree with Prof. Flood that some echoes partially reflected from the D-region have the appearance of volume scattering. This is desirable since the experiment works best if you have a continuous distribution of echoes from all heights. When we were studying quiet days, however, some of the profiles I showed where determined on quietest days when the ionosphere was under regular solar control, and there were no disturbances, many of these days were plagued by reflections from discrete heights. You have both kinds of data. It really depends on what is going on the D-Region. Of course this is over Ottawa. I know Ottawa data best. It is very difficult to unambiguously interpret the data. When you see there are small inflections on the $A_x$ variation as a function of height which occur regularly, we have been very careful analyzing the data to deduce electron density under those conditions An additional problem is the finite pulse width. Some of our data were deconvoluted to get rid of the pulse width problem, but you cannot arbitrarily deconvolute data when you have preferred heights. If you read the Coyne and Belrose paper and the Montbreand and Belrose paper on the subject addressing quiet day electron densities and effective electron loss rates, you will find that we were very careful on how we analyzed the data in presence of preferred heights.
RESPONSE: I have looked at some data from Brazil and more recently from Red Lake, Canada, and also some data from Montpeil, New Zealand. If I exclude the data from Red Lake, most of it seems to follow the Raleigh hypothesis which would be expected for volume scattering. Looking at the February eclipse data of 1979, its remarkable that anyone could operate the experiment in Canada. I congratulate you on being able to do that. That data is certainly very different from anything I have ever seen before.


PAPER: 2. STUDIES OF THE D-REGION BY THE PARTIAL REFLECTION OF MF RADIO WAVES.
AUTHOR: W. Flood
COMMENTER: T. B. Jones
QUESTION: 1. One of the major criticisms of the cross-correlation analysis is the assumption of a specular reflection. The Fourier analysis you have applied to some extent overcomes this difficulty. Could you please comment on the influence of multi-reflection on your data and on the integration times you applied to your data? Did you consider isolating the dominant signal component by Doppler filtering or some other technique?
2. Did your results give any indication of a turbulent layer at the 80-85 kilometer level? If so how did you interpret the results from such reflections?

RESPONSE: 1. If the reflections from the upper atmosphere were truly specular, the angular spectrum of the downcoming waves would be a delta function (not necessarily at the zenith angle) and the magnitude of the spatial cross-correlation function would be unity-at least over the range of antenna separations normally used in drift experiments. Consequently ionospheric drifts could not be measured. The drift experiments require the detection of the drift of a diffraction pattern implying something more than the specular reflections. The spatial correlation function should be narrow but not so narrow that wide angular spectra are also implied. Wide angular spectra would imply altitude smearing in the drift measurements. In this paper we have seen that above 80 Km the average half power semi-cone angle is approximately $13°$ which implies that even for very short pulse lengths, echoes are being received over an altitude range of $R(1-\cos 13°)$. Where R is the nominal altitude of the echo.
In passing I note that cone angle-altitude smearing might be responsible for the two component drift velocities reported by the investigation at Tromso.
Integration times for cone angle as well as partial reflection data varied from 10-20 minutes. Single magneto-ionic component D-Region echoes faded relatively slowly and five minutes of data "integration" was necessary to get sufficient independent samples for meaningful averages. The longest runs were restricted to 20 minutes. It was difficult to find periods which were even quasi-stationary for longer than 20 minutes.

I should comment that during the partial reflection experiment we noted times when during a 20 minute run, successive five minute runs showed quite different mean values of $A_0$ for example. Yet the $A_x/A_0$ ratios for each five minute period did not differ substantially. I think ten minute averages are better than five minute averages.

In terms of isolating the dimensional signal component by Doppler filtering, I suppose you are referring to how we checked out the von Biel system by using "quiet" E-Region echoes. In that case we selected the obviously strongest echo (stronger by 10's of Db's) which had a range extent of less than (say) 6 kilometers. No Doppler filtering was used although these echoes (polarized transmission and reception) faded very slowly. For these selected echoes twenty minute averages were employed.

2. . am not clear as to what you mean by a turbulent layer at 80-85 kilometers. The amplitude distributions I've reported indicates that volume scatter from fluctuations in refractive index is the most likely mechanism for D-Region backscatter at all altitudes. Turbulence can easily be adduced as the source of the refractive index fluctuation. This is not to say that the turbulence is equally strong at all altitudes. If there were a level of intense turbulence in the region between 80-85 kilometers one might expect an enhanced return at these altitudes. My first recollection of the data is that in terms of $A0_h$ the mean backscatter amplitude as a function of altitude, there is no indication of any such strong turbulence region. However on my return home I will review the data and if I find any such indication I will notify the editor so it can be noted in the proceedings

PAPER: 3. VLF/LF PULSE REFLECTION MEASUREMENTS OF THE POLAR D-REGION DURING QUIET AND DISTURBED IONOSPHERIC CONDITIONS
AUTHOR:  J. P. Turtle
COMMENTER: E. R. Swanson
QUESTION: The absolute heights you give depend on the calculation of the groundwave delay. Given the extremely low ground conductivity in the area, calculation of ground wave delay could be difficult or perhaps somewhat uncertain. Is this a practical limitation in height accuracy?
RESPONSE: Our transmitter and receiver in Greenland are separated by 106 kilometers, and due to the fact that the skywave travels a longer path, because of our short pulse, the ground wave is received considerably before the sky wave and for this short separation between transmitter and receiver we do not need to calculate the transmission time for the ground wave. I had not made clear how close our stations were to each other.

PAPER: 3. VLF/LF PULSE REFLECTION MEASUREMENTS OF THE POLAR D-REGION DURING QUIET AND DISTURBED IONOSPHERIC CONDITIONS
AUTHOR:  J. P. Turtle
COMMENTER: J. S. Belrose
COMMENT: I would like to comment on two points relating to your observations in winter, where at Thule the sun never rises. These comments are based on our partial reflection observations made at Resolute Bay during the Arctic winter and observations made at Cambridge, England where the phase height of reflection of VLF waves (16 Hz) steeply incident on the ionosphere was measured.
The first point is that while electron production rates at night are small, they are sufficient to maintain electron densities large enough to reflect VLF waves. Ionization of NO by Lyman alpha in the night glow is the most likely source of ionization, and therefore we would expect that there would be a small daily variation of VLF phase heights at night in December. When the night is longest and the variation can be observed.
The second point relates to the reflection heights at night in winter and summer. Since the height of a constant pressure isopath is lower in winter than in summer we can expect that the reflection heights will be lower in winter than in summer. A given electron production rate occurs at a given pressure level rather than a given height.

PAPER: 3. VLF/LF PULSE REFLECTION MEASUREMENTS OF THE POLAR D-REGION DURING QUIET AND DISTURBED IONOSPHERIC CONDITIONS
AUTHOR:  J. P. Turtle
COMMENTER:  W. C. Bain
QUESTION: You say in your paper that in undisturbed conditions there will be no reflections from heights below 70 km. However in the literature you have given results taken on your system in the Eastern United States and they showed marked reflections at these heights. I believe that in the U. S. you had a longer path-length. Do you think that the absence of these reflections in Greenland is due to the short path used there or to a real difference in the ionosphere?
RESPONSE: The measurements referred to in the Eastern U. S. which show daytime reflections below 70 km were made on a 260 km transmission path. The Greenland measurements were made on a 106 km path with thus a much steeper ionospheric incidence angle. The absence of observed reflections below 70 km in Greenland is most probably due to the steep incidence angle rather than a real ionospheric difference.

PAPER 3. VLF/LF PULSE REFLECTION MEASUREMENTS OF THE POLAR D-REGION DURING QUIET AND DISTURBED IONOSPHERIC CONDITIONS
AUTHOR:  J. P. Turtle
COMMENTER:  F. J. Kelly
COMMENT:  I would like to comment on the scattered Lyman Alpha effect that contributes to the

D-Layer. The normal terminology for the scattering body is the Geo-Corona. i.e. The local hydrogen gas cloud around the earth.

PAPER: 3. VLF/LF PULSE REFLECTION MEASUREMENTS OF THE POLAR D-REGION DURING QUIET AND DISTURBED IONOSPHERIC CONDITIONS
AUTHOR: J. P. Turtle
COMMENTER: J. Aarons
QUESTION: What is the effect of solar cycle on your data?
RESPONSE: A preliminary comparison of our VLF ionosounding data between 1976 (low solar activity) and 1980 (high solar activity) has been made. This indicates somewhat lower reflection heights but similar reflection coefficients with increasing solar activity.

PAPER: 3. VLF/LF PULSE REFLECTION MEASUREMENTS OF THE POLAR D-REGION DURING QUIET AND DISTURBED IONOSPHERIC CONDITIONS
AUTHOR: J. P. Turtle
COMMENTER: J. B. Reagan
QUESTION: The data presented for the June 6, 1979 SPE indicate that no diurnal variation occurs at approximately 60 km altitude even though such variation occurs during a normal day. Chemistry modeling and electron density measurements made in the D-Region during the large SPE of 4 August 1972 clearly indicate a diurnal variation (see the paper #33 by Reagan et al at this meeting) at 60km altitude. Could you explain this apparent discrepancy in results?
RESPONSE: The reflection of the VLF ionosounding pulse occurs at an electron density of about 200-300/cm.³. The diurnal variation referred to by Reagan (Figure 5 Paper 33) remained well above this level. It is possible that the VLF ionosounder is too sensitive to have recorded this variation.

PAPER: 4. THE INFLUENCE OF PRECIPITATING ENERGETIC PARTICLES ON THE PROPAGATION MEDIUM
AUTHOR: W. L. Imhof
COMMENTER: F. J. Kelly
QUESTION: 1. In cosmic rays I understand there is a phenomenon called a Forbush decrease, which is supposed to be typical of disturbed conditions?
    2. Is there some computer program generally available to give models of the ionosphere versus incident particle?
    3. On the solar protons you mentioned a cutoff latitude. Should there also be a longitudinal variation?
    4. Does the model in which cutoff latitude varies with $k_p$ depend on the whole magnetic field flipping and the magnetopause changing its location?
    5. I always thought of the cutoff latitude as being dependent on the particle energy?
    6. How is that affected by a solar flare?
RESPONSE: 1. Yes, this is correct, it does have an effect on the cosmic ray density.
    2. The energy deposition profiles that I showed were calculated with some computer programs available at our laboratory (called AURORA programs), this takes into account the electron scattering as well as the Bremstrahlung produced by the electrons. There are also codes available for calculating the energy deposition from solar protons as well. These are generally available.
    3. There is a longitudinal variation in the sense that the magnetic latitude is at different geographic latitude depending on the longitude at which you are located, because of the offset in the earth's magnetic field. There is also of course a local time variation.
    4. The data I showed were actual measurements and just a least squares fit to the data. There are calculations which have been made by Smart and others, that do calculate this cutoff latitude. It generally has been consistent with measurements.
    5. The cutoff latitude is just in simple terms a matter of the gyro-radius of the particles and how low in latitude they can have access, but the local time variations do depend on the details of the earth's magnetic field.
    6. The earth's magnetic field also changes and there is a local time dependence.

COMMENT:UNKNOWN :The phenomena that changes the cutoff latitude during a large solar particle event is the fact that the low energy plasma from the sun disturbs the earth's magnetic field greatly. It opens up the polar cap and brings it down to lower latitudes. The high energy solar particles can then penetrate.

PAPER: 4. THE INFLUENCE OF PRECIPITATING ENERGETIC PARTICLES ON THE PROPAGATION MEDIUM
AUTHOR: W. L. Imhof
COMMENTER: Mr. P. A. Kossey
QUESTION: There is a latitudinal effect. Proton dumps that occur at low latitudes, particularly around the South Atlantic anomaly where the magnetic field is particularly weak. These effects I believe tend to occur after the effects are noticed in the Polar Region. Do you have an estimate on what the relative effect might be in the vicinity of the south Atlantic anomaly?
RESPONSE: Those events don't affect directly the entry of solar protons, but are more associated with protons trapped in the earth's radiation belts where the field lines are such that high energy protons can get to the lowest altitude in the region of the south Atlantic anomaly. At the times of large magnetic storms although it is not known in detail there is evidence of more precipitation occurring. But there are of different origin than the direct access from the sun.

PAPER: 5. VLF/LF PULSE REFLECTION STUDIES OF THE DAYTIME C LAYER OF THE LOWER IONOSPHERE
AUTHOR: MR. P. A. Kossey
COMMENTER: J. B. Reagan
QUESTION: The C-Layer behavior that you describe including the diurnal, seasonal and solar cycle variations may be explained by the variations in atomic oxygen at the reflection

altitudes that you measure rather than changes in cosmic ray intensity. Neutral and ion chemistry modeling work performed at our laboratory has shown the important relationship between the concentration of atomic oxygen in the lower D-Region and the resulting electron density.
RESPONSE: In this complex region of the ionosphere I suspect that there are a number of processes which contribute to the variability of our pulse reflection data. Your comment on atomic oxygen concentrations and how changes related to them may partially account for our results is very interesting. However, I believe that in addition to such effects, there are changes in the cosmic ray intensity. Particularly over the solar cycle and with latitudes which also contribute subst.tially to the variability in the pulse reflection data.

PAPER: 5. VLF/LF PULSE REFLECTION STUDIES OF THE DAYTIME C-LAYER OF THE LOWER IONOSPHERE
AUTHOR: P. A. Kossey
COMMENTER: W. C. Bain
QUESTION: I should like to comment on the relation between some of these results and earlier measurements on VLF Propagation. I think Kossey reported that he saw much less of this layer at 63 kilometers in the summer than in the winter. On the old measurements of propagation at 16KHz near vertical incidence, in fact, the signals were a good deal stronger in the winter than in the summer. Now if you ascribe this difference to the presence of some absorbing layer which is a bit lower down than the main reflection level for steep incidence waves, this would indicate that the C-Layer was rather weaker in the winter than in the summer which seems to be the wrong way around to tie up with these observations and clearly any explanation would have to take this into account. I might just mention that though Kossey suggested that perhaps the ionization had moved downwards in the summer from 63 Kms., perhaps a similar effect could be obtained by spreading it out so that the gradients were rather smaller in the summer.

RESPONSE: Yes, I think that's right. I wanted to make a very clear point that we are observing pulse reflections and what we see is in some ways tied to the geometry of the experiment and the frequencies contained within the pulse, which we can translate then if you like into an effect of conductivity that we might be able to detect or not detect by pulse reflection. The absence of reflection could be either explained by changes in density with altitude or in terms of reflection properties, change in gradient. This is a very important point you made.

PAPER: 5. VLF-ATMOSPHERICS AS A TOOL FOR PROBING VLF-PROPAGATION CONDITIONS
AUTHOR: J. E. Schafer
COMMENTER: E. R. Swanson
QUESTION: With your multiple receiver locations you should also be able to locate thunderstorms by the intersections of bearing lines. Has this been done and compared with the results you usually obtain?

RESPONSE: By cross-bearings, yes. That has been one of our main aims. We have our station; at such distances that we can make cross bearings, as many as possible, to optimize our VLF propagation model. Thats the main aim, to use these exact determinations of location for a better understanding of the propagation model.

PAPER: 6. VLF-ATMOSPHERICS AS A TOOL FOR PROBING VLF-PROPAGATION CODITIONS
AUTHOR: J. E. Schafer
COMMENTER: I. Fonteyne
QUESTION: La question que je voulais poser c'était sur le détermination de l'angle de l'azimuth de l'éclaire? Comment, je n 1 pas bien compris quel est le principe qui dans l'antenne fait que on peu déterminer l'azimuth de l'antenne, la direction dans la quelle est l'eclair?
       La deuxieme question qui est liée a cela, est-ce-que la dispersion que l'on voit sur l'azimuth et la courbe en cloche Gaussian, n'est pas simplement une erreur-l'erreur de mesure de la direction, autrement dit est-ce-que la zone d'éclair n'est pas vraiment très constante, plus constante que vous ne le pensiez, et est-ce-que la dispersion, la courbe en cloche "Gaussian" que nous avions n'est pas due a l'erreur de mesure.
RESPONSE: 1. We used conventional direction finding techniques with two crossed loops and the basis of such measurements are of course the fact that the magnetic field is horizontal and directed orthogonal to the direction of propagation.
       2. It might be possible of course that we have some measurement errors but as you have seen, the deviations to the right and to the left side are more or less equal. The shape of th. distribution can be quite well fitted with a normal distribution. That shows us that the errors are more or less random. It does not matter if there are errors, if we have sufficient pulses, say two per minute for 20 minutes. That is often enough to determine the peak value. Random disturbances should not matter.

PAPER: 7. THE HIGHER ORDER MODE IN THE LOWER VLF-RANGE MEASURED AT MEDIUM DISTANCES
AUTHOR: W. Harth
COMMENTER : B. Burgess
COMMENT: The round trip delay measurements that you showed are compared with Wait's night time model. They seem to be similar to measurements we have made on the OMEGA transmissions of 10.2 to 11.3 and 13.6 Kilohertz. The measurements we made at night time flying eastward indicated that the modal interference extended out to 6 or 7000 kilometers. Note that Wait's models did not fit that. I am wondering how dependent you are on the model for interpretation of results. It might be a point worth looking into.
RESPONSE : Of course there are a lot of models which are more sophisticated than Wait's model, but the advantage of Wait's model is that it is a simple model and we can work with it. On the other hand thunderstorms are not fixed transmitters. The change of the transmitter itself and also the geographical distribution and size of the cloud and the source itself give us to much inaccuracy in our calculations. So we can say the model is good enough for practical purposes.

PAPER: 7. THE HIGHER ORDER MODE IN THE LOWER VLF-RANGE MEASURED AT MEDIUM DISTANCES
AUTHOR: W. Harth
COMMENTER: E. R. Swanson
COMMENT: I would not particularly question your application of Wait's results for daytime conditions. However, at night I share some of the concern of Burgess. In particular the mode constants show complicated variation with path orientation and latitude.

PAPER 8 : SIMULATED WAVE PARTICLES INTERACTIONS DURING ELF-VLF TRANSMISSION
AUTHOR : M. Garnier
QUESTIONER : W. Harth
QUESTION : On your slides was it frequency versus power spectrum or time and occurrence?
RESPONSE : It was frequency versus spectral amplitude.

PAPER 9 : GENERATION OF ELF AND VLF WAVES BY MODULATED HF HEATING OF THE POLAR ELECTROJET
AUTHOR : P. Stubbe
QUESTIONER : R. H. Doherty
QUESTION : Does this phenomena occur all the time or sometimes, if sometimes what is the percentage of time.?
RESPONSE : I should have said that. It depends very much on the magnetic activity. The correlation between VLF strength and magnetic activity as far as we see it on our magnetometer is an overall good correlation, though not in detail. When there is strong magnetic activity then we have strong signals. If we want to have strong signals at low activity then we have to work with a higher power. We get some signal almost all the time it is seldom that it is dead silent, but the strength of the effect depends strongly on the magnetic activity, that is on the strength of the current flowing in the E-Layer.

PAPER 9 : GENERATION OF ELF AND VLF WAVES BY MODULATED HF HEATING OF THE POLAR ELECTROJET
AUTHOR : P. Stubbe
QUESTIONER : J. S. Belrose
QUESTION : 1. Was it day or night when you made your observations?
        2. Thinking back to the early days of the Luxemburg experiment, where a high power low frequency radio transmission modulated another low frequency transmission, the time constant of the ionosphere with which the electron temperature can follow the frequency modulation on the radio wave is on the order of 40 microseconds at 70 Kilometers and 2 milliseconds at 85 Kilometers. Two Kilohertz was roughly the maximum frequency at which the electron temperature could follow the radio waves at heights around 85 kilometers. You were showing frequencies well in excess of that.
RESPONSE : 1. That is not critical. When there is magnetic activity we get this effect.
        2. These are the characteristic times based on the coefficients one finds in current literature and so represent the best of present knowledge in these characteristic times. It goes from $10^{-5}$ sec at 60 kilometers to $10^{-3}$ at 90 kilometers. From the standpoint of characteristic time there is no reason why we should not be able to excite a few kilohertz.

PAPER 9 : GENERATION OF ELF AND VLF WAVES BY MODULATED HF HEATING OF THE POLAR ELECTROJET
AUTHOR : P. Stubbe
QUESTIONER : T. B. Jones
QUESTION : Very interesting work. I wonder whether it was possible to excite some of these VLF waves into the Whistler Mode and whether you had looked for this?
2. Where is the conjugate point to Tromso? If you looked in the other hemisphere?
3. If people can excite whistlers from places like Siple it seems you could certainly do it with "an antenna" that high up in the atmosphere.
RESPONSE : You mean upward propagating waves. Our colleagues at Lyngby, Denmark who are working with GEOS data looked into this. But it was at an early stage when we had relatively little power. They looked at the spectrograms and did not integrate over a long period. On this basis my answer is no. They had not found anything.
2. The conjugate point is in Antarctica. Dr. Dowden who is involved in this work has access to a station at Mawson which is 600 Kilometers from the conjugate point, this will also be activated for future work
3. From a power point of view I would say this is much more than Siple can do. But this does not mean the effects are much more exciting. I would say the number of ducts that we find at L=6 is so low that it is a rare event to get to waves into the magnetosphere.

PAPER 9 : GENERATION OF ELF AND VLF WAVES BY MODULATED HF HEATING OF THE POLAR ELECTROJET
AUTHOR : P. Stubbe
QUESTIONER : B. Burgess
QUESTION : You were measuring on the ground at a distance of 17 Kilometers from the transmitter, but have you made observations at other distances?
RESPONSE : We made measurements at Andalsness and Kiruna which are at distances of 100 and 300 km, and Penn State. The Penn State observations were not certain.

# OVERVIEW OF ELF PROPAGATION

Peter R. Bannister
Submarine Electromagnetic Systems Department
Naval Underwater Systems Department
New London, Connecticut, 06320 U.S.A

## SUMMARY

The extremely low frequency (ELF) band (30 to 300 Hz) has serious deficiencies compared with conventional radio frequencies. It is characterized by a very restricted bandwidth (low data rates) and an extremely large wavelength (inefficient antennas). For special applications, however, involving some of the propagation paths conducted through rock or sea water, it offers the possibility of communication where conventional bands offer none. In the case of long-range communication with submerged submarines, it can also provide low-loss highly-stable propagation in the earth-ionosphere waveguide.

This paper presents a general overview of ELF propagation. It also compares recently derived simple-form approximate expressions (relating ELF propagation constants to realistic-ionospheric conductivity profiles) with experimentally derived results for daytime and nighttime propagation conditions. Current (unpublished) data measured, simultaneously, in Connecticut and other, more distant, locations are presented to elucidate anomalous ELF nighttime field strength degradations.

## PROPAGATION IN THE EARTH-IONOSPHERE WAVEGUIDE

The energy of propagation radio waves is principally confined to the shell between the earth and ionosphere; this space is frequently denoted as the terrestrial waveguide. For long waves, the effective waveguide height, h, is comparable to a free space wavelength, $\lambda$, and the characteristics of wave propagation are determined by the properties of the guide boundaries.

A number of propagating modes have distinct cut-off frequencies similar to those in the microwave range. However, unlike the highly conducting guides of the microwave range, the upper boundary of the terrestrial waveguide is diffuse and a poor conductor; the finite conductivity of the earth's surface is also important. In the ELF range, h is less than $\lambda$ and only one waveguide mode propagates. For VLF, h exceeds $\lambda$ and there are several propagating modes. In the LF range, the number of significant propagating modes may exceed twenty.

Several field representations can be used to characterize the terrestrial propagation of radio waves. The fields in a uniform spherical shell between the earth and ionosphere can be expressed as a summation of spherical harmonics, which involves Legendre polynomials and spherical Bessel functions of integer order n. This series converges very slowly. The number of terms required is of the order of $10k_0a$, where $k_0 = 2\pi/\lambda$ and a is the radius of the earth. Although this series is directly applicable in the ELF range, its exceedingly slow convergence may preclude its use at LF.

The Watson transformation changes the series of spherical harmonics into a residue, or mode series, where the fields are expressed using Legendre functions and spherical Bessel function of complex order $\nu$. Each term of the mode series can be identified as an azimuthal wave propagating in the $\theta(=\rho/a)$ direction with a distinct phase velocity and attenuation rate.

At ELF, h is of the order of 45 to 90 km. Because h is much less than $\lambda$, the waveguide is below cut off for all but the lowest order mode (i.e., the TEM mode). The electric and magnetic fields are wholly transverse to the direction of propagation in the TEM mode, with the electric field vertical and uniform and the magnetic field horizontal and uniform. In practice, inhomogeneities and non-uniform surface conditions perturb the ideal TEM field configuration and the result is the quasi-TEM mode.

Attenuation in the earth-ionosphere waveguide at ELF for the quasi-TEM mode is low, on the order of 1 or 2 dB/Mm. The effective conductivity of the ionosphere ($10^{-5}$ to $10^{-7}$ S/m) is usually much lower than that of the ground ($10^{-4}$ to 5 S/m), and so the surface impedance of the ground is typically much smaller than the surface impedance of the ionosphere. Thus, the attenuation in the guide is attributable mainly to power absorption by the ionosphere.

The same principles apply to radiation and propagation in the earth-ionosphere waveguide that apply to radiation and propagation above a conducting half space. The significant difference is the attenuation of the fields in the atmosphere. In the case of the simple conducting half-space, the principal field is essentially detached from the half space, with the result that the weakening it experiences as a result of leakage of its power down into the ground is negligible, for practical purposes. In the case of the waveguide, on the other hand, the wave is bounded above and below by finitely conducting media and is, therefore, strongly coupled to them. The rate of power loss into the conducting media is then no longer negligible compared with the total power carried by the propagating field within the guide. The effect is clearly stated in the expression for the waveguide attenuation rate $\alpha$, where $\alpha$ is seen to be inversely proportional to h. In physical terms, this states that the rate of power leakage out of the guide is proportional only to the intensity of the field in the guide, whereas the rate of power flow along the guide is proportional to the intensity of the field and to the volume of the guide. Thus, as the guide decreases in height, the constant power leakage is being subtracted from a smaller total power flow. More rapid depletion is the result (Burrows, 1978).

Apart from this difference, the same principles apply. The launching of the principal field from a vertical electric current source and a horizontal magnetic current source proceeds as though the walls were perfectly conducting. (The same is true of a horizontal electric current source if it is mathematically represented by its equivalent horizontal magnetic current source.) The principal fields then propagate away from the source region with either negligible attenuation, in the case of the half space, or small but definite attenuation in the case of the guide.

Thus, the principal fields directly provide the vertical electric field, $E_v$, and horizontal magnetic field, $H_h$, at the field point. Secondary field components arise because the surface impedance $\eta_g$ of the ground is not zero. Therefore, the horizontal electric field is equal to $\eta_g H_h$ and perpendicular to the horizontal magnetic field, while the vertical magnetic field is related to the circulation of the horizontal electric field. The specific value of the vertical magnetic field is often uncertain, since it is sensitive to the lateral rate of change of surface impedance. It should be noted that the secondary fields are very small in absolute magnitude compared with the principal fields and are of no practical significance, except in the immediate vicinity of the surface. They are of fundamental importance at the surface, however, because certain ELF antennas depend upon the existence of the secondary field (Burrows, 1978).

When the source of the field point is buried, the vertical field components suffer a jump-discontinuity as the field point descends through the surface, (the level depends on the permittivity, or permeability constrast between the ground and the atmosphere). The horizontal field components, on the other hand, are continuous. Further increases in depth reduces their amplitude in an exponential fashion for a homogeneous ground and, in a more complicated but calculable manner, for a layered ground structure. Completely parallel remarks apply to burying the sources.

The preceding few paragraphs have described the propagation of ELF waves in a planar parallel plate waveguide model of the earth-ionosphere guide. The attenuation in that guide is low enough, however, for round-the-world propagation to occur. The planar model is therefore, inadequate when the distance from the source to the field point is of the same magnitude as, or greater than, the radius, a, of the earth.

The general nature of ELF propagation around the earth has been the subject of theoretical study for many years and is, apparently, well understood. The texts by Wait (1970), Galejs (1972) and Burrows (1978) described the theory in the form accepted today and provide a bibliography of earlier work. Reference may also be made to a special issue of the IEEE Transactions on Communications edited by Wait (1974) and a collection of papers by Bannister, et al. (1980).

There are a number of effects attributable to the curvature of the earth's surface that might be significant. For example, the curvature of the guide may modify the relationship between the various field quantities by introducing a marked radial dependence. Second, the energy guided between the walls has a constant height of wavefront but a width of wavefront that is smaller than if the guide were planar. Thus the guide curvature has the effect of channelling the same amount of power flux through a small cross section, (an effect known as spherical focusing). The result is an increase in the power flux density and, therefore, in field quantities. Third, the closure of the guide around the earth changes it from an infinite structure into a finite one. The field does not simply propagate continuously away from the field point to infinity, as it does in the planar model. Instead, it eventually returns to the source point after one complete encirclement of the earth. In principle, the field continues to circulate indefinitely. This means that the field at any point is the sum of the field at the point arising from propagation over the shorter great-circle path from the source, and that arising from propagation over the longer great-circle path. Subsequent encirclements by the two waves propagating in opposite directions may also contribute. Moreover, if the frequency is such that the wave phase changes by $2\pi n$ (where n is an integer) when it completes one complete circuit, the closed guide is a cavity-in-resonance. A fourth effect is the geomagnetic field, which varies in intensity and direction as the point of observation moves about the earth. At any single location, the geomagnetic field interacts with the changed particles of the ionosphere to produce, in effect, an anisotropic conducting medium. Since the tensor describing the conductivity is not symmetrical, electromagnetic processes involving the ionosphere will not occur in strict conformity with the reciprocity theorem. This effect is made more complicated by the variation in direction of the geomagnetic field from place to place (Burrows, 1978).

It turns out that the first and fourth of these possible effects are not of practical significance. The ionospheric height is of the order of 45 to 90 km, which is only about one one hundredth of the earth's radius. Thus no local effects attributable to the earth's curvature are observed. Also, the electrical mis-match between the atmosphere and the ionosphere is so large at ELF, and the transition between them so abrupt, that very little penetration of the ionosphere occurs. Thus the ionosphere acts so much like a perfect reflector that any effect of the anisotrophy on the guided ELF wave can be shown theoretically to be small (Wait, 1962, pp. 300ff.), and has been measured to be so experimentally (Bernstein et al., 1974; Bannister, 1975).

Since the local effect of the curvature is small, the wave propagates in the curved guide with the same parameters as it would in the planar guide. The only effect of the spherical focusing, therefore, is to increase the power flux density in accordance with the reduction in the area of the wavefront. The width of the wavefront, at a great circle distance from the source, is smaller by the factor $\sin(\rho/a)/(\rho/a)$ than it would have been at the same range $\rho$ in a planar guide. Therefore, the power flux density is increased at this distance by the reciprocal of this factor, and the field quantities by the reciprocal of its square root (Burrows, 1978).

## FIELD STRENGTH CALCULATIONS

The expressions most often employed for calculating the fields in the earth-ionosphere waveguide (radiated by sources near the surface) are based upon a simple theoretical model that assumes the earth and ionosphere to be sharply bounded and homogeneous. But the ionosphere, which has a greater influence on propagation than does the ground, is neither homogeneous nor sharply bounded. Therefore, a question arises concerning the usefulness of a simple model.

It is necessary to know whether there are simple curves showing the variation with frequency of parameters equivalent to those of the h, S, and $\eta_g$ parameters of the simple theory, that can be used to calculate the fields with sufficient accuracy for communication system design. (The real part of S is c/v, the ratio of the speed of light in free space to the wave speed in the guide. The imaginary part is proportional to the attenuation rate in the guide.) The real ionosphere may be essentially different in its properties from a well behaved, sharply bounded model. In fact, theoretical calculations using certain layered ionospheric structures have produced propagation data exhibiting resonant absorption and

strong dispersion (Galejs, 1972, pp. 254ff; Barr 1977; Pappert and Moler, 1978; Pappert, 1980; Pappert and Shockey, 1978). On the other hand, experimental measurements of the properties of the guide have consistently shown them to be, on the average, relatively stable and predictable and, in particular, to be accurately represented by the simple formulas (Burrows, 1978).

The experimental corroboration of the simple formulas does not, of course, mean that the ionosphere is actually sharply bounded and homogeneous; direct measurements of its conductivity profile show that it is not. Rather, the corroboration supports the view that, over the frequency range of interest, simple curves exist of parameters equivalent to h, $\eta_g$, and S that can be used in the formulas to obtain accurate field estimates.

The next question to be asked about the simple theory is whether the parameters (e.g., the effective ionospheric height and propagation constant it requires as input) can be readily obtained. It seems likely, based on the theoretical work of Jones (1967, 1970); Greifinger and Greifinger (1978, 1979); Booker (1980); Behroozi-Toosi and Booker (1980), and the experimental propagation measurements of Ginsberg (1974); Bannister (1974a, 1975, 1979); Bannister et al. (1974a); White and Williams (1974) that they can be calculated accurately if enough ionospheric data were available. However, the calculation would not be wholly convincing without periodic experimental verification. The experimental verification in itself is a measurement of the parameters, and so establishes their magnitudes and behavior in time and space directly. Then the interpretation in terms of ionospheric physics is superfluous, apart from the reassurance that it can give that the measurements are consistent with other data (Burrows, 1978).

The substantial body of propagation data now available from measurements of sferics (the propagating electromagnetic pulse originating from a lighting stroke), from Schumann resonances and measurements of signals radiated from man-made sources presents a coherent quantitative description of propagation parameters. Thus, for the initial design of an ELF communications system using the earth-ionosphere waveguide, estimates of numerical values to be used for the parameters can be obtained from existing data. Before the final design, however, propagation measurements over the path planned for the system should be made. By using long integration times on reception, together with phase-synchronous detection, one can achieve the required accuracy using a test transmitter that is a very small version of the one planned for the final system (such as the U.S. Navy's ELF Wisconsin Test Facility (WTF)).

Instead of the parameters h, $\eta_g$, and S appearing in the theoretical propagation model, it is convenient to measure a composite of the three called the excitation factor, $\epsilon$, defined by

$$\epsilon = \left| \frac{\eta_g}{h \sqrt{\omega \mu_0 S}} \right|$$

(1)

and also the modified form of S, which is the attenuation factor as defined by

$$\alpha = 0.0290 \, \omega U m |S|$$

(2)

giving the attenuation in dB/Mm. (It should be noted that the $\epsilon$ defined here is not the same as the excitation factor $\Lambda_n$ used by Wait (1970) and Galejs (1972) for a different purpose.) The utility of these two factors is demonstrated by substituting them in asymptotic form for the horizontal electric current source. Thus,

$$|(H_\phi)_d| \sim Idl\epsilon \left| \frac{k_0}{2\eta_0} \left( \frac{\omega \mu_0}{2\pi} \right)^{1/2} \right| \left( \frac{\rho/a}{\sin \theta} \right)^{1/2}$$
$$\times \frac{10^{-\alpha \rho/1.9 \times 10^7}}{(k_0 \rho)^{1/2}} \cos \phi.$$

(3)

There are essentially six distinct factors in this propagation formula. The first is the source strength Idl. The second is $\epsilon$. The third is a collection of free-space parameters, all of which are determined exactly once the frequency is specified. The fourth is the spherical focusing factor. The fifth is the radial propagation loss factor, including both the exponential decay due to absorption and the $\rho^{-1/2}$ decay due to spreading. The sixth defines the directional dependence of the radiated field. Once the current moment Idl, frequency $\omega$, and coordinates $\delta$, $\phi$ of the field point are specified, only two parameters are left undetermined, i.e., $\epsilon$ and $\alpha$. Thus, when these two are evaluated, the field calculation can proceed (Burrows, 1978).

Recently, Greifinger and Greifinger (1978, 1979a), Booker (1980) and Behroozi-Toosi and Booker (1980) have derived simple-form approximate expressions for the TEM eigenvalues (propagation constants) for ELF propagation in the earth-ionosphere waveguide. They demonstrated that eigenvalues obtained by their methods were in excellent agreement with full-wave numerically calculated eigenvalues. The Greifinger's showed that the propagation constant depends on four parameters, two altitudes and a scale height associated with each. The lower altitude is the height at which the conduction current parallel to the magnetic field becomes equal to the displacement current. The associated scale height is the local scale height of the parallel conductivity. Under daytime ionospheric conditions, the upper altitude is the height at which the local wave number becomes equal to the reciprocal of the local scale height of the refractive index. Under the simplest nighttime conditions, the second set of parameters is replaced by the altitude of the E region bottom and the local wave number just inside the E-region. The relative phase velocity depends, in first approximation, only on the ratio of the two altitudes. The attenuation rate depends on the other two parameters, as well. The two principal attenuation mechanisms are Joule-heating by longitudinal currents in the vicinity of the lower altitude and energy leakage of the whistler component of the ELF wave at the upper altitude.

In a lesser known publication, the Greifingers (1979b) have extended the results presented in their earlier two papers to a more general class of ionospheric conductivity profiles. Their expressions allow the rapid computation of ELF phase speeds, attenuation rates, and excitation factors for a wide range of

ionospheric conditions without the necessity of lengthy fullwave computer calculations. The results can be applied to the rapid evaluation of the effects of a variety of ionospheric disturbances, both natural and artificial, on ELF communication systems.

Booker (1980) has combined the reflection theory of Booker and Lefeuvre (1977) with the Greifingers treatment (1978, 1979) of the effect of ionization below the level of reflection. The theory allows for the influence of the earth's magnetic field, reflection from the gradient on the under side of the D region (or, at night, of a ledge below the E region), reflection from the gradient on the underside of the E region, and reflection from the gradient on the topside of the E region.

We have used (Bannister, 1979a) the recently developed theory of the Greifingers' (1978) and the Wait VLF exponential ionospheric conductivity profile to determine TEM propagation constants for ELF daytime propagation in the earth-ionosphere waveguide. We determined that the resulting values of ELF attenuation rate, phase velocity, and approximate ionospheric reflection height are in excellent agreement with measured data.

For daytime propagation, the Greifingers' expressions for $\alpha$ and $c/v$ are

$$c/v \sim 0.985\sqrt{h_1/h_0}.\tag{4}$$

and

$$\alpha \sim 0.143/\sqrt{h_1/h_0}\left(\frac{\zeta_0}{h_0} + \frac{\zeta_1}{h_1}\right)\quad dB/Mm\tag{5}$$

where $h_0$ is the altitude where $\sigma = \omega\epsilon_0$; $h_1$ is the altitude where $4\omega\mu_0\sigma\,\zeta_1^2 = 1$; and $\zeta_0$ and $\zeta_1$ are the conductivity scale heights at altitudes $h_0$ and $h_1$, respectively.

From (4) and (5) we can see that the phase constant depends primarily on the two reflecting heights and is essentially independent on the conductivity scale heights. On the other hand, for a single scale-height conductivity profile (i.e., $\zeta_1 = \zeta_0$), the attenuation rate is directly proportional to scale height.

The single scale-height profile employed by Wait (1970) for determining VLF propagation parameters is

$$\omega_r(z)\quad \sigma(z)/\epsilon_0 \cdot 2.5 \times 10^5 \exp[(z - H)/\zeta_0].\tag{6}$$

where H is the (arbitrary) reference height. The altitudes $h_0$ and $h_1$ may be determined from

$$h_0 \cdot H \quad \zeta_0 \ln\left(\frac{2.5 \times 10^6}{2\pi f}\right)\tag{7}$$

and

$$h_1 \quad h_0 + 2\zeta_0 \ln\left(\frac{2.39 \times 10^4}{f\zeta_0}\right)\tag{8}$$

Note that in (6), (7), and (8) all heights and scale heights are in kilometers.

The Greifingers (1979b) have also shown that the effective waveguide height of reflection is roughly $h_0$, rather than the higher reflecting height $h_1$. This is in excellent agreement with the effective reflection heights inferred from the Sanguine/Seafarer propagation measurements. The fact that it is the lower height is not really that surprising since the horizontal rate of energy flow is essentially constant up to an altitude $h_0$, above which it falls off very rapidly with altitude.

The most common values of H and $\zeta_0$ employed in interpreting VLF daytime propagation measurements are H = 70 km and $\zeta_0$ = 1/0.3=3.33 km. By using these values in (4), (5), (7), and (8) we can readily determine $h_0$, $h_1$, c/v, and $\alpha$ at ELF. For example, at 75 Hz, $h_0 \sim 49.1$ km, $h_1 \sim 79.5$ km, c/v $\sim 1.26$, and $\alpha \sim 1.5$ dB/Mm. Furthermore, at 1000 Hz, $h_0 \sim 57.7$ km, $h_1 \sim 70.8$ km, c/v $\sim 1.10$, and $\alpha \sim 16.6$ dB/Mm.

The theoretically determined values of the ELF daytime attenuation rate are plotted in figure 1 for frequencies of 5 to 2000 Hz. Also plotted, are various experimentally determined values of $\alpha$. These are all determined from controlled source measurements, except for the 7.8, 14, and 20 Hz attenuation rates, which were inferred from Schumann resonance measurements (Chapman et al., 1966). The 45 and 75 Hz data points are average values determined from the 1970-72 Project Sanguine/Seafarer propagation measurements (Bannister, 1975), the 156 Hz value is from Ginsberg (1974), and the 400 Hz value is from Kuhnle and Smith (1964). The 630-1950 Hz data points were obtained by employing the Navy VLF antenna at Jim Creek, WA, as the source (Ginsberg, 1974). From figure 1 it can be seen that there is excellent agreement throughout the ELF range between the theoretical (employing the Wait exponential ionospheric - conductivity profile) and experimentally determined values of ELF daytime attenuation rates.

The theoretically determined values of the ELF daytime phase velocity are plotted in figure 2 for frequencies of 5 to 1000 Hz. Also plotted are various experimentally determined values of c/v. These values were all determined from measurements of atmospherics. The 7.8, 14, and 20 Hz values were inferred from Schumann resonance measurements (Chapman et al., 1966), the 50-225 Hz values are from Hughes and Gallenberger 1974, and the 300-900 Hz measurements are the two station results of Chapman et al. (1966). From figure 2 we see that there is excellent agreement between the theoretical and experimentally determined values of c/v for frequencies greater than 50 Hz and fair agreement for frequencies less than 50 Hz.

Under nighttime propagation conditions, a sharp E region bottom is usually encountered before the altitude $h_1$ is established. The electron density undergoes a very sharp increase in passing through the bottom, above which it can be quite variable. The Greifingers' (1979) have considered the simple model where the density above this bottom varies slowly on the scale of the local wavelength. The result is

$$c/v \sim \sqrt{h_E/h_o}$$

(9)

and

$$a \sim 0.143f \sqrt{h_E/h_o} \left( \frac{t_o}{h_o} + \frac{1}{\pi k_o n_E h_E} \right)$$

(10)

where $h_E$ is the altitude of the E region bottom and $k_0 n_E$ is the E region local wave number. Comparison with the daytime results (4) and (5) shows that the altitude of the E region bottom has replaced the frequency-dependent altitude $h_1$ as a parameter and the local wavelength just inside the E region, has replaced $\delta_1$.

We have also employed Waits' nighttime ionospheric conductivity model (with a reference height of 90 km and scale height of $1/0.4 = 2.5$ km) in conjunction with the Greifingers' nighttime theory. We also assumed the height of the E region bottom was 90 km and its conductivity was approximately $8 \times 10^{-6}$ Siemens/meter. The resulting values of attenuation rate are in excellent agreement with the 45 to 800 Hz controlled source measurements. Also, the 45, 75, and 150 Hz effective waveguide reflection heights (approximately 75 km) are in excellent agreement with those inferred from the Sanguine/Seafarer measurements.

## ADDITIONAL EXAMPLES OF LOCALIZED NIGHTTIME ANOMALIES

The most important extremely low frequency (ELF) earth-ionosphere waveguide propagation parameters are the attenuation rate, phase velocity and excitation factor. We have shown (Bannister, 1975) that, on the average, the ELF attenuation rate is directly proportional to the excitation factor. The fact that these two quantities are proportional is not really that surprising since, for single layer and exponentially varying ionospheric conductivity models, both are inversely proportional to the ionospheric reflection Height (Bannister, 1975; 1979a). What this suggests is that, on the average, if the nighttime (or daytime) excitation factor is increased (or decreased), then the nighttime (or daytime) attenuation rate is also increased (or decreased).

On several occasions during the past decade, the 40 to 80 Hz ELF nighttime field strength measured at sites in the northeastern U.S. (i.e., Connecticut and Maryland) has displayed rapid decreases of from 4 to 8 dB in several hours (Bannister, 1974b; 1975; 1979b; 1980; Bannister et al., 1974b; Bannister and Williams, 1976; Davis, 1974; 1976). These severe nighttime disturbances sometimes occur during the several days following magnetic storms when similar but less pronounced behavior is found to coincide with phase disturbances on very low frequency (VLF) paths across the northern United States (Davis, 1976).

We have shown (Bannister, 1980) that the Connecticut nighttime field strength amplitude was usually at a minimum between 0600 and 0800 GMT, whereas the nighttime relative phase was at a maximum approximately 1 hour earlier. The time of the lowest nighttime field strengths coincides with the farthest southern displacement of the auroral oval and, presumably, indicates the time at which precipitated energetic electrons would reach their southern most extent in the middle latitudes.

The Connecticut and Maryland measurement sites are located approximately 1.6 Mm from the transmitting source, which is the U.S. Navy ELF Wisconsin Test Facility (WTF). Intuitively, for such short paths, it seems extremely unlikely that changes in attenuation rate would be the explanation of these signal decreases. However, the required changes (i.e., increases) in effective ionospheric reflecting height would also be an unrealistic consideration.

It has been postulated (Sechrist, 1972; Davis, 1974; 1976; Spejeldvik and Thorne, 1975a, b) that levels of the D region controlling ELF propagation in the earth-ionosphere waveguide are strongly influenced by energetic electron precipitation. Recently reported measurements (Wratt, 1977; Dickinson and Bennett, 1978) are consistent with the theoretical results of Spjeldvik and Thorne (1975a, b) regarding ionization caused by precipitation of energetic electrons during the recovery phase of magnetic storms. Because energetic particle precipitation into the D region tends to increase ionization, making the ionosphere more "daylike" by lowering the effective reflecting height and improving excitation, the observed nighttime field strength decreases are in the opposite sense to what would have been expected.

Imhof et al. (1978), from coordinated satellite and ELF field strength measurements, have found that direct particle precipitation into the atmosphere can cause ELF transmission anomalies. In these anomalies the signal strengths may be either attenuated or enhanced depending upon the spacial extent and location of the ionization. The effect appears to be due primarily to changes in the excitation factor. Other factors, such as standing wave effects, may also be of importance (Davis, 1976).

Several authors (Barr, 1977; Pappert and Moler, 1978) have also made calculations regarding the influence of a sporadic-E layer that encompasses the nighttime propagation path. They showed that the presence of nocturnal sporadic-E produced marked maxima and minima in the propagation characteristics of ELF radio waves. One physical explanation for the enhanced absorption can be explained in terms of an attenuation resonance between waves reflected from normal E region heights and from the sporadic-E region. The results of typical theoretical calculations (Pappert and Shockey, 1978) depicting the changes in attenuation rate and phase velocity due to a nocturnal sporadic-E layer are presented in figures 3 and 4.

Pappert (1980) and Pappert and Shockey (1978) have investigated the effects of a more realistically sized patch of sporadic-E on nighttime propagation in the lower ELF band. Their results indicate that a sporadic-E patch of 1 Mm by 1 Mm which causes phase shifts and attenuation rate enhancements consistent with full wave model evaluations can account for the 6 to 8 dB fades observed in the Connecticut and Maryland measurements. Patches 1 Mm by 0.5 Mm can account for more commonly observed fades in the 3 to 4 dB range. Of the cases examined, deepest fades occur when the disturbance falls over the receiver and the depth of the fades in those instances changes very little with the location of the disturbance along the great circle path connecting transmitter and receiver. In other words, a receiver moving beneath a traveling but otherwise invariant ionospheric disturbance would experience a very nearly constant fade (Pappert, 1980).

It should be noted that actual measurements of sporadic E conditions have not been made at the receiving sites when WTF was transmitting. Attempts to explain the observed ELF signal fades in terms of absorption due to sporadic E conditions can, therefore, not be conclusive, but the theoretical efforts in this area point out the potential influences of sporadic E on ELF propagation.

Field and Joiner (1979) employed an integral equation approach for analyzing propagation in the earth-ionosphere waveguide where conditions change over distances comparable with a Fresnel zone. They derived an expression for the relative errors introduced by neglecting transverse ionospheric gradients over the path and found that full-wave methods must be applied when the effective width of a localized disturbance is less than two-thirds of the width of the first Fresnel zone. They also concluded that the WKB approximation significantly overestimates the propagation anomaly when the distrubance is centered near the propagation path and underestimates the anomaly when the disturbance is centered far off-path.

Subsequently, Field and Joiner (1981) extended their analysis by analyzing ELF propagation for both widespread and bounded inhomogeneities. Their solutions showed that such a disturbance behaves like a cylindrical lens filling a narrow aperture. Lateral diffraction, focusing, and reflection can cause the transverse electromagnetic (TEM) mode to exhibit a transverse pattern of maxima and minima beyond the disturbance and a standing-wave pattern in front of it. The focusing and diffraction diminish when the transverse dimension of the disturbance approaches the width of the first Fresnel zone, typically, several megameters. Their analysis shows that reflection from widespread inhomogeneities can be important in two situations: first, for great-circle propagation paths that are nearly tangential to the boundary of the disturbed polar cap; and, second, when the TEM mode is obliquely incident on the day/night terminator, in which case a phenomenon analoguous to internal reflection can occur.

On many measurement dates during 1976, nighttime field-strength-amplitude measurements taken at the Connecticut site were found to be minimum from 0600 to 0800 hours GMT. Conversely, nighttime relative phase was found to be at maximum approximately 1 hour earlier (Bannister, 1980). This phenomenon is further illustrated in Figure 5. A comparison of 34 nighttime minimum amplitude times, with corresponding maximum relative phase times, yielded an average minimum nighttime field strength amplitude time of approximately 0700 GMT and an average maximum nighttime relative phase time of approximately 0600 GMT.

On 18 September 1976 (Figure 5), the nighttime field strength amplitude steadily decreased 5 dB from 2300 to 0630 GMT and then steadily increased 5 dB from 0630 to 1200 GMT. Meanwhile, the nighttime relative phase increased 20° from 0230 to 0500 GMT, and then decreased 15° from 0500 and 0800 GMT.

The average nighttime field strength reduction during those 34 nights was approximately 3 dB, while the average nighttime relative phase increase was approximately 20° (about the same phase change associated with the sunrise-sunset terminators crossing the WTF-Connecticut path). Intuitively, an increase in phase would be due to an increase in the reflecting height and thus a decrease in the electron density near the normal reflection height (~ 75 km, Bannister, 1975). However, this would require an unrealistic nighttime reflection height of approximately 125 to 150 km.

A more plausible explanation is that the field strength amplitude reduction (accompanied by a relative phase increase) is due to the presence of a nocturnal sporadic-E layer. This is in agreement with the results of Pappert and Shockey (1978) who showed that phase increases of 30° are possible in the neighborhood of the attenuation rate resonance caused by waves reflected from normal E region heights and from the sporadic E region.

During January 1977, simultaneous field strength measurements were taken in Connecticut and aboard three submarines located in the North Atlantic/Norwegian Sea area (approximately 5 Mm from WTF). A comparison of the 3 and 6 January data taken aboard all three submarines with the data taken in Connecticut is presented in figure 6. On 3 January, we see that from 0000 to approximately 0400 GMT, the nighttime field strengths were fairly constant at all four receiving locations. However, the field strengths measured by each of the three submarines (which were less than 2 Mm apart in latitude) were substantially different. The average field strength measured during the 0000-0400 GMT nighttime period was ~ -150 dBA/m aboard submarine 1, ~ -154 dBA/m aboard submarine 2 and ~ -157 dBA/m aboard submarine 3, a 7 dB difference! From 0500 to 1800 GMT, the data tracked very well from submarines 2 and 3, while during the WTF daytime period (1400-1800 GMT), the data taken aboard all three submarines were quite similar.

On 6 January (figure 6), from 0200 to 0530 GMT, the field strengths measured by submarines 1 and 3 were approximately 4 dB different in magnitude. However, from 0600 to 1000 GMT, the data from all three locations tracked very well, with peak-to-trough variations of 3 and 4 dB. The 0200 to 0530 GMT variations were probably caused by localized anomalies, while the 0600 and 1000 GMT variations were probably at WTF, or along the whole path due to particle bombardment during the 29 December 1976 magnetic storm recovery period. Another possible explanation for these anomalous nighttime submarine results (figure 6) is that the receivers are on great-circle paths that are nearly tangential to the disturbed polar cap, in which shadow zones and interference patterns could occur (Field and Joiner, 1981).

During the magnetically quiet period of early March 1977, field strength measurements were taken in Connecticut and aboard a submarine located in the North Atlantic (approximately 4 Mm from WTF). Many nighttime field strength variations were observed at both receiving locations.

Figure 7 plots the 1 to 3 March 1977 nighttime field strengths measured at both locations against GMT. Note that the Connecticut and submarine field strength versus GMT plots are displaced by 4 hours. During these three nights, the observed peak-to-trough variations were 6 to 8 dB in Connecticut and 7 to 11 dB at the submarine receiving location. Because (1) the late February/early March period was magnetically quiet and (2) the decreases in the nighttime field strengths occured at different times at the two receiving sites; the prime candidate for the cause of these anomalies is a moving nocturnal sporadic-E layer.

Presented in figure 8 are the 4 to 6 March 1977 nighttime field strengths measured at the two receiving locations. The field strength versus GMT plots (which are very similar at both receiving locations) are displaced by 4 hours on 4 and 5 March and by 2 hours on 6 March. The peak-to-trough variations is a moving nocturnal sporadic-E layer.

Figure 9 plots the 10 and 11 March 1977 field strengths versus GMT. For these plots, the time displacement is only 2 hours. On 10 March, the nighttime peak-to-trough variation was ~ 6 dB in Connecticut and ~ 8 at the submarine receiving location. During 11 March, the Connecticut nighttime field strength gradually decreased ~ 3 dB over a 6 hour period, while the submarine field strength decreased ~ 6 dB. One cause of these variations could be a moving sporadic E layer. Another cause could be particle bombardment during the 9 March magnetic storm recovery period.

Another interesting anomalous nighttime propagation condition is presented in figure 10. On 17 March from 0100 to 0600 GMT, both the Connecticut and Submarine nighttime field strengths were 2 to 3 dB lower than on the previous nights, which is indicative of a propagation anomaly along the whole path or at WTF. On both 26 January and 17 March, from 0630 to 0800 GMT (i.e., the last 1 1/2 hours of the nighttime period), the field strength in Connecticut decreased by only ~ 1 dB. However, the field strength at the submarine location decreased by ~ 7 dB (on 17 March) and by ~ 9 dB (on 26 January). These 0630 to 0800 field strength degradations must be caused by local ionospheric anomalies.

## CONCLUSIONS

In this paper, we have presented a tutorial overview on ELF propagation. Much of the material was excerpted from the excellent book "ELF Communications Antennas" by M. L. Burrows (1978). It is recommended reading for anyone seriously interested in ELF communications.

We have also compared recently derived simple form approximate expressions (which relate ELF propagation constants to realistic ionospheric conductivity profiles) with experimentally derived results for both daytime and nighttime propagation conditions.

On several occasions during the past few years, the ELF nighttime field strength measured in northeastern United States has displayed rapid decreases of from 4 to 8 dB in several hours. The time of the lowest nighttime field strengths (0600-0800 GMT) coincides with the farthest southern displacement of the auroral oval and presumably indicates the time at which precipitated energetic electrons would reach their southernmost extent into the middle latitudes. Therefore a probable cause of some of these localized ELF nighttime field strength variations (which are certainly not restricted to measurement locations in the northeastern United States) are changes in reflection height along the propagation path (which can lead to standing wave effects) because of particle bombardment.

Another possible explanation for these anomalous nighttime results is that the receivers are on great-circle paths that are nearly tangential to the disturbed polar cap, in which shadow zones and interference patterns could occur.

Simultaneous measurements taken in Connecticut and the North Atlantic area during the magnetically quiet period of early March 1977 (where nighttime propagation anomalies occured 2 to 4 hours apart) have indicated that another cause for some of these anomalies is a moving nocturnal sporadic-E layer.

It now appears that theory has advanced to the point where substantial benefit would result from a concurrent measurement program simultaneously involving nocturnal ELF propagation and sporadic-E soundings over and about the propagation path. ELF measurements provide the only means yet of remotely monitoring ionization phenomena in an altitude range not accessible to other techniques, and may be extremely useful in untangling the mysteries of this region.

# REFERENCES

Bannister, P .R. (1974a), "Far-field Extremely Low Frequency (ELF) Propagation Measurements," 1970-72, IEEE Trans. Commun., COM-22(4), 468-474.

Bannister, P. R. (1974b), "A Possible Explanation of the Nighttime Variations of ELF Signal Strengths in Connecticut, IN ELF-VLF Radio Wave Propagation." edited by J. Holtet, pp. 279-283, D. Reidel, Dordrecht, Netherlands.

Bannister, P. R. (1975), "Variations in Extremely Low Frequency Propagation Parameters, J. Atmos. Terr. Phys.," 37(9), 1203-1210.

Bannister, P. R. (1979a), "Some Notes on ELF Earth-ionosphere Waveguide Daytime Propagation Parameters", IEEE Trans. Antennas Propagat., AP-27(5), 696-698.

Bannister, P. R. (1979b), "Summary of Extremely Low Frequency (ELF) Field Strength Measurements Made in Connecticut During 1975," Radio Sci., 14(1), 103-108.

Bannister, P. R., et al (1980, "Extremely Low Frequency (ELF) Propagation," 550 pp., NUSC Scientific and Engineering Studies, Naval Underwater Systems Center, New London, CT 06320.

Bannister, P. R., and F. J. Williams (1976), "Further Examples of the Nighttime Variations of ELF Signal Strengths in Connecticut, J. Atmos, Terr. Phys.," 38(3), 313-317.

Bannister, P. R., F. J. Williams, A. L. Dahlvig, and W. A. Kraimer (1974a), "Wisconsin Test Facility Transmitting Antenna Pattern and Steering Measurements," IEEE Trans. Commun., COM-22(4), 412-418.

Bannister, P. R., F. J. Williams, J. R. Katan, and R. F. Ingram (1974b), "Nighttime Variations of Extremely Low Frequency (ELF) Signal Strengths in Connecticut," IEEE Trans. Commun., COMM-22(4), 474-476.

Barr, R. (1974), "The Effect of Sporadic-E on the Nocturnal Propagation of ELF Radio Waves, J. Atmos. Terr. Phys.," 39(11/12), 1379-1387.

Behroozi-Toosi, A. B. and H. G Booker (1980), "Application of a Simplified Theory of ELF Propagation to a Simplified Worldwide Model of the Ionosphere, J. Atmos. Terr. Phys.," 42(11/12), 943-974.

Bernstein, S. L., M. L. Burrows, J. E. Evans, A. S. Griffiths, D. A. McNeill, C. W. Neissen, I. Richer, D. P. White and D. K. William (1974), "Long Range Communication at Extremely Low Frequencies," Proc. IEEE, 62(3), 292-312.

Booker, H. G. (1980), "A Simplified Theory of ELF Propagation in the Earth-ionosphere Transmission Line, J. Atmos. Terr. Phys.," 42(11/12), 929-941.

Booker, H. G. and F. Lefeuvre (1977), "The Relation Between Ionospheric Profiles and ELF Propagation in the Earth-ionosphere Transmission Line, J. Atmos. Terr. Phys.," 39(11/12), 1277-1292.

Burrows, M. L., ELF Communications Antennas (1978), Peter Peregrinus Ltd., Stevenage, England, 245 pp.

Chapman, F. W., D. Llanwyn Jones, J. D. W. Todd and R. A. Challinor (1966), "Observations on the Propagation Constant of the Earth-ionosphere Waveguide in the Frequency Band 8 c/s to 16 kc/s, Radio Sci.," 1(11), 1273-1282.

Davis, J. R. (1974), "ELF Propagation Irregularities on Northern and Midlatitude Paths, in ELF-VLF Radio Wave Propagation," edited by J. Holtet, pp. 263-277, D. Reidel, Dordrecht, Netherlands.

Davis, J. R. (1976), "Localized Nighttime D Region Disturbances and ELF Propagation, J. Atmos. Terr. Phys.," 38(12), 1309-1317.

Dickinson, P. H. G. and F. D. G. Bennet (1978), "Diurnal Variations in the D Region During a Storm After-effect, J. Atmos. Terr. Phys.," 40(5), 549-558.

Field, E. C., and R. G. Joiner (1979), "An Integral-Equation Approach to Long-Wave Propagation in a Non-Stratified Earth-Ionosphere Waveguide," Radio Sci., 14(6), 1057-1068.

Field, E. C., and R. G. Joiner (1981), "Effects of Lateral Ionospheric Gradients on ELF Propagation," Radio Sci., (to be published).

Galejs, J. (1972), "Terrestrial Propagation of Long Electromagnetic Waves," Pergamon Oxford, 362 pp.

Ginsberg, L. H. (1974), "Extremely Low Frequency (ELF) Propagation Measurements Along a 4900 km Path," IEEE Trans. Commun., COM-22(4), 452-457.

Greifinger, C. and P. Greifinger (1978), "Approximate Method for Determining ELF Eigenvalues in the Earth-ionosphere Waveguide," Radio Sci., 13(5), 831-837.

Greifinger, C. and P. Greifinger (1979a), "On the Ionospheric Parameters Which Govern High-latitude ELF Propagation in the Earth-Ionosphere Waveguide," Radio Sci., 14(5) 889-895.

Greifinger, C. and P. Greifinger (1979b), "Extended Theory for Approximate ELF Propagation Constants in the Earth-Ionosphere Waveguide," DNA Report No. 5561T, R&D Associates, Marina del Rey, CA 90291, 1 September.

Hughes, H. G. and R. J. Gallenberger (1974), "Propagation of Extremely Low Frequency (ELF) Atmospherics Over a Mixed Day-Night Path, J. Atmos. Terr. Phys.," 36(10), 1643-1661.

Imhof, W. L., J. B. Reagan, E. E. Gaines, T. R. Larsen, J. R. Davis, and W. Moler (1978), "Coordinated Measurements of ELF Transmission and the Precipitation of Energetic Particles into the Ionosphere," Radio Sci., 13(4), 717-727.

Jones, D. L. (1967), "Schumann Resonances and ELF Propagation for Inhomogeneous Isotropic Profiles, "J. Atmos. Terr. Phys., 29, 1037-1044.

Jones, D. L. (1970), "Numerical Computations of Terrestrial ELF Electromagnetic Wave Fields in the Frequency Domain," Radio Sci., 5(5), 803-809.

Kuhnle, P. I. and R. D. Smith (1964), "Experimental Research Investigation of Extremely Low Frequency Propagation," Rome Air Development Center, Rome NY, Rep. RADC-TDR-64-360 (AD609719), December.

Pappert, R. A. (1980), "Effects of a Large Pitch of Sporadic-E on Nighttime Propagation at Lower ELF, J. Atmos. Terr. Phys.," 42(5), 417-425.

Pappert, R. A. and W. F. Moler (1978), "A Theoretical Study of ELF Normal Mode Reflection and Absorption Produced by Nighttime Ionospheres, J. Atmos. Terr. Phys.," 40(9), 1031-1045.

Pappert, R. A. and L. R. Shockey (1978), "Effects of Strong Local Sporadic-E on ELF Propagation," NOSC TR 282, 15 August.

Sechrist, C. J., Jr. (1972), "Thermospheric Circulation," edited by W. L. Webb p. 261, MIT Press, Cambridge, MA.

Spjeldvik, W. N. and R. M. Thorne (1975a), "The Cause of Stor   After Effects in the Middle Latitude D Region, J. Atmos. Terr. Phys.," 37(5), 777-795.

Spjeldvik, W. N. and R. M. Thorne (1975b), "A Simplified D-Region Model and its Application to Magnetic Storm After Effects, J. Atmos. Terr. Phys.," 37(10), 1313-1325.

Wait, J. R. (1970), "Electromagnetic Waves in Stratified Media," Pergamon, NY, 608 pp.

Wait, J. R. editor (1974), "Special Issue on Extremely Low Frequency (ELF) Communications," IEEE Trans. Commun., COM-22(4).

White, D. P. and D. K. William (1974), "Propagation Measurements in the Extremely Low Frequency (ELF) Band," IEEE Trans. Commun., COM-22(4), 457-467.

Wratt, D. S. (19744), "Variations in Electron Density in the Middle Latitude D-Region Above Urbana, Illinois, J. Atmos. Terr. Phys.," 39(5), 607-617.
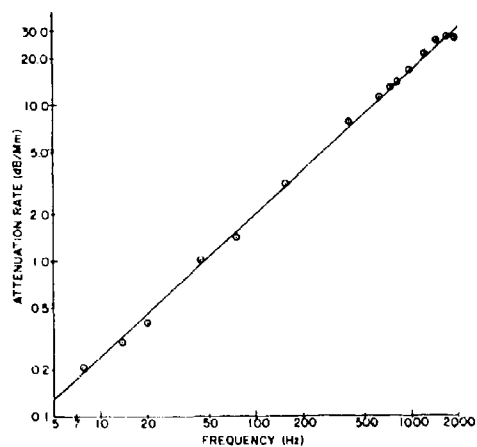
Fig. 1. ELF daytime attenuation rates versus frequency. $\omega_r = 2.5 \times 10^5 \exp[0.3(z-70)]$. ○ Measurements.
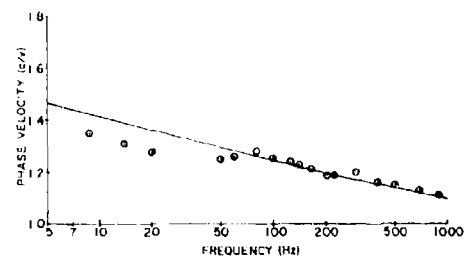


Fig. 2. ELF daytime phase velocity versus frequency. $\omega_r = 2.5 \times 10^5 \exp\{0.3(z-70)\}$. ○ Measurements.
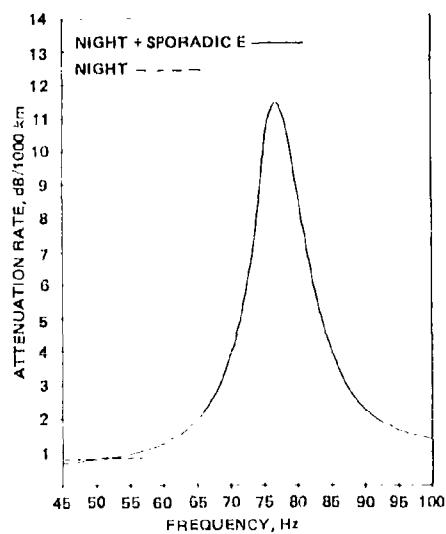


Fig. 3. Attenuation versus frequency.
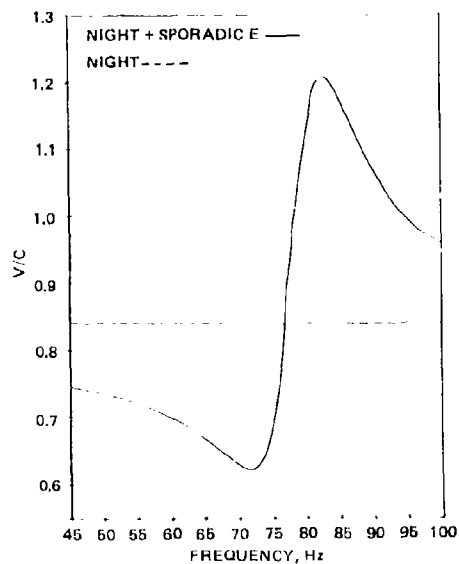


Fig. 4. Phase speed over free space speed versus frequency.
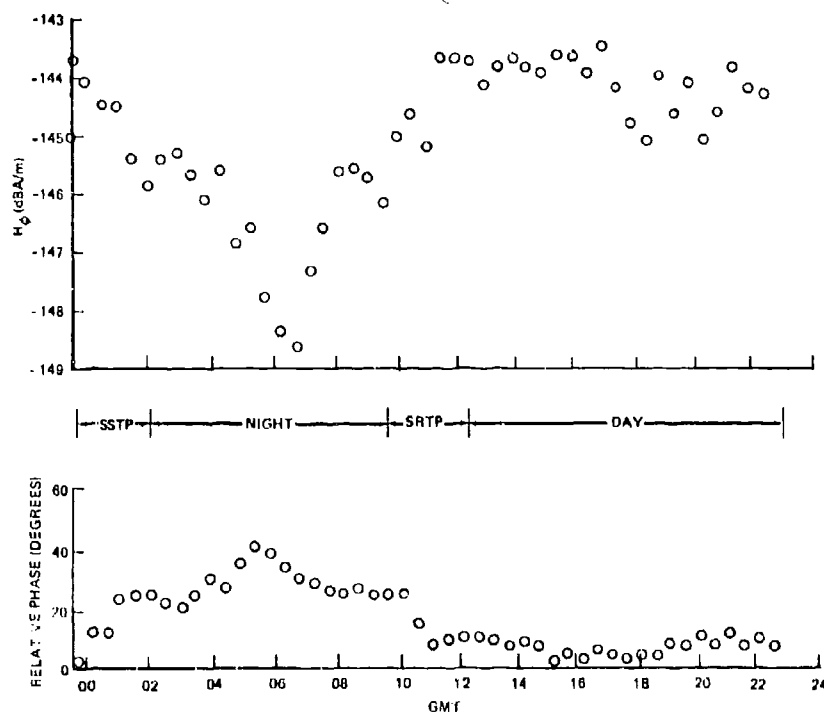
Fig. 5. 18 September 1976 Connecticut field strength versus GMT.
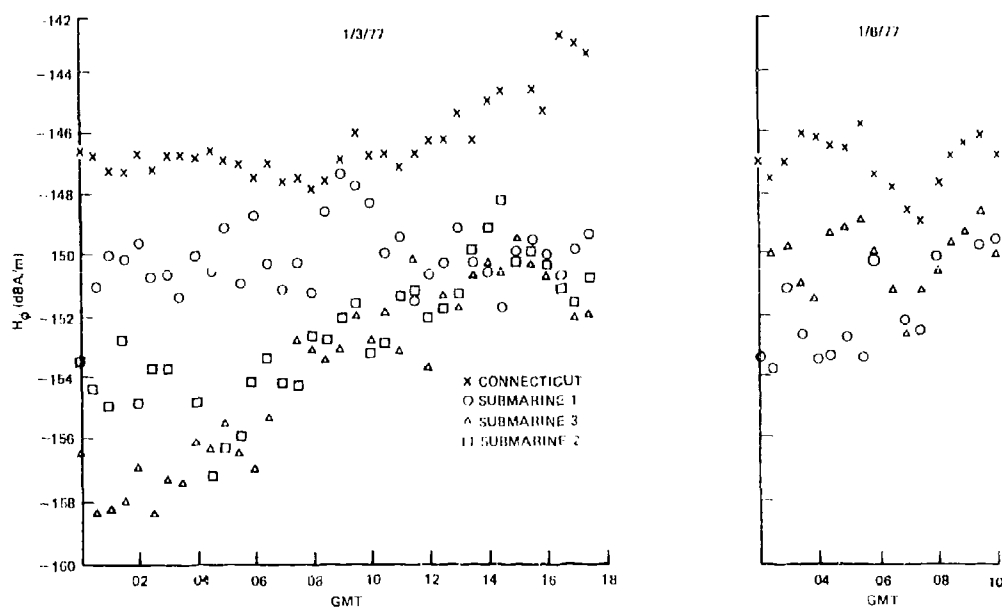


Fig. 6. 3 and 6 January 1977 comparison of Connecticut and submarine data.
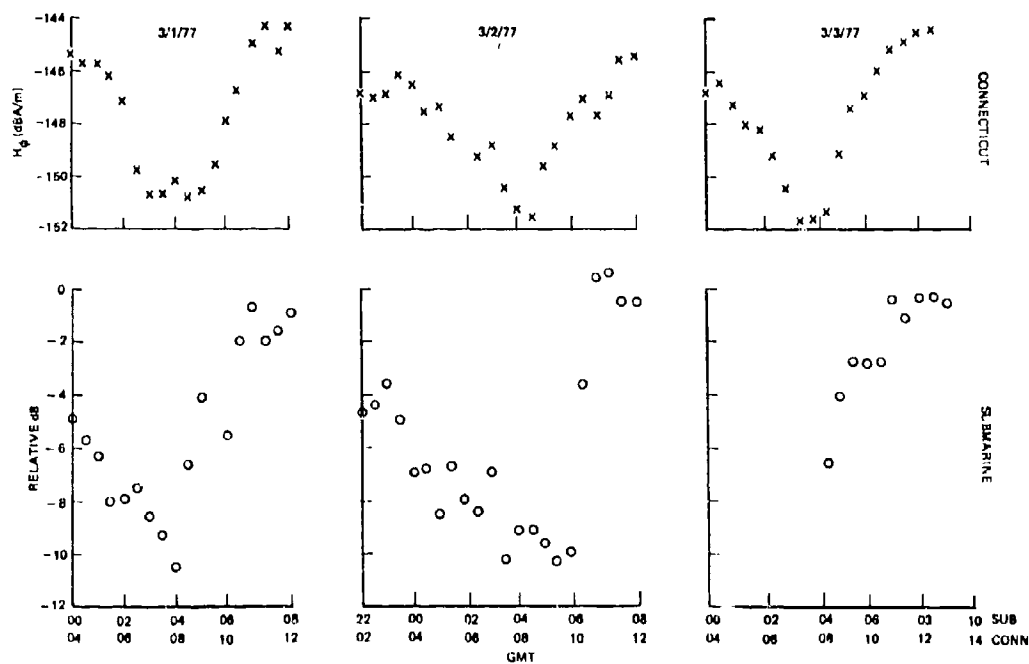
Fig. 7. 1 to 3 March 1977 comparison of Connecticut and submarine data.
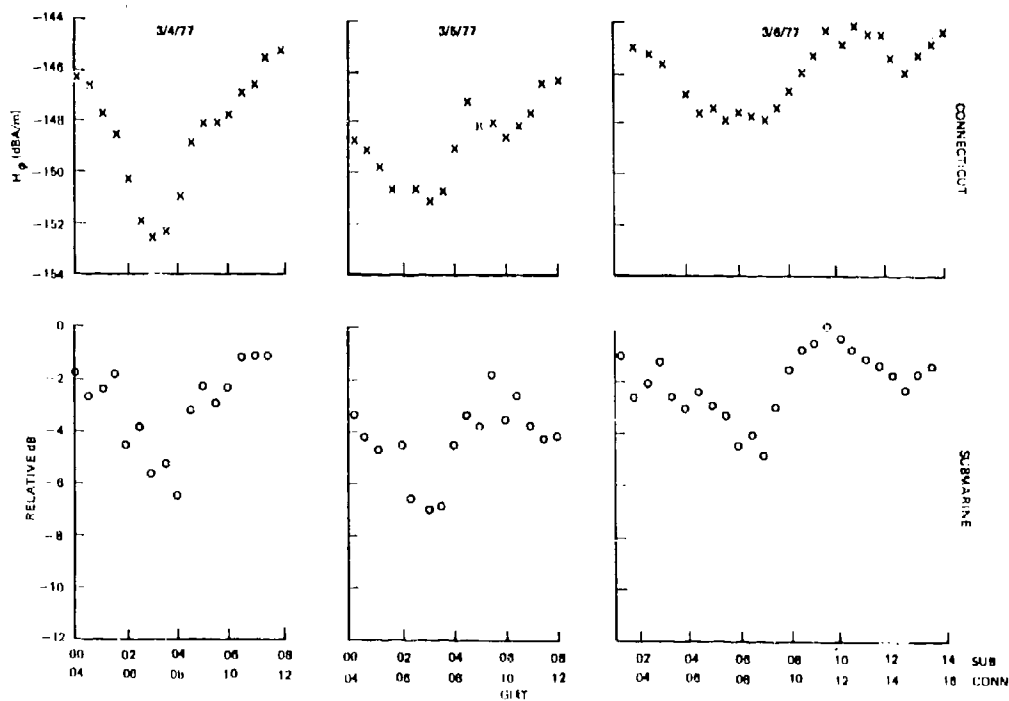


Fig. 8. 4 to 6 March 1977 comparison of Connecticut and submarine data.
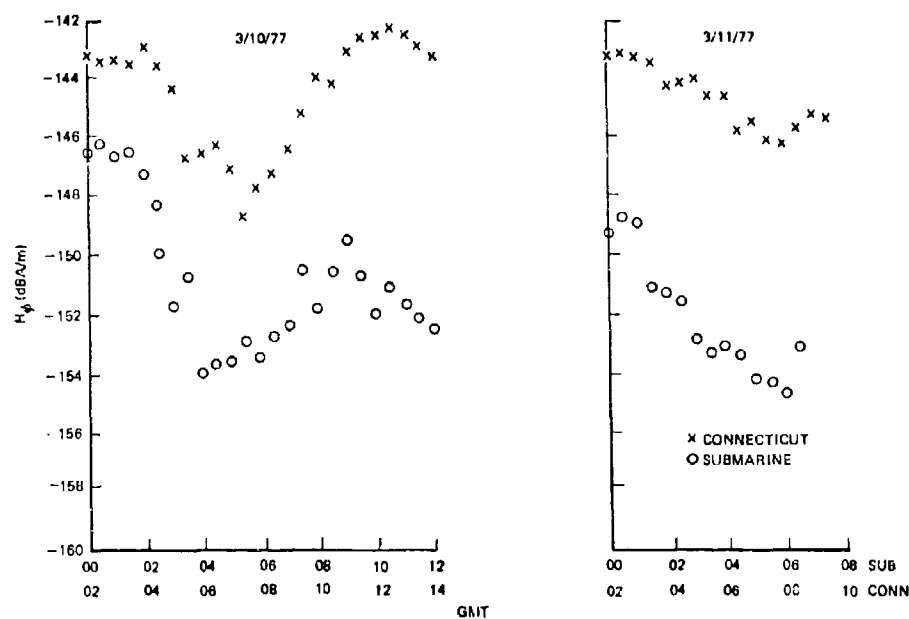
Fig. 9. 10 and 11 March 1977 comparison of Connecticut and submarine data.
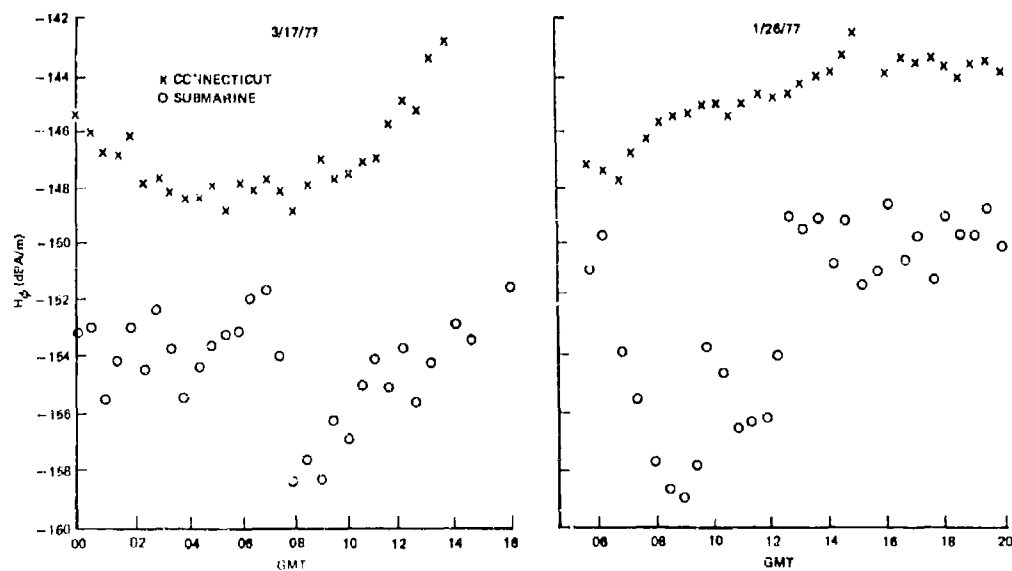


Fig. 10. 26 January and 17 March 1977 comparison of Connecticut and submarine data.

## ELF PROPAGATION IN DISTURBED ENVIRONMENTS

Edward C. Field, Jr.
Pacific-Sierra Research Corporation
1456 Cloverfield Boulevard
Santa Monica, California 90404

### SUMMARY

This paper describes how long-range ELF propagation is affected by ionospheric disturbances such as solar particle events or nuclear environments, which substantially constrict the earth-ionosphere waveguide. A few of our results also pertain to more common ionospheric phenomena, such as sporadic-E patches. Stratified disturbances usually cause both the excitation factor and the attenuation rate of the TEM waveguide mode to increase. Thus, the signal increases somewhat at short distances, but decreases by several decibels at long distances. The main loss mechanism is Ohmic heating of heavy ions in the lower ionosphere.

Even widespread disturbances must often be treated as nonstratified, since they can cause the properties of the earth-ionosphere waveguide to change markedly over the huge ELF wavelength or Fresnel zone. We treat such lateral inhomogeneities by recasting the wave equation as a two-dimensional integral equation. Numerical solutions show that a localized disturbance behaves like a cylindrical lens filling a narrow aperture. Lateral diffraction, focusing, and reflection can cause the TEM mode to exhibit a transverse pattern of maxima and minima beyond the disturbance, and a standing wave pattern in front of it. Such phenomena can contribute to spatial fluctuations occasionally observed on ELF transmissions. The focusing and diffraction diminish when the transverse dimension of the disturbance approaches the width of the first Fresnel zone—typically, several megameters.

## 1. INTRODUCTION

Natural and man-made ionospheric disturbances can significantly affect the long-range propagation of extremely-low-frequency (ELF) and very-low-frequency (VLF) signals. This paper is concerned with ELF propagation; a companion paper [Field, 1981] considers VLF propagation. Long-wave signals propagate in the waveguide bounded sharply on the bottom by the earth and diffusely on the top by the ionosphere. We focus on severe disturbances caused by energetic radiation, which produces anomalous ionization in and below the lower ionosphere and thus constricts the earth-ionosphere waveguide. However, our integral-equation approach for treating nonstratified disturbances—and a few of our results—also pertains to more common ionospheric phenomena, such as sporadic-E patches.

We treat the ELF (30 to 300 Hz) and VLF (3 to 30 kHz) bands separately because they differ in the following important respects. First, only the transverse electromagnetic (TEM) mode is below cutoff at ELF, whereas several modes are above cutoff and mutually interfere at VLF. Second, only vertically polarized signals propagate well at ELF, whereas both transverse magnetic (TM) and transverse electric (TE) modes can propagate at VLF. Third, even a geographically widespread disturbance can cause the properties of the earth-ionosphere waveguide to change markedly over the huge ELF wavelength or Fresnel zone, and give rise to phenomena—lateral reflection, diffraction, and focusing—that are usually unimportant at VLF.

This paper gives numerical calculations of attenuation rates and signal strengths for stratified disturbances having a wide range of intensities. In addition, we calculate the lateral signal structure caused by disturbances that are narrower than a Fresnel zone and must therefore be treated as nonstratified.

## 2. NORMAL AND DISTURBED IONOSPHERIC MODELS

Many types of ionospheric disturbances can cause ELF propagation anomalies. X-rays from solar flares ionize the D- and E-layers of the ionosphere over the sunlit hemisphere. Energetic electrons and protons from solar particle events (SPE) ionize the polar cap at altitudes well below those from which ELF waves are usually reflected. High-altitude nuclear bursts produce various prompt and delayed ionizing radiations, including $\gamma$-rays, $\beta$-particles, and neutrons. The $\gamma$-rays penetrate to even lower altitudes than energetic protons from a strong SPE, and thus can cause much more severe distortions of the earth-ionosphere waveguide.

Extensive calculations for numerous specific disturbances have been made throughout the ELF/VLF research community. Here we concentrate on SPE and nuclear disturbances, which cause ionization well below the normal ionosphere. They constrict the earth-ionosphere waveguide, and usually degrade propagation. We do not consider disturbances—such as X-ray flares—that occasionally enhance propagation.

Figure 1 shows height profiles of electron and positive ion density calculated from models of nominal nuclear environments consisting of widespread, high-altitude fission debris. The profiles shown are convenient for calculating the dependence of the waveguide propagation parameters on the intensity of a disturbance. They span a wide range of intensities, but, because propagation depends on ionization height gradient as well as intensity, they do not cover all possible cases. Specific events must therefore be analyzed individually. The "moderate" and "intense" profiles represent levels of ionization typical of strong SPEs as well as spread-debris environments. We can therefore use them to infer effects of both natural and man-made disturbances.

Before presenting the numerical results, we briefly discuss the relative importance of electrons and heavy ions. We ignore the geomagnetic field because, for the disturbances considered here, the most important processes occur at altitudes where the electron and ion collision frequencies, $\nu_e$ and $\nu_i$, exceed the corresponding gyrofrequencies. The ionospheric refractive-index height profile is thus the basic input to ELF predictive codes. Electrons and many species of heavy ions contribute to the refractive index. In practice—as in Fig. 1—ionic species are classified simply as "positive" or "negative," each

type having properties determined by averaging over the species actually present. Further, it is usually assumed that such generic ions have equal masses $M_i$ and collision frequencies $\nu_i$. The refractive index n then takes the simplified form

$$n^2 - 1 \approx -1 \frac{q^2}{\omega \varepsilon_0 M_e \nu_e} \left( N_e + \frac{2M_e \nu_e}{M_i \nu_i} N^+ \right) , \tag{1}$$

where q is the electron charge, $\omega$ is the angular frequency, $N_e$ is the electron density, and $N^+$ is the density of the "average" positive ion. The factor of two in Eq. (1) occurs because the positive and negative ion densities are nearly equal at altitudes where ions are important.

The values of $M_i$ and $\nu_i$ at a given altitude are poorly known. We use an atomic weight of 32 for $M_i$, but--depending on altitude--values as low as 19 or as high as 50 to 60 are possible. Similarly, $\nu_i$ could be anywhere from a tenth to a fortieth of $\nu_e$. We follow current convention in assuming $\nu_i = \nu_e/20$, and use a nominal profile for $\nu_e$ (e.g., Pappert and Moler [1974]).

Figure 1 shows that ions greatly outnumber electrons at the lower altitudes, where they dominate propagation despite their larger mass. By inserting the assumed numerical values into Eq. (1), then comparing the first and second terms in the parentheses, we find that a transition from electron to ion dominance occurs at the altitude where

$$N_e \sim \frac{N^+}{1500} . \tag{2}$$

For the models shown in Fig. 1, this criterion implies that signals confined mainly to altitudes below, say, 50 to 55 km are more strongly affected by ions than electrons. Of course, that transition altitude will shift if different values are assumed for the masses or collision frequencies.

## 3. EFFECTS OF STRATIFIED DISTURBANCES

This section describes the effects of ionospheric disturbances so geographically widespread that lateral gradients can be ignored.

### 3.1. Propagation Equations

The equations governing ELF propagation are available from many sources (e.g., Galejs [1972]), so need not be repeated here. We solve them numerically, accounting for the vertical inhomogeneity of the ionosphere and curvature of the earth. Our method is essentially that described by Budden [1961] or Field [1969]. To define the notation and illustrate the key dependences, we recapitulate the equation for the spatial dependence of the fields.

An ELF transmitting antenna would probably be oriented horizontally and operated in the endfire mode to excite the quasi-TEM mode--the only one that propagates well. The expression for the horizontal magnetic intensity H is

$$H = - \frac{iLLf}{120\pi} \sqrt{\frac{2\pi\mu_0}{c}} \frac{\Lambda_h}{\sqrt{\sigma_g \, c/v}} \cdot \frac{\exp\left( -\frac{2\pi i}{\lambda} \frac{c}{v} d \right) \exp\left( -\frac{\beta d}{8.7} \right)}{\sqrt{a} \, \sin \, d/a} \quad A/m , \tag{3}$$

where IL is the electric dipole moment of the transmitting antenna, f is the wave frequency, $\Lambda_h$ is the excitation factor for a horizontal dipole in the endfire direction, $\sigma_g$ is the effective ground conductivity in the vicinity of the transmitter, c is the speed of light, d is the distance from the source, and a is the earth's radius. The mode parameters that depend on the ionosphere and must be calculated numerically are the excitation factor $\Lambda_h$, the attenuation rate $\beta$ in decibels per megameter of propagation (dB/Mm), and the relative phase velocity, $v/c$. Although most quantities are in MKS units, we express all distances (L, $\lambda$, d, a) in megameters.

### 3.2. ELF Mode Parameters

The amplitude of a long-range ELF signal is most sensitive to changes in, first, the attenuation rate $\beta$; and, second, the excitation factor $\Lambda_h$. Figure 2 shows the dependence of $\beta$ on the intensity of the disturbance. The results are for 45 and 75 Hz, which approximate the frequencies most likely to be used in an ELF communication system. The extreme left side of Fig. 2 corresponds to the normal daytime model shown in Fig. 1, whereas the extreme right side corresponds to the very intense disturbance. In addition, our calculations employed 12 intermediate levels of disturbance, including the moderate and intense profiles in Fig. 1.

Figure 2 shows that the assumed disturbances can cause the attenuation rate to increase by 1 or 2 dB/Mm relative to normal daytime conditions, depending on the frequency. Although the curves span a wide range of intensities, they do not cover all cases because the waveguide characteristics depend on the spectrum of ionizing radiation as well as the intensity. In fact, calculations not repeated in detail here show that certain moderate-to-severe SPEs can cause the attenuation rate to approach 4 dB/Mm at 75 Hz. Moreover, Pappert [1980] showed that sporadic-E patches could cause the normal daytime attenuation rates as great as 10 dB/Mm at frequencies around 75 Hz. However, these large attenuation rates can occur only over fairly localized (1 Mm × 1 Mm) regions, and only for a narrow (~5 Hz) frequency band that resonates with the vertical structure of the patch.

The behavior of the excitation factor is so simple that we need not plot it. In the idealized limit of a perfectly reflecting, sharply bounded ionosphere at a height $H_0$ above ground, $\Lambda_h$ is equal to $1/2H_0$.

Even for diffuse ionospheric boundaries, as are treated in this paper, the magnitude of $\Lambda_h$ is of the same order as the reciprocal of the nominal ionospheric reflection heights. Thus, an ionospheric disturbance that lowers the effective reflection height will increase $\Lambda_h$. The very intense disturbance in Fig. 1 enhances the excitation of the TEM mode by about a factor of two.

### 3.3. Field Strength versus Distance

Figure 3 plots ELF field strength as a function of distance, with daytime conditions and 1 W of power radiated at 75 Hz from a horizontal electric dipole. The normal curve shows signal strength versus distance for the normal model of Fig. 1 and a path over seawater. The other curve pertains to the intense disturbance of Fig. 1, and could represent either a very strong SPE or a spread-debris nuclear environment. Comparison of the two curves shows that the disturbed signal falls below the normal one, provided that at least 3 Mm of path are exposed. At shorter ranges, however, the signal is stronger in disturbed than in normal conditions. Such short-range enhancement occurs because the disturbance constricts the earth-ionosphere waveguide and increases the excitation factor. The enhanced excitation is overcome by increased attenuation for long paths.

The behavior illustrated in Fig. 3 is typical of that calculated for strong, stratified disturbances that cover both terminals and the entire propagation path. Such environments can degrade long-haul ELF signals by several decibels—a much weaker effect than the tens-of-decibels degradation that can be suffered at VLF. However, the difficulty of radiating power at ELF can make a signal loss of even a few decibels significant.

If a disturbance covers most of the propagation path but not the terminals, the benefit of enhanced excitation will be lost and the signal degradation can be worse than shown in Fig. 3. That situation can occur, for example, on a transpolar link during an SPE. Conversely, if a disturbance affects only the region near a terminal, a signal enhancement can occur regardless of pathlength. Such disturbances are nonstratified, and can produce reflections and diffraction accounted for in Sec. 4.

Our calculations assume a perfectly conducting ground and neglect the geomagnetic field. Heating of the ground and leakage through the ionosphere are therefore not a factor, and the attenuation is entirely due to heating losses suffered in the ionosphere. Figure 4 shows the height profiles of total and ion heating loss; the difference between the two curves is due to electron heating. We see that ion heating is the dominant loss mechanism for the ELF TEM mode under strongly disturbed conditions. The disturbance constricts the earth-ionosphere waveguide and confines the fields largely to altitudes below 50 km. Calculations not repeated here show that ion heating—though nonnegligible—is relatively less important under normal conditions.

### 4. EFFECTS OF NONSTRATIFIED DISTURBANCES

Even such large inhomogeneities as sporadic-E patches, the polar cap boundary, the ionospheric depression from a nuclear burst, and the day/night terminator can cause the properties of the earth-ionosphere waveguide to change markedly over the huge wavelength or Fresnel zone of an ELF signal. Such inhomogeneities therefore cannot always be assumed stratified. This section describes our integral equation method for analyzing the effects of nonstratified disturbances and gives some numerical examples.

### 4.1. Integral-Equation Approach

Under conditions in which the ionosphere is laterally uniform, the field can be written [Galejs, 1972]

$$F_0 = A\Lambda_0 F_0(z)\widetilde{E}_0(x, y) \quad V/m , \tag{4}$$

where $E_0$ is the vertical component of the electric field; A is a constant involving dipole moment, wave frequency, and ground conductivity; $\Lambda_0$ is the excitation factor of the TEM waveguide mode; $F_0(z)$ is the height gain function, normalized to unity at $z = 0$; x, y, and z are cartesian coordinates, with z denoting altitude; and the subscript 0 denotes undisturbed, laterally homogeneous conditions.

The lateral dependence of the field is governed by the function $\widetilde{E}_0$, which satisfies the two-dimensional wave equation

$$\left(\nabla_T^2 + k^2 S_0^2\right)\widetilde{E}_0 = 0 , \tag{5}$$

where $\nabla_T^2$ is the two-dimensional Laplacian, k is the free-space wave number, and $S_0$ is a waveguide propagation constant determined by imposing boundary conditions on $F_0$ at the ground and in the ionosphere. At large lateral distances d from the source,

$$E_0 \propto \exp(-ikS_0 d) . \tag{6}$$

Thus, $\mathrm{Re}S_0$ is the ratio of the speed of light to the phase velocity of the TEM waveguide mode, and $\mathrm{Im}S_0$ is proportional to the attenuation coefficient $\beta$ such that

$$\beta = -8.6k\,\mathrm{Im}S_0 \quad dB/Mm , \tag{7}$$

where k is expressed in $Mm^{-1}$.

In the presence of lateral ionospheric gradients, fields cannot be expressed as products of vertical and radial functions, as they are in Eq. (4). But when irregularities are large enough to significantly affect ELF propagation, scales for lateral variations of the ionospheric refractive index tend to be much longer than those for vertical variations. We therefore argue that the waveguide propagation parameters depend mainly on the local ionosphere, and that separation of the fields into vertical and lateral functions is an approximately correct procedure. The ground-level field [note that $F(z = 0) \equiv 1$] can then be written

$$E \approx A\Lambda(x, y)\widetilde{E}(x, y) , \tag{8}$$

where the lateral dependence resides mainly in $\widetilde{E}$, satisfying

$$\left[\nabla_T^2 + k^2 S^2(x, y)\right] \widetilde{E} = 0 , \tag{9}$$

Unlike $S_0$, the function $S(x, y)$ exhibits a spatial dependence, which accounts for lateral ionospheric gradients. That dependence precludes analytic solution of Eq. (9) in all but a few special cases.

4.2. Laterally Bounded Disturbances

To calculate the propagation anomaly due to a laterally bounded disturbance, it is convenient to recast the wave equation as an integral equation. We define a propagation function W, denoting the fractional amount by which the disturbed lateral wave function $\widetilde{E}$ differs from the undisturbed function $\widetilde{E}_0$; specifically,

$$\widetilde{E}(x, y) \equiv W(x, y)\widetilde{E}_0(x, y) . \tag{10}$$

Then, by applying the two-dimensional Green's theorem, and following the procedure of Field and Joiner [1979], we find that W satisfies the following equation if the transmitter is a horizontal electric dipole:

$$W(x, y) = 1 - \frac{ik^2}{4} \int \int_{-\infty}^{\infty} dx'\, dy' \left[S^2(x', y') - S_0^2\right]\left(\frac{x'r}{xr_1}\right)\frac{H_0^{(2)}(kS_0 r_2)H_1^{(2)}(kS_0 r_1)}{H_1^{(2)}(kS_0 r)} W(x', y') , \tag{11}$$

where H is the Hankel function and the geometric terms are as defined in Fig. 5. Equation (11) is similar to that used to analyze ground wave propagation over nonuniform terrain (e.g., by Hufford [1952]).

To illustrate the dependence of the fields on key parameters, we represent the disturbed region shown in Fig. 5 by

$$S^2(x, y) - S_0^2 = \left(S_1^2 - S_0^2\right)\exp\left[-\frac{(x - \bar{x})^2}{(\Delta x)^2}\right]\exp\left[-\frac{(y)^2}{(\Delta y)^2}\right] , \tag{12}$$

where $S_1^2$ denotes the value of the waveguide propagation constant at $x - \bar{x}$, $y = 0$. The disturbance is assumed to center on the x-axis, and y denotes the transverse location of the receiver. Adjusting $S_1^2 - S_0^2$, $(\Delta x)^2$, $(\Delta y)^2$, and $\bar{x}$ hence allows Eq. (12) to represent disturbances with different strengths, lateral gradients, and longitudinal positions. The disturbance effectively vanishes when $|x - \bar{x}|$ or y becomes several times greater than $\Delta x$ or $\Delta y$, respectively. Although the numerical results pertain to the model described by Eq. (12), our algorithm for solving Eq (11) works equally well for any bounded disturbance.

4.3. Numerical Results

Figure 6 plots the magnitude of W as a function of the off-path distance y for a strong, longitudinally confined ($\Delta x = 0.5$ Mm) disturbance, with curves shown for several effective half-widths $\Delta y$. Our calculations employ values of $S_1$ and $S_0$ corresponding to the intense disturbance and normal profiles in Fig. 1. In Fig. 6a, W is computed from the simple nondeviative WKB formula

$$W_{WKB} \sim \exp\left\{-ik \int_0^r \left[S(x', y') - S_0\right] dr'\right\} , \tag{13}$$

where the integration path is the straight line connecting transmitter and receiver. The figure shows that Eq. (13) gives the intuitively expected result; namely, W is smallest for $y = 0$, where the direct path intersects the peak of the disturbance, and approaches unity for $y \gg \Delta y$—when the direct path effectively misses the disturbance.

On the other hand, W calculated from the integral equation (11) is shown in Fig. 6b to exhibit a pattern on the line $x = 10$ Mm: a maximum for $y = 0$, a minimum a few megameters off-path, and then increasing

with off-path distance. That counterintuitive full-wave behavior of W is due to focusing and diffraction--the effects of which are ignored in the nondeviative WKB formula.

Focusing occurs because wave normals bend toward regions where $S(x, y)$ is large. The disturbance therefore causes the waveguide to behave as a converging cylindrical lens. Diffraction occurs because the effective aperture filled by the "lens" is approximately $2\Delta y$, which is smaller than or comparable to a Fresnel zone for the parameters used here. Focusing actually overcomes anomalous attenuation through the center of the narrowest disturbances, causing $|W|$ to exceed unity. The diffraction/focusing pattern smoothes out as $2\Delta y$ approaches the width of the first Fresnel zone--about 6 Mm for the 10 Mm pathlength used here. The differences between Figs. 6a and 6b illustrate the importance of using full-wave analysis at ELF, even for disturbances of considerable lateral extent.

To illustrate the longitudinal dependence of the field, Fig. 7 plots $|W|$ as a function of the longitudinal distance x for a strong disturbance of half-width $\Delta x = 0.5$ Mm and transverse half-width $\Delta y = 1$ Mm, centered on the direct path. The standing wave pattern in front of the disturbance is caused by reflections from the longitudinal gradient; it is much less pronounced for larger values of $\Delta x$. The magnitude of W gradually recovers toward unity behind the disturbance, because the Fresnel zone broadens--and is therefore less completely filled by the disturbance--as the propagation path lengthens. Such a recovery does not occur for disturbances that are unbounded in the transverse direction.

## 5. DISCUSSION

Our calculations cannot be directly compared with measurements until controlled-source ELF experiments are carried out under disturbed conditions. However, the literature survey of Field [1978] identified a number of atmospheric noise measurements relevant to the effects of ionospheric disturbances on ELF propagation. The measurements pertain to the behavior of ELF/VLF noise intensity and earth-ionosphere cavity resonances during (1) several SPEs, (2) more than 30 solar flares, and (3) the Starfish high-altitude nuclear detonation. They permit several key theoretical predictions to be verified semiquantitatively.

There is substantial agreement between calculations and ELF/VLF noise intensity measured during solar flares. Experiments [Sao and Jindoh, 1966; Sao et al. 1970] consistently show that nearly all flares cause the intensity to increase at frequencies between 30 Hz and 1 kHz, decrease between 5 and 10 kHz, and again increase between 10 and 30 kHz. Calculations show that such flares reduce the waveguide attenuation rate at frequencies where noise enhancement is measured, but raise it in spectral regions where the noise usually diminishes. This agreement, which occurs over three frequency decades, supports results of the computational models for stratified disturbances.

Measurements of ELF noise intensity during two SPEs were reported by Larsen [1974], but too few data were gathered to determine conclusively whether SPEs alter ELF atmospheric noise levels. Measurement of the behavior of a transpolar ELF signal during an SPE would provide valuable data, particularly if the ionospheric height profile is measured simultaneously.

Although the Schumann resonance band (8 to 30 Hz) is somewhat lower than the ELF communications band (45 to 80 Hz), both propagate in the TEM waveguide mode. Data on Schumann resonances may therefore be meaningfully compared with the outputs of ELF propagation codes. Such a comparison semiquantitatively supports the validity of the calculations. Specifically, the calculations predict that either Starfish or the SPEs would cause the frequencies of the Schumann resonance peaks to shift downward by 0.5 to 1 Hz and the Qs of the resonances to decrease. The shift in resonant frequencies is due to the depressed ionosphere reducing the phase velocity of the signal; the decrease in Q is caused by an increase in the attenuation rate in the earth-ionosphere waveguide. Measurements by Balser and Wagner [1963], Gendrin and Stefant [1962], Teply et al. [1963], and Nelson [1967] support these predictions.

To our knowledge, no ELF measurements have been made that could directly confirm or deny our predictions for nonstratified disturbances. However, the conclusion that disturbances varying over a wavelength or a Fresnel zone will cause reflection or diffraction--and must be analyzed with full-wave methods--appears intuitively correct. Moreover, although our models are based on daytime SPEs or nuclear environments, the signal structure predicted for localized disturbances resembles that calculated by Pappert [1980] for sporadic-E patches. Finally, our predicted standing wave and diffraction patterns could contribute to the anomalous lateral fluctuations occasionally observed on ELF transmissions from the Wisconsin Test Facility [Bannister, 1981].

## REFERENCES

BALSER, M., and C. A. WAGNER, 1 July 1963, "Effect of a High-Altitude Nuclear Detonation on the Earth-Ionosphere Cavity," *J. Geophys. Res.*, Vol. 68, No. 13, pp. 4115-4118.

BANNISTER, P. R., 1981, "Overview of ELF Propagation," presented at AGARD 29th Symposium on Medium, Long and Very Long Wave Propagation (at Frequencies Less than 3000 kHz), Brussels, Belgium, 21-25 September 1981, Paper 10.

BUDDEN, K. G., 1961, *The Waveguide Mode Theory of Wave Propagation*, Logos Press, London.

FIELD, E. C., 1969, "Propagation of ELF Waves under Normal or Naturally Disturbed Conditions," *J. Geophys. Res.*, Vol. 74, pp. 3639-3650.

FIELD, E. C., 1 December 1978, *ELF Propagation under Disturbed Conditions: Comparison of Theory with Available Data*, Defense Nuclear Agency, Report DNA 4700F.

FIELD, E. C., 1981, "VLF Propagation in Disturbed Environments," presented at AGARD 29th Symposium on Medium, Long and Very Long Wave Propagation (at Frequencies Less than 3000 kHz), Brussels, Belgium, 21-25 September 1981, Paper 17.

FIELD, E. C., and R. G. JOINER, 1979, "An Integral-Equation Approach to Long-Wave Propagation in a Non-Stratified Earth-Ionosphere Waveguide," *Radio Sci.*, Vol. 14, No. 6, pp. 1057-1068.

GALEJS, J., 1972, *Terrestrial Propagation of Long Electromagnetic Waves*, Pergamon Press, New York.

GENDRIN, R., and R. STEFANT, 29 October 1962, "Effet de l'explosion thermonucléaire à très haute altitude du 9 julliet 1962 sur la résonance de la cavité terre-ionosphère. Resultats expérimentaux," *Comptes Rendus* (Paris, France), Tome 255, No. 18, pp. 2273-2275.

HUFFORD, G., 1952, "An Integral Equation Approach to the Problem of Wave Propagation over an Irregular Surface," *Quart. Appl. Math.*, Vol. 9, pp. 391-403.

LAPSEN, T., 1974, "ELF Noise Measurements," in J. A. Holtet (ed.), *ELF/VLF Radio Wave Propagation*, D. Reidel Publishing Co., Dodrecht-Holland, pp. 233-238.

NELSON, R., 12 May 1967, *Ionospheric Perturbations and Schumann Resonance Data*, Ph.D. thesis, Massachusetts Institute of Technology, Department of Geology and Geophysics.

PAPPERT, R. A., 1980, "Effects of a Large Patch of Sporadic-E on Night-Time Propagation at Lower ELF," *J. Atmos. Terr. Phys.*, Vol. 42, No. 5, pp. 417-425.

PAPPERT, R. A., and W. F. MOLER, April 1974, "Propagation Theory and Calculations at Lower Extremely Low Frequencies (ELF)," *IEEE Trans. Comm.*, Vol. COM-22, pp. 438-451.

SAO, K., and H. JINDOH, 1966, "SEA Phenomenon on E.L.F. Atmospherics," *J. Atmos. Terr. Phys.*, Vol. 28, pp. 97-98.

SAO, K., et al., 1970, "Sudden Enhancements (SEA) and Decreases (SDA) of Atmospherics," *J. Atmos. Terr. Phys.*, Vol. 32, pp. 1567-1576.

TEPLY, L., et al., 26 December 1963, *Sub ELF Geomagnetic Fluctuations: Vol. III, Observations of Transient and Background VLF, ELF, and Sub ELF Electromagnetic Effects Produced by High-Altitude Nuclear Detonations*, Lockheed Missiles and Space Company, Report AF 19(628)-462.
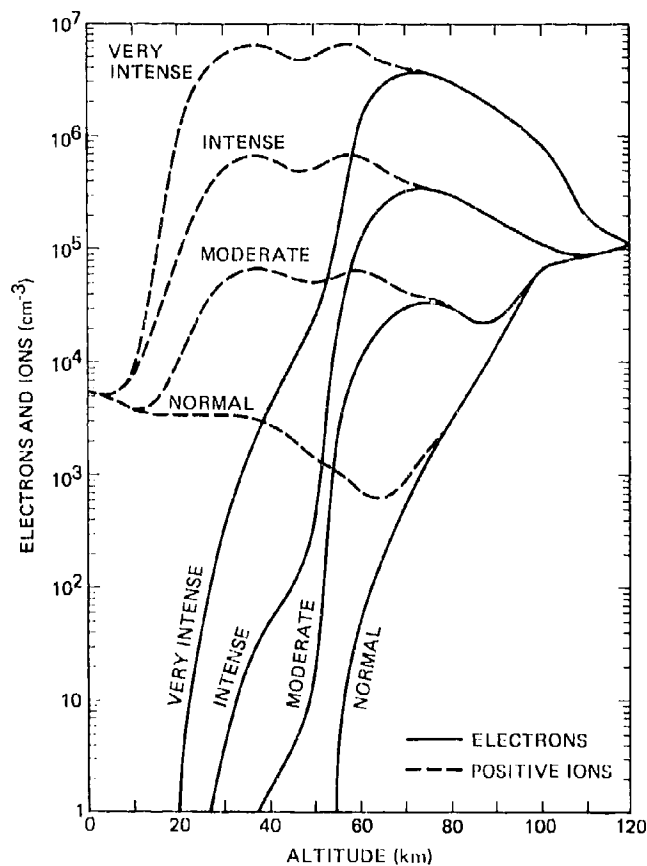
Figure 1. Electron and ion density profiles for nominal daytime normal
and disturbed environments
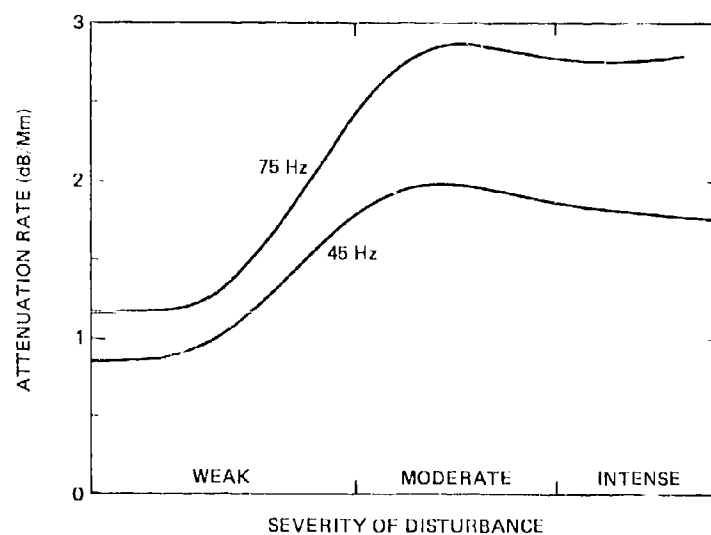


Figure 2. Attenuation rate β in disturbed environments. The in-
tensity of the disturbance varies continuously from normal
daytime conditions (extreme left) to very intense (extreme
right)
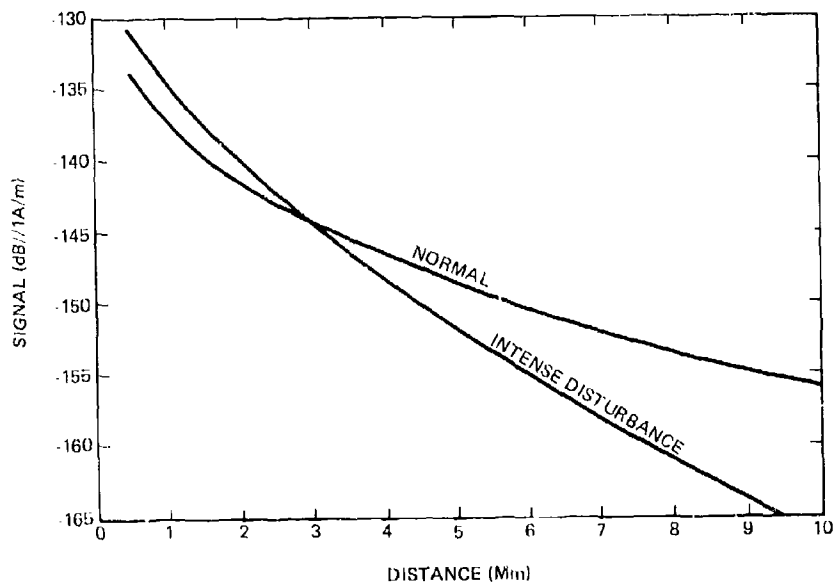
Figure 3. Daytime electric field strength versus distance d: 1 W radiated power and f = 75 Hz
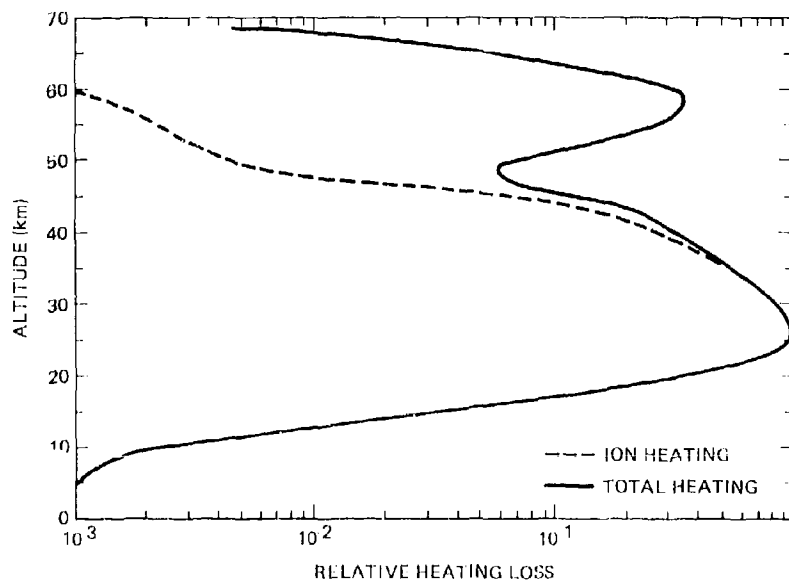


Figure 4. Ionospheric heating loss profiles for TEM mode and intense disturbance: f = 75 Hz
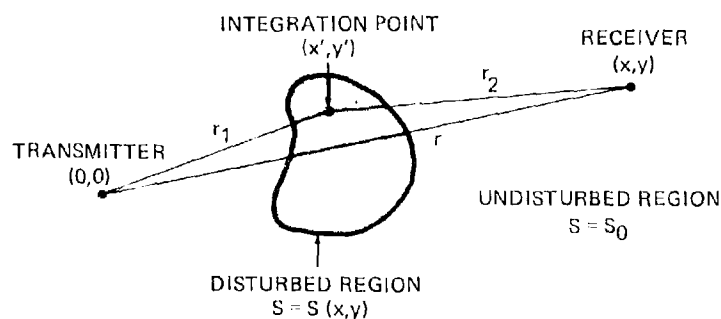
Figure 5.  Schematic of propagation for laterally bounded ionospheric disturbance

(a) WKB APPROXIMATION
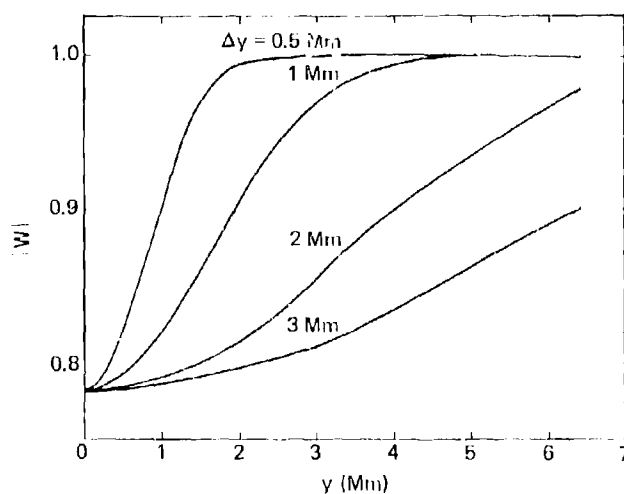


(b) INTEGRAL EQUATION
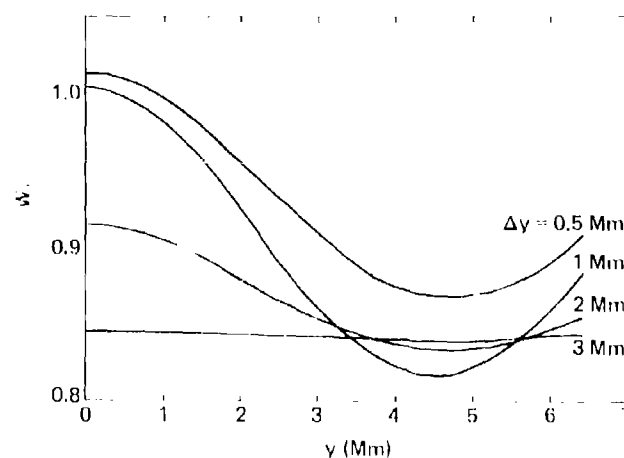


Figure 6.  Amplitude of W versus off-path distance y for intense disturbance of half-width Δy:  x = 10 Mm, x = 5 Mm, Δx = 0.5 Mm, and f = 75 Hz
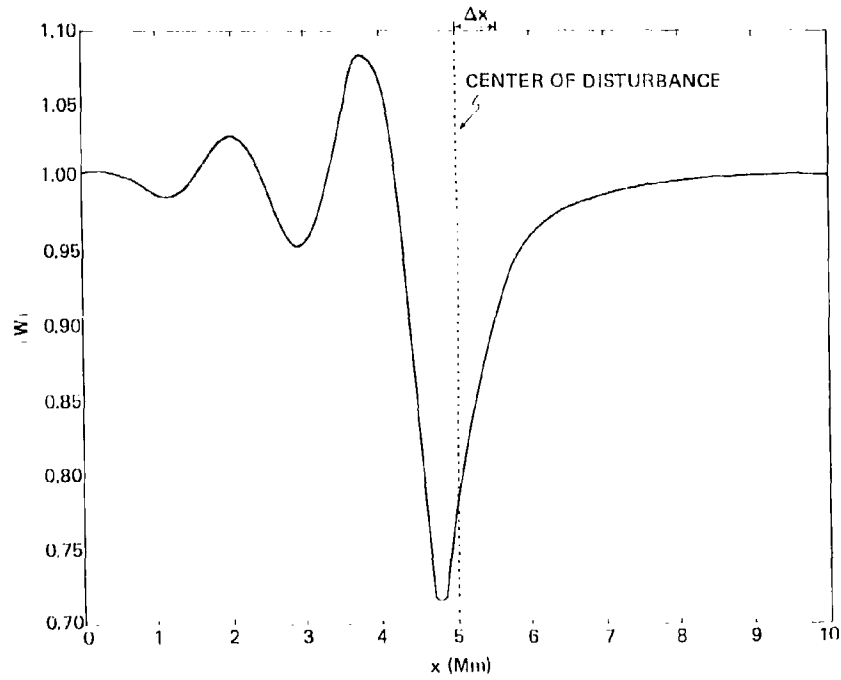
Figure 7. Amplitude of W versus longitudinal distance x for intense
disturbance of half-width $\Delta y = 1$ Mm: $\bar{x} = 5$ Mm, $\Lambda x = 0.5$ Mm,
and $f = 75$ Hz

ELF PROPAGATION IN POLAR AREAS, MEASUREMENTS
AND THEORETICAL FIELD STRENGTH PREDICTIONS

T. R. Larsen

Norwegian Defence Research Establishment
Kjeller, Norway
and
W. L. Imhof, R. C. Gunton
J. B. Reagan, E. E. Gaines, and R. E. Meyerott

Lockheed Palo Alto Research Laboratory
Palo Alto California 94304

ABSTRACT

ELF field strength propagation data as recorded in polar areas by the U. S. Naval Research Laboratory
frequently show periods of abnormally low values. It has been speculated that these disturbances are
due to precipitating particles causing enhanced ionization in the lower ionosphere, but no direct
relationship has so far been advanced. The paper will discuss the influence of the ionosphere upon ELF
propagation at 75 HZ. Results will be presented for the propagation path from the U.S. Navy ELF
Wisconsin Test Facility transmitter to Tromsø, Norway. This 6 megameter path crosses the Greenland
icecap and passes twice through the auroral regions. In these studies full wave computations have been
made using the waveguide mode program developed by Naval Ocean Systems Center, San Diego. The propaga-
tion path has been divided into eight segments taking into account in an approximate way the varying
boundary conditions of the actual waveguide. Results will be presented and discussed for conditions
ranging from ambient to severely disturbed. Modeling has been done for disturbed ionospheric conditions
such as sporadic E-layers, relativistic electron precipitation, auroral events and solar proton events.
Detailed electron and ion density profiles have been deduced from satellite observations in the vicinity
of the path. The importance of the electron as well as the ion concentrations will be discussed.

## 1. INTRODUCTION

Extremely low frequency (ELF) transmissions at nighttime are known to be quite variable. Transmissions
from the U.S. Navy operated Wisconsin Test Facility (WTF) to receiving sites both at middle and high
latitudes are observed to experience anomalous and significant signal strength reductions of up to 3-5dB
on approximately 60 to 80 nights per year. In recent years, it has been recognized that at least some
of the observed anomalies are due to enhanced ionization caused by precipitation of energetic electrons
and protons into the earth's atmosphere.

The paper will describe measurements and theoretical field strength calculations in relations to polar
propagation paths. The various possible ionospheric variations giving rise to propagation anomalies are
discussed. Initially, a brief description is given of the ELF waveguide model used by the authors as
well as a short summary of recent advances in the treatment and understanding of ELF propagation.

## 2.0 PROPAGATION OF ELF WAVES – THEORETICAL APPROACHES TO THE CALCULATION OF FIELD STRENGTHS

### 2.1 The NOSC Model Computer Program

A waveguide model computer program that has been used extensively over the last years and which is also
being used by the present authors at Lockheed Palo Alto Research Laboratory (LPARL), was developed at
Naval Ocean Systems Center (NOSC). This program is well documented in the literature (see e.g. Sheddy
1968; Pappert, 1970; Pappert and Moler, 1974). The program is based upon the formalism developed by
Budden (1961) and Budden and Daniell (1965) for electromagnetic wave propagation in the terrestrial
waveguide. Special emphasis has been given to its applicability in the extremely low frequency (ELF)
range.

The program allows for a terrestrial waveguide with the following characteristics:

- Arbitrary electron and ion density distributions with height
- Variable electron and ion collision frequency height profiles
- The lower boundary of the waveguide is assumed to be a smooth homogeneous earth with arbitrary
  conductivity and permittivity
- Allowance is made for the anisotropy of the ionosphere; arbitrary values for the strength and
  direction of the earth's magnetic field may be applied
- Horizontal inhomogeneties (along the propagation path) may be taken into account by segmenting the
  path into regions having different height profiles for the waveguide parameters listed above.

The computer program is thus capable of treating waveguides that are reasonable model representations of
the actual complex terrestrial waveguide. The program does not allow for variatiton of the guide
parameters perpendicular to the propagation path, therefore uniform conditions have to be assumed over
distances extending a Fresnel Zone or more to either side of the path. This restriction has long been
recognized as a major limitation of the model.

### 2.2 Recent Developments

In actual radio wave propagation situations both lateral and transverse variations can be expected to
occur over most paths, especially at high latitudes. Recently, off-path effects have been considered
and important steps have been taken in approaching formulations that address the real three-dimensional
problems, at least in an approximate way (Pappert, 1980; Field and Joiner, 1979; Greifinger and Grei-
finger, 1978, 1979; Booker, 1980) as briefly described below.
Pappert (1980) treating localized disturbances in a surface propagation model coupled with a moments

method, finds that a thick ionization patch at E-region heights can produce 6-8dB fades in signal strength for a 1.6Mm propagation path. Deepest fades occur when the disturbed area is well within the first Fresnel Zone, and varying amount of fade is predicted depending on size and location of the disturbance area. When the center of the disturbance is located outside the second Fresnel Zone, ne predicts that most of the amplitude fades are damped out.

Field and Joiner (1979) use an integral-equation approach for analyzing propagation in the earth-ionosphere waveguide where conditions change over distances comparable with a Fresnel Zone. They derive an expression for the relative errors introduced by neglecting transverse ionospheric gradients over the path and find that full wave methods must be applied when the effective width of a localized disturbance is less than two-thirds of the width of the first Fresnel Zone. These authors also conclude that the WKB approximation significantly over-estimates the propagation anomaly when the disturbance is centered near the propagation path and underestimates the anomaly when the disturbance in centered far off path (c.f also Field, 1978, 1979, Field et al., 198

Further physical insight into ELF propagation and ionospheric parameters has been achieved by Greifinger and Greifinger (1978, 1979) in associating the eigen value solution mainly with ionospheric properties at two well defined altitudes where maximum ohmic heating occurs. Along with two scale heights at these altitudes, they derive an approximate solution for the ELF mode at high latitudes. They show that the lower altitude region of interest occurs where the conduction current parallel to the magnetic field becomes equal to the displacement current. At these heights the associated scale height is that of the parallel conductivity. At the other height regions the scale height in question is that of the refrac-tive index. For daytime conditions the authors find that this upper height level is situated where the local wave number becomes equal to the reciprocal of the local scale height of the refractive index. With knowledge of these four parameters an approximate wave solution may be found. The authors conclude that the principal attenuation mechanisms are Joule heating by longitudinal currents in the vicinity of the lower altitude and energy leakage of the whistler component of the ELF wave at the upper altitude.

Booker (1980) presents an extensive survey of ELF propagation and outlines a theory for propagation in the earth-ionosphere transmission line based on the work of Greifinger and Greifinger (1979) and the earlier theory by Booker and Lefeuvre (1977). His method greatly advances the physical understanding of the complex reflection and absorption processes. Booker (1980) draws attention to several important results important for understanding ELF propagation, among others:

- At ELF the transition from nearly horizontal phase propagation to nearly vertical propagation takes place in a refracting stratum at the bottom of the ionosphere.
- Between the bottom of the ionosphere and the level of ELF reflection, change of phase can as a first approximation be calculated on the basis of vertical propagation in free space.
- The reflecting stratum is located approximately at the level where the ionosphere fails to respond as a doubly refracting medium to the ELF waves.
- Thus, above the reflecting level the ionosphere is a slowly-varying, non-isotropic medium, whereas below it, the ionosphere behaves essentially as an isotropic medium.

In this theory Booker includes the magnetic field and derives a propagation model with worldwide application.

## 3.0 ELF TRANSMITTER AND PROPAGATION PATH CHARACTERISTICS

A thorough and comprehensive treatment of man-made ELF experiments is given in a special issue of IEEE Transaction of Communications (April 1974). Limited experimental activity has continued since 1974 using the U.S. Navy's experimental transmitter facility in Wisconsin.

### 3.1 The U.S. Navy ELF Transmitter (Wisconsin Test Facility - WTF)

The Navy ELF Wisconsin Test Facility (WTF) consists of two 22.5 km north-south antennas, and one 22.5 km elevated east-west antenna. Each antenna is grounded at both ends. The antenna array pattern can be steered to any particular receiving direction. The transmitter has been operated in the 45 and 75 Hz bands with antenna currents of 300 A. The antenna radiation pattern and soil conductivity ( ..) under the antenna, have been measured by Bannister & Williams (1974), and all ELF field strength values presented here have been normalized to nominal antenna characteristics and the revised antenna radiation pattern (Bannister et al., 1974) is applied.

### 3.2 The Ionospheric Conditions Near the Transmitter

In Figure 1 is indicated the location of the transmitter as well as positions of selected magnetic L-shells. The Booker excitation circle (Booker, 1973) is plotted for a frequency of 75 Hz (radius equals $\lambda_0/2\pi$, where $\lambda_0$ is the free space ELF wavelength). Superposed on the figure is the counting rate of precipitating energetic electrons (> 150 keV) as measured of a pass by the 1972-076B satellite. Such latitude variations of the incoming fluxes are quite typical, and will cause marked local perturbations in the ionized state of the ionosphere below 100 km.

Thus, in this case homogeneous ionospheric conditions do not exist over the whole excitation region of the transmitter. Experience from several years of satellite measurements indicate the precipitating electrons in the L range of 3-5 are probably present most of the time, exhibiting dynamic time and spatial variations.

Such findings complicate the ELF field prediction schemes, and this problem has yet not been attacked fully from a theoretical point of view. In model calculations homogeneous conditions over the trans-mitter area are assumed.

## 3.3 ELF Path Characteristics

The NOSC ELF computer code allows calculations to be made with the propagation path divided into a number of segments, within which the propagation medium and boundary conditions are kept constant. Table 1 lists for the path WTF to Tromsø the segmentation and data for the various segments as used by the authors.

| Segment No. | Segment | Distance Range from WTF (km) | Conductivity (mho/m) | Rel. Perm. $E/E_o$ | Mag. Field $(Wb/m^2)$ | Co-dip (deg.) | Prop Direct. (azimuth in degrees) |
|---|---|---|---|---|---|---|---|
| 1 | Transmitter Area | 0-200 | $3.2 \times 10^{-4}$ | 15 | $5.94 \times 10^{-5}$ | $15.5^{\circ}$ | $20^{\circ}$ |
| 2 | Canada | 200-1000 | $1.0 \times 10^{-3}$ | 15 | $6.05 \times 10^{-5}$ | $11.6^{\circ}$ | $27^{\circ}$ |
| 3 | Hudson Bay | 1000-1800 | 4.0 | 81 | $6.00 \times 10^{-5}$ | 7.7 | $52^{\circ}$ |
| 4 | North Canada | 1800-2900 | $1.0 \times 10^{-3}$ | 15 | $5.83 \times 10^{-5}$ | $6.4^{\circ}$ | $89^{\circ}$ |
| 5 | Davis Straight | 2900-3300 | 4.0 | 81 | $5.72 \times 10^{-5}$ | $6.6^{\circ}$ | $102^{\circ}$ |
| 6 | Greenland Ice Cap | 3300-4400 | $1.0 \times 10^{-5}$ | 5 | $5.50 \times 10^{-5}$ | $8.0^{\circ}$ | $115^{\circ}$ |
| 7 | Norwegian Sea | 4400-5800 | 4.0 | 81 | $5.26 \times 10^{-5}$ | $10.6^{\circ}$ | $122^{\circ}$ |
| 8 | Receiver Area (Tromso,Norway) | 5800-6000 | $1.0 \times 10^{-3}$ | 15 | $5.23 \times 10^{-5}$ | $12.2^{\circ}$ | $128^{\circ}$ |

Table 1   Data for segmented propagation propagation path WTF to Trmosø.

Other paths have been segmented in a similar manner (Imhof et al., 1977).

Effects of changes in the ionospheric conditions due to different solar zenith angles along the propagation paths (local time dependency) have also been considered and will be further discussed in section 7.

## 4.0 ELF PROPAGATION MEASUREMENTS AND PREDICTIONS

A number of reports present results from recording of WTF signals propagated over different paths in the USA  and to Europe (Bannister and Williams, 1974; Bannister, 1974; Davis, 1974, 1976):

Data for paths such as:

- WTF to Connecticut, USA          (1.6 Mm path length)
- WTF to Greenland                     (3.6 Mm path length)
- WTF to Tromsø, Norway            (6.0 Mm path length)
- WTF to Pisa, Italy                     (7.5 Mm path length)

have been collected indicating the diversity of different propagation media analyzed.

The measurements have yielded several general features of ELF propagation, viz:

- Seasonal changes in ionospheric characteristics influence ELF propagation, e.g. through variation in the attenuation rates and relative excitation factors.
- Daytime attenuation rates at 75 Hz are higher than nighttime values, typical ambient values are 1.1-1.3 dB/Mm at day and 0.8-1.0 dB/Mm at night.
- Nighttime propagation is more variable than daytime propagation.
- Polar cap and auroral zone effects are found in ELF propagation.

Such findings, reported e.g. by Bannister (1974) are also reflected in theoretical field strength predictions using propagation models with ambient and disturbed ionospheres (Pappert and Moler, 1974; Pappert, 1978, 1980; Field and Joiner, 1979; Imhof et al., 1976, 1977, 1978a, 1980).

## 4.1  Short Path Propagation

Results of some short path measurements (< 2000 km path length) have shown that anomalous signal reductions of 3 dB and more may occur with a frequency of ⊆ 30% of all nights. These signal strength reductions have been speculated to be caused by precipitation of electrons from the radiation belts resulting in enhanced ionization in the lower atmosphere. Attempts to correlate the anomalous signal strength behaviour with geomagnetic indices indicating the degree of disturbed magnetospheric conditions, have met with limited success.

As an example of short path measurements we show in Figure 2 the nighttime values obtained by Bannister and Williams (1974) for the years 1970-73 for the WTF to Connecticut path.  Signal strength variations,

possibly seasonal, are seen. The average value of all observations, however, agrees to within 0.1 dB of the predicted ambient night value as calculated by the present authors. Furthermore, 'n Figure 3 is depicted an anomalous signal reduction event occuring on 19 April 1973. The signal reduction lasting several hours amounted to ≃ 5 dB as compared witn night values before and after the event. It has not yet been possible to associate such signal attenuation with a discrete electron precipitation event using satellite data coordinated in time and space with the propagation anomaly.

## 4.2 Long Distance Propagation

Long distance ELF propagation also shows signal fades which do not directly seem to be associated with the intensity of energetic particle precipitation. Figures 4 and 5 show ELF measurements by 'avis & Mayers (1975), and Bannister (private communications, 1978), respectively, togecher with plots of magnetic disturbance indicators. In Figure 5 energetic electron fluxes precipitating over/near the path are also given. No simple, systematic relation between low signal strengths, precipitating electron fluxes or geomagnetic disturbed periods is evident.

## 5.0 DISTURBED PROPAGATION CONDITIONS

In the following a discussion of possible influences of energetic electron precipitation (REPs and auroral events) and of sporadic E-layers on ELF propagation is presented.

## 5.1 Propagation During REP Conditions

Relativistic electron precipitation events frequently cause excess ionization in the ionospheric D-region to persist for one to several hours over relatively large geographical areas. Larsen (1974) infers that the disturbed area may extend over 2000 km in longitude. Satellite measurements indicate that the precipitation area may cover several degrees in latitude and one may therefore assume that the REPs may have such large geographic extentions that they can influence ELF propagation.

Examples of precipitating electron energy spectra measured at satellite altitudes are shown by Imhof et al., (1981, this issue). Often the spectrum "peaks" at energies between 800 - 1500 keV. Ion pair production rates from such events are high enough to give substantial increases in the electron density down to 50 - 60 km in altitude. Although such precipitation in the cases considered is observed in a limited latitude interval over/near the propagation path - it is not unreasonable to assume, as a first approximation, that precipitation also occurs     her longitudes simultaneously, cf Figure 6. With this assumption, it is possible to extimate t     ects on propagation over selected paths, cf Tables 2 and 3. It will be noted that signal enhancemeurs are predicted for all these nighttime REPs, by 1 dB or more when the effects occur over the transmitter (receiver) or tenths of dB when the effects are localized to limited areas over the paths. REP conditions over the complete path would markedly enhance the signal (by several dB). Similar findings are derived for auroral precipitation conditions.

| Event Date | Observed Invariant Latitude Range of Precipitation | Path Segment for Precipitation | Calculated Field Strength at 75 Hz WTF-Tromso (dB wrt to 1A/m) | Predicted Change From Ambient Night (dB) |
|---|---|---|---|---|
| Ambient Night | - | - | -154.7 | - |
| 26 March 1976 | $57.5° - 64.8°$ | 0 - 900 km | -153.6 | +1.1 |
| 19 April 1977 | $61.5° - 65.7°$ | 0 - 900 km | -153.5 | +1.2 |
| | | 200 - 900 km | -154.6 | +0.1 |
| | | whole path | -151.9 | +2.8 |
| 7 May 1977 | $65.2° - 68.9°$ | 0 - 1800 km | -153.4 | +1.3 |
| | | 1000 - 1800 km | -154.4 | +0.3 |
| | | whole path | -151.9 | +2.8 |

Table 2    Calculated field strengths for electron precipitation events. Transmissions from the WTF to the receiving station at Tromsø, Norway.

| Profile<br>Date | Path Segments<br>for Precipitation | Calculated Field<br>Strength at 75 Hz<br>(dB wrt 1 A/m) | Predicted Change<br>from Ambient Night<br>(dB) |
|---|---|---|---|
| Ambient Night | | −152.3 | − |
| 19 April 1977 | 0 − 1200 km | −152.1 | +1.2 |
| | 300 − 1200 km | −152.2 | +0.1 |
| 7 May 1977 | 0 − 1200 km | −151.2 | +1.1 |
| | 300 −− 1200 km | −152.1 | +0.2 |

Table 3   Calculated field strengths WTF − Greenland (3.5 Mm path) for 19 April and 7 May 1977 precipitating electron profiles.

In some cases REP ionization profiles have also resulted in predicted signal decreases. The position of the disturbed area in relation to the physical propagation path is the deciding factor (Imhof et al., 1978b).

In addition to direct ionization due to the electrons during an REP event, there is also some secondary ionization due to bremsstrahlung x-rays produced by the electrons. This contribution is usually neglected, but in some cases it ought to be considered. In some of the cases studied, the x-rays dominated as ionization source between 40 and 60 km, filling in the "valley" between the profile of the electron ionization and that of the galactic cosmic rays. Inclusion of the x-ray contribution resulted in one case in a predicted field strength enhancement of 0.7 dB over the signal strength computed without the x-ray ionization (calculated for the 1.6 Mm path: WTF − Connecticut).

In summary, ELF measurements (coordinated with satellite particle measurements) and ELF computer code predictions, have given the following conclusions:

- From both the satellite and ELF station measurements it has been found that direct particle precipitation into the atmosphere can cause ELF transmission anomalies. In these anomalies the signal strengths may be either attenuated or enhanced depending upon the path characteristics and details of the ion pair production profiles. Nighttime REP events may on the average improve ELF propagation conditions.
- Variations in the nighttime ELF signal strengths on a fine time scale are observed which may be due entirely to electron precipitation, but cannot be accounted for quantitatively due to present limitations in the measurements and computational techniques.
- The geometry for the effect of electron precipitation on nighttime ELF transmission is very complex and as a result the need for new techniques for mapping electron precipitation profiles simultaneously over a broad spatial region has become apparent.

5.2  Possible Influence of Sporadic E-Layers on ELF Propagation

Attempts to explain observed ELF signal variations in terms of excessive losses in sporadic E-layers have resulted in predicted signal fades of the right magnitude (Pappert 1978, 1980; Barr, 1977; Imhof et al., 1976, 1977, 1978a, 1980) both for short and long paths.

Measured $E_s$ layers are very thin (3-4 km or thinner), but they may extend over large geographical areas, up to 1 Mm and more (Whitehead, 1970). These layers do not reside at a constant height, but seem to move towards lower heights with time. One example of a sporadic E-layer measured at Wallops Island (Voss, private communication 1979; Smith and Miller, 1980) is shown in Figure 7.

Propagation characteristics at 75 Hz for such a profile indicate significant departures from ambient conditions, viz:

Ambient night:  Attenuation rate, $\alpha$ = 1.07 dB/Mm; Phase velocity/free space velocity, $v/c$ = 0.85

$E_s$ :  Attenuation rate, $\alpha$ = 1.83 dB/Mm; Phase velocity/free space velocity, $v/c$ = 0.75
In such cases the attenuation rate vs. frequency exhibits a pronounced peak, up to 10 dB/Mm or more. The frequency of this peak varies with thickness and height position of the $E_s$ layer. In this specific case, no peak was found in the attenuation rate vs. frequency when the $E_s$ layer was situated at 105 km where it originally was observed.

A resonant absorption effect may explain the high attenuation rates (cf Imhof et al., 1976, 1977; Pappert, 1978, 1980). Large values for the attenuation rates can furthermore result from reflections at more than one level in the ionosphere (Barr, 1977).

Amplitude variations on longer propagation paths may also tentatively be explained by sporadic E layers, in as much as propagation characteristics for such profiles indicate attenuation effects, but the degree of attenuation depends on the position of the $E_s$ layer with respect to the propagation path. As an example, in Table 4 is shown some computed field strength values for $E_s$ conditions over three selected areas for the path WTF to Tromsø, Norway. The values marked $E_s$ x 10 are calculated for an increase in the electron density of the $E_s$ layer (only) by a factor of 10, cf Figure . Apparently the geographic

position of the $E_S$ layer with respect to the propagation path and its intensity must be known in order to predict ELF field strength values for comparison with measured values.

| | Field strength dB WRT/A/m |
|---|---|
| Ambient night | − 154.7 |
| $E_S$ over receiver, ambient elsewhere | − 155.5 |
| $E_S$ over Norwegian Sea, ambient elsewhere | − 156.5 |
| $E_S$ x 10 over Norwegian Sea, ambient elsewhere | − 165.9 |

Table 4  Calculated field strengths at 75 Hz for propagation WTF to Tromsø, Norway.

Effects are predicted for an $E_S$ over Norwegian Sea area (~ 1400 km in lateral size) amounting to ~ 2 dB attenuation. For the very enhanced $E_S$ (Peak electron density of $1.5 . 10^6$ el/cm$^3$) a major signal fade in excess of 10 dB is predicted.

We may thus conclude that idealized $E_S$ disturbances have produced severe ELF attenuation in model calculations, but actual measurements of $E_S$ conditions have not been made during the operation of the Navy's ELF transmitter. Attempts to explain the observed ELF signal fades in terms of absorption due to $E_S$ conditions, can therefore not be conclusive, but the theoretical efforts in this area point out potential important considerations of $E_S$ effects on an ELF communication system.

## 6.0  CALCULATIONS FOR SIMULATED SPE CONDITIONS

There have been no actual measurements of signals from WTF during a solar particle event (SPE). Calculations, for simulated conditions, however, indicate that significant signal strength reductions could occur. The total amount of signal absorption would depend on the position of the ELF transmission path in relation to the extent of the disturbed area.

### 6.1  SPE Simulations Using Data from the August 1972 Event

Imhof et al., (1980) summarized their findings using simulated data from the August 1972 particle event as follows:

- SPE nighttime conditions as observed during the August 1972 event, will decrease the ELF signal at 75 Hz by several dB over a polar propagation path (WTF to Tromsø) for uniform conditions along the whole path.
- The received ELF field strength for such a path is predicted to be reduced by an additional 1-3 dB when the WTF transmitter area is outside the SPE disturbed area.
- The ELF signal strength was found to be sensitive to changes in the ion densities at heights below 45-50 km.

Additional calculations gave similar results also for daytime SPE conditions.

### 6.2  Sensitivity of ELF Field Strengths Using Other Simulated SPE Conditions

Since these studies emphasized the importance of SPE conditions in absorbing energy from the ELF waves, it was of interest also to make computations for other solar particle events, having energy spectra of different spectral shape and intensity. Results will be given for the following cases:

SPE of 12 Nov. 1960    1980 UT

SPE of  2 Nov. 1969    1948 UT

SPE of  4 Aug. 1972    1508 UT

The deduced electron and positive ion densities for these cases are plotted in Figure 8. It may be inferred that the November 1960 event had a harder proton spectrum yielding higher $N^+$ densities below 30 km than the August 1972 PCA. Above 80 km, however, the ionization due to the protons during the 1960 and 1969 events was below the normal ionization levels of the solar radiation and the daytime ambient $N_e$ and $N^+$ curves have been used from 80 to 160 km for these two cases.

Care has been taken to include proper ion densities at all heights. The values for the positive ions above 40 km are obtained using the chemistry code of Gunton et al., (1977). At lower altitudes the values for the positive ion density $N_+$ are obtained using the formula

$$N_+ \quad \sqrt{q/\alpha_i(h, T)}$$

where $\alpha_i$ is the height and temperature dependent ion-ion recombination rate and q is the ion pair production rate.

The calculated results are given in Table 5. As can be noted attenuation of up to 6-8 dB over ambient conditions is predicted for these SPE conditions.

| SPE | Calculated Field Strength (dB/1A/m) | |
|---|---|---|
| 12 Nov 1960 | −162.8 dB; | 8.1 dB below ambient |
| 2 Nov 1969 | −155.7 dB; | 1.0 dB below ambient |
| 4 Aug. 1972 | −160.4 dB; | 5.7 dB below ambient |

Table 5  Calculated ELF signal strengths at 75 Hz for the path WTF to Tromsø during solar proton events.

For these simulated cases, ambient conditions were assumed over the WTF transmitter area. In Table 6 is listed the S-values (sin ($\Theta$), the eigen-angle solution) for three selected segments of the path, representing a range in ground conductivity and different propagation with respect to the earth's geomagnetic field. For comparison, a recent S-value computed by Field et al. (1980) at 75 Hz for a "strong PCA" case is included.

| Segment | SPE 12 Nov 1960 | SPE 2 Nov 1969 | SPE 2 Aug 1972 |
|---|---|---|---|
| #6 Greenland Icecap, $\sigma = 10^{-5}$ mho/m | 1.4526-0.3084 i | 1.3563-0.1916 i | 1.4308-0.2725 i |
| #7 Norwegian Sea, $\sigma = 4$ mho/m | 1.3656-0.2139 i | 1.2681-0.1104 i | 1.3337-0.1725 i |
| #8 Tromsø Land, $\sigma = 10^{-3}$ mho/m | 1.3748-0.2252 i | 1.2767-0.1187 i | 1.3433-0.1830 i |
| Field (1980) Value for "strong PCA" | $S_1 = 1.50-0.25$ i | | |

Table 6  Computed values for S (= sin ($\Theta$)) at 75 Hz for various segments along propagation path WTF to Tromsø. Also given is the value deduced by Field et al., (1980) for "strong PCA" case.

## 6.3  Sensitivity of ELF Waves to Absorption by Ions at Low Altitudes During SPE Conditions

In this section we will briefly discuss the importance of ions below 45-50 km altitude in determining the absorption of ELF waves. Calculations were made at 75 Hz for the WTF to Tromsø path. To achieve this we have modified the 4 Aug 1972 and 12 Nov 1960 ion profiles at low altitudes, and calculated the effects. Figures 9 and 10 show the modifications and the corresponding computed field values, respectively.

It can be concluded that the ions formed by the high energy tail of the precipitating protons below 45-50 km are significant. In the case of the Nov 1960 event the ions below 40-45 km would cause about 8 dB attenuation over the 6 Mm path to Tromsø. The region 20-45 km seems to be the most important height range for this attenuation, but enhanced densities even below 20 km cause some absorption.

Figure 9, showing the modifications to the daytime 4 Aug 1972 (Test Case #1), also indicates effects due to a postulated "extreme" case for ion densities below 20 km. Here the ion densities are almost two orders of magnitude above ambient at 10 km level. The amount of ohmic heating that occurs at these altitudes is strongly reduced and only a minor (~ 1dB) amount of excess absorption takes place.

From the present and earlier studies the following conclusions can be drawn regarding importance of ions:

- Relatively little ELF attenuation seems to occur below about 20 km. For extreme cases with high $N^+$ densities some ELF attenuation is predicted to occur even at these altitudes.
- In the height range 20-45 km ions dominate as cause for the ELF wave attenuation through ohmic dissipation during disturbed conditions. Such ohmic losses may account for 50-60% of the total wave absorption, and they maximize around 30-40 km for the profiles analyzed.
- At heights above 45-50 km the ion contribution to the ionospheric conductivity decreases fast relatively to the electron component which rapidly becomes the dominant part at these and higher altitudes.

## 6.4  Sensitivity of ELF Waves to Changes in Electron Densities at Low Heights During SPE Conditions

During SPE daytime conditions the electron densities around 40 to 50 km may be 4-5 orders of magnitude above the ambient values. Clearly some uncertainty will be connected with the deduced electron densities ($N_e$) due to changes in reaction rate coefficients etc. A simple test on the sensitivity of the ELF field strengths to $N_e$ changes at low heights can be made by moving the lower part of the $N_e$ profile up and down, say 5 km, and perform field strength calculations for these cases.

As an example we have taken the 4 Aug 1972 SPE Day Test case #1 and modified it below 60 km in the way suggested above. The $N^+$ curve was kept unchanged as were the electron densities above 65-70 km.

Such calculations indicate that for a solar proton event like that on Aug 72 an uncertainty in the lower part of the $N_e$ profile of $\pm$ 5 km, would yield a $\pm$ 1 dB uncertainty in the field strength value.

It may be noted that lowering the profile at low altitudes by 5 km (making the ionosphere 5 km thicker) increases the expected signal level essentially through a lower value for the attenuation constant. Conversely, raising the $N_e$ profile by 5 km, resulted in increased attenuation rates by 0.3-0.4 dB/Mm.

## 7.0 EFFECTS OF CHANGE IN SOLAR ZENITH ANGLE ALONG THE PROPAGATION PATH

Over a long propagation path the solar zenith angle ($\chi$) will change according to the local time, as will the ionospheric conditions since the effective recombination rates for free electrons are dependent upon time of day. Thus, even during a solar proton event when the ionization rate can be assumed to be constant over the whole disturbed polar cap region, the electron density height profile will vary with position.

In order to estimate the magnitude of this effect during a SPE, the 4 Aug 1972 1144 UT-ionization profile was used to calculate the $N_e$ profiles at different solar zenith angles, cf Figure 11. Waveguide calculations were made for several simulated "seasons", e.g. for a spring equinox situation (21 March 22 UT) with propagation from day conditions over the transmitter ($\chi = 68.5^\circ$) into night with $\chi = 110^\circ$ at the receiver (Tromsø, Norway). Runs were also made with either day- or night conditions over the complete path. Results, shown in Table 7 indicate that for more accurate prediction estimates of signal strength for a path like WTF to Tromsø, the effects of the solar zenith angle variation should be included.

| Solar Zenith | Path Segment | Calculated Field Strength at 75 Hz (dB wrt 1A/m) | Calculated Change from Ambient Night (dB) |
|---|---|---|---|
| a) $79.5^\circ$ | Whole path | -156.5 | -1.9 |
| b) $110.0^\circ$ | Whole path | -159.6 | -4.9 |
| c) $79.5^\circ$<br>$89.5^\circ$<br>$95.0^\circ$<br>$110.0^\circ$ | 0 - 2900 km<br>2900 - 3300<br>3300 - 4400<br>4400 - 6000 | -158.1 | -3.4 |

Table 7  Calculated field strengths WTF - Norway for SPE of 4 Aug 72. Variations in electron density with solar zenith angle. In case c) four representative electron density profiles have been used as indicated

## 8.0 CONCLUDING REMARKS

Additional experimental work is needed to resolve with greater certainty the potential influence and consequences of various geophysical phenomena upon ELF propagation.

Special initiatives are desired to further develop three-dimensional models in order to incorporate more complex waveguide conditions in theoretical analyses of ELF propagation. Efforts to study non-homogenous excitation regions are encouraged.

<div align="center">REFERENCES</div>

Bannister, P. R., Far field extremely low frequency (ELF) propagation measurements, 1970-1972, IEEE Trans. Com., Comm-22, 468, 1974.

Bannister, P. R., F. J. Williams, J. R. Katan, and R. J. Ingram, Results of far field measurements made in Connecticut from June 1970 to May 1973. NUSC Technical Report 4617, Naval Underwater Systems Center, New London Laboratory, 1973.

Bannister, P. R., and F. J. Williams, NUSC Technical Report 4719, Naval Underwater Systems Center, New London Laboratory, 1974.

Bannister, P. R., F. J. Williams, A. ? Dahlvig, and W. A. Kraimer, Wisconsin Test Facility transmitting antenna pattern and steering measurements, IEEE Trans. Comm., Comm-22, 412, 1974.

Barr, R., The effect of sporadic-E on the nocturnal propagation of ELF radio waves, J. Atmos. Terres. Phys., 39, 1379, 1977.

Booker, H. G., The ionosphere as the secondary conductor of a transformer for ELF, Radio Science, 8, 757, 1973.

Booker, H. G., and F. Lefeuvre, The relation between ionospheric profiles and ELF propagation in the earth-ionosphere transmission line, J. Atmos. Terres. Phys., 39, 1277, 1977.

Booker, H. G., A simplified theory of ELF propagation in the earth-ionosphere transmission line and its worldwide application, ONR Report N00014-78-C-0682-0001, UCSD, La Jolla, California, 31 March 1980.

Budden, K. G., Radio waves in the ionosphere, Cambridge University Press, 1961.

Budden, K. G., and G. J. Daniell, Rays in magnetoionic theory, J. Atmos. Terres. Phys., 27, 3, 395, 1965.

Davis, J. R., ELF propagation irregularities on northern and mid-latitude paths, in ELF-VLF Radio Wave Propagation, J. Holtet, ed., D. Reidel Publ. Company, Dordrecht-Holland, 263-277, 1974.

Davis, J. R., and W. O. Meyers, NRL Report 7924, Naval Research Laboratory, Washington, D.C., 1975.

Davis, J. R., Localized nighttime D-region disturbances and ELF propagation, J. Atmos. Terres. Phys., 38, 1309, 1976.

Field, E. C., Measurement of ELF propagation and ionospheric parameters during polar-cap-absorption events (PCA), PSR Note N201, Pacific Sierra Research Corporation, Santa Monica, California, April 1978.

Field, E. C., and R. G. Joiner, An integral-equation approach to long-wave propagatio. in a nonstratified earth-ionosphere waveguide, Radio Science, 14, 1057, 1979.

Field, E. C., S. J. Gayer, and B. P. D'Ambrosio, ELF propagation in the presence of nonstratified ionospheric disturbances, PSR Report 1013, Pacific Sierra Research Corporation, Santa Monica, California, June 1980.

Greifinger, C., and P. Greifinger, Approximate method for determining ELF eigen values in the earth-ionosphere waveguide, Radio Science, 13, 831, 1978.

Greifinger, C., and P. Greifinger, On the ionospheric parameters which govern high-latitude ELF propagation in the earth-ionosphere waveguide, Radio Science, 14, 889, 1979.

Gunton, R. C., R. E. Meyerott, and J. B. Reagan, Ion and neutral chemistry of the D-region during the intense solar particle event of August 1972, Final Report LMSC-D556351, Lockheed Palo Alto Research Laboratory, January 1977.

Imhof, W. L., T. R. Larsen, J. B. Reagan, Analysis of satellite data on precitating particles in coordination with ELF propagation anomalies, LMSC-D502063, Lockheed Palo Alto Research Laboratory, Palo Alto, California, 30 April 1976.

Imhof, W. L., T. R. Larsen, J. B. Reagan, and E. E. Gaines, Analysis of satellite data on precipitating particles in coordination with ELF propagation anomalies, LMSC-D560323, Lockheed Palo Alto Research Laboratory, Palo Alto, California, 30 June 1977.

Imhof, W. L., T. R. Larsen, E. E. Gaines, J. B. Reagan, R. C. Gunton, and R. E. Meyerott, Analysis of satellite data of precipitating particles in coordination with ELF propagation anomalies, LMSC-D633266, Lockheed Palo Alto Research Laboratory, Palo Alto, California, 30 November 1978a.

Imhof, W. L., J. B. Reagan, E. E. Gaines, T. R. Larsen, J. R. Davis and W. Moler, Coordinated measurements of ELF transmissions and the precipitation of energetic particles into the ionosphere, Radio Science, 13, 717, 1978b.

Imhof W. L., R. C. Gunton, T. R. Larsen, E. E. Gaines, J. B. Reagan, and R. E. Meyerott, Study of ELF propagation anomalies as related to improved knowledge of electron density profiles produced by energetic particle precipitation, LMSC-D681778, Lockheed Palo Alto Research Laboratory, 30 January 1980.

Larsen, T. R., Preliminary discussion of ELF/VLF propagation data, in ELF-VLF Radio Wave Propagation, 263-77, J. Holtet, ed., D. Reidel Publishing company, Dordrecht-Holland, 1974.

Pappert, R. A., Effects of elevation and ground conductivity on horizontal dipole excitation of the earth-ionosphere waveguide, Radio Science, 5, 579-590, March 1970.

Pappert, R. A., and W. F. Moler, Propagation theiry and calculations at lower (ELF) extremely low frequencies, IEEE Trans. Comm., COM-22, 4, 438-451, April 1974.

Pappert, R.A., Effects of a large patch of sporadic-E on nighttime propagation at lower ELF, J. Atmos. Terres. Phys., 42, 417, 1980.

Sheddy, C. H., A general analytic solution for reflection from a sharply bounded anisotropic ionosphere, Radio Science, 3, 792-795, August 1968.

Smith, L. G., and K. Miller, Sporadic-E layers and unstable wind shear, J. Atmos. Terres. Phys., 42, 45, 1980.

Whitehead, J. D., Production and prediction of sporadic E, Rev. Geophys. Space Phys., 8, 65, 1970.
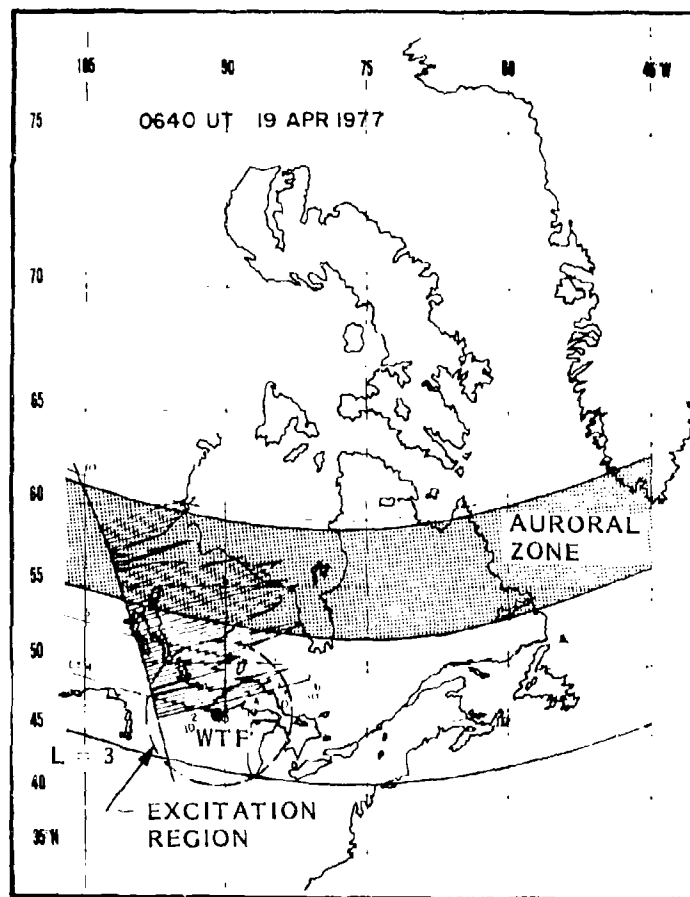
Figure 1. Location of the Wisconsin Test Facility (WTF) and positions of the auroral zone and selected magnetic L-shells. The Booker excitation region is also shown along with the intensity of precipitating electrons measured on a satellite pass.
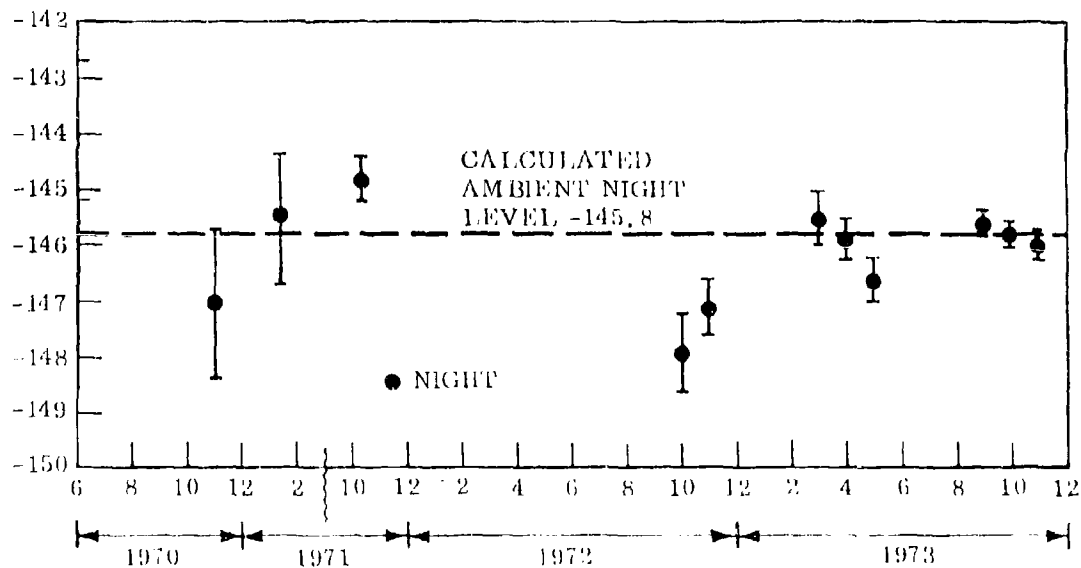


Figure 2. 75-Hz monthly nighttime field strength averages for 1970-73 for the path WTF to Connecticut (Bannister and Williams, 1974). The error bars mark the 80% confidence intervals. Also shown is the LPARL calculated ambient field strength level.
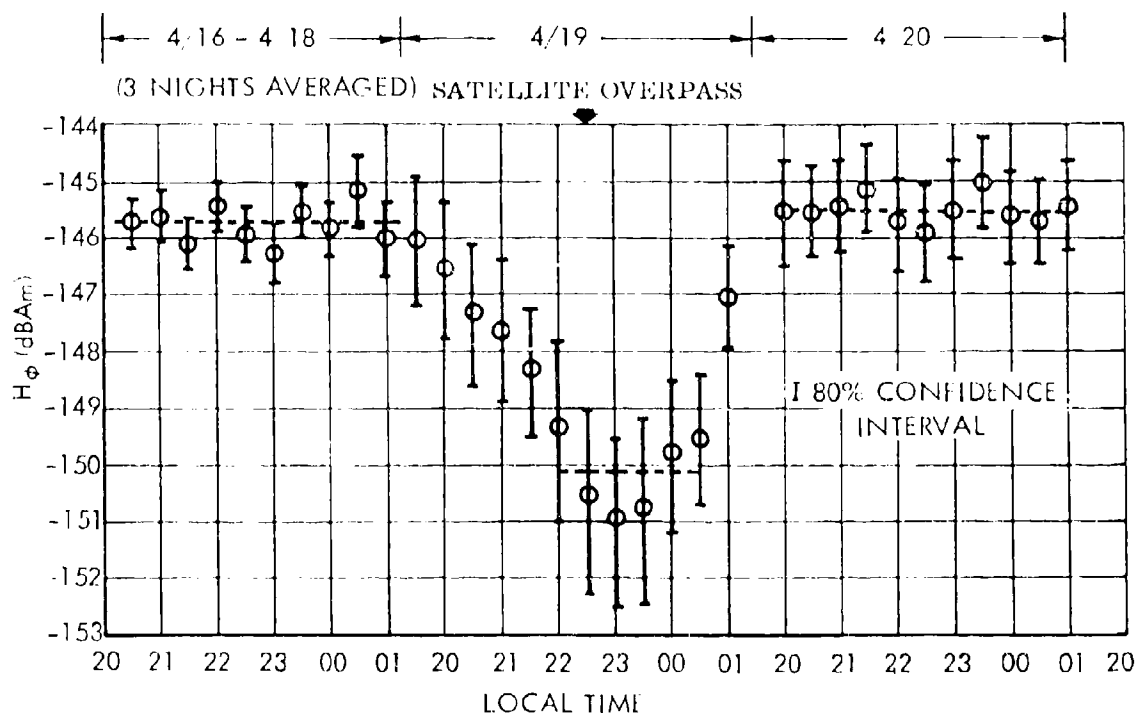
Figure 3    16-20 April 1973 Connecticut 76-Hz Nighttime Field Strengths versus Local Time (Effective Integration Time = 30 min/sample).  (Bannister et al., 1973).
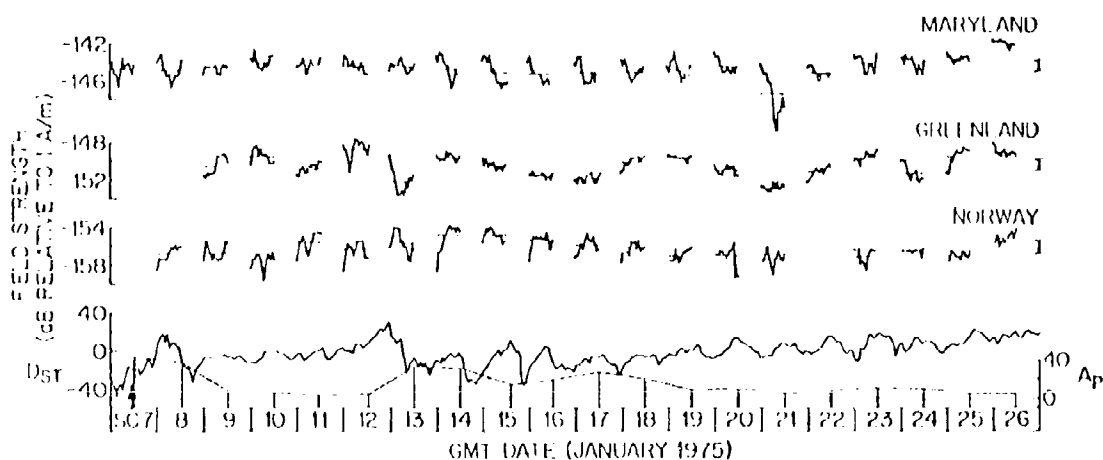


Figure 4    ELF field strengths at 42 Hz of WTF transmissions to Maryland, U.S., Greenland and Norway. The geomagnetic indices ($D_{ST}$ and $A_p$) are given (Davis and Meyers, 1975).
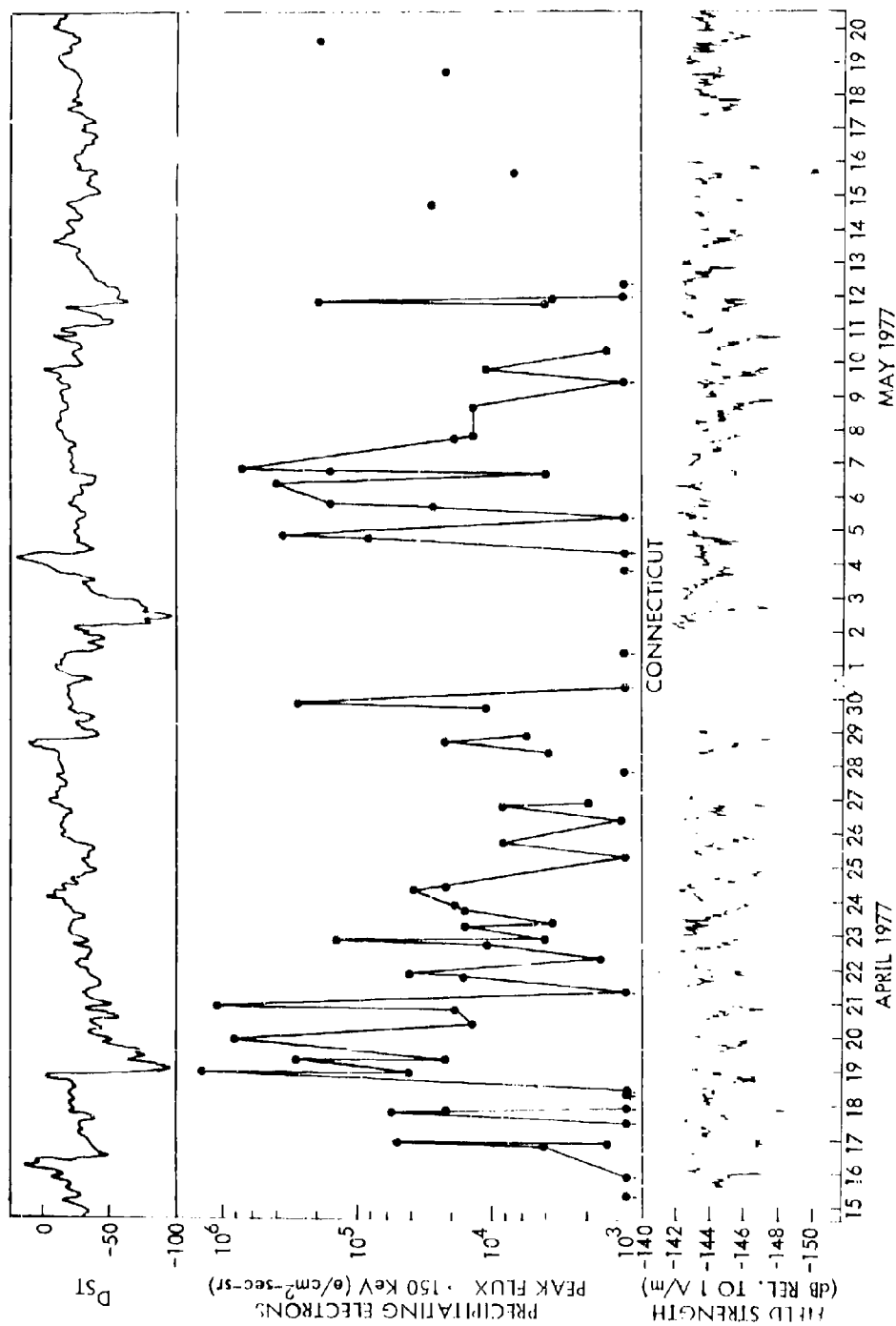
Figure 5    The ELF field strengths as measured at the Connecticut receiving station. Also plotted are the fluxes of precipitating electrons > 150 keV measured on the S72-1 satellite. The $D_{st}$ geomagnetic index is plotted in the upper section.
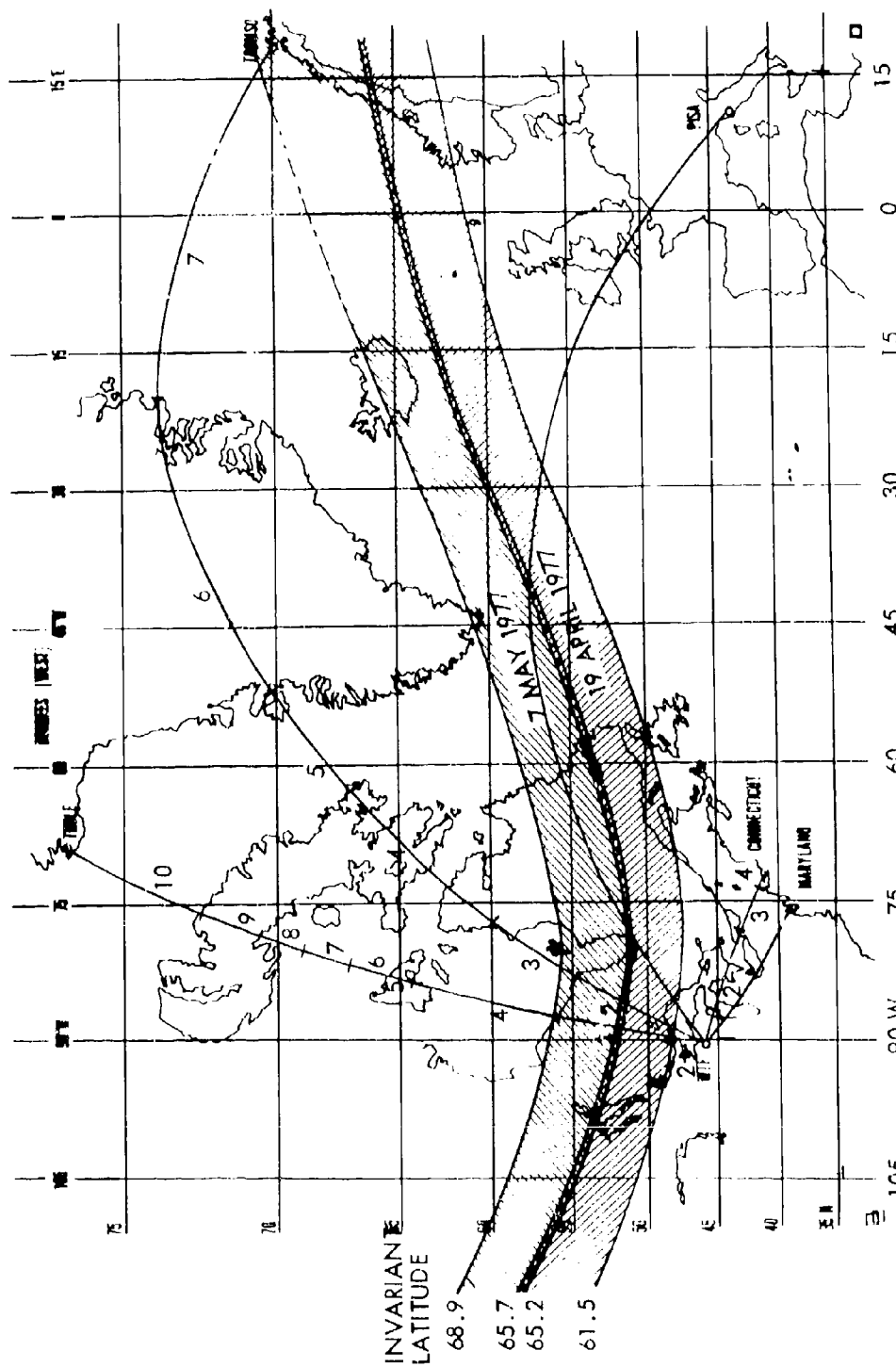
Figure 6 Plots of electron precipitation bands for the REP events of 19 April and 7 May 1977. The bands are assumed to follow invariant magnetic latitude contours. Also shown are great circle paths from WTF to several ELF receiving stations with the segments used in ELF propagation calculations.
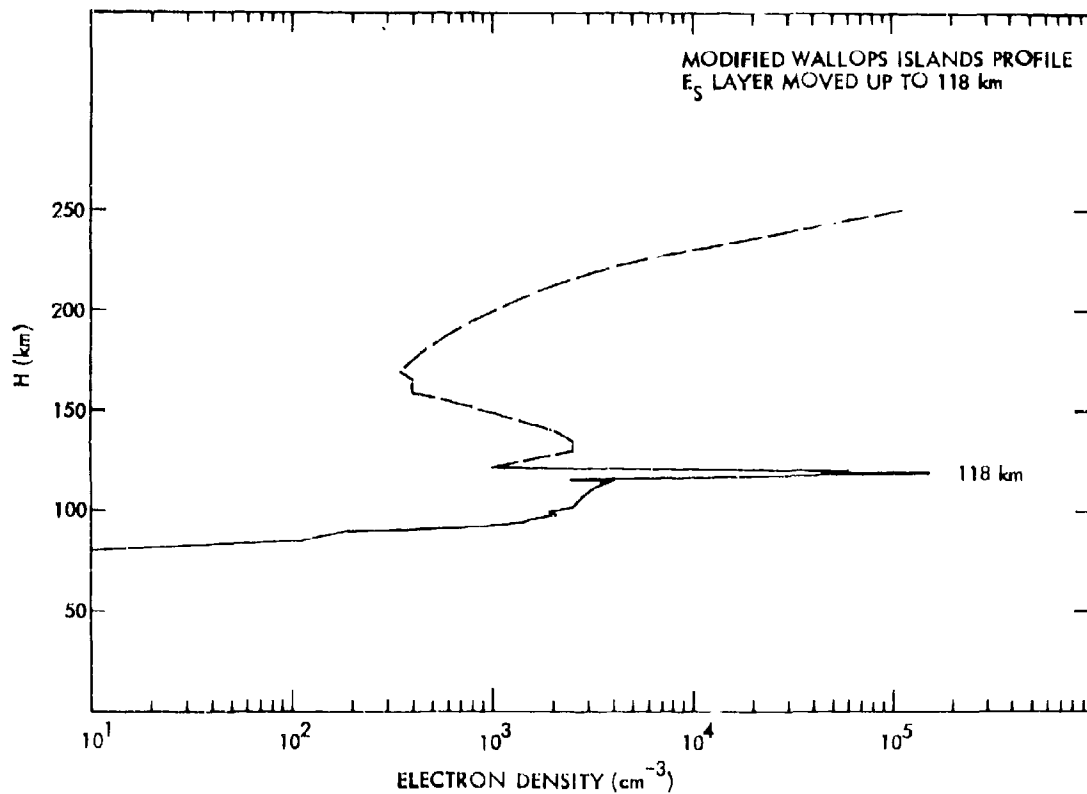
Figure 7    Sporadic E-layer profiles used in calculations based on the measurements of Voss (private communication 1977). The original $E_s$ layer was observed at 105 km, but has been raised to 118 km for these computations. Variations of the original profile include increase of the spike by a factor of 10.
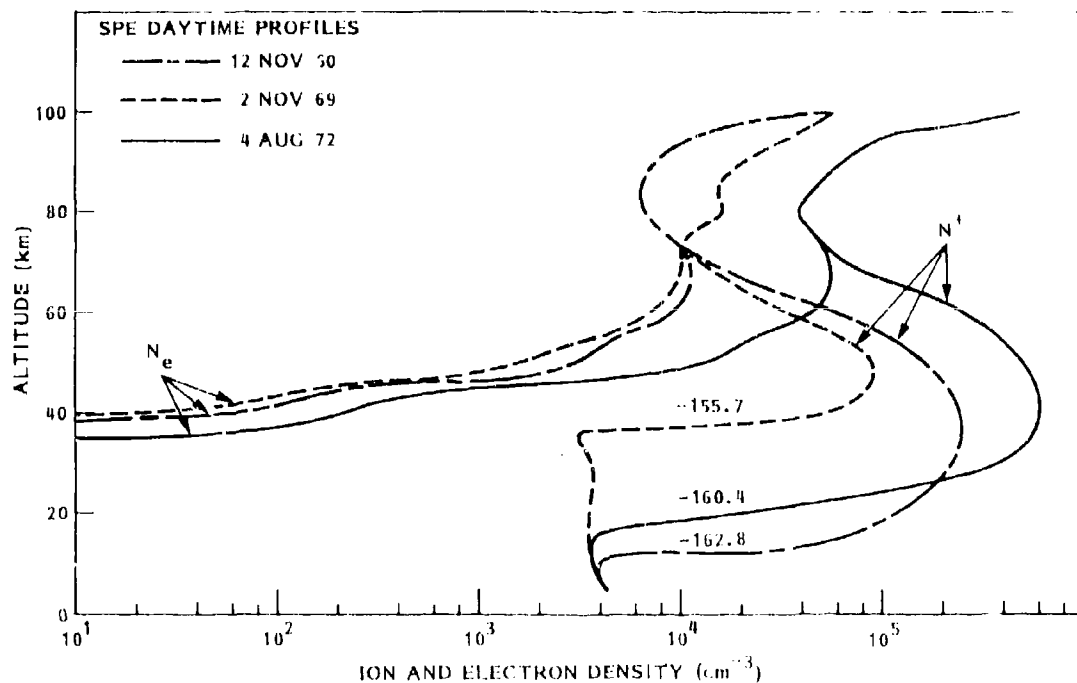


Figure 8    Electron and positive ion densities vs. altitude for three PCA test profiles. The numbers on the curves are the calculated signal strengths in dB at 75 Hz for the Tromsø path.
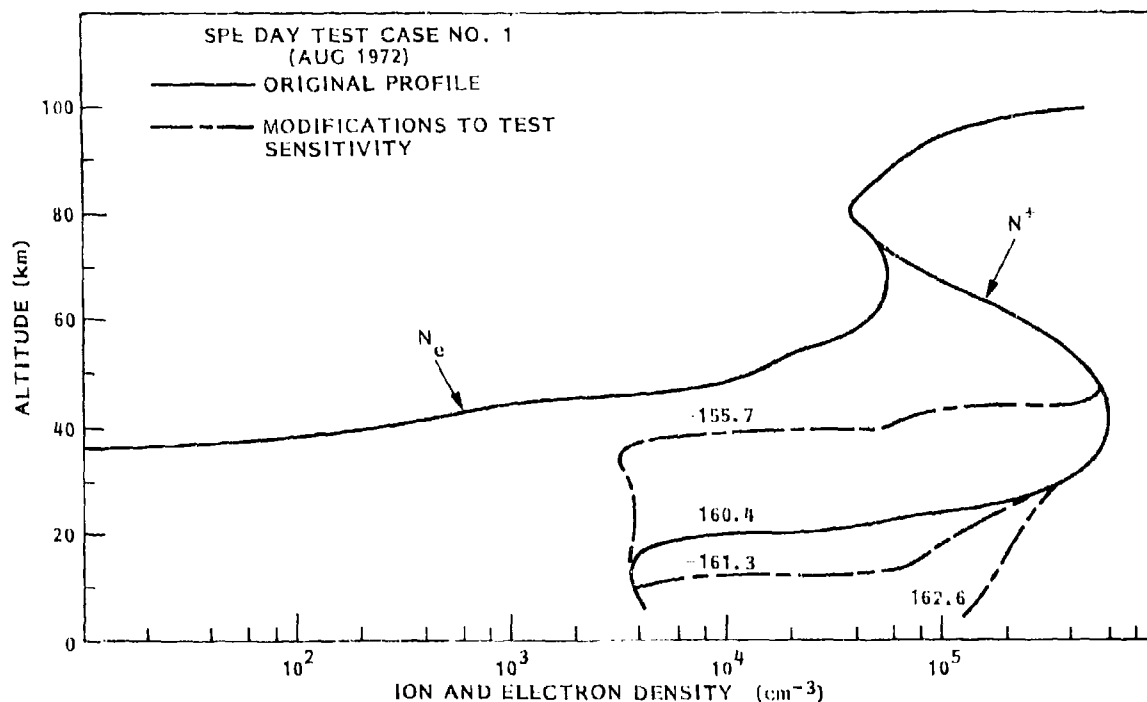
Figure 9    Electron and ion density profiles for the PCA Day Test Case #1 and modifications of the ion profile to test sensitivity of the signal strength over the WTF to Tromsø path to such variations. The numbers on the curves are calculated field strengths in dB at 75 Hz.
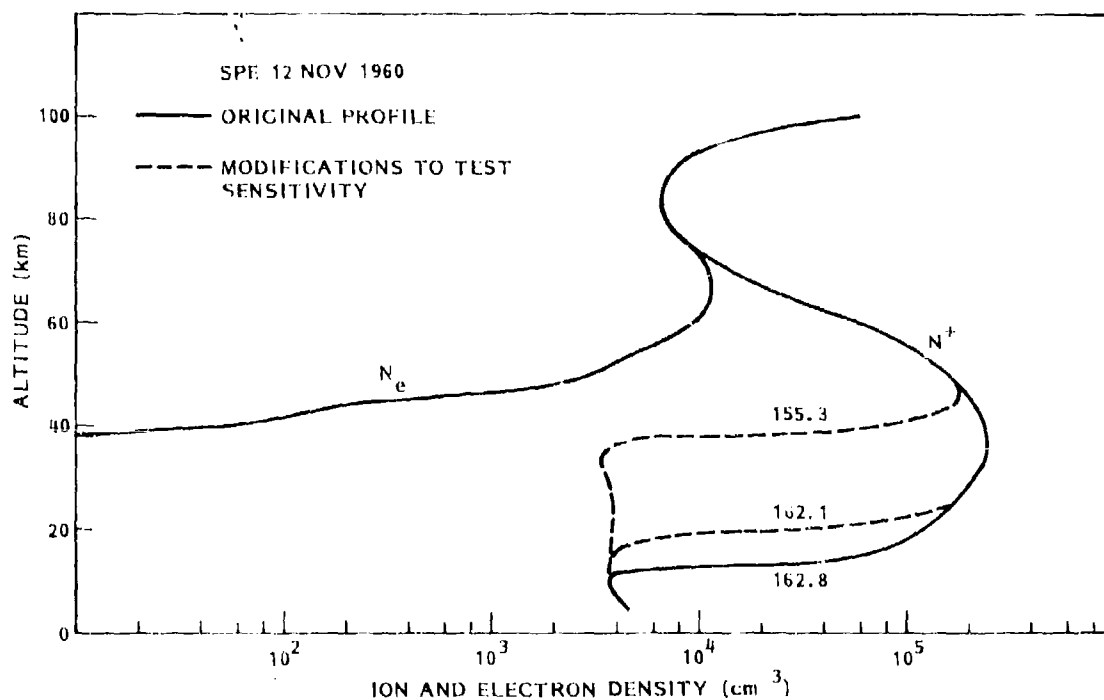


Figure 10    Electron and ion density profiles for the PCA of 12 Nov 1960 along with modifications in the positive ion portions to test sensitivity of the signal strength to such modifications. The numbers on the profiles are calculated field strengths in dB at 75 Hz over the WTF to Tromsø path.
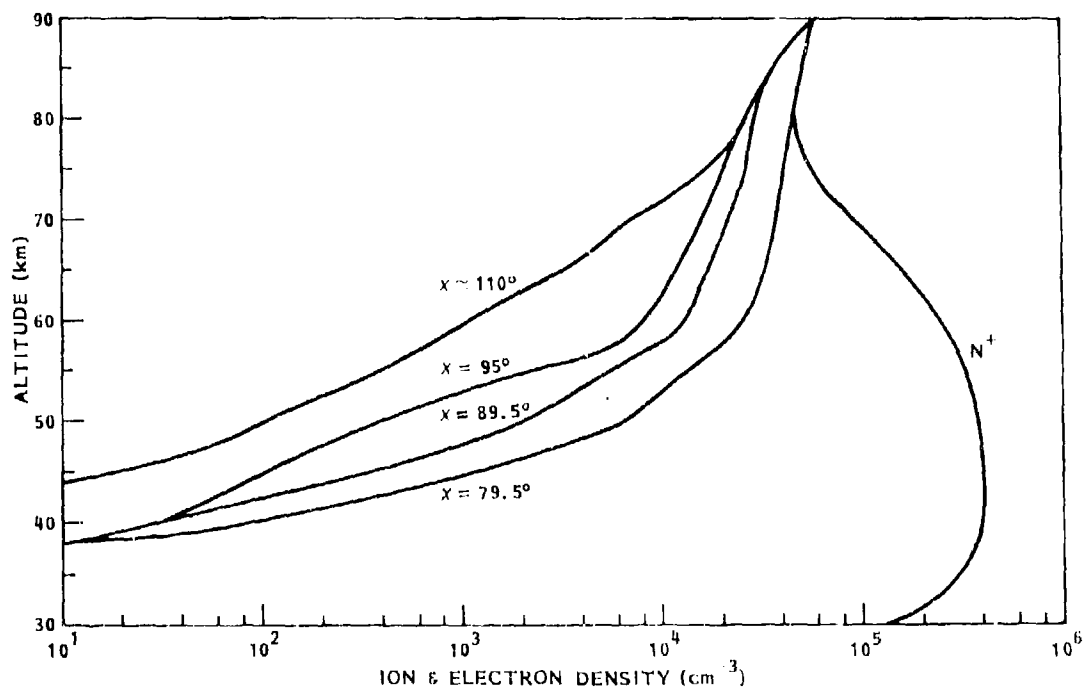
Figure 11    Electron density profiles for the 4 Aug 72 (1144 UT) solar particle event at the four
indicated solar zenith angles.  The positive ion density, taken to be independent of solar
zenith angle, is also shown.

# ELF NOISE SURVEYS - A REVIEW

Emil F. Soderberg
Naval Underwater Systems Center
New London, Connecticut    06320

## SUMMARY

Noise measurement surveys have been made in various geographical areas to determine the characteristics of ELF noise in power spectral variation with season and time of day, and of noise correlation between widely separated locations. By far, the majority of measurements have been made at ground stations, with a small number having been made above the earth and in space, and even fewer having been made in the sea. The various surveys are reviewed and the ELF noise characteristics in each area are discussed.

## INTRODUCTION

A variety of noise sources contributes to the electromagnetic radiation found in the extremely low frequency range (3-3000 Hz). Lightning discharges, power line frequencies and power line harmonic radiation, and magnetospheric plasma wave phenomena all produce energy whose frequencies fall partially or wholly within this band, and thus represent present or potential subjects of interest to the consideration of using various parts of the ELF band for communication purposes.

There have been quite a few noise surveys made in the range 3-3000 Hz to determine the characteristics and intensity of the electromagnetic background at various locations about the earth. Most of these measurements have been made at ground stations around the world, a small number have been made above the earth and in space, and even fewer have been made in the sea. They have been made for a variety of reasons: for the purpose of studying propagation effects, for determining communication background noise, for examining the effects of magnetospheric processes upon power line transmission systems, and conversely, for studying the effects of powerline harmonics upon ionospheric and magnetospheric processes. Even though each of them has been done for a specific purpose, and the data has been analyzed within the framework of a particular objective, they all contribute to a body of information that constitutes what we may call an ELF noise data base.

The purpose of this report is to briefly review the various noise surveys that have been made, and to note some of the ELF noise measurement resources that exist (Tables 1, 2 and 3) and some of the literature that contain data on noise in the ELF band. In the following sections we will take a look at ELF noise measurement surveys in the areas of terrestrial noise, plasma wave noise and ELF noise in the sea.

## TERRESTRIAL NOISE

The dominant source of natural ELF terrestrial noise is worldwide thunderstorm activity. The nearly constant occurrence of lightning discharges gives rise to a broad spectrum of energy which, in the ELF band, propagates throughout the earth-ionosphere cavity with relatively low attenuation. Climatological data (Handbook of Geophysics) show that Southeast Asia, Central Africa, and South and Central America are regions of maximum activity, with an overall worldwide average of almost 2000 lightning centers existing at any one time over the earth's surface. The mean number of lightning discharges is on the order of 30 to 100 per second. In the frequency range of interest here, two types of lightning are responsible for the observed radiation: cloud-to-cloud discharges in the tropics that produce large transient signals below 40 Hz (Kemp, 1971), and cloud-to-ground discharges that have a long discharge-current time constant and produce "slow tail" atmospherics with energy above 40 Hz (Pierce, 1960).

At the lower end of the ELF band, the energy from vertical (cloud-to-cloud and cloud-to-ground) lightning strokes excite the earth-ionosphere cavity and give rise to resonance peaks in the noise spectrum, called the Schumann resonances (covered in a section below). Studies of the characteristics of these resonances (relative mode amplitudes, mode-splitting, resonance Q) may be used to give indications of the locations of thunderstorm centers and information about the propagation path between the receiver and the noise sources.

Observations of atmospheric noise in and above the Schumann resonance region have been made by Watt and Maxwell (1957), Maxwell (1967), Ogawa et al. (1966), Barr (1970), and others. Horner (1970) discusses the use of atmospherics for studying the ionosphere. Barr (1970) has investigated the region between 20 Hz and 12 kHz, and particularly the attenuation band near 3 kHz. Similarly, Dinger et al. (1980) report measurements in the range 1-4 kHz, noting a diurnal variation that suggested the existence of a large propagation anisotropy in the nighttime earth-ionosphere waveguide at 3 kHz. Fraser-Smith and Helliwell (1980) describe the variations in amplitude and rate of occurrence of ELF sferics in Antarctica caused by a solar proton event (SPE), and note that man-made lower-ELF signals propagating over paths passing through the polar regions are likely to be somewhat reduced in strength during the first 24 hours of a moderately large SPE.

Very striking displays of energy are seen in the whistlers, which although mainly VLF phenomena, extend down into the ELF range. Throughout the ELF band are also seen the effects of man-made noise at the power line frequencies and their harmonics. These are examined in the sections below.

Measurements of these ELF band emissions have been made at many ground stations around the world. Table 1 is a partial listing of the ground stations having the capability for measuring noise in the ELF range. The list is in the process of being updated, and several of the entries include the latest information available from the investigators themselves through their very kind cooperation with the author.

## Schumann Resonance Studies

Observations of the noise in the range 3-40 Hz reveals the presence of noise peaks at approximately 7.5, 14, 21, 26 and 32 Hz. These earth resonances, predicted by W. O. Schumann in 1952, have been studied extensively since that time, and treatises such as Polk (1981) and Bliokh et al. (1980) summarize the work to date. The Schumann-ELF natural background is a closely ordered worldwide phenomenon. Its continuity, limited dynamic range and predictable diurnal pattern set it clearly apart from solar-dependent geomagnetic activity (Shand, 1966). The levels of the Schumann resonances are quite low and unless the measurement locations are far from sources of man-made noise, the interference (from power lines, railway systems, telephone ringing systems) is orders of magnitude larger than the Schumann oscillations (Polk, 1980). Shand (1966) compared results of observations at widely spaced stations from Canada to the Antarctic and presents some of the data showing the amplitude-time characteristics and power spectrum plots. Dinger and Goldstein (1980) report magnetometer measurements of the ambient fields in the range 0.3-40 Hz at California and Norway, in which Schumann resonances with a particularly high ratio of signal-to-instrument noise were observed, with six orders of the resonances typically visible. Sao et al. (1973) investigated Schumann resonances in Japan, comparing levels under quiet and severely disturbed states of the ionosphere. Other examples of Schumann resonance spectra are found in the report by Jones and Kemp (1970) in which they investigate discrete events of considerably large amplitude occurring in the Schumann resonance range.

## Project Sanguine Noise Studies

The ELF noise surveys conducted under Project Sanguine (now called Seafarer) were directed toward the determination of design parameters for a receiving system for FBM submarines. The intent of the program was to take advantage of the much lower attenuation of the signal in sea water at extremely low frequencies, so that submarines could run submerged at greater depths and still reliably receive command-control signals from the mainland. An entire issue of the IEEE Transactions on Communications (Vol. COM-22, no. 4, April 1974) has been devoted to papers on Project Sanguine, and more recently Wait (1977) has presented an overview of the Sanguine program.

The noise measurements were conducted in a number of areas in which a submarine was likely to operate. Extensive measurements were reported by Evans and Griffiths (1974) in Malta, Saipan, Norway, Greenland, Hawaii, Florida, Massachusetts, Idaho, and in the North Atlantic. Wideband recordings (5-320 Hz) were made using a whip antenna and two orthogonal horizontal loop antennas at each site. The extent of the noise recording program is indicated in reports by Griffiths (1972, 1975) in which it is noted that for Malta (winter 1986-1969) there are 200 tapes, for Norway (winter, spring, summer 1969) 140 tapes, and for Saipan (summer, fall 1969) 160 tapes. Later on, in May 1972, in Saipan and Greece there were noise recordings of 300 hours and 200 hours, respectively. Larsen (1974) reports the results of 12 months of continuous ELF measurements in Tromsø during 1969 and 1970,and presents some 3-400 Hz data taken at Lavangsdalen.

Narrowband (1 Hz) ELF noise data was recorded at Malta, Guam and Tromsø to study atmospheric noise level statistics. Ginsberg (1974) reports the results of measurements using a "Portable Atmospheric Noise Data Acquisition" (PANDA) system, in which the vertical electric field and two orthogonal horizontal magnetic field components were measured at four discrete frequencies between 20 and 200 Hz, in a nominal 1 Hz bandwidth. The noise surveys at Malta and Guam were quite extensive, with seven seasons of data (October 1968 to April 1970) taken at Malta and four seasons of data (June 1969 to April 1970) taken at Guam. Tromsø measurements covered the winter-spring season from January to May 1969.

Davis and Meyers (1976) made wideband (2-130 Hz) ELF noise recordings for five one-month periods, in all seasons, during 1974 and 1975 at a receiving site near Tr , Norway. Similar measurements were made near Pisa, Italy, for three one-month periods: July-Aug 1975, October-November 1975, and March-April 1976 (Goldstein et al., 1977).

Some of these data have been analyzed broadband (Griffiths, 1972, 1975; Evans and Griffiths, 1974; Larsen, 1974), but most of the emphasis has been on analyzing the noise in terms of receiver design. The non-Gaussian nature of the atmospheric noise has important implications for design considerations. Since most of the energy in atmospheric noise at ELF is contained in discrete lightning impulses, a simple noise clipping circuit in the receiver can remove most of these pulses and thus reduce the noise energy considerably without significantly reducing the signal energy (Bernstein et al., 1974). In the Project Sanguine analyses, the clipped noise was denoted by $N_e$, the "effective atmospheric noise density," and the wideband linearly recorded noise by $N_0$, the "actual atmospheric noise density." In cases where the recorded noise has been clipped ($N_e$), the actual noise is lost, and cannot be recovered for use in any further analysis of atmospheric noise statistics. This appears to be the case for recordings made after 1969 (R. Ingram, personal communication).

# ELF NOISE SURVEYS – A REVIEW

Emil F. Soderberg
Naval Underwater Systems Center
New London, Connecticut    06320

## SUMMARY

Noise measurement surveys have been made in various geographical areas to determine the characteristics of ELF noise in power spectral variation with season and time of day, and of noise correlation between widely separated locations. By far, the majority of measurements have been made at ground stations, with a small number having been made above the earth and in space, and even fewer having been made in the sea. The various surveys are reviewed and the ELF noise characteristics in each area are discussed.

## INTRODUCTION

A variety of noise sources contributes to the electromagnetic radiation found in the extremely low frequency range (3-3000 Hz). Lightning discharges, power line frequencies and power line harmonic radiation, and magnetospheric plasma wave phenomena all produce energy whose frequencies fall partially or wholly within this band, and thus represent present or potential subjects of interest to the consideration of using various parts of the ELF band for communication purposes.

There have been quite a few noise surveys made in the range 3-3000 Hz to determine the characteristics and intensity of the electromagnetic background at various locations about the earth. Most of these measurements have been made at ground stations around the world, a small number have been made above the earth and in space, and even fewer have been made in the sea. They have been made for a variety of reasons: for the purpose of studying propagation effects, for determining communication background noise, for examining the effects of magnetospheric processes upon power line transmission systems, and conversely, for studying the effects of powerline harmonics upon ionospheric and magnetospheric processes. Even though each of them has been done for a specific purpose, and the data has been analyzed within the framework of a particular objective, they all contribute to a body of information that constitutes what we may call an ELF noise data base.

The purpose of this report is to briefly review the various noise surveys that have been made, and to note some of the ELF noise measurment resources that exist (Tables 1, 2 and 3) and some of the literature that contain data on noise in the ELF band. In the following sections we will take a look at ELF noise measurement surveys in the areas of terrestrial noise, plasma wave noise and ELF noise in the sea.

## TERRESTRIAL NOISE

The dominant source of natural ELF terrestrial noise is worldwide thunderstorm activity. The nearly constant occurrence of lightning discharges gives rise to a broad spectrum of energy which, in the ELF band, propagates throughout the earth-ionosphere cavity with relatively low attenuation. Climatological data (Handbook of Geophysics) show that Southeast Asia, Central Africa, and South and Central America are regions of maximum activity, with an overall worldwide average of almost 2000 lightning centers existing at any one time over the earth's surface. The mean number of lightning discharges is on the order of 30 to 100 per second. In the frequency range of interest here, two types of lightning are responsible for the observed radiation: cloud-to-cloud discharges in the tropics that produce large transient signals below 40 Hz (Kemp, 1971), and cloud-to-ground discharges that have a long discharge-current time constant and produce "slow tail" atmospherics with energy above 40 Hz (Pierce, 1960).

At the lower end of the ELF band, the energy from vertical (cloud-to-cloud and cloud-to-ground) lightning strokes excite the earth-ionosphere cavity and give rise to resonance peaks in the noise spectrum, called the Schumann resonances (covered in a section below). Studies of the characteristics of these resonances (relative mode amplitudes, mode-splitting, resonance Q) may be used to give indications of the locations of thunderstorm centers and information about the propagation path between the receiver and the noise sources.

Observations of atmospheric noise in and above the Schumann resonance region have been made by Watt and Maxwell (1957), Maxwell (1967), Ogawa et al. (1966), Barr (1970), and others. Horner (1970) discusses the use of atmospherics for studying the ionosphere. Barr (1970) has investigated the region between 20 Hz and 12 kHz, and particularly the attenuation band near 3 kHz. Similarly, Dinger et al. (1980) report measurements in the range 1-4 kHz, noting a diurnal variation that suggested the existence of a large propagation anisotropy in the nighttime earth-ionosphere waveguide at 3 kHz. Fraser-Smith and Helliwell (1980) describe the variations in amplitude and rate of occurrence of ELF sferics in Antarctica caused by a solar proton event (SPE), and note that man-made lower-ELF signals propagating over paths passing through the polar regions are likely to be somewhat reduced in strength during the first 24 hours of a moderately large SPE.

Very striking displays of energy are seen in the whistlers, which although mainly VLF phenomena, extend down into the ELF range. Throughout the ELF band are also seen the effects of man-made noise at the power line frequencies and their harmonics. These are examined in the sections below.

## Whistlers

Whistlers are mainly VLF phenomena, but their lower frequencies often extend into the ELF band. They are observed mainly in the range 300 Hz to 30 kHz, and are produced by the electromagnetic impulses of lightning as a result of interaction with the earth's magnetic field lines. The energy from the lightning impulse enters the ionosphere where it is guided by the earth's field into the opposite hemisphere. Dispersion in the ionosphere stretches the original impulse into a gliding tone, which is called a whistler. Bullough and Sagredo (1973) describe their direction finding studies of whistlers, to locate where each whistler emerges from the ionosphere. The determination of whistler location provides information on the spatial distribution of thermal plasma, so that the location of the plasmapause can be monitored (Rycroft, 1974). The rich variety of whistler structure has been well documented and illustrated, and references such as Katsufrakis (1964), Helliwell (1965) and Heacock (1974) provide many examples of whistlers and other emissions in the ELF/VLF range.

## Power Line Harmonic Radiation (PLHR)

Harmonics of the fundamental frequency (50 or 60 Hz) are produced on power lines when transient loads are applied or non-linear rectifiers are used. The resulting power line harmonic radiation (PLHR), which has frequency components up to 8 kHz, has been observed to stimulate strong wave-particle and wave-wave interactions in the magnetosphere. The PLHR wave may be amplified in its passage through the interaction region, and as it echoes from hemisphere to hemisphere inside whistler ducts, new emissions may be triggered, adding to the complex structure of the received signals (Park et al., 1980). Many striking examples of PLHR-induced activity are shown by Park (1977), with most of the energy concentrated in the VLF range but with some effects extending into the ELF band. A study by Barr (1979) of the ELF radiation from the New Zealand power system shows no power line harmonics above 1500 Hz, but there is a strong 300 Hz signal radiated from the d.c. power grid. He suggests that it might be profitable to search for correlations between magnetospheric ELF signals recorded on satellites and the location of the world's d.c. power lines, rather than to concentrate only on the effect of a.c. power grids.

## ELF NOISE FROM PLASMA WAVE PHENOMENA

The term "plasma waves" refers to waves that are generated in plasma or have their wave characteristics significantly modified by the presence of plasma. They may be predominantly electromagnetic (having both electric and magnetic fields produced by current fluctuations) or electrostatic (having only an electric field produced by charge fluctuations). Shawhan (1979) in his review of magnetospheric plasma wave research provides a listing of some 27 plasma wave phenomena, along with their typical locations, observed frequencies, and a brief statement about their wave properties. Of these phenomena, 22 contain energy with frequencies that fall partially or wholly within the ELF band, and some of these, at least, may be significant to prospective communication applications in this region.

In the area of the magnetosheath and the bow shock are found electrostatic turbulence between 200 Hz and 4 kHz, and electromagnetic turbulence from 20 Hz to 4 kHz. Electromagnetic wave packets, referred to as lions roars, occur at about 120 Hz with durations of about 2 seconds, and seem to be related to the level of geomagnetic activity. Above 500 Hz there is a weak broadband radiation apparently associated with energetic electrons in the outer radiation zone. In the magnetotail and plasma sheet is observed a broadband electrostatic noise in the range of 10 Hz to several kHz which is both intense and frequent and seems to be associated with streaming keV protons. Broadband electrostatic emission in the region of the polar cusp extends up to 100 kHz but peaks in the 10-50 Hz range. Also associated with the cusp is a 1-300 Hz band of magnetic noise.

Auroral hiss occurs in the kHz range and can be observed both on the ground and from satellites. Intense electrostatic wave turbulence occurs at about 100 Hz with amplitudes up to 50 mV/m. At higher altitudes the noise peaks in the 10-50 Hz range with amplitudes of 10 mV/m. Plasmaspheric hiss, in the range 100-1000 Hz, is found throughout the plasmasphere, particularly during periods of magnetic activity.

Certain of these plasma wave effects are observable at ground stations. Because of the shielding effect of the earth's magnetic field, the energetic particles, electrons and ions, mainly influence the high latitude ionosphere, and as a result the observations of plasma wave processes have been concentrated in the higher latitudes. Investigations such as reported by Holtet and Egeland (1969) show bands of emission in the ELF range that are attributable to these magnetospheric processes. Sato et al. (1980) describe observations of polar chorus, quasi-periodic emissions, and auroral hiss at high latitude stations in Antarctica and Iceland. Coordinated measurements between ground and satellite stations are being conducted to provide comparative data for the study of these phenomena (Perraut et al., 1978; Sato et al., 1980).

There are quite a few satellites that have the capability for measuring the effects of plasma wave phenomena in the ELF range. Some of these are listed in Table 2. Most of the satellites listed can detect both electric and magnetic fields although some have only magnetic sensors. The references in Table 2 contain examples of the various types of ELF plasma wave emissions. Much of the data is the form of frequency-time spectrograms which provide a very effective means for qualitative analysis and for comprehension of the behavior of the phenomena. Data such as these provide a data base for the study of background noise as it affects potential ELF space communications.

## ELF NOISE IN THE SEA

ELF noise in the sea consists almost entirely of atmospheric noise-related energy. There may be some relatively local contributions from industrial noise and power transmission lines, but the dominant contribution appears to come from thunderstorm activity. Because of the low attenuation of waves propagating in the earth-ionosphere waveguide, lightning strokes all over the earth contribute to the atmospheric noise at any point over the ocean. Nearby thunderstorms contribute large but relatively infrequent impulses, while the numerous remote thunderstorms provide a background of smaller but denser impulses. The atmospheric noise, then, consists of impulsive waves with random arrival angles and times.

The majority of the arriving waves, those from remote thunderstorms, are transverse magnetic (TM) waves, i.e., having a vertical electric field and a horizontal magnetic field. In the earth-ionosphere cavity, when the free-space wavelength is large compared with the height of ionosphere, as is the case for the frequencies considered here, only the TM mode can propagate. The transverse electric (TE) mode is completely attenuated beyond the immediate vicinity of the source (Wait, 1970; Polk, 1981).

If we assume an arriving impulse to be a TM mode plane wave, its vertical electric field $E_V$ and horizontal magnetic field H are related by

$$H = \left(\frac{\epsilon_0}{\mu_0}\right)^{1/2} E_V \qquad (1)$$

Since tangential H is continuous across the air-sea boundary, H just below the surface is also given by (1). For propagation in a lossy medium, where the conduction current is much greater than the displacement current ($\sigma \gg \omega\epsilon$), the horizontal electric field $E_H$ just below the surface is related to the horizontal magnetic field H just below the surface by the wave impedance of sea water, so that

$$E_H = H \left(\frac{i\omega\mu_0}{\sigma}\right)^{1/2} \qquad (2)$$

or

$$E_H = E_V \left(\frac{i\omega\epsilon_0}{\sigma}\right)^{1/2} \qquad (3)$$

The horizontal electric field in the sea, $E_H$, is polarized in the direction of propagation of the plane wave above the sea.

As this refracted wave ($E_H$, H) propagates downward into the sea, it is attenuated by the lossy medium. The horizontal electric field E at depth z below the surface is given by

$$E = E_H e^{-z/\delta} \qquad (4)$$

where $\delta = \sqrt{2/\omega\mu\sigma}$.

Measurements of ELF electric fields in the sea have been made by a number of investigators, using surface ships and platforms as well as deep submersibles. In 1966, Selzer and others (1966, 1968) reported electric and magnetic measurements made using the French bathyscaphe "Archimede" in deep waters of Greece, Puerto Rico, Toulon, and the Island of Madeira. Similar work was done using the Cousteau "Diving Saucer" off the coast of Baja California (Soderberg, 1966, 1969), and later using the Westinghouse Deepstar 4000 in deep waters near the Bahamas (Soderberg, 1976) to measure the horizontal electric field at several depths between the ocean surface and the ocean bottom.

These deep water measurements showed the fields to be attenuated with depth as expected from eq. (4) above (with some qualifications), falling to indistinguishable levels at some intermediate depth. In all cases, however, as the bottom was approached there was an increase in noise level that suggested a contribution from below. It was speculated, but not proved, that this noise may have been atmospheric noise conducted from shore outward along the ocean bottom.

Open ocean measurements made from a surface ship were reported by Soderberg and Finkle (1970). Data taken simultaneously in and above the sea showed the close correlation between the horizontal electric field in the water and the vertical field in the air. More recent surface ship measurements of in-water electric fields have been reported by Artamonov et al. (1979) in the Black Sea and by Karnaushenko (1980) in the Black Sea, the Tyrrhenian Sea and the tropical parts of the North Atlantic.

Shallow water measurements have been reported by Brock-Nannestad (1965, 1966), Strarup (1966), Strarup and Tacconi (1968), and Tacconi (1974, 1981). The ELF electric fields in these waters are strongly dependent upon the bottom conductivity and the geometry of the body of water, and are studied to investigate the complex relationship between the fields in the air, earth, and water near a shoreline.

Relatively few studies have been made in the area of ELF noise in the sea (see Table 3). A significant factor has been the prohibitive cost of ship support for at-sea expeditions of this type, especially when there has been no demonstrated urgency to support an application such as communications. One may argue that the problem is only to know what the ELF noise level is over the ocean by extrapolation from land measurements, and from there, simply use a graph of boundary loss and depth attenuation to find the noise in the sea. But from an earth physics standpoint, one would be quite interested in, for example, investigating the effects of discontinuities in sea water electrical conductivity at edges of the Gulf Stream, and in studying the distribution of noise as a function of distance from a coastline. Much interesting work remains to be done in this area.

## CONCLUDING REMARKS

The study of ELF noise is of importance in establishing the limiting factors affecting communications in this frequency range. The many noise surveys done throughout the past several decades have revealed the variety of natural noise background characteristics to be dealt with, in terms of geographic location, time and season, and the medium in which the receiver is located. Developments in technology have brought about new concepts in measurement techniques, increased instrument sensitivities, and new capabilities in transporting instrumentation to remote places, into the sea, and into space. The present knowledge of ELF noise sources represents a significant body of information upon which could be built a more extensive data base for predicting the expected noise levels at receiver locations. The combined efforts of the several multi-station ELF noise monitoring facilities now operating and those proposed to be established, would represent an important step in providing the variational data needed for noise prediction.

# REFERENCES

Anderson, R. R., and D. A. Gurnett, "Plasma wave observations near the plasmapause with the $S^3$-A satellite," J. Geophys. Res., vol. 78, no. 22, pp. 4756-4764, 1973.

Armstrong, J. C., and A. J. Zmuda, "Triaxial magnetic measurements of field-aligned currents at 800 kilometers in the auroral region: initial results," J. Geophys. Res., vol. 78, no. 28, pp. 6802-6807, 1973.

Artamonov, L. V., and G. V. Molochnov, "An experimental assessment of the capability to receive an extremely low frequency electrical field in the sea," (in Russian), Geofizicheskaya Apparatura, no. 67, pp. 12-16, 1979.

Barrington, R. E., T. R. Hartz, and R. W. Harvey, "Diurnal distribution of ELF, VLF, and LF noise at high latitudes as observed by Alouette 2," J. Geophys. Res., vol. 76, no. 22, pp. 5278-5291, 1971

Barr, R., "The ELF and VLF amplitude spectrum of atmospherics with particular reference to the attenuation band near 3 kHz," J. Atmos. Terr. Phys., vol. 32, pp. 977-990, 1970.

Barr, R., "ELF radiation from the New Zealand power system," Planet. Space Sci., vol. 27, pp. 537-540, 1979.

Bernstein, S. L., M. L. Burrows, J. E. Evans, A. S. Griffiths, D. A. McNeill, C. W. Niessen, I. Richer, D. P. White, and D. K. Willim, "Long-range communications at extremely low frequencies," Proc. IEEE, vol. 62, no. 3, pp. 292-312, March 1974.

Bliokh, P. V., A. P. Nicholaenko, Yu. F. Fillippov, Schumann Resonances in the Earth-Ionosphere Cavity, (English edition), Institute of Electrical Engineers IEE electromagnetic wave series, vol. 9, Peter Peregrinus Ltd, New York, 1980.

Brock-Nannestad, L., "EM phenomena in the ELF range: Natural background noise and instrumentation for its measurement," NATO Saclant ASW Research Centre, Technical Report 37, 15 June 1965.

Brock-Nannestad, L., "Electromagnetic background noise in the ELF range," AGARD Conference Proceedings No. 20, Sub-Surface Communications, pp. 543-556, 1966.

Bullough, K., and J. L. Sagredo, "VLF goniometer observations at Halley Bay, Antarctica - I. The equipment and the measurement of signal bearing," Planet. Space Sci., vol. 21, pp. 899-912, 1973.

Bullough, K., M. Denby, W. Gibbons, A. R. W. Hughes, T. R. Kaiser, and A. R. L. Tatnall, "E.l.f./v.l.f emissions observed on Ariel 4," Proc. R. Soc. Lond. A., vol. 343, pp. 207-226, 1975.

Burtis, W. J., "Electron concentrations calculated from the lower hybrid resonance noise band observed by OGO 3," J. Geophys. Res., vol. 78, no. 25, pp. 5515-5523, 1973.

Chukanov, A. A., and N. G. Kleimenova, "Magnetic activity and subauroral ELF-VLF chorus," Geomagn. and Aeron. (transl.), vol. 15, no. 2, pp. 314-315, 1975.

Davis, J. R., and W. D. Meyers, "ELF atmospheric noise excision by wideband clipping," Radio Sci., vol. 11, no. 12, pp. 991-999, December 1976.

Dinger, R. J., W. D. Meyers, and J. R. Davis, "Experimental measurements of ambient electromagnetic noise from 1.0 to 4.0 kHz," NRL Report 8413, Naval Research Laboratory, Washington, DC, 31 July 1980.

Dinger, R. J., and J. A. Goldstein, "Spatial coherence measurements and evaluation of a noise reduction technique for ambient noise from 0.3 to 40 Hz," NRL Report 8430, Naval Research Laboratory, Washington, D.C., 15 October 1980.

Dunckel, N., and R. A. Helliwell, "Whistler mode emissions on the OGO 1 satellite" J. Geophys. Res., vol. 74, no. 26, pp. 6371-6385, 1969.

Egeland, A., "ELF (500-1000 cps) emissions at high latitude," in Natural Electromagnetic Phenomena Below 30 KC/S, Proc. NATO Adv. Study Inst., pp. 157-166, Plenum Press, New York, 1964.

Ejiri, M., K. Tsuruda, Y. Watanabe, A. Nishida, and T. Obayashi," Impedance and electric field observations in the magnetosphere with satellite JIKIKEN (EXOS-B)," J. Geomag. Geoelectr., vol. 33, pp. 101-110, 1981.

Evans, J. E., and A. S. Griffiths, "Design of a Sanguine noise processor based upon world-wide extremely low frequency (ELF) recordings," IEEE Trans. Communications, vol. COM-22, no. 4, pp. 528-539, April 1974.

Fraser-Smith, A. C., and J. L. Buxton, "Superconducting magnetometer measurements of geomagnetic activity in the 0.1-14 Hz frequency range," J. Geophys. Res., vol. 80, pp. 3141-3147, 1975.

Fraser-Smith, A. C., and R. A. Helliwell, "ELF sferic occurrences in the Antarctic during a solar proton event: case study of occurrences at Byrd Station during the event of June 9, 1968," J. Geophys. Res., vol. 85, no. A5, pp. 2296-2306, 1980.

Ginsberg, L. H., "Extremely low frequency (ELF) atmospheric noise level statistics for Project Sanguine," IEEE Trans. Communications, vol. COM-22, no. 4, pp. 555-561, April 1974.

Goldstein, J. A., W. O. Meyers, and J. R. Davis, "ELF nonlinear noise processing experimental measurements, Part 3 – Synoptic sample of diurnal and seasonal noise variation in Italy," Memorandum Report 3543, Naval Research Laboratory, Washington, D.C., July 1977.

Griffiths, A. S., "ELF noise processing," Technical Report 490, Lincoln Laboratory, MIT, Lexington, Massachusetts, 13 January 1972.

Griffiths, A. S., "Measurements of ELF noise processing," Technical Note 1975-33, Lincoln Laboratory, MIT, Lexington, Massachusetts, 2 September 1975.

Gurnett, D. A., and L. A. Frank, "ELF noise bands associated with auroral electron precipitation," J. Geophys. Res., Vol. 77, no. 19, pp. 3411-3417, 1972.

Gurnett, D. A., and L. A. Frank, "Plasma waves in the polar cusp: Observations from Hawkeye 1," J. Geophys. Res., and vol. 83, no. A4, pp. 1447-1462, 1978.

Gurnett, D. A., and R. R. Shaw, "Electromagnetic radiation trapped in the magnetosphere above the plasma frequency," J. Geophys. Res., vol. 78, no. 34, pp. 8136-8149, 1973.

Gurnett, D. A., L. A. Frank, and R. P. Lepping, "Plasma waves in the distant magnetotail," J. Geophys. Res., vol. 81, no. 34, pp. 6059-6071, 1976.

Gurnett, D. A., G. W. Pfeiffer, R. R. Anderson, S. R. Mosier, and D. P. Cauffman, "Initial observations of VLF electric and magnetic fields with the Injun 5 satellite," J. Geophys. Res., vol. 74, no. 19, pp. 4631-4648, 1969.

Guthart, H., T. L. Crystal, B. P. Ficklin, W. E. Blair, and T. J. Yung, "Proton gyrofrequency band emissions observed aboard OGO 2," J. Geophys. Res., vol. 73, no. 11, pp. 3592-3596, 1968.

Handa, S., T. Ogawa, and M. Yasuhara, "Damping coefficients of Q-type bursts in the Schumann resonance frequency range," Contributions of the Geophys. Inst., Kyoto Univ., No. 11, pp. 11-15, 1971.

Handbook of Geophysics, rev. ed., Macmillan, New York, 1961.

Heacock, R. R., "Whistler-like pulsation events in the frequency range 20 to 200 Hz," Geophys. Res. Lett., vol. 1, pp. 77-79, 1974.

Helliwell, R. A., Whistlers and Related Ionospheric Phenomena, Stanford University Press, Stanford, California, 1965.

Helliwell, R. A., "Whistlers and VLF emissions", in Physics of the Magnetosphere, Carivallano, McClay, Radosky (eds.), D. Reidel Publ. Co., Dordrecht-Holland, pp. 106-147, 1968.

Helliwell, R. A., and S. B. Mende, "Correlations between λ4278 optical emissions and VLF wave events observed at L ~ 4 in the Antarctic," J. Geophys. Res., vol. 85, no. A7, pp. 3376-3386, 1980.

Holtet, J. A., "Propagation effects observed in ELF and VLF signals in the ionosphere," in ELF-VLF Radio Wave Propagation, J. A. Holtet (ed.), pp. 351-359, D. Reidel Publ. Co., Dordrecht-Holland, 1974.

Holtet, J., and A. Egeland, "Experimental and theoretical investigations of naturally occurring electromagnetic radiation in the audio-frequency range," Physica Norvegica, vol. 3, no. 3, pp. 223-239, 1969.

Horner, F., "The use of atmospherics for studying the ionosphere," J. Atmos. Terr. Phys., vol. 32, pp. 609-621, 1970.

James, H. G., "VLF saucers," J. Geophys. Res., vol. 81, no. 4, pp. 501-514, 1976.

Jones, D. L., "Extremely low frequency (ELF) ionospheric radio propagation studies using natural sources," IEEE Trans. Communications, vol. COM-22, no. 4, pp. 477-484, April 1974.

Jones, D. L., and D. T. Kemp, "Experimental and theoretical observations on the transient excitation of Schumann resonances," J. Atmos. Terr. Phys., vol. 32, pp. 1095-1108, 1970.

Karnaushenko, N. N., A. S. Kukushkin, V. N. Lobachev, and S. F. Nuzhdin, "Studies of the vertical structure of the natural electromagnetic field in the sea in the tropical Atlantic," (in Russian), Morskiye Gidrofizicheskiye Issledovaniya, no. 2(89), Acad. Nauk, Ukr.SSR, Sevastopol, 1980.

Katsufrakis, J., "Whistlers and ELF emissions," in Natural Electromagnetic Phenomena Below 30 KC/S, Proc. NATO Adv. Study Inst., pp. 261-286, Plenum Press, New York, 1964.

Kemp, D. T., "The global location of large lightning discharges from single station observations of ELF disturbances in the earth-ionosphere cavity," J. Atmos. Terr. Phys., vol. 33, pp. 919-927, 1971.

Kleimenova, N. G., "Some spectral peculiarities of ELF-VLF emissions at subauroral ground stations," in ELF-VLF Radio Wave Propagation, J. A. Holtet (ed.), pp. 365-367, D. Reidel Publ. Co., Dordrecht Holland, 1974.

Kurimoto, K., "Preliminary results of the simultaneous observation of whistlers in low latitudes," J. Geomag. Geoelectr., vol. 32, pp. 575-579, 1980.

Labson, V. F., and H. F. Morrison, "Measurement of the natural audio band electromagnetic field," paper to be presented at the Society of Exploration Geophysicists Annual Meeting, 1981.

Larsen, T.R., "ELF noise measurements," in ELF-VLF Radio Wave Propagation, J. A. Holtet (ed.), pp. 223-238, D. Reidel Publ. Co., Dordrecht-Holland, 1974.

Likhter, Ja., I., and S. S. Sazhin, "On the frequency shift in modulated VLF emissions," J.Atmos.Terr.Phys., vol. 42, pp. 381-384, 1980.

"MONSEE Nov 77": Directory of Solar-Terrestrial Physics Monitoring Stations, H. E. Coffey and M. A. Shea (eds.), MONSEE Special Publication No. 1, AFGL-TF-77-0255, November 1977, obtainable from the National Technical Information Service (NTIS).

Matsumoto, H., S. Miyatake, K. Tsuruda, A. Morioka, J. Ohtsu, H. Oya, and I. Kimura, "VLF wave observation by satellite JIKIKEN (EXOS-B)," J. Geomag. Geoelectr., vol. 33, pp. 63-72, 1981.

Maxwell, E. L., "Atmospheric noise from 20 Hz to 30 kHz, Radio Sci., vol. 2 (New Series), no. 6, pp. 637-644, June 1967.

Muzzio, J. L. R., and J. J. Angerami, "OGO 4 observations of extremely low frequency hiss," J. Geophys. Res., vol. 77, no. 7, pp. 1157-1173, 1972.

Ogawa, T., Y. Tanaka, T. Miura, and M. Yasuhara, "Observations of natural ELF and VLF electromagnetic noises by using ball antennas," J. Geomag. Geoelec., vol. 18, pp. 443-454, 1966.

Parady, B., and L. J. Cahill, Jr., "ELF observations during the December 1971 storm," J. Geophys. Res., vol. 78, no. 22, pp. 4765-4770, 1973.

Park, C. G., "VLF wave activity during a magnetic storm: a case study of the role of power line radiation," J. Geophys. Res., vol. 82, no. 22, pp. 3251-3260, 1977.

Park, C. G., R. A. Helliwell, and F. Lefeuvre, "Ground observations of power line radiation coupled to the ionosphere and magnetosphere," Proc. Fifth. Int. Wroclaw Sympos. on EMC, pp. 341-349, September 1980.

Perraut, S., R. Gendrin, C. de Villedary, D. Fouassier, J. Lavergnat, J. P. Meunier, B. Morlet, J. Bitterly, Y. Corcuff, M. Tixier, F. Glangleaud, M. Fehrenbach, and G. Weill, "French mobile station for recording geophysical data: description; initial results of the conjugated campaign in association with GEOS-1," Proc. Esrange Sympos., Ajaccio, 24-29 April 1978, pp. 73-84, ESA SP-135, June 1978.

Pierce, E T., "Some ELF phenomena," J. Res. NBS-D. Radio Propag., vol. 64D, no. 4, pp. 383-386, 1960.

Polk, C., "Sources, propagation, amplitude and temporal variation of extremely low frequency (0-100 Hz) electromagnetic fields," in Biological and Clinical Effects of Low-Frequency Magnetic and Electric Fields, J. G. Llaurado, A. Sances, Jr., and J. H. Battocletti, C. Thomas Publ., pp. 21-48, 1974.

Polk, C., "Natural and man-made noise in the earth-ionosphere cavity at extremely low frequencies," Proc. Fifth Int. Wroclaw Sympos. on EMC, pp. 903-911, September 1980.

Polk, C., "Schumann resonances," Chapter 3 in Handbook of Atmospherics, H. Volland (ed.), CRC Press, Boca Raton, Florida, 1981.

Russell, T. R., R. E. Holzer, and E. J. Smith, "OGO 3 observations of ELF noise in the magnetosphere," J. Geophys. Res., vol. 74, no. 3, pp. 755-777, 1969.

Rycroft, M. J., "Whistlers and discrete ELF/VLF emissions," in ELF-VLF Radio Wave Propagation, J. A. Holtet (ed.), pp. 317-334, D. Reidel Publ. Co., Dordrecht-Holland, 1974.

S-300 Experimenters, "Measurements of electric and magnetic wave fields and of cold plasma parameters on-board GEOS-1. Preliminary results," Planet. Space Sci., vol. 27, pp. 317-339, 1979.

Sao, K., M. Yamashita, S. Tanahashi, H. Jindoh, and K. Ohta, "Experimental investigations of Schumann resonance frequencies," J. Atmos. Terr. Phys., vol. 35, pp. 2047-2053, 1973.

Sato, N., M. Ayukawa, and H. Fukunishi, "Conjugacy of ELF-VLF emissions Near L-6," J. Atmos. Terr. Phys., vol. 42, pp. 911-928, 1980.

Scarf, F. L., and C. R. Chappell, "An association of magnetospheric whistler dispersion characteristics with changes in local plasma density," J. Geophys. Res., vol. 78, no. 10, pp. 1597-1602, 1973.

Scarf, F. L., R. W. Fredericks, E. J. Smith, A. M. A. Frandsen, and G. P. Serbu, " OGO 5 observations of LHR noise, emissions, and whistlers near the plasmapause at several earth radii during a large magnetic storm," J. Geophys. Res., vol. 77, no. 10, pp. 1776-1793, 1972.

Scarf, F. L., L. A. Frank, K. L. Ackerson, and R. P. Lepping, "Plasma wave turbulence at distant crossings of the plasma sheet boundaries and the neutral sheet," Geophys. Res. Lett., vol. 1, p. 189, 1974.

Selzer, E., "Mesures électromagnétiques effectuées en mer profonde à bord du bathyscaphe Archimède," Ann. de l'Inst. Oceanographique, vol. 46, no. 1, pp. 19-28, 1968.

Selzer, E., L. Launay, and S. W. Lichtman, "Electrical environment determinations at great ocean floor depths using the bathyscaphe Archimedes," IEEE 1966 Ocean Electronics Symposium Technical Proceedings, Honolulu, Hawaii, August 1966.

Shand, J. A., "Some quantitative characteristics of the Schumann-ELF natural electromagnetic background," Can. J. Phys., vol. 44, no. 3, pp. 449-459, 1966.

Shawhan, S. D., "Magnetospheric plasma wave research," Rev. Geophys. and Space Phys., vol. 17, no. 4, pp. 705-724, June 1979.

Singh, D. P., S. K. Jain, and B. Singh, "Propagation characteristics of VLF hiss observed at low latitude ground stations," Ann. Geophys. vol. 34, no. 1, pp. 37-45, 1978.

Smith, R. L., N. M. Brice, J. Katsufrakis, S. D. Shawhan, J. S. Belrose, and R. E. Barrington, Nature, vol. 204, p. 274, 1965.

Smith, E. J., R. E. Holzer, and C. T. Russell, "Magnetic emissions in the magnetosheath at frequencies near 100 Hz," J. Geophys. Res., vol. 74, no. 11, pp. 3027-3036, 1969.

Smith, E. J., A. M. A. Frandsen, B. T. Tsurutani, R. M. Thorne, and K. W. Chan, "Plasmaspheric hiss intensity variations during magnetic storms," J. Geophys. Res., vol. 79, no. 16, pp. 2507-2510, 1974.

Soderberg, E. F., "Undersea ELF measurements of the horizontal E-field to depths of 300 meters," AGARD Conference Proceedings No. 20, Sub-Surface Communications, pp. 453-470, 1966.

Soderberg, E. F., "ELF noise in the sea at depths from 30 to 300 meters," J. Geophys. Res., vol. 74, no. 9, 2376-2387, 1969.

Soderberg, E. F., "A study of the distribution of extremely low frequency electromagnetic fields in the ocean near a shoreline," Naval Underwater Systems Center Technical Report 5441, New London, Connecticut, 1976.

Soderberg, E. F., ad M. Finkle, "A comparison of ELF atmospheric noise spectra measured above and in the sea," AGARD Conference Proceedings No. 77, Electromagnetics of the Sea, pp. 13-1 to 13-13, November 1970.

Strarup, T., "Equipment for measuring the horizontal electric field at sea in the frequency interval of 1-32 cps," NATO Saclant ASW Research Centre, Technical Memorandum No. 96, 31 January 1966.

Strarup, T., and G. Tacconi, "High sensitivity equipment for measuring the horizontal electric field strength component in the frequency interval of 1-32 Hz on the sea bottom in shallow water," NATO Saclant ASW Research Centre, Technical Memorandum No. 141, 15 May 1968.

Tacconi, G., "The measurement of the ELF horizontal electric field component of the background noise in the sea," in ELF-VLF Radio Wave Propagation, J. A. Holtet (ed.), pp. 239-243, D. Reidel Publ. Co., Dordrecht-Holland, 1974.

Tacconi, G., "Sloping bottom effects on e.m. underwater propagation at ELF," paper presented at this meeting, NATO AGARD symposium on Medium, Long and Very Long Wave Propagation (At Frequencies Less Than 3000 kHz)," September 1981.

Taylor, W. W. L., and R. R. Anderson, "Explorer 45 wave observations during the large magnetic storm of August 4-5, 1972," J. Geophys. Res., vol. 82, no. 1, pp. 55-66, 1977.

Taylor, W. W. L., and D. A. Gurnett, "The morphology of VLF emissions observed with the Injun 3 satellite," J. Geophys. Res., vol. 73, no. 17, pp. 5615-5626, 1968.

Thorne, R.M, E. J. Smith, R. K. Burton, and R. E. Holzer, "Plasmaspheric hiss," J. Geophys. Res., vol. 78, no. 10, pp. 1581-1596, 1973.

Tomizawa, I., and T. Yoshino, "Study of power line radiation, I. Balloon observation," Reports of the University of Electro-communications, vol. 30, no. 1, pp. 101-108, August 1979.

Vernova, L. V., Ya. I. Likhter, and Ya. P. Sobolev, "Ion-cyclotron noise in the topside ionosphere," Geomag. Aeron., vol. 18, no. 5, pp. 581-585, 1978.

Vozoff, K., L. Holcomb, and R. Hales, "Synoptic recording system for AMT fields," paper to be presented at the IAGA Meeting, Edinburgh, August 1981.

Watt, A. D., and E. L. Maxwell, "Characteristics of atmospheric noise from 1 to 100 kc, Proc. IRE, vol. 45, pp. 787-794, June 1957.

Wait, J. R., Electromagnetic Waves in Stratified Media, Pergamon Press, 2nd Ed., Oxford-New York, 1970.

Wait, J. R., "Propagation of ELF electromagnetic waves and Project Sanguine/Seafarer," IEEE J. Oceanic Engrg., vol. OE-2, no. 2, pp. 161-172, April 1977.

Watenabe, S., and T. Ondoh, "Propagation of trans-equatorial deuteron whistlers in the low altitude topside ionosphere," J. Atmos. Terr. Phys., vol. 42, pp. 427-435, 1980.

White, D. P., and D. K. Willim, "Propagation measurements in the extremely low frequency (ELF) band," IEEE Trans. Communications, vol. COM-22, no. 4, pp. 457-467, April 1974.

Zakharov, A. V., and S. N. Kuznetsov, "Lifetime of the earth's radiation belt electrons and VLF emission," Geomag. Aeron., vol. 18, no. 2, pp. 232-233, 1978.

TABLE 1

GROUND STATIONS WITH ELF MEASUREMENT CAPABILITY

| Research Group | Station Location<br>Note: Parentheses ( )<br>denotes geomagnetic<br>coordinates | Frequency Range | Sensors | References<br>("p.c." means personal<br>communication) |
|---|---|---|---|---|
| Radio Research Laboratories<br>Space Physics Section<br>Tokyo, Japan | Kashima, Japan<br>(25.8N 204.4E)<br>Syowa, Antarctica<br>(69.7S 77.7E) | 50 Hz – 30 kHz | Electric dipoles-<br>all E components | T. Ondoh<br>(p.c. April 1981) |
| Space Physics Group<br>University of Sheffield, U.K. | Halley, Antarctica<br>75.55 26.9W | 100 Hz – 20 kHz | Crossed loop<br>ELF/VLF wideband<br>goniometer | A. J. Smith<br>(p.c. March 1981) |
| Laboratory of Physics of the<br>Upper Atmosphere<br>Saint Julien l'Ars, France | Kerguelen<br>49.35S 70.20E<br>Belgrano<br>77.8S 321.7E<br>Poitiers<br>46.6N 0.3E | 10-450 Hz<br>400 Hz – 10 kHz<br><br>1–16 kHz | AC magnetometers<br><br>Vertical E<br>Crossed loops | Y. Corcuff<br>(p.c. April 1981) |
| Physics Department<br>University of Otago<br>Dunedin, New Zealand | Campbell Island<br>52.5S 169.20E<br>Dunedin<br>45.79S 170.48E<br><br>Hobart<br>42.5S 147.20E | 300 Hz – 10 kHz<br>1-15 kHz<br>300 Hz – 10 kHz<br>1-15 kHz<br>1-30 kHz<br>290 Hz – 10 kHz<br>1-15 kHz<br>1-20 kHz | NS magnetic | MONSEE Nov 77, pp 219,220,222 |
| Ionospheric Research Group<br>CNET<br>St. Maur, France | Sogra<br>62.80N 46.25E | 10 – 1000 Hz<br>500 Hz – 12 Hz | | MONSEE Nov 77, p 230 |
| Department of Physics<br>University of Sheffield, U.K. | Halley Bay, Antarctica<br>74.5S 26.6W<br>Eskros<br>62.0N 6.8W<br>Bradfield<br>53.4N 1.9W | 500 Hz – 11 kHz | VLF goniometer with 2<br>crossed vertical loops | Bullough and Sagredo (1973) |
| Chubu Institute of Technology<br>Kasugai, Japan | Hajahima (Bonin Is.)<br>(16.5N 208.8E)<br>Yamaoaka, Japan<br>(24.7N 203.6E)<br>Chubu<br>35.2N 137.01E | 300 Hz – 9 kHz<br><br><br>1-16 kHz | 5 m loop | Kurimoto (1980)<br><br>MONSEE Nov 77, p 219 |
| National Institute of Polar<br>Research<br>Tokyo, Japan | Syowa, Antarctica<br>69S 39.6E<br>Mizuho, Antarctica<br>70.7S 44.3W<br>Husafell, Iceland<br>64.7N 20.9W | 200 Hz – 20 kHz | Loop antennas | Sato et al. (1990) |
| Research Institute of<br>Atmospherics<br>Nagoya University<br>Nagoya, Japan | Kagoshima<br>31.4PN 130.71E<br>Moshiri<br>44.36N 142.27E<br>Sakushima<br>34.73N 137.05E | 500-8000 Hz | | MONSEE Nov 77, p 223<br><br>MONSEE Nov 77, p 227<br><br>MONSEE Nov 77, p 229 |
| Department of Science<br>Antarctic Division<br>Melbourne, Australia | Davis<br>68.50S 77.96E | 400 Hz – 10 kHz | | MONSEE Nov 77, p 219 |
| Taunus Observatory<br>Kleiner Feldberg/Ts<br>West Germany | Mobile station:<br>Kaamanen, Finland<br>Kiiminki, Finland<br>Hamburg Hallig, W.Ge. | 300 Hz – 5 kHz | Vertical E | G. Mattern<br>(p.c. May 1981) |
| Institute of Geophysics<br>Genua, Italy | Robarent<br>44.30N 07.88E | 1-15 kHz<br>(not operating<br>at present) | NS magnetic | A. Elena (p.c. May 1981) |
| Geophysical Observatory<br>Christchurch<br>New Zealand | Mobile station:<br>Eauder<br>Five Rivers<br>Stewart Island | 50 Hz – 3 kHz | Vertical E | Barr (1979) and<br>(p.c. May 1981) |
| Physics Department<br>King's College, Strand<br>London, U.K. | Various:<br>South England | 5-120 Hz | Vertical E<br>NS, EW solenoids | D. L. Jones (p.c. March 1981) |
| Geophysical Institute<br>Kyoto University<br>Kyoto, Japan | Aso Volcanic Laboratory | 5-32 Hz<br>4-28 Hz | NS, EW solenoids<br>NS, EW electric<br>vertical electric | Ogawa et al. (1966)<br>Handa et al. (1971) |
| Department of Electrical<br>Engineering<br>University of Rhode Island<br>Kingston, Rhode Island | West Greenwich<br>41°47N 71°44W | 3-37 Hz | NS, EW loops<br>Vertical E | C. Polk<br>(p.c. May 1981) |
| Norwegian Defense Research<br>Establishment<br>Kjeller, Norway | Lavangsdalen, Norway | 3-400 Hz | NS, EW air core loops | Larsen (1974) |
| The Norwegian Institute of<br>Cosmic Physics<br>Oslo, Norway | Lavangsdalen, Norway<br>69.5N 19.3E | 1-100 Hz<br>100-2000 Hz<br>< 2 kHz | | Holter (1974) |
| Auroral Observatory<br>University of Tromsø<br>Tromsø, Norway | Tromsø<br>69.70N 19.00E | | | MONSEE Nov 77, p 233 |

TABLE 1 (CONT'D)

GROUND STATIONS WITH ELF MEASUREMENT CAPABILITY

| | | | | |
|---|---|---|---|---|
| Kiruna Geophysical Observatory<br>Kiruna, Sweden | Kiruna<br>67.8N | 10 Hz - 1 kHz<br>500 Hz - 10 kHz | Horizontal loop | Egeland (1964) |
| Naval Research Laboratory<br>Washington, DC | China Lake, California<br>36°N 118°W | 0.3-40 Hz<br>(not operating<br>at present) | SQUID magnetometer | Dinger and Goldstein (1980) |
| Lincoln Laboratory<br>Massachusetts Institute of<br>Technology<br>Lexington, Massachusetts | Various:<br>see references | 5-320 Hz | Crossed loops<br>Vertical whip | Evans and Griffiths (1974)<br>White and Willim (1974)<br>Griffiths (1975) |
| RCA Laboratories<br>Princeton, New Jersey | Portable:<br>Malta<br>Guam | 20-200 Hz<br>four single<br>frequencies | 2 orthogonal loops<br>for horizontal magnetic<br>2 m vertical whip | Ginsberg (1974) |
| Physical Dynamics, Inc.<br>La Jolla, California | Mobile station | DC - 500 Hz | Fluxgate magnetometer | J. Solinsky<br>(p.c. May 1981) |
| Radioscience Laboratory<br>Stanford University<br>Stanford, California | Byrd Station<br>79.98S 120.02W | 75 Hz<br>1.2 kHz<br>2-4 kHz | Loop antennas:<br>NS, EW, vertical<br>Vertical whip | Fraser-Smith and Helliwell (1980)<br>Helliwell and Mende (1980) |
| | (Various locations) | (10-500 Hz)<br>(200 Hz - 32 kHz) | (Crossed loops) | (R. A. Helliwell, July 1980,<br>unpublished document) |
| Centre de Recherches en Physique<br>de l'Environnement<br>CNET, Issy les-Moulineaux, France | Kerguelen<br>Kilpisen, Norway | 30-450 Hz | Ferrite probe | R. Gendrin (p.c. April 1981)<br>S. Perraut (p.c. April 1981) |
| Institute National d'Astronomie<br>et de Geophysique, France | Mobile station:<br>Skibotn, Norway<br>69.4N 20.3E<br>Husafell, Iceland<br>64.4N 20.8E | 0.1-10 Hz<br>30-600 Hz<br>300 Hz - 10 kHz | Fluxmeter | Perraut et al. (1978) |
| Engineering Geoscience<br>Department<br>University of California<br>Berkeley, California | San Antonio Valley | 1 Hz - 25 KHz | NS, EW coils | V. F. Labson, H. F. Morrison<br>A. Becker (p.c. April 1981) |
| Centre for Geophysical<br>Exploration Research<br>Macquarie University<br>North Ryde, NSW, Australia | Near Sidney | 0.1 Hz - 10 kHz | 3 magnetic components<br>3 electric components | K. Vozoff (p.c. April 1981) |
| Physics Department<br>University of Natal<br>Durban, S. Africa | Sanae<br>70.30 S 357.65E | | 1. m loop | MONSEE Nov 77, p 230 |
| University of Electro-<br>Communications<br>Chofu, Japan | Sugadaira<br>36.5IN 138.35E | <14 kHz | 30 x 20 m delta loop | MONSEE Nov 77, p 231 |
| Space Science Center<br>University of New Hampshire<br>Durham, NH | Siple, Antarctica<br>Roberval, Canada<br>South Pole, Antarctica | 0.005-10 Hz | Induction antenna<br>3 magnetic components | R. L. Arnoldy<br>(p.c. Feb. 1981) |
| Institute of Physics of the<br>Earth<br>University of Paris, France | Garchy<br>47°18N 03°06E | 10-3 - 10 Hz | 3 magnetic components | L. Selzer<br>(p.c. April 1981) |
| Geophysical Institute<br>University of Alaska<br>Fairbanks, Alaska | College, Alaska<br>Macquarie Island, Australia<br>Sodankyla, Finland<br>Oulu, Finland<br>Nurmijarvi, Finland | 0-10 Hz | Coils and fluxgates:<br>3 magnetic components<br>Earth current probes | J. V. Olson (p.c. March 1981, |
| Institute of Physics of the<br>Earth<br>Moscow | Sogra<br>Dolgoschelle<br>Kerguelen<br>Herd | | | Kleimenova (1974) |

TABLE 2

SOME SATELLITES THAT HAVE PROVIDED ELF DATA

The references contain examples of ELF plasma wave emissions

| | | |
|---|---|---|
| Alouette 2 | 73 m electric dipole; magnetic antenna; 50 Hz – 30 kHz | Barrington et al. (1971) |
| Ariel 3<br>Ariel 4 | Loop antenna<br>750 Hz – 18 kHz | Bullough et al. (1975) |
| GEOS 1 | 3-axis 42 m electric dipole 15 Hz – 76 kHz<br>DC-ULF magnetometer 0.1 – 450 Hz<br>ULF-VLF magnetometer 450 Hz – 20 kHz | S-300 Experimenters (1979) |
| Hawkeye 1 | Electric antenna, triaxial magnetometer | Gurnett and Frank (1978) |
| IMP 6 | Orthogonal long wave electric 7.7, 53, 93 m wires<br>3 orthogonal loop antennas 20 Hz – 200 kHz | Gurnett and Shaw (1973) |
| IMP 8 | 121 m electric dipole – 40 Hz – 2 MHz<br>Triax search coil magnetometer – 40 Hz – 117 kHz | Gurnett et al. (1976) |
| Injun 3 | Loop antenna | Smith et al. (1965), Taylor and Gurnett (1968) |
| Injun 5 | 2.8 m electric dipole<br>.56 m magnetic loop ant. – 30 Hz – 10 kHz | Gurnett et al. (1969)<br>Gurnett and Frank (1972) |
| Interkosmos 3<br>Interkosmos 5 | 70 Hz – 20 kHz | Likhter and Sazhin (1980)<br>Zakharov and Kuznetsov (1978) |
| Interkosmos 14 | | Vernova et al. (1978)<br>IMS Newsletter, No. 4, p. 4, 1974 |
| ISIS 1<br>ISIS 2 | 73 m electric dipole – 50 Hz – 27 kHz | James (1976)<br>Watanabe and Ondoh (1980) |
| JIKIKEN (EXOS – B) | 103 m electric dipole<br>15 m loop antenna 150 Hz – 9.5 kHz | Ejiri et al. (1981)<br>Matsumoto et al. (1981) |
| OGO 1 | Search coil magnetometer | Dunckel and Helliwell (1969) |
| OGO 2 | Electric; magnetic | Guthart and Crystal (1968) |
| OGO 3 | Electric antenna<br>Search coil magnetometer 15 Hz – 12.5 kHz | Burtis (1973)<br>Russell et al. (1969) |
| OGO 4 | Magnetic<br>ELF 15 Hz – 1 kHz; VLF 300 Hz – 12.5 kHz | Muzzio and Angerami (1972)<br>Hollet (1974) |
| OGO 5 | Electric dipoles<br>Search coil magnetometer | Scarf and Chappell (1973), Scarf et al. (1972)<br>Thorne et al. (1973), Smith et al. (1969) |
| OGO 6 | Electric Dipole, Search coil magnetometer 4 Hz – 4 kHz | Smith et al. (1974) |
| OV1-17 | Electric dipole | |
| S³-A (Explorer 45) | 2 orthogonal 5 m dipoles<br>Search coil magnetometer, 3 – 1000 Hz | Anderson and Gurnett (1973)<br>Parady & Cahill (1973), Taylor & Anderson (1977) |
| Triad | Triaxial magnetometer | Armstrong (1973) |

TABLE 3

MEASUREMENTS OF ELF NOISE IN THE SEA

| Location | Platform | Sensor | Sensor Depth | Water Depth | Frequency Range | Reference |
|---|---|---|---|---|---|---|
| Puerto Rico Trench<br>Greece<br>Madeira Islands<br>Toulon | Archimede<br>"<br>"<br>" | Electrode pair<br>& solenoid<br>"<br>" | 8000 m<br>5000 m<br>5000 m<br>2500 m | 8000 m<br>"<br>"<br>" | 20-300 Hz<br>0-300 Hz<br>"<br>" | Selzer (1966, 1968) |
| Baja California | Diving Saucer | Electrode Pair | 30-300 m | 860 m | 4-1000 Hz | Soderberg (1966, 1969) |
| Grand Bahamas | Deepstar 4000 | " | 30-1200 m | 1220 m | 4-1000 Hz | Soderberg (1976) |
| Gulf of La Spezia | Floating platform | " | 10 m | shallow | 1-32 Hz | Brock Nannestad (1965, 1966) |
| Gulf of La Spezia | " | " | 10 m | 150 m | 1-32 Hz | Strarup (1966) |
| Gulf of La Spezia | " | " | 25 m | 25 m | 1-32 Hz | Strarup and Tacconi (1968) |
| Tyrrhenian Sea | Ship | " | | | 1-32 Hz | Tacconi (1974) |
| North Atlantic | Oceanographic Ship | " | 25 m | 5000 m | 4-1000 Hz | Soderberg and Finkle (1970) |
| Black Sea | " | " | 10-70 m | 500 m | 20-1500 Hz | Artamonov and Molochnov (1979) |
| Tyrrhenian Sea<br>Tropical N. Atlantic<br>Kandraky area<br>Black Sea | "<br>"<br>"<br>" | Electric<br>magnetic sensors<br><br> | 10-100 m<br>10-100 m<br>10-50 m<br>10-100 m | | 10-200 Hz | Karnaushenko et al. (1980) |

DISCUSSION EPP FALL 81 MEETING
MEDIUM, LONG, AND VERY LONG WAVE PROPAGATION
(AT FREQUENCIES LESS THAN 3000 KHZ)

SESSION 2

PAPER: 10. OVERVIEW OF ELF PROPAGATION
AUTHOR: P. Bannister
COMMENTER: E. R. Schmerling
QUESTION: You showed some very impressive agreement between measured attenuation versus distance and your theoretical computations. Do you have any idea what solar cycle variations might be expected? These would be of two kinds. The first type is the charge in the ionosphere over the epoch of the solar cycle. The second type is the varying effects of particle precipitation which seem to maximize during the falling part of the sunspot cycle. Do you have any feeling for this?
RESPONSE: The measurements taken so far do not extend over a sunspot cycle. We have measurements taken in 1970 to 1972. One path was from the transmitter to Alaska. We also measured in Greenland, Norway, and Greece. There was some directional dependence upon these paths. But the directional dependence of the attenuation rate was very small, on the order of 0.2 to 0.3 dB per megameter.

PAPER: 10. OVERVIEW OF ELF PROPAGATION
AUTHOR: P. Bannister
COMMENTER: P. Kossey
QUESTION: Could you comment on the possible interference effects arising from forward and backpath signals at ELF?
RESPONSE: The author showed an example of three weeks average data taken in the Pacific at a distance of 11.5 Megameters. There appeared to be interference around sunset over Wisconsin, where the direct path is a daytime path and the excitation factor over the transmitter is changing. The excitation factor was lower at night. The path coming the other way is mostly night-time propagation. The difference between the two paths is approximately 6 to 10 dB. You can get some interference pattern depending on the relative phasing. We have some other measurements taken in a different area where it looks like it is a possibility you can get substantial interference from an around the world path, which shows you that the attenuation rates are low on the average.
You won't see the interference on a night-time path which has low attenuation. The path around the other way has higher attenuation since it is in daytime.

PAPER: 10. OVERVIEW OF ELF PROPAGATION
AUTHOR: P. Bannister
COMMENTER: T. B. Jones
QUESTION: Since so much of your explanation of these disturbances hinges on the Sporadic-E-Layer being formed at night particularly, do you have observations where you knew that a Sporadic E-Layer was present? For example from the ionosondes in the US.

RESPONSE: No, we don't. That is one reason why we want to take some Sporadic-E measurements at the same time we are taking nightime propagation measurements

PAPER: 10. OVERVIEW OF ELF PROPAGATION
AUTHOR: P. Bannister
COMMENTER: J. B. Reagan
QUESTION: What is known if anything about how much of the ELF energy leaks up into the magnetosphere through the D-Region?
RESPONSE: As far as I know, there is not much known about this. With some of Booker's recent calculations you can get a rough idea of what does leak through. From what I remember from his last paper I would say 10 to 15 per cent.

PAPER: 11 ELF PROPAGATION IN DISTURBED ENVIRONMENTS
AUTHOR: E. C. Field
COMMENTER: F. J. Kelly
COMMENT: A very nice talk. You might find some confirmation in the calculations by Galejs, reference some of his work back in 1970. He made a similar calculation but employing a different integral. His work was presented at one of our VLF Propagation Meetings before he died in 1974. You might want to look at his work to help confirm some of your calculations.
RESPONSE: Thank you, I will.

PAPER: 11 ELF PROPAGATION IN DISTURBED ENVIRONMENTS
AUTHOR: E. C. Field
COMMENTER: J. S. Belrose
QUESTION: At VLF, the ice-caps in Greenland and Antarctic are very important. Especially during disturbance events when the lower boundary of the ionosphere moves down to very low heights. Has any work been done to show whether it has an effect at ELF?
RESPONSE: I have not done specific calculations at ELF to see what the effect of the ice-caps would be, but the frequency is so low, I think even $10^{-5}$ mhos per meter wouldn't affect propagation very much.
Dr. Imhof's paper addresses this.

PAPER: 11 ELF PROPAGATION IN DISTURBED ENVIRONMENTS
AUTHOR: E. C. Field
COMMENTER: L. Brock-Nannestad

PAPER: 11 ELF PROPAGATION IN DISTURBED ENVIRONMENTS
AUTHOR: E. C. Field
COMMENTER: L. Brock-Nannestad
QUESTION: What happens to the phase during strong disturbances?
RESPONSE: The phase changes by several tens of degrees. Although we have performed a large number of phase calculations. I have .... in the interest of brevity... restricted the presentation to the effects of disturbances on amplitude.

PAPER: 12 ELF PROPAGATION IN POLAR AREAS, MEASUREMENTS AND THEORETICAL FIELD STRENGTH PREDICTIONS
AUTHOR: W. L. Imhof
COMMENTER: E. R. Schmerling
COMMENT : I am puzzled at the large effects due to Sporadic-E. I wonder if you could comment? In other parts of your paper the thrust has been on the electron concentration in the 40 to 100 km. region as being important. Generally speaking sporadic-E is around 105 kilometers
RESPONSE : It is clearly some kind of resonant effect that none of us has understood in great detail.
(E. C. Field Comment) The effect would be most important at fairly high latitudes at night when ELF signals can leak out of the wave-guide and strike a resonant effect almost like a quarter wave plate effect with a Sporadic-E region. Under daytime conditions or at low latitudes where the energy does not get up that high, then you would not expect very much of an effect.

PAPER: 12 ELF PROPAGATION IN POLAR AREAS, MEASUREMENTS AND THEORETICAL FIELD STRENGTH PREDICTIONS
AUTHOR: W. L. Imhof
COMMENTER : F. J. Kelly
COMMENT: I want to thank the author for a very fine presentation. Most authors today have centered attention on the E Layer as the likely cause of "anomalous" propagation. When Bales did some calculations on sporadic E effects, in the early 70's, he found that a resonance between the E-Layer and the F-Layer also played an important role in determining the attenuation of ELF waves at night. Since the F-Region has its own variability with troughs and depletions sometimes occurring, we have an extra complication that enters into the explanation of any observed effects.

A REVIEW OF THE ANALYTICAL TECHNIQUES FOR DETERMINING

THE PHASE AND AMPLITUDE OF A VLF RADIO WAVE PROPAGATING

IN THE EARTH-IONOSPHERE WAVEGUIDE

T.B. Jones and K. Mowforth
Physics Department
University of Leicester
Leicester, England

## SUMMARY

The terrestrial propagation of VLF radio waves can conveniently be considered in terms of a conducting spherical earth surrounded by a concentric electron-ion plasma into which waves are launched from a Hertzian dipole source situated on the earth's surface. The application of Maxwell's equations and the appropriate boundary conditions, allows the vertical electric field strength to be calculated at any point remote from the transmitter. The form of the solution is a series summation of zonal harmonics which requires a large digital computer for its evaluation. This direct approach forms the zonal harmonic or spherical wave analysis method.

Before the advent of large computers an approximation was developed to enable the series summation to be undertaken. This consists of forming a complex integral for the Hertz vector which is expressed as a sum of residues which, after suitable transformation, become the waveguide modes. The propagation is then described in terms of the propagating modes in the spherical waveguide formed by the earth as one wall and the ionosphere as the other.

A somewhat different approach is employed in the wave-hop technique. Here the propagation path is divided into three principal regions and solutions obtained which are not unlike those of geometrical optics. This method achieves high speed of computation and is applicable to frequencies well above the upper limit of the VLF band.

The variation of the phase and amplitude of a VLF wave as a function of distance from the transmitter has been calculated by means of each of the three analysis techniques for several earth ionosphere models and the results compared with each other at various radio frequencies.

## 1.    INTRODUCTION

Low and very low (LF, VLF) frequency radio waves are reflected from the lowest part of the ionosphere and extensive studies of their reflection processes have been carried out since the earliest days of radio. These investigations show that, apart from the sunrise and sunset periods, the propagation is character- ized by high stability both in phase and amplitude. Furthermore, little attenuation of the waves takes place at reflection and as a result they can propagate to very great distances via the ionosphere.

The great disadvantage of the VLF and LF bands is the limited bandwidth available and the high cost and low efficiency of the transmitting installations. Because of these factors the HF bands have been more extensively developed. In recent years there has been a renewed interest in the low frequency bands primarily due to their use in navigational aids. The inherent phase stability of the propagation is an essential feature of any world-wide navigation system. The large skin depth in the earth's surface for these waves has also been exploited recently for sub-surface communications, geological prospecting and mine rescue applications.

In order to determine the likely performance of a VLF/LF radio system the phase and amplitude must be determined as a function of distance from the transmitter for various ionospheric conditions and ground conductivities. Three principal analytical techniques are currently in use. The object of this paper is to describe these methods and to compare the results obtained using them.

## 2.    CALCULATION OF REFLECTION COEFFICIENTS

At low and especially at very low frequencies, the medium through which the wave propagates can vary appreciably in the space of one wavelength. Thus conventional ray optics used to describe the propagation of HF radio waves through the ionosphere no longer applies. Full wave solutions are required in which the wave fields are calculated at many points in the course of one wavelength. A number of full wave methods are currently available.

The differential equations governing the propagation of radio waves in the ionosphere are linear and homogeneous, thus the sum of any solution is itself a solution. In the usual methods of calculation the differential equations satisfying some field component of the wave are first formulated. Solutions are then obtained at great heights, well above the reflection levels, and these correspond to purely upgoing waves. Connection formulae are applied to obtain solutions down through the ionosphere. Below the ionosphere these are separated out into upgoing and downgoing waves. From these the reflection coefficients are calculated, which will depend on the polarization of the incident wave. In general, the incident and reflected waves do not have the same polarization and the reflection properties must be completely specified by the four parameters $_{\parallel}R_{\parallel}$, $_{\parallel}R_{\perp}$, $_{\perp}R_{\perp}$, $_{\perp}R_{\parallel}$.

Numerical methods for full wave solution of the wave equations have been extensively discussed in the literature. These methods differ in detail but to illustrate the procedure the Pitteway (1965) solution is outlined since this one has been extensively used by many groups of workers.

The equation of motion of a single electron in the wave field may be written as

$$\underline{P} = e_o \underline{\underline{M}} \underline{E} \tag{1}$$

where the susceptibility tensor $\underline{\underline{M}}$ is given by

$$\underline{\underline{M}} = -X \begin{bmatrix} U & jY_z & -jU_y \\ -jY_z & U & jY_x \\ jY_y & -jY_x & U \end{bmatrix}^{-1} \tag{2}$$

The conventional notation of the magneto-ionic theory is used throughout.

Following Pitteway (1965) the coordinate axes are defined by the earth's field, and are chosen so that $Y_x$ vanishes. Y is assumed constant at all heights.

The four wave field equations can be written in matrix form

$$\underline{e}' = jk\underline{\underline{T}}\underline{e} \tag{3}$$

where e is the column vector

$$\underline{e} = \begin{vmatrix} E_x \\ -E_y \\ H_x \\ H_y \end{vmatrix}$$

and $\underline{\underline{T}}$ is a 4 x 4 matrix.

$$\underline{\underline{T}} = \begin{bmatrix} -jlB_1 & lB_2 & lmB_3 & 1 - l^2B_3 \\ jmB_1 & -mB_2 & 1 - m^2B_3 & lmB_3 \\ -lm + jB_4 & 1 - l^2 - B_5 + XY_y^2/\alpha & -mB_2 & lB_2 \\ 1 - m^2 - B_5 & -lm - jB_4 & -jmB_1 & jlB_1 \end{bmatrix}$$

where

$$B_1 = XUY_y/\alpha$$
$$B_2 = XY_yY_z/\alpha$$
$$B_3 = U(U^2 - Y^2)/\alpha = 1 + X(U^2 - Y_z^2)/\alpha$$
$$B_4 = XY_z(U - X)/\alpha$$
$$B_5 = XU(U - X)/\alpha \qquad \alpha = U(U^2 - Y^2) - X(U^2 - Y_z^2)$$

The incident wave normal has direction cosines l, m, n and the functional dependence comes through the variation of X and U with height.

The four linear differential equations (3) are integrated numerically. The computer forms derivatives of (3) at the starting values (at great heights) and uses these to calculate the wave fields at a slightly lower height. Fourth-degree polynomials are used to fit the solutions of the differential equations by calculating four separate sets of derivatives at each height. The process is then repeated towards the bottom of the ionosphere until free space is reached. Here the solution is separated into upgoing and downgoing components and the reflection and conversion coefficients determined.

Care must be taken during the numerical integration to ensure that the two solutions remain independent. Suitable constraints are applied to the solutions at each integration step so that the second solution is not swamped by the dominant solution. Full details of these techniques are given by Pitteway (1965).

A somewhat different approach to full-wave calculations has been proposed by Altman (1970) and Altman and Cory (1962). Here the Pitteway method is modified to give 'full-wave' ordinary and extraordinary transfer coefficients for slabs of the ionosphere of various thickness. The ratio of the transmitted or reflected energy flux to the incident value is then calculated for each slab. This full-wave slab approach proved time-consuming since each slab requires a separate numerical integration and little information can be stored for subsequent calculations. To overcome this drawback a generalized thin-film optical analysis was developed by Altman and Cory(1967, 1970). The ionosphere is divided into a large number thin layers and 2 x 2 transfer matrices calculated at each layer interface. Multiple reflection within each elementary layer generates a geometric series of matrices which when summed, yield overall 2 x 2 transfer coefficient matrices of the layer. An iterative procedure repeats the process layer after layer so that the thickness of the resulting slab increases progressively downwards giving the overall reflection and transmission coefficient matrix of the total ionospheric region in terms of the characteristic magneto-ionic modes.

Various other types of numerical full-wave analysis have been developed, e.g. Inoue and Horowitz (1966) and Johler and Harper (1962). They all enable the complex reflection and conversion coefficients to be

determined for any given height distribution of electron density and collision frequency. Parameters such as the wave frequency, path azimuth, angle of incidence, and geomagnetic field intensity are easily varied. Thus the reflection parameters of VLF and LF waves can be calculated for conditions representative of any time of day, season and geographical location. Clearly this technique provides a powerful tool in the design and operation of any VLF/LF radio wave system.

## 3.    TERRESTRIAL PROPAGATION

In the theoretical treatment of long distance terrestrial propagation of VLF/LF waves it is customary to divide the paths of the waves into regions inside and outside the ionosphere and to treat these separately. Thus the reflection coefficient matrix $\underline{R}$ of the form,

$$\underline{\underline{R}} = \begin{bmatrix} {}_{\parallel}R_{\parallel} & {}_{\parallel}R_{\perp} \\ {}_{\perp}R_{\parallel} & {}_{\perp}R_{\perp} \end{bmatrix} \tag{4}$$

is calculated for a realistic model ionosphere (i.e. one which is anisotropic and vertically inhomogeneous) using one of the full-wave techniques derived in the previous section. The model can be analytical or based on experimentally measured electron density and collision frequency profiles. Propagation below the ionosphere to great distances from the transmitter is then usually considered in terms of the propagating modes in the spherical waveguide formed by the earth as one wall and the ionosphere as the other.

The mathematical treatment of the propagation in such a waveguide, where the ionosphere is represented by a concentric isotropic electron-ion plasma, was developed many years ago (Watson, 1919). Solutions are expressed in terms of a series of zonal harmonics, which will be derived briefly here.

Consider a spherical coordinate system for a model terrestrial sphere of radius $r = a$ surrounded by a concentric plasma extending from $r = c$ to $r = \infty$ (Fig.1). Here the propagation media are characterized by their electric constants, expressed in terms of the wave number k. Hence, neglecting the earth's magnetic field,

For $a \le r \le c$   $\quad k = k_1 = \dfrac{\omega}{c} \eta_1$ $\tag{5}$

where    $\eta_1$   refractive index of region 1

$\omega$   $= 2\pi f$ , f = radio frequency.

For $0 < r < a$   $\quad k = k_2 = \dfrac{\omega}{c} \sqrt{\varepsilon_2 - \dfrac{i\sigma\mu_0 c^2}{\omega}}$ $\tag{6}$

where    $\varepsilon_2$   = relative dielectric constant

$\sigma$   = ground conductivity

$\mu_0$   $= 4\pi \times 10^{-7}$ Hm$^{-1}$

For $c < r$   $\quad k = k_3 = \dfrac{\omega}{c} \sqrt{1 - \dfrac{i\omega_N^2}{\omega(\nu + i\omega)}}$ $\tag{7}$

where    $\omega_N$   = plasma frequency = $\dfrac{Ne^2}{\varepsilon_0 m}$

N   = number density of electrons

e   = electron charge

m   = electron mass

$\nu$   = electron collision frequency.

The electrodynamic fields $\underline{E}$ and $\underline{H}$ are derived from Maxwell's equations,

$$\underline{\nabla} \times \underline{E} + \mu_0 \frac{\partial}{\partial t} \underline{H} = 0 \tag{8}$$

$$\underline{\nabla} \times \underline{H} - \varepsilon_0 \frac{\partial}{\partial t} \underline{E} = \underline{J} \tag{9}$$

where $\underline{J}$ is the conduction or convection current. The fields are treated as continuous time harmonic waves, e.g.

$$\underline{E} = |\underline{E}| \exp(j\omega t - ikD) \tag{10}$$

where D is the distance from the source of frequency $f = \omega/2\pi$.

The six components of the fields (namely $E_r$, $E_\theta$, $E_\phi$, $H_r$, $H_\theta$, $H_\phi$) may be calculated by a differentiation process from a single vector $\underline{\pi}$, the Hertz vector, provided the scalar $\pi$ satisfies the wave equation,

$$(\nabla^2 + k^2)\pi = 0 \tag{11}$$

In particular the field component $E_r$ is given as (Hertz, 1889, Debye, 1909),

$$E_r = \left[\exp(i\omega t)\left[\frac{-1}{rb\sin\theta}\right]\frac{\partial}{\partial\theta}\left[\sin\theta\,\frac{\partial\pi^e}{\partial\theta}\right]\right] \qquad b = a + (\text{altitude of transmitter}) \qquad (12)$$

where $\pi^e$ refers to vertical electric source dipole, provided the problem can be reduced to one of two dimensions,

$$\frac{\partial\pi}{\partial\varphi} = 0 \qquad (13)$$

The model for the source or transmitter is specified by the primary Hertz vector (Johler & Berry 1962),

$$\pi_o^e = I_o l\left[\frac{\mu_o c}{4\pi}\right]\exp\frac{\left[e\omega t - ik_1 D\right]}{-ikD} \qquad (14)$$

where the source dipole current moment $I_o l = \frac{4\pi}{\mu_o c}$ .

The solution of the wave equation (11) given the condition (13) depends upon the separation of the variables $\theta$ and $r$,

$$\pi = f(r)\,F(\theta) \qquad (15)$$

It can be shown (Stratton, 1941) that the solutions may be written as a series of zonal harmonics of the form,

$$\left[\beta_n\,\psi_n(kr) + \gamma_n\,\zeta_n^{(2)}(kr)\right]\,P_n(\cos\theta) \qquad (16)$$

where $\beta_n$ and $\gamma_n$ are constants and

$$\psi_n(z) = \frac{\pi z}{2}\,J_{n+\frac{1}{2}}(z) \qquad (17)$$

$$\zeta_n^{(2)}(z) = \frac{\pi z}{2}\,H_{n+\frac{1}{2}}^{(2)}(z) \qquad (18)$$

$J_{n+\frac{1}{2}}(z)$ and $H_{n+\frac{1}{2}}^{(2)}(z)$ are Bessel and Hankel functions of order $(n+\frac{1}{2})$ and argument $z$ (Watson, 1958).

Forming a solution of the type given by (16) and applying boundary conditions to determine the constants $\beta_n$ and $\gamma_n$ (Johler & Berry, 1962; Johler & Berry, 1964) the following rigorous solution for the special case of $a = b = r$ may be obtained,

$$E_r = \frac{I_o l}{k_1^2 a^4}\,\frac{\mu_o c}{4\pi}\,\sum_{n=0}^{\infty} n(n+1)(2n+1)P_n(\cos\theta)\zeta^{(2)}(k_1 a)\psi(k_1 a)$$

$$X\left[1 + R_n^{(s)}\cdot\frac{-\zeta^{(2)}(k_1 a)}{\psi(k_1 a)}\right]\left[1 + T_n^{(s)}\cdot\frac{-\psi(k_1 a)}{\zeta^{(2)}(k_1 a)}\right]\left[1 - R_n^{(s)}\,T_n^{(s)}\right] \qquad (19)$$

where $R_n^{(s)}$ and $T_n^{(s)}$ are reflection coefficients containing focussing or convergence-divergence factors,

$$R_n^{(s)} = \frac{-\zeta^{(1)}(k_1 a)}{\zeta^{(2)}(k_1 a)}\,R_n \qquad (20)$$

$$T_n^{(s)} = \frac{-\zeta^{(2)}(k_1 c)}{\zeta^{(1)}(k_1 c)}\,T_n \qquad (21)$$

$R_n$ and $T_n$ are non-spherical reflection coefficients and are defined in terms of the functions (17) and (18) by Johler, 1964 .

Equation (19) has been derived for an isotropic plasma and attention is now turned to the generalization of this solution to the case of an inhomogeneous anisotropic ionosphere. The presence of the earth's magnetic field allows transverse electric (TE)in addition to transverse magnetic (TM) propagation notwithstanding the pure TM source dipole. In the anisotropic case (Johler & Harper, 1962; Johler, 1962) the reflection coefficient R of equation (19) is replaced by $R_e$ and $R_m$ , the vertical electric and magnetic reflection coefficients. The coefficient T is also replaced by a matrix whose elements are $T_{ee}$, $T_{me}$, $T_{em}$ and $T_{mm}$. These terms may in fact be identified with the reflection coefficients $\|R\|$ , $\perp R\|$ , $\|R_\perp$ and $\perp R_\perp$ of equation (4). Equation (19) then becomes,

$$E_r = \frac{I_o l}{k_1^2 a^4}\,\frac{\mu_o c}{8\pi}\,\sum_{n=0}^{\infty} n(n+1)(2n+1)P_n(\cos\theta)\zeta^{(2)}(k_1 a)\zeta^{(1)}(k_1 a)(1+R_{e,n})$$

$$X\,\frac{|I + \rho_n\,R_{e,n}\,T_n|}{|I - \rho_n\,R_{e,n}\,T_n|} \qquad (22)$$

$$\text{where} \quad I = \begin{bmatrix} 1 & 0 \\ 0 & 1 \end{bmatrix} \tag{23}$$

$$R_e = \begin{bmatrix} R_e & 0 \\ 0 & -1 \end{bmatrix} \tag{24}$$

$$\rho = \frac{\zeta^{(1)}(k_1 a)\zeta^{(2)}(k_1 c)}{\zeta^{(2)}(k_1 a)\zeta^{(1)}(k_1 c)} \cdot \begin{bmatrix} 1 & 0 \\ 0 & -R_m \end{bmatrix} \tag{25}$$

$$T = \begin{bmatrix} T_{ee} & T_{em} \\ T_{me} & T_{mm} \end{bmatrix} \tag{26}$$

## WAVEGUIDE MODE SOLUTIONS

The series (22) is slowly convergent, each mode n being a solution of Maxwell's equations, as is the mode sum. Watson (1918,1919) proposed a representation of zonal harmonics series as a contour integral essentially to aid computation. By transforming the contour, Watson was then able to express the integral approximately as a sum of residues which converges rapidly. By carrying out such a transformation the following solution may be obtained (Wait, 1962),

$$E_r \sim K \sum_{s=1}^{\infty} \Lambda_s \exp(-i \sin\theta_n \frac{d}{a}) \tag{27}$$

where K is a constant depending on transmitter power and other parameters, a is the earth's radius and d is the great circle distance from the transmitter to the receiver. $\Lambda_s$ is known as the excitation factor of mode s and is essentially a measure of the magnitude of this mode at launch. $\theta_n$ is the characteristic angle (complex) of the s-th mode.

The solution (27) is the basic waveguide mode solution and has been found especially useful at VLF. At these frequencies only two modes are usually required to give a good approximation for $E_r$. However at LF as many as ten modes may be needed, and difficulties are encountered because the modes all lie close together. It then becomes difficult to keep track of the various modes. Degenerate solutions are also possible and again it becomes difficult to distinguish between two modes (Budden & Eve, 1975).

Both the waveguide mode technique, and the wavehop method(described below) are well developed for the case of a homogeneous earth-ionosphere duct. Variations in ground or ionospheric conductivities complicate the analysis considerably. Ground discontinuities involve mode-conversions at the discontinuity and as a consequence propagation must be considered in two dissimilar waveguides. The ionosphere, however, changes much less abruptly, and is more difficult to handle. For realistic modelling of the upper boundary the problem becomes exceedingly cumbersome to solve.

## SPERICAL WAVE-GEOMETRIC SERIES SOLUTION

A rather different approach to the solution of the wave equation has been proposed by Johler, 1964 and 1966. This utilizes the expansion of the determinant ratio of equation (22) in terms of a geometric series,

$$\frac{|I + \rho_n T_n|}{|I - \rho_n R_{e,n} T_n|} = |I + (I + R_{e,n}) \sum_{j=1}^{\infty} (\rho_n R_{e,n} T_n)^{j-1} \rho_n T_n| \tag{28}$$

This leads to the spherical wave-geometric series solution,

$$E_r = E_{r,o} + \sum_{j=1}^{\infty} E_{r,j} \tag{29}$$

where j = 0 is the ground wave and j = 1,2,3... are the ionospheric waves.

The geometric series representation permits the introduction of local reflection coefficients as depicted in figure 2. It should be noted here that these series representations are wave solutions and not geometric-optical rays. In the ray limit (Johler, 1964) the geometric-optical rays are an approximate solution, valid only at short distances. A study of the angles of incidence of the j series waves of equation (29) leads to the interesting conclusion that local reflection regions at the ionosphere can be considered. Thus, as indicated in figure 2 the wave j = 1 has a reflection region centered about the path mid-point and denoted (1,1). A reflection coefficient matrix T(1,1) is then ascribed to this region. In this manner an inhomogeneous earth-ionosphere duct may be modelled. This approach to low frequency radio wave propagation has only become practical since the advent of fast digital computers. For example at a radio frequency of 20 kHz a summation over ten j-terms may be required, however each j-series term requires a summation of approximately 28,000 terms of the n-series denoted in equations (22) and(28). Such a calculation was impossible before the advent of digital machines.

## WAVE-HOP SOLUTION

Berry (1964) and Berry and Chrisman (1965) have developed another computation technique which follows the spherical wave-geometric series approach, equation (29). Application of the first part of Watson's technique, i.e. expressing the series as a contour integral results in an equation for the ionospheric waves, gives

$$E_{r,j} = \frac{i}{k_1^2 a^4} \frac{\mu_0 c}{8\pi} \int_0^\infty \frac{F(\nu - \frac{1}{2})}{\cos \nu\pi} \zeta_{\nu-\frac{1}{2}}^{(2)}(k_1 a) \zeta_{\nu-\frac{1}{2}}^{(1)}(k_1 a)(1 + R_e)^2 C_j \, d\nu \qquad (30)$$

where 
$$R_e = R_e(\nu - \tfrac{1}{2})$$
$$C_j = C_j(\nu - \tfrac{1}{2})$$
$$F(\nu - \tfrac{1}{2}) = 2\nu(\nu^2 - \tfrac{1}{4}) P_{\nu - \frac{1}{2}}(-\cos\theta)$$

and $(\rho_n T_n R_{e,n})^{j-1} \rho_n T_n = p^j \begin{bmatrix} c_j & x_j \\ y_j & z_j \end{bmatrix}$

This equation forms the solution known as the Wave-Hop approach and has been found especially applicable at LF. In order to numerically solve the equation it is convenient to divide the propagation path into several regions and apply various approximate methods as follows, (see figure 3),

(i) Close to the transmitter – geometrical optics

(ii) Beyond region (i) to a point near the caustic – saddle point approximation

(iii) Near the caustic – numerical integration

(iv) Beyond the caustic – residue series.

The wave hop techniques advantages result firstly from the fact that the series for $E_r$ is highly convergent from VLF right through LF and into the MF radio frequencies. Secondly, no complicated iterative schemes are required to solve modal conditions which apply in the waveguide mode approach. However, in common with the mode theory this method has not been formulated in a way that lends itself to the modelling of discontinuities within the earth-ionosphere duct.

## 4.    NUMERICAL COMPARISONS OF THEORETICAL TECHNIQUES

A series of computations have been carried out assuming a vertical electric source current moment,

$$I_0 l = \frac{4\pi}{\mu_0 c}$$

on the surface of the earth. A vertically inhomogeneous, anisotropic concentric plasma has been modelled from published D-region electron density and collision-frequency height profiles. In all calculations the full-wave method of Pitteway (1965) has been employed to obtain ionospheric reflection coefficients as a function of angle of incidence.

Results of the three analytical techniques described in the previous sections are compared in figures 4 and 5 for radio frequencies of 16 kHz and 20 kHz respectively. The electron density profile is that due to Deeks (1966) and is applicable to noon, summer, sunspot minimum conditions. A standard mono-energetic CIRA (1965) collision frequency profile has been adopted. The magnetic field parameters are those appropriate to northward propagation at U.K. latitudes, while the ground conductivity is assumed to be that of sea water. At 16 kHz (figure 4) all three analyses indicate a large minima in vertical electric field strength at a range of approximately 400 km from the transmitter. This minimum is the result of strong destructive interference between the ground wave and first hop (j = 1) propagation modes of the Spherical Wave theory. Beyond this distance undulations in field strength as a function of distance result from further interference between higher order terms of the geometric series. Differences in the field strengths determined by the three techniques are less than 3 dB except in the region of the first deep minimum. Here the Wave Hop method predicts a deeper fade, the signal level being approximately $4\frac{1}{2}$ dB smaller than that calculated by the other two theories.

The situation at 20 kHz (figure 5) differs from the 16 kHz results in that the first deep minimum is less pronounced and an almost equally deep fade is apparent at a distance of about 1600 km. Amplitude differences between the three analytical techniques at this frequency are as large as 3 dB at some ranges from the transmitter.

A further comparison between the Spherical Wave and Waveguide Mode formulations is presented in figure 6. Calculations carried out by Synder and Pappert(1969) with exponential Wait and Spies (1964) type profiles have been made in a parametric study of VLF modes below various anisotropic ionospheres. A Waveguide Mode result by Synder and Pappert(1969) for southwards propagation across sea at a geomagnetic dip angle of $60^\circ$ is reproduced in figure 6 (broken line). The radio frequency is 19.8 kHz and the exponential D-region electron density profile is parameterized by $\beta = 0.5$ km$^{-1}$, h$'$ = 90 km (Wait and Spies, 1964). A Spherical Wave calculation for the same ionospheric model and path parameters has been carried out and the results are indicated by the solid line of the figure. In general, the agreement is good over distances as great as 18000km (better than 4 dB except in the region of the first minima). However, the depth of the amplitude fades appears to be greater for the Waveguide Mode technique, and beyond about 6000 km the Spherical Wave method predicts higher amplitude levels.

A comparison of the Spherical Wave and Wave Hop formulations at several frequencies between 10 and 60 kHz is presented in figures 7, 8 and 9. The ionospheric profiles adopted are the same as those of figures 4 and 5, but propagation is now towards the east. Figures 7 and 8 illustrate the nature of the changes in vertical electric field strength with distance at 10, 20, 30, 40, 50 and 60 kHz. At ranges greater than 1000 km the decrease in field strength at 10 kHz is almost exponential, however, at 30 and 60 kHz deep fades are present. As the radio frequency is increased differences between the two theoretical approaches

become more apparent. In general, amplitude minima occur slightly further away from the transmitter with the Wave Hop method compared with those of the Spherical Wave theory. The depth of minima are also different, particularly at the higher frequencies (e.g. 60 kHz). It should be noted that for the frequencies of the VLF Omega navigation system (10.2 - 13.6 kHz) the agreement between the two techniques is excellent. The reason for the discrepancies at higher VLF and LF frequencies is not at present understood.

Illustrated in figure 9 are the variations in phase of the total electric field as a function of distance from the transmitter, at 10, 20 and 30 kHz. As expected, rapid phase variations are well correlated with the amplitude fades indicated in figure 7.

Figure 10 indicates changes in vertical electric field strength for two different ground conductivities; sea ($\sigma$ = 5 mhos/m) and land ($\sigma$ = .01 mhos/m). The results obtained by the three analytical techniques for a frequency of 13.6 kHz are reproduced in the figure. The results are in good agreement for both conductivities, the largest discrepancies occurring in the region of the first deep fade at about 400 km.

## 5. CONCLUSIONS

The three commonly used techniques for calculating the variation of phase and amplitude of VLF waves as a function of distance from the transmitter have been compared. Various ionospheric models and wave frequencies have been considered and propagation over both land and sea-water examined. In general, consistent results are obtained and the differences are considerably smaller than those errors likely to occur from uncertainties in the validity of the model adopted for any given ionospheric conditions. For the higher VLF and LF frequencies the Wave Hop method is to be preferred since it requires the least computing time. However, throughout the VLF range the Spherical Wave technique has considerable potential in its ability to model waveguides of varying height.

### REFERENCES

Altman, C and Cory, H. (1967). Applications of thin-film optics to very low frequency radio propagation in the ionosphere. Conf. on M.F., L.F. and V.L.F. Radio Propagation, IEE Conf. Publ. 36, pp 98-105, London.

Altman, C. and Cory, H. (1970). Multiple reflection processes in the D and E regions at low and very low frequencies. J. Atmos. Terr. Phys., 32, pp 1439-55.

Altman, C. and Fijalkow, E. (1970). Coupling processes in the D and E regions at low and very low frequencies, II. J. Atmos. Terr. Phys., 32, pp 1475-88.

Berry, L.A. (1964). Wave hop theory of long distance propagation of LF radio waves. Radio Sci. 68D, No 12, pp 1275-1272.

Berry, L.A. and Chrisman, M.E. (1965). The path integrals of LF/VLF wave hop theory. Radio Sci., 64D, pp 1469-1480.

Budden, K.G. and Eve, M. (1975). Degenerate modes in the earth-ionosphere waveguide. Proc. Roy. Soc. (London) A342, pp 175-190.

Debye, P. (1909). Der Lichtdruck auf Kugeln von beliebigem Material. Ann. Physik (Leipzig) 30, pp 57-136.

Hertz, H. (1889). Die Kräfte Electrischer Schwingungen behandelt nach der Maxwell' schen Theorie. Ann. Physik und Chemie, Neue Folge 30, 1, Leipzig.

Inoue, Y. and Horowitz, S. (1966). Numerical solution of full-wave equation with mode coupling. Radio Sci., 1, pp 957-70.

Johler, J.R. (1962). Propagation of the low-frequency radio signal. Proc. IRE, 50, pp 404-427.

Johler, J.R. (1964). Concerning limitations and further corrections to geometric-optical theory for LF, VLF propagation between the ionosphere and the ground. Radio Sci., 68D, pp 67-78.

Johler, J.R. (1966). Zonal harmonics in low frequency terrestrial radio wave propagation. NBS Tech. Note, TN335.

Johler, J.R. and Berry, L.A. (1962). Propagation of terrestrial radio waves of long wavelength - theory of zonal harmonics with improved summation techniques. Radio Sci., 66D, pp 737-73.

Johler, J.R. and Berry, L.A. (1964). A complete mode sum for LF, VLF, ELF terrestrial radio wave fields. NBS Monograph 78.

Johler, J.R. and Harper, J.D. (1962). Reflection and transmission of radio waves at a continuously stratified plasma with arbitrary magnetic induction. Radio Sci. 66D, pp 81-99.

Pitteway, M.L.V. (1965). The numerical calculation of wave fields, reflection coefficients and polarizations for long radio waves in the lower ionosphere. I. Phil. Trans. Roy. Soc., A275, pp 219-41.

Stratton, J.A. (1941). Electromagnetic Theory. McGraw-Hill F    Co., Inc., New York.

Synder, F.P. and Pappert R.A. (1969). A parametric study of VLF modes below anisotropic ionospheres. Radio Sci., 4, pp 213-226.

Wait, J.R. (1962). Electromagnetic waves in stratified media. Pergamon Press.

Wait, J.R. and Spies, K.P. (1964). Characteristics of the earth-ionosphere waveguide for VLF radio waves. NBS Tech. Note 300.

Watson, G.N. (1918). The diffraction of electric waves by the earth. Proc. Roy. Soc. (London) 95, pp 83-99.

Watson, G.N. (1919). The transmission of electric waves round the earth. Proc. Roy. Soc. (London) 95, pp 546-563.

Watson, G.N. (1958). Bessel functions, 2nd edition. CUP.

CIRA (1965). Cospar International Reference Atmosphere 1965. North-Holland Publishing Company.
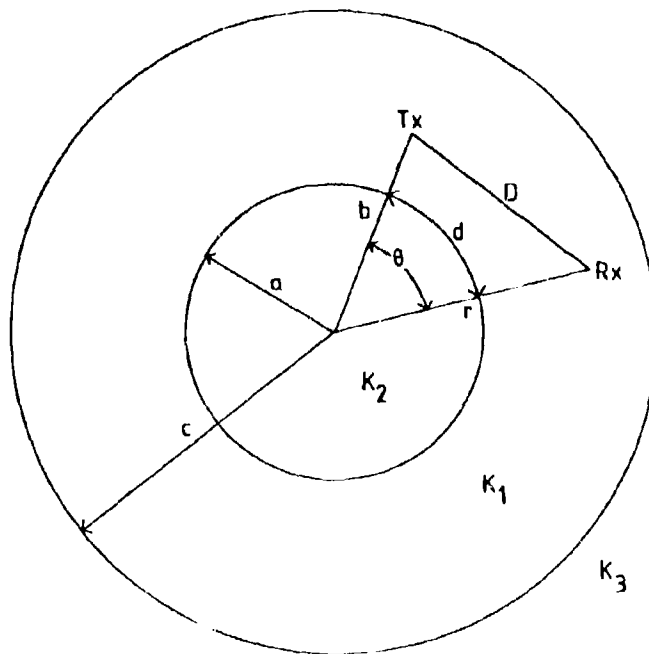


Fig.1 Earth-ionosphere model for a terrestrial sphere of radius $r = a$, surrounded by a concentric plasma from $r = c$ to $r = \infty$
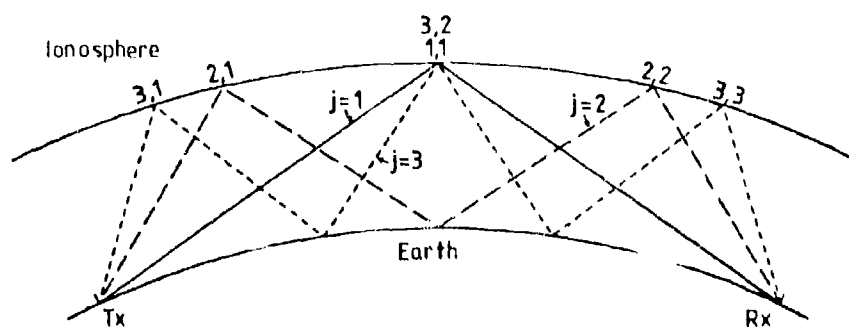
Fig.2   Schematic representation of ionospheric waves, j = 1, 2, 3 . . . using optical rays, illustrating local reflection regions (j, k), where j = order of term of the geometric series and k = order of the reflection region
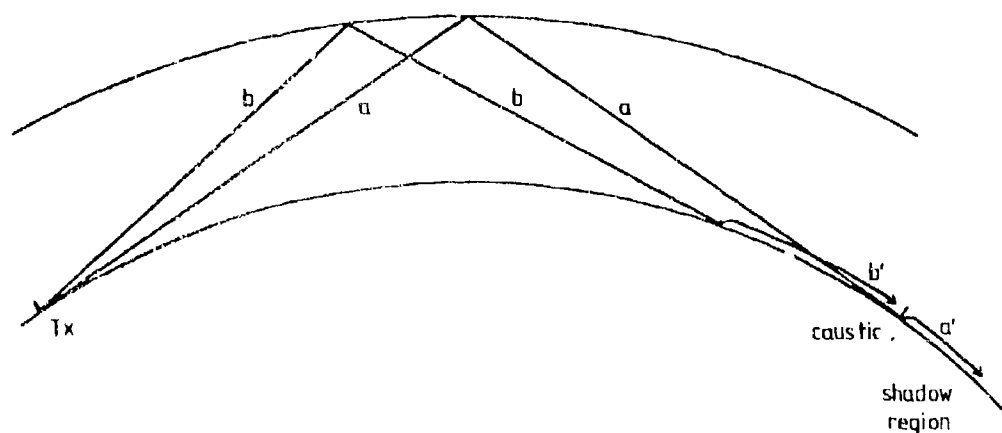


Fig.3   Physical interpretation of wave hop paths in the region of the caustic. Downcoming waves (a and b) excite ground waves (a′ and b′) which propagate into the shadow region
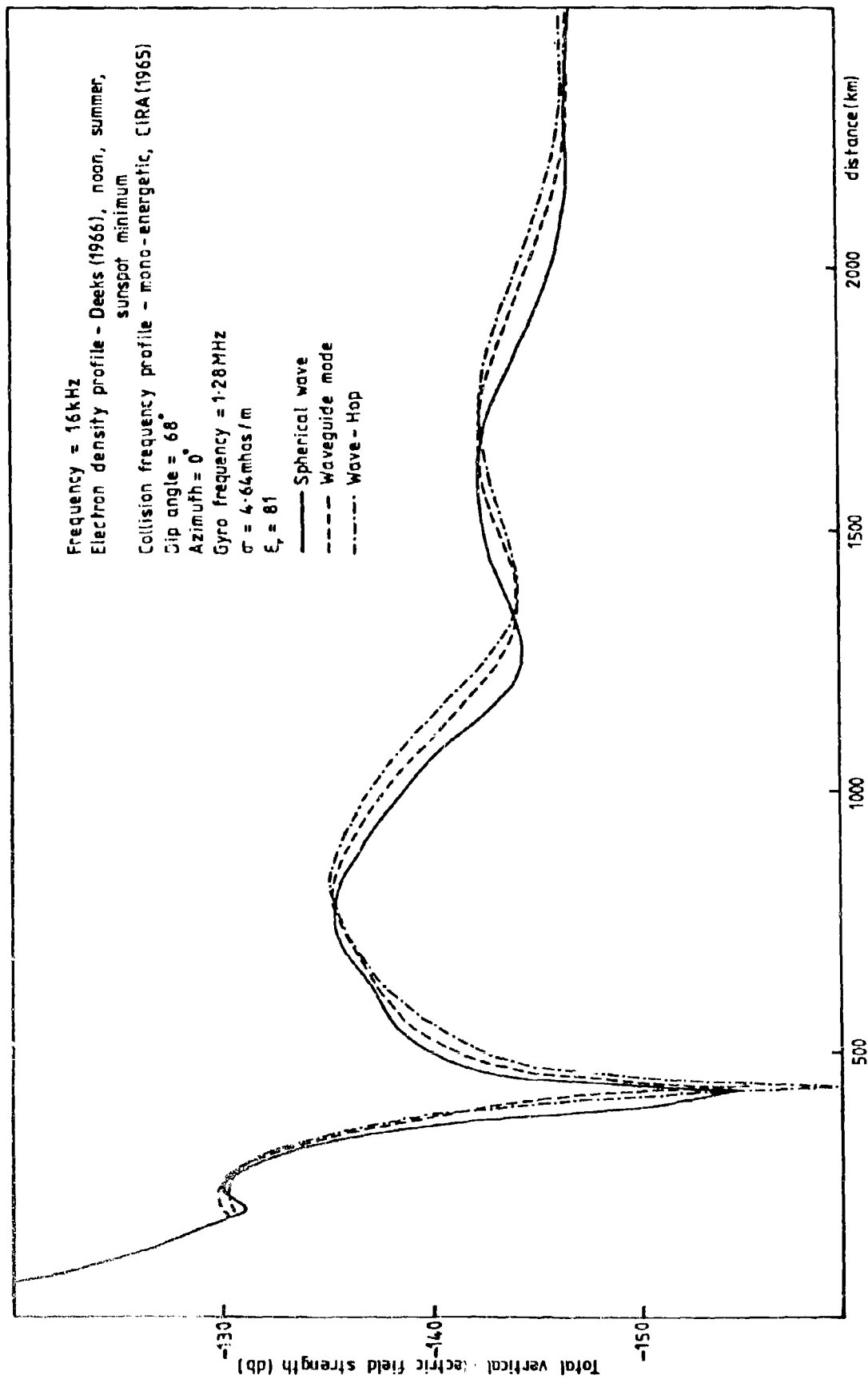
Fig.4  Comparison of spherical wave, waveguide mode, and wave-hop techniques at 16 kHz
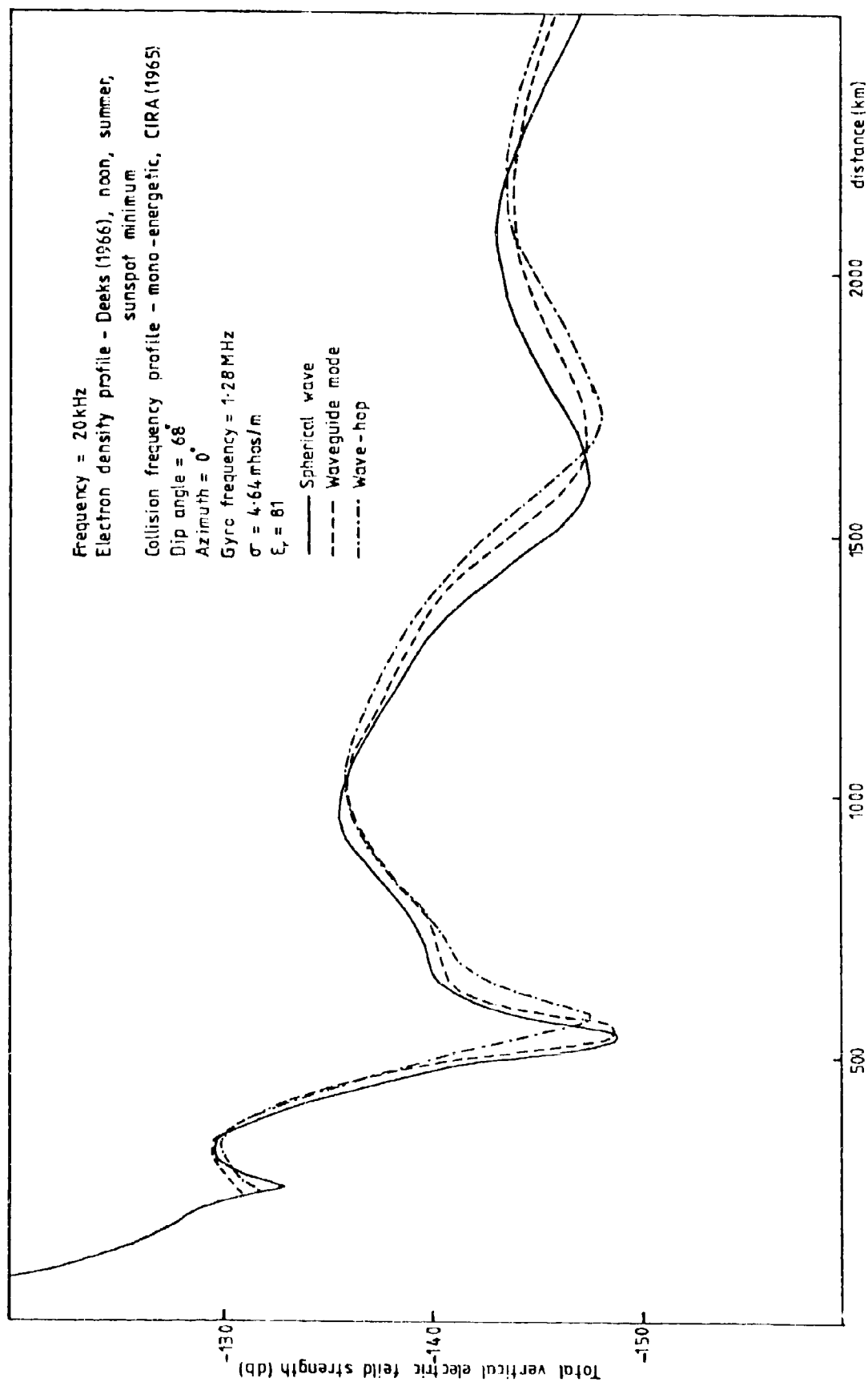
Fig.5 Comparison of spherical wave. waveguide mode. and wave-hop techniques at 20 kHz
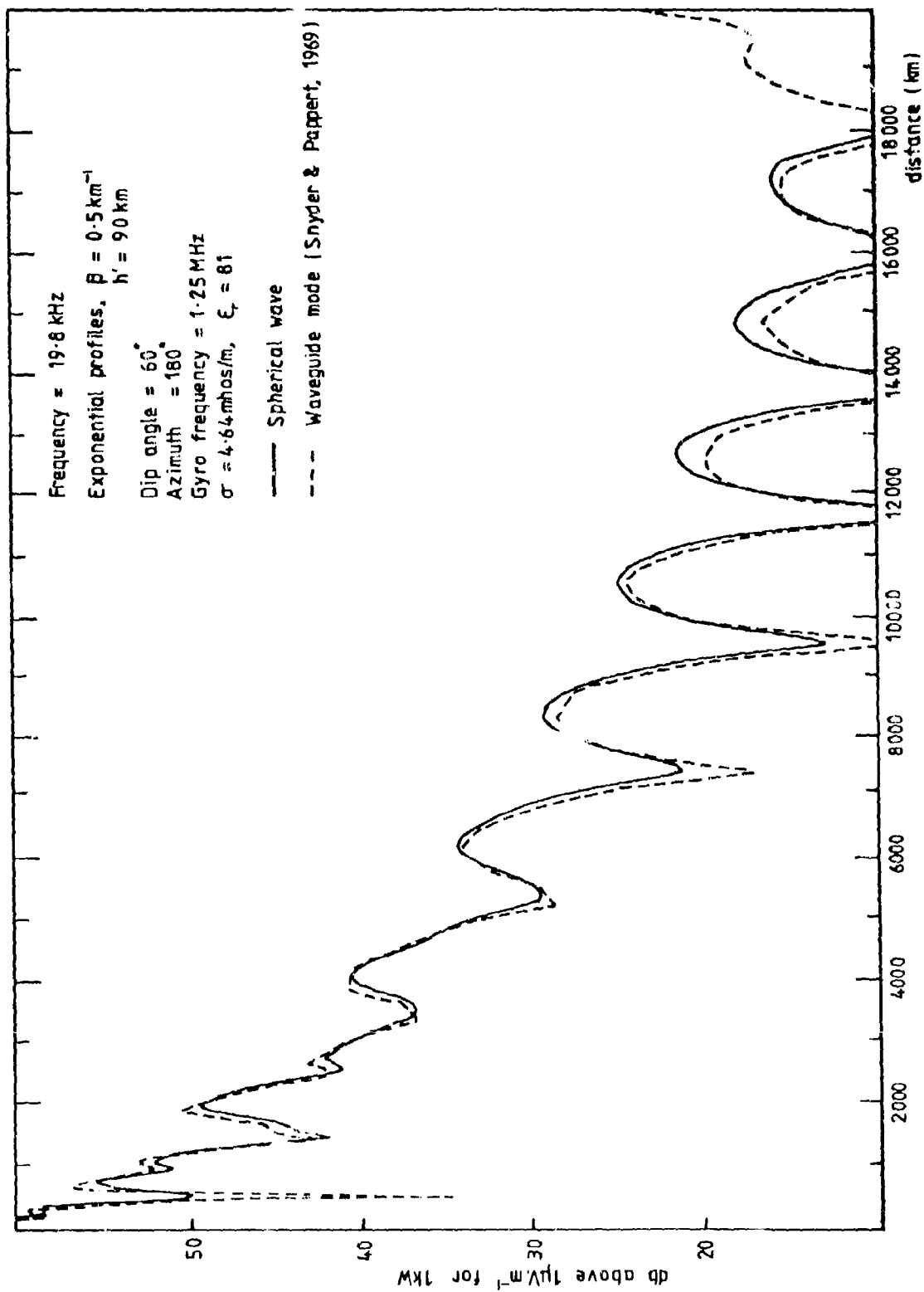
Fig.6  Comparison of spherical wave and waveguide mode (Snyder & Pappert, 1969) techniques
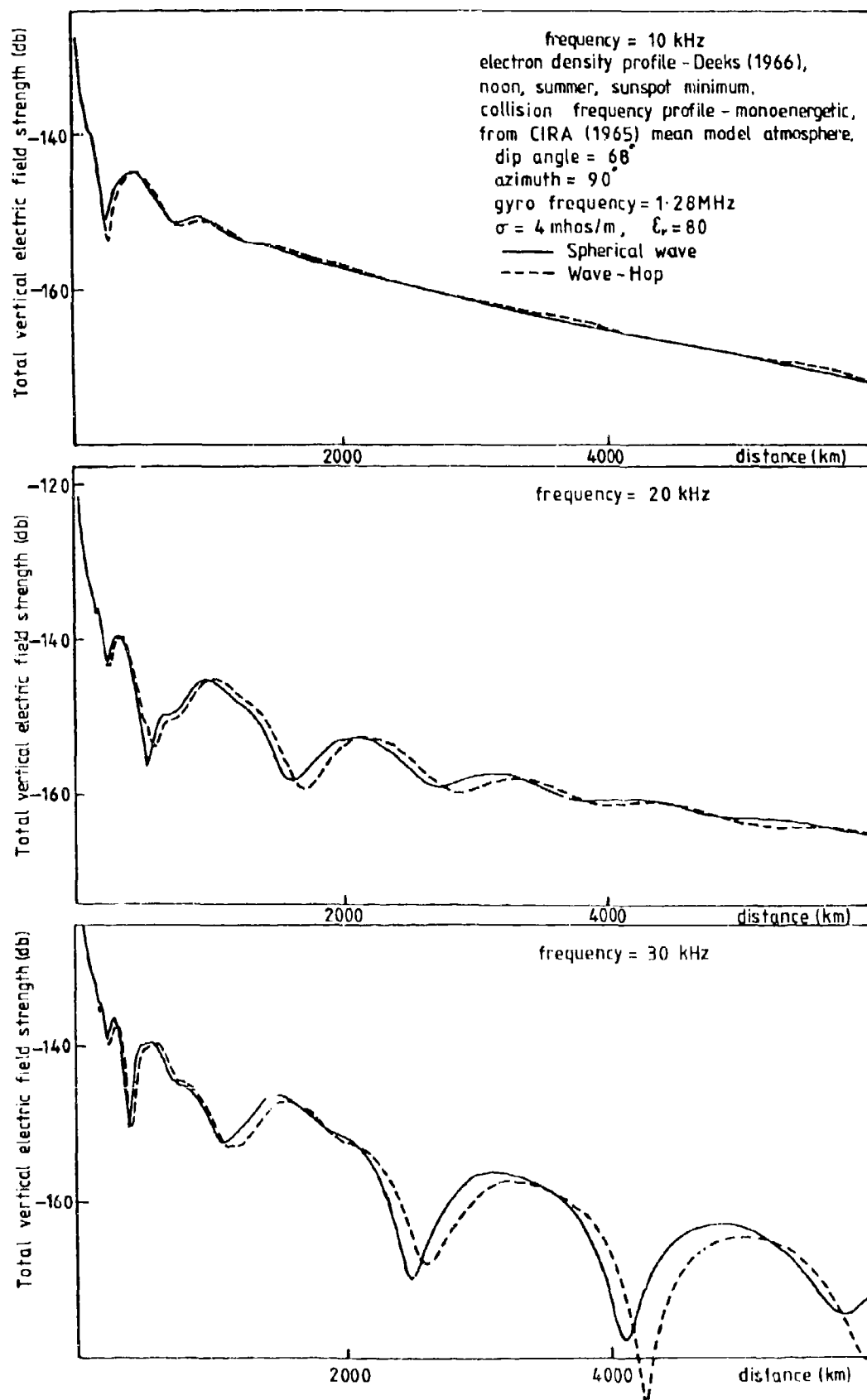
Fig.7 Comparisons of the spherical wave and wave-hop techniques at 10, 20 and 30 kHz
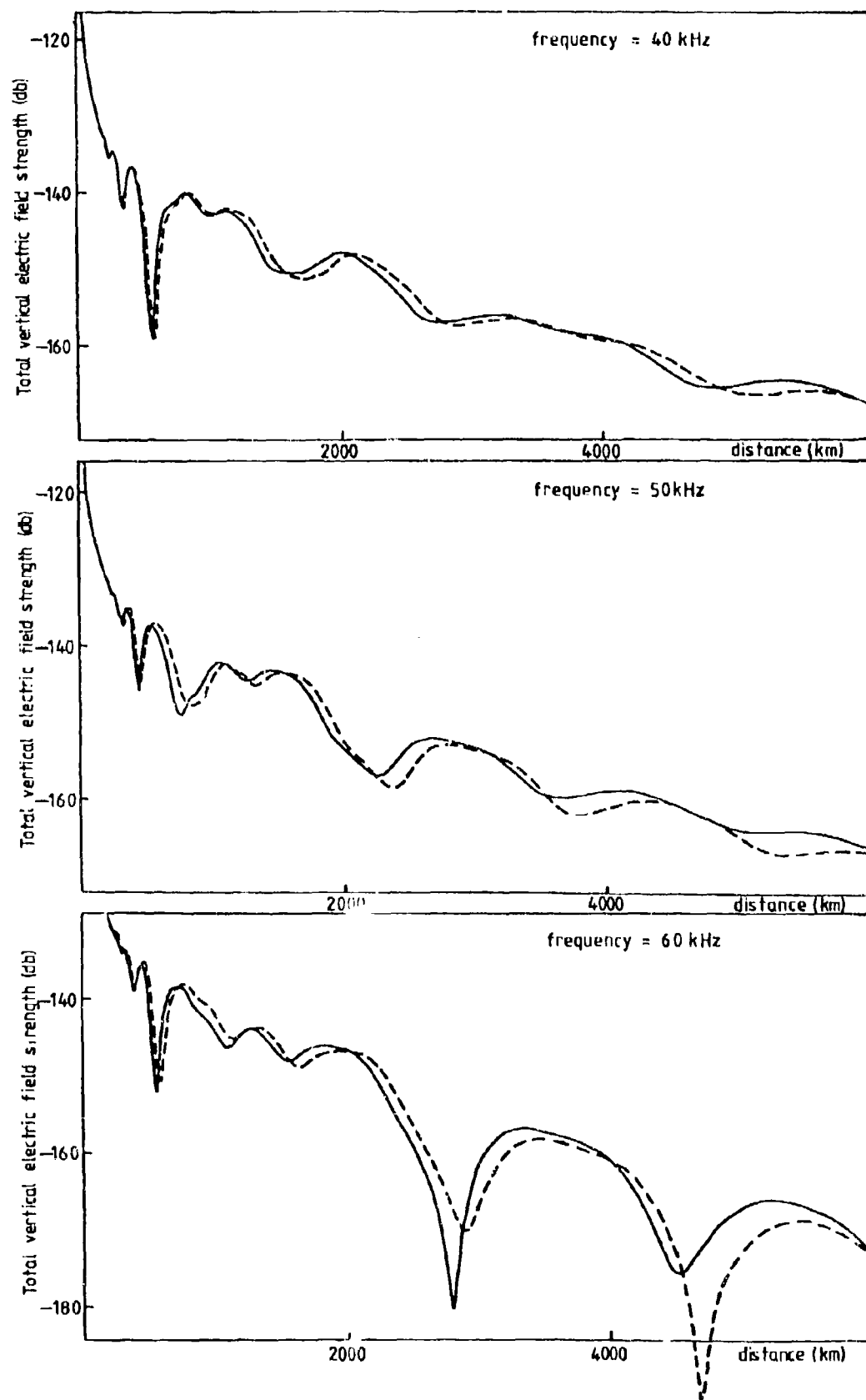
Fig.8 Comparisons of the spherical wave and wave-hop techniques at 40, 50 and 60 kHz
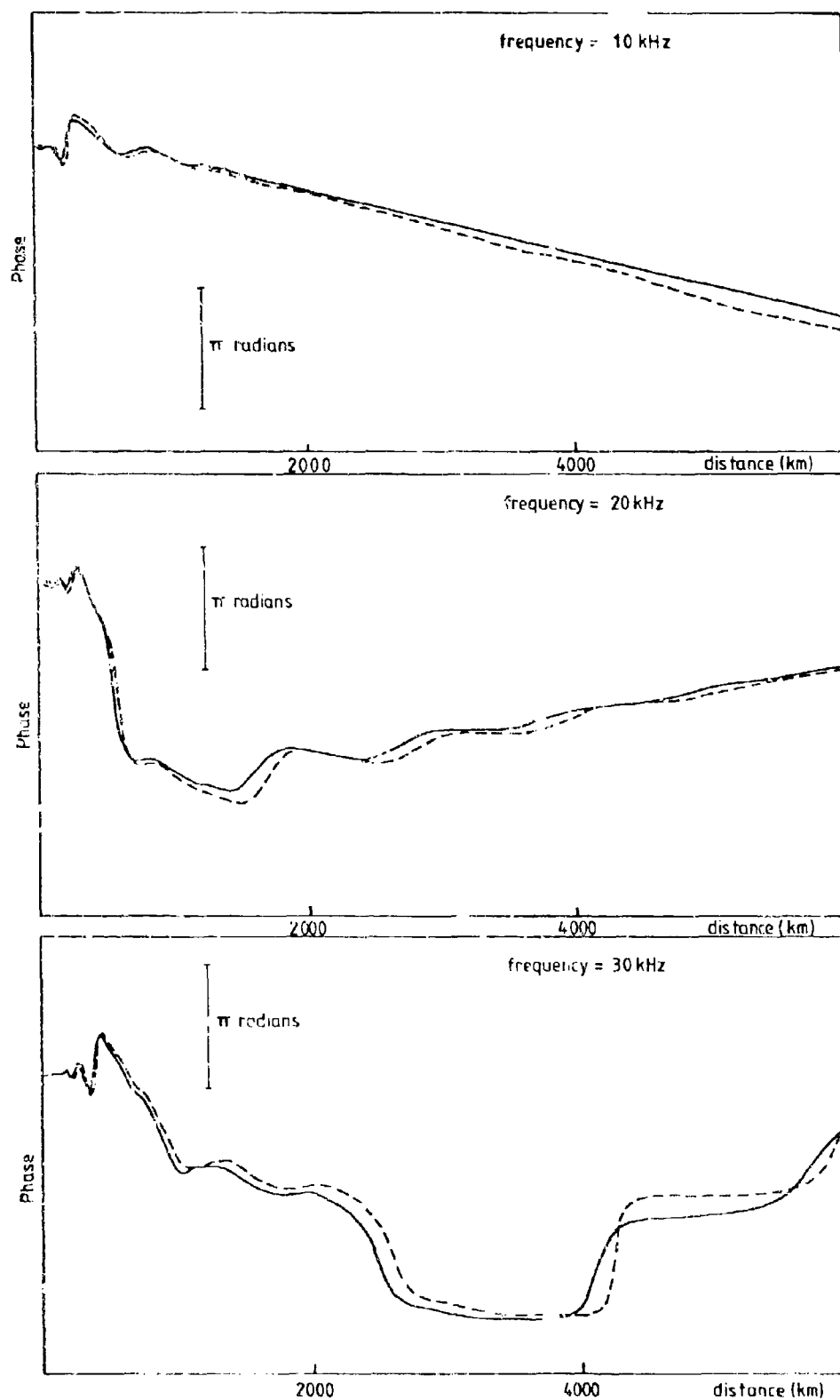
Fig.9   Comparisons of the spherical wave and wave-hop techniques at 10, 20 and 30 kHz.
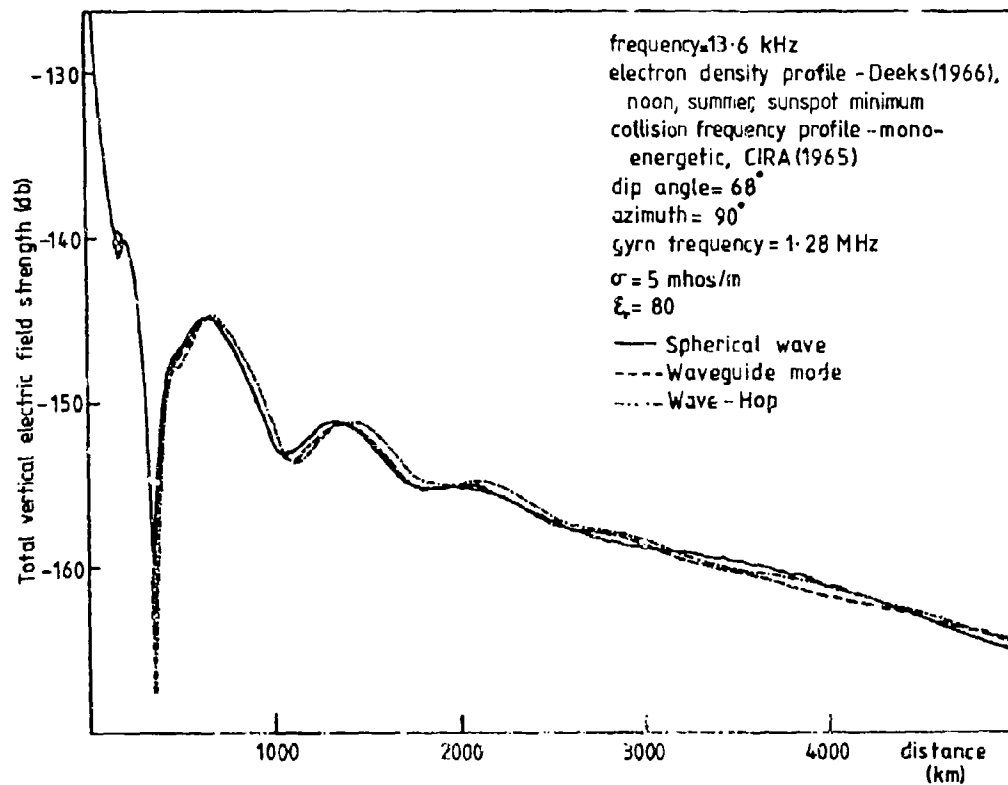
Fig.10(a)   Comparison of spherical wave, waveguide mode, and wave-hop techniques
– propagation over sea
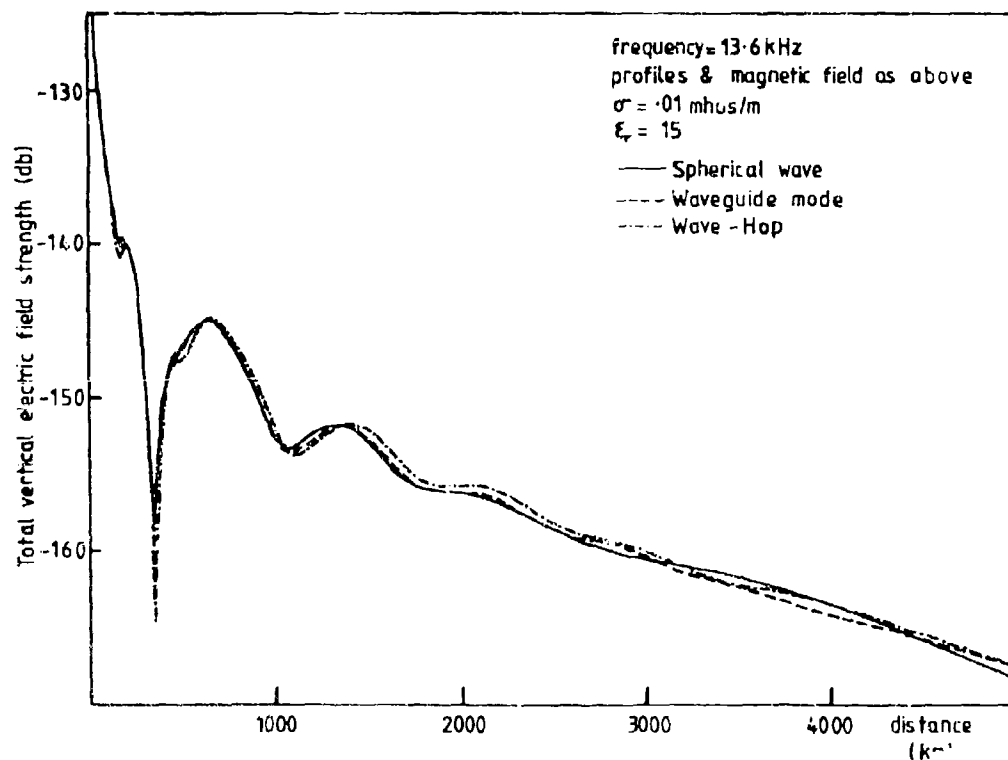


Fig.10(b)   Comparison of spherical wave, waveguide mode, and wave-hop techniques
propagation over land

# VLF PROPAGATION IN DISTURBED ENVIRONMENTS

Edward C. Field, Jr.
Pacific-Sierra Research Corporation
1456 Cloverfield Boulevard
Santa Monica, California 90404

## SUMMARY

This paper addresses long-range VLF/LF propagation of TM and TE signals at frequencies from 10 to 50 kHz. Model ionospheres corresponding to solar proton events or spread-debris nuclear environments are used in full-wave calculations. Such disturbances constrict the earth-ionosphere waveguide, increasing excitation factors and attenuation rates. The signals are therefore usually degraded beyond a few megameters, although either enhancement or degradation can occur at shorter distances. Ohmic heating of heavy ions in the lower ionosphere is the main loss mechanism for intense disturbances.

Only TM modes are efficiently radiated by ground-based transmitters. However, TE signals can be important for air-to-air links with terminal elevations of 20 kft or more, and nearly horizontal trailing-wire antennas. Air-to-air TE signals propagate better than TM modes over poorly conducting ground such as exists throughout Greenland and much of Canada, and can fill nulls in the TM signal. For paths over highly conducting ground, TM modes suffer less degradation than TE signals during intense disturbances; but, for ground conductivities less than about $10^{-4}$ mhos/m, TM signals are more adversely affected than TE signals.

## 1. INTRODUCTION

Natural and man-made ionospheric disturbances can significantly affect the long-range propagation of low-frequency (LF), very-low-frequency (VLF), and extremely-low-frequency (ELF) signals. This paper is concerned with VLF and LF propagation at frequencies from 10 to 50 kHz; a companion paper [Field, 1981] considers ELF propagation. Both papers focus on disturbances that are geographically widespread and depress the upper boundary of the earth-ionosphere waveguide--for example, nuclear environments and strong solar particle events (SPE). The companion paper presents detailed models of normal and disturbed ionospheres that are not repeated here.

Unlike at ELF, where only the transverse electromagnetic (TEM) mode can propagate, several transverse magnetic (TM) and transverse electric (TE) modes are above cutoff at VLF/LF. Under most conditions, only TM modes are of practical interest, because TE modes are difficult to excite from ground-based transmitters. Therefore, TM-mode attenuation in ambient and disturbed environments has been thoroughly studied and documented. However, antennas at altitudes of several kilometers can radiate or receive TE modes reasonably well. Moreover, since trailing-wire antennas on high-speed aircraft are nearly horizontal, they are more efficiently coupled to horizontally polarized than to vertically polarized signals. Thus, TE modes cannot be neglected for airborne antennas, particularly on northerly paths where low ground conductivity can severely attenuate TM modes.

This paper compares TE and TM signals for a wide range of disturbance intensities and ground conductivities. We give numerical results for excitation factors, height gain functions, and attenuation rates for the first few TM and TE modes, and detailed plots of multimode field strength as a function of distance for antenna altitudes of 0 and 40 kft.

## 2. PROPAGATION EQUATIONS

The detailed equations governing VLF propagation have appeared elsewhere (e.g., Galejs [1972], Wait [1970], Field et al. [1976]), so need not be repeated here. We solve them numerically, accounting for the vertical inhomogeneity of the ionosphere and curvature of the earth. To define the notation and illustrate the key dependences, we recapitulate the equations that govern the electric field when geomagnetic anisotropy can be neglected. That approximation is very accurate when the upper boundary of the earth-ionosphere waveguide is depressed far below its normal level; and it is fairly accurate for long-range propagation under normal daytime conditions.

### 2.1. Transverse Magnetic Modes

Typically, VLF/LF transmitters are vertically oriented, and their fields are composed of a superposition of TM waveguide modes. The vertical electric field is given by

$$E_V = -120\pi i \, e^{-\pi i/4} \, \frac{IL \cos \psi}{\sqrt{\lambda d}} \sqrt{\frac{d/a}{\sin d/a}} \sum_{\ell} S_{\ell}^{3/2} \, \Lambda_{\ell} \exp\left(-\frac{\beta_{\ell} d}{8.7}\right) \exp\left(-\frac{2\pi i}{\lambda} \frac{c}{v_{\ell}} d\right) G_{\ell}(h_T) G_{\ell}(h_R) \quad V/m \, ,$$

(1)

where the subscript $\ell$ denotes quantities associated with the $\ell$th TM mode, IL is the effective electric dipole moment of the transmitting antenna; $\lambda$ is the free-space wavelength; d is the distance from the transmitter; a is the earth's radius; and c is the speed of light. We have included a factor $\cos \psi$-- where $\psi$ is the angle between the dipole orientation and the vertical--to account for inclined transmitting antennas. Of course, $\cos \psi = 1$ for a vertical electric dipole. Although most quantities are in MKS units, we express all distances (L, $\lambda$, d, a) in megameters.

The quantity $S_{\ell}$ is essentially the eigenvalue of the $\ell$th TM mode and must be computed numerically. At VLF, however, S has a magnitude close to unity, so the term $S_{\ell}^{3/2}$ in Eq. (1) does not appreciably influence the field. The magnitude of the vertical electric field depends on the state of the ionosphere through three parameters: $\Lambda_{\ell}$, the excitation factor for the TM mode; $\beta_{\ell}$, the attenuation rate in decibels per megameter of propagation (dB/Mm); and $G_{\ell}$, the height gain function for transmitter and receiver

heights $h_T$ and $h_R$, respectively. The phase of the $\ell th$ mode is governed by the relative phase velocity, $v_\ell/c$. These propagation parameters must all be computed numerically for model ionospheres having arbitrary height profiles.

## 2.2. Transverse Electric Modes

Airborne VLF/LF transmitters use trailing-wire antennas whose primary orientation is often horizontal. Such antennas radiate a complicated superposition of TM and TE modes. Here we avoid much of that complexity by considering broadside propagation, where the great-circle path connecting transmitter and receiver is perpendicular to the plane containing the inclined electric-dipole transmitting antenna.

The vertical electric field produced by the vertical component of the inclined transmitting antenna is given by Eq. (1). The broadside horizontal electric field produced by the horizontal component is given by

$$E_H = -120\pi i \ e^{-\pi i/4} \ \frac{IL \sin \psi}{\sqrt{\lambda d}} \ \sqrt{\frac{d/a}{\sin d/a}} \ \sum_\ell \ S_m^{-1/2} \ \Lambda_m \ \exp\left(-\frac{\beta_m d}{8.7}\right) \exp\left(-\frac{2\pi i}{\lambda}\frac{c}{v_m}d\right) G_m(h_T)G_m(h_R) \qquad V/m \ , \tag{2}$$

The symbols are the same as in Eq. (1), except that m denotes the $mth$ TE mode.

## 3. MODE STRUCTURE

Equations (1) and (2) show that each mode's contribution to the total field is proportional to the product of four quantities: the excitation factor $\Lambda$, the transmitter height-gain function $G(h_T)$, the receiver height-gain function $G(h_R)$, and the propagation factor exp $(-\beta d/8.7)$. This section gives calculated values of the four quantities for the normal daytime model ionosphere* presented in the companion paper [Field, 1981] and a ground conductivity $\sigma_g$ of $10^{-3}$ mhos/m. Section 4 presents results showing the effects of ionospheric disturbances and various ground conductivities on mode parameters and the total field.

## 3.1. Excitation Factors

The excitation factor $\Lambda$ accounts for the efficiency with which a mode is launched by a ground-based transmitter. Usually, $\Lambda$ is normalized to unity for TM-mode excitation by a vertical dipole in an idealized waveguide sharply bounded by perfect conductors. Such normalization is accomplished by factoring out the "height" of the ionosphere, which is well defined in the idealized situation [Galejs, 1972]. However, our diffuse ionospheric models have no well-defined boundary. Consequently, the excitation factors computed here have units of inverse distance, and are smaller than those of other authors [Wait and Spies, 1964; Galejs, 1972] by a factor roughly corresponding to the average height of the ionospheric region causing the strongest reflections. That is, our excitation factors are defined to include the dependence on the effective width of the waveguide.

Figure 1 shows the frequency dependence of the calculated excitation factor magnitudes $\Lambda_\ell$ and $\Lambda_m$ for the first three TM modes ($\ell = 1, 2, 3$) and first two TE modes (m = 1, 2) for normal daytime conditions and $\sigma_g = 10^{-3}$ mhos/m. A ground dielectric constant of 10 is assumed throughout. At the lower frequencies, multiplying $\Lambda_\ell$ by nominal daytime reflection heights of $6 \times 10^4$ to $7 \times 10^4$ m gives a result near unity.

The first three TM modes are excited about equally at the lower VLF frequencies, but, above about 30 kHz, the higher order TM modes are much more effectively excited than the first. On the other hand, the TE modes are excited much less effectively than the TM modes. Indeed, $\Lambda_\ell$ exceeds $\Lambda_m$ by four or five orders of magnitude. Such behavior prevents ground-based transmitters from radiating TE signals efficiently at low frequencies. Again, the second mode is more effectively excited than the first.

## 3.2. Height Gain Functions

The height gain functions of a waveguide mode account for the transmitter and receiver elevation. A mode's contribution to the total field is proportional to the product of the excitation factor, the transmitter height-gain function, and the receiver height-gain function. The latter two functions are identical and, therefore, equal when both terminals are at the same altitude. In that case, a mode's relative importance at a given altitude is proportional to the product of the excitation factor and the square of the height gain function.

Figure 2 shows the altitude dependence of the height gain functions $G_\ell$ and $G_m$ for the first three TM modes ($\ell = 1, 2, 3$) and first two TE modes (m = 1, 2) for normal daytime conditions, $\sigma_g = 10^{-3}$ mhos/m, and a frequency of 20 kHz. These functions exhibit the classic height dependences for antennas over a highly conductive ground. That is, the TM-mode functions approximate unity over most of the waveguide, except for some rather sharp nulls; but above a few kilometers, the TE-mode functions increase sharply to values over 100.

For elevated antennas, the large TE-mode height gain function mitigates the effects of the small excitation factor, and these modes can be excited nearly as effectively as TM modes. More precisely, at altitudes where the height gain functions have achieved nearly their maximum value, the quantity $\Lambda_m G_m^2$ is of the same order of magnitude as the quantity $\Lambda_\ell G_\ell^2$. Figure 2 shows that, even for aircraft altitudes as low as 5 to 10 km, the TE-mode functions are very large.

*Some of the results given below are calculated from an exponential fit to this normal conductivity height profile. Differences between these results and those from the actual profile are minor.

At higher frequencies, the height profiles of $c_{\ell,m}$ resemble those shown in Fig. 2 for 20 kHz. The main difference is that the height gain function of the first TM mode develops a broad maximum in the 40 to 60 km altitude range as the frequency increases above 30 kHz. Such "whispering gallery" behavior is not important for the ground-based and airborne terminals considered here, but could be significant for very high, balloon-borne terminals. We also note that--at altitudes above a few kilometers--the TE-mode functions are nearly proportional to $\sigma_g^{1/2}$

### 3.3. Attenuation Rates

Figure 3 plots attenuation rate as a function of frequency for the first three TM modes ($\ell$ = 1, 2, 3) and the first two TE modes (m = 1, 2) for normal daytime conditions and $\sigma_g$ = $10^{-3}$ mhos/m. The higher order modes are more heavily attenuated than the lower, which often allows them to be neglected at VLF for long pathlengths. At the higher frequencies, the attenuation of the higher order modes can be mitigated by efficient excitation. It is therefore necessary to retain many terms in the mode sum, as in Eqs. (1) and (2), throughout the LF band under normal conditions. In that case, geometric optics is often a more convenient approach to propagation analysis than is mode theory. In intense disturbances, however, higher order modes are much more severely attenuated than lower, and the mode sum can be used well into the LF regime. Figure 3 shows that the first TE mode is slightly less attenuated than the first TM mode, although that result depends on the specific normal daytime conditions and ground conductivity assumed. Results for the dependence on ground conductivity are detailed below.

### 4. EFFECTS OF IONOSPHERIC DISTURBANCES

This section gives numerical results showing the effects of ionospheric disturbances and various ground conductivities on VLF/LF mode parameters and field strengths. The nominal ionospheric models used in our calculations are presented in the companion paper [Field, 1981]. We selected them as a convenient means of parameterizing the dependence of the fields on the intensity of a disturbance. Ionospheric disturbances having different characteristics from those considered here are, of course, possible. Therefore, specific events must be modeled individually.

### 4.1. Attenuation Rates

Figure 4 shows the attenuation rate of the first TM mode as a function of the severity of the disturbance for several VLF/LF frequencies and a perfectly conducting ground. Figure 5 shows analogous results for the first TE mode. For all cases shown, the TE mode is more heavily attenuated than the TM mode. However, the TM mode can be the more heavily attenuated for poorly conducting ground. In the VLF band, the TE-mode attenuation becomes prohibitive for intense disturbances.

It is instructive to inquire why, for example, the TE mode at 20 kHz is attenuated by about 30 dB/Mm during an intense disturbance, whereas the TM mode is attenuated by less than 10 dB/Mm--despite similar TE and TM ionospheric reflection coefficients at oblique incidence. A simple physical explanation can be obtained by interpreting the modes as plane waves, with the real part of S [Eqs. (1) and (2)] being the sine of the incidence angle. To satisfy the boundary conditions, the TE mode must be more steeply incident on the ionosphere than the TM mode. For an intense disturbance and 20 kHz, for example, our calculations give incidence angles (i.e., eigenangles) of about 82 and 78 deg for the first TM and TE modes, respectively. The steeper incidence angle makes the TE ionospheric reflection coefficient a few decibels smaller than the TM coefficient. It also makes the skip distance of the TE-mode plane wave significantly shorter than that of the TM mode. Thus, the TE mode suffers more ionospheric reflections per megameter than the TE mode and, therefore, greater attenuation.

Figure 6 shows the ground conductivity dependence of the attenuation rates of the first TM and TE modes at 20 kHz. Results are given for normal daytime conditions and a moderate disturbance, which could be an SPE. The disturbance increases the attenuation rate of both polarizations over normal values. The TE attenuation rate is virtually independent of ground conductivity, whereas the TM rate exhibits a strong, broad maximum for conductivities between $10^{-5}$ and $10^{-4}$ mhos/m, where the TM eigenangle is near the Brewster's angle of the ground. The TM mode propagates somewhat better than the TE mode for the most common ground conductivities, but propagates much worse over low-conductivity ground, such as occurs throughout Greenland and much of Canada. The extreme sensitivity of the TM mode to ground conductivity--combined with uncertainty about the values of that parameter--results in great uncertainty in calculations of transpolar signals from vertical VLF transmitters, particularly during ionospheric disturbances.

Although Fig. 6 pertains to a frequency of 20 kHz, curves for other frequencies exhibit the same general behavior. The main difference is that the Brewster's-angle peak in the TM attenuation rate occurs at higher values of $\sigma_g$ for higher frequencies, and vice versa.

The companion paper [Field, 1981] shows that ions are the primary influence on propagation if important reflections occur below the altitude where the positive ion density exceeds the electron density by a factor of about 1500. Here we quantify the effect of ions by calculating the fraction $F_i$ of the total Ohmic heating in the ionosphere attributable to ions. For simplicity, we use a perfectly conducting ground. Thus, the attenuation in the waveguide is entirely due to ionospheric joule heating, and $1 - F_i$ is the fractional contribution of the electrons. Also, to indicate the extent of uncertainties due to poorly known parameters, we calculate $F_i$ using $\nu_i/\nu_e$ = 1/10 and 1/40, which defines the range of uncertainty in the ratio of ion- to electron-collision frequencies.

Figure 7 shows $F_i$ for the first TM and TE modes at 20 kHz, with $\nu_i/\nu_e$ = 1/10 and 1/40. For $\nu_i/\nu_e$ = 1/40, ionic heating is the dominant loss mechanism for moderate and intense disturbances. For $\nu_i/\nu_e$ = 1/10, the effects of ions are considerably reduced, but still dominant for intense disturbances. Relative ionic losses are somewhat greater for the TE mode than for the TM.

### 4.2. Excitation Factors and Height Gain Functions

Figure 8 is analogous to Fig. 6, but plots the TM excitation factor rather than the attenuation rate. Like $\beta_\ell$, $\Lambda_\ell$ exhibits a strong Brewster's-angle maximum at low conductivities. Also, the disturbance, which

constricts the waveguide, increases the value of the excitation factor, since $\Lambda_\varrho$ is roughly proportional to the inverse of the waveguide width. The height gain function of the first TM mode is nearly unity at altitudes below about 20 km, regardless of the strength of a disturbance. It is therefore not shown.

The dependence of the TE mode on conductivity is much simpler than that of the TM mode, so is also not shown. Briefly, the excitation factor is proportional to $1/\sigma_g$ and--above a few kilometers--the height gain function is proportional to $\sigma_g^{1/2}$. Thus, the product $\Lambda_m \, G_m(h) \, G_m(h_R)$ that appears in Eq. (2) is nearly independent of ground conductivity, as is the TE-mode attenuation rate (Fig. 6). Unlike TM signals, therefore, TE signals between *airborne* terminals are nearly independent of ground conductivity.*

Like the TM excitation factor, the TE excitation factor is roughly inversely proportional to the waveguide width and increases during a disturbance that depresses the lower ionosphere. Thus, for both TM and TE signals, enhanced excitation competes with increased attenuation during a widespread disturbance.

### 4.3. Field Strength versus Distance

Figure 9 plots the electric field strength as a function of distance over a seawater path, for 100 kW of power radiated at 20 kHz from a vertical antenna. The parameters used here were chosen to illustrate the effects of a widespread disturbed environment, rather than to represent some specific event or path. The two curves were calculated from Eq. (1), using a full-wave propagation code to determine the mode parameters. The "normal" curve exhibits nulls and enhancements at ranges up to several megameters, caused by interference among several TM waveguide modes. At greater distances, the higher order modes, which are more heavily attenuated than the first mode, diminish in importance and the signal falls off smoothly with distance.

The two curves reveal several differences between the signals in normal and disturbed environments. First, and most important, the disturbed signal falls well below the normal signal, if at least 2 or 3 Mm of path are exposed. Such behavior is typical of strong SPEs and certain nuclear environments, and results when widespread ionospheric disturbances depress the ionospheric reflection heights, causing severe signal degradation on long-haul VLF links. Second, the mode interference pattern is nearly absent in the disturbed environment, indicating that heavy attenuation of higher order modes leaves only the first mode to contribute significantly. Third, at ranges under, say, 1.5 Mm, the signal can be stronger in the disturbed than in the normal environment, because the disturbed environment destroys interference nulls and increases the excitation factor. Of course, a disturbance covering most of the path, but not the terminals, would increase the attenuation but not the excitation.

TE-mode signals can be efficiently transmitted and received by antennas that are a few kilometers above the ground. TE signals have the following potential advantages for air-to-air links: (1) trailing-wire antennas tend to be nearly horizontal; (2) the deep TM interference nulls can be filled; (3) TE modes cannot be as efficiently transmitted as TM modes by ground-based terminals (except under normal nighttime conditions, where geomagnetic conversion is strong), and hence provide some protection against interference from low-altitude sources; (4) atmospheric noise is believed to be lower in the TE than in the TM mode; and (5) TE modes propagate better than TM modes over poorly conducting ground, such as exists throughout Greenland and much of Canada.

The greatest disadvantages of TE-mode links are that they (1) are more vulnerable than TM modes to degradation in disturbed environments, except for propagation over low-conductivity ground; and (2) do not propagate quite as well as TM modes under most normal conditions.

These assertions can be verified by inspecting the behavior of the mode parameters calculated here. However, they are also illustrated by Fig. 10, which directly compares the horizontally and vertically polarized 20 kHz electric fields radiated broadside to a trailing-wire antenna at an altitude of 40,000 ft and inclined 10 deg relative to the horizontal ($\psi = 80$ deg). We assume the receiver to also be at 40,000 ft, and both terminals to be within the disturbed region. Since Fig. 10 is intended for comparison, rather than to represent some specific link, we show only relative field strengths.

Under normal conditions, the TE signal is stronger than the TM at all distances, owing to the relatively high assumed altitude and the nearly horizontal antenna orientation--the ratio of TE to TM field strength being proportional to $\tan \psi$. However, even for terminals at 20,000 ft, the TE and TM modes are comparable at most ranges; and, since the TE and TM nulls occur at different ranges, each polarization fills in the nulls of the other. The TE signal is more adversely affected by the disturbance than the TM signal, which is dominant for distances beyond about 1 Mm. As indicated by Fig. 6, the TE signal would be stronger than the TM signal if $\sigma_g \lesssim 10^{-4}$ mhos/m, which is the case for large segments of transpolar paths.

### 5. DISCUSSION

No experiments have simultaneously measured VLF/LF propagation and ionospheric-conductivity height profiles between 35 and 75 km during a widespread disturbance. We therefore cannot make detailed comparisons between theory and experiment. Nonetheless, many data verify the following three aspects of our calculations: (1) an intense widespread ionospheric disturbance will substantially degrade long-path VLF signals, (2) poorly conducting ground, such as exists throughout Greenland and much of Canada, causes considerable TM signal loss; and (3) an ionospheric disturbance degrades TM signals much more severely on paths over poorly conducting ground than over seawater.

Westerlund and his colleagues [1969 and 1973] found that VLF signals propagating across Greenland are sharply degraded by the poorly conducting ice. Moreover, their data showed that SPEs cause much greater signal loss on paths that cross Greenland than on seawater paths. Oelberman et al. [1969] measured SPE effects on VLF propagation, and found that the Seattle-to-Switzerland signal typically decreased 10 to 20 dB during an event.

---

*For ground based terminals, $G_m = 1$. The excitation of TE modes then is proportional to $1/\sigma_g$ and prohibitively difficult except for very poorly conducting ground.

Field, Greifinger, and Schwartz [1972] compared calculations with data from a laboratory model that simulated VLF TM propagation in the earth-ionosphere waveguide. Both calculations and data showed that (1) lowering the waveguide's upper boundary increased the signal's attenuation, (2) severe attenuation occurred over a simulated icecap, and (3) lowering the waveguide boundary caused much greater anomalies over the simulated icecap than over simulated seawater. Mode-coupling at the seawater/icecap boundary was noted in the data but not included in the calculations.

These data pertain solely to TM signals from ground-based vertical transmitters. To our knowledge, no data exist for long-range TE signals propagating through disturbed regions or over the icecap. Transpolar transmission between two aircraft at VLF/LF would therefore be a worthwhile experiment.

## REFERENCES

FIELD, E. C., 1981, "ELF Propagation in Disturbed Environments," presented at AGARD 29th Symposium on Medium, Long and Very Long Wave Propagation (at Frequencies Less than 3000 kHz), Brussels, Belgium, 21-25 September 1981, Paper 11.

FIELD, E. C., C. GREIFINGER, and K. SCHWARTZ, 1 March 1972, "Transpolar Propagation of Long Radio Waves," *J. Geophys. Res.*, Vol. 77, No. 7, pp. 1264-1278.

FIELD, E. C., et al., December 1976, *Effects of Antenna Elevation and Inclination on VLF/LF Signal Structure*, Air Force Systems Command, Rome Air Development Center, RADC-TR-76-C-375.

GALEJS, J., 1972, *Terrestrial Propagation of Long Electromagnetic Waves*, Pergamon Press, New York.

OELBERMAN, E. J., et al., February 1969, *Coordinated High-Latitude Experiments for the Simulation of Nuclear Burst Effects on VLF Systems*, HRB-Singer, State College, Penn., Report 336-F.

WAIT, J. R., 1970, *Electromagnetic Waves in Stratified Media*, Pergamon Press, New York.

WAIT, J. R., and K. P. SPIES, 1964, *Characteristics of the Earth-Ionosphere Waveguide for VLF Radio Waves*, U.S. Department of Commerce, National Bureau of Standards, Washington, D.C., Technical Note 300.

WESTERLUND, S., and F. H. REDER, 1973, "VLF Radio Signals Propagating over the Greenland Ice-Sheet," *J. Atmos. Terr. Phys.*, Vol. 35, pp. 1475-1491.

WESTERLUND, S., et al., 1969, "Effects of Polar Cap Absorption Events on VLF Transmissions," *Planet. Space Sci.*, Vol. 17, pp. 1329-1374.
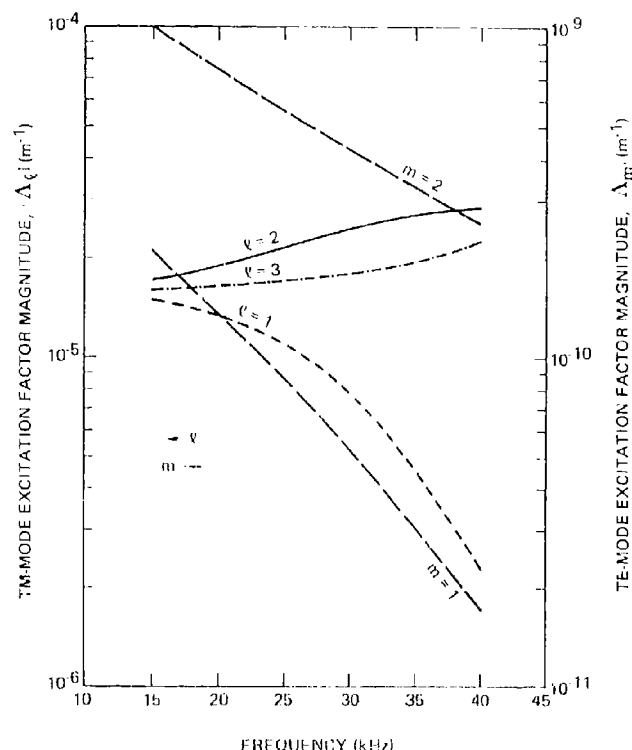
Figure 1. Excitation factor $\Lambda$ versus frequency $f$ for first three TM modes and first two TE modes: normal daytime conditions and $\sigma_g = 10^{-3}$ mhos/m
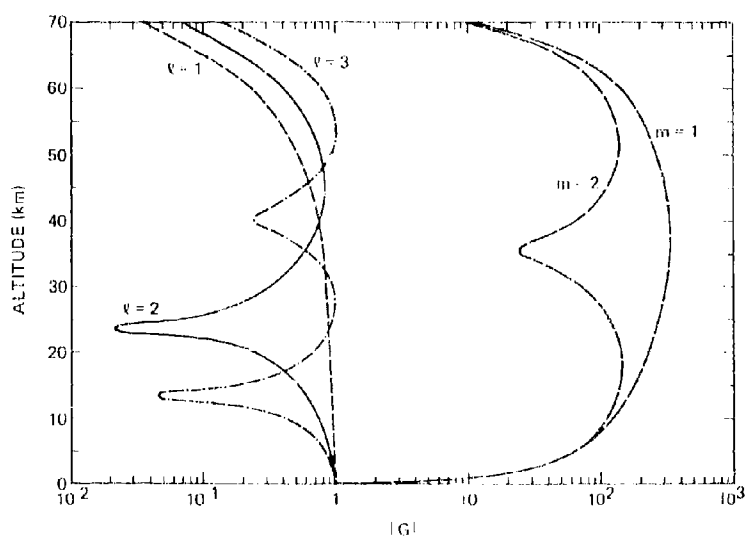


Figure 2. Height gain function $G$ versus altitude for first three TM modes and first two TE modes: normal daytime conditions, $\sigma_g = 10^{-3}$ mhos/m, and $f = 20$ kHz
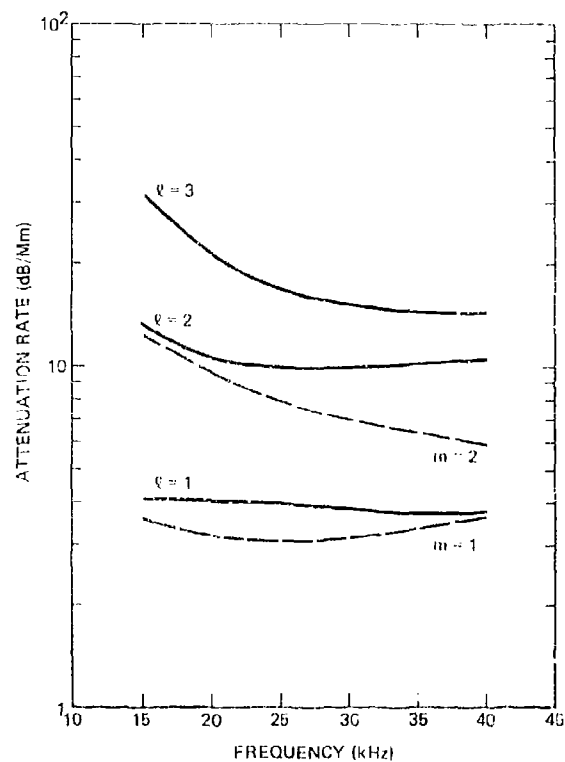
Figure 3. Attenuation rate $\beta$ versus frequency f for first three TM modes and first two TE modes: normal daytime conditions and $\sigma_g = 10^{-3}$ mhos/m
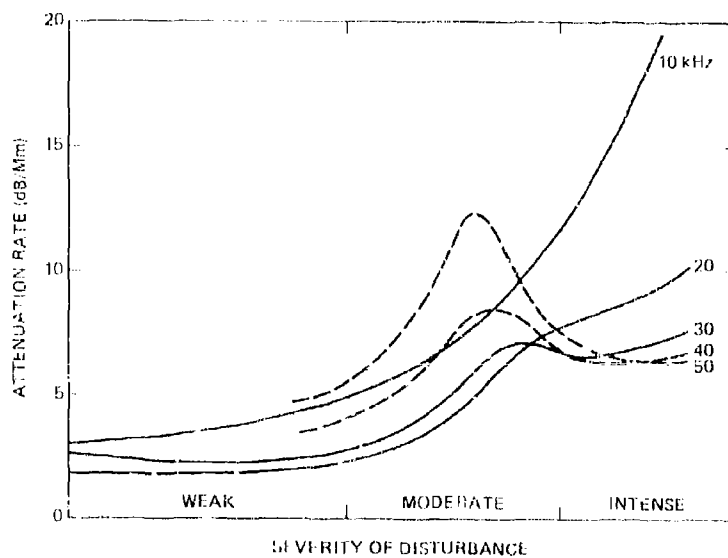


Figure 4. Attenuation rate $\beta$ of lowest order TM mode: $\sigma_g = \infty$. The intensity of the disturbance varies continuously from normal daytime conditions (extreme left) to very intense (extreme right).
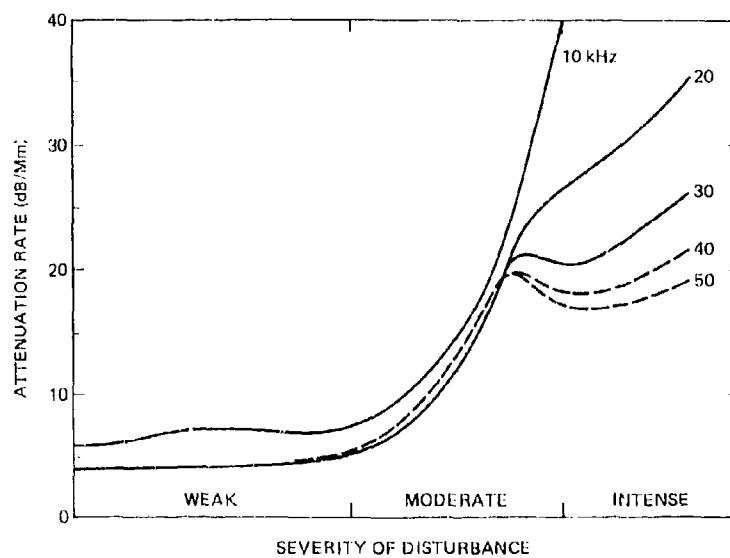
Figure 5. Attenuation rate β of lowest order TE mode: $\sigma_g = \infty$. The intensity of the disturbance varies continuously from normal daytime conditions (extreme left) to very intense (extreme right).
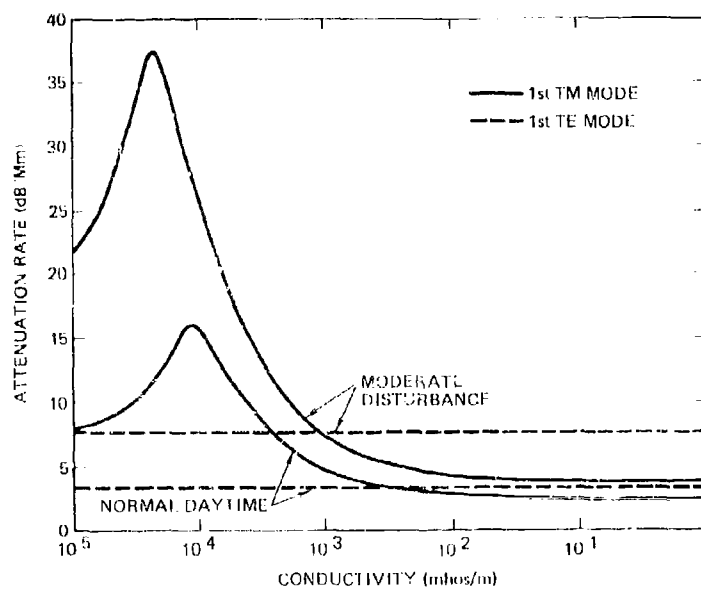


Figure 6. Attenuation rate β versus ground conductivity $\sigma_g$ for normal daytime and moderately disturbed conditions: $f = 20$ kHz
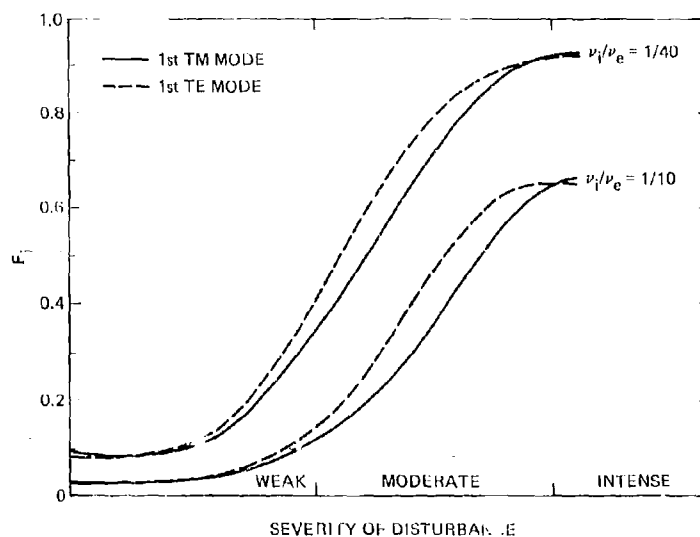
Figure 7. Fraction of ionospheric Ohmic heating due to ions versus severity of disturbance: f = 20 kHz
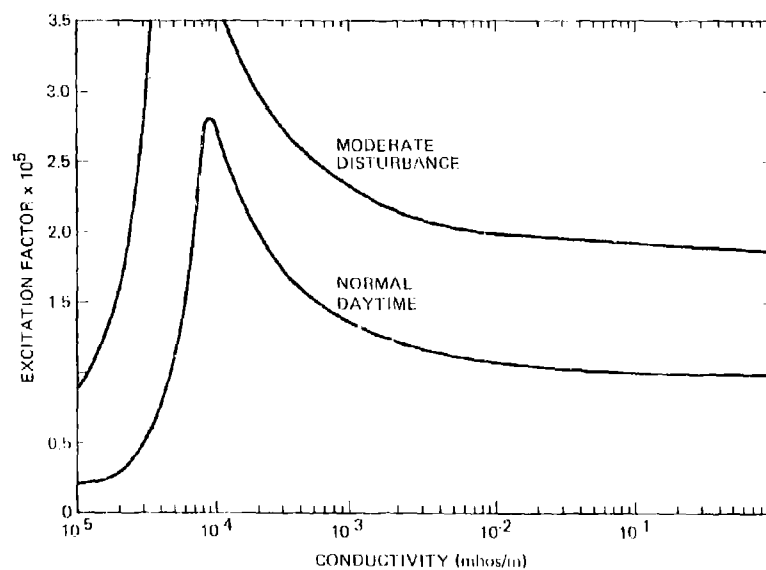


Figure 8. Excitation factor A of lowest order TM mode versus ground conductivity σ_g for normal daytime and moderately disturbed conditions: f = 20 kHz
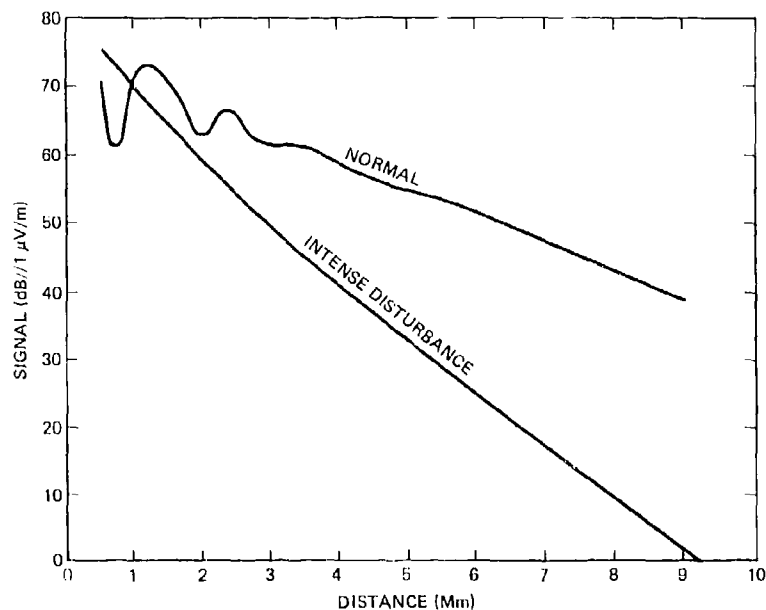
Figure 9: Daytime electric field strength $E_V$ versus distance d: vertical transmitter, seawater path, 100 kW radiated power, $\sigma_g$ = 4 mhos/m, and $f$ = 20 kHz.
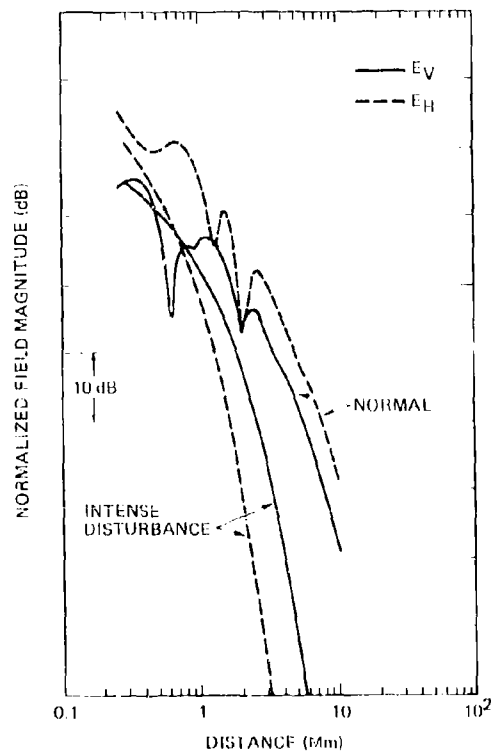


Figure 10: Broadside vertically and horizontally polarized electric field strength versus distance d: transmitting antenna at altitude of 40 kft and inclined 10 deg to the horizontal; $\sigma_g \sim 10^{-3}$ mhos/m and $f$ = 20 kHz

# MULTIPATH VLF PROPAGATION EFFECTS ON
# CORRELATION RECEIVERS

F. J. Kelly
E.O. Hulburt Center for Space Research
Ionospheric Effects Branch
Space Sciences Division

and

J. P. Hauser, H. M. Beck, and F. J. Rhoads
Information Technology
Communication Sciences Division

## ABSTRACT

The effect of electromagnetic propagation at very low frequency in the earth ionosphere waveguide can distort wideband communication waveforms and produce a splitting of the correlation peak of the received signal at a modal interference null where multipath signals arrive out of phase. Propagation from an inclined dipole antenna trailed behind an orbiting aircraft can cause split correlation pattern to fluctuate throughout the orbit period. For the case of an MSK (minimum-shift-keying) signal format, expressions and graphs are given for the correlation vector, as a function of receiver synchronization time and aircraft flight direction.

# MULTIPATH VLF PROPAGATION EFFECTS ON
# CORRELATION RECEIVERS

## INTRODUCTION

The propagation of very-low frequency (VLF) waves over terrestrial paths is often treated by considering the space between the earth and the ionosphere to be the interior of a waveguide, with the earth as a lower boundary and the D and E layers of the ionosphere as an upper boundary. Ordinarily several waveguide modes can propagate with low attenuation in the guide. Where two modes have approximately equal strength and arrive with approximately 180° phase shift between their wave components, a modal interference null ' said to occur. Typical examples of such modal interference nulls are shown in Fig. 1, taken from ...ds and Garner [1]. The predicted curves for Fig. 1 were those generated using the theoretical wave guide formulation of Wait and Spies [2].
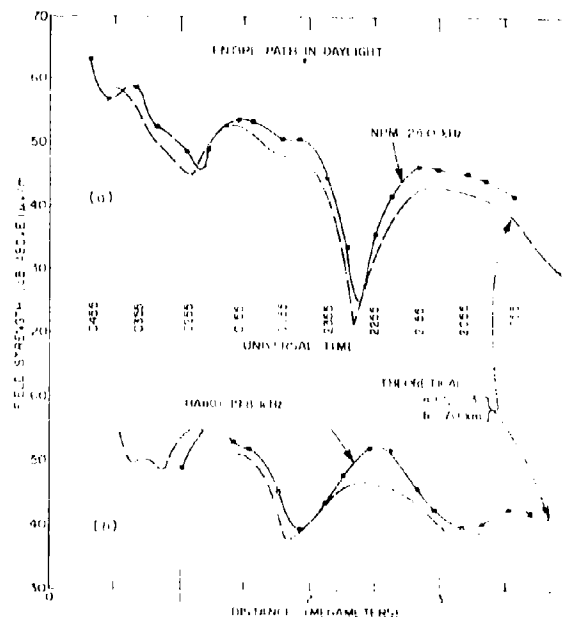


Fig. 1 — Comparison of theoretical results from Wait and Spies [2] with observed records in flight from San Francisco to Honolulu, May 18 19, 1965, for radiated power $P$ = 1 kW

When an airborne facility transmits VLF waves using a trailing-wire antenna, a complicated time-varying field is produced at a receiver [3,4]. The inclined antenna can be considered a superposition of an elevated vertical and horizontal antenna. Both quasi-transverse magnetic and electric modes are generated by the inclined antenna. The amplitudes of these modes vary with the angle between the horizontal component of the antenna and the direction to the receiver. If the horizontally and vertically

electron density models. The position of the first major interference null at 1200 km predicted by the $\beta = .3$ km$^{-1}$, h = 72.0 km ionosphere agrees better with the data in Figure 6 for both the ground level and 24,000 ft. altitude predictions. Predictions for 11,000 ft. altitude were also made, and they are practically identical to the predictions for the ground based receiver. For example, in the null at 1,000 km range the field strength was only changed by 1 dB for the $\beta = .3$ km$^{-1}$, h = 72 km ionosphere prediction.

The waveguide mode program predictions in the present report are made using exponential ionosphere models characterized by parameters and h as in References 5 through 9. In these cases, the electron density, $N_e(z)$, and collision frequency, $\nu_e(z)$, are given at height z, by

$$N_e(z) = 1.43 \ 10^7 \exp [(\beta - .15) z - \beta h] \tag{1}$$

$$\nu_e(z) = 1.82 \ 10^{11} \exp (-.15z) \tag{2}$$

where h and z are in km, $N_e(z)$ is in cm$^{-3}$, and $\nu_e(z)$ is in sec $^{-1}$. Reference 5 recommends a $\beta = .3$ km$^{-1}$, h = 72 km profile for daytime midlatitude (continental U.S.) fall paths and for summer arctic paths. The $\beta = .5$ km$^{-1}$, h = 70 km profile is recommended for midlatitude fall paths (Pacific). The wave-hop prediction program uses a more complicated ionospheric model which depends on $\chi$, the zenith angle of the sun measured at the mid-point of the propagation path. The electron density, $N_e(z, \chi)$, is given by

$$N_e(z, \chi) = N_E (z, \chi) + N_C (z, \chi) \tag{3}$$

where

$N_E(z, \chi)$ is an exponential layer profile, and

$N_C(z, \chi)$ is a cosmic-ray "C-layer" profile.

The exponential layer profile is given by

$$N_E(z, \chi) = 10^3 \exp [b (z-h)] \tag{4}$$

where

| | |
|---|---|
| h = (92-14.5 cos $\chi$) km | for $\chi <$ 102.25° |
| h = 95 km | for $\chi \geq$ 102.25° |
| b = .2 km$^{-1}$ | for $\chi \leq$ 70° |
| b = [.2 + .0233 ($\chi$ - 70°)] | for 70° $< \chi \leq$ 100° |
| b = .9 km$^{-1}$ | for $\chi >$ 100° |

The "C-layer" profile is given by

$$N_C (z, \chi) = N_1 \exp (1 - x - \exp (-x)) \tag{5}$$

where

$$x = (z - h_1) / H \tag{6}$$

and

| | |
|---|---|
| H = 3.3 km | for all $\chi$ |
| h$_1$ = 65 km | for $\chi \leq$ 90.3° |

$$h_1 = [65 + 1.03 (X - 90.3°)] \text{ km for } X > 90.3°$$

The values of $N_1$ used in (5) are given by

$$N_1 = 80 \text{ cm}^{-3} \qquad\qquad\qquad \text{for } X \leq 90°$$

$$N_1 = (80 + 10 \cdot 2(90° - X)) \text{ cm}^{-3} \quad \text{for } 90° < X \leq 95°$$

$$N_1 = 4(97 - X) \text{cm}^{-3} \qquad\qquad \text{for } 95° < X \leq 97°$$

$$N_1 = 0 \qquad\qquad\qquad\qquad \text{for } X > 97°$$

The collision frequency $\nu_e(z)$, used with the wave-hop program is given by

$$\nu_e(z) = \exp\left( \sum_{i=1}^{9} a_i \, x^{i-1} \right) \tag{7}$$

and the $a_i$ coefficients are given as follows:

$$a_1 = 2.588 \times 10 \cdot \qquad a_4 = -1.172 \times 10^{-5} \qquad a_7 = 1.351 \times 10^{-10}$$

$$a_2 = -1.210 \times 10^{-} \qquad a_5 = 1.749 \times 10^{-6} \qquad a_8 = 4.111 \times 10^{-13}$$

$$a_3 = 1.462 \times 10^{-3} \qquad a_6 = 2.948 \times 10^{-8} \qquad a_9 = -3.289 \times 10^{-15}$$

Figure 9 shows sample graphs of the ionospheric electron density profiles described here.

Figure 10 shows field strength versus distance for the 47.45 kHz Iceland transmitter measured during the September flight from Keflavik, Iceland to Patuxent River Naval Air Station in Maryland. The aircraft flew at 18,000 ft. during the early portion of the flight until the distance from Keflavik was about 1950 km and was at 24,000 ft. altitude for the rest of the data. Waveguide mode predictions using a $\beta = .3 \text{ km}^{-1}$, h = 72 km ionosphere model and the wave-hop program predictions agree with the data fairly well out to 2,200 km. There is an unexplained difference between both theoretical predictions and the experimental data beyond 2,200 km, where landfall over Canada occurred. The change in ground conductivity between sea water and land may contribute to the observed difference.

Figure 11, which shows a field strength versus distance plot of the 80.05 kHz transmission from Iceland during the September flight from Iceland to Patuxent River, there is also an unexplained disagreement between the wave-guide mode ($\beta = 3 \text{ km}^{-1}$, h = 72 km) theory and the experimental data beyond 2,200 km. The wave-hop model disagrees with the data over a greater range. There were no solar flares reported during the period of the flight that would explain the disagreements seen on 80.05 kHz and 47.45 kHz.

Figure 12 gives field strength versus distance for the 55.5 kHz transmissions from Thurso, Scotland received on the aircraft as it approached Thurso during the flight from Keflavik to Rota. The aircraft was at 11,000 ft. altitude during the first portion of the flight. When the aircraft was about 780 km from Thurso, the altitude was increased to 27,000 ft. to avoid bad weather and maintained there. A waveguide mode prediction using the $\beta = .3 \text{ km}^{-1}$, h = 72 km ionosphere for a receiver at 11,000 ft altitude (dashed line) shows an increase in the depth of the interference null in comparison to the 25,000 ft. altitude prediction (solid line) but little change of null location. The choice of a slightly different ionospheric height and a value of $\beta$ may produce better agreement.

Figure 13 presents field strength versus distance data for the Thurso transmitter on the outbound portion of the Keflavik to Rota flight, and on the inbound portion of the return flight. The data and theoretical predictions

shown here are in reasonably good agreement. For this prediction a ($\beta$ = .3 km$^{-1}$, h = 72 km) ionospheric profile was used. It was essential that the value of poor ground conductivity ( $\sigma$ = .001 mho/m) be used in this case. A prediction for this path using the conductivity of sea-water ( $\sigma$ = 4 mho/m) gave a completely different prediction which disagreed greatly with the measured data.

Data taken at a higher LF frequency are given in Figure 14, which shows the measured and the theoretical field strength versus distance plots for a Greece transmitter at 148.5 kHz for the daytime flight from Athens to Rota using an NM-12AT field intensity meter on the long wire antenna. The theoretical data were obtained from the wave-hop prediction program and are for a receiver on the ground. The experiment and theory agree fairly well in this case.

Figure 15 shows field strength versus distance plots for the 148.5 kHz Greece transmitter during a September nighttime flight in the Eastern Mediterranean area. The solid line shows the experimental values while the dashed line gives the theoretical values generated by the wave-hop prediction method. It can be seen that the theoretical model predicts the general behavior of the signal reduction with distance from the transmitter and also predicts the fairly sizeable and rapid oscillations of field strength versus distance. However, the experimental and theoretical curves do not agree in detail. The observed field varies up and down in strength more rapidly than the predicted field.

Figure 16 shows field strength versus distance data measured during a daytime calibration flight on September 14, 1976 off the East Coast of the United States. The aircraft was flying a polygonal figure during the time when these data points were recorded using the long wire antenna. It is shown that although the aircraft turned through 360° of heading from the Annapolis transmitter, the total change in field strength observed during the polygon can be very well attributed to the normal theoretical variation of field strength versus distance given by the solid lines in both figures. In this figure an X is plotted to indicate points at which the same field strength value was measured at the same distance but with two different aircraft headings. Because the long wire antenna exhibited the property of an isotropic receiving antenna, no correction factor depending on aircraft heading had to be added to the measured field strength values shown in the other figures of this paper.

Figure 17 shows a field strength versus distance plot of data taken on the long wire antenna using the NM-12AT during the incoming flight from Athens toward the LF transmitter at Morocco on 57.0 kHz. The theoretical data are obtained from the wave-hop computer program.

The comparisons that have been made so far with the experimental data indicate a preference for the use of a $\beta$ = .3 km$^{-1}$, h = 72 km ionosphere in the waveguide program. The wave-hop program agrees as well with most of the data - except for the 80.05 kHz data in Figure 11. The $\beta$ = .5 km$^{-1}$, h = 70 km ionosphere profile used with the waveguide program does not agree even qualitatively with the data. At nighttime the large, rapid oscillations of the field strength with distance are qualitatively explained by the wave-hop prediction model.

3.       THE MARCH 1977 DATA

The emphasis on the March 1977 experiments was to obtain nighttime data over paths similar to those of the previous experimental period. Certain changes in the aircraft paths were introduced because of the maintainance schedules of the Thurso, Scotland transmitter. The Thurso transmitter was off the air during the return period; so a flight through Great Britain was not made on the return trip. The return flights were from Rota, Spain to the Azores; from the Azores to Keflavik, Iceland; from Keflavik back to the Azores; and a final flight from the Azores to Patuxent River, Naval Air Station in Maryland, USA.

Figure 18 shows the nighttime propagation data taken during a flight from Keflavik out over the Norwegian Sea and return. The theoretical prediction of the wave-hop program is shown as a heavy line and the measured field strength values are lighter lines. The times when the aircraft was at the various locations are indicated on the figure. Two severe discrepancies are apparent between the theoretical predictions and the experiments. First, the groundwave attenuation near the transmitter appears to be much greater than predicted by the model giving a 10 dB discrepancy at a range of 500 km. Second the field pattern contains a rapidly oscillating component that is not contained in the predictions. The enhanced ground wave attenuation might be corrected by a change in our assumed values for Icelandic ground conductivity. The extra microstructure in the field strength versus distance plot may be caused by additional horizontal or vertical structure in the ionospheric electron density.

During a nighttime flight in from Athens to Athens (Fig. 19) on 58.3 KHz there was much better agreement between theory and experiment between 0 - 500 km. However the observed microstructure is much greater than that predicted by theory.

During the flight from Keflavik to Rota the aircraft overflew the Thurso transmitter. The data on Fig. 20 were obtained at 55.5 KHz. There is fairly reasonable agreement in overall field strength magnitude over a great deal of the path, but the position and depth of the nulls between .3 Mm and 1.0 Mm are not reproduced very closely. Also, the microstructure is not reproduced either.

The flight path from Athens to Rota is shown in Fig. 21. The data from this flight measuring the Morocco transmissions on 57.0 KHz are shown in Fig. 22. A greater degree of microstructure is evident than in predicted by the theoretical model. Also the theoretically predicted nulls at 1.48 Mm and 1.88 Mm were not observed in the measured data. On the same flight the transmissions of the Greece Station at 58.3 KHz were also monitored. The measured interference null pattern persists out to about 1.6 Mm while the theoretical pattern smooths out at about .9 Mm. The difference between the observed field strength and the theory is quite large also (between 10 - 20 dB) at the extreme range. The values of field strength generated by the Greece transmitter on 148.5 KHz is shown on Fig. 23. In this case we see lots of microstructure; but surprisingly the experimental fields usually exceed the theoretical fields - reversing the situation of the previous figure.

The experimental and theoretical data taken during the flight from Rota, Spain to the Azores is shown in Fig. 24. Here the overall agreement between theory and measured data is good.

The data taken on the flights from the Azores to Iceland and return are shown in Figures 25 - 28. The comparison of data on Fig. 25 and Fig. 26 which are both Keflavik transmissions on 80.0 KHz indicate quite a wide variability from night to night in the propagation of the waves. The data taken on the Morocco transmissions during the return flight from Azores to Patuxent River, Maryland are shown in Fig. 29.

In summary this research points to several directions of progress in the future. First, we need a good wave-hop program for elevated receivers. Second, we need to include realistic inhomogeneities in the model or introduce a statistical factor to take this microstructure into account. Third, because the field values and patterns can change dramatically from night to night, our data collection and ionospheric models must account for the dynamic situation occurring in the lower ionosphere where the waves reflect. In a certain sense the entire concept of a single fixed strength prediction utilizing the mathematical power of the wave-hop or waveguide program is challenged by the variation of the ionosphere.

A review of the findings of other scientist on the horizontal structure of the lower ionosphere during nighttime makes one strongly suspect that the field strength ripples that we observe are caused by similar structures in the ionosphere. It may be that gravity waves are a source of these oscillations (refs. 10 through 12); or there may exist a general patchiness caused by meterological phenomena affecting the production or recombiniation processes. To investigate this possibility some separate lower ionospheric probe like a vertical ionosonde or partial reflection device or airglow monitor might be benefically included in a future aircraft experiment if feasible.

## BIBLIOGRAPHY

1.      Berry, L.A., J.E. Herman, 1971, "A Wave-Hop Propagation Program for an Anisotropic Ionosphere", OT/ITS RR11, Institute for Telecommunication Sciences, Boulder, Colorado 80302

2.      Pappert, R.A., W.F. Moler, and L.R. Schockey, 1970, "A FORTRAN Program for Waveguide Propagation Which Allows Both Vertical and Horizontal Dipole Excitation", Naval Electronics Laboratory Center Interm Report No. 702 for DASA.

3.      Berry, L.A. and R.M. Jones, 1970, "A Time-Varying Electron Density Model for LF/VLF Propagation Calculations", Telecommunications Tech. Memo OT/ITSTM 3. The ionosphere model is also contained in a Defense Communications Agency Report, "LF-VLF Field Strength and Radio Noise at High Latitudes: Comparison of Measurements and Predictions", 1974, DCA 960-TP-74-43.

4.      Lewis, R.A., "The Wave-Hop Fields for an Inclined Dipole Over a Spherical Earth With an Anisotropic Ionosphere", JT Technical Report (unpublished, private communication).

5.      Gardiner, R.S., 1974, "Comparison of Predicted VLF/LF Signal Levels With Propagation Data", Defense Communications Agency Report, 960-TP-74-5.

6.      Rhoads, F.J. and W.E. Garner, 1967, "An Investigation of the Modal Interference of VLF Radio Waves", Radio Science, V.2, pp. 539-546.

7.      Wait, J.R. and K.P. Spies, 1964, "Characteristics of the Earth-Ionosphere Waveguide for VLF Radio Waves", National Bureau of Standards Technical Note 300.

8.      Burgess, B. and T.B. Jones, 1967, "Solar Flare Effects and VLF Radio Wave Observations of the Lower Ionosphere", Radio Science, V.2, pp. 619-626.

9.      Morfitt, D.G., 1976, "Determination of Effective Ionospheric Electron Density Profiles for VLF/LF Propagation", Defense Communications Agency, C650-TP-76-4.

10.     Paulson, M.R., E.E. Gossard and W.F. Moler, 1964, "The Nature and Scale Size of Irregularities in the D-Region of the Ionosphere as Observed on a Near Vertical Incidence VLF Sounder", AGARDograph 74, Propagation of Radio Waves at Frequencies Below 300 kc/s", Ed. W.T. Blackband (Macmillan, New York).

11.     Richter, E.W., J.R. Rowlett, C.S. Gardner and C.F. Sechrist, Jr., 1981, "Lidar Observation of the Mesopheric Sodium Layer Over Urbana, Illinois", Journal of Atmos. & Terres. Phys., 43, 327-337.

12.     Drobjev, V.I., V.M. Krasnov, and N.M. Saliwov, 1979, Temporal Variations of Ionospheric Waves in the D and F Regions", Journal Atmos. and Terres. Phys., 41, 1011-1013.

# LF PROPAGATION TEST ITINERARY
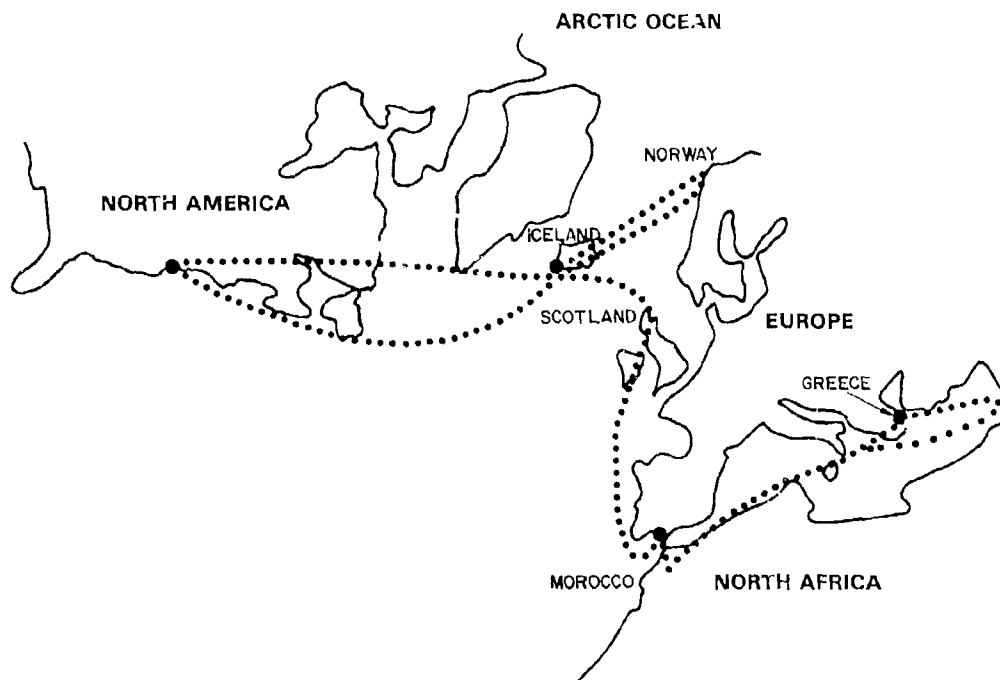


Fig. 1 The experimental flight paths.
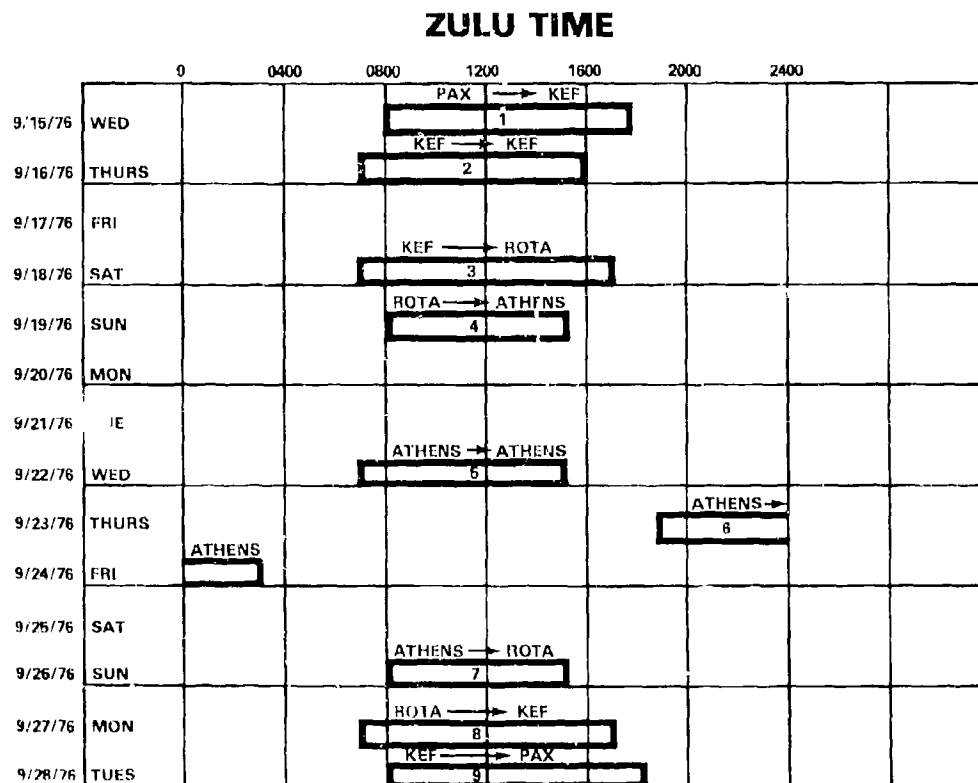


Fig. 2 Scheduled times for the September flights. The flights were accomplished within these time blocks.
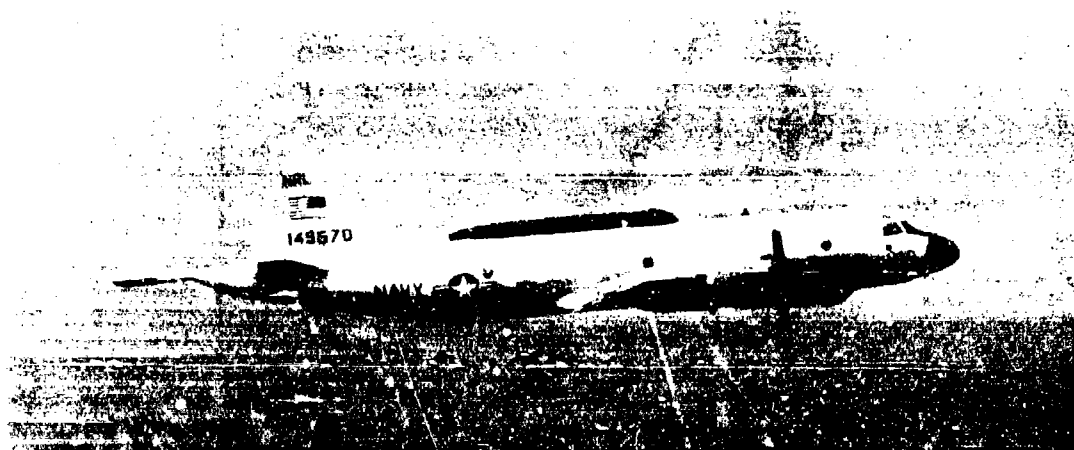
Fig. 3   The NRL RP-3A used for the experiments.

# AIRBORNE RECORDING SYSTEM
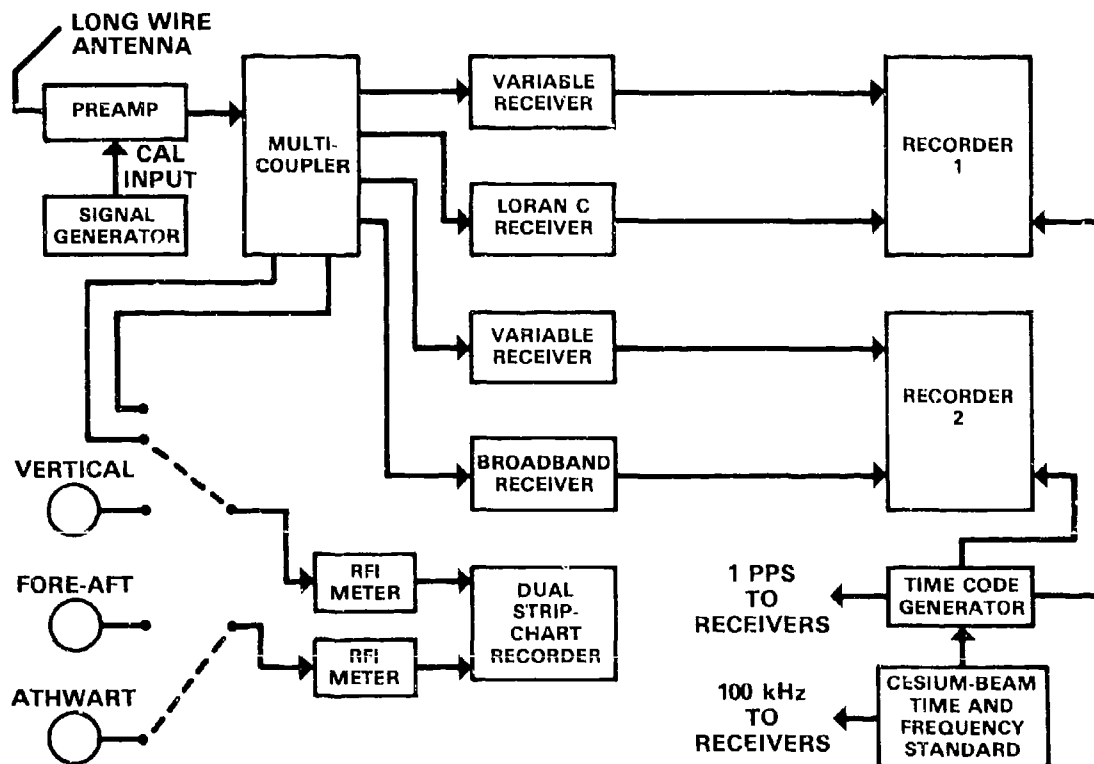


Fig. 4   Block diagram of the aircraft recording and field measurement systems. Similar recording and measurement systems were installed near the four LF transmitter sites in Iceland, Scotland, Morocco and Greece.
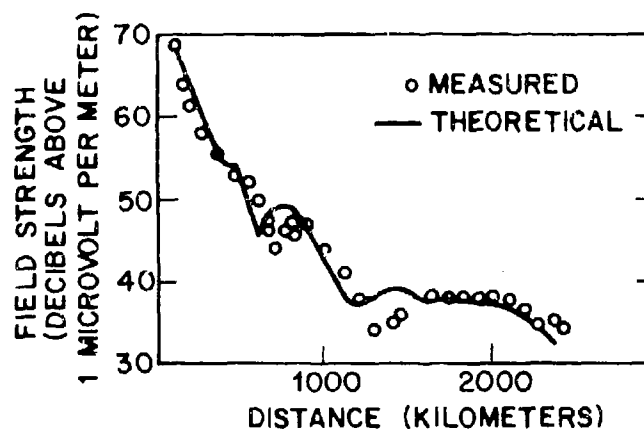
Fig. 5  Field strength versus distance plot of the 57.0 kHz transmissions from a Morocco transmitter measured using an NM-12AT field intensity meter during daytime flight from Rota, Spain to Athens, Greece. The long wire antenna was used, the field strengths are normalized to those produced by a 1 kW radiated power transmitter.
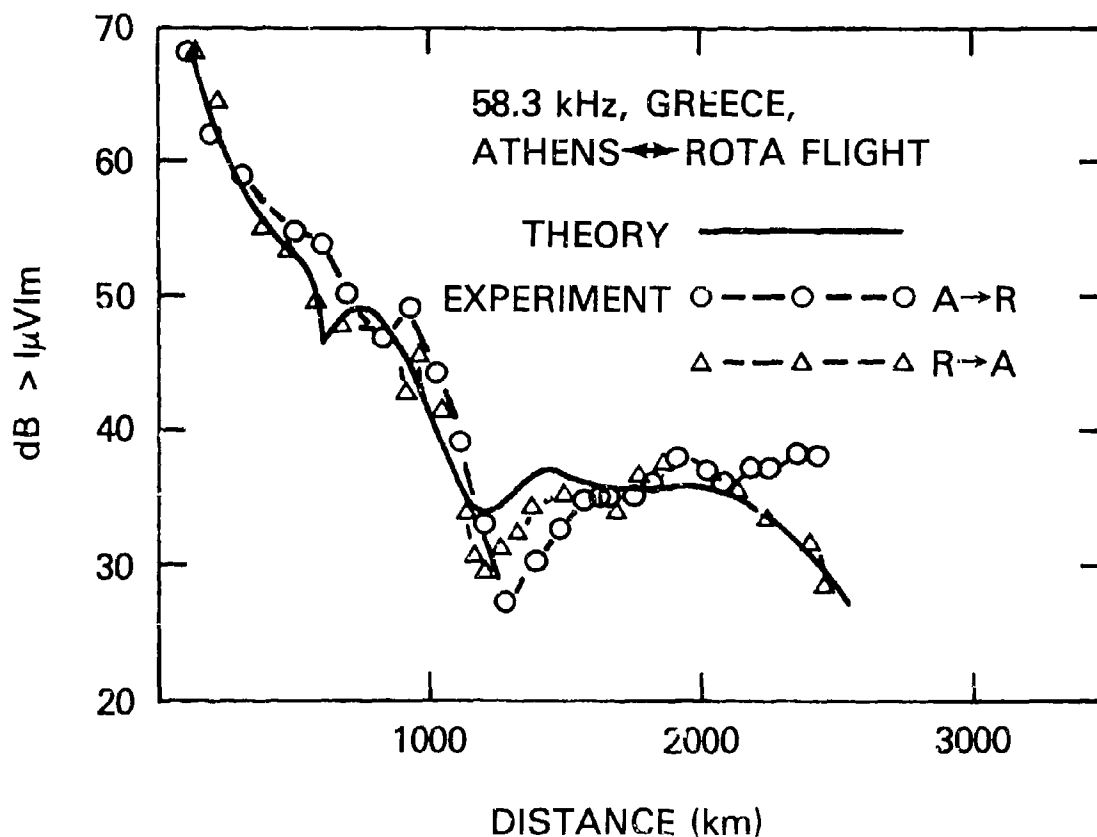


Fig. 6  Field strength versus distance plot of the 58.3 kHz transmissions from the Greece transmitter measured using an NM-12AT field intensity meter while flying during daytime from Rota, Spain to Athens, Greece and return. On the flight to Greece the long wire antenna was used, on the return flight a fore-and-aft loop antenna was used for most of the flight. The field strengths were normalized to those produced by a 1 kW radiated power transmitter. The theoretical curve used here was generated from the wave-hop program.
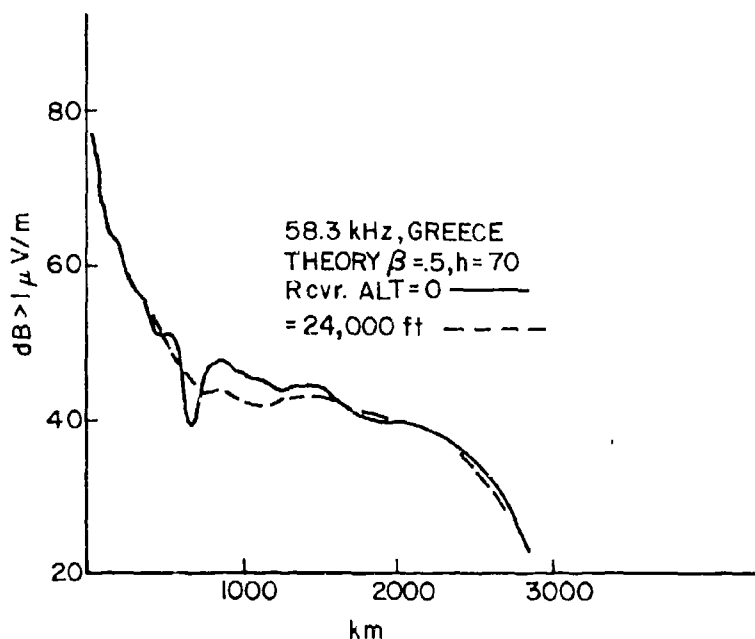
Fig. 7   Theoretical field strength versus distance plots from a Greece
transmitter on 58.3 kHz normalized to one kilowatt radiated poser.
An ionospheric electron density profile having a $\beta = 0.5$ km$^{-1}$ and
h = 70.0 km was used to make these predictions using a waveguide
mode program.  Two different receiver altitudes are shown.
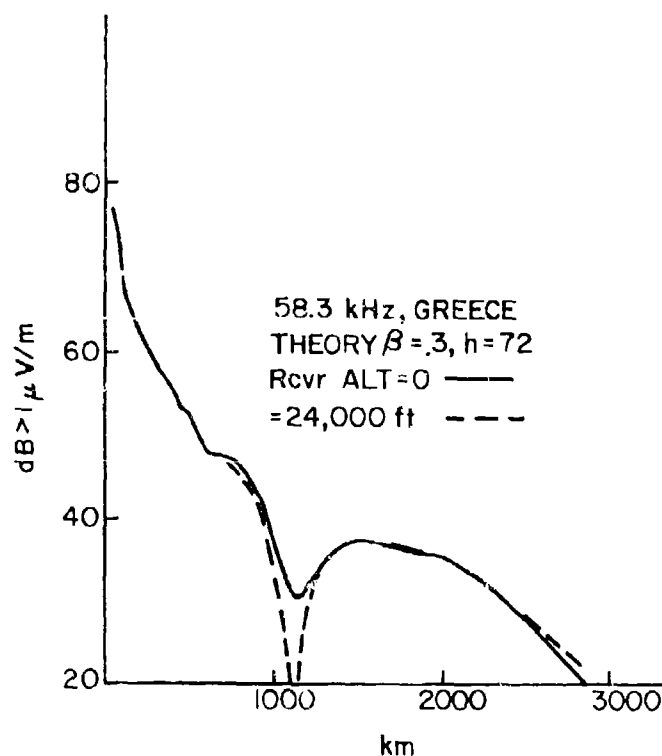


Fig.  8   Theoretical field strength versus distance plots from a Greece
transmitter on 58.3 kHz normalized to one kilowatt radiated power.
An ionospheric electron density profile having a $\beta = 0.3$ km$^{-1}$ and
h = 72 km was used to make these predictions using a waveguide mode
program.  Two receiver altitudes are shown.
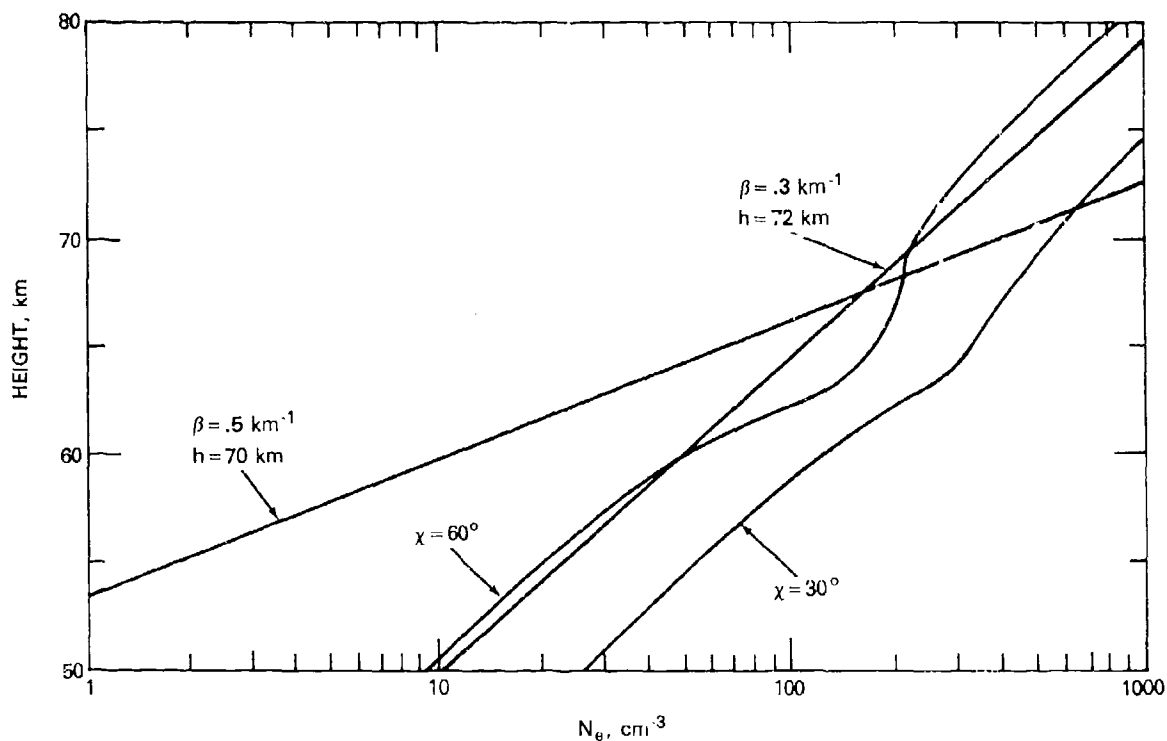
Fig. 9    Model electron density profiles used in making the theoretical
          propagation predictions.
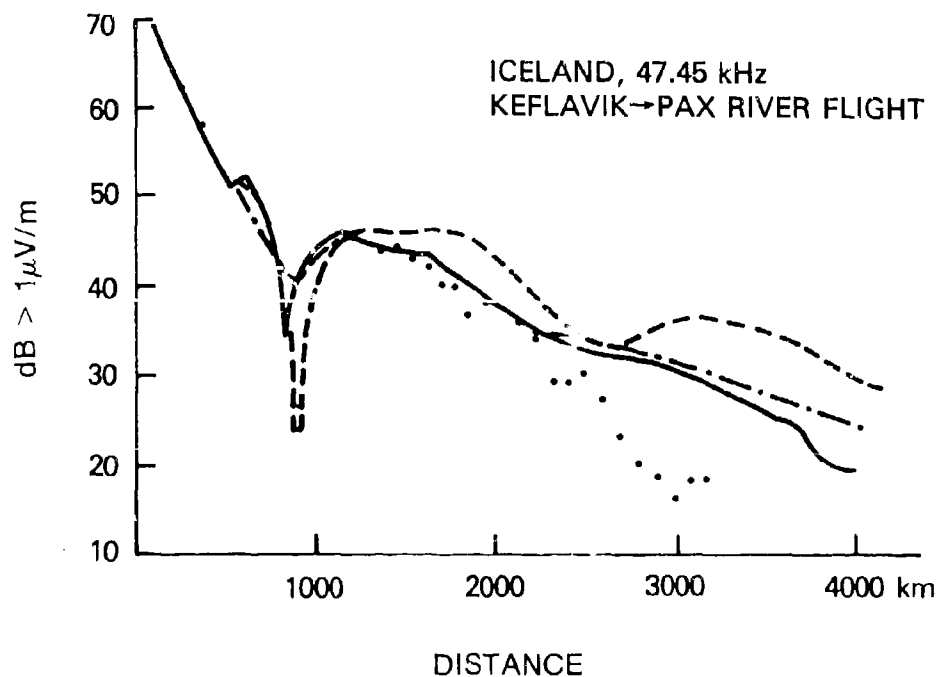


Fig. 10   Field strength versus distance plots from the Iceland transmitter
          on 47.45 kHz measured using a NM-12AT field intensity meter during
          the daytime flight from Keflavik, Iceland to Patuxent River Naval
          Air Station in Maryland.  The long wire antenna was used.  The solid
          theoretical curve was generated using the wave-hop program.  The
          dashed and dash-dot theoretical curves represent the $\beta$ = .5 km$^{-1}$,
          h = 70 km and the $\beta$ = .3 km$^{-1}$, h = 72 km ionospheric model
          predictions respectively for a receiver altitude of 25, 000 ft.
          using the waveguide program.

ICELAND, 80.05 kHz
KEFLAVIK→PAX RIVER FLIGHT
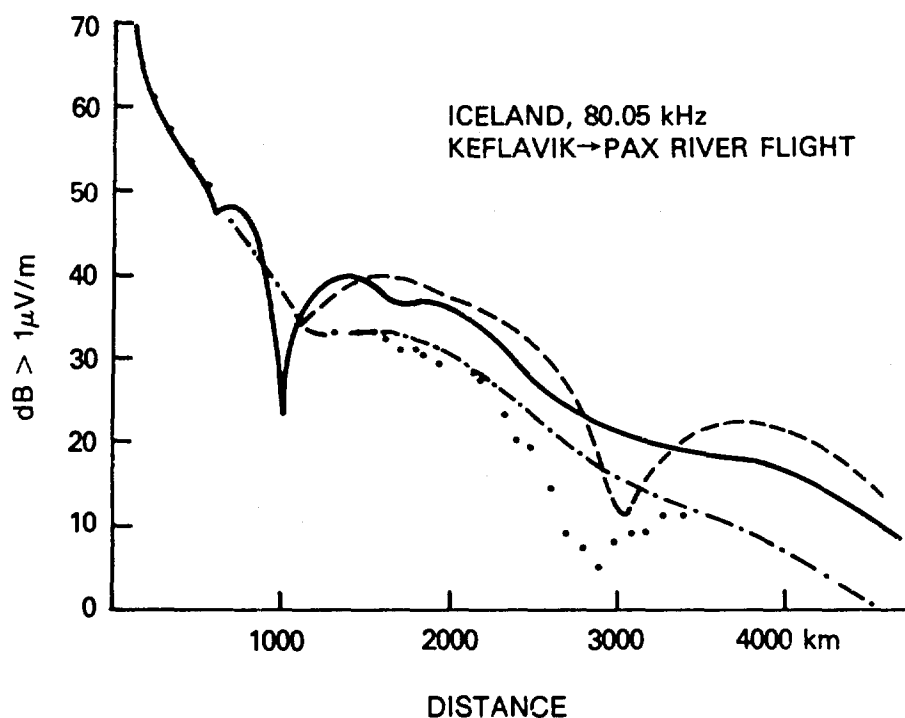
Fig. 11    Field strength versus distance plots from an Iceland transmitter
on 80.05 kHz measured using an NM-12AT field intensity meter during
the daytime flight from Keflavik, Iceland to Patuxent River Naval
Air Station in Maryland.  The long wire antenna was used.  The solid
theoretical curve was generated using the wave-hop program.  The
field strengths are normalized to those produced by a 1 kW radiated
power transmitter.  The dashed and dot-datshed curves are the same
as for Figure 10.
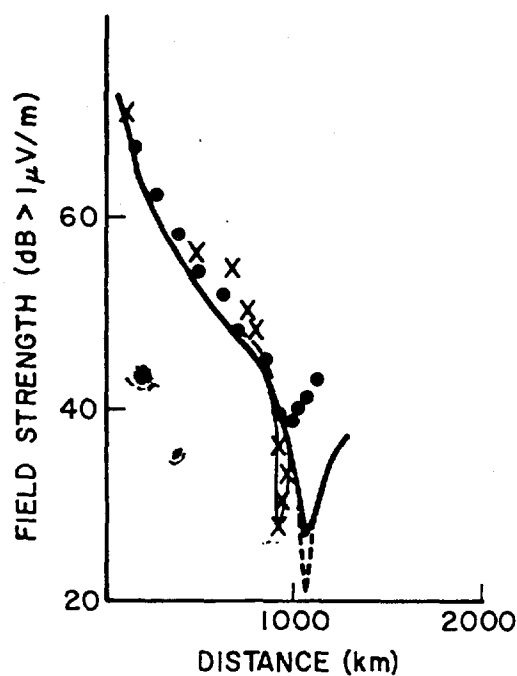


Fig. 12    Field strength versus distance plots from the Thurso, Scotland
transmitter on 55.5 kHz obtained during the flight from Iceland to
Thurso (x's) and from Thurso to Iceland (dots) on the long wire
antenna.  The heavy solid line and the dashed line are waveguide
mode predictions using a $\beta$ = .3 km$^{-1}$, h = 72 km ionosphere profile
for receiver altitudes of 25,000 ft and 11,000 ft respectively.  The
light solid line is added to guide the eye through the data at the
sharp interference null.
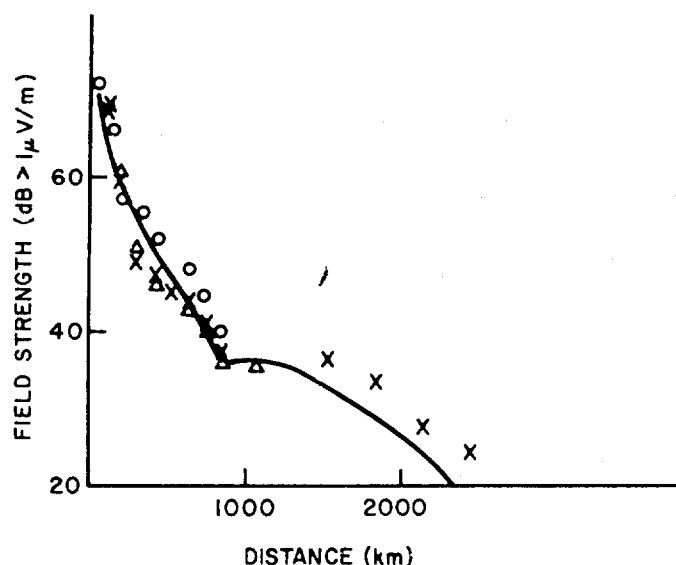
Fig. 13 Field strength versus distance plots from the Thurso, Scotland transmitter on 55.5 kHz measured from tape recordings made of the long wire antenna signal (x's), and from NM-12AT measurements using the fore-and-aft loop ( 's) on the Thurso to Rota flight, and from a NM-12AT measurements of the long wire antenna signal (o's) during the return flight from Rota to Thurso. The solid line is a waveguide mode prediction of the field strength using a ( $\beta$ = .3 km$^{-1}$, h = 72 km) ionospheric profile and a ground conductivity of .001 mho/m which is characteristic of Northern Scotland. The receiver altitude assumed in the prediction is 25,000 ft. The field strengths are normalized to a transmitter producing one kilowatt of radiated power.
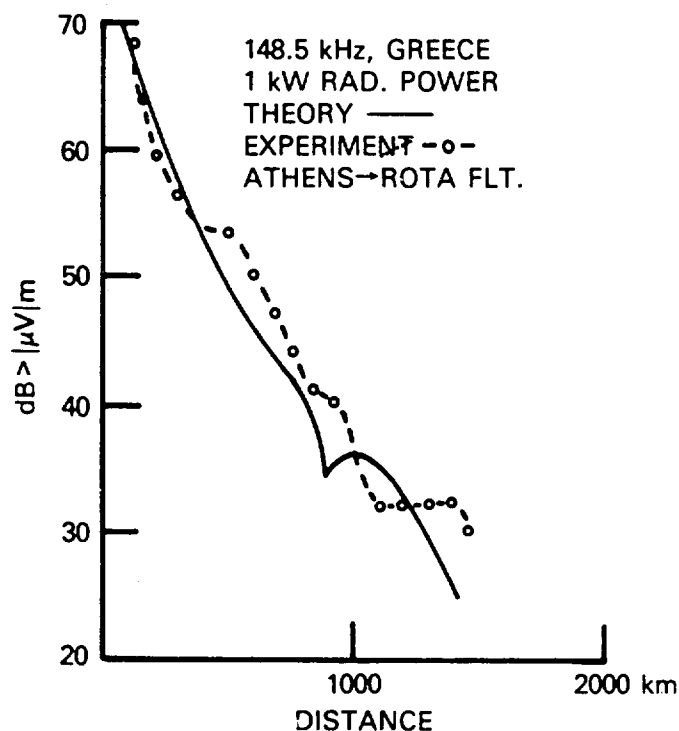


Fig. 14 Field strength versus distance plot of the 148.5 kHz transmissions from the Greece transmitter measured using an NM-12AT field intensity meter while flying during daytime from Athens, Greece to Rota, Spain via Morocco. The long wire antenna was used. The fields are normalized to those produced by a 1 kW radiated power transmitter. The solid theoretical curve was made by the wave-hop computer program.
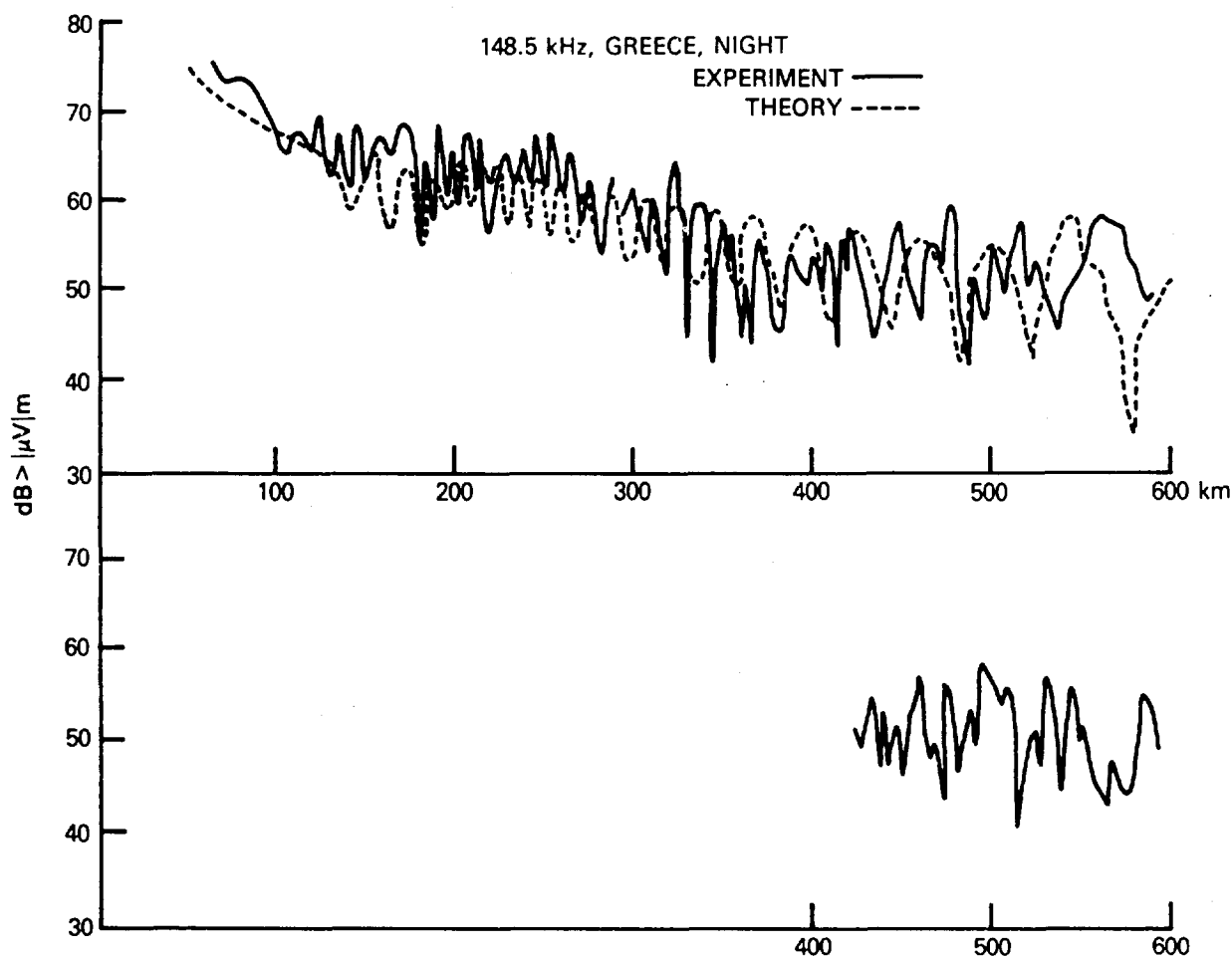
Fig. 15 Field strength versus distance plots of the 148.5 kHz transmission from a Greece transmitter measured using an NM-12AT field intensity meter during a nighttime flight originating in Athens. The long wire antenna was used. The field strengths are normalized to those produced by a 1 kW radiated power transmitter. This data was collected when the aircraft was west and south of Athens. The dashed line is a theoretical prediction generated by the wave-hop program. The upper figure shows data from the flight between Athens and a point in the Mediterranean (36° 59'N, 17° 27'E) southwest of Athens. The lower figure shows data obtained during the subsequent portion of the flight from this point direct to a point (35° 13.5'N, 23° 41'E) southeast of Athens.
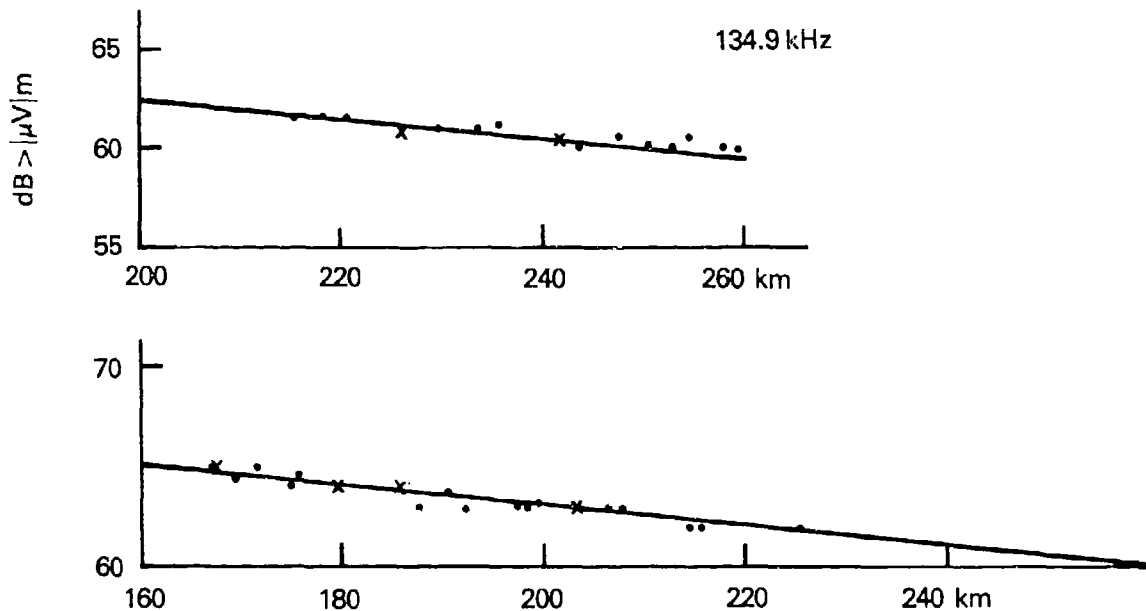
Fig. 16    Field strength versus distance data from the Annapolis, Maryland
transmitters.  This data was taken while the aircraft made two
12-sided polygonal flights to determine the antenna pattern of the
long-wire and loop antennas on board the aircraft.  The crosses
indicate the coincidence of 2 data points where the aircraft was at
the same range but different antenna bearings to the Annapolis
transmitter.  These data are consistent with an omnidirectional
reception pattern for the long wire antenna under daytime
propagation conditions to within about ±0.5 dB average error.  The
solid lines indicate the theoretical field strength versus distance
(normalized to 1 kW radiated power) obtained from the wave-hop
program.  The data and predictions on the lower graph are for 51.4
kHz.

MOROCCO, 57.0 kHz
GREECE→ROTA FLT.
INBOUND TO MOROCCO

Fig. 17    Field strength versus distance measured during the inbound flight
           toward the Morocco transmitter on the flight from Athens.   The
           fields are normalized to 1 kW radiated power from the transmitter.
           The dots represent the experimental points and the solid line is the
           prediction of the wave-hop program.  When the aircraft was 180 km
           from the transmitter, it increased its altitude from 12,000 to
           18,000 ft. and maintained that altitude.



Fig. 18    Field strength versus distance data for Keflavik transmissions
           on 80.1 KHz during flight from Keflavik, Iceland to the northeast
           during nighttime of 3 to 4 Mar 1977 at an altitude of approximately
           23,000 feet.  Experimental data are shown by the light line.
           Theoretical predictions are the heavy line.

**GREECE NIGHT**
**MAR 10**
**2131 Z**
**58.3 kHz**
**1.00 kW**

Fig. 19  Field strength versus distance data for Greece transmissions
on 58.3 KHz during flight from Athens, Greece to the west during
nighttime of 10 to 11 Mar 1977 at an altitude of approximately
22,000 feet.  Experimental data are shown by the light line.
Theoretical predictions are the heavy line.

**KEF → ROTA**
**FLIGHT #3**
**MAR 5**
**0339 Z**
**THURSO**
**55.5 kHz**
**1.00 kW**
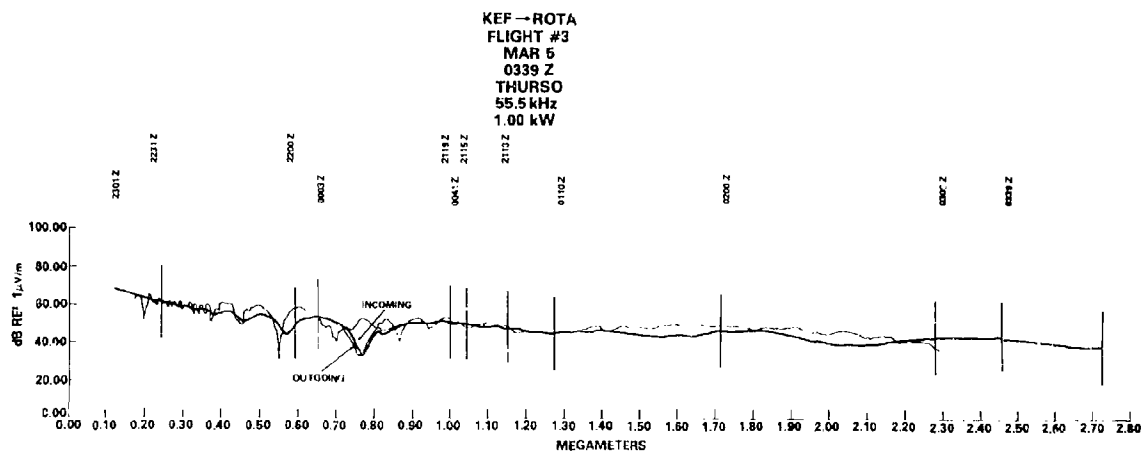
Fig. 20  Field strength versus distance data for Thurso transmissions
on 55.5 KHz during flight from Keflavik, Iceland to Rota, Spain
during nighttime of 5 to 6 Mar 1977 at an altitude of approximately
23,000 feet.  Experimental data are shown by the light line.
Theoretical predictions are the heavy line.
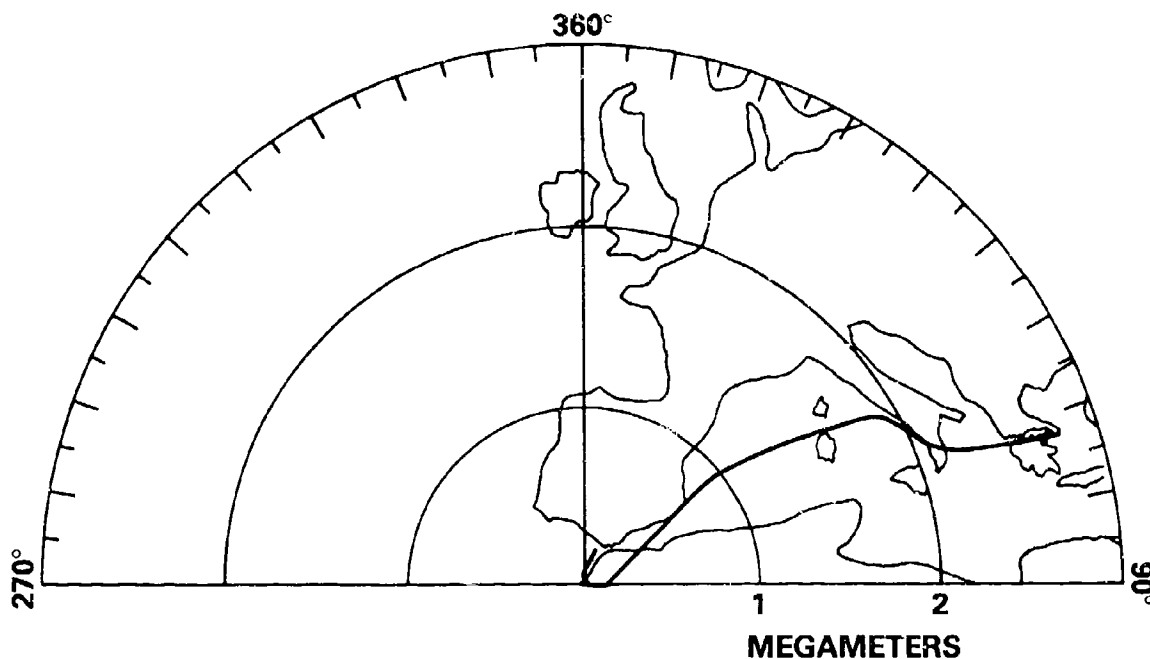
Fig. 21    Map showing path traversed on flight from Athens to Rota.
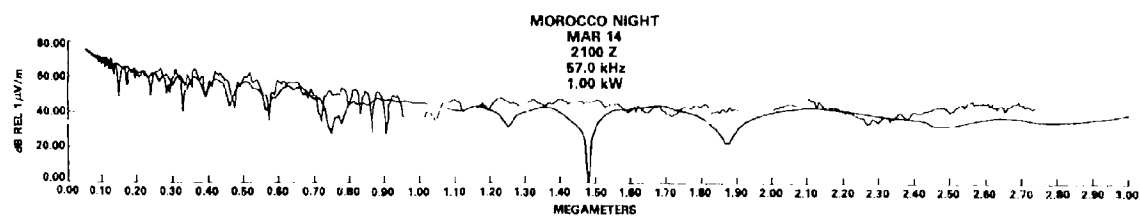


Fig. 22    Field strength versus distance data for Morocco transmissions
on 57.0 KHz during flight from Athens, Greece to Rota, Spain during
nighttime of 14 to 15 Mar 1977 at an altitude of approximately
20,000 feet.  Experimental data are shown by the light line.
Theoretical predictions are the heavy line.

GREECE NIGHT
MAR 15
0134 Z
58.3 kHz
1.00 kW
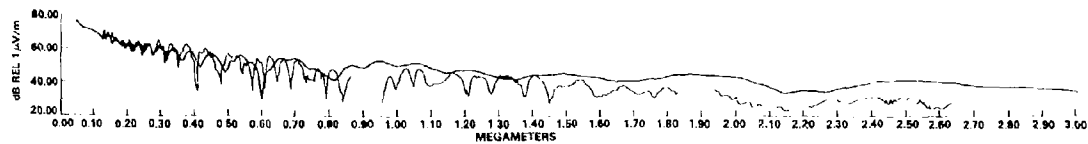
Fig. 23   Field strength versus distance data for Greece transmissions
          on 58.3 KHz during flight from Athens, Greece to Rota, Spain during
          nighttime of 14 to 15 Mar 1977 at an altitude of approximately
          20,000 feet.  Experimental data are shown by the light line.
          Theoretical predictions are the heavy line.
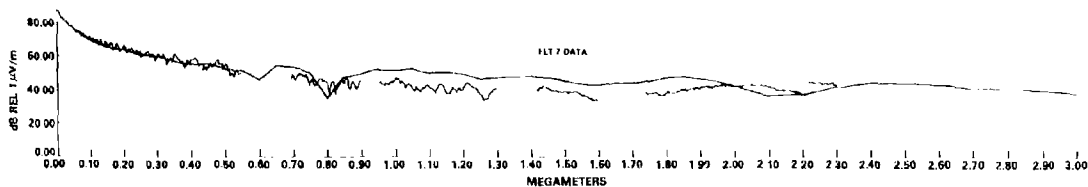
Fig. 24   Field strength versus distance data for Morocco transmissions
          on 57.0 KHz during flight from Rota, Spain to Lajes, Azores during
          nighttime of 15 to 16 Mar 1977 at an altitude of approximately
          21,000 feet.  Experimental data are shown by the light line.
          Theoretical predictions are the heavy line.

GREECE NIGHT
MAR 15
0134 Z
148.5 kHz
1.00 kW
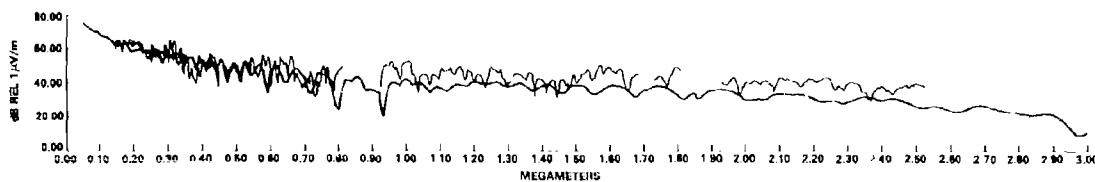
Fig. 25   Field strength versus distance data for Greece transmissions
          on 148.5 KHz during flight from Athens, Greece to Rota, Spain during
          nighttime of 14 to 15 Mar 1977 at an altitude of approximately
          20,000 feet.  Experimental data are shown by the light line.
          Theoretical predictions are the heavy line.

**MOROCCO NIGHT**
**MAR 22**
**0235 Z**
**57.0 kHz**
**1.00 kW**

FLT 10 DATA
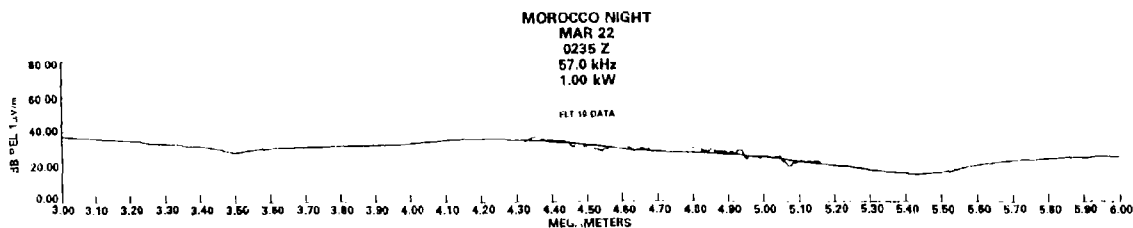
Fig. 26    Field strength versus distance data for Morocco transmissions
on 57.0 KHz during flight from Lajes, Azores to Patuxent River,
Maryland, USA during nighttime of 21 to 22 Mar 1977 at an altitude
of approximately 20,000 feet.  Experimental data are shown by the
light line.  Theoretical predictions are the heavy line.

**FLT 8**
**ICELAND NIGHT**
**MAR 17**
**2215 Z**
**47.4 kHz**
**1.00 kW**
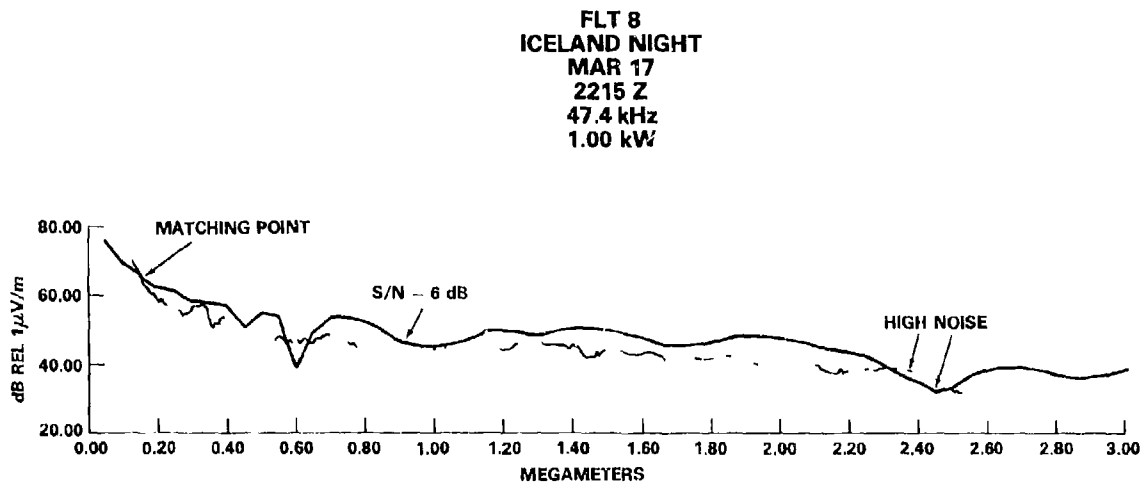
Fig. 27    Field strength versus distance data for Iceland transmissions
on 47.45 KHz during flight from Lajes, Azores to Keflavik, Iceland
during nighttime of 17 to 18 Mar 1977 at an altitude of
approximately 23,000 feet.  Experimental data are shown by the light
line.  Theoretical predictions are the heavy line.

**FLT 8**
**LAJES→KEFLAVIK**
**ICELAND NIGHT**
**MAR 17**
**2215 Z**
**80.0 kHz**
**1.00 kW**
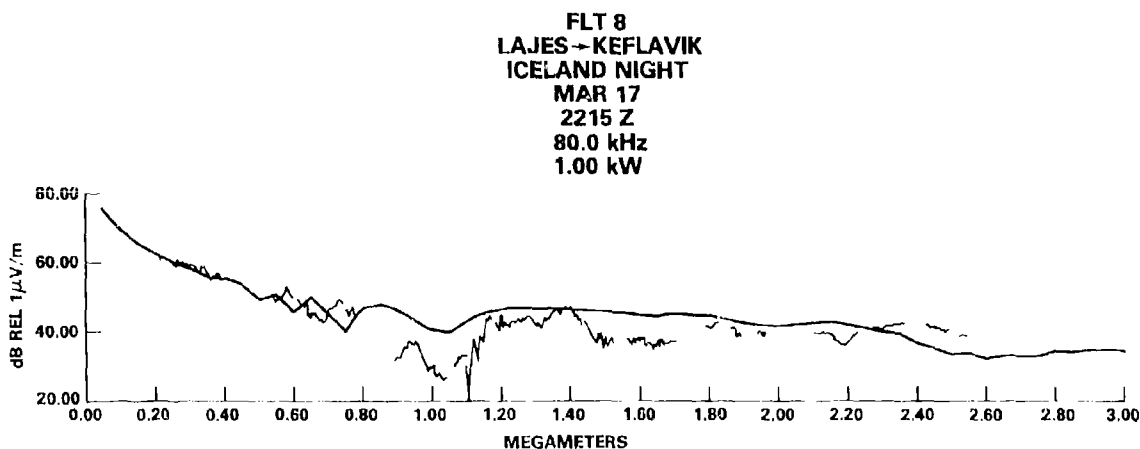
Fig. 28    Field strength versus distance data for Iceland transmissions
on 80.0 KHz during flight from Lajes, Azores to Keflavik, Iceland
during nighttime of 17 to 18 Mar 1977 at an altitude of
approximately 23,000 feet.  Experimental data are shown by the light
line.  Theoretical predictions are the heavy line.

**FLT 9**
**ICELAND NIGHT**
**MAR 20**
**0115 Z**
**80.0 kHz**
**1.00 kW**
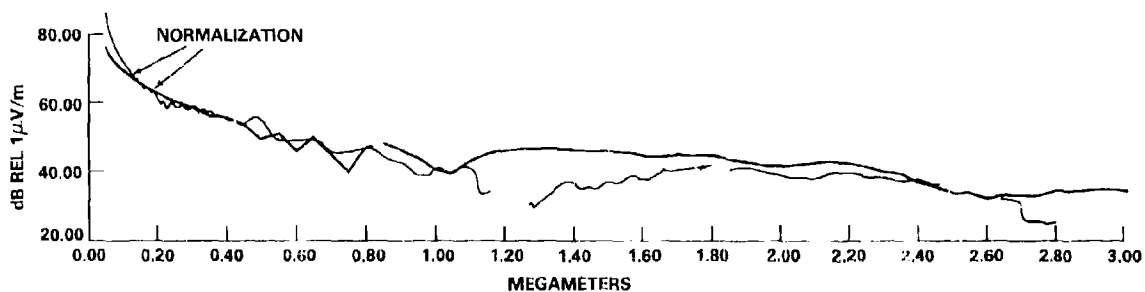


Fig. 29    Field strength versus distance data for Iceland transmissions
           on 80.0 KHz during flight from Keflavik, Iceland to Lajes, Azores
           during nighttime of 19 to 20 Mar 1977 at an altitude of
           approximately 24,000 feet.  Experimental data are shown by the light
           line.  Theoretical predictions are the heavy line.

# MEASURE OF E.C.D., TIME OF ARRIVAL, AMPLITUDE AND PHASE OF BOTH GROUND AND REFLECTED WAVES OF LORAN-C PULSES

J-C. Liévin, J-P. Hamaide,  W. Scholiers, J-P. Lechien
Université Libre de Bruxelles
Campus Plaine, C.P. 222, Boulevard du Triomphe,
1050 Bruxelles (Belgium)

## SUMMARY

We are studying the LORAN-C pulses emitted at 100 kHz by the Sylt station (Federal Republic of Germany) and received at Brussels situated at 514 km.  The pulses are analysed digitally.  After deconvolution of the received wave, the ground wave (measured before with high precision) is subtracted to obtain the reflected wave on the ionosphere.  This analysis provides accurate results for time of arrival, amplitude, phase, ECD of both ground and reflected waves.  The heights of the D layer of the ionosphere are also given.

## 1.    EXPERIMENTAL SET UP

The experimental set up (Guillaume, F., 1977) is composed by a home-made reception system for the LORAN-C signals (fig. n° 1).  Data acquisition and signal averaging are performed on-line by a MOTOROLA 6800 micro-computer.  The sampling frequency is 400 kHz and 256 data are memorized for a time interval of 640 $\mu$s.  The averaged pulse is obtained after a summation that depends of the noise amplitude.  The impulse response of the antenna-receiver system is measured by the same way : a 60 ns duration pulse is emitted by an auxiliary loop.

The preprocessed data are sent by a telex line to a CDC 6600 computer for complete processing (deconvolution and subtraction).  Now, the subtraction is done on-line by the micro-computer.

## 2.    NOISE AT THE OUTPUT OF THE RECEIVING SYSTEM

An amplitude difference of a factor 4 is currently observed for noise during a period of 24 hours.  To improve the speed of the data acquisition, we intend to adjust the number of the pulses averaged $(\eta)$ to the amplitude of noise $(\sigma_I)$ for a given accuracy $(\sigma_M)$ .   A study of correlation shows that the white noise hypothesis cannot be kept, as a set-off, noise is stationary for time up to 20 min.  This leads to the empirical relation

$$\sigma_M = a(\eta) \frac{\sigma_I}{\sqrt{\eta}}$$

where $\sigma_M$ is the standard deviation after a mean of $\eta$ pulses
    $\sigma_I$ is the standard deviation for one pulse
  $a(\eta)$ is an empirical factor
    $[a(256) = 1.09 ; a(512) = 1.18 ; a(1024) = 1.53]$.

## 3.    DECONVOLUTION

It is well known that the effect of a filter on a L.F. pulse is to produce on the carrier a delay depending mainly on the phase characteristics of the filter at the tuned frequency.  On the other hand, the slope of the envelop will also be affected.  Both delays – on the envelop and on the carrier – are in general different.

The utility of deconvolution appears in    . n° 2.  The external edges of the transfert function $H(\gamma)$ of LORAN-pulses must be corrected in taking into account of the transfert function of the receiving system $G(\gamma)$

The general procedure for deconvolution is given in the figure n° 3 where $h(t)$ represents the received wave and $g(t)$ the impulse response of the receiving system.  The method consists of determining the best number of Fourier coefficients i.e. the band-width of the transfert $H(\gamma)$ for a good restitution of the pulse at the antenna $f(t)$ (in amplitude and phase).  A band-width of 81.25 kHz to 118.75 kHz for $G(\gamma)$ was chosen.  A reconstruction of the form of the envelop at $10^{-3}$ of relative amplitude and a phase restoration at 10 ns is obtained.  This choice has been studied in detail (Lechien, J-P.) and will not be discussed here.

The fig. n° 4 shows for one particular case the difference in amplitude and phase between a non deconvolued pulse and a deconvolued one.

It is $f(t)$ that will be utilized for further calculations.

## 4.    OBTAINMENT OF THE REFLECTED WAVE

The received wave at Brussels (the total wave) is formed by the sum of the ground and the reflected wave on the D layer of ionosphere.  (Fig. n° 5).  Let us remark that the received ground and reflected waves are different of the emitted wave because of the dispersive effect of the propagation medium (respectively the whole sea-ground and ionosphere).

The fig. n° 6 gives an illustration of this wave superposition.

The total wave f(t) is represented by

$$f(t) = \sum_{i=0}^{1} f_i (A_i, t-t_i) \sin \left[ \omega (t-t_i) + \varphi_i \right]$$

where i = 0 charactrizes the ground wave and
    i = 1 the reflected wave
    $f_i$ is the form of the envelop
    $t_i$ the time of arrival of the pulse measured on the leading edge of the en  lop at 6) % of the maximum amplitude.
    $A_i$ the maximum amplitude of the envelop
    $\varphi_i$ the phase of the carrier
    ($t_i$ and $\varphi_i$ are measured related to the local clock).

The principal parameters studied in the experimental results are :

a) $\Delta t = t_1 - t_0$   the difference of time of arrival between the reflected and the ground wave

b) $ECD_0$ and $ECD_1$ (envelop to cycle discrepancy) is the interval between the time of arrival of the envelop and the phase (zero crossing of the carrier around the $t_i$ points).

We can extract the reflected wave from the measured wave f(t) by subtraction of the received ground wave. To perform a precise subtraction, the more exact form of the ground wave must be known : that is the more difficult point of our work.

5.    EVALUATION OF THE RECEIVED GROUND WAVE

The effect of dispersion is neglected and, therefore, the emitted wave can be taken instead of the received ground wave when we perform the subtraction.

We went (in July 1979) in the neighbourhood of the emitter (at 30 km) to measure accurately the emitted wave (not disturbed there by the reflected wave. First, the form observed is not the theoretical one ($t^2 e^{-\alpha t}$ announced in the literature) but presents many reboundings. The difference in the form of the two envelops is shown in the fig. n° 7. The carrier is not represented for the theoretical form. For clearness, we shall use this simplification many times in the following figures.

Using this emitted wave, and taking into account of the measured ECD of each pulse, many hundred pulses, spread on several days were interpreted. The results of subtractions are good but the form of the reflected wave presents a few irregularities when their relative amplitude $A_r$ is less than 25 % .

At the present time, we observe an unexpected difference between the wave form measured now and that obtained in July 1979. This deviation is explained by the existence of two power amplifier tank circuits having not the same turning frequency (Johnson, D., 1981). This fact gives no problem for navigation or clock synchronization but for subtraction, the precise knowledge of the two forms are needed. The results presented in this paper use the form measured in July 1979.

6.    EXPERIMENTAL RESULTS

6.1. Virtual height of the D layer of ionosphere

The difference of time of arrival between the ground wave and the reflected wave $\Delta t$, are directly interpreted in distance difference travelled by the two waves. From that, the virtual height of reflection is obtained. In this work, we admit an optical reflection on the D layer (fig. n° 5). Only simple reflection has been observed.

In the fig. n° 8, an example of subtraction is presented. In this pulse, the reflected wave arrives 103 $\mu$s after the ground wave ( $\Delta t$) that corresponds to h = 86 km, and his relative amplitude Ar is equal to 57 % . The validity of the subtraction can be tested in observing the form of the envelop and also in the constancy of the phase of the reflected wave.

A set of measurements during 24 h, is given : $\Delta t$ in $\mu$s on the upper part and Ar in percentage on the lower part of fig. n° 9.

During the night, $\Delta t$ varies around 105 $\pm$ 5 $\mu$s that leads to a virtual high of h = 87 $\pm$ 2.5 km. These variations observed during the night have a real physical meaning (movement of the height of the D layer) and are not due to a lack of precision of the measure.

During the day, we observe $\Delta t = 68 \pm 5$ $\mu$s i.e   . = 70 $\pm$ 2.5 km.

The relative amplitude Ar imposes two remarks :

a) the amplitude of the reflected wave is greater during the night than during the day. Sometimes (as around 04h30), the reflected wave is more important than the ground wave.

b) during the day, $\Delta r$ is often less than 25 % . In these conditions, we cannot obtain reliable values for $\Delta t$ and $ECD_1$ (dashed lines on the figures).

These remarks are valid for all our measurements made at different period of the year.

7.　　MEASURE OF E.C.D.

In order for a precise time user to determine his local clock error, he must know the propagation delay from the LORAN-C transmitter to his receiving antenna. For that, a quantitative measure of the dispersion of the propagation media, is necessary. The difference between the ECD of the received ground wave ($ECD_0$) and the emitted wave, give this information.

The fluctuations (in $\mu$ s) of $ECD_0$ and $ECD_A$ are presented as a function of time on the upper and the lower part of the fig. n° 10.

The mean value $\langle ECD_0 \rangle$ is equal to $2.6 \pm 1 \mu$s. The ECD measured in the neighbourhood of the emitter is $6.3 \pm 0.1 \mu$s. That leads to an ECD difference of $3.7 \mu$s for a distance of 514 km (190 km for sea propagation and 324 km for earth propagation).

The $\langle ECD_0 \rangle$ measured for days during Nov. and Dec. 1978 fluctuate around $2.6 \pm 2 \mu$ s.

The $\langle ECD_0 \rangle$ measured during Nov. 1979 and May 1980 fluctuate around $3.5 \pm 2 \mu$s giving $2.8 \mu b$ for ECD difference. For me, this discrepancy could be due to the change of transmitter.

Using the parametric curves giving the secondary phase correction factor as a function of distance and conductivity (Potts, C., 1972), we obtain $2 \mu$s. This value according to $3.7 \mu$s (1978) and $2.8 \mu$s (1980) is rather good on account of the approximation done on the sea ($\sigma$ = 5 m hos/m) and on the earth conductivity ($\sigma$ = 0.005 mhos/m). The variations of $ECD_A$ are given but not discussed.

8.　　CONCLUSIONS

Our results on the height of the D layer are in agreement with the values given in the litrature (Rawer, K., 1973). We intend to improve the form of the received ground wave to reduce the threshold of the reflected wave detection by taking dir,ersion into account.

Continuous and automatic processing will give throughover the year
- the profile of the D layer
- an evalua on of dispersion (E.C.D.$_0$ )

9.　　ACKNOWLEDGEMENT

10　　REFERENCES

- Guillaume, F., Liévin, J-C., De Prins, J., 1977, Study of L.F. and V.L.F. Time Signals by Digital Method, Atlantic City (New Jersey), presented at the 31st Annual Frequency Symposium.

- Johnson, B.D., 1981, Private Communication, U.S. Coast Guard Sylt.

- Lechien, J-P., Thèse de Doctorat, to be published.

- Liévin, J-C., Scholiers, W., Lechien, J-P., Detrie, R., 1980, Study of ground and Reflected waves of Loran-C Pulses by Digital Method, Braunschweig, Conference on Precision Electromagnetic Measurements (C.P.E.M. 80).

- Pott, C., Wieder, B., 1972, Precise Time and Frequency Dissemination via the Loran C System Proceedings of the IEEE, vol. 60, n° 5, May.
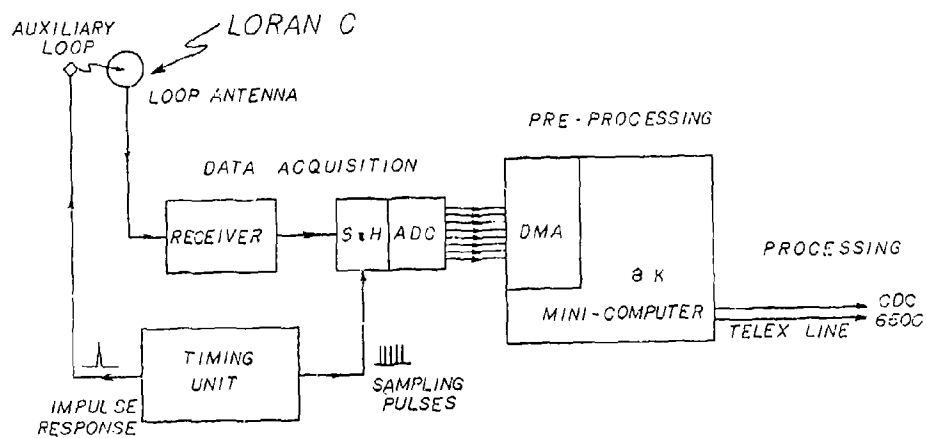
Figure 1



Figure 2



Figure 3

SYLT – NOV. 16 –1978 – 14h16

Figure 4



D LAYER of IONOSPHERE

Figure 5

$$f(t) = \sum_{i=0}^{1} f_i(A_i, t - t_i) \sin\left[w(t - t_i) + \varphi_i\right]$$
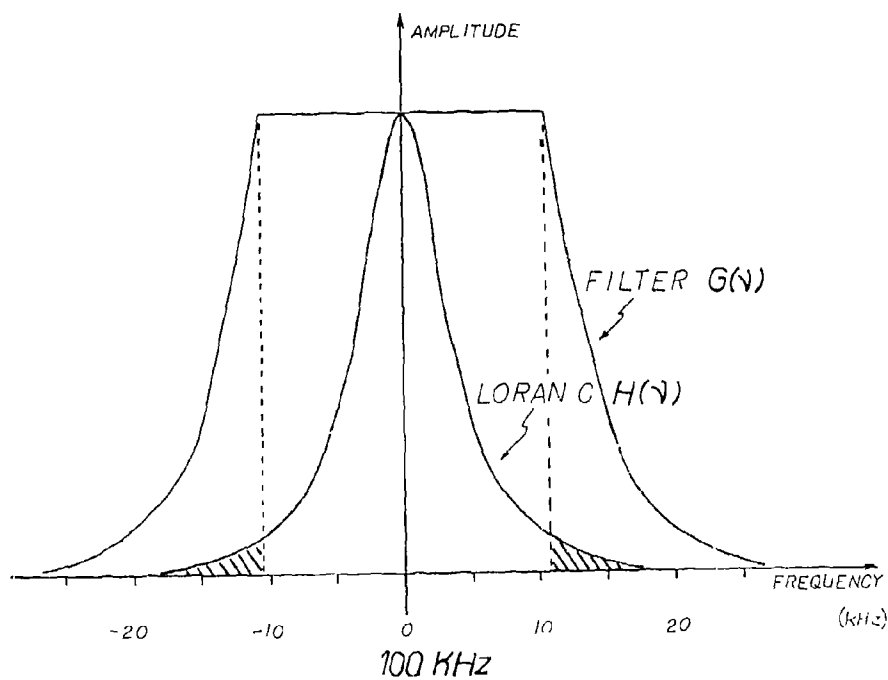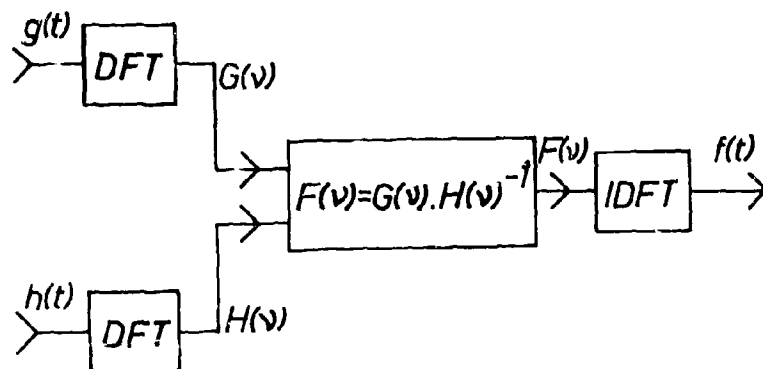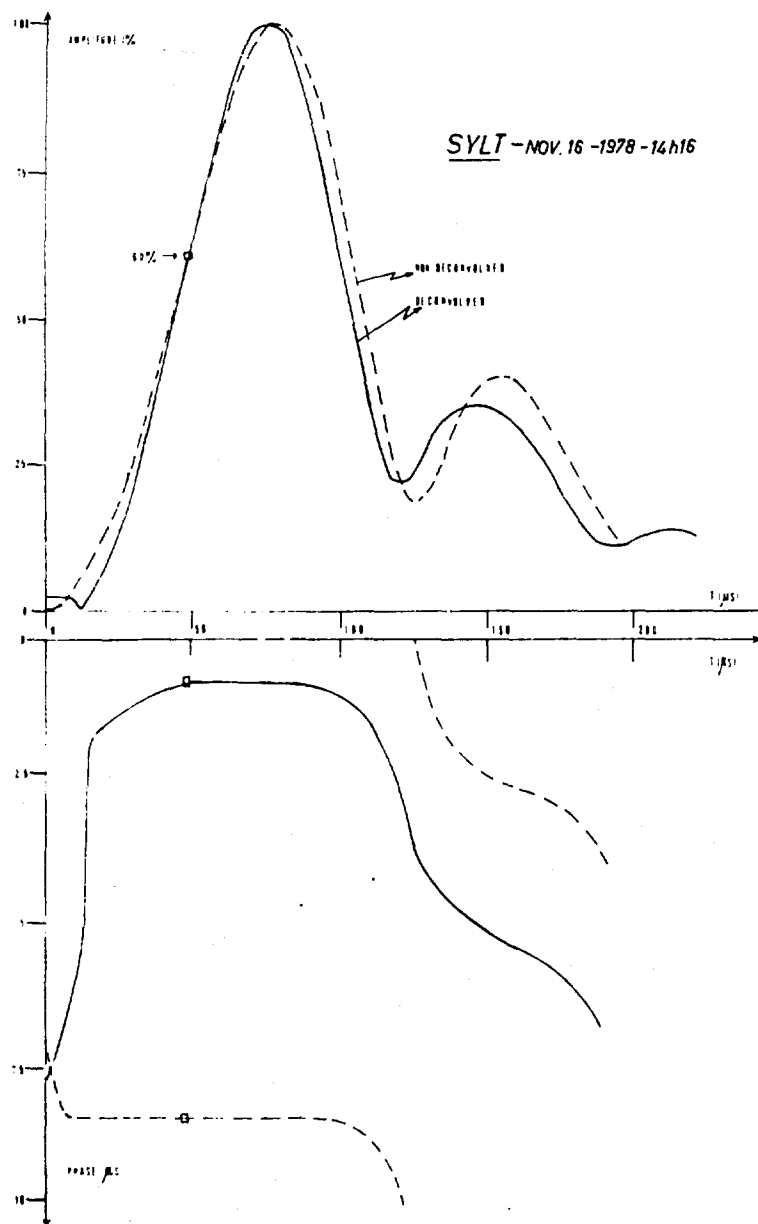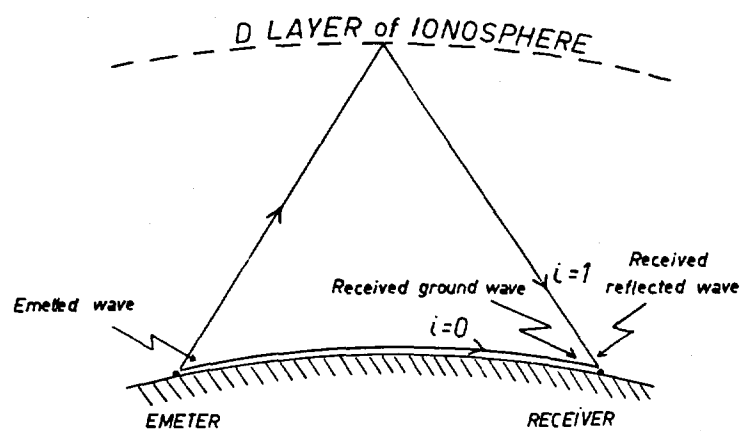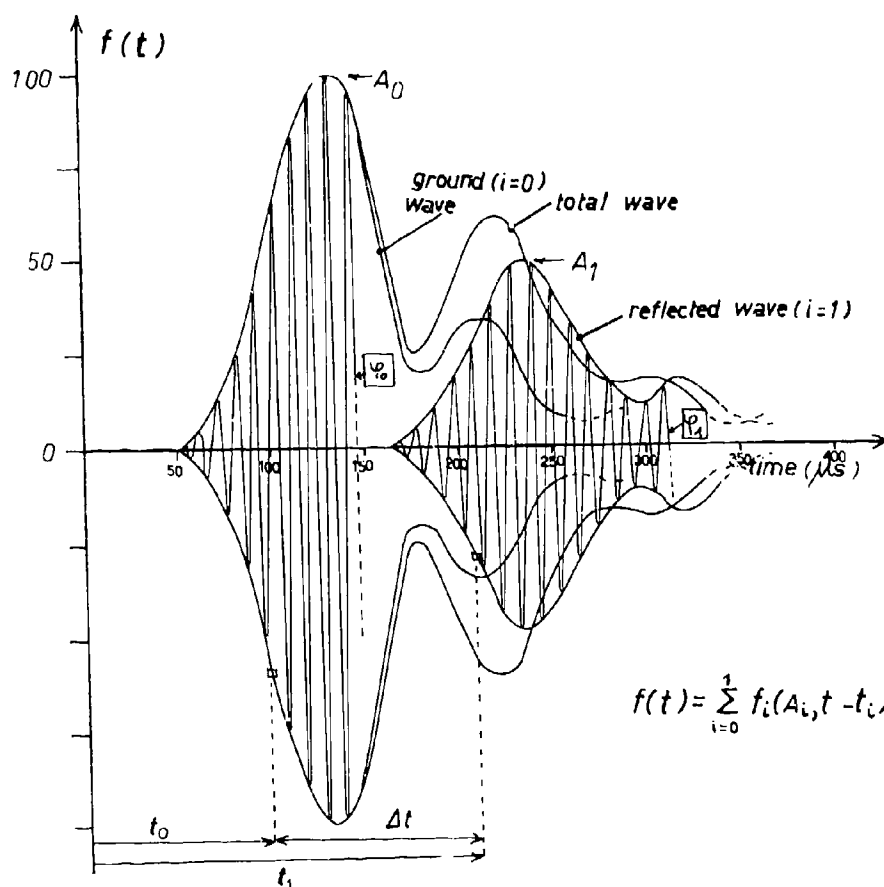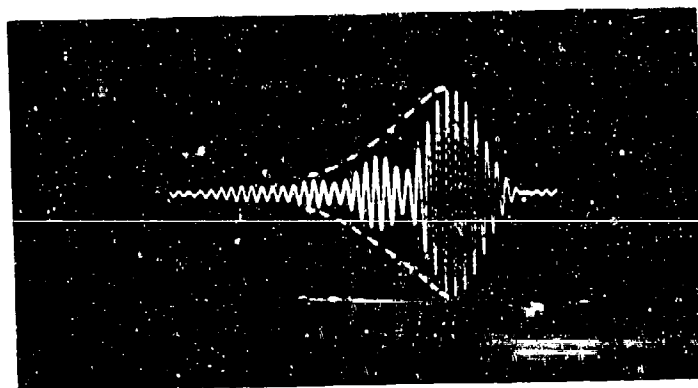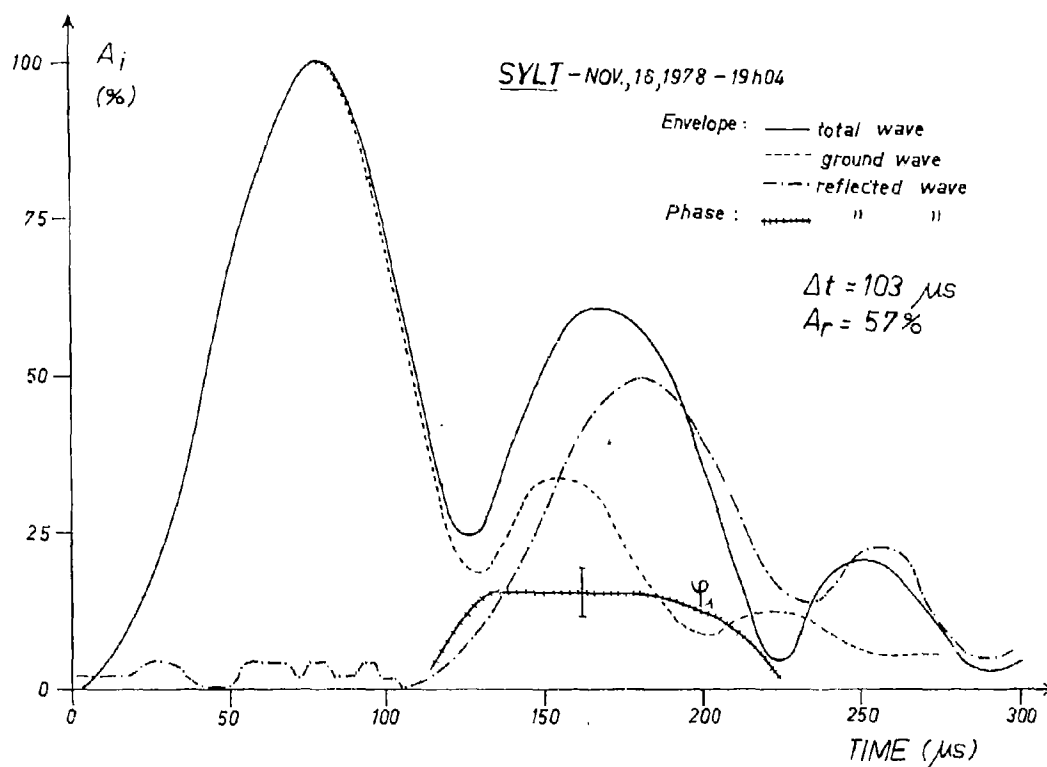
Figure 6



Figure 7

Figure 8
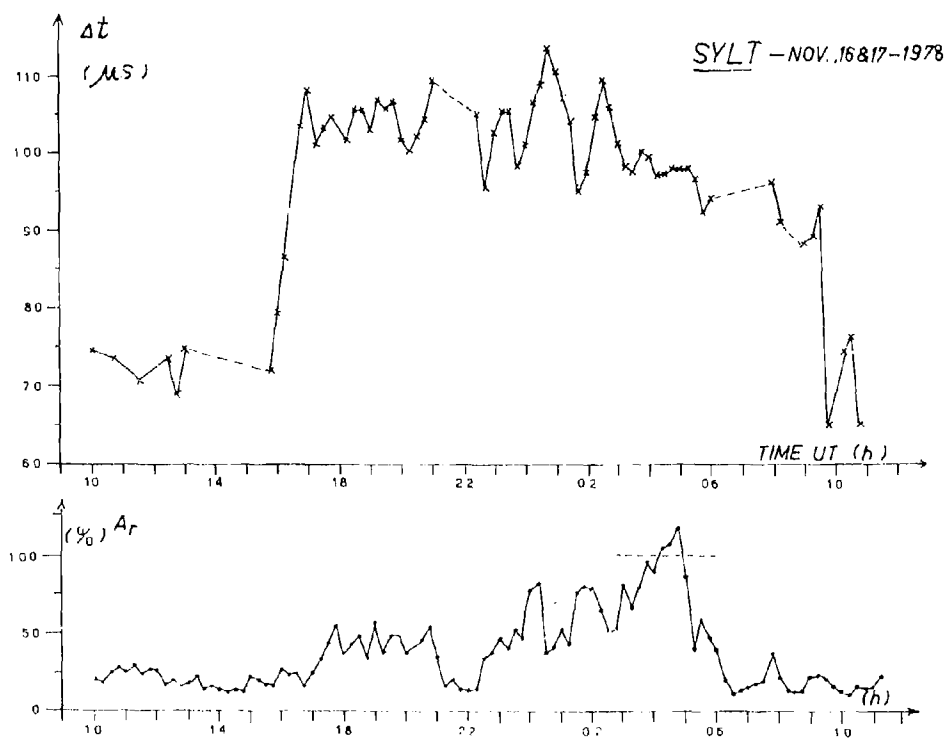


Figure 9
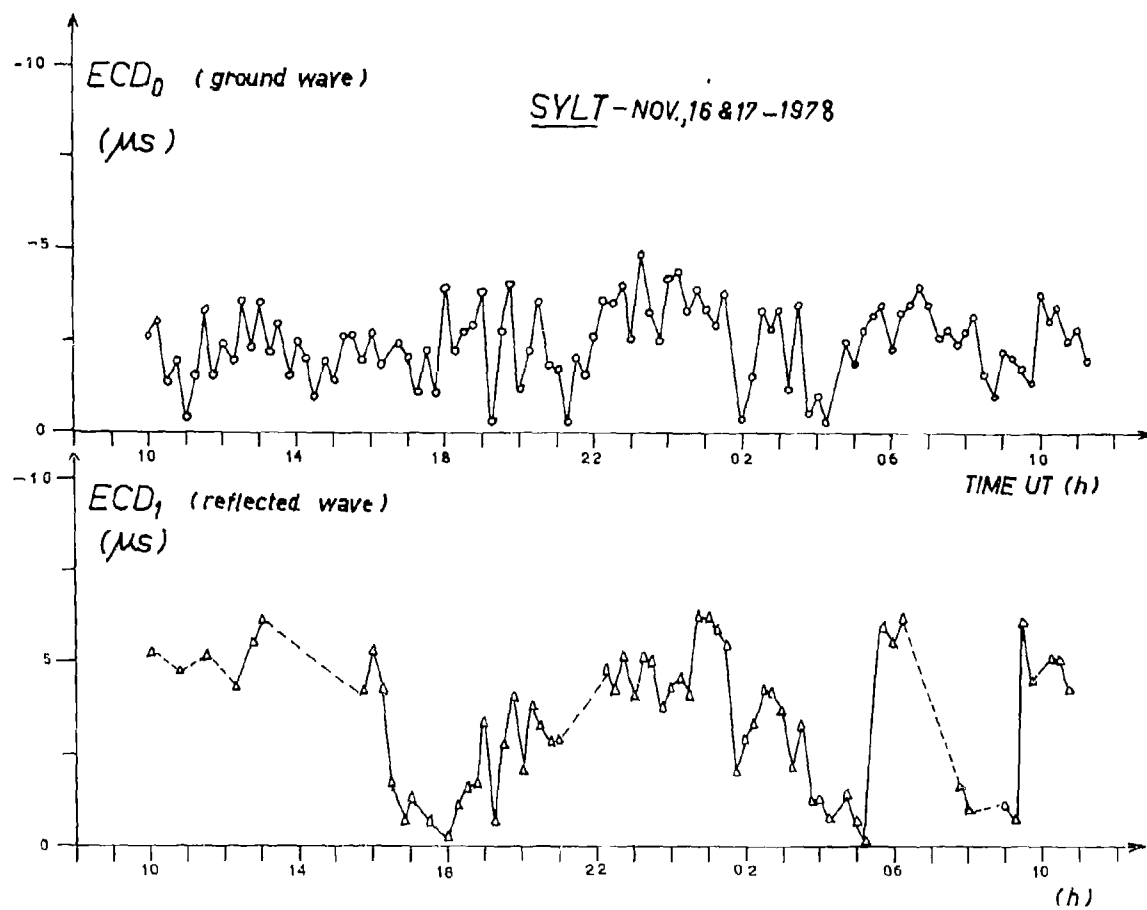
Figure 10

CONSIDERATIONS SUR LA ZONE DE SERVICE D'UN
EMETTEUR DE RADIODIFFUSION PUISSANT EN ONDES KILOMETRIQUES

par

J.Fonteyne
T.D.F., 21-27 rue Barbes
B.P. No.518
92542 Montrouge, Cedex
France

## 1 - PRÉSENTATION

La France est l'un des pays les mieux desservis en radiodiffusion dans la bande
kilométrique. En effet, 4 émetteurs fonctionnant dans cette bande sont reçus :

> ALLOUIS, émetteur de la radiodiffusion nationale (164 kHz, 2 000 kW,
> programme France Inter de Radio France),
>
> + DROITWITCH BBC 200 kHz ) 3 mV/m à Paris
>
> + DONEBACH 155 kHz
>
> + TIPAZA ALG 254 kHz
>
> SAARLOUIS, en Sarre RFA (182 kHz, 2 000 kW, programme Europe 1,)
>
> RADIO MONTE CARLO (218 kHz, 1 400 kW) et enfin,
>
> RADIO LUXEMBOURG à Marnach (236 kHz, 2 000 kW).

Aussi, l'on s'est très tôt préoccupé de la qualité de la desserte, surtout pour
l'émetteur d'ALLOUIS car le but de cet émetteur a toujours été la desserte de tout
le territoire.

Cette recherche des conditions d'écoute et de l'amélioration du confort passe par
l'établissement de cartes de zones de couverture (contours de champ), par l'étude
d'un diagramme de rayonnement favorable, et le contrôle de ce diagramme, la déter-
mination de l'effet d'une interférence entre l'onde de sol et l'onde ionosphé-
rique, ainsi que la recherche et l'élimination des perturbations radioélectriques,
en liaison avec une réglementation antiparasite adéquate.

## 2 - DÉTERMINATION DES COURBES DE CHAMP

Il n'est pas toujours aisé de déterminer les courbes de champ d'un émetteur, et la
superficie couverte est telle que l'on ne peut faire des mesures dans tous les
lieux habités.

Les courbes de champ montrées ici (figure 1) pour l'émetteur d'ALLOUIS sont le ré-
sultat de 2 000 mesures environ, sur 72 axes partant du centre émetteur, et éloi-
gnées de 10 km environ. De plus, de nombreuses mesures complémentaires ont été ef-
fectuées, soit qu'elles correspondaient à des axes d'autres émetteurs, soit
qu'elles semblaient nécessaires pour confirmer des mesures ou pour préciser la va-
leur du champ dans des zones habitées. Toutes ces mesures sont des mesures d'onde
de sol. En particulier, toutes les mesures en des points éloignés de plus de
400 km de l'émetteur ont été effectuées en dehors des périodes hivernales et dans
des conditions d'horaires strictes.

On pourrait en déterminer la conductivité du sol pour la fréquence en question
(164 kHz).

## 3 - DIAGRAMME DE RAYONNEMENT

L'excentricité - légère - du centre émetteur d'ALLOUIS, mais surtout la  diffé-
rence de conductivité du sol entre le nord (plaines généralement riches et culti-
vables) et le sud (avec en particulier le Massif Central, les Alpes et les
Pyrénées) ont incité les responsables à moduler légèrement la puissance apparente
rayonnée de l'émetteur.

L'antenne est constituée de 2 pylônes, dans l'axe Nord-Sud, et éloignés de 457 m
(soit   /4). Sur chaque pylône, de 350 m de haut, la dernière couronne de haubans
ne comporte aucun isolateur. Les autres haubans n'ont d'isolateurs qu'au niveau du
pylône et au sol. L'étude en a été effectuée dans le but de permettre l'écoulement
des charges statiques et de protéger les autres couronnes de haubans contre les
coups de foudre (Lacharnay, 1975).

Pour faciliter l'alimentation, un seul pylône est actif, et l'autre est refermé à la base sur une capacité. Le diagramme de rayonnement horizontal (figure 2), qui est à comparer avec la zone de couverture présente bien un maximum assez large vers le sud.

Le diagramme vertical dans l'axe des pylônes (figure 3) montre bien que le rayonnement d'un pylône ainsi réalisé s'apparente à celui d'un simple pylône quart d'onde alimenté à la base.

Ces mesures de diagramme par hélicoptère sont effectuées systématiquement par TDF, pour tous les émetteurs du réseau principal, que ce soit en radiodiffusion ou en télévision, à l'aide d'un équipement embarqué comprenant un mini-ordinateur. Les diverses données (champ pour 1 à 5 fréquences, données de position) sont enregistrées sur bande magnétique, ce qui permet de tracer dès la fin du vol le diagramme mesuré (Massucci, 1979).

## 4 - EFFETS DE LA RÉFLEXION IONOSPHÉRIQUE

Au-delà d'une certaine distance, la mesure du champ doit être effectuée avec précaution, car dès la tombée du jour, et même toute la journée en hiver, l'influence de l'onde ionosphérique est loin d'être négligeable (figure 4). Elle se manifeste par une augmentation importante du champ, accompagnée d'une variation lente du niveau. Mais les récepteurs s'accommodent bien d'une telle réception, car les variation sont lentes et la CAG a largement le temps de réagir. Par contre, la réflexion ionosphérique entraîne aussi une augmentation du niveau des émetteurs partageant le canal. Si la situation d'Allouis sur ce plan là est très bonne (voir le tableau I), il n'en est pas de même des autres émetteurs qui desservent la France. C'est ainsi que la couverture nocturne confortable de Europe 1 était assurée avec un champ minimal de 100 mV/m jusqu'à ce que l'on ait pu trouver un partage en fréquence plus favorable. Europe 1 à 185 kHz et Oranienb à 179 kHz.

La transmodulation ionosphérique figure parmi les effets les plus importants et les plus nuisibles de la réflexion ionosphérique.

Deux zones de gênes dues à la transmodulation limitent actuellement le service en bande kilométrique en France : la Bretagne où Europe 1 (et aussi, dans une moindre mesure, Luxembourg) subissent une transmodulation due à Allouis, et le midi de la France où Allouis subit une transmodulation de la part de Radio Monte Carlo.

Dans ce cas particulier, le taux de transmodulation dépasse par moments (en automne, en fin d'après-midi) 10% à 300 kHz, ce qui correspond à une qualité totalement inexploitable.

### TABLEAU I

Emetteurs partageant le canal et reçus en B. km en France

| ALLOUIS 164 kHz | SAA LOUIS 185 kHz | MONTE CARLO 218 kHz | LUXEMBOURG 236 kHz |
|---|---|---|---|
| Tachkent | Oranienbourg | Oslo | Kichiniev |
| 150 kW, 5200 km | 750 kW, 600 km | 200 kW, 1750 km | 1000 kW, 1700 km |
| | Ankara | Baku | Archangelsk |
| | 1200 kW, 2300 km | 500 kW, 3500 km | 150 kW, 2600 km |

## 5 - LES PERTURBATIONS RADIOÉLECTRIQUES

La bande kilométrique est particulièrement sensible aux perturbations radioélectriques, d'une part aux bruits naturels et d'autre part aux parasites dits industriels. L'utilisation intensive de cette bande en France entraîne un nombre important de réclamations, et une recherche active des appareils et installations perturbateurs.

Actuellement, les 20 à 30 000 réclamations annuelles sont traitées par une centaine d'agents régionaux, qui recherchent les appareils perturbateurs et les remèdes. La bande kilométrique est particulièrement affectée par les installations électriques, les appareils électroménagers et les installations de réception(voir le tableau II).

Les appareils électroménagers provoquent 1600 réclamations par an en bande kilométrique, contre 800 dans les autres bandes de radiodiffusion ou télévision. Ce sont essentiellement les dispositifs de commande à thyistors (variateurs, gradateurs d'éclairage domestique) et les contacteurs ou thermostats qui sont à l'origine des perturbations.

Les installations électriques provoquent 900 réclamations par an en bande kilométrique, contre 400 dans les autres bandes. Là encore, les dispositifs de commande et les contacteurs constituent l'essentiel des perturbations.

Enfin, les installations réceptrices provoquent 500 réclamations par an en bande kilométrique, contre 500 dans l'ensemble des autres bandes. La plus grande perturbation provient dans ce cas d'harmoniques de la fréquence de balayage des récepteurs de télévision. C'est ainsi que les émissions à 819 lignes du premier réseau de télévision correspondent à une fréquence de balayage de 20,475 kHz, et l'harmonique 8 (163,8 kHz) provoquait un battement gênant avec Allouis 164 kHz. L'on a dû décaler Allouis à 163,84 kHz pour que le battement soit moins gênant.

Le même problème se pose avec l'harmonique 14 du système à 625 lignes (218,75 kHz) sur Radio Monte Carlo 218 kHz et l'harmonique 15 (234,38 kHz) sur Radio Luxembourg (236 kHz).

Il résulte de tout cela que la France a très tôt été obligée d'instaurer une réglementation sévère pour les perturbations dans la bande kilométrique. La mise en harmonie avec les autres pays de la CEE (Directive 76/889 CEE) pour les appareils domestiques et les outils portatifs a entraîné une augmentation du niveau admissible des perturbations radioélectriques, et donc du champ à protéger. L'augmentation de 4 dB des perturbations radioélectriques à 150 kHz, déjà adoptée par le CISPR (Comité International Spécial des Perturbations Radioélectriques), et soutenu par certains pays de la CEE réduirait encore la couverture en radiodiffusion de notre pays, et n'est donc pas acceptable.

CONCLUSION

L'utilisation de la bande kilométrique pour la radiodiffusion permet une couverture quasi totale d'un pays comme la France avec un seul émetteur, mais entraîne aussi des contraintes, en particulier la nécessité de bien protéger la pureté du spectre, d'une part vis à vis des émetteurs étrangers, d'autre part vis à vis des perturbations radioélectriques.

L'installation pour la desserte d'un même pays, de plusieurs émetteurs de grande puissance en bande kilométrique entraîne cependant des transmodulations ionosphériques inévitables dont il faut tenir compte pour éviter une réduction trop importante de la zone de service.

Références bibliographiques

Lacharnay, "Antenne de radiodiffusion O.km protégée contre les charges statiques", Radiodiffusion-Télévision n° 36, février - mars 1975.

Massucci, "Relevé de diagrammes de rayonnement d'antenne d'émission à l'aide d'un hélicoptère", Revue de l'UER, technique n° 173, février 1979


Bibliographie

Radiodiffusion-Télévision, document n° 1.78 : "Radiodiffusion en ondes kilométriques et hectométriques" par Lacharnay S.

TABLEAU 2

Classification des sources de réclamations en
radiodiffusion sonore
Année 1980

| | | O KM | O HM | O DAM | II M.F |
|---|---|---|---|---|---|
| **I-S-M** | TOTAL A | 31 | 12 | | 4 |
| INDUSTRIELS ET SCIENTIFIQUES | | | | | |
| FREQENCES AUTORISEES | | 11 | 7 | | 3 |
| AUTRES FREQUENCES | | 6 | | | |
| MEDICAUX | | | | | |
| FREQENCES AUTORISEES | | 3 | 4 | | 1 |
| AUTRES FREQUENCES | | 2 | | | |
| A ETINCELLES | | 9 | 1 | | |
| **ENERGIE ELECTRIQUE** | TOTAL B | 157 | 31 | 23 | 70 |
| LIGNES > 100 KV ALT. | | | | | |
| LIGNES AERIENNES | | 4 | 1 | 10 | 13 |
| STATIONS | | | | | |
| LIGNES > 100 KV CONT. | | | | | |
| LIGNES AERIENNES | | | | | |
| STATIONS | | 7 | | | |
| LIGNES DE 1 100 KV | | | | | |
| LIGNES AERIENNES | | 118 | 16 | 11 | 56 |
| STATIONS | | 2 | 2 | 1 | |
| LIGNES DE 450 V A 1KV | | | | | |
| LIGNES AERIENNES | | 3 | 2 | 1 | 1 |
| STATIONS | | 1 | | | |
| BASSE TENSION < OU = 450V | | | | | |
| LIGNES AERIENNES | | 11 | 3 | | |
| STATIONS | | 1 | | | |
| TRACTIONS ELECTRIQUES | | | | | |
| CHEMINS DE FER | | 2 | | | |
| TRAMWAYS | | 2 | 2 | | |
| TROLLEYBUS | | 6 | 5 | | |
| **INSTALLATIONS ELECTRIQUES** | TOTAL C | 928 | 119 | 20 | 25 |
| GENERATEURS | | 1 | | | |
| MOTEURS P > 700 W | | 41 | 12 | 4 | |
| CONTACTS | | 184 | 30 | 7 | 12 |
| SYSTEMES D ALLUMAGE | | 31 | 7 | | 1 |
| REDRESSEURS | | 15 | 4 | 1 | |
| CONVERTISSEURS | | 4 | 1 | | |
| VARIATEURS | | 547 | 58 | 5 | 5 |
| CLOTURES ELECTRIQUES | | 143 | 7 | 3 | 7 |
| **APPAREILS ELECTROMENAGERS** | TOTAL D | 1565 | 235 | 39 | 35 |
| MOTEURS P < 700 W | | 92 | 21 | 5 | 1 |
| CONTACTS,THERMOSTATS | | 664 | 141 | 33 | 32 |
| CDES A DIODE,THYRISTOR (P<1000W) | | 809 | 73 | 1 | 2 |
| **LAMPES A DECHARGES** | TOTAL E | 212 | 57 | 4 | 12 |
| LAMPES A FLUORESCENCE | | 63 | 35 | 2 | 1 |
| ENSEIGNES AU NEON | | 146 | 21 | 2 | 11 |
| LAMPES A FILAMENT | | 3 | 1 | | |
| **INSTALLATIONS RECEPTRICES** | TOTAL F | 493 | 28 | 4 | 16 |
| RECEPTEURS RADIO | | 32 | 4 | 1 | 10 |
| RECEPTEURS T.V | | 449 | 20 | 3 | 1 |
| SYSTEMES D ANTENNE ACTIVE | | 3 | 3 | | 5 |
| RECEPTEURS AUTRES QUE R ET TV | | 9 | 1 | | |
| **ALLUMAGES MOTEURS** | TOTAL G | 2 | 2 | 1 | 5 |
| **AUTRES SOURCES** | TOTAL H | 12 | 1 | | 2 |
| A+B+C+D+E+F+G+H | TOTAL I | | | 91 | |

Courbes de Champ de
l'émetteur 0km d'ALLOUIS

F = 163,84 kHz     Pn = 2100 kW
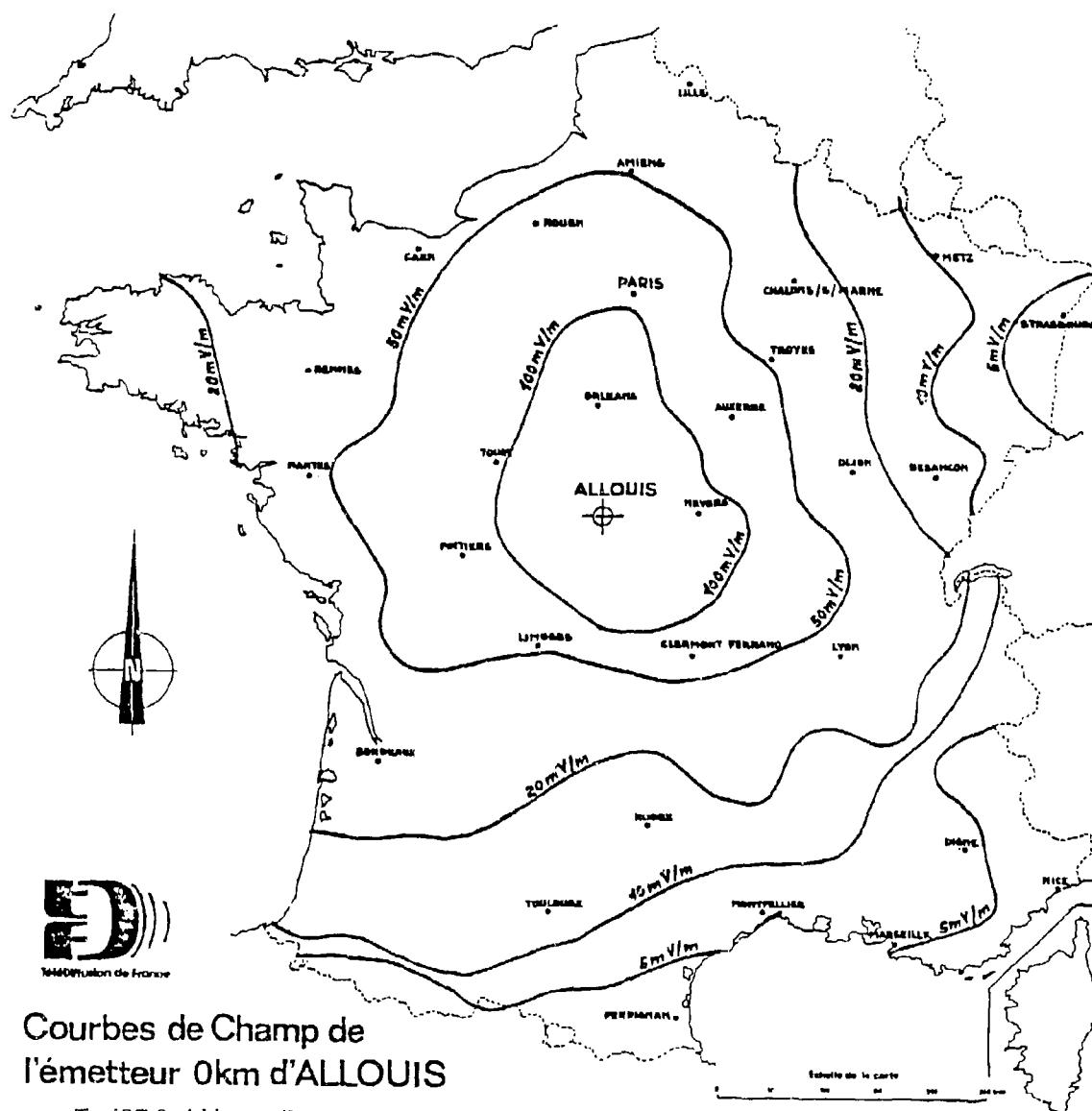
Figure 1

# ÉMETTEUR Okm : ALLOUIS

FREQUENCE: 164 kHz
Polarisation : V

## DIAGRAMME DE RAYONNEMENT A SITE CONSTANT : 1°

Gain/antenne verticale courte : 0,53 dB

Ng

P. nominale   2100 kW
P.A.R.V.      2375 kW
F.C.M.        203,3 dB (µV)
(Niveau OdB de l'échelle)

Échelle linéaire en champ

dB

Axe d'alignement
des pylônes

Distance des mesures :

——— 5 km

——— 7 km

—·—· 20 km

— — — Gabarit du diagramme théorique calculé à partir
des courants à la base des pylônes.

—●— Azimuts des vols verticaux

457m   Hauteur des
pylônes 350 m

| Configuration de l'antenne | |
|---|---|
| Pylône NORD : | Alimenté |
| Pylône SUD : | Fermé sur capacité |
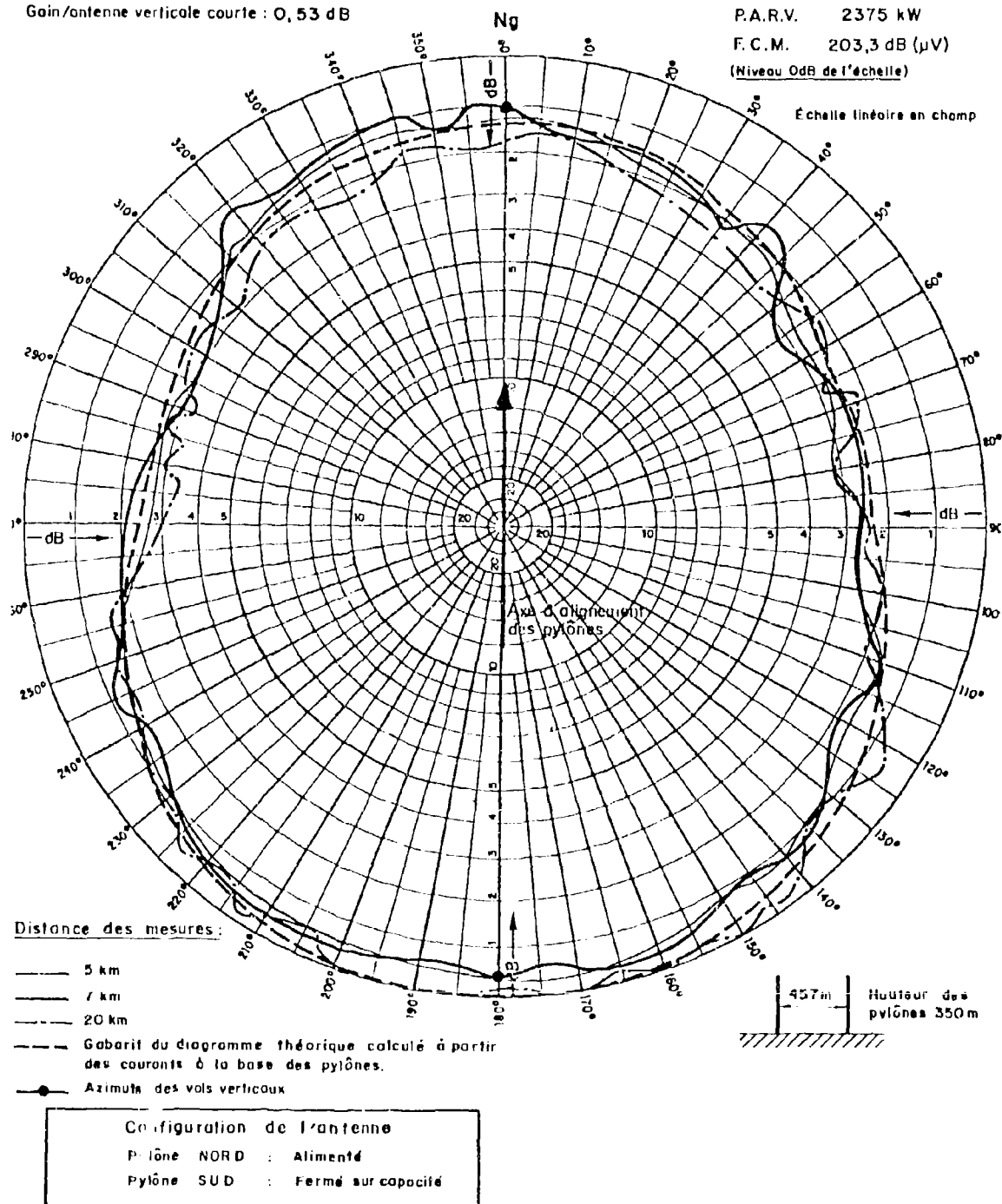
Figure 2

# ÉMETTEUR  O km : ALLOUIS

FRÉQUENCE: 164 kHz
Polarisation : V

## DIAGRAMME DE RAYONNEMENT VERTICAL

Gain/antenne verticale courte : 0,53 dB
Distance de la mesure : 4000 m

P. nominale   2100 kW
P.A.R.V.        2375 kW
F.C.M.         203,3 dB (µV)
(Niveau OdB de l'échelle)

Echelle linéaire en champ

Az : 180°

Az : 0°

——— Mesure en hélicoptère
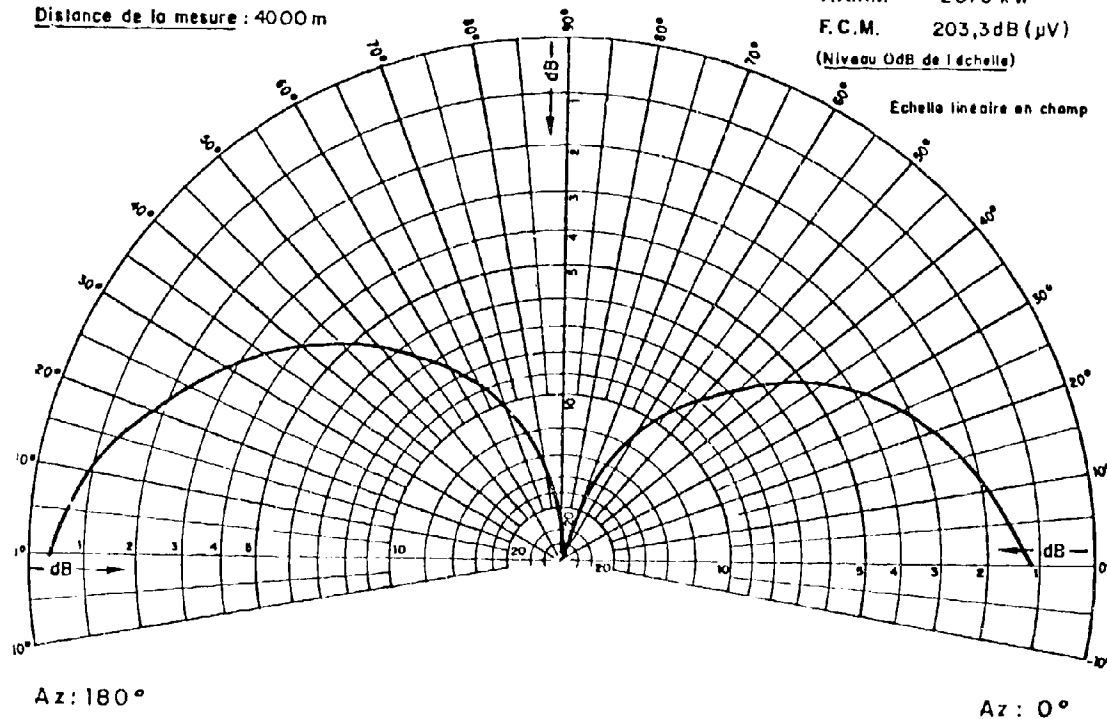
Configuration  de l'antenne
Pylône   NORD   :  Alimenté
Pylône   SUD     :  fermé sur capacité

Figure 3

Monte Carlo — Limours
218 kHz , 630 km

mesures de jour
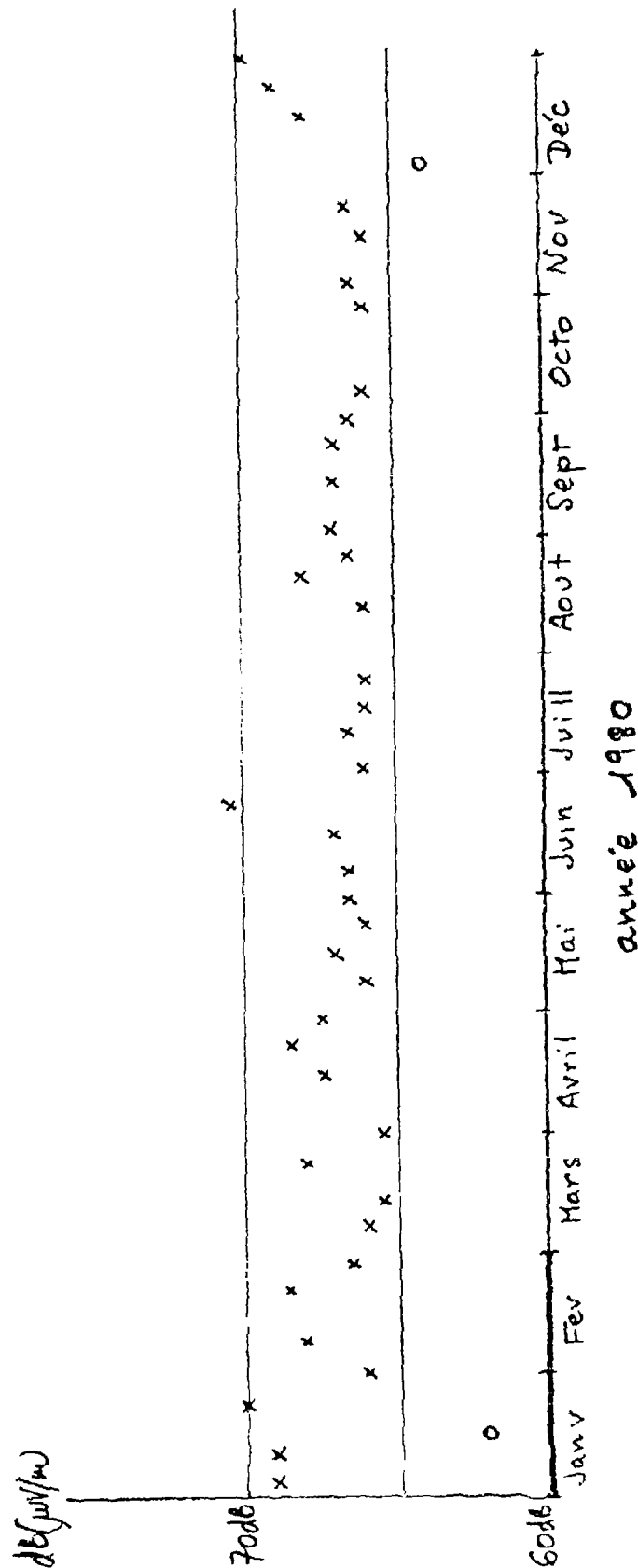
Figure 4

DISCUSSION EPP FALL 81 MEETING
MEDIUM, LONG, AND VERY LONG WAVE PROPAGATION
(AT FREQUENCIES LESS THAN 3000 KHZ)

SESSION 4

PAPER : 22. LF PROPAGATION : AN OVERVIEW
AUTHOR :   J. S. Belrose
COMMENTER : R. H. Doherty
COMMENT : The one-hop Loran-C measurements in the Hawaiian area showed results very similar to
the European observations. The one-hop Loran-C measurements in the Aleutians showed results
identical to your Canadian ones. During the late 1960's when we ran the Hands experimental
station in Boulder, the east coast to boulder measurements would show the typical trapezoid
like you see in Canada during the summer months and then we would switch over to the Cos Chi
pattern during the winter months. We could almost detect when this would happen particularly in
the spring around 21 March. It was not so clear in the fall. That of course doesn't tell what
happens over a solar cycle, it was only for three or four years.

RESPONSE : Thank you I guess that indicates a limitation to my overview, which should have been
covered.

PAPER : 22. LF PROPAGATION : AN OVERVIEW
AUTHOR :   J. S. Belrose
COMMENTER :   J. S. Reagan
COMMENT   :   The difference in the diurnal pattern of VLF and LF phase between Canada and Europe
at the same magnetic latitude may be explained by the difference in the magnetospheric electron
population above the ionosphere at the two locations i. e. a difference in the flux densities
of energetic electrons in the Van Allen radiation belts. Due to the existence of the south
Atlantic magnetic anomaly between North America and Europe the electron population over North
America is approximately 1000 times higher than over Europe on the same L-shell. These
energetic electrons mirror down low in the atmosphere where they create a "drizzle" ionization
in the D-region that is probably sufficiently intense to effect sensitive VLF and LF
propagation. The larger fluxes over North America would result in stronger effects at Ottawa,
for example, than over an equivalent station in Europe. Seasonal effects in the density of the
neutral atmosphere will effect the height where these electrons are stopped, and hence the
height profile of the ionization will vary with the season. The electron population is ever
present but varies in intensity as a function of latitude, longitude and magnetic activity.

RESPONSE   :   A drizzle from the radiation belts has been the explanation of the magnetic storm
after effect for quite some time But the concept of it going on day-after-day is something I
had not entertained. The ionization densities due to this "drizzle" are undoubtedly small,
although as you say they could be sufficient to affect LF phase and amplitude, since a marked
effect is not discernible in measured electron density profiles. The electron density at say 60
Km during the day at $x=60°$, is about $10^2$ electrons over Thumba, in India, Wallops Island, and
Ottawa, as well as in Europe. The drizzle phenomena however would affect mainly the change
ionization over dawn, which has not been studied in any detail.

PAPER : 22. LF PROPAGATION : AN OVERVIEW
AUTHOR :   J. S. Belrose
QUESTIONER : W. C. Bain
QUESTION   :   When you were speaking of the phase changes in European circuits, is it the case
that besides the phase changes during the day, there is also a substantial phase change before
ground sunrise?

RESPONSE : The changes before ground sunrise have been interpreted by me as due to an amplitude
change and a polarization change rather than a height change. There is however a height change
in VLF propagation as observed by yourself and others at 16 Hz over paths of about 600 Km.

PAPER : 24. LOW FREQUENCY RADIO WAVE PROPAGATION IN THE ATLANTIC AND MEDITERRANEAN AREA
AUTHOR :   F. J. Kelly
COMMENTER :   J. S. Belrose
COMMENT : In CCIR reports concerned with low frequency and very low frequency propagation the
recommendation was made therein that aircraft data (Hollingworth patterns) measured by flying
between transmitters and fixed receivers in fact over-flying the receivers could provide useful
data which would help in the interpretation of the fixed receiver data and the fixed receiver
data would also help in providing a reference as to whether or not propagation was normal on
that day. Though that recommendation has been with us for some time, very few experiments have
been done. I would like to comment on measurement of phase with an aircraft-borne receiver. In
the measurements at 30 KHz that were made in Canada we recorded phase as well as amplitude, but
we never got anything useful out of the phase, because the phase change with distance was so
rapid that when you subtracted the phase change due to distance change you were left with a
very uncertain residual which did not change systematically with distance.

PAPER : 24. LOW FREQUENCY RADIO WAVE PROPAGATION IN THE ATLANTIC AND MEDITERRANEAN AREA
AUTHOR :   F. J. Kelly
QUESTIONER :  W. C. Bain
QUESTION  :  I  suggest  that  it  would help in using your data for the purposes of scientific
research if you could plot the portion of the results near to the transmitter  in  a  different
way. I would reccommend the use of a linear instead of a decibel scale in that region, possibly
also using (signal strength x distance)

RESPONSE : Thank you for the suggestion.

PAPER : 24. LOW FREQUENCY RADIO WAVE PROPAGATION IN THE ATLANTIC AND MEDITERRANEAN AREA
AUTHOR :   F. J. Kelly
QUESTIONER :   T. B. Jones
QUESTION  :  The agreement you obtained between the calculated and measured field strengths was
on the whole rather good. Did you consider  using  more  realistic  D-Region  electron  density
profiles? This could probably reproduce some of the day-to-day variability which you observed.
RESPONSE : We have used  several  experimental  profiles,  one  using  a  C-Layer  for  daytime
comparisons. For the nighttime comparison we used only the model proposed by Berry and Herman.

PAPER : 25. MEASURE OF THE ECD TIME OF ARRIVAL, AMPLITUDE AND PHASE OF BOTH GROUND AND SKYWAVES
OF LORAN C-PULSES
AUTHOR :   J. C. Leivin
QUESTIONER :   J. S. Belrose
QUESTION  :  I  spoke  earlier this morning about the difficulties in separating ground and sky
waves in C-W experiments. Your work  reveals  that  this  is  also  the  case  for  the  pulsed
experiment.
In your figure 8, where you show $\Delta T$ as a function of the time of day, the  variation  is  rather
trapezoidal. It would be interesting to know if this is consistent from day-to -day.

RESPONSE : Yes, it is. It is sharp at sunrise.

PAPER : 25. MEASURE OF THE ECD TIME OF ARRIVAL, AMPLITUDE AND PHASE OF BOTH GROUND AND SKYWAVES
OF LORAN C-PULSES
AUTHOR :   J. C. Leivin
QUESTIONER :   J. Schaefer
QUESTION  :  Are  you able to deduce a real D-Layer profile from your measurements (rather  than
only a certain reference height)?
RESPONSE  :  The heights given by the method proposed is one of the parameters useful for clear
understanding of the D-Layer of the ionosphere.

# MEDIUM FREQUENCY PROPAGATION : A SURVEY

P. Knight

British Broadcasting Corporation

Broadcasting House, London W1A 1AA

## SUMMARY

At medium frequencies, ground waves and sky waves are both of equal importance. Ground waves provide stable signals during the day, when sky waves are k. At night sky waves propagate to considerable distances with very little attenuation but are mo  ariable.

Published ground-wave propagation curves apply to and which is smooth and of uniform conductivity, but this condition is rarely satisfied in practice. The paper describes methods for calculating field strengths along mixed land-sea paths, over irregular terrain and through built-up areas.

An interesting feature of sky-wave propagation arises because the Earth's gyromagnetic frequency lies within the frequency band being considered. This gives rise to polarisation coupling loss, which is of considerable importance in tropical regions, and to further coupling loss between hops on multi-hop paths. Enhanced ionospheric cross-modulation also occurs at the gyromagnetic frequency.

## 1. INTRODUCTION

At medium frequencies (300 - 3000 kHz) ground-waves and sky-waves are both of equal importance. Ground waves are used extensively for broadcasting at the lower frequencies in the band. They provide stable signals, especially during the day, when sky-waves are greatly attenuated by the lower ionosphere. At night sky-waves are able to propagate to considerable distances with very little attenuation.

Section 2 of the paper discusses the practical aspects of ground-wave propagation. Propagation curves, such as those published by the CCIR, apply to land which is smooth and of uniform conductivity, but this condition is rarely satisfied in practice. The ground may be of variable conductivity and sections of the propagation path may be over sea water, which has a much greater conductivity than dry land. A method for calculating field strength along mixed land-sea paths is described and the effect of irregular terrain is also considered. It is shown that propagation through cities and built-up areas can be explained by assuming that the ground behaves as an inductively-loaded surface.

Section 3 is concerned with sky-wave propagation, where a transition between E - layer reflection and propagation via the F layer occurs in the frequency band being considered. At the lowest frequencies in the band, waves are reflected from the lower side of the E layer with relatively little loss, because they do not penetrate very deeply into the layer. At higher frequencies, sky-waves may traverse the E layer and be reflected from the F layer; their propagation then has more in common with the type of propagation observed at h.f. An interesting feature of sky-wave propagation arises because the Earth's gyromagnetic frequency lies within the m.f. band. As a consequence, the extraordinary wave of the magnetic-ionic theory is greatly attenuated and only the ordinary wave propagates efficiently.

## 2. GROUND-WAVE PROPAGATION

Ground waves propagate efficiently between vertical antennas close to the ground. The transmission loss between a pair of antennas depends on the ground conductivity and frequency, on Earth curvature and on the roughness of the intervening terrain. It is also influenced by buildings and trees on the propagation path. Before considering these effects in detail, it is instructive to consider propagation between two elevated antennas situated above a plane earth and to see how the transmission loss is modified when the frequency decreases and when the antennas are close to the ground.

### 2.1. Propagation over a plane earth

Fig. 1 shows two antennas A and B situated above a uniform plane earth. Suppose that A radiates a wave of either polarisation. If the distance AP is sufficiently great, the wave incident at P is indistinguishable from a plane wave, and the Fresnel plane-wave reflection coefficients may be used to calculate the reflected-wave field strength. The voltage induced in antenna B by the direct and ground-reflected waves is then given by

$$V = QI \left[ \frac{Q_1 e^{-jkr_1}}{r_1} + \frac{Q_2 R e^{-jkr_2}}{r_2} \right] \qquad (1)$$

where I is the current in antenna A, $Q$, $Q_1$ and $Q_2$ are constants and R is the appropriate reflection coefficient, provided the distance between the antennas is large compared with the wavelength $\lambda$. The constants $Q_1$ and $Q_2$ take account of the vertical radiation patterns of the antennas, and $k = 2\pi/\lambda$.

Before proceeding further, the reflection mechanism must be considered. Antenna A induces currents in the ground; if the ground behaves as a conductor the current is a conduction current and if it behaves as a dielectric the current is a displacement current. Re-radiation by these currents generates the reflected wave.

A useful concept is that of the first Fresnel zone on the ground. This is an elliptical area shown in Fig. 1 which contains the optical reflection point P. Contributions from the boundary of the zone lag behind the contribution from P by 180°. Contributions from within the zone re-inforce each other, but contributions from points outside the zone differ widely in phase and tend to cancel. Thus the contributions from within the zone are mainly responsible for the reflected wave, and the size of the zone therefore influences the

strength of the reflected wave.

When both antennas are at a finite distance from P the area of the zone is slightly less than it would be if one of the antennas were at infinity. If the reduction in area exceeds, say, 10%, the reflected-wave term in Equation (1) will be in error. In practice it transpires that Equation (1) is nearly always valid at u.h.f. and v.h.f., frequently at h.f. but seldom at m.f. and l.f.

When the use of Equation (1) is not justified a correction term may be added as follows

$$V = Q1 \left[ \underbrace{\frac{Q_1 e^{-jkr_1}}{r_1}}_{\text{Direct wave}} + \underbrace{\frac{Q_2 \, Re^{-jkr_2}}{r_2}}_{\text{Reflected wave}} + \underbrace{\frac{Se^{-jkr_2}}{r_2}}_{\text{Surface wave}} \right] \tag{2}$$

$$\underbrace{\hspace{6cm}}_{\text{space wave}}$$

The direct and reflected waves are together known as the space wave. The correction is called the surface wave because it is the only term which remains when both antennas are very close to the ground.

The factor S in Equation (2) is a complicated function of the ground constants, polarisation and antenna positions. Its derivation, first given by SOMMERFELD (1909), is complicated but Sommerfeld's formulae have been arranged in a convenient form by NORTON (1936,37). A more detailed discussion is given by JORDAN and BALMAIN (1968).

When both antennas are very close to the ground, $\psi_1 = \psi_2 \simeq 0$, $Q_1 = Q_2$, $r_1 = r_2$ and R = -1 for both vertical and horizontal polarisation. Equation (2) then simplifies to

$$V = Q1 \, \frac{S \, e^{-jkr}}{r} \tag{3}$$

where r is distance between the antennas. It can be shown from Norton's equations that S diminishes very rapidly with increasing distance with horizontal polarisation but not with vertical polarisation. Horizontally-polarised surface waves suffer such rapid attenuation that they need not be considered further.

At l.f. and m.f., the use of elevated transmitting aerials is impracticable because the wavelength is of the order of 1 km. Vertical aerials erected on the ground are efficient radiators of vertically-polarised surface waves, known as ground waves. These waves have a vertical electric-field component $E_z$ accompanied by a smaller component $E_\rho$ which acts in the direction of propagation. The wave also contains a transverse magnetic-field component $H_\phi$ which is approximately equal to $-E_z/\eta_0$, where $\eta_0$ is the intrinsic impedance of free space. Of the two electric-field components, $E_z$ predominates. The vector product of $E_z$ and $H_\phi$ describes the power flow in the direction of propagation. The smaller vector product of $E_\rho$ and $H_\phi$ corresponds to a downward flow of power into the Earth's surface and accounts for the attenuation of the wave which is additional to that due to the inverse distance term. The attenuation is greatest when the ground is a poor conductor, and it increases as the frequency increases.

The ground wave would be attenuated even if the ground were a pure dielectric, because $E_\rho$ would still be finite and the downward power flow would still occur. The power entering the earth would not be dissipated, however, but would propagate downwards without loss. With a pure dielectric, $E_z$ and $E_\rho$ would be in phase and the wavefront above the Earth's surface would be tilted downwards.

In a further simplification (NORTON 1936,37,1941), the modulus of $E_z$ is expressed in the form

$$E_z = \frac{300 \sqrt{P}}{r} A \tag{4}$$

where A is called the ground-wave attenuation factor and P is the radiated power. Equation (4) then gives the field strength produced by a short vertical aerial radiating P kW; if r is in metres, $E_z$ is in V/m and if r is in km, $E_z$ is in mV/m. The quantity $300\sqrt{P}$ is sometimes called the cymotive force.

Fig.2 shows computed values of A expressed in terms of two parameters p and b, called the numerical distance and phase constant respectively. These parameters are defined as follows

$$p \simeq \frac{\pi r}{\lambda x} \cos b \tag{5}$$

$$b \simeq \arctan \frac{\epsilon_r + 1}{x} \tag{6}$$

where

$$x = \frac{18 \times 10^3 \sigma}{f} \tag{7}$$

$\sigma$ is the ground conductivity in S/m and f is the frequency in MHz. $\epsilon_r$ is the dielectric constant.

To illustrate the application of Norton's method, it is used here to calculate the field strength at a distance of 15 km from a short vertical aerial radiating 10kW at 1MHz, assuming the ground conductivity to be $10^{-2}$ S/m and its dielectric constant equal to 10.

The cymotive force with which the aerial radiates is $300\sqrt{10}$. In the absence of ground wave attenuation (i.e. with a perfectly conducting earth), the field strength at 15 km would be $300\sqrt{10}/15 = 63.1$ mV/m.

For the stated ground constants, $\epsilon_r = 10$ and x = 180. Equations (5), (6) and (7) give p ≈ 0.74 and b ≈ 31°. The ground-wave attenuation factor given by Fig.2 is 0.51. The actual field strength is therefore 63.1 x 0.51 = 32 mV/m or 90 dB relative to 1 μV/m.

## 2.2. The effect of Earth curvature

Although the theory which has been described above assumes that the Earth is flat, this does not give rise to serious errors at m.f. for distances less than 100 km. At greater distances, however, Earth curvature increases ground-wave attenuation.

The formal solution for propagation over a spherical Earth was first derived by VAN DER POL and BREMMER (1937) and is extremely complicated. However Norton has again presented the result in a form which can be readily applied; full details are given in NORTON (1941).

In applying Norton's method a factor which has to be considered is the effective radius of curvature of the Earth. At v.h.f. and u.h.f., the effect of atmospheric refraction can be taken into account by assuming that the Earth has an effective radius which is 1.33 times the true radius. At very low frequencies, however, the thickness of the atmosphere is small compared with the wavelength and it has no significant effect; at these frequencies, therefore, the true radius must be assumed. At l.f. and m.f. the atmosphere has some effect on ground-wave propagation and it has been shown (ROTHERHAM, 1970) that this can be taken into account by multiplying the true radius by frequency-dependent factors which are less than 1.33; at 1 MHz, for example, the effective radius is about 1.25 times the true radius.

In practical applications it is more convenient to make use of propagation curves, such as those published by the CCIR (1974), which have been calculated by the methods described above.

## 2.3. Mixed-path propagation

Published propagation curves are calculated on the assumption that the ground conductivity has a uniform value over the entire path. This assumption is seldom true in practice.

For an all-land path with variable conductivity, sufficient accuracy can usually be obtained by assuming a weighted mean conductivity for the whole path and then using the appropriate propagation curve. This method is not sufficiently accurate for mixed land-sea paths, however, because the conductivities of land and sea differ by a factor of about $10^3$.

The following semi-empirical method due to MILLINGTON (1949) is found to give reliable results for mixed paths and should always be used for mixed land-sea paths. Suppose that 100 km of land is followed by 50 km of sea. For the first 100 km the propagation curve for land must apply; for the remainder of the path the propagation curve for sea can be moved downwards and joined to the land curve, as shown in Fig.3. The field strength at 150 km is therefore represented by the point Y. If the direction of propagation is reversed, 50 km of sea is followed by 100 km of land. Use of the sea curve for the first 50 km, and the land curve, suitably displaced, for the remainder of the path gives a second field-strength value Y'. The field strength should, however, be independent of the direction of propagation because the principle of reciprocity must apply. Thus neither Y nor Y' is correct, but it has been shown that reliable results are obtained if Y and Y' (in dBs) are averaged, giving the value denoted by F in Fig.3.

Millington's method may be extended to paths containing more than two sections of different conductivity, by using the appropriate propagation curve for each section of the path in turn. As before, calculations are performed for both directions of propagation and then averaged.

## 2.4. Ground-wave propagation through urban areas

It has been found that the attenuation of ground waves passing through urban areas cannot be described by assuming that the ground is equivalent to a poor conductor. Furthermore, it is found that the ratio of the electric and magnetic field strengths is not equal to the intrinsic impedance of free space but may be somewhat smaller, because currents flowing in all types of vertical conductors, such as house wiring and plumbing, and even in trees, enhance the magnetic field but tend to reduce the electric field (CAUSEBROOK 1978a).

Measurements have shown that the ground-wave attenuation factor A does not decrease uniformly with increasing distance (as in Fig.2) but may fall rapidly to a fairly deep minimum, after which it increases before falling again. Fig.4 shows ground-wave attenuation factors measured on a typical path through London.

A theory which describes m.f. ground-wave propagation through built-up areas has been developed (CAUSEBROOK 1978b). Moderately built-up areas, such as residential suburbs, are represented by a randomly-distributed array of vertical unipoles, while more densely built-up areas, such as city centres, are represented by a grooved surface, the grooves corresponding to streets. Both representations are equivalent to an inductive ground plane. If the Sommerfeld-Norton theory is extended to this type of surface it is found that the ground-wave attenuation factor, when represented on the complex plane (see Fig.4 of CAUSEBROOK 1978b), contains a zero in the inductive region. If the line representing a path through a built-up area passes near this zero, then the theoretical ground-wave attenuation factor will vary in the same way as the measured values shown in Fig.4.

## 2.5. The effect of ground irregularity

An integral-equation method for calculating ground-wave attenuation over irregular paths has been described (MONTEATH, 1978). This method is based on the Compensation Theorem (MONTEATH, 1951), which leads to an equation of the form

$$G(R) = 1 - \sqrt{\frac{jR}{\lambda}} \int_0^R \frac{\psi + \eta_r}{r(R-r)} e^{-j2\pi t/\lambda} G(r) \, dr \qquad (8)$$

Here $G(R)$ is the complex ground-wave attenuation factor between two antennas A and B separated by irregular ground as shown in Fig.5; over a plane earth the modulus of $G(R)$ is represented by the quantity A of Equation (3). $G(r)$ is the ground-wave attenuation factor for propagation between A and an intermediate point P. Other symbols in Equation (8) not represented on Fig.5 are defined as follows:

> $\lambda$    free-space wavelength
> $\eta_r$    relative surface impedance (MONTEATH,1973)
> $t$    the path difference APB-AB

The integral of Equation (8) is evaluated numerically. As this requires a knowledge of $G(r)$ for a number of points between A and B, $G(R)$ must be evaluated initially for some minimum distance. The calculation is then rep...ed for twice this distance, using the value just derived for the intermediate value of $G(r)$. The path is then extended by a further increment, with two intermediate values of $G(r)$, in order to calculate a third value of $G(R)$, and so on. The first value of $G(R)$ is calculated from one of Norton's formulae on the assumption that a uniform plane earth exists over the first interval. Experience with real ground profiles has shown that intervals of 2 km give adequate accuracy at 1 MHz.

In addition to hills and valleys, the method takes both Earth curvature and varying ground conductivity into account. Computations made over idealised ground profiles, for which solutions can be derived by other means, have shown that the method is reliable and accurate. When applied to real ground it has been found that undulations approaching one wavelength in height have very little effect on ground-wave attenuation. Much larger variations in attenuation, however, would be expected in mountainous areas, where the terrain irregularities may be several wavelengths high.

## 2. SKY-WAVE PROPAGATION

One of the principal characteristics of the 300 to 3000 kHz band is that sky waves propagate efficiently at night but are greatly attenuated during the day. The attenuation occurs in the lower part of the E layer, sometimes known as the D region. At sunset the D region decays rapidly and waves can then be reflected from the E or F layers, with much less attenuation.

The critical frequency of the normal E layer is about 1500 kHz at sunset but it then falls rapidly as a result of electron – ion recombination and tends to a value of about 500 kHz late at night. Sky waves may be reflected from the E layer, or they may penetrate the E layer and be reflected from the F layer, depending on the frequency, path length and time of night. Simultaneous reflection by both layers is also possible in some circumstances. This possibility is illustrated in Fig.6 where waves penetrate the E layer at P and Q but are reflected at S because here the angle of incidence is greater than at P and Q.

Although daytime propagation is relatively unimportant it cannot be entirely disregarded at the upper end of the band, since ionospheric attenuation decreases with the square of the frequency. Nor can it be entirely disregarded at the lower end of the band, where partial reflection from the lower edge of the D region may occur, especially in winter at temperate latitudes.

As the wave propagates from transmitter to receiver it is subject to a number of different types of loss which are illustrated in Fig.7. These losses are considered in detail in the sections which follow. To simplify the discussion it is assumed here that all antennas transmit and receive vertical polarisation (VP); most transmitting antennas operating in the 300 – 3000 kHz band radiate VP and the majority of receiving antennas are more sensitive to the vertically-polarised component of the downcoming wave than to the horizontal component.

Some of the losses described are peculiar to the 300 – 3000 kHz band because the gyromagnetic frequency lies within this band. Enhanced ionospheric cross-modulation also occurs at and near to the gyromagnetic frequency; this is described in Section 3.6.

## 3.1. Ground loss at transmitter and receiver

The strength of the transmitted wave, and the voltage induced in the receiving antenna, are both modified by ground loss, which would be zero only if the ground were flat and perfectly conducting in the vicinity of the antennas. With imperfectly-conducting flat ground the loss in decibels at each terminal would be given by

$$L_g = 6 - 20 \log_{10} \left| 1 - R_v(\alpha) \right| \qquad (9)$$

where $R_v(\alpha)$ is the Fresnel plane-wave reflection coefficient for vertically polarised waves at the radiation angle being considered. Since $R_v$ tends to $-1$ at grazing incidence, the loss would tend to infinity at very low angles if the Earth were flat. However the loss is modified by Earth curvature and has a finite value at grazing incidence (WAIT and CONDA, 1958). Wait and Conda's theory can be used to estimate losses for the negative radiation angles which apply when waves diffract around the curvature of the Earth, as shown in Fig.8.

The field-strength reduction which would occur if flat perfectly-conducting ground were replaced by an imperfectly-conducting curved Earth is shown in Fig.9, which was calculated from Equation (9) for radiation angles above 5° and from Wait and Conda's theory for lower angles, assuming the radius of the Earth to be increased by a factor of 1.25 to allow for atmospheric refraction. Fig.9 should be used in conjunction with Fig.8, which shows radiation angles for hop lengths up to 3000 km.

On single-hop paths involving diffraction around the curvature of the Earth, it is reasonable to assume that the negative radiation angles at both ends of the path are equal if the ground conductivities at the two terminals are similar. When the conductivities are very different, however, this may not be true but calculations have shown that the total ground loss on such paths does not depend critically on the way in which the total diffraction angle is shared between the two ends of the path. It may therefore be assumed to be equally divided between the two ends and given by Fig.8(b) even when the conductivities are dissimilar.

Ground loss may be defined as the field-strength reduction which occurs above a curved Earth when land replaces sea water. Ground loss may therefore be derived from Fig.9 by subtracting field-strength reductions for sea water from those for ground of the appropriate conductivity. The corresponding increase which occurs when land is replaced by sea water is known as sea gain. Fig.10, which shows the sea gain which occurs at 1 MHz when land having a conductivity of 10 mS/m is replaced by sea water, has been adopted by the CCIR in a field-strength prediction method (CCIR, 1978). The increase will be doubled if both terminals are near the sea. The increase rises to a maximum when the path length is about 2000 km because here the one-hop mode predominates and is propagated at a very low angle. The increase rises to a further maximum at about 4000 km; here the 2-hop mode predominates.

The full increase shown in Fig.10 will only apply if the transmitter or receiver is within a few km of the sea. Fig.11 shows how the field-strength depends on the actual distance from the sea (measured in the direction of propagation) when one terminal of a 1500 km path is moved inland, assuming ground of average conductivity (10 mS/m) and a frequency of 1 MHz. Fig.11 is calculated from a formula derived by ANDERSON (1963), and the theory has been confirmed experimentally (KNIGHT and THODAY, 1969).

Sea gain is also influenced by the extent of the sea; for example, it will be considerably reduced if the sea consists only of a narrow channel. This aspect has also been studied by Anderson but the solution is very complicated. An approximation to Anderson's formula has been derived (KNIGHT, 1975a) and has been adopted by the CCIR (1978).

## 5.2. Polarisation-coupling loss

The gyromagnetic frequency, which depends on the strength of the Earth's magnetic field, varies between 800 kHz in equatorial regions and 1600 kHz near the magnetic poles. It therefore always lies within the band of frequencies being considered in this paper. At the gyromagnetic frequency, the extraordinary wave of the magneto-ionic theory (RATCLIFFE, 1959) is so greatly attenuated that it makes a negligible contribution to the received signal; furthermore the attenuation exhibits a broad maximum centred on the gyromagnetic frequency. As a consequence, the extraordinary wave can be disregarded for all practical purposes within the medium-frequency broadcasting band (approximately 550 to 1600 kHz) and even at 3000 kHz its rate of attenuation is two or three times greater than that of the ordinary wave. In the discussion which follows it will be assumed that the extraordinary wave is completely absorbed.

Conventional aerials radiate vertically-polarised waves. At m.f. the wave which is accepted by the ionosphere and which propagates further, usually has a different polarisation and may not be excited efficiently by the incident wave. The wave which emerges from the ionosphere is in general elliptically polarised and may not excite the listener's receiving aerial efficiently, because aerials near the ground are most sensitive to vertical polarisation.

The fraction of the incident power which is lost on entry into the ionosphere is called the polarisation coupling loss. Further polarisation coupling loss occurs when the wave which emerges from the ionosphere induces a voltage in the receiving aerial. The coupling losses which occur at the two ends of the path are caused by essentially the same mechanism and are unchanged if the direction of propagation is reversed.

It has been shown (PHILLIPS and KNIGHT, 1965) that when the transmitting aerial radiates vertical polarisation, the coupling loss in decibels is given by

$$L_c = 10 \log_{10} \left[ \frac{1 + M^2}{\cos^2 \psi + M^2 \sin^2 \psi} \right] \tag{10}$$

where M is the axial ratio of the ordinary-wave polarisation ellipse and $\psi$ is the angle by which its minor axis is tilted from the horizontal plane. Formulae for calculating M and $\psi$ in terms of frequency, magnetic-dip latitude, direction of propagation and angle of incidence at the ionosphere are given by Phillips and Knight.

Curves which give polarisation coupling losses at individual terminals are contained in Fig.12. Although polarisation coupling loss depends to some extent on frequency and angle of incidence at the ionosphere, Fig.12 may be used with negligible error for all frequencies in the m.f. band and for radiation angles up to 20° from the horizontal. The direction of propagation $\chi$ is defined in the inset; on short paths the values of $\chi$ for the two terminals tend to be complimentary and the coupling losses tend to be equal. On long paths, however, the coupling losses at transmitter and receiver must be calculated separately because the magnetic dip latitudes and directions of propagation (relative to magnetic north) at the terminals will, in general, be somewhat different.

Since the major axis of the elliptically-polarised ordinary wave which is accepted by the ionosphere, and also that of wave which emerges, is parallel to the direction of the Earth's magnetic field, polarisation coupling losses are low in temperate latitudes, because the Earth's magnetic field is almost vertical. At the magnetic equator, however, the Earth's field is horizontal and polarisation coupling losses on East-West paths are large.

In the CCIR field-strength prediction method (CCIR, 1978), polarisation coupling losses in temperate latitudes are assumed to have a fixed value of 1 dB at each terminal and are included in the general propagation formula. An empirical formula based on Fig. 12 of this paper is used to calculate the

additional polarisation coupling loss which occurs in tropical latitudes.

## 3.3.   Ionospheric absorption

This section considers first the residual ionospheric absorption which remains late at night when solar activity is low.   It then goes on to consider short period and day-to-day variation of field strength, diurnal and seasonal variations, and the effect of solar activity.

Because sky waves are so variable, field-strength measurements made on a single night are of little value; even if measurements were made at the same hour for 25 consecutive nights the median field strength might still be 2 dB in error.   Assessments of the effects of interfering sky-wave signals should always take this variability into account and it is unrealistic to predict sky-wave field strengths to fractions of a decibel.

### 3.3.1.   Residual night-time absorption

The Earth's magnetic field has two distinct effects on ionospheric absorption.   Firstly it is responsible for the auroral zones, regions centred on the magnetic poles where absorption losses are high.   Distance from the auroral zone is believed to be of considerable importance; for example, ionospheric losses in North America are known to be greater than in Europe (BARGHAUSEN, 1966).   Secondly the rate of attenuation of a wave in the ionosphere depends on the angle between its direction of propagation and the direction of the Earth's magnetic field, the rate of attenuation being least when these two directions are parallel.

These two effects in combination cause ionospheric losses on north-south paths to be less than on east-west paths.   Long north-south paths usually pass through equatorial regions, where propagation tends to be parallel to the Earth's field and auroral effects are absent.   On the other hand, east-west paths tend to be transverse to the Earth's field, and some east-west paths (especially those across the North Atlantic) are close to the auroral zone.

The way in which ionospheric losses would vary if auroral effects were absent has been studied by means of an extensive series of ray-tracing computations, using an ionospheric model assumed to be common to all geographical areas. (OLVER et al 1971).   A detailed study was made of propagation from hypothetical transmitters situated in Europe and Africa.   In Europe, ionospheric losses were found to be almost independent of direction of propagation; this is to be expected because the Earth's magnetic field is almost vertical.   Losses on east-west paths in Europe and Africa were found to be similar; this is also to be expected because east-west propagation tends to be transverse to the Earth's magnetic field at all latitudes.

Ordinary-wave losses computed for the frequency range 500 - 1500 kHz for single-hop east-west paths are shown by unbroken lines in Fig.13.   Although the losses decrease with increasing frequency, the reduction is less than might be expected, because waves of higher frequencies penetrate more deeply into the ionosphere and the distance traversed within the ionosphere is greater than at lower frequencies. Consequently the variation of the total loss with frequency is much smaller than would otherwise be the case.   Fig.13 shows that losses for low-angle modes tend to be almost independent of hop length because of the very small variation of the angle of incidence at the ionosphere.

Propagation parallel to the Earth's magnetic field was studied by computing losses on single-hop north-south paths with reflection points above the geomagnetic equator.   Although most of the computations involved reflection over Africa, some additional computations were made for other equatorial regions since some dependence on the strength of the Earth's magnetic field was expected.   The strength of the Earth's field was, however, found to have negligible influence on the computed losses, which were also found to be almost independent of frequency.   The results of the computations for equatorial north-south paths are shown by the broken curve of Fig.13.

In the auroral zones, ionospheric losses are somewhat greater than those shown in Fig.13.   The auroral zones are centred on the magnetic poles and have an outer radius of 4000 km.   Areas which are affected by increased losses include Canada and the northern USA, the North Atlantic and the northern part of the USSR. In this region, ionospheric losses are independent of the direction of propagation because the Earth's magnetic field is almost vertical.

Fig.13 does not apply when waves penetrate the E layer and are reflected by the F layer; this is most likely to occur at frequencies above 1500 kHz.   Outside the auroral zone the residual night-time absorption loss $L_A$ tends to be independent of path azimuth and is given approximately by the following semi-empirical formula due to Wakai (CCIR 1980):

$$L_A = \frac{7 + 0.019d}{10 + f^2} \quad dB \qquad (13)$$

where d is the path length in km and f is the frequency in MHz.

### 3.3.2   Short-period and day-to-day variation

The ionosphere is a turbulent medium and sky-wave field strength varies continuously.   Short period variations, occuring within periods measured in minutes usually follow a Rayleigh distribution, although larger variations may be observed if two or more propagation modes are received simultaneously.   However, the median field strength measured during a short period generally differs from that measured at the same time on the previous night and it has been found that the day-to-day variation of the median field strength often obeys a distribution which resembles the log-normal (KNIGHT, 1977).   The combined effect of the short period and day-to-day variation causes the instantaneous field strength to exceed the median value by more than 6 dB for about 10% of the total time, during short periods centred on a specific hour, on a series of nights.

### 3.3.3. Diurnal variation

Ionospheric absorption is smallest and field strengths are largest late at night. The absorption increases rapidly at sunrise and decreases from its day-time value almost as rapidly at sunset. Field-strength variations have been measured during the sunset and sunrise periods, and throughout the night, on many paths in different parts of the world. The results have been compared (KNIGHT,1977) and it has been found that these variations are largely independent of frequency (within the m.f. broadcasting band) and of path length. An average curve which shows the additional absorption which occurs around sunset and sunrise, and during the early part of the night, can therefore be drawn; it has been adopted by the CCIR and is reproduced in Fig.14 (CCIR,1978).

For single-hop paths, the sunset and sunrise times of Fig.14 are those observed at the path mid-point. For multi-hop paths the absorption variation is mainly controlled by the hop nearest to the terminal where the sun sets last or rises first, because the remainder of the path is then in darkness. Sunset and sunrise times for paths longer than 2000 km are therefore taken at points 750 km from the appropriate terminal.

The absorption rises to a maximum at about mid-day and Fig.15 shows the corresponding field-strength reduction, measured on a 361 km path in Japan (WAKAI et al, 1969). Fig.15 shows the tendency for day-time field strengths to be greater in winter than in summer. Measurements made at Helsinki of a large number of European transmissions have shown that sky waves received over single-hop paths near mid-day in December are 20 to 40 dB weaker than at night, throughout the frequency range 500 - 1600 kHz (EBU, 1967).

### 3.3.4. Seasonal variation

As described in the previous section, there is a tendency for day-time field strengths to be greater in winter than in summer. At night there is a tendency for field-strength maxima to occur in spring and autumn, except at vertical incidence, when the maximum occurs in the summer. Considerable differences have been observed from one path to another; for a more detailed discussion see KNIGHT 1977.

### 3.3.5. Solar-cycle variation

There is a tendency for night-time sky-wave field strength to decrease with increasing solar activity. The decrease seems to be most pronounced in North America, where reductions of more than 6 dB have been observed on typical paths at the peak of the solar cycle (BARGHAUSEN and LILLIE, 1965). Smaller reductions have been observed in Europe and Australia. In tropical regions, there is unlikely to be any appreciable field-strength reduction because ionospheric absorption at night is relatively small.

Regression analysis indicates that the field-strength reduction is proportionable both to sunspot number R and to the path length p, and can be represented by the formula

$$L_R = 10^{-2}\,bpR \qquad dB \tag{12}$$

where p is in km and b is a constant which depends on geographic location. According to the CCIR, b = 4 for North America, 1 for Europe and Australia and 0 elsewhere (CCIR, 1978).

There is very little information about the effect of solar activity on daytime propagation although measurements made in India at 1500 kHz show field strengths decreasing with increasing solar activity (as at night) because of greater ionospheric absorption (SATYANARAYANA SARMA et al., 1970).

### 3.4. Intermediate reflection loss

Intermediate reflection loss occurs between hops on multi-hop paths and is closely related to polarisation coupling loss. It occurs for the same reason, i.e. because the extraordinary wave is almost completely absorbed and only the ordinary wave propagates

The mechanism is illustrated in Fig.16. When the elliptically-polarised downcoming wave is reflected at the ground its strength is reduced and its polarisation ($P_1$) is modified. The new polarisation $P_2$ will not necessarily match the polarisation $P_3$ which the ionosphere would like to accept for onward propagation of the ordinary wave. The intermediate reflection loss is the sum of the ground reflection loss and the coupling loss between the polarisations $P_2$ and $P_3$; these two losses cannot be considered separately.

There are three situations in which the loss may be large:

1. In temperate latitudes when the downcoming wave is incident at the Brewster angle, because the ordinary wave is essentially vertically polarised.

2. For east-west propagation with sea reflection at $45°$ dip latitude, when the ordinary wave re-enters the ionosphere as the extraordinary wave and is absorbed.

3. For north-south propagation with sea reflection at the magnetic equator, when the ordinary wave is again converted into the extraordinary wave and absorbed.

Intermediate reflection loss is, in general, non-reciprocal, i.e. its value changes if the direction of propagation between two given terminals is reversed. The non-reciprocal effect is most apparent when waves are reflected from land at angles near the Brewster angle, waves propagating towards the west suffering the greater loss. Waves reflected from the sea, however, have similar losses in both directions of propagation.

A general formula for intermediate reflection loss is derived in PHILLIPS and KNIGHT, (1964). This loss is a function of a large number of variables and should, ideally, always be computed. To enable losses to be estimated from curves, however, the following simplifying assumptions have been made elsewhere (KNIGHT,

1975b):

1. The dip latitude and direction of propagation at the points where the wave leaves the ionosphere, and re-enters after reflection, are the same as the value at the Earth reflection point, except on north-south paths near the equator, where an allowance has been made for the change in dip latitude.

2. The frequency is approximately equal to the gyromagnetic frequency.

3. The angle of incidence at the ionosphere is $80^\circ$; this angle is approximately correct for hop lengths greater than 1000 km.

4. The reflection coefficient for horizontally-polarised radiation is -1.0.

Fig.17 shows intermediate reflection losses, computed with these assumptions, for five directions of propagation relative to magnetic north and for a range of dip latitudes. The curves are plotted as a function of $\alpha(\sigma/F)^2$ where $\alpha$ is the radiation angle in degrees, $\sigma$ is the ground conductivity in mS/ and F is the frequency in MHz. Because of the simplifying assumptions, Fig.17 should not be used for values of $\alpha$ greater than $10^\circ$.

The theory described above makes no allowance for Earth curvature, which would be expected to have a significant effect when $\alpha$ is less than $2^\circ$. Although the effect of Earth curvature on intermediate reflection loss has not yet been studied, it is possible that, at grazing incidence, the loss may tend to a value of about 6 dB under all circumstances. Although greater losses would be incurred with negative radiation angles because of diffraction, multi-hop paths involving negative radiation angles are unlikely to contribute significantly to received signals.

### 3.5. Field-strength calculation

So many factors are involved in m.f. sky wave propagation that it is difficult to draw a universal set of propagation curves. A number of methods can be used to calculate field strengths and to construct propagation curves for particular areas, and directions of propagation.

In the wave-hop method (KNIGHT,1975b) each propagation mode is considered separately. The free-space field strength is augmented by convergence gain (BRADLEY,1970) and the losses described in Sections 3.1 to 3.4 are then subtracted. Since the various modes arriving at the receiver are randomly phased, they are added on a power basis. The result gives the estimated median field strength for late at night at periods when solar activity is least. Corrections must be applied to derive field strengths for other times of day and for periods of greater solar activity, and to estimate the values exceeded for various percentage times.

The wave-hop method is too complicated and time consuming for planning purposes and a simpler method has therefore been adopted by the CCIR (CCIR 1978). This is based on a propagation formula derived from measurements made in the USSR (CCIR,1972) which has been found to be reasonably consistent with measurements made elsewhere. Corrections are applied for polarisation coupling loss and sea gain, extending the validity of the formula to tropical regions and coastal areas. Corrections are also applied for diurnal variation and solar activity.

### 3.6 Ionospheric cross-modulation

Another feature of m.f. propagation which is affected by the Earth's magnetic field is ionospheric cross-modulation. When the region of the ionosphere traversed by a sky-wave is strongly illuminated by a high-power disturbing transmitter, the audio-frequency modulation of the latter may be superimposed on the carrier of the former and cause interference. This cross-modulation, also known as the Luxembourg effect, is caused by a non-linear process in the ionosphere. The mechanism has been fully described by HUXLEY and RATCLIFFE (1949). Briefly, the disturbing transmitter varies the collision frequency of the ionosphere in step with its modulation and this, in turn, varies the attenuation suffered by the traversing wave, leading to cross-modulation.

Ionospheric cross-modulation is mainly confined to the l.f. and m.f. broadcasting bands, and the high-power transmitters which are in common use today may cause serious interference to sky-wave broadcasting services. Because of the large numbers of transmitters in these bands, ionospheric cross-modulation is difficult to distinguish from co-channel interference and even more difficult to measure. Numerous measurements have, however, been made in the past when these bands were less congested.

The depth of the transferred modulation depends both on the modulation depth of the disturbing transmitter and on the strength of the disturbing wave at the base of the ionosphere. To enable measurements to be compared they must first be standardised by calculating the cross-modulation which would have been observed if the disturbing transmitter had radiated with certain specified characteristics.

In a comparison of all known measurements (KNIGHT, 1973), estimates were made of the cross-modulation levels which would have been observed had the disturbing transmitters radiated from short vertical aerials with a power of 100 kW and been modulated at 300 Hz to a depth of 80%. This relatively low power was adopted as a reference because many of the measurements were made with powers of this order.

Fig. 18 shows the result of this comparison; full details are given in the reference. The horizontal frequency scale is normalised to the gyromagnetic frequency $F_H$ because cross-modulation rises to a maximum at the gyromagnetic frequency, the width of the maximum depending on the collision frequency at the height where cross-modulation takes place. If the Earth's magnetic field were absent, cross-modulation would decrease approximately as $1/F_D^2$, where $F_D$ is the frequency of the disturbing transmitter.

The enhanced cross-modulation near the gyromagnetic frequency is a direct result of the high rate of

attenuation of the extraordinary wave generated by the disturbing transmitter. As a result an appreciable fraction of the radiated power is dissipated in a relatively small volume, causing electron heating and a significant increase in collision frequency. This in turn greatly increases the attenuation of waves traversing the same region of the ionosphere and is responsible for the increased cross modulation.

## 4. THE COMBINED EFFECT OF GROUND WAVES AND SKY WAVES

At m.f. the ground wave and sky wave can be considered separately because the distance between the ground and the ionosphere is several hundred wavelengths. Interference between the two waves, however, does have to be considered. In some situations the ground wave predominates and at other times the sky wave is stronger.

During the day, sky-wave propagation is relatively unimportant and ground waves provide stable signals. They are therefore widely used for broadcasting. For example a 100 kW transmitter can provide a good service out to a radius of 100 km and a satisfactory service at twice this distance. At night, however, the service is limited by sky-wave interference. The sky-waves may be generated by the same transmitter or they may originate from distant transmitters using the same frequency.

Although sky waves generated by the same transmitter carry the same modulation as the ground wave, it is slightly delayed in time and this gives rise to unacceptable distortion if the two waves are of comparable amplitude. The distortion can be tolerated, however, if the ground wave is at least 10 dB stronger than the sky wave. With a simple transmitting antenna this reduces the radius of the service area to about 80 km at night, regardless of the transmitter power. Some increase in this radius can be achieved by the use of specially designed transmitting antennas which minimise high-angle radiation and so reduce the sky-wave field strength at the edge of the service area, but this is seldom worthwhile today because of the great increase in the number of transmitters sharing the same frequency. Since these co-channel transmitters usually radiate different programme material, careful planning is required to protect ground-wave service areas from harmful sky-wave interference. Ideally, high-power transmitters sharing a common frequency should be separated by at least 1000 km.

Sky waves can be used to supplement ground waves at night, using a separate transmission on a different frequency, or they may be used to serve areas which are much larger than can be covered by ground waves. Sky waves can propagate to considerable distances. For example, European broadcasting transmitters have been regularly observed in southern Africa and both North and South America.

## 5. ACKNOWLEDGEMENT

## 6. REFERENCES

ANDERSEN, J.B., 1963. The radiation field from a vertical dipole on an inhomogeneous ground. Electromagnetic Waves and Antennas, Pergamon Press, pp.1099-1112.

BARGHAUSEN, A.F. and LILLIE, D.A., 1965. Some evidence of the influence of long-term magnetic activity on medium frequency sky wave propagation. Proc.Instn.elect.electron.Engrs.Vol.53,pp.2115-6.

BARGHAUSEN, A.F., 1966. Medium-frequency sky-wave propagation in middle and low latitudes. IEEE Trans. Broadcasting, Vol. BC-12, pp.1-14.

BRADLEY, P.A., 1970. Focusing of radio waves reflected from the ionosphere at low angles of elevation. Electronics Letters, Vol. 6, pp. 457-8.

CAUSEBROOK, J.H., 1978a. Electric/magnetic field ratios of ground waves in a realistic terrain. ibid., Vol.14, pp. 614-5.

CAUSEBROOK, J.H., 1978b. Medium-wave propagation in built-up areas. Proc. Instn. elect. Engrs. Vol.125, pp.804-8.

CCIR, 1972. Night-time sky-wave propagation curves for the 150 - 1600 kHz broadcasting band for distances greater than 300 km from the transmitter. CCIR Doc. 10/82.

CCIR, 1974. Ground-wave propagation curves for frequencies below 10 MHz. CCIR Recommendation 368-2.

CCIR, 1978. Prediction of sky-wave field strength between 150 and 1500 kHz. CCIR Recommendation 453-3.

CCIR, 1980. Supplement to Report 252-2.

EBU, 1976. Daytime LW/MW field-strength measurements. EBU Doc. Com T(B) 213.

HUXLEY, L.G.H. and RATCLIFFE, J.A., 1949. A survey of ionospheric cross-modulation. Proc. Instn. elect. Engrs., Vol.96, Part III, pp.433-40.

JORDAN, E.C. and BALMAIN, K.G., 1968. Electromagnetic waves and radiating systems (chapter 16), Prentice-Hall (second edition).

KNIGHT, P. and THODAY, R.D.C., 1969. Influence of the ground near transmitting and receiving aerials on the strength of medium-frequency sky waves. Proc. Instn. elect. Engrs., Vol.116, pp.911-919.

KNIGHT,P. 1973. L.F. and M.F. propagation : a study of ionospheric cross-modulation measurements. BBC Engineering, No. 94, pp.12-21.

KNIGHT,P., 1975a. LF and MF propagation : an approximate formula for estimating sea gain. British Broadcasting Corporation Research Report No. 1975/32.

KNIGHT, P., 1975b. MF propagation : a wave-hop method for ionospheric field-strength prediction. BBC Engineering, No.100, pp.22-34.

KNIGHT, P., 1977. LF and MF propagation : a study of sky-wave field-strength variation. British Broadcasting Corporation Research Report No. 1977/12.

MILLINGTON, G., 1949. Ground-wave propagation over an inhomogenous smooth earth. Proc. Instn. Elect. Engrs., Vol. 96, Part III, pp. 53-64.

MONTEATH, G.D., 1951. Application of the compensation theorem to certain radiation and propagation problems. Proc. Instn. elect. Engrs., Vol. 98, Part IV, pp. 23-30.

MONTEATH, G.D., 1973. Applications of the electromagnetic reciprocity principle. Oxford, Pergamon Press.

MONTEATH, G.D., 1978. Computation of groundwave attenuation over irregular and inhomogeneous ground at low and medium frequencies. British Broadcasting Corporation Research Report No. 1978/7.

NORTON, K.A. 1936,37. The propagation of radio waves over the surface of the Earth and in the upper atmosphere. Part 1, Proc. Instn. radio Engrs., Vol.24, pp.1367-87 (1936). Part 11, ibid., Vol.25, pp. 1203-36 (1937).

NORTON, K.A. 1941. The calculation of ground-wave field intensity over a finitely conducting spherical earth. Ibid., Vol.29, pp. 623-39.

OLVER, A.D., LYNER, A.G. and KNIGHT, P., 1971. A computer programme for calculating sky-wave field strengths at medium frequencies. EBU Review, No. 125A, pp. 18-27.

PHILLIPS, G.J., and KNIGHT, P., 1965. Effects of polarisation on a medium-frequency sky-wave service, including the case of multihop paths. Proc. Instn. elect. Engrs., Vol. 112, pp.31-39.

RATCLIFFE, J.A., 1959. The magneto-ionic theory and its applications to the ionosphere. Cambridge University Press.

ROTHERHAM, S., 1970. Ground-wave propagation at medium and low frequencies. Electronic Letters, Vol.6, pp.794-5.

SATYANARAYANA SARMA, M., GOPAL RAO, M.S.V and ANJANEYULU, C., 1970. Ionospheric absorption measurements at 1.55 MHz by the URSI A$_3$ method, Indian J. pure and applied Phys., Vol.8, pp.523-25.

SOMMERFELD, A., 1909. The propagation of waves in wireless telegraphy. Ann. Physik, Vol. 28, p 665.
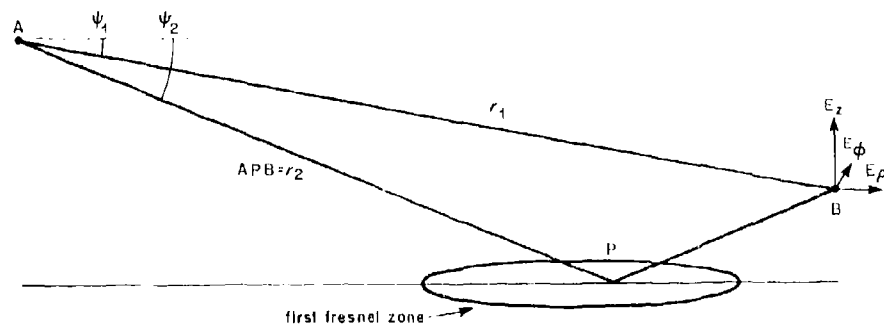
FIG.1 AERIALS ABOVE A PLANE EARTH
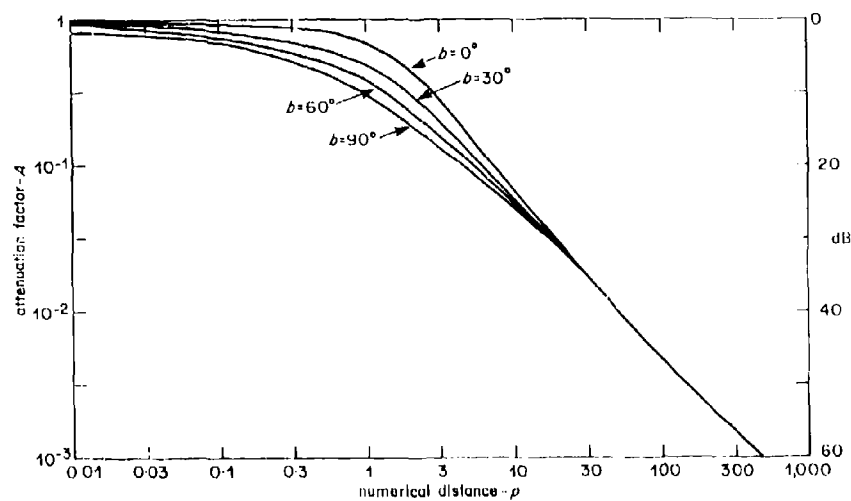


FIG.2 GROUND-WAVE ATTENUATION FACTOR
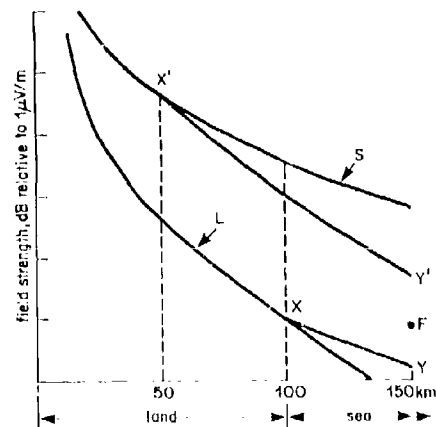


FIG.3 MILLINGTON'S METHOD FOR MIXED-PATH PROPAGATION

L = Land Propagation Curve.  XY = Sea Curve, lowered
S = Sea Propagation Curve.  X'Y' = Land Curve, Raised
F = Average of Values Y and Y'
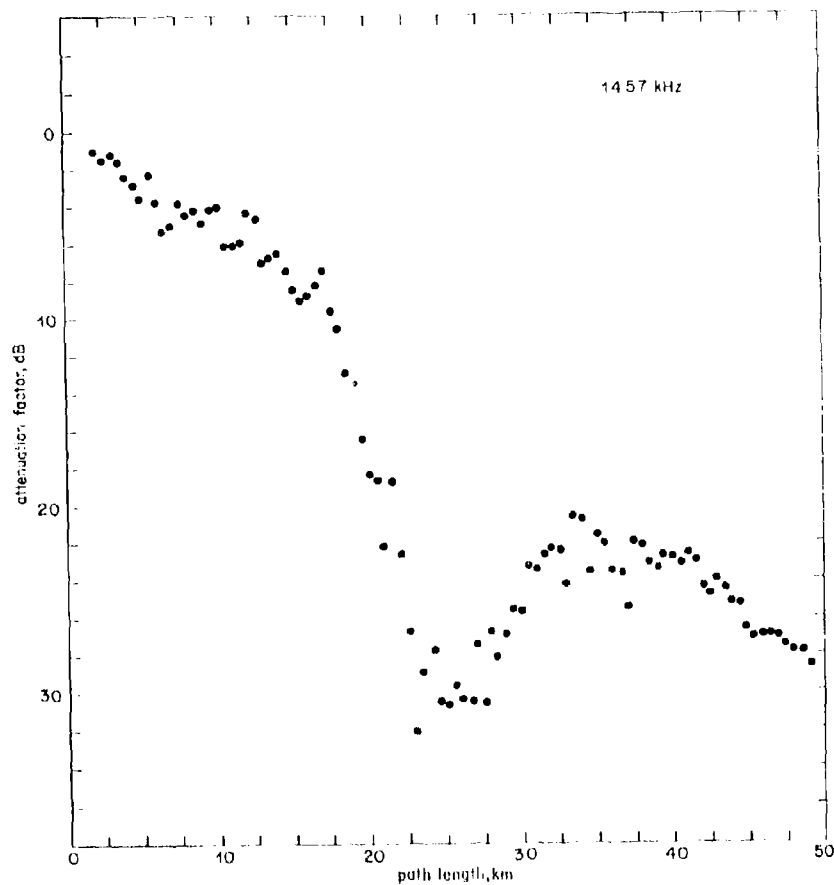
FIG.4  GROUND-WAVE ATTENUATION FACTORS MEASURED ON A PATH THROUGH LONDON
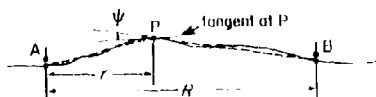


FIG.5  PROPAGATION OVER IRREGULAR GROUND
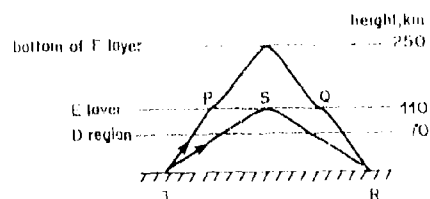


FIG.6  SIMULTANEOUS E AND F LAYER REFLECTION
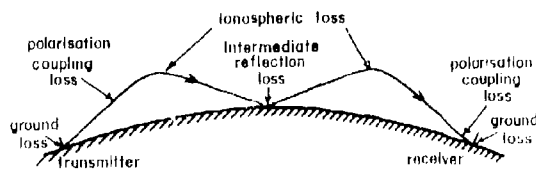


FIG.7  LOSSES ON A TWO-HOP SKY-WAVE PATH
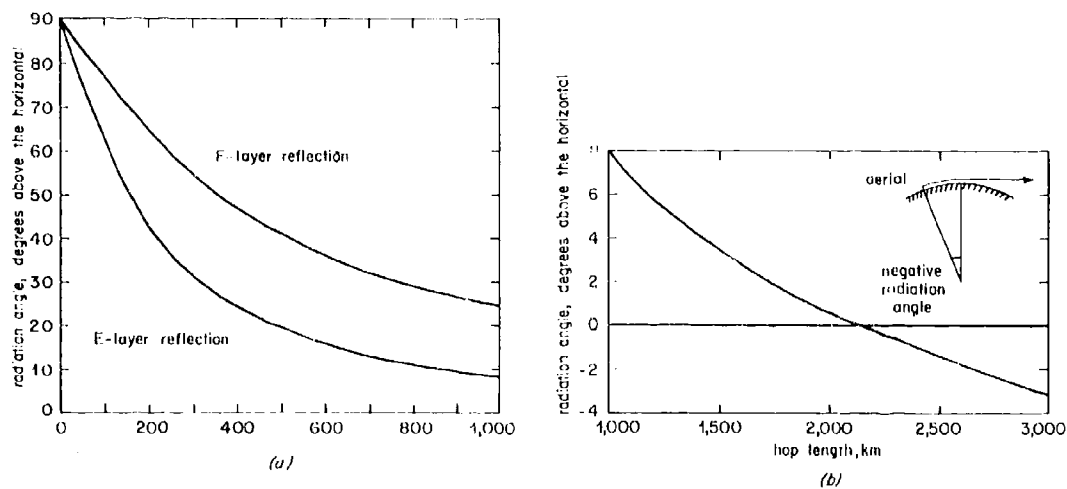
FIG. 8   RADIATION ANGLE

(a) short distances   (b) longer distances : E-layer reflection only
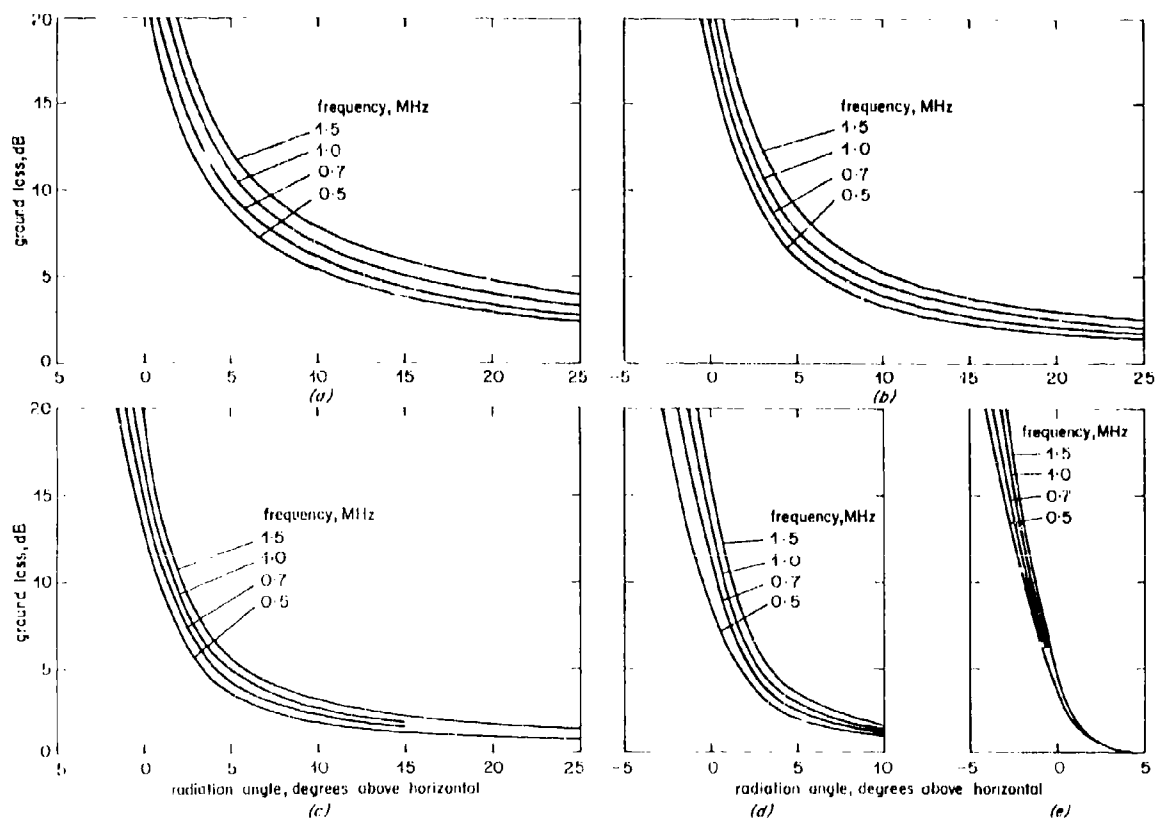


Fig. 9   GROUND LOSS

(a) ground conductivity 1 mS/m   (b) ground conductivity 3 mS/m

(c) ground conductivity 10 mS/m   (d) ground conductivity 30 mS/m   (e) sea water
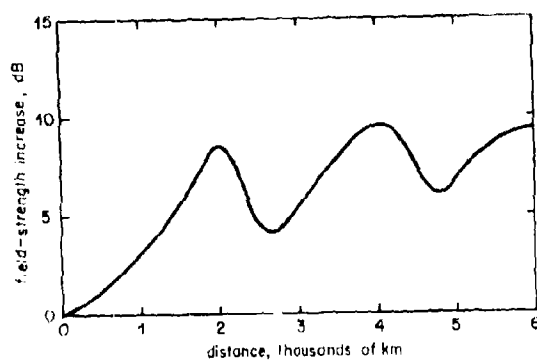
FIG. 10   EFFECT OF REPLACING LAND
AT TRANSMITTER OR RECEIVER, BY SEA
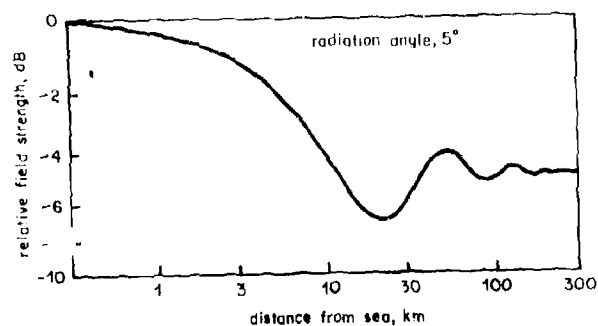
FIG. 11   VARIATION OF FIELD STRENGTH
WITH DISTANCE FROM SEA
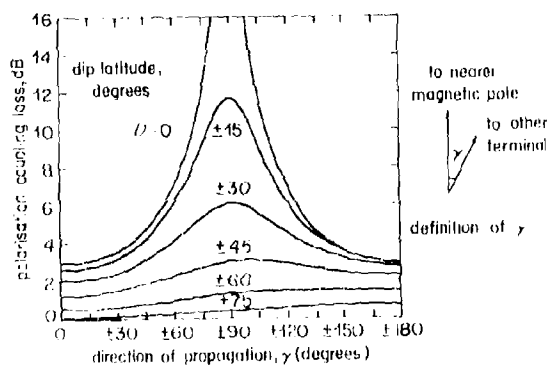


FIG. 12   POLARISATION COUPLING LOSS
AT TRANSMITTER OR RECEIVER
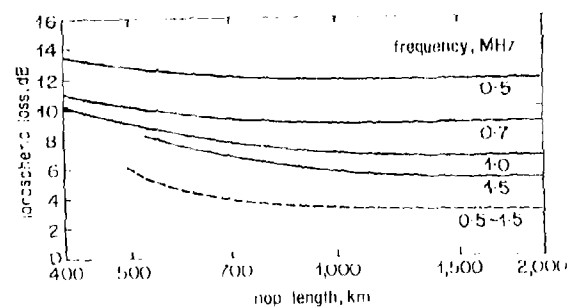
FIG. 13   COMPUTED IONOSPHERIC LOSSES

——— East-west propagation at all latitudes (0 - 90°)

— — North-south propagation at magnetic equator (D 0
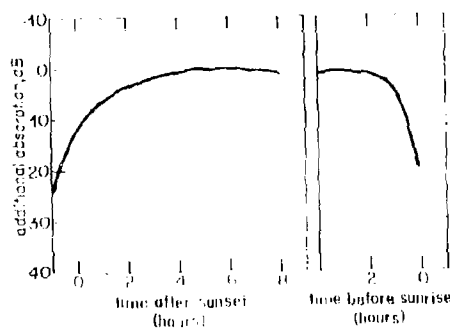


FIG. 14   DIURNAL VARIATION OF IONOSPHERIC ABSORPTION
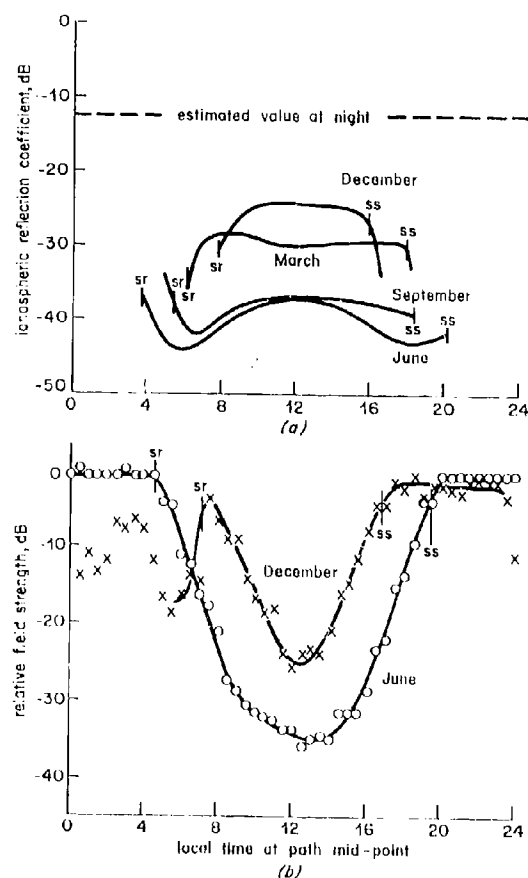
FIG. 15  DIURNAL VARIATION

Measured at 1850 kHz on a 361 km path in Japan in 1964.
(From WAKAI et al, 1969)

SR   Ground sunrise at path mid-point
SS   Ground sunset at path mid-point

The points indicate monthly median values for half-hour periods



P₁    polarisation of downcoming wave

P₂    polarisation of wave after ground reflection

P₃    polarisation of wave accepted by ionosphere
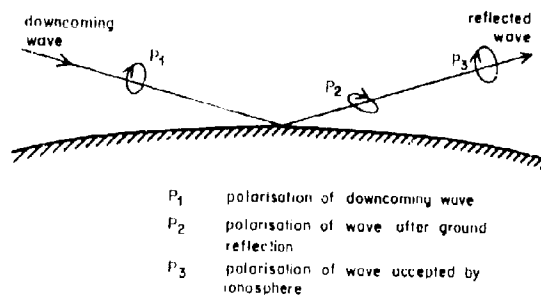
FIG. 16   INTERMEDIATE REFLECTION LOSS
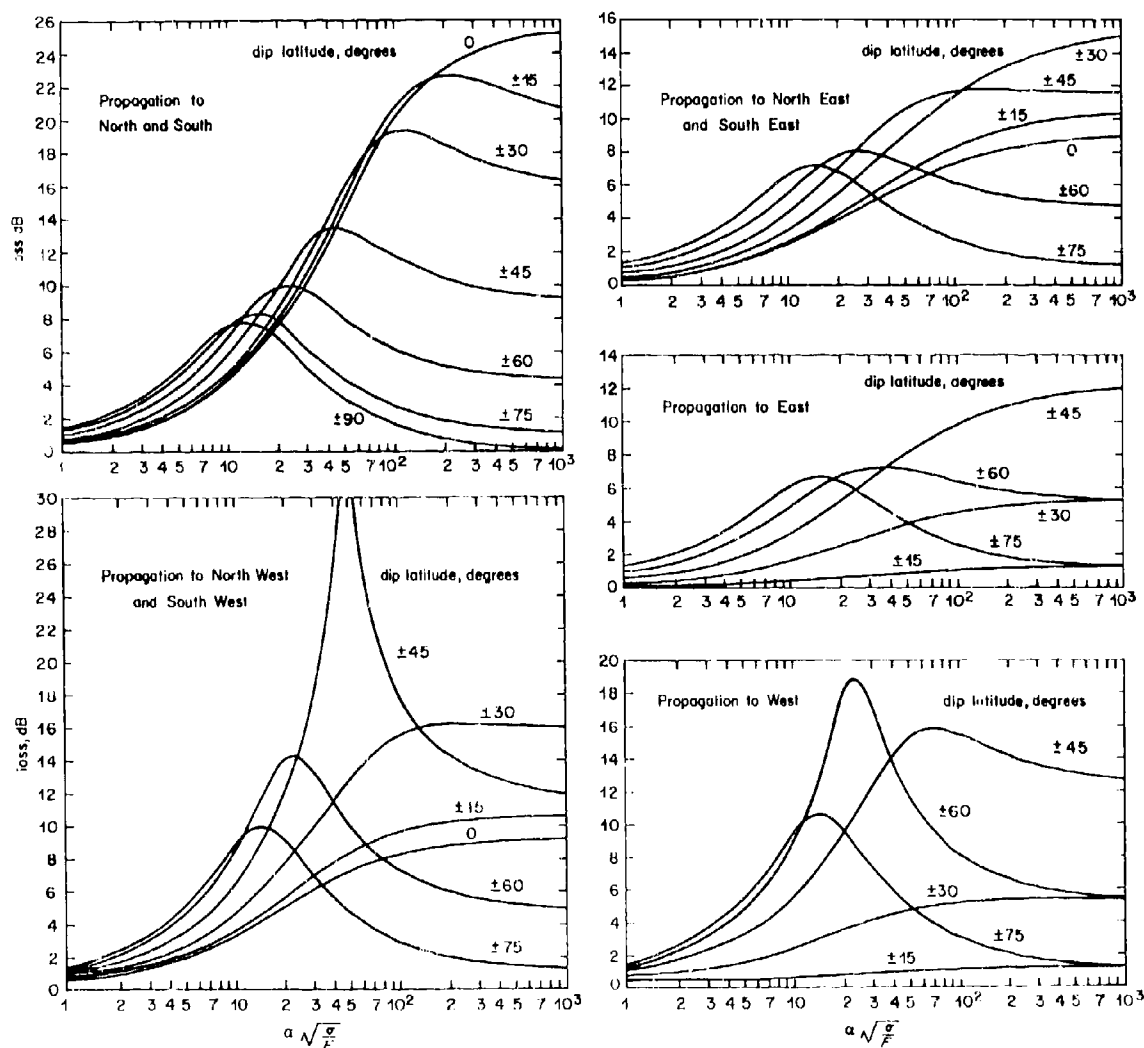
FIG. 17   INTERMEDIATE REFLECTION LOSS

$\alpha$ = angle of arrival, degrees to horizontal   $\sigma$ = ground conductivity, mS/m
F = frequency, MHz   For sea water, $\sigma \simeq 4000$ mS/m
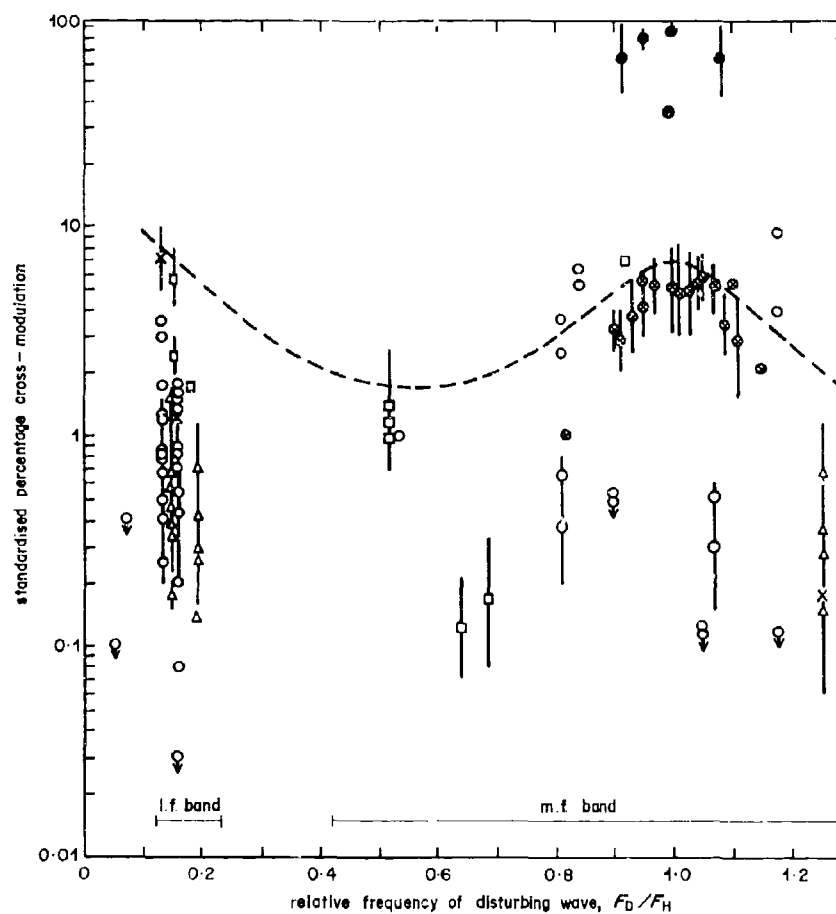
FIG. 18  COMPARISON OF IONOSPHERIC CROSS-MODULATION MEASUREMENTS

--- Semi-empirical upper limit

Vertical lines represent a range of median values measured during the course of a night, or on different nights. Arrows pointing downwards indicate measured values which are less than the value shown.

# REDUCTION IN MF SKYWAVE FIELD STRENGTH AT NIGHT DUE TO
# MAGNETIC-STORM AND WINTER-ANOMALY-RELATED ABSORPTION

E.L. Hagg
Communications Research Centre
P.O. Box 11490, Station "H"
Ottawa, Ontario, Canada
K2H 8S2

## ABSTRACT

Results from a detailed analysis of one year of previously published field strength measurements, taken during high solar activity in 1947-48 at Ottawa on the 1020 kHz KDKA Pittsburg emissions, show that the strength of the night-time skywave is controlled by absorption from two apparently unrelated geophysical effects. One of these is the magnetic-storm and post-storm effect and the other is the winter anomaly effect. The former effect was dominant throughout the year and was the only factor controlling the field strength during the March through September period. The two-monthly median field strength for this period showed a smooth decrease with increased magnetic activity, from 5 to 19 dB relative to an experimentally determined unabsorbed value. The latter effect was present sporadically during the October through February period. The reduction in field strength due to the winter anomaly alone was from 6 to 11 dB.

## 1.0 INTRODUCTION

It is well known that at the higher geomagnetic latitudes the solar cycle has a considerable influence on the strength of the night-time MF skywave. Long-term skywave field strength measurements, made at night in the 550-1600 kHz broadcast band, show the annual median field strength to be highest at sunspot minimum (Damelin, 1971; Wang, 1977). The geomagnetic storm activity is then also at a minimum. This activity increases with increasing solar activity and as a result the annual median field strengths then decrease because of magnetic-storm-associated ionospheric (D-region) absorption. However, while field strengths are highest at sunspot minimum, there is evidence that at other times the field strengths are more closely related to magnetic activity than to the mean sunspot number (Barghausen and Lillie, 1965). One of the factors that control MF field strength at night is therefore likely to be the magnetic-activity-related absorption. Studies based on vertical incidence absorption measurements made during the day on frequencies between 1.7 and 4.0 MHz show that anomalously high absorption occurs during the winter months (Davies and Hagg, 1954; Beynon and Williams, 1976a). Most of this absorption was not associated with magnetic activity and was therefore related to the well-known winter anomaly effect, first discovered by Appleton (Appleton, 1937). MF skywave field strength, measured nightly on 1.02 MHz AM broadcast emissions during high solar activity, was found to be anomalously low from time to time during the winter months even during periods of relatively low magnetic activity (Mather, 1949). It is therefore reasonable to suggest that such low values of field strength could be caused by winter-anomaly-related absorption occurring at night.

The purpose of this paper is to explain and determine quantitatively the factors that controlled the nightly field strength on 1.0 MHz over a 534 km path in North America, during one year at high solar activity. The paper is based on previously published field strength measurements that were taken nearly every night at Ottawa, Canada, on the 1.02 MHz KDKA Pittsburg, U.S.A. emissions (Mather, 1949). The measurements were taken during the 2nd and 3rd hour after ground sunset relative to the most western point of the path. The midpoint of the path was located at 43° geographic and 54° geomagnetic latitude. The measurement period was from May 1st, 1947 through April 30th, 1948. The mean sunspot number for the period was 146.1. Because of the very solid data base which contained measurements for 361 nights out of 366, it has been possible to determine that there were two types of absorption effects which contributed to the reduction of the night-time field strength.

## 2.0 ANALYSIS AND RESULTS

### 2.1 Approach to the Analysis

A somewhat unorthodox approach to the analysis was required in order to explain and determine quantitatively the factors that control the strength of night-time MF skywave. After evaluating some preliminary test results, it became clear that it would be necessary to:

a) determine an experimental median unabsorbed field strength from which a quantitative estimate of the absorption could then be made;

b) separate the months October through February from the remaining 7 months in the analysis because these months showed evidence of absorption that was not related to magnetic activity;

c) divide the data into 2-month periods because the estimated error was deemed too large (up to $\pm$ 7 dB) in the monthly median field strength;

d) develop a method for relating skywave field strength to magnetic activity which is superior to that using the mean Kp sum.

That the steps under b) c) and d) were neces⁙⁙ y is to some extent illustrated in Figure 1 where the monthly median field strength and the corresponding mean Kp sum are plotted for the 12 months of data. For this data, the error was estimated by multiplying the quartile range, Q.R., by $\sqrt{2/N}$ where N is the number of observations. Note that the median field strength for January is 16 to 17 dB lower than that for May, June or July even though the magnetic activity, as indicated by the mean Kp sum, was lower in January than in the summer. The monthly mean sunspot numbers are also shown on the figure and appear unrelated to median field strength and mean Kp sum. That the relationship between monthly median field strength and the corresponding mean Kp sum is not very close is clearly illustrated in Figure 2. One of the reasons for this is that the mean Kp sum can be a poor indicator of both the number and severity of the magnetic storms in a given month. For example, in Figure 2 the field strength for March 1948 is 8 dB lower than that for June 1947, yet according to the mean Kp sum the magnetic activity was lower in March than in June. If days having Kp sums $\geq 29-$ are defined as magnetically disturbed, then there were 5 such days in March with daily Kp sums of $55+$, $37_0$, $37_0$, $37_0$ and $33-$. In June there were only 3 such days with Kp sums of $42_0$, $35_0$ and $32-$. The magnetic storm activity was therefore greater in March than in June, although the mean Kp sums for these months indicated the opposite. Thus the mean Kp sum is not a very useful parameter for relating median MF skywave field strength to geomagnetic storm activity and will not be used in this analysis.

An additional reason for the poor correlation shown in Figure 2 is that anomalous absorption, which was not related to geomagnetic activity, occurred sporadically during the October through February period. Evidence that such absorption occurred will be developed in the next two subsections.

## 2.2 Determining the Experimental Median Unabsorbed Field Strength

As mentioned under a) in sub-section 2.1, a value for median unabsorbed field strength was required. The first step was to exclude, as far as possible, nightly measurements affected by absorption related to magnetic storm and post-storm effects. These effects are illustrated in Figure 3 where the nightly field strength and the daily Kp sums are compared for the period January 30th - February 29th, 1948. There were three minor storms in this period, the first on February 3rd, the second on the 15th - 16th and the third on the 23rd. The maximum daily Kp sums for these storms were $32+$, $31+$ and $29_0$ respectively. In all three cases, the maximum absorption, as evidenced by the maximum reduction in field strength, occurred from 1 to 3 days after the storm peaked, which, for the February 15th - 15th and 23rd storms was $\approx 40$ dB down relative to the pre-storm values. Studies using D-region electron density profiles and satellite particle data have shown precipitating energetic particles to be the dominant source in contributing to the increased D-region electron density and hence to the absorption that occurs during the post-storm period (Larsen et al., 1976; Montbriand and Belrose, 1976).

The following stringent criteria were used for excluding data likely to be affected by magnetic storm and post-storm effects:

a) a daily (24 hour) Kp sum of $\geq 29-$ was defined as magnetically disturbed; nightly measurements then taken were excluded, (a lower value than $29-$ would have been more effective for excluding these effects, but the number of data points remaining would then have been too few to be statistically significant);

b) measurements taken the night before the Kp sum rose to $\geq 29-$ were also excluded if this sum was $\geq 20+$; this was a precaution against including a partially disturbed day that could have affected the measurement;

c) the post-storm effects were reduced, if not completely eliminated, by excluding measurements for a 9 day period after the Kp sum had fallen below $29-$; the one exception to this rule was for the very large magnetic storm which peaked on March 15th, 1948 (daily Kp sum of $55+$) for which the post-storm effects appeared to last for 16 days; these were therefore excluded.

Apart from the exception under c) above, a selected period began on the 10th night after the Kp sum had fallen below $29-$ provided the period contained at least 10 consecutive nights of measurements for which the daily Kp sum did not exceed $28+$. The periods, separated into summer and winter, are listed in Table I below. For the purpose of this study, summer is defined as April through August and winter as October through February.

## TABLE I

| Summer: | Winter: |
|---|---|
| May 1 to May 12, 1947 | Oct. 29 to Nov. 7, 1947 |
| June 27 to July 16, 1947 | Nov. 21 to Dec. 4, 1947 |
| April 1 to April 20, 1948 | Dec. 19 to Jan. 1, 1948 |
| | Jan. 18 to Feb. 2, 1948 |

The median field strength for combined summer and winter periods, as well as for summer alone and winter alone is listed in Table II below.

## TABLE II

| | Total Nights | Median Field Strength (dB>1µV/m) | (Q.R.) $\sqrt{2/N}$ |
|---|---|---|---|
| Combined summer and winter period | 105 | 55.6 dB | 2.3 dB |
| Summer period alone | 52 | 59.2 dB | 2.4 dB |
| Winter period alone | 53 | 49.8 dB | 3.2 dB |

Since the median value for the winter period is 9.4 dB lower than that for the summer, a type of absorption which does not appear to be related to magnetic storm and post-storm effects occurred during the winter. The median value of 59.2 dB >1 µV/m obtained for the summer period is therefore selected to represent the experimental unabsorbed median field strength. This value will hereinafter be referred to as the EUM.

The nightly field strength for the periods in Table II have been sorted into cells of 5 dB and plotted individually as normalized distributions in Figures 4a, b and c. The distribution for the combined summer and winter period in Figure 4a shows a major peak in the percentage occurrence centered at 55 dB and a minor at 38 dB. The distribution for the winter period in Figure 4b is similar, except that the two peaks, separated by about 15-17 dB, have an almost equal percentage occurrence. The peak centered at about 38 dB >1 µV/m is uniquely a winter phenomenon because the distribution for the summer period in Figure 4c shows only a single peak, centered at about 58 dB >1 µV/m.

### 2.3 Methods for Relating Median MF Field Strength to Geomagnetic Activity

In this subsection all of the field strength data obtained throughout the year (361 nights) are included in the analysis. For reasons mentioned under subsection 2.1, the data have been divided into two-month periods and the five months October through February separated from the remaining seven months in the analysis. For the sake of brevity the latter months (May through September 1947 and March - April 1948) will hereinafter be referred to as March through September.

### 2.3.1 First Method

By making an arbitrary assumption that days having Kp sums of $\geq 36_0$ are definitely disturbed magnetically, it is possible to show that the two-monthly median values of field strength, computed from the March through September data, decrease linearly with an increase in the percentage of such days. This is shown in Figure 5, where a straight line has been drawn through the median values which fit the line within 1 dB or better. The EUM value is indicated at the top left by a circle. The two-monthly median values, computed from the October through February data, are lower by 4 to 9 dB relative to the straight line. Evidently additional absorption, which was not related to definitely disturbed days, occurred during the October through February period.

While Figure 5 shows that field strength and magnetic storm activity are closely related during the March through September period, two main objections can be raised against this method of analysis. The first objection is that equal weight is given to all values of Kp sums $\geq 36_0$. Magnetic-storm and post-storm-related absorption effects are likely to be greater for days with Kp sums of say $40_0$ to $60_0$ than for days with $36_0$. The second objection is that the method excludes days with Kp sums $\leq 36$-. Magnetic-storm and post-storm-related absorption effects may also occur for days with Kp sums of, say 29- to 36-, albeit to a lesser extent.

### 2.3.2 Second Method

This method which largely overcomes the two objections discussed above, is based on the mean of the 6 most magnetically-active days in a two-month period, as defined by their daily Kp sums. This method was chosen because preliminary tests showed that the mean of the 5, 6 or 7 most magnetically-active days all gave a remarkably close fit to the two-monthly median field strength, computed from the March through September data. For <5 or >7 such days the fit deteriorated. The main objection that can be raised here is that the method is empirical, i.e. it was selected because it gave a close fit to the March through September field strength data, but more serious objections can be raised against methods based on the mean Kp sum or on the percentage or days the daily Kp sum was $\geq$ a certain value.

A plot of two-monthly median field strength versus the mean of the 6 most magnetically-active days, as determined from their daily Kp sums, is shown in Figure 6. A smooth curve has been drawn through the 2-monthly median values computed from the March through September data, terminating on the left at the EUM value. These values fit the curve to within a fraction of 1 dB. The values computed from the October through February data are lower by 6 to 11 dB relative to those indicated by a smooth curve. This difference represents a quantitative estimate of absorption that does not appear related to geomagnetic activity and is evidence that winter anomaly absorption occurred at night, from October 1947 through February 1948, on the 1.02 MHz KDKA Pittsburgh-Ottawa path. (For the sake of brevity, winter anomaly absorption will hereinafter be referred to as WAA).

## 2.4 Additional Evidence of WAA

It is known that post-storm effects have a seasonal variation and that these effects are largest during the winter season    (Belrose and Thomas, 1968). One can therefore argue that the anomalously low field strengths observed during the October through February period were simply due to enhanced post-storm effects. However, results presented earlier in subsection 2.2 that were based on data from which most, if not all, post-storm effects had been excluded, showed the field strengths to be 9-10 dB lower in the winter relative to those in the summer.

That absorption related to magnetic storm and post-storm effects was not the only factor controlling MF field strength at night in the winter  is illustrated in Figure 7.  Here the nightly field strength for the two 27 day periods November 23 - December 19 (indicated by dots) and December 21 - January 16 (indicated by crosses) are compared against each other and against the daily Kp sum. Note that the daily Kp sums are remarkably similar for both periods.  A relatively minor storm occurred on December 6 (Kp sum $33_0$) and again 27 days later on January 3 (Kp sum 35+).  Two of the five pre-storm nights prior to the December 6 storm (December 2 and 4) show low values of field strength, whereas all five nights prior to the January 3 storm (December 29 - January 2) show low values.  The field strengths during the post-storm period January 4-7, related to the latter storm, were 25 - 30 dB lower than those during the post-storm period December 7-10, related to the December 6th storm.  This difference in field strength is likely due to high WAA being present throughout the pre- and post-storm periods December 28 - January 7, but not throughout the pre- and post-storm periods December 1-10.

High WAA is also the likely reason for the six lowest values of field strength in the November 23rd - December 19th period, which occurred on the nights of November 28th, 29, December 2nd, 4th, 15th and 19th.  These values were 6 to 27 dB lower than those that occurred on the storm and post-storm nights of December 6th, 7th, 8th and 9th.  Thus it appears that WAA can occur independently of storm and post-storm effects.

## 3.0  DISCUSSION

While the winter anomaly has been studied intensively by many workers, using groundbased as well as rocket- and satellite-borne measurements, the primary reason for this anomaly is by no means fully understood.  Recent studies show that the anomaly may be caused mainly, if not exclusively, by "meteorological" effects that occur at D-region levels and below, i.e. winds, temperature perturbations and related changes in the D-region constituents which produce electron density enhancements within the region (Offerman, 1979).  However, the physical processes involved continue to be uncertain.  Results presented in the previous sections show that WAA can also occur at night, in the absence of sunlight, during the October through February period.  A study of 2.0 MHz absorption data, recorded during the day at Prince Rupert, B.C., for the period April 1949 through March 1950 (mean sunspot number 124) showed that WAA occurred, in this case also, during the October through February period (Davies and Hagg, 1954).  The magnitude of the WAA in the Prince Rupert case was 10 - 15 dB, whereas that estimated for the 1.02 MHz Pittsburg to Ottawa path was 6 - 11 dB.

From the evidence presented in subsection 2.4 it appears that WAA can at times occur without being in any way related to storm and post-storm effects.  This suggests that WAA can also occur in the absence of precipitating energetic particles.  However, it is possible that there may have been some contribution to the WAA by a weak background "drizzle" of precipitating particles associated with very minor magnetic disturbances, too small to be classified as "storms".  Nevertheless, such precipitation, if it occurred, is unlikely to have been the dominant factor responsible for the observed WAA.

The measurements on which this paper is based were obtained between the 2nd and 3rd hour after ground sunset.  The high absorption observed during the post-storm periods (see Figure 3) was undoubtly related to enhancements in D-region electron density that were present after sunset. Such enhancements are known to develop quickly at dawn, disappear slowly after sunset and persist only weakly throughout the night (Belrose and Thomas, 1968; Belrose, 1972).  Electron density profiles, based on rocket measurements made on days when WAA was present, show enhancements between 75-90 km with a maximum at the 80-83 km level (Beynon and Williams, 1976b).  Such enhancements may also persist for some time after sunset and are the likely reason why WAA was observed at 2-3 hours after ground sunset on the 1.02 MHz Pittsburg to Ottawa path.

## 4.0  SUMMARY

A detailed analysis of one year of night-time field strength measurements, made during high solar activity at Ottawa on the 1.02 MHz KDKA Pittsburg emissions, has yielded the following results:

The two-monthly median field strengths showed reductions of up to 19 dB relative to an experimentally determined unabsorbed value.  The absorption responsible for this reduction was associated with two apparently unrelated geophysical effects:

a)  the magnetic storm and post-storm effect;

b)  the winter anomaly effect.

The absorption associated with the effect under a) was the dominant factor in reducing the median field strength.  For the months May through September 1947 and March - April 1948 it was this factor alone that controlled the skywave field strength.  The two-monthly median field strength for these

months showed a smooth decrease with increased magnetic activity, from 5 to 19 dB relative to the experimentally determined unabsorbed value.

The absorption associated with the effect under b) occurred sporadically during the October through February period. The reduction in the two-monthly median field strength due to this effect alone was from 6 to 11.0 dB.

## REFERENCES

APPLETON, E.V., 1937, "Regularities and irregularities in the ionosphere", Proc. R. Soc. 162, 451.

BARGHAUSEN, A.F. and LILLIE, D.A., 1965, "Some evidence of the influence of long-term magnetic activity on medium frequency skywave propagation", Proc. IEEE 53, 2115-2116.

BELROSE, J.S., 1972, "Synoptic studies of D-region ionization changes and electron densities by the partial reflection differential absorption experiment", Aeron. Rep. 48, 307, Univ. of Ill., Urbana.

BELROSE, J.S. and THOMAS, L., 1968, "Ionization changes in the middle latitude D-region associated with geomagnetic storms", J. Atmos. Terr. Phys. 30, 1397-1413.

BEYNON, W.J.G. and WILLIAMS, E.R., 1976a, "The long-term variation in the ionospheric winter absorption anomaly", J. Atmos. Terr. Phys. 38, 423-429.

BEYNON, W.J.G. and WILLIAMS, E.R., 1976b, "Rocket measurements of D-region electron density profiles", J. Amos. Terr. Phys. 38, 1319-1325.

DAMELIN, J., 1971, "Long-term skywave field strength measurements in the 550-1600 kHz frequency band", FCC Report No. R-7103.

DAVIES, K. and HAGG, E.L., 1954, "Ionospheric absorption measurements at Prince Rupert", J. Atmos. Terr. Phys. 6, 18-32.

LARSEN, T.R., REAGAN, J.B., IMHOF, W.L., MONTBRIAND, L.E. and BELROSE, J.S., 1976, "A coordinated study of energetic electron precipitation and D-region electron densities over Ottawa during disturbed conditions", J. Geophys. Res. 81, 2200-2211.

MATHER, G.R., 1949, "Periodic skywave recording", R. ST. SR5, Dept. of Transport, Canada.

MONTBRIAND, L.E. and BELROSE, J.S., 1976, "Changes in electron precipitation inferred from spectra deduced from D-region electron densities during a post-magnetic storm, J. Geophys. Res. 81, 2213-2221.

'FFERMAN, D., 1979, "Recent advances in the study of the D-region winter anomaly", J. Atmos. Terr. Phys. 41, 735-752.

WANG, J.C.H., 1977, "Prediction of medium frequency field strength in North America", IEEE transaction on broadcasting, BC 23, No. 2, 43-48.
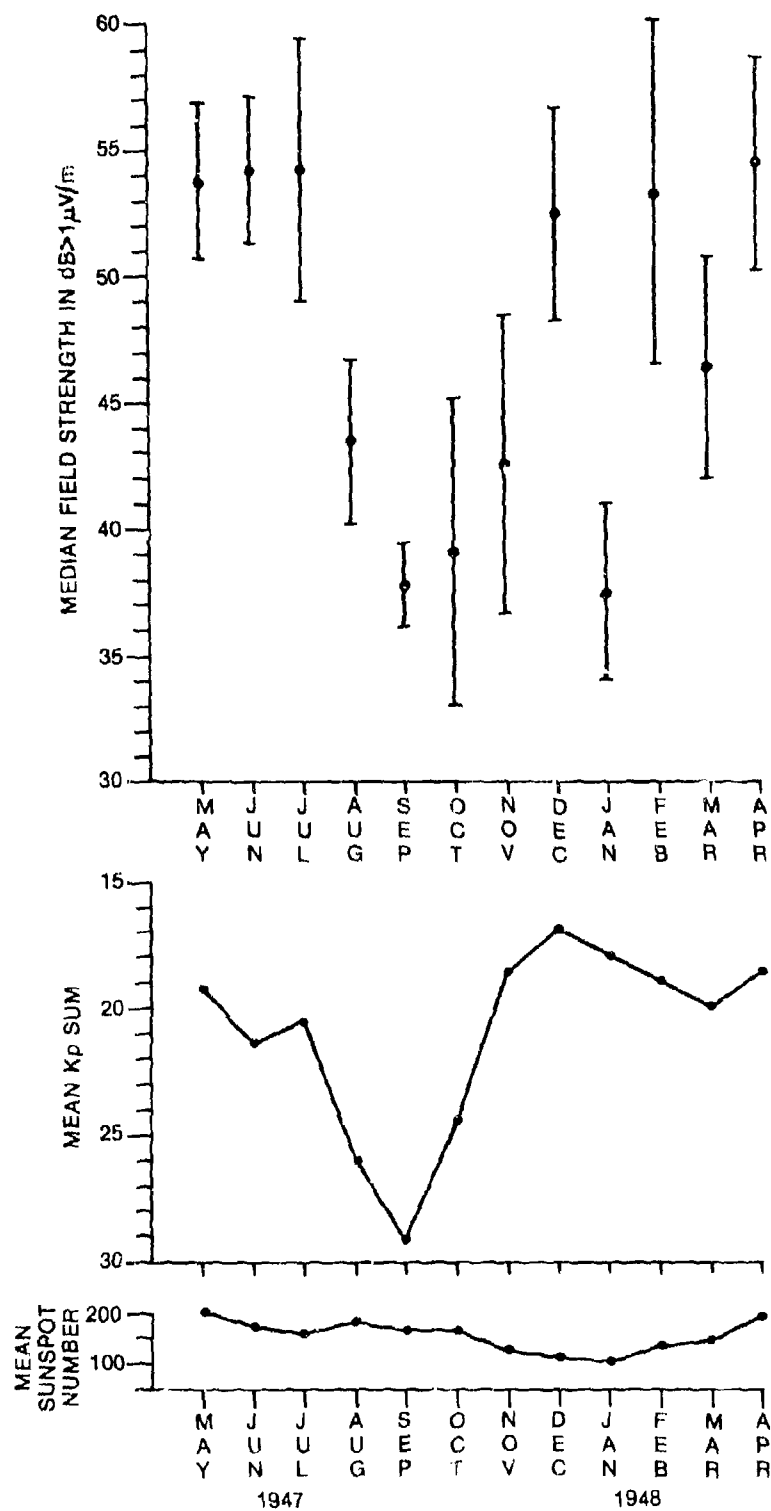
Figure 1.   Monthly median field strength from May 1947 through April 1948 for the 1.02 MHz KDKA Pittsburg-Ottawa path.  Also shown are the monthly mean Kp sums and the monthly mean sunspot number.
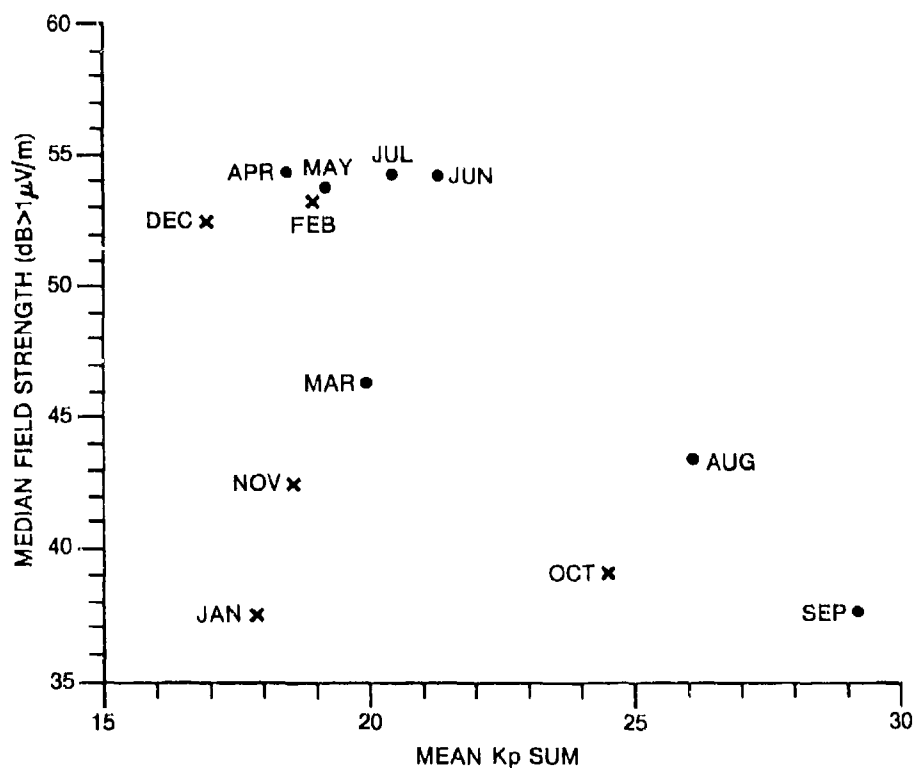
Figure 2.   Monthly median field strength from May 1947 through April 1948 plotted against the monthly mean Kp sum.
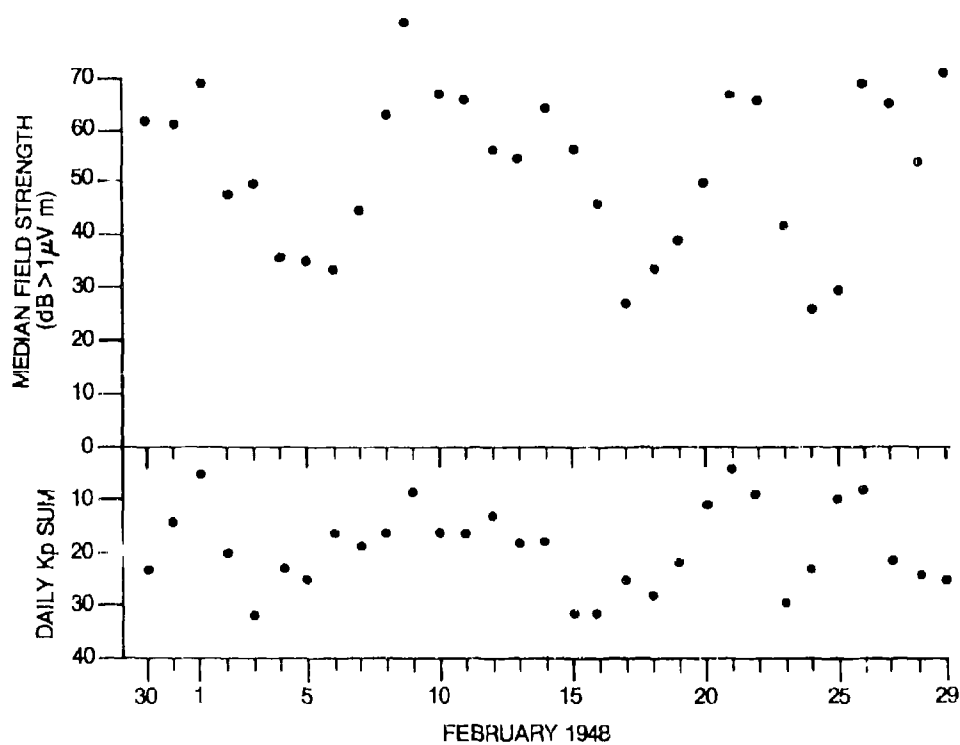


Figure 3.   Nightly field strength and daily (24 hour) Kp sum plotted from January 30th through February 29th, 1948, illustrating the magnetic storm and post-storm effects on the night-time field strengths.
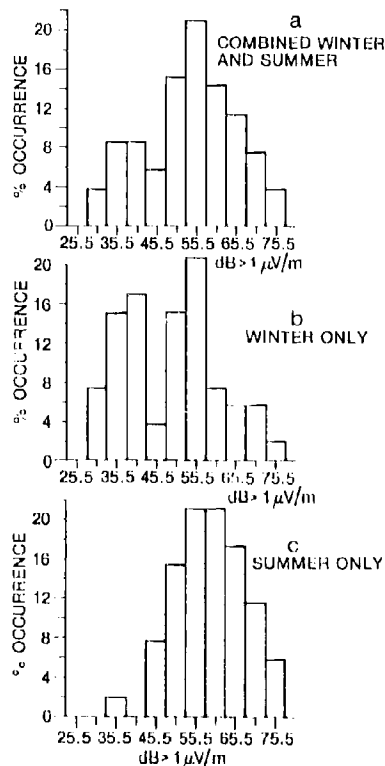
Figure 4.   Normalized distributions of field strength for indicated data periods
(listed in Tables I and II) for which most of the magnetic-storm and
post-storm effects have been excluded.
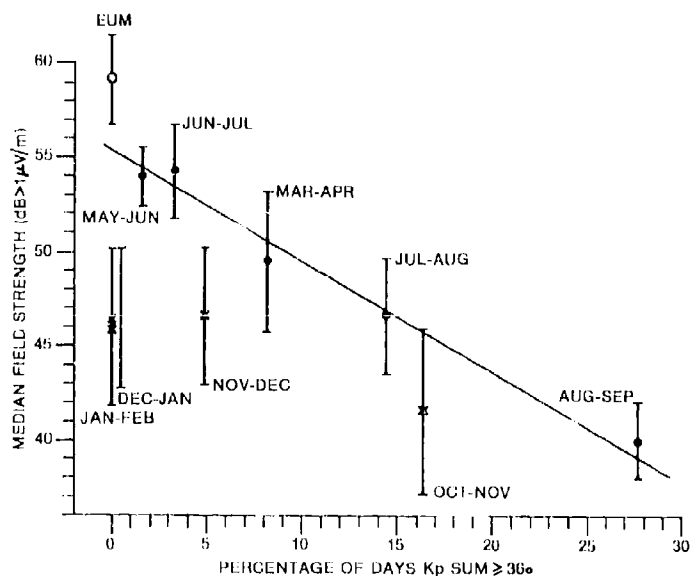


Figure 5.   Two-monthly median field strength based on the May 1947 through April
1948 data, plotted against the percentage of days Kp sum $\geq 36_0$.  Median
values based on the March through September data decrease linearly
with increasing percentage of such days.  Median values based on the
October through February data are lower by 4 to 10 dB relative to
the straight line.  The experimental median unabsorbed value is
indicated by EUM.
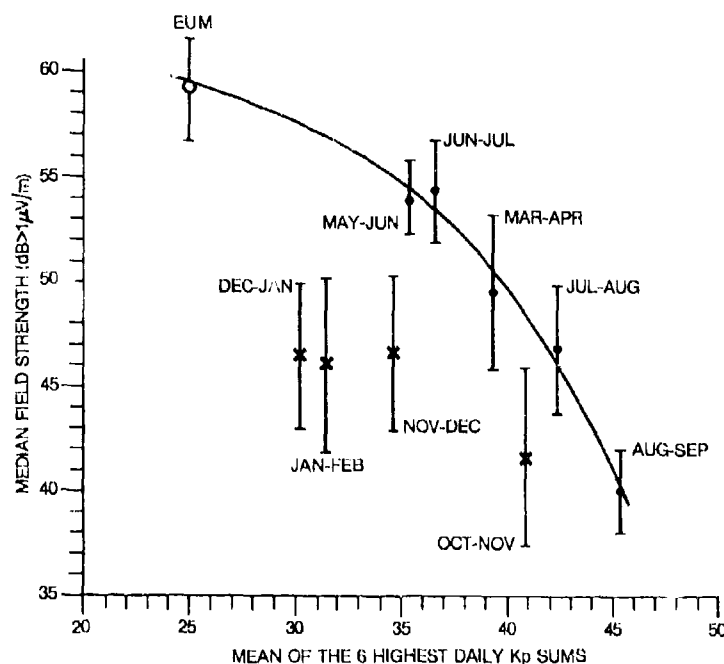
Figure 6.　Two-monthly median field strength based on the May 1947 through April 1948 data, plotted against the mean of the 6 highest daily Kp sums. The smooth curve drawn through the median values based on the March through September data fit these values to within a fraction of 1 dB. The median values based on the October through February data are lower by 6 to 11 dB relative to those indicated by the smooth curve.
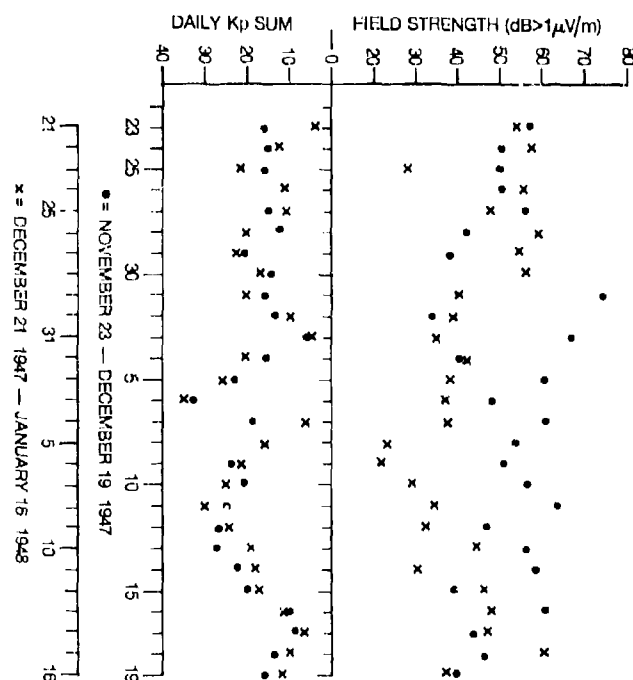


Figure 7.　Nightly field strength for the two 27 day periods November 23rd – December 19th (indicated by dots) and December 21st – January 16th (indicated by crosses) are compared against each other and against the daily Kp sum. Although the Kp sums are remarkably similar for both periods, the field strength is generally lower for the December 21st – January 16th period. This is likely due to higher WAA in this period.

# ON THE DISTORTIONS OF THE MODULATED RADIOWAVES IN THE IONOSPHERE

by

M.Cutolo, S.Feliziani and E.Moriconi
Istituto di Fisica, University of Bari, Bari, Italy
Istituto di Matematica, University of Camerino, Italy
Centro Studi di Radiopropagazione, University, Naples

## ABSTRACT

During the years 1957, 1958 and 1959 many experiments were made by one of us (M.C.) on the Phenomenon called "Ionospheric Self-modulation" at oblique incidence.

The Transmitter was Radio AFN Frankfurt (872 kHz, 150 kW) that emitted its own carrier at 150, 100 and 50 kW, at 60% of modulation. The frequency of modulation varied from 30 Hz to 5000 Hz. Each frequency of modulation was emitted for two consecutive minutes. For the first minute the power was 150 kW and for the second 50 kW and viceversa.

The receiving Station was located in Naples (Italy) at the Institute of Technical Physics of the University of Naples. The measurements were made with the envelope method. In this way we had the envelope of the modulated wave on the screen of an oscilloscope linked to the output of the second I.F. of the reciever.

During the experiments we made 111,273 measurements of which 8188 were affected by sensitive distortions due to the Ionosphere. In this paper we work with these distortions.

As the transmissions were made with different powers it has been easily noticed that the distortions depend on the EMITTED POWERS. This was clearly demonstrated by diagrams and tables. The amplitudes of the first, second and third harmonics change in function of the emitted power. This dependence is important because it is necessary to know if the phenomenon is "linear" or "non linear" to build a theory. Using the Vilienskij's equations it is possible to calculate the modulation percentages of each harmonic. We see in this way that the percentages of second and third harmonic are too low as regards to those of first harmonic and to the emitted percentage of AFN Frankfurt.

After this verification we hope to be able to build a useful theory to explain the reasons of the distortions in our experiments.

## 1. INTRODUCTION

The passage of a radiowave through the Ionosphere often produces some distortions of its own envelope. As we know the mechanism producing the distortions of the envelope of a radiowave has always been the subject of long discussions. Some people believe that the distortions are due to the interference, in the receiving antenna, of electro-magnetic rays that have crossed different paths in the Ionosphere, some others think that the interference occurs in the plasma, some other people believe instead, that the distortions are due to non linear processes of the same Ionosphere.

To eliminate the above perplexity we have thought to take advantage of the experiments organized by USA Air Force to study ionospheric self-modulation phenomenon. In fact, to study the eventual dependence of this phenomenon on power, Radio AFN Frankfurt, that worked as the transmitter, made rapid variations of its own electromagnetic power during its work.

It appears that some distortions clearly depend on power and that therefore they are of a non linear nature.

## 2.  EXPERIMENTAL METHOD

A long series of experiments was made by Cutolo and collaborators from July 1957 to November 1959 using as a transmitter, AFN Frankfurt (Federal Germany). The aim of these experiments was that of studying the dependence of Selfmodulation (decrease or increase of the percentage of modulation of a modulated radiowave when this passes through the Ionosphere) on the transmitted power.

As it is reported in the article (1) the "knowledge of the dependence is necessary to build a theory capable to explain the mechanism producing the phenomenon. In fact if the dependence occurs we can use the interaction theory; on the contrary the dispersion of the ionized medium, the interference or other phenomena are to be taken into consideration. The importance of the concept of non linearity in the Ionosphere is reported in the quoted article".

Radio Frankfurt (872 kHz, 150 kW) emitted its modulated carrier with different power that is 150 kW, 100 and 50 kW and viceversa. The percentage of modulation was always constant that is 60%. The frequencies of modulation were 50 Hz, 200, 400, 500, 700, 1150, 1300, 1600 and 3300 Hz.

Each frequency of modulation was emitted for two minutes. For the first minute the power was 150 kW, second minute 50 kW and for the third was again 150 kW.

The receiving station, located in Naples at the Technical Institute of the University, consisted of an antenna and a super-heterodine receiver. The output of the second I.F. was linked to an oscillograph to obtain the envelope of the modulated wave. A camera photographed the oscillograms. The receiver was calibrated by an audiofrequency generator.

The experiments were always made during the night from 0115 to 0325 T.E.M.

## 3.  HARMONIC ANALYSIS GRAPHICALLY

Figure 1 is an example of the distorted envelope. To find the harmonics that produce the distortions of the wave envelope we used the graphic method. To avoid long and laborious calculations we adopted a simple mathematic diagram with 24 ordinates and 7 constants. It is founded on the Bessel functions that give the constants of Fourier series.

This series is the following:

$$y = a_0 + a_1 \cos x + a_2 \cos 2x + \ldots a_p \cos px$$

where the constants $a_0, a_1, a_2 \ldots b_1, b_2, \ldots$ are given by:

$$a_0 = \frac{1}{n} \Sigma y_k = \frac{1}{n} (y_0 + y_1 + \ldots y_{n-1})$$

$$a_r = \frac{2}{n} \Sigma y_k \cos zx_k = \frac{2}{n} (y_0 \cos zx_0 + y_1 \cos zx_1 + \ldots)$$

$$b_r = \frac{2}{n} \Sigma y_k \sin zx_k = \frac{2}{n} (y_0 \sin zx_0 + y_1 \sin zx_1 + \ldots)$$

The first analysis consisted in calculating all amplitudes of the harmonics constituting the wave.

The coordinates of each sampled photogram are registered on magnetic disk sequentially and grouped in frequency classes. The theoretical curve suggested by the mathematical model at hand, is there fitted to each series of coordinates in order to produce the first three harmonics and their ratios. The result has been printed only if the theoretical curve differed from the experimental curve for a small error.

## 4.  DISCUSSION OF THE RESULTS

During the experiments 8188 oscillograms had the envelope distorted. The number of the distortions was different for each frequency of modulation. Each of these was emitted for one minute. During the minute we made 22 measurements for each frequency of modulation. Figure 1 is an example of the distorted envelope.

To understand the reasons of the distortions we considered it opportune to calculate the amplitudes of first, second and third harmonics with the method above illustrated. The calculation of the amplitudes of the harmonics were made with an opportune program with the computer.

The number of the distortions was different for each frequency of modulation. To have the same statistic we made the mean of 22 measurements for the first, second and third harmonic of each frequency of modulation. That is 22 measurements for each harmonic and for power 50 kW and for 150 kW.

Figure 2 is the diagram of 1 harmonic of each frequency of modulation and for 50 and 150 kW. Each point of the diagram is the mean of 22 measurements.

Figure 3 is the diagram of 2 harmonics for each frequency of modulation for 50 and 150 kW. Figure 4 is the diagram of third harmonic.

Seeing the diagram of Figure 2(a) we note that the amplitudes of first harmonic for each frequency of modulation is smaller at 150 kW than that at 50 kW, except the frequencies 200 and 1600 Hz where the variation of the amplitude is small and it has an opposite behaviour. Figure 3 gives the behaviour of second harmonic. We see that the variation of the amplitudes are larger and more regular except the frequencies 1600 and 3300 Hz where the amplitude is larger at 150 kW than at 50. Figure 4 represents the behaviour of third harmonic. Its amplitude is larger than the first and second harmonic except the frequencies 1150, 1300 and 1600 where the variation is very small and opposite.

Studying the diagrams we believe we have been able to ascertain that the amplitudes of the harmonics vary with the power and that probably the phenomenon of distortion is consequently NON LINEAR.

## 5. CALCULATION OF THE PERCENTAGE OF MODULATION OF THE HARMONICS

As it is written in the paper (1) the measurement of the modulation percentage was made by envelope method there described. As in this case the modulation envelope is distorted, it is impossible to use the above method. Therefore we prefer to calculate the percentage by J.M.Vilenskij theory published in 1953 and improved by V.M.Fain and S.A.Zhevakin in 1956. To calculate the current that the electric field of the radiowave generates in the Ionosphere, Vilenskij makes use of electron distribution function that gives the Davidov equation.

If a modulated radiowave passes through the Ionosphere we have $E = E_0 (1 + M \cos nt)$ where $n$ is the angular frequency of modulation and $M$ is the percentage of modulation transmitted by AFN Frankfurt.

Owing to non linearity of the Ionosphere it is possible the generation of harmonics of the carrier and of frequency of modulation. We have ignored the harmonics of the carrier frequency because we don't have any experimental data.

If $n$ is small, that is $n \ll (2m/M)\nu_{eff} = G\nu_{eff} \cdot 1400$ the percentages of modulation of the frequencies from 1 to 1000 Hz of the first harmonic $n$, of second $2n$ and of third $3n$ are respectively:

$$M'_n = \frac{M(1 - 3\gamma \cdot \frac{3}{4}\gamma M^2)}{1 \cdot \gamma \cdot \frac{3}{2}\gamma M^2}$$

$$M'_{2n} = \frac{\frac{3}{2}\gamma M^2}{1 - \gamma - \frac{3}{2}\gamma M^2}$$

$$M'_{3n} = \frac{\frac{1}{4}\gamma M^3}{1 - \gamma - \frac{3}{2}\gamma M^2}$$

where $M$ is the percentage of modulation of the transmitter, $M'_n$, $M'_{2n}$, $M'_{3n}$ the percentages of first, second and third harmonic of the signals received in Naples and $\gamma$ is a constant.

If $\quad M = 0.6; \quad \gamma = 10^{-2}; \quad G = 2 \times 10^{-3}; \quad \nu_{eff} = 7 \times 10^{-5}$

we have that:

$$M'_n = 58\%; \quad M'_{2n} = 13.5\%; \quad M'_{3n} = 1.3\%.$$

The value of $G = 2m/M = 2 \times 10^{-3}$ (where $m$ is the mass of the electron and $M$ is the mass of heavy particles that is, ions, atoms, molecules) as correctly measured by R.Smith in 1966 (4).

Except the percentage of the first harmonic, the percentages of the second and third harmonic are very small compared with the percentages of the first harmonic and of $M$.

If $n \cdot 2m/M\nu_{eff} = 1400$ that is for frequencies higher than 1400 the percentage of the first harmonic is:

$$M'_n = \frac{M}{1 - \gamma\left(1 + \frac{M^2}{2}\right)} = \frac{0.6}{1 - 10^{-2}\left(1 + \frac{|0.6|^2}{2}\right)} = 0.6072 = 60.7\%.$$

The value of the percentages of $M'_{2n}$ and $M'_{3n}$ are more difficult to calculate because the formulas hold the value of the electric field that the wave has in the Ionosphere. We are not able to calculate this last value because we don't know the correct path of the wave during its propagation from Frankfurt to Naples.

## 6. CONCLUSION

The examination of the diagrams of Figures 2, 3, 4 shows that the amplitudes of the three harmonics clearly vary with the power of the transmitter. Therefore we think that probably the phenomenon of distortion is not linear. Utilizing Vilenskij equations we have also calculated the percentages of modulation of the harmonics for each frequency of modulation.

Concluding: when a modulated radiowave propagates through the Ionosphere the non linear properties of the plasma can generate some distortions of the modulation envelope.

The importance of this result is the following: If the phenomenon of distortion depends on the power it is non linear and therefore the mechanism of its generation can be explained by interaction theories of V.A.Bailey, V.L.Ginzburg, A.V.Gurevich, M.Sodha and of many others. On the contrary, if the phenomenon were linear (it is not our case) that is it does not depend on the power, the mechanism of its generation can be due to dispersion of the plasma, to interference, in the receiving antenna or in the Ionosphere, of rays that have crossed different paths in the Ionosphere or to other reasons.

Non linearity means that the electrons acquire a fair amount of energy from the electric field of the radio wave crossing the plasma. Since the mass of the electron is very small compared with that of the molecules and the ions, the electron does not transfer to the latter all the energy acquired from the electric field so that it heats up, with the result that the dielectric permittivity of the plasma begins to depend on the electric field of the radio wave. Consequently the polarization and the conduction current are no longer proportional to E (electric field of the radio wave), so that all the electro-dynamic processes, in particular the propagation of radio wave, acquire the property of no longer being linear, with the consequent violation of the principle of superposition.

## 7. ACKNOWLEDGEMENTS

## 8. REFERENCES

1. Cutolo, M.        *Ionospheric Self-modulation etc.*, see page 30-7 of this AGARD Conference Proceedings
   Gaffuri, G.       1981.

2. Vilenskij, J.M.   *Zhurnal experim. Theor. Fiziki*, T.26, 42, 1954.

3. Zhevakin, S.A.    *Soviet Phys. Jept*, 3, No.3, 417, 1956.
   Fain, V.M.

4. Smith, R.A.       *Proc. Conf. Phys. Low Ionosphere*, p.235 and 335, Ottawa, 1966.

5. Bailey, V.A.      *Radio Science*, Vol.69D, Section D, p.9, 1965.

6. Ginzburg, V.L.    *Sov. Phys. Uspekhi*, 3, 115, 175, 1960.
   Gurevich, A.V.

7. Gurevich, A.V.    *Non Linear Phenomena in the Ionosphere*, Springer Verlag, New York, Heidelberg, Berlin,
                     1978.

8. Sodha, M.S.       Br. J. appl. Phys., 16, 1923, 1965.
   Kaw, P.K.

Fig.1 Example of a distorted wave envelope. The frequency of modulation is 200 Hz, the modulation percentage transmitted by AFN Frankfurt is 60%; the emitted power 50 kW
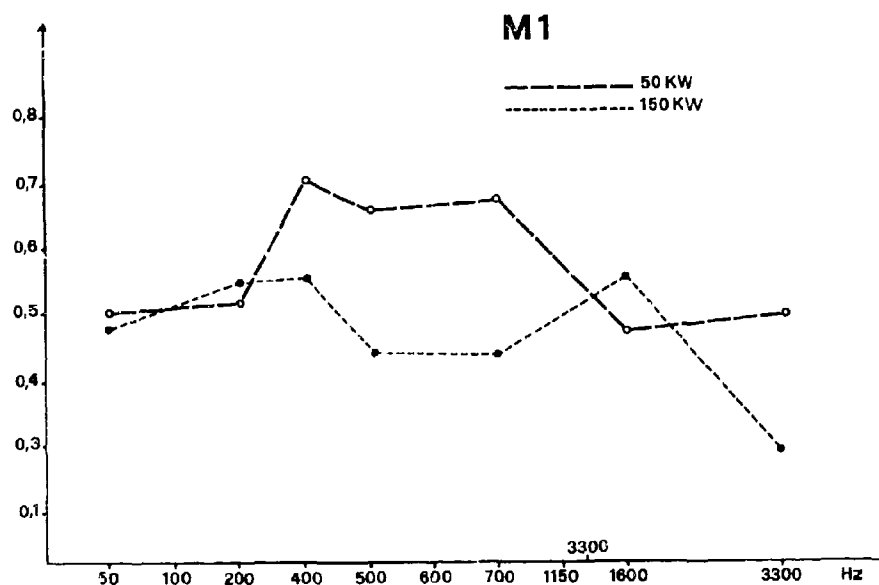


Fig.2 Diagram of first harmonic. On the abscissae there are the frequencies of modulation while on the ordinates the mean of 22 measurements of the amplitudes of second harmonic for each frequency of modulation and for 50 kW and 150 kW

Fig.3    Diagram of second harmonic for the power 50 and 150 kW
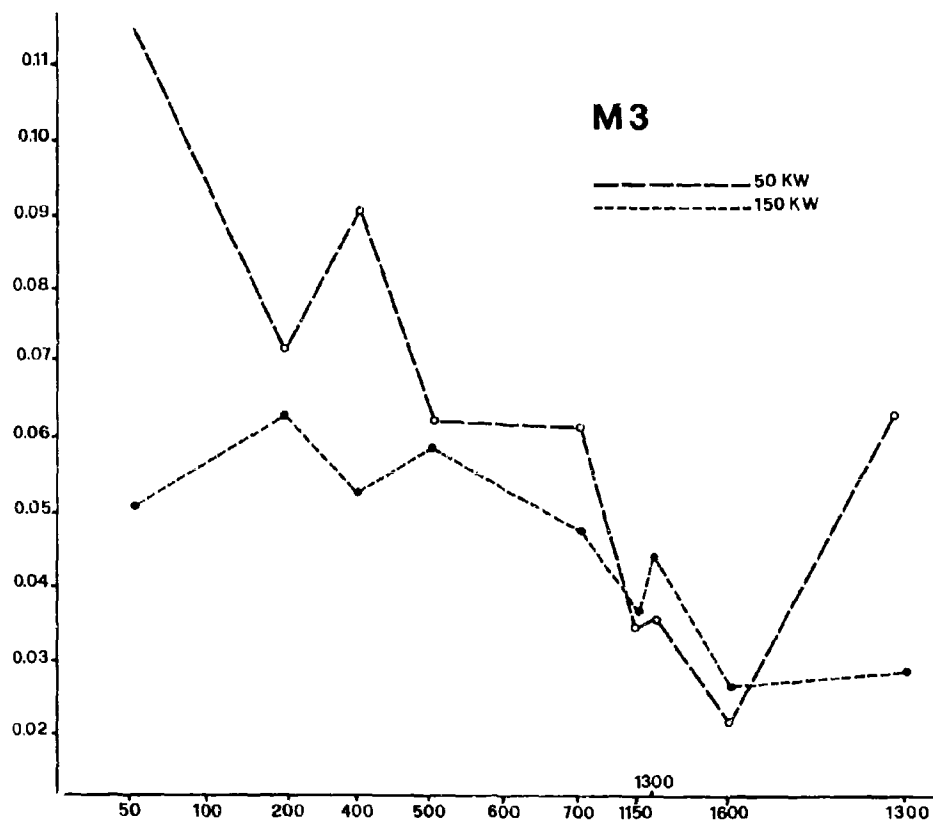


Fig.4    Diagram of the third harmonic for the power 50 and 150 kW;
the meaning of the abscissae and ordinates is that described above

# IONOSPHERIC SELF-MODULATION OF A MODULATED RADIOWAVE WITH FREQUENCY FAR FROM LOCAL GYROFREQUENCY

by

M.Cutolo and G.Gaffuri

Istituto di Fisica, University of Camerino, Camerino, Italy
Istituto di Fisica, University of Bari, Bari, Italy
Centre Studi di Radiopropagazione, University, Naples, Italy

## ABSTRACT

A long series of experiments on self-modulation (increase or decrease of the percentage of modulation of a modulated radio-wave when it passes through the Ionosphere) was made by M.Cutolo and collaborators from 1957 to 1959, to study the dependence of the phenomenon on the power transmitted. The transmitter was Radio AFN Frankfurt (872 kHz, 150 kW) and the receiving station was in Naples. The experiments were always made during the night (0115 - 0325). The measurements were made with the envelope method and always with same statistics.

Radio AFN Frankfurt emitted its carrier frequency with different frequencies of modulation and different powers (150, 100, 50 k). Each frequency of modulation (30 - 5000 Hz) was emitted for 4 consecutive minutes. For the first minute the power was 150 kW, second minute 100 kW, third minute 50 kW, and for the fourth was again 150 kW.

The first characteristic is the finding, for the first time, an increase in the percentage of modulation received with regard to the percentage emitted by the transmitter. The most important observation, however, is the clear dependence of demodulation or the over-modulation on the electromagnetic power. Figure 1 clearly shows this dependence.

Our discussion of the theories made to date to explain the self-modulation shows that no theory is able to explain the phenomenon because the powers considered in the theories are higher than those used by us in our experiments. If we develop an exponent of an equation in a MacLauren series and give a limit to the value of the exponent, we think that the Carlevaro theory could be able to interpret some of the behaviours observed by us. So we have that $\nu_0$ varied during the experiments from $8.20 \times 10^4$ to $3.60 \times 10^6$.

## INTRODUCTION

The concept of non-linear processes in a plasma.

As it is known "non linear processes" in an ionized medium (plasma) are very important not only for the propagation of the radio-waves but also for the applications in the telecommunications and in military operations.

The first non linear phenomenon was discovered by B.D.H.Tellegen in 1933 and it is the Luxembourg effect.[1] V.A.Bailey and D.F.Martyn[2] and then V.A.Bailey alone built the theory suggesting also the possibility to generate the Luxembourg effect with resonance[3]. The early experiments of Luxembourg effect with resonance called gyrointeraction, were made with success by M.Cutolo and collaborators between 1964 and 1950 (Ref.4). In 1957 V.L.Ginzburg used the kinetics theory of Boltzman to explain the mechanism of that phenomenon[5].

Ginzburg and Gurevich made the theory of the effect called also cross modulation or interaction of radiowaves[6]. In 1956 A.V.Gurevich introduced the concept of "plasma field"[7] and developed the theory of self-action and interaction of strong radiowaves in the lower Ionosphere. If a radiowave with carrier frequencies not too high and with power not low propagates through the Ionosphere the electric field E of the wave gives to the electrons a fair amount of the energy. If the propagation occurs in the D region or in nocturn E layer where the number of electrons is very small (at night $\sim 100$ electrons/cm$^3$ or less) and the mean free path is considerable, the electron has time to acquire a fair amount of

energy from the electric field of the radiowave crossing the regions mentioned above. But since the mass of the electron is very small compared with that of molecules and the ions, the electron does not transfer to the latter all the energy acquired from the electric field so that it heats up, with the result that the dielectric permettivity of the plasma begins to depend on the electric field E. It follows that the polarization and the conduction current are no longer proportional to E, so that all the electro-dynamic processes, in particular the propagation of radiowaves, acquire the property of no longer being linear, with the consequent violation of the principle of superposition[7].

The "plasma field E p" according to A.V.Gurevich is the following

$$E_p = \sqrt{\left[ 3KT \frac{m}{e^2} G_{eff}(T) (w^2 + \nu_{eff}^2) \right]}$$

where K is Boltzman's constant, T the temperature of the heavy particles (molecules, atoms, ions), m and e the mass and the charge of the electron, $G_{eff}$ is the fraction of energy lost by an electron in a single collision, w the angular frequency of the radiowave and $\nu_{eff}$ is the actual number of collisions per second (collision frequency).

If E is $E \ll E_p$ the electric field is said to be weak and therefore it has no effect on the ionized gas (plasma). But if $E > Ep$ (or $E \gg Ep$) the field is said to be strong (or very strong) and so it is able to change substantially the properties of the plasma, as mentioned before.

Conclusion: non linear ionospheric property means that in the plasma the electrons heat up more than the molecules with the result that $\epsilon_0$ is no longer constant but begins to depend on the electric field E.


## SELF-MODULATION

As it is known the phenomenon called by Cutolo[8] Ionospheric Self-demodulation was observed, for the first time, in May 1948, during the Italian experiments on "Luxembourg effect with resonance" or better "Gyrointeraction"[3].

Self-demondulation consists in the decrease of the received modulation percentage with an increase of the modulation frequency. This phenomenon has been observed with carrier frequency varying around the local gyrofrequency. The knowledge of the dependence on power is necessary to build a theory capable to explain the mechanism producing the phenomenon. In fact if the dependence occurs we can use the interaction theory; on the contrary the dispersion of the ionized medium, the interference or other phenomena are to be taken into consideration. Up to today we don't know whether the phenomenon depends on the electromagnetic power emitted by the radio Station or not.

To study the eventual dependence on power a long Series of experiments of self-demodualtion was made by Cutolo and collaborators from 1957 to 1959. Thanks to US Air Forces we used Radio AFN Frankfurt as the transmitter. The receiving station was in Naples, at the Institute of Technical Physics of the University.

Radio AFN Frankfurt (Federal Germany) (872 kHz, 150 kW) emitted its carrier frequency with different frequencies of modulation and different powers (150, 100, 50 kW). Each frequency of modulation (30 3000 Hz) was emitted for 4 consecutive minutes. For the first minute the power was 150 kW, second minute 100 kW, third minute 50 kW, the fourth was again 150 kW and vice-versa 50, 100 and 150 kW.

The measurements were made with the envelope method in the receiving station in Naples. The envelope method consists of reading the maximum value A and the minimum B of the envelope (Fig.1). The percentage M of the direct ray or M' of the echo was calculated by means of the formula:

$$M \text{ (or } M') = (A - B)/(A + B) \times 100$$

including the required corrections: the influence of the receiver, the thickness of the oscillograph trace, etc.

By this method we made the measurements at H.F. or at I.F. (intermediate frequency) and not at audiofrequency as the researcher J.W.King did. In his paper published on Journal of Atmospheric and Terrestrial Physics in 1959 (Ref.9) Dr King asked Cutolo what precaution he used to eliminate the influence of the selective fading on the measurements. The precaution consisted of using the envelope method. In fact by this method it was possible to ignore the distorted envelopes (due eventually to selective fading) from those that were perfectly sinusoidal (not due to selective fading) and so the researcher (M.C.) was able to show that Demodulation and Overmodulation were not due to selective fading.

The first characteristic of the experiments is the infrequent presence of selective fading and distortions of the wave envelope compared to that found in former experiments. The second characteristic is the observation, for the first time, of an increase of the percentage of the received modulation, with regard to the percentage emitted by the transmitter. An other important observation, however, is the CLEAR dependence of the demodulation or the overmodulation on the electromagnetic power.

For all those reasons we called the phenomenon SELF-MODULATION and not SELF-DEMODULATION.

The principal results are the following.

Figure 2 clearly shows the dependence of the phenomenon on power. On the abscissae there are the frequencies of modulation with which the carrier was modulated for a minute in the transmitting station. The ordinates are the percentage of modulation received in Naples, after the passage of the radio-waves through the ionosphere. The dotted line parallel to the X-axis is the percentage of modulation (60%) emitted by AFN Frankfurt. All the points below the dotted line represent the demodulation, the points above, the over modulation undergone by the wave in the plasma. Each point is the mean of the sixty observations made during an exact minute of transmission. The vertical line represents the fluctuation of the received modulation during the minute. As you see the percentage of received modulation varies, for every frequency of modulation, with the powers. In fact, at 150 kW the percentage M' for the frequency 30 Hz is 33.5%; at 100 kW is 39.2%; at 50 kW is 47.0%; then it returns to 33.6% at 150 kW. And so for all other frequencies, at least up to 1000 Hz.

The solid line is the theoretical curve calculated by us, as we will see later.

A very interesting observation is the following: as the power varies there is not only a dependence of M' on the power, but as this varies the behaviour of the phenomenon changes. While in Figure 3 at a power of 150 kW there is demodulation at low frequencies and a tendency to retake 60% at high frequencies, in the case of 50 kW there is a sensitive over-modulation at low frequencies of modulation and demodulation at high frequencies.

In Figure 4 it is noted with interest that while for the power of 150 kW (Fig.4(a)) there is only demodulation, for the power of 50 kW (Fig.4(b)) there is only overmodulation.

In Figure 5 the percentages of demodulation clearly depends on power. In fact the demodulation is more sensitive at 150 kW then at 50 kW.

Figure 6 is a typical example of overmodulation and that is, of gain of percentage of modulation with regard to that emitted by the transmitter. In these figures at a power of 50 kW there is greater overmodulation than at 150 kW.

As we said before the solid lines of the figures are the theoretical curves obtained by the Authors. The dependence of the phenomenon on the power in the cases we have observed shows that the experimental results can be analysed by the interaction theory. Some analyses start from BAILEY's equation. Hibbers (1955) (Ref.10) and Carlevaro (1956) (Ref.11) presented a linear solution of that equation.

## THEORETICAL REMARKS

The CARLEVARO's solution is the following:

$$\frac{M'^2}{M^2} = \frac{1 - 4\rho(1-\rho)\cos^2\psi}{(1 - M^2\cos^2\psi)^2} \qquad [1]$$

where M is the depth of the transmitted modulated wave, M' the received percentage after the passage of the radio-wave through the ionosphere, $tg\psi = nG\nu$, n = is the angular frequency of modulation, G is the mean relative energy loss in a collision, $\rho = \alpha/2[w(w + GQ_0]$, $\nu$ is the collision frequency of the electrons in the presence of the radiowave, $Q_0$ is the thermal energy of the electrons in absence of the radio-waves, w is the mean value of the work done by the electric field of the radio-wave on an electron between two consecutive collisions and $\alpha$ is the total absorption coefficient.

If the wave is modulated the electric field $E = E_0(1 + M \sin nt)$.

If we indicate with Eu the amplitude of the electric field after is passage through the ionized layer we have

$$Eu = e^{-\alpha}Em(1 + M \sin nt) \exp[-\alpha\rho M \cos\psi \sin(nt - \psi)] \qquad [2]$$

where all symbols are known.

If $\alpha\rho M \cos\psi$ is small with respect to 1, the second exponential of 2 can be developed in MacLauren series

$$Eu = e^{-\alpha}Em[1 - \rho M^2\cos^2\psi][1 + a \sin nt + b \cos nt + c \cos(2nt - \psi)] \qquad [3]$$

where 
$$a = M\frac{1 - \alpha\rho\cos^2\psi_1}{1 - \rho M^2\cos^2\psi_1}; \qquad b = M\frac{\alpha\rho\cos\psi_1\sin\psi_1}{1 - \rho M^2\cos^2\psi_1}; \qquad c = \frac{\rho M^2\cos\psi_1}{1 - \rho M^2\cos^2\psi_1}.$$

The depth of modulation of the wave after its passage through the layer is

$$M^2 = a^2 + b^2 .$$

Resolving a and b by [3] one has the Carlevaro's Equation [1] reported above.

Figure 7 shows a diagram (Carlevaro, 1956) in which one sees that for each value of M there are four values of $\rho$, and for each of these values of $\rho$ there are four characteristic behaviours a, b, c, d. Now we make a brief critical analysis of the final part of Carlevaro's work and this is to show how all the behaviours suggested by him do not correctly represent the phenomenon.

To obtain [3] and [4] from which we soon have [1], one has developed in MacLauren series the exponent of [2] given a limit to the value of the exponent. To calculate Eu with a fixed percentage precision one must approximate the exponential with the same precision. If the maximum imprecision is 10% the exponent must be less than 0.4 for each value of $\psi$, that is

$$\rho M \cos \psi_1 \leqslant 0.2 .$$ [4]

If we want the curve M' in function of the frequency of modulation to have the fixed precision on the whole band of frequencies (beginning from n = 0) one must have $\left(\text{remembering that } \mathrm{tg}\psi = \dfrac{n}{G\nu}\right)$

$$\rho M \leqslant 0.2 .$$ [5]

We have added the dotted line $\rho M = 0.2$ in Figure 7 and the curves that have fixed precision are those below this line. If the point $(\rho; M)$ is not below the dotted line, that is [5] is not valid, the curve has the fixed precision beginning only from the minimum value for which [4] is valid.

It is easy to demonstrate that there is a clear dependence of $\rho$ on $\dfrac{n}{G\nu}$ when $\rho M \cos \psi = 0.2$ is valid for the same values of M. From this it is also easy to calculate the curve $(\rho; G\nu; M)$ that has the limitation [4].

With the approximation that it is possible to make in the case of the experiments $\dfrac{w_0}{GQ_0} \ll 1; \nu \simeq \nu_0$

$$M'(F) = \frac{M\sqrt{1 - 4\rho(1 - \rho)\cos^2 \psi_0}}{1 - \rho M^2 \cos^2 \psi_0}$$

where

$$\cos \psi_0 = \frac{[G\nu_0]^2}{[G\nu_0]^2 + 4\pi^2 F^2}$$

F is the frequency of modulation ($F = n/2\pi$), $\nu_0$ is the collision frequency in absence of an electric field, $Q_0$ is the thermal energy in absence of the radiowave.

To determine the parameters $(\rho; [G\nu_0])$ giving the curve M'(F) closest to the experimental is closest to the experimental points, we have applied a method of research of the minimum in the following manner.

We have defined a function of $\rho$ and $[G\nu_0]$ according to the following expression

$$\epsilon(\rho; [G\nu_0]) = \frac{\sum\limits_{i=1}^{N} \xi_i}{N}$$

where N is the number of the experimental points available and

$$\xi_1 = |M'(F_c; \rho; [G\nu_0]) - M_{si}|$$

is the absolute value of the difference between the experimental value at a frequency of modulation and the corresponding value of the function M'(F). The minimization of the function and the determination of the corresponding couple of parameters $(\rho; [G\nu_0])$ were made by means of a HP 9100 B computer. The results are given in the single figures. As can be seen analyzing the function M'(F) two pairs of parameters exist $(\rho_1; [G\nu_0]_1)$ and $(\rho_2; [G\nu_0]_2)$ that give the same curve and therefore both make the function minimum. For this reason some of the experimental curves are interpretable with two couples of different parameters.

To make sure that the curves calculated with the parameters so determined enter totally or partially in the specified limits earlier we proceeded as follows: Given that the curves taken into examination were all obtained in experiments in which M = 0.6 the condition (5) is satisfied for $\rho \leqslant 0.3$. The curves that are obtained, therefore, with these values of $\rho$ come within the precision fixed on the whole band of frequencies beginning from F = 0. For $\rho > 0.33$ the curves are only partially acceptable and precisely only beginning from a frequency $F^x$, for which the condition (4) is satisfied.

To calculate $F^x$ a graph can be used, from which, assigned a value of $\rho$, it is possible to determine the value $n^x/[G\nu_0]$ that satisfies the (13). From this value, $([G\nu_0])$ being known, it is easy to calculate $F^x$.

We were able to build 18 diagrams of which we report here only 4.

From the examination of all the measurements it appears that $\nu_0$ varied during the experiments from $8.20 \times 10^4$ to $3.6 \times 10^6$. From analysis of the diagrams the following results are obtained:

(a)   for diagram 4a it was not possible to determine any couple of parameters because the function $\epsilon(\rho ; [G\nu_0])$ does not give well-defined minima.

(b)   for diagrams 6a, 6b, 6c, 3b, the parameters were determined with the method described, but no couple can be accepted because each of them is such that the experimental points used in the determination are all, or at least the most significant, outside the valid portion of the curve.

(c)   the analysis of the remaining diagrams has furnished for each a double couple of parameters that lead to the same curve of these couples, however, only the first is acceptable because the second has a $\rho$ such that the experimental points are in the same condition as those in the diagrams of item (b).

The values of the constants used in the above calculations are: $E_0 = 7.21 \times 10^{-7}$ (P power in kW) is the electric field in the self-modulation zone (half path between Frankfurt and Naples); $G = 5 \times 10^{-3}$ mean relative energy loss in a collision (King 1957); $T = 200°$ K, temperature of the ionosphere in the self-modulation zone.

## CONCLUSION

From examination of the diagrams it appears that self-modulation may have three different behaviours illustrated in the figures and that the most interesting is cerainly *overmodulation*.

The diagrams show, in particular Figure 2, that the phenomenon clearly depends on the power emitted and therefore it is a non-linear phenomenon.

From the brief discussion made about the Carlevaro-Hibberd's theories, it is found that these are not able to explain all the behaviours indicated in the figures. It is easily demonstrated that other well-known theories don't explain all experimental behaviours.

The theories of Carlevaro and Hibberd are substantially the same. But Carlevaro has the merit of having indicated the solution of the Bailey equation and a diagram which foresees the possibility of having overmodulation as well as demodulation. Viceversa the Hibberd theory, in the form in which it has been presented by the author, foresees only a demodulation at low audio frequencies and shows that the percentage of demodulation is small. Despite the fact that F.H.Hibberd was convinced of the existence of only demodulation decreasing with the increasing of the frequency of demodulation, our study has shown that his theory also foresees overmod    ion as well as notable demodulation.

We did not publish up to date all the long series of the experiments, because we have hoped to be able to find a theory capable to interpret all behaviours of the observed phenomena.

The publication of the results of the complete series of experiments will be published elsewhere.

## ACKNOWLEDGEMENTS

## REFERENCES

1.   Tellegen, B.D.H.        Nature 131, 840, 1933.

2.   Bailey, V.A.          Phil. Mag. 18, 369, 1934.
     Martyn D.F.

3.   Bailey, V.A.          Phil. Magazine, Part I, 23, No.157, 929-960, 1937.
                           Phil. Magazine, 26, No.176, 425-543; 956 Nuovo Cim. 4, 1439, 1938.
                           Rado Sc. D, 69, 9, 1965.

4. Cutolo, M.    Alta Freq. 15,111, 1946; Nature, Lond. 180, 834, 1947.
   Carlevaro, M.    Nuovo Cim. 5, 1, 1948; Alta Freq. 18, 169, 1948.
   Ferrero, R.    Nature, Lond. 166, 98, 1950; ibidem, 176, 314, 1951.
   Gherghi, M.    Nuovo Cim. 9, 687 and 9, 5, 1952.
   Motzo, M.

5. Ginzburg, V.L.    *Propagation of Electromagnetic Waves in Plasma*, (Amsterdam: North-Holland), 1961.

6. Gurevich, A.V.    *Non Linear Effect in the Ionosphere*, Springer (Berlino), 1978.

7. Ginzburg, V.L.    Soviet. Phys. Usp. 3, 115; ibidem 3, 175, 1960.
   Gurevich, A.V.

8. Cutolo, M.    Nuovo Cim., Suppl. 4, 1450, 1952.
   Bonghi, G.C.
   Immirzi, F.
   Cachon, P.

9. King, J.W.    J. Atmos. Terr. Phys., 14, 41, 1959.

10. Hibberd, F.H.    J. Atmos. Terr. Phys., 6, 268-279, 1955.

11. Carlevaro, M.    Nuovo Cim., Supp. 4, 1422-1229, 1956.

12. Pozzi, A.    Plasma Phys. Editor. C.N.R., Rome, p.165, 1965.
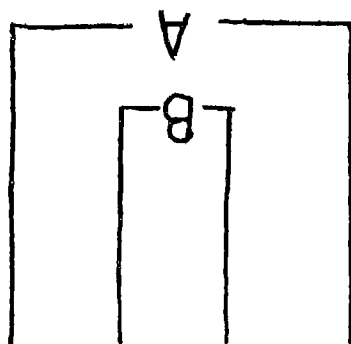
Fig.1 Oscillogram obtained at the output of the intermediate frequency (I.F.) of the receiver

$$M = \frac{A - B}{A + B} \times 100$$
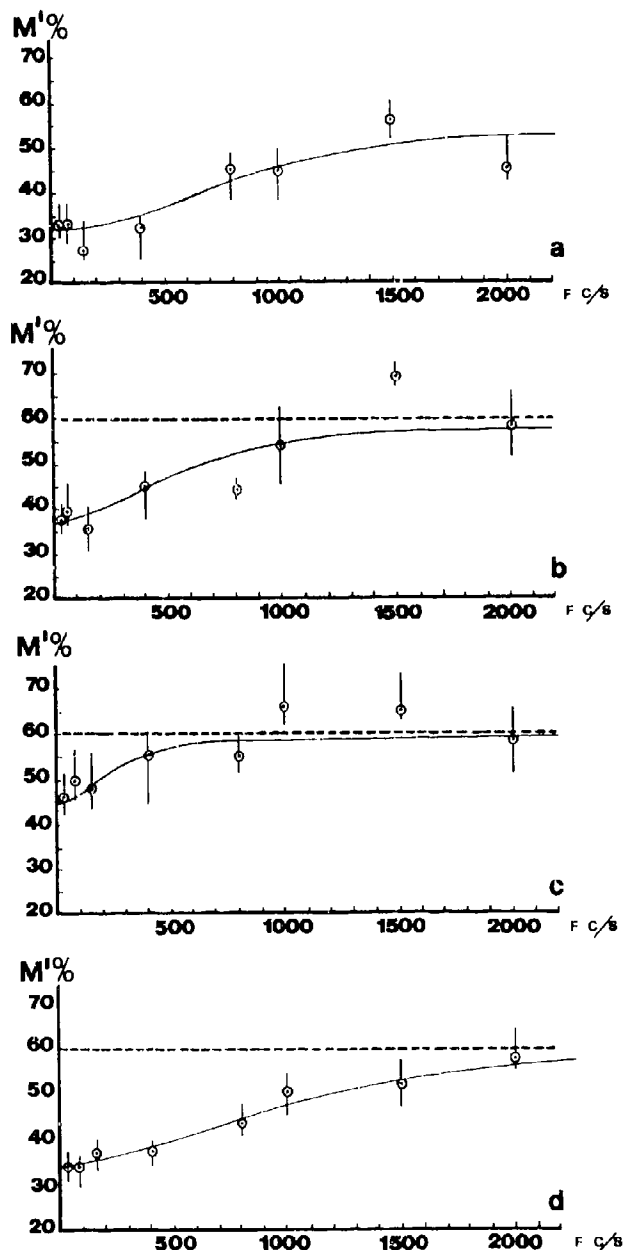
Fig.2    Experiment of 28/3/1958

(a)    150 kW  $\epsilon = 3.61\%$;   $\rho = 0.25$;   $G\nu_0 = 9,200\ \text{sec}^{-1}$;   $F^x = 0\ \text{Hz}$
150 kW  $\epsilon = 3.65\%$;   $\rho = 0.71$;   $G\nu_0 = 12,000\ \text{sec}^{-1}$;   $F^x = 3,500\ \text{Hz}$
Of the two determining couples of parameters only the first is acceptable because the experimental points were outside the portion of valid curve corresponding to the second couple of parameters.

(b)    100 kW  $\epsilon = 2.77\%$;   $\rho = 0.20$;   $G\nu_0 = 4,700\ \text{sec}^{-1}$;   $F^x = 0\ \text{Hz}$
$\epsilon = 2.69\%$;   $\rho = 0.74$;   $G\nu_0 = 6,400\ \text{sec}^{-1}$;   $F^x = 2,000\ \text{Hz}$
In this case too only the first couple of parameters is acceptable.

(c)    50 kW  $\epsilon = 2.67\%$;   $\rho = 0.13$;   $G\nu_0 = 2,200\ \text{sec}^{-1}$;   $F^x = 0\ \text{Hz}$
50 kW  $\epsilon = 2.68\%$;   $\rho = 0.78$;   $G\nu_0 = 3,300\ \text{sec}^{-1}$;   $F^x = 1,280\ \text{Hz}$
In this case too only the first couple of parameters is acceptable.

(d)    150 kW  $\epsilon = 1.18\%$;   $\rho = 0.24$;   $G\nu_0 = 7,900\ \text{sec}^{-1}$;   $F^x = 0\ \text{Hz}$
$\epsilon = 1.12\%$;   $\rho = 0.71$;   $G\nu_0 = 9,700\ \text{sec}^{-1}$;   $F^x = 2,900\ \text{Hz}$
Also in this case only the first couple of parameters is acceptable.
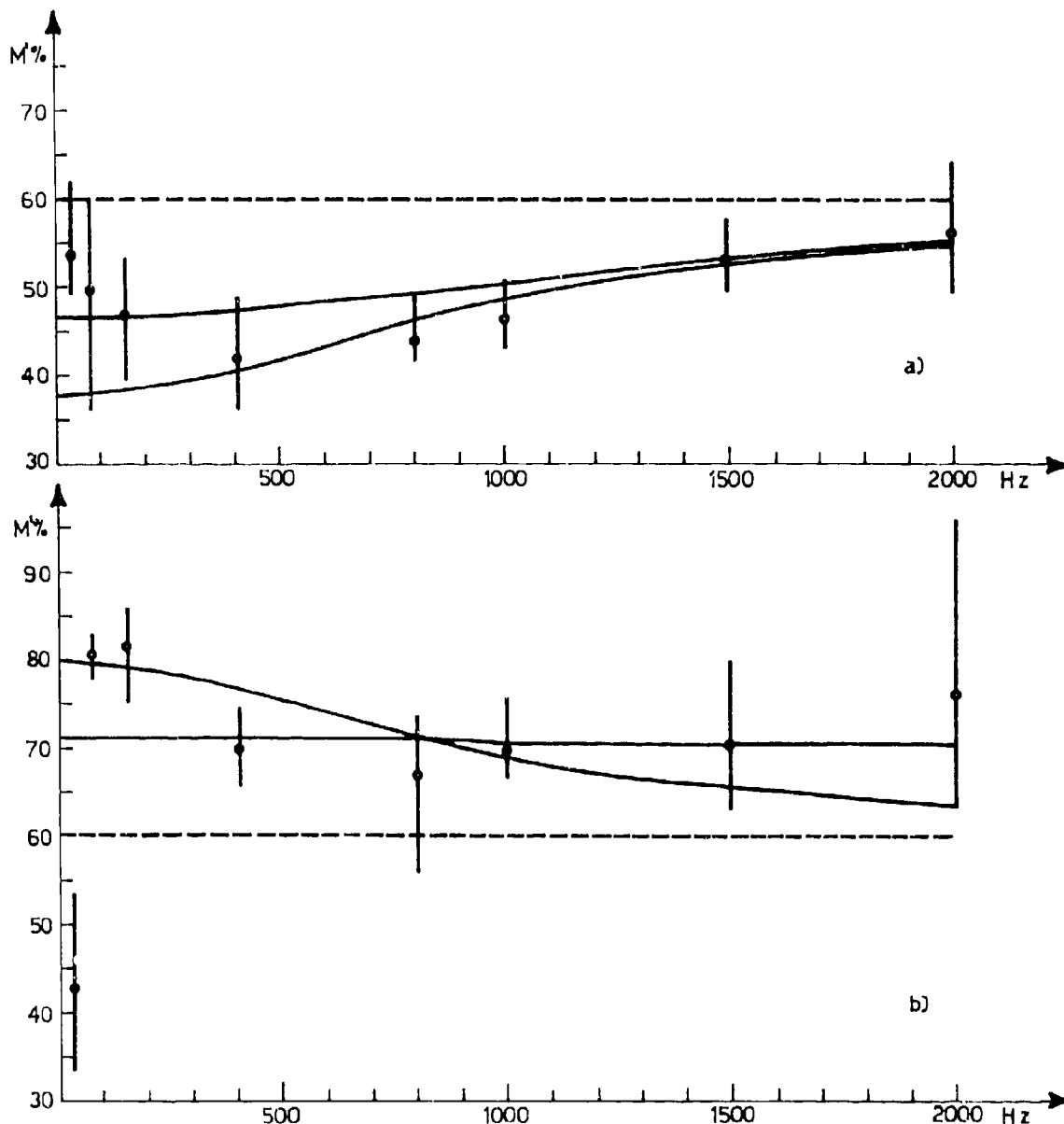
Fig.3   Experiments of 16/1/1958

$$\epsilon = 3.45\%; \quad \rho = 0.13; \quad G\nu_0 = 11,000 \ \text{sec}^{-1}; \quad F^x = 0 \ \text{Hz} \quad (\text{Curve 1})$$

(a)   150 kW   $\epsilon = 1.14\%; \quad \rho = 0.21; \quad G\nu_0 = 7,800 \ \text{sec}^{-1}; \quad F^x = 0 \ \text{Hz} \quad (\text{Curve 2})$

$$\epsilon = 1.09\%; \quad \rho = 0.73; \quad G\nu_0 = 11,000 \ \text{sec}^{-1}; \quad F^x = 3,400 \ \text{Hz}$$

The second and the third couple of parameters were determined not considering
the experimental points with frequencies of modulation 30/70/150 Hz. Of the
couples of parameters determined the second may be held to be valid because it
leads to an $\epsilon$ minor to that of the first. The third couple must be discarded
because the experimental points are outside the portion of valid curve
corresponding to it.

(b)   50 kW   $\epsilon = 7.42\%; \quad \rho = 0.90; \quad G\nu_0 = 41,000 \ \text{sec}^{-1}; \quad F^x = 16,000 \ \text{Hz} \ (\text{Curve 1})$

$\epsilon = 4.48\%; \quad \rho = 0.94; \quad G\nu_0 = 7,000 \ \text{sec}^{-1}; \quad F^x = 2,900 \ \text{Hz} \ (\text{Curve 2})$

The second couple of parameters was determined not considering the experimental
point with frequency of modulation 30 Hz. Neither of the two couples is acceptable
because both lead to portions of valid curves that do not contain the experimental
points.
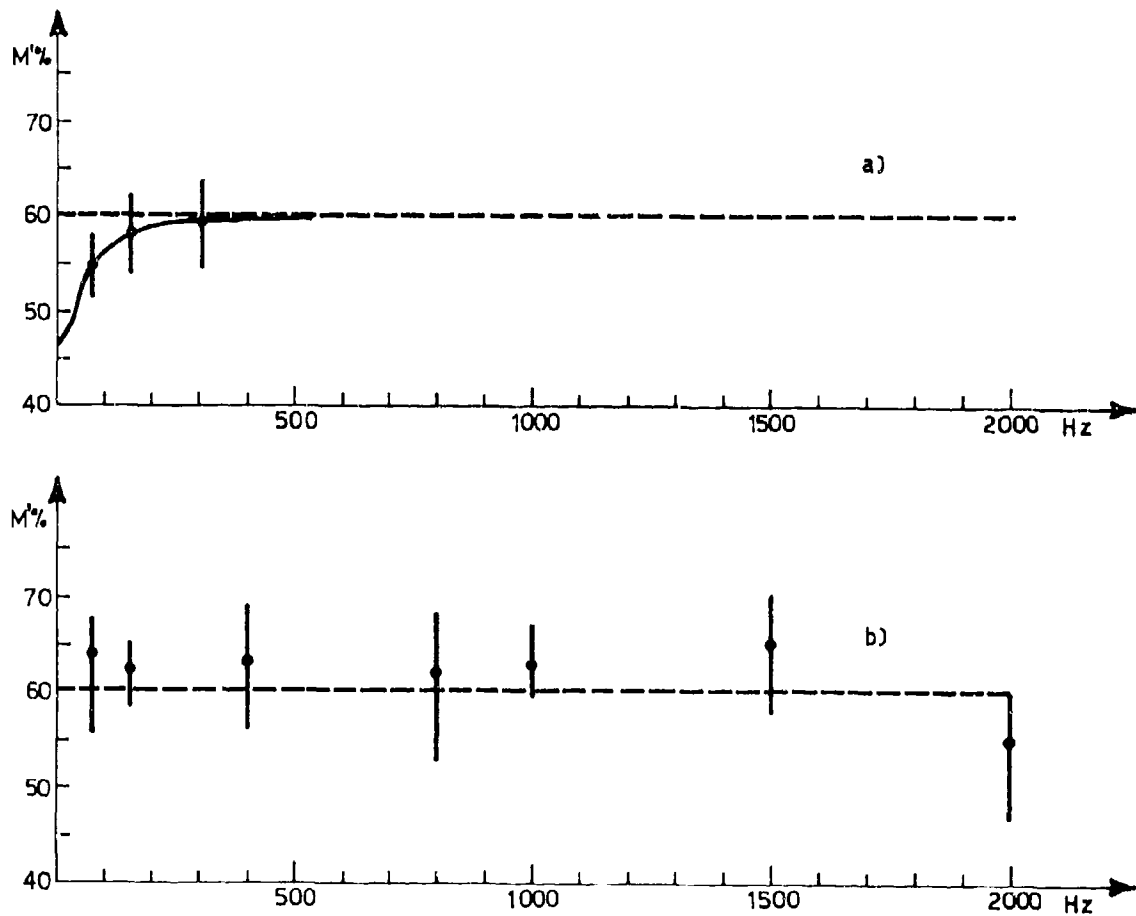
Fig.4 Experiment of 24/1/1958

(a) 150 kW $\epsilon = 0.22\%$; $\rho = 0.13$; $G\nu_0 = 410 \text{ sec}^{-1}$; $F^x = 0 \text{ Hz}$
$\epsilon = 0.20\%$; $\rho = 0.80$; $G\nu_0 = 870 \text{ sec}^{-1}$; $F^x = 300 \text{ Hz}$
Of the two couples of parameters only the first is acceptable because the
experimental points are outside the portion of valid curve corresponding to the
second couple of parameters.

(b) 50 kW. It was not possible to interpret this diagram because the function did not
present a very clear minimum.
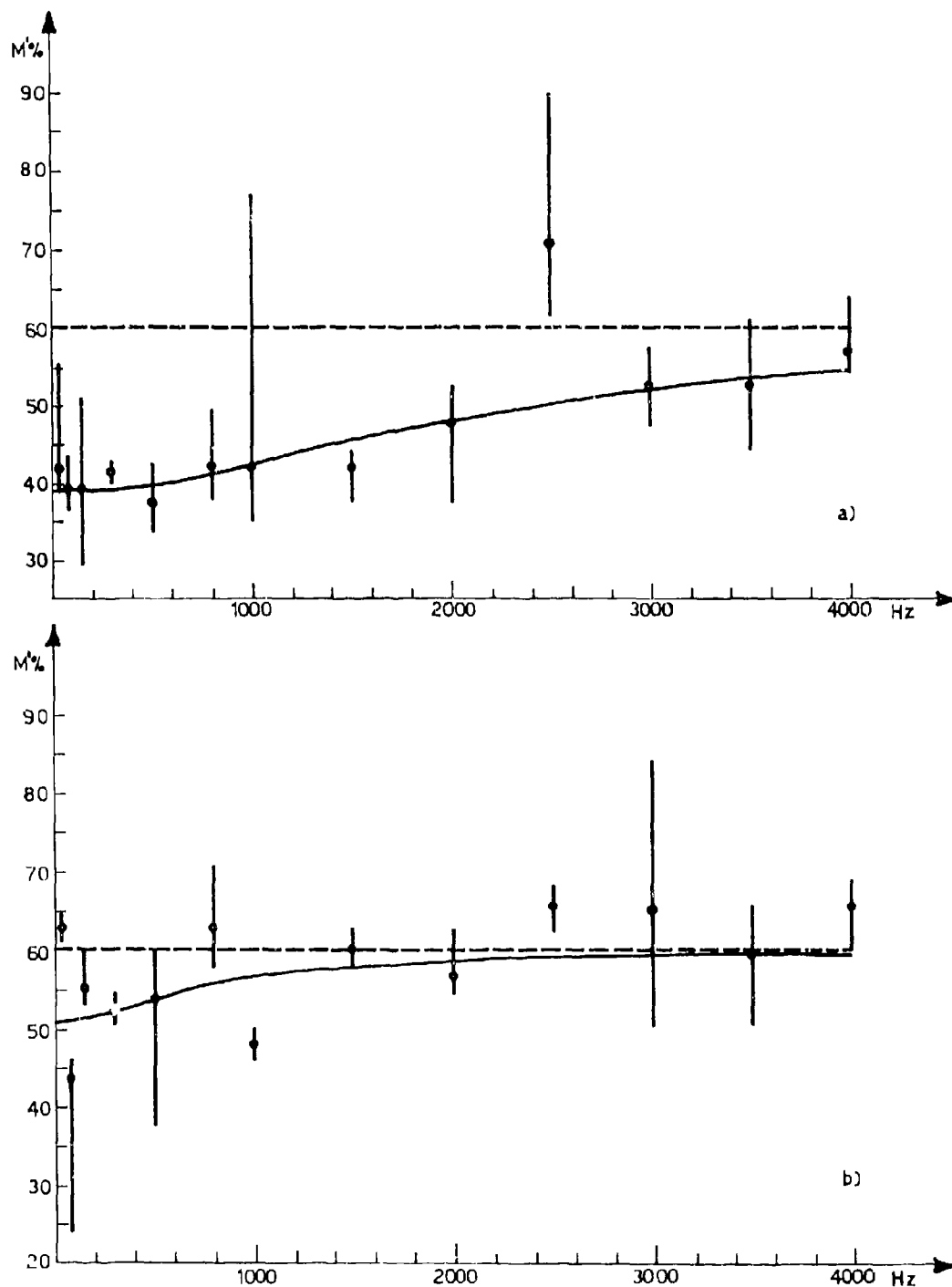
Fig.5   Experiment of 17/5/1958

(a)   150 kW    $\epsilon = 1.36\%$;   $\rho = 0.20$;   $G\nu_0 = 12,000 \ sec^{-1}$;   $F^x = 0 \ Hz$
                $\epsilon = 1.26\%$;   $\rho = 0.74$;   $G\nu_0 = 24,000 \ sec^{-1}$;   $F^x = 7,3000 \ Hz$

Of the two couples of parameters only the first is acceptable because the
experimental points are outside the portion of valid curve corresponding to the
second couple of parameters.

(b)   50 kW     $\epsilon = 4.56\%$;   $\rho = 0.09$;   $G\nu_0 = 5,100 \ sec^{-1}$;   $F^x = 0 \ Hz$
                $\epsilon = 4.53\%$;   $\rho = 0.84$;   $G\nu_0 = 7,600 \ sec^{-1}$;   $F^x = 2,600 \ Hz$

For reason above also in this case only the first couple of parameters is acceptable.
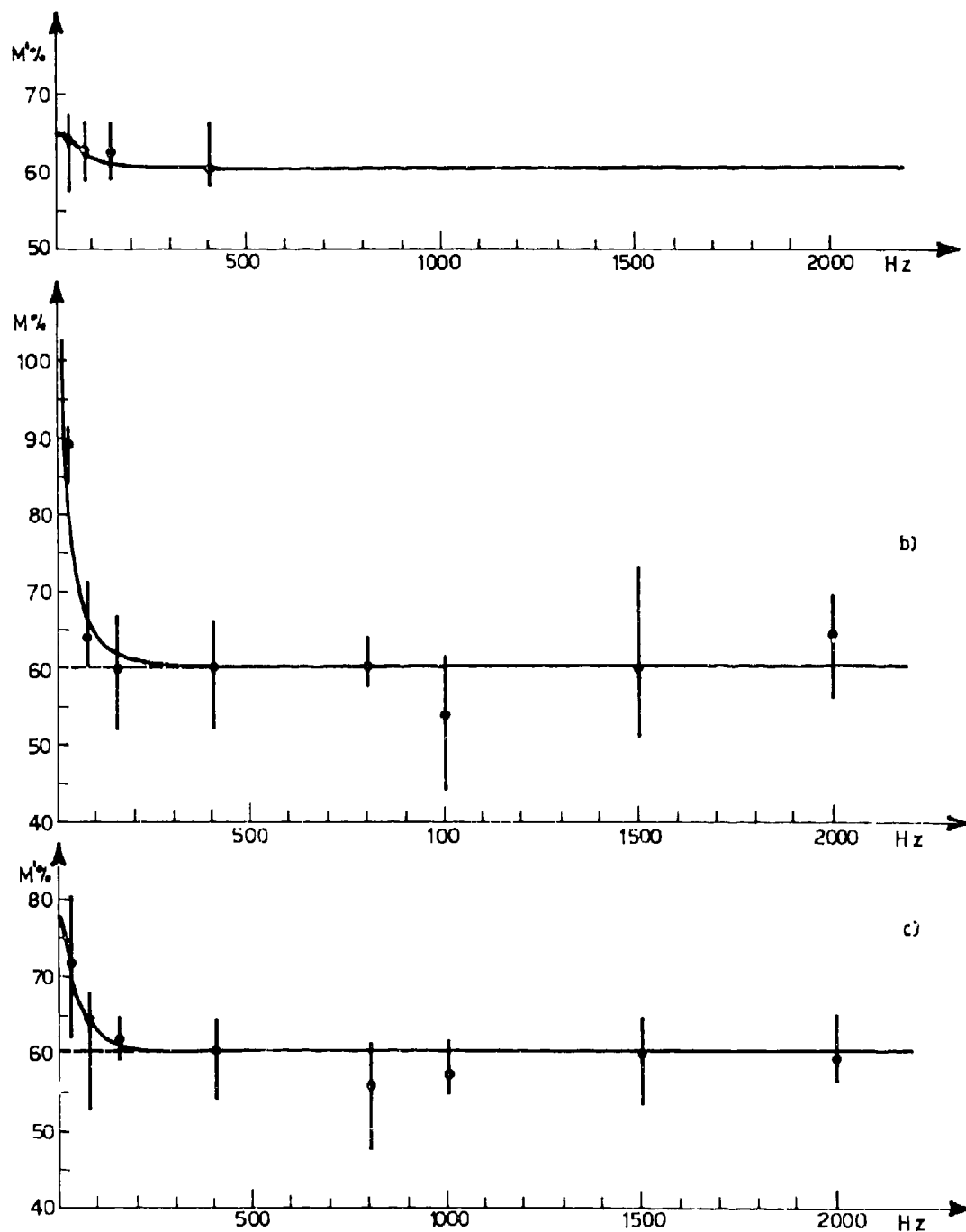
Fig.6   Experiment of 21/1/1958

(a)   150 kW $\epsilon - 1.15\%$; $\rho - 0.93$; $G\nu_0 - 310$ sec$^{-1}$; $F - 128$ Hz
Parameters not acceptable because the greater part of the experimental points used in the determination were outside the portion of the valid curve.

(b)   50 kW  $\epsilon - 2.21\%$; $\rho - 1.20$; $G\nu_0 - 170$ sec$^{-1}$; $F^x$  94 Hz
Parameters in the same condition as those above.

(c)   150 kW $\epsilon - 0.47\%$; $\rho - 0.87$; $G\nu_0 - 400$ sec$^{-1}$; $F^x - 151$ Hz
Parameters in the same condition as those above.
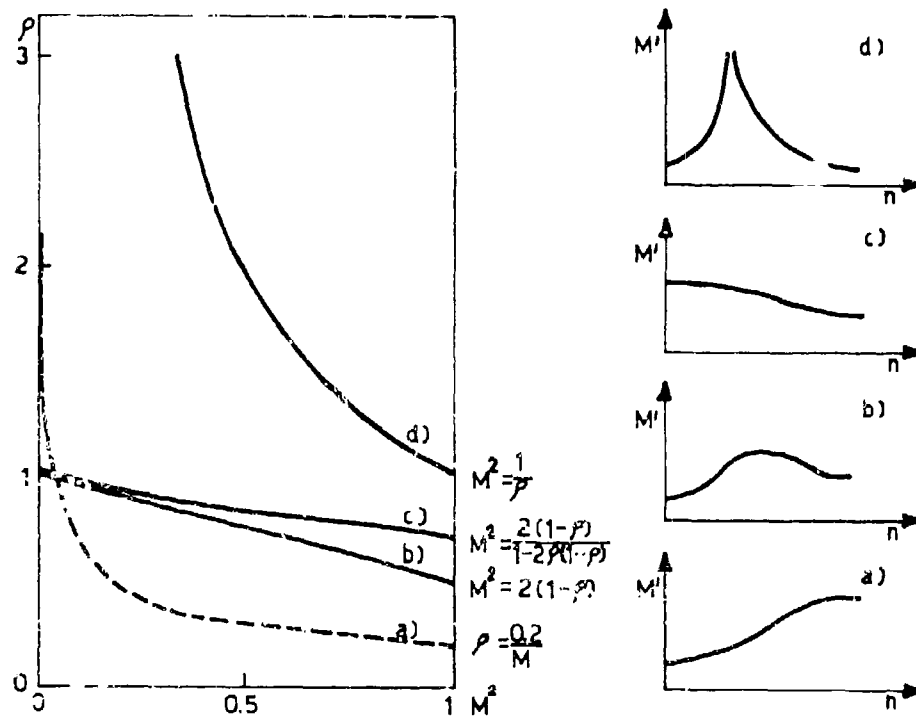
Fig.7  Experiment of 17/11/1959
  (a)  150 kW  $e = 1.27\%$;  $\rho = 0.852$;  $G\nu_0 = 3.900$ sec$^{-1}$;  $F = 1,400$ Hz
       This couple of parameters can not be accepted because the experimental points
       are outside the portion of valid curve corresponding to it.

  (b)  50 kW. It was not possible to interpret this diagram because the function $\epsilon$ did
       not present a very clear minimum.

# CALCULATION OF THE RESIDUAL MODULATION OF A MODULATED RADIOWAVE
## REFRACTED BY IONOSPHERE

L. Carlomusto

Centro Linceo Interdisciplinare di Scienze Matematiche e loro

Applicazioni, Accademia Nazionale dei Lincei - Roma

Università degli Studi di Camerino

ABSTRACT.

The aim of this work is the numerical calculation of the residual modulation of a modulated radiowave with variable power refracted by the Ionosphere. To do that we calculate and discuss the solution of an important equation of the Ionosphere: Bailey's equation.

Using this equation we try to solve the problem of a wave refracted by Ionosphere with the macroscopic theory; the last theory has, as regards that microscopic, two advantages: the possibility to found mathematics formulae more manageable and that to give results more easily comparable with the experimental results. In fact the solution of the Bailey's equation is utilized to obtain macroscopic quantities that we can comparable with the teoretical and the experimental results obtained by other workers.

## 1. INTRODUCTION.

First time the problem of the calculation of the residual modulation of a modulated radiowave refracted by Ionosphere was investigated by A. Pozzi (1962),(1964), who obtained results with waves of high power. Successively A.V. Gurevich (1978), with different method, obtained results with waves of low and high power.

Sperimentally results was obtained by M. Cutolo (1960),(1974).

## 2. CALCULATION OF THE SOLUTION OF THE BAILEY'S EQUATION.

We suppose that the electromagnetic field $E_i$ incident is modulated with an audiofrequency $n/2\pi$ and with a percentage of modulation M

$$E_i = E_o(1 + M \text{ sen } nt) \tag{1.2}$$

the equation of the motion of the electrons is

$$\frac{dv}{dt} \frac{2T}{v_o^2} + \frac{TG}{v_o^2} (v^2 - v_o^2) = w_o(1 + M \text{ sen } nt)^2 \tag{2.2}$$

where $v$ is the collision frequency of the electrons with neutral particles, and $v_o$ is the umperturbed collision frequency.

G is the mean relative energy loss in a collision, T represents the energy in condition of the thermal equilibrium. If we suppose that

$$v = v/v_o \qquad ed \qquad nt = \pi/2 - 2z$$

the adimensional equation (2.2) becomes:

$$\frac{dv}{dz} = C_1(v^2-1) - C_1C_2(1+M \cos 2z)^2$$

where

$$C_1 = \frac{Gv_o}{n} \; ; \; C_2 = \frac{w_o}{GT}$$

If $v = -\frac{1}{C_1}\frac{u'}{u}$ the last equation becomes:

$$u'' + (t_o + 2t_1\cos 2z + 2t_2\cos 4z)u = 0$$

where

$$t_o = -C_1^2 C_2\left(1+\frac{M^2}{2}\right) \; ; \; t_1 = -C_1^2 C_2 M \; ; \; t_2 = -C_1^2 C_2 \frac{M^2}{4}$$

This last equation has been solved by Hills infinite determinants. The solution of v is therefore the following:

$$v = -\frac{1}{C_1}\frac{2(\mu a_1 - 2b_1)f(z)\cos 2z - 2(\mu b_1 + 2a_1)\text{sen}2z + \mu f(z)}{2a_1\cos 2z - 2b_1 f(z)\text{sen}2z + 1} \tag{3.2}$$

where, for values not to high of $w_o$, $\mu = -\sqrt{-t_o}$

$$f(z) = \frac{\alpha e^{\mu z} - e^{-\mu z}}{\alpha e^{\mu z} + e^{-\mu z}} \qquad\qquad \alpha = e^{-\mu\frac{\pi}{2}}\frac{C_2(\mu + 2\mu b_1 + 2a_1) - (1 - 2b_1)}{C_1(\mu - 2\mu b_1 + 2a_1) + (1 - 2b_1)}$$

$$a_1 = \frac{t_1(t_2 - t_o + 4 - \mu^2)}{(t_o-4)^2 + \mu^2(\mu^2 + 2t_o + 8) - t_2^2} \qquad\qquad b_1 = \frac{\mu\mu t_1}{(t_o-4)^2 + \mu^2(\mu^2 - 2t_o + 8) - t_2^2}$$

If we suppose that approximately $f(z) = 1$, (3.2) becomes:

$$v = -\frac{1}{C_1}\mu\frac{2m\,\text{sen}\,x - 2n\cos x + 1}{2a_1\,\text{sen}\,x - 2b_1\cos x + 1} \tag{4.2}$$

where

$$m = a_1 - \frac{2b_1}{\mu} \; ; \qquad n = b_1 + \frac{2a_1}{\mu}$$

Expanding the (4.2) by Fourier's series, limited only at first term, we finally obtain for the function $v/v_o$ the expression:

$$\frac{v}{v_o} = \alpha_o + \alpha_1\cos x + \beta_1\,\text{sen}\,x \tag{5.2}$$

where $\alpha_o = \sqrt{-t_o}/C_1$

$$\alpha_1 = \frac{32}{C_1 t_1}\frac{(4+t_2)(1-t_o)}{(t_2+4)^2 - 16t_o} \; ; \quad \beta_1 = \frac{-128}{C_1 t_1}\frac{(1-t_o)\sqrt{-t_o}}{(t_2+4)^2 + 16t_o}$$

## 3. NUMERICAL DETERMINATION OF THE RESIDUAL MODULATION.

After these developments, (1.2) becomes:

$$E_i = E_o(1 + M\,\text{sen}\,x) \tag{1.3}$$

and the refracted wave will have instead the intensity:

$$E_r = E_i e^{-\gamma v} \tag{2.3}$$

where $\gamma$ is the mean value of the total absorption's coefficient. We will utilize an approximate value of $\gamma$ but such that does'nt influence much the determination of the residual modulation M".

The expansion of $E_r$ by Fourier's series, limited only at first term, gives:

$$E_r = E_{rm} (1 + a \ sen \ x + b \ cos \ x)$$

The residual modulation M" is:

$$M''^2 = a^2 + b^2$$

Utilizing the Fourier's tecnique and neglecting the contribution of the subsequent harmonics, we find a and b:

$$a = M - \frac{1}{(\alpha_1^2+\beta_1^2)^{\frac{1}{2}}} \frac{I_1\left[\gamma(\alpha_1^2+\beta_1^2)^{\frac{1}{2}}\right]}{I_o\left[\gamma(\alpha_1^2+\beta_1^2)^{\frac{1}{2}}\right]} \quad ; \qquad b = -\frac{\alpha_o}{(\alpha_1^2+\beta_1^2)^{\frac{1}{2}}} \frac{I_1\left[\gamma(\alpha_1^2+\beta_1^2)^{\frac{1}{2}}\right]}{I_o\left[\gamma(\alpha_1^2+\beta_1^2)^{\frac{1}{2}}\right]}$$

where $I_o$ and $I_1$ are the Bessel's functions.

Utilizing the values of $\alpha_o, \alpha_1, \beta_1$, and M we have:

$$M''^2 = M^2 + \frac{1+\alpha_o^2}{\alpha_1^2+\beta_1^2}(\frac{I_1}{I_o})^2 - \frac{2M}{(\alpha_1^2+\beta_1^2)^{\frac{1}{2}}}(\frac{I_1}{I_o}) \tag{3.3}$$

knowing the parameters of the incident wave and the value of $\gamma$, equation (3.3) gives the possibility to calculate the residual modulation.

## 4. DISCUSSION OF THE RESULTS.

The formula (3.3) has quantities not directly depending upon the parameters of the incident wave and the examined conditions. For these reasons we are able to calculate the expressions of (3.3) in function of $C_1 = Gv_o/n$ and $C_2 = w_o/(GT)$:

$$1 + \alpha_o^2 = 2 + C_2(1 + \frac{M^2}{2}) \tag{1.4}$$

$$(\alpha_1^2+\beta_1^2)^{\frac{1}{2}} = \frac{32\left[1+C_1^2(1+C_2+C_2\frac{M^2}{2})\right]}{C_1^3 C_2 M\left[16+C_1^2(\frac{C_2^2 M^4 C_1^2}{16} + 6C_2 M^2+16+16C_2)\right]^{\frac{1}{2}}} \tag{2.4}$$

Utilizing (1.4),(2.4) and (3.3) and the values of the Bessel's functions (that are calculated with another program) has been calculated the residual modulation M" in function of $1/C_1$.

We use very low values of $C_2$ because the solution (3.2) has been obtained with low power (small values of $w_o$).

Fig. 1 gives the values of the residual modulation obtained for $M = 0.6$ and $\gamma = 1.5$ for some values of $C_1$.

We observe that for values of $C_2$ around 0.1 we have always demodulation but not excessive. For values of $C_1$ around 1.0 we observe first an overmodulation also high, then a light demodulation. For values higher of $C_1$ the demodulation disappears completely.

## 5. CONCLUSION.

In this paper it has been calculated numerically the residual modulation for waves with low power refracted by Ionosphere. The obtained results agree and complete those had previousley by Pozzi (1962),(1964) with waves of high power.

Comparing instead our results with those theoretical obtained by A.V. Gurevich (1978), but with a different method, we see that, for power not excessively low, the agreement is excellent. But variyng the modulation frequency A.V. Gurevich always obtaines both overmodulation and demodulation; instead, with low power and with low frequency of modulation, we have only demodulation.

This good result appears more important when we compare our numerical results with those sperimentally obtained by M. Cutolo (1960),(1974). In fact in the experimental data of residual modulation now available up to date we see numerous cases in which it is possible to have demodulation only, with low power and with low frequency of modulation. Such data, and not only those in which we have both overmodulation and demodulation, are now in good agreement with the theoretical and numerical data discussed in this paper.

## 6. REFERENCES.

- CUTOLO,M., 1960,"Some Considerations on ionospheric self-modulation at oblique incidence", Istituto di Fisica Tecnica, University of Naples, Italy.

- CUTOLO,M., 1974,"The ionospheric propagation of the modulated waves with carrier frequencies far from and variyng around the girofrequency", AGARD Conference Proceedings N° 138.

- GUREVICH,A.V., 1978,"Nonlinear Phenomena in the Ionosphere", Springer, Berlino.

- POZZI,A., 1962,"Moto di elettroni nella Ionosfera in presenza di campo elettrico alternativo modulato", Nuovo Cimento, 26 S.10.

- POZZI,A., 1964,"Alcuni problemi non lineari dell'assorbimento ionosferico", Consiglio Nazionale delle Ricerche, Roma, Italy.
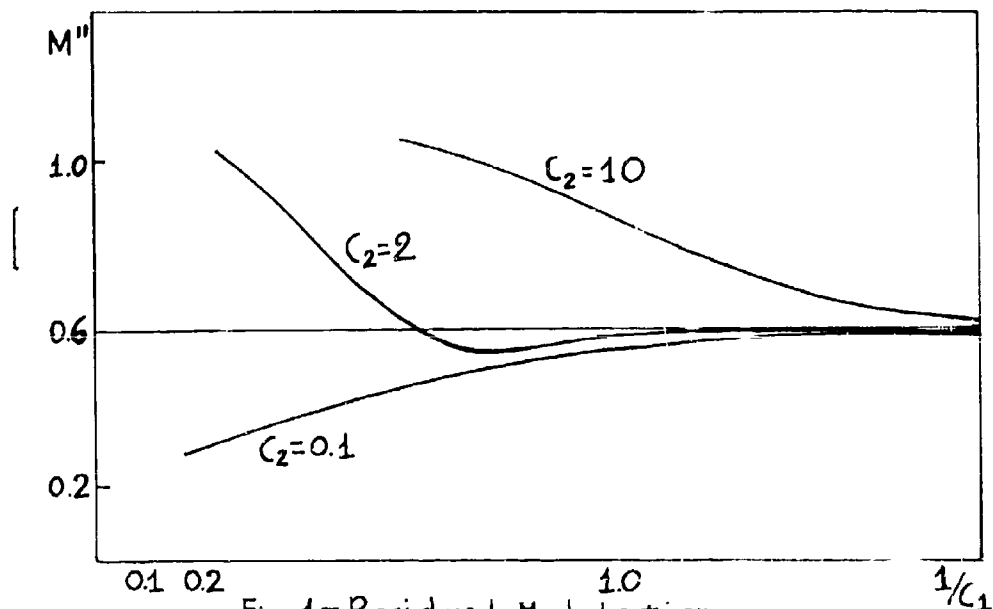
Fig. 1 - Residual Modulation

# MEDIUM WAVE MULTI-SECTION GROUNDWAVE PROPAGATION IN MARMARA AND WEST BLACK-SEA REGION-NUMERICAL RESULTS

A.HIZAL and A.F.FF?

Electrical Engineering Department
Middle East Technical University
Ankara-Turkey

## SUMMARY

A numerical study of MF ground wave propagation in the Marmara and West Black Sea region, near Istanbul is presented. The numerical results are obtained by two methods: (i) the flat-ground two and four-section ground-wave propagation formulas based on the approach by King, Maley and Wait and (ii) the integral equation solution based on the formulation by Ott (i.e. PROGRAM WAGNER). The results obtained up to 400 km from the station indicates that MF (0.5 MHz) ground wave is a suitable mode of propagation for PTT ship-to-shore communication system.

## I. INTRODUCTION

Groundwave propagation along mixed paths has been investigated both numerically and experimentally previously: by King and Maley, (1965) and King et.al. (1966) for flat grounds and by Ott (1979) for irregular and inhomogeneous grounds. For flat grounds, the integral expressions developed by King et.al. (1965, 1966) in elliptical coordinates proved to be accurate and can be used also for propagation paths oblique to the land-sea boundaries. For irregular terrain such as hills higher than a wavelength and for continuously changing surface impedance, the integral equation method by Ott (1979) as incorporated in PROGRAM WAGNER, is suitable.

In the present work a groundwave propagation study in the Marmara and West Black Sea region of Turkey is made in order to assess the performance of PTT's MF coastal maritime communication systems from the propagation point of view. In Fig.1, the region of interest and the location of the station are indicated. To the West of Istanbul (Çatalca Plain) where the station is located, the ground is mostly flat with small hills up to about 200 meters. The ground in this region may be assumed to be moderately wet. The other characteristics of the terrain in the Marmara region are: the existence of Marmara Island about 670 meters high, Kapıdağ peninsula about 780 meters high, Gemlik Peninsula about 900 meters high, Istanbul-Izmit path almost flat with hills about 400 meters high near Izmit. To the south of the Dardanelles is placed the Biga peninsula where there are Hills up to about 1700 meters for some propagation paths. In general the Marmara region has a climate which is a mixture of mediterranean and temperate climates, the ground in this region is moderately wet most of the year. Marmara and Aegean Seas are moderately salty while Black-Sea is considerably less salty.

We are interested in the attenuation factor in the sea sections of the paths, with a maximum total path length of about 400 km. Under these conditions flat ground modelling of the paths seems to be sufficient. It is reported that, (Ott, 1971), for a sea-land-sea path the attenuation factor in the land section is drastically different for calculations assuming a flat island and a realistic island with a hill several wavelengths in altitude. However, the attenuation function on the sea-section after that island is not significantly different for the two cases above.

In this paper we shall present the result of computations for the attenuation factor in various propagation paths indicated in Fig.1. For two of the paths with a second land portion, the flat-ground and the irregular-ground (i.e. those obtained by PROGRAM WAGNER) results will be presented. In the first section of the paper a brief review of the theory will be given as a new formula is developed for the four section flat-ground path.

## 2. THEORY

For the two-section propagation path shown in Fig.2, King and Maley (1965, 1966) has developed a formula in the elliptical co-ordinates for the attenuation factor $F(d,Z,Z_1)$ using the compensation theorem and the method of stationary phase integration (e.g. Monteath, 1973):

$$F(d,Z,Z_1) = F(d,Z) + (\frac{id}{\lambda})^{\frac{1}{2}} \int_0^{\theta_1} (\frac{Z-Z_1}{\eta_0}) F(r,Z) F(R,Z_1) d\theta \qquad (1)$$

where

$$\theta_1 = \cos^{-1}\{(2x_1/d)-1\}, \quad r=(d/2)(1-\cos\theta), \quad R=d-r$$

$$\eta_0 = \sqrt{\mu_0 / \varepsilon_0} : \text{Intrinsic impedance of the free-space.}$$

$$Z = (\eta/\eta_o) \sqrt{\eta_o^2 - \eta^2} \qquad : \text{Surface impedance of the land for the vertical polarization}$$

$$\eta = \sqrt{i\omega\mu_o/(\sigma + i\omega\varepsilon)} \qquad : \text{Intrinsic impedance of the land}$$

For the sea, $Z$ and $\eta$ are to be replaced by $Z_1$ and $\eta_1$, respectively.

$$F(r,Z) = 1-i \sqrt{\pi p} \, e^{-p} \, \text{erfc} \, (i \sqrt{p}) \qquad (2)$$

is the Sommerfeld attenuation factor. $\text{erfc}(\ ) = (2/\sqrt{\pi})\int_z^\infty e^{-t^2} dt$ is the complementary error function and $p=(-ikr/2)(Z/\eta_o)^2$ is the numerical distance. Formula (1) has been proved to be very accurate when the source (A) and the observation point (B) are several wavelengths away from the coast. Expression (1) is easy to integrate numerically using Gaussian-quadrature. To obtain a formula amenable for iteration the reciprocity theorem may be used in the original compensation formula by replacing $F(r,Z)F(R,Z_1)$ in (1) by $F(R,Z)F(r,Z,Z_1)$. But it is found that such an iteration scheme is not necessary and (1) is quite accurate.

For the three-section paths King et.al. (1966) have developed a formula similar to (1) which contains the two-section result given by (1) in the integrand. For our purposes we need a formula which is suitable for a four-section path such as a land-sea-land-sea path where the second-land portion is either an island or a peninsula, typical characteristic feature of the Marmara region. Although such a formula did not appear previously, it is a straightforward procedure to develop it using the electromagnetic compensation theorem (Monteath, (1973). Referring to Fig.3 the mutual impedance change can be expressed by

$$Z'_{AB} - Z_{AB} = \iint_S (Z'-Z) \, \vec{h}_{At} \cdot \vec{h}'_{Bt} \, ds \qquad (3)$$

where $\vec{h}_{At}$ and $\vec{h}'_{Bt}$ are the tangential magnetic fields due to unit currents at A and B, the latter being open circuited. The primed situation refers to the case where the second land portion S exists. We have $Z=Z_1$ and $Z'=Z_2$ and S is the surface between $\theta_1$ and $\theta_2$. The unprimed situation refers to the case where only land (Z) and sea ($Z_1$) exists. When (3) is evaluated in elliptical co-ordinates and invoking the stationary phase-approximation one obtains

$$F_{AB}=F(d,Z,Z_1) + (\frac{id}{\lambda})^{\frac{1}{2}} \int_{\theta_1}^{\theta_2} \{\frac{Z_1-Z_2}{\eta_o}\} \, F(r,Z,Z_1)F(R,Z_1,Z_2) d\theta \qquad (4)$$

where $\qquad |\vec{h}_{At}| \propto F(r,Z,Z_1) \quad \text{and} \quad |\vec{h}'_{Bt}| \propto F(R,Z_1,Z_2)$

$\theta_o = \text{Cos}^{-1}\{(2x_1/d)-1\}$ , $\theta_2 = \text{Cos}^{-1}\{(2x_2/d)-1\}$

$\theta_1 = \text{Cos}^{-1}\lfloor\{2(x_2+y_2)/d\}-1\rfloor$ and $F(d,Z,Z_1)$ is given by (1).

$F(r,Z,Z_1)$ and $F(R,Z_1,Z_2)$ are also given by (1) with the replacement of the set $\{d,Z,Z_1\}$ by $\{r,Z,Z_1\}$ and $\{R,Z_1,Z_2\}$, respectively, Calculation of (4) is made numerically, evaluating the integral by the Gaussian quadrature method. It is evident that considerably longer computer time is needed in this case, compared to the two-path case to calculate the attenuation factor. Theoretical and experimental investigation made by King and Maley (1966) has revealed that formulas developed for the perpendicular incidence can be used for the oblique incidence for angles of incidence up to about $70^o$ from the normal. Consequently in the present calculations we shall use either (1) or (4), for the paths shown in Fig.1 with flat ground approximation. Once the attenuation factor has been computed the vertical electric field can be calculated from

$$E_A = -i \frac{L_A I_A}{\lambda} \eta_o \frac{e^{-ikd}}{d} F \qquad (5)$$

where $L_A$ is the effective height of the transmitter antenna, $I_A$ is the antenna current and $F=F(d,Z,Z_1)$ or $F=F_{AB}$ .

For the inhomogeneous and irregular paths, the integral equation approach developed by Ott (1979) will be used. The theory of the integral equation approach is described in detail by Ott (1979) and Ott (1971), previously. A computer program based on the integral equation, known as PROGRAM WAGNER, had been tested previously for various irregular terrains and the numerical results were compared with measured values. PROGRAM WAGNER has been implemented in our computer facility IBM 370/145 and used for the two paths shown in Fig.1, namely Kapıdağ-Biga-Lesbos path and the Gemlik Bay path.

## 3. NUMERICAL RESULTS

All the numerical results are for f=500 kHz ( $\lambda$ =600 m):

### (a) Two-section flat-ground paths

For the Black-Sea region near İstanbul we have chosen three paths for which the land portion is assumed to have $\epsilon_r$=15, $\sigma$=0.008 mho/m and the sea has $\epsilon_r$=80 and $\sigma$=3 mho/m. $x_1$, the distance of the transmitter to the coast for the three-paths, are $x_1$=15 km, 20 km, and 35 km, respectively. The results are shown in Fig.4.

For the Marmara Sea which is more salty than the Black Sea we shall assume $\epsilon_r$=80 and $\sigma$=4 mho/m. We have chosen four paths described by the sets 1: {$x_1$=32.5 km,$\epsilon_r$=15, $\sigma$=0.01}, 2: {$x_1$=25 km, $\epsilon_r$=15, $\sigma$=0.01}, 3: {$x_1$=10 km, $\epsilon_r$=8, $\sigma$=0.002} and 4: {$x_1$=70 km, $\epsilon_r$=15, $\sigma$=0.008}. The results of the computations are shown in Fig.5.

### (b) Four-section flat ground paths

We shall describe four such paths:(i) $x_1$=25 km, $x_2$=110 km, $y_2$=15 km (Kapıdağ) $\epsilon_r$=15, $\sigma$=0.01, $\epsilon_{r2}$=8, $\sigma_2$=0.002 mho/m, (ii) $x_1$=12.5, $x_2$=52.5, $y_2$=18 (Gemlik Bay), $\epsilon_r$=8, $\sigma$=0.002, $\epsilon_{r2}$=8, $\sigma_2$=0.002, (iii) $x_1$=35, $x_2$=117.5, $y_2$=12.5. (Marmara Island), $\epsilon_r$=15, $\sigma$=0.001, $\epsilon_{r2}$=8, $\sigma_2$=0.002, (iv) $x_1$=30, $x_2$=155, $y_2$=130 (Aegean Sea path 1 ) $\epsilon_r$=15, $\sigma$=0.01, $\epsilon_{r2}$=10, $\sigma_2$=0.008. The results of the computations for the attenuation factor beyond the second land portion in the sea are presented in Fig.6.

### (c) Comparisons with the irregular terrain (WAGNER) results

For the two paths i.e. Gemlik and Kapıdağ-Biga-Lesbos paths (Aegean Sea Path 2) PROGRAM WAGNER is used to obtain numerical results for the attenuation function for the flat-ground and the topographic ground cases. The computer program is first tested by repeating several test runs reported by Ott (1971). In the calculations, the topographic features were taken into consideration with an accuracy of 25 m. ($\lambda$/24). The field points were taken at $\lambda$/3 intervals in sea-to-land transitions and in regions of rapid terrain variations. The ground constants for the paths are taken to be the same as those for the corresponding flat-ground paths, since a detailed experimentally measured ground conductivity map of Turkey is not available. The terrain profile and the numerical results for the two paths under consideration are presented in Figs.7 and 8. Flat-Ground results obtained by formulas (1) and (4) are superposed on these curves. It is observed that on the sea section of the paths, flat-ground results do not deviate significantly from those for the topographic cases, while on the land sections attenuation functions for the two cases differ significantly. Thus it may be found advantageous, from the point of view of computational economy, to use the simpler formulas (2) or (4) if the region of interest happens to be over the sea, especially when the hills are of heights below roughly a wavelength.

A common feature observed is the steep rise of the attenuation function over the land section where a rising terrain is found.

While it is evident that from the view point of ship-to-shore communications, the land based station must be as close to the coastline as possible, when other factors require that the station must be inland, it should be situated on a hill if the land section to the shore includes high terrain irregularities.

## 4. CONCLUSION

The numerical study presented in this paper revealed that the Çatalca Plain (the site of the station) is a suitable site to establish a modernized MF maritime communication system for the West Black Sea, Marmara Sea and the upper Aegean Sea of the Marmara Region of Turkey. The predicted attenuations up to about 400 km are needed in estimating the requirements on the transmitter power and the effective antenna height for managable signal to noise ratios in the regions of interest at this particular frequency.

The four section formula (eq.4) obtained during the course of this work represents an efficient technique for predicting attenuation for the last sea section of the propagation path and its accuracy is found to be sufficient for the present application.

## 5. REFERENCES

KING, R.J. and MALEY, S.W., 1965, "Model Experiments on Propagation of Groundwaves Across an Abrupt Boundary at Perpendicular Incidence", Radio Science Vol.69 D., No.10, pp.1375-1381.

KING,R.J., et.al., 1966, "Groundwave Attenuation Along Three Section Mixed Paths", Proc. IEE, Vol.113, No.5, pp.747-751

OTT, R.H., 1979, "Theories of Groundwave Propagation Over Mixed Paths", AGARD Cong. Proc. No.269 on Terrain Profiles and Contours in Electromagnetic Wave Propagation", Paper No.6-1.

KING, R.J. and MALEY, S.W., 1966, "Model Experiments on Propagation of Groundwaves Across and Abrupt Boundary at Oblique Incidence", Radio Science, Vol.1, No.1, pp.111-115.

OTT, R.H., 1971, "A New Method of Predicting HF Groundwave Attenuation Over Inhomogeneous, Irregular Terrain", OT/ITS Research Report 7, Institute of Telecommunication Sciences, Bo.Co., U.S.A.

MONTEATH, G.D., 1973 "Applications of the Electromagnetic Reciprocity Principle", Pergamon Press.
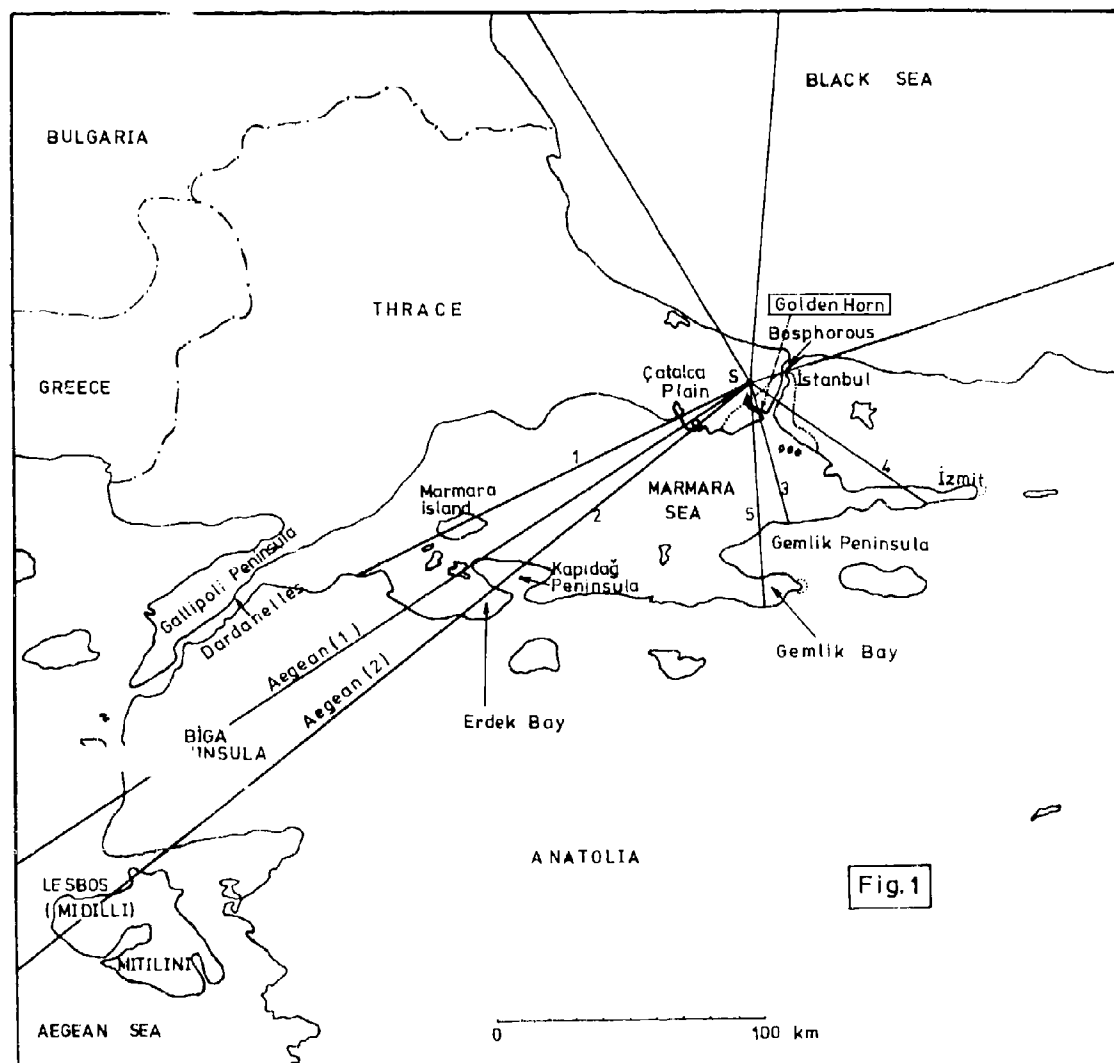
Fig. 1
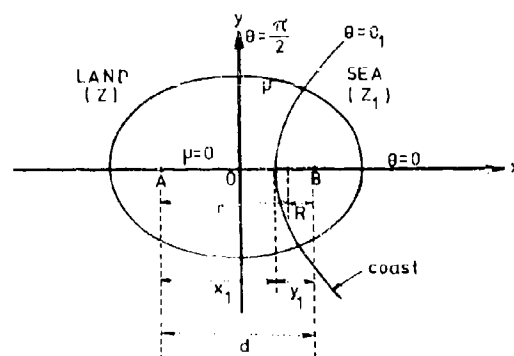


Fig 2
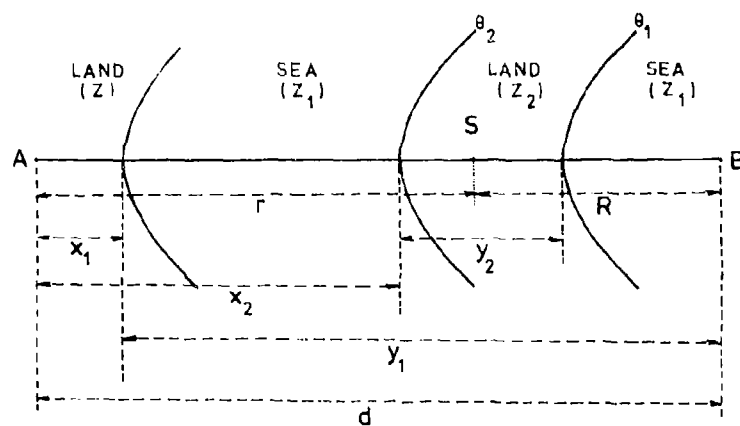
**Fig.3**
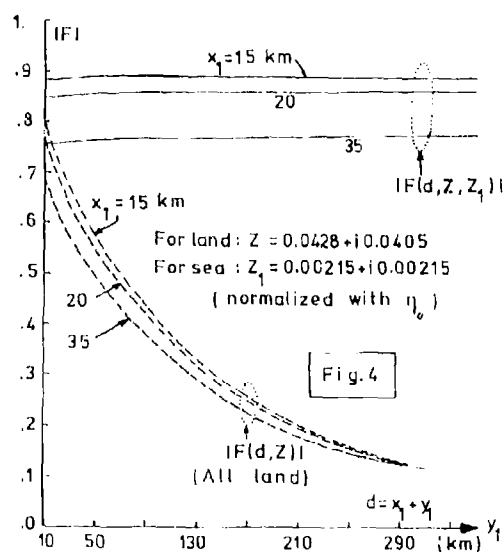


For land: $Z = 0.0428 + i0.0405$
For sea: $Z_1 = 0.00215 + i0.00215$
( normalized with $\eta_0$ )

$|F(d,Z,Z_1)|$

$|F(d,Z)|$ (All land)

$x_1 = 15$ km
20
35

$d = x_1 + y_1$

**Fig.4**



$2(x_1 = 25$ km$)$
$1 (32.5$ km$)$
$3 (10$ km$)$
$4 (70$ km$)$

---- $|F(d,Z)|$ (All land)
—— $|F(d,Z,Z_1)|$

$d = x_1 + y_1$

**Fig.5**



Kapıdağ path ( 2 )

Aegean-Sea path (1)

Marmara Island path (1)

Gemlik Bay (5)

—— $|F(d,Z,Z_1)|$
—— $|F_{AB}^E|$
---- $|F(d,Z)|$ (All land)

$d = x_1 + y_1$

**Fig.6**

Gemlik Path Fig.7



Aegean (2) Path Fig. 8

DISCUSSION EPP FALL 81 MEETING
MEDIUM, LONG, AND VERY LONG WAVE PROPAGATION
(AT FREQUENCIES LESS THAN 3000 KHZ)

SESSION 5

PAPER : 28. MEDIUM FREQUENCY PROPAGATION : A SURVEY
AUTHOR :   P. Knight
QUESTIONER :   F. J. Kelly
QUESTION  :   Sammadar of  the U. S. Coast Guard has been studying the effects of tropospheric
index of refraction changes on 100 KHz ground wave phase. Have you any information on this
effect of tropospheric weather on MF groundwave phase and amplitude?
RESPONSE : I think the wavelength is too large for day-to-day variations in the weather to have
very much  effect on ground wave field strengths. We do observe seasonal variations due to the
ground being more moist in the winter, and being a better conductor, therefore giving rise to
higher  field  strengths.  In calculating ground wave field-strengths we do take account of the
variation of refractive index with height  by assuming an  artificial  increased radius of
curvature  of  the earth. There is a very good paper by Rothran of Marconi Company who produced
factors by which one multiplies the radius of the earth at lower frequencies. In the MF Band we
take a factor of 1.25.   4/3 is typically employed at higher frequencies. I don't think however
that you will see day-to-day variations.

PAPER : 30. ON THE SELF-MODULATION AND DISTORTION OF MF WAVES IN THE IONOSPHERE
AUTHOR : M. Cutolo
QUESTIONER :   F. J. Kelly
QUESTION : What was the location of the interaction region and the geometry of the path?

RESPONSE  :  The transmitter was in Frankfort, the receiver in Naples, and the disturbed region
at the midpoint. Total distance about 1000 kilometers.

PAPER : 30. ON THE SELF-MODULATION AND DISTORTION OF MF WAVES IN THE IONOSPHERE
AUTHOR :  M. Cutolo
QUESTIONER : J. Fonteyne
QUESTION : Il aurait ete interessant de mesure le champ, et
ussi d'avoir une sequence sans modulation. Y a til de tells mesure simultanees?
RESPONSE : I hope to do this next experiment.

PAPER : 30. ON THE SELF-MODULATION AND DISTORTION OF MF WAVES IN THE IONOSPHERE
AUTHOR :   M. Cutolo
QUESTIONER :   P. A. Kossey
QUESTION : At what hours were the phenomena most clearly observed.?
RESPONSE : Our observations were made during the night from midnight to 6:30  in  the  morning.
During the day it is impossible to receive Frankfurt in Naples.

PAPER : 31. MEDIUM WAVE MULTIPATH PROPAGATION IN MARMARA AND WEST BLACK-SEA REGION.
AUTHOR : A. Fer
QUESTIONER :   F. J. Kelly
QUESTION : Did you consider using Millington's method as described by   Knight earlier?
RESPONSE  :  Yes, we considered it, it would have taken a shorter time, however the technique I
described is a rigorous analysis as opposed to Millington's semi-empirical  formulation. While
Monteath has given a proof of Millington's method, it is nevertheless a semi-empirical formula.
On the four section path we did not have any experimental evidence on hand to  see  whether  it
worked  satisfactorily. Furthermore the extension of King, Monteath, and Wait's results for the
three section path was a simple  process  based  on  the  compensation  theorem.  It  takes  an
extremely short time in a 37145 computer for example. We believe the results are more accurate.

PAPER : 31. MEDIUM WAVE MULTIPATH PROPAGATION IN MARMARA AND WEST BLACK-SEA REGION.
AUTHOR :   A. Fer
QUESTIONER : J. Fonteyne
QUESTION : La théorie c'est très bien, mais les essais  practiques  seraient  nettement  mieux,
dont  mon idée était de savoir si vous comptiez faire vraiment des essais avec un emetter situé
a' l'endroit de réception, ou avec des émetteurs a' des différents emplacements pour bien verifié
toutes  ces courbes et ces variations de conductivité. Je crois que ça c'est peut-être la chose
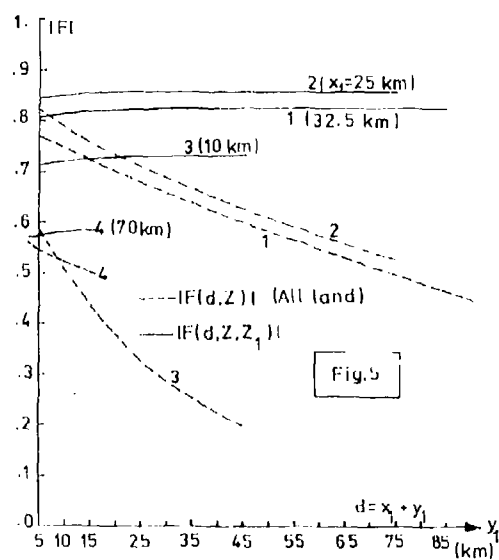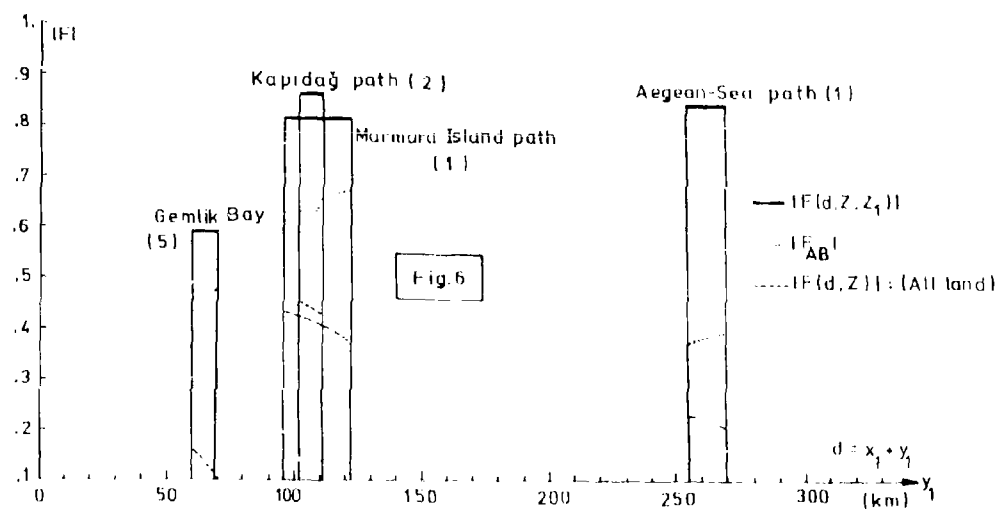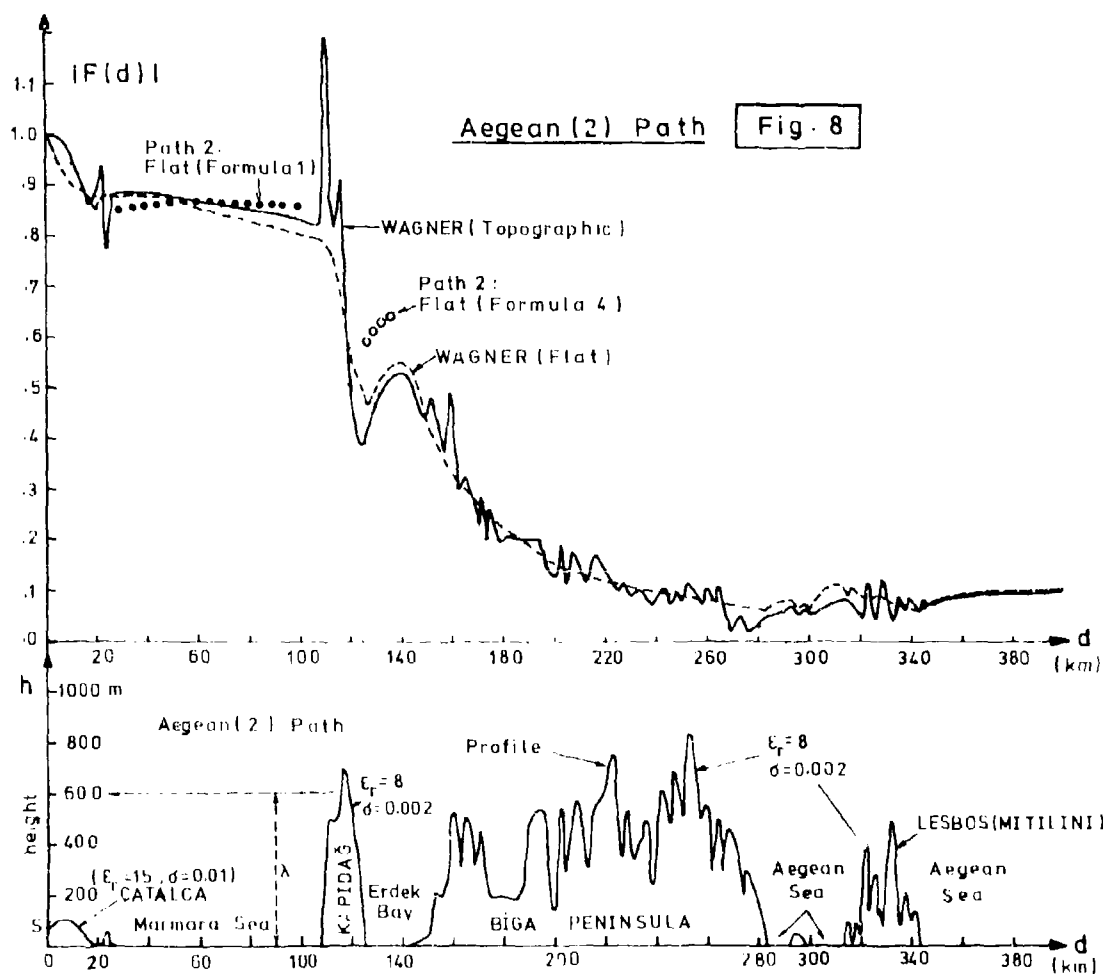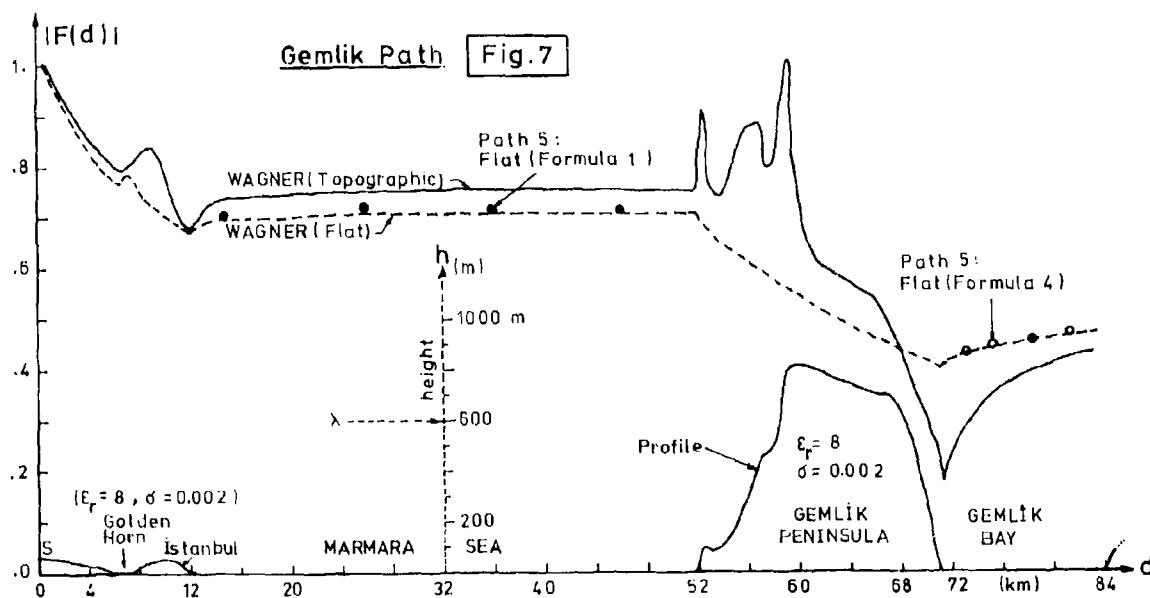plus importante pour nous, pour nous permettre de dire quelle est la méthode la meilleure?
RESPONSE  :  Well,  I  think  as  you  say experimental justification and confirmation of these
results is definitely necessary. To me,  it  seems,  about  the  best  method  we  can  use  in
connection  with  any  specific problem is to apply the rigorous integral equation technique of
Randy Ott's program WAGNER. It seems to take into accrum  all the characteristics of  interest.
However  it's  so  expensive.  We  feel  that this particular technique is somehow a compromise
between  the simple formula of Millington, which I suppose we should have  compared  graphically
here,  and  the more rigorous technique. Millington's formula is I believe only applicable to a
case where the transmitter is very far from the coastline, and near  the  boundary  region  the
results  it  gives  are not supposed to be very accurate. This was one of the considerations in
our case. When we take the limiting case of the transmitter far away from the coastline and the
point of observation far from the coastline, our formula reduces to Millington's formula. Which
is to be expected.

PAPER : 31. MEDIUM WAVE MULTIPATH PROPAGATION IN MARMARA AND WEST BLACK-SEA REGION.
AUTHOR :   A. Fer
COMMENTER :   L. W. Barclay
COMMENT : Following the other discussion on this paper I should like to comment 1.) I have made
some  comparisons between Millington's and Ott's methods, although not over such severe terrain
profiles as those in Turkey, and found the two methods to be  in  good  agreement  particularly
over the sea.

2.) One of the papers (I believe in "NATURE")  published  by  Millington
showed  good  agreement  between  his  mixed  path  method  and  experimental  results when the
transmitter was close to the coast. I should also like to draw attention to the recent paper by
Damboldt  at  the  IEE  Antennas and Propagation Conference (1981) where, results obtained from
measurements over multisection mixed paths in the Baltic sea area are given.

# NUMERICAL MODELING OF THE PROPAGATION MEDIUM AT ELF/VLF/LF

D. G. Morfitt
J. A. Ferguson
F. P. Snyder
Electromagnetic Propagation Division
Naval Ocean Systems Center
San Diego, CA 92152

## SUMMARY

A reliable knowledge of radio signal amplitude and phase characteristics is required to design and maintain communications and navigational circuits at elf/vlf/lf. The ability to accurately predict signal levels as a function of propagation frequency and range is of considerable importance in achieving reliable communication coverage. Detailed computational models (computer programs) based on multimode theory have been developed. These models have been found to account for the signal variability as a function of propagation distance that occurs in nature. Computed results are, however, very sensitive to the choice of model parameters used as inputs to the calculations. In particular, the ionospheric electron density, ion density and collision frequency profiles are important quantities which are required to adequately depict the real propagation environment. This paper presents an overview of some available procedures for determining ionospheric profiles to be used in computing reliable predictions of elf/vlf/lf signal levels.

## 1. INTRODUCTION

The propagation of low frequency, very low frequency and extremely low frequency radio waves is of considerable practical importance for communications, for navigation systems, and for worldwide frequency and time comparisons. The propagation of elf/vlf/lf radio waves is characterized by high stability in both phase and amplitude. Little attenuation of the waves occurs in the ionospheric reflection process and as a result they propagate to very great distances. These waves also penetrate further into seawater than do waves of higher frequencies. The signals are not greatly affected by most natural-occurring ionospheric disturbances apart from the polar cap events, and radio communications can usually be maintained under conditions that make communication very difficult at higher frequencies. Because of these propagation characteristics, vlf and lf systems are prime components in emergency communications networks. Marine communicators are highly dependent upon the vlf radio frequency band for broadcast communications to ships at sea. Concurrently, some communicators have specific interest in propagation on frequencies at the lower end of the lf range for transmission between inflight aircraft. Elf transmission would be useful for communication to submerged vessels since these frequencies penetrate further into the sea than other frequency bands.

A review of the propagation characteristics of radio waves at these frequencies is presented by Thrane (1979). Some of the most important computational methods that are available for predicting the phase and amplitude of long waves are briefly discussed as are some navigation and communication applications. A recent review by Burgess and Jones (1975) also describes the propagation of vlf and lf radio waves with reference to systems applications. Elf communications are described by Wait (1974).

In order to design and maintain communications circuits at elf/vlf/lf, a reliable knowledge of radio signal amplitude and phase characteristics is required. Accurate propagation prediction techniques would prove invaluable in helping to meet these needs. Considerable theoretical work at elf/vlf/lf frequencies has been conducted since the early 1960s. The works of Budden (1961), Wait (1970) and Galejs (1972) describe the basic theory of radio wave propagation at long wavelengths. Detailed computational models which characterize propagation at these frequencies, have been developed. These models have been found to account for the signal variability as a function of propagation distance that occurs in nature. Of the several propagation models that have been developed for computing field strengths at elf/vlf/lf, those developed at the United States Naval Ocean Systems Center (NOSC) will be utilized in this paper because of the many special computational options they contain.

Computed results are very sensitive to the choice of model parameters used as inputs to the calculations. In particular, the ionospheric electron density, ion density and collision frequency profiles along with proper values of the earth's magnetic field parameters, ground conductivity, and dielectric constant are important quantities which are required to adequately depict the real propagation environment. A determination as to which ionospheric density profiles should be used as inputs to the propagation model is examined through application of three procedures. The first approach is to acquire experimentally measured long path propagation data and then to "best fit" these data by calculating the field strength amplitude along the appropriate propagation path using a variety of ionospheric profiles. A second approach is to survey the literature for published profiles of ionospheric density vs height. A regression analysis is then performed in terms of temporal and geophysical variations to determine the required profiles. A third approach is to utilize the International Reference Ionospheric Model. This model is assumed to provide useful ionospheric profiles with no dependence on the theoretical assumptions. The ionospheric profiles produced by the second and third methods are input to the propagation model and compared to the measured data of method one. This comparison gives a check of the latter two methods, as to their usefulness in signal level predictions.

## 2. PROPAGATION MODEL

The propagation of elf, vlf and lf terrestrial radio waves to great distances is conveniently represented in terms of waveguide mode theory. The NOSC waveguide model is chosen for the analysis presented in this paper because it allows for changes in the waveguide parameters (i.e. ionospheric profiles, the earth's magnetic field and the earth's conductivity and dielectric constant) along the propagation path.

It has been determined by Pappert (1981) that the waveguide procedure is useful for computing fields at frequencies as high as 300 kHz for daytime propagation conditions. The frequency limit for nighttime propagation is at least 60 kHz (Morfitt, 1977).

The NOSC waveguide model is described in a series of papers by Pappert (1968, 1970, 1972, 1974 and 1975). In general this technique obtains the full wave solution for a waveguide that has the following characteristics: (1) arbitrary electron and ion density distributions and collision frequency (with height) and (2) a lower boundary which is a smooth homogeneous earth character zed by an adjustable surface conductivity and dielectric constant. The model allows for earth curvature, ionospheric inhomogeneity, and anisotrophy result ng from the earth's magnetic field. The model also allows for the calculation of both horizontal and vertical components of the electric field at an arbitrary height in the waveguide. Air-to-air, ground-to-air or air-to-ground vlf/lf propagation problems involving a horizontally inhomogeneous waveguide channel may be treeted.

The energy within the waveguide is considered to be partitioned among a series of modes. Each mode represents a resonant condition, i.e., for a discrete set of angles of incidence of the waves on the ionosphere, resonance occurs and energy will propagate away from the source. The complex angles ($\theta$) for which this occurs are called eigenangles 'or "modes"). They are obtained using a "full-wave" procedure, such as described by Morfitt and Shellmai 76). The set of complex modal solutions is determined from the full-wave computer program for a spec d earth-ionosphere waveguide are summed at arbitrarily selected distances from the transmitter to obt .n the calculated vlf/lf field at those distances. This simple model is called horizontally homogeneous and can be applied to most daytime propagation paths with unvarying ground conductivity. Generally the parameters of the waveguide must be varied to describe the real propagation paths properly. Such paths cross land-sea and day-night boundaries and regions through which the geomagnetic field variations are significant. The modeling of such paths is accomplished by dividing them into horizontally homogeneous segments. As an example, a land-sea boundary might mark the end of one segment and the beginning of the next. Two methods are used for computing fields over these segmented paths. One method is the so-called WKB (Wait, 1964) while the second is mode conversion (Pappert and Snyder, 1972). The WKB procedure is a technique that utilizes average values of the mode constants along the propagation path. This method is accurate when changes in the modal parameters are sufficiently gradual along the path. For those propagation conditions where the properties of the earth-ionosphere waveguide can not be considered as slowly varying, the mode conversion technique must be applied. At each boundary, conversion coefficients are calculated to relate modes in one segment to those in the next. The mode conversion model allows for an arbitrary number and order of modes on each side of each waveguide discontinuity. The mode conversion model can be applied even in the event that the propagation path has only slowly varying waveguide parameters.

3. PROPAGATION AT ELF

Propagation at elf is presented in terms of theory and experiment in Wait ('1974). Pappert and Moler (1974), showed very good results between calculations and experimental measurements during undisturbed ionospheric conditions. The models of the electron and ion densities which were used in these calculations are given in Figure 1. Measured elf signal levels have been found to experience large amplitude fades during nighttime propagation (Davis, 1976). Barr (1977) and Pappert (1980) have suggested that sporadic-E layering in the ionospheric height regions between 110 and 130 kilometers (km) could produce these effects.

4. PROFILES FROM LONG PATH VLF/LF MEASUREMENTS

The ionospheric region of greatest importance to vlf/lf propagation is that from about 50 km up to about 120 km (the D and E regions). This region is not easily studied by ground based probing experiments, which tend to be plagued either by large error factors in estimates of the ionization densities at various heights or by poor height resolution (Trane, 1974). Rocket soundings provide more accurate measurements but are very limited in their temporal and geographical distributions.

Propagation studies using long-path vlf and lf data provide an indirect but useful description of the ionosphere for propagation prediction. The important ionospheric parameter needed to simulate actual propagation data is the ionospheric conductivity profile through which the radio waves must pass. This parameter is the principal unknown in the propagation models and is a function of the height variation of electron and ion density distributions and collision frequenices. The procedure using long path propagation measurements, attempts to determine the ionospheric conductivity profile indirectly by comparing fields calculated with the waveguide computer program to the measured fields. The ionospheric profile input to the waveguide calculations is varied until acceptable agreement with measurement is reached.

For propagation at vlf/lf during ambient conditions, only the electron density distribution need be considered in calculations. The ion distributions may be neglected. For this ionospheric model, the conductivity parameter ($\omega_r$) is a function of the electron density divided by the electron-neutral particle collision frequency. One of the simplest ionospheric profiles is an exponential variation of conductivity with height. It can be specified by only two parameters, scale height and reference height. Following Wait and Spies (1964) the conductivity parameter $\omega_r(h)$ is taken to be of the form $\omega_r(h) = 2.5 \times 10^5$ exp ($\beta(h-H')$), where h is the ionospheric height, $\beta$ is a gradient parameter in inverse height units and H' is a reference height. The value of the electron density N (h), in electrons/cubic centimeter, is calculated as a function of height, h in kilometers by the equation $N(h) = 1.43 \times 10^7$ exp ($\beta(h-H')$ $-0.15h$) where $\beta$ is in km$^{-1}$ and H' is in km. The collision frequency is given by $\nu(h) = 1.82 \times 10^{11}$ exp ($-0.15h$), where $\nu$ is the number of collisions per second.

The process of varying the ionospheric model (i.e. the values of $\beta$ and H'), calculating fields and comparing the calculations with measurements is greatly facilitated by the use of these exponential profiles. The usefulness of this simple ionospheric model is a result of its ease of application and its success in modeling experimentally measured data as demonstrated by Bickel et al. (1970), Morfitt (1977) and Ferguson (1980). The most usable measured data are collected at a large number of points along a great circle propagation path which includes the transmitter. The easiest way to collect such data is aboard an aircraft.

In general, the ionospheric models determined from the above procedure must be considered to represent an averaged ionosphere since the modeling assumes that the ionosphere was static during any aircraft flight period. The data fitting procedure attempts to find a calculated pattern of amplitude as a function of distance which agrees with the large scale pattern of the measured data. Thus, many small amplitude variations are averaged. It is possible that profiles of more complex forms than the exponential could be found to produce a better fit to measured data in some instances, but since the propagation paths considered are quite long, any profile determined to produce a best fit to the data is really an average profile for the total path.

Some exponential profiles are illustrated in Figure 2 for daytime conditions and in Figure 3 for nighttime conditions. The daytime curves are compared in Figure 2 to that derived by Bain and Harrison (1972) for summer during sunspot maximum conditions. The nighttime curves are compared in Figure 3 to that of Thomas and Harrison (1970).

Field strength levels produced from waveguide multimode computations, using various values of the $\beta$ and H' parameters of the electron density profile, are compared to experimentally recorded long path propagation data. These data have been obtained by recording signals from the vertically polarized transmitters: (NSS) Annapolis, Maryland; (NAA) Cutler, Maine; (NLK) Jim Creek, Washington; (NPM) Lualualei, Hawaii; (WWVL and WWVB) Fort Collins, Colorado; (GYN) Preston, England; (GBR) Rugby, England and the NOSC - 10 frequency sounder, Hilo, Hawaii. The comparisons between the waveguide computations and the experimental data are illustrated in plots of the vertical electric field against propagation distance. These plots show a vertical scale with dB above one microvolt per meter, normalized to one kilowatt of radiated power (dB/$\mu$V/m/kW). The horizontal scale is in megameters, Mm, from the transmitter (1 Mm = 1000 km).

### 4.1 Daytime Propagation in the Pacific

Figure 4 shows the comparison between fields as computed by the NOSC waveguide program and data recorded aboard an inflight aircraft in June 1965. The Figure illustrates that the profile $\beta = 0.5$ km$^{-1}$, H' = 70 km (or $\beta = 0.5$, H' = 70) gives signal levels in close agreement with recorded data. Figure 5 gives a summary of other comparisons using this profile with data recorded at various frequencies for propagation over midlatitude seawater paths in the summer. These data were all recorded at times of sunspot minimum. Propagation measurements were also made on 2 and 3 February 1974. Vlf/lf (10-60 kHz) signals were recorded aboard an inflight aircraft at an altitude of 9 km (30,000 ft) as it flew between Hawaii and Southern California. The signals were transmitted and recorded by the NOSC multifrequency sounder. Figures 6 and 7 show the experimental data values and corresponding calculated fields. The results indicate that the summer electron density profile, ($\beta = 0.5$, H' = 70), needs to be replaced by a profile with $\beta = 0.3$ and H' = 72-75 for daytime propagation over the Pacific during winter. These data were also recorded during sunspot minimum. The fact that the best-fit profiles for the aircraft flights of 2 February and 3 February are not the same illustrates the variability of daytime ionospheric propagation.

### 4.2 Daytime Propagation Across the Continental United States

Data obtained from propagation measurements carried out across the continental US during daytime transmissions are also examined. Aircraft measurements recorded by NOSC in June of 1958 during sunspot maximum are shown in Figure 8. It is of interest to note that while the profile ($\beta = 0.5$, H' = 70) provided good fits to summer propagation data recorded over the Pacific Ocean, the profile ($\beta = 0.3$, H' = 72) tends to simulate the signal levels better for propagation over this continental path. Other daytime measurements of vlf/lf propagation data have been carried out by Morgan (1966). The measured values were made on nine radials extending outward from transmitters located at Fort Collins, Colorado. The transmitter frequencies were 20 kHz (WWVL) and 60 kHz (WWVB). These measurements were made from ground vehicles at various positions along each radial. The data were obtained during September and October in 1964 and 1965. These were times of sunspot minimum. Figure 9 illustrates the comparison between data recorded at 60 kHz on the radial to Palm Beach, Florida. The profile ($\beta = 0.5$, H' = 70) does not describe the measured fields. The profile ($\beta = 0.3$, H' = 72) gives signal levels which are in much better agreement with data. Comparisons between calculation and measurement for all of the Morgan radials at both 20 and 60 kHz show that the profile ($\beta = 0.3$, H' = 72) gives very good agreement in almost all cases (Morfitt, 1977).

### 4.3 Daytime Propagation over the Greenland Ice Cap

Experimental measurements at 45 kHz have been obtained by Burgess in July 1970 aboard an inflight aircraft over Greenland during sunspot maximum conditions. These transmissions originated in England. Comparison of these field strength measurements to computed field strength predictions is shown in Figure 10. The profile ($\beta = 0.3$, H' = 72) was used as input to the mode conversion calculations for simulating the measured data.

### 4.4 Propagation through the Terminator

Fixed site measurements were made during sunrise conditions on the Hawaii to Southern California path over a four day period in October 1968. This was a time of sunspot maximum. The transmitter was the NOSC multifrequency sounder. Figure 11 illustrates the field strength calculations as compared to experimental measurements (Pappert and Morfitt, 1975). The mode conversion result simulates the data much better than that of WKB. The modeling was done assuming the daytime profile was ($\beta = 0.3$, H' = 70) and the nighttime profile was taken as ($\beta = 0.5$, H' = 86).

### 4.5 Nighttime Propagation in the Pacific

To examine the characteristics of vlf signal strengths for propagation during nighttime conditions, measurements were made aboard inflight aircraft, at an altitude of 3 km (10,000 ft), during January and February . This was at time of sunspot maximum. One of the signals monitored was NPM, Hawaii on 23.4 kHz. The propagation paths originated from Hawaii and terminated at Seattle, Washington; Ontario, California; Samoa and Wake Island. Results presented by Bickel et al. (1970) showed that a profile with ($\beta = 0.5$, H' = 85.5-87) would match the NPM data very well for the first two paths. The Samoa path was modeled

to some degree by the (H' = 85.5) profile but the WKB methods were required because of the rapid change of magnetic parameters with distance. The Wake Island data could not be modeled because the ionosphere was apparently changing with time.

Propagation data were also recorded during the February 1969 flights using the NOSC multifrequency sounder. Ten vlf frequencies were transmitted and recorded. These were approximately: 9.3, 10.9, 14.0, 15.6, 17.1, 21.8, 24.9, 26.5, 28.0 and 31.2 kHz. Comparisons between waveguide predictions and some of the multifrequency sounder data are shown in Figure 12 for the Hawaii to Ontario, California path. Here it is observed that the profile ($\beta$ = 0.5, H' = 87) represents these measured fields very well at 14.0, 17.1 and 21.8 kHz. A somewhat modified profile would be required to obtain better fits to the data at 10.9, 24.9 and 28.0 kHz. Results of calculations based on other choices of the $\beta$, H' conductivity parameters show that the required profile is found to vary with propagation frequency. At 9.3 kHz the values are ($\beta$ = 0.35, H' = 87) while at 31.1 kHz the values are ($\beta$ = 0.6, H' = 88).

In an attempt to obtain more definitive nighttime propagation data for the 10-60 kHz frequency range, additional measurements were taken on 30 January and 1 February 1974 over the Hawaii to Southern California path. The propagated signal were transmitted by the NOSC multifrequency sounder. These sounder data w re recorded aboard an inflight aircraft at an altitude of 9 km (30,000 ft). This was a time of sunspot minimum. Comparisons between calculations and the multifrequency sounder data are shown in Figures 13 and 14. The profiles determined to give best fit to the data of Figure 13 show values of ($\beta$ = 0.3-0.7) with (H' = 88-89). For Figure 14 the values are ($\beta$ = 0.3-1.2) and (H' = 87-88). It is of interest to note that the best fit exponential profile varies with propagation frequency. As the frequency is increased, the value of the conductivity gradient is found to increase. The reference height parameter H', however, is found to remain somewhat constant at the higher frequencies.

The electron density profiles determined to fit both the 7 February 1969 data (Figure 12) and the 1974 data from 1 February (Figure 13) appear to follow a similar relationship between propagation frequency and the profile gradient parameter $\beta$. In the case of the aircraft flight on 30 January 1974 (Figure 14), the recorded data tend to require a larger value of $\beta$ in order to produce an acceptable fit to the field strength levels. The explanation for the differences in best-fit electron density profile between the 30 January and the 1 February data is not known.

4.6  Nighttime Propagation Over the Continental United States and Higher Latitudes

Data from fixed vlf transmitters over propagation paths other than the Hawaii to Southern California path have been examined by Ferguson (1980). These data were collected on twenty-eight higher latitude paths during aircraft flights in 1957, 1969 and 1974-1977. Figure 15 shows one example of these measurements giving the results of "best-fit" fields for flights between NLK and NSS during the winter of 1969. This was a time of sunspot maximum. The best fit for these data gave values of ($\beta$ = 0.6, H' = 76-82). These values for H' are remarkable since the nominal range of H' for nighttime data at lower latitudes is 86-89 km. These data indicate a disturbance of the ionosphere. The 76 km value is nearly as low as the nominal daytime range of 70-74 km. The available data suggest that the boundary of the very low values of H' is in the vicinity of 70° magnetic dip. For propagation paths at latitudes south of this 70° dip line, the previously determined H' of 87 km is found.

The results obtained by Ferguson over the higher latitude paths are consistent with those of Westerlund and Reder (1973) for a very short path (350 km) from Omega, Norway to Kiruna, Sweden. Values of H' lower than the middle-latitude nighttime profile indicate a source of ionization not present at low latitudes. A likely source for this additional ionization is particle precipitation (Gough and Collins, 1973). In a study to coordinate satellite measurements of electron fluxes and ground-based measurements of D-region ionization, Larsen et al., (1976) showed that precipitating electrons can be the dominant source of ionization at D-region heights. The satellite results clearly indicate that the southern-most boundary of the precipitation varies from day to day. In one instance the minimum detectable flux level was exceeded at a magnetic latitude of about 57° (magnetic dip at the ground = 72°). The electron flux increased to a plateau at about 61° (Jip - 74.5°). In another instance this transition took place about 44° (dip = 62.5°) to 48° (dip 65.8°). In both instances the transition region is about 4° of magnetic latitude. These observations were used in establishing a tentative geophysical model for propagation calculations. Latitudes north of the transition region were called high latitudes. The propagation paths examined by Ferguson included some flights within the transition region and others totally within the high latitudes.

Analysis of the long path data measurements suggests the following table of exponential electron density profiles for vlf/lf propagation prediction, Morfitt (1977) and Ferguson (1980).

Table 1. Suggested profiles based on long-path vlf/lf propagation data.
(Frequencies, F, are in kHz)

| Seasonal-Diurnal Propagation Condition | H' (km) | $\beta$ (km$^{-1}$) | Magnetic Dip (°) |
|---|---|---|---|
| Summer day | 70 | 0.5 | |
| Summer night | 87 | 0.0077F + 0.31 | |
| Winter day | 74 | 0.3 | |
| Winter night | 80 | 0.035F - 0.025 (10 < F < 35) | 90-75 (high latitudes) |
| | | Linear change between high and middle latitudes | (transition latitudes) |
| | 87 | 0.0077F + 0.31 | <70 (middle latitudes) |

## 5. PROFILES FROM THE LITERATURE

Observations of the D-region have been made at scattered stations since 1948. Methods used for these observations include partial reflection, rockets, wave interaction, vlf/lf reflection and incoherent scatter. Examination of the available literature pertaining to D-region electron density profiles illustrates the enormous complexity of the situation. The aeronomy of the region is very complex and is not completely understood. There is also the complicated dependence of the electron density on such environmental conditions as latitude, solar zenith angle and season.

There are several reviews of measurements and resulting electron density profiles [Thomas, 1974; Thrane, 1974; Belrose and Segal, 1974; and Sechrist, 1974]. The literature is so vast and the experimental results so scattered throughout that it is difficult to obtain a coherent picture of the situation.

There have been many attempts to determine an applicable electron desity from propagation measurements. One of the more successful results was obtained by Bain and Harrison (1972). They found an electron density profile which fit 16 kHz data in England for sunspot maximum conditions during summer.

Some investigators have attempted to produce a series of D-region electron density profiles which would describe the ionosphere for daytime and nighttime conditions. In the determination of these profiles, the effects of different solar activities, season, solar zenith angle and geographical latitude were included. The most notable results have been [Deeks, 1966; Krashushkin and Khyazeva, 1970; Bain, 1974; Davis and Berry, 1977; Rawer et al., 1978; and McNamara, 1979]. All of these procedures have met with varying degrees of success.

### 5.1 The Davis-Berry Exponential Model

The Davis and Berry (1977) model of the electron density profile of the ionospheric D-region is an attempt to systematize exponential profiles derived from experimental observations. A total of 570 electron density profiles were used in the analysis. About 40% of the total number are from Ottawa, Canada; Wallops Island, Virginia; or University Park, Pennsylvania which are fairly clo _ together (on a global scale). Very few were from latitudes greater than 70°, and the majority of measurements were made during the daytime. The range of sunspot numbers from 10 to 125 is well represented in the data.

The model takes into account solar zenith angle, solar cycle, seasonal, latitudinal and magnetic activity variations. Their assumption is that for the purpose of predicting vlf/lf propagation, the variation of electron density with height can be represented by the exponential relationship $N(h) = N_0 \exp(\alpha(h-H'))$, where $N_0$ = electron density at some reference height, $H'$ and $\alpha$ = scale height.

They show how to obtain $N_0$, $H'$ and $\alpha$ from a given electron density profile, as found in the literature, and an assumed collision frequency profile. These parameters, $\alpha$ and $H'$ were subjected to a multiparameter linear regression analysis. The resultant expressions from this approach give the reference height, $H'$ in the form $H' = a + b \times$ (zenith angle) + $c \times$ (latitude) + $d \times$ (solar activity) + $e \times$ (month) + $f \times$ (magnetic index). The scale height, $\alpha$, is of the form $\alpha = a + b \times$ (zenith angle) $\times c$ (month) + $d \times$ (magnetic index). The model is not a function of the propagation frequency.

The exponential profile notation can be related to the $\beta$ and $H'$ notation described earlier by $\beta = \alpha + 0.15$. Calculations for $\beta$ and $H'$ at noon and midnight for summer and winter at sunspot minimim and midlatitude conditions illustrate that the daytime values compare favorably with those determined from long path data. For nighttime the vaues of $H'$ are too small. At higher latitudes the nighttime exponential profiles derived empirically by Ferguson (1980) are not reproduced by the Davis-Berry model.

### 5.2 The McNamara Model

Davis and Berry's set of electron density profiles has been extended by McNamara (1979) to include a total of 700 experimental profiles. These have all been digitized and made completely computer accessible. Each profile has associated with it the following conditions of its observation: year, month, day, local time, smoothed monthly sunspot number, latitude, longitude, method of observation, an index of magnetic activity, and a special case parameter. This last parameter indicates whether the profile was obtained under normal conditions or under conditions such as eclipses, auroral absorption events, and so on. The procedure developed by McNamara uses the extended set of profiles and a multiple linear regression technique to provide a model of the electron density at heights from 55 through 90 km in steps of 5 km. The McNamara model gives electron densities, at each height, in the form $\log_{10}N = a + b \times$ (zenith angle) + $c \times$ (latitude) + $d \times$ (solar activity) + $e \times$ (season) + $f \times$ (magnetic index). The exact form of each of the contributing terms is chosen so as to be physically realistic, to linearize the regression equation, and to minimize the standard deviation of each coefficient. It is assumed that the terms in the expansion are independent. The McNamara model differs from that of Davis and Berry in that the resulting profiles are not restricted to the exponential form. Results of comparing calculations using the McNamara profiles to measured data are shown in Figures 16 and 17 for daytime and nighttime conditions. The daytime prediction is favorable while the nighttime agreement is poor. More examples need to be examined, however, to provide for a full test of this model.

### 5.3 The International Reference Ionosphere 1978

The "International Reference Ionosphere" project (Rawer et al., 1980) is a joint URSI and COSPAR effort which began in 1969. It is intended to summarize the most important features of the terrestrial ionosphere. The IRI is intended to combine approved experimental results consisting of in situ rocket observations combined with radio propagation experiments between the ground and the rocket, so as to provide a useful ionospheric reference with no dependence on theoretical assumptions. The IRI profiles are obtained from computer models composed of a set of independent functions, each valid in a particular height range, representing averages of measured ionospheric parameters.

The following analysis is taken from Snyder and Ferguson (1981). Table 1 gives a set of exponentially varying D-region electron density profiles recommended for computing vlf/lf field strengths for long path propagation. Some of the vlf propagation data used to construct Table 1 are used to examine the IRI model. For daytime, one propagation path was from NPM (Hawaii) to San Francisco, California during the summer of 1965 with a smoothed spot number of 20. This data is shown in Figure 5. A second daytime propagation path was from Hawaii to San Diego, California during the winter of 1974 with a smoothed sunspot number of 20. The transmitter for this case was the NOSC multifrequency sounder located at Hilo, Hawaii. These data are shown in Figures 6 and 7. For nighttime, one propagation path was from Hawaii to San Diego, California during the winter of 1974 with a smoothed sunspot number of 20. This data is shown in Figure 13. A second nighttime propagation path was from Hawaii to Ontario, California during the winter of 1969 with a smoothed sunspot number of 120. This data is shown in Figure 12. In both nighttime cases, the transmitter was the NOSC multifrequency sounder. All signal amplitudes, for daytime and for nighttime, were recorded aboard an airplane flying between the transmitter and the path end points.

Two electron density profiles for the NPM to San Francisco path are shown in Figure 18a. Both the IRI-78 and the exponentially varying profile ($\beta = 0.5$, H' = 70) are included. A plot of the ionospheric conductivity parameter, $\omega_r$, is shown in Figure 18b for both the IRI and the exponential profiles. The conductivity parameters differ considerably throughout the height range presented. However, they are nearly the same in the vicinity of the reference height for the exponential profile. It is this similarity in the height range near the reference height that will result in nearly identical mode sums for the two profiles.

Figure 19 shows the measured and computed daytime vlf field strengths for the NPM to San Francisco propagation path at 19.8 and 24.0 kHz. For this low sunspot number, summer case, there is excellent agreement between the computed and experimentally measured results. The signal amplitudes differ by only a few dB, except at the null locations. Furthermore, the null locations are in agreement to within 100 to 200 km. The computed and measured daytime amplitudes for the multifrequency sounder to San Diego propagation path are shown in Figure 20. For this case, vlf signals were measured on two flights of the airplane on consecutive days, one flying from San Diego area towards the sounder location and the other flying in the opposite direction. The season for this case is winter rather than summer, although the sunspot number is the same as for the data in Figure 19. The difference between the two sets of measured amplitudes is an indication of the daily variability of the vlf signal strengths as a function of distance. The best agreement between computed and measured amplitudes is for the lower frequency. There is relatively poor agreement for the higher frequencies.

Comparisons of the measured and computed field strengths for the nighttime San Diego path are shown in Figure 21 and for the Ontario path in Figure 22. A striking feature of both Figure 21 and 22 is the almost total lack of similarity between the computed and measured field strengths. In general, there is no similarity in null locations or the amplitudes. The measured data are typically 10 to 20 dB lower than the computed amplitudes.

In view of the results presented in the foregoing sections, no attempt was made to determine an improved set of parameters for the daytime IRI-78 profiles. Some limited data have been examined (although not presented) which indicate, that the IRI-78 D-region model may be inadequate for long path vlf field strength calculations under conditions of high sunspot number. It should also be recalled that the simple model of the IRI-78 profiles is inadequate to provide a good fit to daytime vlf propagation data over a large frequency band as has been indicated in the multifrequency sounder to San Diego analysis.

The IRI-78 profile model has been shown to be inadequate for computing long path vlf signals for nighttime conditions, at least for the winter season. Measured data for nighttime conditions for two different sunspot numbers indicate a sunspot dependence in the ionospheric profile. The IRI-78 model does not reflect a similar dependence. Numerous modifications to the parameters of the IRI-78 nighttime model were examined in an attempt to find a reasonable set of parameters for vlf long path nighttime propagation modeling. The procedure adopted was to start with the given parameters for the IRI-78 and modify certain individual parameter in small steps attempting to approach a better agreement between the computed and measured field strengths. The results of such modifications in every case lead to a set of parameters which produced electron densities similar to the exponential electron densities of table 1. Therefore, the IRI-78 nighttime D-region electron densities are found to be generally too large, a result just the opposite of that reported Singer et al. (1980).

6. CONCLUSION

Several procedures that are used to infer ionospheric electron density profiles have been examined. Resulting profiles have been input to a computer program that computes signal levels versus propagation distance. Field strength values obtained are compared to long path propagation data. It is found that a proper choice of exponential profile tends to produce field strength levels that simulate the experimental data somewhat better than the comparison determined by the use of profiles taken from the models of Davis-Berry, McNamara or the IRI-78. This observation is especially true for propagation during nighttime.

7. REFERENCES

BAIN, W.C. (1974), The use of Vlf propagation results in ionospheric modelling. ELF-VLF Radio Wave Propagation, ed. J.A. Holtet, 151-163, D. Reidel Publishing Co., Dordrecht, Holland.

BAIN, W.C. and HARRISON, M.D. (1972), Model ionosphere for D region at summer noon during sunspot maximum. Proc. IEEE, 119, 790-796.

BARR, R. (1977), The effect of sporadic-E on the nocturnal propagation of ELF radio waves. J. Atmos. Terr. Phys., 39, 1379-1387.

BELROSE, J.S. and SEGAL, B. (1974), On interpretation of CW propagation data for long radio waves. Methods of Measurements and Results of Lower Ionosphere Structure. COSPAR Symposium, Akademic-Verlag, Berlin, 77-109.

BICKEL, J.E., FERGUSON, J.A. and STANLEY, G.V. (1970), Experimental observations of magnetic field effects on VLF propagation at night. Radio Science, 5, 19-25.

BUDDEN, K.G. (1961), The waveguide-mode theory of wave propagation. Prentice Hall.

BURGESS, B. and JONES, T.B. (1975), The propagation of LF and VLF radio waves with reference to some systems applications. The Radio and Electronics Engineer, 45, 47-61.

DAVIS, J.R. (1976), Localized night'ime D-region disturbances and ELF propagation. J. Atmos. Terr. Phys., 38, 1309-1317.

DAVIS, R. M., Jr. and BERRY, L.A. (1977), A revised model of the electron density in the lower ionosphere. Tech. Rep. TR 111-77, 58 pp., Defense Commun. Agency Command Control Tech. Center, Washington, DC, NTIS, AD 17883.

DEEKS, D.G. (1966), D-region electron density distributions in middle latitudes deduced from the reflection of long radio waves. Proc. Roy. Soc. A. 2, 91, 413-437.

FERGUSON, J.A. (1980), Ionospheric profiles for predicting nighttime vlf/lf propagation. Naval Ocean Systems Center Technical Report 530, NTIS, ADA 085399.

GALEJS, J. (1972), Terrestrial propagation of long electromagnetic waves. Pergamon Press, New York, Oxford.

GOUGH, M.P. and COLLIN, H.L. (1973), Energetic electron precipitation as a source of ionization in the nighttime D-region over the mid-latitude rocket range, South Uist. J. Atmos. Terr. Phys., 35, 835-850.

KRASHUSHKIN, P.Y.E. and KNYAZEVA, T.A. (1970), Diurnal seasonal, and 11-year variations of the electron density profile in the lower ionosphere. Geomagnitism and Aeronomy, 10, no. 6, 769-789.

LARSEN, T.R., REAGAN, J.B., IMHOF, W.L., MONTBRIAND, L.E. and BELROSE, J.S. (1976), A coordinated study of energetic electron precipitation and D-region electron concentrations over Ottawa during disturbed conditions. Journal of Geophysical Research, 81, 2200-2211.

McNAMARA, L.F. (1979), Statistical model at the D-region. Radio Science, 14, 1165-1173.

MORFITT, D.G. (1977), Effective electron density distributions describing vlf/lf propagation data. Naval Ocean Systems Center Technical Report 141, NTIS, ADA 047508.

MORFITT, D.G. and SHELLMAN, C.H. (1976), MODESRCH, an improved computer program for obtaining elf/vlf/lf mode constants. Naval Electronics Laboratory Center Interim Report 77T, NTIS, ADA 032473.

MORGAN, G.I. (1966), Measured daytime field intensities in the United States at vlf, lf and mf. Gautney and Jones Communications, Inc. TR-60, 0141.002, NTIS, AD 843730.

PAPPERT, R.A. (1968), A numerical study of vlf mode structure and polarization below and anisotropic ionosphere. Radio Science, 3 (new series) 219-233.

PAPPERT, R.A. (1979), Effects of a large patch of sporadic-E on nighttime propagation at lower elf. J. Atmos. Terr. Phys., vol 22, 417-425.

PAPPERT, R.A. (1981), Lf daytime earth-ionosphere waveguide calculations. Naval Ocean Systems Center Technical Report 647, N IS, ADA 096098.

PAPPERT, R.A. and BICKEL, J.E. (1970), Vertical and horizontal vlf fields excited by dipoles of arbitrary orientation and elevation. Radio Science, 5, 1445-1452.

PAPPERT, R.A. and MOLER, W.F. (1974), Propagation theory and calculations at lower extremely low frequencies (elf). IEEE Transactions on Communications, COMM-22, 438-451.

PAPPERT, R.A. and MORFITT, D.G. (1975), Theoretical and experimental sunrise mode conversion results at vlf. Radio Science, 10, 537-546.

PAPPERT, R.A. and SNYDER, F.P. (1972), Some results of a mode-conversion program for vlf. Radio Science, 7, 913-923.

RAWER, K., BILITZA, K. and RAMAKRISHNAN, S. (1978), Goals and status of the International Reference Ionosphere. Rev. Geophys. and Space Phys., 16, no. 2, 177-181.

SECHRIST, C. F., Jr. (1974), Comparisons of techniques for measurement of D-region electron densities. Radio Science, 9, 137-149.

SINGER, W., TAUBENHEIM, J. and BREMMER, J. (1980), A test of the IRI lower ionosphere models by comparison with radio propagation data. J. Atmos. Terr. Phys., 42, 241-248.

SNYDER, F.P. and FERGUSON, J.A. (1981), The use of the International Reference Ionosphere (IRI-78) models for calculating long path fields at vlf. Published in The effect of the ionosphere on radiowave systems. J.M. Goodman, editor, US Government Printing Office, Washington, DC.

THOMAS, L. (1974), The temporal and geographic variations of D-region electron concentrations; methods and measurements and reslts of lower ionosphere structure. Edited by K. Rawer, Akademic Verlag, Berlin.

THOMAS, L. and HARRISON, M.D. (1970), The electron density distributions in the D-region during the night and pre-sunrise period. J. Atmos. and Terr. Phys., 32, 1-4.

THRANE, E.V. (1974), Ionospheric profiles up to 160 km: A review of techniques and profiles. In Methods of Measurement and Results of Lower Ionosphere Structure, edited by K. Rawer, Akademic-Verlag, Berlin.

THRANE, E.V. (1979), Propagation of long radio waves in the earth's environment. AGARD Conference Proceedings no. 99, Aerospace Propagation Media Modelling and Prediction Schemes for Modern Communications, Navigation and Surveillance Systems.

WAIT, J.R. (1964), Two dimensional treatment of mode theory of the propagation of vlf radio waves. Radio Science 68D, 81-93.

WAIT, J.R. (1970), Electromagnetic waves in stratified media. Pergamon Press, New York.

WAIT, J.R. (ed) (1974), Special issue on extremely low frequency (elf) communications. IEEE Transactions on Communications, COM-22, 4.

WAIT, J.R. and SPIES, K.P. (1964), Characteristics of the earth-ionosphere waveguide for vlf radiowaves. NBS Technical Note 300.

WESTERLUND, S. and REDER, F.H. (1973), Vlf radio signals propagating over the Greenland ice-sheet. J. Atmos. Terr. Phys., 35, 1475-1491.

8. ACKNOWLEDGEMENT
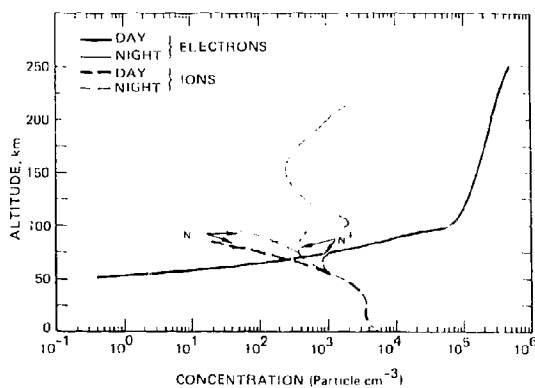
Figure 1. Ambient day and night constituent profiles.
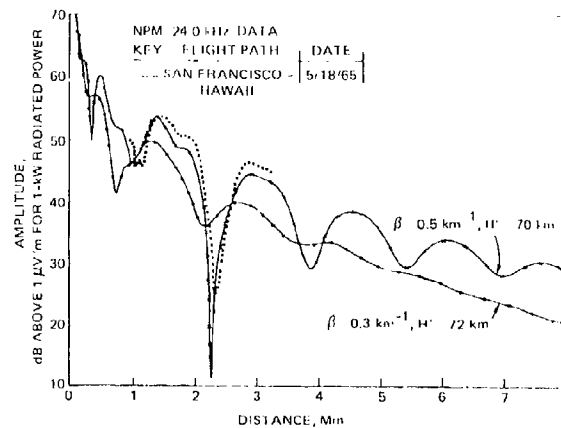


Figure 4. Propagation over the Pacific Ocean (daytime, summer). (NPM 24 kHz).
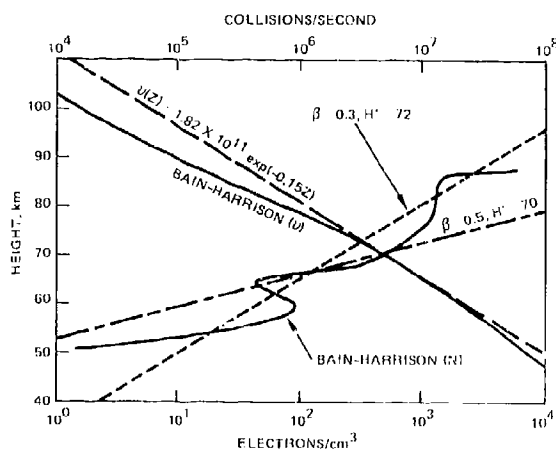


Figure 2. Daytime electron density profiles and collision frequency profiles.
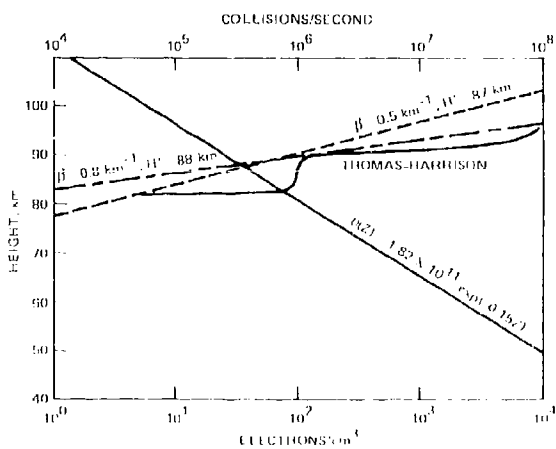


Figure 3. Nighttime electron density profiles and collision frequency profile.
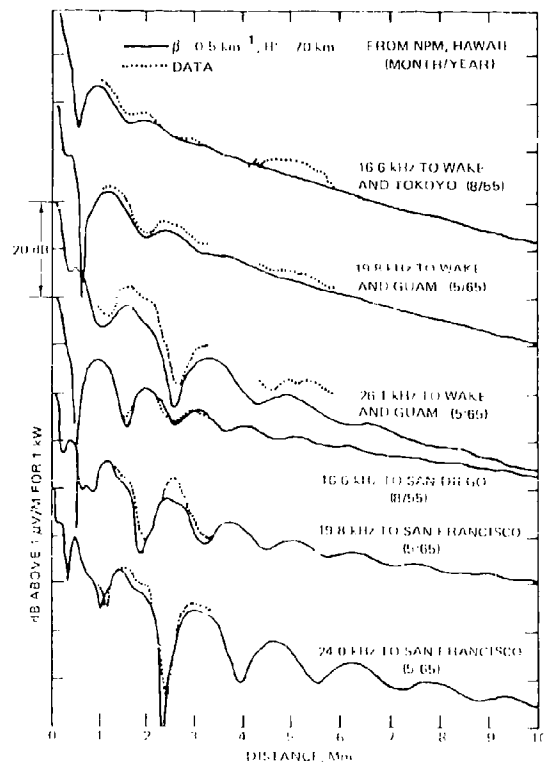


Figure 5. Propagation over the Pacific Ocean (daytime, summer) various VLF frequencies.
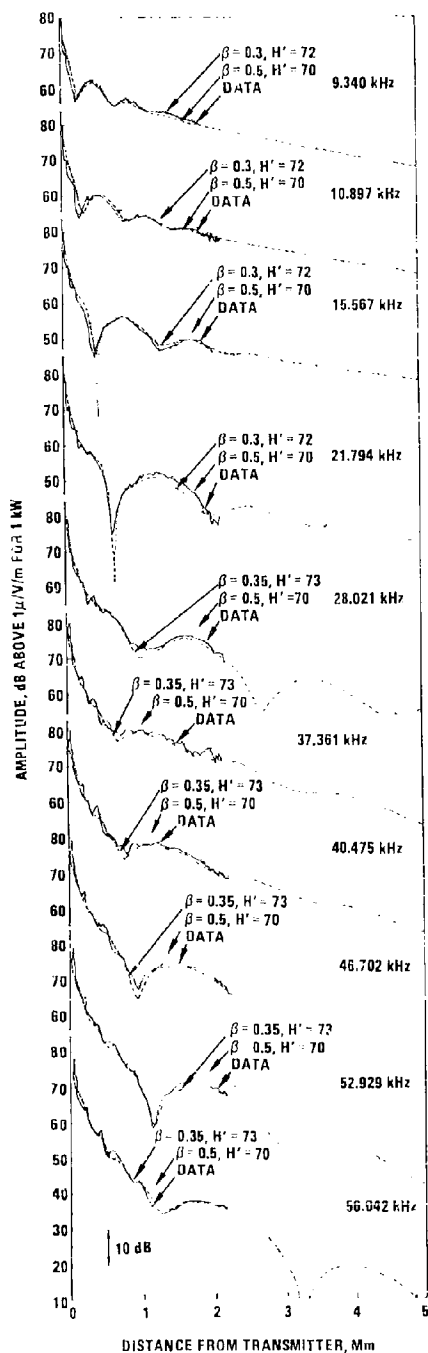
Figure 6. Measured and computed daytime signal levels on the Hawaii to San Diego path. Hawaii transmitter, aircraft flight, February 2, 1974
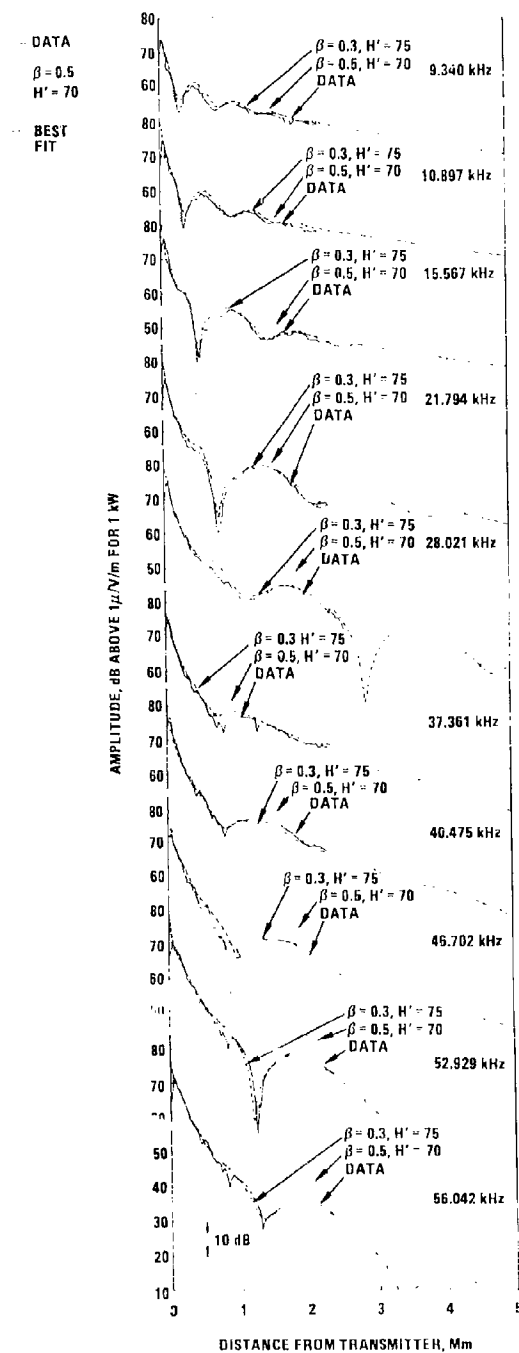
Figure 7. Measured and computed daytime signal levels on the Hawaii to San Diego path. Hawaii transmitter, aircraft flight, February 3, 1974.
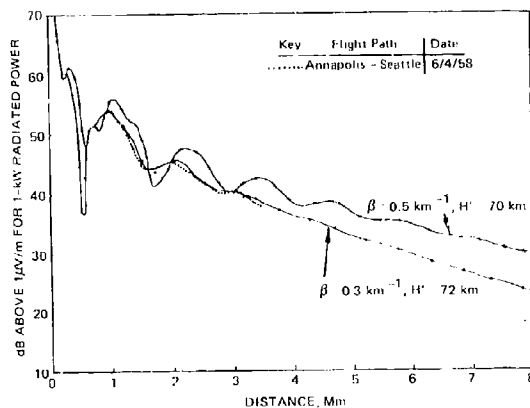
Figure 8. Daytime propagation across the continental United States (NLK 18.6 kHz).
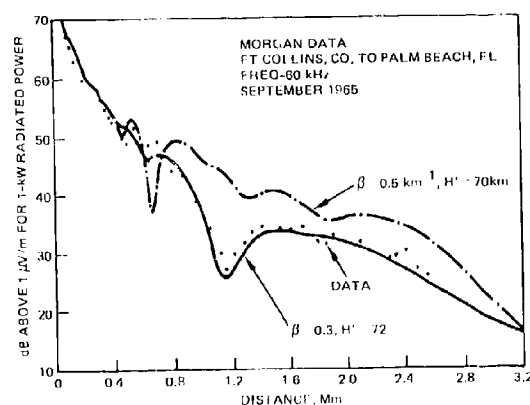


Figure 9. Daytime propagation across the continental United States (WWVB 60 kHz).
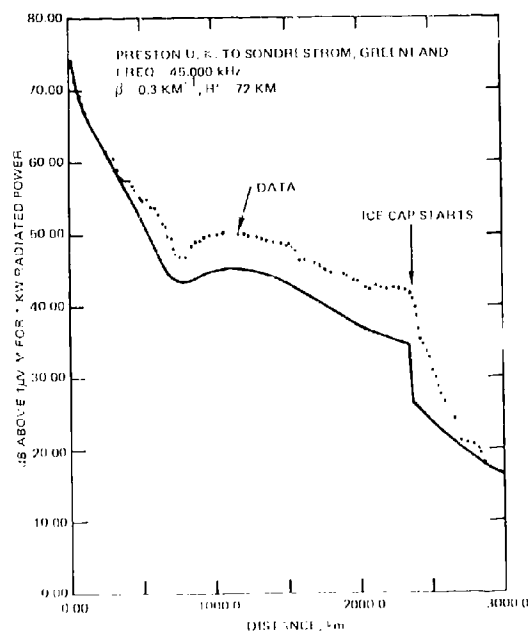


Figure 10. Daytime high-latitude propagation across the Greenland ice cap (45 kHz).
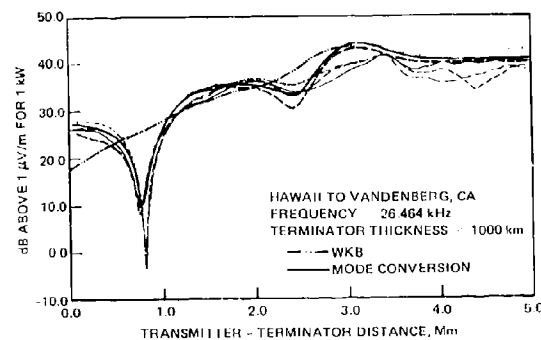


Figure 11. Vlf propagation through the sunrise terminator.
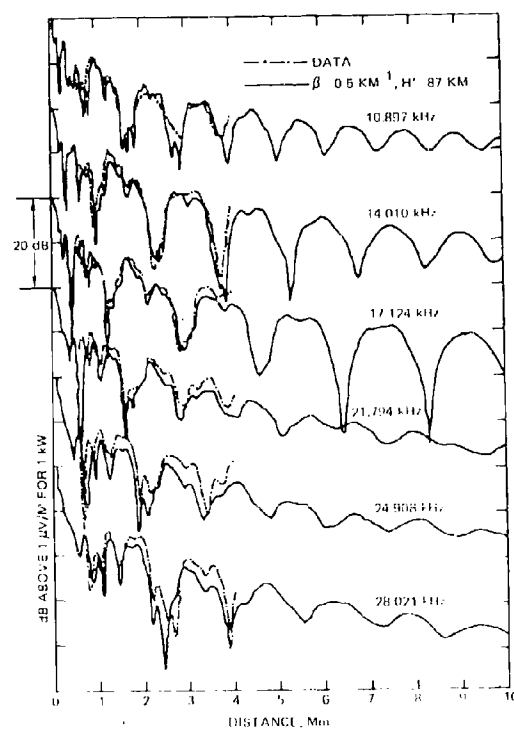


Figure 12. Multifrequency sounder data over the Pacific, Hawaii to Southern California (Ontario) path (nighttime winter), 1969.
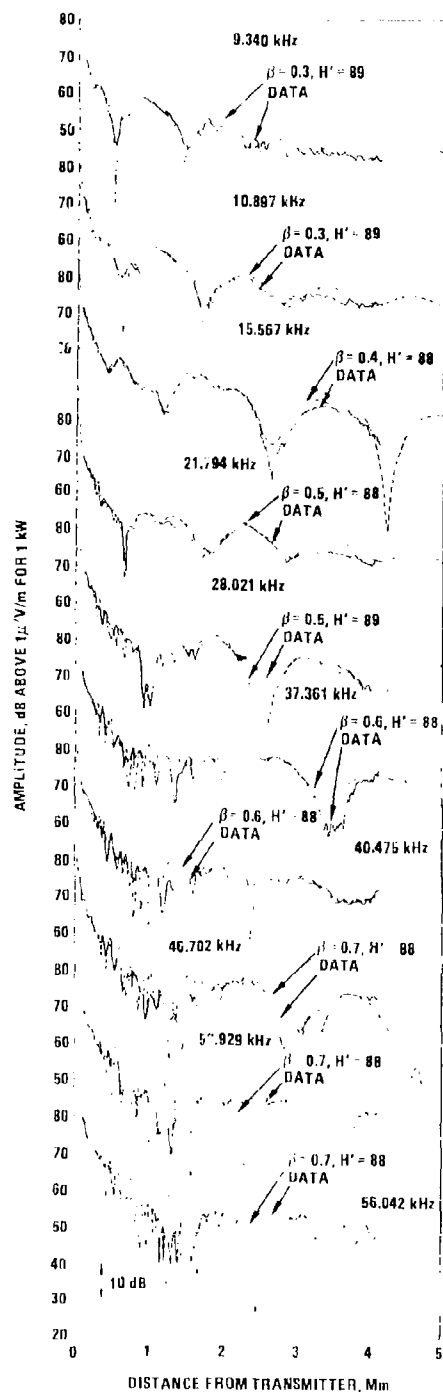
Figure 13. Measured and computed nighttime signal levels on the Hawaii to San Diego path. Hawaii transmitter, aircraft flight, February 1, 1974
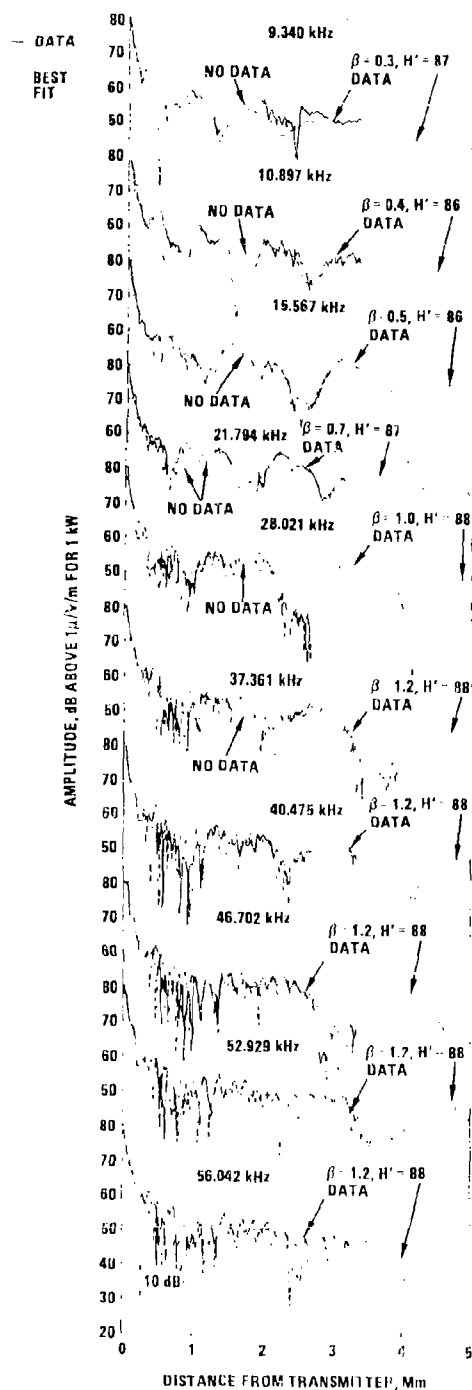
Figure 14. Measured and computed nighttime signal levels on the Hawaii to San Diego path. Hawaii transmitter, aircraft flight, January 30, 1974.
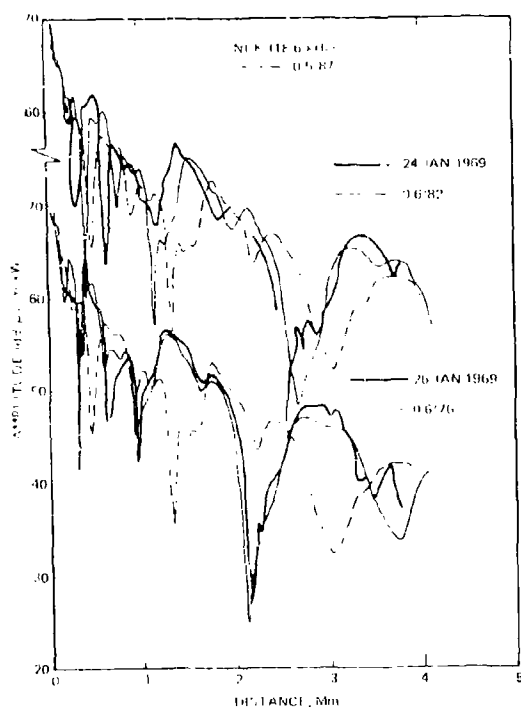
Figure 15. Best fit to measurements. NLK toward NSS, 1969 — Nighttime



Figure 17. Nighttime propagation, Hawaii to San Diego, California, NOSC Sounder, 15.567 kHz, February, 1974.
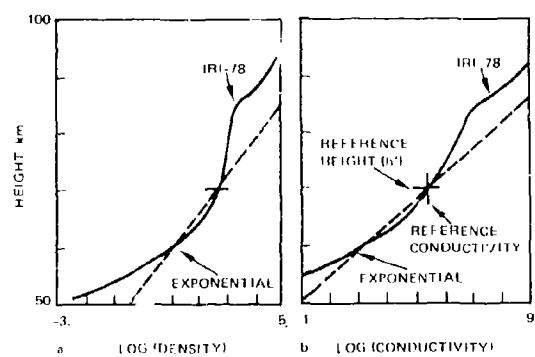


Figure 18. Electron density and conductivity parameters NPM to San Francisco – Day



Figure 16. Daytime propagation, Hawaii to San Diego California, NOSC Sounder, 56.0 kHz, February 1974
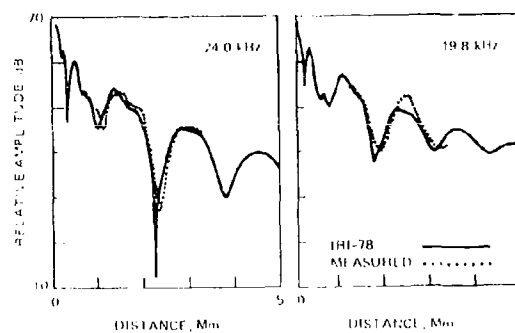


Figure 19. Computed and measured signal strengths NPM to San Francisco – Day
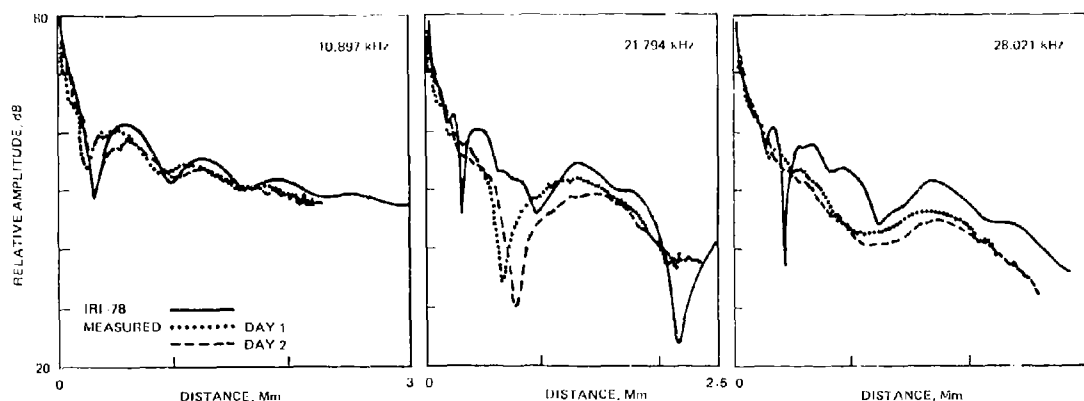
Figure 20. Computed and measured signal strength sounder to San Diego – Day.
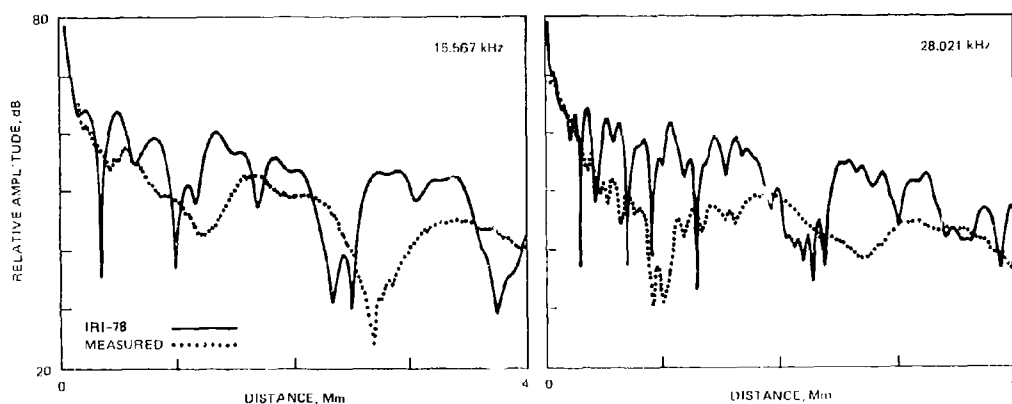


Figure 21. Computed and measured signal strengths sounder to San Diego – Night.
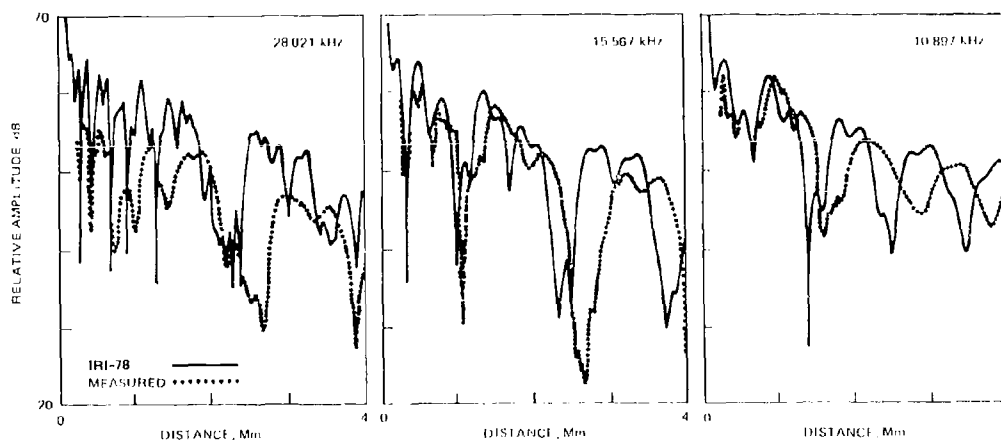


Figure 22. Computed and measured signal strengths sounder to Ontario – Night.

# MODELING OF THE AMBIENT AND DISTURBED IONOSPHERIC
## MEDIA PERTINENT TO ELF/VLF PROPAGATION

J. B. Reagan, R. E. Meyerott, R. C. Gunton
W. L. Imhof, and E. E. Gaines
Lockheed Palo Alto Research Laboratory
Palo Alto, California 94304 USA

and

T. R. Larsen
Norwegian De ( ice Research Establishment
Kjeller, Norway N-2007

## SUMMARY

Propagation at ELF and VLF in the earth's waveguide occurs principally between the ground and that part of the ionosphere between 20 and 120 km. An attempt has been made to model the ion and electron concentrations and the electrical conductivity in this portion of the ionospheric media during ambient and solar disturbance periods. Based on an evaluation of recent data a new ambient daytime electron density profile is proposed for ELF/VLF propagation studies. Several solar particle events (SPE) ranging from moderate to intense in magnitude and differing in spectral hardness have been modeled using satellite, balloon and ground-based data to define the source terms and in some cases the electron density profiles. A time dependent ion/neutral chemistry computer code has been used to calculate the resulting ion, electron and conductivity profiles in a manner that is consistent with the measurements. During intense SPE's it is shown that the conductivity at 40 km, a height critical to ELF propagation, can be increased over 200 times. The sensitivity of ELF propagation at 75 Hz across a transpolar path between the United States and Norway to these enhanced conductivity profiles as well as to varying diurnal conditions has been evaluated using available electromagnetic propagation codes. It is shown that during daytime conditions in an intense SPE the effective bottom of the ionosphere is lowered from an ambient 52 km altitude to between 33 and 40 km, depending on the intensity of the event. The corresponding top of the ionosphere where ELF reflection ultimately occurs is also lowered from 90 km to between 58 and 65 km. The principal attenuation occurs near the bottom of the ionosphere in the height range 20 - 40 km where the waves suffer ohmic dissipation with the dominant ion population. A secondary loss occurs near the top of the ionosphere due to ohmic dissipation with the enhanced electron density. In a typical transpolar link the signal strength in an intense SPE is calculated to be attenuated by 5 to 8 dB over ambient conditions. Differing ion and electron profiles along the propagation path due to varying diurnal conditions can result in up to 3 dB difference in the received signal strength. The ionospheric modeling provides the basis for future field experiments with ELF propagation under solar particle disturbed conditions.

## 1. INTRODUCTION

The propagation of extremely low frequency (ELF) waves in the earth's ionospheric cavity is subject to nighttime amplitude attenuations of several dB (Davis 1974, 1976; Davis and Meyers, 1975; Larsen, 1974), some of which are believed to be of ionospheric origin, but the causes and effects are not understood at present. These anomalies result both from signal absorption and from changes in excitation of the waves into the propagation medium, a wave-guide formed by the earth and the lower ionosphere. The conditions of the ionosphere are subject to major day/night differences and indeed the ELF signal strengths do display diurnal variations. Calculations of ELF transmissions have shown that the signal strengths may depend in a complex manner on the ionization profiles in the waveguide. The conductivity of the earth depends on whether the propagation is over rock, sea water, ice cap, etc. The conductivity of the atmosphere depends on the deposition of ionizing particles in the atmosphere by cosmic rays, solar protons and electrons and magnetospheric electrons and x-rays from the sun (see Imhof et al., 1981).

Successful correlations between anomalous ELF signal strengths and the presence of precipitating electrons in the waveguide have been established (Imhof et al., 1976; Reagan et al., 1978). The conclusions drawn from these coordinated measurements are that the signal strengths may be either attenuated or enhanced depending upon the geometry and details of the ion and electron density profiles that result from magnetospheric electron precipitation into the ionosphere. The spatial features and the temporal/spatial/spectral fluctuations of the energetic electron precipitation are highly variable making the ionospheric modeling of this disturbance difficult.

In contrast to electron precipitation energetic proton precipitation at high latitudes during solar particle events (SPE) is more uniform, spatially extended, and more temporally stable. In this paper the efforts at modeling the ion and electron concentrations and the electrical conductivity in the ionosphere between 25 and 120 km altitude during several SPE's will be presented. The approach is to start with an ionospheric model for ambient daytime and nighttime conditions against which disturbed conditions can be compared. Based on the analysis of recent experimental data it is proposed that a new daytime ambient ionosphere profile be adopted for ELF/VLF propagation studies.

The SPE's of 12 November 1960, 4 August 1972 and 3 November 1969 have been analyzed. A combination of satellite, balloon and rocket data have been used to define the solar proton spectra incident on the atmosphere during these events. From these data ion production rate profiles in the atmosphere have been derived. In the case of the 4 August 1972 and 3 November 1969 SPE's, extensive correlative data on the in situ electron and ion densities are also available from ground-based radar and direct rocket measurements. These or relative data have enabled us to develop and test a comprehensive one-dimensional, time-dependent chemistry program that couples the complex ion and neutral reactions in a fast running computer code. The chemistry code allows us to predict the ion, electron and conductivity profiles for any diurnal and seasonal condition based on a given ion production rate profile.

The code enables us to model the diurnally varying ionospheric conditions over a long distance transpolar ELF path. The ion and electron density profiles derived in this manner have been input to electromagnetic propagation codes that predict the signal attenuation at ELF. Long propagation paths have been segmented to treat varying ground conductivity and ionospheric conditions (see Larsen et al., 1981). It must be emphasized that no transpolar ELF propagation experiments during SPE conditions have yet been conducted and experimental verification of this modeling remains to be accomplished.

## 2. AMBIENT IONOSPHERE

### 2.1 Daytime Ion and Electron Profiles

In developing our ambient model for the lower ionosphere considerable use has been made of measured electron density profiles. Several measured daytime profiles are shown in Figure 1. A profile from Knapp (1966) that has been used previously for many ELF propagation studies (Pappert and Moler, 1974; Imhof et al., 1980; Reagan et al., 1978) and another proposed by Booker (1980) for a solar zenith angle of $75^{\circ}$ are also shown in Figure 1. All of the experimental profiles are based on mid-latitude measurements made at a solar zenith angle near $\chi = 60^{\circ}$. Each of the three profiles within the range 60 to 160 km represents a concensus by the authors of a number of measurements. The E region profile of Maeda (1972) was based on winter, low solar activity conditions and differs very little from the Knapp (1966) profile. The Mechtly et al. (1972) curve is a mean of quiet sun measurements. The curve of Mitra and Chakrabarty (1971) is a concensus of measurements made by a number of different methods in the 65-90 km range. The altitude profile below 60 km is based on the work of York (1980) who has reevaluated rocket-borne probing techniques for measuring electron densities. This re-analysis has led to considerably larger electron densities below 55 km than specified by the Knapp (1966) or Booker (1980) ambient day profiles. The profile shown in Figure 1 between 40 and 70 km is based on measurements reported by York (1980) made at White Sands, New Mexico in October at a solar zenith angle near $60^{\circ}$.

Based on these recent results, we propose that the ambient electron profile shown in Figure 2 be used for comparison purposes to represent daytime conditions in future ELF propagation studies. Of course, ambient electron density profiles depend on solar zenith angle, latitude, season and solar activity and no single profile can represent all of these conditions. Figure 2 also shows a positive ion ambient profile resulting from the new electron profile. Positive ion densities were calculated using the following relations from lumped parameter ionization theory:

$$N^+ = N_e + N^-  \tag{1}$$

$$Q = \alpha_D N^+ N_e + \alpha_I N^+ N^-  \tag{2}$$

Equation (1) specifies charge neutrality while Equation (2) is the steady-state condition where Q is the ion pair production rate, $\alpha_D$ is the electron-ion recombination rate, and $\alpha_I$ is the ion neutralization rate. Equations (1) and (2) may be combined to yield

$$N^+ = \frac{\left[ N_e^2 \left( \frac{\alpha_D}{\alpha_I} - 1 \right)^2 + \frac{4Q}{\alpha_I} \right]^{1/2} - N_e \left( \frac{\alpha_D}{\alpha_I} - 1 \right)}{2}  \tag{3}$$

The value $3 \times 10^{-6}$ cm$^3$ sec$^{-1}$ was assumed for $\alpha_D$ and values of $\alpha_I$ were calculated from the following equation that includes two- and three-body interactions with neutrals.

$$\alpha_I = 5 \times 10^{-8} + 6 \times 10^{-6} PT^{-5/2} \text{ cm}^3 \text{ sec}^{-1}  \tag{4}$$

The two-body coefficient of $5 \times 10^{-8}$ cm$^3$ sec$^{-1}$ is based on the recent work of Smith and Church (1977) and the three-body coefficient is a function of altitude through the pressure P(dynes/cm$^2$) and the temperature T(degrees K) of the atmosphere. Values of $\alpha_I$ range from $5.16 \times 10^{-8}$ cm$^3$ sec$^{-1}$ at 60 km to $5.16 \times 10^{-7}$ cm sec$^{-1}$ at 20 km for an atmospheric model representing $65^{\circ}$N latitude in August. The values of ambient production rate, Q, due to galactic cosmic rays (GCR) above 18 km were calculated from the formula of Heaps (1978) for average solar conditions and a magnetic latitude of $57^{\circ}$N. The GCR production rates were augmented with Lyman alpha production rates above 70 km.

Also shown in Figure 2 are the electrical conductivities at a frequency of 75 Hz associated with the proposed daytime ambient electron and ion profiles. Free electrons, due to their much higher mobility, dominate the total conductivity down to an altitude of ~47 km in this daytime model even though their concentration is lower than the positive ions below about 70 km. Below 40 km the conductivity of the ionosphere is determined by the ions with low atomic mass (<100 amu) and high mobility even though complex cluster ions (Meyerott et al., 1980) and even multiple-cluster ions (Arnold et al., 1981) with high atomic mass (>200 amu) are present.

The horizontal lines in Figure 2 labeled $H_0$ and $H_1$ are the two crucial altitudes for ELF propagation at 75 Hz in this daytime model. These two parameters result from the approximate approach of Greifinger and Greifinger (1978) to the full wave solution for the ELF propagation constants. $H_0$ is located at 52 km in

this daytime model and represents the altitude where the displacement and conduction currents are equal, i.e., the lower boundary of the ionosphere. $H_1$ is located at 90 km and repr-sents the upper boundary of the waveguide where ultimate reflection of the ELF wave takes place. $H_1$ is the altitude at which the character of the propagation process changes from wave-like to diffusion-like. Greifinger and Greifinger (1978) have shown that ELF propagation is determined primarily by the properties of the ionosphere in the vicinity of these two well-defined altitudes where maximum ohmic dissipation takes place. It is therefore in these altitude regions that the conductivity profile must be known with some confidence if measured ELF attenuation rates and phase constants are to be compared with modeling.

When the proposed daytime profile was input to an ELF propagation code developed by the Naval Ocean Systems Center—NOSC (Sheddy, 1968; Pappert, 1970; Pappert and Moler, 1974) the signal strength was calculated to be attenuated by an additional one decibel compared to using the Knapp (1966) profile for the 6000 km path from Wisconsin to Norway. This results from the fact that the electron density in the proposed profile near the $H_0$ altitude is 100 times higher than in the previously used profile.

## 2.2 Nighttime Ion and Electron Profiles

For ambient nighttime propagation the electron and ion profiles shown in Figure 3 are proposed. The profiles are in basic agreement with the earlier model of Knapp (1966). Propagation calculations using these profiles have also been shown to be in good agreement with measured signal strengths at 75 Hz in Norway (Imhof et al., 1976). The $H_0$ and $H_1$ altitudes for a frequency of 75 Hz are also plotted in Figure 3. As a result of the lower electron density at night the effective bottom of the ionosphere, $H_0$, is raised to 72 km from the 52 km calculated for the daytime. The effective upper edge, $H_1$, is 88 km which is relatively unchanged from the daytime equivalent altitude of 90 km. The principal day/night effect on ELF waves is therefore the raising of the lower edge of the ionosphere by ~20 km at night.

## 3. SOLAR DISTURBANCE EVENTS

Solar particle events (SPE) potentially provide the most significant and persistent natural disturbance to a long distance ELF communication system. During such events which may occur 6 to 7 times per year near solar maximum and have a duration of two to ten days, energetic solar protons, alpha particles and electrons cover the entire polar cap regions rather uniformly down to ~$60^\circ$ magnetic latitude. The region irradiated covers some 17 percent of the earth's surface area. Transpolar ELF communication paths would be particularly effected. We have attempted to model the ionospheric conditions existing during several SPE's measured to date and to estimate the effects on a transpolar ELF link operating at 75 Hz.

## 3.1 Summary of Past SPE's

Figure 4 shows the ion-pair production rates in the atmosphere due to the major SPE's of solar cycle 19 and 20 as taken from Reagan et al. (1981) with the 3 November 1969 event added from Swider (1975). These production rates were generated from the "hardest" proton spectra in each event. Also shown for comparison is the production rate due to galactic cosmic rays at solar maximum and minimum. As can be readily seen, all of these SPE's greatly exceed the cosmic ray production source that is responsible for the ambient ionization in the lower atmosphere by large factors. At the daytime $H_0$ altitude of 52 km the ion production rate in the 4 August 1972 event is $10^5$ times the cosmic ray production rate. The 4 August 1972 SPE dominates in ion production rate over all of the other events in cycles 19 and 20 at altitudes above 26 km. Below 26 km the events of 12 November 1960 (1930 UT) produced a higher ionization rate than the August 1972 event. The significance of this intense ionization at the lower altitudes will be seen later. The SPE's of 4 August 1972 and 12 November 1960 would be classified as "intense" while the event of 3 November 1969 would be termed "moderate" in effects on ELF.

## 3.2 Ion and Neutral Chemistry Modeling

Extensive efforts have been made to model the ion and neutral chemistry behavior of the D-region during the SPE's of 3 November 1969 (Swider al., 1971, 1978; Gunton et al., 1977) and 4 August 1972 (Reagan and Watt, 1977; Reagan et al., 1981). In our laboratory a one-dimensional, time-dependent chemistry code has been developed that couples the complex neutral and ion reactions in a fast running computer code (Gunton et al., 1977). The code uses as input the ion-pair production rate profiles derived from satellite, balloon and rocket data. A standard CIRA atmospheric model is used and the concentrations of key minor constituents are adjusted for latitude, season and diurnal conditions. The ion-pair production rates are introduced at the local time of the SPE superimposed on the seasonal and diurnal chemistry cycle for any given geographic location. The code then follows the changes in the neutral and ion chemistry corresponding to the production rate temporal behavior for several days at that location. The code can be adjusted and run several times to simulate the initial and subsequent diurnal conditions across a long ELF communication path at the time of a SPE. A subroutine calculates the electron, ion and total conductivity as well as the $H_0$ and $H_1$ parameters using the approximate method developed by Greifinger and Greifinger (1978).

In the November 1969 SPE, extensive measurements of in situ electron and ion concentrations were made (Swider, 1975) and in the August 1972 SPE electron density profiles were measured at some 100 times during the event (Watt, 1975; Reagan and Watt, 1976; Reagan, 1977; Imhof et al., 1981). A comparison between the calculated electron density using the chemistry code during the 4 August 1972 SPE and the electron density measured with the Chatanika radar is shown in Figure 5. The agreement between the calculated and measured temporal behavior at 60 km over a several day period is quite good except in deep twilight. Figure 5 also shows the SPE-induced changes in the positive ion and atomic oxygen concentration superimposed on their normal diurnal behavior. Equally good agreement was obtained with the chemistry code during the November 1969 SPE despite the different seasonal, diurnal and ionization level conditions.

## 3.3 SPE Ion and Electron Density Profiles

Figure 6 shows the ion and electron density profiles resulting from the chemistry code modelling for a daytime case ($\lambda = 79^\circ$) near the peak of the 4 August 1972 event (1508 UT). The positive ion densities

reached $6 \times 10^5$ cm$^{-3}$ near 40 to 45 km, some 200 times higher than the ambient daytime values shown in Figure 2. The corresponding electron density at 40 km was ~1000 times higher than ambient. The conductivity at 75 Hz due to electrons exceeded that due to the ions down to an altitude of ~40 km. The bottom of the effective ionosphere to ELF waves ($H_0$) dropped to 33 km from 52 km as a result of this intense ionization at the lower altitudes. The upper end of the ionosphere ($H_1$) where total reflection is expected to occur also dropped from 90 km to 58 km according to our calculations.

The ion and electron profiles for this case were also input to a computer program at the NOSC that calculated the profile of the relative heating loss and the absorption (dB/1000km) of the 75 Hz waves (private communication, W. Moler, 1978). The relative heating loss per unit volume profile is also shown in Figure 6. The peak heating loss per unit volume comes near 36 km altitude where the ions dominate the conductivity, which is consistent with the location of the $H_0$ parameter using the Greifinger and Greifinger (1978) approach. A secondary heating peak caused by the enhanced electron conductivity is shown at 60 km, once again consistent with the $H_1$ altitude. Most of the absorption of the 75 Hz wave occurs between 30 and 40 km in this case and no additional attenuation occurs above ~65 km.

The corresponding profiles for the "moderate" SPE of 3 November 1969 (0000 UT) are shown in Figure 7. A peak ion density of $10^5$ cm$^{-3}$ was reached at 48 km. The electron conductivity exceeded the ion conductivity down to ~40 km as in the previous case. However, the absolute conductivity at this altitude was only one-tenth that in the August 1972 case. The $H_0$ and $H_1$ altitudes are at ~42 km and ~63 km, respectively.

Finally, the ion and electron density for the 12 November 1960 SPE (1930 UT) are shown in Figure 8. In this event the ion-pair production rates shown in Figure 4 were used with the effective electron and ion loss rate coefficients calculated from our chemistry modeling of the August 1972 SPE to obtain the electron and ion densities. As a result of the very "hard" proton spectra in this event, ion densities in excess of $1 \times 10^5$ cm$^{-3}$ were calculated as low as 20 km and exceeded ambient levels down to ~12 km. The calculated $H_0$ and $H_1$ altitudes are ~37 km and ~65 km, respectively.

### 3.4 ELF Signal Attenuation Results

The ion and electron density profiles shown in Figure 6, 7 and 8 were input to the NOSC propagation code to determine the effects of the SPE's on a transpolar signal at 75 Hz. The path considered was from Wisconsin in the United States to Tromso, Norway. For these calculations the transmitter was assumed to be experiencing ambient conditions. In actuality the existing experimental ELF transmitter in Wisconsin is located at an invariant latitude of 60° and therefore is at the edge of the polar cap, i.e. the geomagnetic cutoff of a SPE would be very close to the transmitter. If the transmitter were located inside the polar cap, calculations have shown that the signal strength in the overhead segment would actually be enhanced due to improved excitation coupling.

The path was segmented into eight parts as described in a companion paper in these proceedings (Larsen et al., 1981). For the November 1969 case the first five segments were assumed to be in daylight and the remainder in night. In the other two SPE's all of the segments beyond the transmitter region were assumed to be in daylight. The results shown in Table 1 were obtained.

Table 1. Calculated Signal Attenuation at 75 Hz on a Transpolar ELF Path During Solar Particle Events

| SPE Date | Time | Classification of Event | Signal Attenuation Below Ambient |
|---|---|---|---|
| 12 Nov 1960 | 1930 UT | Intense | 8.1 dB |
| 4 Aug 1972 | 1508 UT | Intense | 5.7 dB |
| 3 Nov 1969 | 0000 UT | Moderate | 1.0 dB |

From Table 1 it can be seen that weak to moderate SPE's that possess "soft" proton spectra which result in the principal ion-pair production occurring near 55 ~ 60 km will cause only nominal attenuation over ambient ELF signal strengths under daytime conditions. If the SPE occurs at nighttime the change in signal strength will be greater. Intense SPE's that possess "hard" proton spectra which result in the peak ionization occurring at altitudes below 40 km such as the 4 August 1972 and the 12 November 1960 events will cause significant attenuations of 5 to 8 dB over ambient daytime signal levels. The attenuation in these cases will be somewhat higher under nighttime conditions. The November 1960 SPE resulted in a larger signal attenuation at 75 Hz than the 4 August 1972 SPE because of the higher positive ion densities existing in the former event below 30 km.

### 3.5 Diurnal Effects

Over a long propagation path the solar zenith angle ($\chi$) will change according to the local time, as will the ionospheric conditions since the effective recombination rates for free electrons are dependent upon time of day. Thus, even during a SPE when the ionization can be assured to be constant over the whole disturbed polar cap region, the electron density profile will vary with position.

In order to estimate the magnitude of this effect, the 4 August 1972 SPE ionization profile at 1144 UT was used to calculate the electron density profiles at different solar zenith angles. For simplicity, no change was assumed to take place in the positive ion profile. The latter assumption is only truly valid at the lower altitudes. The NOSC propagation code was run for a variety of such diurnal profiles. A comparison of the extreme cases where the entire path is in daytime or nighttime reveals a difference of approximately 3 dB in the received signal strength on a transpolar path. While the approach was only an approximation, the effect appears significant and indicates that in future ELF system modeling consideration of the diurnal conditions along the path must be taken into account.

## 4.0 Conclusions

The present modeling of the ambient and SPE disturbed ionosphere has resulted in the following conclusions pertinent to ELF propagation studies.

o A new daytime ion and electron density profile for the lower ionosphere under ambient conditions is proposed that should provide closer agreement between calculated and measured signal strengths on long propagation paths.

o Using a time dependent chemistry code that couples ion and neutral chemistry the ion and electron density and the conductivity profiles in the intense SPE of 4 August 1972 and the moderate SPE of 3 November 1969 have been derived. The lumped parameter coefficients derived from these analyses have been applied to the SPE of 12 November 1960.

o During intense SPE's the conductivity of the lower ionosphere can be raised by several orders of magnitude. Below 40 km the conductivity is determined by ions with relatively low mass and high mobility even though complex ions with high atomic mass are present. Above this altitude free electrons determine the conductivity.

o The bottom of the effective ionosphere to ELF waves is shown to be lowered in an intense SPE from 52 km to ~35 km under daytime conditions as a result of the enhanced conductivity. The principal absorption of ELF waves occurs near the lower edge of this ionosphere as the result of ohmic heating losses to the dominant ion population.

o The top of the effective ionosphere where ELF reflection ultimately occurs is also lowered from near 90 km to approximately 60 km in an intense SPE. A secondary ohmic heating loss to free electrons occurs at this altitude.

o When input to an ELF propagation code the ion and electron density profiles derived for the intense SPE's produce a calculated 5 to 8 dB attenuation in the signal strength at 75 Hz on a transpolar path.

o SPE's having "hard" proton spectra that produce intense positive ion densities below 40 km have the most significant effect on ELF propagation.

o Diurnal variations in the ionospheric composition across a transpolar ELF path could result in an much as 3 dB difference in signal strength during an intense SPE.

o The ionospheric modeling attempted in this paper needs to be tested with field experiments involving transpolar ELF propagation during a large SPE. No such tests have been performed to date.

REFERENCES

Booker, H. G., 1980, "A Simplified Theory of ELF Propagation in the Earth-Ionosphere Transmission Line and Its Worldwide Application," J. Atmos. Terr. Phys., 42, pp. 929-941.

Davis, J. R., 1974, "ELF Propagation Irregularities on Northern and Mid-Latitude Paths," in ELF-VLF Radio Wave Propagation, J. Holtet, ed., D. Reidel Publ. Co., Dordrecht-Holland, pp. 263-277.

Davis, J. R., and W. O. Meyers, 1975, Naval Research Laboratory Report NRL 7924, Washington, D.C.

Davis, J. R., 1976, "Localized Nighttime D-Region Disturbances and ELF Propagation," J. Atmos. Terr. Phys., Vol. 38, p. 1309.

Greifinger, C., and P. Greifinger, 1978, "Approximate Method for Determining ELF Eigen Values in the Earth-Ionosphere Waveguide," Radio Science, 13, 831.

Gunton, R. C., R. E. Meyerott, and J. B. Reagan, 1977, "Ion and Neutral Chemistry of the D-Region During the Intense Solar Particle Event of August 1972," Final Report, LMSC-D556351, Lockheed Palo Alto Research Laboratory, Palo Alto, California 94304.

Heaps, M. G., 1978, "Parametrization of the Cosmic Ray Ion-Pair Production Rate Above 18 km," Planet. Space Sci., 26, 573.

Imhof, W. L., T. R. Larsen, J. B. Reagan, and E. E. Gaines, 1976, "Analyses of Satellite Data on Precipitating Particles in Coordination with ELF Propagation Anomalies," Lockheed Palo Alto Research Laboratory Report, LMSC-D502063, Palo Alto, California 94304.

Imhof, W. L., R. C. Gunton, T. R Larsen, E. E. Gaines, J. B. Reagan, and R. E. Meyerott, 1980, "Study of ELF Propagation Anomalies as Related to Improved Knowledge of Electron Density Profile Produced by Energetic Particle Precipitation," Lockheed Palo Alto Research Laboratory Report LMSC-D681778, Palo Alto, California 94304.

Imhof, W. L., R. C. Gunton, J. B. Reagan, R. E. Meyerott, E. E. Gaines, and T. R. Larsen, 1981, "The Influence of Precipitating Energetic Particles on the Propagation Medium," Paper I-4 in the Proceedings of AGARD Symposium on Medium, Long and Very Long Wave Propagation (at Frequencies Less Than 3000 KHz), Brussels, Belgium.

Knapp, W., 1966, General Electric-TEMPO Report RPT 66TMP-83.

Larsen, T. R., 1974, "Preliminary Discussion of ELF/VLF Propagation Data," in ELF-VLF Radio Wave Propagation, J. Holtet, ed., D. Reidel Publ. Co., Dordrecht-Holland, pp. 263-277.

Larsen, T. R., W. L. Imhof, R. C. Gunton, J. B. Reagan, E. E. Gaines, and R. E. Meyerott, 1981, "ELF Propagation in Polar Areas, Measurements and Theoretical Field Strength Predictions," Paper II-12 in the Proceedings of the AGARD Symposium on Medium, Long, and Very Long Wave Propagation (at Frequencies Less Than 3000 KHz), Brussels, Belgium.

Maeda, K., 1972, "E-Region Electron Density Profiles," Space Research, 12, 1229.

Mechtly, E. A., S. A. Bowhill, and L. G. Smith, 1972, "Change of Lower Ionosphere Electron Concentrations with Solar Activity," J. Atmos. Terr. Phys., 34, p. 1899.

Mitra, A. P., and D. K. Chakrabarty, 1971, "Models of Lower Ionosphere Electron Density Profiles," Space Research, 11, 1013.

Pappert, R. A., 1970, "Effects of Elevation and Ground Conductivity on Horizontal Dipole Excitation of the Earth-Ionosphere Waveguide," Radio Science, 5, pp. 579-590.

Pappert, R. A., and W. F. Moler, 1974, "Propagation Theory and Calculations at Lower (ELF) Extremely Low Frequencies," IEEE Trans. Comm., COM-22, 4, 438-451.

Reagan, J. B., and T. M. Watt, 1976, "Simultaneous Satellite and Radar Studies of the D-Region Ionosphere During the Intense Solar Particle Events of August 1972," J. Geophys. Res., 81, 4579.

Reagan, J. B., W. L. Imhof, E. E. Gaines, T. R. Larsen, J. R. Davis, and W. R. Moler, 1978, "Effects of Precipitating Energetic Particles on an ELF Communication Link," in the Proceedings of the Symposium on the Effect of the Ionosphere on Space and Terrestrial Systems, J. M. Goodman, ed., Naval Research Laboratory, Washington, D.C.

Reagan, J. B., R. E. Meyerott, R. W. Nightingale, R. C. Gunton, R. G. Johnson, J. E. Evans, W. L. Imhof, D. F. Heath, and A. J. Krueger, 1981, "Effects of the August 1972 Solar Particle Events on Stratospheric Ozone," J. Geophys. Res., 86, 1473.

Sheddy, C. H., 1968, "A General Analytic Solution for Reflection From a Sharply Bounded Anisotropic Ionosphere," Radio Science, 3, pp. 792-795.

Smith, D., and M. J. Church, 1977, "Ion-Ion Recombination Rates in the Earth's Atmosphere," Planet. Space Sci., 25, 433.

Swider, W., R. S. Narcisi, T. J. Keneshea, and J. C. Ulwick, 1971, "Electron Loss During a Nighttime PCA Event," J. Geophys. Res., 76, 4691.

Swider, W., 1975, "Composite PCA '69 Study," Final Report AFCRL-TR-75-0149, Air Force Cambridge Research Laboratory, Bedford, Massachusetts.

Swider, W., T. J. Keneshea, and C. I. Foley, 1978, "An SPE-Disturbed D-Region Model," Planet. Space Sci., 26, 883.

Watt, T. M., 1975, "Effective Recombination Coefficient of the Polar D-Region Under Conditions of Intense Ionizing Radiation," DNA Report 3663T, Stanford Research Institute, Menlo Park, California.

York T. M., 1980, "Comparison of Electron Densities in the Middle Atmosphere Indicated by Rocket Borne Probing Techniques," Report PSU-IRL-IR-69, Ionosphere Research Laboratory, Pennsylvania State University, University Park, Pennsylvania.
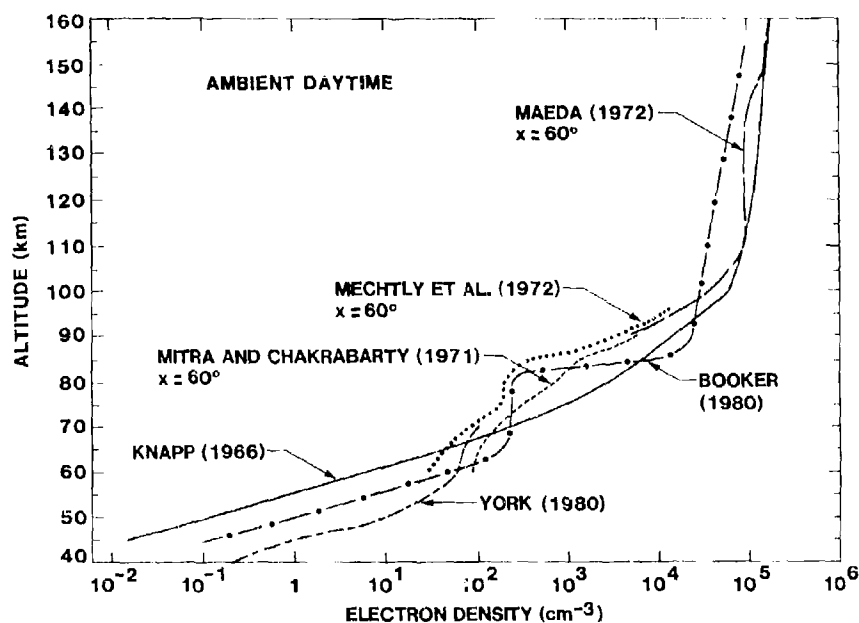
Figure 1. Altitude profiles of some recent daytime measurements of electron density compared with ambient daytime profiles used in previous ELF propagation studies.
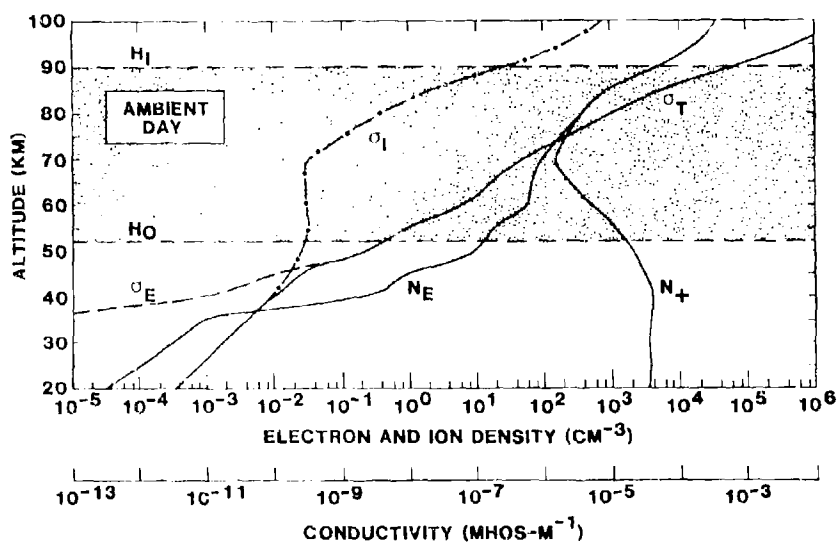


Figure 2. Proposed ambient daytime ion ($N^+$) and electron ($N_E$) density profiles and the corresponding conductivity profiles ($\sigma_I$, $\sigma_E$, and $\sigma_{Total}$). The bottom and top of the effective ionosphere to 75 Hz waves are shown as $H_0$ and $H_1$, respectively.
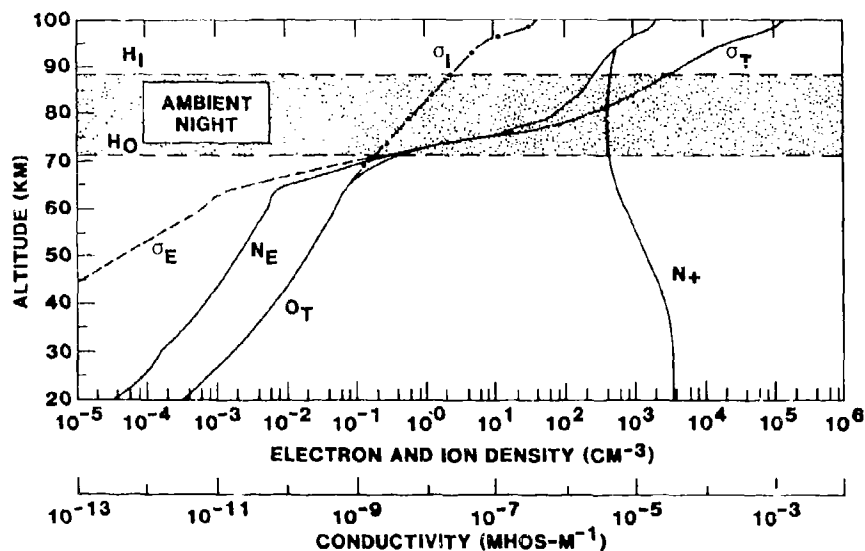
Figure 3. Altitude profiles of electron and positive ion densities ($N_E$, $N^+$) in cm$^{-3}$, electron, ion, and total conductivities ($\sigma_E$, $\sigma_I$, $\sigma_{Total}$) at 75 Hz for an ambient night. The bottom and top of the effective ionosphere to ELF waves at night are shown as $H_0$ and $H_1$, respectively.
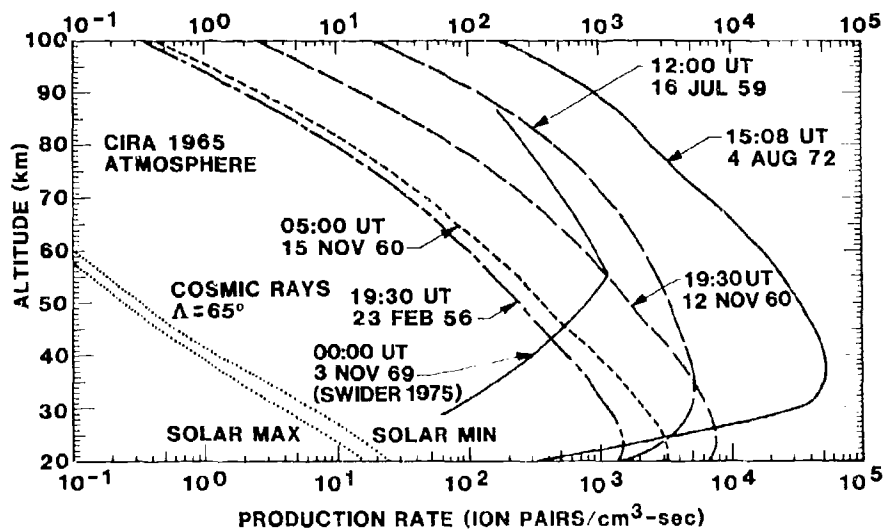


Figure 4. Solar proton induced ion production rates during the major solar particle events in solar cycles 19 and 20 from Reagan et al. (1981) with the 3 November 1969 curve added from Swider (1975). The cosmic ray ionization for solar maximum and minimum is shown for comparison. The 4 August 1972 SPE dominates in ion production rate over all of the other events in cycles 19 and 20 at altitudes above 26 km.
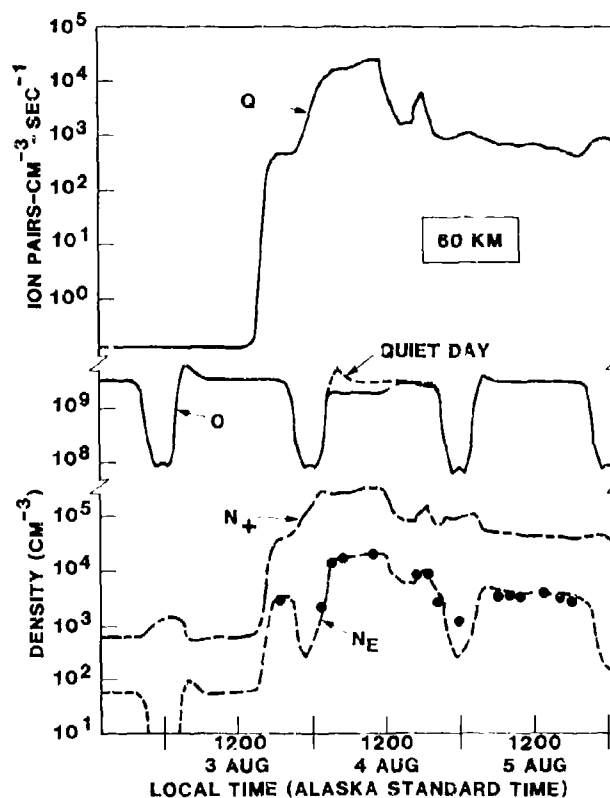
Figure 5. Experimental ion pair production rate and calculated electron density, positive ion density, O atom density vs. time at 60 km altitude during the SPE of August 1972. The dots are the experimental electron density data from Chatanika radar measurements for comparison with the chemistry code derived electron densities.
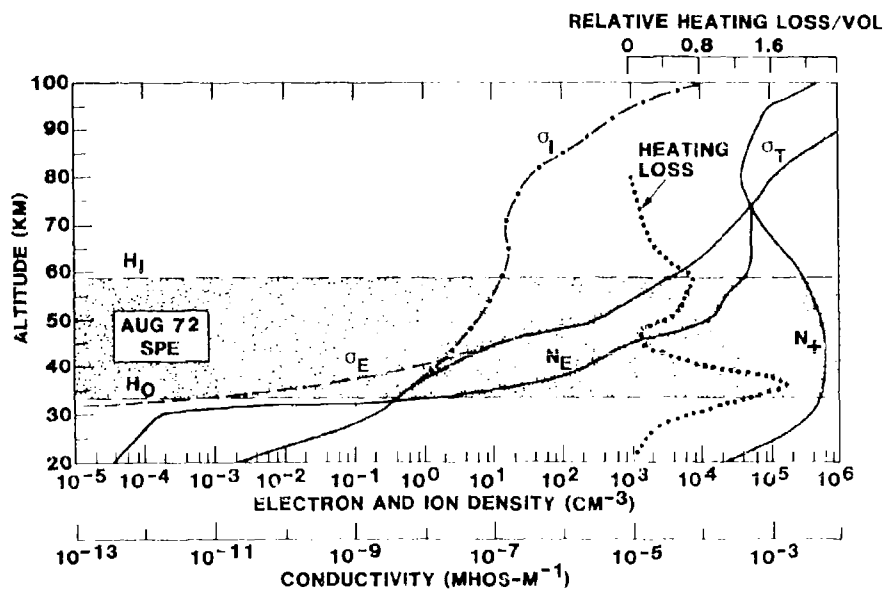


Figure 6. The calculated profiles of the electron and positive ion densities ($H_E$, $N^+$) and the electron, ion, and total conductivities ($\sigma_E$, $\sigma_I$, $\sigma_T$) near the peak time (1508 UT) of the 4 August 1972 SPE. The bottom and top of the effective ionosphere to 75 Hz waves are shown as $H_I$ and $H_0$, respectively. Also shown as heavy dots is the relative heating loss per unit volume profile.
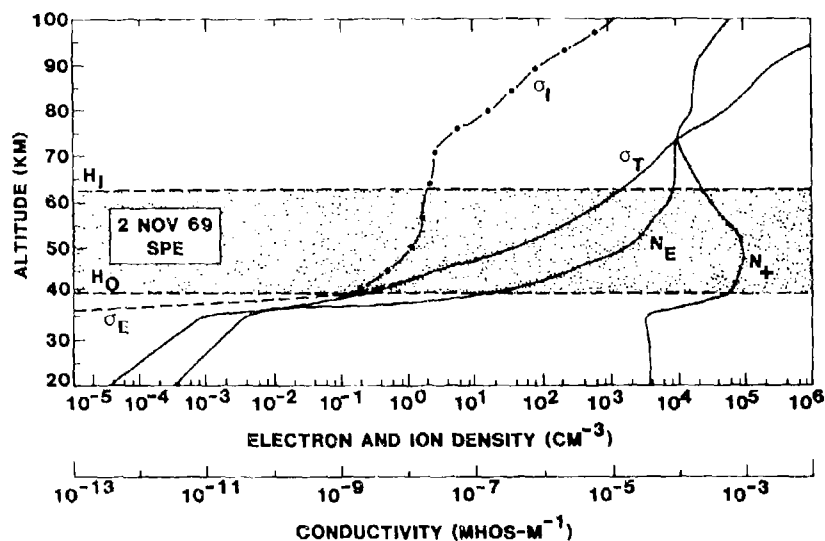
Figure 7. The calculated profiles of the electron and positive ion densities ($N_E$, $N^+$) and the electron, ion, and total conductivites ($\sigma_E$, $\sigma_I$, $\sigma_T$) at 0000 UT on 3 November 1969 during a SPE. The bottom and top of the effective ionosphere to 75 Hz waves is shown as $H_0$ and $H_1$, respectively.
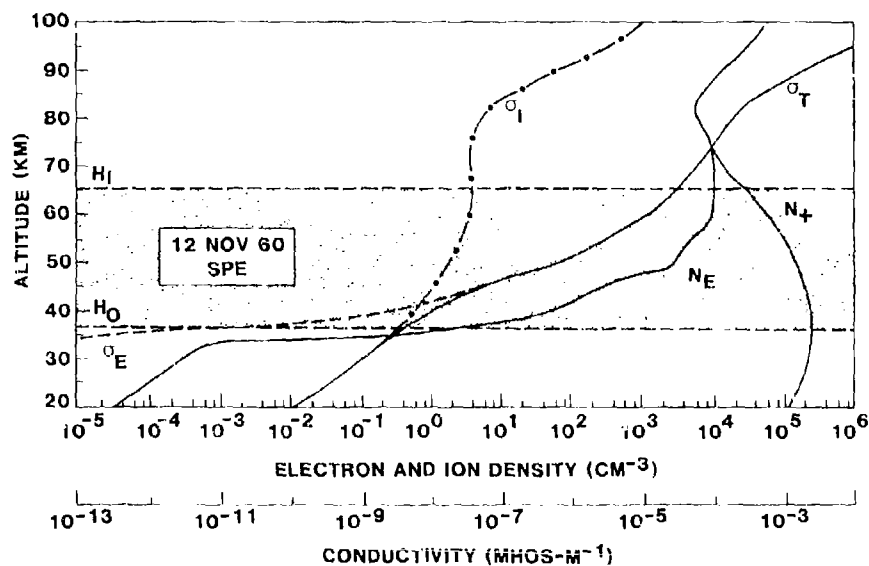


Figure 8. The calculated profiles of the electron and positive ion densities ($N_E$, $N^+$) and the electron, ion, and total conductivities ($\sigma_E$, $\sigma_I$, $\sigma_T$) at 75 Hz at 1930 UT on 12 November 1960 during a SPE. The bottom and top of the effective ionosphere to 75 Hz waves are shown as $H_0$ and $H_1$, respectively.

# MODELS OF THE MIDLATITUDE D REGION AT NOON

W. C. Bain
SERC, Rutherford and Appleton Laboratories
Chilton, Didcot, Oxon. OX11 0QX, UK

## SUMMARY

Bain and Harrison have previously given a model for the electron-density distribution in the D region of the ionosphere for summer noon at sunspot maximum. Here two further models are derived in a similar way, for equinox noon and for winter noon. Propagation results are calculated from these models for various frequencies in the range 16-85 kHz and for certain distances below 1000 km, and are compared with measurements made over the same frequency/distance combinations. Satisfactory agreement is obtained. Some difficulties in dealing with winter conditions are pointed out, including those associated with the 'winter anomaly in absorption'.

A number of models prepared by other workers are considered and propagation results are calculated from them for comparison with observed data. The models examined are by Deeks, Jones and Spracklen, Bremer and Singer, Azarnin and Orlov, and McNamara. The models of McNamara are treated in some detail and are shown to be unsuitable for calculations of propagation over the frequency and distance ranges dealt with here. The other models are considerably better but all show some disagreement with the measurements cited.

## 1. INTRODUCTION

To enable one to carry out calculations of VLF or LF propagation for path lengths less than 1000 km, the CCIR (1978) have provided a set of curves of reflection coefficient. These curves were drawn to fit as closely as possible the rather limited observed data, and their use relies on the assumption that the reflection coefficient is the same if the parameter $f \cos i$ is the same ($f$ is frequency and $i$ is the angle of incidence). No account is taken of any azimuth dependence. Calculations made from these curves must be subject to appreciable errors, and it may well be that better propagation results could be obtained by making full-wave calculations from model ionospheres consisting of a height distribution of electron density. If this approach is to be successful satisfactory model ionospheres are required, and the noon models set out in this paper are intended for this purpose.

A previous paper by Bain and Harrison (1972) gave a model for the D region of the ionosphere at midlatitudes at summer noon during sunspot maximum. The agreement between propagation results observed and calculated from this model was very satisfactory. It was particularly good in the case of the Hollingworth pattern at 16 kHz, which is quite sensitive to changes in electron density below 75 km. The model was actually derived by starting from a rocket measurement of the distribution of electron concentration taken at the same time as the Hollingworth pattern. The combined Faraday and differential Doppler techniques used in the rocket are believed to be the most accurate method for determining electron density in the height range 70-90 km (THRANE, 1973). The rocket profile only contained values for heights above about 70 km, so it was extended arbitrarily down to 50 km. Propagation calculations were then made from this profile for frequencies from 16 to 100 kHz and it was modified until a reasonable fit was obtained with observations. Only very small changes were made to the profile above 70 km because of the reliability of the rocket results, but the values below that height were modified without inhibition. The final profile is shown in Fig. 1. The propagation data used in constructing the model were for paths less than 1000 km, and it might therefore be expected to give its best results for such distances, but Jones (1981) has found that it gives good results for atmospherics propagated over large distances at frequencies below 1 kHz.

In the propagation calculations mentioned above a collision-frequency profile must be specified, and as in Bain and Harrison (1972) the following relation between monoenergetic collision frequency ($\nu_M$) and atmospheric pressure p was used.

$$\nu_M = 7.5 \times 10^5 \, p \quad \text{(SI units)}$$

p was obtained from a reference atmosphere (CIRA, 1972) for a latitude of 52.5°N.

It is clearly desirable to be able to calculate propagation data at all times of the year, so models for equinox and winter noon are presented here; this is in accordance with a CCIR request (CCIR, 1978). The models cannot be expected to give as accurate results for a particular time as will the summer model since the variability of signal strength increases as summer changes to winter; calculations from them should only be taken as giving median propagation data. Bain and Harrison (1972) stated that the results applied to sunspot maximum conditions and here too propagation results only for these conditions are used. However, sunspot-cycle variations in VLF propagation are often not very great, and in the absence of sunspot-minimum models it is probably worth while to use the models presented here at all times in the sunspot cycle.

## 2. THE EQUINOX MODEL

The equinox model was derived in a similar way to the summer model. However resources did not permit the simultaneous measurement of a Hollingworth pattern and a rocket profile of electron density, as was done previously. Instead, all rocket profiles taken under the appropriate conditions were plotted and an average curve drawn through them. Because such results are not reliable below about 70 km the average profile was extended arbitrarily below this height. This profile was used as a starting point and modified until it gave reasonable propagation results at frequencies from 16 to 100 kHz; it is shown in Fig. 1. The calculated results are compared in Table 1 with observed data, which are all rather old and appear in papers by Straker (1955), Bracewell et al. (1951, 1954), Weekes and Stuart (1952a,b) and Williams (1951).

The results from this model are quite satisfactory; they certainly represent a better fit to the observations than do the calculations from any of the measured profiles cited by Bain (1974). The model is plotted along with all comparable rocket profiles in Fig. 2 and can be seen to lie within their bounds above 70 km. The results of calculations from some of these profiles appear in Bain (1974), but not from all of them since they do not all cover a sufficient range of electron concentration. As a rough guide to the acceptability of the model calculations in this and subsequent tables, the observed conversion coefficients and phases at 16 kHz are probably accurate to about 20% and 30° respectively. At higher frequencies the accuracy will be less, say 50% and 60°.

TABLE 1    Observed and calculated VLF and LF propagation data for equinox

| Freq. (kHz) | Angle of inc. (deg) | Magnetic azimuth (deg) | Parameter observed or calculated | Observed value | Calculated from model |
|---|---|---|---|---|---|
| 16.0 | 32 | 111 | $_{,,}R_{\perp}$ | .20 | .15 |
| 16.0 | " | " | $_{,,}R_{,,}$ | .20 | .21 |
| 16.0 | " | " | pol. phase | 90° | 104° |
| 16.0 | " | " | phase of $_{,,}R_{\perp}$ rel to GW | 300° | 291° |
| 31.15 | 20 | 1 | $_{,,}R_{\perp}$ | .04 | .030 |
| 31.15 | " | " | pol. phase | 90° | 66° |
| 43.2 | 39 | 80 | $_{,,}R_{\perp}$ | .005 | .0081 |
| 43.2 | " | " | pol. phase | 47° | 29° |
| 70.8 | 34 | 100 | $_{,,}R_{\perp}$ | .007 | .0052 |
| 70.8 | " | " | pol. phase | 90° | 141° |
| 85.0 | 76 | 240 | $_{,,}R_{,,}$ | .05 | .047 |

## 3.    THE WINTER MODEL

The winter model was derived in a similar way to the equinox model and is also shown in Fig. 1. There were however additional complications in the derivation, the main one being the presence or absence of the 'winter anomaly in absorption'. The propagation measurements used were made in England, where typical winter conditions mean that a moderate winter anomaly would exist. Rocket profiles have therefore been left out of account if they were taken at times of weak or intense winter anomaly. This may not matter greatly, as the winter anomaly affects profiles principally above 80 km except in very intense anomalies, and propagation at frequencies below 100 kHz is not greatly affected by changes at these levels during the day. Another difficulty arises because VLF propagation is much influenced by the parameter $\ell n \sec \chi$, where $\chi$ is the zenith angle of the sun. The winter noon observations of propagation were made when this angle was near to 75°, and $\ell n \sec \chi$ changes rapidly with $\chi$ around this value. It was found that to obtain an appreciable number of rocket profiles for use in the modelling procedure a rather greater range of values of $\ell n \sec \chi$ had to be permitted than might be desirable.

The comparison of observed and calculated results is given in Table 2; the references to the observed results are as in Section 2 except that data from Williams (1951) were not used.

Again the results from the model are satisfactory and agree with observations better than those from any of the measured profiles cited by Bain (1974). Figure 3 shows the model plotted with a number of comparable rocket profiles; it can be seen to lie within their bounds above 73 km. This height is greater than at equinox because the lower electron densities below 75 km result in the rocket results becoming unreliable at a greater height than at equinox. Propagation calculations for some of the profiles are given by Bain (1974).

## 4.    OTHER MODELS

Models of the D region have been produced by various other workers, such as Deeks (1966), Jones and Spracklen (1976), Bremer and Singer (1977), Azarnin and Orlov (1976), and McNamara (1979). Their summer models are shown in Fig. 4. The models of McNamara and the propagation results they give are considered first, since these models are now frequently cited. They were not of course constructed primarily to give radio propagation results and McNamara himself pointed out their limited usefulness in such calculations for reflection heights in the 80-90 km range. Table 3 indicates that they are also not very satisfactory for calculations in which the reflection height is below 80 km as it is in nearly all cases here; note that the values of angle of incidence and of magnetic azimuth are nearly the same as for the corresponding case in Table 1.

Most of the calculated values are considerably in error although the reflection heights at 16 kHz in summer and equinox are good, as is shown by the phase values. One or two of the calculated conversion coefficients at the higher frequencies are also acceptable. It must be concluded, however, that the models of McNamara (1979) are not suitable for use in calculations of VLF and LF propagation.

The models produced by the other workers mentioned above give much better propagation results. A

TABLE 2   Observed and calculated VLF and LF propagation data for winter

| Freq. (kHz) | Angle of inc. (deg) | Magnetic azimuth (deg) | Parameter observed or calculated | Observed value | Calculated from model |
|---|---|---|---|---|---|
| 16.0 | 31 | 111 | $_{,,}R_\perp$ | .27 | .22 |
| 16.0 | " | " | $_{,,}R_{,,}$ | .27 | .37 |
| 16.0 | " | " | pol. phase | $90^{\circ}$ | $117^{\circ}$ |
| 16.0 | " | " | phase of $_{,,}R_\perp$ rel to GW | $240^{\circ}$ | $216^{\circ}$ |
| 31.15 | 20 | 1 | $_{,,}R_\perp$ | .17 | .14 |
| 31.15 | " | " | pol. phase | $90^{\circ}$ | $93^{\circ}$ |
| 43.2 | 39 | 80 | $_{,,}R_\perp$ | .19 | .15 |
| 43.2 | " | " | pol. phase | $47^{\circ}$ | $104^{\circ}$ |
| 70.8 | 34 | 100 | $_{,,}R_\perp$ | .06 | .074 |
| 70.8 | " | " | pol. phase | $90^{\circ}$ | $129^{\circ}$ |
| 85.0 | 76 | 180 | $_{,,}R_{,,}$ | .10 | .091 |

TABLE 3   Comparison of observed data with calculations from the models of McNamara

| Freq. (kHz) | Parameter | Summer | | Equinox | | Winter | |
|---|---|---|---|---|---|---|---|
| | | Obs. | Cal. | Obs. | Cal. | Obs. | Cal. |
| 16.0 | $_{,,}R_\perp$ | .12 | .044 | .20 | .056 | .27 | .136 |
| 16.0 | phase of $_{,,}R_\perp$ rel to GW | $360^{\circ}$ | $370^{\circ}$ | $300^{\circ}$ | $287^{\circ}$ | $240^{\circ}$ | $160^{\circ}$ |
| 31.15 | $_{,,}R_\perp$ | .005 | .0078 | .04 | .0097 | .17 | .030 |
| 43.2 | $_{,,}R_\perp$ | < .003 | .0032 | .005 | .0018 | .19 | .034 |
| 70.8 | $_{,,}R_\perp$ | .002 | .00008 | .007 | .0019 | .06 | .022 |

TABLE 4   Comparison of observed data with calculations from various models

| Freq. (kHz) | Parameter | Season | Observed value | Calculated from model of | | |
|---|---|---|---|---|---|---|
| | | | | Jones and Spracklen | Bi... and Singer | Azaroin and Orlov |
| 16.0 | $_{,,}R_\perp$ | Summer | .12 | .080 | .092 | .089 |
| 16.0 | phase of $_{,,}R_\perp$ rel to GW | " | $360^{\circ}$ | $251^{\circ}$ | $288^{\circ}$ | $307^{\circ}$ |
| 31.15 | $_{,,}R_\perp$ | " | .005 | .0119 | .0123 | .0016 |
| 43.2 | $_{,,}R_\perp$ | " | < .003 | .0017 | .0031 | .0041 |
| 70.8 | $_{,,}R_\perp$ | " | .002 | .0016 | .0021 | .0074 |
| 16.0 | $_{,,}R_\perp$ | Winter | .27 | .208 | – | .184 |
| 16.0 | phase of $_{,,}R_\perp$ rel to GW | " | $240^{\circ}$ | $45^{\circ}$ | – | $245^{\circ}$ |
| 31.15 | $_{,,}R_\perp$ | " | .17 | .081 | – | .125 |
| 43.2 | $_{,,}R_\perp$ | " | .19 | .037 | – | .125 |
| 70.8 | $_{,,}R_\perp$ | " | .06 | .050 | – | .062 |

selection of these, for summer and winter conditions, are given in Table 4.

The models of Jones and Spracklen (1976) are extensions of those of Deeks (1966) and these can be treated together. Their summer model can be seen to give good values for conversion coefficient but the results are not so good in the winter. In both cases the reflection height at 16 kHz is too high, by at least 3 km; the summer result might be expected from the position of the curves relative to the Bain and Harrison model near 70 km in Fig. 4. Bremer and Singer (1977) have a sunspot maximum model only for summer; the conversion coefficients are quite good but the reflection height at 16 kHz is again too high. Azarnin and Orlov (1976) have summer and winter models suitable for comparison with observed data; their summer model does not give good results for the coefficients or the reflection height but their winter model is rather better in these respects.

5.      CONCLUSION

Models for the D region have been produced for equinox and winter noon which give satisfactory results for propagation at frequencies below 100 kHz, although all tests here are for distances less than 1000 km. None of the models produced elsewhere can match these results, though they may of course be better in other respects, e.g. at higher frequencies.

6.      REFERENCES

AZARNIN, G. V. and ORLOV, A. B., 1976, "Model of the lower daytime ionosphere for computing VLF fields", Geomagn. and Aeron. 14, 266-270.

BAIN, W. C. and HARRISON, M. D., 1972, "Model ionosphere for D region at summer noon during sunspot maximum", Proc. IEE, 119, 790-796.

BAIN, W. C., 1974, "Use of LF and VLF propagation data in studies of electron density profiles at mid-latitudes", Indian J. Radio and Space Physics, 3, 113-118.

BELROSE, J. S., ROSS, D. B. and McNAMARA, A. G., 1972, "Ionization changes in the lower ionosphere during the solar eclipse of 7 March 1970", J. Atmos. Terr. Phys., 34, 627-640.

BEYNON, W. J. G. and WILLIAMS, E. R., 1976, "Rocket measurements of D region electron density profiles", J. Atmos. Terr. Phys., 38, 1319-1325.

BRACEWELL, R. N., BUDDEN, K. G., RATCLIFFE, J. A., STRAKER, T. W. and WEEKES, K., 1951, "The ionospheric propagation of low and very-low frequency radio waves over distances less than 1000 km", Proc. IEE, 98, Pt. III, 221-236.

BRACEWELL, R. N., HARWOOD, J. and STRAKER, T. W., 1954, "The ionospheric propagation of radio waves of frequency 30-45 kc/s over short distances", Proc. IEE, 101, Pt. IV, 154-162.

BREMER, J. and SINGER, W., 1977, "Diurnal, seasonal and solar-cycle variations of electron densities in the ionospheric D- and E-regions", J. Atmos. Terr. Phys., 39, 25-34.

CCIR, 1978, "Recommendations and Reports", Pt. VI, 216-239 (Report 265-4).

CIRA, 1972, "COSPAR International Reference Atmosphere", Akademie-Verlag, Berlin.

DEEKS, D. G., 1966, "D-region electron distributions in middle latitudes deduced from the reflection of long radio waves", Proc. R. Soc. A291, 413-437.

DICKINSON, P. H. G., HALL, J. E. and BENNETT, F. D. G., 1976, "Rocket measurement of electron concentration in the lower ionosphere at two European locations", J. Atmos. Terr. Phys., 38, 163-173.

JONES, D. L., 1981, Private communication.

JONES, T. B. and SPRACKLEN, C. T., 1976, "Polarisation of VLF radiowaves reflected from the ionosphere", Proc. IEE, 123, 11-122.

McNAMARA, L. F., 1979, "Statistical model of the D region", Radio Sci., 14, 1165-1173.

MECHTLY, E. A., SECHRIST, C. F. and SMITH, L. G., 1972a, "Electron loss coefficients for the D region of the ionosphere from rocket measurements", J. Atmos. Terr. Phys. 34, 641-646.

MECHTLY, E. A., BOWHILL, S. A. and SMITH, L. G., 1972b, "Changes of lower ionosphere electron concentration with solar activity", J. Atmos. Terr. Phys., 34, 1899-1907.

SECHRIST, C. F., MECHTLY, E. A. and SHIRKE, J. S., 1969, "Co-ordinated rocket measurements on the D region winter anomaly", J. Atmos. Terr. Phys., 31, 145-153.

STRAKER, T. W., 1955, "The ionospheric propagation of radio waves of frequency 16 kc/s over short distances", Proc. IEE, 102C, 122-133.

THRANE, E. V., 1973, in "Methods of measurement and results of lower ionosphere structure", Akademie-Verlag, Berlin, 5-21.

WEEKES, K. and STUART, R. D., 1952a, "The ionospheric propagation of radio waves with frequencies near 100 kc/s over short distances", Proc. IEE, 99, Pt. IV, 29-37.

WEEKES, K. and STUART, R. D., 1952b, "The ionospheric propagation of radio waves with frequencies near 100 kc/s over distances up to 1000 km", Proc. IEE, 99, Pt. IV, 38-46.

WIDDEL, H. V., ROSE, G., SPENNER, K., FRIEDRICH, M. and TORKAR, K. M., 1979, "Electron densities during winter anomalous absorption of different intensity", J. Atmos. Terr. Phys., 41, 1105-1119.

WILLIAMS, C., 1951, "Low-frequency radio-wave propagation by the ionosphere, with particular reference to long-distance navigation", Proc. IEE, 98, Pt. III, 81-99.
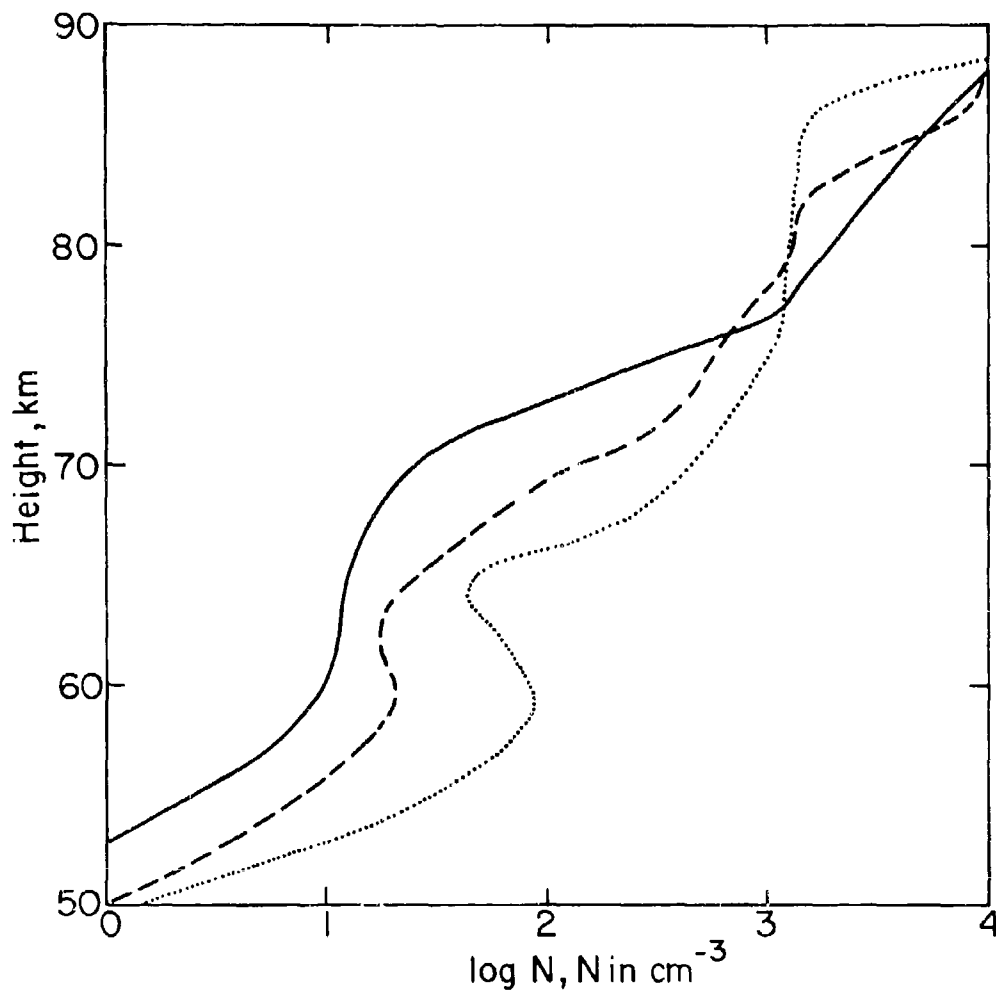
1. Models of the electron-density distribution at noon for

     winter ————————

     equinox – – – – – – –

     summer · · · · · · ·
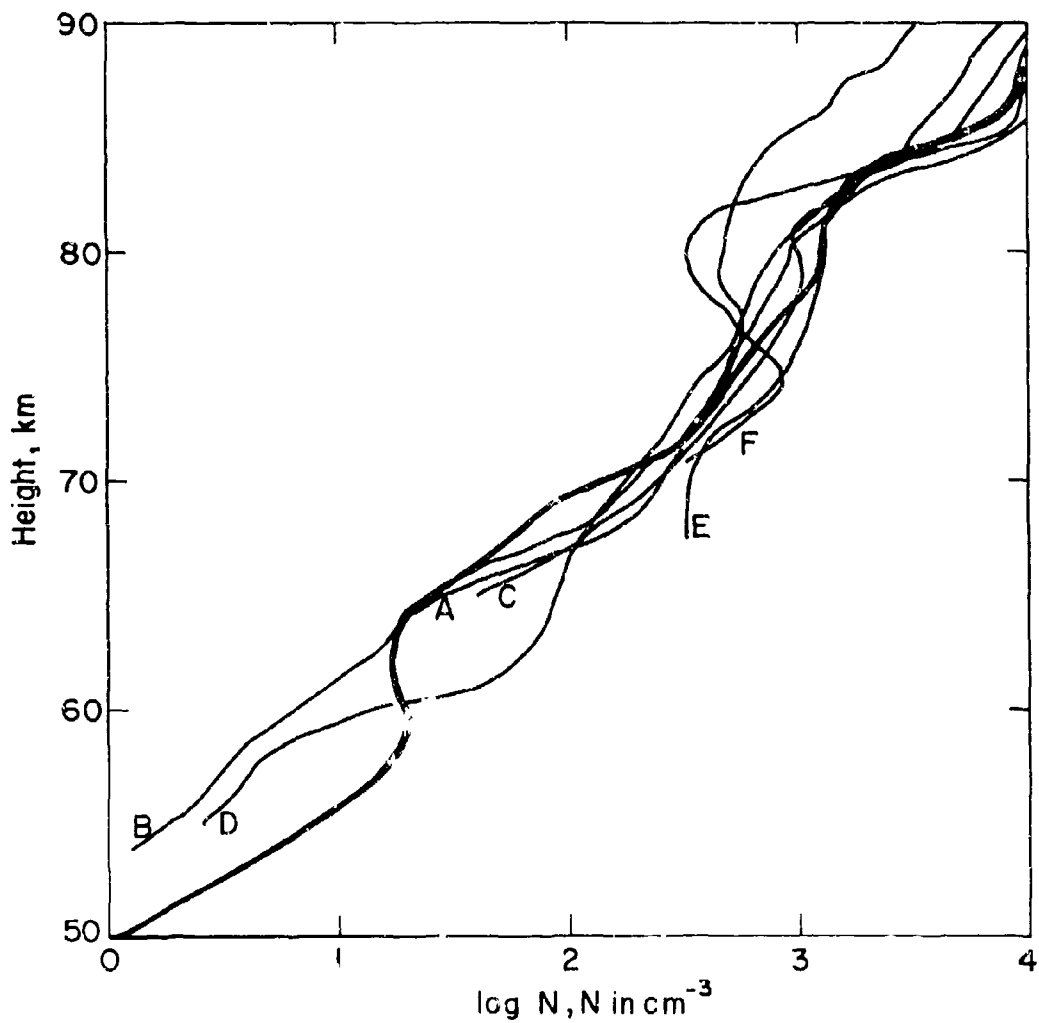
2.    Equinox noon distribution of electron density

Thick curve : model

A : Belrose et al (1972), E Quoddy, 7 Mar 1970.

B : Mechtly et al (1972a), Wallops I, 7 Mar 1970.

C : Mechtly et al (1972b), Wallops I, 17 Apr 1969.

D : Mechtly et al (1972b), Wallops I, 10 Sep 1969.

E : Dickinson et al (1976), S Uist, 29 Aug 1972.

F : Beynon and Williams (1976), S Uist, 18 Sep 1970.
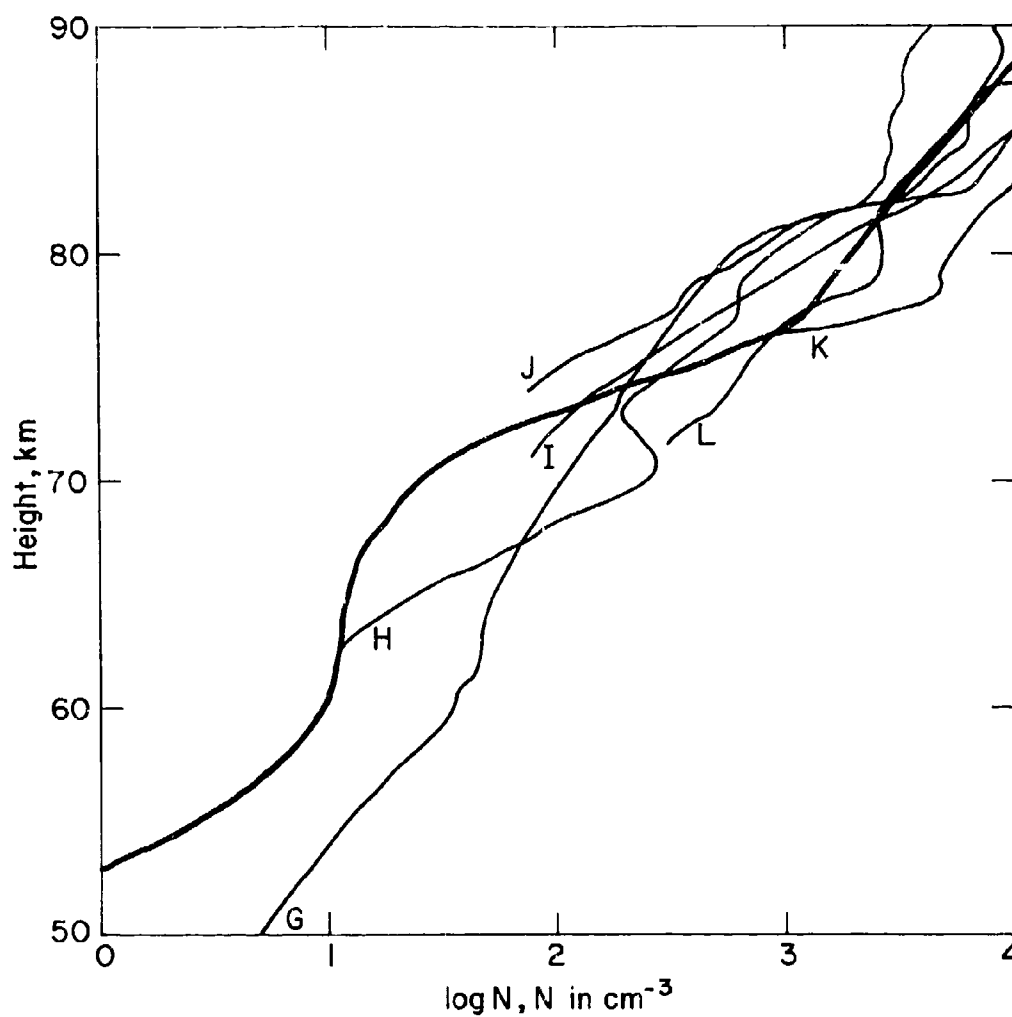
3.   Winter noon distributions of electron density

Thick curve : model

G : Sechrist et al (1969), Wallops J, 10 Jan 1966.

H : Sechrist et al (1969), Wallops T, 31 Jan 1967.

I : Beynon and Williams (1976), S Uist, 5 Dec 1968.

J : Dickinson et al (1976), S Uist, 5 Dec 1968.

K : Dickinson et al (1976), S Uist, 3 Dec 1971.

L : Widdel et al (1979), Arenosillo, 4 Jan 1976.

D REGION MODELS, SUMMER
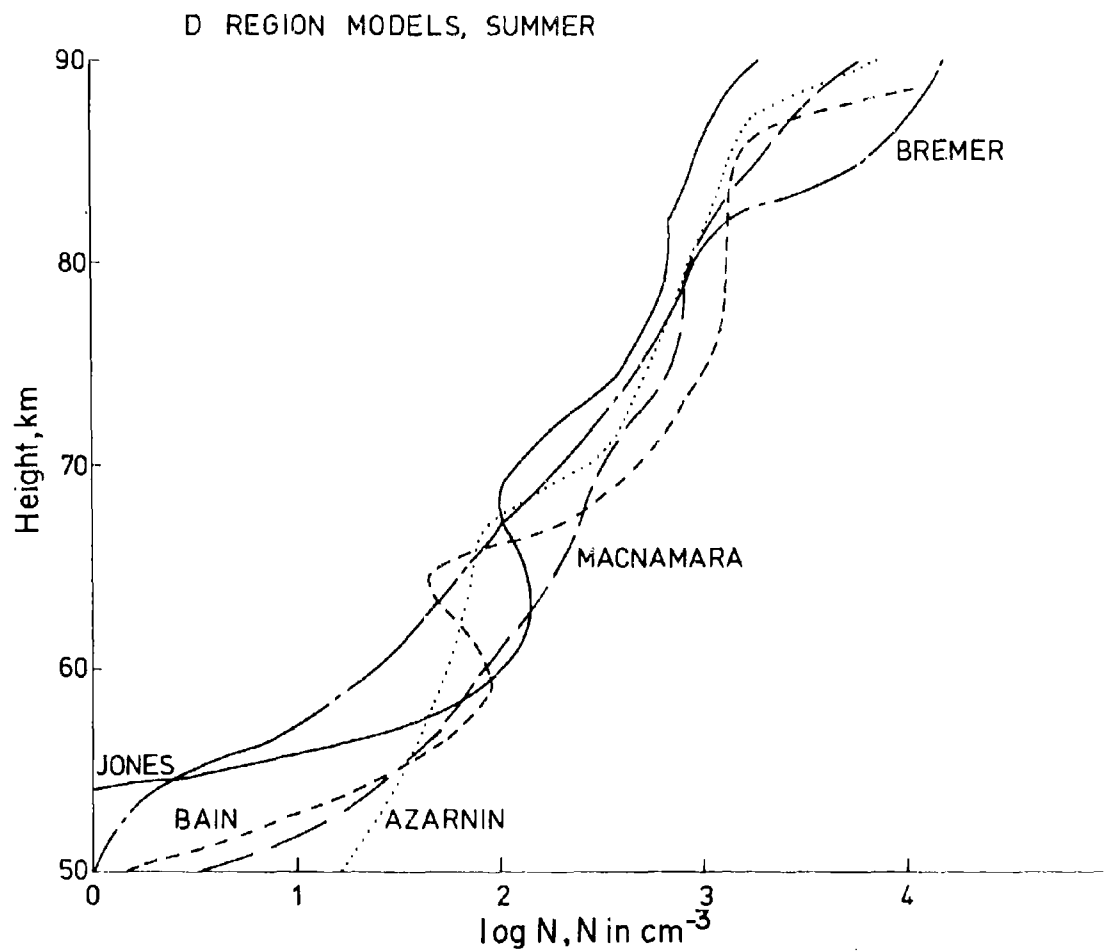


4. Summer noon models of electron density from Azarnin and Orlov (1976), Bremer and Singer (1977), Jones and Spracklen (1976) and Macnamara (1979). Also shown for comparison is the model from Bain and Harrison (1972), which appears in Fig 1 as well.

DISCUSSION EPP FALL 81 MEETING
MEDIUM, LONG, AND VERY LONG WAVE PROPAGATION
(AT FREQUENCIES LESS THAN 3000 KHZ)

SESSION 6

PAPER : 32. NUMERICAL MODELING OF THE PROPAGATION MEDIUM AT
LF/VLF/LF
AUTHOR :   D. G. Morfitt
QUESTIONER :   T. B. Jones
QUESTION : 1. The "average models" of the D-Region electron density profiles  are  very  useful
for  general  system  planning.  However  the  day  to day variability limits the usefulness of
"average" profiles for determining the propagation conditions on any  specific  day.  Have  you
considered  any  form  of  real  time  sensing  (sounding)  to adjust the "average" profiles to
conditions which exist on a particular day?
        2.  Small  changes  in  the  night time profile move the field strength minima with
respect to transmitters. This great sensitivity of the minima to the profile is a major problem
in  obtaining  a useful model for any given set of experimental night time field-strength range
results.

SESSION 6

PAPER : 32. NUMERICAL MODELING OF THE PROPAGATION MEDIUM AT ELF/VLF/LF
AUTHOR :   D. G. Morfitt
QUESTIONER :   T. B. Jones
QUESTION :   1.  The "average models" of the D-Region electron density profiles are very useful
for general system planning. However the day  to  day  variability  limits  the  usefulness  of
"average"  profiles  for  determining the propagation conditions on any specific day. Have you
considered any form of real  time  sensing  (sounding)  to  adjust  the  "average"  profile  to
conditions which exist on a particular day.
        2. Small changes in the night time profile  move  the  field  strength  minima  with
respect to transmitters. This great sensitivity of the minima to the profile is a major problem
in obtaining a useful model for any given set of experimental night time  field  strength-range
results.
RESPONSE : There was a tremendous amount of variation in our experiments.  In  the  propagation
data shown here in February on two different days h' varied between 72 and 75. On the nighttime
data there was also a large variation. The Beta for the higher frequencies  being  0.7  in  one
case  and  1.2 for the next night. Such a change was needed to interpret the variation in field
strength for the two nights.
        However, no measurements such as you mentioned are planned at this time.

PAPER : 32. NUMERICAL MODELING OF THE PROPAGATION MEDIUM AT ELF/VLF/LF
AUTHOR :   D. G. Morfitt
QUESTIONER :   B. Burgess
QUESTION : A very interesting paper. Were you able to make any phase or time delay measurements
on  your  flights? I think when you match profiles to data the phase information is very useful.
Some of the measurements we did on the OMEGA-TRINIDAD which Dr. Jones and his colleagues  tried
to  model  showed  that the signal amplitudes could be matched quite well. But when you came to
match the phase as well this proved very difficult, especially at night time. The model is very
sensitive  to  the  phase  measurements.  The other point I would like to make is that on those
measurements which took on the OMEGA transmissions near Trinidad  and  also  around  ALDRA,  in
Norway in the late 60's, we found that when we flew during nighttime on the ALDRA transmissions
the signal level against distance measurements we obtained were very similar to those  obtained
during  daytime around Trinidad. The daytime ones taken around ALDRA looked very much as if the
levels of the D-Region were much lower than they would have been in the middle latitudes?
The  phase  measurement was important to us because we were mainly interested in navigation. We
found that as one might expect phase is a much more sensitive parameter than amplitude  because
you  only  have  to  move  the reflection point a little bit and you start to advance the phase
where you may not even change the amplitude. Phase is certainly  much  more  sensitive  to  the
model that you use than amplitude.
RESPONSE : In particular we have never been able to get  phase  measurements  on  the  aircraft
flights.  Years  ago when Mr. Hildebrand had the sounder set up in Hawaii, and we had receiving
sights in San Diego, at a fixed sight receiver we did obtain some phase measurements.

PAPER : 32. NUMERICAL MODELING OF THE PROPAGATION MEDIUM AT ELF/VLF/LF
AUTHOR :   D. G. Morfitt
QUESTIONER :   E. R. Swanson
QUESTION : 1. A point already mentioned by Mr. Morfitt but
which may warrant emphasis is that amplitude vs. distance functions will  "look"  similar  with
sleight  height  changes.  That  is, a first approximation is as though the distance scale were
stretched or shrunk. Thus if calculations show a sharp null in a region at a range of 3 Mm  for
one  ionospheric  model, a somewhat different ionospheric model on a particular day might place
the null at 3.1 Mm but there would be  a  null  somewhere  in  the  region.  Except  to  verify
prediction  theories  we  are  rarely  interested  in  predicting field strength for a specific
location. Rather, we want to predict for a region and we want to  predict  not  only  the  most
probable value but also the probability of a significant null. This we can do even if we cannot
predict exactly what the ionosphere will do at some future time.
        2.  Regarding  a  question  by  someone on the lack of phase measurements. There are two
factors weighing heavily against measurement of phase as a function of distance.  First,  phase

is only defined with respect to a local clock coordinated with that at the transmitter. This may require cesium frequency standards and will present problems in initialization. Second, whereas amplitude tends to vary slowly with distance, phase varies approximately one cycle per wavelength. Thus distance must be determined with precision which requires precise location. One degree at 20 kHz corresponds to about 42 meters displacement . Location is rarely known to this precision. Practical measurements include the Omega Phase difference and beat frequency differences as observed by Burgess. However these types of measurements are more difficult to interpret than field strength as a function of distance.

PAPER : 32. NUMERICAL MODELING OF THE PROPAGATION MEDIUM AT ELF/VLF/LF
AUTHOR : D. G. Morfitt
COMMENTER : T. B. Jones (answering as Session Chairman)
COMMENT : It can be done if you use phase difference and use one receiver to lock the other. I always remember being very impressed flying with Burgess and seeing how it locked solid when we flew over GBR. That is the kind of information you want if you are interested in navigation but not for communication.

PAPER : 32. NUMERICAL MODELING OF THE PROPAGATION MEDIUM AT ELF/VLF/LF
AUTHOR : D. G. Morfitt
COMMENTER : J. S. Belrose
You noted that the international reference ionosphere fitted summer but did not fit winter, I must admit your talk is very up-to-date because you are employing this model (or trying to). I have not seen the book yet. I would suspect it is heavily weighted to the middle latitudes because that is where most of the data were taken. You are comparing a path between Hawaii and California. That is fairly near the equator and there would not be much seasonal change. I said earlier in the absence of better data one could look at the pressure profiles to give you some indication of how much difference there should be in the height of the profile from summer to winter. There is very little difference in the height of a constant pressure surface between summer and winter at low latitudes. There is 3 to 4 Kilometers at middle latitudes and 5 to 7 at high latitudes. The profiles simply have to go up and down by that amount, discounting other problems in connection with the way electrons are produced and lost. Electron production has got to be proportional to the pressure. The radiation comes in until it burns itself out and ionization is produced. You have interpreted the data by exponential profiles, but have you looked enough at latitude differences. A method which works worldwide would have to take some account of the reference height of an exponential profile as you go from low to high latitudes and from summer to winter.

PAPER : 33. MODELLING OF THE AMBIENT AND DISTURBED IONOSPHERIC MEDIA PERTINENT TO ELF/VLF PROPAGATION
AUTHOR : J. B. Reagan
QUESTIONER : J. S. Belrose
QUESTION : I certainly agree with your philosophy that experiment is needed to confirm theory, but you seem to be resting very heavily on using ELF for confirmation, even for the quiet day. One would have the impression in looking at your data that ELF is not particularly sensitive to profile change. The change from a normal day to a moderate event is only one decibel. Do you have any feel for the sensitivity of the ELF confirming the normal day? It seems you could have relatively wide changes in parameters, and still end up with little change in ELF attenuation. Since the effects are larger on VLF and since VLF data does exist, why has the comparison not been made with VLF field strengths and phase heights.
RESPONSE : That's a good question. You are quite right, ELF is not particularly sensitive during daytime conditions. Of course, this is one of the primary reasons why it is being considered for communication systems, among others. The work we have done suggests it takes intense events which dump energy well down in the bottom of the D-Region in order to effect ELF propagation significantly. VLF would be much more sensitive and therefore more sensitive to the average solar particle event, which is well known. We have not done any modeling work involving VLF during solar particle events. But, I think if we get a campaign going in this solar maximum as we are now hopeful of doing, one would want to study both VLF and ELF propagation. Since we have a number of VLF paths currently in operation, one would want to operate both, take the data on both, do the chemistry modeling and apply it to both frequency ranges.

PAPER : 34. MODELS OF THE MIDLATITUDE D REGION AT NOON
AUTHOR : W. C. W. C. Bain
COMMENTER : P. A. Kossey
COMMENT : I was interested in the technique of forcing the models to agree with data over a fairly broad frequency range plus in addition to that working with the conversion coefficient and phase height. We found in our limited attempts to model with our data that we can easily do very well if we limit the frequency range, and if we forget about the conversion coefficient, etc. So when you force the model to agree with the wave polarization over a broad frequency band. As Dr. Bain has done, it is apparent that this is the way to go and in fact it is a very large task. I am very impressed by the results he has obtained.
I believe Dr. Bain was the first one by, looking at interference patterns back in 1952, to speculate on this C-layer which has been rather controversial and is still quite little understood. His paper with Bracewell which compared steep and oblique incidence observations of GBR (16kHZ) speculated on such a layer being there, and a lot of work has gone on now, showing that that is certainly the case.

PAPER : 34. MODELS OF THE MIDLATITUDE D REGION AT NOON
AUTHOR : W. C. Bain

QUESTIONER :   T. B. Jones
QUESTION  :  One  of  the problems in all this modeling work is the limited set of experimental data that one starts with. Dr. Bain showed four frequencies, two conversion  coefficients  both in  amplitude and phase. There was some work done by Shellman at San Diego, and by ourselves at Leicester which quantifies the errors that one will get either in electron density or in height and  its a tradeoff between whether you get good height or good electron density. This work was the so-called inversion technique. I think one has to be very  careful  in  all  this  type  of modeling in not trying to abstract too much detail from the set of data that one has. For those interested I would refer them to both Dr. Shellman's work and our own. It is  very  interesting when  you  try  to  quantify  exactly how much detail one can extract from a given data set.  I think you will find you need a very substantial data set, if you  are  to  go  for  a  detailed profile, which you would ideally like to utilize for propagation calculations.

PAPER : 34. MODELS OF THE MIDLATITUDE D REGION AT NOON
AUTHOR :   W. C. Bain
QUESTIONER :   J. B. Reagan
QUESTION : In the data that you showed there is easily an order of magnitude spread  in  either the  summer  time  or  winter  time  model  at  any given altitude. Could you comment from your experience on how much of that might be real variation in the D-Region and how much of it might be due to experimental error in the various techniques that are used.
RESPONSE : That is difficult to answer if we take the experimental results, certainly there are errors there,  I  cited  in  the  paper,  I  think,  some estimates of errors, about 20% at 16 Kilohertz and 50% at higher frequencies, so we have by no means achieved a tremendous  accuracy there. I don't know that I can make any other useful comments on your question.

PAPER : 34. MODELS OF THE MIDLATITUDE D REGION AT NOON
AUTHOR :  W. C. Bain
QUESTIONER :   T. B. Jones
QUESTION : Returning to this point of fitting  a  profile  to  agree  with  data  over  a  wide frequency  range.  If  you  try  to  fit VLF and HF data, the profile has to account for the HF absorption as well. That is a whole different problem, if you must fit both VLF and LF, as will as HF absorption, this is an even more stringent test.
RESPONSE : I think you will find that the winter profiles do go up in electron density to above 80 Km. This would tie up with some of the anomalous absorption in winter, in fact the profile I gave was meant to tie up with a profile in winter over the UK when you would expect a  moderate winter anomaly to be present.

# OMEGA

by

E. R. SWANSON
U.S. Naval Ocean Systems Center
San Diego, California 92152 USA

## ABSTRACT

Omega is a very long-range, very low frequency (VLF) radio navigation system which now provides nearly global coverage for ships and aircraft. The final station of eight is now being completed in Australia. Coverage is not only nearly global but is also highly redundant with more than the minimum required number of signals available in most locations. The system is in general use in both the marine and aeronautical environments both commercially and militarily. Acceptance by commercial airlines has been especially rapid. Receivers range from simple phase comparison units which must be supported by specal propagation tables and plotting charts to fully automatic receivers which read out in latitude and longitude after being initialized with no more than approximate location and time. Realizable fix accuracy is usually on the order of one to two nautical miles.

This paper follows overviews of VLF propagation presented by others with some specific comments and observations of application to navigation. Special attention is directed to the subject of signal coverage. For communications, it is only needed to receive a signal with adequate signal-to-noise ratio. For navigation, it is also necessary that the signal have a well defined or characterized phase variation in space. Omega coverage considerations have proved to be more formidable than was originally envisaged.

The paper provides a general overview of Omega with attention to Administration, Synchronization, Traditional Applications, Lane Ambiguity Resolution, Special Applications, and Differential Omega. Combined systems using both Omega and VLF communications signals are mentioned.

## FOREWORD

An overview of any complex subject is always difficult to write. Navigation is both a specialized field with its own unique problems and nomenclature and also an interdisciplinary area which uses results and developments in many other fields. Literature supporting Omega is extraordinarily voluminous and will be found scattered in a number of areas including the geophysical, propagational, electronic and statistical technical literature as well as within the specifically navigational literature. Thousands of publications now exist dealing principally with various aspects of Omega. A professional society also exists to foster use and understanding of the system: The International Omega Association, P.O. Box 2324, Arlington, VA 22202, USA. The association produces various publications including a bibliography conveniently divided into ten subject areas and proceedings of annual meetings (IOA, 1981). Proceedings from the 1980 meeting in Bergen, Norway are now available and total 520 pages thus illustrating the continuing volume of work with Omega (IOA, 1980). Although this paper has been prepared for a propagation panel meeting, it is oriented more generally toward the Omega system than specifically toward its propagational aspects. A paper dealing explicitly with propagation was given by this author at Istanbul in 1976 (Swanson, 1976) and would require little update. A limited discussion of propagation is included based on an abridgment of the Istanbul paper with limited updating. However, the original discussion would be best read in its entirety. Omega propagation has most recently been reviewed by Reder (1981). There is, however, a need for a general review of the system both as a major application of VLF and also as perhaps the world's best source of VLF signals for research purposes. No attempt has been made to provide exhaustive references. Rather, recent work by active authors has been cited as well as certain fundamental works. Where applicable an effort has also been made to cite references in the forthcoming proceedings of the International Omega Association's Montreal meeting thus pointing to a single source for much additional current information.

## 1. OMEGA

Omega is a very low frequency (VLF) navigation system operating in the internationally allocated navigation band between 10 and 14 kHz. Seven stations presently provide nearly global coverage. The final of the eight planned stations is being constructed in Australia and is expected to be completed in May 1982 (Brough, 1981; ONSOD, 1981). The present system is already supporting 10,000 users who are split more or less evenly between the marine and aeronautical communities. Receivers range from relatively simple instruments using only one of the frequencies provided by Omega to complex instruments able to receive all frequencies from all eight Omega stations and process this information to readout directly in latitude and longitude. Commercial acceptance has been particularly rapid in the airborne community within the last few years. It may well be true that Omega has already provided benefits to justify its entire development and implementation costs even though the system is not yet fully completed. Thus although the initial station construction phase of Omega implementation is still in progress and various other aspects warrant research, Omega has been used operationally for many years.

### 1.1 History

Omega has evolved considerably from the initial suggestion by J. A. Pierce in 1947 of the possibility of constructing a long range hyperbolic navigation system based on phase-difference techniques rather than time differences. In particular, a system operating in the vicinity of 50 kHz with a sine wave modulation of 200 Hz was suggested. An experimental system of this type called Radux was constructed by the then Navy Electronics Laboratory (now Naval Ocean Systems Center). Subsequently, in 1955, it was suggested that the Radux information from the LF Signal be combined with a separate VLF transmission near 10 kHz. This system was called Radux-Omega and initial 10.2 kHz transmissions were made in 1955. Later

the LF transmissions were discontinued and ranges were expanded to a single frequency Omega system and, later, a multifrequency Omega system. Omega can thus trace a thirty-four year evolutionary history and has included transmissions at the system base frequency for twenty-six years.

Modern transmissions using stations in Norway, Trinidad, Hawaii, and Forestport, New York began in 1966. Previously, stations were used in a conventional slave-master configuration. Modern transmissions are derived from a bank of cesium frequency standards at each station and each station is controlled as a source of standard signals. The modern arrangement is especially practical for a global system in that the navigator can pair stations in any convenient way to obtain useful hyperbolic geometry and signals. The modern configuration has also proved more reliable than older arrangements.

1.2    Implementation

Practical implementation of Omega requires work in three broad areas: station design and construction; receiver design, manufacture and installation; and propagational theory development and implementation leading to either practical models for incorporation in automatic receivers or charts and tables for use manually. Work in all three areas has been proceeding concurrently for a number of years. However, it is the station construction schedule which has received the most attention. Rather apparently, crude navigation may be attempted with crude receivers and poor propagational knowledge; no navigation can be attempted without signals.

Station sitings are shown in figure 1. All stations shown are presently constructed except the station in Australia. The stations are given in Table I according to letter designation, location, antenna type and operating agency (modified from Tables I and II of Herbert and Nolan, 1975). The nominal radiated power of all stations is 10 kW at 10.2 kHz. As previously noted, the estimated completion date of Australia is May 1982.

TABLE I
TRANSMITTING STATIONS

| STATION | LOCATION | ANTENNA TYPE | OPERATING AGENCY |
|---------|----------|--------------|------------------|
| A | Bratland, Norway | Valley Span | Norwegian Telecommunications Administration |
| B | Liberia | Grounded Tower | Dept. of Commerce, Industry, and Transportation |
| C | Haiku, Hawaii | Valley Span | U.S. Coast Guard |
| D | La Moure, North Dakota, USA | Insulated Tower | U.S. Coast Guard |
| E | La Reunion Isl, Indian Ocean | Grounded Tower | French Navy |
| F | Golfo Nuevo, Argentina | Insulated Tower | Argentina Navy |
| G | Australia | Grounded Tower | Australian Dept. of Transport |
| H | Tsushima Island, Japan | Insulated Tower | Japanese Maritime Safety Agency |

System management has been described by Herbert and Nolan (1975). Omega stations not on U.S. soil are operated by host nation agencies who are responsible for maintaining the Omega signal without interruption and in phase with the world-wide Omega Navigation System. These agencies were listed in Table I. Especially important areas of international cooperation include the coordination of maintenance periods to avoid simultaneous outages of two or more stations thus achieving the reliabilities indicated in section 1.5 and synchronization as described in the following section.

An up to date status report is usually included at annual meetings of the International Omega Association as, most recently, by Vence (1981). Typically included is a discussion of present plans and a summary of continuing programs of the U.S. Coast Guard Omega Navigation System Operations Detail (ONSOD). Plans currently include continuing to operate a global monitoring network, continuing work on signal coverage, and continuing to validate various regions. Validation work has now addressed the Western Pacific (Karkalick, 1978), the North Atlantic (Campbell et al., 1980), and the North Pacific (Levine and Woods, 1981) and the South Atlantic. The U.S. Federal Aviation Agency also maintains a specialized data bank to validate airborne performance (Erickson and Rzonca, 1980). The most recent status report published in a navigation journal was by Vass (1978) and is now somewhat dated but still worth reading.

1.3    Synchronization

Omega is by far the best controlled navigation system from the viewpoint of precise timing (Swanson, 1981a). Observations are taken and calculations performed to determine weekly synchronization adjustments which are then inserted to maintain time at each station. Synchronization within the system is maintained based on observations at sites near each transmitter where remote signals can be compared with those generated locally (Swanson and Kugel, 1971). As equivalent "reciprocal" measurements are made at other stations, the propagation delay can be effectively estimated on an instantaneous path by path basis. Although Omega itself will contain 32 cesium frequency standards when Australia is complete,

synchronization to Coordinated Universal Time (UTC) is based on the U. S. Naval Observatory as a reference. Four independent types of linkage may be available: VLF measurements of the Omega signals received at the Observatory, satellite/TV transfer comparison, Loran-C transfer comparison and portable clock. Non-VLF measurements provide significantly increased accuracy over conventional VLF techniques but are not currently available on a regular basis for all Omega stations. An important link is by satellite to Wahiawa, Hawaii and then by Loran-C transfer comparison to Omega Hawaii. Calculations are based on an elaborate computer program incorporating a Kalman filter (Shane, 1976; Santamore et al., 1976). Synchronization instructions are generated and issued by the Japanese Maritime Safety Agency in Tokyo. At any given time any Omega station is likely to be synchronized to UTC as represented at the U.S. Naval Observatory to one or two microseconds.

## 1.4    Format

Basic Omega signals consist of very low frequency 10.2 kHz continuous wave pulses transmitted sequentially from each station. Since the transmissions are time shared, a commutator is required to separate each station within the 10-second commutation pattern shown in figure 2. The commutation scheme is unambiguous and is synchronized in a known relationship to Coordinated Universal Time (UTC). However, the Omega commutation pattern is no longer simply related to regularly broadcast time pulses as was once the case when UT-2 was broadcast. The commutation pattern was originally defined to commence beginning at 0000 hours and repeat every 10 seconds. Present standard time transmissions employ "leap" seconds which are used typically once or twice per year. For Omega to follow leap seconds would require each user to jump his commutator whenever leap seconds were introduced to standard time. This is operationally inconvenient. Worse, it is potentially dangerous in the event some user does not get informed of the forthcoming time change. A one second change is sufficiently close to a one segment misalignment that it is possible for a receiver to appear to be tracking satisfactorily but actually be tracking on different pairs of signals. The inconvenience during set-up of having off-sets between Omega and International Time must be weighed against the inconvenience and incipient hazard of having occasional leap seconds. At present Omega epoch leads UT by ten seconds which is immaterial considering transmissions at 10.2 kHz alone but of importance considering the full format.

A hyperbolic Omega receiver measures the phase of two or more Omega stations against a reference generated from an internal oscillator. The internal oscillator permits storage of the phase information so that the relative phases of the different stations can be intercompared. Readout is the phase difference in centicycles between selected stations and ordinarily is recorded continuously on strip chart recorders. Since the comparisons are all between signals of the same frequency, no internal ambiguity can arise within the receiver due to circuitry performing frequency translation. Further, a hyperbolic Omega receiver has no intrinsic specification for absolute radio frequency phase shift since shifts common to all stations will be removed in the hyperbolic differencing. The system does, however, have an inherent physical ambiguity. Since adjacent carrier cycles cannot be distinguished, the measured phase of each carrier is inherently ambiguous by an integral number of cycles. Hyperbolic phase differences on a baseline between two stations are ambiguous by the hyperbolic spacing of one-half wavelength (about 8 n.mi. at 10.2 kHz).

Because of continuous operation, the navigational lane ambiguity problem inherent in a single frequency system is hopefully not troublesome to the navigator. However, additional frequencies are included in the full Omega format to permit reestablishment of lane should difficulties occur (Fig. 3). Additional frequencies included for lane identification are 13.6, 11 1/3 and 11.05 kHz. They may be used independently in exactly the same manner as the 10.2 kHz transmissions. However, ambiguities in hyperbolic 13.6 kHz lines-of-position will be coincident with those at 10.2 kHz only every 24 miles. Similarly, LOP's at 11 1/3 will only be coincident every 72 miles and those at 11.05 only every 288 miles. Comparison of the coincidence of lines-of-position obtained at the various frequencies can thus serve to establish the proper lane of the 10.2 kHz carrier within the 288 mile ambiguity of the lowest beat frequency (Pierce et al., 1966; Swanson, 1965; Swanson and Hepperley, 1959; Burgess, 1969; Burgess and Walker, 1970; Swanson, 1978). Some modern receivers do not process information hyperbolically and have a limited lane resolution capability to lane widths of 576 n.mi. (±288 mi.), i.e., the full wavelength of the lowest difference frequency. Several practical aspects of lane resolution should be emphasized: 1) lane is usually established in-port and maintained by continuous tracking; 2) in the event of single station outage using a four station receiver, no ambiguity has occurred; 3) brief outages present no problem since lane is easily re-established by dead reckoning; 4) if a lane ambiguity arises, it is probably not on all LOP's therefore not all need be redetermined; 5) if not all lanes have been lost, lane can be reset by intersecting existing LOP's with only one external navigational LOP such as sun line, depth contour, radar-range, etc.; and 6) if coincidence of lanes is not reasonably "close," navigation directly on the difference frequency is possible, or alternatively, stations may be paired differently to present less accurate fixing within unambiguous, more highly divergent lines-of-position. The latter options are particularly important. Omega lane resolution need never be forced. Lanes may be resolved selectively. If an ambiguity of 8 miles should develop on an LOP, it is still possible to use the 3.4 kHz beat position derived from 13.6 and 10.2 kHz to an unambiguous position accuracy of about two miles. If, at some later time, coincidence improves, then the carrier lane identification can confidently be made (Swanson, 1971).

Figure 3 also shows additional transmissions on unique frequencies indicated by $f_1, f_2, ..., f_8$. They are useful for VLF navigation as described in section 2 and, coincidentally, are very useful for frequency dissemination. The 283 1/3 Hz Omega difference frequency can be used to identify carrier cycles directly in specialized timing applications (Wilson et al., 1972; Chi and Wardrip, 1974; Kugel, 1975 (contains bibliography); Swanson, 1981a).

## 1.5    Practical Navigation

Omega is used primarily because, as Stringer (1970) observed at a meeting of the British Institute of Navigation, "It satisfies the three R's - reliability, redundancy and range." The existing operational stations individually maintained an average 97.5 percent signal availability during 1980 (Rzonca, 1981). The Mean Time Between Failure (MTBF) of receiving equipment has been good ranging from several thousand hours for many designs to 17,000 hours or several years for highly reliable mature designs. Omega is the

first radio navigation system to be deliberately designed to include redundancy. Omega signals propagate to great range. (One significant limitation on use of a signal will often be due to a station interfering with itself through the signal propagation around the world by both a short and long path). In many locations all eight stations may be detectable although perhaps only five or six may be useable. One key to reliability is thus the probability of having more than one transmitter off the air simultaneously. An approach to this type of analysis has been presented by Bruckner and Auerbach (1976) and has been applied to Omega (Frye, 1978). Rzonca (1981) shows simultaneous outages by two stations to have occurred 0.1 percent of the time in 1980 but that the median duration of simultaneous outages was only six minutes and only one exceeded two hours.

Manual Omega navigation requires: antenna, antenn coupler, receiver (preferably with strip chart recorders), predicted propagation correction tables, and perbolic charts (or lattice tables). Equipment was once built by numerous manufacturers. Available c ts and tables are listed in the catalog of the U.S. Oceanographic Office. Once the equipment is installed, it must be properly checked out and synchronized to the commutation pattern. Checkout procedures can vary between equipments of various manufacturers. Synchronization with the commutation pattern is obtained by one of three methods: 1) look at (or listen to) the Omega signals and move the commutator into alignment; 2) knowing the relation between Omega and International Time, start the commutator from a standard 10-second pulse such as might be obtained from WWVB; or 3) knowing the strongest signal in the area, align the commutator until the correct segment corresponds. In practice the third alternative is the most commonly used although, because of anisotropy in signal propagation, a guess of the strongest signal expected in an unfamiliar area can be hazardous. Once commutation is properly established, phase tracks should settle within a few minutes and a fix may be taken. Knowing the actual position and working backwards, correct lane counts can be annotated on strip chart recorders and/or lane counters set. Before sailing, it is desirable to prepare hyperbolic predicted propagation corrections for the station pairs selected for use on the voyage. If the scale of available Omega charts is not satisfactory, lattice tables should be used to plot Omega lanes on the local charts.

Underway, the fixing procedure is simply to read the various phase differences indicated by the receiver, add the respective skywave corrections, and plot the resulting LOP's on the chart. Fix reduction takes only a few minutes. Of course, some reasonableness checks should be made prior to taking the fix. Commutation synchronization can be checked. If the receiver is equipped with a "no signal" light or with field strength indication, the navigator should assure himself that adequate signals are available. Also, strip chart records should be scanned to verify continuous tracking and lane count. Ironically, the high reliability and automatic tracking of Omega place an unusual premium on self-discipline in routinely performing reasonableness checks. If Omega were not reliable, the navigator would appreciate the obvious need for performing elementary checks. However, since a hundred fixes may be obtained without difficulty, it is human nature to assume there will never be any difficulty.

Manual Omega receivers are now largely technologically obsolescent. The foregoing discussion was included for perspective and acknowledgment of the fact that thousands of such equipments still exist and are still being used for navigation. Manual single frequency receivers are still the only types installed on most U.S. Navy surface ships. Fixes of the type obtained from a single frequency manual receiver were recently deduced from observations at fixed sites sampled throughout the world at all times of day and all seasons of the year (Swanson, 1981b). Fix errors are displayed in figure 4 which includes data from some sites which are atypical. Restricting data to conditions more ordinarily encountered lowers the median circular error probable (c.e.p.) to 1.5 n.mi. instead of the 2.0 n.mi. obtained in figure 4. Single frequency results are summarized in Table II. Figures for backup coverage indicate the accuracy available when one of the most desirable signals for navigation is missing.

TABLE II

10.2 kHz FIX ACCURACY
(c.e.p.; n.mi.)

| SITE SELECTION | COVERAGE | |
| --- | --- | --- |
| | PRIMARY | BACKUP |
| CONSERVATIVE | 2.0 | 3.3 |
| TYPICAL | 1.5 | 3.2 |

Modern receivers are computer based and use multiple frequencies, model propagation delays and combine and process information to readout in latitude and longitude. Early in the development of Omega a need was recognized for automatic fix reduction in a rapidly moving airplane especially if the navigation was to be done by the pilot or first officer in a cramped cockpit instead of by a professional navigator with at least some limited area for plotting. The first practical airborne Omega navigation equipment was the AN/ARN-99 developed by Northrup (Smith, 1971) which includes such navigational conveniences as optional readout of "Distance-to-go", bearing to preselected "way" points, ground speed, etc., as well as position. The receiver approach can now be implemented using microprocessors. As costs have decreased and the ability to relieve the user of much of the work load has been demonstrated, automatic receivers have also become attractive to marine users. Although modern receiver designs of various manufacturers differ considerably in detail, use of multiple frequencies and multiple stations with processing to readout the usual convenient navigational parameters is common. One marine receiver is internally integrated with satellite navigation while many airborne receivers include an option to use VLF signals emitted by communications stations (see section 2).

Accuracy specifications for automatic receivers have been addressed by Sakran (1974) and by Special Committee 126 of the Radio Technical Commission for Aeronautics (RTCA). A recent flight evaluation by

Sakran (1981) shows accuracy of one receiver to be 1.24 n.mi. (c.e.p.) over primarily daytime flights in the continental United States. A number of other flight test programs with various equipments over the past several years suggest a typical accuracy of about 1½ n.mi. However, propagation correction coefficients were recently improved (Morris and Swanson, 1980). Table III (from Swanson, 1981b) shows a conservative if somewhat speculative estimate for worldwide 24-hour accuracy of a modern receiver using modern propagation corrections.

## TABLE III

### MULTI-FREQUENCY FIX ACCURACY
### (c.e.p.; n.mi.)

| SITE SELECTION | COVERAGE | |
|---|---|---|
| | PRIMARY | BACKUP |
| CONSERVATIVE | 1.2 | 2.0 |
| TYPICAL | 0.9 | 2.2 |

## 1.6    Special Uses

A number of specialized uses or forms of Omega have developed to exploit particular aspects of the system. Ordinarily, Omega accuracy will not be significantly influenced by poor signal to noise ratio. Usually signals will not be marginal and the primary accuracy limitation will be due to inherent day to day fluctuations in the transfer (or "mapping") function of the propagation medium itself (Swanson, 1970).

Since errors will be introduced by all segments of the long transmission paths to an area, it follows that two receivers in the same area will exhibit similar errors. This spatial correlation results in excellent rendezvous accuracy and also excellent accuracy for relative navigation such as might be needed within a task force or for traffic control. Differential Omega is a system designed to upgrade nominal system accuracy in local areas through use of spatial correlation (Swanson et al., 1974a; Nard, 1981; Watt et al., 1981; Rick, 1981; McKay and Adams, 1981). Although aeronautical use of Differential Omega is still in the development stage, marine use is well advanced. The International Maritime Consultative Organization (IMCO) has adopted a standard for Marine Differential Omega (Pietri, 1980). France has installed full coverage within its own European coastal waters and elsewhere while other nations have also installed Differential Beacons as shown in figure 5. Expansion plans for Differential Omega have been described by Nard (1981).

Differential Omega concepts and principals can be exploited even without formal construction of a Differential Omega navigation system. Oceanographic surveys have exploited differential properties. One scheme to measure winds aloft employs an Omega transponder in a weather balloon. Comparison of the indicated balloon position with the indicated position of similar equipment operated on the ground allows determining the position of the balloon as a function of time and hence calculation of the upper atmosphere winds.

The Omega radio field can also be sensed as an input to what might be called position monitoring systems or cooperative surveillance systems. An early suggestion was the use of Omega for monitoring the location of free drifting weather balloons. An Omega Position and Location Experiment, OPLE, and follow-on experiments for tracking vehicles or traffic control were conducted by NASA (Laughlin et al., 1965; Laughlin, et al., 1967). These systems employed an onboard Omega transponder and a satellite relay to a central processing site. Another similar system was suggested as a position reporting service for use in search and rescue applications. The Global Rescue Alarm Net (GRAN) envisaged that mariners and airmen could carry a small transponder which would telemeter the Omega format through a satellite to ground so that the position of the unit needing rescue could be determined. The system was described by Crawford and Rupp (1972) and showed great technical promise, however, it is not now being pursued. There is, however, a continuing interest in potential position reporting schemes particularly those offering the accuracy possible through the use of Differential Omega techniques (Scull, 1981). In the opinion of this author Omega is a strong contender for many such applications because: 1) the signals are pervasive and not easily blocked or disturbed by foilage or buildings and 2) the required information is very narrow band. The latter characteristic is valuable because it leads to simple low cost methods of providing narrow band reporting telemetry. Choice of a wide bandwidth positioning system will either lead to requirements for wide telemetry bandwidth or substantial and expensive processing by the sensor.

Omega is also used for land navigation in the arctic where reliable alternative methods are not available (Eyre, 1981).

In addition to the spatial correlation features exploited by Rendezvous and Differential Omega, exploitation is made of the dispersive correlation wherein fluctuations on one frequency are closely related to those on a second over the same propagation path. Dispersive correlation significantly reduces the errors expected using beat frequency navigation or lane resolution. A special application called "Composite Omega" has been suggested by J. A. Pierce to take optimum advantage of dispersive correlation (Swanson, 1965; Pierce, 1968; Swanson, 1969; Papousek and Reder, 1973; Pierce, 1974; Brown and Van Allen, 1976).

Auto-correlation of propagation variations is also significant being 8 to 10 hours for normal propagation conditions at night. However, diurnal prediction errors correlate over shorter periods and may become the dominant consideration in practical applications. Measurements by Wright (1969) indicate a potential for determining velocity to 1/3 kt when the propagation paths are either all dark or all sunlit.

There are close theoretical and practical relationships between navigation and timing (Swanson, 1981a). Omega can be used for timing as it is controlled to international time and can disseminate both frequency and epoch (Swanson and Kugel, 1972). The unique frequencies are particularly convenient sources of standard frequency as they may be easily received and used without decommutation. Epoch dissemination is employed within the system for synchronization and also for use as an input to some national time standards (Gupta, 1981). Application also exists for the timing of seismographic arrays (Schneider et al., 1981). A little used capability also exists for timing using lead edge or envelope techniques (Swanson and Adrian, 1973). Accuracies of a few microseconds are possible using carrier phase measurements.

## 2. VLF NAVIGATION

Although this paper explicitly covers Omega, some mention should be made of other VLF navigational techniques. The long range, excellent coverage and reliable reception of Omega are largely characteristics deriving from the frequency band and are not necessarily restricted to the particular navigational implementation we know as Omega (Litchford, 1971; Swanson and Robie, 1973).

Many VLF communications stations throughout the world are stabilized to standard frequency. In the past, transmissions have been continuous wave with on-off keying. Recently, many U S. Naval transmitters were converted to minimum shift keying. For navigational purposes the change constitutes a complication but not an insurmountable difficulty. With simple carrier transmissions from three or more stations, the various signals can be received; then shifted in frequency to some common frequency and then paired and phase differenced (Palmer, 1972). Alternatively, they can be used in a range-range mode against a precision oscillator. Such systems must be initialized. They cannot refine an approximate location as can Omega. In operation a navigation system using such signals is somewhat like an inertial system in that it is exactly correct at the time and place of initialization and then deteriorates with separation and elapsed time. However, the "error drift" is not unlimited as is true with inertial equipment. The error budget for such equipment has been discussed by Swanson and Dick (1975). A substantial number of receivers employing this principle have been manufactured. Flight results from one particular equipment have been described by Tymczyszyn (1975). A recent discussion of performance of an Omega/VLF receiver has been given by Sakran (1981).

Beukers (1973) described a VLF navigation system maintained by the USSR. The frequencies were 11.905, 12.649 and 14.881 kHz with stations located in the e.    est, and center of the Soviet Union. Radiated power appeared high: 50 to 100 kW.

A major difference between Omega and the alternatives is that the Omega system is administered by international agreement and has standards of frequency and phase control and reliability. Other differences stem from the inherent navigational ambiguities present when comparing signals of different frequencies which must be resolved by initialization. However, an important difference occurs when using communications transmissions since they generally fall into the frequency band near or above 20 kHz. This circumstance favors the higher propagational modes and renders the signal structure more complex than with Omega.

## 3. PROPAGATION

The propagation characteristics which permit use of VLF at great range also introduce limitations on Omega. To a greater extent than at higher frequencies, the use of VLF assumes a reliance on nature to provide repeatable propagation. Repeatable propagation usually occurs but with some unwanted temporal and spatial complexity. Also, on occasion, irregular variations occur.

One convenient analytical model for VLF radio propagation is that of a concentric spherical waveguide formed between the earth and the ionosphere. If only one propagation mode is supported by the waveguide, then there will be a simple relationship between phase and distance at long distances from a transmitter. Phase at any given point will be related to distance to the transmitter, ground conditions especially around conductivity, and characteristics of the lower D-region of the ionosphere which forms the upper boundary of  waveguide. As the ionosphere is a magneto-plasma, propagation is anisotropic so that phase is not only a function of distance from a transmitter but also dependent on geophysical path details.

The ionosphere undergoes regular predictable seasonal and diurnal changes as a function of the solar illumination. One practical problem is the prediction and removal of this unwanted temporal variation.

A limitation is the occasional unpredictable variation caused by unpredictable variations in the geophysical environment. The two most important anomalous variations are Sudden Phase Anomalies (SPA's) caused by Sudden Ionospheric Disturbances (SID's) and Polar Cap Absorptions (PCA's). These effects are related to solar flares. SPA's are caused by the X-ray flux impinging on the sunlit ionosphere thus anomalously reducing the width of the waveguide. PCA's result from flares which also emit protons. The charged particles are guided by the earth's magnetic field to the polar regions where they cause an anomalous reduction in the width of the waveguide.

### 3.1 General Characteristics

The concept of a spherical waveguide leads immediately to several valid conclusions. For example, energy will propagate around the world in all directions and may reinforce at the antipodal point from the transmitter. This phenomena has been observed and illustrates the extreme range obtained at VLF. Also, since the lower ionosphere or "D-region" is controlling at VLF, one would expect a severe attenuation when the wavelength becomes comparable with the height of the guide at about 70 to 90 Km, i.e., a frequency of about 4 kHz. A severe increase in attenuation is observed as expected. Another generality, very important to navigation systems, is that if one mode should be dominant, then phase and amplitude should vary   gularly as a function of distance from the transmitter without fluctuations due to interference

between various modes. Note that the regularity is occurring at large distances. This is just the opposite from the usual experience with, say, Loran A, where the groundwave propagation at short distances is regular and multihop skywave can cause irregularities at longer distances.

VLF propagation has been studied for many years. This is due not only to its practical use as the mainstay of fleet communications for a half century but also because of the extreme repeatability of measurements. Although diurnal variations occur, measurements over paths from 5,000 Km to 10,000 Km long typically show repeatability of about 1 dB in field strength while phase variations are measured in microseconds. Although detailed prediction of VLF fields is difficult, some notable success has been achieved (see figure 6 and Morfitt, et al., 1981).

The most accurate theoretical work is now being done using digital computers to solve the waveguide problem. However, expressions developed by J. R. Wait and others provide some insight as has been reviewed by Swa     n (1976).

### 3.1.2 Experimental Observations

The most important changes are the diurnal variations of phase and amplitude. They are typically associated with ionospheric change related to variation of the solar zenith angle over the propagation path being studied. Two typical examples of diurnal variation of amplitude are shown in figures 7 and 8. Note that the field strength tends to be constant at night and decreases following the transit of the sunrise line over the propagation path to a lower value just after the entire path becomes sunlight and finally reaches a nominal value during the day. The decrease just after sunrise is very common for frequencies near 10 kHz and is typically about 4 dB and lasts for about an hour. Although the details of this particular sunrise decrease are not well understood, they presumably are related to both the dynamics of ionospheric disassociation and recombination rates leading to daytime equilibrium, and another phenomena especially important in the 20-30 kHz frequency range, viz: mode conversion caused by the sunrise line. Typical diurnal variation of phase over a long west to east path at 10.2 kHz is shown in figure 9. A constant or "flat" night is observed shifting into a slow variation or "curvature" during the day. At higher frequencies within the VLF range phase tends to be somewhat less stable during the night but more stable in mid-day. Figure 10 shows that the diurnal variation can be considerably more complex than is usually observed at 10.2 kHz. The "steps" during transitions are probably due to modal conversion at the terminator. A theory for the step phenomena has been proposed by Crombie (1964 & 1966) and has had some success over long paths (Lynn, 1971 & 1973). However, if the results shown are close to those for a similar path treated by Pappert and Morfitt (1975), then a more complicated modal conversion model is necessary for this particular path.

As previously mentioned and shown in Figures 7 and 8, field strength is typically repeatable to a standard deviation of about 1 dB from day to day at 10.2 kHz. Repeatability of phase is, however, one of the most useful properties of VLF. Phase variations occur due to ordinary random variations in the ionosphere or, usually to a much lesser extent, to variations in ground conductivity. Occasional larger variations occur. Already mentioned were sudden phase anomalies (SPA's) and polar cap absorptions (PCA's). Typical stabilities appropriate for single propagation paths of various lengths from about 4 Mm to 10 Mm are given in Table IV.

TABLE IV

STANDARD DEVIATIONS OF VLF SIGNALS
(microseconds)

| PERIOD | FREQUENCY | |
|---|---|---|
| | 10.2 kHz | 13.6 kHz |
| DAY | 3 | 2 |
| NIGHT | 5 | 4 |
| TRANSITION | 4 | 4 |

The occasional SID or PCA can cause radical phase variation from nominal. Larsen (1976) presented the morphology and a data base for determining the effects of SID's and PCA's. The data cited by Larsen is valid for determining SID activity over long sunlit paths and PCA activity over long transpolar and transauroral paths near maximum solar activity. The effects have been speculatively extrapolated by Swanson (1974) to more typical conditions (Fig. 11). The renormalization of the function representing SIDs includes extrapolation to typical conditions rather than near-noon, 24-hour operation and allowance for nominal hyprbolic cancellation of phase advances. PCA renormalization is similar except that reduction over the 24-hour day is not applicable. PCA renormalization to nominal solar activity is speculative since there is an insufficient data base near solar minimum. Figure 11 shows that about 2 percent of the time the nominal scatter expected from a normal statistical distribution will be exceeded due to the effect of SIDs and PCAs. The difference is especially important when assessing the probability of some unusual event such as a navigational error greater than 5 miles. (Swanson, 1979). There is virtually no probability of an error greater than 5 miles from the normal distribution (an excursion of over 10 standard deviations). However, figure 24 shows that the probability of an error that large, or greater, due to an SID is 0.02 percent, and from a PCA, 0.2 percent. That is, a PCA could induce an error of that magnitude on one out of 500 occasions. At present the intrinsic association of large navigational errors with geophysical events is mitigated by the occurrence of occasional large errors due to prediction problems or the occurrence of poor geometry as can be seen in figure 4.

In all discussions of the repeatability of phase measurements it is very important to draw the distinction made earlier between day to day statistical scatter, or "noise", and electromagnetic noise. Repeatability is limited by the stability of the transfer or "mapping" function affecting the signal after it leaves the transmitting antenna and until it is received at the receiver (Swanson, 1970). This type of repeatability is effected by random variations in the ionosphere or ground and will not improve by increasing the electromagnetic signal-to-noise ratio. Normally, the signal-to-noise ratio does not significantly affect repeatability except over exceptionally long paths and/or with unusually high local noise.

Natural noise at VLF is primarily due to electromagnetic signals radiated from thunderstorm lightning. The total thunderstorm noise can be computed on a global basis from all "storm centers" (Maxwell and Stone, 1965). In addition, the noise is highly impulsive (Swanson and Adrian, 1973). While the ambient noise is usually high, arctic areas are typicaly quiet and reception of weak signals is common. These characteristics, as well as the wide variation in signal strength which may occur depending on propagation path, combine to give stringent specifications for VLF receivers.

A second area of low signal strength but adequate signal-to-noise ratio is underwater reception. VLF signals are unique in their ability to penetrate sea water to useful depths. At 10 kHz the attenuation rate is about 3 dB/meter which indicates reception at 50 feet 8 Mm removed from a 10 Kw stations.

Propagation blackouts, of the type sometimes experienced at higher frequencies, are rare to the point of being virtually unknown at VLF.

## 3.2 Approaches to VLF Propagation Prediction

Various approaches to VLF propagation prediction have been surveyed by Swanson (1976). The two most important in terms of their application to Omega are full wave waveguide theory using a digital computer and parametric modeling. With Omega, full wave computations provide a suggestion as to how parametric variatons may occur and suggest methods for parameterizing. In addition, the major burden of determining Omega coverage has relied on full wave computation. Phase prediction relies on a parametric model.

### 3.2.1 Full Wave Waveguide

In a simple form, the full wave waveguide approach considers a spatially homogeneous earth-ionosphere waveguide wherein the lower boundary is specified by a specific ground conductivity and the upper boundary by an arbitrary electron density profile. Correct differential equations for propagation are specified and the solution is worked out through appropriate algorithms within a large digital computer. The approach differs from the traditional in which problems in mathematical physics are solved toward as nearly a closed form of solution as possible, and then computations, if any, are used simply to evaluate the solution. Many workers have used full wave solutions in conjunction with wave guide notions. Pappert, Gossard, and Rothmuller (1967), following Budden's formulation, were first to report the results of a program which fully allowed for earth curvature, ionospheric inhomogeneity, and anisotropy. Subsequent contributions on different aspects have been published by various investigators and a more general book was written by Galejs (1972).

Variable propagation conditions along the path have been handled by Bickel using the WKB technique, which is valid provided the propagation parameter variation is slow. An application of full wave theory using an assumed electron density profile and the WKB approximation is shown in figure 6 together with data later observed during flight measurements (Bickel et al., 1970). The agreement is excellent, although the calculations do not include allowance for ionospheric roughness. Gossard and Paulson (1970) have shown typical ionospheric fluctuations at night. Ionospheric roughness is likely to cause increased relative attenuation of higher order modes. Recently theory has been extended to include mode conversion (Pappert and Morfitt, 1975; Pappert and Snyder, 1972; Snyder, 1981; Morfitt et al., 1981).

A problem with full wave modeling is the need for realistic ionospheric and ground parameters, particularly the ionospheric height, electron density gradient, and ground conductivity. Extensive efforts to deduce electron density profiles have been conducted for many years. Most methods of deducing electron density profiles do not work well in the ionospheric D-region. The best data appear to be the result of VLF sounding. Vertical sounding was first conducted at VLF by NELC at Sentinel, Arizona in 1961 (Paulson et al., 1962). Subsequently, more extensive installations were built by Hildebrand at Thule, Hawaii, and in the Mojave Desert. Shellman (1970), using the full wave solution as a subroutine, has developed and refined electron density profile determination from sounding data to obtain confidence limits on the results. Profiles have also been deduced manually by comparing full wave predictions based on various assumed profiles with observed flight data as shown, for example, in a MEECN report (1976).

### 3.2.2 Parametric

Parametric approaches do not intrinsically seek to relate observed radio quantities such as phase or amplitude to inherent geophysical parameters such as electron density profiles. Instead, relevant propagation parameters such as attenuation, velocity, and excitation are assumed to be specified in terms of readily defined path characteristics such as orientation, latitude, ground conductivity, diurnal period, etc.

Parametric approaches have considerable economic advantages. Also, since the bulk of such programs is ordinarily devoted to bookkeeping and summing of the various functions as applied to path segments, the programs are inherently compatible with the full wave solution. The full wave solution provides guidance on the separability of the variables and suggests appropriate functional forms for the variations; the parametric program incorporates these and performs calculations over long paths. Parametric approaches work best when the range of variables which must be considered is least and when the effects of geophysical variations on the propagation parameters can be separated. Although some sophistication can

be economically incorporated into parametric programs to account for variations which are not readily separated, close coupling of propagation parameters is likely to necessitate use of a full wave solution.

In addition to economic advantages, parametric approaches offer a precision and sensitivity not readily obtained with a full wave program. To vary the result of a full wave program, the geophysical input must be changed -- most likely the assumed electron density profile. Such changes of input may cause significant variations in phase and/or amplitude not only at the frequency of interest but at other frequencies as well. With a parametric approach, simpler methods of deducing the parameters are available (Swanson, 1971).

The parametric program of special importance to Omega because of widespread application is the Omega phase prediction program which first became operational in its present format in March 1964. The program is restricted to phase prediction at specified Omega frequencies, but predicts phase 24 hours per day at all seasons. Variations were initially incorporated with orientation, ground conductivity, latitude, sunspot number, and diurnal period. The program has been modified and refined since its inception.

A paper presenting the theoretical formulation used for Omega phase prediction has been written by Swanson (1971). This work was expanded by Swanson and Brown (1972) into a document including not only the background and theoretical formulation of Omega phase prediction but also listing the FORTRAN program used in the production of Omega propagation prediction (or skywave correction) tables used with Omega. More recent program documentation has been written by Morris and Cha (1974). Special constants for use with the program were developed by Tolstoy (1976) and used on an interim basis in the preparation of Predicted Propagation Correction (PPC) tables for the European area. Recently a new revision of global prediction constants has been published by Morris and Swanson (1980) while an alternative parameterization of the dip and bearing relationships has been studied by Gupta and Morris (1981).

### 3.2.3 Statistical

An additional prediction method of limited use with Omega is the statistical approach. A special application is the Force-fit model for use with Omega data. This model has been extensively developed by Kasper (1970) after initial feasibility studies at the Naval Electronics Laboratory Center (NELC). The model is especially interesting in that it operates in conjunction with the Omega Predicted Propagation Correction (PPC) model. The parametric skywave correction model is first applied to account for recognized spatial or diurnal variations, and then an error field is developed for actual observations. Spatial correlation is then evaluated and smoothing conducted to whatever extent may be statistically justified. An alternative algorithm has been recently suggested (Gupta et al., 1981).

### 3.3 Application of Predictions

Prediction of signal amplitude or signal-to-noise ratio is of very little interest. Such predictions are sometimes made as an adjunct to VLF research which will in turn be applied to solve other problems. The day-to-day variation of electromagnetic noise is such that a receiver can inherently determine signal availability at any given time on any given day much better than any general prediction scheme. One use of amplitude prediction is in the preparation of coverage maps (Gupta et al., 1980). They may also be used in choosing which line-of-position to place on navigational charts and which ancillary tables are to be provided in given areas. These latter products are only needed with manual receivers which, as noted, are now becoming technologically obsolescent.

Prediction of geophysical events such as SID's and PCA's is useful only if it is reasonably accurate, addresses events of sufficient magnitude to be of practical interest, and can be disseminated to the navigator in a timely fashion. The dissemination problem precludes much application for some high seas users. However, a monitor has been developed to detect and warn of SID's and PCA's in an air traffic environment (Swanson and Levine, 1978).

The coverage prediction problem with Omega is severe and is primarily the determination of regions of signal self-interference, that is, areas where the phase does not vary regularly with distance due to significant contamination with higher order modes or by presence of the long path signal propagated from the transmitter the long way around the world. The critical problem is not determining signal presence, receivers can measure that quite easily; rather, the problem is the assurance of adequate signal quality. The need is for determining areas where strong signals may be received but where the phase information cannot be reliably related to position. These signals must be "deselected", i.e., excluded, from the navigational solution. The U.S. Coast Guard Omega Navigation System Operations Detail has developed elaborate coverage maps which are continually being refined (Gupta et al., 1980; Vence, 1981). Simplified guidance is provided to the U.S. Navy by bulletins published by the Naval Electronic Systems Engineering Center, Vallejo (NAVSYSENGRCTR, 1981). Work to date has relied heavily on full wave analysis. An effort is also underway by this author to develop coverage guidance parametrically. Coverage guidance is implemented either by furnishing the user with published coverage diagrams or other procedural guidance for signal usage, as an overlay to published Predicted Propagation Corrections (PPC's) for manual use, or by incorporating coverage information within the receiver or a combination of methods. With a manual receiver, the user must determine his signal usage based on the information available to him. With an automatic receiver, relatively elaborate coverage guidance can be incorporated within the software. One receiver uses coverage overlays developed from the full wave modeling. Most receivers incorporate some type of range limitations although range is a poor indication of Omega signal quality. Some also employ bearing restrictions on certain stations so that sectors of known modal interference will not be used. Additionally, automatic receivers employ elaborate combinational filtering which can help protect against adverse effect of modal interference provided there is sufficient signal redundancy. A potential problem with present coverage guidance is that it relies on full wave modeling as conducted using path averaging (WKB) techniques rather than mode conversion. Taguchi (1980) has published data showing cycle slippage in areas where it is not expected. A sample coverage diagram for 10.2 kHz at 1800 GMT in August is shown in figure 12 (from Gupta et al., 1980).

Phase predictions are published by the U.S. Defense Mapping Agency as computed on a large computer using the model developed by this author. Automatic receivers typically include some propagation prediction model although a few exploit relations between frequencies to minimize the need for elaborate propagation prediction. Implementations of propagation predictions within navigational computers range from extremely good approximations of the full model (which are for all intents and purposes identical) to considerable simplifications as described, for example, by Levine (1980). Implementation within a small computer becomes a significant consideration in any proposed improvements in propagation prediction. A perspective can be gained by considering the effect of an eclipse on VLF as has been observed by various workers and subsequently predicted by Noonkester and Sailors (1971). Although eclipses are one of the most predictable phenomena, no attempt is made to incorporate such knowledge into practical predictions.

Additional study of the relationships between the various frequencies could be of value. Automatic receivers can easily determine relative discrepancies between the phases received at various frequencies. If these can be modeled to suggest improvements in signal processing, receivers could adaptively modify their processing according to the deduced conditions.

## 4. CONCLUSIONS

A general review of the Omega system has been presented including a brief discussion of the major propagational characteristics. Navigation now constitutes perhaps the greatest use of the Very Low Frequency band. Omega also provides some of the best controlled and standardized signals in the world for research or other applications.

## REFERENCES

Beuker, J. M., 1974, "A review and Applications of VLF and LF Transmissions for Navigation and Tracking," NAVIGATION, 21, 2 (Summer 1974), pp 117-133.

Bickel, J. E., Ferguson, J. A., and Stanley, G. V., 1970, "Experimental Observations of Magnetic Field Effects on VLF Propagation at Night," RADIO SCI., v. 5, pp 1127-1136, August-September 1970.

Bough, G., 1981, "Status of Omega Australia," (Paper presented at the 6th Ann. Meeting of the Int'l Omega Assoc., Montreal, 18-20 August 1981, and to be published in the Proceedings).

Bruckner, J. M. H., and Auerbach, R. A., 1970, "LF/VLF NAVAID Signal Reliability in Airborne Applications," NAVIGATION, 23, 3. (Fall 1976), pp 209-216.

Burgess, B., 1969, "Propagation effects and lane-ambiguity resolution in Omega, "Proc Instn Elect Engrs, v. 116, 8, pp 1297-1303.

Burgess, B. and Walker, D., 1970, "Effects in Omega from Propagation Variations," J. Inst. of Navigation (Br.), 23, 1, pp 49-59.

Chi, A. R. and Wardrip, S. C., 1974, "Recent Field Test Results Using OMEGA Transmissions for Clock Synchronization," Proc. 6th Annual Precise Time and Time Interval (PTTI) Planning Meeting, 3-5 December 1974, NASA/GSFC Report X-814-75-117, pp 187-197.

Crawford, W. R., and Rupp, W. E., Jr., 1972, "Locating Downed Aircraft by GRAN (Global Rescue Alarm Net)," NAVIGATION, 19, 4, Winter 1972-3, pp 311-316.

Crombie, D. D., 1964, "Periodic Fading of VLF Signals Received Over Long Paths During Sunrise and Sunset," J. Res. Nat. Bur. Stand. Sect. D. 68D(1), pp 27-34.

Crombie, D. D., 1966, "Further Observations of Sunrise and Sunset Fading at Very-Low-Frequency Signals," RADIO SCI., 1(1), pp 47-51.

Eyre, K., 1981, "Further Adventures with the Greek (Land Transit Navigation at High Latitude)," (Paper presented at the 6th Ann. Meeting of the Int'l Omega Assoc., Montreal, 18-20 August 1981, and to be published in the Proceedings).

Frye, E. O., 1978, (Personal communication 15 May 1978).

Galejs, J., 1972, Terrestrial Propagation of Long Electromagnetic Waves, (Pergamon Press), 362 pp.

Gossard, E. E., and Paulson, M. R., 1970, "Effect of Off-Path Reflections on Phase and Amplitude Fluctuations at VLF," AGARD-CP-33, Phase and Frequency Instabilities in Electromagnetic Wave Propagation, K. Davies, Editor, July 1970, pp 239-280.

Gupta, A. Sen., 1981, "Omega VLF Timing in India." (Paper to be published in the Proc. 6th Ann Mtg of the Int'l Omega Assoc., Montreal, 18-20 August 1981.)

Gupta, R., DePalms, L., Donnelly, S., and Morris, P., 1981, "Evaluation of Alternative Force Fit Algorithms for Improving Omega Position Accuracy," (Paper presented at the 6th Ann. Meeting of the Int'l Omega Assoc., Montreal, 18-20 August 1981, and to be published in the Proceedings).

Gupta, R. R., Donnelly, S. F., Morris, P. B., and Vence, R. L., Jr., 1980 "Omega System 10.2 kHz Signal Coverage Prediction Diagrams," Proc. of the 5th Ann. Mtg. of the Int'l Omega Assoc., Bergen, Norway, 5-7 August 1980, pp 22-1 to 22-36.

Gupta, R., and Morris, P., 1981, "Performance of the OMEGA Propagation Correction Model with New Geomagnetic Sub-Models," (Paper presented at the 6th Ann. Meeting of the Int'l Omega Assoc., Montreal, 18-20 August 1981, and to be published in the Proceedings).

Herbert, N. F., and Nolan, T. P., 1975, "The Current Status of the OMEGA Navigation System," Paper presented at the OMEGA Symposium, Tokyo, June 1975 (Abridgement published in Navigation (Japanese), Oct. 1975 n. 47, pp 55-56 (in Japanese)).

IOA, 1981, Bibliography of Omega Publications, (Int'l Omega Assoc., P.O. Box 2324, Arlington, VA 22202).

IOA, 1980, Proc. of the 5th Ann. Mtg. of the Int'l Omega Assoc., Bergen, Norway, 5-7 August 1980.

Kasper, J. F., Jr., 1970, "A Skywave Correction Adjustment Procedure for Improved Omega Accuracy," Proc. of the ION Nat'l Marine Meeting, U.S. Coast Guard Academy, New London, Conn., 12-14 October 1970, v. II, pp 17-30.

Kugel, C. P., 1975, Propagation Effects on the Operation of the Omega Dual-Frequency Timing Receiver, Naval Electronics Laboratory Center Technical Note 3046, 23 September 1975.(*)

Larsen, T. R., 1977, "Omega Accuracy in Polar Regions During Ionospheric Disturbances," AGARD-CP-209 (Propagation Limitations of Navigation and Positioning Systems), published February 1977, pp 18-1 to 18-17.

Laughlin, C., Hilton, G., Hollenbaugh, R. and Lavigne, R., 1965, Meteorological Experiment Using the Omega System for Position Location, NASA GSFC Rept. X-713-65-416, October 1965.

Laughlin, C. R., et al., 1967, PLACE Experiment Description, NASA GSFC Rept. X-133-67-577, November 1967.

Levine, P. H., 1980, "Tests of a Simple Omega Phase Model Including Solar Flare Effects," Proc. of the 5th Ann. Mtg. of the Int'l Omega Assoc., Bergen, Norway, 5-7 August 1980, pp 25-1 to 25-31.

Levine, P., and Woods, R., 1981, "Omega Validation in the Northern Pacific," (Paper presented at the 6th Ann. Meeting of the Int'l Omega Assoc., Montreal, 18-20 August 1981, and to be published in the Proceedings).

Litchford, G., 1971, "Making General Aviation Safer and More Effective through Universal Electronic Design," Astro. and Aero., January 1971, p 36.

Lynn, K. J. W., 1971, "Frequency Dependence of vlf Modal Interference Effects Observed on East-West Propagation Paths," JATP, 33 (No. 6), pp 951-958.

Lynn, K. J. W., 1973, "VLF Mode Conversion Observed at Middle Latitudes," JATP, 35(3), pp 439-452.

McKay, W., and Adams, F., 1981, "Differential Omega Experiment in the Ottawa Area," (Paper presented at the 6th Ann. Meeting of the Int'l Omega Assoc., Montreal, 18-20 August 1981, and to be published in the Proceedings).

Maxwell, E. L. and Stone, D. L., 1965, 10 kc/s Atmospheric Noise Prediction, DECO Rept. 54-F2.

MEECN, 1976, Determination of Effective Ionospheric Electron Density Profiles for VLF/LF Propagation, MEECN Technical Report, Defense Communications Agency, 1 January 1976, C650-TP-76-4.

Morfitt, D. G., Ferguson, J. A., and Snyder, F. P., 1981, "Numerical Modeling of the Propagation Medium at ELF/VLF/LF," These Proceedings.

Morris, P. B., and Cha, M. Y., 1974, Omega Propagation Corrections: Background and Computational Algorithm, Dept. of Transportation, U.S. Coast Guard, Omega Navigation System Operations Detail, Rept. ONSOD-01-74, December 1974, 226 p.

Morris, P. B., and Swanson, E. R., "New Coefficients for the Swanson Propagation Correction Model," Proc. of the 5th Ann. Mtg. of the Int'l Omega Assoc., Bergen, Norway, 5-7 August 1980, pp 26-1 to 26-24.

Nard, G., 1981, "A Differential Omega Update," (Paper presented at the 6th Ann. Meeting of the Int'l Omega Assoc., Montreal, 18-20 August 1981, and to be published in the Proceedings).

NAVSYSENGRCTR, 1981, Naval Electronic Systems Engineering Center, Vallejo, CA documents 14203-124840 and 14203-124804 being AN/BRN-7 and AN/SRN-12 Omega Receiver Navigators and Operators Information Bulletin 3 and 5, respectively. Both May 1981.

Noonkester, V. R., and Sailors, D. B., 1971, "Observed and Predicted VLF Phase Behavior for the Solar Eclipses of September 11, 1969 and March 7, 1970," RADIO SCI, 6, 10 (October 1971), pp 871-878.

ONSOD, 1981, Current weekly status message.

Palmer, W., 1972, Technical Considerations Regarding the GNS System, Winslow Palmer P. E., 114 Montrose Dr., Ft. Myres, Florida 33901.

Pappert, R. A., Gossard, E. E., and Rothmuller, J. J., 1967, "A Numerical Investigation of Classical Approximations Used in VLF Propagation," Radio Sci., v. 2, pp 387-400, April 1967.

Pappert, R. A., and Morfitt, D. G., 1975, "Theoretician and Experimental Sunrise Mode Conversion Results at VLF," Radio Sci., v. 10, n. 5, May 1975, pp 537-546.

Pappert, R. A., Morfitt, D. G., 1975, "Theoretical and Experimental Sunrise Mode Conversion Results at VLF," RADIO SCI., 10, 5 (May 1975), pp 537-546.

Pappert, R. A., and Snyder, F. P., 1972, "Some Results of a Mode-Conversion Program for VLF," RADIO SCI., 7, 10 (October 1972), pp 913-923.

Paulson, M. R., Gossard, E. E., and Moler, W. F., 1962, "The Nature and Scale Size of Irregularities in the D-Region of the Ionosphere as Observed on a Near Vertical Incidence VLF Sounder," ch. 6 in Propagation of Radio Waves at Frequencies below 300 kc/s, W. T. Blackband, ed., NATO/AGARD Avionics Panel, Ionospheric Research Committee, 1962.

Pierce, J. A., Palmer, W., Watt, A. D., and Woodward, R. H., 1966, Omega: A World-Wide Navigational System-System Specifications and Implementation, Published by Pickard and Burns Electronics for the Omega Implementation Committee. (Pickard and Burns Pub. No. 886B). 2nd ed., May 1966.

Pietri, J. M., 1980, "IMCO Resolution on Differential Omega," Proc. of the 5th Ann. Mtg. of the Int'l Omega Assoc., Bergen, Norway, 5-7 August 1980, pp 18-1 to 18-4 (plus 20 page appendix with resolution).

Reder, F., 1981, "Omega and VLF Propagation," (Paper presented at the 6th Ann. Meeting of the Int'l Omega Assoc., Montreal, 18-20 August 1981, and to be published in the Proceedings).

Rick, H., 1981, "A Differential Omega/VLF Navigator," (Paper presented at the 6th Ann. Meeting of the Int'l Omega Assoc., Montreal, 18-20 August 1981, and to be published in the Proceedings).

Rzonca, L., 1981, Worldwide Omega and Very Low Frequency (VLF) Transmitter Outages, January to December 1980, U.S. FAA Rept. FAA-RD-81-29 (Also identified as FAA-CT-81-26), May 1981, 18pp.

Sakran, F. C., Jr., 1981, "U.S. Navy Flight Test Results with the LTN-211 ONS," (Paper presented at the 6th Ann. Meeting of the Int'l Omega Assoc., Montreal, 18-20 August 1981, and to be published in the Proceedings).

Sakran, F. C., Jr., 1974, "Accuracy Specifications for Automatic Omega Navigators," Proc. 2nd Omega Symposium, 5-7 November 1974., Washington, D.C., pp 9-20.

Santamore, H. J., R. N. Schane, S. F. Donnelly, 1976, Omega Synchronization: Current Operations and Future Plans," Proc. 8th Ann. PTTI Applications and Planning Mtg., 1976.

Schneider, J., Mayer R., and Powell, L., 1981, "Application of Omega to Timing and Positioning of Seismograph Arrays," (Paper presented at the 6th Ann. Meeting of the Int'l Omega Assoc., Montreal, 18-20 August 1981, and to be published in the Proceedings).

Scull, D. C., 1981, "Where do we go next in Radio Navigation Planning?" (Paper presented at the 6th Ann. Meeting of the Int'l Omega Assoc., Montreal, 18-20 August 1981, and to be published in the Proceedings).

Shane, R. N., 1976, "Linear, Dynamic Estimation and Control of Omega Radio Navigation System Synchronization," Proc. IEEE Conference on Decision and Control, Clearwater Beach, Florida 1-3 December 1976.

Sherman, C. H., 1970, "Electron-Density Distributions n the Lower Ionosphere with Associated Error Limits Derived from VLF and LF Sounder Data," Radio Sci., v.5, pp 1127-1136, August September 1970.

Smith, E. J., 1971, "AN/ARN-99 Method of Removing Omega Lane Ambiguity," Proc. 1st Omega Symposium, 9-11 November 1971, Washington, D.C., pp 75-82.

Snyder, F. P., 1981, Transequatorial Propagation of Very Low Frequency Radio Waves, Naval Ocean Systems Center Technical Document 431, 15 April 1981. 107pp.

Stringer, F. S., 1970, "A Hybrid System for World-Wide Navigation," Journal of the (British) Institute of Navigation, v. 23, n. 1 p. 26, January 1970.

Swanson, E. R., "Blunders caused by Omega Propagation: SPA's and PCA's," Proc. 2nd Omega Symposium, 5-7 November 1972, Washington, D.C., (U.S. Inst. of Navigation), pp 202-206.

Swanson, E. R., 1977, "The Distribution Pattern of Omega Observations," (British) J. of Navigation, 32, 2, pp 276-278.

Swanson, E. R., 1981a, "Interrelation of Navigation and Timing," (Paper presented at the Int'l Time and Frequency Symposium, New Delhi, February 1981 and to be published in JIETE, November 1981).

Swanson, E. R., 1981b, "Accuracy of Omega Using 1980 PPC's," (Paper presented at the 6th Ann. Meeting of the Int'l Omega Assoc., Montreal, 18-20 August 1981, and to be published in the Proceedings).

Swanson, E. R., 1977, "Propagation Effects on Omega," AGARD-CP-209 (Propagation Limitations of Navigation and Positioning Systems), published February 1977, pp 15-1 to 15-21.

Swanson, E. R., 1965, Omega Lane Resolution: Phase Measurements at Two Very Low Frequencies, Naval Electronics Laboratory Center Report 1305, 5 August 1965.

Swanson, E. R., 1971, "VLF Phase Prediction," VLF-Propagation, G. Bjontegaard, ed., (Proc. from the VLF-Symposium, Sandefjord, Norway, 27-29 October 1971). Norwegian Institute of Cosmic Physics Report 7201, January 1972.

Swanson, E. R., 1970, "Time Dissemination Effects Caused by Instabilities in the Medium," Phase and Frequency Instabilities in Electromagnetic Wave Propagation, K. Davies, Id. (Proc. AGARD/EPC Symposium, Ankara, 9-12 October 1967), pp 181-198.

Swanson, E. R., and Adrian, D. J., 1973, Omega Envelop Capability for Lane Resolution and Timing, Naval Electronic Laboratory Center Technical Report 1901, 20 November 1973 (AD 774891).

Swanson, E. R., Adrian, D. J., and Levine, P. H., 1970a, "Differential Omega Navigation for the U.S. Coastal Confluence Region," NAVIGATION, v. 21, n. 3, Fall 1974, pp 264-271.

Swanson, E. R., and Brown, R. P., 1972, Omega Propagation Prediction Primer, Naval Electronics Laboratory Technical Note 2101, 3 August 1972(*).

Swanson, E. R., and Dick, M. J., VLF Airborne Navigation Requirements, Naval Electronics Laboratory Center Technical Report 1941, 4 February 1975, 22 p. (Also designated as Dept. of Transportation Report FA74-WAI-425-1), (AD A012 581).

Swanson, E. R., and Hepperley, 1969, Composite Omega, Naval Laboratory Center Report 1657, 23 October 1969. (AD 863 791).

Swanson, E. R., and Kugel, C. P., 1972a, "VLF Timing: Conventional and Modern Techniques Including Omega," Proc. IEEE, v. 60, n. 5., May 1972, pp 540-551.

Swanson, E. R., and Kugel, C. P., 1971, Omega Synchronization and Control, Naval Electronics Laboratory Center Technical Report 1757, 19 March 1971 (AD 732 448).

Swanson, E. R., and Robie, F. C., VLF Navigation, Naval Electronics Laboratory Center Technical Document 233, 1 Jan 1973. (AD 761 498).

Taguchi, K., 1980, "Cycle Jump on the Signals of Omega Received in the North Pacific: Experimental Results," Proc. of the 5th Ann. Mtg. of the Int'l Omega Assoc., Bergen, Norway, 5-7 August 1980, pp 23-1 to 23-16.

Tolstoy, A. I., 1976, New Coefficients for the Swanson PPC Model as Utilized by Omega at 10.2 kHz, USCG Omega Navigation System Operations Detail Report ONSOL-01-76, October 1976, 30pp + appendices.

Tymczyszyn, W. R., 1975, "Inflight Worldwide VLF Experience Using Global Navigation GNS-500," Proc. 7th Ann. Precise Time and Time Interval (PTTI Applications and Planning Meeting, 2-4 December 1975, NASA Publ. No. X-814-76-45, pp 521-548.

Vass, E. R., 1978, "OMEGA Navigation System: Present Status and Plans 1977-1980," NAVIGATION, 25, 1 (Spring 1978), pp 40-48.

Vence, R., 1981, "ONSOD Programs," (Paper presented at the 6th Ann. Meeting of the Int'l Omega Assoc., Montreal, 18-20 August 1981, and to be published in the Proceedings).

Watt, T., Karkalik, F., and Abrams, L., 1981, "On the use of Differential Omega for Airborne Navigation in Alaska," (Paper presented at the 6th Ann. Meeting of the Int'l Omega Assoc., Montreal, 18-20 August 1981, and to be published in the Proceedings).

Wilson, J. J., Britt, J. E., and Chi, A. R., 1972, "OMEGA Timing Receiver, Design and System Test," Proc. 4th Ann. Precise Time and time Interval (PTTI) Planning Meeting, 14-16 November 1972, NASA/GFSC Publ. No. X-814-73-72, pp 345-361.

* Naval Electronics Laboratory Center Technical Notes are informal documents which were intended primarily for use within the Center.
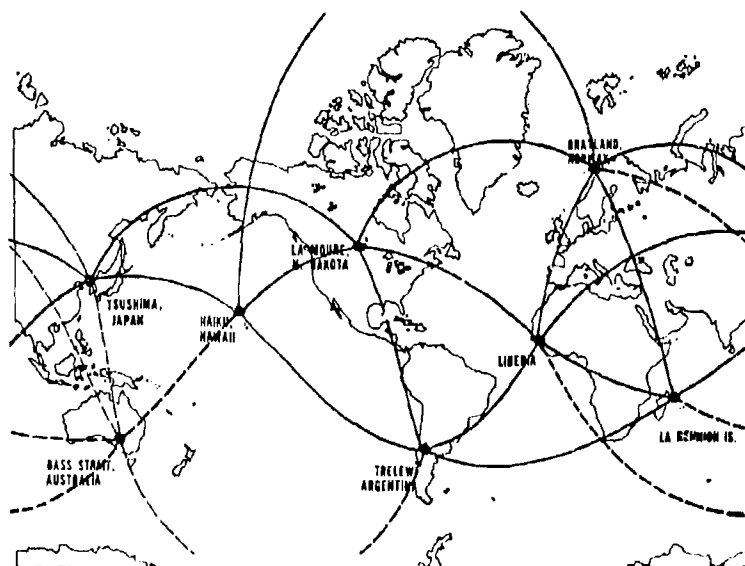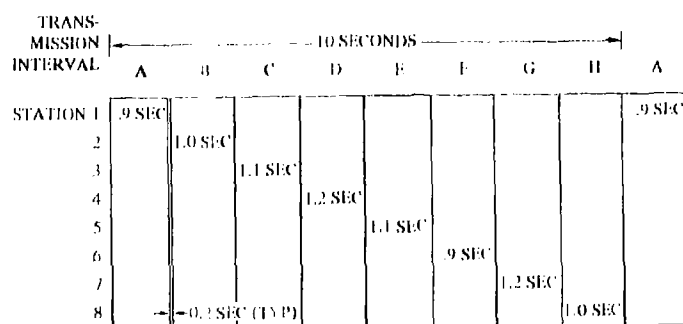
Figure 1. Omega Station Locations.



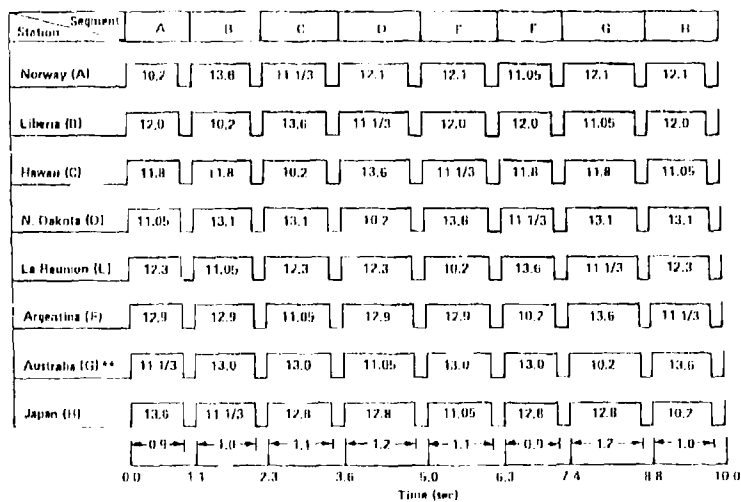Figure 2. Simplified 10.2 kHz Transmission Format.



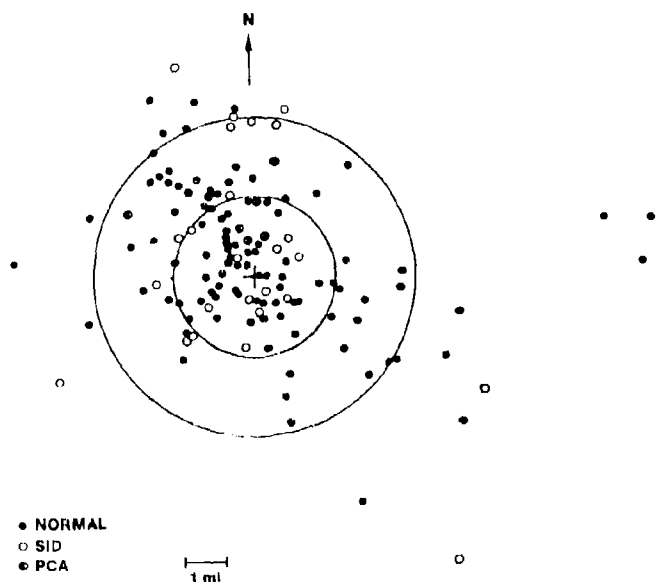Figure 3. Omega Signal Format.

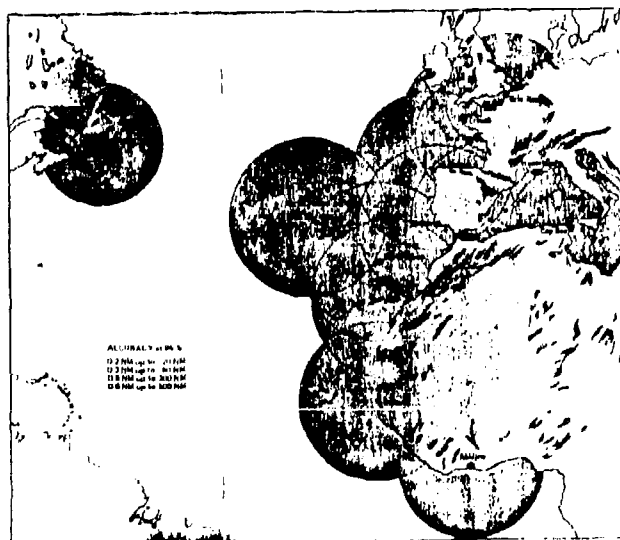Figure 4. Fixes in Areas of Primary Coverage (c.e.p. = 2.0 n.mi.).



Figure 5. Differential Omega Coverage (from SERCEL).
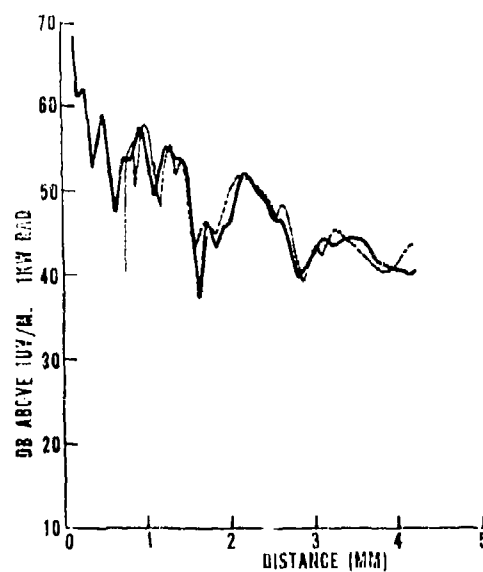


Figure 6. Comparison of Predicted and Observed Amplitude at Night, 23.4 kHz (from Bickel, Ferguson, and Stanley, 1970).
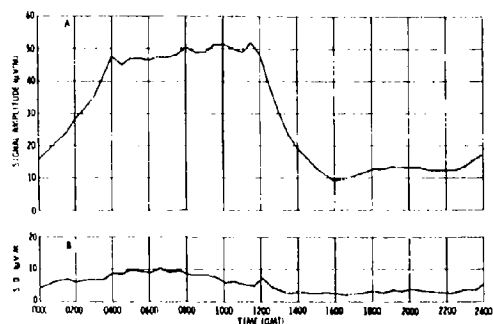
Figure 7. Average Field Strength (A) and Corresponding Standard Deviation (B) for 10.2 kHz Signal Received at Rome, N.Y. from Haiku, Hawaii, 24 October - 10 November 1962.
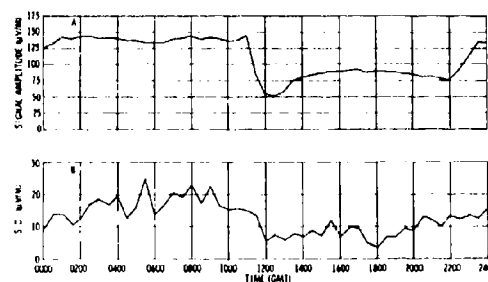
Figure 8. Average Field Strength (A) and Corresponding Standard Deviation (B) for 10.2 kHz Signal Received at Farfan, C.Z., from Forestport, NY, 27 November - 21 December 1962.
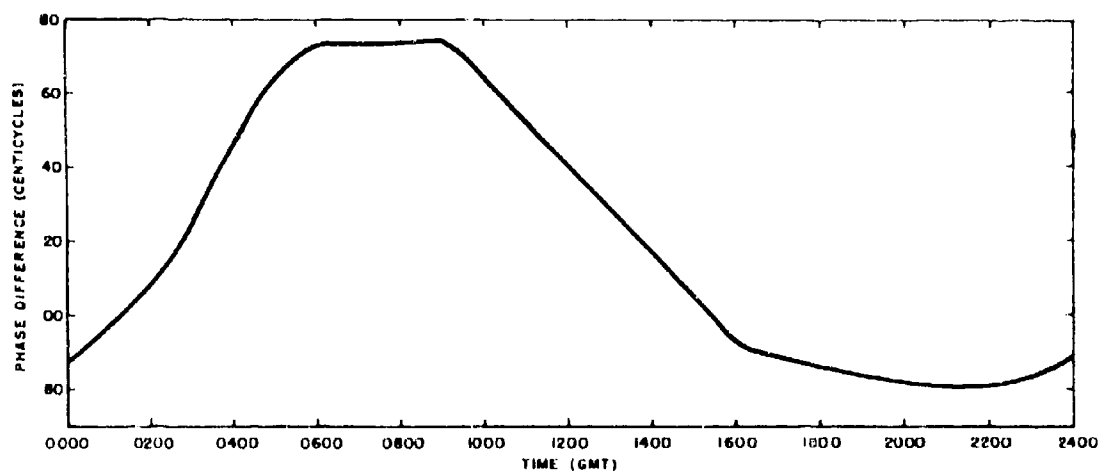


Figure 9. Average 10.2 kHz Phase of Omega Hawaii Received at Forestport, New York, 17 - 24 May 1966. Standard Deviation Approximately 2 Centicycles.



Figure 10. 19.8 kHz NPM (Hawaii) Phase Recorded in San Diego, 9-12 July 1965 (from Bickel).

Figure 11. Typical Probability of Propagation Induced Blunder.



Figure 12. Coverage Prediction Diagram for 10.2 kHz at 1800 GMT in August.
(from Gupta et al., 1980).

# THE EFFECTS OF PROPAGATION ON THE ACCURACIES OF POSITIONS

## DETERMINED USING OMEGA IN THE U.K.

T.B. Jones and K. Mowforth
Physics Department
University of Leicester
Leicester, England

## SUMMARY

The signals from the Omega transmitters located in Norway (A), Liberia (B) and North Dakota (D) have been monitored at three receiving sites within the U.K. Lines of position, (LOPs), have been derived from the relative phases of the received signals and the intersection of the LOPs yields the receiver location. The receiver positions derived in this way have been compared with the known true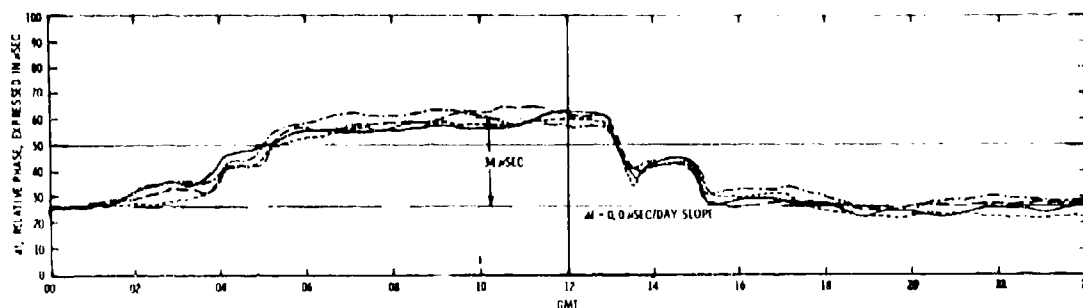 position of the receivers and the error determined. This procedure has been undertaken at hourly intervals for all the data collected during the period January 1978 to December 1979.

Marked diurnal and seasonal changes in position errors are obtained for all three receivers. At the most northerly receiving site, the magnitudes of the errors are different from those observed at the other two locations. This is accounted for in terms of the differences in propagation conditions along the various paths involved.

Error corrections derived from the ONSOD Omega prediction method have been applied and the resulting improvement in accuracy is discussed. A somewhat different correction method, in which the Omega data are combined with a position determination from a satellite navigation system, is also considered.

## 1. INTRODUCTION

An important characteristic of very low frequency (VLF) radio signals propagating to great distances is their inherent phase stability. In the Omega navigation system the phase of the signals received from two spaced VLF transmitters are combined to produce a hyperbolic type of interference pattern. These interference fringes when projected on to the earth's surface define a set of lines of position (LOPs). Position is determined by the intersection of two LOPs which are obtained from two or more pairs of the Omega transmitters.

Measurements of LOPs at three sites within the U.K. exhibit marked diurnal and seasonal variations as a result of changes in the lower ionosphere, moreover, the magnitude of the variations differs between the three sites considered (Jones & Mowforth, 1980). An estimate of the ionospheric errors in the LOPs can be obtained by prediction methods such as that developed by the Omega Navigation Systems Operations Detail (ONSOD). However, these predictions are for average conditions over a 15 day interval, consequently appreciable differences between measured and predicted errors can arise on any given day.

In this investigation the LOPs are combined to produce a ground position 'fix'. This has been compared with the known location of the receiver to determine the radial position errors. The influence of the ionosphere on the position error is discussed and the improvements obtained by applying the ONSOD corrections quantified.

An alternative error correction procedure can be formulated if the true position of the receiver can be determined at intervals by some other means e.g. a navigation satellite. The performance of such a hybrid system is simulated and related to the time period between updates.

The measurements presented indicate that appreciable differences in errors can occur at a given time at various sites within the U.K. when position is determined by means of the same station pairs at each site. The limitations of the error prediction programs are quantified and an alternative approach using satellite derived position fixes is considered.

## 2. OMEGA AND THE DETERMINATION OF POSITION FIXES

The primary Omega navigation signal is transmitted at a frequency of 10.2 kHz (10 kW power) and additional frequencies of 13.6 and 11⅓ kHz are also provided. These transmissions are synchronized (by caesium standards), unmodulated, continuous very low frequency (VLF) waves which in order to prevent signal interference are time sequenced within a ten second period.

Outside the near field zone of each transmitter, a stable signal pattern exists which is repeated in a radial direction every wavelength ( ~ 30 km at 10.2 kHz). The cumulative phase is defined as the total intervening phase between a transmitter and observation point (receiver), and is therefore approximately proportional to the corresponding great-circle distance. The dependence of great-circle distance upon cumulative phase is a function of phase velocity ($v_p$) which is known to vary with radio frequency, ionospheric conductivity and height, ground conductivity, etc (Morris & Hilton, 1974). Hence the assumption of any single value of $v_p$ will nearly always yield erroneous results. To minimize these errors, a nominal value has been selected for the Omega system which is a rough average of (dominant mode) phase velocity over all paths and time, i.e.

$$v_p = \frac{c}{0.9974}$$

The system is usually operated in a hyperbolic mode, that is, the phase difference between the signals received from two transmitters is determined. The locus of geographic positions which give rise to the same phase difference with respect to the two transmitters is a closed curve (LOPs) on the earth's surface, (see figure 1). A navigator can thus fix his position at the intersection of two LOPs obtained from a

minimum of three transmitters. The distance between LOPs differing by $2\pi$ radians in phase is termed a 'lane' ($\approx$ 15 km for 10.2 kHz signals). In general lanes become wider for points off the baseline joining two transmitters.

Locating the intersection of two LOPs on the surface of the earth is generally intractable to all navigators except those equipped with computers. To resolve this difficulty charts have been constructed based on the nominal value of phase velocity.

### 3. MONITORING PROGRAM

A monitoring program undertaken in conjunction with the U.K. Admiralty Compass Observatory (ACO) has been reported on by Jones and Mowforth (1980). This paper is concerned with the ground position data recorded during this study at the following three U.K. locations:

Leicester        (52° 37' 19"N , 1° 7' 22"W)

Farnborough      (51° 17' 17"N , 0° 45' 15"W)

Butt of Lewis    (58° 30' 55"N , 6° 15' 37"W)

Ground positions are calculated from three Omega LOPs as follows:

Norway (transmitter A) – Liberia (transmitter B)       = LOP AB

Norway               – North Dakota (transmitter D) = LOP AD

Liberia              – North Dakota                 = LOP BD

The lane boundary geometries surrounding each receiver location are presented in figure 2. Both 10.2 kHz and 13.6 kHz LOPs are indicated, the latter frequency producing the narrower lanes (see also Table 1). It should be noted that LOP AB lies in a north-west to south-east direction, while LOP AD is orientated almost north-south.

Position fixes, as discussed above, may be calculated from the intersection of a minimum of two LOPs. A third LOP is measured to provide a check and since the resulting error triangle is always less than $\frac{1}{4}$ km for this data, the positions are represented by a "+" at the triangle centroid.

### 4. ERRORS IN GROUND POSITION FIXES

Since the location of each monitor site (static) is accurately known the errors in position fixes determined from Omega can be readily ascertained. To evaluate the effectiveness of the ONSOD corrections, ground position fixes and their associated errors have been calculated from both the raw data set and from data to which the appropriate corrections have been applied. Examples of these results are reproduced in figures 3 to 7 which are based on the geometry of figure 2.

#### 4.1 The position of the Farnborough receiver

(i) <u>10.2 kHz (figure 3)</u>. The positions of the Farnborough receiver determined from the 10.2 kHz signals at two hourly intervals are illustrated in figure 3. All the data collected in the period January 1978 to June 1979 for each time (GMT) stated are included. No attempt has been made to distinguish between data collected at various seasons or months. Data to the left of each diagram is that uncorrected by ONSOD while that to the right has been corrected. Several important features are apparent from these data, and are briefly discussed below.

(a) The distribution of position fixes is spread along an approximately east-west line, along the great circle path from the North Dakota transmitter to the receiver. This is a result of the large variability in signal phase from this transmitter.

(b) Variability in the north-south direction is related to the stability of the AB LOP. Only at dawn ($\sim$ 06:00 GMT) and to a lesser extent, dusk ($\sim$ 18:00 GMT) is the scatter in this direction large, due to the rapid phase changes in LOP AB at these times.

(c) Uncorrected position fixes drift diurnally towards the receivers' true location and then away again. This phenomena is a natural consequence of the strong diurnal phase change patterns present in all Omega LOPs (especially AB). Further reference to this effect is made in section 5.

(d) ONSOD corrected data in general shows improvements in position fix accuracy over the uncorrected data, but the scatter in the east-west direction is not reduced. At times the corrected data overshoots the receivers' true location (e.g. 00:00 GMT) and this is a consequence of the large systematic differences recorded between LOP AB and the prediction curves at night (Jones & Mowforth, 1980).

(ii) <u>13.6 kHz (figure 4)</u> Position fixes determined from the 13.6 kHz Farnborough data are presented in figure 4. In general similar comments to those above apply at this frequency. However, the mean position of fixes is different at the higher frequency (refer also to section 5). In addition, the overall scatter of position fixes appears to be less at 13.6 kHz (section 5).

#### 4.2 The position of the Leicester receiver

As a consequence of the similarity in LOP data between Farnborough and Leicester the ground position fix distributions agree closely. Improvements obtained by application of ONSOD corrections are also similar in magnitude. For comparison of these distributions and those recorded at the Butt of Lewis, the Leicester 10.2 kHz data reproduced is restricted to the period 24/3/79 to 13/8/79 (figure 5) which coincides with the availability of the North of Scotland observations.

4.3    The position of the Butt of Lewis receiver

Butt of Lewis position fixes are presented in figures 6 (10.2 kHz) and 7 (13.6 kHz), 10.2 kHz results being compared with corresponding Leicester measurements in figure 5.

(i)    10.2 kHz (figure 6).

(a)    Butt of Lewis night-time fixes are in general distributed at a greater distance from the receivers' true location than those recorded in Leicester.

(b)    The scatter of position fixes in an east-west direction appears slightly greater at certain times at Leicester (e.g. 14:00 GMT). This may be a consequence of remaining differences between the coverage of data in the period indicated (i.e. there is no Butt of Lewis LOP data from 16th June to 14th July).

(c)    Following point (b), the north-south scatter appears slightly greater at the Butt of Lewis (e.g. 16:00 GMT). This may also be related to the differences in the diurnal variations of LOP AB at the two locations.

(d)    ONSOD corrected fixes are generally more accurate at the Butt of Lewis than at Leicester. Differences between the sites (corrected data) appear more prominent at night (20:00 – 04:00 GMT) than during the day (06:00 – 18:00 GMT).

(ii)    13.6 kHz (figure 7).    Position fixes determined from 13.6 kHz Butt of Lewis LOPs are illustrated in figure 7. The comparative statements made above between Leicester and Butt of Lewis 10.2 kHz data are generally valid at 13.6 kHz. Differences between the position fixes recorded at the two frequencies in Scotland are also apparent as was the case for Farnborough (compare figures 6 and 7).

5.    DIURNAL VARIATION IN MEAN POSITIONS

The greatest ionospheric influence which affects VLF radio wave propagation is the diurnal variation in electron density. It is this change which must be modelled if accurate predictions of the propagation errors are to be achieved. The existing ONSOD predictions partly meet this objective but, as indicated above, the degree of success is rather variable. To quantify these differences the diurnal variations of errors in position fix have been investigated in detail.

Illustrated in figures 8 to 12 are mean hourly position fix plots, recorded at each monitoring location. Both uncorrected and ONSOD corrected data are included, the former always exhibiting a clockwise rotation. These diagrams essentially quantify the mean diurnal pattern in position fixes for the data presented in figures 5 to 7. The form of this pattern is particularly important since it could well provide the basis of a simple prediction program for the U.K. area.

When ONSOD corrections are applied the diurnal variations in mean position fixes are destroyed, the remaining distribution being a function of the correction accuracy. Histograms, illustrating radial standard deviations (RSDs) about the mean positions are also included in the figures. Generally only small reductions in RSD are apparent after application of ONSOD corrections. The behaviour of these data are summarized below.

5.1    Discussion of mean ground position distributions

(i)    Farnborough monitor, 10.2 kHz (figure 8).    Farnborough, 10.2 kHz mean position fix distributions are indicated in figure 8. A minimum radial error (~ 0.5 km) occurs around 10:00 GMT prior to correction by ONSOD.         The maximum radial error (~ 9 km) present in the uncorrected data set occurs at 20:00 GMT. ONSOD corrections reduce radial errors to 5 km or less, however RSDs at dawn and dusk are larger than at other times. This is a consequence of the difficulties in predicting LOP variations at these times.

(ii)    Farnborough monitor, 13.6 kHz (figure 9).    The magnitude of the 13.6 kHz diurnal pattern (figure 9) is reduced and displaced some 10 km from the receiver's true location. RSDs of both corrected and uncorrected data are approximately 1 km less than those at 10.2 kHz. There is however a prominent increase in RSD around 08:00 after ONSOD predicted propagation corrections (PPCs) have been added.

(iii)    Leicester monitor, 10.2 kHz (figure 10).    Similar diurnal patterns in uncorrected mean position fixes are observed at Leicester. A more direct comparison of the Butt of Lewis and Leicester 10.2 kHz results (24/5/79 – 13/8/79) is presented in figure 10. Variations between this diurnal pattern and that of figure 8 (Farnborough) are due principally to the differences in the time periods over which the data originate rather than due to change in receiver location.

Radial standard deviations increase slightly during the dawn period (06:00 – 07:00 GMT) after addition of ONSOD corrections.

(iv)    Butt of Lewis monitor, 10.2 kHz (figure 11).    Figure 10 (Leicester, 10.2 kHz) may be compared with a similar data set recorded in Scotland (figure 11) which has the following features. Firstly, the shape and location of the diurnal variation is different at the two locations. Secondly, application of ONSOD PPCs generally result in more accurate position fixes at the Butt of Lewis, and their distributions differ from one site to the other. Thirdly, RSDs are similar at the two locations, the maximum differences being of the order of 1 km (at dawn and dusk).

(v)    Butt of Lewis monitor, 13.6 kHz (figure 12).    In common with the Farnborough measurements at this frequency (figure 9) uncorrected fixes form a diurnal pattern located some distance (~ 10 km) from the receivers' true location. ONSOD corrections destroy the variation and RSDs are slightly less (~ 1 km) at 13.6 kHz than those observed on 10.2 kHz in Scotland.

## 5.2 Concluding note

The analysis presented in this section (5) has illustrated both the systematic and random variations in Omega position fixes derived from three LOPs (AB, AD and BD). Such variations have been quantified in terms of radial distances from the true position and radial standard deviations about hourly mean position fixes. The distributions observed are a result of the combination of some or many of the effects described by Jones and Mowforth, 1980, and the above analysis has to a certain extent indicated their relative magnitude. For example, variations in LOP AD produce a very prominent trend in position fix distributions, and contribute substantially to the observed level of RSD, at Leicester and Farnborough.

Furthermore, the results presented above provide a clear indication of the nature of the improvements possible with the application of ONSOD PPCs and highlight the differences in system performance in the north and south of the U.K.

## 6. REAL TIME UPDATING OF OMEGA POSITION FIXES

The magnitude and variability of the diurnal LOP errors have been investigated and the effectiveness of ONSOD predictions discussed. An alternative method of correcting the navigation errors can be postulated if the position of the receiver is accurately determined by some other method at certain times. For example, real time updates of position could be obtained from a satellite navigation system or from the retransmission in a Differential Omega system. Errors due to the differences in receiver positions in the latter system have been examined by Jones and Mowforth, 1980. The alternative technique of combining Omega with satellite navigation has already been developed by some commercial companies, and this type of updating method is of interest.

### 6.1 Omega/satellite receiver simulation

A navigation satellite can provide a very accurate position fix at certain times of the day, i.e. when the satellite is above the operator's horizon. From these fixes the errors in Omega LOPs at the particular time and location of the observation can be determined. This information then provides an additional correction to the Omega position fixes and this can form the basis of a correction to be applied during the period when the satellite is not available.

The possible improvements achieved with such an Omega/satellite receiver have been examined by combing Omega LOP data previously presented with a simulated satellite aid. The satellite derived positions (or updates) are assumed to have no associated error and to be available at regular six hourly intervals (00:00, 06:00, 12:00 and 18:00 GMT). One further simulation for which the satellite updates are available hourly is also included.

The results of this analysis are presented in figures 13 to 17 in the form of circular error probability (cep) versus radial error in kilometers. Navigation radial errors are usually quantified in terms of a particular cep level; a radial error of 7 km (95% cep) being generally quoted for Omega (Maenpa, 1978). That is, 95% of all Omega derived fixes (including PPCs ) should be less than 7 km from the receiver's true location. The Admiralty have adopted a 98% cep level for their statements of system performance and therefore both 95% and 98% levels are indicated in the figures. A summary of these radial errors is presented in table 2.

The data have been assessed by the four methods indicated below and illustrated in figures 13 to 17.

(a) Position fixes determined from totally uncorrected LOP data.

(b) Position fixes determined from LOP data combined with ONSOD PPCs.

(c) Position fixes determined from LOP data with satellite updates only.

(d) Position fixes determined from LOP data combined with ONSOD corrections and satellite updates.

LOPs AB, AD and BD have been utilized in this analysis.

### 6.2 Radial error distributions (hourly data, updates six-hourly)

(i) Farnborough monitor, 10.2 kHz (figure 13). Radial error dir    ations recorded at Farnborough during the period January 1977 to June 1978 on 10.2 kHz are indicated i    gure 13. The improvements possible through the application of methods (b) - (d) above are immediate. apparent from the diagram, method (d) providing the most accurate position fixes. Note that with techniques (c) and (d), i.e. those involving satellite updates, about 17% of the position fixes have no associated radial error, and correspond to the times when the satellite update correction is first applied in each six-hourly interval.

(ii) Farnborough monitor, 13.6 kHz (figure 14). Distributions at 13.6 kHz differ from those at 10.2 kHz, large radial errors being recorded in the 13.6 kHz uncorrected data. ONSOD corrections are more accurate at this higher frequency producing small radial errors. Satellite updating combined with uncorrected data results in a radial error distribution not unlike the most accurate distribution indicated in figure 13 (satellite updates plus ONSOD corrected data, 10.2 kHz).

(iii) Leicester monitor, 10.2 kHz (figure 15). Leicester 10.2 kHz radial error distributions over the period 24/5/79 to 13/8/79 are presented in figure 15. These data are compared below with those from the Butt of Lewis.

(iv) Butt of Lewis monitor, 10.2 kHz (figure 16). Comparing figures 15 (Leicester, 10.2 kHz) and 16 (Butt of Lewis, 10.2 kHz) an interesting difference in the distributions for uncorrected data is apparent. The shallow ledge present in figure 16 is probably due to the more dominant phase change present over the Liberia path which tends to segregate the position fixes more effectively into two regions; one

close to, and the other further away from, the receiver's true location.

These data further quantify the improved performance of the ONSOD corrections at the Butt of Lewis. Their accuracy here is such as to render unnecessary the inclusion of satellite updates at six-hourly intervals.

(v) Butt of Lewis monitor, 13.6 kHz (figure 17). A large bias is evident in the 13.6 kHz uncorrected Scottish data as indicated by figure 17. ONSOD corrections appear more effective in reducing radial errors at this site compared with those obtained on 10.2 kHz. The combination of both correction techniques (method (d) above) results in greater radial errors at large ceps. This is a result of the introduction of overcorrection by the satellite updates.

6.3 Comparisons with nominal Omega accuracy

The nominal value of radial error in Omega is 7 km at a cep of 95%. It is apparent from table 2 that this is never achieved in the U.K. except when some form of correction is applied. Navigation at Farnborough with 10.2 kHz transmissions only just meets this nominal figure when both ONSOD PPCs and satellite updates are combined. The situation at 13.6 kHz is better due to greater accuracy of the ONSOD PPCs.

Three situations are considered from the Leicester 1979 data, and discussed below:

(a) 10.2 kHz Leicester, hourly data for the period January to December 1979 is examined. Nominal Omega performance is achieved with either ONSOD PPCs or with satellite updates plus PPCs.

(b) 10.2 kHz Leicester, hourly data for the period 24/3/79 to 13/8/79. The trends here are essentially the same as those above (January-December 1979), differences being accounted for by the reduction in the size of the data set.

(c) 10.2 kHz Leicester, five minute data recorded during 1979 but unlike situation (a) and (b), with hourly satellite updates. Under these conditions very marked improvements are possible with a Omega/satellite system, radial errors at best being reduced to 2.4 km (95% cep).

Finally, Butt of Lewis results (hourly data, six hourly updates) are indicated in table 2, where at both 10.2 kHz and 13.6 kHz radial errors are about 4½ km (95% cep) with just the addition of ONSOD corrections.

7. CONCLUSIONS

A detailed analysis of the experimentally determined performance of the Omega system at three locations within the U.K. has been undertaken. The validity of the ONSOD LOP corrections for these locations has been assessed by comparison with the observations and their diurnal and seasonal variations quantified. From this study a number of systematic differences and biases are apparent between the ONSOD predicted LOPs and the experimental data. Major prediction errors are evident at dawn (and to a lesser extent at dusk) for some of the propagation paths. Under certain situations the prediction program overestimates the day/night phase changes leading to further large systematic errors. The limitation of any long-term prediction program due to the day-to-day variability of the ionospheric D-region is also noted.

The changes in the receiver's apparent positions were determined from three LOPs. The variation in Omega performance accuracy was investigated by calculating the differences in the measured error of the same LOP at three U.K. locations. From these analyses it is apparent that the performance of Omega at Farnborough and Leicester is very similar, but there are marked differences between the Butt of Lewis errors and those for the two southerly receivers.

The differences in radial errors in position have been further quantified in the context of an Omega/satellite combined system. This analysis highlights the possible advantages and limitations of such a system and has further emphasised the differences in performance within the U.K.

Further work is required to determine the origins of the errors noted in the prediction technique and to explain the differences observed in accuracy within the U.K. area.

REFERENCES

Jones, T.B. and Mowforth, K.E. (1980). Experimental validation of the ONSOD Omega prediction method. AGARD Conf. on The Physical Basis of the Ionosphere in the Solar-Terrestrial system. AGARD-CP-295.

Morris, P.B. and Milton, Y.C. (1974). Omega propagation corrections: background and computational algorithm. ONSOD Report No. ONSOD-01-74.

Maenpa, J.F. (1978). Hybrid satellite/Omega navigation in the HX 1105. Proc. of the 3rd Annual Meeting, International Omega Association.

| Monitor site | LOP | Lane Width (km) | |
|---|---|---|---|
| | | 10·2 kHz | 13·6 kHz |
| Leicester | AB | 14·7 | 11·0 |
| | AD | 24·0 | 18·0 |
| | BD | 17·6 | 13·2 |
| Farnborough | AB | 14·7 | 11·0 |
| | AD | 25·0 | 18·6 |
| | BD | 17·6 | 13·2 |
| Butt of Lewis | AB | 15·4 | 11·6 |
| | AD | 19·2 | 14·4 |
| | BD | 17·5 | 13·2 |

Table 1   Omega lane widths at the U.K. monitoring sites.

| LOCATION | FREQ. (kHz) | DATA PERIOD | DATA TYPE | SATELLITE UPDATE INTERVAL | UNCORRECTED DATA | | ONSOD CORRECTED | | SATELLITE CORRECTED | | ONSOD PLUS SATELLITE CORRECTIONS | |
|---|---|---|---|---|---|---|---|---|---|---|---|---|
| | | | | | 95% | 98% | 95% | 98% | 95% | 98% | 95% | 98% |
| Farnborough | 10·2 | Jan. 1978 – Jun. 1979 | Hourly | 6 hourly | 11·5 | 13·9 | 8·6 | 11·1 | 8·9 | 10·6 | 7·0 | 8·3 |
| Farnborough | 13·6 | Jan. 1978 – Jun. 1979 | Hourly | 6 hourly | 14·9 | 16·8 | 6·9 | 8·4 | 6·3 | 7·4 | 6·9 | 8·0 |
| Leicester | 10·2 | Jan. -Dec. 1979 | Hourly | 6 hourly | 10·6 | 12·0 | 6·8 | 8·5 | 7·7 | 9·4 | 6·0 | 7·3 |
| Leicester | 10·2 | 24/3/79 -13/8/79 | Hourly | 6 hourly | 10·8 | 11·9 | 6·0 | 7·6 | 8·1 | 10·3 | 5·1 | 6·3 |
| Leicester | 10·2 | Jan. -Dec. 1979 | 5 minute | Hourly | 10·7 | 12·3 | 6·8 | 8·7 | 2·5 | 3·4 | 2·4 | 3·6 |
| Butt of Lewis | 10·2 | 24/3/79 -13/8/79 | Hourly | 6 hourly | 11·2 | 12·2 | 4·5 | 5·7 | 7·6 | 8·5 | 4·2 | 4·7 |
| Butt of Lewis | 13·6 | 24/3/79 -13/8/79 | Hourly | 6 hourly | 14·3 | 14·7 | 4·6 | 5·4 | 5·5 | 6·1 | 6·2 | 7·1 |

Table 2   Measured radial errors at the three U.K. monitoring sites at
95% and 98% circular error probability levels (all radial errors
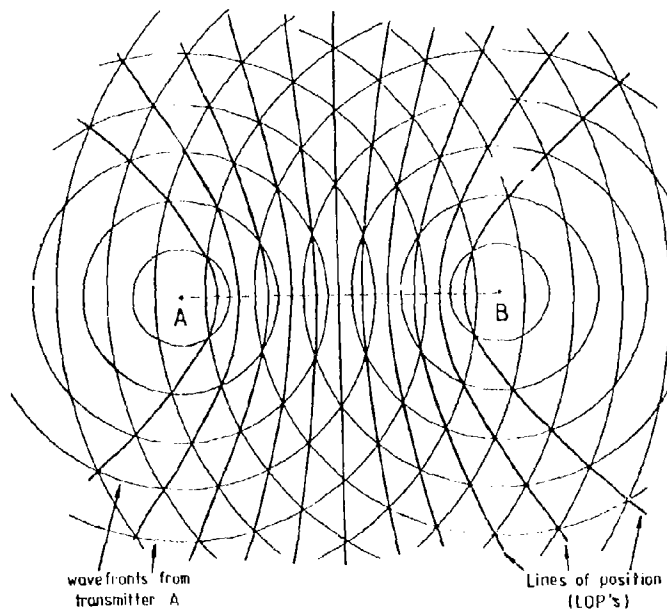in km).

wavefronts from
transmitter A

Lines of position
(LOP's)

Figure 1    Lines of position (LOPs) formed by two radio transmitters
A and B (the baseline is indicated by the broken line).



Leicester, 10 2 kHz
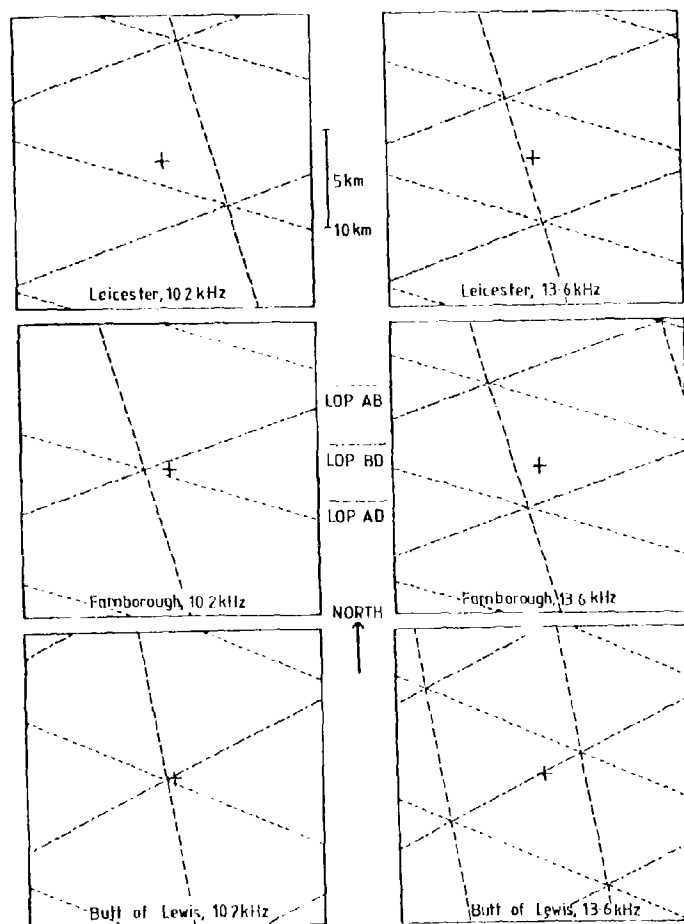
Leicester, 13 6 kHz

5 km

10 km

Farnborough, 10 2 kHz

Farnborough, 13 6 kHz

LOP AB

LOP BD

LOP AD

NORTH

Butt of Lewis, 10 2kHz

Butt of Lewis, 13 6 kHz

Figure 2    Omega lane boundary geometry at the U.K. monitoring sites.
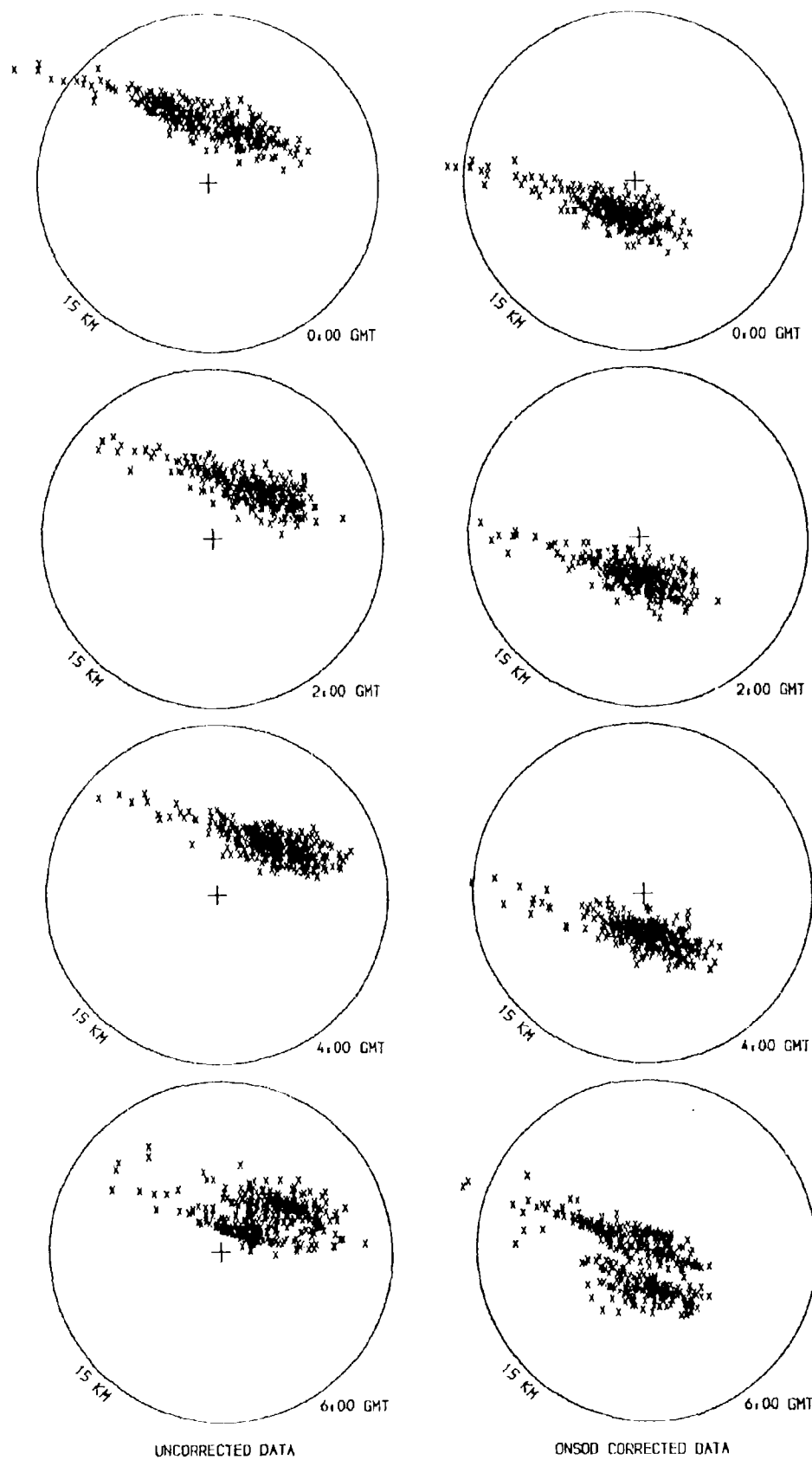
UNCORRECTED DATA          ONSOD CORRECTED DATA

Figure 5(a)  Position fix distributions, Farnborough, Jan.1978-June 1979,
10.2 kHz, 00:00-06:00 GMT.

Figure 3(b)   Position fix distributions, Farnborough, Jan.1978-June 1979, 10.2 kHz, 08:00-14:00 GMT.

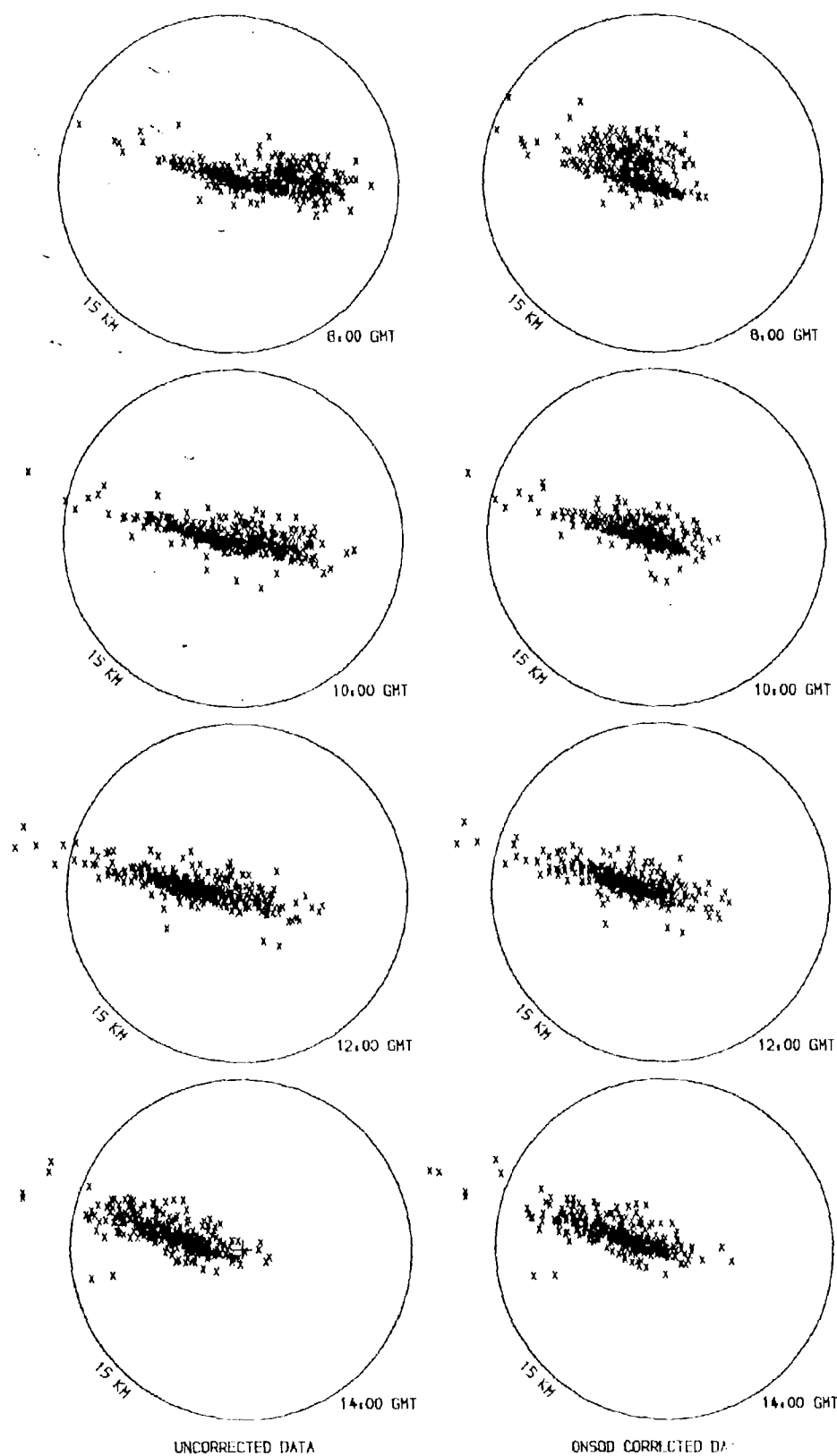UNCORRECTED DATA                    ONSOD CORRECTED DATA
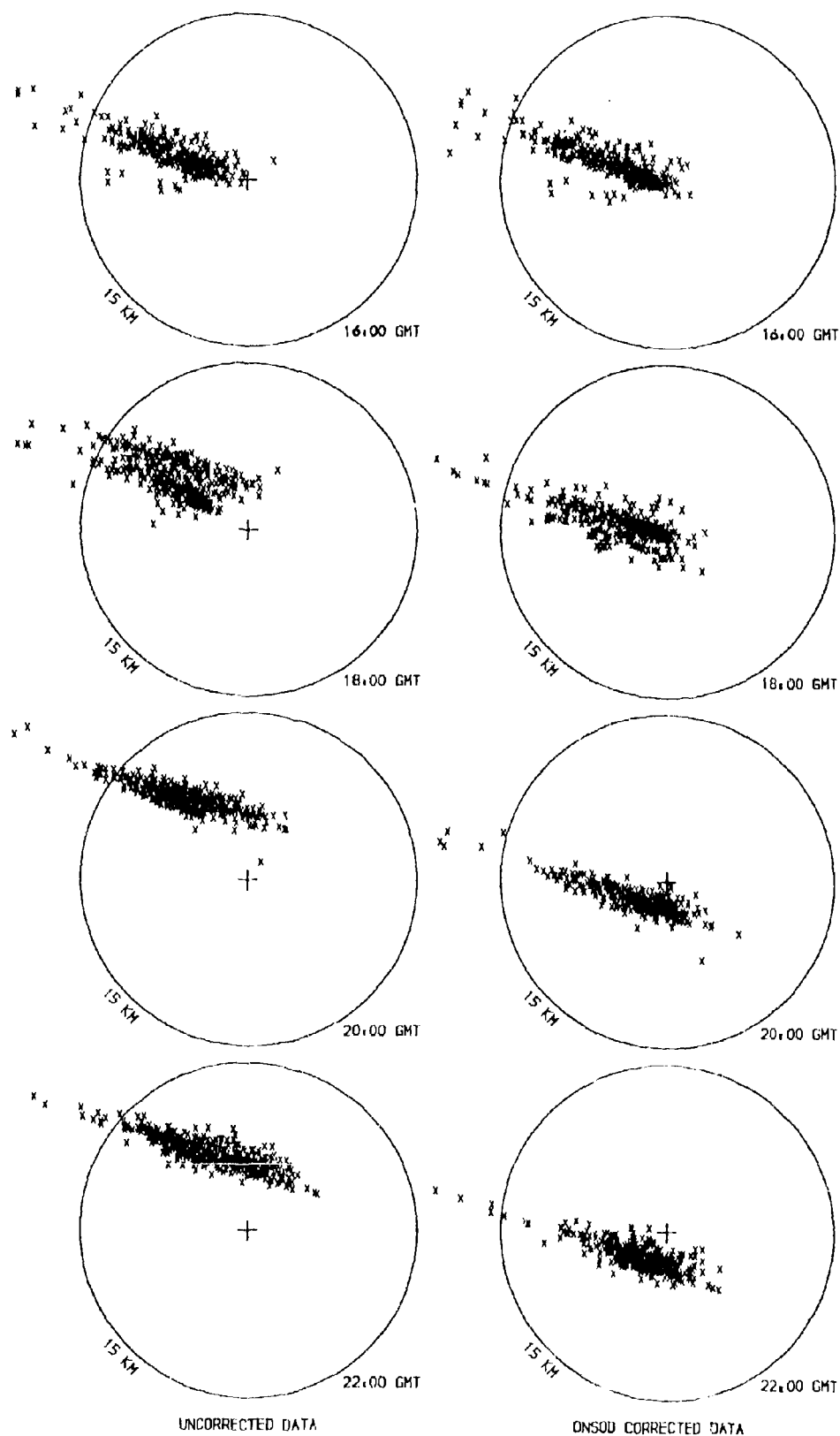
Figure 5(c)   Position fix distributions, Farnborough, Jan.1978-June 1979,
10.2 kHz, 16:00-22:00 GMT.

Figure 4(a)   Position fix distributions, Farnborough, Jan.1978–June 1979,
13.6 kHz, 00:00–06:00 GMT.

UNCORRECTED DATA                    ONSOD CORRECTED DATA
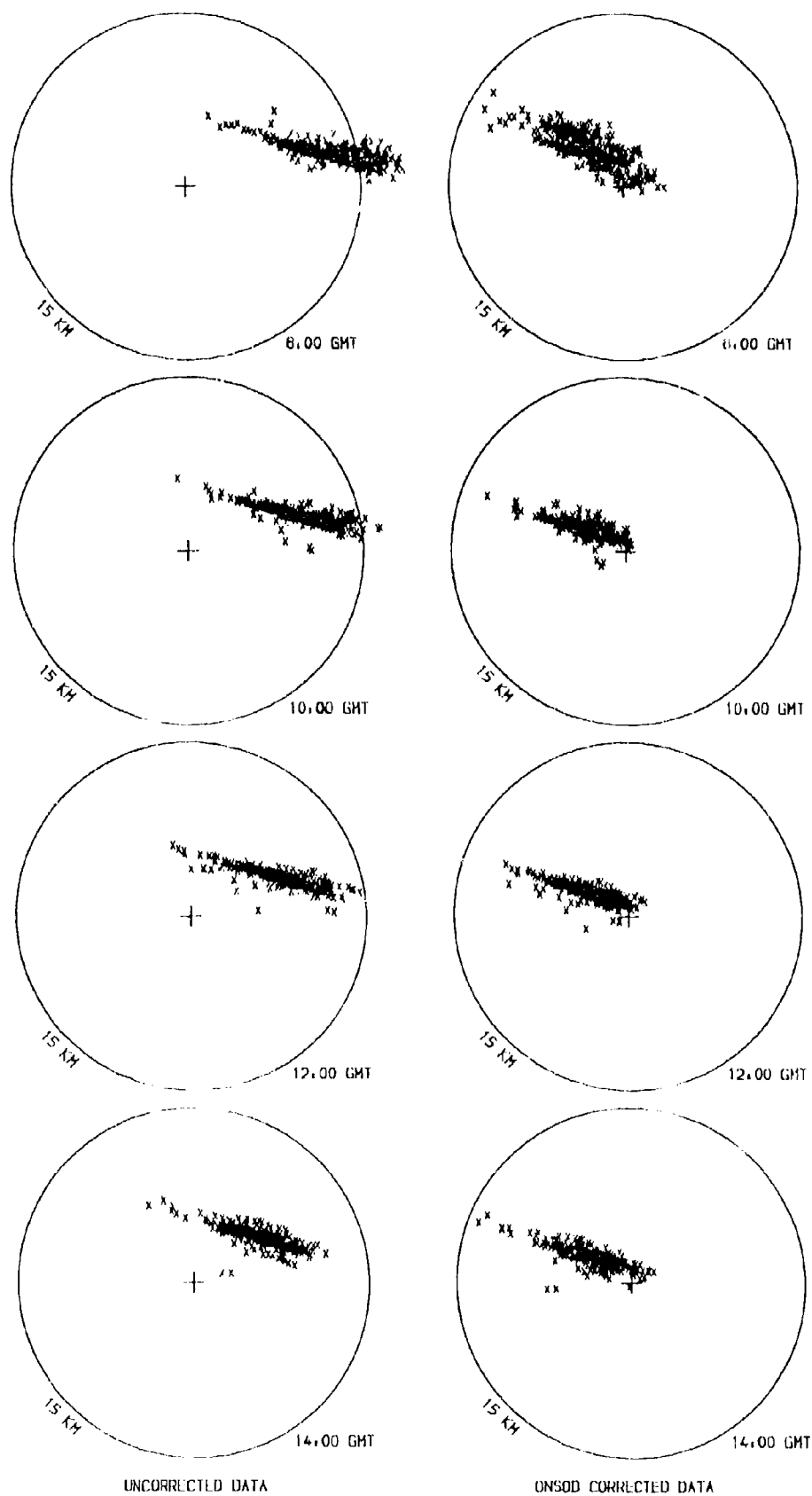
Figure 4(b)   Position fix distributions, Farnborough, Jan. 1978-June 1979,
13.6 kHz, 08:00-14:00 GMT.

UNCORRECTED DATA                    ONSOD CORRECTED DATA
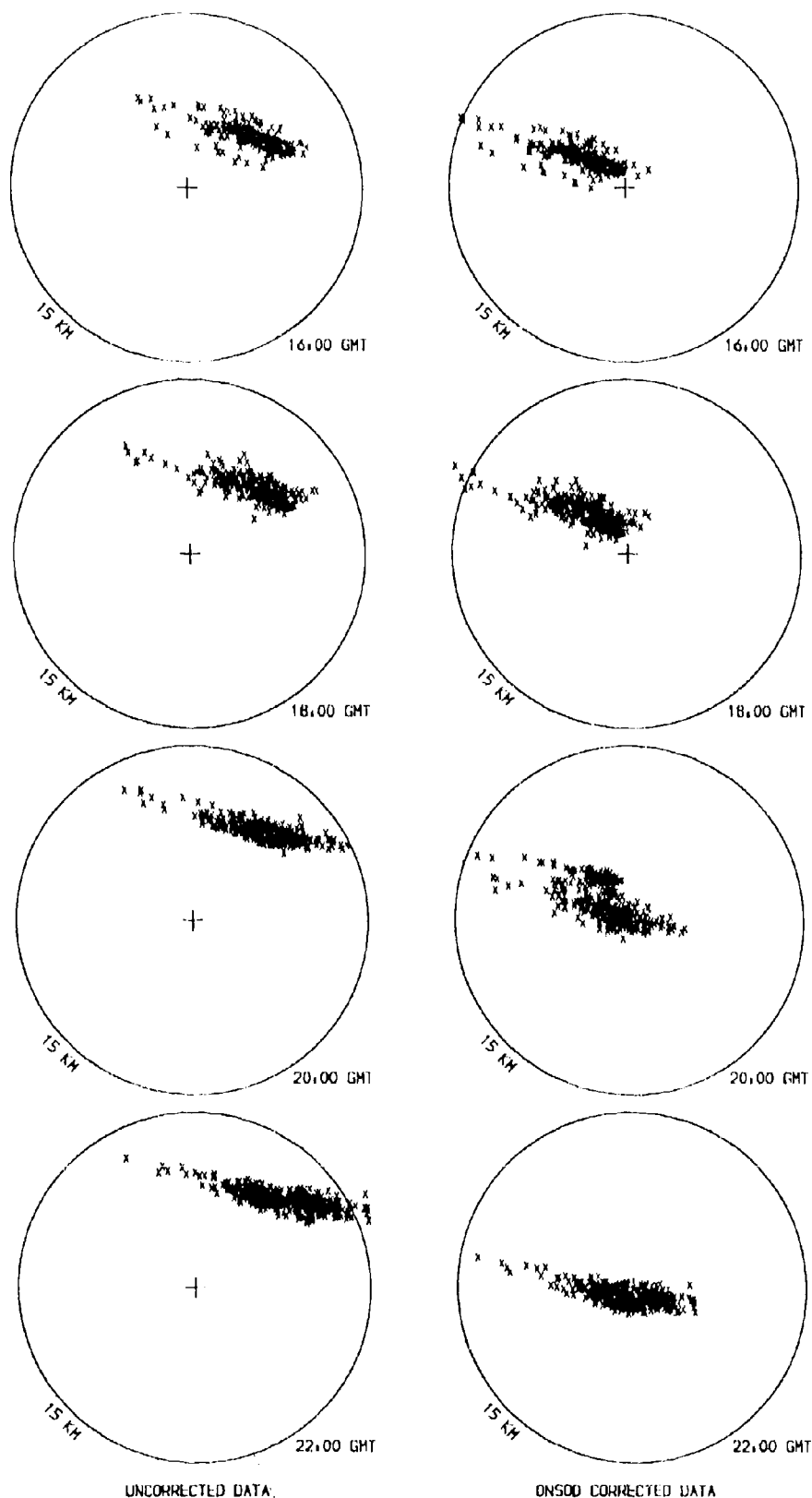
Figure 4(c)   Position fix distributions, Farnborough, Jan.1978–June 1979,
15.6 kHz, 16:00–22:00 GMT.

UNCORRECTED DATA                    ONSOD CORRECTED DATA

Figure 5(a)   Position fix distributions, Leicester, 24 March 1979-15 August
1979, 10.2 kHz, 00:00-06:00 GMT.

Figure 5(b) Position fix distributions, Leicester, 24 March 1979-15 August 1979, 16.2 kHz, 08:00-14:00 GMT.

UNCORRECTED DATA           ONSOD CORRECTED DATA

Figure 5(c) Position fix distributions, Leicester, 24 March 1979-13 August 1979, 10.2 kHz, 16:00-22:00 GMT.

Figure 6(a)  Position fix distributions, Butt of Lewis, 24 March 1979 14 August 1979, 10.2 kHz, 00:00-06:00 GMT.
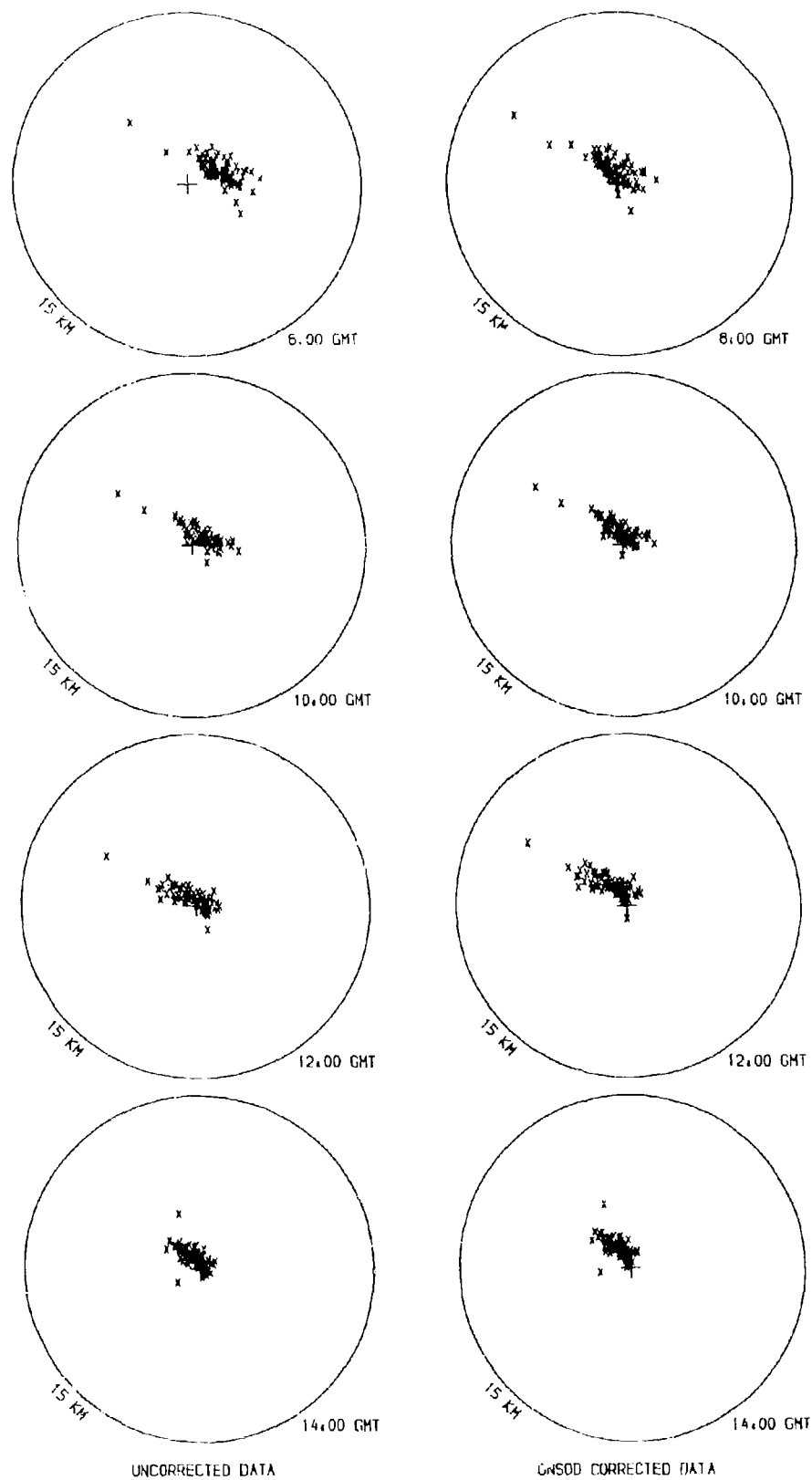
Figure 6(b)   Position fix distributions, Butt of Lewis, 24 March 1979-13 August
1979, 10.2 kHz, 08:00-14:00 GMT.
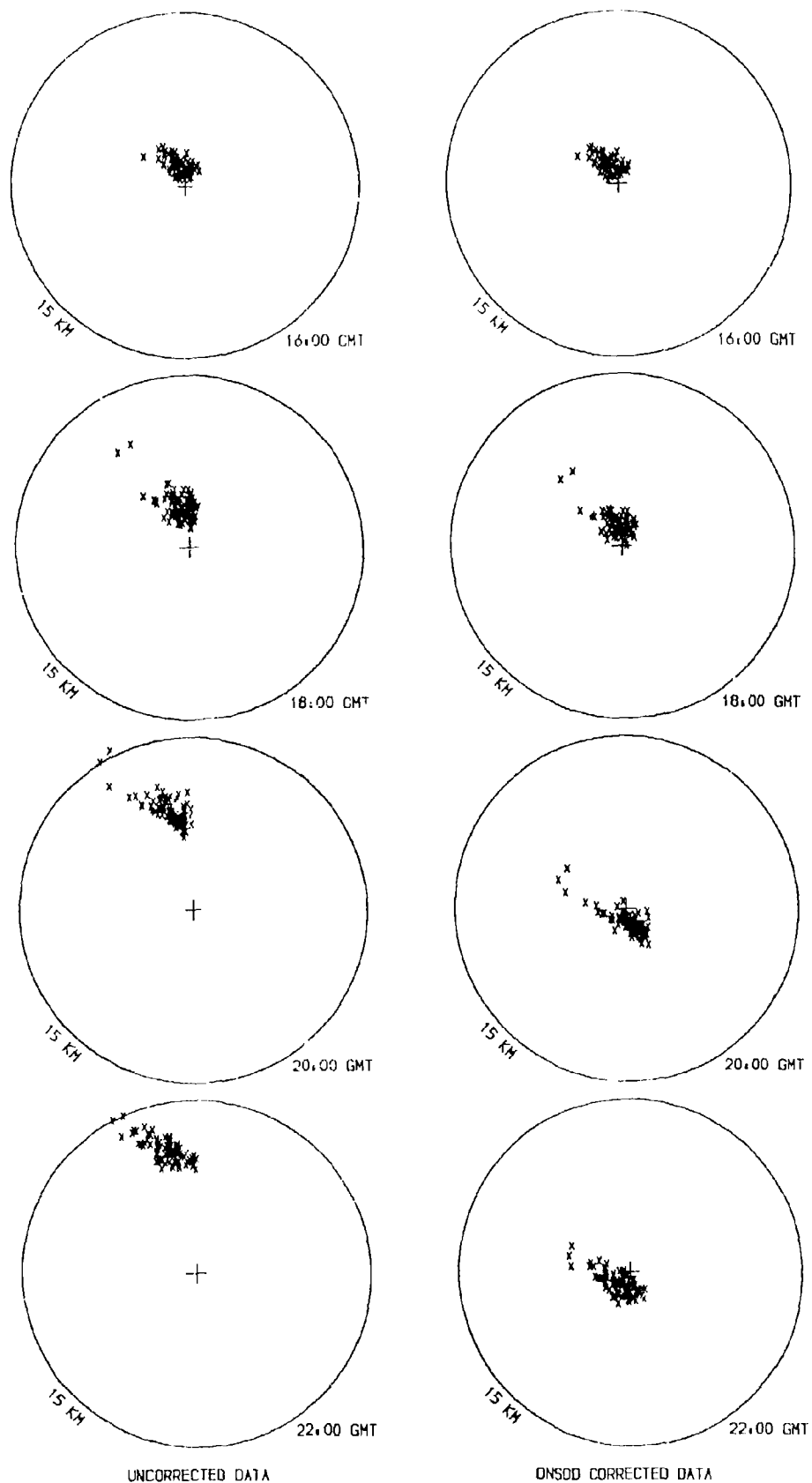
Figure 6(c)  Position fix distributions, Butt of Lewis, 24 March 1979–13 August
1979, 10.2 kHz, 16:00–22:00 GMT.
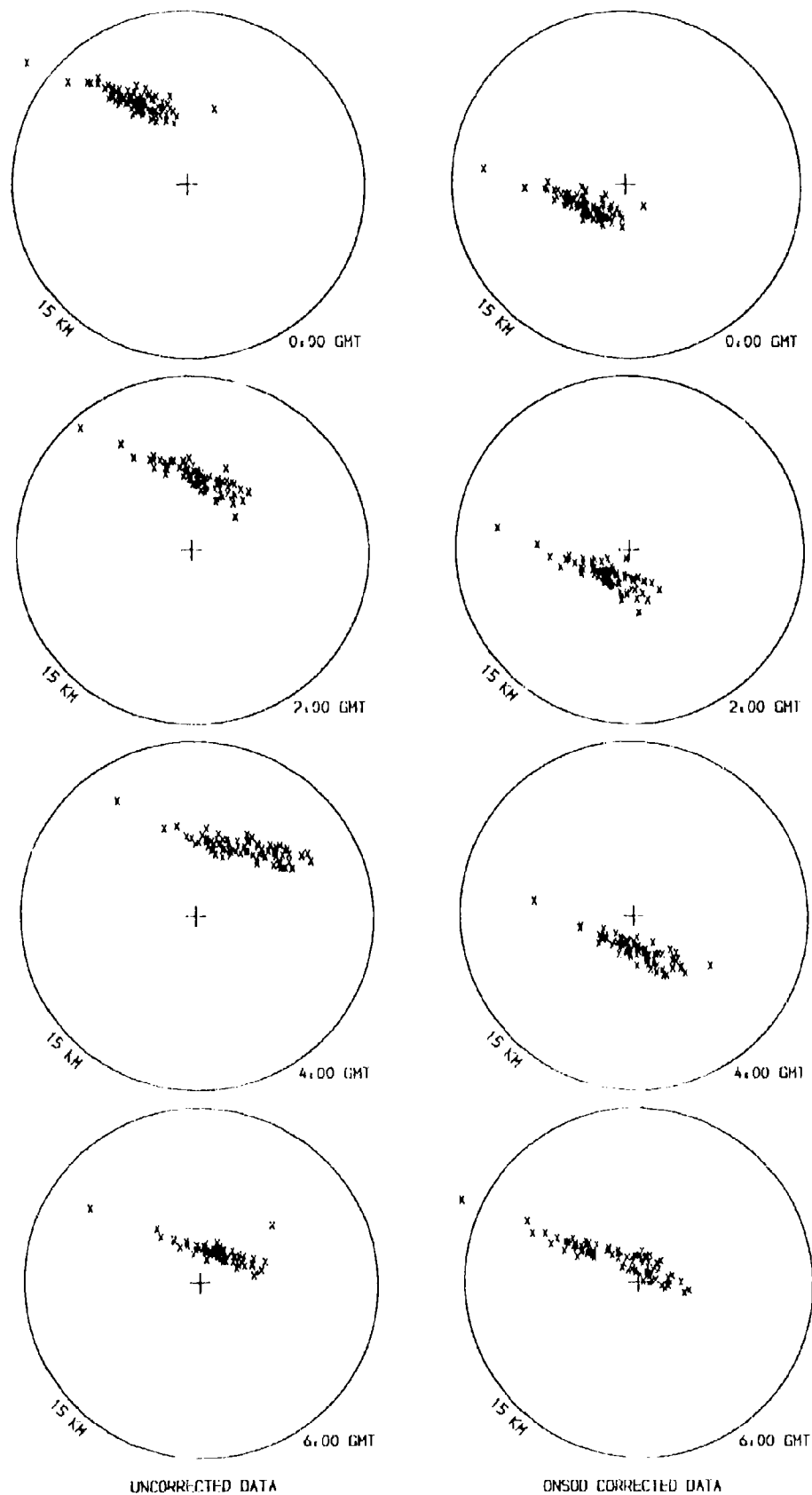
UNCORRECTED DATA

ONSOD CORRECTED DATA
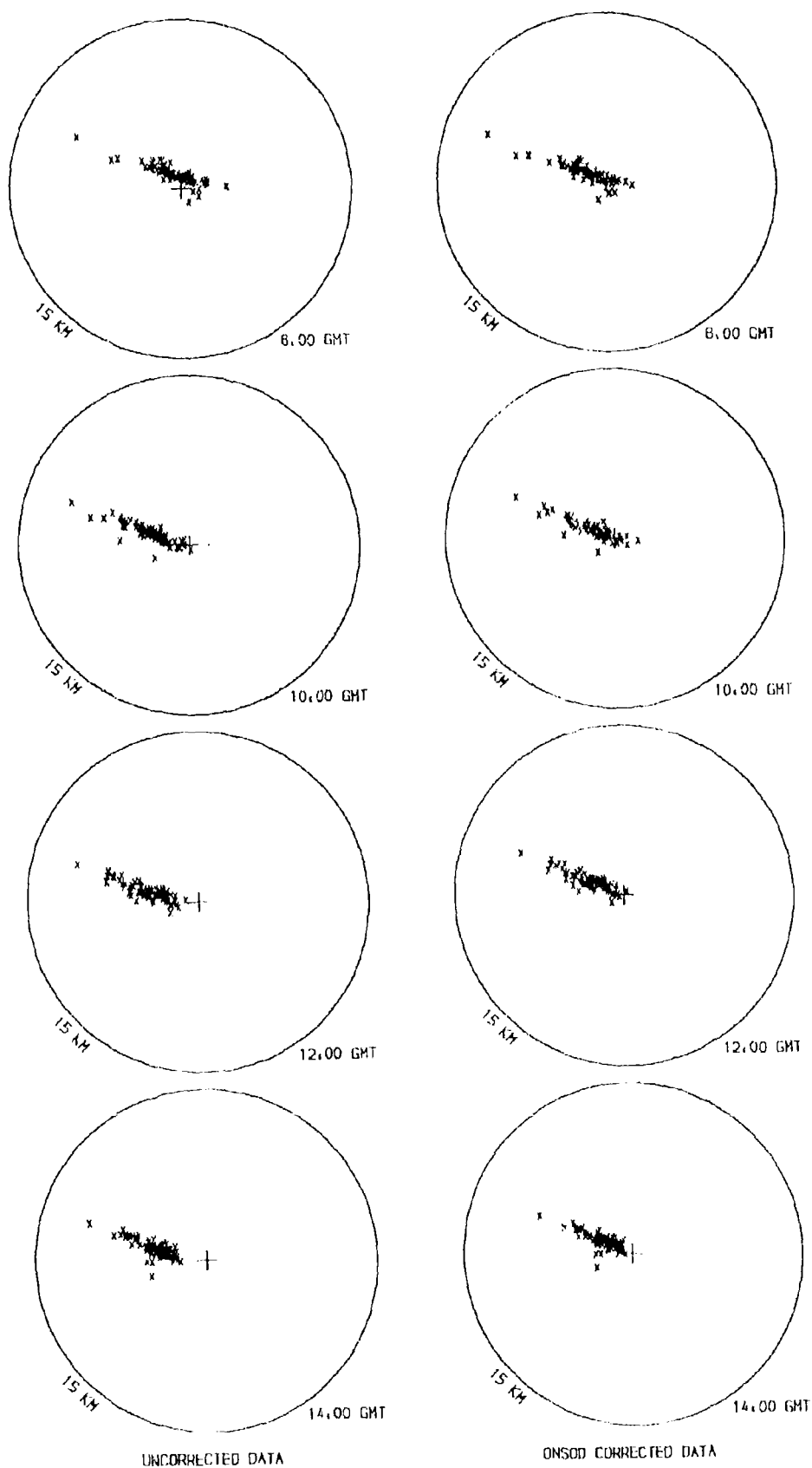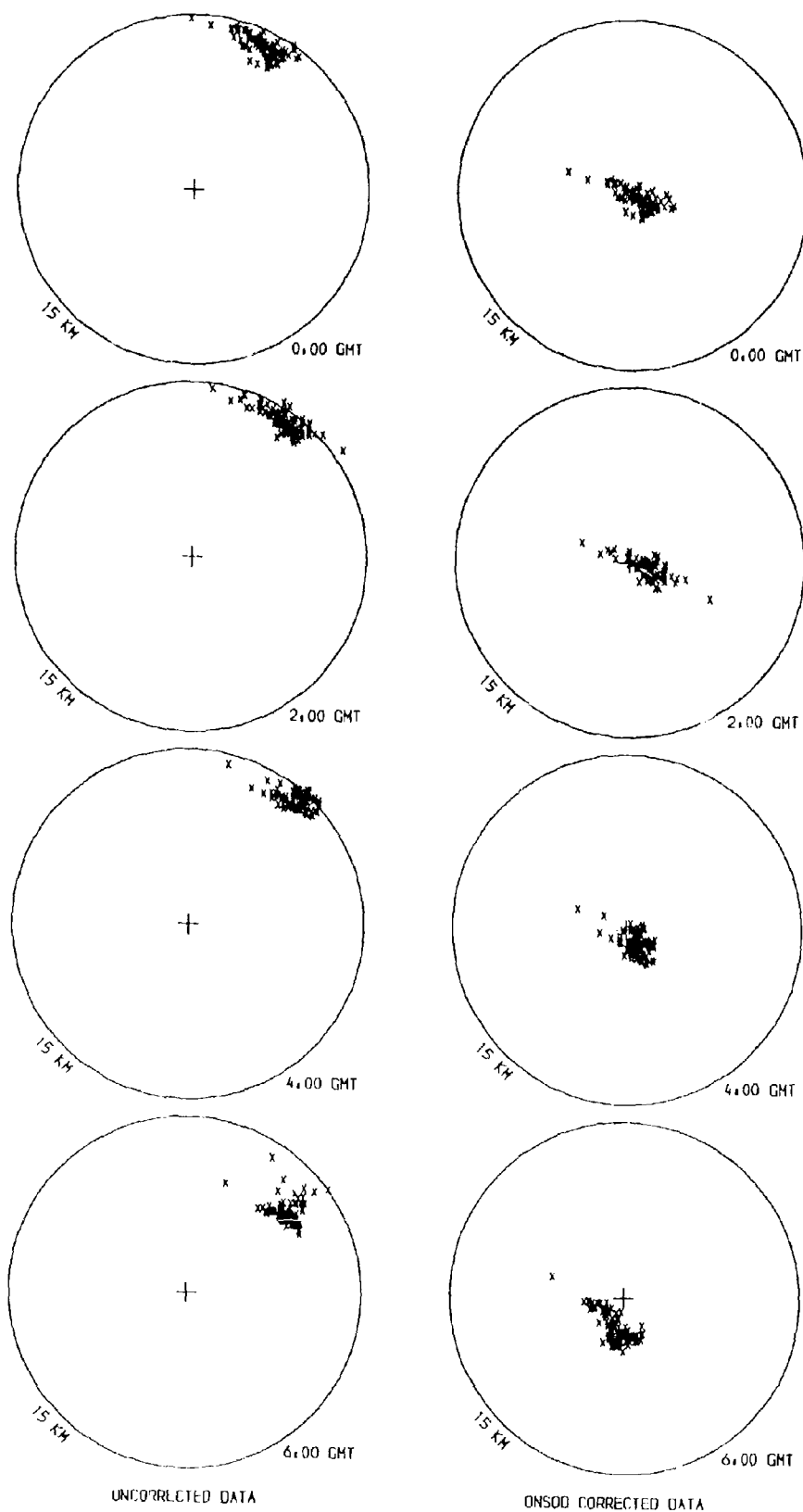
Figure 2(a)   Position fix distributions, Butt of Lewis, 14 March 1979-15 August
1979, 13.6 kHz, 00:00-06:00 GMT.

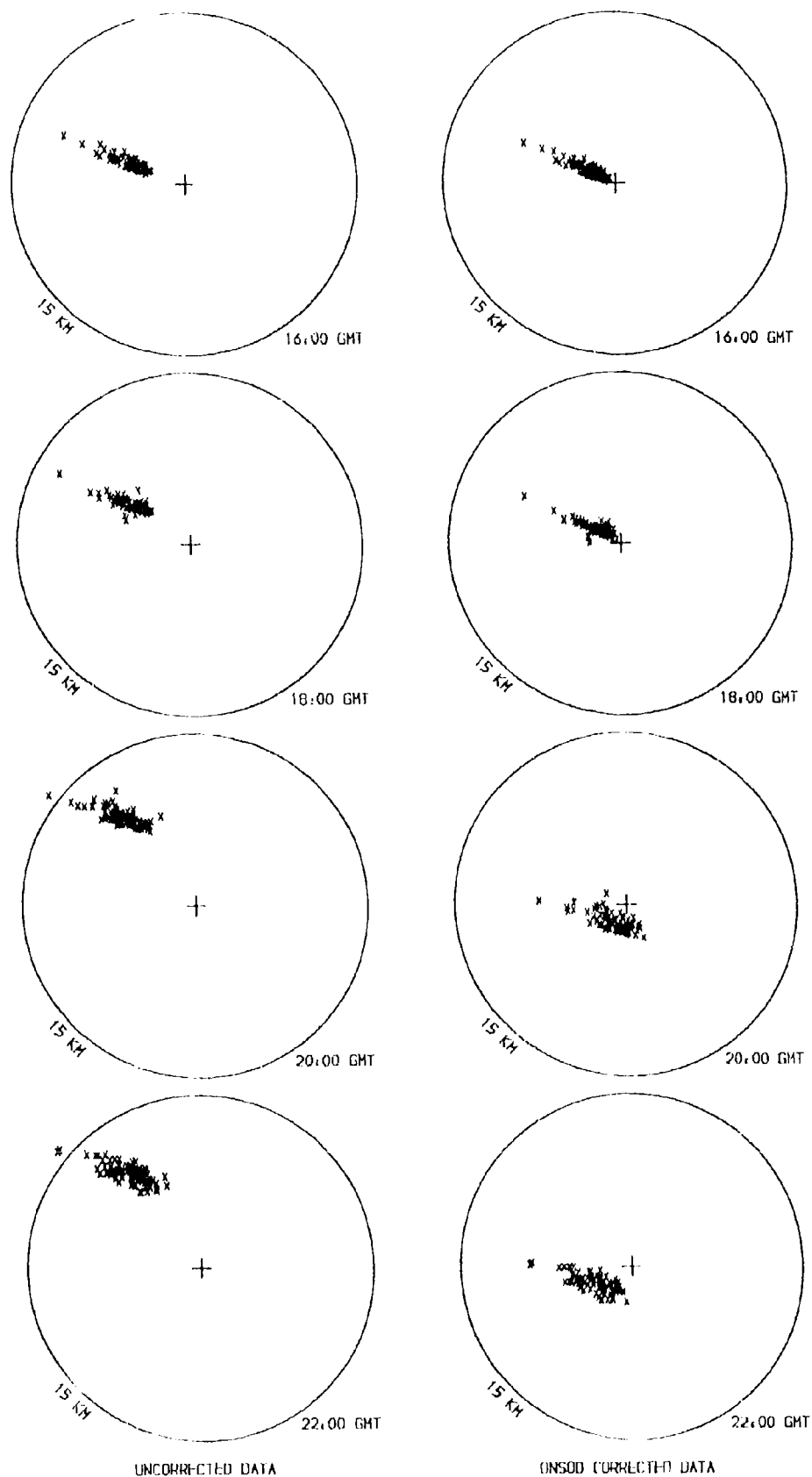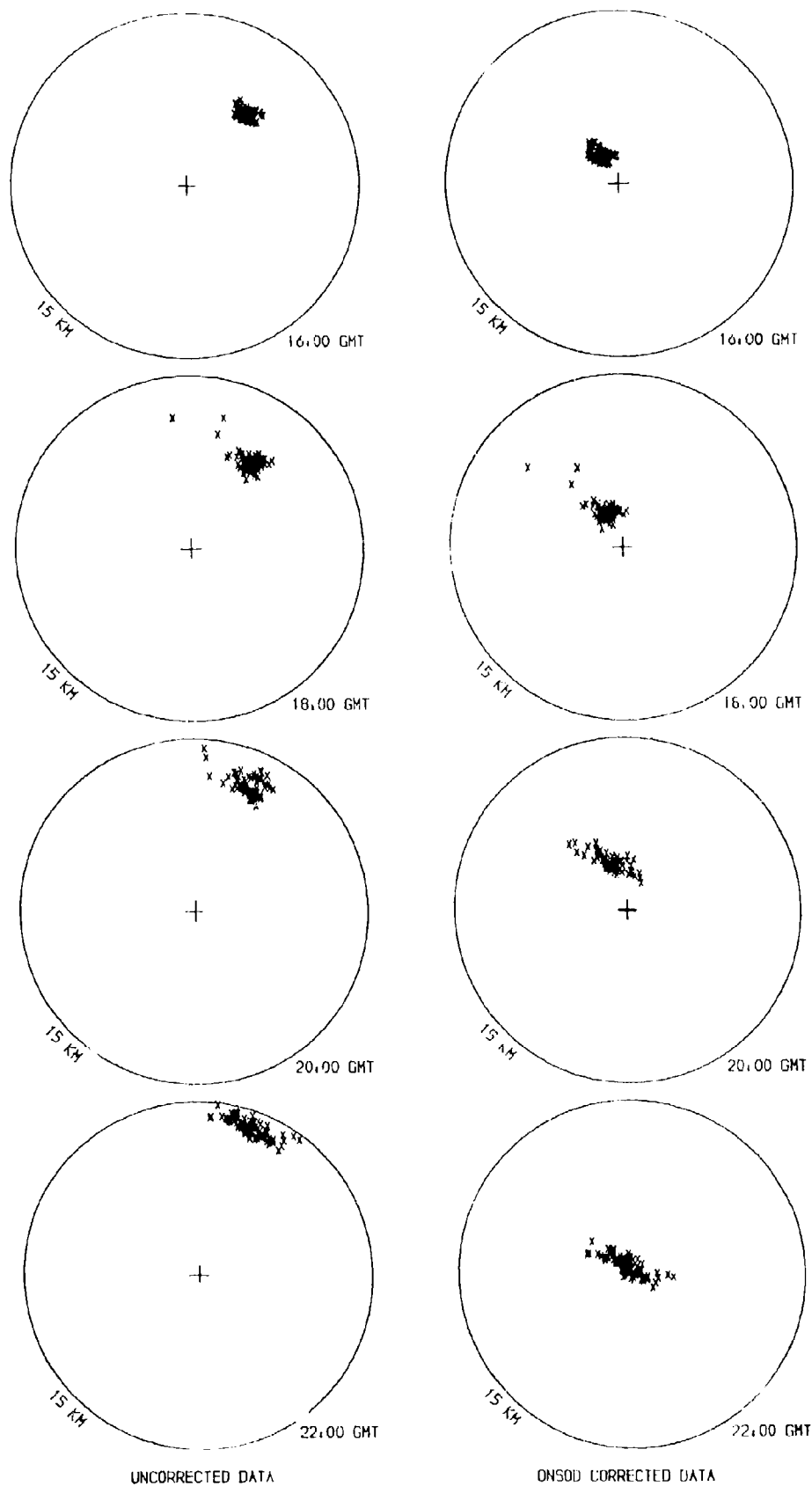Figure 7(b)  Position fix distributions, Butt of Lewis, 14 March 1979-13 August 1979, 12.6 kHz, 08:00-14:00 GMT.

UNCORRECTED DATA        ONSOD CORRECTED DATA
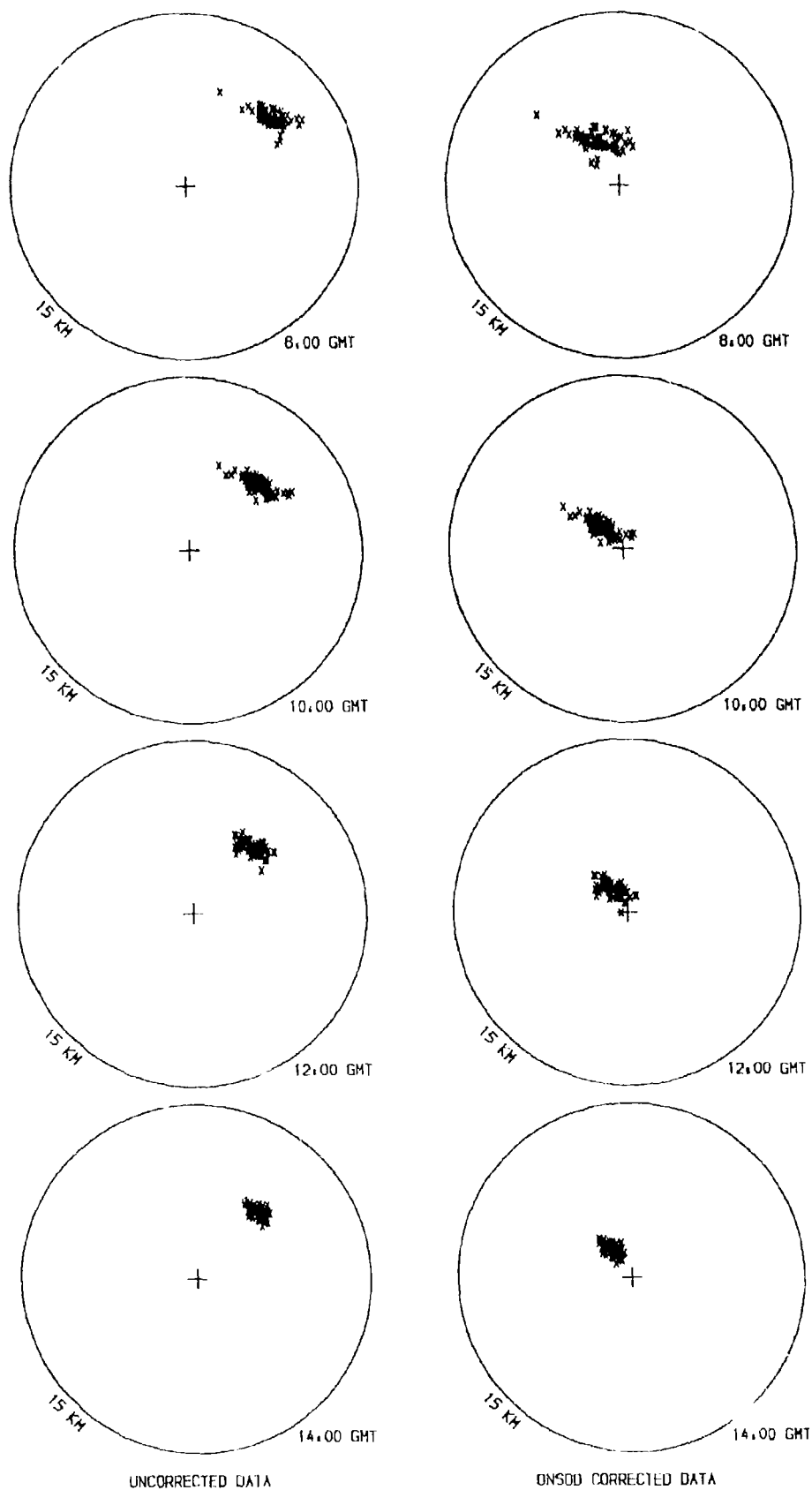
Figure 7(c)  Position fix distributions, Butt of Lewis, 14 March 1979-13 August 1979, 13.6 kHz, 16:00-22:00 GMT.
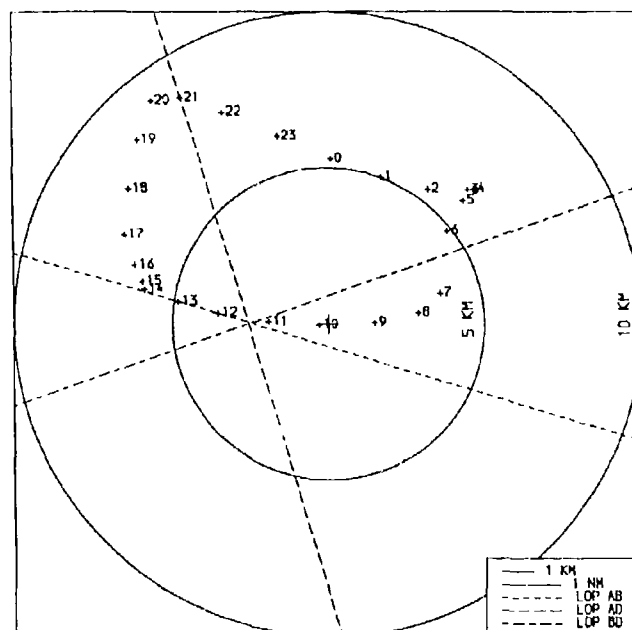
UNCORRECTED FARNBOROUGH HOURLY MEAN POSITION FIXES, JAN 1978 – JUN 1979, 10.2KHZ
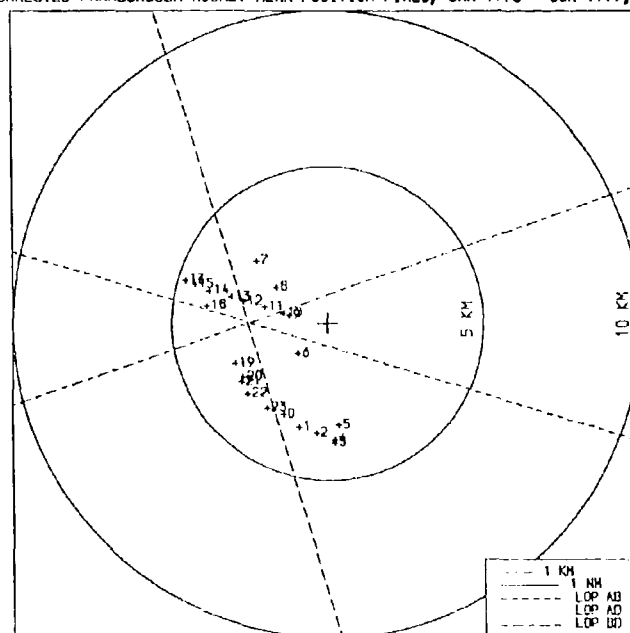
ONSOD CORRECTED FARNBOROUGH HOURLY MEAN POSITION FIXES, JAN 1978 – JUN 1979, 10.2KHZ

UNCORRECTED DATA      CORRECTED DATA

RADIAL STANDARD DEVIATION ABOUT THE MEAN POSITIONS
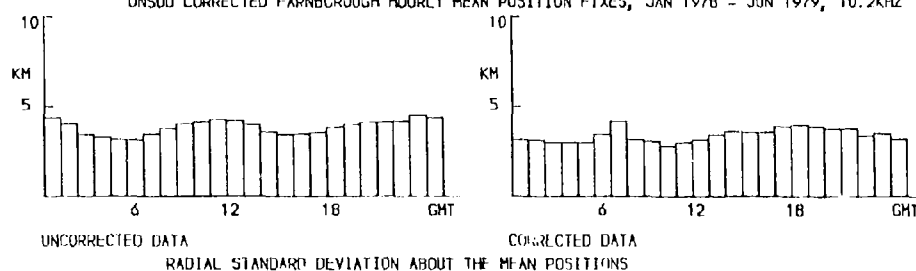
Figure 8      Farnborough hourly mean position fixes, Jan. 1978–June 1979, 10.2 kHz. Uncorrected data, corrected data and Radial Standard Deviations about the mean positions.
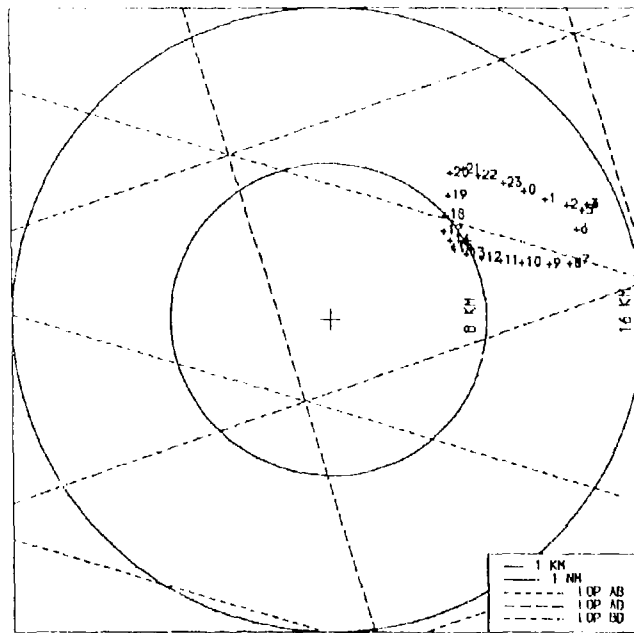
UNCORRECTED FARNBOROUGH HOURLY MEAN POSITION FIXES, JAN 1978 – JUN 1979, 13.6KHZ
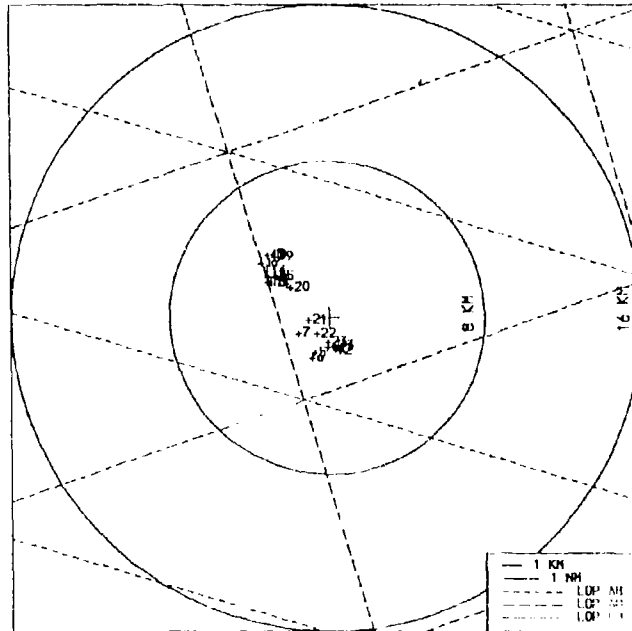
ONSOD CORRECTED FARNBOROUGH HOURLY MEAN POSITION FIXES, JAN 1978 – JUN 1979, 13.6KHZ

UNCORRECTED DATA

CORRECTED DATA

RADIAL STANDARD DEVIATION ABOUT THE MEAN POSITIONS
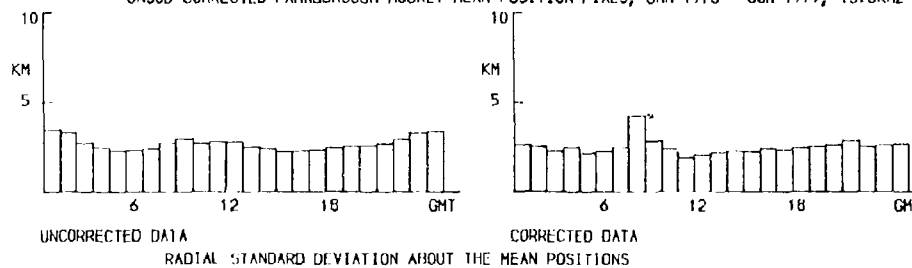
Figure 9    Farnborough hourly mean position fixes, 24 March 1979-14
            August 1979, 13.6 kHz.  Uncorrected data, corrected data and
            Radial Standard Deviations about the mean positions.
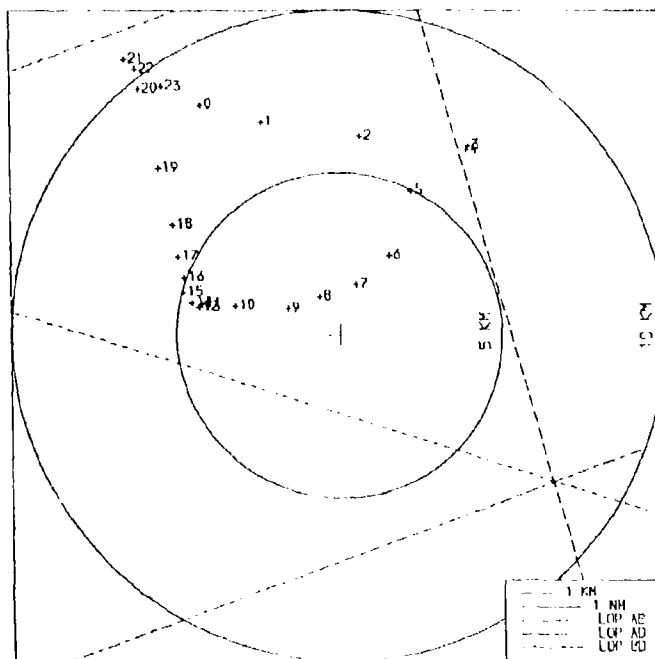
UNCORRECTED LEICESTER HOURLY MEAN POSITION FIXES, 24/3/79 TO 13/8/79, 10.2 KHZ
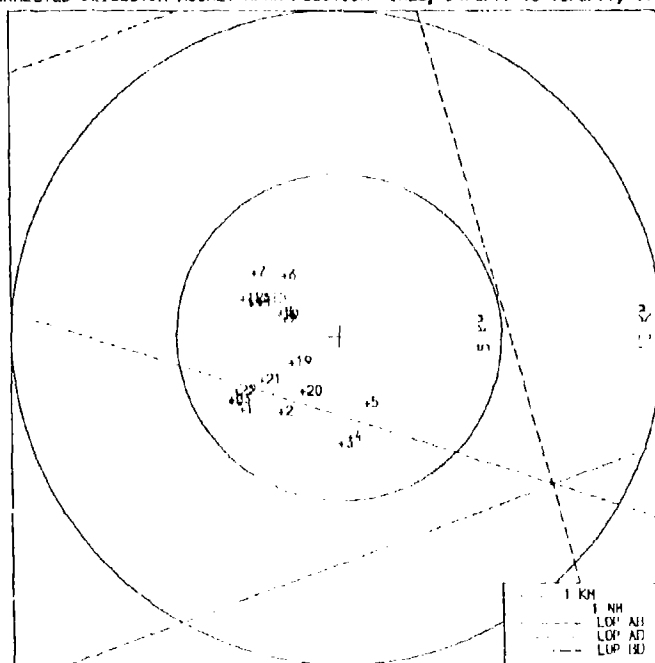
ONSOD CORRECTED LEICESTER HOURLY MEAN POSITION FIXES, 24/3/79 TO 13/8/79, 10.2 KHZ

UNCORRECTED DATA

CORRECTED DATA

RADIAL STANDARD DEVIATION ABOUT THE MEAN POSITIONS
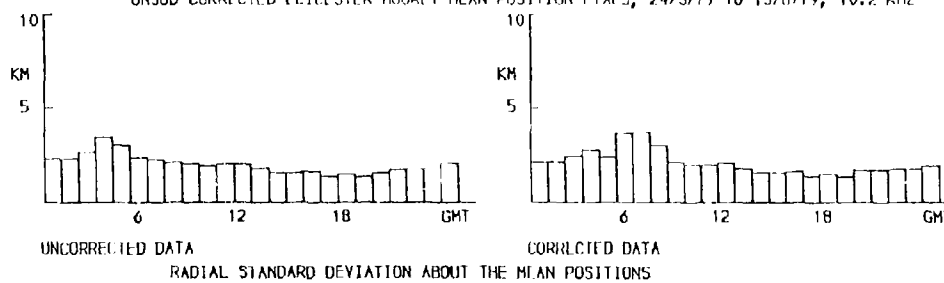
Figure 10    Leicester hourly mean position fixes, 24 March 1979-13
            August 1979, 10.2 kHz.  Uncorrected data, corrected data and
            Radial Standard Deviations about the mean positions.

UNCORRECTED BUTT OF LEWIS HOURLY MEAN POSITION FIXES, 24/3/79 TO 13/8/79, 13.6KHZ

ONSOD CORRECTED BUTT OF LEWIS HOURLY MEAN POSITION FIXES, 24/3/79 TO 13/8/79, 13.6KHZ
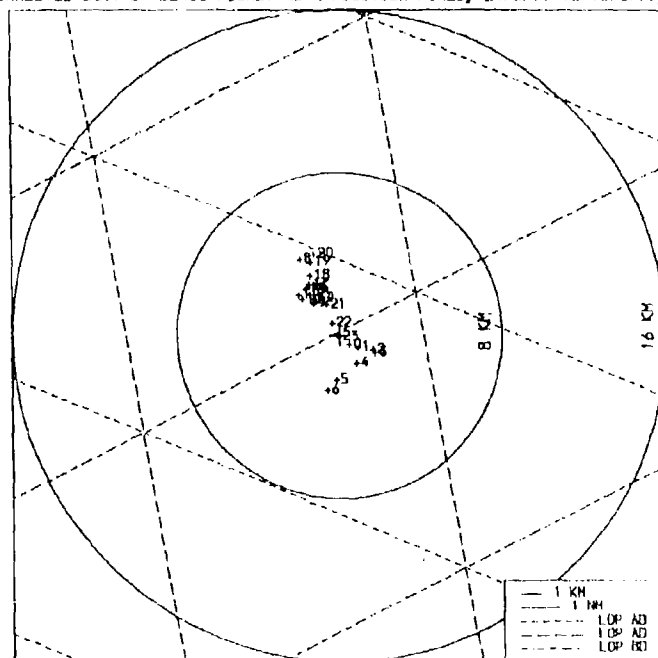
UNCORRECTED DATA

CORRECTED DATA

RADIAL STANDARD DEVIATION ABOUT THE MEAN POSITIONS
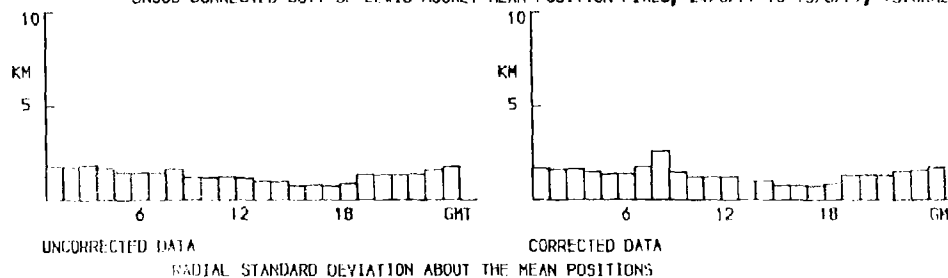
Figure 11    Butt of Lewis hourly mean position fixes, 24 March 1979-13
            August 1979, 10.2 kHz. Uncorrected data, corrected data and
            Radial Standard Deviations about the mean positions.

UNCORRECTED BUTT OF LEWIS HOURLY MEAN POSITION FIXES, 24/3/79 TO 13/8/79, 10.2KHZ

ONSOD CORRECTED BUTT OF LEWIS HOURLY MEAN POSITION FIXES, 24/3/79 TO 13/8/79, 10.2KHZ
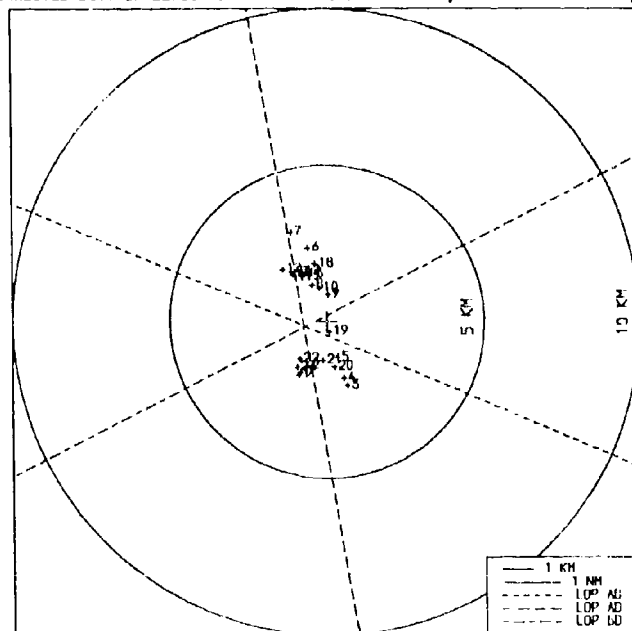
UNCORRECTED DATA

CORRECTED DATA

RADIAL STANDARD DEVIATION ABOUT THE MEAN POSITIONS
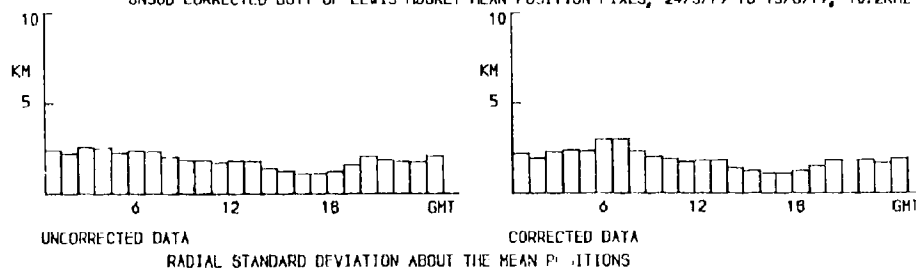
Figure 12    Butt of Lewis hourly mean position fixes, 24 March 1979–
13 August 1979, 13.6 kHz.  Uncorrected data, corrected data
and Radial Standard Deviations about the mean positions.
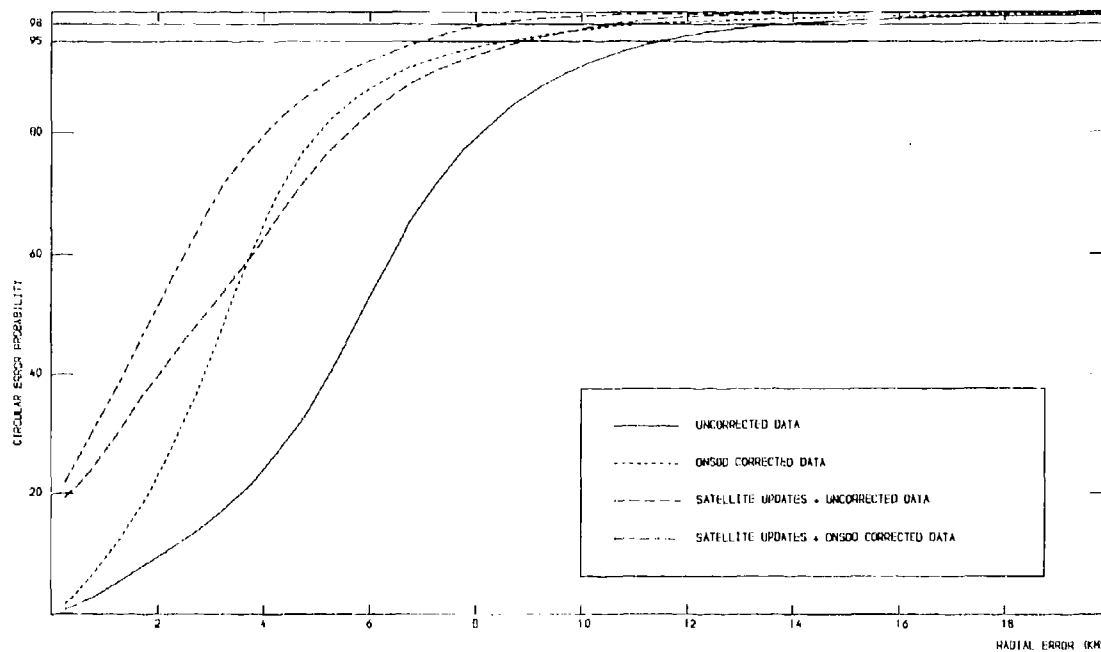
Figure 13    Radial error distributions at Farnborough, Jan. 1978–June
1979, 10.2 kHz.  Satellite updates every 6 hours.
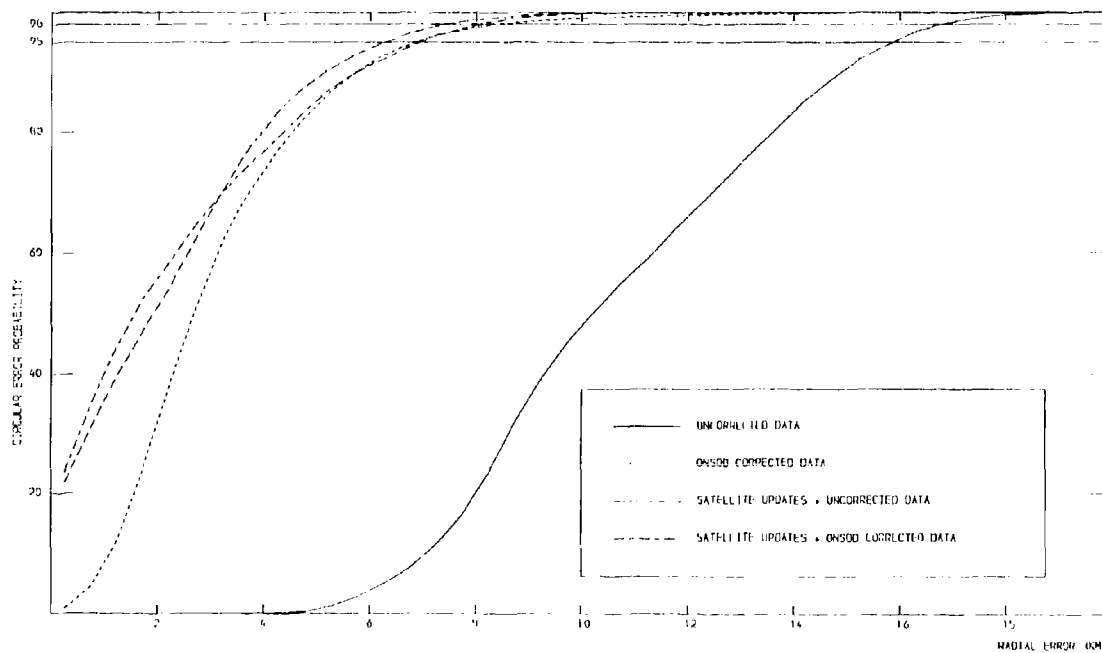


Figure 14    Radial error distributions at Farnborough, Jan. 1978–June
1979, 13.6 kHz.  Satellite updates every 6 hours.
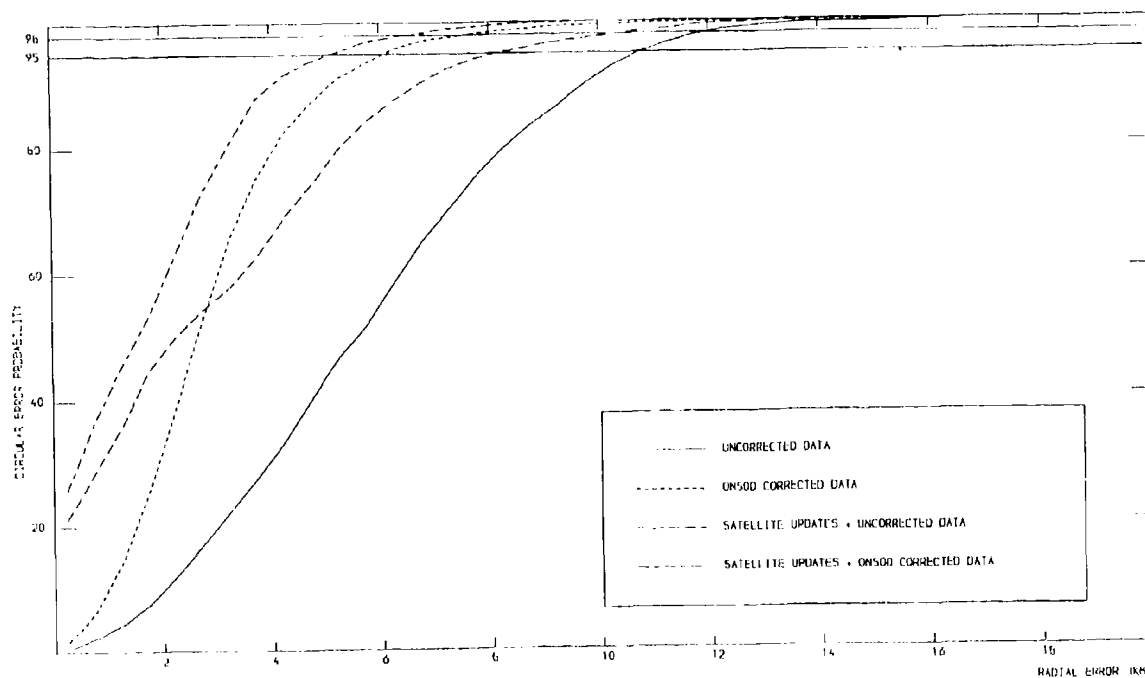
Figure 15    Radial error distributions at Leicester, 24 March 1979–
13 August 1979, 10.2 kHz.  Satellite updates every 6 hours.
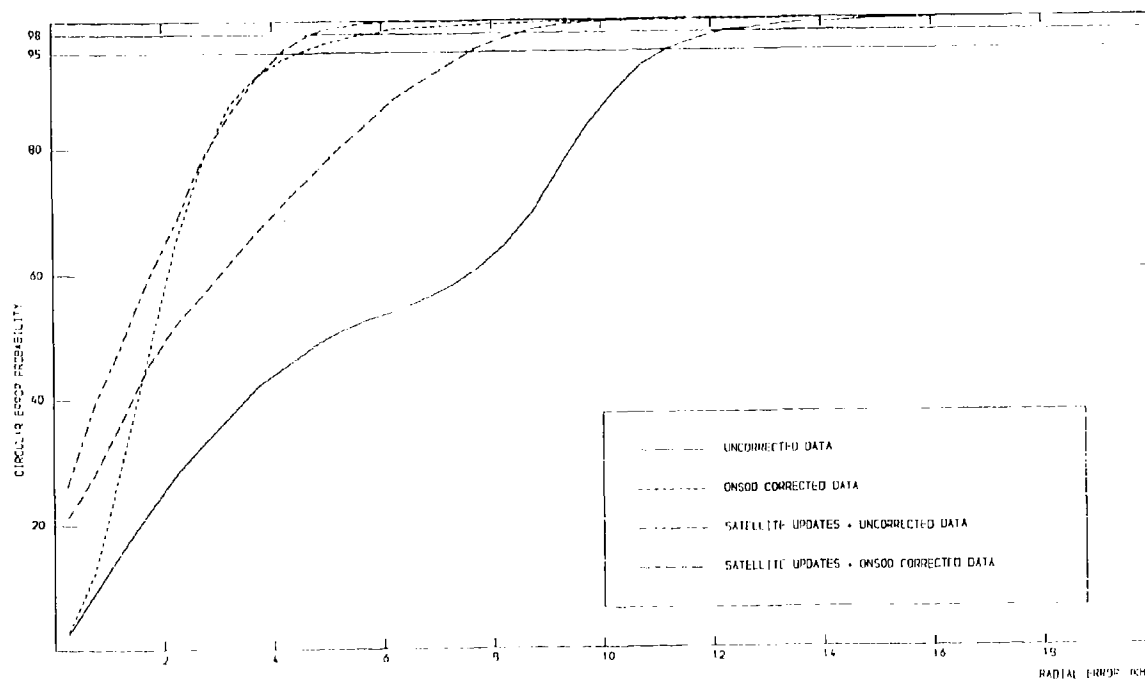


Figure 16    Radial error distributions at the Butt of Lewis, 24 March
1979–13 August 1979, 10.2 kHz.  Satellite updates every 6 hours.
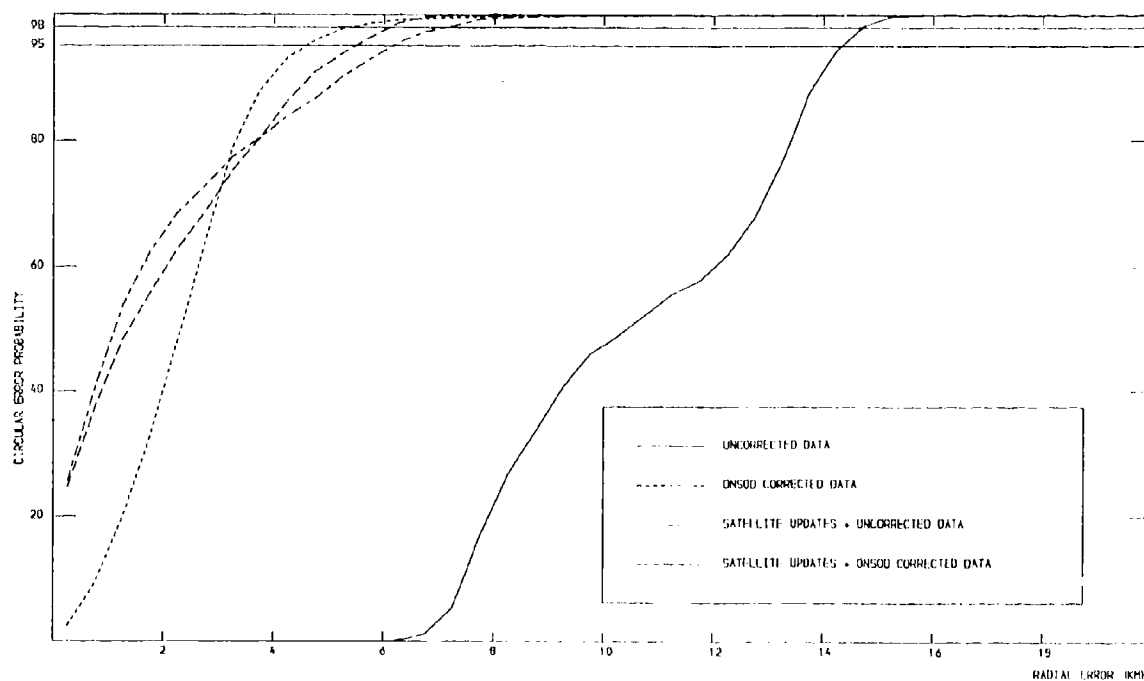
Figure 17    Radial error distributions at the Butt of Lewis, 24 March
1979-15 August 1979, 13.6 kHz.  Satellite updates every 6 hours.

# THE USE OF VLF COMMUNICATIONS FOR NAVIGATION

by

C.D. Hardwick
Flight Research Laboratory
National Aeronautical Establishment
National Research Council of Canada
Ottawa, Ontario K1A OR6, Canada

## Summary

This paper outlines current methods of VLF navigation and makes necessary comparisons with other systems. Some performance results are presented, both for typical stand-alone systems and for one that is optimally integrated with a simple Doppler sensor. Finally, a small and logical modification to the stations is suggested that would greatly enhance the effectiveness of VLF navigation.

## Introduction

The extensive redundant coverage of the world by signals from VLF Communication stations whose carriers are cesium stabilized to about $1\times10^{-12}$, affords a simple and inexpensive method of navigation. This navigation capability is particularly useful in remote areas where there is no other form of radio navigation available and in some cases, can relieve government agencies of the huge expense of providing radio nav facilities. Figure 1 shows typical coverage from one of the more powerful transmitters. (Hauser, J.P., 1974).

## Transmission Characteristics

The VLF Comm. Stations (Table 1) are operated primarily by the U.S. Navy for communicating with NATO surface and submarine vessels, although GBR has time keeping and other functions as well. Operation is continuous except for four to six hours a week of regularly scheduled maintenance and each station has a daily retuning period of 10 minutes. There is considerable redundancy in the stations' power amplifiers so that unscheduled outages due to lightning striking the massive antenna structures (a very common occurrence),are usually kept to less than 30 seconds (Patch, H., 1975). Communication is by teletype using frequency shift keying (FSK) or more commonly, minimum shift keying (MSK), (de Buda, R., 1976).

## Receivers and Navigation Methods

A navigation receiver in its very simplest form consists of a short (and highly mismatched) antenna, a broad-band preamplifier, a selective phase-linear gain stage for each frequency of interest and finally, a narrow-band phase-lock loop (PLL) to track the phase of one of the two frequency components of the FSK or MSK.*

| Letter Designation | Call Sign | Location | Frequency (KHz) | ERP (KW) |
|---|---|---|---|---|
| M | NAA | Cutler, Maine | 17.8 | 1000 |
| A | NSS | Annapolis, Maryland | 21.4 | 400 |
| W | NLK | Jim Creek, Wash. | 18.6 | 130-250 |
| L | NPM | Lualualei, Hawaii | 23.4 | 630 |
| J | NDT | Yosami, Japan | 17.4 | 40 |
| S | NSS | North West Cape, Australia | 22.3 | 1000 |
| R | GQD | Anthorne, U.K.** | 19.0 | 80 |
| G | GBR | Rugby, U.K. | 16.0 | 250 |
| 0 | JXN | Helgeland, Norway | 16.4 | 150 |

** Not cesium stabilized

### TABLE 1 - VLF COMMUNICATIONS STATIONS

If the phases of a minimum of two stations are compared against a frequency standard (or clock) of at least $1\times10^{-10}$ stability, navigation is possible in circular geometry across the face of the earth (Fig.3a). If the receiver's clock is of lesser quality, the addition of a third station's phase allows clock error to be calculated; this is equivalent to navigating in hyperbolic geometry (Fig. 3b). In either mode, it is normal to use more than the minimum number of stations, giving an over-determined set of equations that is solved by some weighted least squares method, with each station's weight usually being a function of geometry, signal to noise ratio and propagation factors. Because distances across the earth from observer to the stations are large, a good model of the geoid is required in order to compare expected phase distances with those given by the receiver; the navigation equations are solved using plane trigonometry to adjust the expected position to that corresponding to the phase measurements and one has a very simple VLF navigation system.

It should be noted that because the carriers of the VLF stations are not necessarily related to the epoch, phase measurements must always be made relative to a known starting position. In a moving vehicle, if phase tracking of one station is temporarily lost, its hardware or software tracking loop must

---

* Because each sideband of MSK switches $\pm180^{0}$ in phase to give a four-state code, a frequency doubler is usually used before the gain stages to give unambiguous phase at either sideband.

be "told" where it is within ½ wavelength using circular geometry (or within ¼ wavelength in hyperbolic mode); this is usually possible through the position keeping capability of the remaining stations or by some other on-board system capable of short-term navigation such as Doppler/heading reference. If all VLF signals in a stand-alone system are lost, nothing can be done except to reinitialize it at a known position.

## Propagation Effects

The observed phases of VLF signals are subject to predictable effects such as diurnal change of the ionosphere, long-path signal interference with the (normal) short path signal and higher mode effects close to the transmitter (Belrose, J.S., 1968). A certain amount of care in selection of stations and particularly the elimination of any station whose reception path is subject to a moving day-night terminator, can minimize these problems. However, the unpredictable effects such as sudden iono-spheric disturbances (SID's) or polar cap anomalies (PCA's) limit the accuracy of a stand- lone VLF nav system; these effects are somewhat moderated by the use of more than the minimum number of signals, in that the effect of a SID, for example, is not necessarily highly correlated over all signal paths.

## Accuracy

There is not a large database whereby firm statistics for expected VLF accuracy can be set. This is particularly true for operation where signal paths are predominantly in darkness. Project "Speckled Trout" (1980), flying mainly trans-Atlantic and South West Pacific routes over a six month period, reports average circular error for their VLF system of 3.44 Km (27 flights for 104.4 hours).

Another example (mainly daytime paths) that can be considered typical is for two survey operations, totalling thirty flights of three to four hours duration*. The terminal errors were as follows:

|                      | Average Radial Error | Std. Deviation |
|----------------------|----------------------|----------------|
| Caribbean Area       | 4 1  Km              | 3.7  Km        |
| Canadian High Arctic | 2.52 Km              | 1.96 Km        |

Occasional short term position errors of up to 400m can often be observed, lasting from one to five minutes.

In our experience, the above results can be considered typical. For nighttime, where the ionosphere is less well defined, errors can be expected to increase by about a factor of 1.5.

The last section of this paper shows how navigation accuracy can be greatly increased by using VLF in conjunction with another inexpensive source of navigation information.

## Comparison With Other Remote Area Nav Systems

To appreciate the advantages and disadvantages of VLF for remote area navigation, certain characteristics of several other contending systems must be briefly sketched.

a)    Global Positioning System (GPS). This system, with its predicted maximum accuracy in three dimensions of less than 10m, will undoubtedly meet the requirements of the vast majority of the world's navigators. However, the positioning and maintaining of 24 satellites is a very costly undertaking and the implementation dates keep slipping. Furthermore, accessibility to the entire system could be denied for strategic reasons to any user other than NATO military and the costs of user equipment are expected initially to be quite high.

b)    Inertial Navigation Systems. Although not radio based, these are attractive for remote area navigation; currently available systems give accuracies in the order of 1.8 Km/hr. Their disadvantage is that the error build-up with time is unbounded and their cost of acquisition and maintenance is high relative to other systems.**

c)    Decca and Loran-C. Systems of this type provide considerably more accuracy than VLF, with Loran-C giving about 300M day or night. Their disadvantage is that their coverage is currently limited to mainly Maritime areas. Typical maximum usable range is 2000 Km over sea water; to provide worldwide three-station coverage, particularly over low conductivity areas such as arctic tundra where the necessary ground wave is severely attenuated, would be a costly project involving many governments.

d)    Omega. We must pause longer here than with the previous systems because Omega and VLF Comm. navigation are logically complementary to each other, are adjacent in the VLF spectrum and share many common characteristics. Unlike VLF comm., Omega is not a continuous transmission (Swanson, E.R., 1975); four frequencies between 10.2 and 13.6 KHz are time shared over ten seconds between eight stations, seven of which are currently fully operational. Radiated power is limited to 10 KW to prevent long path inter-ference between stations in adjacent time slots on the same frequency and because of the problems associated with loading the antennas in the 200 milliseconds allowed between the nominal one second transmissions. The difference in radiated power between Omega and VLF comm. can result in a 20 to 30 db receiver S/N advantage for the latter, which can be very important for operation in areas of high background noise. There are, in fact, various areas where Omega coverage is a problem, such as the South Atlantic or, sad to say, the west central part of the U.S. and Canada. It is for this reason that most Omega system manufacturers are now providing VLF tracking as a back-up in such areas.

---

*    Data from the NAE Convair-580 aircraft.

**   A new generation of inertial systems is becoming available with accuracies of <0.18 Km/hr. This one order increase in accuracy will initially have a corresponding cost factor.

Because all Omega transmissions are carefully synchronized to the UTC epoch, it can be considered, in a limited sense, an absolute positioning system; initialization at a known point is not categorically necessary, which is an advantage compared to VLF. In a phase measurement navigation system, the lower the frequency, the greater is the distance between points of equal phase. In Omega, the maximum unambiguous distance is given by a hypothetical frequency derived from the difference of two of the signal frequencies, namely

$$11.333 \text{ KHz} - 11.05 \text{ KHz} = 0.2833 \text{ KHz with } \lambda = 1061 \text{ Km}$$

If assumed position is within $\frac{1}{4} \lambda$ or 265 Km of actual, correct position can be determined and the correct wavelength at all the Omega frequencies can be established. Unfortunately, this technique requires a minimum of six clean phase measurements (actual algorithms usually use correlated information from all the frequencies to build up a difference frequency) and in conditions of low S/N, where restart capability is most often needed, correct cycle identification does not always work (Beukers, J.M., 1974).

Another advantage that Omega enjoys over VLF is that propagation performance for the 10.2 and 13.6 KHz on a worldwide basis has been extensively modelled (Swanson, E.R. and Brown, R.P., 1972) and coefficients and submodles have been continuously updated since 1970 using force-fit techniques based on a large bank of observed data (Gupta, R., 1981). A numerical model for propagation at the higher VLF frequencies is said to exist, but it not in the public domain. Since all Omega manufacturers use predicted propagation corrections (PPC's) in one form or another, a given Omega solution can be expected to have the edge on corresponding VLF solution with the important proviso that there is adequate Omega coverage. A series of flights covering most of the continental United States using Omega augmented with VLF and Omega only (unfortunately not concurrently) gave

|        | Ω/VLF    | Ω Only   |                    |
|--------|----------|----------|--------------------|
| R.M.S. | 4.07 Km  | 3.33 Km  |                    |
| C.E.P. | 2.78 Km  | 2.22 Km  | (SaKaran, F.C., 1981) |

In the past, one of the biggest differences between VLF Comm and Omega has been in complexity and performance of mobile receivers. For the VLF, a hardware second order tracking loop (i.e. zero phase error for a constant velocity), with a very narrow bandwidth and thus, good noize immunity, is simple to mechanize. For Omega, a similar hardware filter that has to slew to the correct phase, achieve lock at the start of a one second burst and then track correctly, must have a wider bandwidth and the mechanization can be quite difficult. Until recently, Omega receivers have been dependent on rather high quality velocity information ("rate aiding") from some other system to achieve quieter phase tracking. However, software tracking loops such as now can be mechanized in microprocessor-based receivers are flexible and can use the time skew of the Omega information to generate the equivalent of velocity data to allow tracking at effectively narrow bandwidths.

## Non-Technical Problems Associated with VLF Navigation

VLF Navigation has not found wide acceptance except with those who actually use it. The reason for this is largely non-technical. Navigation is a highly polarized discipline, mainly because equipment manufacturers and agencies that underwrite the cost of developing a particular system have an understandable interest in protecting their investments against competing systems. In the case of VLF, however, there were no facility development costs to the navigation community (it was a windfall) and for a number of years, there were only two small manufacturers of VLF navigation systems.

Advocacy of a particular system unfortunately permeates government regulatory and military agencies and it is not uncommon to find vigorous, single-minded policies to this effect. For example, the U.S. Navy, the underwriter of Omega development, was not pleased that their communications stations were being used successfully for world wide navigation for a number of years before Omega became operational.

Between the U.S. Navy Communication Command and the VLF navigators, there is a tacit understanding that the requirements of the latter group will be accommodated provided this is not taken as a commitment to navigation--i.e. operational flexibility must be retained. As a matter of record, retuning times have been staggered between stations to provide continuity of navigation coverage and the U.S. Naval Observatory receives and forwards forecasts of non-routine shutdowns and of reports of non-scheduled outages. This sort of arrangement, however effective, does not meet the requirements of regulatory agencies that approve, for example, air traffic separation limits based on navigational capability and who require that a radio navigation aid be committed to its task without qualification. However, for those who actually use the VLF navigation facility, the current arrangement is quite satisfactory.

## A Small Change to Improve Greatly the Usefulness of VLF Comm Signals

As stated previously, the carriers of the VLF stations, although cesium stabilized, are not related to the UTC epoch. However, in order to allow coherent reception techniques, the mark and space frequencies are controlled to be self-coherent, with the transition from one to the other always occurring at zero phase (Fig. 3). The point at which transition occurs corresponds to a phase-stable signal, commonly 50 or 100 Hz depending on type of modulation and data rate. At NAE, a decoder (Hardwick, C.D. and Barszczewski, A., 1976) was built to reconstruct and track the 50 Hz signals from NAA (Cutler) and from the late lamented NBA (Panama, 24.0 KHz), when both these stations were still transmitting FSK. Over the short periods we ran the experiment, it was observed that the 50 Hz had very close to the same phase stability as its carrier. This led to the conclusion that if the VLF carriers (and thus the 50 Hz transitions) were related to the epoch, the 50 Hz signal, whose phase information would be unambiguous over approximately 6000 Km*, would be exceedingly useful for navigation and time keeping.

---

* For MSK at the current baud rate of 200, the shift is ±50 Hz, resulting in a 100 Hz signal. This would give 3000 Km of unambiguous phase.

Private conversations between the author and U.S. Naval Research Laboratory personnel indicate that it would not be difficult to keep the transmitters related to UTC, since the cesium standards, far field monitors and control circuitry are all in place for the purpose of keeping the FSK or MSK phase coherent. It would be a matter of resetting certain counters in the modulators and letting them start in synchronization with a cesium derived signal on transmitter start-up. A simple mechanization would cost an estimated \$300 to \$1000 per station* which is very little compared to capital and operating costs. Zero phase at each transmitter would probably not be tied to the UTC second as is the case for the Omega stations, but the offset would be fixed, measurable and monitorable**, which would be just as useful.

The applications of a time stabilized low frequency modulation are very numerous, the most important of which are as follows:

1. World-wide time/keeping capability to several μSec.

2. "Absolute" worldwide hyperbolic positioning with ambiguity ≈ 1500 or 750 Km
   (i.e., $\lambda/4$) for FSK and MSK respectively.

3. A potential aid to Omega lane resolution difficulties.

4. Unambiguous position reporting via satellite for Search and
   Rescue, vehicle or ship location, etc. etc.

The navigation (or time-keeping) accuracy obtainable using 50 to 100 Hz difference frequencies would be dependent on the degree to which propagation anomalies over a given path correlate as frequency difference decreases. Intuitively, it would seem that correlation should increase with decreasing frequency difference and this has been verified to some extent in low power experiments around 12 KHz with difference frequencies as low as 200 Hz (Rawles, A.T. and Burgess, B., 1967). Records using 20.0 and 20.5 KHz (more representative of the VLF Comm frequencies) show a very stable difference frequency on the daylight path from Boulder to Ottawa, a 4 μSec wander during nighttime and a 8 μSec peak-to-peak disturbance during the dawn transition, the latter corresponding to a 28 μSec shift in the individual carriers (Belrose, J.S., 1968). The same experiment indicated that using a 100 Hz difference (19.9 or 20.0 KHz), the dawn perturbation of the difference signal was still observable but very much smaller.

With the VLF Comm stations in their present configuration, adequate experimental data could be gathered to define performance at small difference frequencies. If there were a prospect of the stations being stabilized as suggested, there might then be sufficient incentive for such experiments to be carried out.

## Example of VLF Accuracy Using Optimum Integration of Nav Information

It is evident that no navigation system (including VLF) is ideal. However, the good characteristics of one system can complement those of another provided the data are handled in a optimal fashion. To date, there has been little tendency in this direction on the part of manufacturers, primarily because each is intent on optimizing his own particular system.

The example that follows is the result of blending Doppler velocity/heading reference with VLF phase data in a Kalman mechanization in the NAE Convair-580 research aircraft (Leach, B.W., 1981). Doppler gives good high resolution velocity data on the short term, but small velocity and heading bias errors quickly integrate to unacceptable position-errors on the longer term. On the other hand, VLF gives rather noisy short-term data, but its long term position accuracy is good provided that propagation changes (bias build-ups) can be detected. Figure 4 shows that Doppler/heading biases can be computed quite quickly; thereafter, a "calibrated" doppler system can recognize bias build-ups in the VLF phase data. In this example, the bias of station R (GQD, 19.0 KHz), which is not cesium stabilized and hence drifting in phase, was tracked and the station was actually usable for navigation. In Figure 5, the build-up of error using a Doppler-only mechanization, is evident. The second trace ("complementary filter") is the result of smoothing VLF with doppler and in the long term shows some improvement. The bottom trace ("smart" Kalman filter) shows the very bounded error when the filter is given a priori information (hence "smart") as to which stations are expected to be subject to propagation errors***. The *a priori* information on transmission path behaviour is given to the filter in the form of expected noise variance for each station and is obviously infinitely more compact than a detailed propagation model.

## Conclusion

VLF Communications provides a viable means of navigating in any part of the world and is particularly useful where dedicated nav aids are not available. As a stand-alone system, it is very cost-effective for the small user. It has not found favour with regulatory agencies, but the fact that there are now over 4000 airborne systems in operation (1981), attests to its usefulness.

Navigation performance improves proportionally to the amount of available raw data used in the solution, provided it is used in a near optimal manner, as illustrated by the foregoing VLF-Doppler example. Unfortunately, this approach can be non-cost effective because system manufacturers tend to concentrate on one source of data. One encouraging recent trend is the very logical integration of VLF and Omega data by a number of manufacturers.

---

\* This minimum system would require some input from an operator; a completely servoed system would be somewhat more expensive.

\*\* Possibly by the U.S. Naval Observatory?

\*\*\* At present, the filter cannot sort itself out if all the stations are expected to have equally variable phase biases. A smarter K.F. is being developed to do this.

The effectiveness of VLF navigation could be greatly increased by relating the FSK and MSK modulations of the Comm stations to UTC via their cesium frequency standards, a modification that would involve minimum expense. The result would be global absolute positioning and time distribution system that would have many useful applications.

References

1. Hauser, James P., et al, September 1974 — Coverage Predictions for the Navy's Fixed VLF Transmitters. NRL Memorandum Report 2884, Naval Research Laboratory, Washington, D.C.

2. Patch, H., et al November 20, 1975 — VLF Debate. Canadian Aeronautics and Space Institute, Ottawa.

3. de Buda, R. 1976 — Fast FSK Signals And Their Demodulation. Canadian Electrical Engineering Journal, Vol. 1, 1976.

4. Belrose, J.S. 1968 — LF and VLF Radio Wave Propagation. Section IV, AGARD Lecture Series "Radio Wave Propagation", July 1968.

5. Project Speckled Trout, 1980 — Report No. 80-3, 1st Airborne Command Control Squadron, Andrews AFB, Washington, D.C., 20331.

6. Beukers, J.M. 1974 — A Review and Applications of VLF and LF Transmissions for Navigation and Tracking. Navigation Vol. 21, No. 2.

7. Swanson, E.R. 1975 — Omega Format Optimization. NELC Technical Report, 1966, Naval Electronics Laboratory Center, San Diego.

8. Swanson, E.R. Brown, R.P. 1972 — Omega Propagation Primer. NELC Technical Note TN2101.

9. Gupta, P. Morris, P. 1981 — Performance of the Omega Propagation Correction Model with New Geomagnetic Sub-Models. Proceedings of the International Omega Association, Sixth Annual Meeting (Montreal).

10. SaKaran, F.C. 1981 — U.S. Navy Flight Test Results with the LTN-211 ONS. Proceedings of the International Omega Association, Sixth Annual Meeting (Montreal).

11. Hardwick, C.D. Barszczewski, A. 1976 — Determination of Absolute Position by Demodulating the VLF Communications Signals. Canadian Aeronautics and Space Journal, Vol. 22, No. 4.

12. Leach, B.W. February 1981 — A Kalman Filter Approach to Navigation on the NAE Convair 580 Aeromagnetics Research Aircraft. Aeronautical Report LR-604. (NRC No. 19271).

LONG WAVE PROPAGATION CENTER
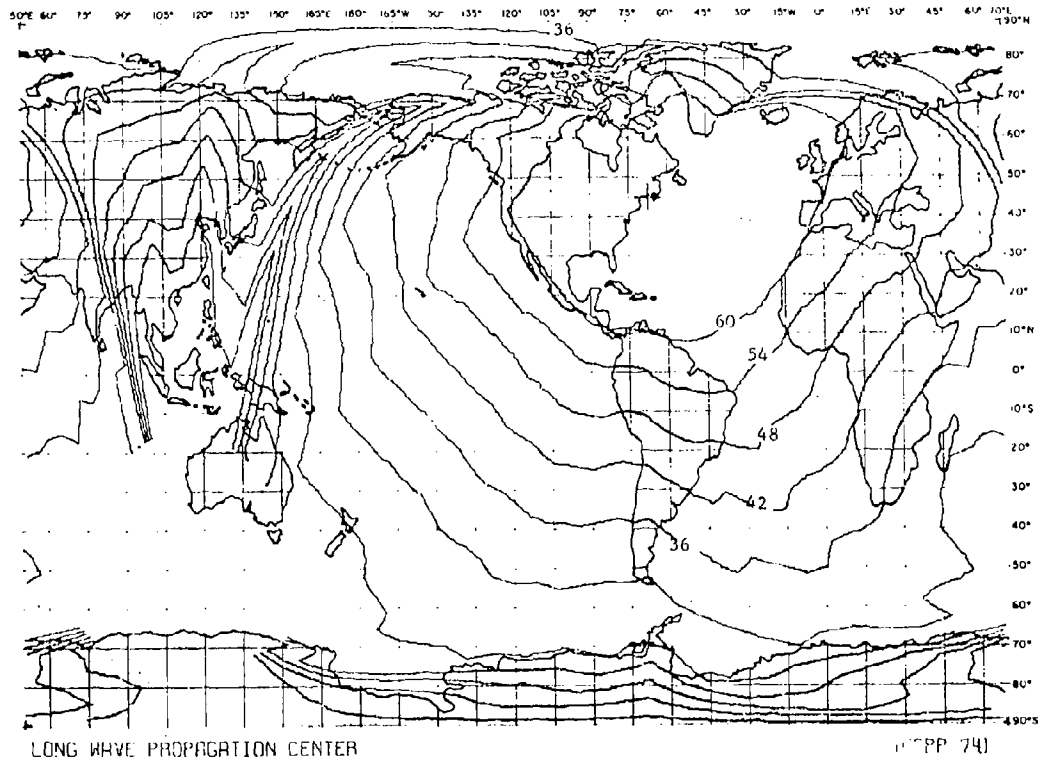
FIG. 1: SIGNAL LEVEL CONTOURS IN dB > 1μV/M NAR (17.8KHz, 1000KW),
CUTLER SUMMER 99% TIME AVAILABILITY
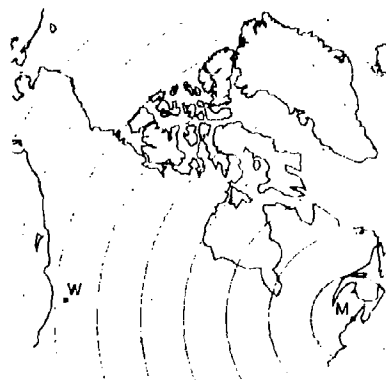


FIG. 2(a): CIRCULAR GEOMETRY



FIG. 2(b): HYPERBOLIC GEOMETRY

20 mS

| | f₁ | f₀ | f₀ | f₁ | f₁ | f₀ | f₁ | f₀ | f₁ | |
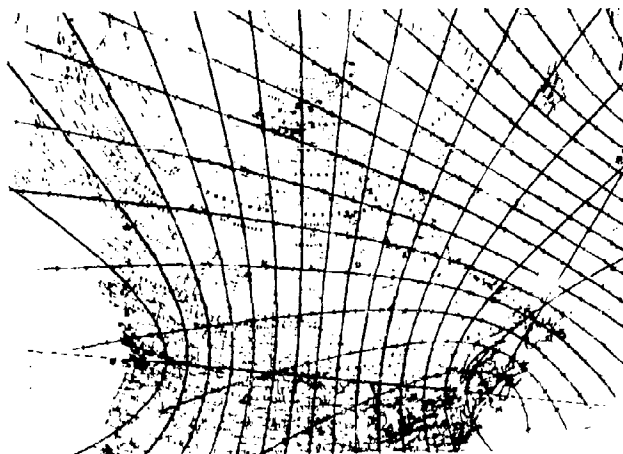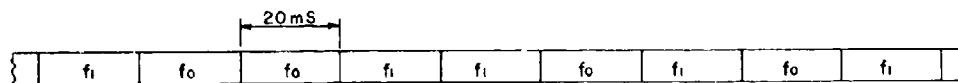
WHERE    $f_1 = f_0 + 50 \text{ Hz}$

FIG. 3(a):  TYPICAL TRANSMISSION FORMAT (FSK)



$f_1$ ⟵ | ⟶ $f_0$
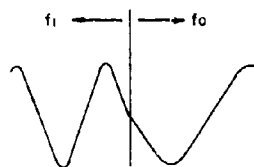
FIG. 3(b):  INTERCEPT BETWEEN THE CARRIER AND THE SHIFTED FREQUENCY



LAT/LONG IN DEG

DOPPLER BIAS

PLOTOUT. 8    JUL. 07 1980 08.40.55

VLF BIAS

FIG. 4:  SMART KALMAN FILTER STATE ESTIMATES FOR REAL DATA

FIG. 5: TOTAL POSITION ERRORS — REAL DATA

# LORAN-C: AN OVERVIEW OF OPERATIONAL AND PROPAGATION CHARACTERISTICS
by

Robert H. Doherty & J. Ralph Johler
Colorado Research & Prediction Laboratory, Inc.
1808 South Flatiron Court
Boulder, Colorado 80301

## ABSTRACT

Loran-C is a low frequency (90 to 110 kHz) pulse radio navigation system. Loran-C is ordinarily configured geographically as a chain which consits of a master station and two or mo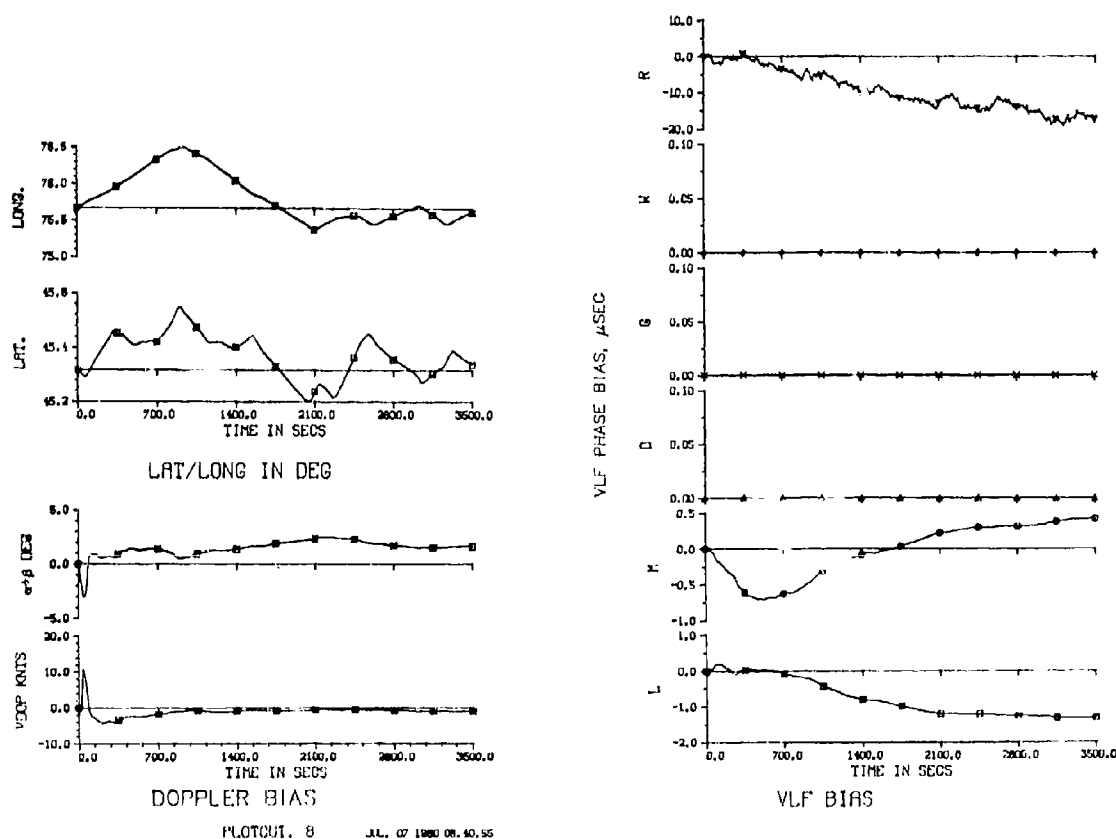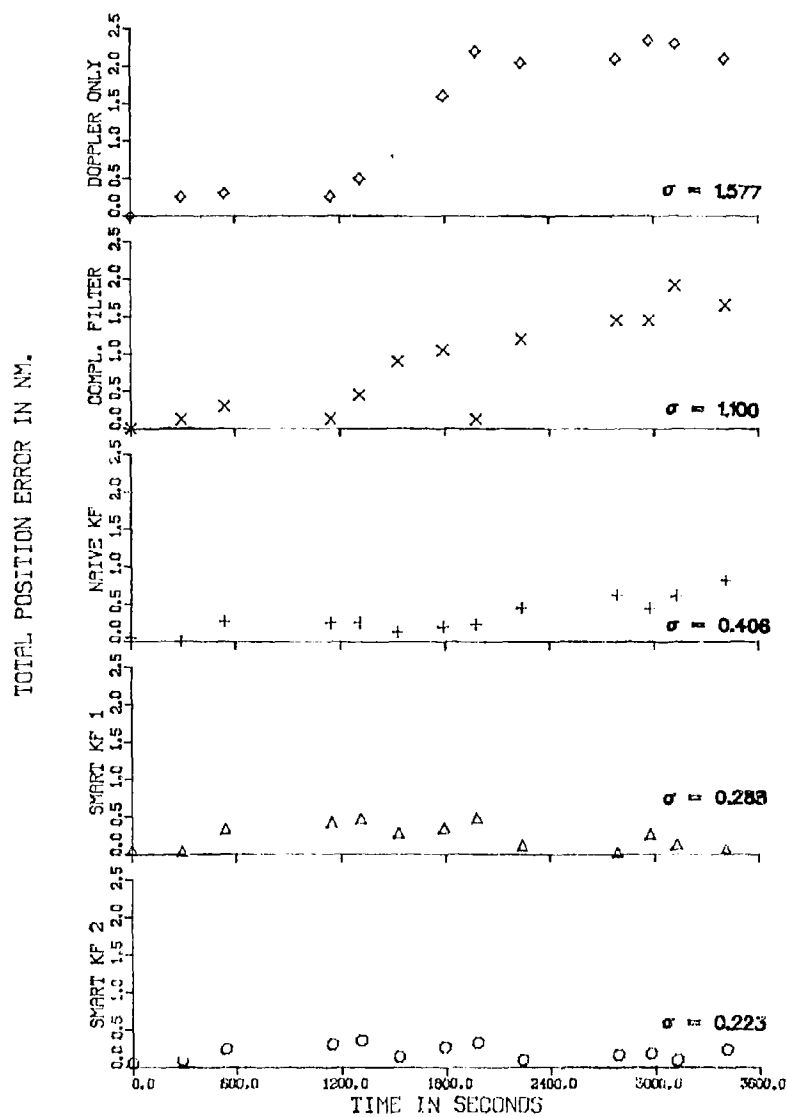re secondary stations oriented to provide an optimum coverage area. The pulse format and phase stability of the system are of paramount importance for both navigation and the companion use of the for time synchronization. All Loran-C chains operate at the same frequency, utilizing differences in repetition rates to distinguish one chain from another. This tecnique operates well in prime service areas, but introduces a problem known as the phenomenon of cross rate interference. This phenomenon manifests itself in remote or marginal service areas. A signal phase coding technique is used for searching and identifying stations, such techniques are also benificial for reducing interference from CW signals.

The need for a low frequency loran system was born out of the shortcommings of the standard loran system used during World War II. Many early tests of low frequency loran culminated in the testing of CYTAC by the U.S. Air Force in the early and mid 1950's. This was a tactical bombing system, and was a direct predecessor to Loran-C. Following a decision by the U. S. Coast Guard to implement Loran-C as a general purpose navigation system, several chains were installed world wide and 24 stations were operational in the early 70's. A U. S. government-wide decision in the early 70's declared that Loran-C would be the primary U. S. Coatal confluence navigation system. Consequently in the last decade 20 new stations have been added covering all of the U. S. coastlines and the Great Lakes region.

Since the Loran-C ground wave is very stable in time, and since the primary usage has been over sea water paths, the major calibration efforts for the systems have been oriented toward measurements. Ground wave radio propagation has been well defined by Maxwellian theory and limitations as well as calibration of the Loran-C systems are theoretically possible. Considerable improvements in the potential Loran-C usage over land paths could be achieved by applying appropriate theoretical work. The unique nature of the Loran-C pulse transmission allows one to separate ground wave and sky wave transmission. Also, the pulse provides a transient capable of validating transient propagation theory. Therefore, the Loran-C transmissions have proven to be very effective diagnostic tools for validating ground impedance and tropographic models used in propagation theories. Continued efforts in this direction will undoubtedly lead to improved prediction and calibration procedures for use with all Loran-C systems.

## 1.0 INTRODUCTION

Present day loran, more precisely, Loran-C, is the result of more than 40 years of system development. The need for a long-range, high-accuracy radio navigation system was critical from the begining of WWII. Conventional methods of navigation at that time were virtually useless for convoys and aircraft on anti-submarine patrol in the North Atlantic during fog and foul weather.

The first and most widely known system used the frequency band just below 2 MHz. For all practical purposes, the first system was useful over sea water only due to the high rate of attenuation of the 2 MHz signal over land. At that time, however, there existed a pressing need for navigation at sea, and the system satisified that need very well. For many years it was called "Standard Loran" and was later designated as "Loran-A". The merit of the wartime system was evidenced by the fact that it continued in service until completely replaced by Loran-C by the end of 1980. A comprehensive treatment of the loran development up to the end of WWII is given by Pierce et al.(1948).

Toward the end of WWII, military requirements demanded navigational coverage over land and at greater ranges than previously required. Those requirements were not satisfied until long after the cessation of hostilities but, broadly speaking, those requirements initiated a series of developments which finally produced Loran-C, a 100-kHz pulse navigation system. Thus, during the late 1950s and early 1960s, the Department of Defense instituted a program designated to develope a new generation of radionavigation aids. The result was CYTAC, a land based bombing system, later renamed Loran-C by the U. S. Coast Guard. Loran-C has greater range and is more accurate than Loran-A ( Hefley,1972). The recent development of low cost receivers has brought the use of Loran-C within the grasp of thousands of commercial and sport fishermen, and much of the entire recreational boating community. Today Loran-C service is available throughout the coastal waters of the contiguous 48 states, the Great Lakes, Alaska (except for the North slope) and most of the Hawaiian waters as well as many other areas in the Northern Hemisphere (See Figure 1).

## 2.0 LORAN-C CONCEPTS AND TECHNICAL BACKGROUND

Loran-C is a hyperbolic radionavigation system utilizing pulse transmissions to: (1) seperate master and secondary stations (2) seperate ground wave from sky wave transmissions (3) reduce interference effects from in band CW transmissions. The characteristics of the Loran-C receiving equipment have been especially suitable to make use of computer technology. Therefore equipment that required support vehicles shown in Figure 2 in 1954 can be easily carried in the palm of one hand today.

### 2.1 Pulse Propagation Characteristics

Figure 3 illustrates a single Loran-C pulse as seen at the transmitting station and a series of Loran-C pulses from a Master and two Secondary stations as they might be seen at a receiving site. Each transmitter sends a group of eight pulses (for visual identification nine pulses from the Master) in a designated time sequencing arrangement. Each series of eight pulses are phase coded by transmitting a pulse with either 0 or 180 degrees added to the phase in some sequence. Thus, the Master station is coded in one configuration and all Secondaries in another configuration. This phase coding allows the reciever to distinguish the Master transmission, each particular Secondary is determined by time position following the Master. In addition to allowing for identification the phase coding reduces interference from CW transmissions because Loran-C pulses will be monitored in 0 or 180 degree aspect depending on the transmitted code. Figure 4 illustrates how the Loran-C system is capable of operating solely on ground wave, and therefore remains free from sky wave interference in the navigational operation. From this figure it is also easy to see how by simply moving the sampling point to the peak of the first hop sky wave it is possible to monitor nearly pure sky wave signals as discussed in section 5 of this paper.

### 2.2 Digital Aspects of System and Equipment Size Reduction

Receiving equipment measures the difference in time of arrival of each Secondary transmission and the single Master transmission for a Loran-C chain. Different Loran-C chains are seperated by the fact that they operate on different repetition rates. Time Difference (TD) measurements are made in the recieving equipment in two steps. A course measurment to whithin +/- 5 microseconds is made on the pulse envelope. Secondly, the fine measurement is made on the CW part of the signal within the pulse. This is a measurement made on a 100 kHz carrier to within .01 to .1 microseconds depending on equipment and integration times. Since the two measurements are made seperately a difference in readings can occur, and indeed propagation theory says such a difference should change with distance. This difference is called Envelope to Cycle Difference (ECD). With the exception of initially determining the envelope sampling point, all of the proceedures described above fall within the normal scope of present day computer technology. Therefore, within the past 25 years it has been possible to reduce 7 relay racks of equipment down to a hand held size of approximately 10 pounds.

## 3.0 THE OPERATIONAL SYSTEM

Present day Loran-C operational systems, as described by the U. S. Coast Guard (1980), cover large portions of the Northern Hemisphere and all of the U. S. Coast Lines as shown in Figure 1. In all of the Loran-C chains, Service Area Monitors (SAMs) are used to keep the transmissions controlled in the service area. Also, Loran-C chains are normally calibrated by making many measurements throughout the entire service area of the chain. All of these measurements are analized in a pseudo-empirical, pseudo-statistical manner in order to determine the chain parameters, primarily the emission delays associated with each secondary transmitting station. A best fit of the data to scaled areas assigned conductivity values, and fit to curves similar to those in Figure 5 are used for this calibration. The phase corrections are determined by assuming reciprocity and empirically summing in both directions. Unlike the integral equation technique (see 4.1) this process can not account for rough terrain.

### 3.1 Typical Operation Using Area Monitors

All, or almost all, Loran-C chains are operated by using a monitor in or near the primary service area to feed back information to keep both the envelope and phase numbers constant in the service area. The service area monitor procedure somtimes leads to ambiguities if more than one area monitor is available in the service area. Since only one location can be held absolutely constant, either one monitor must be chosen for control or an averaging process must be employed.

3.1.1 Temporal variation manifestation — There is some temporal variation in the Loran-C signal, and if they are held constant in one location, they will not be constant in other locations. Although, it is probably desirable to keep the system as nearly constant as possible in the primary service area, it should be considered that use of the system far from the primary service area could be enhanced with a local area monitor providing corrections for any equipment used in that area. This would be particularly true where temporal variations were the greatest, over land paths subject to below freezing temperatures, see description in section 4 of this paper.

3.1.2  Cross rate interference - All Loran-C chains are operated at 100 kHz and all chains have identical phase codes and pulse separations. Rate sequencing is employed to separate each chain from all others. This involves different repetition rates for different chains. Whereas this technique works well to separate chains instrumentally, unwanted signals from chains not being used are continually drifting through the time domain for the signals being monitored. This is a small problem when the desired signal level is high and the undesired signal level is low, but it can become a significant problem in fringe areas where the undesired signal level may exceed the desired signal level, especially when sky wave interference is considered. Special receivers could be built for fringe area use where digital techniques were used to blank out times when strong interfering Loran-C signals were present, but this practice is not followed in ordinary Loran-C receivers.

## 3.2  Typical Calibration of Operational System

Typical calibration of Loran-C chains are made by taking measurements at known points within the service area, and using a best fit to this data to determine the correct numbers for the service area monitor to hold.    The actual emission delay numbers for the secondary stations are also determined in this process. As pointed out by Johler and Doherty (1976) for the Mediterranean chain and Doherty and Johler (19  ) for the U.S. West Coast chain, this process may yield errors of several hundred nanoseconds (i. e. tenths of microseconds).    This, in turn, could produce errors of several hundreds of feet when introduced into a geographical coordinate conversion scheme.

3.2.1  Spatial variation manifestation - In the above mentioned references and also in Burch et. al.(1976) the Loran-C spatial variations are treated extensively. The existence of spatial variations over land paths is a well known phenomena. Many Loran-C measurements over land paths and along coast lines where land paths are involved between the transmitter and receiver show these variations.   Section 4 of this paper gives a brief theoretical explanation for these variations and a method whereby the variations could be theoretically predicted if this were desired. To date all Loran-C usage has been predicated upon the repeatability and measurability of the Loran-C system and few attempts have been made to improve the predictability of the system.

3.2.2  ECD and other operational aspects - As mentioned previously, ECD (envelope to cycle difference) occurs throughout the Loran-C service area. The ECD       nts a serious problem when it exceeds 5 microseconds, and thus causes a cycle error. This co    on can exist over extremely rugged terrain, as can be seen from the theory. An especially serious case may be encountered where the signal passes over a very rugged coast line. In this case a serious error can occur close to the shore line in a dangerous area. Also this error occurs in the fringe area of reception; this area of reception is variable depending upon the sophistication of the receiving equipment. Again in terms of problem areas associated with ECD very little propagation theory has been consulted or utilized.

## 4.0  RADIO PROPAGATION AND A PREDICTION POTENTIAL

Overland static grid Loran-C propagation (Grid Warp) is uniquely predictable using the integral form of Maxwell's Equations as demonstrated by Johler(1971). See figure 6 for an artists concept of the static grid warp phenomena. The demonstrated high-precision repeatability of Loran-C time differences (TDs) has provided a mechanism with sufficient resolution to detect the extremely small phase variations caused by propagation anomalies. This propagation theory allows for prediction of the even smaller temporal variations through the introduction of the refractive index lapse rate changes. Considerable theoretical work has demonstrated that the temporal variations of the Loran-C signal are related to the changes in the refractive index lapse rate (change of refractive index with altitude).

## 4.1  Theory of Propagation Related to Spatial Variations (Grid Warp)

A numerical solution of an integral equation representation of the ground wave over irregular, inhomogeneous earth has been employed to calculate amplitude and phase of the propagated continuous wave as a function of frequency. A computer simulation again using numerical methods, transforms this result to the time domain yielding the impulse response. Then the impulse response is convolved with the Loran-C pulse function, that has been transformed from the time domain to the frequency domain. A final result demonstrates the propagation of both pulse envelope and the cycles under the envelope in the presence of irregular, inhomogeneous ground. In the particular case of the Loran-C pulse, it is concluded that both the phase delay and the ECD is a unique function of the particular type of terrain over which the wave propagates, and it is, at the present state of the art, necessary to introduce such terrain into the propagation theory to give a unique prediction of the pulse propagation time (Johler and Horowitz 1974). As demonstrated by Johler et. al.(1979), a data base determination necessary to exercise the above programs would not be particularly difficult to obtain, however it does not presently exist. Until such a data base does exist the true prediction capability of Loran-C cannot be exploited over land paths, even though the propagation theory is understood and available in computerized form. A review of various approximations to the theoretical propagation solution is given by Samaddar(1979).

### 4.2 Theory of Propagation Related to Temporal Variations

Normally temporal variations in the overland propagation of the Loran-C signal are an order of magnitude smaller than the spatial variations. Moreover, temporal variations over sea water paths are extremely small. The apparent exception occurs for over land paths subjected to sub-freezing temperatures. The phase variations in these cases are at least an order of magnitude greater than can be explained by primary wave propagation time being influenced by the surface refractive index ( $n d./c$ where $n$ is the surface index of refraction, c is the velocity of light in a vacuum, and d is the distance). The variations must be explained in terms of $\alpha$, the lapse rate of the refrative index and the fact that the secondary phase correction is a function of $\alpha$ to the 2/3 power (Doherty 1975). The basis for the effect being more pronounced for sub freezing temperatures relates to the relation between the dry term and the wet term for the refractive index (Samaddar, 1980; Doherty and Johler 1975). During periods of cold temperatures, Loran-C can be significantly effected by changes in weather conditions.

### 4.3 Computer Technology and Prediction Capabilities

Computerized prediction programs for spatial variations were described above, and a suggested computerized prediction program for temporal variations was proposed by Campbell et. al.(1979). With the advent of smaller and smaller computers containing larger and larger memory capabilities it is possible to anticipate a Loran-C receiver with full prediction capability contained therein. However, in the interim it seems reasonable to concentrate some effort on obtaining an adaquate data base for computer predictions and also to implement area monitors with both spatial and temporal propagation prediction capability. Monitors of this type along with localized communications capability could provide a very accurate differential Loran-C positioning capability.

### 5.0 MEASUREMENT VERIFICATION OF PROPAGATION EFFECTS

Loran-C measurements of both ground wave and sky wave propagation phenomena have provided unique verification of many of the low frequency radio propagation theories. Also the measurements have provided mechanisims for event detection, and inputs to stimulate new thoughts on various propagation and constituent determinations. These measurements have been rather unique in that the pulse transmissions allow for separation of the ground wave and sky wave effects. Individual ground wave measurements and individual sky wave measurements at these frequencies are rare, especially over long periods of time and over widely seperated geographical locations.

### 5.1 Ground Wave Propagation

Ground wave measurements made on the Loran-C signals generally fall into one of two categories. Rather short term data taken at many locations is defined in terms of spatial variations due to terrain irregularities and ground inhomogenetics of surface and sub-surface conductivities. Long term data taken at fixed locations generally is interpreted in terms of temporal variations. The best source of this type of data has been from the Loran-C system itself, i.e. long term recordings of signals between two Loran-C transmitting sites. Therefore, spatial variations observed from many measurements over short durations and temporal variations observed from fewer observations for long time periods comprise the Loran-C ground wave data base.

5.1.1 Verification of spatial variations in Death Valley – An example of spatial variations is shown in Figure 7. Here a comparison of computed (solid curve) phase variations and measured phase values (points numbered 1-9 and lettered A-P) in the vacinity of Death Valley California is presented. This is extremely rugged country and the measurements were made in a vehicle confined to existing roads. Therefore, it was impossible to make the measurements over exactly the same straight line path where the calculations were made. The extremes of the measurements and the extremes of the calculations agree quite well. Doherty (1975) gives a more complete description of these measurements, and Johler and Horowitz (1975) give a description of the theoretical calculations that are compared to the data.

5.1.2 Explanation of temporal variations – Figure 8 illustrates temporal variations derived from measurements made over a two year period between the Dana, Indiana transmitter and the Carolina Beach, North Carolina transmitter. During winter months this path is subject to sub-freezing temperatures over land areas. Propagation over this baseline path shows an increasing speed of propagation (decreased delay time) associated with the colder temperatures in the winter months. Also the signal velocity becomes more variable during the colder periods. Both of these phenomena and weather related frontal movements have been associated with the Loran-C phase through the lapse rate of the refractive index and particularly the increased importance of the dry term of this lapse rate during cold weather (Doherty and Johler,1975; Samaddar,1980).

### 5.2 Sky Wave Propagation

Loran-C signals have always been recognized as a potential source of unique sky wave information. By sampling the pulse waveform at a point near the peak of the first hop reflection it is possible to observe nearly uncontaminated sky wave propagation. Diurnal, locational and seasonal variations in the ionospheric D-region can be monitored from long term observations of these signals. Also short term perturbations of the D-region such as caused by high altitude nuclear tests, daytime solar flares or solar

eclipses, and nightime particle precipatation events can be observed from monitoring the Loran-C sky waves. Through a cooperative program between the U.S. Coast Guard and the Boulder Radio Laboratories of the U.S. Department of Commerce, Loran-C sky wave data was gathered for 12 years (1962-1974) at approximately 16 Loran-C secondary stations throughout the world. Information presented in the remainder of this section is derived from these measurements.

5.2.1 Nuclear tests - Detection of high altitude nuclear tests through the perturbations produced in the ionospheric D-region provided the incentive to initiate the sky wave monitoring program. These effects could be sudden as explained by Jean et.al. (1965) or they could be long lasting over several days as shown by Doherty (1970). During the initial period of the sky wave monitoring program several U. S. and Russian high altitude nuclear tests were detected in this Loran-C sky wave monitored data.

5.2.2 Eclipses - Total or near total solar eclipses occurred over some of the sky wave monitored paths in July 1963 and again in March 1970. These eclipses allowed one to study the sunset-sunrise effect over a very short time period and without the oblique path atmosphere being present. A study of these results allowed an interpretation of the D-region from a chemical constituent viewpoint (Doherty, 1970, Doherty, 1971a). Seasonal variations in the ionospheric D-region also became a factor in these interpretations.

5.2.3 Solar flares - During daylight hours the phase and amplitude of the Loran-C sky wave signals is normally very stable. There are detectable changes in the daylight results both with latitude at a given time and with season at a given latitude. Solar X-ray events, normally associated with solar flares, are easily observable on both the phase and amplitude of these Loran-C sky wave recordings.

5.2.3.1 Normal and abnormal flare effects - Figure 9 shows signatures of solar events as seen on several Loran-C paths. A significant result of flare signatures at this LF frequency and for a one hop propagation path is that phase advances or phase retardations can occur, and amplitude increases or amplitude decreases can also occur (Subrahmanyam, et al., 1974 ). It seemed that there were certain times or locations when one or another of these effects appeared dominant. Therefore, it was decided to undertake a statistical study of flare effects for one year period at three different latitudes (Doherty, 1980).

5.2.3.2 Variation of effects with latitude and season - Figure 10 shows the percent of flares demonstrating an amplitude enhancement at three different latitudes as a function of season. Amplitude enhancements occur nearly 100 % of the time in the summer and more frequently at low latitudes than at high latitudes. Figure 11 shows the percent of flares with a phase advance at the same three latitudes as a function of season. The fact that nearly all low latitude flares and most mid latitude flares show phase advances even in the winter suggests that a different portion of the D-region is determining the phase changes than the one determining the amplitude changes. The complete study referenced above analyzed the results as a function of solar zenith angle both during summer months and during winter months at each latitude. This study definitely suggests that general changes in the ionospheric D-region occur as a function of latitude for a given season and also occur as a function of season for a given lattiude. Similar interpretations have also been reached from other studies.

5.3 Ionospheric interpretations from sky wave measurements

In summary, studies of the Loran-C sky wave measurements were used in order to attempt a better understanding of the ionospheric D-region. In addition to the use of the data to better understand the daytime ionosphere (Doherty, 1968 and 1970), night time events of a particle precipitation nature were observed (Doherty, 1971 a and b). The observations reported herein represented the results of very limited analysis of the existing data. No doubt a thorough analysis of this data would yield many more interesting phenomena.

6.0 UNTAPPED POTENTIALS FOR LORAN-C

Current Loran-C radio navigation equipment has demonstrated a repeatable precision index of less than 0.01 microsecond/kilometer. Thus, two colocated receivers measuring the same time difference will deviate less than this amount as to the standard deviation of their measured time difference. It is therefore concluded that operation of Loran-C in a differential mode is a feasible technique for such practical applications such as collision avoidance, instrument landing systems, air traffic control, precise location of surface vessels used out of sight of land in underwater exploration, and ground based vehicle location in non-urban environment (Doherty and Johler, 1975-76). It is also the opinion of these authors that the computerized aspects of the Loran-C system, both configured and potential, make it a very powerful tool for future positioning capabilities and other applications. Solution and useage of radio propagation prediction methods for the Loran-C system can further enhance the potentials of future usage.

6.1 Ultimate Absolute Accuracy Potential Over Land Areas Dependent On Prediction

Comprehensive use of Loran-C over land for aircraft or for ground based vehicles depends upon the ability to eliminate the errors due to both the spatial variations and those due to the temporal variations. Presently attempts to solve these problems are limited to calibration by measurements alone and the potential use of a monitor to detect and report temporal variations.

6.1.1 Spatial calibration by prediction – Calibration by prediction (Burch et. al. 1976) could ultimately be a cheaper, more useful, and more accurate method for treating spatial variations. Furthermore, this technique lends itself directly to a computer solution that could eventually be implemented directly into a receiver. Furthermore, this is the only calibration technique that will work where measurements cannot be made or independent location information is not available.

6.1.2 Temporal prediction from weather information – Prediction of temporal variations from weather data is theoretically less well defined than the spatial prediction problem. This is because the rigorous theory relating the alpha factor precisely to surface and upper level weather conditions has not been solved. However long term weather predictions such as shown in figure 8 could be predicted using a computer program, and also shorter term fluctuations could be predicted using a somwhat more empirical approach (Dean, 1978, Campbell et.al.,1979) utilizing the relation between the dry term of the refractive index and the phase changes observed during cold weather.

6.2 Computer Technology Enhances Future Potentials

Three areas of future Loran-C operation lend themselves well to computerized enhancement for the system. The receiver may be improved by incorporating predictions, both spatial and/or temporal as described above. The receiver operation may also be inhanced by computerized removal of harmfull cross rate interference. Computerized techniques can first determine if the interference is harmfull, and if so, autcmatically remove the harmfull interference by eliminating the contaminated samples from the desired signal. The third area where future computerization can enhance the system opertation is in connection with area monitor operation, both for the system area monitor and for supplemental area monitors used in a differential operation.

6.2.1 Predictions incorporated in computerized receivers – It is possible at the present time to incorporate land sea boundaries and rather elementary predictions into existing Loran-C receivers. It is not inconceivable with bubble memory capabilities that the entire world land mass impedances and terrains could be incorporated into Loran-C recieivers. In the meantime, if the world wide data base existed, predictions of phase corrections could be made for all Loran-C operational systems. These phase corrections could be used to develope algorithms that could easly be incorporated in existing type computerized receivers.

6.2.2 Computerized reduction of cross rate interference in fringe areas – If Loran-C receivers were built to monitor several different chains at once, information on location could be derived from more than one pair of time differences. Also the information from other than the primary chain being monitored could be used to determine the severity of cross rate interference on the primary chain. If this severity exceeded a predetermined level the cross rate interference could be eliminated by removing the signal samples which are subject to this contamination.

6.2.3 Improving area monitor and differential loran operation with computer propagation – The first place where computerized propagation predictions should be incorporated into the Loran-C system is at the service area monitors. Where these monitors are used to control the system by introducing corrections into the secondary transmitters, the calculations would indicate when the corrections were due to propagation changes and when the changes were due to equipment fluctuations or malfunctions. Particularly in the case where transmitters are operated in an unattended mode, this information would be usefull to warn operators to check the transmitter facilities.

The second situation where the propagation predictions would be benificial arises when applied to area monitors that are not controlling the operating system, but are used to enhance Loran-C in a differei ial mode. In this case, where corrections would need to be supplied to the operating receivers for maximum positioning accuracy, calculated propagation corrections for different receive locations would greatly enhance the accuracy. This is pariicularly true since the propagation corrections are always nonlinear, and the location of the receiver within the Loran-C service area is extremely important. Computerized propagation predictions enhanced by area monitor observations as feedback to the prediction algorithms provides a possibility of a bootstrap type operation that could give excellant positional information from the Loran-C system.

## 7.0 CONCLUSIONS

Loran-C is a viable radio navigation system in the continental U. S. and along all of the U. S. and most Canadian coast lines. Also most northern routes over the Atlantic or Pacific Ocean are covered. The use of Loran-C by the fishing and recreational industries should guarantee the existence of the system for many years to come. Most users of the system do not require absolute accuracy and the excellent repeatable accuracy always inherent in the system suffices for their requirements. Loran-C could provide precise geographic coordinate determinations for the more demanding user, but it will be necessary for this user to create a data base adaquate to make the necessary propagation predictions. Temporal variations in the propagation time, which tend to degrade the repeatable accuracy, become most significant over land paths subjected to sub-freezing temperatures. Where these effects occur the more demanding user may wish to obtain a weather data base, and a propagation prediction mechanism utilizing this data base. The only missing elements for spatial predictions is the lack of the surface and sub-surface data base with properly assigned impedances. The missing elements for temporal predictions is the lack of a weather data base and the correlation between alpha factor and the weather parameters. Conversley only a time varying alpha data base would be needed to achieve temporal variation predictions.

## 8.0 REFERENCES

BURCH, L. B., R. H. DOHERTY and J. R. JOHLER, 1976, Loran Calibration by Prediction, Navigation: Journal of The Institute of Navigation, 23, 195-200.

CAMPBELL, L. W.,R. H. DOHERTY and J. R. JOHLER, 1979, Loran-C System Dynamic Model, Temporal Prpopagation Variation Study, Report No. DOT-CG-D57-79, AD- A076214 (Prepared for: U.S. Department of Transportation, United States Coast Guard, Office of Research and Development, Washington, D.C. 20590).

DEAN, W. N., 1978, Diurnal Variations in Loran-C Groundwave Propagation, Proc. 9th Annual PTTI Planning Meeting,(Technical Information Division, Code 250, Goddart Space Flight Center, Greenbelt,MD 20771)

DOHERTY, R. H., 1968, Importance of Associative Detachment and Dissociative Attachment in the Lower Ionosphere as Shown by LF Radio Measurements, JGR Space Physics, 73, 2429-2440.

DOHERTY, R. H., 1970, Changes in D-region Chemistry Consistent with Radio Observations, Jour. of Atm. and Terr. Phys. 32, 1519-1533.

DOHERTY, R. H., 1971a, LF Observations During a Solar Eclipse and Suggested Particle Precipitation Between March 6 and 14, 1970, World Data Center A, Upper Atmosphere Geophysics, Report UAG-12 PartIII, 437-447.(U. S. Department of Commerce, NOAA Laboratories, 325 Broadway, Boulder, CO 80302).

DOHERTY, R. H., 1971b, Observations Suggesting Particle Precipation at Latitudes Below 40 deg. N,Radio Science, 6, 639-646.

DOHERTY, R. H., 1975, Spatial and Temporal Electrical Properties Derived from LF Pulse Ground Wave Propagation Measurements, AGARD-CP-144 Paper No. 30.

DOHERTY, R. H., 1980, Unpredicted Variation in D-region Response to Solar X-ray Events, Solar-Terrestial Predictions Proceedings, Volume 4: Prediction of Terrestial Effects of Solar Activity, Richard F. Donnelly, Editor,D3-35 - D3-47 (U. S. Department of Commerce, NOAA Laboratories, 325 Broadway, Boulder, CO 80302).

DOHERTY, R. H. and J. R. JOHLER, 1975-76, Unexploited Potentials of Loran-C, Navigation: Journal of The Institute of Navigation, 22, 343-351.

DOHERTY, R. H.,and J. R. JOHLER, 1975, Meteorological Influences on Loran-C Ground Wave Propagation, Jour. of Atm. and Terr. Phys. 37,1117-1124.

DOHERTY, R. H.,and J. R. JOHLER, 1978, Interpretation of West Coast Loran-C Errors Using Programmable Calculator Analysis Techniques, Proceedings of the Seventh Annual Technical Symposium,The Wild Goose Association, 4 Townsend Rd. Acton, MA 01720, 227-237.

HEFLEY, G.,1972, The Development of Loran-C Navigation and Timing, National Bureau of Standards Monograph 129, (Superintendent of Documents, U.S. Government Printing Office, Washington, D.C. 20402).

JEAN, A. G., C. E. HORNBACK, R. H. DOHERTY, J. R. WINKELMAN, and R. T. MOORE, 1965. Techniques for Detection of High-Altitude Nuclear Explosions, Proc. of the IEEE, 53, 2088-2008.

JOHLER, J. R.,1971, Loran Radio Navigation Over Irregular, Inhomogeneous Ground With Effective Ground Impedance Maps, Telecommunications Research and Engineering Report No. 22 (Superintendent of Documents, U.S. Government Printing Office, Washington, D.C. 20402).

JOHLER, J. R. and R. H. DOHERTY, 1976, Significance of Ground Wave Propagation Anomalies observed During a Loran-C Chain Validation, OT/ITS Technical Memorandum 76-223 (U.S. Department of Commerce, 325 Broadway, Boulder,CO 80302 ).

JOHLER, J. R., R. H. DOHERTY and A. R. COOK, 1979, Loran-C Pulse Transient Propagation, Report No. DOT-CG-D-52-79, AD-A077551 (Prepared for: U.S. Department of Transportation, United States Coast Guard, Office of Research and Development, Washington, D.C. 20590 ).

JOHLER, J. R., and S. HOROWITZ, 1975, Propagation of a loran pulse over irregular, inhomogeneous ground, AGARD-CP-144 Paper No. 28.

PIERCE, J. A.,R. H. WOODWARD, and A. A. MCKENZIE ,1948, Loran, 4, Loran radiation series, McGraw-Hill Book Co.,Inc., New York, N.Y.

SAMADDAR, S. N., 1979, The Theory of Loran-C Ground Wave Propagation-A Review, Navigation: Journal of The Institute of Navigation, 26, 173-187.

SAMADDAR, S. N., 1980, Weather Effect on Loran-C Propagation, Navigation: Journal of The Institute of Navigation, 27, 39-53.

SUBRAHMANYAM, C. V.. SASTRI , J. HANUMATR, and S. D. DESPHANDE, 1974, Study of Solar Flare Signatures on LF Field Strength over Tashkent-Delhi Path, Indian Journal of Radio and Space Physics, 3, 153-157.

U. S. COAST GUARD, 1980, Loran-C User Handbook, U.S. Department of Transportation, Coast Guard, Comdtinst M16562.3.
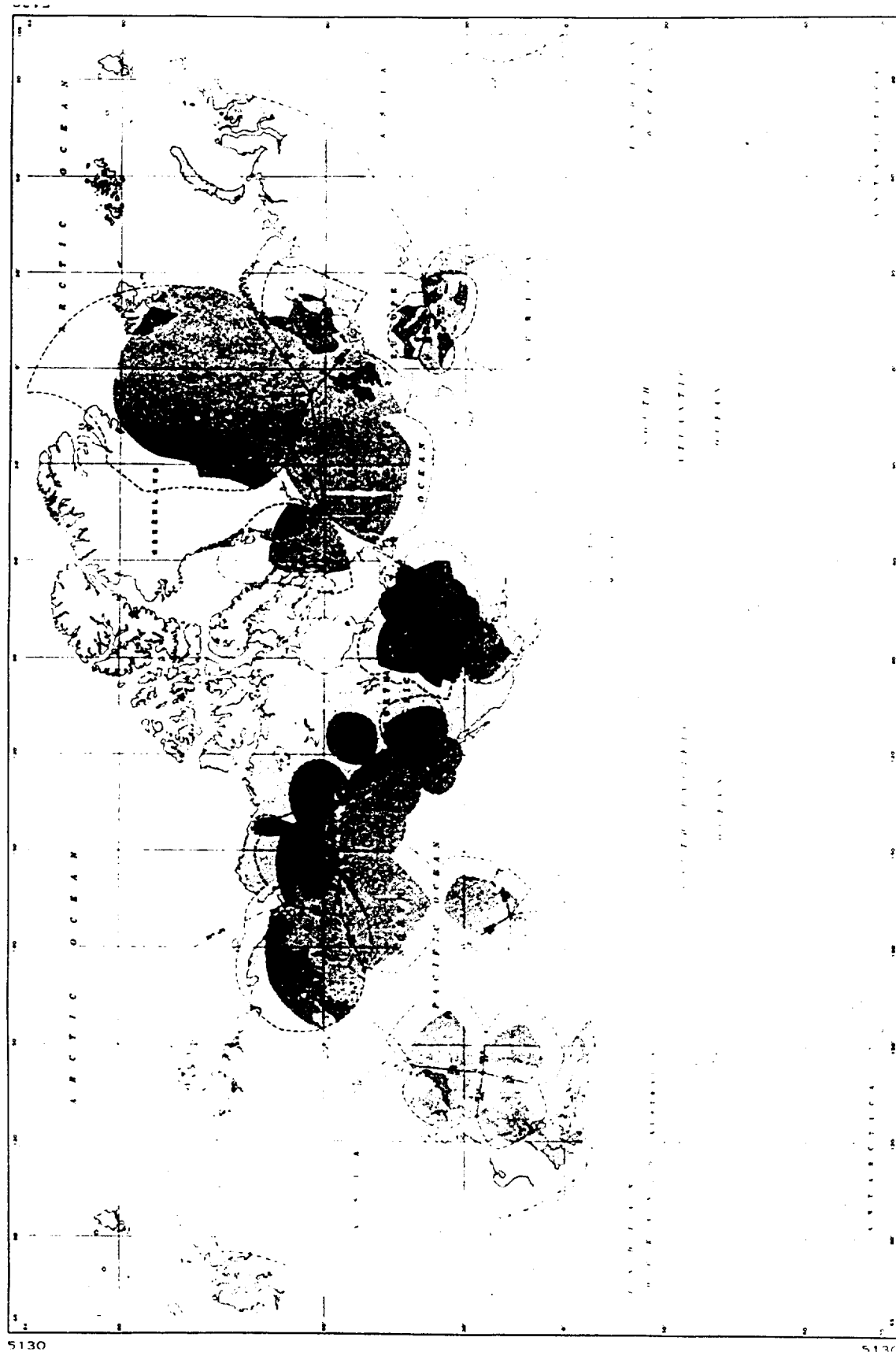
Fig.1 Service area coverage diagram
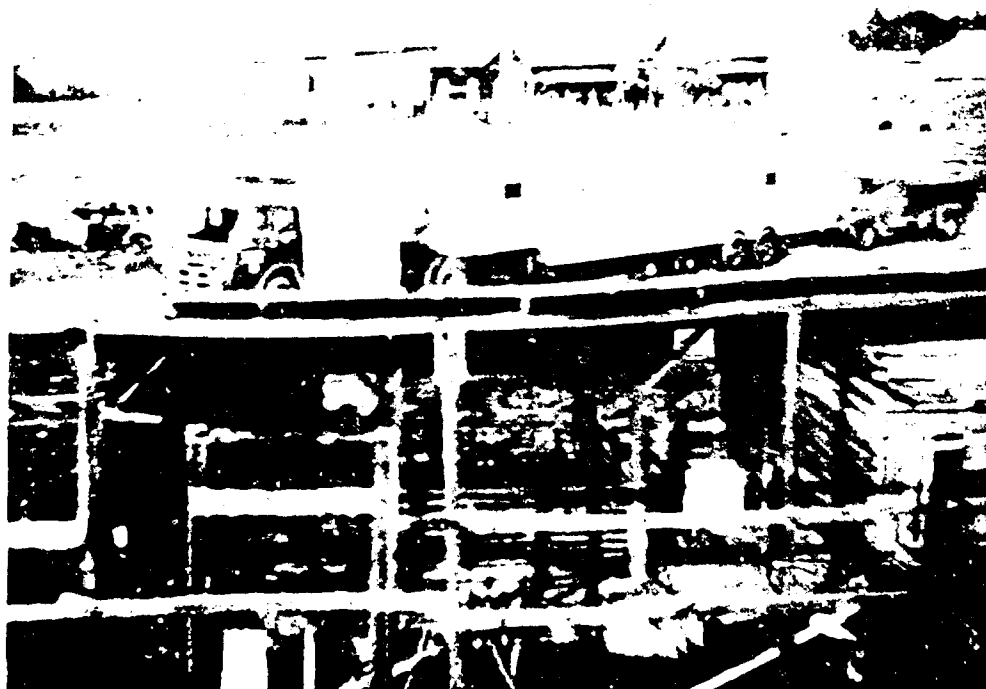
Fig.2    Trailer housing CYTAC receiver and support vehicles in 1954
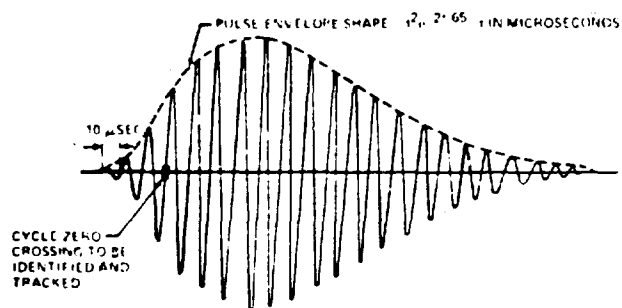


LORAN-C PULSE
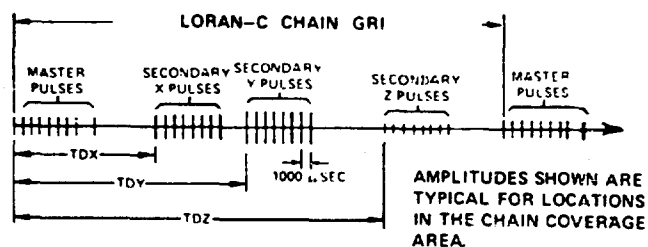


EXAMPLE OF RECEIVED LORAN-C SIGNAL

Fig.3    Signal format for one pulse and for three separate transmitters
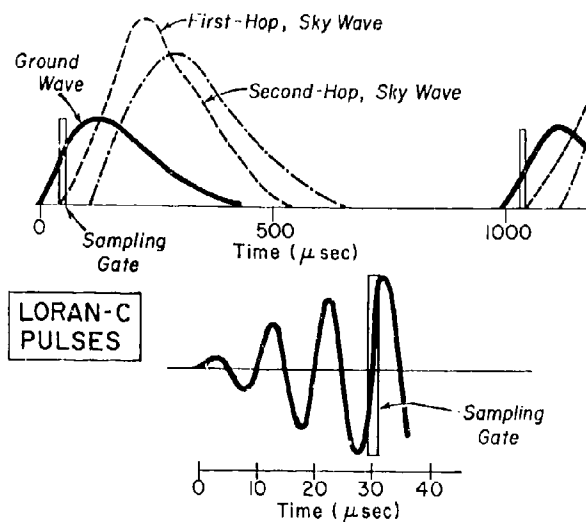
Fig.4    Loran-C pulse form and sampling point determination



| | α | = 0.85 | | |
|---|---|---|---|---|
| Curve | σ | ε₂ | \|x\| | Arg x |
| 1. | 5. | 80–15 | .001055 | .7854 |
| 2. | .0557 | 15 | .01 | .7788 |
| 3. | .0139 | 15 | .02 | .7717 |
| 4. | .0051 | 17 | .033 | .7762 |
| 5. | .0027 | 52 | .045 | .8377 |
| 6. | .00076 | 75 | .08 | 1.038 |
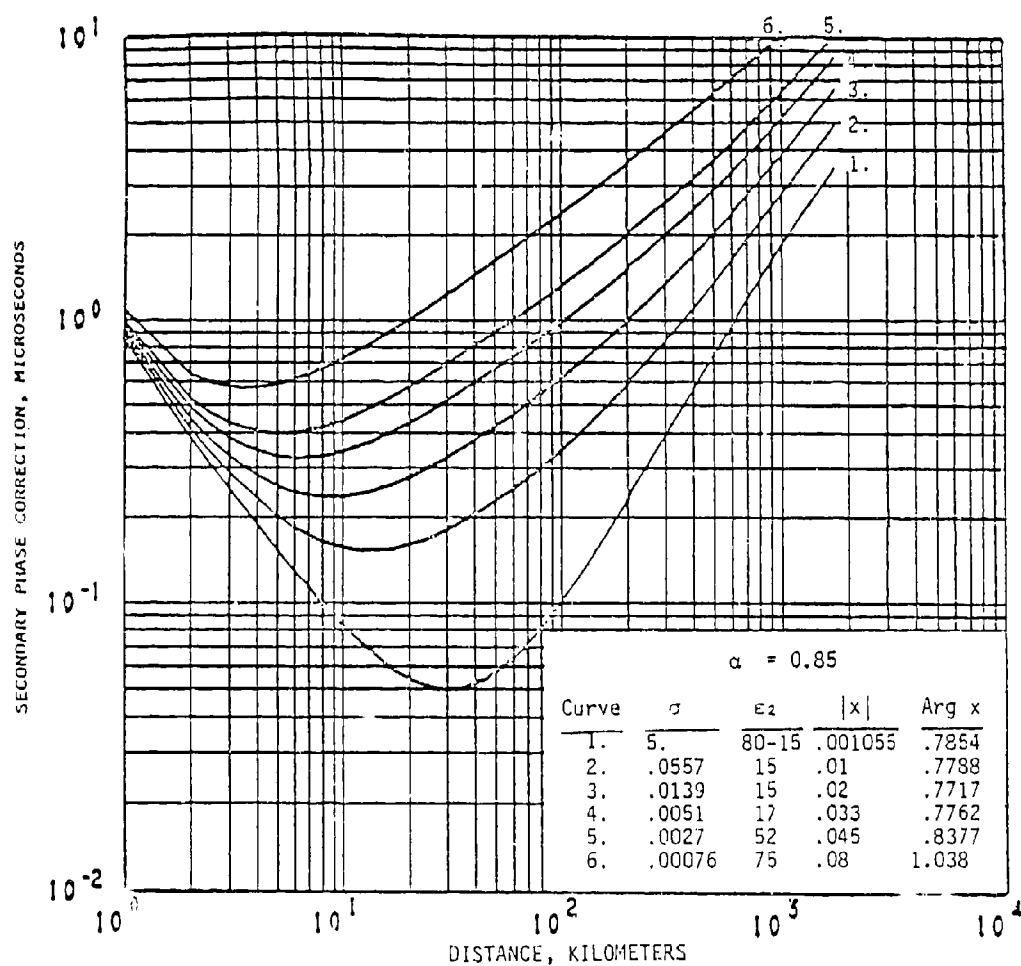
Fig.5    Secondary phase correction in microseconds as a function of distance for various values
of ground impedance or conductivity
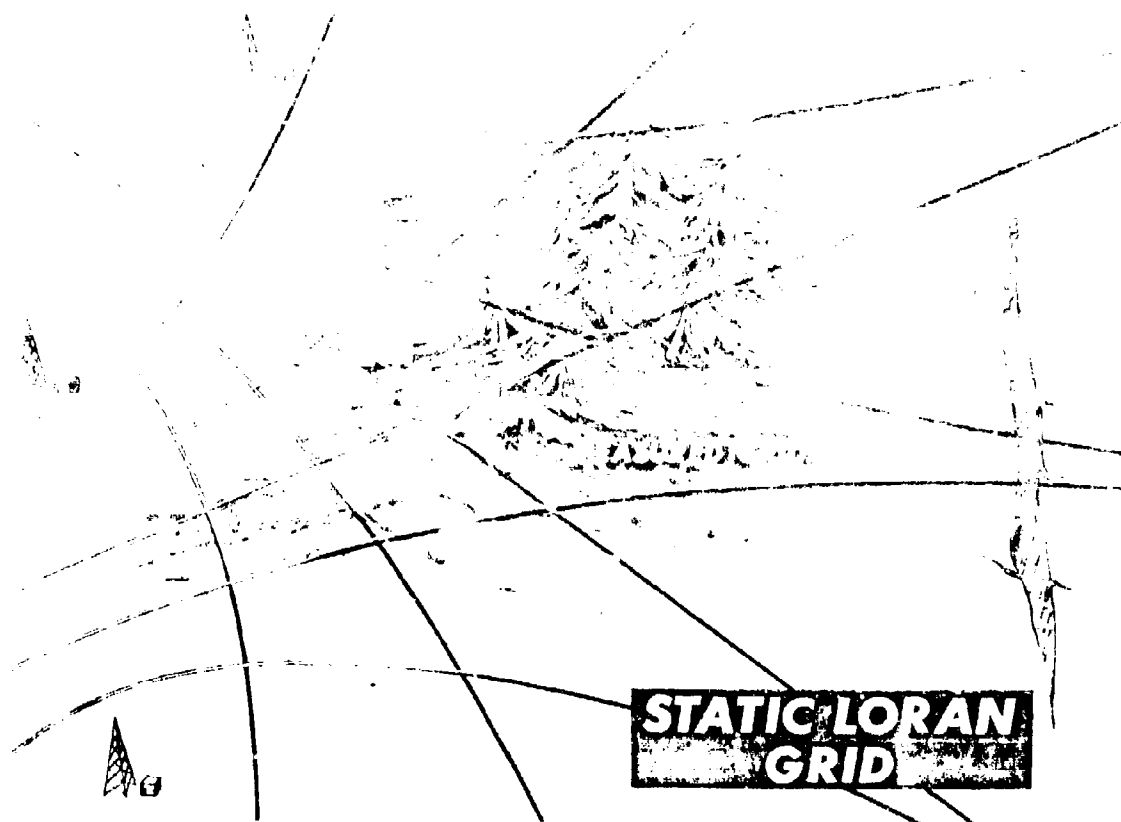
Fig.6    Loran-C static grid depicting a conceptual effect of terrain anomalies (grid warp)
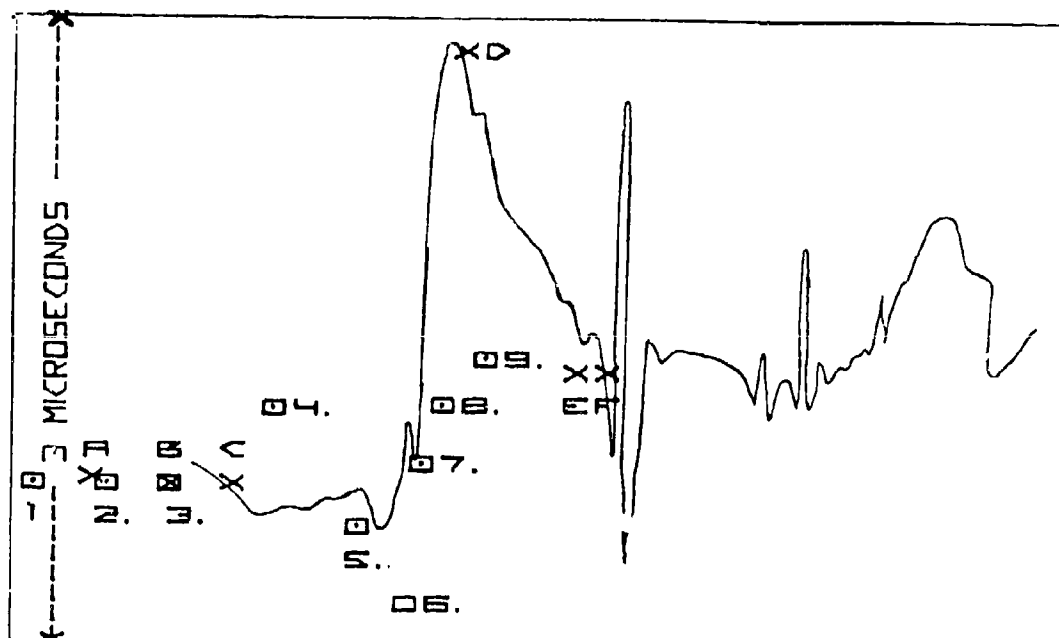


Fig.7    Predicted curve versus measured data points in Death Valley (observed grid warp)
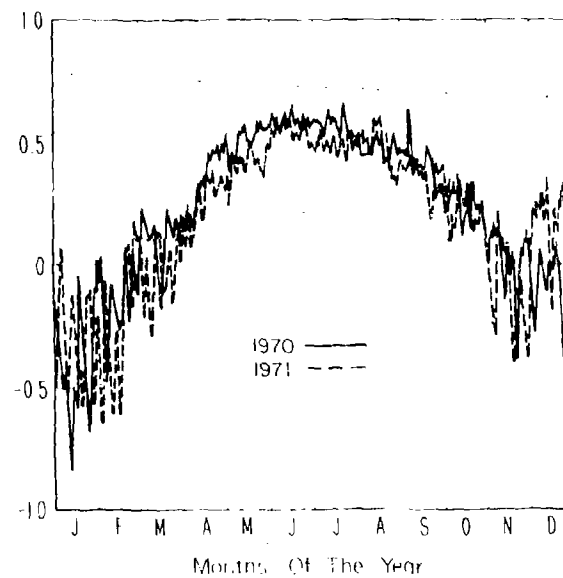
Fig.8  Two seasons temporal variations between Dana, Ind and Carolina Beach, N.C.
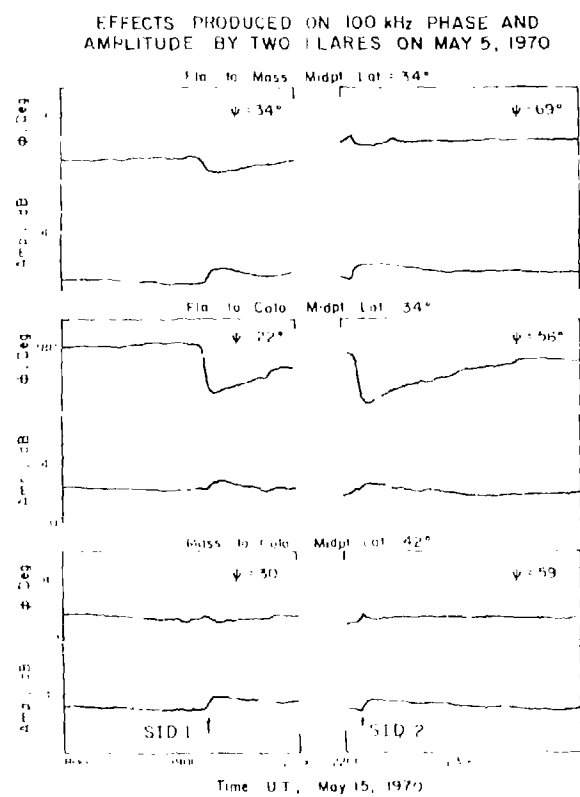


Fig.9  Typical sky wave effects of several solar flares
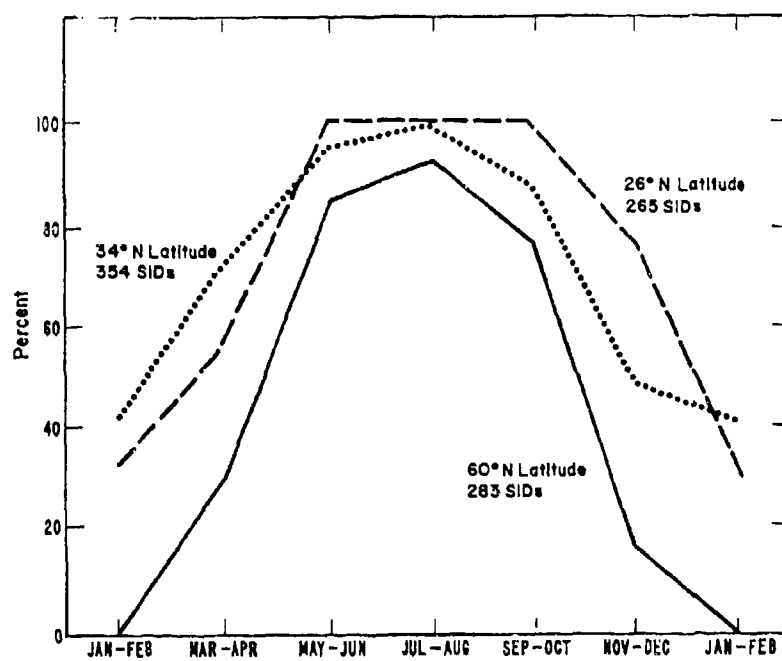
Fig.10  Percent of flare events with amplitude enhancements at three latitudes for all seasons
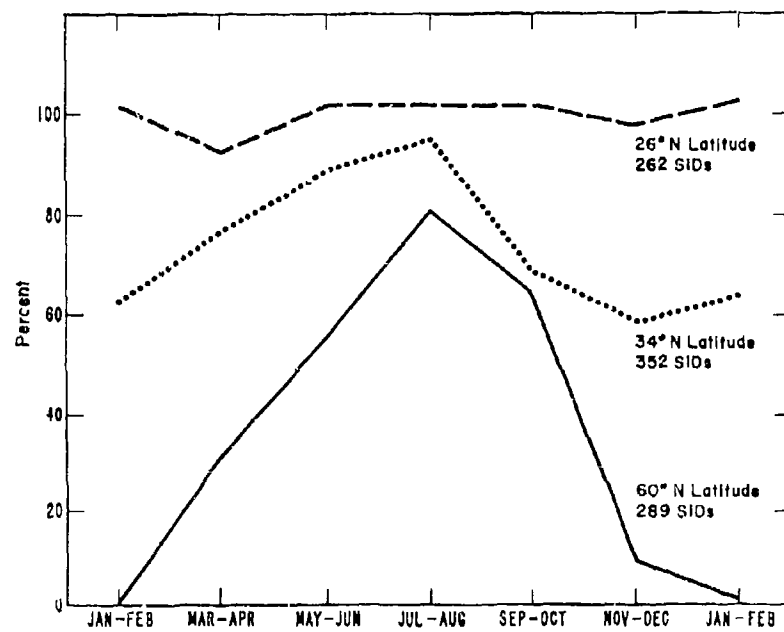


Fig.11  Percent of flare events with phase advances at three latitudes for all seasons

# ELECTROMAGNETIC FIELDS OF DIPOLE ANTENNAS IN THE PRESENCE OF LAYERED MEDIA

J. A. Kong, W. C. Chew and T. M. Habashy
Department of Electrical Engineering and
Computer Science and Research Laboratory
of Electronics
Massachusetts Institute of Technology
Cambridge, Massachusetts  02139 USA

## SUMMARY

The electromagnetic fields due to a dipole antenna in the presence of layered media have been formulated in integral forms and solved with the following techniques:  the brute force integration methods; the modal approach by finding the residues for the integrals; the image-source approach by using the saddle point method; and hybrid techniques with combinations of the above approaches.  For wavelengths $\lambda > 3$ Km  and observation points less than  $\lambda/20$,  quasi-static near field approximations can be applied.  It is found that for very long wavelengths or for sufficiently thin layer thickness the normal mode approach is more useful, whereas for shorter wavelength or for thicker layers, the image method is more efficient and accurate.  In the intermediate range, when the number of normal modes required exceeds  20  or the number of images exceeds  10,  the hybrid methods then become necessary.  The various numerical results are illustrated and compared with experimental data.

## 1.    INTRODUCTION

In this paper, we study the problem of electromagnetic radiation from a dipole antenna in the presence of a two-layer medium [Fig. 1] with the integral reflection coefficient formulation for the field quantities [Kong, 1972, 1975, 1981].  Several mathematical techniques will be applied to the solution of the integrals:  (1) brute force numerical integration methods,  (2) multi-image approach with the saddle point method,  (3) normal mode approach with the residue method,  (4) hybrid approach with combinations of the above methods, and  (5) uniform asymptotic approximation with the generalized Weber functions [Bleistein, 1967; Chew and Kong, 1981; Felsen and Ishihara, 1977; Ishihara and Felsen, 1979; Kong et al., 1974, 1977; Tsang et al., 1973, 1974; Wait, 1970, 1971].  Both quasi-static limits and asymptotic far field solutions will be examined and discussed. Numerical results will be obtained, illustrated, and compared with experimental measurements.

## 2.    FORMULATIONS AND SOLUTIONS

Consider a dipole antenna submerged in a conducting medium as shown in Fig. 1.  Let the antenna be a horizontal electric dipole (HED).  The  z-component of the electric field vector is found to be [Kong, 1981]

$$E_z = -\frac{iIl}{8\pi\omega\epsilon_o} \int_{-\infty}^{\infty} dk_\rho k_\rho^2 [1 - R_{01}^{TM}] \, S^{TM} \, H_1^{(1)}(k_\rho\rho) \, \cos\phi \, e^{i(k_{1z}d + k_{oz}h)} \tag{1}$$

where

$$R_{01}^{TM} = \frac{1 - \epsilon_o k_{1z}/\epsilon_1 k_{oz}}{1 + \epsilon_o k_{1z}/\epsilon_1 k_{oz}} \tag{2}$$

$$R_{12}^{TM} = \frac{1 - \epsilon_1 k_{2z}/\epsilon_2 k_{1z}}{1 + \epsilon_1 k_{2z}/\epsilon_2 k_{1z}} \tag{3}$$

$$S^{TM} = \frac{1 - R_{12}^{TM} e^{i2k_{1z}(H-d)}}{1 + R_{01}^{TM} R_{12}^{TM} e^{i2k_{1z}H}} \tag{4}$$

$k_{oz} = (k_o^2 - k_\rho^2)^{1/2}$,  $k_{1z} = (k_1^2 - k_\rho^2)^{1/2}$,  $k_{2z} = (k_2^2 - k_\rho^2)^{1/2}$,  $k_o^2 = \omega^2\mu_o\epsilon_o$,  $k_1^2 = \omega^2\mu_o\epsilon_1$,  $k_2^2 = \omega^2\mu_o\epsilon_2$.  $Il$ is the dipole moment,  $H_1^{(1)}(k_\rho\rho)$  is the first order Hankel function of the first kind, and  $\phi$  is the azimuthal angle with respect to the  x-axis in the  xy-plane.

In the long wavelength region when  $\lambda > 30$ Km  and for observation distance less than  $\lambda/10$,  we can apply the quasi-static approximation by neglecting the displacement currents.  Under the quasistatic approximation,  $R_{01}^{TM} \approx 1$,  $1 - R_{01}^{TM} \approx -2ip \, \epsilon_o k_{1z}/\epsilon_1 k_\rho$,  where  $p = \pm 1$  and the sign of  $p$  should be kept constant along a particular path of integration to maintain analytical continuity.  We have

$$S^{TM} \approx \frac{1 - R_{12}^{TM} e^{i2k_{1z}(H-d)}}{1 + R_{12}^{TM} e^{i2k_{1z}H}} \ . \tag{5}$$

In the multi-image approach, we assume $|R_{12}^{TM} e^{i2k_{1z}H}| \ll 1$ which is valid for large layer thickness. We expand $S^{TM}$ to obtain

$$S^{TM} = 1 + \sum_{m=1}^{\infty} (-R_{12}^{TM})^m e^{i2k_{1z}mH} + \sum_{m=1}^{\infty} (-R_{12}^{TM})^m e^{i2k_{1z}(mH-d)} \ . \tag{6}$$

Substituting (6) in (1) yields

$$E_z = \frac{pI\ell}{4\pi\omega\varepsilon_1} \cos \phi \int_{-\infty}^{\infty} dk_\rho k_\rho k_{1z} \hat{H}_1^{(1)}(k_\rho\rho) \ e^{i(k_\rho\rho + k_{1z}d) - pk_\rho h}$$

$$+ \frac{pI\ell}{4\pi\omega\varepsilon_1} \cos \phi \sum_{m=1}^{\infty} \int_{-\infty}^{\infty} dk_\rho k_\rho k_{1z} (-R_{12}^{TM})^m \hat{H}_1^{(1)}(k_\rho\rho) \ e^{i[k_\rho\rho + k_{1z}(2mH+d)] - pk_\rho h}$$

$$+ \frac{pI\ell}{4\pi\omega\varepsilon_1} \cos \phi \sum_{m=1}^{\infty} \int_{-\infty}^{\infty} dk_\rho k_\rho k_{1z} (-R_{12}^{TM})^m \hat{H}_1^{(1)}(k_\rho\rho) \ e^{i[k_\rho\rho + k_{1z}(2mH-d)] - pk_\rho h}$$

$$\tag{7}$$

where $\hat{H}_1^{(1)}(k_\rho\rho) = H_1^{(1)}(k_\rho\rho) e^{-ik_\rho\rho}$. Each term of the series is evaluated by the saddle point method with the pole singularities between the original path of integration and the steepest descent path properly accounted for. The first term in (7) is the half-space solution in the absence of the bottom surface. Each integral in the two summations can be identified with an image field [Fig. 2].

In the normal mode approach, we solve for the zeros of

$$1 + R_{12}^{TM} e^{i2k_{1z}H} = 0. \tag{8}$$

The field is then obtained with the residue calculus

$$E_z = \sum_{n=0}^{\infty} E_{zn} + E_b \tag{9}$$

where $E_{zn}$ represents normal mode solutions for each residue and $E_b$ represents the branch point contributions.

In the hybrid image-mode approach, $S^{TM}$ is expanded into a partial sum plus a remainder term as follows:

$$E_z = \frac{pI\ell}{4\pi\omega\varepsilon_1} \cos \phi \int_{-\infty}^{\infty} dk_\rho k_\rho k_{1z} \hat{H}_1^{(1)}(k_\rho\rho) \ e^{i(k_\rho\rho + k_{1z}d) - pk_\rho h}$$

$$+ \frac{pI\ell}{4\pi\omega\varepsilon_1} \cos \phi \sum_{m=1}^{N} \int_{-\infty}^{\infty} dk_\rho k_\rho k_{1z} (-1)^m (R_{12}^{TM})^m \hat{H}_1^{(1)}(k_\rho\rho)$$

$$e^{i[k_\rho\rho + k_{1z}(2mH+d)] - pk_\rho h}$$

$$- \frac{pI\ell}{4\pi\omega\varepsilon_1} \cos \phi \sum_{m=1}^{N} \int_{-\infty}^{\infty} dk_\rho k_\rho k_{1z} (-1)^{m-1} (R_{12}^{TM})^m \hat{H}_1^{(1)}(k_\rho\rho)$$

$$e^{i[k_\rho\rho + k_{1z}(2mH-d)] - pk_\rho h}$$

$$+ \frac{p I \ell}{4 \pi \omega \epsilon_1} \cos \phi \int_{-\infty}^{\infty} dk_\rho k_\rho k_{1z} \ S^{TM} (-1)^{N+1} \ (R_{12}^{TM})^{N+1} \ \hat{H}_1^{(1)} (k_\rho \rho)$$

$$e^{i\{k_\rho \rho + k_{1z}[2(N+1)H+d]\} - pk_\rho h} . \tag{10}$$

This equation can be put in the following descriptive form

$$E_z = \sum_{n=0}^{N} (\text{images}) + \sum_{n=K}^{\overline{K}} (\text{modes}) + R_N \tag{11}$$

where $N$ is the number of images and $R_N$ is a residue term resulting from the contour deformation in the resulting remainder term.

The criterion of choosing $N$ and $K$ can be determined as follows [Felsen and Ishihara, 1977; Ishihara and Felsen, 1979]: Let $N$ be the number of images and $K$ be the first contributing mode. $N$ and $K$ satisfy the inequality

$$M_K > N > M_{K-1}$$

where

$$M_K = \frac{1}{2H \ \text{Real}(k_{1zK})} \ \{p(k_{\rho K}'' - k_1')h + (k_1' - k_{\rho K}')\rho\} - \frac{d}{2H} \tag{12}$$

$k_{\rho K} = k_{\rho K}' + i k_{\rho K}''$ and $k_{1zK}$ is the value of $k_{1z}$ evaluated at the pole $k_{\rho K}$. The real number $M_K$ is the value of $m$ at which the steepest descent path (SDP) defined by

$$ik_\rho \rho + ik_{1z}(2mH + d) - pk_\rho h = ik_1 \rho - pk_1 h - S \tag{13}$$

passing through the branch point at $k_\rho = k_1$ will also pass through the pole at $k_{\rho K}$. It is seen from (12) that as $\rho$ is increased, the value of $M_{K-1}$ starts to increase and will eventually approach the value $N$. Thus when $\rho$ is increased such that $M_{K-1} > N$ then the first excluded mode (i.e. the $(K-1)$th mode) must be added to the modal sum. Similarly, as $\rho$ is decreased such that $M_K < N$, then the $K$th mode should be removed from the modal sum. Alternately, if the number of modes $(\overline{K} - K)$ is kept constant, then the number of images $N$ must be adjusted with varying $\rho$ such that all possible images $N < M_K$ are included.

For high frequencies, we consider the case for which $h = d = 0$. We expand

$$\frac{X_{01} R_{12} X_{10} \ e^{i2k_{1z}H}}{1 - R_{01}R_{12} \ e^{i2k_{1z}H}} = \sum_{m=1}^{\infty} X_{01}X_{10} \ R_{10}^{m-1} \ R_{12}^m \ e^{i2k_{1z}mH} . \tag{14}$$

where $X_{\alpha\beta} = 1 + R_{\alpha\beta}$. A typical expression for the TM field components takes the form

$$T = \int_{-\infty}^{\infty} dk_\rho \ \frac{k_\rho}{k_{oz}} \ X_{01} \ H_0^{(1)} (k_\rho \rho) \ e^{ik_{oz}z} + \sum_{m=1}^{\infty} \int_{-\infty}^{\infty} dk_\rho \ \frac{k_\rho}{k_{oz}} \ X_{01}X_{10} \ R_{10}^{m-1} \ R_{12}^m \ H_0^{(1)} (k_\rho \rho)$$

$$e^{ik_{oz}z + i2k_{1z}mH} . \tag{15}$$

For each image source term in the above expansion, there is a saddle point at $k_{\rho s} = k_1 \sin \alpha_m$ with $\alpha_m = \tan^{-1}(\rho/2md)$. For TM waves there is an additional pole

$$k_{\rho p} = k_1 \left[ \frac{\mu_o \varepsilon_1 / \mu_1 \varepsilon_o - 1}{(\varepsilon_1/\varepsilon_o)^2 - 1} \right]^{1/2} \tag{16}$$

and a branch point on $k_\rho = k_o$ which can be removed by the transformation $k_\rho = k_o \sin \beta$ and $k_{oz} = k_o \cos \beta$. After such a transformation, a typical image-source term in (15) becomes

$$T_m = \int_\Gamma d\beta k_o \sin \beta \, B_m(\beta) \, \tilde{H}(\beta) \, e^{iR_m[\cos \alpha_m (k_1^2 - k_o^2 \sin^2 \beta)^{1/2} + k_o \sin \alpha_m \sin \beta]} \tag{17}$$

where

$$R_m = [\rho^2 + (2md)^2]^{1/2} \tag{18}$$

$$B_m(\beta) = X_{01}X_{10} R_{10}^{m-1} R_{12}^m e^{ik_{oz}z}]_{k_\rho = k_o \sin \beta} \tag{19}$$

$$\tilde{H}(\beta) = H_o^{(1)}(k_o \rho \sin \beta) e^{-ik_o \rho \sin \beta} \tag{20}$$

and $\Gamma$ is the original path of integration on the $\beta$-plane as shown in Fig. 3.

The transformation gives rise to three colinear saddle-points at

$$\beta_{m1} = \sin^{-1}\left[\frac{k_1}{k_o} \sin \alpha_m\right]$$

$$\beta_{m2} = \pi/2$$

$$\beta_{m3} = \pi - \sin^{-1}\left[\frac{k_1}{k_o} \sin \alpha_m\right].$$

The steepest descent path and the branch cut for $\mathrm{Re}[k_{1z}] = 0$ are shown in Fig. 3 for $\alpha_m > \theta_o = \sin^{-1}(k_o/k_1)$.

The removal of the branch point at $k_\rho = k_o$ converts the problem into the asymptotic evaluation of an integral with a singularity close to three colinear saddle-points. Bleistein [1967] described the more general problem of asymptotic integral equation with multiple saddle points and many nearby singularities in terms of generalized Weber's functions. Making use of the generalized Weber's functions, the integrals are evaluated and compared with the ordinary saddle-point methods and experimental results.

## 3. RESULTS

In Figs. 4 and 5 we compare the results for the real and imaginary parts of $E_z$ as calculated with the brute force numerical integral method, the hybrid, the normal mode and the image expansion approaches. It is noted that the quasi-static near field approximation is valid for frequencies less than 100 KHz and for measurement distance less than 1/20 of the free-space wavelength. For higher frequencies or large layer thickness, the multi-image method gives accurate results in an efficient way while for lower frequencies or small layer thickness, the normal mode approach is more attractive. In the intermediate range the hybrid mode approach becomes useful.

At higher frequencies when the quasi-static approximation is no longer applicable, the generalized Weber's functions to approximate the fields are used instead of the ordinary saddle point methods. In Fig. 6, we show the results for $E_z$ component due to a horizontal magnetic dipole and compare the two methods with numerical integrations. The ordinary saddle point result is seen to be inaccurate. However, when $d$ is large, as $\alpha_m \neq \theta_o$ we can show that GOA is a special case of generalized Weber's function approximation.

The TE field of a horizontal electric dipole is dual of the TM field of a horizontal magnetic dipole. For $\mu_1 = \mu_o$, the Sommerfeld pole is at infinity, the generalized Weber function approximation reduces to that of a three-saddle-point analysis repre-

sentable in terms of parabolic cylinder functions. Figure 7 shows the comparison of a three-saddle-point analysis and the geometrical optics approximation when compared with measurement results obtained from a model tank experiment. The three-saddle-point result is demonstably superior to the geometrical optics approximation (GOA).

## ACKNOWLEDGEMENT

## REFERENCES

BLEISTEIN, N., 1967, "Uniform asymptotic expansions of integrals with many nearby stationary points and algebraic singularities", J. Math. and Mech., 17, 533-559.

CHEW, W. C., and J. A. KONG, 1981, "Electromagnetic field of a dipole on a two-layer Earth", Geophysics, 46, 309-315.

FELSEN, L. B., and T. ISHIHARA, 1977, "Hybrid ray-mode formulation of ducted propagation", J. Acoust. Soc. Am., 65, 595-607.

ISHIHARA, T., and L. B. FELSEN, 1979, "High-frequency fields excited by a line source located on a concave cylindrical impedance surface", IEEE Trans. on Ant. and Prop., 172-179.

KONG, J. A., 1972, "Electromagnetic fields due to dipole antennas over stratified anisotropic media", Geophysics, 37, 958-996.

KONG, J. A., 1972, "Theory of Electromagnetic Waves", Wiley-Interscience, New York.

KONG, J. A., (Ed.), 1981, "Research Topics in Electromagnetic Wave Theory", Chapter 10, 211-234, Wiley-Interscience, New York.

KONG, J. A., L. C. SHEN, and L. TSANG, 1977, "Fields of an antenna submerged in a dissipative dielectric medium", IEEE Trans. on Ant. and Prop., AP-25, 887-889.

KONG, J. A., L. TSANG, and G. SIMMONS, 1974, "Geophysical subsurface probing with radio frequency interferometry", IEEE Trans. on Ant. and Prop., AP-22, 616-620.

TSANG, L., R. BROWN, J. A. KONG, and G. SIMMONS, 1974, "Numerical evaluation of electromagnetic field due to dipole antennas in the presence of stratified media", J. Geophysical Res., 79, 2077-2080.

TSANG, L., and J. A. KONG, 1973, "Interference patterns of a horizontal electric dipole over layered dielectric media", J. Geophysical Res., 78, 3287-3300.

WAIT, J. R., 1970, "Electromagnetic Waves in Stratified Media", Pergamon Press, New York.

WAIT, J. R., (Ed.), 1971, "Electromagnetic Probing in Geophysics", Golem Press, Boulder, Colorado.

MEDIUM (0)
(AIR REGION)

$\varepsilon_0$, $\mu_0$

RECEIVER

MEDIUM (1)
(SEA WATER)

$z = d$

DIPOLE SOURCE
(I$\ell$)

$z = 0$

$\varepsilon_1{}'$, $\mu_0$

$\varepsilon_1 = \varepsilon_1{}' + i \dfrac{\sigma_1}{\omega}$

$z = -(H-d)$

MEDIUM (2)
(GROUND)

$\varepsilon_2{}'$, $\mu_0$

$\varepsilon_2 = \varepsilon_2{}' + i \dfrac{\sigma_2}{\omega}$
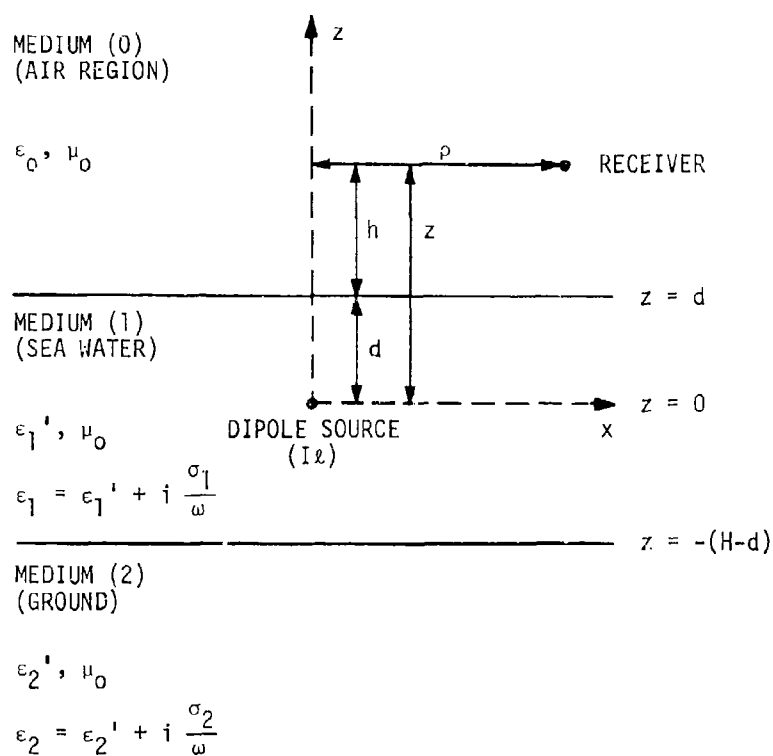
Figure 1    A dipole antenna submerged within a conducting
medium.

$\varepsilon_0$, $\mu_0$

RECEIVER

DIPOLE
SOURCE
(d)

H

$\varepsilon_1{}'$, $\mu_0$

$\varepsilon_2{}'$, $\mu_0$

IMAGE (1)
(2H - d)

IMAGE (1')
(2H + d)
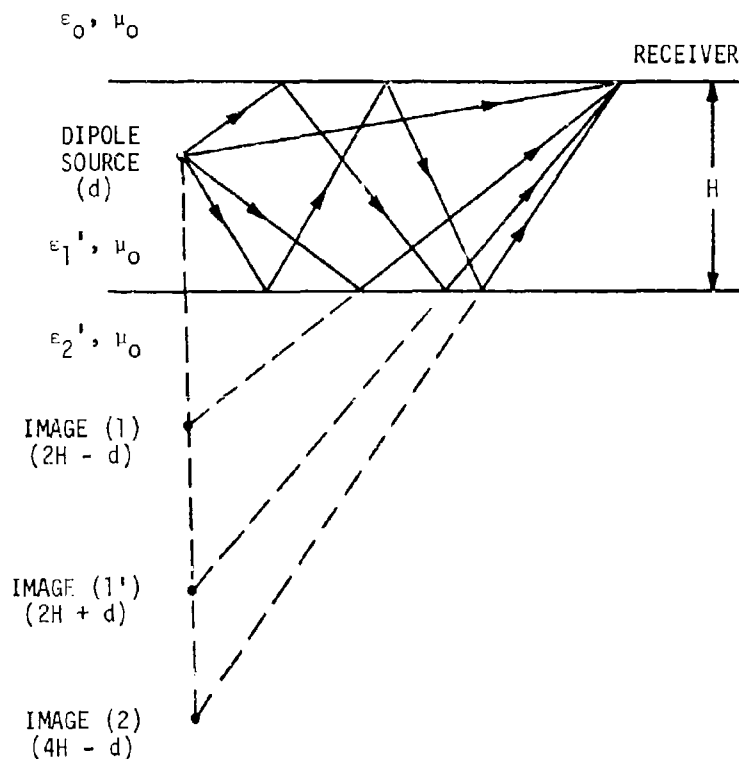
IMAGE (2)
(4H - d)

Figure 2    Dipole source and its images for a two-layer
medium.
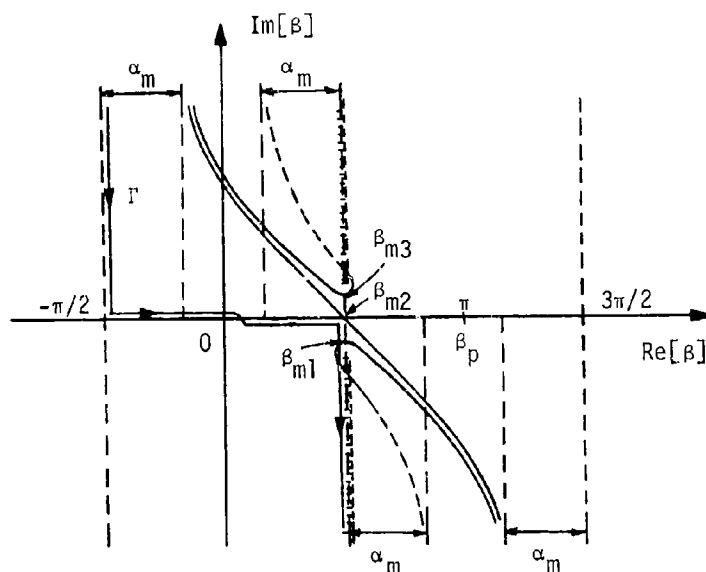
Figure 3    Steepest-descent paths on β-plane that pass
through three colinear saddle points when $\alpha_m > \theta_o$.
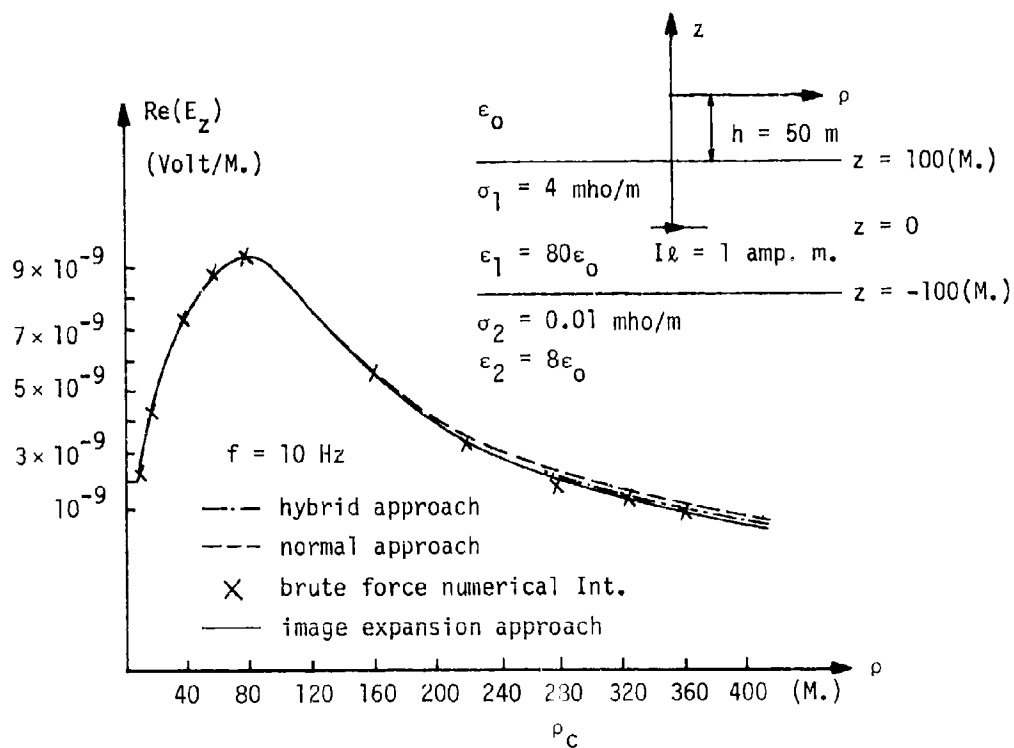


Figure 4    The real part of $E_z$ as calculated by the four
methods.
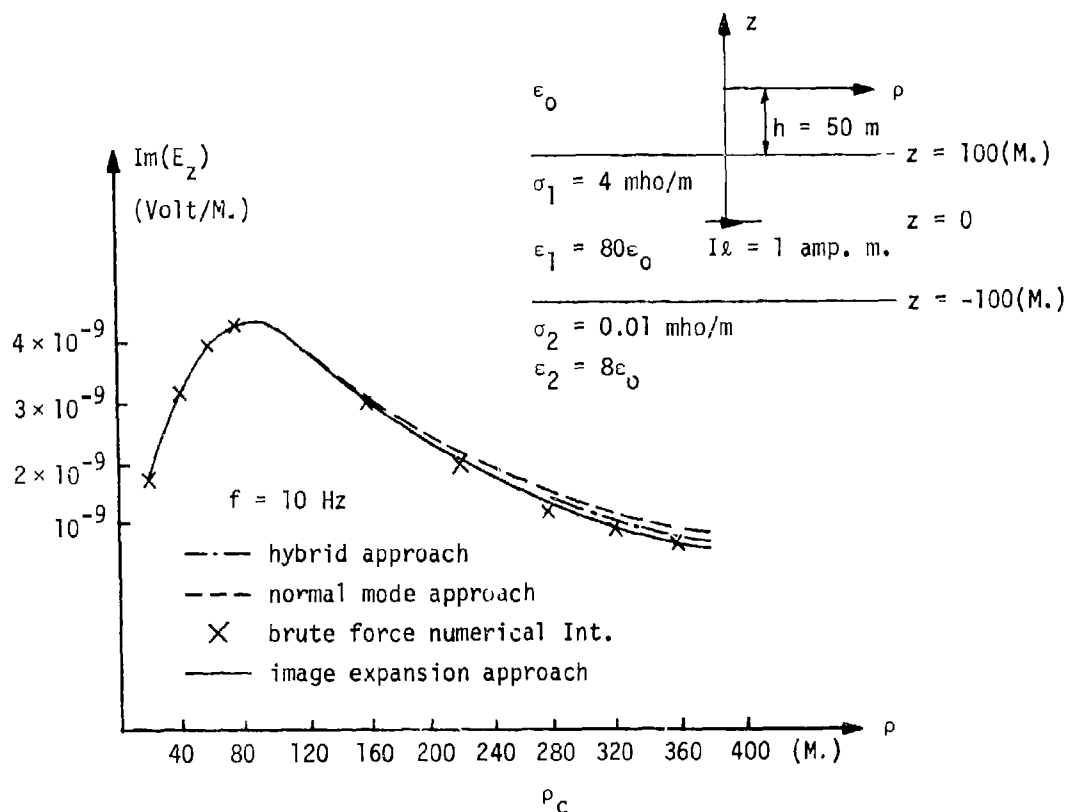
Figure 5    The imaginary part of $E_z$ as calculated by the four methods.
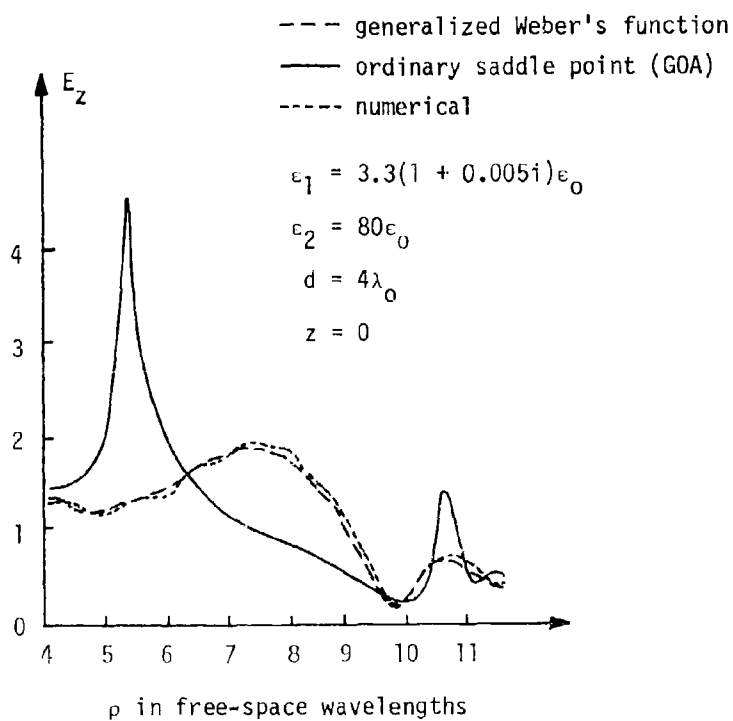


Figure 6    $E_z$ component in the broadside direction of an HMD normalized with respect to $I\ell/4\pi\omega\epsilon\lambda^2$.
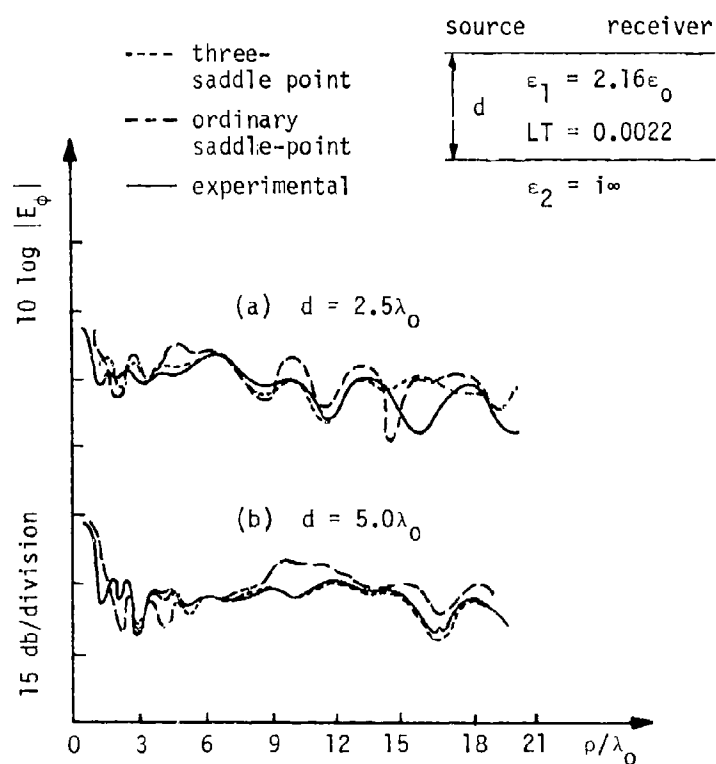
Figure 7   $E_\phi$ component from various theories in comparison
with experimental results from model tank.

NEW TECHNOLOGY FOR ELF RADIATORS : A REVIEW OF AIRBORNE, ROCKET-BORNE AND SPACE-BORNE ANTENNAS

Mario D. Grossi
Raytheon Company
Portsmouth, R.I.,02871,U.S.A.

## SUMMARY

Engineering practicality and ecological and societal acceptability of a ELF system depend essentially upon the design parameters of the radiator at the transmitting terminal. The ecological problem virtually vanishes when the ELF radiator is either airborne, rocket-borne or space-borne. However, the feasibility issue centers now on the achievable intensity of the electric or magnetic moments, owing to the limited availability of primary power. The technological outlook is, however, promising. Long wires that trail an airplane or are suspended vertically from it, similar to the VLF TACAMO antenna, can be used as effective electric dipoles. Airborne loops, cryogenic and non-cryogenic, are also a possibility. For the rocket-borne and the space-borne cases, recent studies of the deployment in orbit of a metal wire several hundred kilometers long, kept aligned along the vertical by gravity gradient forces, have shown that there is a large source of electrodynamic primary power, due to the $\underline{v} \times \underline{B}$ phenomenon, that could be utilized to energyze the ELF system. A Shuttle-borne experiment is in preparation, to be conducted on the occasion of an orbital Shuttle mission of the mid '80s.

## 1. INTRODUCTION

The engineering solutions considered thus far by the designers of ELF radiators have been strictly limited to ground-based configurations. These unusually large radiators have been the object of a long-lasting controversy : their societal acceptability has proved to be problematic, mostly because of their environmental impact. These problems have held back, in fact, their full scale development for at least two decades.

The large ELF ground antenna proposed in the mid '60s for Project SANGUINE was supposed to be installed in Wisconsin and to cover there an area of 13,750 Km$^2$ of low conductivity soil. It was designed to use a total wire length of about 1,000 Km, with the wire cut in 10 segments, each about 100 Km long, with all segments parallel and spaced 10 Km apart. A total of 100 transmitter modules would have required a primary power of 25 Megawatt. Current in the wire was supposed to reach 77.1 A, with a total electric moment of 7.71 10$^8$ Am.

Of the smaller SEAFARER antenna, also in the ELF band, two versions were designed in the mid '70s, one for installation in Wisconsin and one in Michigan. The Wisconsin antenna was supposed to have a total wire length of 750 Km and to cover an area 3,368,75 Km$^2$. All wire segments were supposed to be parallel and spaced about 1 Km apart, with a total of 40 terminal grounds. A set of four transmitters required a 5 MW primary power line. The Michigan antenna was designed to use a total length of 649.37 Km buried wire and to cover a 4,550 Km$^2$ area. Wire segments were supposed to be all parallel and spaced 8.37 Km apart, with a total of 66 terminal grounds. The required level of primary power was 5 MW.

Because of societal opposition against the large ELF antennas above , "Austere ELF" antenna concepts were elaborated upon, in the late '70s. A proposed scheme is depicted in Figure 1 and Figure 2. The first Figure depicts an ELF antenna existing at Clam Lake, Wisconsin. It is a center-driven, end-grounded, telephone pole mounted wire configuration, with a limit of 300 A wire current imposed by environmental constraints. The plan was to feed this antenna with a transmitter that was phase-locked, via telephone line, to a similar transmitter at the ELF installation of K.I. Sawyer AFB, Michigan, that is 265 Km away. This second installation ( see Figure 2) was actually never built. Its design consists of three arms, with length 48.5 up to 64.5 Km, and with a total wire length of 210 Km.

Even with these reduced configurations, opposition to ground based ELF antennas has, however, not subsided and although plans are being again laid out for a ground ELF installation, the environmentalists too are mapping the course of their counteraction.

## 2. AIRBORNE, ROCKET-BORNE AND SPACE-BORNE ELF RADIATOR CONFIGURATIONS

The ecological problems virtually vanish  when the ELF radiator is airborne, rocket-borne or spaceborne. Feasibility and practicality now center on the achievable intensity of the electric or magnetic moment, owing to the limited availability of primary power that characterizes such airborne, rocket-borne and space-borne platforms.

The technological outlook is, however, promising. Long wires that trail an airplane or are suspended vertically from it can be used as effective electric dipoles. Airborne loops, cryogenic and non-cryogenic, are also a possibility. One of the most succesful developments of airborne long-wire antennas is the VLF antenna of the TACAMO system, used for submarine communications. This antenna has been in operation for several years, as the radiator of the airborne TACAMO station ( see Figure 3). It is a 10 Km wire that acquires a nearly vertical configuration when deployed from a EC-130 G/Q airplane that moves in a tight-turn flight pattern above the ocean area of interest. The antenna is fed by a VLF transmitter with 200 Kw output power, installed on the EC-130 G/Q. Investigations on the use in the ELF band of such 10 Km wire ( and of an even longer wire), deployed from airplanes, helicopters, or from high-altitude balloons, are in progress.

As far as the case is concerned of ELF antennas mounted on rockets, on board the Shuttle Orbiter, on S.O.C. (Space Operational Center), or on other orbiting vehicles (Grossi, 1973), recent studies have provided analytical proof of the feasibility of the orbital deployment of a metal wire that is several hundred kilometers long. This wire may acquire several positions of equilibrium, one of which is the vertical orientation, stabilized by gravity-gradient forces. Another is the trailing, horizontal position that is stable when the wire is terminated with a large balloon, that provides a sufficiently strong braking force because of the air drag due to the residual air density at the Shuttle orbital heigth.

When vertically oriented, the wire, for most of the orbital inclinations of the Shuttle ( exclusive of the polar and of the near-polar ones) generates a large amount of electrodynamic DC power, by the $\underline{v} \times \underline{B}$ mechanism and by the additional interactions between the terminating electrodes and the ionosphere. This DC power can be converted into electromagnetic radiation at ELF by the so-called Alfven Wings mechanism. In this case, the orbiting vertical wire, moving at orbital speed in the magneto-ionic medium of the Earth ionosphere, functions at the same time as a DC power generator, and as a ELF radiator.

In alternative, the DC power generated by the vertical orbiting wire can be converted to ELF by a static DC/AC converter on board the Shuttle Orbiter and can be used to feed another wire antenna deployed by the same orbiting vehicle, possibly in the horizontal direction. Figure 4 shows a deployment sequence of a rocket-borne wire antenna that could produce about 50 Kw of DC primary power by the $\underline{v} \times \underline{B}$ phenomenon, of which about 45 Kw could be available, net of ohmic losses, for the excitation of the Alfven Wings mechanism. Two space-borne configurations, that use basically the NASA TSS (Tethered Satellite System) facility on board the Shuttle Orbiter are illustrated in Figure 5 and Figure 6. The TSS system is expected to be an orbital reality in the mid '80s.

As a part of TSS, mechanisms of wire deployment and retrieval, and a possible control system, are illustrated in Figure 7 and Figure 8. The controls are designed to minimize in-plane and out-of-plane oscillations of the long wire, of the type illustrated in Figure 9, that are expected to insurge during the various phases of the orbital operations of TSS.

## 3. THEORETICAL BACKGROUND

### 3.1 Introductory remarks

The generation and injection of electromagnetic waves in space plasma by means of a long tether in Earth orbit, at ionospheric heigths, is a comprehensive subject, since there are several electrodynamic phenomena associated with the moving tether (Dobrowolny, 1981), some of which potentially usable for ELF emissions.

The configuration on which we will mostly concentrate in this lecture pertains a metallic tether connected to the Shuttle at one end, and to a conducting balloon at the other end. The tether can be deployed both upwards and downwards with respect to the Shuttle Orbiter. This amounts, from the electrodynamics point of view, to exchanging the polarity of the two end electrodes ( the balloon and the conducting part of the Shuttle) with respect to the ionospheric plasma. The numerical results provided in this section have been obtained primarily for a tether that moves perpendicularly to the geomagnetic field lines at the Shuttle velocity $v_0 = 7.8$ Km/sec. Length and radius of the long wire are taken to be $L = 100$ Km and $r_w = 0.5$ mm. The motion of this long metal wire in the Earth ionosphere will lead to the generation of electromagnetic waves in different frequency bands from ULF to HF , through several generation mechanisms (Williamson and Banks, 1976; Dobrowolny et al., 1979; Dobrowolny, 1979; Banks et al., 1982).

As the tether system moves through the Earth magnetic field, a polarization electric field $\underline{E} = -\underline{v} \times \underline{B}$ is seen along the tether from the plasma rest frame ( we refer, for the moment, to the case of a perfectly conducting tether). With the Earth magnetic field $B = 0.3$ Gauss, we obtain a maximum potential difference between the ends of the system: $V_0 = 2.34 \ 10^4$ Volt ( when $\underline{v}$ is perpendicular to $\underline{B}$ ). A corresponding potential difference is therefore seen to be applied between the lines of force that pass through the terminations of the system and leads to propagation of waves away from the region of the disturbance. Electromagnetic power generation is thus achieved without the use of on-board transmitters and without pulsing the tether current. The source of primary energy is provided by the tether's motion. As it has been pointed out (Grossi and Colombo, 1978; Dobrowolny, 1979), this electrodynamic interaction, and corresponding wave generation, is similar to the interaction of certain celestial bodies with plasmas, such as the one of Jupiter's moon Io with the jovian magnetosphere. Recent Voyager I measurements performed inside the Io's tube of flux ( Ness et al, 1979) have confirmed the occurrance of this interaction.

By appropriately modulating an electron emitter on board the Shuttle Orbiter, one can then obtain pulsating currents in the conducting tether ( Banks et al., 1980) and this can maximize emissions at the modulating frequency. An on-board transmitter can also be used to feed the tether as a normal driven antenna ; such a transmitter is essential in the case of horizontal tether oriented in the direction of motion, where there is no natural current flowing in the wire. There would be no dynamical problems with this configuration. In fact, the horizontal tether, if terminated at the free end by a balloon (that operates as a aerodynamic brake) would be a stable system configuration (Colombo, 1980).

In configuration A of Figure 10 (balloon downwards with respect to Shuttle Orbiter), and under the assumption that the Shuttle is kept at low potentials with respect to the medium, large potential drops may be present between the balloon surface and the ionospheric plasma. Then, as pointed out by Dobrowolny (1979), secondary electrons can be produced by the impact of energetic ions on the surface of the balloon. These secondaries may then be accelerated away from the balloon along magnetic lines towards the Earth atmosphere. Thus, generation of accelerated electron beams is another phenomenon that might be associated with the tether's interaction with the surrounding medium. This has been suggested by a number of authors (Goldreich and Lynden-Bell, 1969; Gurnett, 1972; Hubbard et al, 1976) in studies of the interaction of Io with Jupiter's magnetosphere.

The generation of accelerated electron beams may also give rise to instabilities, through electron cyclotron resonance interactions, and may produce whistlers and wave at even a higher frequency. At the altitudes of interest, the electron cyclotron frequency is $f_{ce} \cong 0.8$ MHz and the electron plasma frequency $f_{pe}$ ranges between 5 and 11 MHz. It is therefore in the HF band where wave generation by accelerated electron beams should be expected.

### 3.2 Current-Voltage Chracteristics of the orbiting wire

The tether-balloon system, while moving across magnetic lines, carries a current due to the collection of ionospheric ions and electrons at its ends ( the balloon at one end, and the conducting part of the Shuttle

surface at the other, estimated to have an area of approximately 35 $m^2$). The condition that must be imposed in order to derive current and potentials is that of the balance of charged particle fluxes between the two end electrodes. The current collected at the Shuttle end, $i_s$ must be equal and opposite to the current $i_B$ collected at the balloon end :

$$i_s(V_s) = - i_B (V_B) \qquad (3.1)$$

This equation holds for a wire system that does not use neither ion nor electron guns on board the Shuttle. For the potentials $V_s$ and $V_B$ , we have :

$$\left| V_s - V_B \right| = \left| \underline{v}_o \times \underline{B} \cdot L \right| \qquad (3.2)$$

where L is the tether length. Hence (3.1) is an implicit equation for one of the potentials, for example $V_s$ . Having determined $V_s$, the $V_B$ is obtained from (3.2), and the current $I_c = \left| i_s \right| = \left| i_B \right|$ is calculated from the solutions found for the potentials.

The model that has been used for charged particle collection is the following (Anderson et al., 1979; Dobrowolny, 1981). For the attracted particle contribution to the current referring to particles of species j ( we use j =i or e, for ions and electrons respectively), we can write:

$$\frac{i_j \text{ attracted}}{i_{jo}} = f(V) \qquad (3.3)$$

where the normalizing electron and ion currents are given by :

$$i_{eo} = \frac{1}{8} \; n_\ell \left| e \right| \; v_{the} \; A \qquad (3.4)$$

$$i_{io} = \frac{1}{4} \; n_\ell \; Z \left| e \right| v_o \; A \qquad (3.5)$$

where A is the collecting area, $n_\ell$ is the electron density and $v_{the}$ is the thermal velocity. The function f depends from the electron potential V, through :

$$\phi^* = \left| \frac{eV}{kT_e} \right| \left( \frac{\lambda_{de}}{R} \right)^{4/3} \qquad (3.6)$$

where $T_e$ is the electron temperature, $\lambda_{de}$ is the Debeye length , and R is the electrode's radius. The function $f(\phi^*)$ is plotted in Figure 11. The plot was derived by combining different models for particle attraction by large electrodes at large and moderate potentials ( Alpert et al., 1965; Linson, 1969).

For the repelled particle contribution to the current, we use simply :

$$\frac{i_j \text{ repelled}}{i_{jo}} = e^{-\left| \frac{eV}{kT_e} \right|} \qquad (3.7)$$

where V is now the repelling potential. Approximate results for current and potentials as a function of balloon radius, obtained with the model of a perfectly conducting tether, are given by Anderson et al., (1979). Recently a more accurate method (Arnold and Dobrowolny, 1980) has been developed, based on a transmission line analogy of the tether system, to compute the stationary state governed by (3.1). This was done by solving a time dependent problem, and hence the transient of the tether system toward the stationary state was also obtained.

It must be noticed that the equilibrium current i in the tether , obtained by the method outlined above, is a very non linear function of the equilibrium potential difference ($V_s - V_B$ ), also obtained from the calculation approach above. The various results for current and potentials versus balloon radius do not correspond therefore to a ohmic relation between i and $V_s - V_B$ , involving the tether resistance $R_w$ . It is however true that, in all cases, the current values obtained must be smaller than the ohmic limit that corresponds to the total electromotive potential available, i.e. :

$$i < i_R = \frac{\left| \underline{v}_o \times B \cdot \underline{L} \right|}{R_w}$$

Figure 12 gives an example of calculation of the Shuttle potential ($V_s$) and of the ballon potential ($V_B$) for the case in which neither electron nor ion guns are used on board the Shuttle Orbiter, and for a downwards configuration ( Case A of Figure 10). The wire is assumed to be made of aluminum. Figure 13 gives the current in the wire as a function of balloon radius, again for Configuration A and for two values of wire resistivity ( $\rho = 0.03 \mu \Omega m$ for aluminum and $\rho = 0.15 \mu \Omega m$ for piano-wire steel ).In all cases the principal limitation for the current in the tether is the tether resistance. For the two values of resistivity considered above, the limiting values are :

$$i_R = 1.23 \text{ A} \qquad \text{for } \rho = 0.15\mu \, \Omega \text{ m}$$

$$i_R = 6.1 \text{ A} \qquad \text{for } \rho = 0.03\mu \, \Omega \text{ m}$$

These limiting values are, however, not reached in systems that do not use electron or ion emitters, even with very large ballon radii. These emitters are essential when it is required to boost the current in the tether at its highest values.

Let's consider now the case in which an electron gun or an ion gun is used on board the Shuttle Orbiter. In Configuration A (Figure 10), we need an ion gun on board the Shuttle and it must be used in such a way as to keep very small its potential with respect to the plasma ( $V_s \cong 0$ ). The balloon will be at the potential $-|V_B|$, where:

$$|V_B| = \Delta\phi_0 - R_w i \tag{3.8}$$

and $\Delta\phi_0 = |\underline{v}_0 \times \underline{B} \cdot \underline{L}|$. The current i will be given by the equation:

$$i = i_B = i_{i0} \, f \, (|V_B|) \tag{3.9}$$

For a given balloon radius $R_B$, the actual values of current in the tether and potential of the balloon are obtained from the intersection of the two curves $i(V_B)$ given by (3.8) and (3.9). The results of the calculations are given in Figure 14. The achieved increase in current can be appreciated by comparing Figure 14 with Figure 13. Figure 15 shows the level of current in the wire achievable for Configuration B, when an electron gun is used on board the Shuttle. It can be seen in the Figure that for balloon radius larger than about 10 meter , it is possible to approach the resistive limit of the current.

As it can be seen in Figure 3, that applies to cases when neither an ion nor an electron gun is used, the Configuration A balloon can be charged to a very high and negative potential. The ions that impact on the balloon surface can thus reach high energies through the accelerating sheath region surrounding the balloon and can cause significant emissions of secondary electrons. Since this effect produces a change in the current, and hence in the voltages, it must be taken into account in computing current-voltage characteristics. The effect is also of interest because the secondary electrons, accelerated away from the balloon through the sheath region, can produce electromagnetic waves, as already mentioned in this lecture. This effect has been included in the software that computes current-voltage characteristics of the tether.

3.3 Partition of the primary electrodynamic power into the various loads

In view of the potential uses of the orbiting tether as a ELF generator, it is of relevance to analyze how the primary electrodynamic power of the tether system ( that originates from the $\underline{v} \times \underline{B}$ phenomenon) is divided into different loads. The power level that we calculate from the equation:

$$P_1 = \left| V_s - V_B \right| i \tag{3.10}$$

by using the results of the computation of current and potentials, does contain the effect of the ohmic losses in the wire (i.e. $\left| V_s - V_B \right| = V_0 - R_w i$ ). The power dissipated in ohmic losses is:

$$P_2 = R_w i^2 \tag{3.11}$$

If there is no effect of secondary electron emission, we can say that the total power $P_4$ available for exciting wave processes outside the tether is $P_1$. That is, $P_4 = P_1$. When acceleration of secondary electrons takes place, an overestimate for the power level $P_3$ that goes in accelerating electrons can be obtained by assuming that , in passing through the sheath surrounding the balloon, the electrons gain all the energy $|eV_B|$. Then,

$$P_3 = \left| V_B \right| i_{sec} \tag{3.12}$$

where $i_{sec}$ is the current of secondary electrons. This is an overestimate, partly because the emitted secondaries are accelerated through the sheath region only through the component of the electric field that is parallel to $\underline{B}$ , which inserts a numerical factor $( < 1)$ in (3.12). In this equation, we have

$$i_{sec} = i^{(i)} \, (V_B) \, \delta \, (|V_B|) \tag{3.13}$$

where $\delta$ is the yield, a function of the total balloon potential with respect to the plasma. At equilibrium we have:

$$i_{sec} = i \frac{\delta(V_B)}{1 + \delta \, (V_B)} \tag{3.12}$$

where i is the total current. Consequently, we have:

$$P_3 = |V_B| \, i \, \frac{\delta}{1+\delta} \tag{3.13}$$

In the general case $P_3 \neq 0$ and the power level $P_4$ available for wave generation, is given by: $P_4 = P_1 - P_3$. There might be another dissipative phenomenon: the generation of microturbulence in the charged sheath surrounding the balloon, and this could absorb power. Thus, $P_4$ must be considered rather an upper limit for the power that is expected to be available for wave generation. Numerical examples of calculations for the various power levels considered above are presented in Figure 16.

### 3.4 The phenomenon of the Alfven Wings

The concept of the Alfven Wings was introduced by Drell et al (1965) and further developed by Chu and Gross (1966). It has gained recently experimental support from the Voyager 1 observations of magnetic field perturbations associated with the flux tube of the moon Io in Jupiter's magnetosphere (Ness et al, 1979) and from further work that did follow, once the observations were analyzed (Neubauer, 1980). Figure 17 (Banks et al, 1980), gives a pictorial view of the current wings associated with a TSS moving in the Earth ionosphere. The basic features of the disturbance associated with the TSS are as follows. Since the ionospheric conductivity parallel to the Earth magnetic field is extremely large at altitudes above the E layer, and much larger than the transverse conductivity, the magnetic field lines can be regarded as equipotential. The ionospheric state is perturbed by the motion of the tether, or by any large conductors, across magnetic lines. From the rest frame of the plasma, it is seen a polarization electric field $\underline{E} = - \underline{v}_0 \times \underline{B}$, if we consider the tether fully conducting. A corresponding potential difference is, therefore, seen between the lines of force touched by the two terminating ends of the system. This perturbed state tries to readjust itself to the previous equilibrium state (with no potential difference across field lines) through the propagation of waves from the region of disturbance. These waves, and the associated currents parallel to $\underline{B}$ lines, carry away the applied potential differences, or the equivalent transverse space charge. The angular frequency $\omega$ of the radiated wave is constrained to satisfy the equation $\omega = k_y v_0$, where $k_y$ is the wave number and y is the direction of motion of the TSS system. An estimate for $k_y$ is given by $k_y = 2\pi/d_y$ where $d_y$ is the conductor's dimension in the direction of motion. We obtain for the frequency $f^* = v_0/d_y$.

It is important to realize that $f^*$ must be interpreted as an upper limit of the frequencies contained in the disturbance. If $f^* < f_{ci}$ (cyclotron frequency for the ions), all the power contained in the disturbance goes into hydromagnetic waves and, in particular, into Alfven waves. This happens for the case of Io. In the case of the TSS, this occurrance materializes when the balloon radius $R_B$ is larger than a critical value $R_B^*$ : $R_B \Rightarrow R_B^* \simeq (20 \sin\alpha)$ meter, where $\alpha$ is the angle between velocity and magnetic field.

The coupling of the tether system to the plasma medium occurs through the radiation of waves. In particular, if a current $J_\parallel$, parallel to magnetic field lines, is associated with these waves, it continues the tether current into the ionosphere, down to E layer altitudes, where perpendicular current closure can take place. This parallel wave current is beyond the so-called "DC current model" of Io, proposed by Goldreich and Lynden-Bell (1969). According to this model, the flux tube containing Io would actually be frozen to this moon and thus would follow its motion around Jupiter, with up and down going parallel currents at the boundaries of the tube (the Alfvenic currents) and circuit closure provided by Io at one side and by the Jupiter ionosphere at the other side.

An equation of general validity, not limited to the case of small amplitude waves, is the following (Jeffrey and Taiuti, 1964):

$$\underline{v} \pm \frac{\underline{B}}{(\mu_0 \rho_p)^{1/2}} = constant \qquad (3.14)$$

where $\underline{v}$ and $\underline{B}$ are the fluctuations of velocity and magnetic field in the wave, and $\rho_p$ is the plasma mass density. The constant can be evaluated from the background properties of the plasma. In the rest frame of the plasma, then, we have:

$$\underline{v} \pm \frac{\underline{B}}{(\mu_0 \rho_p)^{1/2}} = \underline{v}_A = \frac{\underline{B}_0}{(\mu_0 \rho_p)^{1/2}} \qquad (3.15)$$

where $\underline{B}_0$ is the Earth magnetic field. For infinite conductivity along magnetic lines, we have $E_\parallel = 0$ and the Ohm's law reduces to

$$\underline{E}_\perp + \underline{v} \times \underline{B} = 0 \qquad (3.16)$$

Taking now the divergence of this equation and combinig it with (3.15), we arrive at the equation:

$$\nabla_\perp \cdot \underline{E}_\perp = \mu_0 v_A J_\parallel$$

which relates the space charge, or potential difference, across field lines with the parallel current associated with the wave. In the case of the TSS, space charge corresponds to the electromotive force applied by the orbiting wire between two diffent field lines. On the other hand, by combining Maxwell's equations:

$$\nabla \times \underline{E} = - \frac{\partial \underline{B}}{\partial t}$$

$$\nabla \times \underline{B} = \mu_0 \underline{J}$$

we arrive at the equation :

$$\nabla\nabla \cdot \underline{E} - \nabla^2 E = \mu_0 \frac{\partial \underline{J}}{\partial t} \qquad (3.17)$$

projecting along the magnetic field (z) direction and taking into account that:

$$\frac{\partial}{\partial t} (\nabla_\perp \cdot E_\perp) = \mu_0 \frac{\partial J_z}{\partial t} \qquad (3.18)$$

By combining (3.17) with the equation $\nabla_\perp \cdot E_\perp = \mu_0 v_A J_\shortparallel$, already introduced, we can write:

$$\frac{\partial}{\partial t} (\nabla_\perp \cdot E_\perp) = v_A \frac{\partial}{\partial z} (\nabla_\perp \cdot E_\perp) \qquad (3.19)$$

which tells us that the transverse space charge propagates at the Alfven speed, within the MHD framework and parallel to magnetic field lines. Actually the Alfvenic current flows at an angle $\theta_A$ with respect to the field lines given by $\theta_A = \arctan \frac{v_0}{v_A}$ . In our case $\theta_A \simeq 0.55^0$ and therefore, to all practical purposes, we can speak of parallel motion. In order to have an Alfvenic disturbance, we must consider for the balloon a very large dimension. Then, by assuming that the current is uniformly distributed across the tube of flux defined by the balloon boundary, we can write

$$J_\shortparallel = \frac{I_{AW}}{\pi R_B^2} \qquad (3.20)$$

and, consequently :

$$I_{AW} \sim \frac{\pi}{2} R_B \frac{1}{\mu_0 v_A} \cdot E_\perp \qquad (3.21)$$

The perpendicular electric field, taking ohmic losses in the tether into account, is given by :

$$E_\perp = E_{\perp 0} - \frac{R_W I_{AW}}{L} \qquad (3.22)$$

where $E_{\perp 0}$ is the total Lorentz field and, for motion perpendicular to $\underline{B}$ : $E_{\perp 0} = v_0 B = 0.23$ Volt/m. We can therefore write for the Alfvenic current $I_{AW}$ :

$$I_{AW} = \frac{I_0}{1 + \frac{\pi}{2} \frac{R_B}{L} \frac{R_W}{\mu_0 v_A}} \qquad (3.23)$$

where:

$$I_0 = \frac{\pi}{2} R_B \frac{1}{\mu_0 v_A} E_{\perp 0} \qquad (3.24)$$

is the total parallel current in Alfven waves, which we would have for a perfectly conducting tether.

Figure 18 illustrates the Alfvenic current $I_{AW}$ as a function of balloon radius for a tether length L = 100 Km and two values of wire's resistivity. We have taken in our calculations $v_A = 800$ Km/sec as an average value for the Alfven speed between 100 and 300 Km altitude. The curves of the Figure have validity for $R_B \simeq 20 \sin\alpha$ meter, as the current $I_{AW}$ applies to waves in the hydromagnetic range of frequencies. The current $I_{AW}$ is not the current $I_c$ in the tether, which originates from the particle collection at the terminating end electrodes. Figure 19 provides their ratio. In the cases of the Figure, the Alfvenic current always exceeds the collection current $I_c$. Unless there is a mechanism, not included in our analysis, that establish a limit for $I_{AW}$, the Alfven Wings should be able to carry away along magnetic lines of force the electromagnetic perturbation produced by the TSS, however large this might be.

Concerning the amount of power associated with the Alfven Wings, this quantity can be obtained by multiplying the wave energy density W by the volume filled by the wave energy in one second. This volume, in turn, is given by the cross section of the tube of flux delimited by the system boundary ( let's call this cross section A) multiplied by the wave group velocity $v_G$. Thus $P_{AW} = W 2A v_G$, where the factor 2 indicates wave propagation in two opposite directions with respect to the tether system, toward the conjugate regions of the low ionosphere. For Alfven waves, the following equation applies: $W_{WA} = B^2/2\mu_0$, where B is the magnetic field of the perturbation. By having $v_G = v_A$, we obtain $P_{AW} = B^2 A v_A/\mu_0$. For this equation to be valid, $R_B \gtrsim (20 \sin\alpha)$ meter. The perturbing magnetic field is calculated in terms of the transverse electric field across the balloon cross-section: $B = E_\perp/v_A$. By taking into account the resistive losses in the tether, we obtain the expression for the power of the Alfvenic waves:

$$P_{AW} \sim \frac{(E_{\perp 0} - R_{W} i)^2}{\mu_o v_A} \pi R_B^2 \qquad (3.25)$$

where the current i must be computed as a function of balloon radius. The input impedance $Z_{AW}$ of the tube of flux can be computed from

$$Z_{AW} = \frac{\Delta v^2}{P_{AW}} \qquad (3.26)$$

where $\Delta v = 2 R_B E_{\perp}$. From (3.25) and (3.26) we obtain $Z_{AW} = \frac{4}{\pi} \mu_o v_A$. At the altitudes of interest, a typical value of this impedence is $Z_{AW} \cong 1.3$ ohm.

Figure 20 shows results of calculations for the power $P_{AW}$ as a function of balloon radius.

## 4. NUMERICAL ESTIMATES OF FIELD INTENSITIES AT THE EARTH SURFACE

Calculations of the field intensity achievable at the Earth surface with the rocket-borne ELF radiator of Figure 4 are reported in Table I. These calculations are based on the Alfven Wings mechanism. Similar calculations have been performed for the system configuration of Figure 5. This is a Shuttle-based vertical tether system substantially more powerful than the system in igure 4, with a tether length of 400 Km. Table II contains the results of the calculations performed for this system configuration.

The configuration of Figure 6 is the most complex of the ones that we have considered. In it, the vertical wire generates DC power that is converted to ELF by a DC/AC static converter. The excitation of the Alfven Wings mechanism is minimized in order to reduce radiation losses. The ELF power obtained by static conversion is utilized to feed the horizontal dipole, characterized by an electric moment $I\ell = 3.2 \; 10^6$ Am.

#### TABLE I

##### PERFORMANCE PARAMETERS OF ROCKET-BORNE ELF WIRE ANTENNA

| | |
|---|---|
| Wire Length | 100 Km |
| Wire diameter | 2 mm ( aluminum wire coated with dielectric) |
| Wire ohmic resistance | 1 Kohm |
| Current in Wire | 2 Amp |
| Mass of wire | 850 Kg |
| Balloon radius | 50 m |
| Electrodynamic power generated | 47 Kw |
| Power Losses ( ohmic losses) in the wire | 4 Kw |
| Net available electro-dynamic power | 43 Kw |
| Ionospheric transmission losses | 6 dB |
| Conversion losses electro-dynamic power to electromagnetic power | 30 dB (initial estimate) |
| E.m. field at hot spot on the Earth surface | $H_{\parallel}$ = 1 milligamma |
| Noise level in 1 Hz bandwidth | Noise = 0.1 milligamma |
| Signal-to-Noise Ratio in 1 Hz bandwidth | SNR = + 20 dB |

#### TABLE II

##### SHUTTLE-BORNE, VERTICALLY DEPLOYED, ELF ANTENNA. PERFORMANCE PARAMETERS

| | |
|---|---|
| Wire length | 400 Km |
| Wire diameter | 2 mm (aluminum wire with dielec. coating) |
| Mass of Wire | 3.4 Tons |
| Wire ohmic resistance | 4 Kohm |
| Current in the wire | 8 A |
| Balloon radius | 50 m |
| Electrodynamic power generated | 750 Kw |
| Power losses in the wire (ohmic losses) | 250 Kw |
| Net available electrodynamic power | 500 Kw |
| Ionospheric transmission losses | 6 dB |
| Conversion losses Electrodynamic-to-electromagnetic power | 30 dB (initial estimate) |
| E.m. field intensity at hot spot on the Earth surface | $H_{\parallel}$ = 3 milligamma |
| Noise level in 1 Hz bandwidth | Noise = 0.1 milligamma |
| Signal-to-Noise ratio in 1 Hz bandwidth | SNR = + 18 |

Pappert (1973) has developed a theory of excitation by an orbiting dipole of quasi-TM and quasi-TE guided modes in the Earth-Ionospheric cavity. When working, for instance, at 75 Hz, the horizontal wire of Figure 6 would generate field intensities at the Earth surface comparable to the ones computed by Pappert (1973) for the "Austere ELF" transmitting facility, as plotted in Figure 21 and Figure 22. Signals would have substantial intensity at distances of several megameters far from the vertical that contains the orbitin transmitter.

## 5. CONCLUSIONS

New vistas in ELF radiators derive from the present-day activities to design and construct long metal wires for orbital use. It is expected that in the mid-'80s demonstration flights of the TSS facility

will be conducted by NASA, aimed at the experimental verification that deployment and retrieval operations are  feasible and safe  and that the several electrodynamic uses of the tether are possible, as predicted theoretically. The importance of even producing just DC power becomes evident, when we call to mind that the Shuttle has a serious shortage of electric power and a level , for instance, of 30 Kw coming from the use of the tether would double the present amount of primary power available from the on-board battery system. The demonstration flights would also verify the existance of the Alfven Wings mechanism, and of other radiation schemes, with direct bearing on the feasibility and practicality of Shuttle-mounted and rocket-mounted ELF antennas. It is reasonable to expect that in the time frame 1985-1990, these long orbiting wires will be far enough in their development to be available for use in operational ELF communication systems.

## 6. REFERENCES

Alpert Ya. L. et al, 1965, Space Physics with artificial satellites, Book published by Consultant Bureau, New York, N.Y.

Anderson M.P. et al, 1979, Orbiting tether's electrodynamic interactions, Final Report, NASA Contract NAS5-25077, April.

Arnold D.A. et al., 1980, Transmission line model of the interaction of a long metal wire with the ionosphere, Radio Science, 15, 1149-1161.

Banks P. et al, 1980, Tethered Satellite System, Facility Requirements Definition  Team Report, CASS, Utah State U. Logan, Utah, April.

Black K.M. et al., 1978, Tacamo, Signal, Vol. 33, No. 1 September, pp. 6-13.

Chu C.K. and R.A. Gross, 1966, Alfven waves and induction drag on long cylindrical satellites, AIAA Journal, Vol. 4, No. 12, pp. 2209-2214, December.

Colombo G., 1980, Private Communication.

Dobrowolny M, G. Colombo , M.D.Grossi, 1976, Electrodynamics of long tethers in the near-Earth environment, SAO Report in Geoastronomy N.3, October ( reissued April 1979).

Dobrowolny M. et al., 1979, Mechanisms of electrodynamic interactions between a tethered satellite system and the ionosphere, SAO Reports in Radio & Geoastronomy No. 6, August,

Dobrowolny M. , 1979, Wave and particle phenomena induced by an electrodynamic tether, SAO Special Report No. 388, November.

Dobrowolny M., 1981, Theoretical Investigation of the generation and injection of e.m. waves in space plasma by means of a long orbiting tether, Final Report, NASA Contract NAS8-33520, February.

Drell S.D. et al, 1965, Drag and propulsion of large satellites in the ionosphere : an Alfven propulsion engine in space, Journal of Geophysical Research, Vol. 70, 3131- 3145.

Goldreich P. and Lynden-Bell D., 1969, Io, a Jovian unipolar inductor, Astrophysical Journal , 156, pp. 59-78.

Grossi, M.D., 1973, A ULF dipole antenna on a space-borne platform of the PPEPL class, Letter Report to NASA-MSFC, Contract NAS8-28203, May 11.

Grossi M.D. and G. Colombo, 1978, Interactions of a tethered satellite system with the ionosphere, Proceedings of UA/NASA Workshop on the uses of a tethered satellite system, ed. S.T.Williams, Huntsville, Alabama, pp. 176-181.

Gurnett D.A., 1972, Sheath effects and related charged particle acceleration by Jupiter's satellite Io, Astrophysical Journal , 175, pp. 525-533,

Hubbard R.F. et al , 1976, Io as an emitter of 100 KeV electrons, Journal of Geophysical Research, 79, pp. 920-928.

Jeffrey A, and T. Taiuti, 1964, Non-linear wave propagation, New York, N.Y. , Academic Press.

Linson L.M., 1969, Current-voltage characteristics of an electron-emitting satellite in the ionosphere, Journal of Geophysical Research, 74, pp. 2368-2375.

NASA, 1976, Shuttle/Tethered Satellite System, Conceptual Design Study , Technical Memorandum, NASA TMX-73365, December.

Ness N.F. eta al, 1979, Magnetic field studies at Jupiter by Voyager 1, Prelimibary results, Science 204, pp. 982-987.

Neubauer, F.M., 1980, Non-linear standing Alfven wave current system at Io: theory, Journal of Geophysical Research, 85, pp. 1171-1178.

Pappert, R.A., 1973, Excitation of the Earth-ionosphere waveguide by point dipoles at satellite heights, Radio Science , 8, No. 6, pp. 535-575

Starkey R.J., Jr,,1980-1981, The renaissance in submarine communications, Military Electronics/Counter-

measures, Nov. 1980, pp. 38-47; Dec. 1980, pp. 52-57; Jan. 1981, pp. 26-39, Feb. 1981, pp.29-34.

Weiffenbach G,C. and J.F. McCarthy, 1975, Skyhook : an experiment on the dynamics of tethered satellites, SAO/MIT Proposal to NASA, P-577-11-75, November 7.

Williamson R.P. and P.M. Banks, 1976, The tethered balloon-current generator: a space Shuttle-tethered sub-satellite for plasma studies and power generation, Final Report, NOAA Contract USDC-NOAA 03-5-022-60, January.
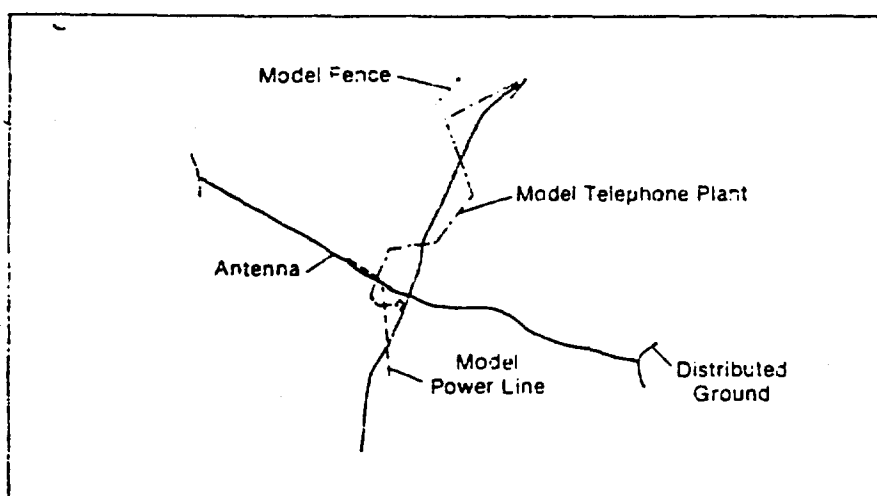


Fig.1   Clam Lake, WI ELF Test Site, 14 x 14 mi (22.5 x 22.5 km) center driven, end-grounded antenna farm having proven strategic submarine communications capability (Starkey, 1981)
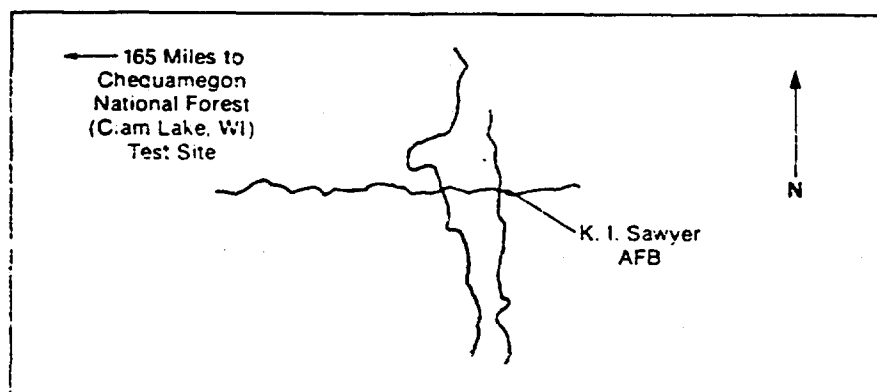


Fig.2   Proposed Michigan portion of Austere ELF with three 30–40 mi (48.3 – 64.4 km) antenna limbs connected electromagnetically with the Clam Lake, WI test site via leased telephone cables (Starkey, 1981)

# VLF COMMUNICATIONS
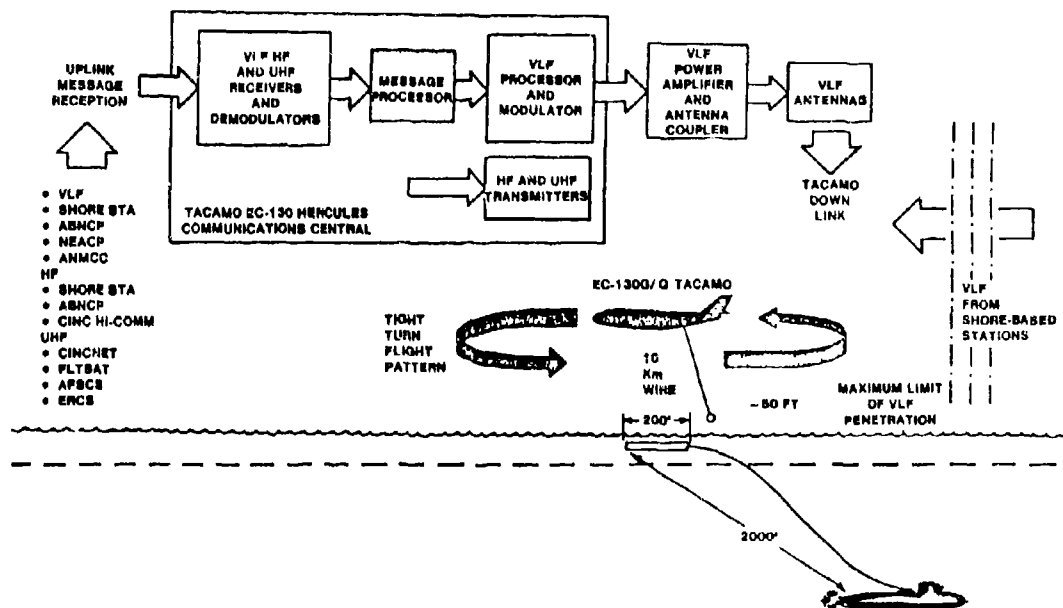


Fig.3  TACAMO VLF airborne station with 10 km vertical wire antenna (Black et al, 1978)

# SPACEBORNE ELF–DEPLOYMENT SEQUENCE, ROCKET-BORNE
# EMERGENCY COMMUNICATION SYSTEM AT ELF
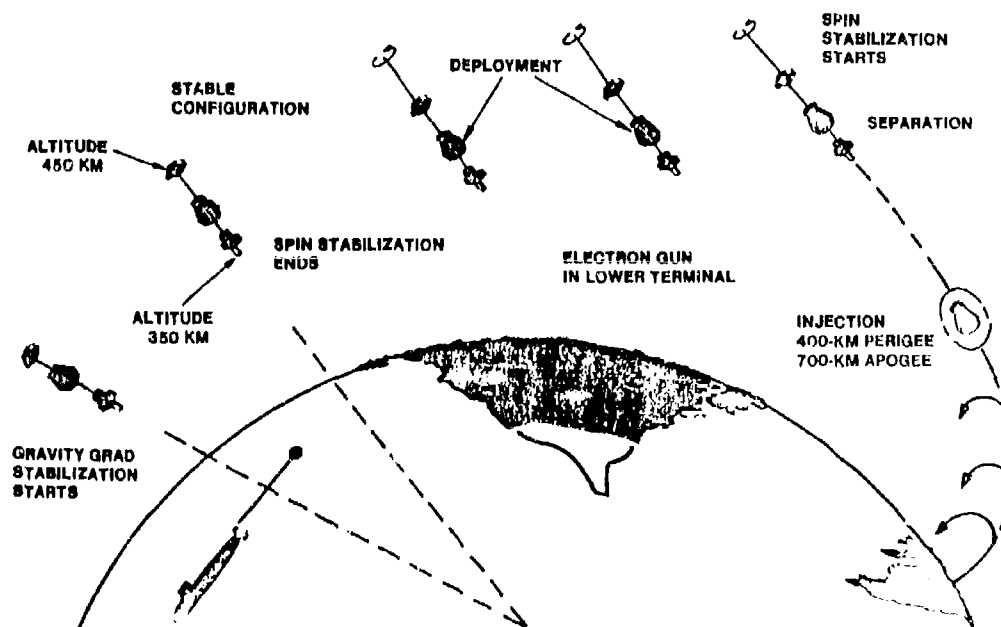


Fig.4   Deployment sequence of a rocket-borne ELF wire antenna (Weiffenbach and McCarthy, 1975)

## SPACEBORNE ELF—SHUTTLE-MOUNTED ELF TRANSMITTER AND ANTENNA—1ST EXAMPLE OF POSSIBLE SYSTEM CONFIGURATION
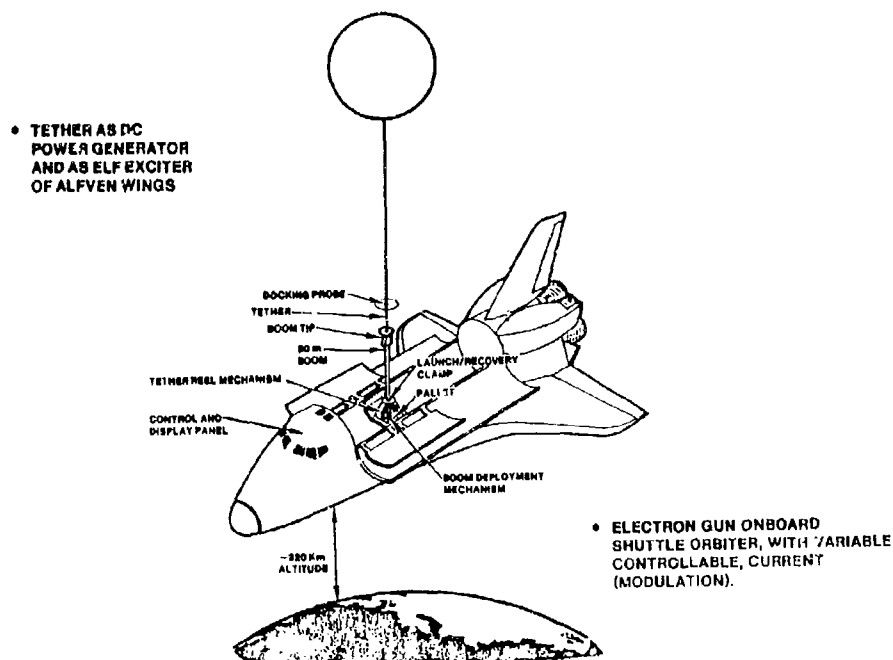


Fig.5 Vertical metal wire of the shuttle-borne TSS facility, used for DC power generation and for excitation of Alfvén Wings radiation at ELF

## SPACEBORNE ELF—SHUTTLE-MOUNTED ELF TRANSMITTER AND ANTENNA—2ND EXAMPLE OF POSSIBLE SYSTEM CONFIGURATION
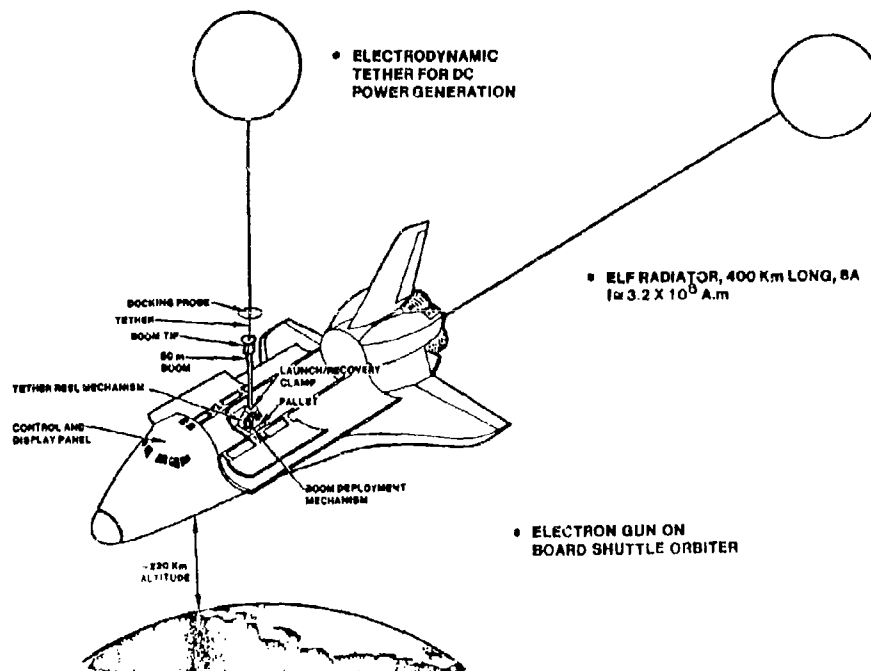


Fig.6 Vertical wire DC power generator and horizontal ELF radiator. The two wires can also be used as a V antenna, requiring balanced excitation at the vertex of the V
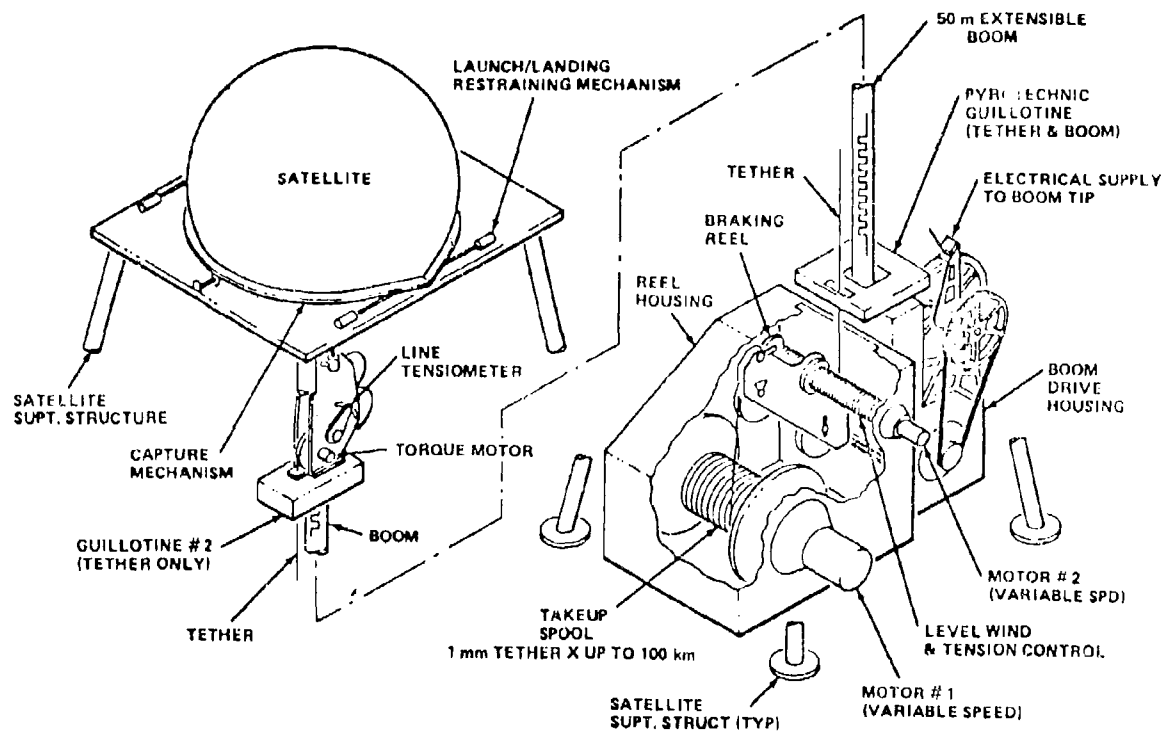
Fig.7 The reel and the boom mechanism of the TSS (Tethered Satellite System)
Shuttle-borne facility (NASA, 1976)
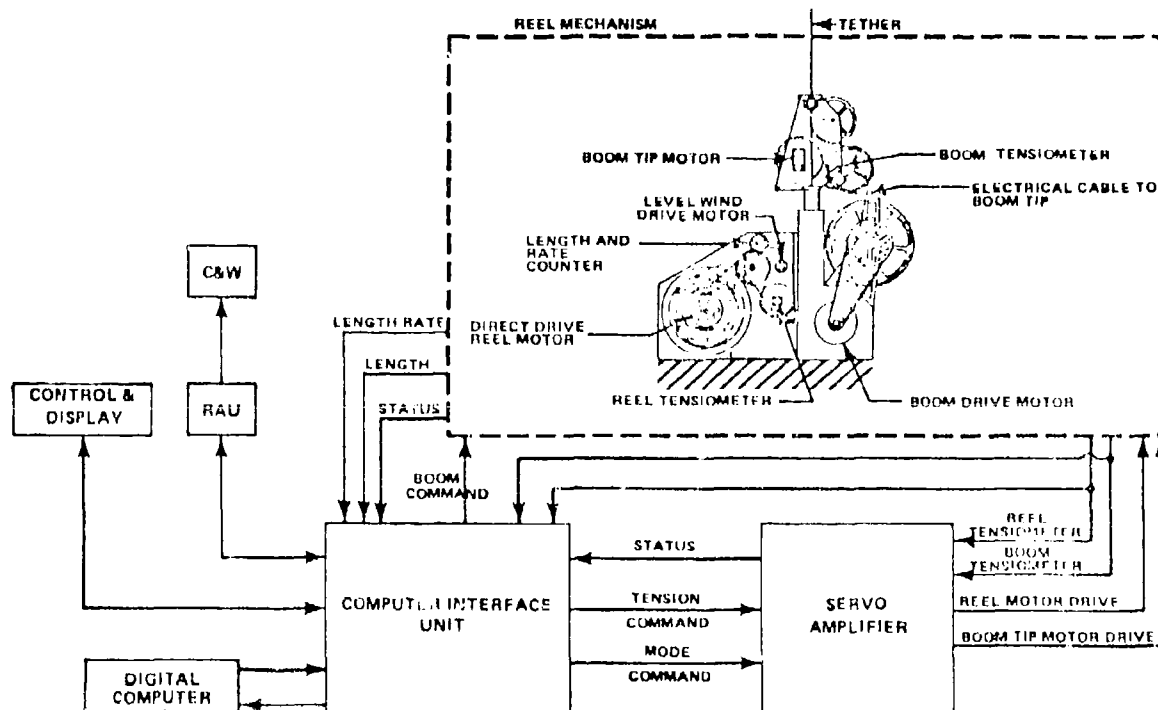


Fig.8 Block diagram of the tether control system, Shuttle-borne TSS facility (NASA, 1976)
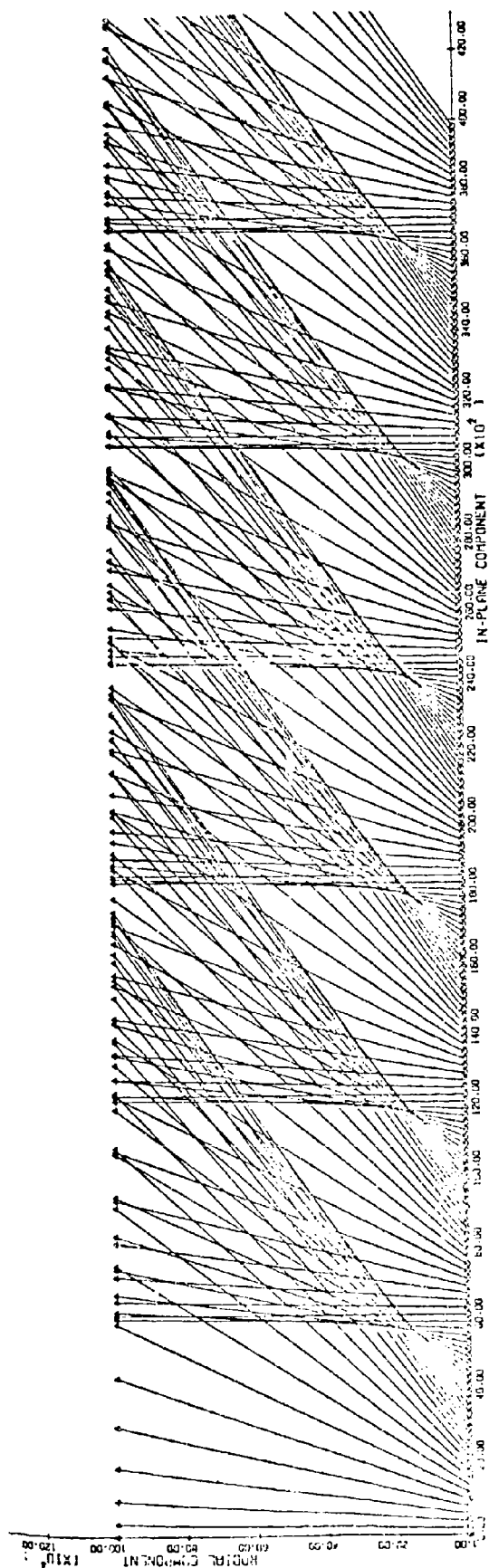
Fig. 9   Tether's pendular swing.   The wire is deployed upwards. is 10 km long and has a current
of 0.1 A.   In the figure, the scale of the x-axis is 100 times more expanded than the scale of the y-axis
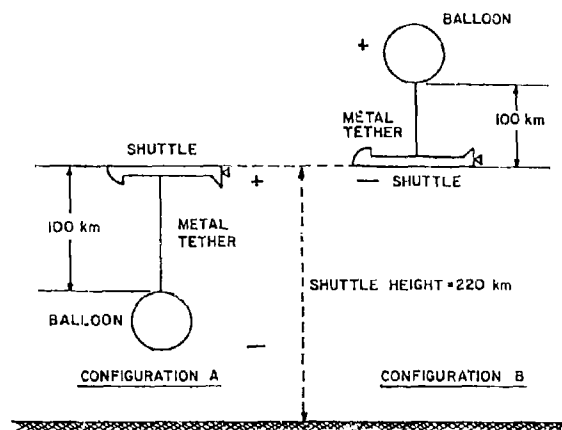
Fig.10  Shuttle-based electrodynamic tether
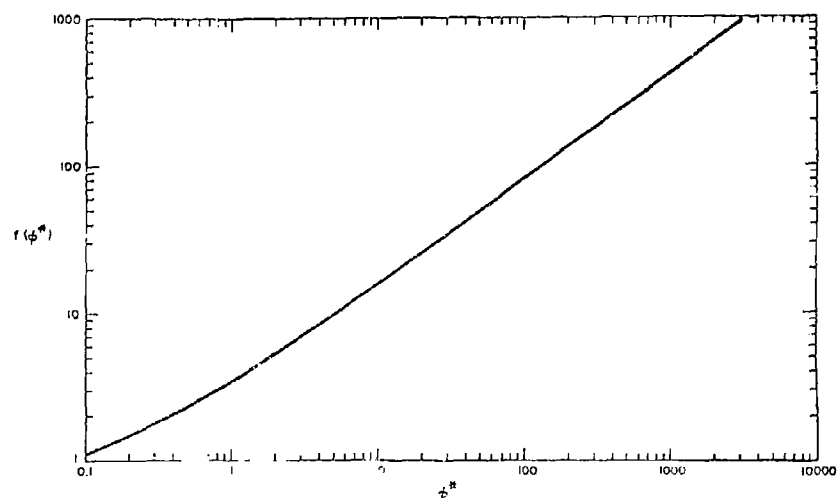


Fig.11  Graph of the function f($\phi^*$)
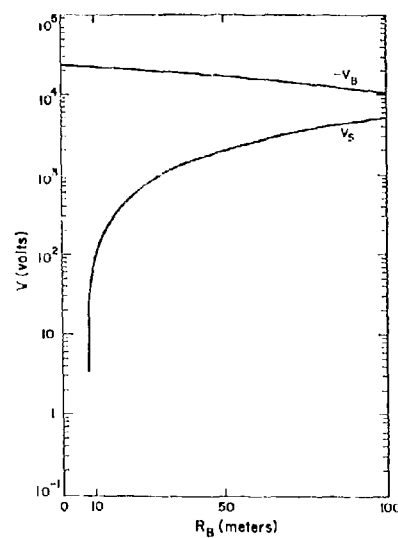


Fig.12  onfiguration A: Voltages versus $R_B$ for $L = 10^5$ m, $\rho = 0.03\mu\Omega$m
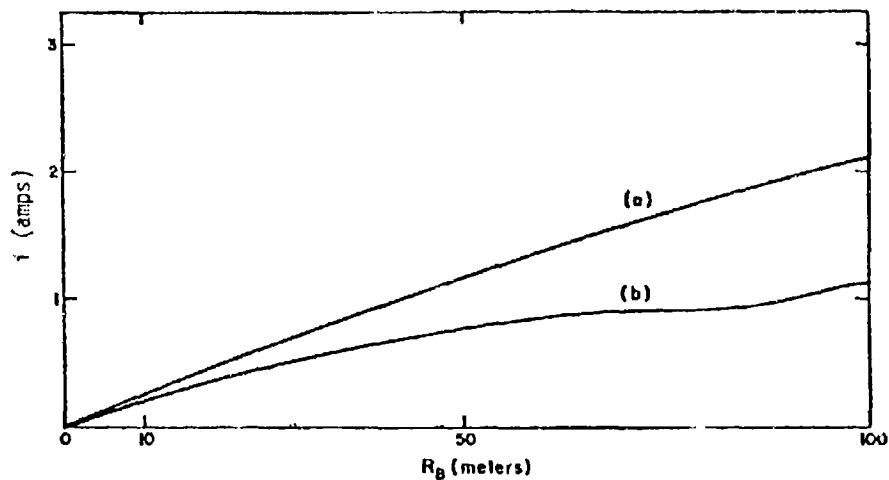
Fig.13   Configuration A:  Current versus $R_B$ for $L = 10^5$ m.  (a) $\rho = 0.03\mu\Omega$m;  (b) $\rho = 0.15\mu\Omega$m
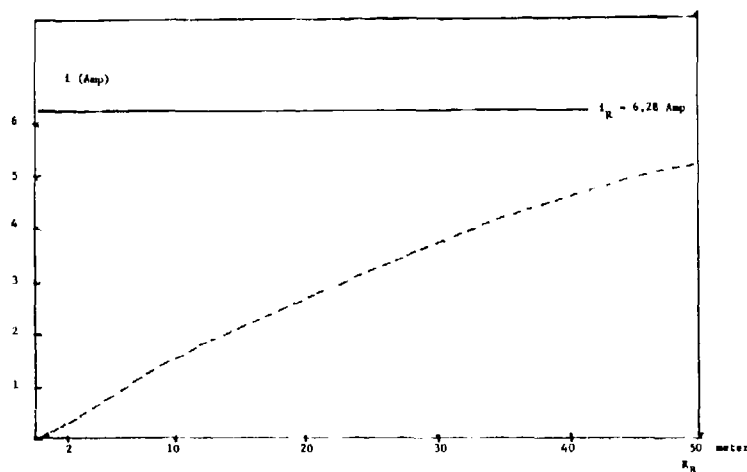


Fig.14   Currents versus $R_B$, Configuration A, $L = 100$ km, $\rho = 0.03\mu\Omega$m, $r_w = 0.5$mm.
There is an ion gun onboard the Shuttle, so that $V_S \simeq 0$
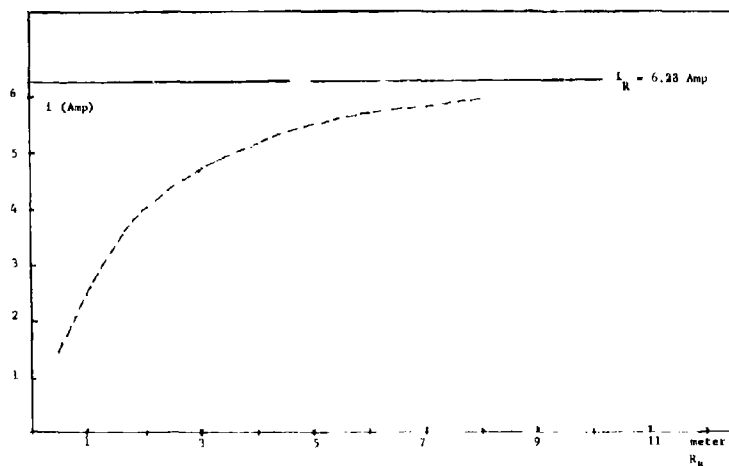


Fig.15   Currents versus $R_B$, Configuration B, $l = 100$ km, $\rho = 0.03\mu\Omega$m, $r_w = 0.5$mm.
An electron gun is onboard the Shuttle, so that $V_S \simeq 0$
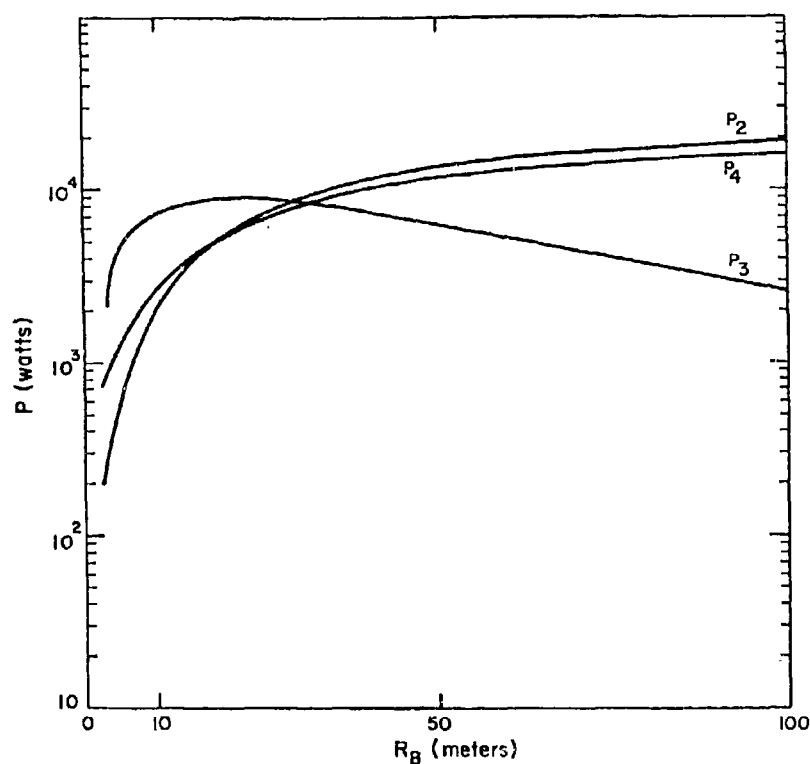
Fig.16   Power into ohmic dissipation ($P_2$), acceleration of secondary electrons ($P_3$) and
wave radiation ($P_4$):   Configuration A, $L = 10^5$ m, $\rho = 0.03 \mu\Omega$m
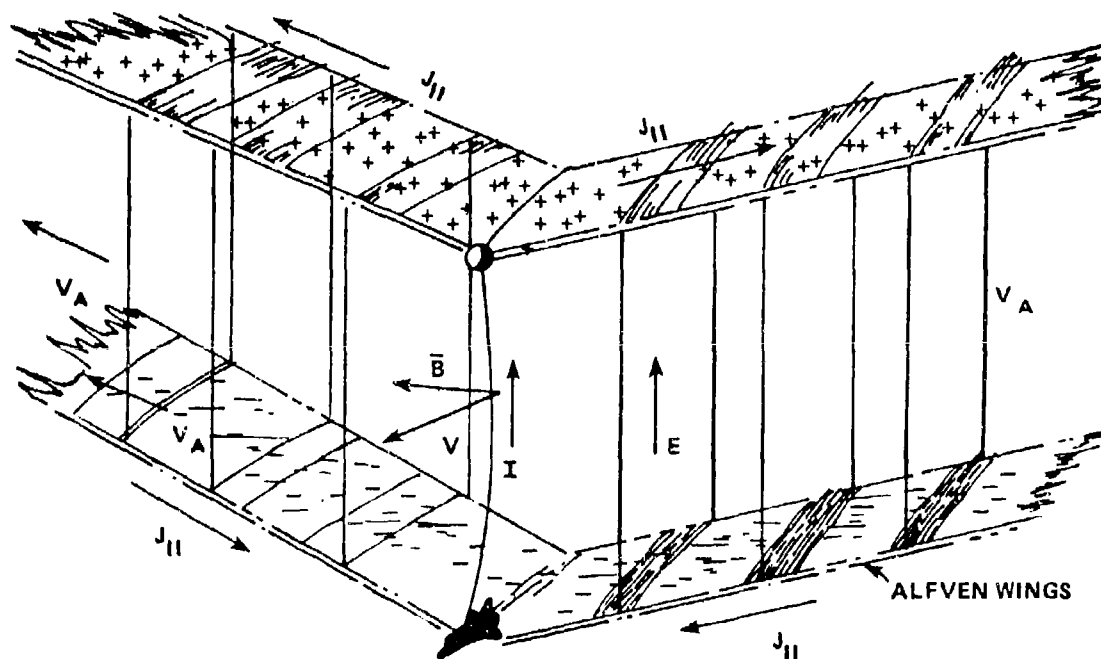


Fig.17   Schematic view of the upper and lower current sheets which spread out from the electrodynamic
tether system.  The periodic darkened regions represent the outward propagation of ww frequency
Alfven waves along the magnetic field.  There is a net positive charge excess on the top wing and a
net negative charge density on the lower wing (from Banks et al., 1980)
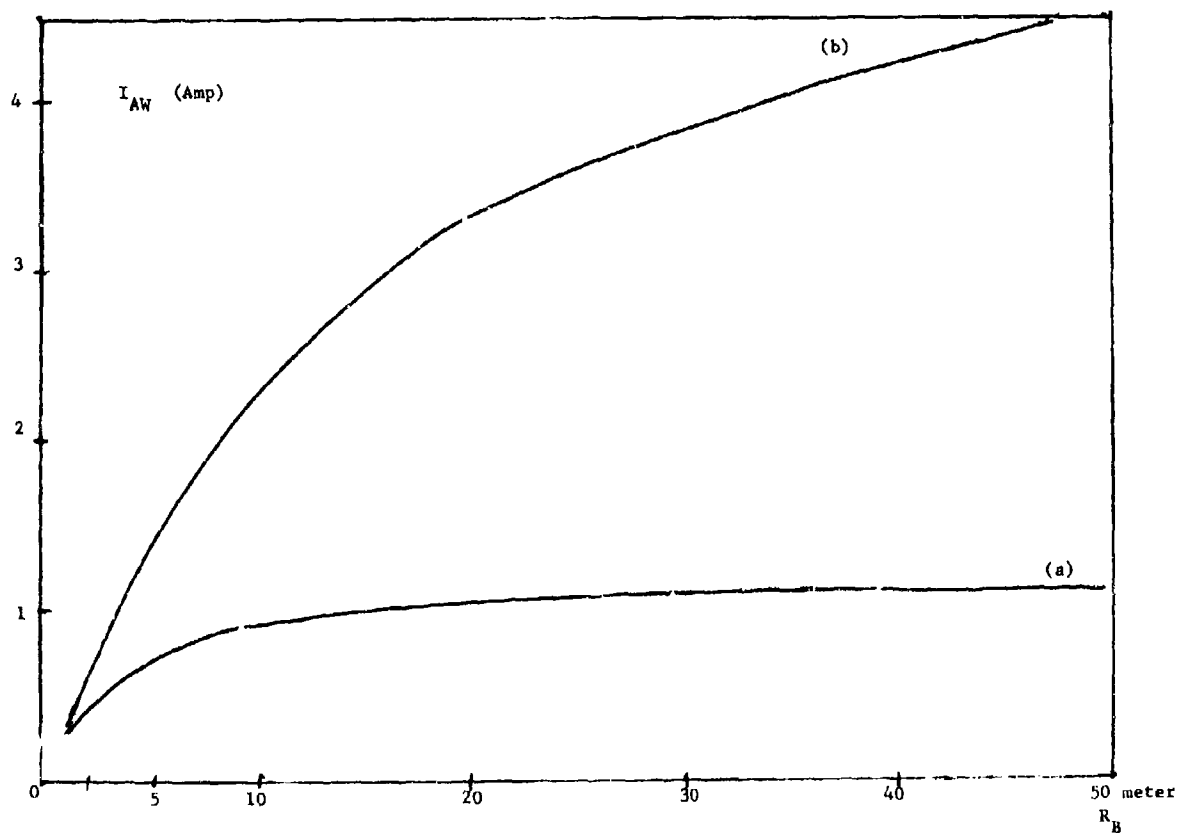
Fig.18   Alfvenic current versus balloon radius $R_B$:  (a) $\rho = 0.015\mu\Omega m$;  (b) $\rho = 0.03\mu\Omega m$
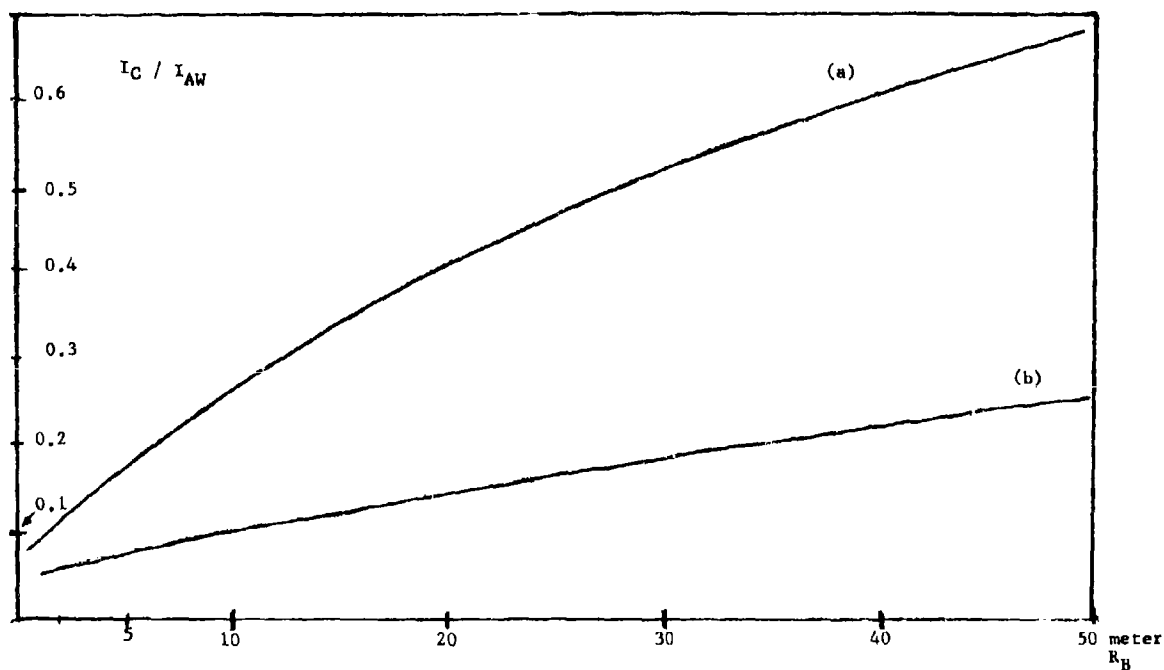


Fig.19   Ratio between collection current ($I_C$) and Alfvenic current ($I_{AW}$) versus balloon radius $R_R$, Configuration A:  (a) $\rho = 0.15\mu\Omega m$;  (b) $\rho = 0.03\mu\Omega m$
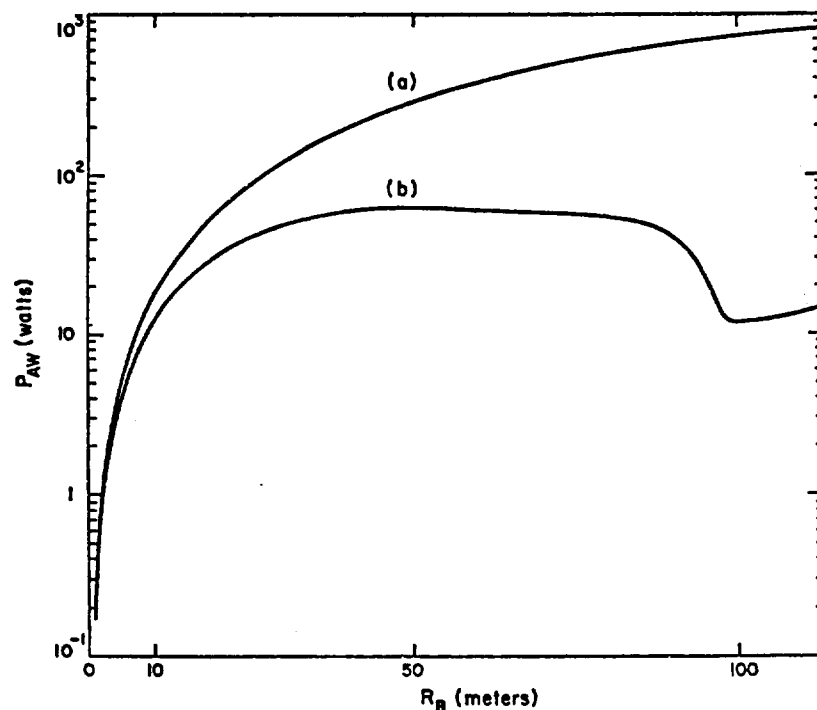
Fig.20  Power in Alfven wave from a single balloon versus balloon radius:
Configuration A, (a) $\rho = 0.03\mu\Omega$m;  (b) $\rho = 0.15\mu\Omega$m
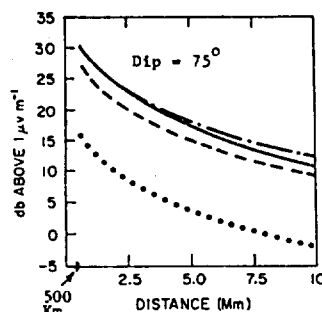


NOTE

Dip is at 0° at the
magnetic equator

Fig.21  Signal levels versus distance.  Signal levels for electric-dipole sources referred to a current moment
for $3.18 \times 10^6$ amp-m.  Signal levels for magnetic dipole sources referred to a current loop of $2.02 \times 10^{10}$
amp-m².  The azimuth is 90°, the dip is 75°; and the frequency is 75Hz Legend:
— — — — ground-based electric dipole, end fire, $\sigma = 10^{-4}$ mho m$^{-1}$; . . . . . vertical electric dipole,
500 km; ———— horizontal electric dipole, broadside and end fire, 500 km; — · — horizontal
magnetic dipole, broadside and end fire, 500 km (from Pappert, 1973)
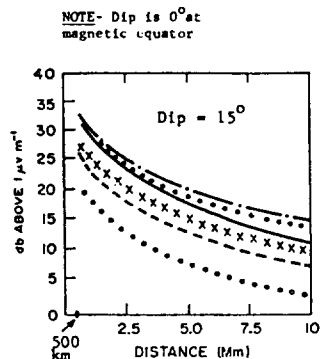
NOTE- Dip is 0°at
magnetic equator



Fig.22  Signal levels versus distance.  Signal levels for electric dipole sources referred to a current moment
of $3.18 \ 10^6$ amp.m.  Signal levels for magnetic dipole sources referred to a current loop of $2.02 \ 10^{10}$
amp.m².  The azimuth is 90°, the dip is 15°, and the frequency is 75 Hz.  Legend:
— — — — ground-based electric dipole end fire, $\sigma = 10^{-4}$ mhos/m; . . . . . . . vertical electric dipole,
500 km; ————horizontal electric dipole, end fire, 500 km;  o o o o o o o o horizontal electric
dipole, broadside, 500 km;  x x x x x horizontal magnetic dipole, end fire, 500 km;  — · — ·
horizontal magnetic dipole, broadside, 500 km (from Pappert, 1973)

# SQUID TECHNOLOGY AND ITS COMING IMPACT
## ON COMMUNICATION SYSTEMS

Claudia D. Tesche
LuTech, Inc.
P. O. Box 1263
Berkeley, California 94701
U.S.A.

## ABSTRACT

The dc SQUID (Superconducting Quantum Interference Device) is a low noise flux-to-voltage transducer used in sensitive superconducting magnetometer systems. These systems show great promise as detectors of electromagnetic signals at frequencies ranging from $10^{-2}$ Hz to $10^6$ Hz. The dc SQUID consists of a superconducting loop interrupted by two Josephson junctions. A lumped circuit element model for the dc SQUID is presented. The magnetic field resolution of a pick-up coil coupled inductively to the device is derived as a function of the device parameters. The operation and resolution of a typical system is described. The recent development of high resolution devices with energy factors approaching the quantum limit is described. The magnetic field resolution of these devices is expected to approach $2 \times 10^{-18}$ THz$^{-1}$ at frequencies above a KHz. Low frequency resolution is presently limited by 1/f noise in the device.

## 1. INTRODUCTION

In recent years, superconducting circuit elements have been used with great success in a wide variety of electromagnetic devices. For example, the most sensitive magnetometers and linear amplifiers and the most stable voltage sources are now fabricated from superconducting devices employing Josephson junctions. In addition, superior superconducting parametric amplifiers, analog-to-digital converters and integrated circuit logic and memory devices have also been developed. The performance of the superconducting devices has commonly exceeded that of the conventional room temperature devices by an order of magnitude or better (McDonald, D.B., 1981).

In this paper, the development of an extremely sensitive superconducting magnetometer, the dc SQUID (Jaklevic, R.C., ..., 1964), will be reviewed. In the past three years, the energy resolution of this device in the laboratory has been improved by three orders of magnitude over commercially available superconducting magnetometers. The intense interest in the fabrication of superconducting devices ensures the development of reliable instruments with unprecedented resolution for field use in the very near future. The availability of such devices as detectors for low frequency electromagnetic radiation promises to have an impact on communication systems.

## 2. THE DC SQUID: AN OVERVIEW

The dc SQUID (Superconducting Quantum Interference Device) consists of a superconducting loop of inductance L interrupted by two Josephson juctions (Fig. 1). The junctions are biased at a fixed dc current I. The voltage drop, $\bar{V}$, across the SQUID is a function of the flux, $\Phi_a$, threading the superconducting loop. A small change in the input flux $\Delta\Phi_a$ produces a small change in the output voltage $\Delta\bar{V} = (\partial\bar{V}/\partial\Phi_a)\Delta\Phi_a$. Thus the dc SQUID is a flux to voltage transducer characterized by a forward transfer function, $\partial\bar{V}/\partial\Phi_a$.

The Josephson elements used in the device are typically thin film Josephson junctions (Josephson, B.D., 1962). These devices can be characterized by a lumped circuit element model (RSJ model) shown in Fig. 2 (Stewart, W.C., 1968, McCumber, D.E., 1968). The ideal Josephson junction critical current is $I_0$. A shunt resistance R and junction self capacitance C are in parallel with the junction. The Johnson noise associated with the normal resistance R is a major source of noise in the SQUID. The thermal fluctuations in the voltage across the shunt resistors generate fluctuations in the output voltage. The flux sensitivity of the isolated SQUID is determined by dividing the rms output voltage noise by the forward transfer function. Since the Johnson noise sources scale with the temperature, excellent sensitivity is obtained for devices operated at 4 K.

The flux resolution of the dc SQUID is a function of the applied flux (Tesche, C.D., ..., 1977). In fact, the dc SQUID operates like an interferometer. The average voltage $\bar{V}$ is a periodic function of the applied flux $\Phi_a$ with period $\Phi_0 = h/2e \approx 2 \times 10^{-15}$ Wb (see Fig. 3). At values $\Phi_a = n\Phi_0/2$ ($n = 0, \pm 1, \pm 2, ...$), the forward transfer function vanishes. As a result, the dc SQUID is usually operated in a flux locked loop (see Fig. 4) (Clarke, J.,...,1976). An ac modulation flux $\Phi_m$ with peak-to-peak amplitude $\Phi_0/2$ and frequency $\omega_m$ is applied to the SQUID. If the applied flux $\Phi_a = n\Phi_0/2$, the voltage across the SQUID oscillates at twice the modulation frequency. Small changes in $\Phi_a$ away from this value produce a component in the output voltage at $\omega_m$. This component is amplified and lock-in detected. Thus, the dc output voltage, $V_0$, is proportional to the change in applied flux, $\Delta\Phi_a$. A feedback current generated by $V_0$ is used to null out the change in applied flux. The modulation frequency places an upper limit on the detectable signal frequency. A typical value for the modulation frequency is 100 KHz, although in principle, values in the MHz range could be used. A dc SQUID operated as a small signal amplifier (no modulation) could conceivably be operated up into the GHz range.

The dc SQUID can be used directly as a magnetometer. The input inductance is then the loop inductance L. The SQUID can also be coupled inductively through a coupling coil $L_i$ to a pick-up coil $L_p$ (see Fig. 5). The pick-up coil configuration can be varied at will. In general, the resolution of the magnetometer is optimized for $L_i \approx L_p$ (Clarke, J., ..., 1979). In addition, good coupling must be maintained between the coupling coil $L_i$ and the SQUID loop L. This places a practical limit on the size of the pick-up coil. Since the applied flux is proportional to the area of the pick-up coil, the magnetic field resolution is limited by both the intrinsic SQUID loop inductance L and by the effective flux noise at the

SQUID input. SQUID loop inductances are typically $L \sim 10pH - 1nH$. As a result, pick-up coil inductances are relatively small. The magnetic field resolution is a result of the intrinsically low dc SQUID flux noise rather than the use of a large cross section pick-up coil. For a solenoidal pick-up coil of radius 0.05 m and length 0.2 m, a resolution $\bar{B} \sim 2 \times 10^{-18}$ T in a 1 Hz bandwidth is obtainable.

Finally, the resolution of the device is also limited by low frequency (1/f) voltage noise observed at the device output (Clarke, J.,...,1976). The source of this noise is not well understood at this time. In fact, although much progress has been made in reducing the Johnson noise contribution to the output voltage noise, the low frequency component has not been similarly reduced. Characterizing the source of this noise remains one of the outstanding problems in the development of the dc SQUID.

The ideas summarized in this section will be expanded upon in the rest of this paper. A lumped circuit element model for the device is developed in Section III. Low frequency noise is discussed in Section IV. An analysis of the resolution of the dc SQUID magnetometer is presented in Section V. Finally, fabrication techniques and device operation are discussed in Section VI.

## 3. A LUMPED CIRCUIT ELEMENT MODEL FOR THE DC SQUID

The behavior of ordinary circuit elements can be adequately described by a set of classical variables, such as current, voltage, magnetic flux, etc. However, to adequately describe superconducting circuit elements, a new parameter must be introduced. This parameter is the quantum mechanical phase, $\delta$. In a superconducting material, the motions of a substantial fraction of the conduction electrons becomes correlated at low temperatures. As a result, quantum mechanical interference effects become observable on a macroscopic scale. In order to describe these interference effects, a complex macroscopic wave function $\psi = A \exp(i\delta)$ is assigned to the superconducting electrons. The phase of the wave function is the additional parameter needed to describe the superconducting circuit elements. Although the absolute value of the phase is not observable, the phase difference across a superconducting circuit element is observable. Two examples are given below.

### 3.1 The Josephson Tunnel Junction

In the Josephson tunnel junction (Josephson, B.D., 1962), two pieces of superconductor are separated by an insulating barrier (Fig. 2a). Current can flow in the superconducting material with no loss. However, the maximum lossless current that can flow through the junction, $I_J$, is a function of the phase drop $\Delta\delta$ across the junction.

$$I_J = I_0 \sin \Delta\delta. \tag{1}$$

The critical current $I_0$ is a function of the junction size, materials and temperature. If the current through the junction exceeds the critical current, the excess flows through the normal resistance R and self capacitance C (see Fig. 2). In this case, the phase drop oscillates in time, with frequency proportional to the voltage drop, V, across the normal elements

$$V = \frac{\Phi_0}{2\pi} \frac{d\Delta\delta}{dt} \tag{2}$$

### 3.2 Flux Quantization in a Superconducting Loop

In a loop made of normal metal, variations in the flux threading the loop generate a voltage drop around the loop. In a superconducting loop, there is no loss in the ring. Thus, persistent currents are generated around the ring which perfectly screen the changes in applied flux. The phase drop around the loop is proportional to the total flux (applied flux + screening flux) through the ring, $\Delta\delta/2\pi = \Phi_T/\Phi_0$. Since the wave function must be single valued, $\Delta\delta = 2\pi n$ ($n = 0, \pm 1, \pm 2, ...$). Thus the total flux through the ring is quantized, $\Phi_T = n\Phi_0$.

In the dc SQUID, the superconducting ring is interrupted by two Josephson junctions. In this case, $\Delta\delta = \Delta\delta_1 - \Delta\delta_2 + 2\pi n$, where $\Delta\delta_1$ and $\Delta\delta_2$ are the phase drops across the junctions. Thus for screening current J and loop inductance L,

$$\frac{\Delta\delta_1 - \Delta\delta_2}{2\pi} = \frac{LJ + \Phi_a - n\Phi_0}{\Phi_0} \tag{3}$$

Note that the derivative of Eqn (3) is Faraday's law of induction.

### 3.3 The DC SQUID

The lumped circuit element model for the dc SQUID is shown in Fig. 1 (Tesche, C.D., ..., 1977). The dc SQUID consists of two Josephson junctions in a superconducting loop of inductance L. The junction critical current is $I_0$, and self capacitance is C. The normal shunt resistance is R. If the external flux applied to the SQUID is $n\Phi_0$, no screening currents are generated around the loop. The dc bias current I can be increased to $2I_0$ before a voltage drop $\bar{V}$ begins to appear across the junctions. If the applied flux is increased, however, a screening current is generated around the loop (Eqn. 3). As a result, the lossless components $I_J$ are reduced (Eqn. 1). At bias current $2I_0$, the voltage across the junctions oscillates non-sinusoidally at frequency $\omega_J = 2\pi\bar{V}/\Phi_0$ (Eqn. 2). The time averaged voltage $\bar{V} \sim I_0 R \approx \mu V$. This corresponds to a frequency $\omega_J \approx 10^9$ rad sec$^{-1}$. In practice, this places an upper limit on the signal frequency, $\omega_s < \omega_J$.

A major source of noise is the Johnson noise generated in the shunts. The voltage noise generated across the output can be estimated by removing the Josephson junctions from the circuit. The voltage power spectral density $S_V$ for a device at temperature T is then white at frequencies $\omega \ll \omega_J$, with $S_V = 4k_B T (R/2)$. (The inductance L is usually chosen such that $2LI_0 \sim \Phi_0$.) The variance in the voltage $\Delta V^2$ in a band width B is $\Delta V^2 = S_V B$. A numerical simulation of the dc SQUID circuit indicates that the actual voltage noise is increased by a factor $\gamma_V \approx 10$, where $\gamma$ depends on the circuit parameters (Tesche, C.D.,...,1977).

The circulating current noise is estimated in the same fashion (Tesche, C.D.,...,1979). At frequencies $\omega \ll \omega_J$, $S_J = \gamma_J 2k_B T/R$, where $\gamma_J$ depends on the device parameters. A typical value is $\gamma_J \sim 10$. If the junctions are removed, the current and voltage noises are uncorrelated. However, the nonlinearities in the junctions introduce substantial correlation near the optimal bias point.

In most applications, the current noise is unimportant. In that case, the voltage noise can be expressed as an equivalent flux noise through the loop, $S_\Phi = S_V/(\partial V/\partial \Phi_a)^2 \sim \gamma_V 2k_B T \, L/R$. For a device operated at 4K, with $L \simeq 1nH$, $R \simeq 1\Omega$, $S_\Phi \simeq 10^{-5}\ \Phi_0 Hz^{-1} = 2 \times 10^{-20}$ Wb $Hz^{-1}$. Devices have been fabricated with $S_\Phi$ as low as $10^{-7}\ \Phi_0 Hz^{-1}$.

A useful figure of merit related to the flux sensitivity is the energy factor referred to the SQUID loop inductance, $S_E = S_\Phi/2L$. The energy factor can be expressed as a function of the geometric factors, L and C, and temperature T under the following conditions. First, the screening factor $\beta = 2LI_0/\Phi_0 = 1$. A detailed numerical simulation indicates that this is the optimal choice under most circumstances (Tesche, C.D., ..., 1977). Second, in order to eliminate hysteresis in the I-V characteristics, the junction hysteresis parameter $\beta_C = (2\pi I_0 R/\Phi_0)(RC) \lesssim 1$. (Note that $2\pi I_0 R/\Phi_0$ is a characteristic frequency for the junction.) (Stewart, W.C., 1968, McCumber, C.E., 1968). For $\beta = 1$, $\beta_C = 1$, the energy factor for a device limited by the thermal noise in the shunt resistance is

$$S_E = \gamma_E \, k_B T \, (LC)^{\frac{1}{2}},\tag{4}$$

where $\gamma_E$ is a function of the device parameters ($\gamma_E \simeq 10$ is a typical value).

In the limit $\omega_J \simeq (LC)^{\frac{1}{2}} \gg k_B T/\hbar$, the thermal component of the Johnson noise is no longer the dominant noise source. In this case, quantum fluctuation effects appear to limit the energy factor to $S_E \simeq \hbar = 10^{-34}$ $JHz^{-1}$ ((Tesche, C.D., ..., 1977)(Koch, R.H.,...,1981). There appears to be no fundamental limit to the flux noise, however.

## 4. LOW FREQUENCY NOISE

Low frequency noise with a voltage power spectral density $S_F \propto 1/f$ has been observed both in single current biased Josephson junctions (Clarke, J., ..., 1976) and in the dc SQUID (Clarke, J.,...,1979). This noise source dominates the thermal noise for a dc SQUID with moderate energy resolution, $S_E \sim 2.4 \times 10^{-31}\ JHz^{-1}$ at frequencies $f \lesssim 10^{-2}$ Hz (Clarke, J, 1976). In high resolution SQUIDs ($S_E \lesssim 10^{-33}\ JHz^{-1}$), 1/f noise dominates at frequencies $f \lesssim$ 10-100 KHz (Ketchen, M.B.,...,1980).

The source of the 1/f noise in the dc SQUID is not well understood. However, there is some evidence to suggest that the noise is generated by thermal fluctuations within the junction (Clarke, J.,...,1976) (Ketchen, M.B,...,1980)(Voss, R.F.,...,1976). Since the junction critical currents are functions of the temperature, thermal fluctuations produce low frequency variations in the output voltage. For a junction with heat capacity $C_V$ in contact with a heat reservoir at temperature $T$, the mean square fluctuation in the junction temperature is $(\Delta T)^2 = k_B T^2/C_V$. The resultant fluctuation in the junction critical current is $(\Delta I_0)^2 = (\partial I_0/\partial T)^2 \Delta T^2$. The independent fluctuations in the critical currents of the two SQUID junctions generate a fluctuation in the output voltage $(\Delta V) = R_e^2 I_0^2$, where $R_e \simeq R$ (Tesche, C.D., 1981).

The spectral density of the temperature fluctuations appears to vary as 1/f over the frequencies of interest. Experimental results appear to agree with a spectral density for the temperature fluctuations of $S_T = k_B T^2/2\pi C_V f$ (Ketchen, M.B.,..., 1980). The junction heat capacity and self capacitance both scale with the junction area. Thus, the low frequency SQUID energy resolution determined by the 1/f noise sources is

$$S_F = KT^2/Cf\tag{5}$$

where K depends on the device and junction parameters. The practical implication of this expression is the following. If the high frequency energy resolution, $S_E \propto C^{\frac{1}{2}}$, is improved by reducing the junction capacitance C, the energy resolution at low frequencies will deteriorate like $S_E \propto 1/C$. This places a practical limit on the junction capacitance.

## 5. RESOLUTION OF THE DC SQUID MAGNETOMETER

The dc SQUID may be coupled inductively to either a superconducting or normal pick-up coil as illustrated in Fig. 5. The magnetic field resolution in this configuration is a function of both the pick-up loop geometry and the dc SQUID energy factor (Clarke, J.,...,1979). Although the analysis of the superconducting and normal input circuit magnetometers is quite different, the basic results are similar (Tesche, C.D., 1978). We shall focus on the normal case only.

For a pick-up coil of cross sectional area A in a perpendicular magnetic field of rms amplitude B and frequency $\omega$, the effective signal energy in the pick-up coil is $u = \hbar^2 A^{3/2}/2\varepsilon\mu_0$, where $\varepsilon \sim 1$. The effective energy resolution referred to the pick-up coil, $S_C$, depends on the SQUID loop energy factor $S_E$, the coupling efficiency $\alpha^2 = M^2/LL_i$, and the noise flux generated in the input circuit $S_I = M^2 S_J$. The optimal choice of input coil inductance is $L_i = \gamma_C L_p$, where $\gamma_C$ is a parameter of order unity. The optimized energy resolution in that case is $S_C \simeq S_E/\alpha^2$. Thus, the minimum detectable signal energy (unity signal-to-noise) is a bandwidth B is $u = S_E B/\alpha^2$. This corresponds to a mean squared magnetic field of

$$B^2 = \gamma_1 \varepsilon \mu_0 S_E B/\alpha^2 A^{3/2}\tag{6}$$

where $\gamma_1$ is a function of the correlation between the current and voltage noise in the SQUID ($\gamma_1 \sim 1$).

The practical implications of Eqn. 6 are the following. First, although there appears to be a fundamental limit to the energy resolution (with correlation factor) of the dc SQUID, there is no fundamental limit to the magnetic field resolution. The practical limit is the following. The energy resolution $S_E \propto L^{\frac{1}{2}}$

(the capacitance is limited by the 1/f noise). However, it is difficult to couple a large input coil efficiently ($\alpha^2 \sim 1$) to a small SQUID loop inductance. Since $L_p \sim L_i$, the pick-up coil inductance is limited by the size of the SQUID loop. This in turn limits the pick-up area A. Several ingenious geometries have been suggested to maximize the factor $L^2/\alpha^2 A$ (Jaycox, J.M.,...,1980)(Cromar,M.W., to be published). A magnetic field resolution for a quantum noise limited SQUID coupled with $\alpha = 0.5$ to a solenoidal pick-up coil of radius 0.05m and length 0.2m of $B \sim 2 \times 10^{-18}$ THz$^{-1}$ appears achievable.

## 6. FABRICATION AND DEVICE OPERATION

The dc SQUID developed by Clarke, Goubau and Ketchen in 1976 consists of a thin film device evaporated onto a cylindrical 3 mm diameter quartz tube (Clarke, J., 1976). The junctions are Nb-NbOx-Pb tunnel junctions fabricated using shadow mask techniques. The loop inductance $L \sim 1$nH, the junction capacitance C 400 pF, and the junction area $A \sim 10^4$ $\mu m^2$. The input coil is wound directly on the cylindrical tube. The flux noise spectral density in a flux-locked loop is $S_\phi \sim 3 \times 10^{-5}$ $\phi_0$ Hz$^{-1}$ in the white noise region. The 1/f noise sources in the SQUID and associated electronics dominate at frequencies $f \lesssim 2 \times 10^{-2}$ Hz.

Most of the high resolution dc SQUIDs which have been developed in the past three years have been fabricated out of thin film materials deposited on planar substrates (Jaycox, J.M.,...,1980)(Cromar, M.W. to be published)(Voss, R.R.,...,1980)(Ketchen, M.B.,...,1979)(Hu, E.L.,...,1979)(Greiner, J.H.,...,1980) (Laibowitz, R.B.,...,1979). Josephson junctions have been fabricated from Nb, Pb-In alloys, and the IBM Pb-alloy. These junctions are designed for use at liquid He temperatures and below (T $\leq$ 4.2K). The junctions have been patterned using shadow masks for junction areas $A \sim 10^2$ $\mu m^2$ and electron beam lithography for junction areas $A \sim 1\mu m^2$. The SQUID loop area varies from a fraction of a $\mu m^2$ to several $\mu m$. The coupling and pick-up coils are usually patterned on the same substrate.

The dc SQUID and input coil are mounted inside a superinsulated liquid Helium dewar. The dewar is carefully screened to reduce high frequency electromagnetic transients which might cause the device to jump lock. The dewars are lightweight and rugged, and may be operated in the field as long as one month without refill. Moderately sensitive devices have been used successfully in the field for over 6 years. (For a detailed description of this device, see (Clarke, J.,...,1979).

## CONCLUSION

SQUIDs (Superconducting Quantum Interference Devices) are sensitive detectors of changes in magnetic flux. These devices show great promise as extremely sensitive detectors.

The sensitivity of the SQUID to changes in magnetic flux is limited by the intrinsic device noise sources. The dominant noise source for the present generation of devices at frequencies $\sim$ 10-100 KHz is the Johnson noise associated with the resistive Josephson junctions. Below $\sim$ 10-100 KHz, 1/f noise is observed. The ultimate source of this noise is not well understood. The intrinsic sensor noise is characterized by an equivalent flux noise spectral density $S_\phi$ through the SQUID loop. A useful figure of merit is the energy factor $S_E = S_\phi/2L$, where L is the loop inductance. Energy factors in the white noise region of $S_E \sim 10^{-34}$ J/Hz $\sim \hbar$ are anticipated. Magnetic field resolution is limited by the size of the pick-up coil that can be efficiently matched to the SQUID loop. The optimal SQUID loop inductance is usually between 10pH and 1nH. For a solenoid pick-up coil of length 0.2 m by radius 0.05 m, this would correspond to a rms magnetic field resolution in a 1 Hz bandwith above the 1/f region of $\bar{B} = 2 \times 10^{-18}$T. Reduction of the effects of the low frequency noise sources and improvements in thin film coupling schemes are expected to result in similar resolution even at frequencies well below a KHz. Clearly, this development would have an impact on communication systems.

## REFERENCES

CLARKE, J., W.M. Goubau and M.B. Ketchen, 1976, "Tunnel Junction dc SQUID: Fabrication, Operation and Performance," J. Low Temp. Phys., Vol. 25, pp. 99-144.

CLARKE, J. and G. Hawking, 1976, "Flicker (1/f) Noise in Josephson Tunnel Junctions," Phys. Rev., Vol. B14, pp. 2826-2831.

CLARKE, J., C.D. Tesche and R.P. Giffard, 1979, "Optimization of dc SQUID Voltmeter and Magnetometer Circuits," J. Low Temp. Phys., Vol. 37, pp. 405-420.

CROMAR, M.W. and P. Carrelli, to be published, Applied Physics Letters.

GRENIER, H.J., C.J. Kircher, S.P. Klepner, S.K. Lahiri, A.J. Warnecke, S. Basavaian, E.T. Yen, John M. Baker, P.R. Brosious, H.-C.W. Huang, M. Murakami and I Ames, 1980, "Fabrication Process for Josephson Integrated Circuits", IBM J. Res. and Dev., Vol. 24, pp. 195-205.

HU, E.L., L.D. Jackel, R.W. Epworth and L.A. Fetter, 1979, "Experiments on Ge-Sn Barrier Josephson Junctions, IEEE Trans. Magn., Vol. MAG-15, pp. 585-588.

JAKLEVIC, R.C., J. Lambe, A.H. Silver and J.E. Mercereau, 1964, "Quantum Interference Effects in Josephson Tunneling", Phys. Rev. Lett., vol. 12, pp. 159-160.

JAYCOX, J.M. and J.B. Ketchen, 1981, "Planar Coupling Scheme for Ultra-Low Noise dc SQUIDs", IEEE Transactions on Magnetics, Mag. 17, 1.

JOSEPHSON, B.D., 1962, "Possible New Effects in Superconductive Tunneling", Phys. Lett., Vol. 1, pp. 251-253.

KETCHEN, M.B. and R.F. Voss, 1979, "An Ultra-low Noise Tunnel Junction dc SQUID", Appl. Phys. Lett., Vol. 35, pp. 812-815.

REFERENCES (cont.)

KETCHEN, M.B. and C.C. Tsuei, May 6-9, 1980, "Low Frequency Noise in Small Area Tunnel Junction dc SQUIDs", paper presented at the Second International Conference on Superconducting Quantum Devices, Berlin.

KOCH, Roger, D.J. Van Harlington and John Clarke, 1981, "Quantum Noise Theory for the DC SQUID", Applied Physics Letters, Vol. 38, No. 5, pp. 38.

LAILOWITZ, R.B. A.N. Broers, J.T. C. Yeh and J. M. Viggiano, 1979, "Josephson Effect in Nb Nanobridges", Appl. Phys. Lett., Vol. 35, pp. 891-893.

MCCUMBER, D.E., 1968, "Effect of ac Impedance on ( Voltage current Characteristics of Superconductor Weak-Link Junctions", J. Appl. Phys., Vol. 39, pp 113-3118.

MCDONALD, D.B., 1981, "Superconducting Electron: ", Physics Today, Vol. 34, No. 2.

STEWART, W.C., 1968, "Current Voltage Characteristics of Josephson Junctions", Appl. Phys. Lett., Vol. 12, pp. 277-280.

TESCHE, C.D. and J. Clarke, 1977, "DC SQUID: Noise and Optimization", J. Low Temp. Phys., Vol. 29, pp. 301-331.

TESCHE, C.D. and J. Clarke, 1979, "DC SQUID: Current Noise", J. Low Temp Phys, Vol. 37, pp. 397-403.

TESCHE, C.D., 1981, "A Thermal Activation Model for Noise in the dc SQUID", accepted for publication in J. Low Temp Phys.

VOSS, R.F. and J. Clarke, 1976, "1/f Noise from Thermal Fluctuations in Metal Films", Phys. Rev. B13, 556.

FIGURES
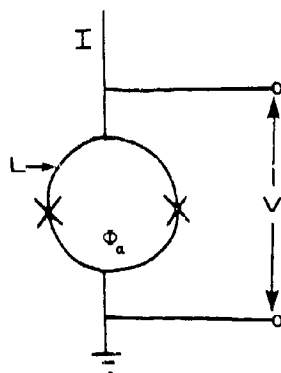


Fig. 1. DC SQUID with loop inductance L biased at dc current I. The voltage V across the Josephson junctions is a function of the flux $\Phi_a$ applied to the loop.
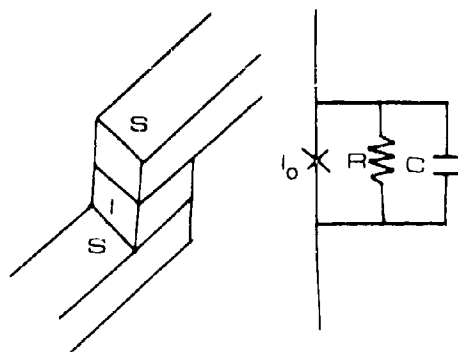


Fig. 2(a). Josephson tunnel junction consisting of a superconductor-insulator-superconductor (SIS) sandwich, (b) RSJ lumped circuit element model.

FIGURES (cont.)
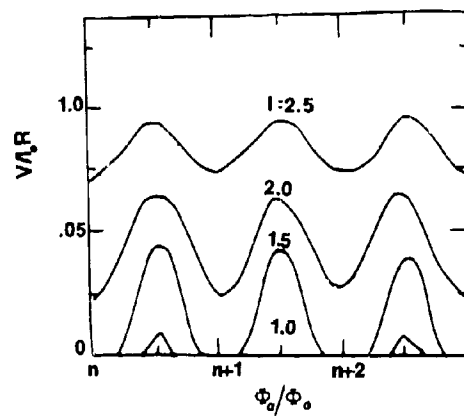


Fig. 3  Plot of typical voltage versus applied flux as a function of bias
current I.  (SQUID parameters R = 1Ω, L = 1nH, $I_0$ = 1μA and T = 1K.)
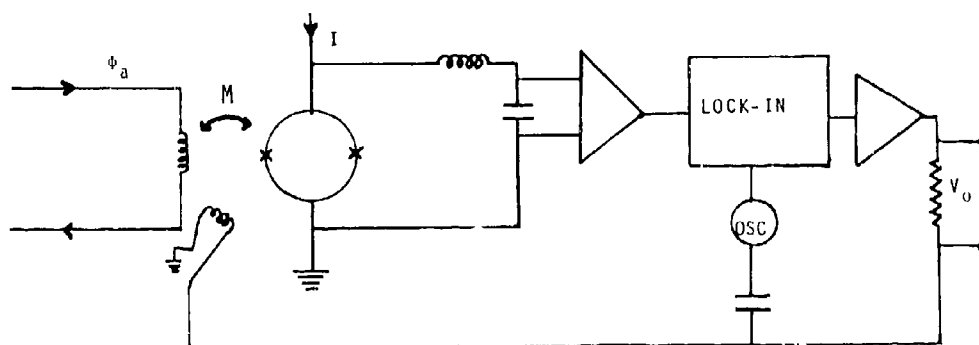


Fig. 4.  DC SQUID magnetometer operated in a flux locked loop.
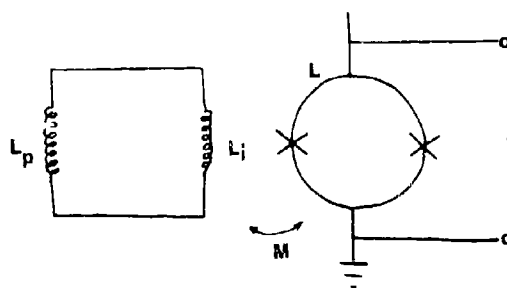


Fig. 5.  DC SQUID magnetometer coupled to an input coil $L_i$ through a mutual
inductance $M = \alpha^2 L L_i$.  The pick-up coil inductance is $L_p$.

DISCUSSION EPP FALL 1981 MEETING
MEDIUM, LONG, AND VERY LONG WAVE PROPAGATION
(AT FREQUENCIES LESS THAN 3000 KHZ)

SESSION 7

PAPER : 36. OMEGA
AUTHOR :   E. R. Swanson
QUESTIONER :   F. J. Kelly
QUESTION : Are the coverage diagrams prepared on a universal time basis, for each season and as
a function of Omega frequency?
RESPONSE  : No, there is a set done for various seasons and hours of the day, and according to
blocks of noise modelling, among other things. Properly done this is an extremely complex  task
and  the  user  is inundated with complexity. I am also looking at other ways which may be more
comprehensible if not better. There is also work to be done at 13.6 kHz, to date all work is at
10.2 kHz only. This is a very formidable problem it uses full wave analysis extensively.

PAPER : 37. THE EFFECTS OF PROPAGATION ON THE ACCURACIES OF POSITIONS DETERMINED USING OMEGA IN
THE UK
AUTHOR :   T. B. Jones
QUESTIONER :   E. R. Swanson
QUESTION : 1. Which prediction coefficients were used? Did they employ the 1971 coefficients as
were used for many years, the new 1980 coefficients or something else?
        2. Your  Farnborough  for the North Dakota transmission data seemed to be scattered
markedly more than some of the other data. Does Farnborough have abnormally high local noise?
        3. You  referred  to prediction errors during disturbed conditions. I am sure there
would be interest in improving predictions  during  these  periods.  However,  one  must  first
predict the disturbance, and its duration and magnitude in advance, to allow for production and
distribution of correction tables.

RESPONSE : 1. It was the interim coefficients before the 1980 coefficients became available.
        2.  No,  if you look at the Leicester data it too has scatter. This I believe is due
to the path being tangential to the auroral zone which results in  additional  scatter  due  to
fluctuations in received phase associated with sub-storm activity.
        3. I think the only way to deal with disturbed conditions is to have  some  form  of
real time monitoring to ascertain the magnitude of the event. From this information it might be
possible to issue a correction for other paths. The problem of getting the information  to  the
user  is  a  formidable  one,  but  one  can env     a scheme something along the lines of the
differential Omega system.

PAPER : 41. NEW  TECHNOLOGY  FOR  ELF  RADIATORS: A  REVIEW  OF  AIRBORNE,  ROCKET-BORNE  AND
SPACE-BORNE ELF ANTENNAS
AUTHOR :   M. D. Grossi
QUESTIONER :   J. Aarons
QUESTION : What would be the environmental impact on the propagation of  other  RF  signals of
this very long wire reflector coming around every 90 minutes.
RESPONSE : The wire is like a very long meteor trail, it will create an echo, but the footprint
is not very large. It is a very thin wire. I hope that will not be an objection.

PAPER  :  41.  NEW  TECHNOLOGY  FOR  ELF  RADIATORS: A  REVIEW  OF  AIRBORNE,  ROCKET-BORNE AND
SPACE-BORNE ELF ANTENNAS
AUTHOR :   M. D. Grossi
QUESTIONER :   J. S. Belrose
QUESTION : 1. Will the wire be rewound on the conclusion of the experiments?
        2. What happens during magnetic storms? Satellite charging  has  been  an  important
problem for ordinary satellites.

RESPONSE : 1. Yes (Retrieval time: 2 hours to 12 hours). It will be reused next mission, etc.
        2. No, but we have considered wire motion from sudden perturbations.
uch  as  might  be caused by air density fluctuations, and ways to stabilize the wire if set in
motion b    lectro-mechanical methods (plasma injection). This technique could also take care of
any  difficulty  encountered  with  the  variable  VxB  force.... a magnetic storm is perhaps a
perturbation on this force (300 γ's compared with the 29,000 γ's of the main field).

PAPER : 41. NEW  TECHNOLOGY  FOR  ELF  RADIATORS: A  REVIEW  OF  AIRBORNE,  ROCKET-BORNE  AND
SPACE-BORNE ELF ANTENNAS
AUTHOR :   M. D. Grossi
QUESTIONER :   J. B. Reagan
QUESTION : What effects will your high power levels at ELF in the shuttle-borne system have  on
the  particle  population of the magnetosphere? A large portion of the radiation belt electrons
resonate with ELF waves. At continued operation you could  precipitate a  significant  fraction
of  the electrons trapped in the radiation belts, and create artificial aurora and interference
to communications over a wide frequency range?
RESPONSE  :  Dr.  Schmerling  was  10  years  ago  interested  mainly in this aspect, and he is
currently considering including an experiment in WISP experiments to  be  carried  out  in  the
space shuttle. Perhaps he could comment.

PAPER  :  41.  NEW  TECHNOLOGY  FOR  ELF  RADIATORS: A  REVIEW  OF  AIRBORNE,  ROCKET-BORNE AND
SPACE-BORNE ELF ANTENNAS
AUTHOR :   M. D. Grossi
COMMENTER :   E. R. Schmerling
COMMENT  :  The  early  philosophy that we had was that if we could put in orbit a long antenna
with a local transmitter providing a radiating field, we could increase by at least 50  dB  the

the EM field causing wave-particle interactions, compared with that presently available in the Siple transmitter. We've not really looked at the electrodynamic stability problem, e. g. how much power must be put into the accellerator to get electrons out of the system? The other point is, where do these electrons come from? In a sense they have to be "sucked" out of the ionosphere, and this provides a further limitation on the current. How many electrons can you draw from the ionosphere, push through the wire and emit at the other end of the accellerator? We have been interested in three aspects: 1) The point of view that Dr. Grossi had that the very long wire would interact with the VxB, could be modulated, producing magneto-hydrodynamic waves and micropulsations; 2) concerning the length of wire, even 1-2 km would be much longer than we've ever had before; and 3) a long wire could be a means of dangling an instrumented package downwards, beneath the shuttle, at low altitudes, in the neighbourhood of 100 km.

PAPER : 42. SQUID SCIENCE AND TECHNOLOGY AND ITS COMING IMPACT ON ULF/ELF COMMUNICATION SYSTEMS
AUTHOR : C. D. Tesche
QUESTIONER : L. Brock-Nannestad
QUES...N : How do you test devices with such high sensitivity? It would seem impossible to find a place quiet enough on earth to test the resolution you have been demonstrating.
RESPONSE : One exploit. one of the properties of superconducting materials. If you have a ring, the screening currents around the ring are perfect and can completely exclude any change of flux through the loop. It is the miser effect. What one does is makes a superconducting cavity and places the device inside the ring. The screening is almost perfect and the field changes inside that cavity are very, very small. In fact most of these devices are operated inside superconducting shields.

COMMENTER : M. D. Grossi
As Dr. Tesche has said, most of these devices are used in a field derivative or secondary derivative mode. Two devices are used, which are say 10 cm apart, and now the noise is in the gradient mode, i. e. it can be cancelled to a high degree because it is correlated in the two loops.

COMMENTER : L. Brock-Nannestad
I was thinking that the SQUID devices would be operated in the differential or gradient mode, however the signal itself, at ELF, is also fairly effectively cancelled. At ELF, which is useful for communications to submarines beneath the surface of the sea, the gradient is very small because of the wavelength.

COMMENTER : M. D. Grossi
The applications that I know of by the Military have always employed the SQUID device in the gradient mode.... never as a total field device. You are right, the signal itself is also cancelled as well as the noise. However, fortunately the noise is cancelled more effectively than the signal. Since the noise frequently originates from nearby sources, its gradient is less than that for the signal. That is the noise is better correlated in the two loops, and so is better cancelled.

COMMENTER : C. D. Tesche
I should say that if one tries to get rid of the correlated noise from nearby sources, one uses two SQUID devices, separated by distances that are large compared with the distance to nearby noise sources. And then one can do a single reference kind of procedure, and that is a very useful and very important idea when using SQUID devices, as for example in magneto-tellurics, or any operational system in the field, where there are moving metal objects.

PAPER : 42. SQUID SCIENCE AND TECHNOLOGY AND ITS COMING IMPACT ON ULF/ELF COMMUNICATION SYSTEMS
AUTHOR : C. D. Tesche
QUESTIONER : T. J. Beahn
QUESTION : We used RF SQUIDS some years ago and finally discontinued their use (in spite of the fact that they performed very well) because of the logistics of helium support and supply. I would suggest that continued work on DeWars, refrigeration, etc. is indeed as important as you have suggested in your talk.
RESPONSE : The problem is recognized and considerable effort is being exerted in the development of cryocoolers.

PAPER : 42. SQUID SCIENCE AND TECHNOLOGY AND ITS COMING IMPACT ON ULF/ELF COMMUNICATION SYSTEMS
AUTHOR : C. D. Tesche
QUESTIONER : E. R. Schmerling
QUESTION : Is there any hope of using superconductors that have higher critical temperatures, which could therefore avoid the requirement for liquid helium.
RESPONSE : There is always hope. The highest $T_c$ is up in the 20's now. The critical points to look at are nitrogen at 70. Liquid hydrogen in the 20's, helium at 4.2. If you can get a good cryo-cooler operating in the 10-15 degree range and use some of these high $T_c$ materials there are possibilities.

## ROUND TABLE DISCUSSION

Participants at Round Table:    J.S. Belrose (Chairman)
                                               B. Burgess
                                               J.B. Reagan
                                               G. Lange-Hesse
                                             J. Fonteyne
                                             T.B. Jones

In his opening remarks J.S. Belrose emphasized that the reason for having the session chairmen around the table was to stimulate discussion from the floor, not to carry out a discourse between the participants at the round table. He noted that he had asked each one of his colleagues to make a few comments about the session that they had chaired, with particular emphasis on: (1) what they thought was new; (2) what research studies needed to be done; and (3) what the direction of new work should be. He stressed, however, that their remarks need not be confined strickly to the session that they had chaired, because there was an over lap between material presented in the various sessions, which is only natural since factors that influence VLF propagation, for example, also affect the frequency bands above and below the frequency range under consideration. He noted that the AGARD/EPP was specially interested in the limitations that the propagation media imposed on system design and performance, and since there would be no round table discussion following the applications session, contributors to this session were particularly invited to contribute to the present discussions.

B. Burgess summarized the papers presented in the session on the Propagation Medium. He noted that the authors of the papers presented in this and following sessions, together with participants from the various Nations, represented a majority of the researchers who were experts in the western world in the area, and so the symposium provided a good forum for these researchers to get together to exchange ideas and to review where they were all going. He noted that ELF propagation research was a prime driver for a lot of the new work presented, and this stemmed largely from USA work in this area, and on the systems application of very-very low frequencies. He noted that W.L. Imhoff's paper on precipitating energetic particles affecting the propagation medium clearly revealed the localized nature of energetic electron events, and that effects on long path propagation could be observed; but he felt that the present state of our knowledge was incomplete. That is while the paper provided a feel for effects observed, more work was needed here. In particular he noted that while solar proton events (SPE) are more wide spread, and in that sense easier to interpret, e.g., comparisons between calculation and observation, that, as J.B. Reagan had indicated, there were no ELF measurements made during SPE's. Concerning the C-layer Burgess noted that the possible existence of such a layer had been speculated many years ago (by Bracewell and Bain in 1952), and yet still today there were uncertainties about its existence as a separate clearly defined layer below the D-layer. He noted that while P.A. Kossey's paper certainly emphasized the role of the C-layer, and that, like the D-layer there were substantial variations from day-to-day, and with season; noteably the "C-layer" was most clearly discernable in winter. He noted that the latitude variation was not at all clear, more data were needed. And that while there were some indications that the variations with the solar cycle were in the way originally suggested, in that the layer was strongest during solar minimum years, this also was not entirely clear. Burgess noted that while the C-layer should dominantly affect ELF and VLF propagation, it seemed however, that long path LF propagation gave the best background information on it. He noted that while J. Schäfer and H. Volland had developed a very useful tool, employing naturally occuring atmospherics, to study VLF propagation; and that while W. Harth had tried to explair the medium distance results in terms of multi-mode propagation employing the simple Wait exponential type profile, he felt more work was needed to utilize more realistic profiles to explain these data. He noted that the last two papers were concerned with wave-particle interaction. Of particular interest was the paper by P. Stubbe who used an HF heater transmitter to in effect produce a large ELF antenna in the sky. This heater facility clearly had the potential to reveal exciting new results on the polar ionosphere, and he encouraged the researchers to continue their work.

B. Burgess pointed out that while the D-region is often described as being relatively stable, compared with the F-region for example, it is in fact quite a variable part of the ionosphere, and one can't really employ a single model profile to explain propagation data. He questioned whether we have in fact progressed very far in modelling the propagation medium? He remarked that in so far as VLF propagation is concerned we haven't a good nighttime profile, particularly the details of the profile, and the ion and electron distribution at the lowest heights. While physics of the lower ionosphere was not a main theme for the symposium, he noted that J.B. Reagan had shown that computer modelling has given results which agreed with some aspects of VLF/ELF propagation. The chemistry of the region is very complex, however computer codes now exist, and Burgess questioned whether we need to know anything further about the physics of the lower ionosphere?

J.B. Reagan summarized the session on ELF Propagation, commenting on various aspects of the work in some detail. He pointed out the various areas of ELF research in which he believed that more work was needed. Concerning propagation theory he remarked that much work had been done in this area, by Galejs, Pappert, Morfitt, Field, Booker, and others; and in particular he noted that approximations had been developed by the Greifingers which provided easily calculatable results. He felt that our knowledge about propagation over great circle paths in a homogeneous ionosphere was well understood; but that propagation take place also over non-great circle paths; and he felt that, concerning our knowledge about disturbance effects, due to energetic particle precipitation, sporadic E, electron ledges, trans-auroral zone propagation, etc. we have only a limited knowledge. He expressed the view that for ELF we should really model in 3 dimensions.

He remarked that while a reasonable data base exists on field strength and phase, and radio noise, and that while propagation models have been developed that predict these field strengths under ambient and mildly disturbed conditions with reasonable accuracy, that there were variations (in magnitude several dBs) that occur from night-to-night and during a night that are not totally understood. He noted that while sporadic-E had been suggested as having a major influence on propagation, that there were no observations to confirm this. He pointed out that no measurements have been made during very intense particle events.

In the area of disturbance modelling Reagan indicated that we need to know the size of the disturbance, its location, and the variability and altitude profile of electron and ion densities. In particular he pointed out that since electron precipitation events were very variable in space and time, and that since the application for ELF was for global communications, we needed to know what is going on on a global scale. He remarked that if we are really going to understand disturbance phenomena we must have the large scale picture of the disturbance, and that this probably can only be got by observing the region from above using satellites; employing in particular a recently developed Bremsstrahlung x-ray experimental technique.

When the electrons interact with the atmosphere, they emit Bremsstrahlung x-rays, that can be detected from satellites. These can be sensed, imaged and from the x-ray spectrum one can derive the incident electron spectrum that caused the x-rays, and in this way we get a global view of electron precipitation; which in the future has to be worked somehow into the propagation models.

Another area that affects ELF propagation modelling is the D-region ion chemistry, and Reagan noted that the ion chemistry was very complex, and that it was being continuously updated as improved reaction rates from laboratory work became available. He noted that more work was needed on the diurnal and seasonal variations of ion chemistry, and particularly the ion chemistry in polar regions. He expressed the view that what is needed is a field program, to establish just how well we are doing in our modelling, and in particular we need a campaign during a large solar particle event, to test both the chemistry and the propagation codes.

And lastly, Reagan remarked that we need a better understanding of the role of the magnetosphere, its influence on the ionosphere, and in turn the influence of the ionosphere on the magnetosphere. He noted that clearly there was a coupling between the two, and until that coupling is better understood, many of the phenomena which still appear as unknowns, will remain as unknowns.

G. Lange-Hesse summarized the papers in the VLF Propagation session. He commented particularly on practical aspects and interest in VLF radio waves. He noted that while principle use of this band was for navigation and communications, because of the large skin depth in the earth's surface, VLF has also been exploited for sub-surface communications, geological prospecting and mine rescue. He pointed out the practical aspects of employing transverse electric modes for air-to-air links, between terminals at 20,000 feet or more. Air-to-air transverse electric modes propagate better than transverse magnetic modes over poorly conducting ground such as exists throughout Greenland and Canada. He noted that the disturbed environment degraded the transverse magnetic mode much more severely on paths over these poorly conducting areas then over sea water. He remarked that little was said about the influence of the disturbed environment and particularly the effects on the transverse electric modes. Concerning practical aspects of employing transverse electric modes for air-to-air communications, Lange-Hesse noted that this polarization should be more practical, since it was operationally easier for high speed aircraft to trail an horizontal long wire antenna.

Finally he drew the attention of the participants to the good experience that German scientists have developed in the use of small rockets for deploying parachute pay loads to study the D-region in the altitude range 35-75km. He drew attention to this because of the possibility of deploying such techniques to study the disturbed environment in-situ.

J.S. Belrose commented on the papers presented in the LF Propagation session. He said that he concurred with Dr. Burgess's concern that we have relatively little information on the C-layer. He addressed particularly the need for measuring ionospheric reflection coefficients in the frequency range (effective frequencies) 20-150kHz, since during summer daytime the reflection coefficient changes by two orders of magnitude. He commented particularly on the interesting results obtained by RADC, and he commented on the excellent continuity of their VLF/LF sounding programme which had been deployed for several years at middle and high latitudes. He drew attention to, however, an in consistency in results that they had obtained in the USA, compared with results that he had presented in his lecture, based essentially on European data. In the frequency range 30-50kHz Belrose noted that the ionospheric reflection coefficient data that he presented showed that the values of the reflection coefficient decreased by a factor of 5 on a summer day, whereas the VLF/LF sounder results showed no decrease at all.

Concerning the difference in the diurnal phase patterns between LF propagation in Europe (cosinusoidal patterns) and Canada (trapezoidal patterns), Belrose noted, once again, J.B. Reagan's comment that a continuous drizzle of electrons from the Van Allen belts contributed to the ionization in the undisturbed D-region. This fact probably accounted for the differences observed, since the effects of such a drizzle would be much stronger in the North America sector compared with Europe because of the South Atlantic anomaly.

J. Fonteyne nous a exposé: Je vous remercie de m'avoir permis de présenter ceci en français. Dans la session que j'ai présidée sur la bande hectométrique il y a eu quatre exposés et ces quatre exposés ont été de nature totalement différente. Tout d'abord M. Knight nous a fait un exposé très général sur l'état des connaissances actuelles à la fois sur la propagation de l'onde de sol et sur la propagation de l'onde ionosphérique et ceci est une constatation de ce que nous savons et à mon sens ne porte pas ni à constations ni à remarques, d'ailleurs il n'y en a pas eu juste après l'exposé. Peut-être aurait-on pu parler des endroits dans lesquels on manque de données ou des endroits dans lesquels nous avons des doutes sur la prévision de la propagation. Ceci m'amène tout de suite à l'exposé de M. Hagg qui est justement

un cas ou M. Hagg dans son exposé a présenté l'anomalie hivernale et les affaiblissements donc dans les latitudes élevées dû à cette anomalie hivernale et aux orages magnétiques et ceci qui est bien connu en bande décamétrique est peut-être moins connu en bande hectométrique (en bande décamétrique c'est HF, en bande hectométrique c'est MF). On se rend compte tout de suite que le problème est complexe et si on a vraiment besoin d'établir des prévisions dans ces régions, il nous faudra faire des mesures complémentaires, refaire des mesures maintenant pour essayer d'améliorer un peu nos prévisions dans ces zones-là. Ensuite en troisième nous avons eu un exposé de M. Cutolo qui nous a parlé des phénomènes de démodulation et de distortion. En fait tout cela c'est quelque chose qui je crois, aurait mérité un peu plus de détails et c'est un effet très général; ce sont les effets de la non-linéarité dans l'ionosphère dans lequel intervient aussi la trans-modulation et peut-être est-ce dû au fait que je suis de la radiodiffusion et que les problèmes de trans-modulation m'intéressent particulièrement dans ce domaine-là et je crois que ça c'est quelque chose qui mérite des explications, des recherches et des études peut-être un peu plus poussées en particulier dans l'exposé de M. Cutolo.Si la démodulation, c'est-à-dire la diminution du taux de modulation de l'émetteur et la distortion de la modulation de l'émetteur est peut-être expliquée d'une manière assez simple peut-être un peu simpliste, l'automodulation est un phénomène dont l'explication est beaucoup moins évidente. Enfin nous avons eu un exposé de M. Fer sur des études théoriques pour l'emplacement d'un centre de réception et donc sur la propagation de l'onde de sol dans des conditions où il y a des discontinuités de conductivité. Je crois, que cet exposé a été suivi d'une discussion déjà assez intéressante et assez intensive et l'on a pensé aux travaux futurs qu'il conviendrait de faire,en particulier la comparaison avec des résultats de mesures effectives et puis la comparaison avec la méthode de Millington qui aussi est une méthode très souvent bien utilisable pour la propagation sur les discontinuités de conductivité. J'avais espéré que l'on ait un peu de temps pour les discussions ou les commentaires venant de l'audience et dans mon idée ces discussions devaient porter essentiellement sur les zones dans lesquelles les données nous manquent et la précision de nos prévisions devrait être améliorée et deuxièmement sur les effets de la non-linéarité de l'ionosphère et tous les désagréments sur les radiocommunications que peuvent apporter ces non-linéarités. Je crois, que ce sont les deux points sur lesquels j'aurais souhaité un peu plus de discussion et un peu plus de travail important.

T.B. Jones spoke about the session he chaired on Numerical Modelling of the Propagation Medium. He remarked that most of what he had intented to say had already been said, and that he agreed entirely with the various comments made. Jones made two general comments at the outset. He noted that the quality of the presentations and the work presented was excellent. He said that he found the papers interesting and well presented, and that the range of material that was covered was he felt large enough to have something of interest for everyone participating on the symposium. He said that he was surprised to learn that there was still an active interest in VLF/ELF propagation, since in the UK present support for such research was at a very low level, and that there was a danger that the knowledge that we have in this area may be lost, in the sense that we are not training new graduate students in the area.

Refering to D.G. Morfitt's paper, Jones pointed out that he was impressed by the good success and usefulness of the simple exponential model to predict long path VLF/LF field strength. He noted that he and his colleagues, W.C. Bain and others, had been so concerned with developing structured D-regions models, since they had been concerned with predicting steep as well as oblique incidence propagation, to the extent that many researchers had     essentially disregarded the simple exponential model; which, he noted could have a great measure of success in predicting long path field strength.

T.B. Jones also commented in the opposite vain on J.B. Reagan's paper. He noted that D-region chemistry was very complicated, in fact to such a degree that very large computer codes were required to cover all the various reactions. He noted that he was interested to see the success that had apparently been achieved in the use of these codes to predict realistic model electron and ion densities under quiet and disturbed conditions.

Concerning collision frequencies, Jones noted that there was no discussion on which collision frequency models should be employed for numerical calculation by full wave analysis of VLF/LF fields, which was a topic that had received considerable discussion at early symposia. (editors note: c.f. Belrose and Segal [1974]).

He concluded his discussion in the same way he began, that is, he expressed the view that he would have liked to have left the meeting with a better idea on where we should go from here, since he felt that while we have much expertise in the area, we are in danger of lossing it, unless we have a well defined goal to aim for, funding support to carry out the work, so that graduate students can be encouraged to work in this area of research.

The chairman then opened the discussion for comment from the floor. H.J. Albrecht noted that communication began at VLF/LF, some 60-70 years ago, and that AGARD had been concerned with research in this area for 20 years. He noted that researchers had been developing D-region profiles, and that discussions of the C-layer had gone on throughout this period. He too raised the question concerning what actually has been accomplished during the past 20 years? He noted that our knowledge about ground conductivities was still inadequate. He also pointed out that while high precision was desirable, we should not forget that for the systems engineer, a tolerance of about 3dB was satisfactory, in-so-far as predicting field strength.

G. Tacconi noted that the propagation was very variable, and he pointed out the need to characterize the channel in terms of statistical probability. He also wondered about the future of ULF (30-300Hz) communications. P. Bannister noted that a new programme for continuation of the USN's programme Sanguine, code named the Seafarer's Program had been proposed, and that various versions of this programme had been suggested (ranging from $5M to $30M). E.C. Field noted that other research, but at a low level of effort, was going on in USA, in short range ULF communications to stationary deeply submerged platforms. He indicated that the data rates proposed were very low (a bit every 10 minutes), that the requirement was for very short range communications to very great depths.

L. Brock-Nannesiad said that he shared Dr. Jones sentiments. That is he too wondered what the future work should be? He noted that while the various papers presented were probably good state-of-the-art reports, that few of the authors gave an indication on what they felt was needed to increase our knowledge in their own particular areas of expertise. He noted that AGARD is a systems oriented organization, and that it is not only a question of continuing good university research, but in translating that research into the philosophy of systems, which could be used by system designers and by the users.

J.S. Belrose addressed this subject by pointing out, as he had at the outset, that the EPP was concerned with, and had been concerned with propagation limitations to system design, and that while panel symposia emphasized, by and large, propagation aspects, that the panel always tried to have a few papers, typically a whole session on applications, and that this symposium was no exception. However he said we had not heard yet from the systems/application people. He therefore invited comment from these workers.

M.D. Grossi noted that AGARD should not only be concerned with the limitations that the propagation media imposes on the utilization of systems, but also the reverse aspect, which was the challenge to use natural phenomena to the advantage of the system users. He noted that some of the papers were indeed related to this latter aspect, viz. the use of the transverse electric mode for air-to-air communications, and he drew reference to his paper (to be presented) on rocket-and satellite (shuttle) borne ELF antennas. He also noted the extremely important application of SQID technology to ELF/ULF receiver design, which was a topic yet to discussed (in the Applications Session).

R.H. Doherty commented that in his view, with few exceptions, the progress that had been reported at this meeting, over what we had seen in previous meeting could almost singularly be attributed to the progress that had occured in the computer explosion; viz. in the ability of computers to solve problems, and, what the future held was an increasing ability to computerize, optimize and miniaturize equipment. He noted that this was, at least, one clear direction toward which future work should be directed.

Returning to limitations in our knowledge about ground conductivities, E.R. Swanson noted we still don't have a decent global ground conductivity map for use at VLF. He noted that researchers were still employing a map (the DECO ground conductivity map) that had been discounted by its authors years ago. He commented that when we have a detailed knowledge about the propagation of skywaves, then we can perhaps work backwards, and analyse field strength data to deduce a decent map of ground conductivities on a global scale. J.S. Belrose noted that some work had been done in this area by NRL, but probably a fresh out look was needed. He noted that CCIR Study Group V was endeavouring to produce world wide ground conductivity maps; and that Canada was participating in this work, but the maps were derived from MF proof of performance records on file for some eighty broadcast stations with the Department of Communications. H.J. Albrecht noted that our knowledge was particularly inadequate in equatorial regions, where there was a strong dependence on ground humidity.

T.J. Beahn mentioned a different aspect, concerning applications. He noted that the attractive part of VLF/ELF communications was obviously the high reliability for long haul circuits, however, offsetting this was the enormous cost of transmitting stations. He wondered whether any of the authors might speculate on novel ways of generating ELF that would get around the enormous cost and enormous size of ELF stations. M.D. Grossi noted that he would speak to this question in the final session of the symposium, viz the application of satellite-borne ELF antennas. J.S. Belrose commented that this was hardly a money saving alternative, and he noted that while various novel ideas had been proposed (such as island slot antennas, antennas laid out on the polar ice-caps, etc.) none were entirely satisfactory.

C.D. Harwick commented on his particular interests in ELF/ULF on the applications side. He noted the use of ELF signals for anti-submarine detection. He mentioned the work done to detect submarines magnetically, and noted that current technology was almost up to threshold of caesium magnetometers, and that we had exceeded the threshold of SQID magnetometers. He said that those considering transmitting at ULF should take into account present users of the band. He noted that even at VLF interference could be a problem. He reminised on a flight into the artic when severe receiver over load was noted due to a USSR station transmiting on 16.2kHz that suddenly appeaed.

Finally J.B. Reagan, concerning future ELF/VLF research, described an experimental programme related to magnetosphere-ionosphere coupling. The research involves collaboration between the Lockheed Group, particularly W. Imhoff and the University of Iowa Group, particularly Dr. Anderson, and envolves the ISEE satellite. High power USN VLF transmitters will be utilized to excite wave-particle interactions. Resonant interaction can cause changes to the pitch angle for mirroring electrons, resulted in some being precipitated. The process is one of resonance, e.g., a VLF wave travelling in a magnetospheric duct resonates with energetic electrons, mirroring on that field line, such that precipitation occurs on the other end of the field line. The low altitude P70A1 Satellite has been used to measure the electrons that are precipating, and at the same time the ISEE satellite was measuring the wave environment further up along the magnetic field line. The results so far obtained are extremely interesting, and suggestive sharp peaks are detected in the electron spectra, which are attributed to wave particle interaction. New experiments are planned for next year involving the use of a new satellite to be launched, that will carry a very comprehensive set of experiments aimed at providing more detail on the electrons that are precipated due to this wave particle resonant interaction. The VLF transmitters will be modulated with unique codes, and an attempt will be made to find the signatures of these codes in the electron spectra. The experimental programme will also utilize the Stanford University VLF transmitter at Siple in the Anarctic. The new satellite will measure precipitating electrons with 1000 times the sensitivity of previous satellites. It is instrumented to look down at the atmosphere to measure the large scale picture by observing the Bremsstrahlung x-rays over a very wide range as the satellite moves in latitude. The Lockheed Group, Reagan said expect to be able to map the precipitation in his way, as well as by optical photometers in three different wavelengths. The experiment should be in operation in the late spring of 1982, and will operate for a period of nine months. He urged that anyone planning related ground based or rocket experiments should be encouraged to cooperate in these studies, so as to add to our knowledge on this phenomena.

J.S. Belrose closed the discussion. He said he didn't know whether the comments made had satisfied Dr. Jones, and others, who were concerned about the direction of future of work in the area, but he noted that various aspects of propagation, and wave particle interactions had been discussed, and he suggested that when the Conference Proceedings were available, and the various participants, and other interested researchers who couldn't participate in the symposium, had the time to read the papers in detail and digest the comments made during the Round Table Discussions, that he was sure that researchers would continue to study the many facinating aspects of long and very long wave propagation.

# APPENDIX

## LIST OF ATTENDEES

| | |
|---|---|
| AARONS, J. Dr | Senior Scientist, Air Force Geophysics Lab., L.G. Hanscom Field, Bedford, MA 01731, US |
| ALBRECHT, H.J. Dr | FGAN, Konigstr, 2, 5307 Wachtberg-Werthoven, Ge |
| AMUNDROD, L. Mr | N.Skrenten 4 C, 1413 Taarnaasen, No |
| BAIN, W.C. Dr | Upper Atmosphere Group, Rutherford & Appleton Labs., Chilton, Didcot, Oxon OX11 0QX, UK |
| BANNISTER, P.R. Mr | Code 3411, Naval Underwater Systems Center, New London, CT 06320, US |
| BARCLAY, L.W. Mr | Directorate of Radio Technology, Waterloo Bridge House, Waterloo Rd., London SE1 8UA, UK |
| BEAHN, T.J. Dr | Dept. of Defense, Ft. George G. Meade, MD 20755, US |
| BELROSE, J.S. Dr | Communications Research Centre, P.O. Box 11490, Station H, Ottawa K2H 8S2, Ca |
| BERENGER, J.P. I.S.C. Mr | ETCA/CAD, 16 bis Ave., Prieur de la Cote D'Or, 94114 Arcueil Cedex, Fr |
| BLOCH, S. Mr | c/o Standard Elektrik, Lorenz AG, Dept. CS/ERGP1, P.O. Box 40 07 49, D-7000 Stuttgart 40, Ge |
| BLYTHE, J.H. Dr | Marconi Research Laboratories, West Hanningfield Rd., Great Baddow, Chelmsford, Essex CM2 8HN, UK |
| BOITHIAS, L. Mr | CNET, 38 rue du General Leclerc, 92131 Issy-les Moulineaux, Fr |
| BONVALOT, Mr | Thomson CSF (DTC/LCV), 16 rue de Fosse Blanc, BP 156, 92231 Gennevilliers/ Cedex, Fr |
| BOSSY, L. Prof. | Institut Royal Meteorologique, 3 Av. Circulaire, B-1180 Bruxelles, Be |
| BROCK-NANNESTAD, L. Mr | Danish Defence Research Est., P.O. Box 2715, DK-2100 Copenhagen 0, De |
| BULAT, T. Dr Assoc. Prof. | I.U. Yerbilimleri Fakultesi, Jedfizik Muh Bolumu, Vezneciler, Istanbul, Tu |
| BURGESS, B. Dr | RN4-Radio & Navigation Dept., RAE Farnborough, GU14 6TD, UK |
| CHARCOSSET, G. Dr | Laboratoire Physique Hte Atmosphere, Faculte des Sciences, 40 Ave. recteur Pineau, 86022 Poitiers, Fr |
| CHIVERS, J.A.S. Dr | Plessey Electronic Systems Research, Roke Manor, Romsey, Hants, SO5 0ZN, UK |
| COSSA, U. Mr | Aeritalia, Cogro Marche 41, 10146 Torino, It |
| COYNE, V.J. Mr | Chief, Strategic Surveillance Br., Surveillance Div., Rome Air Development Center/ OCS, Griffiss AFB, N.Y. 13441, US |
| CUTOLO, M. Prof. Dr | Universita di Napoli, Istituto de Fisica, Univ. Napoli, Via Monteoliveto 3, 80134 Napoli, It |
| DOHERTY, R.H. Mr | CRPLi, 1898 So. Flatiron Ct., Boulder, CO 80301, US |
| DOMINICI, Prof. | Istituto Nazionale di Geofisica, Via Ruggero, Bonghi 11B, 00184 Roma, It |
| ELLINGSEN, E. Mr | E. Lab., Univ. of Trondheim, N-7034 Trondheim-NTH, No |
| FER, A. Ferit Dr | Electrical Engineering Dept., Middle East Technical University, Ankara, Tu |
| FIELD, E. Jr., Dr | Pacific Sierra Research Group, 1456 Cloverfield Blvd., Santa Monica, CA 90404, US |
| FLOOD, W. Dr | U.S. Army Research Office, Dept. of the Army, P.O. Box 12211, Research Triangle Park, N.C. 27709, US |
| FONTEYNE, J. Mr | TDF, 21 27 rue Barbes, B.P. No.518, 92542 Montrouge, Cedex, Fr |
| GARNIER, M. Prof. | 105 rue Anatole France, 92290 Chatenay Malabry, Fr |
| GEEST, van der P.C. Prof. | Royal Military Academy (KMA), Kasteelplein 10, 4811 XC Breda, Ne |
| GROSSI, M.D. Dr | Submarine Signal Division, Raytheon Company, Portsmouth, RI 02871, US |
| HAGG, E.L. Mr | Communications Research Center, Shirley Bay, P.O. Box 11490, Station H, Ottawa, Ontario K2H 8S2 |

| | |
|---|---|
| HARDWICK, C.D. Mr | Flight Research Laboratory, National Aeronautic Establishment, National Research Council, Ottawa, Ontario K1A OR6, Ca |
| HARTH, W. Mr | Institut fur Radioastronomie, Max Planck Institut, Auf dem Hogel 69, 5300 Bonn 1, Ge |
| HECKLER, R. Mr | Rhode und Schwarz Gmbh, Systemtechnik, 4 FK, ÜB Betriebsfunktechnik, Muhldorfstrasse 15, Munchen 80, Ge |
| HECKLER, R.H. Mr | Rhode u. Schwarz, 4FKH, Muehldorfstr. 15, 8 Muenchen 80, Ge |
| HIZAL, A. Dr | ERA Technology Center, Leatherhead, KT22 75A, Surrey, UK |
| HODARA, H. Dr | Vice President, Tetra Tech Inc., 630 North Rosemead Blvd., Pasadena, CA 99107, US |
| HUBERSON, J.A.R. L/Col. | DRET/SDR Telecommunications, 26 Blvd Victor, 75996 Paris Armees, Fr |
| IASELLI, G.P. Colonel | Ministera della Difesa, TELECOMDIFE, Viale Universita 4, 00100 Roma, It |
| IMHOF, W.L. Dr | Lockheed Palo Alto Research Lab., 3251 Hanover Street, Palo Alto, CA 94304, US |
| INGMANN, P.J. Mr | Radioastronomische Institut, Auf dem Higel 21, D5300 Bonn, Ge |
| JABLONSKI, J.C. Mr | 20 Populieren Laan, 2401 Bruxelles, Be |
| JONES, T.B. Prof. | Dept. of Physics, University of Leicester, Leicester, LE1 7RH, UK |
| KELLY, F.J. Dr | Code 4180.3 Space Science Div., Naval Research Laboratory, Washington, D.C.20735, US |
| KNIGHT, P. Dr | Research Dept., British Broadcasting Corporation, Kingswood Warren, Tadworth, Surrey, KT20 6NP, UK |
| KONG, J.A. Dr | Massachusetts Inst. of Technology, Dept. of Electrical Eng. 36 383, Cambridge, Mass. 02139, US |
| KOSSEY, P.A. Dr | Propagation Branch, Rome Air Development Center, Hanscom Air Force Base, MA 01731, US |
| LAMPERT, E.W. Dr | Siemens AG. K SI FR Fu EF 2 , Postfach 70 00 74, D-8000 Munchen 70, Ge |
| LANGE-HESSE, G.L.F. Dr | Max-Planck Institut fur Aeronomie, Postfach 20, D-3411 Katlenburg, Lindau 3, Ge |
| LIEVIN, J.C. Dr | CP222, Campus Plaine, Universite Libre de Bruxelles, Boulevard du Triomphe, B-1050 Bruxelles, Be |
| MATTHIEUSSENT, G. Mr | Laboratoire Physique des Plasmas, Batiment 212, Universite Paris-Sud, 91405 Orsay, Fr |
| MAYROKOUKOULAKIS, Dr | Technology Research Center KETA, Delta Falirou, Palaion Faliron, Athens, Gr |
| MICHA, Captain | Commandant 22eme Wing Logistique, Quartier Roi Albert I, Rue de la Fusee, 70, B-1130 Bruxelles, Be |
| MINNIS, C.M. Dr | URSI Secretariat, Ave. Albert Lancaster 32, B-1180 Bruxelles, UK |
| MORFITT, D.G. Mr | Code 5324, Naval Ocean Systems Center, San Diego, CA 92152, US |
| PALMER, F.H. Dr | National Defence Headquarters, CRAD/DSP-4, 101 Colonel By Drive, Ottawa, Ontario K1A OK2, Ca |
| PFORR-WEISS, I.J. Mr | Farvandsdirektorat, Overgaden O. Vandet 62, DK 1415, Copenhagen, De |
| PILLET, G.M. Miss | C.N.E.T./DICET, 38 40 rue de General Leclerc, 92131 Issy les Moulineaux, Fr |
| PODEVIN, F. Mr | Societe Aerospatiale, Route de Verneuil, 78130 Les Muneaux, Fr |
| RAWLES, A. Mr | STC, P.O. Box 174, The Hague, Ne |
| REAGAN, J.B. Dr | Lockheed Palo Alto Research Lab., 3251 Hanover treet, Palo Alto, CA 94304, US |
| RIGDEN, C.J. Dr | ASWE, Portsdown, Admiralty Surface Weapons Est., Cosham, Portsmouth, Hants PO6 4AA, UK |
| SCHAEFER, J. Dr | Radio Astronomical Institute, University of Bonn, Auf dem Huegel 71, 5300 Bonn 1, Ge |
| SCHEGGI, A.M. Prof. | IROE-CNR, Via Panciatchi 64, Firenze, It |
| SCHMERLING, E.R. Dr | Chief, Plasma Physics Code ST5, Office of Space Science, NASA Headquarters, Washington, D.C. 20546, US |
| SIZUN, H. Mr | C.N.E.T., Route de Tragestel, B.P. 40, 22301 Lannion, Fr |

SODERBERG, E.F. Mr — Code 3422, Naval Underwater Systems Center, New London, Ct. 06320, US

SOICHER, H. Dr — US Army Communications Research and Development Command, CENCOMS DRDCO-COM-RH-5, Fort Monmouth, N J 07703, US

SPRENKELS, Col. D'Aviation Ir — C.Commandant 22eme Wing Logistique, Quartier Roi Albert I, Rue de la Fusee, 70, B-1130 Bruxelles, Be

STUBBE, P. Mr — Institut fur Aeronomie, Max-Planck Institut, 3411 Katlenberg-Lindau 3, Ge

SWANSON, E.R. Mr — Code 824, Naval Ocean Systems Center, 271 Catalina Blvd., San Diego, CA 92152, US

TAAGHOLT, J. Mr — Danish Scientific Liaison Officer for Greenland, Technical University, Bldg. 349, DK-2800 Lyngby, Denmark, De

TACCONI, G. Dr — Instituto di Electrotecnica, Viale Causa 13, 16145 Genova, Universita di Genova, It

TESCHE, C.D. Dr — LuTech, Inc., P.O. Box 1263, 127 University Ave., Berkeley, CA 94701, US

THRANE, E, Prof. — NDRE, P.O. Box 25  N 2007 Kjeller, No

TIXIER, M. Dr — Laboratoire Physique Hte Atmosphere, Faculte des Sciences, 40 Ave. recteur Pineau, 86022 Poitiers, Fr

TURTLE, J.P. Mr — RADC/EEPL, Rome Air Development Center, Hanscom Air Force Base, MA 01731, US

VORST, Van Der A. Prof. — Universite Catholique de Louvain, Laboratoire de Telecommunications et d'Hyperfrequences, Btmt. Maxwell, B-1130 Bruxelles, Be

# REPORT DOCUMENTATION PAGE

| 1. Recipient's Reference | 2. Originator's Reference | 3. Further Reference | 4. Security Classification of Document |
|---|---|---|---|
| | AGARD-CP-305 | ISBN 92-835-0311-2 | UNCLASSIFIED |

**5. Originator**
Advisory Group for Aerospace Research and Development
North Atlantic Treaty Organization
7 rue Ancelle, 92200 Neuilly sur Seine, France

**6. Title**
MEDIUM, LONG AND VERY LONG WAVE PROPAGATION
(AT FREQUENCIES LESS THAN 3000 kHz)

**7. Presented at**
a Meeting of the Electromagnetic Wave Propagation Panel held in
Brussels, Belgium, 21–25 September, 1981.

| 8. Author(s)/Editor(s) | 9. Date |
|---|---|
| Edited by Dr J.S.Belrose | February 1982 |

| 10. Author's/Editor's Address | 11. Pages |
|---|---|
| Communications Research Centre Dept. of Communications, P.O.Box 11490, Station H Ottawa K2H 8S2, Canada | 544 |

**12. Distribution Statement**
This document is distributed in accordance with AGARD
policies and regulations, which are outlined on the
Outside Back Covers of all AGARD publications.

**13. Keywords/Descriptors**

| | |
|---|---|
| Electromagnetic wave transmission | Very low frequencies |
| Medium frequencies | Extremely low radio frequencies |
| Low frequencies | Radio communication |

**14. Abstract**

These Proceedings include the papers and discussions presented at the AGARD Electromagnetic Wave Propagation Panel Symposium on "Medium, Long and Very Long Wave Propagation (at Frequencies less than 3000 kHz)" held in Brussels, Belgium in September 1981.

The Meeting reviewed propagation information at ELF and VLF frequencies. It was intended to summarize the current state of knowledge in this frequency band in the areas of propagation, antennas, and radio communications technology, with speculation on trends and future use.

There were 37 papers presented, 9 on the propagation medium, 4 on ELF propagation, 6 on VLF propagation, 4 on LF propagation, 4 on MF propagation, 3 on numerical modelling of the propagation medium, and 7 on applications.

| | |
|---|---|
| AGARD Conference Proceedings No.305<br>Advisory Group for Aerospace Research and Development, NATO<br>MEDIUM, LONG AND VERY LONG WAVE PROPAGATION (AT FREQUENCIES LESS THAN 3000 kHZ)<br>Edited by Dr J.S.Belrose<br>Published February 1982<br>544 pages<br><br>These Proceedings include the papers and discussions presented at the AGARD Electromagnetic Wave Propagation Panel Symposium on "Medium, Long and Very Long Wave Propagation (at Frequencies less than 3000 kHz)" held in Brussels, Belgium in September 1981.<br><br>P.T.O. | AGARD-CP-305<br><br>Electromagnetic wave transmission<br>Medium frequencies<br>Low frequencies<br>Very low frequencies<br>Extremely low radio frequencies<br>Radio communication |
| AGARD Conference Proceedings No.305<br>Advisory Group for Aerospace Research and Development, NATO<br>MEDIUM, LONG AND VERY LONG WAVE PROPAGATION (AT FREQUENCIES LESS THAN 3000 kHZ)<br>Edited by Dr J.S.Belrose<br>Published February 1982<br>544 pages<br><br>These Proceedings include the papers and discussions presented at the AGARD Electromagnetic Wave Propagation Panel Symposium on "Medium, Long and Very Long Wave Propagation (at Frequencies less than 3000 kHz)" held in Brussels, Belgium in September 1981.<br><br>P.T.O. | AGARD-CP-305<br><br>Electromagnetic wave transmission<br>Medium frequencies<br>Low frequencies<br>Very low frequencies<br>Extremely low radio frequencies<br>Radio communication |
| AGARD Conference Proceedings No.305<br>Advisory Group for Aerospace Research and Development, NATO<br>MEDIUM, LONG AND VERY LONG WAVE PROPAGATION (AT FREQUENCIES LESS THAN 3000 kHZ)<br>Edited by Dr J.S.Belrose<br>Published February 1982<br>544 pages<br><br>These Proceedings include the papers and discussions presented at the AGARD Electromagnetic Wave Propagation Panel Symposium on "Medium, Long and Very Long Wave Propagation (at Frequencies less than 3000 kHz)" held in Brussels, Belgium in September 1981.<br><br>P.T.O. | AGARD-CP-305<br><br>Electromagnetic wave transmission<br>Medium frequencies<br>Low frequencies<br>Very low frequencies<br>Extremely low radio frequencies<br>Radio communication |
| AGARD Conference Proceedings No.305<br>Advisory Group for Aerospace Research and Development, NATO<br>MEDIUM, LONG AND VERY LONG WAVE PROPAGATION (AT FREQUENCIES LESS THAN 3000 kHZ)<br>Edited by Dr J.S.Belrose<br>Published February 1982<br>544 pages<br><br>These Proceedings include the papers and discussions presented at the AGARD Electromagnetic Wave Propagation Panel Symposium on "Medium, Long and Very Long Wave Propagation (at Frequencies less than 3000 kHz)" held in Brussels, Belgium in September 1981.<br><br>P.T.O. | AGARD-CP-305<br><br>Electromagnetic wave transmission<br>Medium frequencies<br>Low frequencies<br>Very low frequencies<br>Extremely low radio frequencies<br>Radio communication |

| | |
|---|---|
| The Meeting reviewed propagation information at ELF and VLF frequencies. It was intended to summarize the current state of knowledge in this frequency band in the areas of propagation, antennas, and radio communications technology, with speculation on trends and future use.<br><br>There were 37 papers presented, 9 on the propagation medium, 4 on ELF propagation, 6 on VLF propagation, 4 on LF propagation, 4 on MF propagation, 3 on numerical modelling of the propagation medium, and 7 on applications.<br><br>Papers and discussions presented at a Meeting of the Electromagnetic Wave Propagation Panel held in Brussels, Belgium, 21–25 September, 1981.<br><br><br>ISBN 92-835-0311-2 | The Meeting reviewed propagation information at ELF and VLF frequencies. It was intended to summarize the current state of knowledge in this frequency band in the areas of propagation, antennas, and radio communications technology, with speculation on trends and future use.<br><br>There were 37 papers presented, 9 on the propagation medium, 4 on ELF propagation, 6 on VLF propagation, 4 on LF propagation, 4 on MF propagation, 3 on numerical modelling of the propagation medium, and 7 on applications.<br><br>Papers and discussions presented at a Meeting of the Electromagnetic Wave Propagation Panel held in Brussels, Belgium, 21–25 September, 1981.<br><br><br>ISBN 92-835-0311-2 |
| The Meeting reviewed propagation information at ELF and VLF frequencies. It was intended to summarize the current state of knowledge in this frequency band in the areas of propagation, antennas, and radio communications technology, with speculation on trends and future use.<br><br>There were 37 papers presented, 9 on the propagation medium, 4 on ELF propagation, 6 on VLF propagation, 4 on LF propagation, 4 on MF propagation, 3 on numerical modelling of the propagation medium, and 7 on applications.<br><br>Papers and discussions presented at a Meeting of the Electromagnetic Wave Propagation Panel held in Brussels, Belgium, 21–25 September, 1981.<br><br><br>ISBN 92-835-0311-2 | The Meeting reviewed propagation information at ELF and VLF frequencies. It was intended to summarize the current state of knowledge in this frequency band in the areas of propagation, antennas, and radio communications technology, with speculation on trends and future use.<br><br>There were 37 papers presented, 9 on the propagation medium, 4 on ELF propagation, 6 on VLF propagation, 4 on LF propagation, 4 on MF propagation, 3 on numerical modelling of the propagation medium, and 7 on applications.<br><br>Papers and discussions presented at a Meeting of the Electromagnetic Wave Propagation Panel held in Brussels, Belgium, 21–25 September, 1981.<br><br><br>ISBN 92-835-0311-2 |

# AGARD

## NATO ⊕ OTAN

7 RUE ANCELLE · 92200 NEUILLY-SUR-SEINE

FRANCE

Telephone 745.08.10 · Telex 610176

## DISTRIBUTION OF UNCLASSIFIED
## AGARD PUBLICATIONS

AGARD does NOT hold stocks of AGARD publications at the above address for general distribution. Initial distribution of AGARD publications is made to AGARD Member Nations through the following National Distribution Centres. Further copies are sometimes available from these Centres, but if not may be purchased in Microfiche or Photocopy form from the Purchase Agencies listed below.

## NATIONAL DISTRIBUTION CENTRES

**BELGIUM**
Coordonnateur AGARD VSL
Etat-Major de la Force Aérienne
Quartier Reine Elisabeth
Rue d'Evere, 1140 Bruxelles

**CANADA**
Defence Science Information Services
Department of National Defence
Ottawa, Ontario K1A OK2

**DENMARK**
Danish Defence Research Board
Østerbrogades Kaserne
Copenhagen Ø

**FRANCE**
O.N.E.R.A. (Direction)
29 Avenue de la Division Leclerc
92320 Châtillon sous Bagneux

**GERMANY**
Fachinformationszentrum Energie,
Physik, Mathematik GmbH
Kernforschungszentrum
D-7514 Eggenstein-Leopoldshafen 2

**GREECE**
Hellenic Air Force General Staff
Research and Development Directorate
Holargos, Athens

**ICELAND**
Director of Aviation
c/o Flugrad
Reykjavik

**ITALY**
Aeronautica Militare
Ufficio del Delegato Nazionale all'AGARD
3, Piazzale Adenauer
Roma/EUR

**LUXEMBOURG**
See Belgium

**NETHERLANDS**
Netherlands Delegation to AGARD
National Aerospace Laboratory, NLR
P.O. Box 126
2600 A.C. Delft

**NORWAY**
Norwegian Defence Research Establishment
Main Library
P.O. Box 25
N-2007 Kjeller

**PORTUGAL**
Direcção do Serviço de Material
da Forca Aerea
Rua da Escola Politécnica 42
Lisboa
Attn: AGARD National Delegate

**TURKEY**
Department of Research and Development (ARGE)
Ministry of National Defence, Ankara

**UNITED KINGDOM**
Defence Research Information Centre
Station Square House
St. Mary Cray
Orpington, Kent BR5 3RE

**UNITED STATES**
National Aeronautics and Space Administration (NASA)
Langley Field, Virginia 23365
Attn: Report Distribution and Storage Unit

THE UNITED STATES NATIONAL DISTRIBUTION CENTRE (NASA) DOES NOT HOLD
STOCKS OF AGARD PUBLICATIONS, AND APPLICATIONS FOR COPIES SHOULD BE MADE
DIRECT TO THE NATIONAL TECHNICAL INFORMATION SERVICE (NTIS) AT THE ADDRESS BELOW.

## PURCHASE AGENCIES

| *Microfiche or Photocopy* | *Microfiche* | *Microfiche or Photocopy* |
|---|---|---|
| National Technical Information Service (NTIS) 5285 Port Royal Road Springfield Virginia 22161, USA | Space Documentation Service European Space Agency 10, rue Mario Nikis 75015 Paris, France | British Library Lending Division Boston Spa, Wetherby West Yorkshire LS23 7BQ England |

Requests for microfiche or photocopies of AGARD documents should include the AGARD serial number, title, author or editor, and publication date. Requests to NTIS should include the NASA accession report number. Full bibliographical references and abstracts of AGARD publications are given in the following journals:

Scientific and Technical Aerospace Reports (STAR)
published by NASA Scientific and Technical
Information Facility
Post Office Box 8757
Baltimore/Washington International Airport
Maryland 21240, USA

Government Reports Announcements (GRA)
published by the National Technical
Information Services, Springfield
Virginia 22161, USA